Mantle Xenoliths from the Marsabit Volcanic Field: A Case Study on the Evolution of the Lithospheric Mantle in a Continental Rift Environment

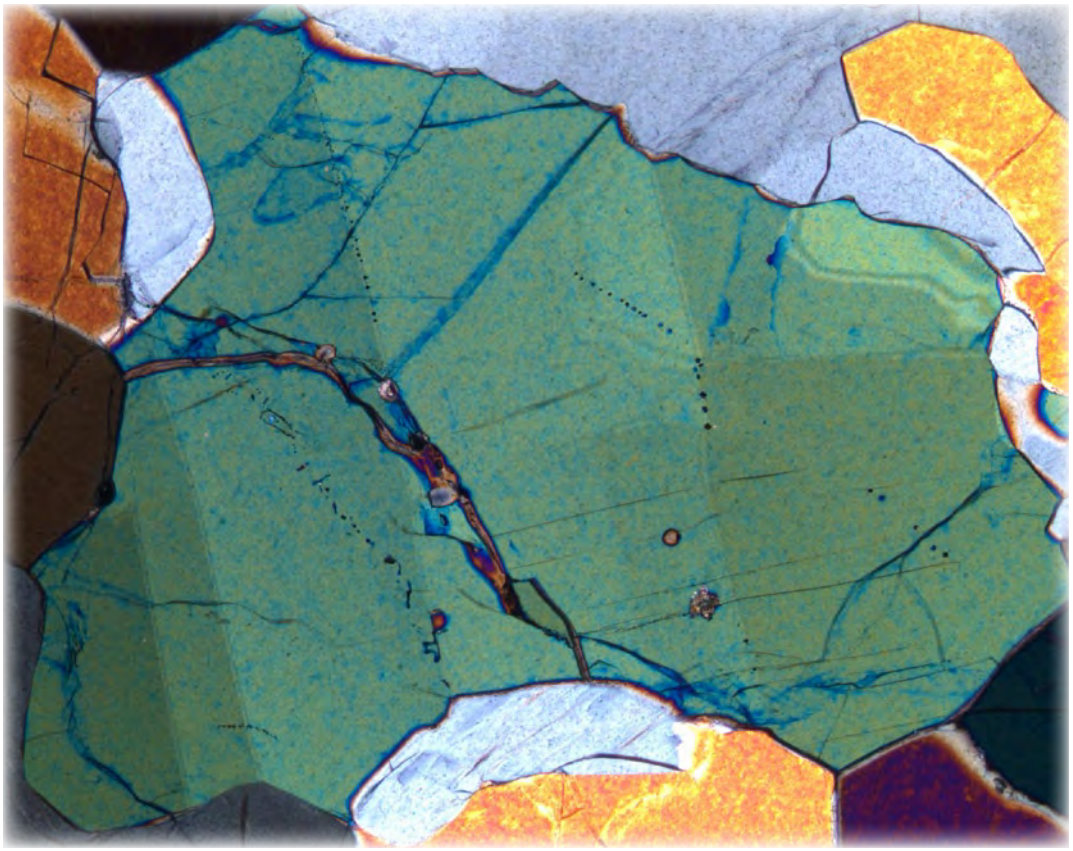
Thèse présentée à la Faculté des Sciences
Institut de Géologie et d'Hydrogéologie
Université de Neuchâtel

pour l'obtention du grade de docteur és sciences

par

Benjamin Kaeser

- Soutenue le 30 novembre 2006 -



Acceptée sur la proposition du jury:

Prof. Angelika Kalt (Neuchâtel; directrice de thèse)
Prof. Rainer Altherr (Heidelberg, DE)
Prof. Dmitri A. Ionov (Saint-Etienne, FR)
Prof. Othmar Müntener (Lausanne, CH)
Prof. Alan B. Woodland (Frankfurt, DE)

Université de Neuchâtel

für Silvia

cover illustration: olivine with inclusion trails concentrated on kink-bands - Group II (grt)-spl lherzolite from Marsabit

Université de Neuchâtel

FACULTE DES SCIENCES
Secrétariat-Décanat de la faculté
- Rue Emile-Argand 11
- CP 158
- CH-2009 Neuchâtel

IMPRIMATUR POUR LA THESE

Mantle Xenoliths from the Marsabit Volcanic Field: A Case Study on the Evolution of the Lithospheric Mantle in a Continental Rift Environment

Benjamin KAESER

UNIVERSITE DE NEUCHATEL

FACULTE DES SCIENCES

La Faculté des sciences de l'Université de Neuchâtel,
sur le rapport des membres du jury

Mme A. Kalt (directrice de thèse),
MM. O. Müntener (Lausanne), A. Woodland (Frankfurt D),
R. Altherr (Heidelberg D) et D. Ionov (St-Etienne F)

autorise l'impression de la présente thèse.

Neuchâtel, le 11 janvier 2007

Le doyen :
J.-P. Derendinger

UNIVERSITE DE NEUCHATEL
FACULTE DES SCIENCES
Secrétariat-décanat de la faculté
Rue Emile-Argand 11 - CP 158
CH-2009 Neuchâtel

■ Téléphone : +41 32 718 21 00 ■ Fax : +41 32 718 21 03 ■ E-mail : secretariat.sciences@unine.ch ■ www.unine.ch/sciences

TABLE OF CONTENTS

I IMPRIMATUR
III TABLE OF CONTENTS
VI ABSTRACT
VIII ACKNOWLEDGMENTS / REMERCIEMENTS / DANKSAGUNG

1 **CHAPTER 1:** Introduction, Geological Setting, Aims and Organisation of the Study

2 INTRODUCTION
2 GEOLOGICAL AND TECTONIC SETTING
2 Geography and surface topography of the EARS
5 Geology of the EARS and its basement
7 Continental rifting events in Africa
9 Volcanism and the 'mantle plume' issue
11 Previous studies on mantle xenoliths from the EARS
14 THE IMPORTANCE OF MARSABIT
15 AIMS AND ORGANISATION OF THE STUDY

17 **CHAPTER 2:** Evolution of the Lithospheric Mantle beneath the Marsabit Volcanic Field (Northern Kenya): Constraints from Textural, P-T and Geochemical Studies on Xenoliths

18 INTRODUCTION
20 ANALYTICAL METHODS
21 SAMPLE SELECTION AND MACROSCOPIC CHARACTERISTICS
22 XENOLITH PETROGRAPHY
25 COMPOSITION OF MINERALS
39 SYNTHETIC SUMMARY OF TEXTURES AND MINERAL COMPOSITIONS
41 THERMOBAROMETRY
48 GEOCHEMICAL AND TEXTURAL EVOLUTION OF THE LITHOSPHERIC MANTLE BENEATH MARSABIT
53 GEODYNAMIC IMPLICATIONS
54 ACKNOWLEDGMENTS

55 **CHAPTER 3:** Crystallisation and Breakdown of Metasomatic Phases in Graphite-bearing Peridotite Xenoliths from Marsabit (Kenya)

56 **INTRODUCTION**
56 **SAMPLE CONTEXT**
58 **ANALYTICAL METHODS**
59 **PETROGRAPHY**
63 **MINERAL COMPOSITION**
74 **DISCUSSION**
74 **Formation of the early assemblages**
80 **The nature of the metasomatising agent(s)**
83 **The origin of the metasomatising melts**
84 **Late assemblages – metasomatic mechanisms**
88 **Time constraints**
88 **SUMMARY & CONCLUSIONS**
90 **ACKNOWLEDGMENTS**

91 **CHAPTER 4:** Li, Be and B Abundances in Minerals of Peridotite Xenoliths from Marsabit (Kenya): Disequilibrium Processes and Implications for Subduction Zone Signatures

92 **INTRODUCTION**
92 **GEODYNAMIC CONTEXT**
94 **MINERALOGICAL AND GEOCHEMICAL CHARACTERISTICS OF THE SAMPLES**
97 **Li, Be AND B ABUNDANCES IN MINERALS**
104 **INTER-MINERAL AND MINERAL/MELT PARTITIONING OF Li, Be AND B: DEGREE OF (DIS)EQUILIBRIUM**
109 **CAUSES FOR DISEQUILIBRIUM: LATE-STAGE DIFFUSION AND REACTION**
113 **THE NATURE OF EARLY METASOMATISM BENEATH MARSABIT AS DEDUCED FROM CLASSICAL AND LIGHT ELEMENT DATA**
119 **SUMMARY AND CONCLUSIONS**
119 **ACKNOWLEDGMENTS**

121 **CHAPTER 5:** Mafic Xenoliths from Marsabit (Northern Kenya): Evidence for Multiple Magmatic Events in the Lithospheric Mantle and Interaction between Perdotite

122 ***PREFACE***
122 **INTRODUCTION**
123 **PETROGRAPHY**
125 **Group V – garnet websterites**
128 **Group VI – grt-free pyroxenites**
129 **COMPOSITION OF MINERALS**
143 **CALCULATED BULK ROCK COMPOSITIONS**
144 **DISCUSSION I: ORIGIN AND EVOLUTION OF THE GRT WEBSTERITES**
156 **DISCUSSION II: ORIGIN AND EVOLUTION OF THE GRT-FREE PYROXENITES**
158 **SUMMARY**

161 **CHAPTER 6:** An Analcime-bearing Olivine Gabbro Xenolith from Marsabit (northern Kenya): Evidence for Alkalic Crustal Intrusions?

162 **INTRODUCTION**
162 **TEXTURES**
162 **MINERAL COMPOSITION**
165 **GROUP VI GABBRO – CRYSTALLISED, SLIGHTLY EVLOVED ALKALIC MELT**

167 **CHAPTER 7:** Summary, Conclusions and Outlook

175 **CHAPTER 8:** Analytical Methods

181 **CITED REFERENCES**

APPENDICES (additional 187 pp.)

ABSTRACT

***Mots clés**: manteau lithospherique, xénolithes mantelliques, péridotite, pyroxénite, géochimie* in-situ*, magmatisme alkaline, métasomatose; éléments en traces, LA-ICPMS, SIMS, rift Est Africain, graben de Anza, Kenya, Marsabit*

***Keywords:** lithospheric mantle, mantle xenoliths, peridotite, pyroxenite, alkaline magmatism,* in-situ *geochemistry, metasomatism, trace elements, LA-ICPMS, SIMS, East African rift, Anza Graben, Kenya, Marsabit*

Mantle xenoliths, rock fragments sampled by magmas during their ascent from depth to the surface, provide direct information on the nature and composition of the Earth's mantle. This thesis is the result of a petrographic, geochemical and petrological case study on mantle xenoliths hosted by Quaternary basanitic and alkali basaltic scoriae of the Marsabit volcanic field (northern Kenya). Magmatic activity is related to the development of the East African rift system. Results from previous seismic, geological and petrological studies show that continental rifting in East Africa is strongly controlled by pre-existing structures in the lithosphere. Further, the nature of the lithosphere has been shown to play a crucial role for the locus and composition of volcanic rocks, as magmas partly derive from, or at least interacted with the lithospheric mantle. The xenoliths from Marsabit provide a direct window in the mantle and allow constraining the nature of the East African Rift lithosphere.

The xenoliths comprise several groups of ultramafic (peridotite) and mafic (pyroxenite and gabbro) rocks. Peridotite includes porphyroclastic or statically recrystallised, formerly garnet-bearing lherzolite (Group I and II, respectively), porphyroclastic spinel harzburgite and dunite (Group III) and mylonitic spl harzburgite and lherzolite (Group IV). Mafic rocks comprise garnet-bearing and garnet-free pyroxenite (Group V and VI, respectively) and gabbro (Group VII).

The integration of textural and compositional data, together with results from thermobarometry and evaluation of mineral zoning indicate a complex evolution of the lithospheric mantle. The possibly oldest features are preserved in the formerly garnet-bearing lherzolites (Group I and II) and in the garnet pyroxenites. These rocks provide evidence of an earlier high-pressure / high temperature stage (~970-1100°C at depths around 60-90 km), similar to non-rifted sub-continental lithospheric mantle such as actually present underneath southern Kenya. This stage most likely corresponds to the lithospheric conditions prior to continental rifting which started during Mesozoic times with the formation of the Anza Graben (an older rift perpendicular to the present-day East African rift). The garnet pyroxenites formed prior to rifting as well. It is suggested that the garnet pyroxenites represent the products of high-pressure crystallisation of opx-saturated melts, possibly formed during Pan-African (Neoproterozoic-Paleozoic) orogenesis. Crustal rocks issued from this time period make up most of the present-day crystalline basement of the Marsabit area.

All peridotite types, as well as the garnet pyroxenites were subjected to later cooling, decompression and pervasive deformation (to very low mantle *P-T* conditions of ~700-800°C at depths ~30-40 km). These features are best explained by continental rifting during Mesozoic-Paleogene times that led to the formation of the Anza Graben.

Subsequently magmatism and metasomatism related to the development of the Tertiary-Quaternary East African rift obliterated features related to Mesozoic-Paleogene rifting. Evidence

for this comes, for example, from the statically recrystallised lherzolites, where textural annealing is associated with a young heating event (up to 1100°C). Heating was accompanied by cryptic metasomatism (i.e., enrichment of clinopyroxene in Fe-Ti and incompatible trace elements). The metasomatising melts were compositionally similar (and possibly genetically related) to the Quaternary basanites erupted at the surface of Marsabit. Probably in the same period, garnet-free pyroxenites (Group VI xenoliths) crystallised from alkaline melts, presumably in dykes within the shallow mantle or at the mantle-crust boundary (between ~30-60 km depths). Also these alkaline melts were most likely related to the lavas erupted at the surface.

Further evidence for Tertiary-Quaternary metasomatism can be found in the porphyroclastic Group III peridotite xenoliths (Group III), which show a textural transition from virtually non-metasomatised spl harzburgite to modally metasomatised amphibole dunite. The latter contain rather unusual mantle minerals such as apatite, graphite, Na-rich phlogopite and katophorite (amphibole). The phase assemblage, as well as major and trace element characteristics indicate that this type of metasomatism resulted from the infiltration of volatile (H_2O, CO_2)-rich silicic melt and/or fluid in a pre-existing heterogeneous and probably reduced mantle. Such melts may have evolved from previous melt-rock reaction processes. In a very late stage (i.e., shortly before the xenoliths were transported to the surface in their host magma), the metasomatic minerals partially melted. This led to the formation of patches consisting of newly formed minerals (microlites) and glass (quenched melt).

The metasomatised harzburgites and dunites are further strongly enriched in the low-atomic mass elements (light elements) Lithium, Beryllium and Boron. Therefore, these elements were investigated with special emphasis. The light elements are now widely used to trace recycled components in mantle and volcanic rocks in subduction zone settings. In the case of Marsabit, the light element systematics could potentially be interpreted as reflecting such components in the mantle, added by ancient, pre-rift subduction events. The detailed investigation of Li, Be and B systematics in minerals from the Marsabit xenoliths, however, clearly points to young disequilibrium features and to modification of light element budgets during very late-stage melting events (i.e. the formation of melt pockets). These results highlight that the application of light element systematics to trace subduction-related components is not un-problematic. This applies in particular to xenoliths where a careful quantification of late-stage metasomatic events with respect to the light elements is necessary.

ACKNOWLEDGMENTS / REMERCIEMENTS / DANKSAGUNG

Meine Dissertation gab mir die Möglichkeit an einem einem begeisternden, aktuellen ‚state-of-the-art' Forschungsprojekt beizutragen. Nebst dem Projekt für sich war jedoch auch (und vor Allem) das Umfeld in Neuchâtel, die Aufenthalte an anderen Instituten und die Teilnahme an zahlreichen Tagungen und Exkursionen Grund, dass die vergangenen vier Jahre eine äusserst ausgefüllte und erfüllende Zeit war. Für die Früchte dieser Arbeit bin ich vielen Leuten zu Dank verpflichtet:

Als erstes möchte ich mich bei meiner Referentin und Betreuerin **Angelika Kalt** bedanken. Sie hat mir den Marsabit-Teil des Kenya Projekts anvertraut und mir so die ersten Einblicke in die faszinierende Welt der Xenolithe und der Mantelpetrologie ermöglicht. Das entgegengebrachte Vertrauen, die mir gelassenen Freiheiten und das stetige Interesse am Fortschritt meiner Arbeit waren sehr wertvoll für mich. Angelika hatte immer ein offenes Ohr für Diskussionen und zahlreiche Gespräche, auch in Momenten zeitintensiver administrativer Arbeiten die am Institut immer wieder anfielen.

Auch bei **Rainer Altherr** möchte ich mich bedanken. Er hat zusammen mit Angelika Kalt das Kenya Projekt auf die Beine gestellt und mir die Marsabit Xenolithe zur Verfügung gestellt. Während meinen Aufenthalten in Heidelberg hatte er zudem immer Zeit und Interesse über den Fortschritt meiner Arbeit zu erfahren.

Ganz im Speziellen will ich mich bei **Othmar Müntener** bedanken. Zahlreichen Diskussionsstunden und etliche Exkursionen zusammen mit ihm verdanke ich einen grossen Teil meines Petrologieverständnisses und bewahrten mich auch davor – als Xenolith-Forscher – den Blick für die grösseren Zusammenhänge der Mantelgeologie zu verlieren.

Un grand merci aussi à **Erwan Bourdon**, pour des heures de discussions non seulement scientifiques mais aussi sur des sujets moins sérieux (et surtout pour l'introduction à certaines spécialités culinaires bretonnes).

Further, I would like to thank **Arjan Dijkstra**: for improving my English style in lots of manuscripts and research proposals, for many discussions (especially on structural features in mantle rocks, which geochemists may sometimes neglect), and for accompanying me during our two-day journey to Montpellier.

Thomas Pettke führte erstklassige LA-ICPMS Messungen durch und hat mir die Möglichkeiten dieser Methode (inklusive der leicht ermüdenden Datenauswertung...) aufgezeigt. Für die jeweils sehr angenehmen Messtage and der ETH Zürich und Diskussionen (nicht nur über Geologie und Spurenelemente) möchte ich mich herzlich bedanken.

Edwin Gnos war immer bereit um Fragen und Probleme bei der Elektronenmikrosonden-Analytik in Bern zu lösen. Auch für so manches interessante Gespräch über Mineralogie und Mikrosonden-Analytik möchte ich mich hier bedanken. Nebst Edwin waren auch **Tom Burri**, **Alfons Berger** und **Ulli Linden** immer für Pannenhilfe an der Mikrosonde bereit.

Mehrere Wochen konnte ich zudem am mineralogischen Institut in Heidelberg verbringen. Unter der Anleitung von **Thomas Ludwig** konnte ich die Technik der Sekundärionen Massenspektrometrie lernen. Thomas war zudem ständig abrufbereit wenn Probleme bei den Messungen auftraten. **Hans-Peter Meyer** hat während zwei Messsessionen in Heidelberg eine jeweils perfekt kalibrierte Elektronenmikrosonde zur Verfügung gestellt. **Ilona Fin** und **Oliver Wienand** (Heidelberg) haben zudem Hochqualitäts-Dünnschliffe für die SIMS Analytik hergestellt.

Für den stets netten Empfang in Heidelberg und die Diskussionen während den Mittagspausen möchte ich mich zudem bei der ganzen Heidelberger-Gruppe bedanken. Dies sind zusätzlich zu den oben genannten: **Melanie Kaliwoda, Angela Helbling, Iris Sonntag, Horst Marschall, Stefan Prowatke, Stephan Klemme, Thomas Zack und Jens Hopp.**

Merci aussi à **André Villard**, qui a produit plus d'une centaine de lames minces pétrographiques, ainsi que des lames polies de haute qualité (et toujours dans les délais) pour les mesures de microsonde électronique, LA-ICPMS ou MEB.

Les analyses MEB ont été effectuées dans l'excellent laboratoire à l'Institut de Microtéchnique à Neuchâtel sous la responsabilité de **Dr Massoud Dadras**.

Ein Dankeschön auch an **Christoph Neururer**, für die Einführung und Hilfe an dem Elektronenmikroskop in Fribourg.

J'aimerais aussi remercier **Prof. Jean-Louis Bodinier** et **Dr. Marguerite Godard** pour leur accueil chaleureux à Montpellier lors de l'introduction des 'plate-models' et les discussions sur les processus métasomatiques dans le manteau.

Ensuite j'aimerais mentionner tous les gens à l'institut de Neuchâtel qui ont contribué à une atmosphère de travail superbe. En particulière, j'aimerais remercier:

Laure Pelletier, ma collègue de bureau, pour une atmosphère de travail toujours 'bon-enfant' et pour toute sorte de discussion sur tous les petits et grands soucis de la vie doctorant.

Alexey Ulianov, mon collègue de travail sur le projet de Kenya, qui m'a beaucoup soutenu au début de mon travail à la microsonde électronique, au MEB, ainsi que en m'introduisant avec enthousiasme dans la pétrologie des roches alcalines.

Tout mes autres copines et copains doctorant-es et maître assistant-es pour les moments merveilleux à Neuchâtel (les apéro, les grillades, les 'bêtes mortes', les 'six packs', et le reste moins culinaire): **Mary-Alix, Virginie, Cécile, Séverine, Christina, Laure et Laure, Melody, Flurin, Stéphane, Alex, Charles, Stéphane 'double-V', Nico, Erwan, Laurent, Haydon, Pascal et Raul**.

Elisabeth Kuster, notre bibliothécaire, qui a toujours été disponible pour toute sorte de commandes pour des 'bouquins' et des articles dans le monde.

Sabine Erb et **Gianfranca Cerrito**, nos secrétaires, toujours là pour écouter nos petits soucis!

et, bien sur, tout le corps professoral, les étudiants et le reste de la communauté à Neuchâtel!

Und, zu guter Letzt, meiner Familie

Silvia, sowie meinen Eltern und meiner Schwester, für die Unterstützung in den letzten 4 Jahren (auch dass ich der Steine wegen nicht die Sicht für die anderen Dinge im Leben verlor) und für den Rückhalt während der letzten 27 Jahren.

This research was supported by the Swiss National Science Foundation (SNF) grant 200021-100647/1. Finanancial support from the SNF (grants 21-26579.89 and 200021-103479/1) for the electron microprobe facility at the Institute of Geological Sciences, University of Bern is acknowledged. Field work in Kenya was financially supported by the Deutsche Forschungsgemeinschaft within the frame of the Collaborative Research Centre 108 (RFB 108) at the University of Karlsruhe.

Chapter 1:

Introduction, Geological Setting, Aims and Organisation of the Study

INTRODUCTION

Information on the structure and composition of the mantle – the Earth's most voluminous part – is mainly based on indirect observation obtained, for example, from seismic investigation or from the interpretation of mantle-derived volcanic rocks. Alternatively, though spatially restricted, direct information can be obtained by studying mantle rocks exposed at the surface. These are either relatively large (km-sized) rock bodies transported to the surface by tectonic processes (e.g., orogenic peridotites, ophiolites or oceanic mantle exhumed on ocean floors), or nodules of mantle rocks (mantle xenoliths, typically cm to 10 cm-sized) sampled by magmas during their ascent to the surface.

Due to their rapid transport to the surface, most xenoliths record the thermal, structural and compositional state of the mantle at the time of sampling by the host magma. Although being disrupted from their structural context, xenoliths thus provide an important tool to quantify mantle conditions beneath regions of volcanic and tectonic activity such as continental rifts.

This is a part of a petrological project on xenoliths related to the Kenya rift international seismic project (KRISP) in the 1990's. The goal of this project is to constrain the thermal, chemical and structural state of the East African lithosphere at different stages of continental rifting. It focuses on the Kenya rift as a part of the East African Rift System (EARS; Fig. 1.1). Complementary to the indirect results from KRISP (e.g., Achauer *et al.*, 1994; Prodehl *et al.*, 1994; Fuchs *et al.*, 1997), the investigation of mantle-derived xenoliths allows to gain first-hand information on the composition and nature of the mantle underlying the EARS. Previous xenolith studies had concentrated mainly on localities in Tanzania, where the rift is actually at the initial stage of its development, or in Ethiopia, where rifting is advanced and already grades into continental-oceanic rift transition. The transition between the beginning (Tanzania) and advanced (Ethiopia) stages of rifting is (broadly) found in Kenya and was largely unexplored before beginning of KRISP.

For the purpose of closing this gap, mantle and crustal xenolith suites from several young (Tertiary-Quaternary) volcanic fields along the Kenya rift were investigated in the framework of the KRISP-related petrological project initiated by Prof. Rainer Altherr (Heidelberg) and Prof. Angelika Kalt (Neuchâtel). The study areas include xenoliths localities from the Chyulu Hills (southern Kenya), Merille, Kulal, and Marsabit in northern Kenya (Fig. 1.2). The present study focuses on ultramafic and mafic xenoliths from the Marsabit volcanic field.

GEOLOGICAL AND TECTONIC SETTING

In the following sections, a detailed description of the topography, geology and geodynamics of East Africa and the EARS is given. This includes an extensive list of references to important geophysical, structural, geological and petrological studies. They all contributed to the fact that the EARS is one of the best studied continental rifts in the world and a classical site for investigating rift tectonics and continental volcanism since pioneering work undertaken more than 100 years ago (e.g., Gregory, 1886, 1921).

Geography and surface topography of the EARS

East Africa is characterised by important topographic variation including two large-scale high elevation plateaus – the East African plateau in the south and the Afar plateau in the north (Fig. 1.1). The EARS partly cross-cuts and contours these plateaus. It extends from the Red Sea – Afar – Gulf of Aden triple junction in the north, to the Lake Malawi in the south (Fig. 1.1). In the southern part, it broadly follows the margin of the East African plateau by splitting into a western and and eastern rift branch (Fig. 1.1). The eastern branch can be further subdivided into the Main Ethiopian rift (MER; Fig.

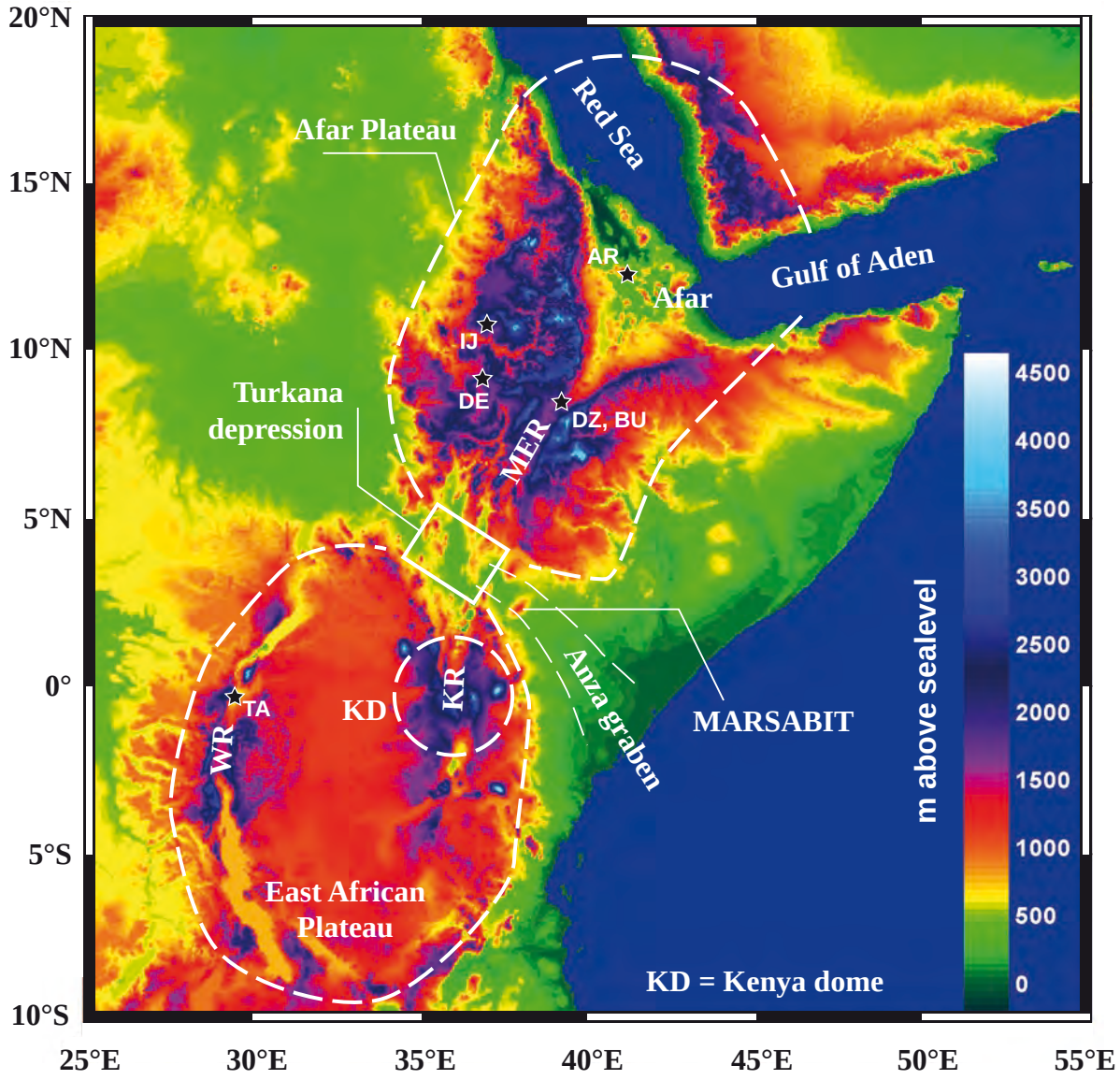
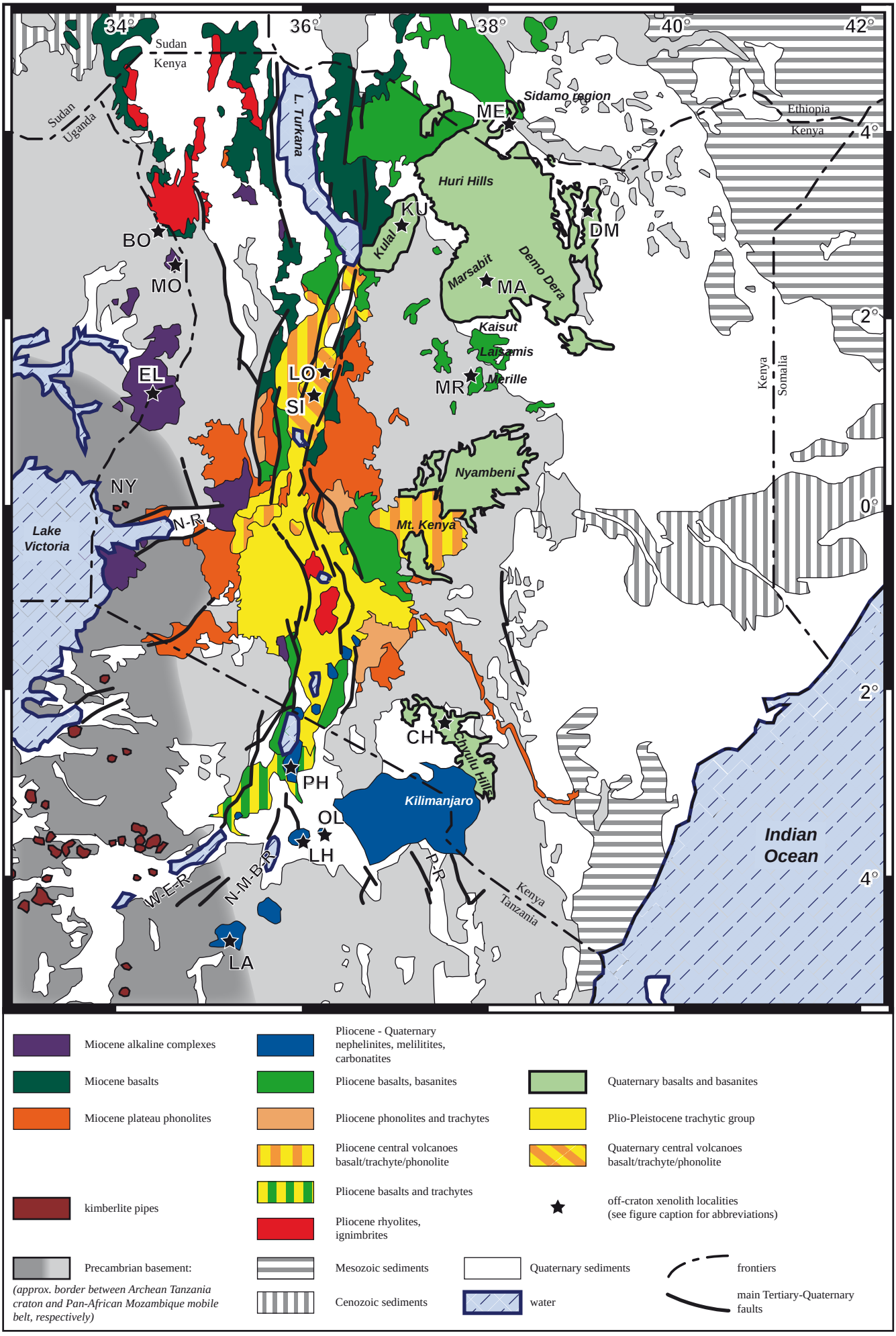


Fig. 1.1. *Main topographic features in East Africa (numerical model; data source: GTOPO30, US Geological Survey). Stars indicate mantle xenolith localities not indicated on Fig. 1.2 (AR: Assab Range; IJ:Injibara; De: Dedessa; DZ: Debre Zeyit; Bu: Butajira; TA: Toro Ankole). For further explanations see text.*

1.1) in the north, and the Kenya rift in the south. The latter extends from the Lake Turkana region to northern Tanzania and has developed along the eastern margin of the Tanzania craton and the northeastern side of the East African plateau. The Kenya rift is characterised by important topographic variation. Its width decreases from 150-200 km in the region of Lake Turkana, to 50-70 km in central Kenya. The narrow rift in central Kenya traverses a high-altitude (~2000 m) dome, situated on the larger scale East African plateau (Fig. 1.1). This so-called 'Kenya dome' (Fig. 1.1) is in strong contrast to the northern part of Kenya where the elevations are of much lesser magnitude (about 400 m above sea level, Fig. 1.1). In southern Kenya and northern


34°
36°
38°
40°
42°
4°
2°
0°
Sudan
Kenya
Sudan
Uganda
L. Turkana
Sidamo region
Ethiopia
Kenya
Huri Hills
Kulal
Marsabit
Demo Dera
Kaisut
Laisamis
Merille
Kenya
Somalia
Nyambeni
Mt. Kenya
Lake
Victoria
N-R
Chyulu Hills
Kilimanjaro
Indian
Ocean
W-E-R
N-M-B-R
P-R
Kenya
Tanzania
BO
MO
EL
LO
SI
NY
KU
ME
DM
MA
MR
CH
PH
OL
LH
LA
Miocene alkaline complexes
Miocene basalts
Miocene plateau phonolites
kimberlite pipes
Precambrian basement:
(approx. border between Archean Tanzania craton and Pan-African Mozambique mobile belt, respectively)
Pliocene - Quaternary nephelinites, melilitites, carbonatites
Pliocene basalts, basanites
Pliocene phonolites and trachytes
Pliocene central volcanoes basalt/trachyte/phonolite
Pliocene basalts and trachytes
Pliocene rhyolites, ignimbrites
Mesozoic sediments
Cenozoic sediments
Quaternary basalts and basanites
Plio-Pleistocene trachytic group
Quaternary central volcanoes basalt/trachyte/phonolite
off-craton xenolith localities (see figure caption for abbreviations)
Quaternary sediments
water
frontiers
main Tertiary-Quaternary faults

Tanzania the rift spreads out into several smaller half grabens (Fig. 1.2: the Eyasi-Wembere rifts, the Natron-Manyara-Balangida rift and the Pangani rift; see Foster *et al.*, 1997, for example).

The Marsabit shield volcano is located in northern Kenya (02°20' N, 37°59'E; Fig. 1.3). It belongs to a series of volcanic fields situated east of Lake Turkana, including Demo Dera (NE of Marsabit), Huri Hills (N of Marsabit; Fig. 1.3), and several smaller eruptive centers south of Marsabit (Kaisut, Laisamis, Merille; Fig. 1.2). Volcanic activity in all these fields is temporally related to the development of the Kenya rift (1.8-0.5 Myr in Marsabit; Brotzu *et al.*, 1984; Key *et al.*, 1987), however, the fields are not within the rift but slightly offset eastwards (Fig. 1.2). In contrast to other volcanic fields which are situated on the eastern rift shoulder (e.g., Nyambeni, Mt. Kenya, Chyulu Hills; Fig. 1.2), Marsabit lies within a topographic depression, in the Anza graben, representing the eastward continuation of the so-called Turkana depression (Fig. 1.1). This zone of low elevation (600 m average altitude) separates the East African plateau from the northern Afar plateau and is interpreted to represent the topographic expression of an older Mesozoic-Paleogene rift (Schull, 1988; Bosworth, 1992; Hendrie *et al.*, 1994; Winn *et al.*, 1993; Morley, 1999; Morley *et al.*, 2006a,b,c), cross-cut by the EARS. This highlights the complex geological context of the Marsabit volcanic field.

Geology of the EARS and its basement

A simplified geological map of Kenya and neighbouring regions is given in Fig. 1.2. The EARS developed mainly within the Precambrian basement of East Africa, which can be subdivided in two major units – the Tanzania (or Nyanza) craton and the Mozambique mobile belt. Outcrops in cratonic units are found in Tanzania, western Kenya, and eastern Uganda. They consist of Archean and Paleoproterozoic granitoids, polymetamorphic rocks, (meta)sediments and (meta)volcanics, including typical greenstone belts (e.g., Holmes, 1951; Pallister, 1971; Bell & Dodson, 1981 and references therein). The oldest rocks record ages in the order of 2.8 Ga (Bell & Dodson, 1981; Meert *et al.*, 1994; Borg & Krogh, 1999; Maboko, 2000; Manya & Maboko, 2003).

The younger Mozambique mobile belt (Holmes, 1951) extends from the Arabian-Nubian Shield (Fig. 1.4; e.g., Vail, 1985) via Ethiopia, Uganda, Kenya and Tanzania to Mozambique, Malawi and Madagascar in the south, and follows (and partly re-works) the eastern margin of the Tanzania craton (e.g., Smith & Mosley, 1993; Smith, 1994; Nyblade & Brazier, 2002). The belt is the result of multiple accretion events during the assembly of eastern Gondwana in Pan-African times (Neoproterozoic to early Paleozoic, see Fig. 1.4; e.g., Meert, 2003, and Fritz *et al.*, 2005 for recent reviews) and includes several metamorphic domains with different ages and *P-T* histories (e.g., Shackleton, 1973; Key *et al.*, 1989; Stern & Dawoud, 1991; Pinna *et al.*, 1993; Shackleton, 1993; Stern, 1994; Appel *et al.*, 1998; Möller *et al.*, 1998; Johnson *et al.*, 2003; Nyamai *et al.*, 2003; Sommer *et al.*, 2003; Ulianov & Kalt, 2006; and references therein). In northeast Africa (i.e., Afar, Ethiopia, northern Kenya) the Mozambique belt and the adjacent Arabian-Nubian Shield, represent mainly the result of the Neoproterozoic East African Orogenesis (720-550 Myr; Meert, 2003 and references therein; see Fig. 1.4).

In northern Kenya, post-Pan African Mesozoic rocks are mostly covered by the voluminous Cenozoic volcanics associated to the EARS, and

Fig. 1.2. *Geological map of Kenya and neighbouring regions compiled on the basis of maps from King (1970), Baker et al. (1971), and the Geological Map of Africa (U.S. Geological Survey, 2002, ArcShape file at www.uni-koeln.de/sfb389). N-R: Nyanza rift; N-M-B-R: Natron-Manyara-Balangida rift; W-E-R: Wembere-Eyasi rift; P-R: Pangani rift. Xenolith localities: ME, Mega; KU, Kulal; MA, Marsabit; MR, Merille; DM, Dulei Mukororí; BO, Bobong; MO, Moroto; EL, Mount Elgon; NY, Nyanza; LO, Lomujal; SI, Silali; CH, Chyulu Hills; PH, Pello Hills; OL, Olmani; LH, Lashaine; LA, Labait*

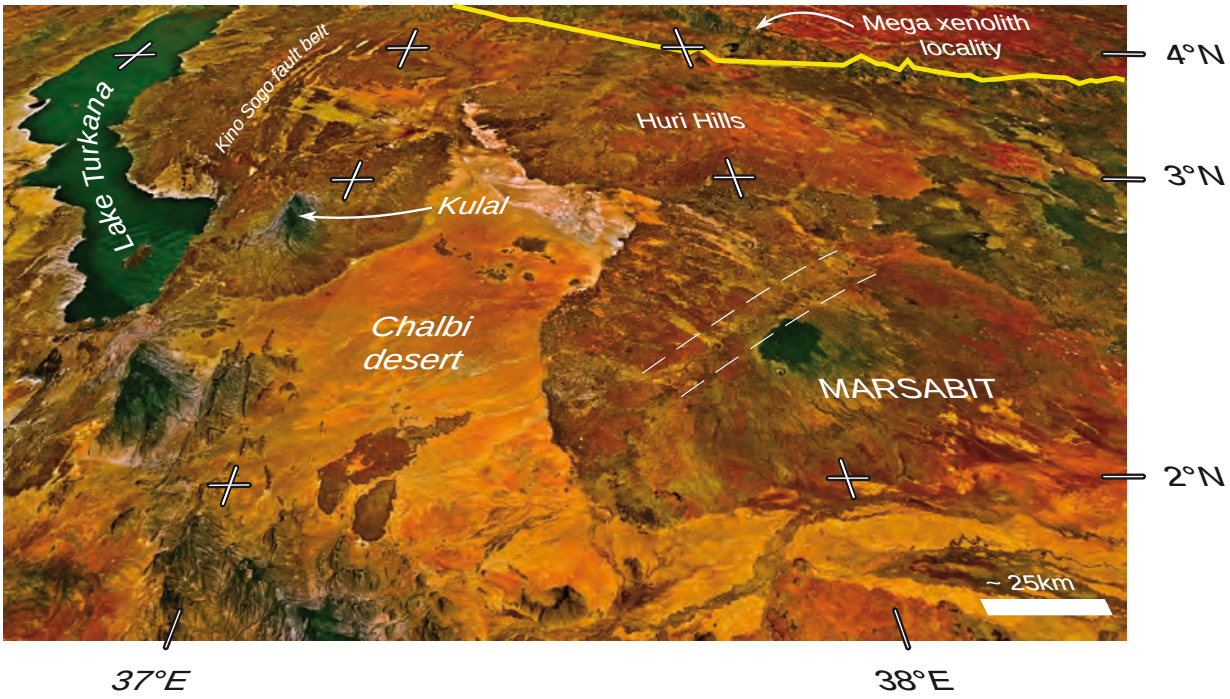


Fig. 1.3. *Satellite image of the Marsabit - Lake Turkana area. The dashed lines on the Marsabit volcanic field indicate the SW-NE lineament of Quaternary cinder cones from which the xenoliths were sampled. The yellow line is the border between Kenya and Ethiopia (Image source: NLT Landsat7, visible colours from NASA worldwind v.1.3.5; height: 36,380 m; tilt: 53°; vertical exageration: 5:1).*

by Quaternary sediments (Fig. 1.2). Southeast of Marsabit boreholes related to oil prospection (up 4391 m deep) reveal an important Cretaceous-Quaternary sedimentary record within the Anza Graben (Winn *et al.*, 1993; Bosworth & Morley, 1994; Morley *et al.*, 2006c). Drilled lithologies are dominated by syn-rift sandstones, subordinate shales and minor diabase intrusions (Winn *et al.*, 1993; Morley *et al.*, 2006c). Jurassic sediments and the crystalline basement were not reached (Winn *et al.*, 1993).

Continental rifting and formation of the EARS started in Cenozoic times, associated with the eruption of various volcanic rocks (see below). Volcanism was most profuse in the eastern branch of the EARS, where > 900'000 km^3 of lava was erupted (Morley, 1999). Much smaller volumes were ejected in the western rift (Ebinger, 1989; Pasteels *et al.*, 1989; Kampunzu & Mohr, 1991; Kampunzu *et al.*, 1998). The rift valley in southern and central Kenya is dominated by voluminous plateau phonolites and trachytes (e.g., Lippard, 1973; see Fig. 1.2). Volcanic rocks covering the northern part of the rift, including volcanic fields east of the main rift axis, such as the Marsabit volcano, consists mainly of basalts, alkali basalts and basanites (King, 1970; Baker *et al.*, 1971; Baker, 1987). Acidic rocks (rhyolites and ignimbrites) occur west of Lake Turkana (Baker *et al.*, 1971). The western shoulder of the Kenya rift contains several alkaline complexes comprising volcanic (nephelinites, phonolites, melilitites and carbonatites), as well as plutonic units (ijolites, alkali syenites and carbonatites; McCall, 1958; King, 1970; Le Bas, 1987). These complexes are distributed on the (partly burried) northeastern margin of the Tanzania craton (the so-called carbonatite belt; Le Bas, 1987; Smith, 1994). Carbonatites are absent on the eastern shoulder of the rift.

The Marsabit complex is underlain by a basal platform of fissure-fed basalt on which alkali

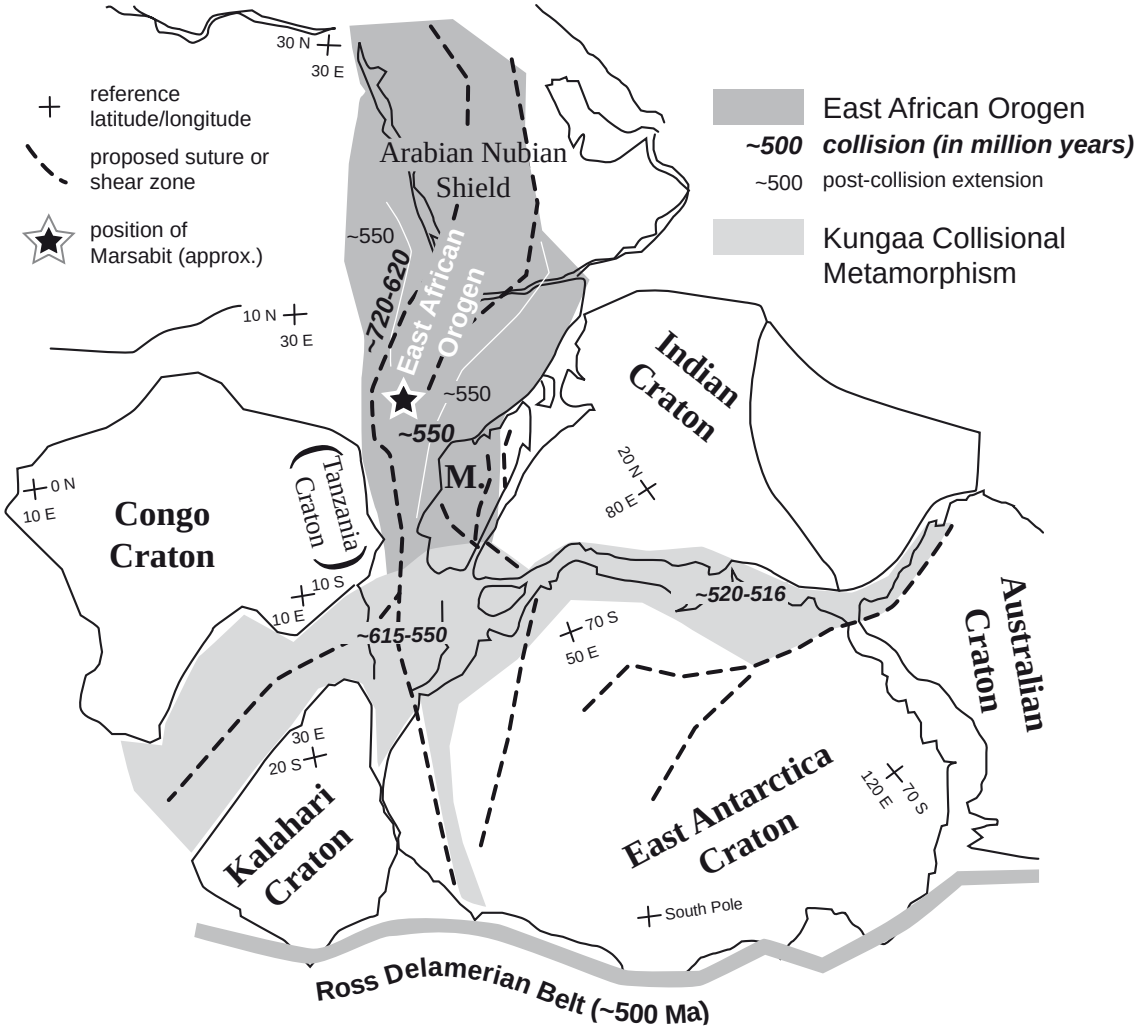


Fig. 1.4. *The Pan-African assembly of Gondwana (redrawn and simplified from Meert, 2003). The star indicates the approximate position of Marsabit.*

basalt and basanite lava flows built the Marsabit volcano. The youngest feature is a broadly SE-NW alignment of numerous maars and cinder cones traversing the summit area of the Marsabit volcano (Williams, 1978; Key *et al.*, 1987; see Fig. 1.3). From these cinder cones the studied xenoliths have been sampled.

Continental rifting events in Africa

After the formation of the Mozambique mobile belt, the African continent was subjected to three main continental rifting events (Fig. 1.5): the development of the Karroo rifts, the West and Central African rift systems (WARS/CARS) and the EARS (as a part of the Afro-Arabian rift system; AARS):

The Karroo rifts

The Karroo rifts (e.g., Cox, 1970) formed from upper Carboniferous (Lambiase, 1989) until Mid Jurassic times (Rabinowitz *et al.*, 1983; Binks & Fairhead, 1992; Winn *et al.*, 1993; Fig 1.5a). In east Africa rifting led to the formation

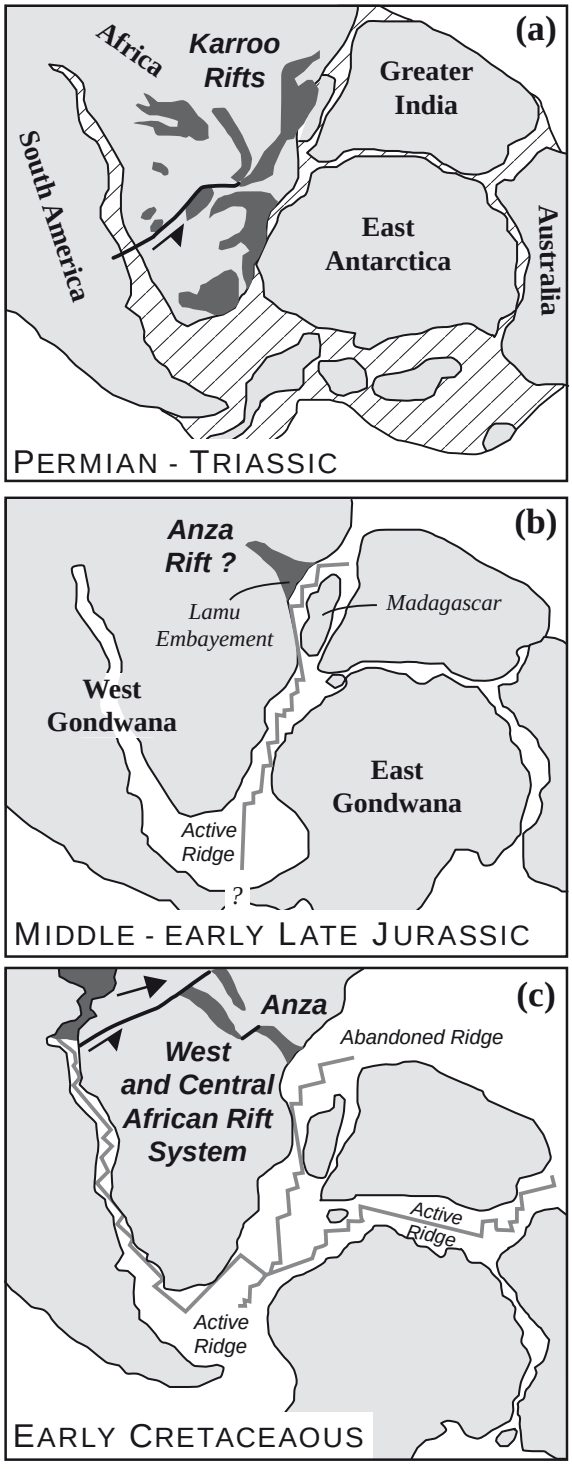


Fig. 1.5. *Continental rifting episodes in Africa prior to the development of the Tertiary-Quaternary East African Rift System (modified from Winn et al., 1993)*

of the Somali-Mozambique basin and the associated break-up of Gondwana. The Lamu embayment in southeast Kenya (Fig. 1.5b) has been interpreted as a failed rift branch, formed during the separation of Madagascar from the African continent (e.g., Reeves *et al.*, 1987; Greene *et al.*, 1991; Morley *et al.*, 2006a). It is not known whether Jurassic (or older Mesozoic) faults extend into the Anza Graben (Winn *et al.*, 1993).

Central- and West African rift system (including Anza graben)

The second rift phase lasted from upper Jurassic to mid Cretaceous times and includes the formation of the WARS and CARS and the associated Anza Graben (Schull, 1988; Fairhead, 1988; Bosworth, 1992; Winn *et al.*, 1993; Ebinger & Ibrahim, 1994; Fig. 1.5c). They developed mainly in response to the opening of the central Atlantic ocean (Fairhead, 1988; Winn *et al.*, 1993, and references therein). The Anza graben is connected with the Sudan basin through a transform fault accross the Kenya rift (Bosworth, 1992; Ebinger & Ibrahim, 1994; Wescott *et al.*, 2006; Fig. 1.5c). Erosion and sedimentary processes obliterated any surface expression of the Anza graben. Geophysical data, however, point to crustal thinning of about 8-10 km and a sediment fill of about 7-10 km (Reeves *et al.*, 1987; Bosworth, 1992; Dindi, 1994). The exact timing of rifting is not well constrained (Morley *et al.*, 2006b). K-Ar dating on basalts from drill holes revealed Neocomian ages (145-125 Ma; Bosworth & Morley, 1994), while sedimentological investigations indicate a maximum age for the onset of rifting corresponding to the Santonian (85.8-83.5 Ma; Winn *et al.*, 1993) or Neocomian (145-125 Ma; Bosworth & Morley 1994).

The Afro-Arabian Rift System, including the East African Rift System

The AARS started to develop in late Eocene times (e.g., Guiraud & Bellion, 1995) and led to the formation of the Gulf of Aden, the Red Sea,

as well as the EARS (Fig. 1.1). In Kenya (and southern Ethiopia) rifting related to the EARS is thought to have initiated in early Miocene times (e.g., Morley, 1999 and references therein). In the Turkana depression, there is, however, evidence that rifting started earlier, during the Paleogene, by reactivation of Mesozoic rifts in Sudan and Kenya (Hendrie *et al.*, 1994; Ebinger *et al.*, 1993; Ebinger & Ibrahim, 1994; Morley *et al.*, 2006a,b). The oldest volcanic rocks in the Turkana region (34.8 Ma; McDougall & Watkins, 2006), directly overlie Precambrian gneisses. This is in line with evidence from other parts of the Kenya rift indicating that the earliest volcanism preceded the earliest known rifting (e.g., Baker & Wohlenberg, 1971; Morley et al., 1992; MacDonald et al., 1994).

Northern Kenya is characterised by a complex history of fault propagation, activation and re-activation. In the Turkana area, rifting and volcanic activity was characterised by a continuous eastward migration. From the Eocene to the Pliocene, the locus of rifting has shifted from basins (half grabens) east of Lake Turkana to a region west of Lake Turkana characterised by a narrow trough populated by swarms of minor faults and dykes (the Kino Sogo fault belt; Fig. 1.3) with eruptive centres lying along the trend of the Main Ethiopian rift (Ebinger & Ibrahim, 1994; Morley, 1999; Morley *et al.*, 2006b).

In the southern Kenya rift crustal extension began around 10 Ma, while splay faults further south (northern Tanzania) initiated at ~5 Ma (Dawson, 1992; Foster *et al.*, 1997; Morley, 1999). In the western branch of the EARS, rifting initiated only during late Miocene times (Ebinger, 1989).

Numerous geophysical studies, in particular the deep seismic refraction profiling program 'KRISP' (Kenya rift international seismic project; e.g., Prodehl *et al.*, 1994; Fuchs *et al.*, 1997), provided important structural details of the lower crust and upper mantle beneath the EARS. Interpretation of seismic refraction and wide-angle reflection data (Mechie *et al.*, 1997) indicates that in the south, beneath the East African dome, the crust is still thick (35 km), whereas, in the north, beneath Lake Turkana, it is thinned to 20 km. The superposition of perhaps three rift systems in the Turkana depression resulted in cumulative stretching factors approaching 2, compared to 1.3-1.4 in central and southern Kenya (Ebinger & Ibrahim, 1994; Hendrie *et al.*, 1994; Mechie *et al.*, 1997). Steady-state geotherms constructed from three different mantle xenolith suites on the eastern side of the Kenya rift indicate lithospheric thicknesses of < 75 km beneath Marsabit (see also Chapter 2 and 5 in this thesis), ~115 km beneath the Chyulu Hills (southern Kenya; Fig. 1.2), and ≥ 145 km beneath Lashaine, northern Tanzania (Henjes-Kunst & Altherr, 1992). The Moho beneath Marsabit lies at <30 km depth (Henjes-Kunst & Altherr, 1992). A zone of low P_n-wave propagation is observed beneath the rift axis of the southern Kenya rift, and can be explained by a lithospheric mantle containing small amounts (3-5%) of melt (Green *et al.*, 1991; Achauer *et al.*, 1994). P_n-wave velocities increases from 7.5-7.7 km/s below the rift axis to 8.0-8.2 km/s beneath the eastern shoulders, providing evidence that the presence of anomalously hot material, as well as crustal thinning, is confined to the central rift axis (Mechie *et al.*, 1997). This is in line with a model where the lithospheric mantle deforms by pure shear beneath the rift axis, and argues against models where lithospheric thinning is offset beneath the rift flanks (e.g., simple-shear models; Mechie *et al.*, 1997).

Volcanism and the 'mantle plume' issue

Cenozoic volcanism in the eastern branch of the EARS started in southern Ethiopia at ~45 Ma (George *et al.*, 1998) and propagated southward with time (e.g., Baker, 1987; Kampunzu & Mohr, 1991). The results of numerous studies on the major and trace element composition and Pb-Nd-Sr isotope signatures of primitive lavas are commonly interpreted in the light of mantle plume-lithosphere interaction (e.g., MacDonald,

1994, Stewart & Rogers, 1996; Furman & Graham, 1999; Rogers *et al.*, 2000; MacDonald *et al.*, 2001; Kabeto *et al.*, 2001; Späth *et al.*, 2001; MacDonald, 2002). According to these workers volcanism is dominated by lithospheric melts, but variable amounts of possibly mantle-plume derived material indicates that melting was triggered by mantle plume-lithosphere interaction. In the Lake Turkana region, the comparison of Sr-Nd-Pb isotope data of mafic Quaternary lavas with petrological and geophysical data indicates that magmas are dominated by sub-lithospheric melts formed at shallow depth below the strongly thinned lithosphere, in equilibrium with fertile spinel peridotite, and that they contain a considerable amount of mantle plume-derived material (Furman *et al.*, 2004 and 2006).

A similar picture was obtained for lavas from the Huri Hills (Class *et al.*, 1994) and mildly alkaline basalts from Marsabit (Volker, 1990). The mildly alkaline lavas from Marsabit are closely associated with strongly alkaline lavas (mainly basanites) whose trace element signatures indicate formation at greater depth in the spinel-garnet field (Volker, 1990). The close temporal relationship of these compositionally different lavas indicates considerable compositional heterogeneity in the mantle beneath Marsabit. Sr, Nd, and Pb isotope data (Volker, unpublished data) suggests that the magma sources comprise components similar to HIMU and EM1 reservoirs defined in oceanic domains (e.g., Hofmann, 1997). The HIMU ('high-μ'; i.e. $^{238}U/^{204}Pb$) signatures may indicate recycled oceanic lithosphere, stored for about 2 Gyr in the mantle (e.g., Zindler & Hart, 1986) and ultimately sampled and transported to the source region of the Marsabit volcanics. However, trace element ratios such as Ba/Th and Rb/Nb in Marsabit lavas clearly deviate from the HIMU-EM1 trend (Volker, unpublished data). Similar results are found for other types of EARS-related magmatic rocks. Carbonatite-nephelinite complexes on the western shoulder of the Kenya rift, for example, have been shown to derive from small isotopically distinct mantle sources which cannot be explained in terms of mantle reservoirs defined for OIB (Kalt *et al.*, 1997). This indicates that the HIMU-EM1 mixing model is in several cases too simple, and that the geochemistry of lavas, including those from Marsabit, may reflect other types of source heterogeneities. The question remains to which degree volcanic products erupted along the EARS reflect lithospheric, asthenospheric and/or mantle plume related material.

The issue of the presence or absence of mantle plumes and their impact on rifting and magmatism in the EARS is still lively debated (Sleep, 1990; Burke, 1996; Ebinger & Sleep, 1998; George *et al.*, 1998; Courtillot *et al.*, 2003; Ritsema & Allen, 2003; Montelli *et al.*, 2004; Anderson, 2005; Anderson & Schramm, 2005; Pik *et al.*, 2006; Sleep, 2006). Models aiming to explain the development of the EARS must account for several pertinent structural and volcanic features. One of them is the extremely large volume of volcanic products erupted in the eastern rift branch; another is the high topography of the Afar and East African plateau, as well as the Kenya dome. Both features are consistent with an active rifting mode caused by one or more upwelling mantle plumes impacting on the lithosphere beneath East Africa (Latin *et al.*, 1993; Slack *et al.*, 1994; Burke, 1996; Simiyu & Keller, 1997; Zeyen *et al.*, 1997; Ebinger & Sleep, 1998; George *et al.*, 1998; Nyblade *et al.*, 2000; Rogers *et al.*, 2000; Nyblade, 2002; MacDonald *et al.*, 2001; Furman *et al.*, 2006). Such an interpretation would be in line with global tomography studies providing evidence for a broad region of low seismic wave velocities extending from the lowermost mantle beneath the SE Atlantic Ocean and SW Africa to the upper mantle beneath East Africa (the 'African Super-Plume'; e.g., Ritsema & van Heijst, 2000; Ni & Helmberger, 2003). Moreover, surface wave tomography studies reveal zones of extraordinarily low seismic velocities beneath the Tanzanie craton (e.g., Weeraratne *et al.*, 2003) and NE Africa/Arabia (Debayle *et al.*, 2001). Beneath the part of the Kenya rift underlain by the Mo-

zambique mobile belt, a low-velocity anomaly persists down to the transition zone (>400 km; Green *et al.*, 1991; Achauer *et al.*, 1994), interpreted to represent a mantle plume impinging on the thick lithosphere of the Tanzania craton and spreading out beneath the adjacent western and eastern rift branches (e.g., Weeraratne *et al.*, 2003).

There is general consensus that East Africa is in part underlain by anomalously hot mantle which most likely triggered rifting and volcanic activity in the EARS. However, it is unclear whether the thermal anomalies represent one or more 'true' mantle plumes beneath Tanzania, Kenya and Afar (i.e., a plume tails starting at the transition zone / lower mantle / core-mantle boundary and a spreading plume head at the asthenosphere-lithosphere; e.g., Burke, 1996; Ebinger & Sleep, 1998; George *et al.*, 1998; Rogers *et al.*, 2000; Lin *et al.*, 2005; Pik *et al.*, 2006), or whether they are part of a broad mantle upwelling beneath southern and east Africa causing 'hot-spot type' volcanism throughout East Africa (the African superplume or superswell; e.g., Lithgow-Bertelloni & Silver, 1998; Courtillot *et al.*, 2003; Benoit *et al.*, 2006; Park & Nyblade, 2006).

In the case of the southern Kenya rift, there are even alternative models which explain the thermal anomalies beneath the Tanzania craton and the Kenya dome by small-scale convection in the shallow mantle at the transition of thick cratonic lithosphere and the thinner edge (King & Ritsema, 2000). It is beyond the scope of this study to go deeper into the anti-plume – pro-plume debate (see Ernst & Buchan, 2001 and Foulger *et al.*, 2005 for recent reviews). However, the results of mantle xenoliths from Marsabit provide evidence of a very heterogeneous lithospheric mantle, modified by various styles of melt intrusion and mantle metasomatism, which – as it will be shown – were able to generate very variable geochemical signatures. Interaction of this heterogeneous lithosphere with the parental EARS magmas must considerably modify the final composition of the volcanic products and lead to large variations in their composition. Against this background, the potential involvement of plume material will be even more difficult to constrain.

Previous studies on mantle xenoliths from the EARS

Studies on mantle xenoliths provide first-hand information on the thermal history and chemical characteristics of the lithospheric mantle beneath the EARS. Whilst the mantle beneath the Tanzania craton was well sampled by numerous xenolith-rich kimberlite pipes (Nixon, 1987), off-craton xenolith localities are not that wide-spread. This is mainly due to the fact that more than 50% of the volcanic rocks in the EARS are transitional basalts and tholeiitic rocks that are typically devoid of mantle xenoliths (Kampunzu & Mohr, 1991). The off-cratonic xenolith localities discussed below are indicated in Fig. 1.1 and 1.2. They are all associated either with nephelinitic-carbonatitic rocks, or with basanites and alkali basalts (Dautria & Girod, 1987). In addition, most of these xenolith-bearing lavas erupted not within the rift itself, but are slightly offset, either on the western or the eastern rift shoulder.

From the western rift branch, only few studies include data on mantle xenoliths. Plagioclase and calcite-bearing lherzolite xenoliths are reported from east Zaïre. It is, however, not clear whether they are cognate to their host lava or of mantle origin (Kampunzu & Mohr, 1991). The most prominent suite consists of strongly metasomatic xenoliths from the Toro Ankole province (Uganda), dominated by clinopyroxenite and some glimmerite with rather unusual phase assemblages (magnetite, titanite, apatite, rare olivine, calcite and K-feldspar; Lloyd & Bailey, 1975; Dautria & Girod, 1987; Lloyd *et al.*, 1987).

Within the eastern branch of the EARS, xenolith-bearing volcanic edifices are known from northern Tanzania, Kenya and Ethiopia. In northern Tanzania, xenoliths are reported from

Pleistocene tuff cones (Dawson, 1992) at Pello Hills, Olmani, Lashaine, and Labait. Reported lithologies include garnet-bearing and garnet-free lherzolite, harzburgite, dunite, wehrlite and alkalic pyroxenite (Dawson, 1964; Dawson *et al.*, 1970; Reid & Dawson, 1972; Dawson & Smith, 1973; Reid *et al.*, 1975; Pike *et al.*, 1980; Henjes-Kunst & Altherr, 1992; Rudnick *et al.*, 1994; Dawson *et al.*, 1997; Johnson *et al.*, 1997; Lee & Rudnick, 1999). The abundance of highly refractory peridotite (Lee & Rudnick, 1999; Dawson, 2002 and references therein), further characterised by strongly refractory Platinum Group Element (PGE) signatures (Rehkämper *et al.*, 1997) testify to extensive depletion of the peridotitic mantle during Archean melting events [i.e., Os isotope depletion ages of ~3.4 Ga for Lashaine (Burton *et al.*, 2000) peridotites and 2.5-2.9 Ga for Labait peridotites (Chesley *et al.*, 1999)]. Results from thermobarometry indicate that the lithospheric mantle beneath the Tanzanian part of the EARS is thick (up to 150 km), characterised by the presence of abundant garnet-bearing peridotite, and equilibrated to steady-state geotherms that correspond to heat flows of 44-45 mW/m^2 (Lashaine; Henjes-Kunst & Altherr, 1992; Rudnick *et al.*, 1994; Dawson, 2002 and references therein) and ~50 mW/m^2 (Labait; Lee & Rudnick, 1999). The Tanzanian mantle seems to be hotter than the actual (measured) surface heat flow of the Tanzania craton (23-47mw/m^2; Nyblade *et al.*, 1990), indicating recent heating (from EARS magmas) that is not yet reflected in the surface heat flow (Lee & Rudnick, 1999).

Mineral and whole rock data of all Tanzanian xenolith suites indicate that early depletion of the peridotitic mantle was partly overprinted by various styles of later metasomatism. The latter includes the formation of amphibole and phlogopite-bearing veins and metasomatism by carbonatite melts (Dawson & Powell, 1969; Rhodes & Dawson, 1975; Ridley & Dawson, 1975; Pike *et al.*, 1980; Jones, 1983; Jones *et al.*, 1983; Dawson, 1987; Dawson & Smith, 1988 and 1992; Nielson, 1989; Johnson *et al.*, 1997; Rudnick *et al.*, 1993, 1994, and 1999; Lee *et al.*, 2000a; Dawson, 2002). Isotope studies indicate multiple metasomatic events including one at around 2.0 Ga (Cohen *et al.*, 1984; Burton *et al.*, 2000), probably in the context of the pre-Pan-African Usagaran orogeny (Dawson, 2002, and references therein). This hypothesis is corroborated by Re-Os studies which yield younger Re-Os ages (~2.0 Ga) for the lower lithosphere beneath Labait, compared to the Archean ages preserved in the shallower lithosphere. This indicates formation and/or modification of the lower lithosphere during the Proterozoic (Chesley *et al.*, 1999). Similarly, Lee & Rudnick (1999) explain the occurrence of abundant deep-seated Fe-rich dunites in the lower lithosphere beneath Labait by refertilisation or incremental accretion of new lithosphere during the interaction with asthenospheric melt, either in Proterozoic times or related to the EARS.

Vauchez *et al.* (2005) explain grain growth and nucleation recrystallisation associated with heating of about 200-250°C in peridotite xenoliths from Labait to reflect infiltration of EARS-related melts above a rising mantle plume. Also texturally young metasomatic features, such as veins cross-cutting peridotite (e.g., Pike *et al.*, 1980; Rudnick *et al.*, 1993 and 1999) or glass-bearing patches in dunites from Lashaine (Dawson, 2002) point to metasomatism by related to the EARS. Indeed, precise dating of metasomatism in the case of Labait xenoliths (using zircon in peridotite-hosted phlogopite veins) yielded Pleistocene ages (400 ± 200 Ka; Rudnick *et al.*, 1999).

In southern Kenya, mantle xenoliths occur in Quaternary basanites from the Chyulu Hills, comprising garnet and spinel peridotite, as well as various types of pyroxenite and granulite (Henjes-Kunst & Altherr, 1992; Garasic, 1997; Ulianov, 2005; Ulianov *et al.*, 2005; Ulianov & Kalt, 2006; Ulianov *et al.*, 2006; Altherr *et al.*, submitted). Detailed thermobarmetric calculations (Henjes-Kunst & Altherr, 1992; Altherr *et al.*, submitted) indicate an actual steady-state geotherm corresponding to a heat-flow of 60-

70 mW/m^2 and a lithospheric thickness of ~115 km, thus slightly 'hotter' and thinner than in northern Tanzania. Pressure estimates indicate a compositional stratigraphy with fertile garnet lherzolite and depleted porphyroclastic spinel harzburgite in the lowermost lithosphere, overlain by depleted garnet harzburgite, (olivine) websterite and spinel lherzolite between ~80-60 km, and depleted granular harzburgite together with websterite and orthopyroxenite at the top between 40 and 60 km (Altherr *et al.*, submitted). All rock types from the shallower lithosphere (80-40 km depth) were subjected to a long period of cooling. Diffusion modelling indicates that cooling most likely started at the end of the formation of the Pan-African orogenic Mozambique belt. In agreement with this, websterite (and orthopyroxenite) in the uppermost mantle, together with Ca-Al-rich lower-crustal granulites, could be explained to have formed in a Pan-African convergent setting (Ulianov, 2005; Ulianov *et al.*, 2005 and 2006). The granulites most likely represent former troctolitic cumulates that underwent metamorphism, possibly in the context of Pan-African collision (Ulianov & Kalt, 2006; Ulianov *et al.*, 2006).

Heat input related to Tertiary-Quaternary rifting was only a local phenomenon, restricted to the shallow lithosphere, probably induced by small amounts of intruding magma of yet unknown origin (Altherr *et al.*, submitted).

Xenolith data from volcanic fields in the northern parts of the Kenya rift and the Main Ethiopian rift are scarce. Xenoliths in the main Ethiopian rift (Fig. 1.1) are reported from the Assab Range, southern Eritrea (Ottonello *et al.*, 1978a; Dautria & Girod, 1987), situated just south of the Afar triple-junction, and from Debre Zeyit and Butajira, near Addis Ababa (Rooney *et al.*, 2005). Xenoliths from Assab comprise mantle-derived deformed spinel peridotite and pyroxenite, as well as lower crustal mafic-ultramafic magmatic cumulates (Ottonello *et al.*, 1978a). The mantle peridotites equilibrated at high temperatures (1050-1100°C; Ottonello *et al.*, 1978a). Their residual major element composition together with strong enrichment in incompatible trace elements (and radiogenic Sr) is interpreted by early depletion followed by fluid metasomatism (Ottonello *et al.*, 1978b, Ottonello, 1980; Betton & Civetta, 1984). Xenoliths from Debre Zeyit and Butajira (Rooney *et al.*, 2005; also within the MER) are dominated by plagioclase-bearing Al-augite xenoliths and megacrysts and contain subordinate lherzolite and norite xenoliths. Al-augite records near-magmatic temperatures (1220-1341°C) and is explained to have formed by fractional crystallisation in veins/dykes intruding the mantle and crust at depths between 1-30 km (max. 0.6 GPa). Rooney *et al.* (2005) interpret these dykes/veins in connection with the development of a proto-ridge axis related to the transition of continental towards oceanic rifting. On the other hand, xenolith localities on the NW Afar plateau (Lake Tana, Dedessa and Injibara area; Fig. 1.1) are dominated by relatively fertile peridotite (Conticelli *et al.*, 1999; Roger *et al.*, 1999). Mineral compositions, textures and results from thermobarometry indicate that the shallow mantle has a relatively uniform composition. It records elevated temperatures (mostly > 950°C) suggesting equilibration to a geotherm of about 90 mW/m^2 (Conticelli *et al.*, 1999). In addition, most peridotites show only small degrees of metasomatism (Rogers *et al.*, 1999).

In southern Ethiopia, mantle xenoliths occur in the Sidamo region, situated north of the Anza graben, on the border of the Afar plateau (Morten *et al.*, 1992; Fig. 1.2). Lithologies include peridotite (exclusively garnet-free), as well as minor pyroxenite (Morten *et al.*, 1992; Bedini, 1994; Conticelli *et al.*, 1999). Peridotite xenoliths provide evidence for various styles of metasomatic modification resulting from the interaction with melt (Bedini *et al.*, 1997; Bedini & Bodinier, 1999; Lorand *et al.*, 2003). In a detailed study, Bedini *et al.* (1997) showed that the different metasomatic expressions can be explained by one single event of melt intrusion. During this process, the lithospheric mantle experienced heating and recrystallisation accompanied by

impregnation by large volumes of basaltic (OIB-like) melt. This process ultimately led to erosion (and thus thinning) of the lithosphere. At the same time, basaltic melts moved upward in the colder shallow mantle. These melts became highly evolved through reactive porous flow and were responsible for metasomatic features in peridotite from the shallower mantle. Bedini *et al.* (1997) explain all these features in the context of EARS-related magmastism in the context of an upwelling mantle plume.

Reisberg *et al.*, (2004) showed that despite strong metasomatic modification, Os isotope ratios of the Sidamo xenoliths still preserve model ages of an ancient, Archean melt extraction event (pre-Pan-African; 2.4-2.8 Gyr). As discussed by Reisberg *et al.* (2004), these ages may indicate an extension of the Archean root of the Tanzania craton under southern Ethiopia (and consequently northern Kenya). On the other hand, they also mention that depleted mantle can survive for a long time in the convecting mantle. Therefore, Archean ages preserved in the mantle beneath Ethiopia must not necessarily correspond to the age of lithosphere stabilisation (i.e., formation of the Tanzania craton). The age of the lithospheric mantle beneath southern Ethiopia and northern Kenya thus remains unconstrained.

Xenolith localities in Kenya (except from the Chyulu Hills; see above) are poorly known and the aim of this project is to close this gap between Ethiopian and Tanzanian xenolith localities. Early studies report mantle and/or crustal xenoliths from other localities within the Kenya rift, as well as from some localities on the western and eastern rift flanks. On the western rift flank mantle xenoliths and xenocrysts (lherzolite, Cr-pyrope, Cr-spinel, Cr-diopside, olivine, enstatite, phlogopite), as well as mantle-derived megacrysts (amphibole and pyroxene) have been reported from Mount Elgon, Moroto and Bobong (Nixon, 1987 and references therein). All these xenoliths occur in nephelinite commonly associated with carbonatite, being part of the carbonatite belt at the border of the Tanzania-Nyanza craton (e.g., Smith, 1994). The occurrence of nearby sporadic alluvial diamonds (Nixon, 1987) suggests that these xenoliths represent cratonic lithosphere. In addition to these locations, one kimberlite pipe in the Nyanza region was shown to contain mantle-derived xenoliths comprising garnet-free but amphibole and phlogopite-bearing spinel dunite and harzburgite, as well as rare olivine orthopyroxenite (Ito, 1986; Nixon, 1987). Due to the lack of Cr-pyrope, the original depth of these xenoliths is unconstrained and it is not clear whether they represent cratonic lithopshere (Nixon, 1987).

Within the central Kenya rift, (crustal?) gabbroic and ultramafic xenoliths are reported from Silali and Lomujal (McCall, 1970; Nixon, 1987). Xenolith-bearing quaternary volcanics east of Lake Turkana are known from Marsabit (Henjes-Kunst & Altherr, 1992; this study), the Merille-Ndonyuo Olnchoro area (Suwa *et al.*, 1975), Dulei Mukorori (Dautria & Girod, 1987) and Kulal. Some data on xenoliths from Merille have been published by Suwa *et al.* (1975) indicating the presence of spinel-facies harzburgite and lherzolite and minor spinel websterite. Symplectitic intergrowths between spinel and pyroxenes possibly indicate the former presence of garnet (Suwa *et al.*, 1975). The Marsabit xenoliths have been studied prior to this work by Henjes-Kunst & Altherr (1992) and Olker (2001) with the aim to constrain their thermal history. As a major result, they have shown that the Marsabit lithospheric mantle preserved compositional and textural features indicating thinning and cooling from a stage similar to the present-day thermal state of the mantle beneath the Chyulu Hills in southern Kenya (see above).

THE IMPORTANCE OF MARSABIT

As outlined above, locus and extent of EARS rifting, as well as the compositional nature of the associated magmatism are governed considerably by the pre-existing structure and composition of the lithosphere attained during its evolution prior to the development of the EARS. In northern Kenya (including Marsabit),

such pre-existing structures are particularly important. The lithosphere beneath this part of the EARS was modified during multiple accretion episodes in Pan-African times (Neoproterozoic – early Paleozoic). From Mesozoic until Paleogene times, up to three continental rifting episodes further modified the Pan-African lithosphere prior to the development of the EARS.

The EARS and the associated volcanic activity are commonly explained by active rifting in the context of one or more mantle plumes, based on geophysical studies and geochemical / isotopic studies on primitive lava. However, given ample evidence for pre-EARS events, it is doubtful whether a plume component can be distinguished un-equivocally from remnants of earlier processes that modified the basement of the EARS. In the context of interpreting compositional features of volcanic rocks and constraining the complex evolution of the Kenya rift in general (and the Marasbit complex in particular), the relationship between pre-EARS heterogeneities and possible 'pristine' material, newly added by an upwelling asthenosphere or mantle plume(s), is critical. In this respect, detailed investigation of mantle xenoliths is a powerful source of information to further elucidate the present lateral and vertical heterogeneity in the lithospheric mantle, and to unravel the sequence of events that produced this heterogeneity.

AIMS AND ORGANISATION OF THE STUDY

This study consists of detailed investigation of textures, mineralogy, major element composition and trace element geochemistry of mantle xenoliths hosted by Quaternary alkali basalts and basanites from the Marsabit volcano. The aim of this work is (1) to obtain information on the mineralogy and major and trace element heterogeneity of the lithosphere underlying Marsabit; (2) to constrain the evolution of the lithospheric mantle beneath Marsabit in *P-T-X* space; (3) to characterise metasomatic events which modified this part of the lithosphere; and (4) to obtain temporal information of the different events, wherever possible.

The above issues (1) and (2) will be mainly addressed in ***Chapter 2***. This chapter (now published in Journal of Petrology; Kaeser *et al.*, 2006) is the result of a detailed study which includes petrography, thermobarometry and major and trace element geochemistry (laser ablation inductively coupled mass spectrometry; LA-ICPMS) of the Marsabit peridotite xenoliths. It provides a classification of the encountered rock types and serves as a basis for ***Chapter 3***. In this chapter, mainly issues (3) and (4) are addressed by dealing with the complex metasomatic enrichment of the Marsabit spinel harzburgite xenoliths in more detail. Results of detailed investigation of the textural context and the composition of metasomatic minerals including *in-situ* trace element analysis (using LA-ICPMS) are presented. These data provide arguments in favour of very young EARS-related metasomatism and highlight the importance of small-scale melt-rock reaction processes creating mantle heterogeneity. In ***Chapter 4***, complementary to Chapter 3, the results of *in-situ* analyses of Li, Be and B ('light element') contents in minerals by SIMS (secondary ion mass spectrometry) are presented. Also the potential and limitations of light element geochemistry for deciphering metasomatic processes in the mantle are discussed. ***Chapter 5*** contains textural, major and trace element data on mafic xenoliths, namely garnet-bearing websterites and subordinate garnet-free pyroxenites. This chapter includes data of an earlier PhD thesis produced at the University of Heidelberg (Olker, 2001). The magmatic and metamorphic evolution of the Marsabit lithopshere (issue 2) is addressed, in particular the question to which extent old Pan-African mantle heterogeneities are preserved and modified during subsequent continental rifting. Also, the role of added mafic material added to the mantle during magmatic activity in the course of rifting (issue 4) is discussed too. The latter issue is further addressed by ***Chapter 6***. This chapter includes textural and compositional data on

Table 1.1: Approximate relative contributions of each author to chapters 2-6

	Chapter 2	Chapter 3	Chapter 4	Chapter 5	Chapter 6
Petrography, including optical microscopy and modal analyses	Kaeser: 100%	Kaeser: 100%	Kaeser: 100%	Kaeser: 80% Olker: 20%	Kaeser: 100%
SEM documentation	Kaeser: 100%	Kaeser: 100%	Kaeser: 100%	Kaeser: 100%	Kaeser: 100%
Electron Microprobe (EMP) analysis	Kaeser: 90% Kalt: 10%	Kaeser: 100%	Kaeser: 100%	Kaeser: 20% Olker: 80%	Kaeser: 100%
LA-ICPMS analysis	Kaeser: 40% Pettke: 60%	Kaeser: 40% Pettke: 60%	-	Kaeser: 40% Pettke: 60%	-
SIMS analysis	-	-	Kaeser: 70% Ludwig: 30%	-	-
Data processing (EMP, LA-ICPMS, SIMS)	Kaeser: 100%	Kaeser: 100%	Kaeser: 100%	Kaeser: 50% Olker: 50%	Kaeser: 100%
Thermobarometric calculations and trace element modelling	Kaeser: 100%	Kaeser: 100%	Kaeser: 100%	Kaeser: 30% Olker: 70%	
Interpretation of data	Kaeser: 50% Kalt: 50%	Kaeser: 60% Kalt: 40%	Kaeser: 60% Kalt: 40%	Kaeser: 40% Olker: 40% Kalt: 10% Altherr: 10%	Kaeser: 100%
Writing manuscript text	Kaeser: 70% Kalt: 30%	Kaeser: 70% Kalt: 30%	Kaeser: 70% Kalt: 30%	Kaeser: 70% Kalt: 30%	Kaeser: 100%
Drawing figures, compiling tables	Kaeser: 100%	Kaeser: 100%	Kaeser: 100%	Kaeser: 95% Olker: 5%	Kaeser: 100%

a single gabbro xenolith and a short discussion on evidence of young plutonic intrusions in the crust. Finally, ***Chapter 7*** contains a summary, conclusions and an outlook for further research to resolve remaining questions. At the end, the applied analytical methods (***Chapter 8***) are outlined, followed by the complete list of ***Cited References***. The very large amount of data is presented in a separate ***Appendices*** volume. The latter includes a petrographic classification of all investigated samples (***A1***), and major element data of minerals including microprobe data including zoning profiles (***A2***) and representative analyses (***A3***; the complete dataset is provided on an enclosed CD). The complete trace element data set is given in ***A4*** (LA-ICPMS data) and ***A5*** (SIMS data). The contribution of all involved authors to each chapter can be summarised as listed in Table 1.1.

Chapter 2: Evolution of the Lithospheric Mantle beneath the Marsabit Volcanic Field (Northern Kenya): Constraints from Textural, *P-T* and Geochemical Studies on Xenoliths

Benjamin Kaeser[1], Angelika Kalt[1] & Thomas Pettke[2,*]

[1] Institut de Géologie et d'Hydrogéologie, Université de Neuchâtel, Rue Emile-Argand 11, CH-2009 Neuchâtel, Switzerland
[2] Isotope Geochemistry and Mineral Resources, Department of Earth Sciences, Federal Institute of Technology, ETH Zentrum NO, CH-8092 Zürich, Switzerland (now at: Institute of Geological Sciences, University of Bern, Baltzerstrasse 1, CH-3012 Bern, Switzerland)

Manuscript published in Journal of Petrology (2006; Volume 47: pages 2149-2184)

ABSTRACT

Xenoliths hosted by Quaternary basanites and alkali basalts from Marsabit (northern Kenya) represent fragments of Proterozoic lithospheric mantle thinned and chemically modified during rifting in the Mesozoic (Anza Graben) and in the Tertiary-Quaternary (Kenya Rift). Four types of peridotite xenoliths were investigated to constrain the thermal and chemical evolution of the lithospheric mantle. Group I, III and IV peridotites provide evidence of an actually cold, highly deformed and heterogeneous upper mantle. Textures, thermobarometry and trace element characteristics of minerals indicate that these low temperatures in the spinel stability field (~750-800 °C at < 1.5 GPa) were attained by decompression and cooling from initially high pressures and temperatures in the garnet stability field (970-1080°C at 2.3-2.9 GPa). Cooling, decompression and penetrative deformation are in line with lithospheric thinning, probably related to the development of the Mesozoic to Paleogene Anza Graben.

Re-equilibrated and recrystallised peridotite xenoliths (Group II) record heating (from ~800°C to ~1100°C). Mineral trace element signatures indicate enrichment by mafic silicate melts, parental to the Quaternary host basanites and alkali basalts. Relationships between mineral textures, *P-T* conditions of equilibration, and geochemistry can be explained by metasomatism and heating of the lithosphere related to the formation of the Kenya Rift, above a zone of hot upwelling mantle.

KEY WORDS: East African Rift System; Anza Graben; in-situ LA-ICPMS; peridotite xenoliths; thermobarometry

INTRODUCTION

In this study we present new data on mantle xenoliths from the East African Rift System (EARS; Fig. 2.1a), one of the world's largest active continental rifts. The EARS extends from the Afar triple junction in the north to Mozambique in the south. Two large-scale topographic elevations separate the EARS in two parts – the Afar dome to the north and the East African dome to the south (Fig. 2.1a). The boundary between them is characterised by the Turkana depression. In this zone of lower elevation, the Tertiary/Quaternary EARS transects an older (Mesozoic) rift – the Anza Graben (Fig. 2.1b). Mantle xenoliths investigated in this study were collected on the Marsabit shield volcano, northern Kenya, in the eastward continuation of the Turkana depression (Fig. 2.1b). Although the Marsabit volcano is situated on continental crust of the Pan-African Mozambique belt, and lies within the NW-SE oriented Anza Graben, volcanic activity is related to the EARS.

Previous geophysical, structural and petrological studies have provided a fairly detailed understanding of the rifting mechanisms related to the formation of the Anza Graben, the EARS, and of the associated volcanic products. The Anza Graben is believed to represent a failed branch of an upper Jurassic – lower Cretaceous rift associated with the separation of Madagascar and the African continent (Reeves *et al.*, 1987; Greene *et al.*, 1991; Ebinger & Ibrahim, 1993; Morley, 1999). The timing of initial rifting in the Anza Graben remains uncertain. K-Ar dating on basalts from drill holes revealed Neocomian ages (145-125 Myr; Bosworth & Morley, 1994) while sedimentological investigations indicate a maximum age for the onset of rifting corresponding to the Santonian (85.8-83.5 Myr; Winn *et al.*, 1993) or Neocomian (145-125 Myr; Bosworth & Morley 1994).

Tertiary volcanism in the Kenya rift (EARS-related) started in southern Ethiopia at ~45 Ma (George *et al.*, 1998) and propagated southward with time (e.g., Baker, 1987). Volcanic activity in

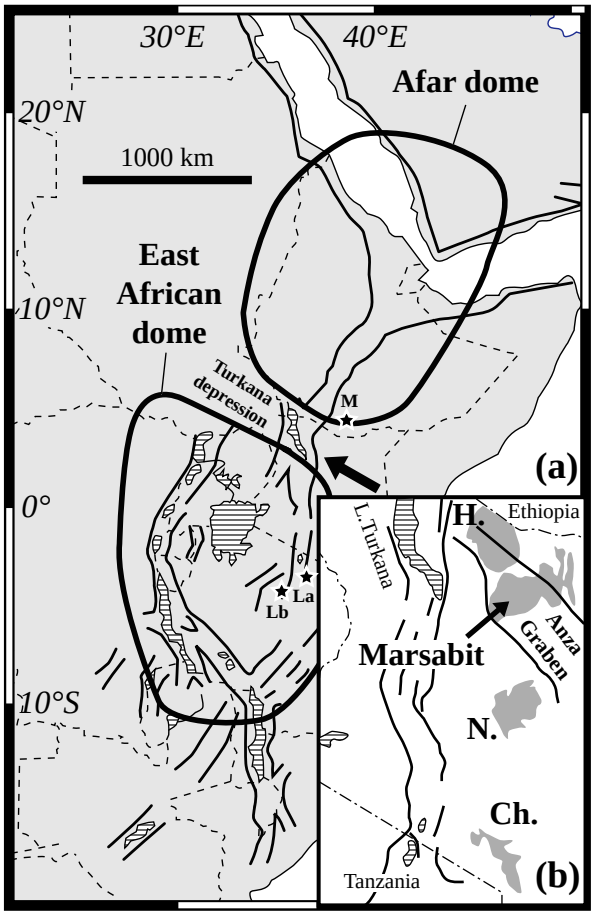


Fig. 2.1. *Geological setting.* ***(a)*** *The East African Rift System, indicating the East African and the Afar domes, separated by the Turkana depression. Small stars indicate the position of some other xenolith-bearing volcanic localities (M: Mega; Lb: Labait; La: Lashaine).* ***(b)*** *Inset shows the main structural features of to the Tertiary Kenya rift (N-S) and the Jurassic-Cretaceous Anza Graben (NW-SE). Quaternary volcanic fields are shown in light grey (H: Huri Hills; N: Nyambeni; Ch: Chyulu Hills; modified from Henjes-Kunst & Altherr, 1992).*

Marsabit started in the late Miocene (7.7-5.4 Ma, Brotzu *et al.*, 1984) with the eruption of fissure-fed basalts. K-Ar dating of the Marsabit shield volcano itself has yielded ages between 0.7-1.8 Myr (Key *et al.*, 1987) and 0.5 Ma (Brotzu *et al.*, 1984), respectively. At ~2 Ma the eruption style changed from hawaiian to strombolian, leading to the formation of the mantle xenolith-bearing cinder cones and maars of alkali basaltic to basanitic composition (Volker, 1990).

A comprehensive model based on seismic refraction – wide-angle reflection experiments (Mechie *et al.,* 1997) indicates that in the south, beneath the East African dome (Fig. 2.1a) the crust is thick (35 km), elevation is high (2-3 km) and the rift is narrow (50-70 km wide). In contrast, in the north, beneath Lake Turkana (Fig. 2.1), the crust thins to 20 km, elevation decreases to about 400 m and the rift widens to 150-200 km. Increasing lithospheric thickness from north to south has also been postulated by Henjes-Kunst & Altherr (1992) on the basis of steady-state geotherms constructed from three different mantle xenolith suites (< 75 km beneath Marsabit, ~ 115 km beneath the Chyulu Hills, southern Kenya, and ≥ 145 km beneath Lashaine, northern Tanzania).

Numerous geophysical studies detected low-velocity anomalies beneath different parts of the EARS, interpreted as anomalously hot upwelling mantle (e.g., Achauer *et al.*, 1994; Prodehl *et al.*, 1994; Fuchs *et al.*, 1997; Debayle *et al.*, 2001; Nyblade *et al.*, 2000; Weeraratne *et al.*, 2003). Whether this hot material is related to one or more mantle plumes (e.g., Ebinger & Sleep, 1998; George *et al.*, 1998) triggering lithospheric thinning in the context of active rifting, or to shallow upwelling asthensophere in the context of passive rifting (e.g., King & Ritsema, 2000), as well as the control of pre-EARS lithospheric structures (e.g., Nyblade *et al.*, 2002) is still a matter of debate. Studies of xenoliths from southern Kenya and Tanzania point to a still thick, less- or non-thinned lithosphere, comprising abundant garnet-bearing peridotite (Dawson *et al.* 1970; Reid & Dawson, 1972; Pike *et al.*, 1980; Jones *et al.*, 1983; Henjes-Kunst & Altherr, 1992; Lee & Rudnick, 1999) that preserved pre-rift features, such as Archean Re-depletion ages (Chesley *et al.*, 1999) or Pan-African metacumulates with Island arc signatures (Ulianov & Kalt, 2006). However, in some parts the deep lithosphere interacted with EARS-related, asthenosphere-derived carbonatitic and silicate melts (Cohen *et al.*, 1984; Dawson & Smith, 1988; Rudnick *et al.*, 1993; Dawson, 2002; Vauchez *et al.*, 2005). Xenoliths from the northern part of the Kenya rift, on the other hand, are dominated by spinel-bearing peridotites in line with a thinner lithosphere (Suwa *et al.*, 1975; Henjes-Kunst & Altherr, 1992; Bedini *et al.*, 1997; Conticelli *et al.*, 1999; Rooney *et al.*, 2005; this study). Geochemical studies of Ethiopian xenoliths (Bedini *et al.*, 1997; Bedini & Bodinier, 1999; Lorand *et al.*, 2003; Reisberg *et al.*, 2004) have shown that the thinned lithospheric mantle interacted with basaltic melts, interpreted as thermo-mechanical erosion of the lithosphere above a mantle plume. Geochemical data on rift-related lavas from different localities along the EARS have been interpreted to reflect the interaction of plume-derived components with the lithospheric mantle (Class *et al.*, 1994; Stewart & Rogers, 1996; George *et al.*, 1998; Rogers *et al.*, 2000; George & Rogers, 2002; Kabeto *et al.*, 2001; MacDonald *et al.*, 2001; Späth *et al.*, 2001; Furman *et al.*, 2004).

Because Marsabit is located on the intersection of three main tectonic features, its mantle xenoliths provide a unique opportunity to put new constraints on the thermal evolution and the compositional nature of the lithospheric mantle beneath this part of the East Africa. The lithosphere beneath Marsabit has a complex multi-stage evolution, most likely beginning with the formation of the Mozambique belt in Proterozoic times, which includes subduction, collision and accretion events between approximately 750 and 615 Ma (e.g., Key *et al.*, 1989; Shackleton, 1993; Stern, 1994; Meert, 2003 and references therein). These events were followed by processes related to continental rifting, first, in the context of the Anza Graben in the Mesozoic and second, during the formation of the EARS in the Tertiary/Quaternary.

The aim of this study is therefore, to decipher different stages in the evolution of the lithosphere, characterised by changing *P-T* conditions (decompression, cooling, heating) and/or metasomatism, and, where possible, to link these stages to the geodynamic context (i.e.

relation to Pan-African-, Anza-, and/or EARS-related porcesses). To this end, we choose a set of xenolith samples that cover the entire range of peridotite types found in volcanic rocks from Marsabit. We combine a 'classical' petrographic-petrological approach, including classification of the mantle xenoliths, major element compositions of minerals, thermobarometry, and mineral zoning patterns, with a detailed study of trace elements in minerals.

ANALYTICAL METHODS

Major elements in minerals were analysed using a CAMECA SX 50 electron microprobe equipped with four wavelength-dispersive spectrometers (Mineralogisch-Petrographisches Institut, Universität Bern) and a CAMECA SX 51 electron microprobe with five wavelength-dispersive spectrometers (Mineralogisches Institut, Universität Heidelberg). Routine analyses were carried out using 15 kV and 20 nA operating conditions on both instruments. Counting times were 20 sec for most elements. Natural and synthetic silicates and oxides were used as standards. Raw data were corrected with a routine PAP program.

Trace element contents in minerals were analysed *in-situ* on polished thin sections (40-50 μm thick), using a laser ablation (LA) instrument equipped with a 193 nm ArF excimer laser (Lambda Physik, Germany) coupled to an ELAN 6100 (Perkin Elmer, Canada) quadrupole inductively coupled plasma mass spectrometer (ICPMS) at the Institut für Isotopengeologie und Mineralische Rohstoffe, ETH Zürich. The instrumental setup and capabilities are described by Günther *et al.* (1997) and Heinrich *et al.* (2003). Operating conditions were similar to those in Pettke *et al.* (2004). Raw data were reduced using the LAMTRACE program. Laser pit sizes were between 14 and 110 μm, depending on grain size and the absence / presence of mineral, fluid or melt inclusions and of exsolution lamellae. Mineral grains were analysed in detail for major elements (electron microprobe) before LA-ICPMS analysis to obtain an internal standard for LA-ICPMS data quantification and to control intra-grain heterogeneities (e.g., zoning).

Original pyroxene and garnet compositions (prior to exsolution or decomposition, respectively) were calculated by reintegration using microprobe analyses of reaction products (orthopyroxene lamellae in exsolved clinopyroxene; spinel, orthopyroxene and clinopyroxene from symplectites for garnet). We measured at least ten different points of each phase used for reintegration in order to obtain statistically significant average compositions of the reaction products. Modal proportions of the phases in each reintegrated area were determined by image analysis using high-quality BSE images. On each pyroxene grain or symplectite cluster, 3-5 different areas of about 100x150 μm were re-integrated in order to be representative. In cases where exsolution lamellae were too small to be individually measured, bulk compositions were obtained by scanning (with EMP) a representative area using a defocused electron beam (~15 μm). Initial garnet compositions were calculated following the method of Morishita & Arai (2003a) which uses the calculated bulk symplectite composition and subtracts the amount of an inferred 'olivine component' (from the reaction grt + ol = spl + opx + cpx) necessary to obtain a 'perfect' garnet stoichiometry. The mean olivine composition of each analysed sample was used as the 'olivine component'. The stoichiometric quality of the resulting garnet composition was then controlled by site assignment of each cation to an ideal garnet composition [$(Fe,Mn,Ni,Mg,Ca,Na)_3(Si,Ti,Al,Cr)_5O_{12}$]. Only calculated garnets satisfying stoichiometry were considered further.

Modal analyses of the whole-rocks (Table 2.1) were obtained by image analysis on different scales. Due to often inhomogeneous distribution of phases we used high resolution rock slice scans to determine the amount of symplectite clusters and clinopyroxene. Spinel contents were calculated from scans of 2-3 different entire

Table 2.1: Mineralogy and textures of the analysed mantle xenoliths from Marsabit

Sample Nr.	*Gr.*	*Texture*	*Lithology*	*Modal composition (vol%)*					
				symplectites (maximum initial grt*)	ol	opx	cpx	spl*	modal metasomatism
Ke 1960/2	I	porphyroclastic	(grt)-spl lherzolite	13.3	44	10.7	32	0.05	Ti-parg (tr.), gl
Ke 1963/1	I	porphyroclastic	(grt)-spl lherzolite	11	50	29	10	tr.	gl
Ke 1963/2	I	porphyroclastic	(grt)-spl lherzolite	15.5	41.1	23.2	19.2	0.05	Ti-parg (0.8 vol%), phl (0.1 vol%)
Ke 1965/4	I	porphyroclastic	(grt)-spl lherzolite	19.4	41	23.9	15.7	0.05	Ti-parg (tr.)
Ke 1958/6	II	strongly recrystallised	(grt)-spl lherzolite	9	59	25	6.6	0.5	-
Ke 1958/13	II	tabular, less recrystal.	(grt)-spl lherzolite	9.9	58.5	20.7	10.3	0.2	gl
Ke 1958/20	II	strongly recrystallised	(grt)-spl lherzolite	14.8	52	23.7	9.3	0.3	-
Ke 1959/24	II	strongly recrystallised	(grt)-spl lherzolite	10.7	63.5	18.7	6.8	0.3	-
Ke 1959/25	II	less recrystallised	(grt)-spl lherzolite	7	63.2	19.9	9	0.9	gl
Ke 781/6	III	porphyroclastic	spl harzburgite	-	72.4	22.6	4.1	0.9	-
Ke 1959/15	III	porphyroclastic	spl harzburgite	5	63	26	5.2	0.7	amph (0.17 vol%), apa (tr.), gl
Ke 1965/1	III	porphyroclastic	spl harzburgite	1.5	70.8	22.9	3.9	0.9	gr (tr.)
Ke 1965/15	III	porphyroclastic	spl harzburgite	-	74.2	18.2	5	-	amph (0.15 vol%), phl (tr.), gr (tr.), apa (tr.), gl
Ke 1961/1	IV	ultramylonitic	spl harzburgite	-	87.5	10.1	1.5	0.8	-
Ke 1968/1	IV	mylonitic	spl lehrzolite	-	62	27.3	8.7	2	-

*: see explanation in section 'Analytical Methods'; **: excluding spinel in symplectites/clusters; ol: olivine; opx: orthopyroxene; cpx: clinopyroxene; spl: spinel; Ti-parg: Ti pargasite; phl: phlogopite; gl: silicate glass+microlites (cpx, ol, chromite, carbonate); amph: Ti-poor amphibole; gr: graphite; apa: apatite; tr.: trace amounts

thin sections from one xenolith. Initial garnet contents were obtained by redrawing the shape of symplectite clusters. The obtained maps were then analysed digitally. The results certainly overestimate the real initial garnet content as the size of symplectites/clusters involves both garnet and olivine consumed during the symplectite-forming reaction. These values must, therefore, be regarded as maximum garnet contents. Clinopyroxene contents were obtained by colour filtering (green for Cr-rich diopside) on rock slice scans. The accuracy of this method was tested on sample Ke 1958/20 in which the clinopyroxene content was also determined by analysis of BSE images (covering an entire thin section) as well as from thin section photomicrographs. Comparison of the results yielded deviations of less than 1% (modal clinopyroxene of 8.3% from thin section photomicrographs, 8.1% from BSE images and 8.7% from colour sampling on rock slice scans), which indicates consistency of the colour sampling method. Values for orthopyroxene and olivine were obtained by manual phase attribution on large-scale thin section photomicrographs. The obtained maps were subsequently digitised and analysed.

SAMPLE SELECTION AND MACROSCOPIC CHARACTERISTICS

The xenoliths investigated in this study were collected by Angelika Kalt and Rainer Altherr (1991 and 1992). They are hosted by basanitic and alkali basaltic scoriae and consist of peridotite, pyroxenite and other, less common, rock types such as ultramafic cumulates and gabbros. The collection of xenoliths from

Marsabit comprises around 300 samples. The xenoliths have diameters from ~3 cm up to 25 cm with an average size of about 10 cm. They have rounded shapes and show sharp contacts with the host lava (Fig. 2.2a). Most xenoliths are fresh, altered samples can be recognised by the reddish colour of olivine grains. This study focuses on peridotite xenoliths. 66 samples were investigated by optical microscopy. They were subdivided in four groups based on their mineralogy and textures: Group I (15 samples) and Group II (20 samples) are clinopyroxene-rich lherzolites and contain abundant spinel-orthopyroxene-clinopyroxene symplectites which are interpreted as breakdown products of former garnet (hereafter referred to (grt)-spl lherzolites). The main petrographic differences are porphyroclastic textures in Group I and recrystallised fabrics in Group II. In the latter, a more or less gradual transition between the two end-members exists. Group III xenoliths (27 samples) are porphyroclastic spinel harzburgites (spl harzburgites). Five samples of this group contain rare symplectites testifying to the former presence of garnet. The last type, Group IV (4 samples) consists of spinel lherzolites and harzburgites characterised by a strongly foliated, mylonitic texture. On the basis of microscopic investigation, 15 representative xenoliths (Group I: 4; Group II: 5; Group III: 4; Group IV: 2) were selected further chemical analysis (Table 2.1).

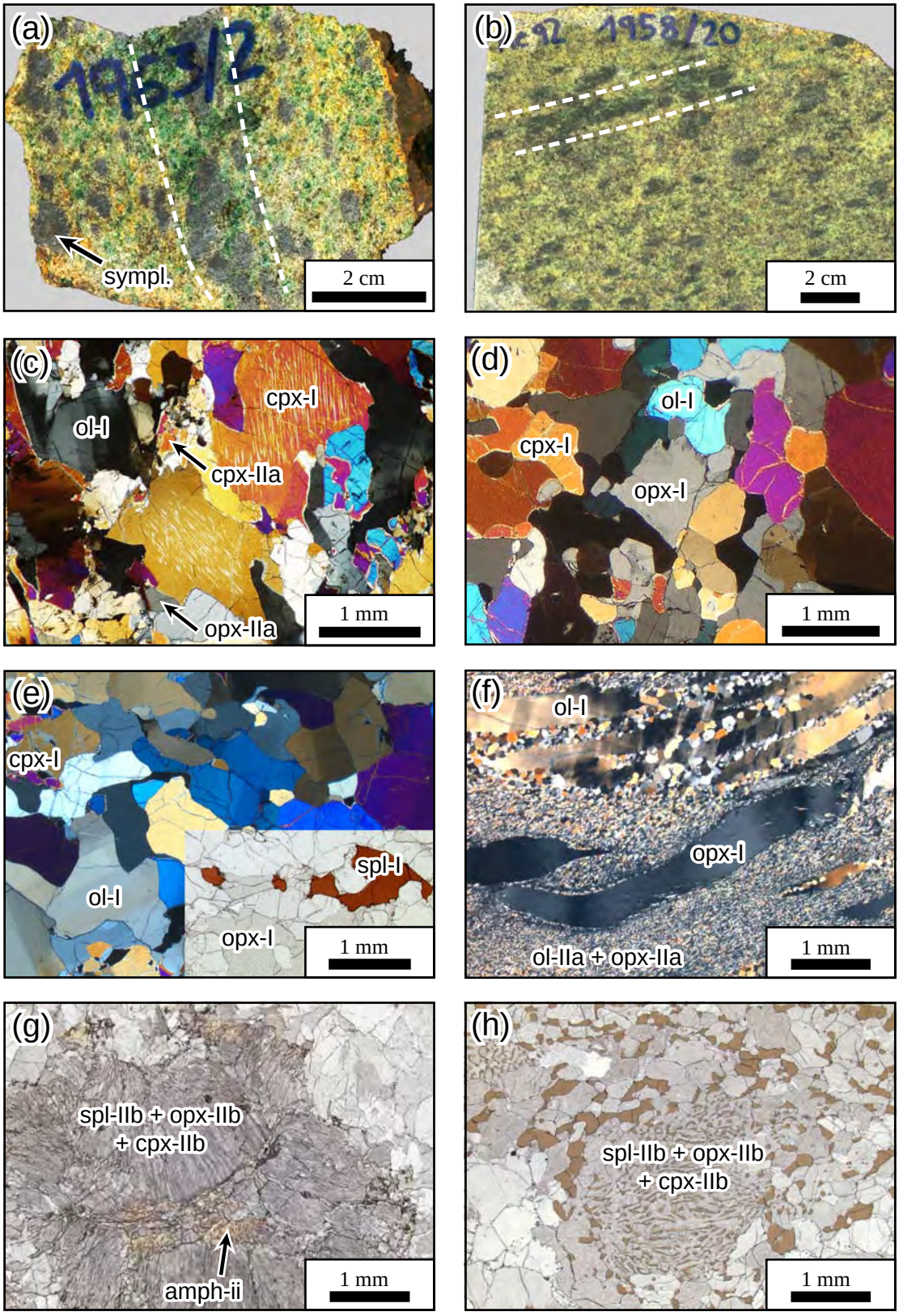
XENOLITH PETROGRAPHY

The textural characteristics of Group I to IV peridotites are illustrated in Fig. 2.2a-h. Most samples are characterised by texturally distinct generations of minerals. They are, however, not necessarily different in terms of composition. In the following, first generation grains (suffix 'I') are either porphyroclasts or form a totally equilibrated texture. Second generation grains are either neoblasts in porphyroclastic samples ('IIa'), or are associated with spl-opx-cpx symplectites/clusters ('IIb').

Group I: porphyroclastic (grt)-spl lherzolite

These coarse-grained rocks contain large porphyroclasts (~1.5-3.5 mm) of kinked olivine (ol-I), orthopyroxene (opx-I) and clinopyroxene (cpx-I) with very irregular, ragged to lobate grain boundaries (Fig. 2.2c). Indications of dynamic recrystallisation (subgrain formation, grain boundary migration) are common. The cores of clinopyroxene porphyroclasts contain exsolution lamellae of orthopyroxene (Fig. 2.2c) which are, in some cases, bent, indicating that exsolution occurred before or during deformation. Clinopyroxene lamellae within opx-I are rarely observed and only very small. Exsolutions in opx-I appears to be related to deformation as

Fig. 2.2. *Photographs (a-b) and photomicrographs (c-h) of peridotite xenoliths from Marsabit:* ***(a)*** *rock slice of Group I (grt)-spl lherzolite (Ke 1963/2); note heterogeneous distribution of symplectite (grey) and clinopyroxene (dark-green); dashed lines denotes diffuse layering parallel to the foliation indicated by the ovoid shape of the symplectites;* ***(b)*** *rock slice of Group II recrystallised (grt)-spl lherzolite (Ke 1958/20; dashed lines indicate layering parallel to the foliation);* ***(c)*** *Group I porphyroclastic (grt)-spl lherzolite (Ke 1963/2); note orthopyroxene exsolution lamellae in cpx-I;* ***(d)*** *Group II strongly recrystallised (grt)-spl lherzolite (Ke 1958/20); note strain-free grains;* ***(e)*** *Group III porphyroclastic spl harzburgite (Ke 1965/1);* ***(f)*** *Group IV ultramylonitic spl harzburgite (Ke 1961/1);* ***(g)*** *fine-grained symplectite with associated Ti-pargasite (amph-ii) in Group I (grt)-spl lherzolite (Ke 1963/2);* ***(h)*** *coarser grained symplectite in Group II (grt)-spl lherzolite (Ke 1958/20); note coarse-grained clusters mantling symplectite.*


(a)
sympl.
2 cm
(b)
2 cm
(c)
ol-I
cpx-I
cpx-IIa
opx-IIa
1 mm
(d)
ol-I
cpx-I
opx-I
1 mm
(e)
cpx-I
spl-I
ol-I
opx-I
1 mm
(f)
ol-I
opx-I
ol-IIa + opx-IIa
1 mm
(g)
spl-IIb + opx-IIb
+ cpx-IIb
amph-ii
1 mm
(h)
spl-IIb + opx-IIb
+ cpx-IIb
1 mm

lamellae are typically confined and oriented normal to kink-bands. Recrystallised neoblasts (ol-IIa, opx-IIa, cpx-IIa and spl-IIa) are of smaller size (~0.25-0.50 mm) and form domains adjacent to first-generation porphyroclasts. The second generation grains are characterised by a lack of exsolution lamellae and a smaller, but nevertheless observable, degree of deformation.

The former presence of garnet is indicated by very fine-grained spinel-orthopyroxene-clinopyroxene symplectites (spl-IIb, opx-IIb, cpx-IIb; Fig. 2.2g) forming round to ovoid aggregates. Such features are often described in mantle-derived peridotites and are interpreted to result from the garnet break-down reaction grt + ol = opx + cpx + spl (e.g., Reid & Dawson, 1972; Wallace, 1975; Henjes-Kunst & Altherr, 1992; Morishita & Arai, 2003a; Altherr *et al.*, in preparation). All Group I samples are characterised by very high clinopyroxene and garnet contents (Table 2.1). On hand-specimen scale, clinopyroxene and symplectites together form layers or diffuse domains, alternating with more olivine-rich domains (Fig. 2.2a).

Abundant Ti-pargasite and rare phlogopite indicate that there has been at least one metasomatic event. Texturally, Ti-pargasite occurs either as large grains which are in textural equilibrium with the surrounding peridotite matrix (amph-i), or associated with spl-IIb around and within symplectites (amph-ii; Fig. 2.2g); or as small domains replacing the rims of cpx-I and IIa (amph-iii). Large amph-i grains are sometimes associated with strongly deformed phlogopite and may contain sulfide inclusions.

Group II: recrystallised (grt)-spl lherzolite

In contrast to Group I, the peridotite xenoliths of Group II are characterised by statically recrystallised, typically strain-free grains forming 120° triple junctions (Fig. 2.2d). As in Group I, spl-opx-cpx symplectites indicate the former presence of garnet. However, they are more coarse-grained and the vermicular symplectite texture is often mantled by coarse spinel and pyroxene grains (Fig. 2.2h). A more or less gradual transition between the porphyroclastic textures of Group I and those of Group II was observed. Less recrystallised samples still contain rare deformed porphyroclasts, whereas strongly recrystallised xenoliths show annealed textures with granuloblastic grains of equant size. Most Group II samples show a foliation defined by elongated symplectites or clusters clearly visible in rock slices (Fig. 2.2b). Sample Ke 1958/13 (less recrystallised) shows a weak tabular fabric. Evidence of modal metasomatism is absent, and thus this group is virtually anhydrous.

Group III: porphyroclastic spl harzburgite

Group III xenoliths are texturally similar to Group I, but contain more olivine and less clinopyroxene. A relation to Group I is further testified by the presence of very rare spl-opx-cpx symplectites, indicating that garnet was also present in this group. Exsolution lamellae in pyroxenes are generally absent. Group III rocks contain large holly-leaf textured spinel (spl-I; Fig. 2.2e), which was never observed in Group I.

In some samples, modal metasomatism has produced very complex microtextures which overprint the primary peridotite mineral assemblage. These are mainly characterised by green, Ti-poor amphibole, phlogopite, ± graphite, ± apatite, forming clusters around primary spinel or veinlets (see also Chapter 3). These assemblages are then partly replaced by pockets of silicate glass associated with microlites of clinopyroxene, olivine and chromite. Compositional data of the silicate glass and of the microlites indicates that their formation is not related to interaction of the xenolith with its host lava (see Chapter 3).

Group IV: mylonitic spl harzburgite

Group IV xenoliths comprise highly deformed spl lherzolite and harzburgite

showing a pronounced foliation (Fig. 2.2f). Xenolith Ke 1961/1 exhibits an ultramylonitic texture, characterised by porphyroclasts (ol-I, opx-I, cpx-I and spl-I) forming highly strained ribbons and stringers (up to ~ 1 cm long; Fig. 2.2f). In contrast, neoblasts (~0.5 -10 μm in size) are completely strain-free with perfect polygonal shapes and 120° triple junctions (Fig. 2.2f). Larger neoblasts are exclusively olivine, recrystallised around olivine porphyroclasts. The more fine-grained matrix consists of ol-IIa + opx-IIa (ratio about 9:1) and only very rare spl-IIa and cpx-IIa. Clinopyroxene porphyroclasts contain relatively thick orthopyroxene and spinel lamellae (> 5 μm), whereas orthopyroxene clasts contain only thin (< 1 μm) but very abundant clinopyroxene (+ spinel) lamellae. Exsolution likely occurred prior to the onset of deformation because lamellae in orthopyroxene are strongly curved.

COMPOSITION OF MINERALS

Major elements

Representative compositions of olivine, orthopyroxene, clinopyroxene, spinel, amphibole, and phlogopite are given in Tables 2.2-5 and in Appendix A3. Results from re-integration of symplectites and exsolved pyroxenes are given in Table 2.6.

Olivine and spinel

Mg-numbers [100*Mg/(Mg+Fe^{2+})] of first generation olivine (Table 2.2) are ~89-90 in Group I and Group II xenoliths. One sample of Group II contains olivine with lower Mg-numbers (86-88; Table 2.2). Olivine from Group III xenoliths has Mg-numbers of ~91-92. Mg-numbers in olivine from the two Group IV samples are high in the harzburgite (Ke 1961/1; ~91-93), and somewhat lower in the lherzolite (Ke 1968/1; ~89-90). CaO contents are low in Group I, III and IV (generally < 0.05 wt%), and slightly higher in Group II (0.05-0.19; and up to 0.3 wt% in Ke 1958/6; see Table 2.2).

Spinel compositions are given in Table 2.2 and the variation with respect to Mg-numbers and Cr-numbers [100*Cr/(Cr+Al+Fe^{3+})] is illustrated in Fig. 2.3.

Orthopyroxene

All analysed samples contain enstatite-rich orthopyroxene with Mg-numbers ranging from ~90 to 93 (Table 2.3). Al_2O_3 contents are quite variable (Fig. 2.4a), mainly due to mineral zoning (see descriptions below). The highest Al_2O_3 contents, together with relatively high CaO contents are found in strongly recrystallised Group II samples (Fig. 2.4a).

Clinopyroxene

Clinopyroxene from all samples are chromian diopsides (Table 2.4). The compositional variation between the different groups is shown in Fig. 2.4b and c, showing largely negative correlations between Mg-numbers and TiO_2 contents, and between CaO and Al_2O_3 contents, with highest Al_2O_3 and TiO_2 contents in Group II clinopyroxene (at relatively low Mg-numbers). In contrast, clinopyroxene from Group III and IV have lower Al_2O_3 and TiO_2 contents at higher Mg-numbers. Group I clinopyroxene is of intermediate composition. Reintegration of exsolved orthopyroxene in cpx-I from Group I slightly decreases Ca contents and Mg-numbers (Table 2.6; Fig. 2.4b and c).

Amphibole and phlogopite

Amphiboles from Group I xenoliths are Ti-pargasites (Table 2.5) with TiO_2 contents of 1.52 – 3.68 wt%. Mg-numbers (88.3-90.2) are similar to those of first generation olivine and orthopyroxene. Large amph-i grains are enriched in K_2O (0.74 – 1.34 wt%), whereas amph-ii and -iii has lower K_2O contents. Group I phlogopite composition is typical for upper mantle micas (e.g., Delaney *et al.*, 1980; Ionov *et al.*, 1997)

Table 2.2: Major element composition of olivine and spinel (representative analyses)

	OLIVINE							SPINEL									
Group	**I**	**I**	**II**	**II**	**III**	**IV**	**IV**	**I**	**I**	**I**	**II**	**II**	**III**	**III**	**III**	**IV**	**IV**
	ol-I	**ol-I**	**ol-I**	**ol-I**	**ol-I**	**ol-I**	**ol-I**	**spl-IIa**	**spl-IIa**	**spl-IIb**	**spl-I**	**spl-IIb**	**spl-I**	**spl-I**	**spl-I**	**spl-I**	**spl-I**
sample	1965/4	1963/2	1958/6	1958/20	1965/1	1961/1	1968/1	1965/4	1960/2	1965/4	1958/20	1959/24	781/6	1965/1	1965/1	1961/1	1961/1
location	core	core	core	core	core	core	core	core	core	sympl	core	cluster core	core	core	rim	core	rim
SiO_2	41.07	40.90	40.03	40.75	41.17	41.48	41.19	0.01	n.d.	0.04	0.06	0.04	n.d.	n.d.	n.d.	n.d.	n.d.
TiO_2	n.d.	n.d.	n.d.	n.d.	0.02	n.d.	0.03	0.02	0.06	0.06	0.19	0.18	0.06	0.11	0.05	0.02	0.01
Al_2O_3	0.02	0.03	0.07	0.05	n.d.	n.d.	n.d.	57.50	51.51	63.40	56.97	53.62	52.24	39.41	41.71	43.34	54.70
Cr_2O_3	n.d.	n.d.	0.05	n.d.	n.d.	0.01	0.02	10.80	17.62	4.36	8.99	12.93	15.58	30.24	27.61	25.42	13.54
Fe_2O_3	-	-	-	-	-	-	-	0.93	0.72	0.81	3.36	3.08	2.07	0.87	1.23	0.92	1.44
FeO	10.33	10.20	11.75	10.19	8.04	7.48	9.37	9.55	10.72	8.62	7.69	8.26	8.77	11.12	10.10	11.50	8.06
MnO	0.13	0.15	0.16	0.14	0.12	0.14	0.09	0.04	0.18	0.16	0.16	0.13	0.12	0.16	0.16	0.21	0.15
NiO	0.34	0.37	0.35	0.35	0.37	0.43	0.35	0.35	0.33	0.42	0.41	0.45	0.39	0.14	0.13	0.12	0.26
MgO	48.97	48.70	47.06	48.70	50.35	51.12	49.62	20.23	18.89	21.30	21.37	20.65	20.11	17.44	18.29	17.36	20.68
CaO	0.03	0.02	0.19	0.10	0.04	0.01	0.01	n.d.	0.01	0.02	0.02	0.03	0.01	0.02	n.d.	0.01	0.01
Na_2O	0.03	n.d.	0.01	n.d.	0.03	0.03	0.02	n.a.	n.a.	n.a.	n.a.	n.a.	n.a.	n.a.	n.a.	n.a.	n.a.
K_2O	0.02	n.d.	n.d.	n.d.	n.d.	0.01	n.d.	n.a.	n.a.	n.a.	n.a.	n.a.	n.a.	n.a.	n.a.	n.a.	n.a.
ZnO	n.a.	n.a.	n.a.	n.a.	n.a.	n.a.	n.a.	0.14	0.18	0.13	0.03	0.04	0.10	0.15	0.10	0.23	0.29
Total	**100.95**	**100.37**	**99.67**	**100.28**	**100.15**	**100.70**	**100.71**	**99.58**	**100.21**	**99.31**	**99.26**	**99.42**	**99.45**	**99.65**	**99.40**	**99.13**	**99.15**
Stoich.	**4O**	**4O**	**4O**	**4O**	**4O**	**4O**	**4O**	**4O**	**4O**	**4O**	**4O**	**4O**	**4O**	**4O**	**4O**	**4O**	**4O**
Si	1.000	1.001	0.995	0.999	1.000	1.000	1.001	0.000	-	0.001	0.002	0.001	-	-	-	-	-
Ti	-	-	-	-	0.000	0.000	0.001	0.000	0.001	0.001	0.004	0.004	0.001	0.002	0.001	0.000	0.000
Al	0.001	0.001	0.002	0.001	-	0.000	-	1.759	1.613	1.893	1.740	1.661	1.630	1.305	1.366	1.421	1.691
Cr	-	-	0.001	-	-	0.000	0.000	0.222	0.370	0.087	0.184	0.269	0.326	0.672	0.606	0.559	0.281
Fe^{3+}	-	-		-	-	-	-	0.018	0.014	0.015	0.065	0.061	0.041	0.018	0.026	0.019	0.028
Fe^{2+}	0.210	0.209	0.244	0.209	0.163	0.151	0.190	0.207	0.238	0.183	0.167	0.182	0.194	0.261	0.235	0.268	0.177
Mn	0.003	0.003	0.003	0.003	0.002	0.003	0.002	0.001	0.004	0.003	0.003	0.003	0.003	0.004	0.004	0.005	0.003
Ni	0.007	0.007	0.007	0.007	0.007	0.008	0.007	0.007	0.007	0.009	0.009	0.010	0.008	0.003	0.003	0.003	0.006
Mg	1.777	1.777	1.745	1.779	1.824	1.837	1.797	0.783	0.748	0.805	0.825	0.809	0.794	0.730	0.758	0.720	0.809
Ca	0.001	0.001	0.005	0.003	0.001	0.000	0.000	-	0.000	0.001	0.001	0.001	0.000	0.001	-	0.000	0.000
Na	0.002	-	0.001	-	0.001	0.001	0.001	-	-	-	-	-	-	-	-	-	-
K	0.001	-	-	-	-	0.000	-	-	-	-	-	-	-	-	-	-	-
Zn	-	-	-	-	-	-	-	0.003	0.003	0.002	0.001	0.001	0.002	0.003	0.002	0.005	0.006
Total	**3.001**	**2.999**	**3.003**	**3.001**	**3.000**	**3.001**	**2.999**	**3.000**	**3.000**	**3.000**	**3.000**	**3.000**	**3.000**	**3.000**	**3.000**	**3.000**	**3.000**
Mg#	***89.4***	***89.5***	***87.7***	***89.5***	***91.8***	***92.4***	***90.4***	***77.6***	***75.9***	***81.5***	***83.2***	***81.7***	***80.3***	***73.6***	***76.4***	***72.9***	***82.1***
Cr#								***11.2***	***18.7***	***4.4***	***9.6***	***13.9***	***16.7***	***34.0***	***30.7***	***28.2***	***14.2***

Fe_2O_3 in spinel is calculated assuming perfect stoichiometry; n.a.: not analysed; n.d.: not detected; -: not calculated

Table 2.3: Major element composition of orthopyroxene (representative analyses)

	ORTHOPYROXENE																		
Group	**I**	**I**	**I**	**I**	**I**	**I**	**I**	**II**	**II**	**II**	**II**	**III**	**III**	**III**	**IV**	**IV**	**IV**	**IV**
	opx-I	**opx-I**	**opx-I**	**opx-I**	**opx-IIa**	**opx-IIa**	**opx-IIb**	**opx-I**	**opx-I**	**opx-I**	**opx-IIb**	**opx-I**	**opx-I**	**opx-I**	**opx-I**	**opx-IIa**	**opx-I**	**opx-I**
sample	1965/4	1960/2	1963/2	1965/4	1963/2	1960/2	1960/2	1958/13	1958/13	1959/24	1959/24	1965/1	1965/1	781/6	1961/1	1961/1	1968/1	1968/1
location	Al-trough	Al-bulge	Al-bulge	rim	n.blast core	n.blast rim	sympl	core	rim	core	cluster core	core*	rim	core	core	n.blast core	core	rim
SiO_2	56.49	55.28	55.63	57.21	55.89	56.86	56.36	55.51	56.67	54.90	54.47	56.57	57.14	55.76	56.70	57.58	54.91	57.05
TiO_2	0.19	0.07	0.10	0.08	0.11	0.07	0.07	0.08	0.03	0.15	0.14	0.04	0.05	0.10	0.02	0.03	0.11	0.02
Al_2O_3	2.31	4.14	3.25	1.66	3.22	2.13	2.77	3.76	2.89	5.28	5.04	2.65	2.03	3.33	2.57	1.06	3.87	1.61
Cr_2O_3	0.35	0.35	0.27	0.11	0.26	0.25	0.12	0.37	0.24	0.49	0.55	0.43	0.22	0.34	0.42	0.09	0.51	0.15
FeO	6.56	6.35	6.46	6.18	6.48	6.16	6.56	6.34	5.92	6.04	6.03	5.33	5.16	5.49	4.83	5.11	5.88	6.28
MnO	0.20	0.21	0.15	0.14	0.20	0.23	0.20	0.13	0.12	0.13	0.11	0.13	0.13	0.16	0.10	0.16	0.15	0.23
NiO	n.d.	0.01	n.a.	n.a.	0.09	0.08	0.08	0.10	n.a.	0.09	n.a.	n.a.	0.11	0.05	0.07	0.08	0.12	0.01
MgO	34.28	33.19	33.89	34.70	33.44	34.36	33.92	33.57	34.27	32.60	32.45	34.73	34.92	33.89	35.17	35.99	33.47	34.66
CaO	0.43	0.32	0.28	0.24	0.38	0.27	0.30	0.38	0.57	1.06	1.07	0.51	0.32	0.49	0.36	0.18	0.37	0.29
Na_2O	0.05	0.06	0.04	0.03	0.04	0.05	0.04	0.09	0.12	0.15	0.16	0.05	0.07	0.03	0.01	0.01	0.06	0.04
K_2O	n.d.	0.01	n.d.	0.01	n.d.	n.d.	0.01	n.d.	n.d.	0.02	0.01	n.d.	n.d.	n.d.	n.d.	0.03	n.d.	n.d.
Total	**100.85**	**99.97**	**100.05**	**100.39**	**100.11**	**100.46**	**100.41**	**100.32**	**100.83**	**100.90**	**100.02**	**100.43**	**100.15**	**99.63**	**100.28**	**100.32**	**99.45**	**100.34**
Stoich.	**6O**	**6O**	**6O**	**6O**	**6O**	**6O**	**6O**	**6O**	**6O**	**6O**	**6O**	**6O**	**6O**	**6O**	**6O**	**6O**	**6O**	**6O**
Si	1.937	1.909	1.920	1.962	1.928	1.951	1.938	1.911	1.936	1.882	1.883	1.936	1.957	1.925	1.938	1.968	1.905	1.960
Ti	0.005	0.002	0.003	0.002	0.003	0.002	0.002	0.002	0.001	0.004	0.004	0.001	0.001	0.003	0.001	0.001	0.003	0.000
Al	0.093	0.169	0.132	0.067	0.131	0.086	0.112	0.153	0.116	0.213	0.206	0.107	0.082	0.136	0.104	0.043	0.158	0.065
Cr	0.009	0.010	0.007	0.003	0.007	0.007	0.003	0.010	0.006	0.013	0.015	0.012	0.006	0.009	0.011	0.002	0.014	0.004
Fe^{2+}	0.188	0.183	0.186	0.177	0.187	0.177	0.188	0.183	0.169	0.173	0.174	0.152	0.148	0.158	0.138	0.146	0.170	0.181
Mn	0.006	0.006	0.004	0.004	0.006	0.007	0.006	0.004	0.004	0.004	0.003	0.004	0.004	0.005	0.003	0.005	0.004	0.007
Ni	-	0.000	-	-	0.002	0.002	0.002	0.003	-	0.003	-	-	0.003	0.001	0.002	0.002	0.003	0.000
Mg	1.752	1.708	1.743	1.774	1.720	1.758	1.739	1.723	1.745	1.666	1.673	1.772	1.783	1.744	1.793	1.834	1.731	1.775
Ca	0.016	0.012	0.010	0.009	0.014	0.010	0.011	0.014	0.021	0.039	0.039	0.019	0.012	0.018	0.013	0.007	0.014	0.011
Na	0.003	0.004	0.003	0.002	0.002	0.003	0.002	0.006	0.008	0.010	0.011	0.003	0.004	0.002	0.001	0.000	0.004	0.003
K	-	0.001	-	0.001	-	-	0.001	-	-	0.001	0.000	-	-	-	-	0.001	-	-
Total	**4.009**	**4.003**	**4.009**	**4.002**	**4.001**	**4.002**	**4.005**	**4.008**	**4.006**	**4.007**	**4.008**	**4.005**	**4.000**	**4.001**	**4.004**	**4.009**	**4.008**	**4.006**
Mg#	***90.3***	***90.3***	***90.3***	***90.9***	***90.2***	***90.9***	***90.2***	***90.4***	***91.2***	***90.6***	***90.6***	***92.1***	***92.3***	***91.7***	***92.8***	***92.6***	***91.0***	***90.8***

*: analysed with defocused beam to include thin exsolution lamellae; n.a.: not analysed; n.d.: not detected; -: not calculated

Table 2.4: Major element composition of clinopyroxene (representative analyses)

	CLINOPYROXENE																	
Group	**I**	**I**	**I**	**I**	**I**	**I**	**I**	**II**	**II**	**II**	**II**	**II**	**III**	**III**	**III**	**IV**	**IV**	**IV**
	cpx-I	**cpx-I**	**cpx-I**	**cpx-I**	**cpx-IIa**	**cpx-IIa**	**cpx-IIb**	**cpx-I**	**cpx-I**	**cpx-I**	**cpx-I**	**cpx-IIb**	**cpx-I**	**cpx-I**	**cpx-I**	**cpx-I**	**cpx-I**	**cpx-IIa**
sample	1963/2	1965/4	1960/2	1965/4	1963/2	1960/2	1960/2	1958/6	1958/13	1958/20	1958/20	1958/20	781/6	1965/1	1965/1	1961/1	1968/1	1968/1
location	Al-trough	Al-bulge	Al-bulge	rim	n.blast core	n.blast rim	sympl	core	core	core	rim	sympl core	core	core	rim	core	core	rim
SiO_2	53.73	52.24	51.95	52.70	52.89	52.72	52.84	50.84	52.35	51.34	51.46	51.27	52.16	53.52	54.03	53.33	52.14	53.70
TiO_2	0.64	0.81	0.65	0.53	0.66	0.46	0.65	0.67	0.40	0.46	0.50	0.49	0.29	0.12	0.10	n.d.	0.44	0.25
Al_2O_3	5.09	6.65	5.85	5.51	6.44	4.88	5.58	7.13	6.35	7.04	7.05	7.10	5.48	3.41	2.89	2.74	5.90	4.14
Cr_2O_3	0.82	1.15	0.68	0.41	0.95	0.83	0.32	0.85	0.94	1.09	0.72	0.69	1.04	1.34	0.80	0.79	1.02	0.45
FeO	2.47	2.08	1.95	2.02	2.20	2.14	2.12	4.27	2.35	3.24	3.28	3.30	2.29	2.05	1.85	1.47	2.19	2.06
MnO	0.06	0.06	0.09	0.10	0.10	0.06	0.07	0.04	0.06	0.11	0.10	0.10	0.04	0.06	0.08	0.05	n.d.	0.01
NiO	0.04	n.a.	0.05	n.a.	n.a.	n.a.	0.03	n.a.	n.a.	n.a.	n.a.	n.a.	0.02	0.03	0.05	n.d.	0.03	0.03
MgO	15.11	14.75	14.62	15.49	14.30	15.04	15.12	15.92	14.76	16.22	16.42	15.89	15.26	16.06	16.82	16.59	14.46	15.24
CaO	20.79	21.30	21.67	21.46	20.89	21.79	21.98	18.50	20.45	19.16	19.39	19.21	21.60	21.70	22.11	23.70	20.86	21.93
Na_2O	2.07	1.92	1.73	1.56	2.19	1.62	1.60	1.42	2.07	1.39	1.36	1.30	1.50	1.31	1.11	0.85	2.22	1.79
K_2O	n.d.	n.d.	0.04	0.02	n.d.	0.01	0.03	n.d.	n.d.	n.d.	0.01	0.01	n.d.	n.d.	n.d.	n.d.	n.d.	0.02
Total	**100.83**	**100.97**	**99.29**	**99.79**	**100.63**	**99.56**	**100.33**	**99.63**	**99.73**	**100.06**	**100.26**	**99.35**	**99.68**	**99.60**	**99.84**	**99.51**	**99.27**	**99.62**
Stoich.	**6O**	**6O**	**6O**	**6O**	**6O**	**6O**	**6O**	**6O**	**6O**	**6O**	**6O**	**6O**	**6O**	**6O**	**6O**	**6O**	**6O**	**6O**
Si	1.926	1.874	1.895	1.907	1.900	1.918	1.905	1.851	1.897	1.856	1.856	1.864	1.897	1.945	1.956	1.943	1.902	1.949
Ti	0.017	0.022	0.018	0.014	0.018	0.013	0.018	0.018	0.011	0.012	0.013	0.013	0.008	0.003	0.003	-	0.012	0.007
Al	0.215	0.281	0.251	0.235	0.273	0.209	0.237	0.306	0.271	0.300	0.300	0.304	0.235	0.146	0.123	0.118	0.254	0.177
Cr	0.023	0.033	0.020	0.012	0.027	0.024	0.009	0.025	0.027	0.031	0.020	0.020	0.030	0.038	0.023	0.023	0.030	0.013
Fe^{2+}	0.074	0.062	0.059	0.061	0.066	0.065	0.064	0.130	0.071	0.098	0.099	0.100	0.070	0.062	0.056	0.045	0.067	0.063
Mn	0.002	0.002	0.003	0.003	0.003	0.002	0.002	0.001	0.002	0.004	0.003	0.003	0.001	0.002	0.003	0.001	-	0.000
Ni	0.001	-	0.002	-	-	-	0.001	-	-	-	-	-	0.001	0.001	0.001	-	0.001	0.001
Mg	0.807	0.789	0.795	0.836	0.766	0.816	0.813	0.864	0.797	0.874	0.883	0.861	0.827	0.870	0.908	0.901	0.786	0.824
Ca	0.799	0.818	0.847	0.832	0.804	0.849	0.849	0.721	0.794	0.742	0.749	0.748	0.842	0.845	0.858	0.925	0.815	0.853
Na	0.144	0.134	0.122	0.109	0.153	0.114	0.112	0.100	0.145	0.097	0.095	0.092	0.106	0.092	0.078	0.060	0.157	0.126
K	-	-	0.002	0.001	-	0.001	0.001	-	-	-	0.001	0.001	-	-	-	-	-	0.001
Total	**4.009**	**4.015**	**4.014**	**4.010**	**4.009**	**4.010**	**4.011**	**4.016**	**4.016**	**4.015**	**4.018**	**4.006**	**4.016**	**4.006**	**4.008**	**4.016**	**4.023**	**4.013**
Mg#	***91.6***	***92.7***	***93.0***	***93.2***	***92.0***	***92.6***	***92.7***	***86.9***	***91.8***	***89.9***	***89.9***	***89.9***	***92.2***	***93.3***	***94.2***	***95.3***	***92.2***	***92.9***

n.a.: not analysed; n.d.: not detected; -: not calculated

Table 2.5: Representative major element composition of Ti-pargasite and phlogopite

	Ti-PARGASITE							PHLOGOPITE	
Group	**I**	**I**	**I**	**I**	**I**	**I**	**I**	**I**	**I**
	amph-i	**amph-i**	**amph-i**	**amph-i**	**amph-ii**	**amph-ii**	**amph-iii**	**phl**	**phl**
sample	1960/2	1963/2	1963/2	1965/4	1965/4	1963/2	1963/2	1963/2	1963/2
location	core	core	rim	core	within sympl	within sympl.	repl. cpx	core	rim
SiO_2	42.86	43.41	43.82	43.74	43.56	43.94	43.55	38.59	38.74
TiO_2	2.89	2.84	2.75	3.56	2.50	3.40	2.78	4.71	4.76
Al_2O_3	14.45	14.55	14.58	13.69	14.46	13.96	13.61	15.52	15.24
Cr_2O_3	0.51	0.69	0.44	0.71	0.67	0.38	1.03	0.89	0.88
FeO	3.64	3.82	3.58	3.57	3.52	3.58	3.42	3.90	3.92
MnO	0.09	0.09	0.06	0.03	0.07	0.07	0.06	0.01	0.01
NiO	0.22	0.10	0.10	0.10	0.12	0.09	0.07	0.26	0.24
MgO	17.23	16.85	17.53	17.86	18.12	17.57	17.75	21.58	21.90
CaO	11.61	11.21	11.31	11.37	11.59	11.64	11.55	0.04	0.04
Na_2O	3.34	3.56	3.43	3.49	3.57	3.72	3.65	0.94	0.92
K_2O	0.74	1.01	0.74	0.21	0.06	0.13	0.35	9.43	9.15
F	n.a.	0.05	n.d.	0.05	n.d.	0.03	n.a.	n.a.	n.a.
Cl	n.a.	n.a.	n.a.	0.02	0.01	n.a.	n.a.	n.a.	n.a.
H_2O*	2.10	2.09	2.13	2.10	2.13	2.12	2.11	4.23	4.24
Total*	***99.67***	***100.25***	***100.48***	***100.48***	***100.38***	***100.61***	***99.94***	***100.09***	***100.03***
Stoich.	**23 O**	**23 O**	**23 O**	**23 O**	**23 O**	**23 O**	**23 O**	**22 O**	**22 O**
Si	6.110	6.155	6.173	6.161	6.137	6.177	6.178	5.464	5.481
Ti	0.310	0.303	0.291	0.378	0.265	0.359	0.297	0.502	0.506
Al	2.427	2.432	2.421	2.272	2.401	2.314	2.276	2.590	2.541
Cr	0.057	0.078	0.049	0.079	0.075	0.042	0.115	0.100	0.099
Fe^{2+}	0.434	0.453	0.422	0.421	0.415	0.421	0.406	0.462	0.464
Mn	0.011	0.010	0.008	0.004	0.009	0.008	0.007	0.001	0.001
Ni	0.026	0.012	0.012	0.011	0.014	0.010	0.008	0.029	0.027
Mg	3.661	3.561	3.682	3.749	3.805	3.683	3.754	4.555	4.618
Ca	1.773	1.703	1.707	1.716	1.749	1.754	1.756	0.006	0.006
Na	0.923	0.979	0.938	0.952	0.975	1.015	1.004	0.257	0.253
K	0.134	0.183	0.133	0.038	0.012	0.023	0.064	1.703	1.651
F	-	0.021	-	0.022	-	0.011	-	-	-
Cl	-	-	-	0.005	0.002	-	-	-	-
H	2.000	1.979	2.000	1.973	1.998	1.989	2.000	4.000	4.000
Total**	***15.867***	***15.868***	***15.837***	***15.781***	***15.855***	***15.805***	***15.864***	***15.669***	***15.646***
Mg#	***89.4***	***88.7***	***89.7***	***89.9***	***90.2***	***89.7***	***90.2***	***90.8***	***90.9***
Cr#	***2.29***	***3.10***	***2.00***	***3.36***	***3.01***	***1.77***	***4.83***	***3.72***	***3.74***

*: calculated based on stoichiometry; **: corrected for F and Cl; ***: without F, Cl, and H;
n.a.: not analysed; n.d.: not detected -: not calculated

Table 2.6: Calculated garnet and pyroxene compositions obtained from reintegration (for explanations see section 'Analytical methods')

	GARNET *(recalculated)*						**ORTHOPYROXENE** *(EMP scan)*						**CLINOPYROXENE** *(recalculated)*					
Group	**I**		**I**		**I**		**I**		**I**		**IV**		**I**		**I**		**IV**	
	(grt-I)		**(grt-I)**		**(grt-I)**		**opx-I**		**opx-I**		**opx-I**		**cpx-I**		**cpx-I**		**cpx-I**	
sample	1960/2		1963/2		1965/4		1960/2		1963/2		1961/1		1960/2		1963/2		1961/1	
remark	bulk sympl.	*2 σ*	bulk sympl.	*2 σ*	bulk sympl.	*2 σ*	tiny cpx lamellae	*2 σ*	tiny cpx lamellae	*2 σ*	opx+spl lamellae	*2 σ*	opx lamellae	*2 σ*	opx lamellae	*2 σ*	opx+spl lamellae	*2 σ*
SiO_2	41.76	*0.18*	41.50	*0.17*	41.10	*0.35*	56.05	*0.14*	56.22	*0.14*	56.31	*0.49*	53.01	*0.23*	53.83	*0.11*	52.48	*0.00*
TiO_2	0.21	*0.03*	0.24	*0.11*	0.23	*0.14*	0.13	*0.02*	0.16	*0.01*	0.01	*0.01*	0.49	*0.06*	0.64	*0.02*	0.03	*0.19*
Al_2O_3	24.82	*0.40*	25.16	*0.44*	25.54	*0.38*	2.53	*0.05*	2.56	*0.12*	2.79	*0.30*	4.21	*0.07*	4.93	*0.10*	3.37	*0.18*
Cr_2O_3	1.82	*0.14*	1.36	*0.13*	2.20	*0.11*	0.37	*0.05*	0.25	*0.01*	0.55	*0.24*	1.24	*0.06*	0.83	*0.04*	1.17	*0.13*
FeO	5.55	*0.12*	5.25	*0.09*	5.29	*0.10*	6.30	*0.14*	6.57	*0.04*	4.87	*0.18*	2.67	*0.06*	2.81	*0.01*	1.64	*0.05*
MnO	0.13	*0.03*	0.12	*0.03*	0.10	*0.03*	0.17	*0.03*	0.16	*0.02*	0.13	*0.03*	0.09	*0.02*	0.09	*0.01*	0.08	*0.03*
NiO	0.05	*0.00*	0.05	*0.00*	0.00	*0.00*	0.09	*0.04*	0.08	*0.02*	0.10	*0.05*	0.05	*0.03*	0.04	*0.02*	0.01	*0.00*
MgO	19.97	*0.41*	18.70	*0.33*	19.19	*0.39*	33.63	*0.13*	34.09	*0.10*	34.61	*0.39*	16.58	*0.19*	16.16	*0.03*	17.27	*0.00*
CaO	5.39	*0.05*	6.74	*0.20*	6.12	*0.07*	0.53	*0.07*	0.57	*0.11*	0.67	*0.53*	19.75	*0.29*	19.56	*0.33*	22.66	*0.46*
Na_2O	0.40	*0.02*	0.53	*0.12*	0.41	*0.13*	0.05	*0.02*	0.06	*0.01*	0.03	*0.02*	1.63	*0.25*	1.96	*0.20*	0.81	*0.52*
K_2O	0.01	*0.02*	0.01	*0.01*	0.01	*0.01*	0.01	*0.01*	0.01	*0.00*	0.01	*0.01*	0.01	*0.02*	0.01	*0.02*	0.01	*0.01*
Total	***100.11***		***99.64***		***100.19***		***99.86***		***100.72***		***100.08***		***99.73***		***100.84***		***99.52***	
Stoich.	**12 O**		**12O**		**12O**		**6O**		**6O**		**6O**		6 O **6O**		6 O **6O**		6 O **6O**	
Si	2.937		2.937		2.895		1.939		1.931		1.932		1.922		1.926		1.913	
Ti	0.011		0.013		0.012		0.003		0.004		0.000		0.013		0.017		0.001	
Al	2.057		2.098		2.120		0.103		0.104		0.113		0.180		0.208		0.145	
Cr	0.101		0.076		0.123		0.010		0.007		0.015		0.036		0.023		0.034	
Fe	0.326		0.310		0.311		0.182		0.189		0.140		0.081		0.084		0.050	
Mn	0.008		0.007		0.006		0.005		0.005		0.004		0.003		0.003		0.002	
Ni	0.003		0.003		0.000		0.002		0.002		0.003		0.002		0.001		0.000	
Mg	2.094		1.972		2.015		1.734		1.745		1.771		0.896		0.862		0.939	
Ca	0.406		0.511		0.462		0.019		0.021		0.025		0.767		0.750		0.885	
Na	0.055		0.072		0.056		0.004		0.004		0.002		0.114		0.136		0.057	
K	0.001		0.001		0.001		0.000		0.000		0.000		0.000		0.000		0.000	
Total	***8.001***		***8.000***		***8.000***		***4.003***		***4.012***		***4.004***		***4.014***		***4.009***		***4.025***	
Mg#	***86.5***		***86.4***		***86.6***		***90.5***		***90.2***		***92.7***		***91.7***		***91.1***		***95.0***	
Cr#	***4.68***		***3.49***		***5.47***		-		-		-		-		-		-	

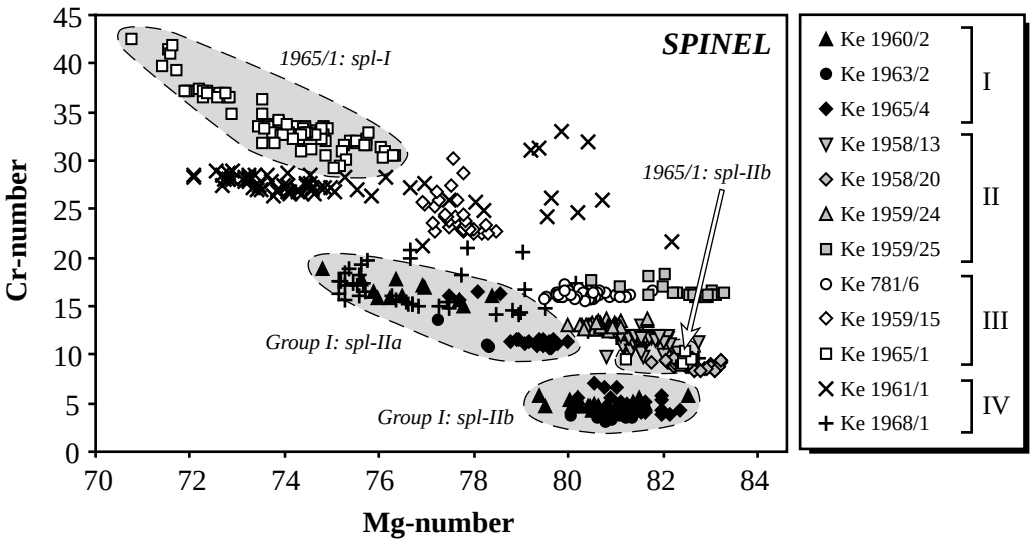


Fig. 2.3. *Variation of Cr# [molar Cr/(Cr+Al+Fe^{3+})] vs. Mg# [molar Mg/(Mg+Fe^{2+})] in spinel. Fe^{3+} calculated assuming perfect stoichiometry. Compositional different spinel generations (when present) are contoured by grey fields.*

with Mg-numbers of ~ 90.9, high Al_2O_3, TiO_2 and Cr_2O_3, as well as considerable Na_2O contents (0.81 – 0.95 wt%; Table 2.5).

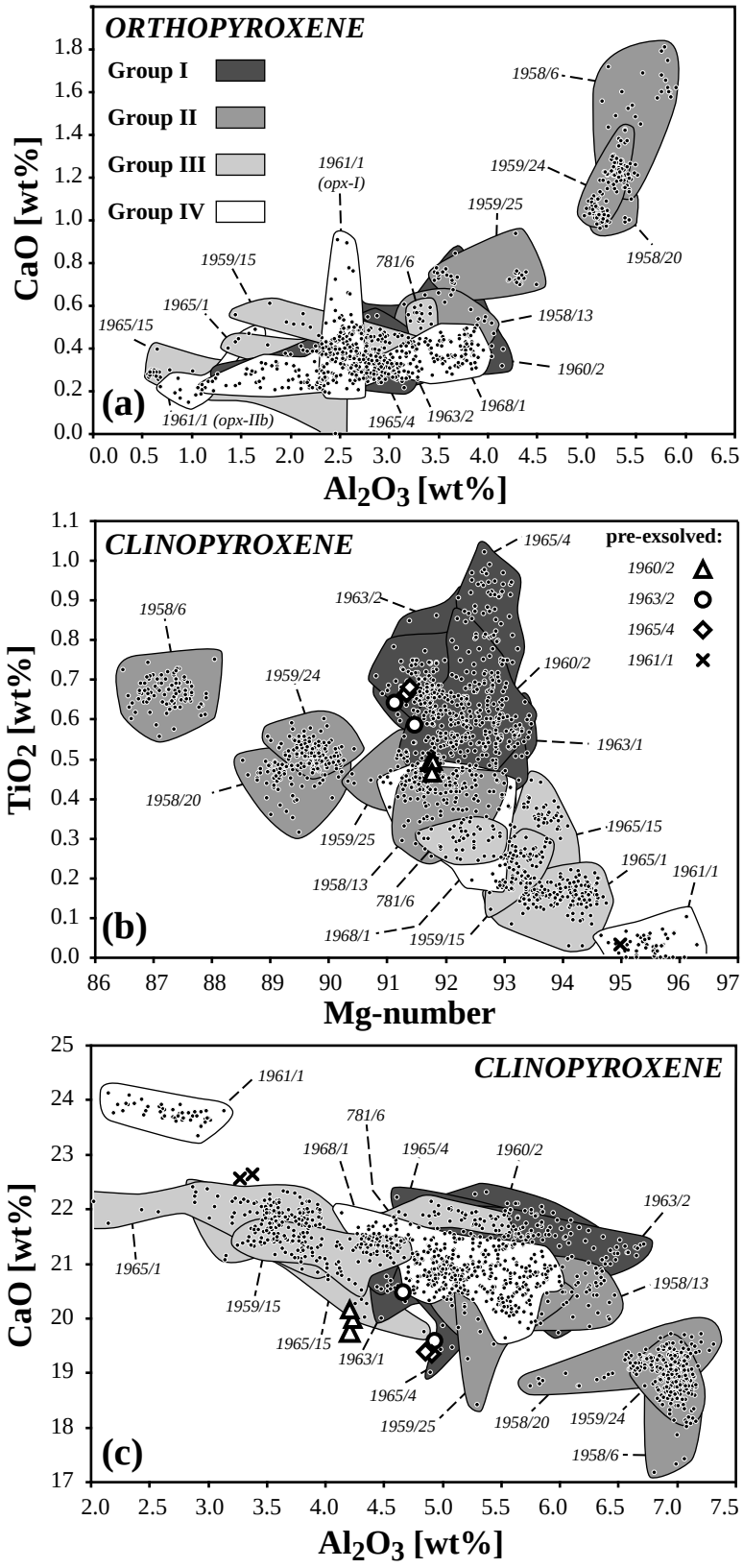
Amphiboles from Group III samples are Ti-poor magnesiokatophorites with high Na_2O and relatively low K_2O contents (3.66-5.65 and 0.23-0.52 wt%, respectively), and high Mg-numbers (91.3-93.0). The associated phlogopite is Ti-poor (≤ 0.5 wt%) as well, and further characterised by very high NaO_2 contents (see Chapter 3).

Major element zoning

Mineral zoning was investigated by microprobe traverses across single grains. Representative zoning patterns for pyroxene are illustrated in Fig. 2.5a-e and 2.6a-e. Representative core and rim values for all analysed samples are given in Appendix A3.

In Group I samples, opx-I typically shows Al zoning patterns with a low-concentration plateau in the core and increasing values toward the rims (Fig. 2.5a). The alumina peak is typically associated with a drastic decrease of concentration within the outermost rim (Fig. 2.5a; hereafter termed the 'Al bulge'). Ca and Cr show plateaus in the cores and outer zones with lower concentrations. Neoblasts (opx-IIa) lack the central Al trough, but show the Al bulge (Fig. 2.5b). Their Ca concentrations correspond to those of opx-I rims and show no zoning. Al and Cr in cpx-I grains show similar patterns as opx-I (Fig. 2.6a-b). Ca and Mg-number profiles are flat or display a slight rimward increase (Fig. 2.6a-c), with rim compositions corresponding to the core composition of cpx-IIa (Fig. 2.6c). Ti and Na patterns are either flat or show slightly decreasing values from cores to rims (Fig. 2.6a-b). Spinel and olivine are not zoned with respect to major elements.

In contrast to Group I, strongly recrystallised (grt)-spl lherzolites (Ke 1958/20 and 1959/24) show much more homogenous grains. Zoning in pyroxenes is generally absent (Fig. 2.5d and 2.6d), but some clinopyroxene grains show Cr contents decreasing from core to rim (Table 2.4 and Appendix A3). There is no difference in composition between larger and smaller grains. Orthopyroxene from the xenolith with a tabular fabric (Ke 1958/13) shows decreasing Al contents from core to rim, accompanied by increasing Ca contents (Fig. 2.5c).


ORTHOPYROXENE
Group I
Group II
Group III
Group IV
1958/6
1959/24
1961/1 (opx-I)
1959/25
1958/20
1959/15
781/6
1965/1
1958/13
1965/15
1960/2
1968/1
(a)
1961/1 (opx-IIb)
1965/4
1963/2
CaO [wt%]
Al2O3 [wt%]
CLINOPYROXENE
pre-exsolved:
1960/2
1963/2
1965/4
1961/1
1965/4
1963/2
1958/6
1960/2
1959/24
1963/1
1958/20
1965/15
1959/25
1965/1
1961/1
1958/13
781/6
1968/1
1959/15
(b)
TiO2 [wt%]
Mg-number
CLINOPYROXENE
1961/1
781/6
1968/1
1965/4
1960/2
1963/2
1965/1
1958/13
1959/15
1965/15
1963/1
1965/4
1959/25
1958/20
1959/24
1958/6
(c)
CaO [wt%]
Al2O3 [wt%]

Al contents in opx-I grains from Group III spl harzburgites decrease from a central plateau towards rims, while Ca and Cr patterns are either flat or decrease towards rims (Fig. 2.5e). With the exception of Al and Cr, which decrease rimwards, clinopyroxene is not zoned (Fig. 2.6e). Large Cr spinel grains (spl-I) show a slight decrease in Cr-number (and increase in Mg-number) from core to rim (not shown).

Al zoning patterns in large opx-I clasts in the Group IV spl lherzolite (Ke 1968/1) show decreasing values from core to rim (Table 2.3). The patterns of all other elements are flat. Both cpx-I and opx-I in the ultramylonitic spl harzburgite (Ke 1961/1) are compositionally homogeneous but contain abundant lamellae of pyroxene (clinopyroxene in opx-I and vice versa) and Cr spinel. Considerable zoning was found in spl-I (Table 2.2) as well as in olivine. Mg-numbers in spl-I increase from core to rim while Cr-numbers exhibit the opposite trend. In the ultramylonitic sample (Ke 1961/1), Cr-numbers again strongly increases within the outermost 20 μm. Ca contents are higher in olivine rims than in cores, whereas Mg-numbers decrease towards the rim.

Trace elements

Representative LA-ICPMS data for all analysed minerals is given in Table 2.7-2.9. Trace element signatures are displayed in Fig. 2.7-2.10. The complete dataset is given in Appendix A4.

Clinopyroxene

Group I cpx-I and IIa are characterised by LREE depletion (Fig. 2.7b) with low $(La/Sm)_N$ values (Fig. 2.8), similar to clinopyroxene of fertile lherzolite (Eggins *et al.*, 1998). Strong compositional zoning was found with respect to the HREEs. Exsolved cores of clinopyroxene have very low HREE contents [$(Eu/Lu)_N \geq 3.18$] whereas rims show flat patterns [$(Eu/Lu)_N$ around 1; Fig. 2.8]. HREEs in the cores of cpx-IIa are similar to cpx-I rims (Fig. 2.7b). Extended trace element patterns (Fig. 2.7a) reveal negative Nb and Ta anomalies. Negative Zr, Hf, and Ti anomalies occur but are often only moderately developed, whereas some rim analyses have marked positive Zr and Hf anomalies (Fig. 2.7a).

Patterns from MREE to HREE in Group II clinopyroxene are flat [$(Eu/Lu)_N = 1.05\text{-}1.75$; Fig. 2.8] and HREE-zoning is not observed. LREEs, on the other hand, show variable patterns ranging from depleted to enriched (Fig. 2.7c-d and 2.8). LREE enrichment is accompanied by higher U and Th abundances. The most enriched signature is observed in clinopyroxene of Ke 1958/13 characterised by its weak tabular fabric (Fig. 2.7c-d). Negative Zr, Hf and Ti anomalies are broadly the same as in Group I clinopyroxene.

The investigated Group III xenolith (Ke 1965/1) contains clinopyroxene variably enriched in LREE's (Fig. 2.7e) with $(La/Sm)_N$ values of the same order of magnitude as in the more recrystallised samples from Group II (Fig. 2.8). The HREEs, on the other hand, show a similar variation as in Group I clinopyroxene, depending on whether they occur close or far away from rare symplectites (Fig. 2.7f). U and Th contents are high (Fig. 2.7e). Negative Zr, Hf and Ti anomalies are more marked than in Group I and II clinopyroxene.

Clinopyroxenes from the mylonitic spl lherzolite (Ke 1968/1) are similar to those of Group

Fig. 2.4. *Major element composition of orthopyroxene and clinopyroxene in the peridotite xenoliths of Marsabit.* ***(a)*** *Al_2O_3 vs. CaO contents of orthopyroxene;* ***(b)*** *Mg# vs. TiO_2 contents of clinopyroxene;* ***(c)*** *Al_2O_3 vs. CaO contents of clinopyroxene. Dots indicate individual analyses while grey-shaded fields attribute them into the four textural groups (I, II, III, IV). Corresponding sample numbers are indicated in italics. Large symbols in* ***(b)*** *and* ***(c)*** *represent re-calculated clinopyroxene compositions prior to orthopyroxene and spinel exsolution (see text for further explanations).*

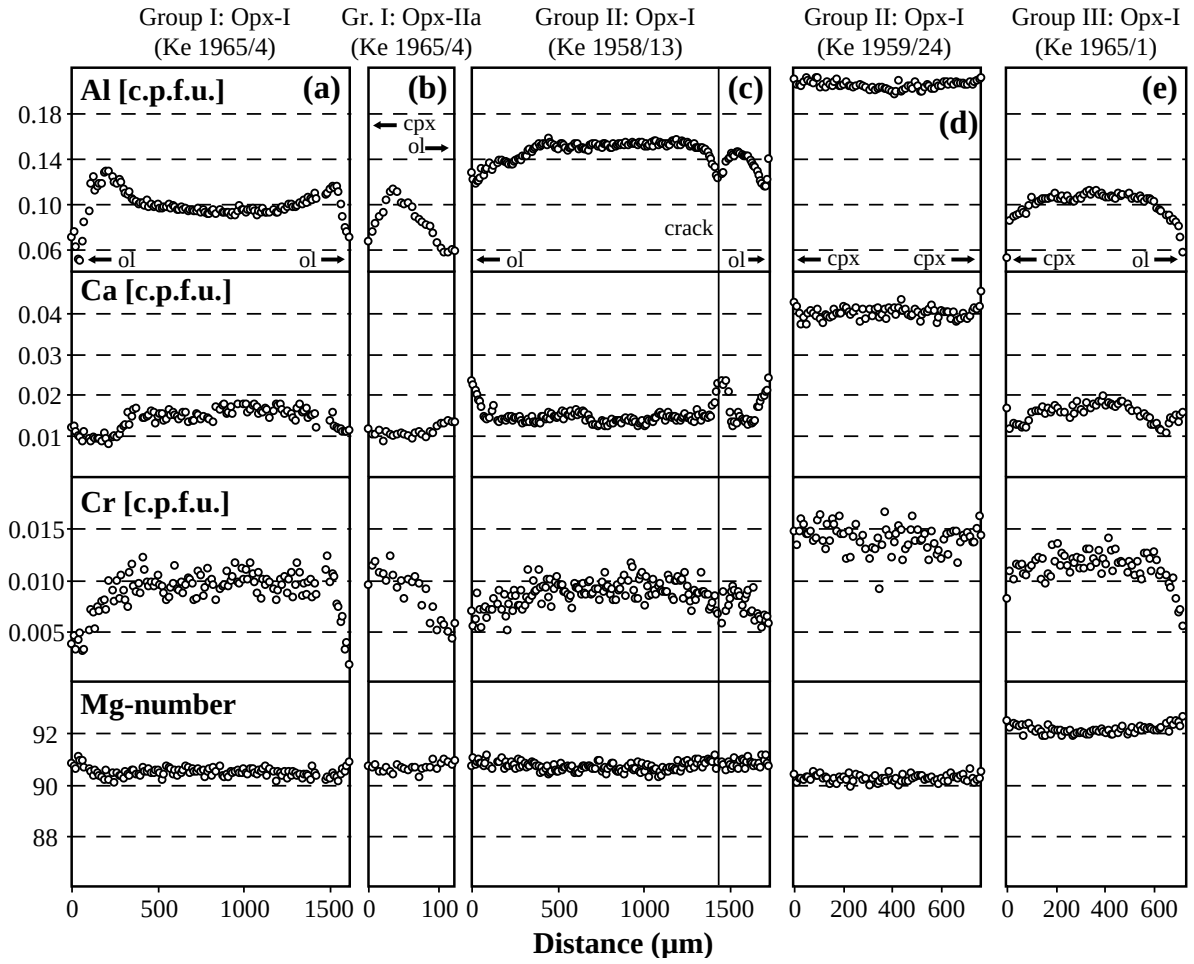


Fig. 2.5. *Major element zoning patterns in orthopyroxene (distance = rim-core-rim; c.p.f.u. = cations per formula unit).* ***(a)*** *opx-I porphyroclast in Ke 1965/4 (Group I);* ***(b)*** *opx-IIa neoblast in Ke 1965/4 (Group I);* ***(c)*** *opx-I in tabular-granuloblastic Ke 1958/13 (Group II);* ***(d)*** *opx-I in equilibrated Ke 1959/24 (Group II);* ***(e)*** *opx-I porphyroclast in Ke 1965/1 (Group III).*

I samples (Fig. 2.7g). REE patterns are convex-upward (Fig. 2.7h), while no compositional differences between porphyroclasts and neoblasts are observed. Trace element characteristics of the ultramylonite (Ke 1961/1) are different (Fig. 2.7g-h). REE patterns are sinusoidal, with LREE abundances strongly fractionated from MREEs (Fig. 2.8). Further, clinopyroxene in Ke 1961/1 is extremely depleted in Ti (<170 µg/g).

Orthopyroxene

Orthopyroxene (Fig. 2.9a-d) from Group I and II have straight REE patterns with positive slopes from LREE to HREE. Group II orthopyroxenes have slightly higher REE concentrations than those from Group I (Fig. 2.9b). Orthopyroxenes from Group III (Fig. 2.9c) show similar patterns. Positive anomalies compared to neighbouring REEs are found for Pb, Hf, Zr and Ti, which is a typical feature of orthopyroxene in upper mantle spl peridotites (Rampone *et al.*, 1991; Eggins *et al.*, 1998). Group IV orthopyroxenes are characterised by lower REE abundances as observed in the associated clinopyroxene (Fig. 2.9d). Orthopyroxene from Ke 1961/1 (ultramylonite) lacks the positive Ti spike (Fig. 2.9d).

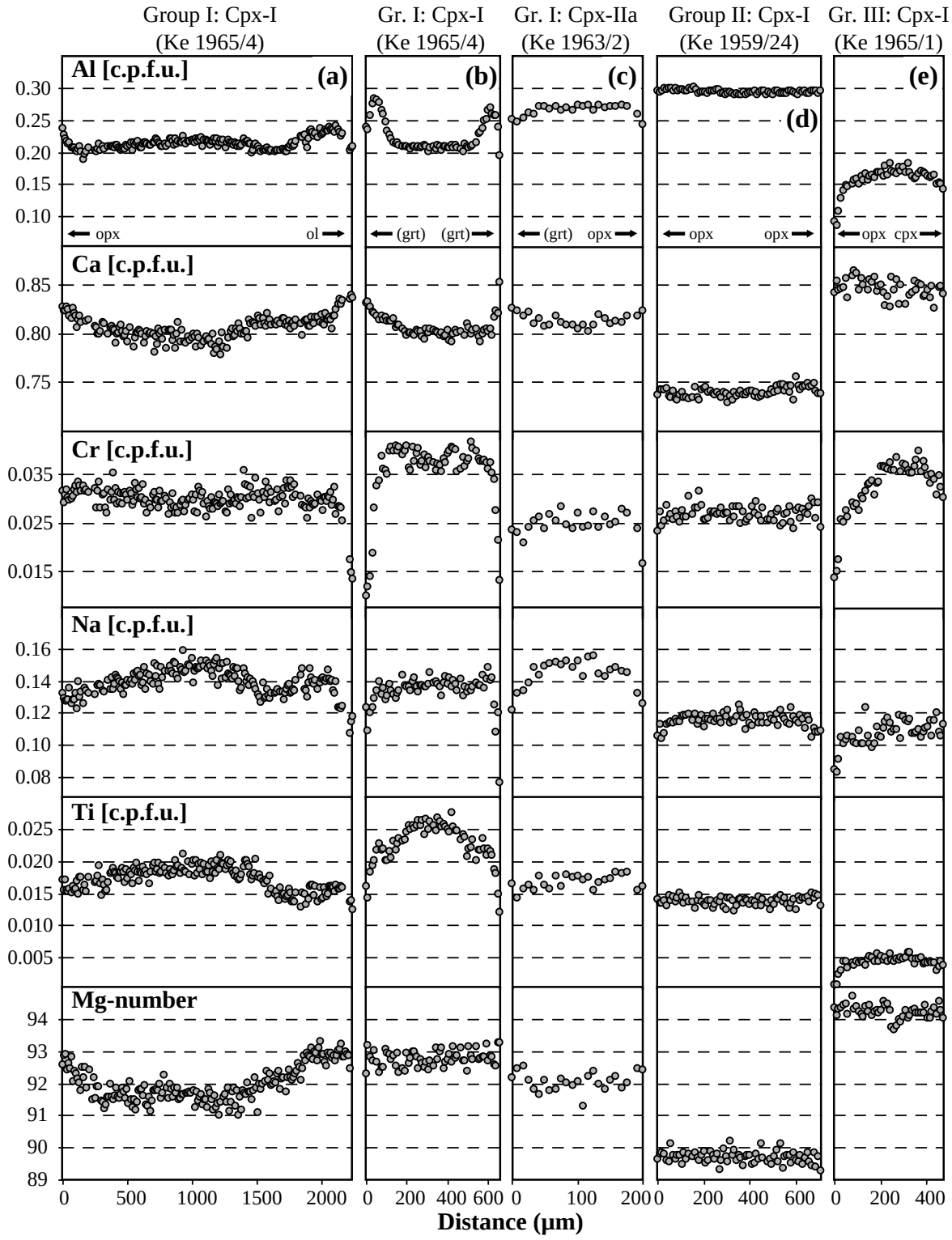


Fig. 2.6. *Major element zoning patterns in clinopyroxene (distance = rim-core-rim; c.p.f.u. = cations per formula unit).* ***(a)*** *cpx-I porphyroclast in Ke 1965/4 (Group I);* ***(b)*** *cpx-I (euhedral inclusion in symplectite) in Ke 1965/4 (Group I);* ***(c)*** *cpx-IIa neoblast in Ke 1963/2 (Group I);* ***(d)*** *cpx-I in equilibrated Ke 1959/24 (Group II);* ***(e)*** *cpx-I porphyroclast in Ke 1965/1 (Group III).*

Table 2.7: Representative trace element composition of clinopyroxene (in µg/g)

	Group I						Group II				Group III		Group IV	
sample	**1963/2**	**1963/2**	**1963/2**	**1963/2**	**1965/4**	**1965/4**	**1958/13**	**1958/20**	**1959/24**	**1959/25**	**1965/1**	**1965/1**	**1961/1**	**1968/1**
location	cpx-I, core	cpx-I, core	cpx-I, rim	cpx-IIa, core	cpx-I, core	cpx-I, rim	cpx-I, core	cpx-I, core	cpx-I, core	cpx-I, core	cpx-I, core	cpx-I, rim	cpx-I, core	cpx-I, core
anal. Nr.	dd08b06	ob29d13	ob29d10	ob29d08	ob28c11	ob28c07	ob29a10	ob29b07	ob28b10	ob28a03	mc22a13	ob28d12	mc22c05	mc22b10
P	30.5	29.0	46.7	35.3	33.3	85.4	53.1	47.4	48.0	25.3	17.9	19.5	11.6	20.3
K	0.86	<0.60	3.20	1.39	1.99	<5.90	4.77	21.7	18.0	<0.68	0.72	<0.78	7.44	0.97
Sc	26.4	23.9	50.9	40.1	27.5	172.7	66.9	55.3	48.9	47.2	141	104	66.2	53.4
Ti	3180	3424	3372	3303	3648	4726	2277	2617	2747	2584	837	998	156	2274
V	326	335	314	326	330	297	259	228	246	294	202	250	178	253
Ni	270	276	231	228	276	277	298	348	364	346	263	290	269	268
Zn	3.86	4.87	3.05	2.72	6.66	3.78	6.18	12.1	14.3	11.0	4.81	6.22	22.1	5.42
Ga	n.a.	8.93	5.34	6.45	8.98	3.14	3.16	4.53	5.00	4.10	1.34	1.54	0.88	3.13
Rb	0.008	<0.009	<0.011	<0.008	<0.010	<0.080	<0.009	0.011	0.012	<0.010	0.010	<0.012	0.043	0.011
Sr	68.6	67.8	57.7	52.8	74.1	50.2	117	113	84.2	53.9	39.6	67.8	33.3	52.6
Y	3.12	3.93	18.8	15.2	3.37	69.6	16.0	14.8	14.6	13.8	41.2	13.1	3.52	5.97
Zr	25.4	21.9	36.1	29.2	23.2	102	40.1	27.4	27.1	19.9	22.3	12.5	21.5	16.9
Nb	0.065	0.105	0.066	0.048	0.23	0.047	0.33	1.20	0.71	0.053	0.072	0.031	0.084	0.038
Cs	<0.004	<0.002	<0.003	<0.003	<0.004	<0.031	<0.002	0.002	0.003	<0.002	0.003	<0.004	0.004	0.006
Ba	<0.021	<0.011	<0.015	0.024	<0.021	<0.108	0.017	0.083	0.057	0.020	0.129	0.255	0.157	<0.014
La	0.99	0.84	0.94	0.81	1.05	0.83	5.99	4.77	1.23	0.82	0.79	4.14	0.20	0.48
Ce	3.62	3.60	3.63	3.16	3.60	2.47	10.4	10.6	3.79	2.54	2.15	5.61	0.917	2.23
Pr	0.75	0.67	0.67	0.59	0.69	0.46	1.18	1.24	0.72	0.48	0.32	0.50	0.29	0.48
Nd	4.66	4.20	4.18	3.99	4.17	3.19	5.61	5.56	4.51	3.20	1.83	2.24	2.97	2.83
Sm	1.42	1.63	1.74	1.74	1.62	2.19	1.76	1.51	1.78	1.40	0.98	0.78	1.84	1.28
Eu	0.58	0.55	0.82	0.75	0.59	0.90	0.82	0.72	0.78	0.66	0.64	0.38	0.55	0.48
Gd	1.42	1.42	2.42	2.14	1.44	6.02	2.11	2.12	2.14	1.93	2.74	1.13	1.01	1.30
Tb	n.a.	0.19	0.48	0.40	0.21	1.54	0.42	0.38	0.43	0.40	0.74	0.25	0.11	0.23
Dy	0.93	1.04	3.20	2.57	0.98	10.8	2.92	2.80	2.70	2.35	6.50	2.09	0.73	1.37
Ho	0.13	0.14	0.74	0.58	0.15	2.89	0.67	0.58	0.57	0.53	1.61	0.51	0.13	0.23
Er	0.27	0.29	2.01	1.76	0.24	8.37	1.93	1.54	1.45	1.35	5.04	1.47	0.41	0.55
Tm	0.037	0.042	0.34	0.24	0.025	1.13	0.24	0.24	0.24	0.20	0.76	0.25	0.059	0.084
Yb	0.19	0.21	2.17	1.78	0.25	6.83	1.87	1.53	1.61	1.35	5.42	1.71	0.52	0.52
Lu	0.017	0.040	0.27	0.26	0.009	1.00	0.24	0.20	0.20	0.20	0.81	0.21	0.075	0.061
Hf	1.10	0.79	1.15	0.99	1.00	3.05	0.96	0.78	0.78	0.68	0.41	0.32	0.34	0.58
Ta	0.017	0.018	0.006	0.012	0.019	<0.033	0.064	0.10	0.050	0.006	0.015	0.009	0.021	0.006
Pb	0.18	0.16	0.17	0.15	0.16	<0.39	0.23	0.098	0.073	0.11	0.38	0.72	0.52	0.085
Th	0.022	0.012	0.009	0.009	0.017	<0.015	0.80	0.15	0.18	0.042	0.014	0.64	0.003	0.005
U	0.004	0.009	0.006	0.006	0.006	0.016	0.191	0.037	0.040	0.013	0.010	0.35	0.007	0.004

n.a.: not analysed

Table 2.8: Representative trace element composition of orthopyroxene, Ti-pargasite, and phlogopite (in µg/g)

	OPX - Group I		OPX - Group II				OPX - Group III		OPX - Group IV		Ti-PARG - Group I			PHL - G.I
sample	**1963/2**	**1965/4**	**1958/13**	**1958/20**	**1959/24**	**1959/25**	**1965/1**	**1965/1**	**1961/1**	**1968/1**	**1963/2**	**1965/4**	**1963/2**	**1963/2**
location	opx-I, core	opx-I, core	opx-I, core	opx-I, core	opx-I, core	opx-I, core	opx-I, core	opx-I, core	opx-I, core	opx-I, core	amph-i	amph-ii	amph-iii	core
anal. Nr.	ob28f06	ob28c10	ob29a04	ob29b12	ob28b07	ob28a05	mc22a12	mc22a09	mc22c11	mc22b13	dd08b13	ob28c05	ob29d04	ob28f09
P	22.3	13.7	20.4	19.8	24.5	16.6	16.7	11.1	12.8	9.39	118	257	137	21.5
K	0.72	0.50	<0.61	<0.47	0.56	<0.58	<0.46	<0.48	<0.50	<0.48	8614	556	4109	82709
Sc	5.17	9.29	10.9	18.9	15.4	14.3	50.9	23.9	18.5	7.08	61.3	139	55.9	2.98
Ti	863	879	443	763	796	555	177	263	56.4	352	15013	12194	17163	23896
V	72.8	69.4	74.3	105	97.7	87.4	48.8	70.2	75.5	68.5	396	270	475	330
Ni	622	562	594	773	760	723	600	592	591	566	745	915	884	1773
Zn	16.0	19.0	22.8	44.0	46.5	37.6	30.0	25.2	23.7	21.1	4.36	13.1	6.77	8.98
Ga	4.19	2.18	2.10	4.65	4.36	3.42	0.71	1.45	0.96	1.96	n.a.	2.28	5.18	6.64
Rb	<0.008	<0.013	<0.011	<0.009	0.002	0.024	<0.007	<0.006	<0.005	<0.005	2.13	0.50	0.73	106
Sr	0.27	0.057	0.094	0.66	0.44	0.10	0.021	0.041	0.095	0.035	157	131	153	33.5
Y	0.38	0.58	0.54	1.25	1.22	0.89	1.64	0.84	0.18	0.12	27.0	112	39.1	0.13
Zr	0.68	0.44	0.90	2.41	2.24	1.04	0.96	0.42	1.15	0.17	36.9	71.5	41.6	2.04
Nb	0.005	<0.004	0.021	0.065	0.044	0.006	0.010	0.012	0.009	0.007	7.70	6.44	2.44	2.66
Cs	<0.002	<0.003	<0.001	<0.002	<0.002	<0.004	<0.001	0.005	<0.003	<0.002	<0.008	<0.093	<0.016	1.29
Ba	0.021	0.018	<0.012	0.026	<0.014	<0.011	<0.016	<0.017	0.039	<0.015	24.2	7.45	12.8	626
La	0.007	<0.003	<0.003	0.021	0.005	0.004	0.002	<0.002	<0.003	<0.002	1.65	1.38	1.70	0.008
Ce	0.022	0.004	0.014	0.10	0.034	0.007	0.008	0.004	0.005	0.002	5.51	3.25	6.19	0.007
Pr	0.002	0.002	0.002	0.015	0.011	0.004	0.005	0.002	0.003	0.002	1.11	0.52	1.09	<0.002
Nd	<0.010	0.011	0.009	0.048	0.030	<0.014	0.008	<0.006	0.015	<0.007	6.66	4.51	7.43	0.015
Sm	<0.006	<0.013	0.021	<0.014	0.054	0.021	<0.011	<0.007	<0.009	<0.015	2.62	3.08	3.20	<0.013
Eu	0.005	0.002	0.006	0.020	0.023	0.004	0.009	0.006	0.009	0.003	1.15	1.75	1.29	0.014
Gd	0.020	0.037	0.021	0.038	0.107	0.031	0.023	0.009	0.022	0.015	3.44	9.24	4.91	<0.015
Tb	0.007	0.007	0.008	0.010	0.015	0.013	0.009	0.008	0.004	0.003	n.a.	2.04	0.87	0.005
Dy	0.048	0.052	0.056	0.172	0.182	0.126	0.162	0.056	0.034	0.013	4.57	17.6	6.27	0.017
Ho	0.011	0.029	0.025	0.047	0.041	0.032	0.062	0.028	0.004	0.006	1.07	4.46	1.56	0.005
Er	0.056	0.057	0.088	0.15	0.16	0.11	0.30	0.14	0.010	<0.005	2.81	11.8	4.29	0.009
Tm	0.008	0.019	0.018	0.036	0.026	0.019	0.066	0.035	0.009	0.003	0.40	1.66	0.61	0.003
Yb	0.090	0.23	0.15	0.29	0.21	0.23	0.69	0.33	0.064	0.025	2.46	10.8	4.16	<0.015
Lu	0.014	0.037	0.035	0.044	0.046	0.037	0.15	0.066	0.013	0.009	0.36	1.56	0.52	0.002
Hf	0.015	0.011	0.045	0.089	0.075	0.028	0.011	0.013	0.022	0.007	1.10	1.65	1.41	0.049
Ta	<0.002	<0.001	<0.002	0.004	0.003	<0.002	<0.001	0.002	<0.002	<0.001	0.15	0.17	0.08	0.13
Pb	0.043	<0.036	0.041	0.033	0.035	0.048	0.021	0.022	0.022	0.014	0.69	<0.93	0.38	0.46
Th	<0.001	0.002	<0.003	0.003	0.002	<0.002	0.002	<0.003	<0.002	0.003	0.012	<0.037	<0.010	0.002
U	0.001	<0.002	0.007	<0.002	0.004	<0.001	0.002	<0.001	<0.002	<0.002	0.008	<0.052	0.015	<0.002

n.a.: not analysed

Table 2.9: Representative trace element composition of olivine and spinel (in µg/g)

	OL - G.I	OL - Group II		OL - Group III		OL - Group IV		SPL - G.I	SPL - Group II		SPL - Group III		SPL - Group IV	
sample	**1963/2**	**1958/20**	**1959/24**	**1965/1**	**1965/1**	**1961/1**	**1968/1**	**1963/2**	**1958/20**	**1959/24**	**1965/1**	**1965/1**	**1961/1**	**1968/1**
location	ol-I, core	ol-I, rim	ol-I, rim	ol-I, core	ol-I, core	ol-I, core	ol-I, core	spl-IIb	spl-I	spl-IIb	spl-I, core	spl-I, core	spl-I, core	spl-I, core
anal. Nr.	ob28f07	ob29b04	ob28b04	mc22a08	mc22a11	mc22c08	mc22b05	ob29d11	ob29b10	ob28b11	ob28d03	mc22a18	mc22c17	mc22b17
Na	14.5	64.8	80.8	17.0	8.46	16.2	6.68	0.50	95.3	3.55	1.19	237	1.91	0.92
Al	21.2	190	213	29.3	30.5	19.1	38.4	341218	307611	306716	246509	222744	264706	290093
P	45	67.5	57.2	26.0	18.4	13.8	30.7	20.7	19.9	19.6	24.2	17.3	18.1	13.2
K	<0.38	<0.36	0.33	0.60	<0.46	0.87	0.58	<112	729	12.4	<81.9	995	<50	<42.9
Ca	121	722	715	185	200	304	33.8	<2.49	2.79	0.32	<1.83	11.9	<1.68	2.32
Sc	0.72	2.91	2.62	2.47	5.19	1.63	0.70	<0.093	0.70	0.58	0.61	2.35	0.38	0.11
Ti	9.23	24.0	36.6	3.25	2.18	1.33	3.26	162	892	1031	560	447	75.1	164
V	1.20	4.16	4.37	1.29	0.86	0.56	0.62	242	363	417	832	540	663	424
Ni	2768	2462	2624	2895	2924	3011	2871	4298	3376	3092	1510	1598	1302	2402
Zn	18.7	57.2	66.5	37.9	49.9	21.4	20.1	1166	764	878	1577	1426	1812	1885
Ga	0.014	0.063	0.11	0.036	<0.01	0.047	0.041	93.7	76.4	90.5	54.3	25.4	23.2	71.2
Rb	<0.004	<0.008	0.002	0.008	<0.005	0.009	0.010	0.056	0.027	0.038	0.061	0.18	0.029	0.042
Sr	<0.002	0.009	0.012	0.004	0.003	0.056	0.006	0.059	0.52	0.037	0.062	0.45	0.095	0.054
Y	0.004	0.071	0.061	0.018	0.047	<0.003	<0.002	<0.008	0.021	0.019	0.023	0.074	0.039	0.024
Zr	0.006	0.034	0.062	0.024	0.028	0.028	0.016	0.078	0.15	0.21	0.38	1.46	0.44	0.29
Nb	<0.003	0.009	0.008	<0.003	0.005	<0.002	<0.002	0.091	0.21	0.21	0.58	0.40	0.32	0.18
Cs	<0.001	0.004	0.001	0.007	0.006	0.003	0.003	<0.013	0.013	0.051	0.073	0.58	0.026	0.046
Ba	<0.014	0.009	0.003	<0.015	<0.019	<0.017	<0.010	<0.045	<0.030	<0.04	0.081	0.31	0.41	0.046
La	<0.001	0.008	0.001	0.003	<0.001	<0.002	<0.003	0.010	0.026	0.029	0.033	0.070	0.036	0.026
Ce	0.001	0.006	<0.001	0.007	<0.002	<0.003	<0.003	0.045	0.20	0.10	0.043	0.18	0.056	0.042
Pr	<0.001	0.001	0.002	0.005	0.002	0.002	0.002	<0.011	0.019	0.016	0.053	0.033	0.029	0.029
Nd	0.004	<0.011	0.002	0.019	<0.009	0.007	<0.006	<0.076	0.060	0.022	<0.033	0.051	<0.023	<0.038
Sm	<0.005	<0.008	0.002	<0.006	<0.006	0.006	<0.007	<0.053	<0.021	0.006	0.077	0.041	0.031	<0.045
Eu	<0.001	<0.003	<0.004	<0.003	<0.002	<0.002	0.003	0.015	0.009	0.031	0.036	0.037	<0.008	0.025
Gd	<0.005	0.006	0.005	<0.006	<0.008	0.006	<0.007	<0.043	<0.021	0.011	<0.021	0.026	<0.043	0.074
Tb	<0.001	<0.001	<0.0008	0.001	<0.001	<0.001	0.004	<0.008	0.005	0.003	0.014	0.016	0.010	0.005
Dy	<0.003	0.012	0.005	0.007	0.004	<0.003	<0.004	<0.026	<0.013	<0.018	0.036	0.019	0.028	<0.013
Ho	0.001	0.003	0.001	0.004	0.003	0.001	<0.001	<0.005	0.009	0.005	0.006	0.031	0.005	0.012
Er	<0.006	0.011	0.010	<0.008	0.007	<0.003	<0.005	<0.044	<0.044	0.009	<0.024	0.066	<0.016	<0.014
Tm	<0.001	0.003	0.004	0.002	0.004	0.001	0.004	<0.004	<0.005	0.014	<0.006	0.020	0.006	0.009
Yb	0.007	0.022	0.021	0.020	0.039	0.006	<0.010	<0.052	<0.020	0.030	<0.030	0.053	<0.044	<0.049
Lu	0.001	0.010	0.007	0.005	0.013	0.001	<0.002	<0.005	0.004	0.012	<0.006	0.016	0.012	0.004
Hf	<0.003	<0.006	0.004	<0.006	0.006	<0.006	<0.004	<0.018	<0.017	0.020	<0.018	0.28	0.053	0.029
Ta	0.002	<0.002	<0.001	0.002	0.003	0.001	0.006	<0.006	0.006	0.015	0.031	0.032	0.011	0.020
Pb	0.035	0.026	0.019	0.019	0.036	0.025	0.018	<0.12	0.24	0.10	0.38	0.72	0.10	0.11
Th	<0.001	<0.001	0.002	0.004	0.002	0.002	<0.001	0.009	<0.008	0.023	0.027	0.045	0.017	0.022
U	<0.001	<0.002	<0.002	0.007	<0.002	0.001	0.002	<0.007	0.012	0.011	0.052	0.072	0.058	0.043

Ti-pargasite and phlogopite

Ti-pargasites from Group I (grt)-spl lherzolite has depleted LREE patterns (Fig. 2.10a). Other characteristics are positive anomalies for Nb, [with $(Nb/Ta)_N$ = 1.76 – 3.15], Sr and Ti, and very strong negative U and Th anomalies. MREE to HREE are similar to those of clinopyroxene in Group I, with amph-i tending towards lower HREE contents than amph-ii and -iii. Further, K-rich amph-i has higher LILE (e.g., Rb, Ba), as well as Pb abundances (Table 2.8; Fig. 2.10a). Group I phlogopite is characterised by very low REE abundances (Fig. 2.10b). In contrast, it is the major repository for the LILEs (Cs, Rb, Ba), and it contains considerable amounts of Nb, Ta, Pb, Sr and Ti (Table 2.8; Fig. 2.10b).

Amphiboles from strongly metasomatised Group III samples are LREE enriched [$(La/Yb)_N$ between 2 and 32; see Chapter 3]. Further, both amphibole and phlogopite are characterised by U-Th enrichment and show marked negative Zr-Hf-Ti anomalies (see Chapter 3).

Olivine and spinel

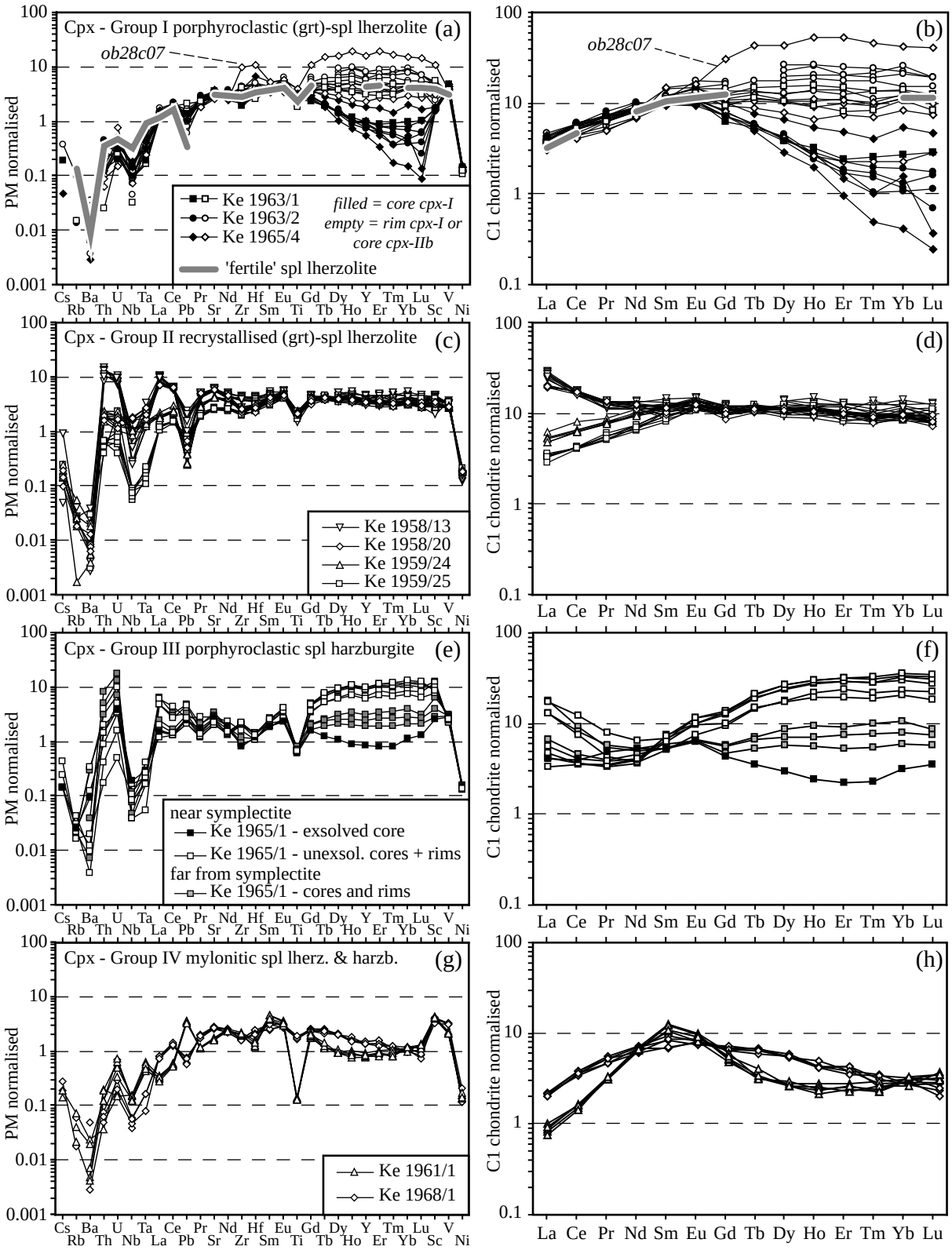
Both olivine and spinel contain incompatible element abundances mostly below the limit of detection (Table 2.9) with the exception of V, Ni, Zn, Ga and Pb and Nb (spinel).

SYNTHETIC SUMMARY OF TEXTURES AND MINERAL COMPOSITIONS

Porphyroclastic peridotites range in composition from lherzolite (Group I) to harzburgite (Groups III and IV). They are characterised by abundant deformation-related microtextures and considerable compositional variation within single xenoliths (intra-grain and between different mineral generations). Textures and compositional features can be interpreted in terms of changing *P-T* conditions, deformation, and variable styles of metasomatism (see discussion below). In Group I rocks, the presence of spl-opx-cpx symplectites, low-Al troughs in the cores of first generation pyroxenes (cpx-I, opx-I), together with exsolution lamellae in the cores of cpx-I are in line with a decompression and cooling event leading to the transition from a former high-pressure/high-temperature (HP/HT) stage to a medium temperature (MT) stage (Fig. 2.11). The formation of symplectites is related to the transition from the garnet- into the spinel-stability field, accompanied by the redistribution of HREEs (and Al) from garnet into pyroxenes (increasing concentrations from core to rims; Takazawa *et al.*, 1996; Glaser *et al.*, 1999; Ionov, 2004). Some cpx-I rims yield anomalously high HREE contents (up to ~50 x chondrite; analysis *ob28c07* in Table 2.7 and Fig. 2.7a-b) that are too high to be in equilibrium with orthopyroxene (apparent $_{Yb}D^{opx/cpx}$ of ~0.02 instead of 0.10-0.20; e.g., Eggins *et al.*, 1998; Bedini & Bodinier, 1999). These rims may be interpreted as selvages overgrown on cpx-I, which inherited the trace element budget of garnet and did not equilibrate with the other peridotite phases (see models proposed by Vannucci *et al.*, 1993, and Takazawa *et al.*, 1996 for former grt websterites from Zabargad, and former grt lherzolites from the Horoman peridotite, respectively].

As spl harzburgites (Group III and IV) contained no or only rare garnet, they lack the Al-trough (Fig. 2.5e and 11), and only large cpx-I grains close to symplectites have preserved the low-HREE signature in their cores. The composition of Group I pyroxene neoblasts corresponds to the high-Al bulge in the porphyroclasts of these rocks (Fig. 2.5b and 2.11), and thus they also recorded the MT stage (Fig. 2.11). Decreasing Al contents towards rims of both porphyroclasts and neoblasts, observed in all porphyroclastic rock types (Group I, III and IV) suggests further cooling to a low temperature stage (MT-LT transition; Fig. 2.11).

In contrast to the porphyroclastic rocks, mineral grains from strongly recrystallised samples (Group II) are generally homogeneous (Fig. 2.11), and there is no compositional


Cpx - Group I porphyroclastic (grt)-spl lherzolite (a)
ob28c07
PM normalised
Ke 1963/1
Ke 1963/2
Ke 1965/4
filled = core cpx-I
empty = rim cpx-I or
core cpx-IIb
'fertile' spl lherzolite
(b)
C1 chondrite normalised
Cpx - Group II recrystallised (grt)-spl lherzolite (c)
Ke 1958/13
Ke 1958/20
Ke 1959/24
Ke 1959/25
(d)
Cpx - Group III porphyroclastic spl harzburgite (e)
near symplectite
Ke 1965/1 - exsolved core
Ke 1965/1 - unexsol. cores + rims
far from symplectite
Ke 1965/1 - cores and rims
(f)
Cpx - Group IV mylonitic spl lherz. & harzb. (g)
Ke 1961/1
Ke 1968/1
(h)
Cs Rb Ba Th U Nb Ta La Ce Pb Pr Sr Nd Zr Hf Sm Eu Ti Gd Tb Dy Ho Y Er Tm Yb Lu Sc V Ni
La Ce Pr Nd Sm Eu Gd Tb Dy Ho Er Tm Yb Lu

variation between different mineral generations. The mineral compositions in Group II samples range between compositions similar to Group I in less recrystallised samples, towards more 'fertile' compositions in strongly recrystallised samples (lower Mg-numbers in olivine and pyroxenes, higher Al in pyroxenes; Fig. 2.4a-c). The Al_2O_3-CaO systematics in pyroxenes of strongly recrystallised Group II samples (Fig. 2.4b-c) is best explained by higher equilibrium temperatures compared to the porphyroclastic rocks (the HT stage; Fig. 2.11). Concerning the relation of Group I and II in terms of their *P-T* evolution, two scenarios are possible: (a) Group II was subjected to decompression (i.e. formation of symplectites after garnet) but, in contrast to Group I, remained at constantly higher temperatures, or (b) Group II was subjected to the same *P-T* evolution as Group I (i.e. decompression and cooling during the HT/HP-MT-LT transition), and experienced a later heating event, overprinting the textural and geochemical record of the earlier event. Several textural and compositional characteristics favour the second scenario. These are: (1) bleb-like or elongated orthopyroxene inclusions in some large clinopyroxene grains in strongly recrystallised samples indicating the presence of former exsolution lamellae; (2) zoning patterns for slow-diffusing elements (e.g., Cr and Al, compared to faster diffusing Ca; Sautter *et al.*, 1988) in opx-I from less recrystallised samples indicating cooling (decreasing Cr and Al from core to rim; Fig. 2.11), followed by heating (rimward increasing Ca; Fig. 2.11); (3) petrographic similarities on the macroscopic scale between Group I and II (i.e. high clinopyroxene and garnet contents and layering; Table 2.1; Fig. 2.1a and b) indicating a common initial bulk composition.

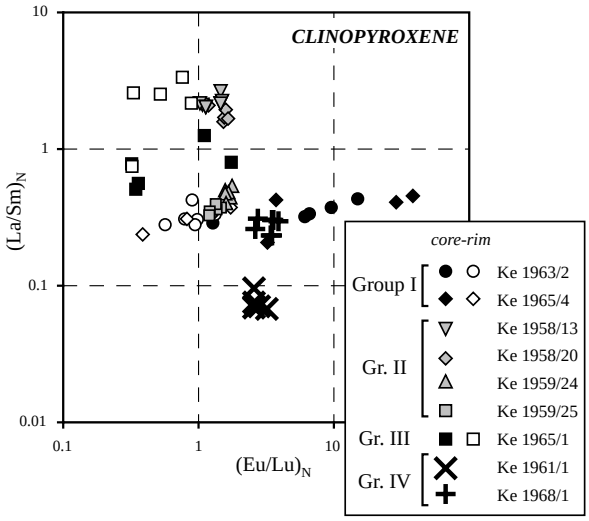


Fig. 2.8. *REE systematics of clinopyroxene in peridotites from Marsabit. $(La/Sm)_N$ and $(Eu/Lu)_N$ are both normalised to C1 chondrite (McDonough & Sun, 1995).*

THERMOBAROMETRY

In the following we present the results of detailed thermobarometric calculations in order to constrain quantitatively the *P-T* evolution during the above presented stages recorded in the lithospheric mantle beneath Marsabit.

Application of geothermobarometers

A large number of thermometers and barometers have been experimentally and empirically calibrated and extensively tested for upper

Fig. 2.7. *Trace element characteristics of clinopyroxene in the peridotite xenoliths of Marsabit. (a-b) Group I porphyroclastic (grt)-spl lherzolite; (c-d) Group II recrystallised (grt)-spl lherzolite; (e-f); Group III porphyroclastic spl harzburgite; (g-h) Group IV mylonitic spl lherzolite and harzburgite. Fertile spl lherzolite [grey line in* ***(a)****] is taken from Eggins et al. (1998). Extended trace element patterns (a, c, e, g) are normalised to primitive mantle, REE patterns (b, d, f, h) are normalised to C1 chondrite (all normalising values from McDonough & Sun, 1995).*

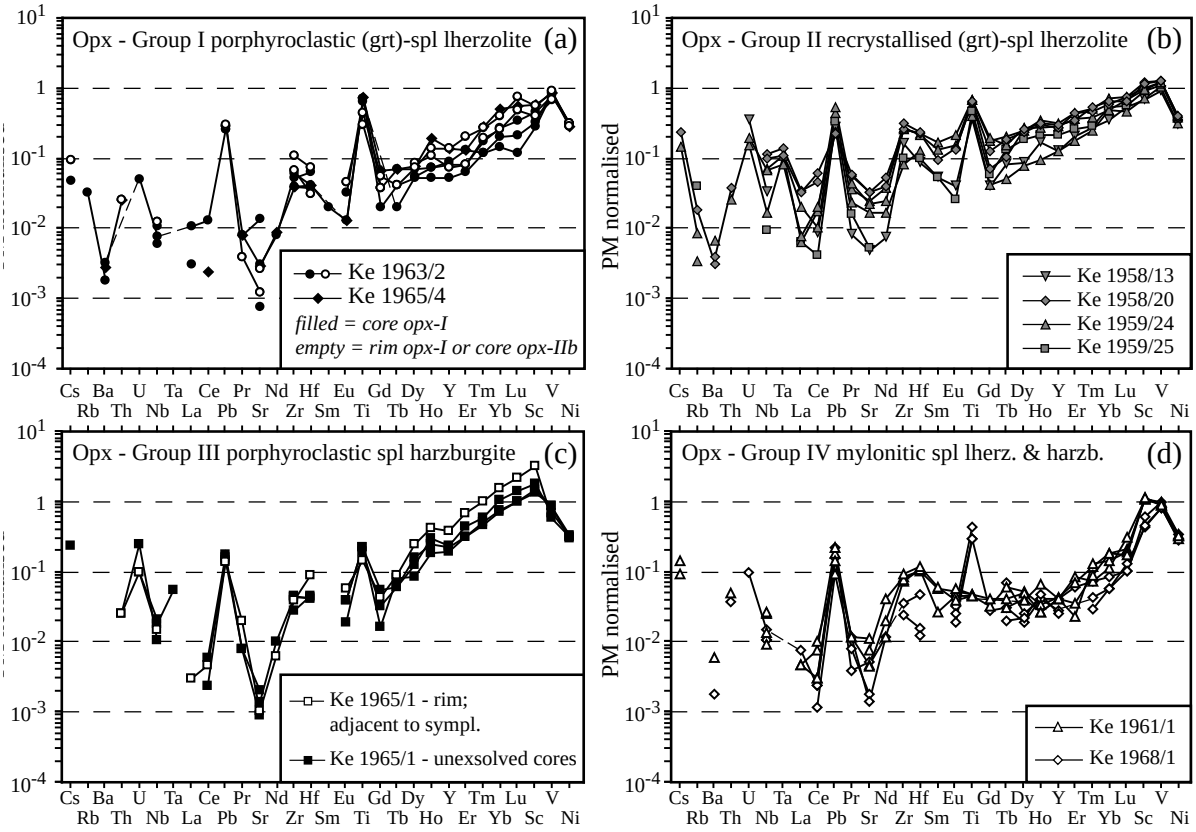


Fig. 2.9. *Trace element characteristics of orthopyroxene in the peridotite xenoliths of Marsabit.* ***(a)*** *Group I porphyroclastic (grt)-spl lherzolite;* ***(b)*** *Group II recrystallised (grt)-spl lherzolite;* ***(c)****; Group III porphyroclastic spl harzburgite;* ***(d)*** *Group IV mylonitic spl lherzolite and harzburgite (values normalised to the primitive mantle values of McDonough & Sun, 1995).*

mantle rocks (Brey *et al.*, 1990; Brey & Köhler, 1990; Werling & Altherr, 1997; Taylor, 1998; Smith, 1999). Thermobarometric calculations in this study were mainly based on the experimentally calibrated thermometers of Brey & Köhler (1990), based on the exchange between enstatite and diopside components in coexisting clino- and orthopyroxene ($T_{2Px\text{-}BK90}$), the Ca content of orthopyroxene in equilibrium with clinopyroxene ($T_{Ca\text{-}opx\text{-}BK90}$), and the partitioning of Na between ortho- and clinopyroxene ($T_{Na\text{-}BK90}$). The barometer based on the Al content in orthopyroxene coexisting with garnet ($P_{Al\text{-}opx\text{-}BK90}$) was only applied to the (grt)-spl lherzolites of Group I, for which the composition of garnet was recalculated using the bulk composition of its breakdown products (fine-grained symplectites). For other samples, minimum pressures for the appearance of garnet were calculated using the spinel composition ($P_{grt\text{-}in\text{-}CWW86}$; Carroll Webb & Wood, 1986). Further temperature constraints were obtained from the Al and Cr contents of orthopyroxene ($T_{Al,Cr\text{-}opx\text{-}WS91}$; Witt-Eickschen & Seck, 1991), the Cr-Al exchange between orthopyroxene and spinel ($T_{opx\text{-}spl\text{-}SS81}$; Sachtleben & Seck, 1981), the Fe^{2+}-Mg exchange between olivine and spinel ($T_{ol\text{-}spl\text{-}B91}$; Ballhaus *et al.*, 1991), and the partitioning of Cr between clino- and orthopyroxene ($T_{Cr\text{-}S99}$; Seitz *et al.*, 1999). Thermobarometric results are given in Table 2.10 and a *P-T* compilation is shown in Fig. 2.12a and b. In order to be consistent with the reconnaissance study of Henjes-Kunst & Altherr (1992), temperatures for assemblages in the stability field of

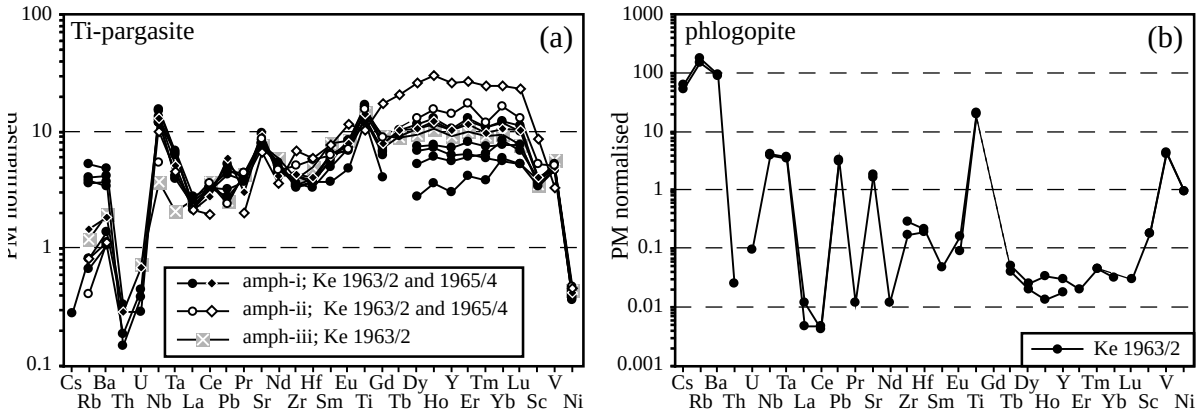


Fig. 2.10. *Trace element characteristics of* ***(a)*** *Ti-pargasite and* ***(b)*** *phlogopite in Group I porphyroclastic (grt)-spl lherzolite from Marsabit (normalised to the primitive mantle values of McDonough & Sun, 1995).*

spinel ('no garnet'; Table 2.10) were calculated assuming a pressure of 1.2 GPa.

General *P-T* evolution of the samples

Thermobarometric calculations yield 966-1075°C at 2.33-2.87 GPa for the initial HP/HT stage (preserved only by Group I rocks). This was followed by cooling (path 1 in Fig. 2.12b) to temperatures of around 800-900 °C (constrained by Group I, III, IV, as well as less recrystallised Group II xenoliths). Maximum pressures after the breakdown of garnet were < 1.5 GPa. The porphyroclastic rocks (Group I, III and IV) further cooled to very low temperatures (LT; around 750°C). Group II peridotites were later subjected to heating (path 2 in Fig. 2.12b) resulting in recrystallisation and equilibration at high temperatures (HT stage; 1000-1200°C). The two proposed *P-T* paths will be now discussed in detail.

Group I, III and IV xenoliths: decompression and cooling

The *P-T* conditions of the HP/HT stage, prior to pyroxene exsolution and garnet breakdown, were estimated by applying the $P_{Al\text{-}opx\text{-}BK90}$ barometer in combination with $T_{2Px\text{-}BK90}$, using the re-integrated composition of clinopyroxene and garnet (Table 2.6). This yields 966-1075 °C at 2.33-2.87 GPa (Table 2.10). Although Fe/Mg ratios in the recalculated garnet were certainly modified during and after the reaction grt-I + ol-I = spl-IIb + opx-IIb + cpx-IIb, this approach is still justified as the $P_{Al\text{-}opx\text{-}BK90}$ barometer does not strongly depend on the garnet composition (Altherr *et al.*, in preparation). We consider $T_{2Px\text{-}BK90}$ based on the re-integrated cpx-I cores to yield relatively accurate results, although the pyroxene's recalculated cores are most likely out of equilibrium with respect to Ca. This is shown in Fig. 2.13, where the Ca content of re-calculated opx-I and cpx-I is compared to the experimentally determined equilibrium partitioning at different pressures (Brey *et al.*, 1990). However, the Ca content of a hypothetical orthopyroxene in equilibrium with the recalculated cpx-I (Fig. 2.13; at 2 GPa similar to that obtained for the HP/HT stage) would yield $T_{Ca\text{-}in\text{-}opx\text{-}BK90}$ of ~1000-1100 °C. This is in good agreement with the above presented results (966-1075 °C) and shows that $T_{2Px\text{-}BK90}$ depends mostly on the Ca content in the clinopyroxene.

Temperatures from $T_{Ca\text{-}opx\text{-}BK90}$ using the measured Ca contents in the cores of Group I opx-I are consistently lower (819-909 °C) than those based on two-pyroxene thermometry. Similar temperatures (differing by less than ~25

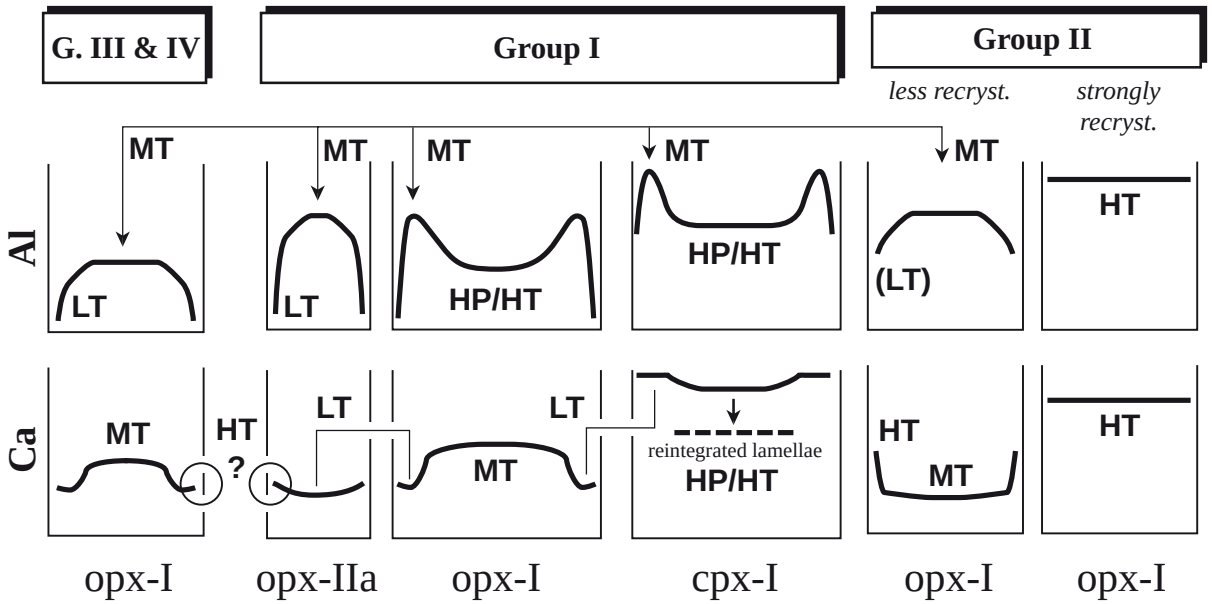


Fig. 2.11. *Interpretation of the observed Al and Ca zoning patterns in pyroxenes of the peridotite xenoliths from Marsabit in terms of changing P-T conditions. HP/HT: high-pressure / high-temperature stage; MT: medium-temperature stage; LT: low-temperature stage; HT: high-temperature stage (for further explanations see text).*

°C within each sample) are obtained by $T_{Al,Cr\text{-}opx\text{-}WS91}$, based on the Al and Cr contents of the high Al bulge of opx-I and of the cores of opx-IIa neoblasts (827-929 °C; Table 2.10). Therefore, we interpret the Ca plateau in opx-I (Fig. 2.5a) to reflect re-equilibration during the MT stage (Fig. 2.11 and 2.12b), i.e., the *P-T* conditions after cooling and decompression. The fact that Al and Ca contents in the opx-I cores represent different *P-T* stages may be explained by the faster diffusion of Ca in pyroxenes compared to Al or Cr (Sautter *et al.*, 1988; Witt-Eickschen & Seck, 1991). Temperature estimates based on the core composition of the neoblasts (opx-IIa and cpx-IIa) give the same temperature range (MT stage), in agreement with the hypothesis that deformation and recrystallisation occurred after and/or during the HP/HT-MT transition.

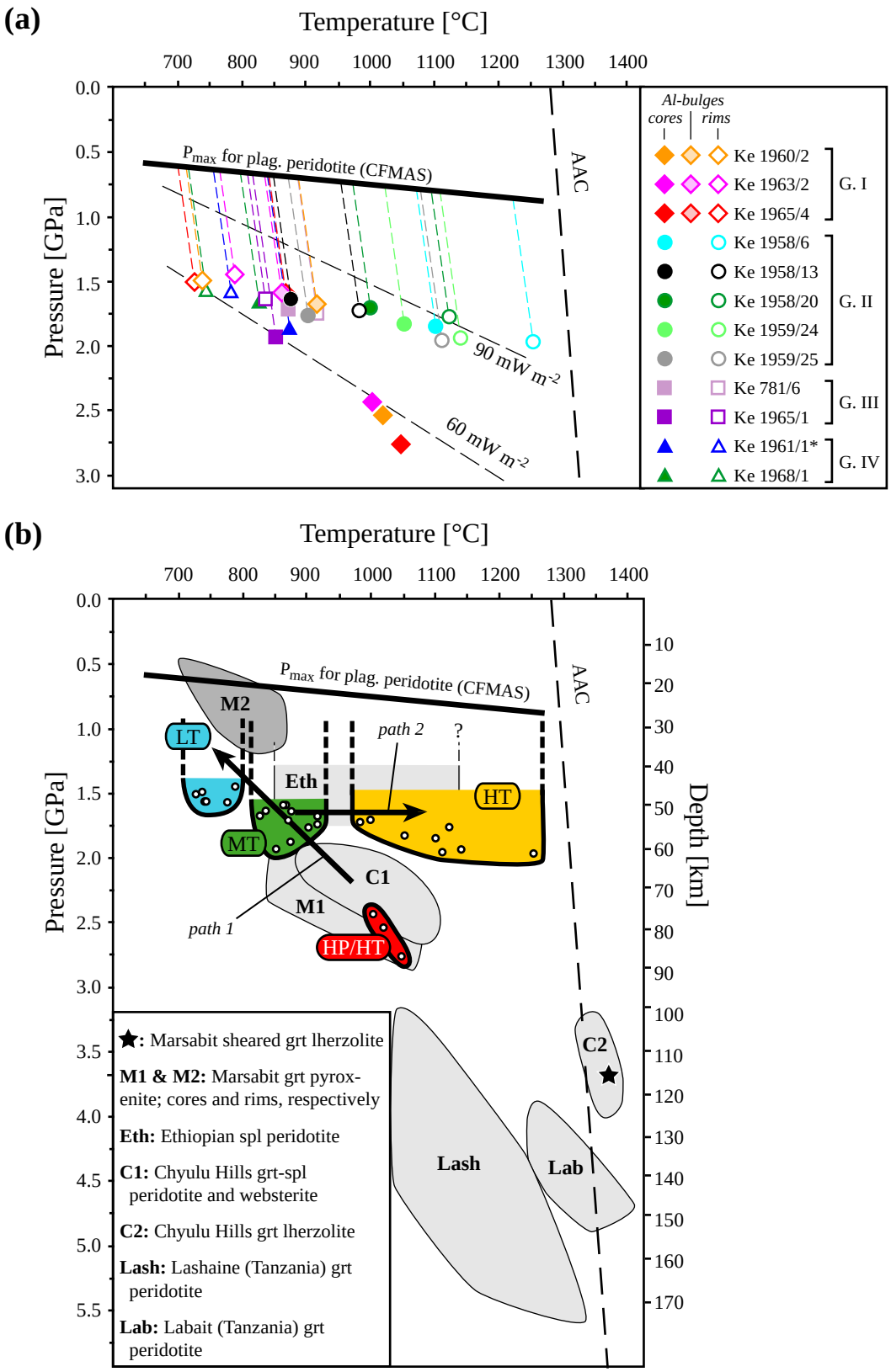
The MT stage is, besides in Group I rocks, also recorded in Group III and IV spl peridotites (e.g., the high Al and Ca plateaus in Group III opx-I; Fig. 2.5e and 2.11). Thermometers applied to the core composition of opx-I, cpx-I, ol-I and spl-I of most Group III and IV samples yield temperatures between 750 and 900 °C (Table 2.10). As cpx-I in Group III generally lacks exsolution lamellae, no information on an eventual higher temperature stage can be obtained. Indications for a former equilibrium at higher pressures can, however, be inferred in Group III samples from the presence of rare symplectites, and from the low HREE contents in some large cpx-I porphyroclasts (e.g., xenolith Ke 1965/1; Fig. 2.7f). This indicates a similar *P-T* evolution of Group I and III samples (i.e. transition from HP/HT to MT).

In addition, all pyroxenes from Group I, III and IV indicate further cooling to a LT stage, as shown by decreasing Al contents towards rims (Fig. 2.5, 2.6 and 2.11). This is supported by lower Ca contents in the rims of large opx-I porphyroclasts (both Group I and III; Fig. 2.5a and e). The ultramylonitic Group IV sample (Ke 1961/1) lacks zoning but cpx-I contains abundant spinel and orthopyroxene lamellae, indicating cooling as well. The degree of cooling may be quantified with the $T_{Al,Cr\text{-}opx\text{-}WS91}$ thermometer. From the Al-bulges to the rims in Group I (Ke

Table 2.10: Results of *P-T* calculations for peridotite xenoliths from Marsabit (*P* in GPa, *T* in °C)

	garnet stability field		***no garnet (temperatures at $P_{assumed}$ = 1.20 GPa)***							
	$T_{2Px\text{-}BK'90}$ / $P_{Al\text{-}opx\text{-}BK'90}$		$P_{grt\text{-}in\text{-}CWW86}$	$T_{2Px\text{-}BK90}$	$T_{Ca\text{-}opx\text{-}BK90}$	$T_{Na\text{-}px\text{-}BK90}$	$T_{Cr\text{-}S99}$	$T_{opx\text{-}spl\text{-}SS82}$	$T_{Al,Cr\text{-}opx\text{-}WS91}$	$T_{ol\text{-}spl\text{-}B91}$
Group I: porphyroclastic (grt)-spl lherz.			(at T = 850°C)							
Ke 1960/2										
cores (recalculated cpx-I, opx-I & grt)	1020 ± 14	/ 2.54 ± 0.12	-	-	-	-	-	-	-	-
Al bulge in opx-I; core in opx-IIa & spl-IIb	-		< 1.51	-	897 ± 12	-	-	-	908 ± 21	-
pyroxene and ol-I rims & spl-IIb	-		< 1.51	701 ± 40	798 ± 16	711 ± 130	-	705 ± 58	-	811 ± 81
Ke 1963/2										
cores (recalculated cpx-I, opx-I & grt)	1004 ± 38	/ 2.44 ± 0.11	-	-	-	-	-	-	-	-
Al bulge in opx-I; core in opx-IIa & spl-IIb	-		< 1.47	-	854 ± 35	-	-	-	850 ± 12	-
pyroxene rims & spl-IIb	-		< 1.47	787 ± 38	799 ± 25	746 ± 41	-	-	792 ± 32	-
Ke 1965/4										
cores (recalculated cpx-I, opx-I & grt)	1048 ± 27	/ 2.76 ± 0.11	-	-	-	-	-	-	-	-
Al bulge in opx-I; core in opx-IIa & spl-IIb	-		< 1.51	-	869 ± 13	-	-	-	844 ± 17	-
pyroxene and ol-I rims & spl-IIb	-		< 1.51	719 ± 38	722 ± 38	716 ± 121	-	658 ± 8	774 ± 54	1011 ± 42
Group II: recrystallised (grt)-spl lherz.										
Ke 1958/6 *(strongly recrystallised)*										
cores	-		< 1.66	1167 ± 59	1097 ± 8	1205 ± 49	1139 ± 92	-	1032 ± 21	-
rims	-		< 1.67	1247 ± 48	1180 ± 27	1270 ± 25	1176 ± 41	-	1048 ± 23	-
Ke 1958/13 *(less recrystallised)*										
cores	-		< 1.66	884 ± 35	855 ± 33	925 ± 42	841 ± 12	862 ± 33	892 ± 28	-
rims	-		< 1.66	992 ± 21	908 ± 40	1002 ± 31	876 ± 84	-	853 ± 19	-
Ke 1958/20 *(strongly recrystallised)*										
cores	-		< 1.63	1119 ± 9	1113 ± 9	1121 ± 32	888 ± 50	1072 ± 18	1000 ± 9	-
rims	-		< 1.63	1109 ± 11	1068 ± 20	1127 ± 30	1100 ± 56	-	1031 ± 37	-
Ke 1959/24 *(strongly recrystallised)*										
cores	-		< 1.69	1103 ± 11	1053 ± 8	1119 ± 32	1052 ± 78	1037 ± 19	1019 ± 15	-
rims	-		< 1.69	1125 ± 10	1077 ± 15	1143 ± 38	1094 ± 54	-	1028 ± 14	-
Ke 1959/25 *(less recrystallised)*										
cores	-		< 1.74	994 ± 13	962 ± 15	1143 ± 38	854 ± 146	-	921 ± 34	-
rims	-		< 1.74	1103 ± 99	1031 ± 66	1141 ± 78	991 ± 145	-	930 ± 20	-
Group III: porphyroclastic spl harzburgite										
Ke 781/6										
cores (& spl-I)	-		< 1.69	822 ± 17	866 ± 16	839 ± 65	866 ± 88	863 ± 29	900 ± 30	-
rims (& spl-I)	-		< 1.69	859 ± 15	907 ± 9	903 ± 111	986 ± 123	855 ± 27	910 ± 41	1331 ± 107
Ke 1965/1										
cores (& spl-I)	-		< 1.93	809 ± 51	864 ± 25	812 ± 131	859 ± 84	756 ± 56	894 ± 27	940 ± 60
rims (& spl-IIb)	-		< 1.62	834 ± 32	834 ± 37	895 ± 61	763 ± 121	-	804 ± 47	1092 ± 55
Ke 1965/15 *(modally metasomatised)*										
cores (no spl-I preserved)	-		-	-	837 ± 46	-	-	-	913 ± 51	-
Group IV: mylonitic spl lherz. & harzb.										
Ke 1961/1 *(ultramylonitic spl harzburgite)*										
cores (opx-I, cpx-I, ol-I & spl-I)	-		< 1.83	834 ± 9	913 ± 18	811 ± 35	950 ± 51	761 ± 25	933 ± 11	792 ± 35
rims (opx-I, cpx-I, ol-I & spl-I), and opx-IIa cores	-		< 1.64	-	762 ± 70	804 ± 241	-	-	782 ± 101	1119 ± 85
Ke 1968/1 *(mylonitic spl lherzolite)*										
cores (opx-I, cpx-I, ol-I & spl-I)	-		< 1.70	722 ± 56	797 ± 32	764 ± 103	791 ± 154	-	848 ± 85	964 ± 58
rims	-		< 1.56	711 ± 62	768 ± 21	725 ± 54	703 ± 147	-	770 ± 46	1381 ± 91

errors = 1σ; for references with respect to thermometers and barometers see text


(a)
Temperature [°C]
700 800 900 1000 1100 1200 1300 1400
Pressure [GPa]
0.0 0.5 1.0 1.5 2.0 2.5 3.0
P_max for plag. peridotite (CFMAS)
AAC
90 mW m-2
60 mW m-2
Al-bulges
cores rims
Ke 1960/2
Ke 1963/2
Ke 1965/4
G. I
Ke 1958/6
Ke 1958/13
Ke 1958/20
Ke 1959/24
Ke 1959/25
G. II
Ke 781/6
Ke 1965/1
G. III
Ke 1961/1*
Ke 1968/1
G. IV
(b)
Temperature [°C]
700 800 900 1000 1100 1200 1300 1400
Pressure [GPa]
0.0 0.5 1.0 1.5 2.0 2.5 3.0 3.5 4.0 4.5 5.0 5.5
Depth [km]
10 20 30 40 50 60 70 80 90 100 110 120 130 140 150 160 170
P_max for plag. peridotite (CFMAS)
AAC
M2
LT
path 2
?
Eth
HT
MT
C1
M1
path 1
HP/HT
C2
Lash
Lab
★: Marsabit sheared grt lherzolite
M1 & M2: Marsabit grt pyroxenite; cores and rims, respectively
Eth: Ethiopian spl peridotite
C1: Chyulu Hills grt-spl peridotite and websterite
C2: Chyulu Hills grt lherzolite
Lash: Lashaine (Tanzania) grt peridotite
Lab: Labait (Tanzania) grt peridotite

1963/2, Ke 1965/4), and from cores to rims in Group III, respectively (Ke 1965/1), a temperature decrease of ~60-90 °C has been calculated (Table 2.10; Fig. 2.12b). Rim temperatures obtained with $T_{2Px\text{-}BK90}$, $T_{Ca\text{-}opx\text{-}BK90}$ and $T_{Na\text{-}px\text{-}BK90}$ (at an assumed pressure of 1.20 GPa) are mostly < 850°C, reaching very low values around 750°C (Table 2.10). In Group I, comparison between results from mineral pairs within (not shown) and outside of symplectites revealed no significant differences. In the ultramylonite (Ke 1961/1: Group IV), neoblast cores (opx-IIa) record very low temperatures as well (Table 2.10), indicating that the mylonitisation occured during the MT-LT transition. Generally, temperatures below ~850 °C must be regarded with caution due to low diffusion rates and proximity to the closure temperature for the diopside-enstatite exchange reaction (e.g., Smith, 1999). However, the results are in quite good agreement with temperatures obtained by $T_{opx\text{-}spl\text{-}SS81}$ and $T_{Cr,Al\text{-}opx\text{-}WS91}$ (Table 2.10). In some samples, calculations using rim compositions and fast reacting thermometers, i.e. based on fast diffusing elements (Mg-Fe in spinel and olivine in the case of $T_{ol\text{-}spl\text{-}B91}$; Chakraborty *et al.*, 1994), result in considerably higher temperatures (1000-1300 °C; Table 2.10). They are either interpreted to be related with the same heating event recognised in the Group II peridotites (the HT event; Fig. 2.11), or to reflect heating by the host basanite during the transport of the xenolith to the surface.

All temperatures calculated for the MT and LT stages correspond to an assumed pressure of 1.2 GPa (Table 2.10) and are projected to maximum pressures based on the Cr content of associated spinel (Fig. 2.12a and b). The maximum pressures for the MT stage after the breakdown of garnet is < 1.51 GPa (Table 2.10), defined by the Cr content of symplectitic spinel of Group I xenoliths (spl-IIb). Similarly low maximum pressures are indicated by the low-Cr rims in the mylonitic spl peridotites (Table 2.2).

Group II xenoliths: heating and recrystallisation

Based on textural evidence, it was suggested that the recrystallised Group II lherzolites represent heated, recrystallised and variously metasomatised equivalents of formerly deformed Group I lherzolites. These assumptions are supported by zoning patterns (Fig. 2.11) and thermobarometric calculations (Table 2.10). Temperatures based on the core composition of minerals from less recrystallised samples (Ke 1958/13 and Ke 1959/25) using slowly reacting thermometers (based on Al and Cr; $T_{Cr\text{-}S99}$; $T_{opx\text{-}spl\text{-}SS82}$; $T_{Al,Cr\text{-}opx\text{-}WS91}$) give similar values (~840-960) as those found for the MT stage in the porphyroclastic rocks (Table 2.10; Fig. 2.12a). In contrast, temperatures using rim compositions and thermometers based on faster diffusing elements ($T_{2Px\text{-}BK90}$, $T_{Ca\text{-}opx\text{-}BK90}$ $T_{Na\text{-}px\text{-}BK90}$) yield higher temperatures (Table 2.10; Fig. 2.12a). This may produce apparently contradictory zoning patterns in some opx-I from less recrystallised Group II xenoliths (Fig. 2.5c):

Fig. 2.12. *P-T estimates for peridotite xenoliths from Marsabit.* ***(a)****: P-T conditions calculated for each individual sample based on evaluation of mineral zoning patterns. Dashed subvertical lines indicate that corresponding symbols represent maximum pressures. Minimum pressures are defined by the absence of plagioclase (from Gasparik, 1987). The steady-state model geotherms (long dash lines) are from Pollack & Chapman (1977), the asthenospheric adiabatic upwelling curve (AAC) is from McKenzie & Bickle (1988).* ***(b)****: Interpretation of our P-T estimates and comparison with thermobarometric results from other xenolith suites along the EARS: Marsabit (Henjes-Kunst & Altherr, 1992, Olker, 2001), Ethiopia (Bedini et al., 1997), Chyulu Hills (Altherr et al., in preparation), Lashaine and Labait (Lee & Rudnick, 1999). P-T path 1 describes decompression and cooling from an initial high-P/high-T stage (HP/HT), via a medium-T stage (MT) to a low-T stage (LT). Group II xenoliths experienced later heating from MT to HT described as P-T path 2 (further explanations in text).*

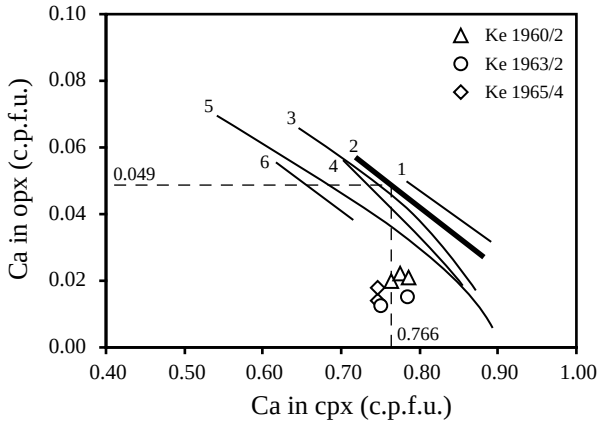


Fig. 2.13. *Ca_{cpx} vs. Ca_{opx} (cations per formula unit; c.p.f.u.) for reintegrated cpx-I and opx-I from Group I porphyroclastic (grt)-spl lherzolite. Comparison with the experimental results of Brey et al., (1990) indicates that the reintegrated cores of cpx-I and opx-I are not in equilibrium with respect to Ca (lines labelled 1-6 represent equilibrium partitioning at 1-6 GPa). Assuming a pressure of 2.0 GPa, the mean Ca content in cpx would be in equilibrium with an opx with about 0.049 Ca p.f.u. (dashed lines), corresponding to temperatures of about 1000-1100°C (applying $T_{Ca\text{-}opx\text{-}BK90}$; Brey & Köhler, 1990; for discussion see text).*

the initial cooling event (MT-LT transition) is still preserved by the more slowly diffusing Al, whereas the subsequent heating is indicated by a rimward increase of the faster diffusing Ca.

The homogeneous mineral composition in the strongly recrystallised samples can be explained by almost complete equilibration at the HT stage. This is supported by temperature calculations which yield consistently high values for both cores and rims, and for all applied thermometers (around 1000-1200 °C at 1.20 GPa; Table 2.10). The only exception is $T_{Cr\text{-}S99}$, which records the MT stage also in one strongly recrystallised sample (Ke 1958/20; Table 2.10).

The recalculated bulk compositions of symplectites/clusters in Group II samples do not satisfy a garnet stoichiometry which is probably due to recrystallisation and equilibration at higher temperatures (Morishita & Arai, 2003a). Therefore, we calculated only maximum pressures from spinel compositions ($P_{grt\text{-}in\text{-}CWW86}$) of 1.63-1.74 GPa (Table 2.10; Fig. 2.12a)

GEOCHEMICAL AND TEXTURAL EVOLUTION OF THE LITHOSPHERIC MANTLE BENEATH MARSABIT

The Marsabit mantle xenoliths reflect the thermal and compositional state of the lithospheric mantle at maximum depths of ~45-60 km at the time of sampling through their host lava. In addition, older episodes of (partial) chemical and P-T equilibration are recorded in the samples to different degrees. In this section we combine *P-T* stages (Fig. 2.11 and 2.12) with textures and geochemical signatures in order to constrain the relative timing of deformation and metasomatism in the lithospheric mantle beneath this part of the EARS (Fig. 2.14). The details outlined below can be summarised as follows: penetrative deformation observed in all porphyroclastic peridotites is related to decompression and cooling from the initial HP/HT stage, representing the oldest preserved feature, to the MT stage. This was accompanied by subsolidus re-distribution of major and trace elements in the context of the transition from garnet to spinel stability. In addition, the penetrative deformation accounts for the generally very fertile character of some xenolith types (Group I), as they most likely represent the result of mechanical addition of pyroxenitic material to the peridotitic mantle. Finally, metasomatism in Group II and III xenoliths, as well as heating and recrystallisation in Group II xenoliths are related to the younger HT stage (subsequent to the MT stage).

Porphyroclastic xenoliths

Group I rocks have anomalous modal compositions (Table 2.1). Their high clinopyroxene and initial garnet contents make them too fertile to represent an ancient melting residue and even conflict with their classification as mantle

peridotite. Calculated bulk rock compositions (not shown) yield up to 6 wt% Al_2O_3, which is considerably higher than primitive mantle estimates (McDonough & Sun, 1995). Other compositional parameters, such as Mg-numbers of olivine (Table 2.2), on the other hand, are in line with fertile lherzolite (89-90; e.g., Pearson *et al.*, 2003). These apparently contradictory features may be explained by metasomatic addition of clinopyroxene and garnet (re-fertilisation), as observed in some cratonic xenoliths (Simon *et al.*, 2003). The lack of enriched trace element patterns in Group I clinopyroxene (Fig. 2.7b), however, argues against this hypothesis. The fact that all of the investigated Group I samples are pervasively deformed is more in favour of a model of mechanical, solid-state mingling of peridotite and pyroxenite (e.g., Bodinier *et al.*, 1988). The result will be heterogeneous zones consisting of more and less pyroxene rich peridotites, respectively olivine websterites. This is observed in some Group I xenoliths (layering; Fig. 2.2a). Similar models, based on petrographic observations, have been proposed in some cases for the peridotite – grt pyroxenite relationship in orogenic peridotite massifs, such as Lherz (Bodinier *et al.*, 1988), Beni Bousera (Kornprobst, 1966; Tabit *et al.*, 1997), Ronda (Schubert, 1977; van der Wal & Vissers, 1996) or Malenco (Müntener & Hermann, 1996). Although garnet websterite form an important part of the Marsabit xenolith suite, no composite xenoliths were found and no trace element data of the pyroxenite xenoliths are yet available, which would allow to further constrain the peridotite-pyroxenite relationship. However, a spatial relationship in the mantle with the porphyroclastic peridotites is supported by thermobarometry, i.e. the *P-T* evolution obtained for the Group I lherzolites is in good agreement with thermobarometric studies on these pyroxenites (cooling and decompression from 1066-926 °C at 2.51-1.41 GPa to 859-712 °C at 1.15-0.75 GPa; Henjes-Kunst & Altherr, 1992; Olker, 2001; see fields M1 and M2 in Fig. 2.12b).

Yet, no data is available for characterising the age and exact nature of the pyroxenitic material. The fact that the clinopyroxene- and (initially) garnet-rich layers are oriented parallel to the foliation indicates that the peridotite-pyroxenite mingling is most likely the result of the penetrative deformation event (or older). Deformation, in turn, is associated with the MT stage (Fig. 2.14), as indicated by textural and compositional features in the Group I rocks (i.e. zoning, *P-T* conditions and high HREE abundances recorded by neoblast cores, as well as bent exsolution lamellae in cpx-I). It is worth to note that the HP/HT and MT stages are manifested in some Group III and IV peridotites as well, indicating a close spatial relationship between all porphyroclastic peridotite types.

In addition to deformation, the porphyroclastic rocks show metasomatic overprint which is different in Group I and Group III. All Group I Ti-pargasites have constant and mostly depleted incompatible trace element abundances (e.g., LREEs, U, Th; Fig. 2.10a), whereas the HREEs show strong variation between the cores of K- and LILE-rich amph-i grains and texturally 'younger' amph-ii and -iii (Fig. 2.10a). The REE signature of amph-i, together with the LREE-depleted nature of the associated clinopyroxenes, suggests that K-rich Ti pargasite (+phlogopite) represent an 'old' modal metasomatic assemblage that re-equilibrated with the surrounding mineral matrix. This resulted in depleted LREEs and low HREEs, in equilibrium with associated clinopyroxene and garnet (Vannucci *et al.*, 1995). Similar Mg-numbers of amphibole and silicates (olivine) further support this idea.

Equilibrium with garnet (low HREEs) indicates an age related to the HP/HT stage. The temperature estimates for the HP/HT stage (Fig. 2.12b) are in line with the experimentally determined stability of Ti-pargasite under upper mantle conditions (1075°C between 1.8 and 2.5 GPa: Niida & Green, 1999). Most likely amph-i and phlogopite belong to the pyroxenite component that was introduced mechanically

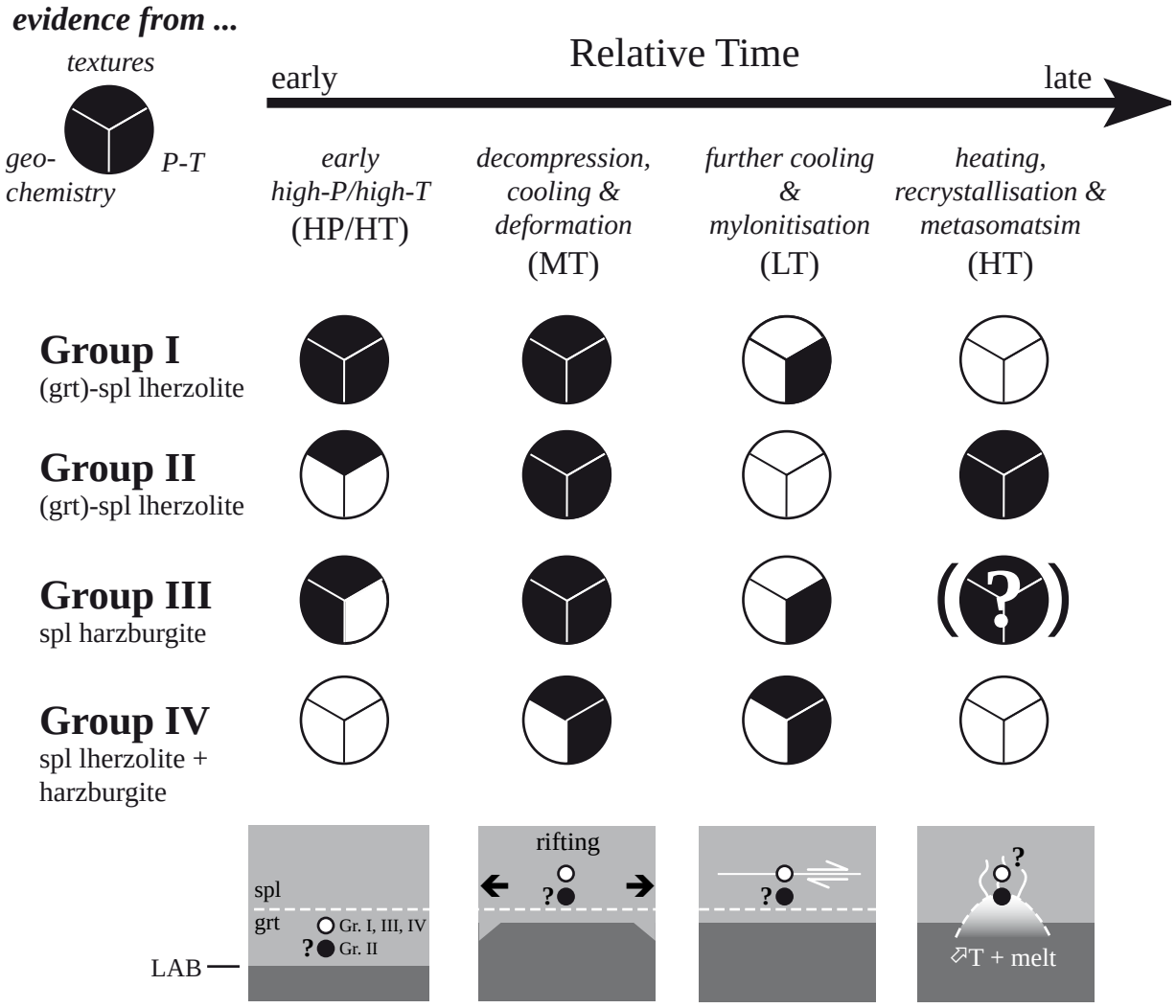


Fig. 2.14. *Schematic representation of the relative timing of events recorded by the Marsabit peridotite xenoliths. Filled sectors of circles denote which events are recorded by a given xenolith type and by which type of evidence (textures, thermobarometry, trace element geochemistry). Block diagrams of the bottom represent simplified cross-sections through the lithospheric mantle and the upper asthenosphere (LAB = lithosphere-asthenosphere boundary) and present a simplified model of lithospheric evolution through time. No absolute timescale can be attributed due to the lack of accurate dating methods (for discussion see text).*

in the peridotite. This is indicated by almost identical compositions of Ti pargasites and phlogopite in the grt websterites (Olker, 2001). This would also explain the confinement of Ti-pargasite to the clinopyroxene-rich Group I rocks. The high-HREE Ti pargasite (amph-ii and -iii) most likely represents secondary amphibole resulting from sub-solidus recrystallisation of primary amph-i during decompression. Re-equilibration with spinel led to HREE-rich, but still LREE-depleted compositions.

The presence of cold mylonites (Group IV) further testifies to zones of strongly focused strain in the shallow lithospheric mantle, most likely associated with the MT-LT transition (Fig. 2.14). Deep-seated shear zones near the asthenosphere-lithosphere boundary (field 'C2' in Fig. 2.12b) are documented by sheared

garnet-bearing lherzolites from the Chyulu Hills, as well as from Marsabit (star in Fig. 2.12b; Henjes-Kunst & Altherr, 1992). Along with the cold, shallow-level, sheared Group IV peridotites from this study, they indicate shear zones at different levels in the lithospheric mantle beneath Marsabit.

Apart from low sulfide contents in Ke 1961/1, the two mylonitic samples show no evidence for metasomatism. The conspicuous trace element signature of cpx-I in the ultramylonitic spl harzburgite (sinusoid REE pattern and extreme Ti depletion; Fig. 2.7g-h) are difficult to explain. The strongly depleted incompatible trace elements, however seem to preclude a metasomatic event.

In contrast to Group I and IV, spl harzburgites of Group III are characterised by variable enrichment in incompatible elements (Fig. 2.7e and 2.8), providing evidence of a different metasomatic event compared to Group I. Detailed descriptions and chemical data will be given in Chapter 3. Metasomatism ranges from cryptic (enrichment of clinopyroxene; Figs. 2.7e-f and 2.8) to modal, the latter resulting in the crystallisation of amphibole, phlogopite, apatite and graphite. Metasomatism led to enrichment of LREEs, Th and U, while Hf, Zr and Ti show negative anomalies (Fig. 2.7e-f). The amphibole and phlogopite compositions point to a Si-Na-rich and relatively Ca-poor metasomatic agent. This, along with the fact that orthopyroxene is a stable phase of the metasomatic assemblages, whereas clinopyroxene is not, argues in favour of a Si-rich, orthopyroxene-saturated fluid or melt, and against a carbonatitic melt. Absence of deformation in the modal metasomatic assemblages, as well as replacement textures indicate that metasomatism post-dates the penetrative deformation. Compositional similarities with respect to the trace element signatures in some Group II xenoliths imply that metasomatism in Group II and III was possibly related to the same, relatively late event (see Fig. 2.14 and discussion below).

Recrystallised xenoliths - cryptic metasomatism

Group II xenoliths provide evidence of the same early *P-T* evolution as Group I (transition from the HP/HT to the MT stage) which was followed by heating to the HT stage (Fig. 2.12b and 14). Importantly, they also contain initial pyroxene-rich layers (Fig. 2.1b) which suggests that they were subjected to the same deformation-related pyroxenite-peridotite mingling as Group I xenoliths (MT stage). Due to the lack of absolute depth constraints (only maximum pressures), we have no information whether Group II xenoliths originated at greater depths than Group I samples, or if they reflect lateral temperature heterogeneities (e.g., proximity to magma intrusions/conduits; note that the deeper position of Group II indicated in Fig. 2.14, is schematic and purely hypothetical).

In addition to heating, Group II samples show evidence of cryptic metasomatism (enriched clinopyroxene trace element patterns; Fig. 2.7c-d). There is a relationship between the degree of recrystallisation, equilibration temperatures and metasomatism: being texturally closest to Group I xenoliths, sample Ke 1959/25 shows clinopyroxene trace element patterns almost identical to Group I clinopyroxene after the breakdown of garnet (Fig. 2.5c-d). From Ke 1959/24 to Ke 1958/20, there is a progressive enrichment in LREE, U and Th. The most enriched signature in these elements is developed in clinopyroxene from the sample with the most pronounced foliation (Ke 1958/13; Fig. 2.5c-d). Thus, the metasomatising agent seems to be focused in zones with an anisotropic fabric.

Ti concentrations in clinopyroxene (in sample Ke 1958/6; Fig. 2.4b), and slightly lower Mg-numbers in olivine and pyroxenes in the strongly recrystallised and heated samples indicate Fe-Ti enrichment, in line with metasomatism and heating by a mafic silicate melt (Menzies *et al.*, 1985; Bodinier *et al.*, 1990; Bodinier *et al.*, 2004). This is further supported

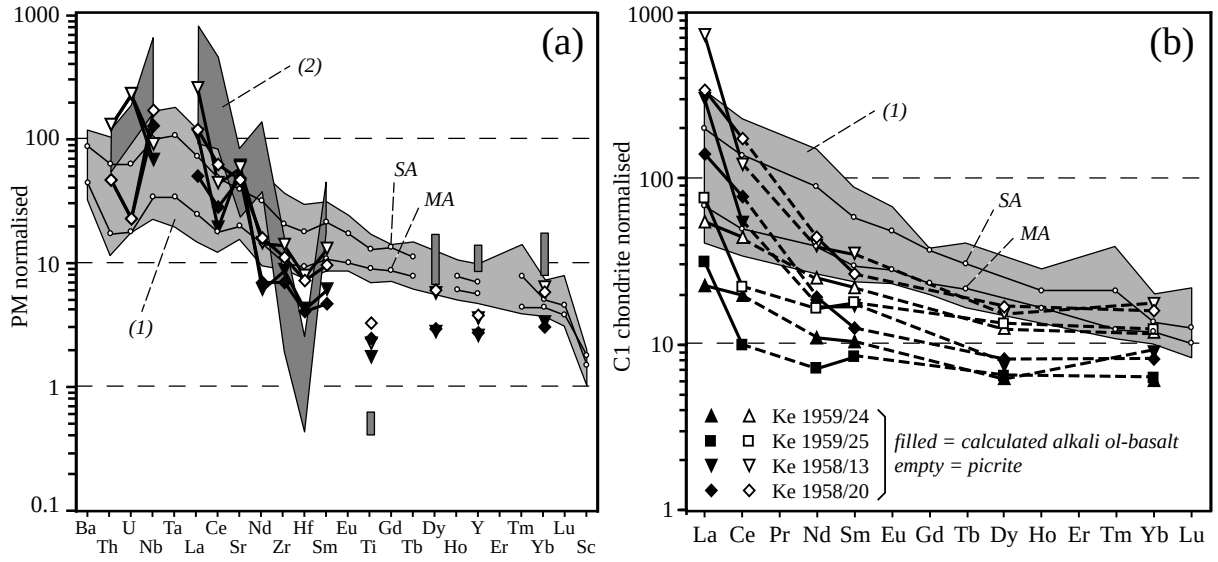


Fig. 2.15. *Primitive mantle* ***(a)*** *and chondrite-normalised* ***(b)*** *trace element patterns of calculated melts in equilibrium with Group II (grt)-spl lherzolite xenoliths from Marsabit (normalising values from McDonough & Sun, 1995). Clinopyroxene/melt partition coefficients for picritic and alkali ol-basaltic melts (Skulski et al., 1994; their runs TS137 and TS139, respectively). Partition coefficients for U and Th are from Wood et al. (1999). SA, MA: average of strongly and mildly alkaline Quaternary basanites and alkali basalts, respectively, from Marsabit (Volker, 1990); (1) compositional range of Quaternary basanites and alkali basalts from Marsabit (Volker, 1990); (2) range of calculated silicate melts in equilibrium with amphibole-rich harzburgites (Group III) from Marsabit (see Kaeser et al., in preparation).*

by the more ferric and Ti-enriched composition of Group II spinel (Table 2.1; Dick & Bullen, 1984; Xu *et al.*, 1998a). In addition, the moderate negative Hf-, Zr- and Ti anomalies in Group II clinopyroxene (Fig. 2.7c) are balanced by slightly positive anomalies in the associated orthopyroxene (Fig. 2.9b). Thus, calculated whole-rock trace element patterns would be devoid of negative anomalies (e.g., Rampone *et al.*, 1991), in line with metasomatism by mafic melts (e.g., Bodinier *et al.*, 1990).

In order to constrain the exact nature of the metasomatising agent responsible for cryptic metasomatism in Group II samples, hypothetical melts in equilibrium with the phase assemblage of each studied Group II xenolith (Table 2.1) were calculated using published clinopyroxene/melt partition coefficients ($D^{cpx/melt}$; see Fig. 2.15 for references). Values for $D^{opx/melt}$ and $D^{ol/melt}$ (for calculation of the bulk rock partition coefficient) were derived from the respective temperature dependent $D^{cpx/opx}$ and $D^{cpx/ol}$, using the equations of Witt-Eickschen & O'Neill (2005). Melts in equilibrium with samples containing LREE-enriched clinopyroxene (Ke 1958/13 and 1958/20) approach the LREE composition of the strongly alkaline host basanites (SA in Fig. 2.15). The less incompatible elements (from Sm to Lu), on the other hand, exhibit lower abundances, and do not overlap with the MREE-HREE range shown by the alkali basalts and basanites. Such type of REE variation is commonly explained by chromatographic trace element fractionation during open system melt percolation (e.g., Navon & Stolper, 1987). In Fig. 2.15, extended trace element patterns for hypothetical melts in equilibrium with the most strongly metasomatised Group II samples are shown. The incompatible element patterns (U, Th, Nb, Ta, LREEs and Sr) of the calculated melt in equilibrium with the enriched, strongly heated, completely equilibrated, and strongly

recrystallised xenolith (Ke 1958/20) indicates that the metasomatising agent was most likely parental to the Quaternary Marsabit basanites and alkali basalts (Fig. 2.15). The less heated and recrystallised, slightly foliated sample (Ke 1958/13) is in equilibrium with a melt with higher abundances of incomaptible elements, bearing some similarities to melts in equilibrium with the amphibole-rich harzburgites (Fig. 2.15 and Chapter 3). This transition from strongly over less heated and recrystallised Group II lherzolites, to modally metasomatised Group III harzburgites, indicates that metasomatism in Group II and III samples is most likely the result of one single event. The different styles of expression either reflect different agents or are the result of reactive fractionation upon melt percolation depending on different temperatures, melt/rock ratios, phase assemblages, modal proportions, and element diffusivities (Vasseur *et al.*, 1991; Bedini *et al.*, 1997; Vernières *et al.*, 1997; Ionov *et al.*, 2002; Bodinier *et al.*, 2004; Xu & Bodinier, 2004; Yu *et al.*, 2006; see also Chapter 3).

GEODYNAMIC IMPLICATIONS

Calculated melts in equilibrium with the heated and recrystallised Group II xenoliths (Fig. 2.15) indicate that the young (HT-related) metasomatic event is most likely related to the Tertiary to Quaternary magmatic activity in Marsabit. Consequently, the HT event was probably part of EARS-related processes. The late heating and melt infiltration (HT stage) produced geochemical signatures similar to those observed in xenoliths from Mega, southern Ethiopia (U-Th-LILE-LREE enrichment; Bedini *et al.*, 1997), which have been modelled in the context of Tertiary, EARS-related thermo-mechanical erosion of the lower lithosphere atop hotter material (e.g., a mantle plume).

For Marsabit, the integration of thermobarometry, compositional data and textures provides evidence that the late heating and melt infiltration (HT stage) post-dates decompression and penetrative deformation during the HP/HT-MT-LT transition (Fig. 2.14). The geodynamic context of decompression and deformation is lithospheric thinning. Beneath the Marsabit area, it was either related to the formation of the Anza Graben and/or to initial EARS-related rifting (HP/HT-MT-LT transition). Absolute time constraints for the age of the HP/HT-MT transition are difficult to obtain. Estimating the maximum age of the HP/HT-MT transition by diffusion modelling using published diffusion coefficients for REEs (van Orman et al., 2001) and Al in clinopyroxene (Sautter *et al.*, 1988) gave unsatisfactory results. The smallest cpx-I grain analysed that still shows HREE zoning has a diameter of 0.6 mm. Assuming a constant temperature of 900°C, after decompression and cooling to the MT stage, it would take maximum 20-170 Ma to completely re-equilibrate the Yb contents in such a grain. However, the xenoliths further cooled to much lower temperatures than 900°C, which would result in considerably longer re-equilibration times (e.g., ~3 Ga at 800 °C). Similarly, calculating the duration of the decompression event using the Al zoning patterns in clinopyroxene (Al increase from core to rim; e.g., Fig. 2.12b) would yield time spans in the order of 10^5 to 10^6 years at 1000°C, ~10^7 years at 900°C, and 10^8 to 10^9 years at 800°C, respectively. Therefore, as the time spans between Mesozoic and Tertiary rifting are relatively short (or even overlapping; Reeves *et al.*, 1987), diffusion modelling is unlikely to better constrain the timing of decompression observed in mantle xenoliths from Marsabit.

However, comparison with geological and geophysical data shows that lithospheric thinning in the course of Mesozoic rifting would be in good agreement with several conclusions from other studies. Cooling, relatively cold deformation, and the lack of metasomatism associated with decompression would be in line with the generally volcanic-poor nature of the whole Mesozoic Central African Rift System (including the Anza Graben; e.g., Reeves et al., 1987; Morley, 1999 and references therein).

Further it would be in line with the picture of the present-day structures beneath the Kenya rift. Anomalously low-velocity material is confined to the surface expression of the present day rift (Mechie *et al.*, 1997 and references therein). This argues in favour of a model where the lithospheric mantle deforms by pure shear beneath the rift axis, and against models where lithospheric thinning is offset beneath the rift flanks, e.g., below Marsabit (Mechie *et al.*, 1997).

Additional arguments in favour of lithospheric thinning in the context of Mesozoic rifting come from other xenolith localities. Although porphyroclastic peridotites occur beneath Mega as well (Bedini *et al.*, 1997), they do not show the intense decompression- and deformation-related features revealed by the samples of Marsabit. This means that the lithospheric mantle beneath Mega experienced probably only EARS-related modifications, in line with the geographic position of Mega at the border of the Afar dome, away from the Anza Graben (Fig. 2.1a). Xenolith localities further to the south, far from the Anza Graben, in southern Kenya and Tanzania, reflect a still thick lithospheric mantle (Fig. 2.12b), but variably metasomatised by EARS-related melts or fluids (e.g., Dawson & Smith, 1988; Rudnick *et al.*, 1993; Henjes-Kunst & Altherr, 1992; Chesley *et al.*, 1999; Lee & Rudnick, 1999; Dawson, 2002). On the contrary, xenoliths from Marsabit, situated above the Anza Graben, record Mesozoic rifting processes in addition to EARS-related metasomatism.

The penetrative deformation during the HT/HP-MT transition resulted in considerable small-scale heterogeneities comprising variously depleted peridotite mingled with originally mafic lithologies (grt pyroxenite). The heated mantle parts (represented by Group II xenoliths), interpreted to have interacted with melts parental to the Marsabit Quaternary magmas, show evidence for such heterogeneities as well. Percolation through, or assimilation of such heterogeneous material may account for the heterogeneous nature of the magmas of this region (Marsabit: Volker, 1990; Huri Hills: Class *et al.*, 1994; see Fig. 2.1b), as reflected by trace element and isotope signatures of the lavas. However, the compositional features observed in the Group II xenoliths do not allow to conclude whether the melts responsible for metasomatism contain a mantle-plume signature or not. Finally, in the mantle lithosphere beneath Marsabit, the thermal conditions prior to decompression and deformation (i.e. the HP/HT stage) were similar to the present-day situation observed in xenoliths from southern Kenya, beneath the Chyulu Hills (Fig. 2.12b; Altherr *et al.*, in preparation; Henjes-Kunst & Altherr, 1992), which is consistent with the conclusions of Henjes-Kunst & Altherr (1992).

ACKNOWLEDGMENTS

Many thanks go to Othmar Müntener. Numerous discussions contributed to the substance of this study. Thanks go also to Edwin Gnos (Bern) and Hans-Peter Meyer (Heidelberg) for assistance with microprobe work. We are grateful to Tanya Furman, Else-Ragnhild Neumann, Elisabetta Rampone, and Yigang Xu for through and constructive reviews which greatly improved the quality of this paper, and Marjorie Wilson for valuable comments and editorial handling. This work is part of a grant from the Swiss National Science Foundation (Nr. 200021-100647/1) to A.K.

Chapter 3: Crystallisation and Breakdown of Metasomatic Phases in Graphite-bearing Peridotite Xenoliths from Marsabit (Kenya)

Benjamin Kaeser[1], Angelika Kalt[1] & Thomas Pettke[2,*]

[1] Institut de Géologie et d'Hydrogéologie, Université de Neuchâtel, Rue Emile-Argand 11, CH-2009 Neuchâtel, Switzerland
[2] Isotope Geochemistry and Mineral Resources, Department of Earth Sciences, Federal Institute of Technology, ETH Zentrum NO, CH-8092 Zürich, Switzerland (now at: Institute of Geological Sciences, University of Bern, Baltzerstrasse 1, CH-3012 Bern, Switzerland)

Manuscript submitted to Journal of Petrology (accepted with moderate revision; stand: 19.01.2007)

ABSTRACT

Mantle-derived xenoliths from the Marsabit shield volcano (eastern flank of the Kenya rift) include porphyroclastic spinel peridotites characterised by variable styles of metasomatism. Petrography indicates a transition from clinopyroxene-bearing cryptically metasomatised harzburgite (LREE, U, and Th enrichment in clinopyroxene) to modally metasomatised clinopyroxene-free harzburgite and dunite. The metasomatic phases include amphibole (low-Ti Mg-katophorite), Na-rich phlogopite, apatite, graphite and metasomatic low-Al orthopyroxene. Transitional samples show that metasomatism led to replacement of clinopyroxene by amphibole. In all modally metasomatised xenoliths melt pockets (silicate glass containing silicate and oxide microlites, carbonates and empty vugs) occur in close textural relationship with the earlier metasomatic phases.

Altogether, the petrography, major and trace element data, as well as constraints from thermobarometry and fO_2 calculations, indicate that cryptic and modal metasomatism is the result of a single event of interaction between peridotite and a SiO_2-Na_2O-CO_2-H_2O-rich melt. The unusual style of metasomatism (composition of amphibole, presence of graphite, formation of orthopyroxene) reflects low *P-T* conditions (~750-850°C at <1.5 GPa) in the wall rock during impregnation and locally low oxygen fugacities. The latter allowed the precipitation of graphite from CO_2. The inferred silicic volatile-rich melt possibly derived from alkaline basic melts by melt-rock reaction during the development of the Tertiary-Quaternary Kenya rift. Glass-bearing melt pockets formed at the expense of the early phases, mainly through incongruent melting of amphibole and orthopyroxene, during heating and probably fluid infiltration related to the magmatic activity that ultimately sampled and transported the xenoliths to the surface.

KEY WORDS: graphite; peridotite xenoliths; Kenya Rift; modal metasomatism; silicate glass

INTRODUCTION

During recent decades numerous studies have described different styles of metasomatism in the Earth's upper mantle. These studies, in combination with experimental work, show that the agents responsible for mantle metasomatism are either mafic silicate melts, carbonate melts or C-O-H-rich fluids (e.g., Menzies & Hawkesworth, 1987; Pearson *et al.*, 2003; Bodinier & Godard, 2003, and references therein). Integration of textural, mineralogical and geochemical data from mantle samples highlights the complexity of mantle metasomatism. They show that metasomatic features are controlled by (1) the composition of the initial metasomatising agent; (2) the pre-metasomatic composition and heterogeneity of the mantle rock; (3) the evolution of the physico-chemical parameters during metasomatism (e.g., porosity, fO_2, *P, T*); (4) element fractionation processes during melt (fluid)-rock interaction; and (5) mineral reactions. Several recent studies have demonstrated that compositional differences between metasomatic products in a single suite of mantle rocks do not necessarily imply different metasomatising events (e.g., Bedini *et al.*, 1997; Ionov *et al.*, 2002; Bodinier *et al.*, 2004; Rivalenti *et al.*, 2004; Ionov *et al.*, 2006). Mechanisms like chromatographic fractionation during melt or fluid percolation (Navon & Stolper, 1987) and melt/fluid-rock reaction (Godard *et al.*, 1995; Vernières *et al.*, 1997) can generate compositionally distinct products, starting from one initial melt or fluid.

We present a study of metasomatised, graphite-bearing xenoliths from Marsabit (northern Kenya), in order to investigate melt-rock reaction and fractionation processes. The products of metasomatism are texturally and compositionally variable and unusual. An early Na-Si-rich assemblage comprises volatile-bearing phases (amphibole, phlogopite, apatite), metasomatic orthopyroxene as well as graphite. Associated with these phases is a second metasomatic assemblage of carbonate-bearing silicate glass patches ('melt pockets'), similar to those described from many other xenolith suites (e.g., Frey & Green, 1974, Dautria *et al.*, 1992; Ionov *et al.*, 1993 and 1994; Zinngrebe & Foley, 1995; Chazot et al., 1996a; Draper & Green, 1997; Yaxley *et al.*, 1997; Coltorti *et al.*, 2000, Laurora *et al.*, 2001; Bali *et al.*, 2002; Ban *et al.*, 2005 and references therein). The approach is based on detailed investigation of trace element variation in minerals and integration of textural constraints, and emphasises that the exotic mineralogy and compositions reflect complex interplay between melt-rock reaction processes, chromatographic trace element fractionation, pre-existing mantle heterogeneity and effects of changing *P, T* and fO_2 during one single metasomatising event. We further present mass balance calculations which show that the melt pockets were formed by incongruent melting of the early assemblage (mainly amphibole and orthopyroxene), most likely triggered by a fluid.

The results indicate that the 'exotic' nature of the metasomatic products reflects a particular pre-existing physical and chemical environment – i.e. low ambient temperatures (and probably pressures) and relatively low oxygen fugacities – rather than an exotic initial metasomatic agent. We will show that metasomatism in this case does not necessitate multiple metasomatic events of different nature, but simply reflects the product of melt-rock reaction, possibly initiated by common, continental-rift related basanites.

SAMPLE CONTEXT

The investigated xenoliths were collected from basanitic to alkali-basaltic (Volker, 1990) scoriae (cinder cones) of the Marsabit shield volcano. Magmatic activity in Marsabit started in the late Miocene, while rocks from the shield volcano yield Pleistocene to Quaternary ages (e.g., Key *et al.*, 1987). Magmatism is thus clearly related to the development of the Kenyan sector of the East African Rift System (EARS). The Marsabit shield volcano is, however, located eastward of the main axis of the EARS, within the Mesozoic Anza Graben (e.g., Morley, 1999 and references therein), the east-

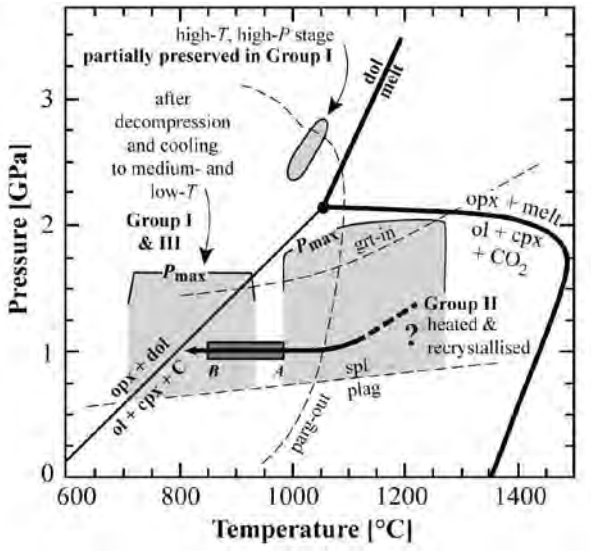


Fig. 3.1. *Pressure-temperature evolution recorded by peridotite xenoliths from Marsabit (light grey fields; summarised from Kaeser et al., 2006), together with reactions relevant for this study: plagioclase-spinel transition in the CFMAS system (Gasparik, 1987); appearance of garnet (grt) in model lherzolite (Klemme & O'Neill, 2000); maximum stability of Ti-pargasite (parg) in model lherzolite (Niida & Green, 1999); solidus of natural carbonated lherzolite and subsolidus decarbonation (opx + dol = ol + cpx + C) modified from Lee & Wyllie (2000) at fO_2 below the CCO buffer (e.g., Woermann & Rosenhauer, 1985). The bold arrow schematically indicates the infiltrating and cooling metasomatising Si-rich melt. The dark-grey field indicates the temperature range (at 0.96 GPa) of co-existing clinopyroxene and hornblende in Si-rich melt (dacite; A = hornblende-out; B = clinopyroxene-out) at H_2O concentrations between ~6 and 10 wt% (Prouteau & Scaillet, 2003). See text for further explanations.*

ward continuation of the Turkana depression (see Fig. 1.1). This region of lower topographic elevation is situated in between two large-scale topographic domes (the Ethiopian plateau in the north and the East African plateau in the south; Fig. 1.1). The Turkana depression is characterised by a strongly thinned lithosphere beneath the main Kenya rift (beneath Lake Turkana). There is still a lively debate on the origin of this depression and on the processes that trigger rifting and volcanic activity in this region. Furman *et al.* (2006), for example, provide a detailed discussion of this topic. The basement of the Anza Graben and the Marsabit complex is made of lithosphere modified throughout the formation of the Mozambique mobile belt in a convergent tectonic setting during Pan-African times (e.g., Meert, 2003 and references therein; see also Chapter 1 for details with respect to the geological and geodynamic context).

In the previous study (Kaeser *et al.*, 2006) we used peridotite xenoliths to constrain the evolution of the lithospheric mantle beneath Marsabit. The peridotites were subdivided into porphyroclastic, formerly garnet-bearing spinel lherzolites [(grt)-spl lherzolites; Group I], recrystallised (grt)-spl lherzolites (Group II), porphyroclastic spl harzburgites (Group III) and mylonitic spl lherzolites and harzburgites (Group IV). For detailed descriptions of textures and mineral chemistry of primary assemblages of all four peridotite types, the reader is referred to Kaeser *et al.* (2006).

Thermobarometry revealed that the porphyroclastic rocks experienced decompression and cooling from 970-1080°C at 2.3-2.9 GPa to ~750-800°C at <1.5 GPa (mainly preserved in Group I xenoliths; see Fig. 3.1). Recrystallised Group II lherzolites underwent a similar early evolution but experienced later heating and re-equilibration at 1000-1200°C (Fig. 3.1).

The present study mainly focuses on metasomatic features in the cooled Group III xenoliths. Group I contains Ti-pargasite and rare phlogopite in chemical equilibrium with the surrounding peridotitic minerals. Textures and trace element geochemistry revealed that this phase assemblage formed during an earlier metasomatic event and recrystallised and re-equilibrated with the peridotitic minerals during decompression and penetrative deformation (Kaeser *et al.*, 2006). Group II (grt)-spl lherzolites were cryptically metasomatised (LREE-U-Th-Nb enrichment in clinopyroxene) by infiltration of alkaline mafic melts, possibly parental to the Quaternary magmas of the Marsabit volcano (Kaeser *et al.*, 2006).

The textural and compositional characteristics of metasomatism in the Group III xenoliths suggest a distinct event compared to metasoma-

Table 3.1: Textures and mineralogical composition of the investigated peridotite xenoliths

Sample Nr.	*Group*	*Lithology*	*Pre-metasomatic and early metasomatic phases (vol%)*									*Modal composition of melt pockets (vol%)*						
			former garnet[1]	Ol	Opx	Cpx	Spl	Am	Phl	Graphite/ Apatite	Melt pockets	Glass	Di_m	Ol_m	Chr_m	Mg-Cc	vugs
Ke 1960/2	I	porphyroclastic (grt)-spl lherzolite	13.3	44.0	10.7	32.0	0.1	tr.	-	-	<0.5	n.d.	n.d.	n.d.	n.d.	n.d.	n.d.
Ke 1963/1	I	porphyroclastic (grt)-spl lherzolite	11.0	50.0	29.0	10.0	tr.	-	-	-	<9.0	n.d.	n.d.	n.d.	n.d.	n.d.	n.d.
Ke 1958/13	II	recrystallised (grt)-spl lherzolite	9.9	58.0	20.2	10.3	0.2	-	-	-	2.0	n.d.	n.d.	n.d.	n.d.	n.d.	n.d.
Ke 1959/25	II	recrystallised (grt)-spl lherzolite	7.0	63.2	19.9	9.0	0.9	-	-	-	<2.0	n.d.	n.d.	n.d.	n.d.	n.d.	n.d.
Ke 1965/1	III-a	porphyroclastic spl harzburgite	1.5	70.8	22.9	3.9	0.9	-	-	tr./-	-	-	-	-	-	-	-
Ke 1959/15	III-b	porphyroclastic spl harzburgite	5.0	63.0	26.0	5.2	0.7	0.2	-	-/tr.	<4.0	21.8	23.4	27.7	4.9	8.1[2]	7.6
Ke 1965/15	III-b	porphyroclastic spl harzburgite	-	71.9	17.7	6.8	0.4	0.2	0.1	0.10/tr.	3.0	21.4	34.0	23.7	2.8	16.0	2.2
Ke 785*	III-c	porphyroclastic spl harzburgite	-	64.0	18.7[3]	-	0.6[4]	1.1	0.9	0.23/-	14.4	21.9	27.0	21.8	5.7	6.7	7.0
Ke 1965/3	III-c	porphyroclastic spl dunite	-	80.1	3.2[3]	-	0.7[4]	-	tr.	-/tr.	16.0	22.7	21.3	29.5	6.6	12.8[5]	7.4
Ke 1965/25	III-c	porphyroclastic amphibole dunite	-	53.6	-	-	-	12.0	tr.	0.25/-	34.2	n.d.	n.d.	n.d.	n.d.	n.d.	n.d.
Ke 1959/27	III-c	porphyroclastic dunite	-	88.5	tr.[3]	-	-	-	-	-	11.5	n.d.	n.d.	n.d.	n.d.	n.d.	n.d.
Ke 1970/6	III-d	recrystallised spl harzburgite	-	87.2	9.5[3]	2.7[6]	0.6[4]	-	-	-	-	-	-	-	-	-	-

Ol: olivine; Opx: orthopyroxene; Cpx: clinopyroxene; Am: amphibole; Phl; phlogopite; Di_m, Ol_m, Chr_m: diopside, olivine and chromite microlites in melt pockets; Mg-Cc: Mg-calcite; [1] spl-opx-cpx symplectites; [2] dolomite instead of calcite; [3] metasomatic, low-Al orthopyroxene (Opx_m); [4] compositionally identical to Chr_m; [5] highly variable (2.4-19.7 vol%) in individual melt pockets; [6] compositionally similar to glass- related Di_m; -: not detected; tr.: traces; n.d.: not determined

tism in Group I xenoliths, post-dating decompression and deformation, and possibly concurrent with late (EARS-related) heating and cryptic metasomatism observed in the recrystallised Group II lherzolites.

ANALYTICAL METHODS

Modal compositions (Table 3.1) were determined from digitised images of thin sections and rock slice scans (for details see Kaeser *et al.*, 2006).

Minerals were analysed for major elements using a CAMECA SX 50 electron microprobe equipped with four wavelength-dispersive spectrometers (Mineralogisch-Petrographisches Institut, Universität Bern) and a CAMECA SX 51 electron microprobe with five wavelength-dispersive spectrometers (Mineralogisches Institut, Universität Heidelberg). Pyroxene, olivine and spinel were analysed using routine operating conditions (focused beam, accelerating voltage of 15 kV, beam current of 20 nA, and counting times of 20 sec for most elements). Silicate glass was analysed with a larger beam size (~10-15 μm) and a lower beam current (15 nA) in order to avoid Na loss during analysis. Natural and synthetic silicates and oxides were used as standards. Carbonates were analysed with a beam current of 10 nA and a beam size of 10 μm, with natural carbonates and sulfates used as standards. The concentrations of H_2O (in amphibole and phlogopite), CO_2 (in carbonates) and Fe^{3+} (in spinel) were calculated based on stoichiometry. The raw data of all microprobe analyses were corrected with a routine PAP program.

Trace element contents in minerals were analysed *in-situ* on polished thin sections (40-50 μm thick), using a laser ablation (LA) instrument equipped with a 193 nm ArF excimer laser (Lambda Physik, Germany) coupled to an ELAN 6100 (Perkin Elmer, Canada) quadrupole inductively coupled plasma mass spectrometer (ICPMS) at the Institut für Isotopengeologie und Mineralische Rohstoffe, ETH Zürich (see Pettke *et al.*, 2004, and references therein for the instrumental setup, capabilities and operating conditions). Raw data were reduced using the LAMTRACE program. Laser pit diameters were between 14 and 110 μm, depending on grain size and the absence / presence of mineral, fluid or melt inclusions and of exsolution lamellae.

PETROGRAPHY

The Marsabit peridotite xenoliths contain two texturally different types of modal metasomatic modification. The first type of metasomatism created volatile-bearing phase assemblages of mainly amphibole and phlogopite (Fig. 3.2a-e). Metasomatism in Group I and III are, however, not related to each other (see above and Kaeser *et al.*, 2006). The second type is characterised by the occurrence of 'melt pockets' (e.g., Ionov *et al.*, 1994): patches and networks of silicate glass associated with microlites of clinopyroxene, olivine and chromite (Fig 2f and 3a-f). In this case glass further encloses globules of carbonates (Fig 3e-f, and 4a-b). The glass-bearing assemblages form at least partly at the expense of the volatile-bearing assemblages. In the following, pre-metasomatic phase assemblages are termed 'primary' (olivine = ol-I, clinopyroxene = cpx-I, orthopyroxene = opx-I; spinel = spl-I), the early volatile-bearing metasomatic assemblages are referred to as 'early metasomatic' and the later glass-bearing assemblages are termed 'late metasomatic' (Na-rich Cr diopside = Di_m; augite = Aug_m; olivine = Ol_m; chromite = Chr_m).

Early metasomatic minerals in Group I (grt)-spl lherzolites are brown Ti-pargasite and phlogopite (Kaeser *et al.*, 2006). Almost all Group I samples contain tiny domains or veinlets of brownish silicate glass and microlites of Ol_m, Aug_m (titaniferous) and Chr_m. In some cases, Ti-pargasite is fringed by glass (+ microlites) selvages, indicating incongruent melting (Ti-pargasite => melt + Ol_m + Aug_m; Fig. 3.3a). Recrystallised (grt)-spl lherzolites (Group II) do not contain volatile-bearing phases, but some samples have glass-bearing patches. In one sample (Ke 1958/13), glass patches further contain considerable amounts of Mg-calcite. In samples equilibrated at high temperatures (~ 1100°C; e.g., Ke 1959/25), glass occurs as minute melt pools and films around spinel and clinopyroxene within recrystallised symplectites, both developing characteristic 'spongy' rims (Fig. 3.3b).

Group III spl harzburgites contain by far the most abundant metasomatic products (early and late). Early metasomatism formed clusters and veinlets of amphibole, phlogopite, graphite, ±apatite, clearly distinct from early metasomatic assemblages in Group I (grt)-spl lherzolites. Based on petrographic investigations, we subdivided Group III peridotites in four types (Type III-a to d). Textural and geochemical features show that the transition from Type III-a to Type III-c (+d) mainly corresponds to the transformation of modally non-metasomatised spl harzburgite to pervasively overprinted amphibole harzburgite-dunite.

Type III-a

This type is classified as porphyroclastic, cpx-I-bearing spl harzburgite, devoid of metasomatic phases, but showing geochemical evidence of cryptic metasomatism (Kaeser *et al.*, 2006 and this study). This rock type was also once garnet-bearing and was subjected to decompression, as is indicated by the presence of rare spl-opx-cpx symplectites (Table 3.1 and Kaeser *et al.*, 2006).

Type III-b

Xenoliths of Type III-b are still cpx-I-bearing spl harzburgites, but they contain metasomatic volatile-bearing phases (Table 3.1). One xenolith (Ke 1965/15) contains veinlets of pale green amphibole, phlogopite, graphite ±apatite (Fig. 3.2e and 3.3c). Graphite occurs as macroscopic flakes (up to 500 µm long; Fig. 3.2e), similar to those described from cratonic, kimberlite-hosted peridotite xenoliths (Pearson *et al.*, 1994). Cpx-I in the vicinity of veinlets is strongly resorbed and develops patches or lamellae of Ti-poor amphibole, indicating metasomatic replacement (Fig. 3.3c). In all Type III-b samples amphibole and clinopyroxene are partially replaced by the late glass-bearing assemblage. Cpx-I is overgrown by a secondary, green Na-rich Cr diopside (Di_m)

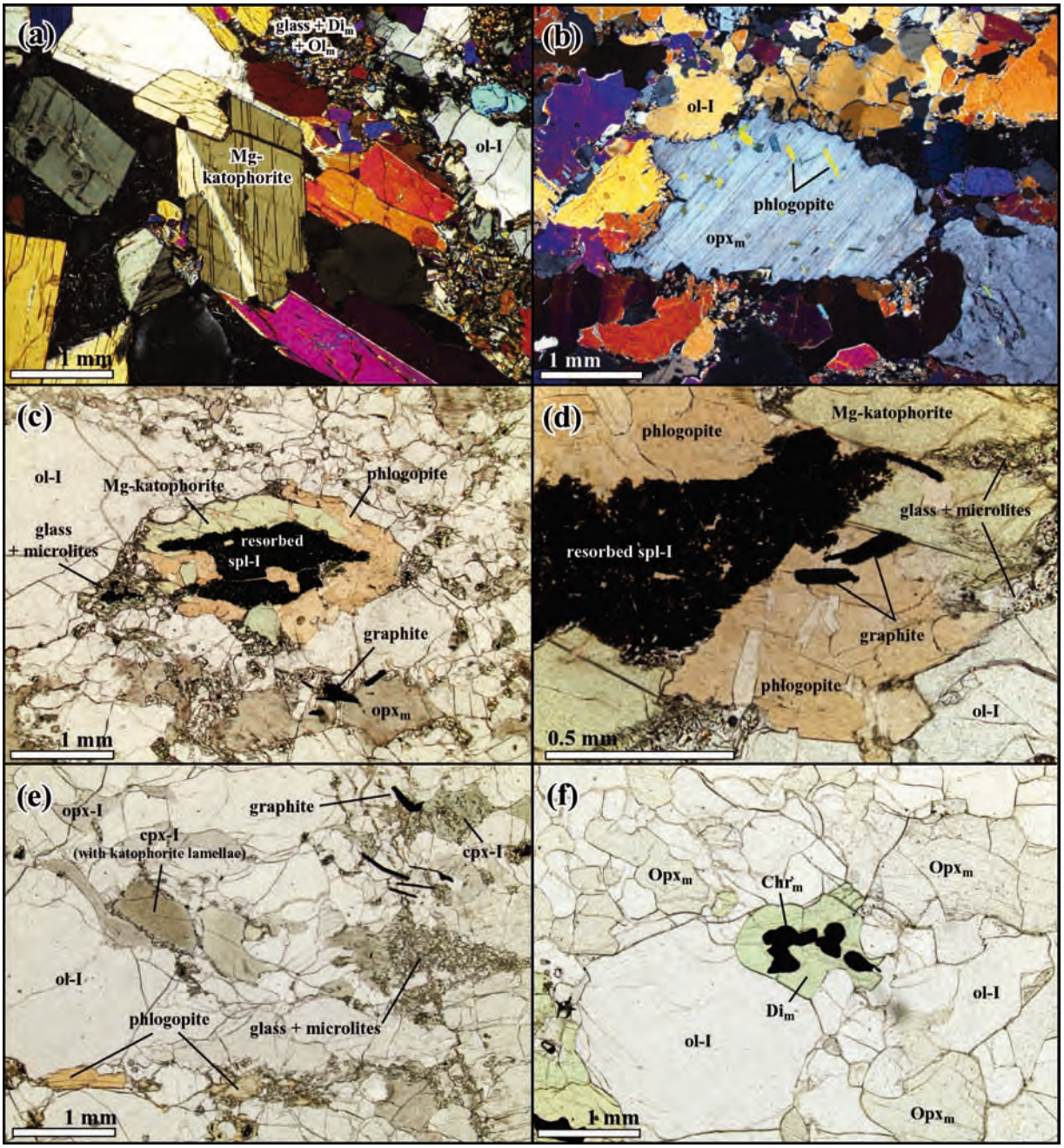


Fig. 3.2. *Photomicrographs showing the textural characteristics of metasomatism in the porphyroclastic spl harzburgites from Marsabit:* ***(a)*** *twinned, euhedral Mg-katophorite in Type III-c amphibole dunite. Note the irregular grain boundaries with glass + microlite bearing melt pockets (sample Ke 1965/25; crossed polars);* ***(b)*** *metasomatic low-Al orthopyroxene (Opx$_m$) in a Type III-c spl harzburgite with euhedral phlogopite inclusions (early metasomatic assemblage). Note irregular, concave grain boundaries indicating later resorption by olivine (sample Ke 785*; crossed polarisers);* ***(c)*** *Type III-c Mg-katophorite and phlogopite clustering around partly resorbed spinel (spl-I), and metasomatic orthopyroxene (Opx$_m$) in contact with partly included graphite (sample Ke 785*);* ***(d)*** *details of Type III-c early metasomatic Mg-katophorite and phlogopite, the latter containing graphite inclusions (sample Ke 785*);* ***(e)*** *Type III-b early metasomatic assemblage including interstitial phlogopite, graphite and clinopyroxene (cpx-I) becoming replaced by Mg-katophorite lamellae (sample Ke 1965/15;);* ***(f)*** *Type III-d spl harzburgite characterised by annealed textures and clusters of chromite (Chr$_m$) enclosed by green Na-rich Cr diopside (Di$_m$; sample Ke 1970/6).*

occasionally enclosing patches of silicate glass ±carbonate (Fig. 3.2c). Di_m further occurs as micro-phenocrysts in melt pockets, sometimes enclosing (resorbed?) orthopyroxene.

Type III-c

Type III-c samples are harzburgites and dunites devoid of cpx-I. Transitional samples (Type III-b to -c) still contain relics of cpx-I. Metasomatic products in Type III-c xenoliths generally occur as clusters of amphibole, phlogopite, graphite and rare apatite. The primary assemblage is dominated by ol-I.

Green, Ti-poor amphibole and phlogopite typically form aggregates around relic, skeletal spl-I (Fig. 3.2c-d). Dunite xenolith Ke 1965/25 is unusual as it contains cm-scale clusters of large, euhedral amphibole crystals (Fig. 3.2a) with small phlogopite inclusions. Single amphibole crystals show magmatic twinning. Graphite is associated with amphibole and phlogopite (sometimes found as inclusions in the latter; Fig. 3.2d) or orthopyroxene (Fig. 3.2c). Straight contacts between amphibole, phlogopite and ol-I indicate textural equilibrium. Phlogopite also occurs as euhedral, randomly dispersed flakes in orthopyroxene (Fig. 3.2b). This, together with compositional arguments (e.g., very low Al contents; see below), suggests that orthopyroxene is related to metasomatism (Opx_m). Sample Ke 1965/3 also contains early metasomatic interstitial apatite.

Late metasomatic assemblages are ubiquitous in Type III-c xenoliths. They form melt pockets, interconnected by glass films along olivine grain boundaries. Euhedral apple-green Na-rich Cr diopside micro-phenocrysts (Di_m; up to 0.3 mm long) in individual melt pockets commonly have the same crystallographic orientation, suggesting growth at the expense of an earlier phase. BSE imaging reveals sector zoning (Fig. 3.3e and 3.4a). Melt pockets in several samples enclose relic, strongly resorbed amphibole grains (Fig. 3.3d). Phlogopite (e.g., in Ke 785*) appears to be less resorbed (Fig. 3.3d). Early amphibole is rimmed by a kaersutitic selvage (Fig. 3.3d), indicating that the early amphibole is not in chemical equilibrium with the silicate glass. When in contact with glass, orthopyroxene is also strongly resorbed. Several features suggest incongruent breakdown by a process similar to the reaction opx + melt $\Rightarrow$ ol + cpx + modified melt (e.g., Shaw *et al.*, 1998): thin glass films are present on orthopyroxene cleavage planes; late euhedral $Ol_m + Di_m \pm Chr_m$ nucleated within orthopyroxene, and primary olivine overgrows orthopyroxene (Fig. 3.2b; development of strongly concave opx grain boundaries). Glass in Type III-b and -c samples contains considerable amounts of rounded carbonates (e.g., Fig. 3.3e), texturally similar to interstitial, glass-related carbonate globules from other xenolith suites (e.g., Ionov *et al.*, 1996; Lee *et al.*, 2000; Laurora *et al.*, 2001; Bali *et al.*, 2002; Demény *et al.*, 2004). BSE imaging and qualitative EDX mapping highlight that carbonate globules consists of clusters of sometimes euhedral Mg-calcite crystals, occasionally showing oscillatory zoning (Fig. 3.4a-b). In sample Ke 1965/15, Mg-calcite is in contact with graphite flakes (Fig. 3.3f), indicating growth of Mg-calcite at the expense of graphite. Glass in some samples (e.g., Ke 1959/15) contains rounded blebs of apatite (Fig. 3.3c), as well as minor amounts of Fe-Ni sulphide globules. Abundant vugs (e.g., Fig. 3.3d) in all types of silicate glass are possibly remnants of an exsolved vapour phase.

Sample Ke 1959/27 (Type III-c) is unusual in several aspects. It contains kaersutite phenocrysts hosted in the glass. Further, Di_m phenocrysts are overgrown by Ti-augite rims, and glass is of untypical dark-brown colour. This xenolith most likely recorded interaction with a melt of host-basanite affinity during ascent to the surface.

Type III-d

This unique xenolith (Ke 1970/6) is a coarse-grained (grainsize up to 4 mm) metasomatic spl harzburgite. Ol-I and Opx_m are almost strainfree. Chr_m occurs as rounded, black grains surrounded by a cluster of apple-green Na-rich Cr diopside (Di_m; Fig. 3.2f) containing melt in-

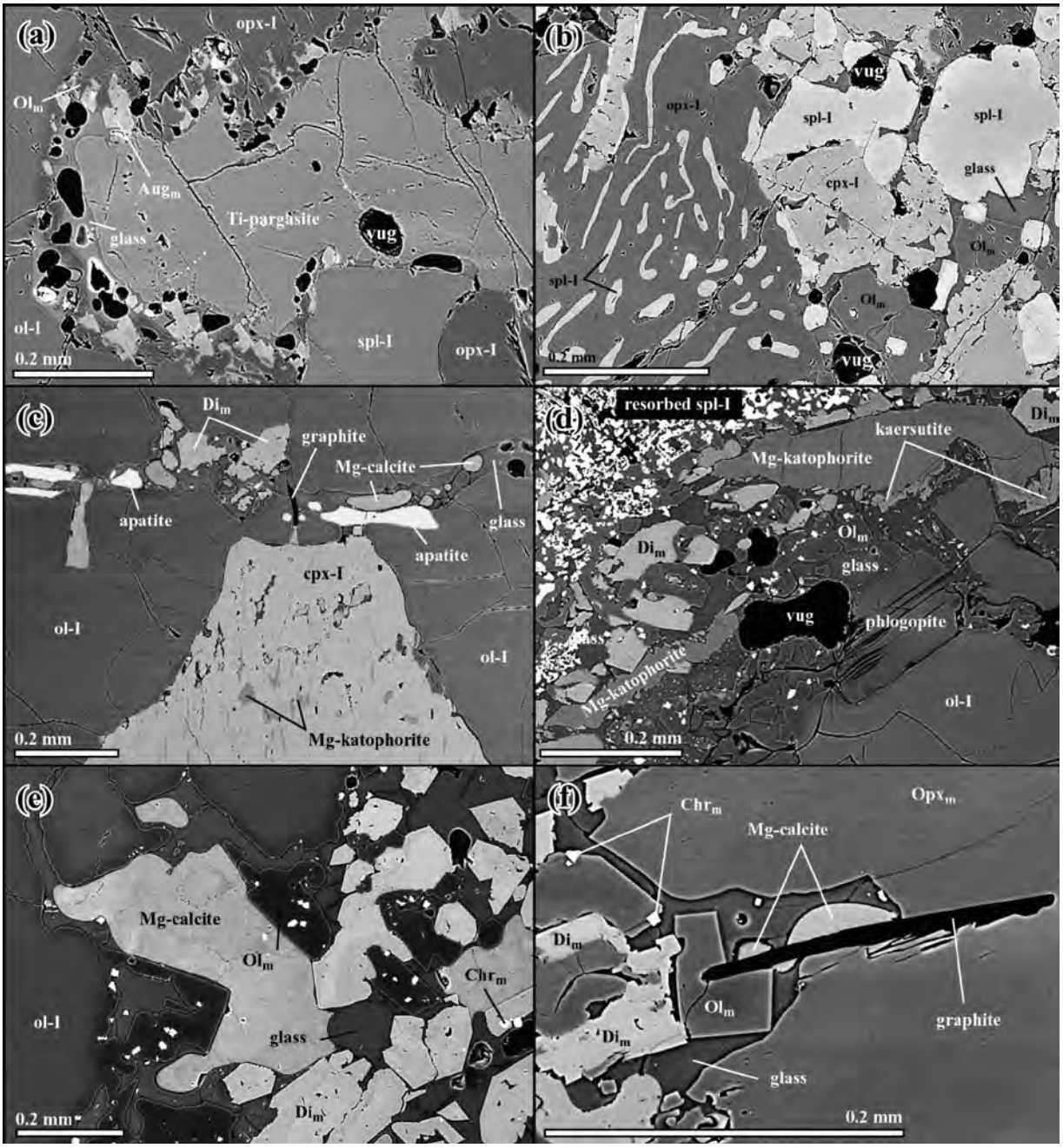


Fig. 3.3. *Backscattered electron images showing textural characteristics and relationships between early and late metasomatic assemblages:* ***(a)*** *Ti-pargasite and primary orthopyroxene (opx-I) in a Group I (grt)-spl lherzolite (Kaeser et al., 2006), partly replaced by silicate glass and secondary Ti-augite (Aug$_m$) and olivine (Ol$_m$; sample Ke 1960/2);* ***(b)*** *spinel-orthopyroxene-clinopyroxene symplectite becoming replaced by the late, glass-bearing assemblage. Note the spongy rims of clinopyroxene (cpx-I) indicating partial melting;* ***(c)*** *Type III-b spl harzburgite showing the textural characteristics of early (graphite, apatite, Mg-katophorite replacing cpx-I) and late (glass, Mg-calcite, Di$_m$) metasomatic assemblages (sample Ke 1965/15);* ***(d)*** *phlogopite and residual Mg-katophorite in a melt pocket in a Type III-c spl harzburgite. Note the more regular grain boundaries of phlogopite compared to Mg-katophorite (the latter is further rimmed by irregular kaersutitic amphibole; sample Ke 785*);* ***(e)*** *silicate glass, Mg-calcite and microlites of Na-rich Cr diopside (Di$_m$), olivine (Ol$_m$), and chromite (Chr$_m$) in a Type III-c spl harzburgite. Note grey tone variation in Di$_m$ indicating sector zoning (sample Ke 1965/3);* ***(f)*** *Relationship between graphite and Mg-calcite in a Type III-b spl harzburgite (sample Ke 1965/15).*

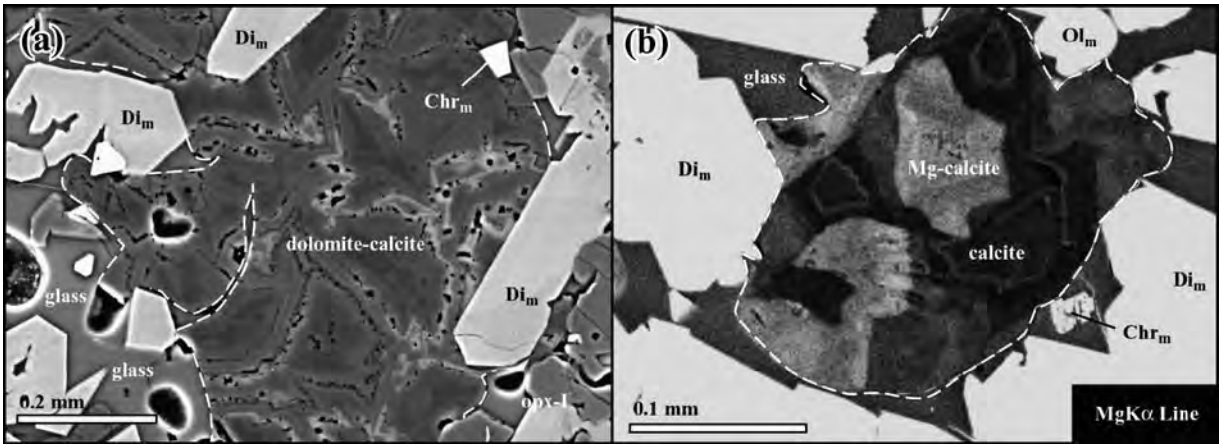


Fig. 3.4. *Oscillatory zoning of carbonate related to silicate glass in porphyroclastic spl harzburgites from Marsabit;* ***(a)*** *zoned, euhedral dolomite crystals (dark) rimmed by fine selvages of calcite (light), together with Na-rich Cr diopside (Di$_m$) and chromite (Chr$_m$; sample Ke 1959/15);* ***(b)*** *qualitative compositional map of carbonates in a melt pocket (sample Ke 1965/3). Lighter grey tones indicate higher Mg contents. Note the euhedral shapes of the carbonate crystals. The dashed white lines highlight the contact of carbonates with the pristine silicate glass.*

clusions. There is no primary clinopyroxene or volatile-bearing phases. Several Opx$_m$ grains show numerous melt inclusions forming continuous films or trails along cleavage planes. These remarkable textural features can be explained by almost complete annealing of a former Type III-c spl harzburgite containing silicate glass + Di$_m$ microphenocrysts, which subsequently recrystallised to form the clinopyroxene clusters around spinel and orthopyroxene with melt inclusions.

MINERAL COMPOSITION

Compositional data (major and trace elements) of non-metasomatic primary phases from all peridotite types, as well as of Ti-pargasite and phlogopite from Group I samples can be found in Kaeser *et al.* (2006). A more complete dataset with respect to the metasomatic phase assemblages is given in Appendices A3 and A4 of this thesis.

Early metasomatic assemblages

Clinopyroxene

'Cryptically' metasomatised cpx-I (Type III-a and -b) are Cr-rich diopsides (Table 3.2) with high Mg#s and low Ti contents typical for enriched mantle peridotites (e.g., Pearson *et al.*, 2003). Trace element data (Table 3.2) show enrichments of U, Th, Sr, and LREEs, varying depletions in HREEs, and marked negative anomalies for HFSEs (Nb, Ta, Zr, Hf, Ti; Fig. 3.5a).

Orthopyroxene

Opx-I from Type III-a and -b is enstatite-rich and has higher Mg#s and lower Al contents than primary orthopyroxene in Group I and II samples. It is HREE-depleted and slightly enriched in U and Th pointing to cryptic metasomatism (Table 3.3). Opx$_m$ (Types III-c and -d) is extremely Al-poor (0.2-1.0 wt% Al_2O_3). LREEs and MREEs are slightly enriched relative relative to HFSEs, which is unusual for mantle-derived orthopyroxene (Rampone *et al.*, 1991).

Amphibole

Green amphiboles (Type III-b and -c) are mostly Ti-poor (Table 3.4) with very high Si and Na contents and high Mg#s (Fig. 3.6a and b). Low-Ti amphibole in Type III-c is Mg-katophorite (Fig. 3.6a; according to Leake *et al.*, 1997), which is an unusual composition for mantle-derived amphibole. Type III-b samples contain less

Table 3.2: Representative analyses of clinopyroxene (oxides in wt%; trace elements in μg/g)

Group	**I**	**II**	**III-a**			**III-b**		**III-c**			**III-d**
Mineral	**Aug_m**	**Aug_m**	**cpx-I**	**cpx-I**	**cpx-I**	**cpx-I**	**cpx-I**	**Di_m**	**Di_m**	**Di_m**	**Di_m**
Sample	1963/1	1959/25	1965/1	1965/1	1965/1	1965/15	1959/15	1965/3	785*	1959/27	1970/6
Texture	micro-xx	spongy	Zone A* core	Zone B* rim	Zone C* core	core	core	micro-xx	micro-xx	micro-xx	
SiO_2	48.54	51.56	52.46	53.22	53.25	53.10	54.10	54.33	53.88	54.29	53.90
TiO_2	2.11	0.38	0.15	0.16	0.14	0.40	0.20	0.12	0.37	0.16	0.07
Al_2O_3	7.82	7.24	3.51	3.56	3.96	4.36	4.25	1.99	2.19	2.75	3.89
Cr_2O_3	1.22	1.08	1.35	1.21	1.12	1.39	1.37	5.45	3.62	2.24	2.84
$FeO_{(tot)}$	2.14	3.48	2.28	1.79	1.74	1.96	2.10	1.83	2.06	2.44	2.53
MnO	0.07	0.09	0.04	0.06	0.02	0.04	0.07	0.09	0.07	0.14	0.04
NiO	0.04	n.a.	0.09	n.a.	n.a.	0.05	0.03	0.04	0.03	0.00	0.00
MgO	15.67	18.26	16.11	16.32	16.09	15.94	15.66	15.85	16.67	16.96	16.04
CaO	22.03	17.47	21.98	22.22	21.71	20.30	19.81	17.38	19.70	19.81	18.41
Na_2O	0.42	0.95	1.27	1.34	1.51	1.93	2.41	2.92	1.67	1.72	2.32
K_2O	0.01	0.03	n.d.	n.d.	n.d.	0.03	0.01	0.01	n.d.	n.d.	0.00
Total	***100.07***	***100.55***	***99.26***	***99.88***	***99.54***	***99.50***	***100.00***	***100.01***	***100.24***	***100.51***	***100.02***
Mg#	***92.87***	***90.35***	***92.66***	***94.19***	***94.28***	***93.55***	***93.02***	***93.92***	***93.52***	***92.54***	***91.89***
Anal-Nr.	*ob29e11*	*ob28a07*	*mc22a16*	*ob28d14*	*ob28d10*	*ob29c15*	*dd09b08*	*dd08d16*	*ob28e04*	*dd08g11*	*ob28g12*
P	39.1	30.9	12.6	16.9	16.8	21.6	65.5	113.5	46.8	61.1	129
K	18.0	<3.97	6.64	0.86	9.85	198	18.6	13.7	112	187	11.4
Sc	169	54.9	41.6	64.6	46.4	24.3	69.2	97.0	108	73.6	78.6
Ti	11871	2157	747	816	828	2027	1053	613	1663	1022	439
V	784	255	233	245	249	275	278	378	525	234	303
Ni	380	536	287	269	277	302	294	368	411	316	329
Zn	6.68	30.9	5.85	5.87	6.79	9.14	13.7	7.93	10.8	15.0	10.9
Ga	3.55	5.92	2.32	1.68	2.39	4.73	n.a.	n.a.	4.40	n.a.	3.58
Rb	<0.090	<0.055	0.015	0.013	0.016	0.16	<0.076	0.051	0.13	0.49	<0.008
Sr	22.6	14.4	52.8	58.0	118	98.6	106	687	47.0	218	484
Y	23.7	13.1	3.62	10.6	2.32	1.65	11.0	73.9	19.9	40.6	43.6
Zr	16.6	5.98	8.35	10.0	7.90	10.4	13.0	22.6	2.29	53.5	17.4
Nb	0.20	0.046	0.13	0.051	0.045	0.14	0.14	3.58	0.070	1.13	1.16
Cs	<0.035	<0.015	0.003	<0.002	<0.002	0.005	<0.032	<0.019	<0.020	<0.018	<0.002
Ba	0.30	<0.062	0.60	0.047	4.23	4.44	0.28	0.47	0.38	6.02	0.085
La	0.23	0.12	0.97	3.04	6.81	2.59	13.9	88.4	2.80	8.82	21.7
Ce	1.76	0.65	2.43	5.03	7.05	5.48	21.6	195	13.7	37.1	90.3
Pr	0.49	0.16	0.45	0.53	0.56	0.73	1.66	23.9	2.64	6.93	16.1
Nd	5.04	1.58	2.39	2.42	2.38	3.57	5.38	99.5	13.3	38.5	86.4
Sm	1.99	0.96	0.78	0.88	0.71	1.17	1.10	18.4	3.9	12.9	21.4
Eu	0.85	0.38	0.35	0.37	0.28	0.43	0.37	6.21	1.36	4.00	7.41
Gd	4.15	1.53	0.85	1.10	0.79	0.87	1.10	14.3	3.87	12.2	16.4
Tb	0.73	0.32	0.13	0.24	0.11	0.10	n.a.	n.a.	0.68	n.a.	2.33
Dy	3.81	2.05	0.72	1.72	0.55	0.49	1.64	13.4	4.96	9.23	11.2
Ho	1.09	0.43	0.13	0.38	0.094	0.068	0.37	2.58	0.81	1.66	1.82
Er	2.17	1.22	0.35	1.18	0.17	0.15	1.17	7.07	2.09	4.15	3.79
Tm	0.45	0.22	0.056	0.19	0.027	0.017	0.16	0.95	0.22	0.53	0.39
Yb	1.97	1.42	0.51	1.28	0.16	0.12	0.95	5.67	1.37	3.36	2.11
Lu	0.27	0.17	0.087	0.18	0.022	0.015	0.22	0.70	0.089	0.42	0.24
Hf	1.00	0.22	0.34	0.31	0.28	0.50	0.25	0.81	0.056	1.02	0.23
Ta	0.034	<0.019	0.011	0.007	0.016	0.021	<0.029	0.657	<0.012	0.043	0.056
Pb	<0.29	<0.23	0.37	0.50	0.58	1.15	0.68	0.23	<0.28	<0.089	0.11
Th	<0.026	<0.008	0.12	0.41	1.31	0.73	4.94	0.45	0.019	0.062	0.062
U	0.020	<0.008	0.076	0.27	0.47	0.28	1.29	0.049	<0.018	0.030	0.017

*: see Fig. 3.13; n.d.: not detected; n.a.: not analysed

Table 3.3: Representative analyses of orthopyroxene, spinel and olivine (oxides in wt%; trace elements in µg/g)

Group	**III-a**	**III-b**	**III-b**	**III-c**	**III-d**	**III-c**	**III-d**	**III-c**	**III-c**	**III-c**	**III-d**
Mineral	**opx-I**	**opx-I**	**opx-I**	**Opx_m**	**Opx_m**	**Chr_m**	**Chr_m**	**ol-I**	**Ol_m**	**ol-I**	**ol-I**
Sample	1965/1	1965/15	1959/15	1965/3	1970/6	1965/3	1970/6	785*	1965/3	1965/25	1970/6
Texture	Zone C* core	core	core	core	core	core	core	core	core	core	core
SiO_2	56.57	56.42	56.15	58.07	57.13	0.12	0.05	40.93	41.35	40.78	40.98
TiO_2	0.04	0.13	0.06	0.01	0.05	0.44	0.16	n.d.	0.01	0.01	n.d.
Al_2O_3	2.65	2.69	2.99	0.46	1.92	12.23	18.80	0.01	0.01	n.d.	0.04
Cr_2O_3	0.43	0.56	0.40	0.32	0.54	54.54	50.43	0.01	0.29	0.01	0.05
Fe_2O_3	-	-	-	-	-	5.54	3.38	-	-	-	-
$FeO_{(tot)}$	5.33	5.68	5.76	5.38	4.86	11.14	12.07	9.39	5.83	11.33	7.71
MnO	0.13	0.14	0.14	0.12	0.12	n.a.	0.05	0.15	0.13	0.27	0.07
NiO	n.a.	0.10	0.09	0.07	0.09	0.15	0.09	0.40	0.24	0.37	0.39
MgO	34.73	34.20	33.80	35.61	34.64	14.80	15.02	49.00	51.82	47.39	50.13
CaO	0.51	0.53	0.48	0.20	0.52	0.03	0.00	0.01	0.08	0.02	0.08
Na_2O	0.05	0.08	0.13	0.09	0.14	n.a.	n.a.	0.01	0.04	n.d.	0.01
K_2O	n.d.	n.d.	n.d.	n.d.	0.01	n.a.	n.a.	0.01	n.d.	n.d.	0.00
Total	**100.44**	**100.52**	**100.00**	**100.34**	**100.03**	**99.10**	**100.08**	**99.93**	**99.80**	**100.18**	**99.47**
Mg#	***92.08***	***91.48***	***91.28***	***92.18***	***92.71***	***70.32***	***68.94***	***90.29***	***94.06***	***88.17***	***92.06***
Anal.Nr.	*ob28d09*	*ob29c12*	*dd09b11*	*dd08c03*	*ob28g04*		*ob28g07*	*ob28e08*	*dd08d03*	*as12a18*	*ob28g11*
Na	341	423	1136	539	1120	n.a.	4.38	29.7	262	64.7	230
Al	15120	14586	17785	1817	10834	n.a.	114911	8.93	82.1	12.0	1201
P	15.6	14.5	17.5	17.5	24.8	n.a.	19.8	42.1	292	105	244
Ca	3163	3016	3881	1487	3895	n.a.	<53.48	82.2	579	200	658
K	1.72	<0.44	<0.35	98.1	1.50	n.a.	<0.86	<0.37	<1.02	1.98	6.30
Sc	8.05	5.46	17.3	2.44	12.4	n.a.	2.80	0.61	4.32	0.94	2.86
Ti	239	619	366	44.9	227	n.a.	956	1.56	8.71	1.70	20.4
V	76.8	90.6	77.2	14.9	63.4	n.a.	925	1.04	3.77	0.96	28.3
Ni	568	646	585	588	748	n.a.	1010	2686	2875	2920	2649
Zn	25.6	30.1	24.5	60.6	37.3	n.a.	732	63.0	66.5	146	69.3
Ga	1.81	3.50	n.a.	n.a.	1.33	n.a.	28.0	0.015	n.a.	0.035	0.77
Rb	<0.009	<0.010	<0.011	0.45	<0.014	n.a.	0.028	<0.008	<0.028	<0.013	0.024
Sr	0.24	0.14	0.44	1.02	1.67	n.a.	0.089	0.017	<0.013	0.045	0.52
Y	0.081	0.073	0.49	0.69	2.02	n.a.	0.025	0.015	0.16	0.10	0.19
Zr	0.23	0.277	0.51	0.038	0.88	n.a.	1.24	<0.005	<0.033	<0.006	0.15
Nb	<0.005	0.020	<0.007	0.18	0.051	n.a.	0.877	<0.003	0.025	0.008	0.035
Cs	<0.002	<0.001	<0.004	0.008	<0.004	n.a.	0.046	<0.002	<0.010	0.004	0.003
Ba	0.056	<0.018	<0.021	7.48	0.035	n.a.	<0.028	<0.016	<0.071	0.17	0.13
La	0.019	<0.002	0.055	0.061	0.045	n.a.	0.039	0.021	<0.004	0.017	0.019
Ce	0.020	0.005	0.046	0.109	0.27	n.a.	0.052	0.023	<0.012	0.027	0.15
Pr	0.002	<0.001	0.005	0.007	0.064	n.a.	0.024	<0.001	<0.011	0.009	0.019
Nd	<0.008	0.010	0.043	0.039	0.42	n.a.	<0.029	<0.007	<0.052	0.018	0.11
Sm	0.014	<0.009	0.016	<0.018	0.19	n.a.	0.022	<0.006	<0.051	<0.009	0.032
Eu	<0.003	<0.002	<0.005	0.012	0.077	n.a.	0.018	<0.002	<0.012	<0.003	0.011
Gd	<0.014	<0.006	0.028	0.021	0.20	n.a.	<0.026	<0.006	<0.041	<0.016	0.035
Tb	0.002	<0.001	n.a.	n.a.	0.045	n.a.	<0.004	<0.001	n.a.	<0.001	0.004
Dy	0.015	0.011	0.086	0.058	0.38	n.a.	0.010	<0.003	<0.043	<0.009	0.041
Ho	0.007	0.003	0.012	0.031	0.069	n.a.	0.003	<0.001	<0.006	0.004	0.010
Er	<0.012	0.008	0.043	0.094	0.22	n.a.	<0.015	<0.006	0.058	0.018	0.027
Tm	0.002	0.001	0.015	0.014	0.031	n.a.	<0.003	<0.001	0.010	0.003	0.004
Yb	0.027	0.011	0.19	0.170	0.28	n.a.	<0.018	0.009	0.064	0.060	0.038
Lu	0.001	0.002	0.026	0.026	0.033	n.a.	0.007	0.002	0.040	0.018	0.008
Hf	0.006	0.010	0.014	<0.009	0.013	n.a.	0.042	<0.003	<0.017	<0.009	<0.006
Ta	<0.001	<0.001	<0.004	<0.005	<0.002	n.a.	0.015	0.001	<0.018	<0.001	<0.001
Pb	<0.028	0.041	0.047	0.074	<0.041	n.a.	0.15	0.036	0.075	0.042	0.046
Th	0.009	<0.002	0.069	0.020	<0.002	n.a.	0.010	0.050	<0.006	0.011	<0.001
U	0.004	<0.001	0.026	0.017	0.004	n.a.	0.017	0.011	<0.006	<0.001	<0.002

*: see Fig. 3.13; n.d.: not detected; n.a.: not analysed

Table 3.4: Representative analyses of amphibole (oxides in wt%; trace elements in µg/g)

Group	**III-b**				**III-c**					
Mineral	**katoph.**	**katoph.**	**katoph.**	**katoph.**	**katoph.**	**katoph.**	**katoph.**	**katoph.**	**kaersut.**	**kaersut.**
Sample	1959/15	1965/15	1965/15	1965/15	785*	785*	1965/25	1965/25	1959/27	1959/27
Texture	residual in m.p.	interst.	interst.	lamellae in cpx-I	residual in m.p.	residual in m.p.	euherdral core	euhedral rim	glass-related	glass-related
SiO_2	45.41	46.03	46.25	48.87	49.55	49.59	49.52	49.53	40.64	41.06
TiO_2	0.15	1.90	2.03	0.99	0.30	0.29	0.22	0.28	6.12	5.77
Al_2O_3	13.65	11.45	11.00	9.15	8.26	8.07	8.77	7.94	14.05	13.95
Cr_2O_3	2.51	1.23	1.48	1.44	2.54	2.63	1.06	1.15	0.31	0.08
$FeO_{(tot)}$	3.50	2.93	3.04	2.78	3.02	2.94	3.59	3.46	5.88	6.15
MnO	0.06	0.03	0.04	0.02	0.08	0.02	0.10	0.08	0.16	0.10
NiO	0.09	0.14	0.09	0.10	0.10	0.06	0.09	0.12	0.10	0.10
MgO	18.83	18.86	18.96	19.97	20.67	20.62	20.00	20.24	15.76	15.45
CaO	8.51	9.74	9.60	9.76	8.05	7.93	8.63	9.09	10.86	10.75
Na_2O	4.74	4.27	4.40	4.32	5.48	5.55	5.29	5.09	2.84	2.94
K_2O	0.49	0.38	0.41	0.31	0.27	0.29	0.28	0.39	1.39	1.38
H_2O*	2.13	2.27	2.27	2.28	2.13	2.13	2.14	2.11	2.05	1.99
F	0.04	n.a.	n.a.	n.a.	n.a.	n.a.	0.02	n.d.	0.06	0.18
Cl	0.14	n.a.	n.a.	n.a.	0.05	0.06	0.04	0.05	n.d.	0.02
Total	***100.25***	***99.22***	***99.54***	***99.99***	***100.50***	***100.18***	***99.73***	***99.52***	***100.22***	***99.92***
Mg#	***90.55***	***91.99***	***91.76***	***92.75***	***92.43***	***92.59***	***90.86***	***91.24***	***82.69***	***81.73***
Anal.-Nr.	*dd09c17*	*ob29c07*	*ob29c08*		*ob28e18*	*ob28e17*	*as12a12*	*as12a08*	*dd08g05*	*dd08f08*
P	445	222	235	n.a.	175	196	206	120	214	266
K	4301	3916	3637	n.a.	2393	2654	2955	3655	13289	12762
Sc	40.2	7.04	6.63	n.a.	35.8	34.5	31.1	35.2	37.5	27.0
Ti	720	9867	9917	n.a.	1732	1898	1421	1589	32154	32071
V	216	317	332	n.a.	289	299	172	187	469	404
Ni	726	842	828	n.a.	811	876	737	813	638	530
Zn	29.8	16.3	15.9	n.a.	18.8	21.4	45.1	45.7	46.3	54.8
Ga	n.a.	9.81	9.39	n.a.	10.3	11.4	8.67	8.72	n.a.	n.a.
Rb	2.79	1.84	1.51	n.a.	0.35	0.50	0.96	1.50	7.44	7.13
Sr	216	325	335	n.a.	70.8	66.7	95.5	117	618	668
Y	10.1	2.69	3.15	n.a.	11.1	12.6	39.0	35.9	31.0	35.5
Zr	5.39	3.70	3.31	n.a.	2.92	2.97	11.4	59.2	93.3	110
Nb	3.39	4.13	4.47	n.a.	1.02	1.21	19.2	70.5	26.5	34.1
Cs	0.006	<0.001	0.005	n.a.	0.006	<0.009	0.008	0.018	<0.019	<0.010
Ba	78.1	61.4	54.0	n.a.	2.59	3.09	8.46	8.41	331	322
La	35.7	11.6	11.0	n.a.	7.04	8.24	17.7	11.3	10.7	13.8
Ce	62.7	22.5	23.1	n.a.	21.7	24.8	62.1	42.6	33.8	44.8
Pr	5.74	2.08	2.24	n.a.	3.01	3.49	8.56	6.23	5.57	7.24
Nd	17.7	7.20	7.79	n.a.	12.8	15.1	36.3	29.6	31.8	39.8
Sm	2.08	1.43	1.43	n.a.	2.85	3.16	7.52	7.40	9.45	11.1
Eu	0.80	0.58	0.60	n.a.	1.08	1.15	2.32	2.52	3.63	3.84
Gd	1.82	0.85	0.88	n.a.	2.25	2.41	7.01	6.92	9.40	9.80
Tb		0.11	0.13	n.a.	0.39	0.50	1.20	1.17	n.a.	n.a.
Dy	1.71	0.57	0.67	n.a.	2.02	2.52	7.35	6.98	7.00	8.19
Ho	0.36	0.10	0.10	n.a.	0.39	0.50	1.55	1.44	1.37	1.47
Er	1.06	0.24	0.27	n.a.	0.97	1.14	4.05	3.82	2.96	3.36
Tm	0.16	0.030	0.033	n.a.	0.12	0.17	0.60	0.58	0.27	0.39
Yb	1.20	0.28	0.30	n.a.	0.77	0.99	4.00	3.86	2.43	2.72
Lu	0.19	0.036	0.038	n.a.	0.079	0.077	0.58	0.44	0.33	0.31
Hf	0.15	0.067	0.054	n.a.	0.065	0.048	0.28	0.78	3.31	3.76
Ta	0.033	0.14	0.14	n.a.	0.002	0.004	0.10	1.07	1.67	1.98
Pb	2.01	3.60	3.74	n.a.	1.42	1.73	1.95	2.22	0.22	0.39
Th	6.82	1.50	1.34	n.a.	1.81	1.96	0.59	0.28	0.10	0.20
U	2.12	0.39	0.39	n.a.	0.40	0.48	0.19	0.12	0.018	0.048

katoph.: Mg-katophorite; kaersut.: kaersutite; interst.: interstitial; m.p.: melt pockets; n.d.: not detected;
n.a.: not analysed; *: calculated assuming 2 H per formula unit; **: corrected for F and Cl

Table 3.5: Representative analyses of phlogopite and apatite (oxides in wt%; trace elements in µg/g)

Type	**III-b**		**III-c**						**III-b**	**III-c**
Mineral	**phlog.**	**phlog.**	**phlog.**	**phlog.**	**phlog.**	**phlog.**	**phlog.**	**Mineral**	**apatite**	**apatite**
Sample	1965/15	1965/15	1965/3	785*	785*	785*	1965/25	**Sample**	1959/15	1965/3
Texture	veinlet	interst.	in opx	in opx	with amph in m.p.	around chromite	incl. in amph	**Texture**	bleb in glass	interst. grain
SiO_2	39.25	39.14	41.71	41.90	41.24	41.34	42.30	**SiO_2**	0.16	0.49
TiO_2	3.13	3.07	0.09	0.53	0.39	0.37	0.27	**Al_2O_3**	0.01	n.d.
Al_2O_3	15.44	15.83	13.60	13.60	13.84	13.77	14.77	**P_2O_5**	37.68	37.15
Cr_2O_3	1.12	1.05	1.32	1.47	1.90	1.97	0.63	**$FeO_{(tot)}$**	0.37	0.29
$FeO_{(tot)}$	3.50	3.47	2.71	0.00	2.89	2.77	3.40	**MnO**	0.06	n.d.
MnO	n.d.	0.02	0.08	3.05	0.04	0.02	0.05	**MgO**	0.84	0.91
NiO	0.23	0.27	0.19	0.23	0.24	0.28	0.23	**CaO**	47.50	42.37
MgO	22.87	22.80	25.77	25.91	25.82	25.28	25.25	**SrO**	0.95	3.97
CaO	n.d.	0.02	0.01	n.d.	0.04	0.01	0.02	**Na_2O**	0.79	1.33
Na_2O	2.15	2.19	2.82	2.58	2.64	2.62	2.08	**La_2O_3**	0.03	0.07
K_2O	7.19	7.07	7.04	7.06	6.74	6.84	6.83	**Ce_2O_3**	0.88	3.47
H_2O*	4.28	4.29	4.16	4.28	4.25	4.24	4.30	**Nd_2O_3**	0.03	0.07
F	n.a.	n.a.	0.12	0.04	0.06	0.05	0.04	**F**	1.39	2.24
Cl	n.a.	n.a.	0.22	0.06	0.07	0.05	0.04	**Cl**	2.87	0.92
Total **	***99.16***	***99.22***	***99.87***	***100.69***	***100.13***	***99.59***	***100.20***	***Total*** **	***93.05***	***92.45***
Mg#	***92.82***	***92.87***	***94.43***	***93.80***	***94.08***	***94.20***	***92.98***	***Mg#***	***80.08***	***84.84***
Anal.-Nr.	*ob29c16*	*ob29c10*	*dd08c05*	*ob28e05*	*ob28e13*	*ob28e07*	*as12a05*		*dd09b14*	*dd08e07*
P	36.9	18.7	48.0	33.9	20.6	18.8	36.2	**P**	129717	139419
K	71711	72575	60747	79052	70997	69992	70189	**K**	110	89.7
Sc	0.99	1.10	1.31	1.30	0.88	0.91	1.60	**Sc**	2.42	0.79
Ti	15500	16408	890	2839	2096	1807	1736	**Ti**	23.5	<2.93
V	255	284	88.8	142	108	130	78.8	**V**	3.65	3.82
Ni	1808	1727	1744	2046	1813	1773	1905	**Ni**	12.1	3.97
Zn	23.4	22.1	35.8	38.2	31.7	32.1	69.5	**Zn**	1.19	0.96
Ga	11.1	9.84	n.a.	21.0	19.0	18.8	23.5	**Ga**	n.a.	n.a.
Rb	185	147	289	183	133	133	342	**Rb**	0.15	0.49
Sr	102	116	77.5	32.5	36.3	35.0	101	**Sr**	7138	42233
Y	0.10	0.086	<0.057	<0.054	0.021	0.006	0.052	**Y**	98.8	1454
Zr	0.19	0.19	0.43	<0.088	0.077	0.070	0.73	**Zr**	3.07	1.01
Nb	5.06	6.28	47.9	1.77	1.02	1.46	21.0	**Nb**	0.24	0.20
Cs	1.75	1.38	2.61	3.99	2.16	1.80	7.98	**Cs**	<0.013	<0.036
Ba	1212	1096	1343	298	277	219	1124	**Ba**	139	126
La	0.10	0.055	0.069	<0.029	0.020	<0.003	<0.045	**La**	7460	19048
Ce	0.027	0.011	<0.075	<0.019	0.14	<0.003	0.078	**Ce**	6844	25945
Pr	0.012	0.008	<0.067	<0.024	0.012	<0.003	<0.019	**Pr**	380	2212
Nd	0.019	0.035	<0.41	<0.079	0.065	<0.009	<0.22	**Nd**	749	6530
Sm	0.015	<0.011	<0.47	<0.090	0.016	<0.010	<0.13	**Sm**	51.5	747
Eu	0.022	0.017	<0.10	<0.026	0.013	0.010	<0.095	**Eu**	14.7	189
Gd	<0.010	<0.011	<0.43	<0.151	<0.011	0.012	0.17	**Gd**	31.4	451
Tb	<0.002	<0.002	n.a.	<0.027	0.002	<0.002	<0.028	**Tb**	n.a.	n.a.
Dy	<0.015	<0.017	0.45	<0.077	<0.007	<0.006	<0.077	**Dy**	19.8	281
Ho	<0.002	<0.003	<0.043	<0.020	0.002	<0.002	<0.028	**Ho**	3.59	51.1
Er	<0.009	<0.013	<0.25	<0.11	<0.016	<0.009	<0.11	**Er**	9.03	119
Tm	<0.002	<0.002	<0.088	<0.013	0.002	0.003	<0.018	**Tm**	1.19	13.8
Yb	<0.014	<0.011	<0.47	<0.15	<0.011	<0.019	<0.17	**Yb**	8.03	72.4
Lu	0.002	<0.002	<0.061	<0.014	<0.002	<0.002	<0.020	**Lu**	1.15	7.42
Hf	0.019	0.018	<0.25	<0.053	<0.012	<0.006	<0.19	**Hf**	<0.023	<0.120
Ta	0.20	0.22	1.40	0.031	0.012	0.009	0.23	**Ta**	<0.015	<0.075
Pb	5.46	5.86	1.25	1.08	0.83	0.98	1.43	**Pb**	43.6	5.77
Th	<0.004	<0.004	<0.080	0.043	0.088	0.056	<0.021	**Th**	2538	1305
U	0.012	0.011	0.069	<0.018	0.038	0.030	0.031	**U**	572	278

interst.: interstitial; m.p.: melt pocket; *: calculated assuming 2 H per formula unit (22 oxygens); **: corrected for F and Cl; n.a.: not analysed; n.d.: not detected

Table 3.6: Representative analyses of silicate glass (oxides in wt%; trace elements in µg/g)

Group	**I**	**II**		**III-b**		**III-c**				**Host**
sample	1963/1	1958/13	1959/25	1959/15	1965/15	785*	1965/25	1965/3	1965/3	
remark	melt pocket	within sympl	next spl	next amph	next cpx	next amph	next amph	melt pocket	next apatite	host basanite*
SiO_2	54.41	52.07	56.94	53.06	57.75	60.96	56.57	59.38	59.74	44.10
TiO_2	2.03	2.57	1.31	0.17	1.57	0.62	0.30	0.24	0.20	2.55
Al_2O_3	19.94	18.96	19.55	24.12	20.53	17.79	23.13	15.75	12.45	13.96
Cr_2O_3	0.02	0.07	0.07	0.05	0.01	0.01	0.01	n.d.	n.d.	n.a.
$FeO_{(tot)}$	2.89	3.24	2.83	1.88	2.47	1.26	2.52	2.95	3.74	12.83
MnO	0.13	0.06	0.06	0.07	0.00	0.01	0.04	0.05	0.08	0.21
NiO	n.d.	n.a.	0.01	n.d.	n.d.	n.a.	0.00	n.a.	0.06	n.a.
MgO	3.40	3.79	3.19	1.82	1.29	1.14	1.22	3.04	3.82	9.38
CaO	8.34	11.87	6.67	5.06	2.57	0.82	0.44	1.24	1.01	10.30
Na_2O	3.72	3.25	6.36	11.07	9.66	9.71	12.99	13.88	13.84	3.74
K_2O	2.30	0.75	0.04	1.54	1.97	3.57	1.38	1.21	1.42	1.46
Cl	0.01	0.22	0.02	0.31	1.06	0.12	0.14	0.23	0.61	n.a.
P_2O_5	0.14	0.15	0.15	0.41	0.08	0.09	0.12	0.49	2.33	0.59
Total	***97.35***	***96.99***	***97.20***	***99.56***	***98.96***	***96.09***	***98.88***	***98.45***	***99.29***	***99.12***
Mg#	***67.72***	***67.62***	***66.76***	***63.29***	***48.16***	***61.75***	***46.32***	***64.74***	***64.58***	***56.58***
Anal.-Nr.	*ob29e07*	*dd08a08*	*dd09a05*	*dd09c05*	*ob29c11*	*ob28e09*	*as12a09*	*dd08d14*	*dd08e08*	
P	130	179	144	1061	448	230	503	1519	6738	n.a.
K	25085	8111	419	12563	16408	32515	15882	9265	11277	n.a.
Sc	30.2	69.4	13.2	1.79	1.84	1.25	0.068	0.22	1.02	23.7
Ti	12900	14226	6346	665	7329	0.041	0.46	0.80	1.403	15311
V	95.6	390	119	107	26.5	0.081	0.42	0.85	2.921	n.a.
Ni	27.6	49.1	33.9	12.8	37.1	0.25	0.95	2.06	4.462	191
Zn	52.0	21.8	11.5	9.62	10.3	0.022	1.23	10.1	7.839	n.a.
Ga	9.77	n.a.	n.a.	n.a.	17.3	0.82	1.12	4.38	10.3	n.a.
Rb	24.6	10.8	0.43	18.1	26.3	0.44	3.08	6.67	12.0	36.9
Sr	146	289	257	427	488	4.06	1.51	9.70	13.6	792
Y	16.3	33.9	13.9	5.43	1.45	0.58	2.56	6.11	15.3	29.9
Zr	36.1	59.8	74.3	4.66	17.1	0.98	4.34	10.4	17.1	216
Nb	4.94	63.8	2.88	4.16	16.1	1.58	4.03	10.6	24.5	64.7
Cs	0.41	0.078	<0.085	0.14	0.46	2.55	8.40	7.97	26.0	n.a.
Ba	174	536	9.50	238	261	7.61	66.0	57.8	36.5	563
La	1.70	13.7	3.36	69.8	18.3	1.79	4.19	14.1	37.9	46.2
Ce	5.16	20.3	8.79	94.7	25.6	54.6	6.27	17.6	39.8	82.3
Pr	0.89	2.20	1.74	6.55	1.94	11.0	46.0	44.0	50.8	n.a.
Nd	5.98	11.1	5.78	14.6	6.03	0.99	1.52	4.47	72.4	40.0
Sm	1.53	3.57	1.81	1.42	0.48	3.30	11.6	30.4	97.5	8.51
Eu	0.73	1.18	0.67	0.41	0.35	79.6	92.0	210	151	2.67
Gd	2.56	4.47	2.00	0.62	0.51	7.52	26.2	61.9	158	7.29
Tb	0.44	n.a.	n.a.	n.a.	0.086	2.60	136	234	164	1.11
Dy	2.83	5.72	2.68	0.90	0.27	4.66	7.04	18.5	247	n.a.
Ho	0.63	1.36	0.76	0.23	0.037	10.1	33.0	99.3	256	1.14
Er	1.83	3.84	1.79	0.45	0.38	14.4	89.0	221	1008	n.a.
Tm	0.20	0.53	0.15	0.09	<0.039	129	168	405	1099	0.52
Yb	2.27	3.66	1.99	0.62	0.23	2953	1966	1213	1163	2.20
Lu	0.25	0.52	0.25	0.14	0.050	30.8	138	333	1265	0.31
Hf	1.14	1.61	1.94	0.26	0.52	188	881	1644	4997	5.04
Ta	0.18	2.05	0.15	<0.080	0.33	0.14	0.76	1.10	<0.87	4.03
Pb	0.73	0.59	0.69	5.41	44.8	<5.75	9.83	17.0	<19.9	n.a.
Th	0.053	1.55	0.39	19.4	2.96	19.4	22.0	n.a.	n.a.	5.06
U	0.029	0.34	0.055	5.45	0.69	0.20	0.71	n.a.	n.a.	1.26

*: average composition of the strongly alkaline basanites from Marsabit (Volker, 1990); n.d.: not detected; n.a.: not analysed

Table 3.7: Representative analyses of carbonates (oxides in wt%; trace elements in µg/g)

Group	II	III-b	III-c	III-c	III-c
Mineral	**Mg-Cc**	**Dol**	**Mg-Cc**	**Mg-Cc**	**Mg-Cc**
Sample	1958/13	1959/15	785*	1965/3	1965/3
Texture	in glass	in glass	in glass	in glass	in glass
SiO_2	n.a.	n.a.	n.a.	n.d.	0.03
FeO_{tot}	0.07	0.16	0.10	0.10	0.06
MnO	0.04	0.01	n.d.	n.d.	n.d.
MgO	1.25	19.22	1.90	1.25	5.17
CaO	54.43	31.89	53.77	53.91	48.53
Na_2O	n.d.	0.03	0.04	n.d.	0.03
K_2O	n.a.	n.a.	n.a.	0.01	n.d.
SrO	n.d.	0.03	0.08	0.04	0.21
BaO	n.d.	0.03	n.d.	n.a.	n.a.
CO_2*	44.14	46.18	44.42	43.77	43.91
Total	***99.93***	***97.56***	***100.32***	***99.09***	***97.94***
Mg#	***96.95***	***99.54***	***97.13***	***95.54***	***99.31***
Ca#*	***96.90***	***54.39***	***95.31***	***96.87***	***87.09***
Anal-Nr.	*dd08a07*	*dd09c12*	*ob28e15*	*dd08d10*	*dd08d11*
P	196	220	137	580	589
K	8.67	9.70	6.42	10.5	15.5
Sc	1.54	<0.65	0.27	<0.27	<0.076
Ti	111	9.75	24.2	5.28	1.96
V	0.96	<0.85	<0.42	<0.37	0.21
Ni	11.6	9.00	5.17	<2.94	5.93
Zn	1.72	4.59	1.13	2.96	0.45
Ga	n.a.	n.a.	<0.13	n.a.	n.a.
Rb	<0.12	0.084	<0.074	<0.060	0.046
Sr	55.8	593	371	251	4274
Y	3.99	0.12	1.30	7.04	0.15
Zr	1.20	2.61	0.12	0.97	7.56
Nb	0.80	1.44	0.056	6.92	1.85
Cs	0.087	<0.063	<0.018	<0.039	<0.008
Ba	0.44	1.26	<0.24	0.29	27.1
La	0.88	0.34	0.84	13.6	0.25
Ce	1.70	0.32	1.34	9.97	0.23
Pr	0.17	0.060	0.18	0.95	0.026
Nd	0.89	0.30	0.68	2.28	0.078
Sm	0.26	<0.44	0.074	0.48	<0.018
Eu	0.095	<0.12	0.051	0.20	<0.008
Gd	0.46	<0.37	0.14	0.51	0.026
Tb	n.a.	n.a.	0.036	n.a.	n.a.
Dy	0.36	<0.19	0.089	0.58	<0.038
Ho	0.097	<0.029	0.044	0.11	<0.006
Er	0.38	<0.117	0.083	0.33	<0.019
Tm	0.075	<0.052	0.016	0.084	<0.006
Yb	0.24	<0.43	0.14	0.27	<0.040
Lu	<0.023	<0.072	0.011	0.066	<0.008
Hf	<0.065	<0.16	<0.036	<0.074	<0.013
Ta	<0.036	0.048	<0.016	<0.031	0.008
Pb	<0.15	<0.24	<0.21	0.74	0.18
Th	<0.039	0.021	<0.017	<0.028	<0.005
U	0.14	0.60	0.86	6.00	1.48

Mg-Cc: Mg-calcite; Dol: dolomite; n.d.: not detected;
n.a.: not analysed; *: calculated from stoichiometry; **: Ca/(Ca+Mg)

silicic edenite-Mg-katophorite (Fig. 3.6a). Amphibole lamellae in cpx-I (in Type III-b) have similar compositions. Cr contents (Fig. 3.6b) are high only in amphiboles related to metasomatic replacement of spl-I. F and Cl contents in all amphiboles are low (Table 3.4). Trace element patterns show enrichment in U and Th, strongly negative Hf and Zr anomalies, and enrichment of LREEs over HREEs (Fig. 3.7a-b). Amphibole from sample Ke 1965/15 shows the lowest HREE concentrations, but in contrast, exhibits a conspicuous positive Ti anomaly (Fig. 3.7b). Nb and Ta vary considerably with highest abundances in euhedral Mg-katophorite (Table 3.4; Fig. 3.7c). Compared to typical mantle amphiboles the Mg-katophorites show a large compositional range (e.g., Fig. 3.8a). They are, however, remarkably depleted in LILEs (e.g., 1.26-83 µg/g Ba compared to 75-1400 µg/g as reported for mantle amphibole from several off-craton xenolith suites; see Ionov *et al.*, 1997), and show low LILE/LREE ratios (Fig. 3.8b).

Phlogopite

Phlogopites (Table 3.5) have very high Na_2O contents (up to 2.88 wt%). Ti concentrations are mostly very low (Fig. 3.9a), and Mg#s are high (> 93). F and Cl contents are low (Table 3.5). Generally, Na-rich phlogopites have higher U and Th concentrations and lower HFSE contents than phlogopite from the Group I (grt)-spl lherzolites (Fig. 3.9a). Some trace elements show very broad ranges within different samples (e.g., Nb ranging from 1.02 µg/g in Ke 785* to 47.9 µg/g in Ke 1965/3).

Apatite

Considerable differences were found between the two textural types of apatite (early in sample Ke 1965/3 and phosphate globules associated with glass). Microprobe analyses only poorly satisfy apatite stoichiometry and show quite low totals (Table 3.5). This is most likely due to the abundant inclusions, which are in-

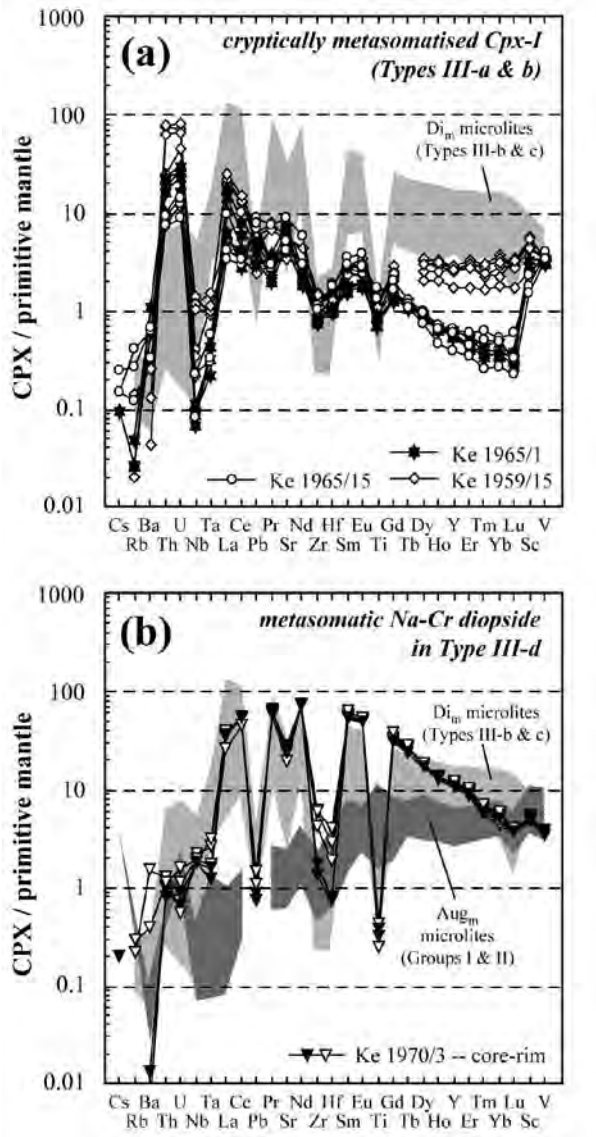


Fig. 3.5. *Trace element composition of clinopyroxene from the porphyroclastic spl harzburgites from Marsabit (normalised to the primitive mantle values of McDonough & Sun, 1995);* ***(a)*** *Trace element patterns of primary cryptically metasomatised clinopyroxene (cpx-I) in Type III-a and -b spl harzburgites;* ***(b)*** *Trace element patterns of Na-rich Cr diopside (Di_m) from the recrystallised Type III-d spl harzburgite. The shaded fields indicate the compositional range of glass-related clinopyroxene (Na-rich Cr diopside, Di_m = light grey; (Ti)-augite, Aug_m = dark grey).*

evitably included in the analysis. Early apatite is F-rich (1.89 – 2.53 wt% F) with variable Cl contents (0.92 – 1.57 wt%). It has extremely high LREE contents (up to 3.75 wt% Ce_2O_3, measured with electron microprobe), and very high SrO (3.38 – 5.24 wt%). The elevated MgO (~1.06 wt%) and Na_2O (~1.37 wt%) contents and FeO_{tot} of 0.19 – 0.31 wt% are typical for upper mantle apatites (O'Reilly & Griffin, 2000).

In contrast, apatite globules in silicate glass are Cl-rich (2.96 – 3.14 wt% Cl) and have lower F, Ce_2O_3, SrO and Na_2O, but slightly higher FeO_{tot} contents (Table 3.5). Both types of apatite are strongly LREE-enriched [$(La/Yb)_N$ up to 783] and are the major host for U and Th (up to 33'500 times primitive mantle values) but with Nb, Ta, Zr, Hf and Ti extremely depleted compared to the REEs (Fig. 3.9b).

Late (glass-bearing) assemblages

Silicate glass

Representative microprobe and LA-ICPMS analyses of silicate glass are given in Table 3.6, selected compositional plots are displayed in Fig. 3.10a-f. Generally, glass is siliceous (up to 66 wt% SiO_2) and peraluminous (12.45-25.07 wt% Al_2O_3) with similar characteristics (very low MgO and FeO, high alkalis) to that in many other xenolith suites (e.g., Ionov *et al.*, 1994; Zinngrebe & Foley, 1995; Chazot *et al.*, 1996; Neumann & Wulff-Pedersen, 1997; Draper & Green, 1997; Coltorti *et al.*, 2000; Laurora *et al.*, 2001; Shaw & Klügel, 2002; Ban *et al.*, 2005). Mg#s are commonly high (up to ~70; Fig. 3.10b). All compositional parameters are clearly distinct from the xenolith-hosting basanites (Fig. 3.10a-f).

Although broad compositional ranges are observed, several characteristics allow distinguishing between glass hosted by Group I and II and glass in Group III xenoliths: the latter are generally more Si-rich, have higher alkali contents (broadly phonolitic with Na_2O up to 14.11

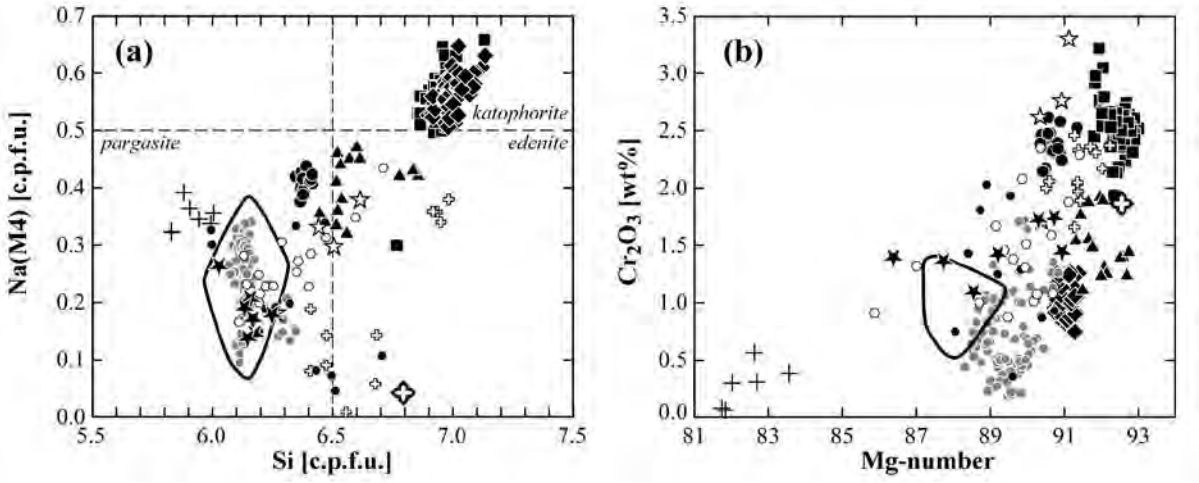


Fig. 3.6. *Major element characteristics of amphiboles from porphyroclastic spl harzburgites from Marsabit, compared to compositions of mantle-derived amphibole from other localities (Mg-number = Mg/(Mg+Fe_{tot}) in molar proportions; for symbol legend and references see Fig. 3.8).*

wt%; Fig. 3.10a) and lower Ti concentrations (Fig. 3.10c). With respect to trace elements, alkali-rich glass (Type III-b and -c) is always LREE-enriched [$(La/Yb)_N$ up to 77] at variable absolute REE concentrations (Fig. 3.11a; Yb_N from 1.4 up to 91.0). Zr, Hf, and Ti are depleted relative to the REEs, and in Nb and Ta relative to Th and U.

Glass from the virtually anhydrous Group II samples (Ke 1958/13 and Ke 1959/25) is compositionally close to glass from Group I (grt)-spl lherzolites (basaltic to trachyandesitic compositions; Fig. 3.10b). Trace element patterns range from LREE-depleted to slightly enriched, while absolute LREE concentrations are lower than in the alkali-rich glass (Group III-b and –c). Negative HFSE anomalies are lacking and Nb and Ta are enriched relative to Th and U. The trace element composition of silicate glass always mirrors the composition of the associated early metasomatic phases (i.e. amphibole in most cases but also clinopyroxene, phlogopite, apatite, spinel and orthopyroxene).

Glass within the Type III-c dunite Ke 1959/27 and from the margin of xenolith Ke 1965/15 (contact with host lava) show some important differences compared to glass from the other samples, i.e. enrichment in FeO and SiO_2 contents, close to the composition of the host basanite (Fig. 3.10a-f and 3.11b).

Clinopyroxene microlites

Glass-related clinopyroxenes from Group I and II are augites (Aug_m), while glass-bearing assemblages from Type III-b and c contain Na-rich Cr diopsides (Di_m; up to 3.23 wt% Na_2O and 6.45 wt% Cr_2O_3; Fig. 3.11a and b). Both Aug_m and Di_m show considerable heterogeneity (Table 3.2) which is mostly the result of sector zoning (e.g., Fig. 3.3e). Di_m is similar to glass-related clinopyroxene reported from other localities (e.g., Dautria *et al.*, 1992; Hauri *et al.*, 1993; Ionov *et al.*, 1996; Ban *et al.*, 2005). Mg#s are very high (up to 94.9). Clinopyroxene from the kaersutite-bearing dunite (Ke 1959/27) is strongly zoned with Di_m cores enclosed by Aug_m rims, accompanied by a significant decrease of Mg#s.

Trace element patterns in both Di_m and Aug_m are similar in shape to the associated glass (except LILEs: Cs to U; Fig. 3.11a). Negative HFSE anomalies are mostly due to higher REE abundances, i.e. the absolute concentrations of HFSEs are more or less the same as in cpx-I from Type III-a and -b (see Fig. 3.5a; no real

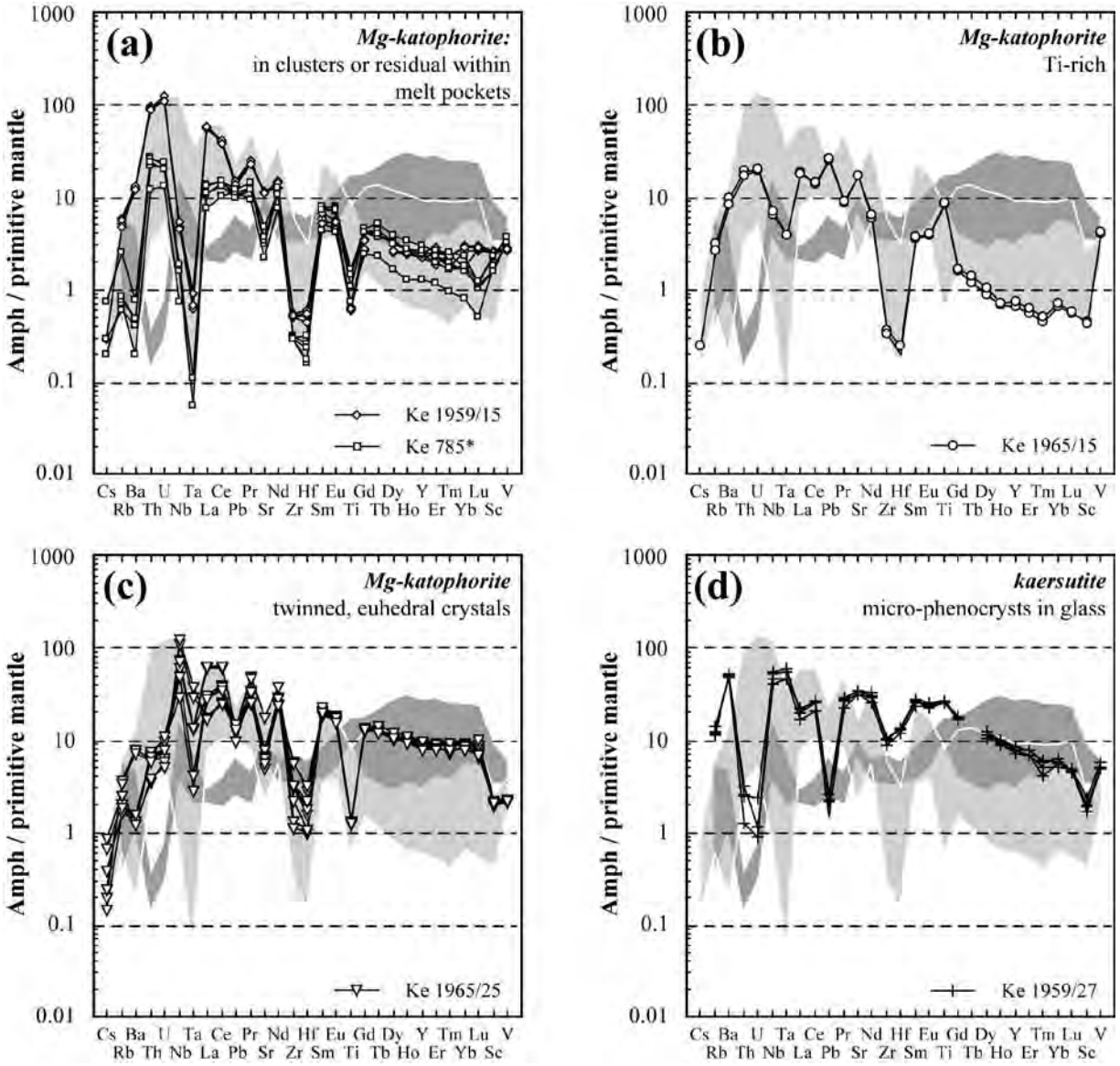


Fig. 3.7. *Trace element composition of amphibole from porphyroclastic spl harzburgites from Marsabit (normalised to the primitive mantle values of McDonough & Sun, 1995); Mg-katophorite in Type III-b and -c xenoliths* ***(a-c)****, and glass-related kaersutite* ***(d)****. The shaded fields indicate the compositional variation of all Mg-katophorite analyses (light grey), and the compositional range of LREE-depleted Ti-pargasite from the Group I (grt)-spl lherzolites (dark grey; Kaeser et al., 2006).*

HFSE depletion). Di_m from the annealed Type III-d spl harzburgite (Ke 1970/6) has identical trace element characteristics compared to glass-hosted Na-rich Cr diopside (Fig. 3.5b).

Olivine, spinel, kaersutite

Compared to ol-I, glass-related Ol_m is more magnesian (Table 3.3; up to Fo94.6) and enriched in Ca. Ol-I in contact with glass develops strong compositional gradients approaching the composition of Ol_m at rims. Spinel microlites (Chr_m) are Mg-rich chromites (Cr# up to 66.5). They are enriched in (calculated) Fe_2O_3 compared to spl-I.

Kaersutite occurs as tiny rims on amphibole in Type III-b and c, and as micro-phenocrysts in sample Ke 1959/27. Reaction rims are character-

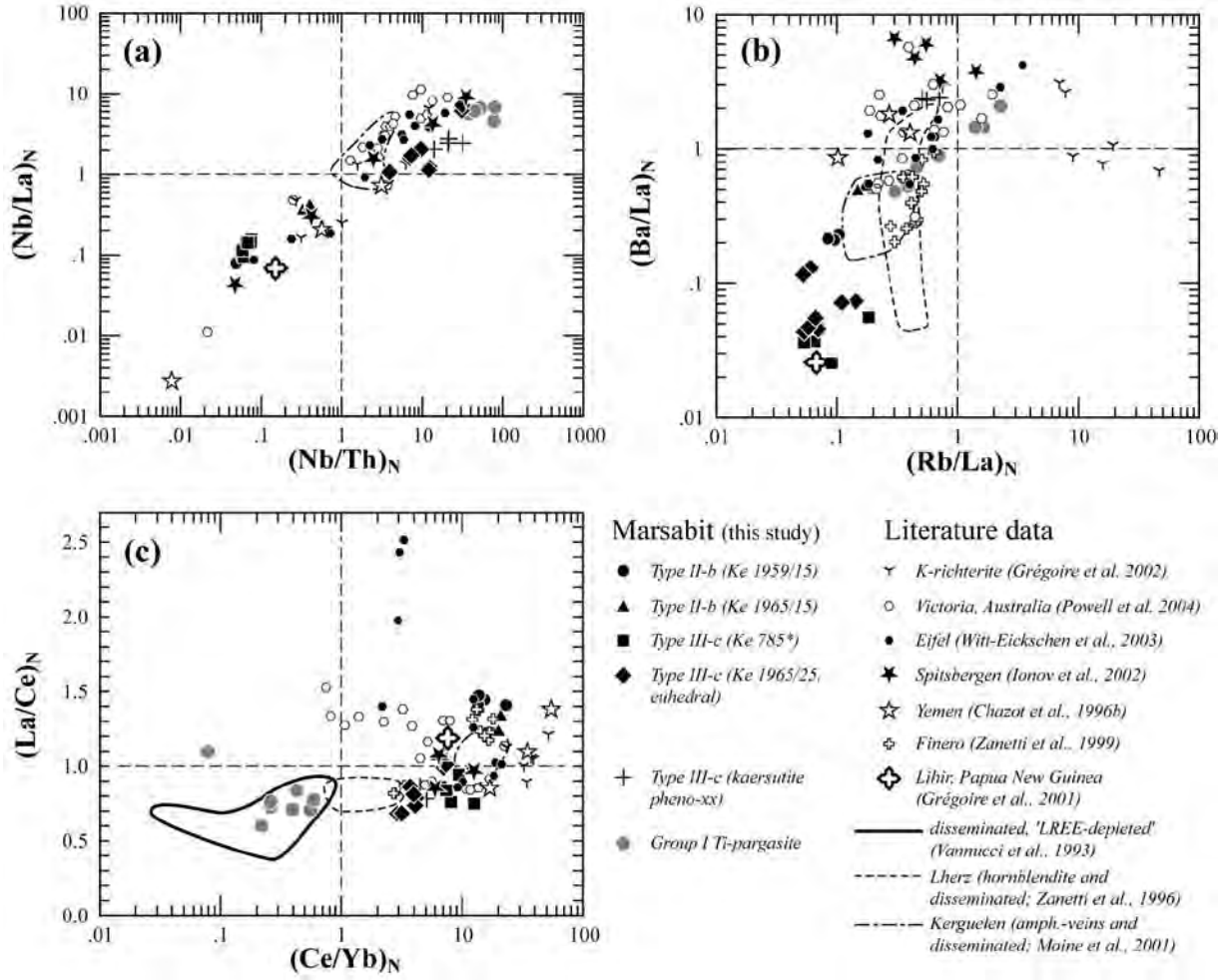


Fig. 3.8. *Selected trace element parameters of amphiboles from the porphyroclastic spl harzburgites from Marsabit compared to those of mantle-derived amphibole from other mantle xenolith suites and from peridotite massifs (see text for explanations). Concentrations (ratios) normalised to the primitive mantle values of McDonough and Sun (1995).*

ised by higher Mg#s than the 'primary' amphibole. They are too narrow to be analysed for trace elements. Kaersutite micro-phenocrysts in sample Ke 1959/27 have low Mg# (about 82) and high K_2O contents (Table 3.4). Major element characteristics as well as trace element patterns (convex upward REE patterns, high Nb-Ta, low U-Th; Fig. 3.6d) are similar to hornblendites and amphibole megacrysts from alkaline magmas (e.g., Shaw and Eyzaguirre, 2000).

Carbonates

Most glass-related carbonate globules contain Mg-calcite (Table 3.7) with an average Mg# of 96.5 and Ca/(Ca+Mg) between 0.87 and 0.98. In sample Ke 1965/3, MgO correlates positively with SrO (up to 5.35 wt% MgO and 0.89 wt% SrO). Other elements show very low concentrations (Table 3.7). One sample (Type III-c Ke 1959/15) contains zoned crystals ranging from dolomitic to calcitic in composition. Carbonates have low REE contents with flat to slightly LREE-enriched patterns (Fig. 3.12). Extended trace element plots exhibit a very broad range of concentrations in different samples (e.g., Pb; Fig. 3.12). Large positive peaks for U, Pb and Sr are typical. In addition, U and Nb are strongly enriched compared to Th and Ta, respectively. Hf, Zr and Ti show very low concentrations.

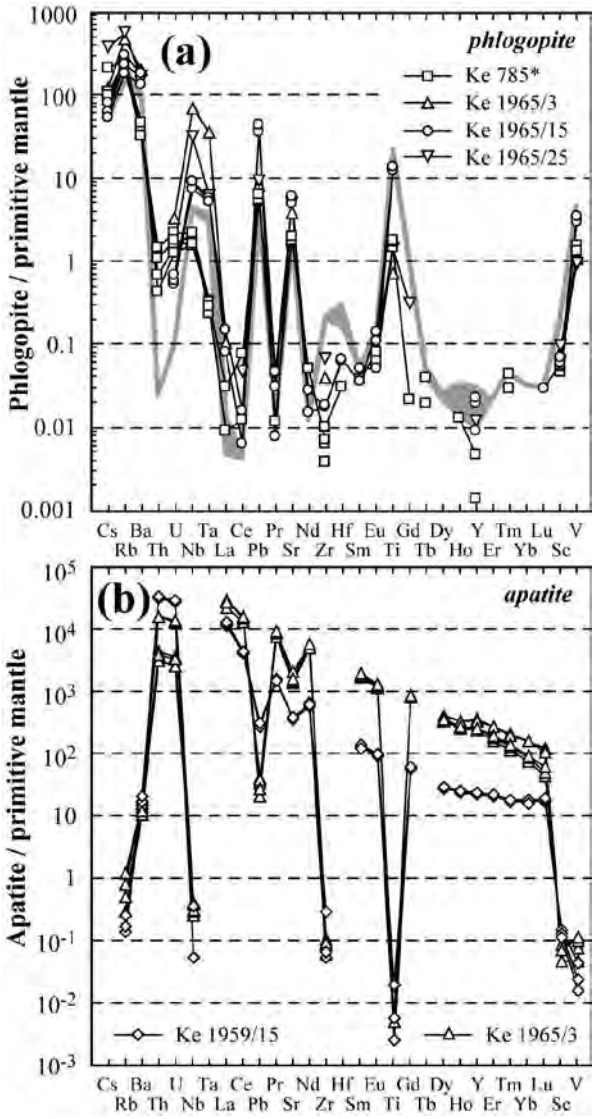


Fig. 3.9. *Trace element patterns of* ***(a)*** *phlogopite, and* ***(b)*** *apatite from porphyroclastic spl harzburgites from Marsabit (concentrations normalised to the primitive mantle values of McDonough & Sun, 1995). The grey field in* ***(a)*** *indicates the composition of Ti-rich phlogopite in Group I (grt)-spl lherzolites (Kaeser et al., 2006).*

Overall, major and trace element characteristics of the carbonates are similar to carbonates found in other peridotite xenoliths (e.g., Ionov, 1998; Lee *et al.*, 2000; Laurora *et al.*, 2001; Ionov & Harmer, 2002; see Fig. 3.12).

DISCUSSION

Despite large compositional variations, numerous common textural and compositional features indicate that the early metasomatic assemblages in all Group III samples formed during one single metasomatic event. In the following discussion, we argue that during a first metasomatic stage, the primary (pre-metasomatic) phase assemblage in Group III spl harzburgites was partially replaced by metasomatic minerals, finally resulting in clinopyroxene-free amphibole- and phlogopite-bearing dunite and harzburgite (Type III-c). The initial metasomatic agent was most likely an evolved Si-rich melt, and the transition from peridotites of Type III-a to -c can be explained by progressive melt-rock reaction. We will show that the late (glass-bearing) assemblages are closely related to the early metasomatic assemblages, mainly representing break-down products.

Formation of the early assemblages

Transition from cryptic (Type III-a) to modal (Type III-b and c) metasomatism

Formation of new phases requires (i) a melt/fluid freezing out and crystallising (decreasing melt mass) and/or (ii) liquid-solid or sub-solidus reaction. Textural features such as spinel being replaced by amphibole and phlogopite (e.g., Fig. 3.2c) indicate melt(fluid)-rock reaction. The geochemical signatures observed in the different peridotite types thus most likely reflect complex mixtures of pre-existing compositional heterogeneities coupled with metasomatic modification. This is illustrated best in sample Ke 1965/1 (Type III-a), the least metasomatised xenolith in this study. It can be subdivided into three parts containing clinopyroxene with different REE signatures (Zone A, B and C in Fig. 3.13). The LREEs are increasingly enriched

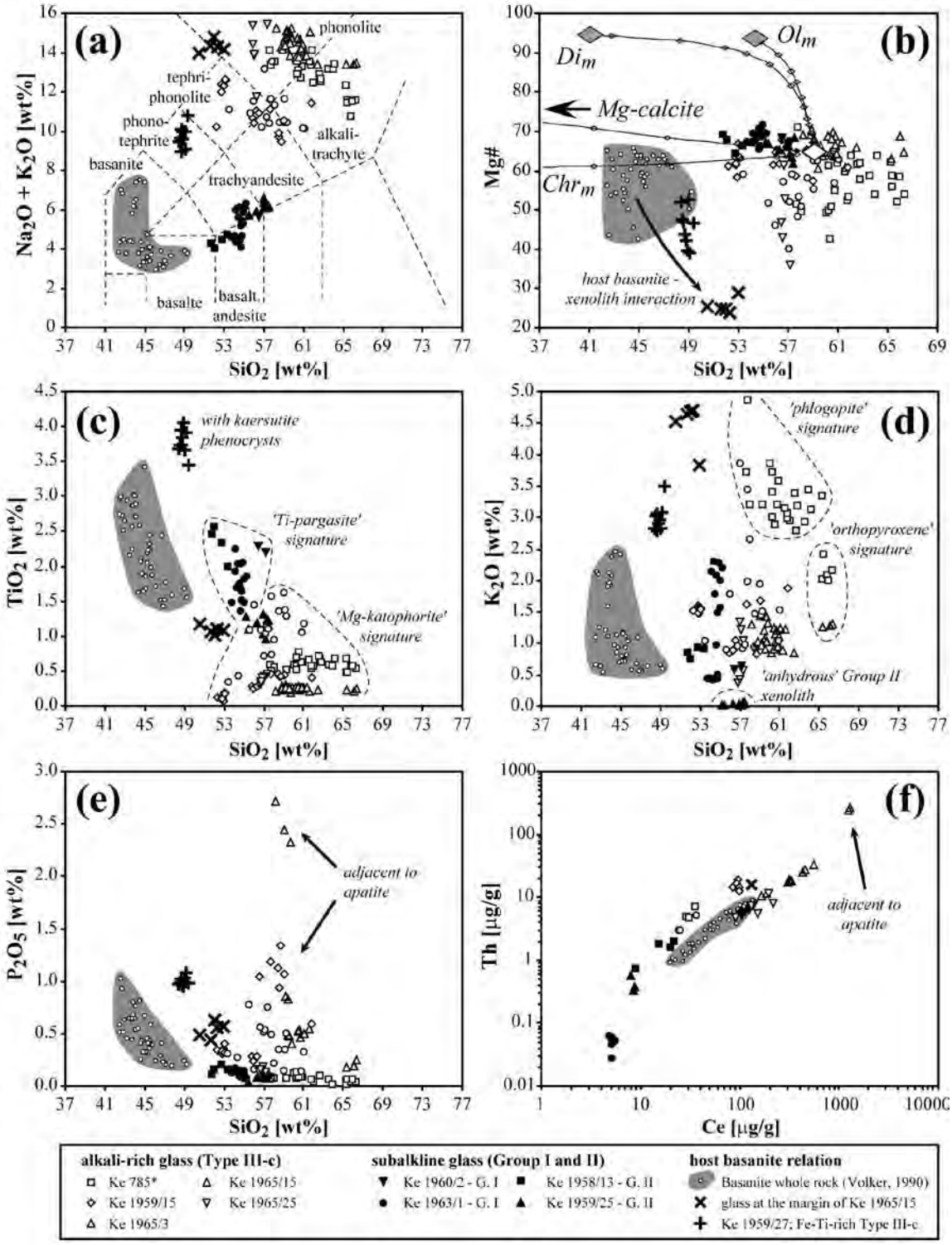


Fig. 3.10. *Total alkalis vs. SiO_2* ***(a)****, Harker-type co-variation diagrams* ***(b-e)*** *and incompatible trace element co-variation diagram* ***(f)*** *showing the compositional variability of silicate glass found in the porphyroclastic spl harzburgites from Marsabit. In* ***(b)*** *binary mixing lines between a typical composition of alkali-rich glass (large empty diamond) and the associated microlites are shown (each increment = 10 wt%). They illustrate that the glass does not represent the derivate of host lava infiltration and fractional crystallisation.*

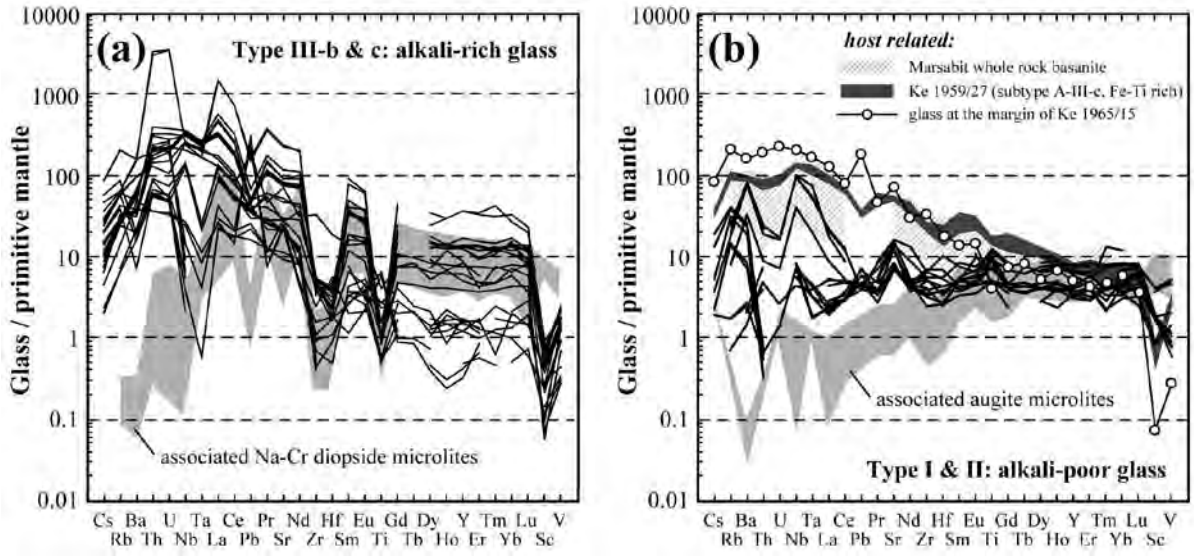


Fig. 3.11. *Trace element patterns of* ***(a)*** *alkali-rich glass in Type III-b and -c spl harzburgite and amphibole dunite, and* ***(b)*** *alkali-poor glass in Group I and II (grt)-spl lherzolites. The grey fields outline the compositional range of the associated Na-rich Cr diopside* ***(a)*** *and augite* ***(b)****. The compositions of the host basanites and alkali basalts and of glass related to xenolith-lava interaction are shown in* ***(b)****.*

from Zone A to C, indicating increasing cryptic metasomatism. HREE abundances, on the other hand, are very heterogeneous in the least metasomatised Zone A, moderately depleted in Zone B, and homogeneously low in the most metasomatised Zone C (containing graphite; Fig. 3.13), similar to REE patterns in clinopyroxene from the amphibole and phlogopite-bearing Type III-b sample (Ke 1965/15; Fig. 3.5a).

The decoupling of strongly (LREEs, Th, U) from moderately incompatible elements (HREEs) can be explained by chromatographic fractionation during percolation of small amounts of melts or fluids through an initially non-metasomatised peridotite (Navon & Stolper, 1987; Godard *et al.*, 1995; Vernières *et al.*, 1997; Bedini *et al.*, 1997; Ionov *et al.,* 2002). Upon reaction with the wall-rock, a fluid or melt will become progressively enriched in incompatible elements as a function of increasing distance from its initial source. This is due to the fact that elements with higher $^{mineral/melt}D$-values (e.g., HREEs) are selectively removed from a percolating melt/fluid when it exchanges with the surrounding minerals. This results in faster moving chemical fronts of incompatible elements compared to those of more compatible elements. This is consistent with the geochemical signature of cpx-I from the least metasomatised part of sample Ke 1965/1 (Zone A; Fig. 3.13) that already started to re-equilibrate with respect to the incompatible elements (i.e. addition of Th, U and LREEs), while more compatible elements still reflect pre-metasomatic heterogeneities. In this particular case, these are extreme HREE variations, most likely reflecting the earlier garnet breakdown (Kaeser *et al.*, 2006). On the other hand, more intensely metasomatised parts (e.g., Zone C in sample Ke 1965/1 and sample Ke 1965/15) are characterised by clinopyroxene trace element patterns where mildly incompatible elements have also been modified (e.g homogeneously depleted HREEs; Fig. 3.5a and 3.13).

Similarly, the modal and compositional differences between Type III-b and -c can be explained by melt percolation and associated trace element fractionation. Compared to Type III-b, higher abundances of metasomatic phases in Type III-c suggests that higher amounts of flu-

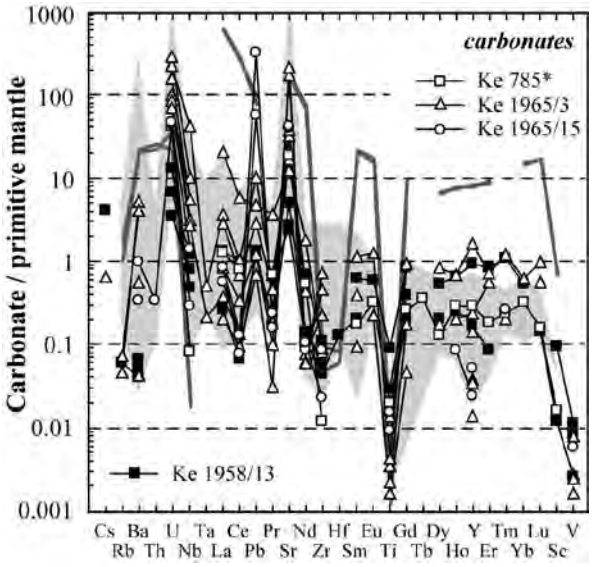


Fig. 3.12. *Trace element patterns of glass-hosted carbonates in peridotite xenoliths from Marsabit (concentrations normalised to the primitive mantle values of McDonough & Sun, 1995). The grey field in* ***(c)*** *outlines the compositional range of carbonates found in other peridotite xenoliths (Ionov & Harmer, 2002 and references therein). Carbonate material interpreted as quenched carbonatite melt, found in peridotite xenoliths from Kerguelen (Moine et al., 2004) is shown for comparison (dark-grey line).*

id/melt crystallised in, or passed through, these rocks. The amphibole-rich dunite (Ke 1965/25), for example, contains low-Ti Mg-katophorite exhibiting the lowest $(La/Yb)_N$ and $(La/Ce)_N$ ratios, and high $(Nb/La)_N$ and $(Nb/Th)_N$ ratios (Fig. 3.8a and c), indicating a moderately fractionated metasomatic agent. Mg-katophorite from the phlogopite-rich harzburgite (Ke 785*; Type III-c), and amphiboles from the more cpx-rich harzburgites (Type III-b) show progressively more fractionated patterns (e.g., Fig. 3.8c) and decreasing abundances in 'amphibole-compatible' elements (e.g., Nb; Fig. 3.7a). Thus, the transition from Type III-c to -b could reflect increasing distance between the site at which the xenolith was sampled and the source of the 'initial' metasomatising agent (Ionov *et al.*, 2002, Bodinier *et al.*, 2004). Judging from the abundance of modal metasomatic phases, the amphibole dunite (Ke 1965/25) was probably closest to the source of the metasomatising agent. The phlogopite-rich nature of Ke 785*, which indicates higher K and LILE (Cs, Rb, Ba) contents in the remaining agent is in line with a more fractionated melt or fluid, at somewhat greater distance from the metasomatic source.

The Nb abundances in amphiboles agree with this model as well. For example, amphibole from Ke 1965/25 has comparatively high Nb concentrations (Fig. 3.7c), in line with relatively high $^{amph/melt}D_{Nb}$ values constrained by different studies (e.g., Ionov and Hofmann, 1995; LaTourrette *et al.*, 1995). In Ti-poor systems, such as in this study, Nb uptake by amphibole is even enhanced due to increased D_{Nb} values (Tiepolo *et al.*, 2001). Consequently, in an event during which amphibole crystallises continuously, the remaining fluid/melt will get progressively depleted in Nb (Ionov *et al.*, 2002), resulting in formation of Nb-depleted amphiboles further away from the source (Ionov *et al.*, 2002); such Nb-depleted amphibole is found in sample Ke 785*, as well as in Type III-b xenoliths (e.g., Ke 1959/15; Fig. 3.7a). Amphibole signatures from xenolith suites modelled successfully in the context of percolative trace element fractionation (e.g., Spitsbergen; Ionov *et al.*, 2002) show similar ranges, e.g., in Nb/Th ratios (Fig. 3.8a) as documented for our samples. This further supports the hypothesis that similar percolation mechanisms acted in the mantle beneath Marsabit.

The role of pre-existing heterogeneities and exotic minerals

Although a model based on trace element fractionation during melt percolation is supported by textures and can account for many compositional features, some compositional peculiarities remain unclear. First, clinopyroxene and amphibole in several samples (Ke 785*, 1965/1 and 1965/15) are characterised by extremely low HREE abundances, more than one order of magnitude lower than in amphiboles from the

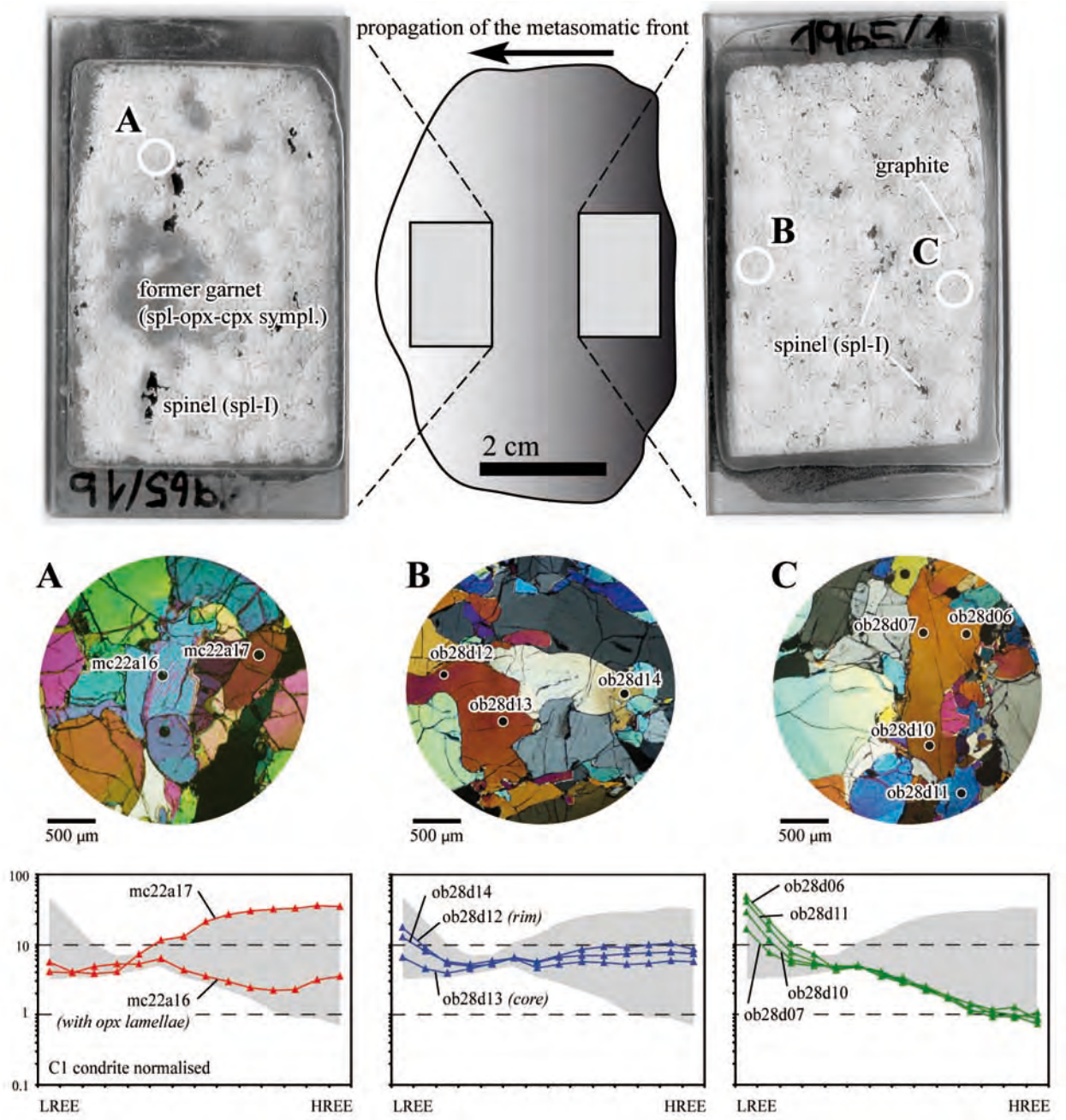


Fig. 3.13. *Detailed REE systematics in primary clinopyroxene (cpx-I) in a porphyroclastic, cryptically metasomatised spl harzburgite (sample Ke 1965/1) displaying the transition from Type III-a (Zone A and B) to Type III-b (Zone C) on a scale of few centimetres. The numbers on the photomicrographs (crossed polars) correspond to single laser ablation microprobe pits (for explanations see text).*

strongly metasomatised amphibole dunite Ke 1965/25 (Fig. 3.5a, 3.7a-c). The main phases that crystallise during metasomatism are low-Ti Mg-katophorite and phlogopite. However, $_{HREE}$-$D^{amph/melt}$ (e.g., LaTourrette *et al.*, 1995) indicate that amphibole crystallisation alone is unlikely to deplete the metasomatic agent to such a high degree in HREEs. The same probably accounts for the extreme Nb depletion in amphiboles from Ke 785*, relative to the other Type III-c xenolith (Ke 1965/25; see also Ionov *et al.*, 2002).

Further, clinopyroxene, phlogopite and amphibole in the Type III-b sample Ke 1965/15 show all, on one hand, strongly fractionated REE patterns (e.g., high La/Ce in amphibole; Fig 8c), but on the other hand, are characterised by a positive Ti anomaly, decoupled from other HFSEs (e.g., Hf and Zr; Fig. 3.7b). Trace element fractionation during amphibole crystallisation (i.e. formation Type III-c amphibole dunites), however, should lower Ti contents in the remaining fluid or melt (e.g., Moine *et al.*, 2001).

Based on textures, mineralogy and dominating common compositional features, the hypothesis that Type III-b and -c xenoliths were metasomatised by completely independent metasomatic agents can be ruled out. Therefore, two other possibilities remain to account for the above described inconsistent observations: (1) inference of other phases, reactants or products, that are able to fractionate specific trace elements, present in the mantle beneath Marsabit but not present in the few investigated samples, or (2) pre-metasomatic compositional heterogeneities, similar to the inherited HREE variation in Type III-a clinopyroxene (see above).

Garnet would be a strong sink for HREEs, but metasomatism occurred in the spinel field, after decompression, with maximum pressures of <1.5 GPa (Kaeser *et al.*, 2006), so garnet had already broken down to symplectites (Fig. 3.13). Percolation of melt through garnet-bearing websterites, prior to metasomatism in Ke 1965/1 and 1965/15, could be an alternative. Websterites have been interpreted to occur in close spatial relationship with porphyroclastic peridotites in the shallow mantle beneath Marsabit (Kaeser *et al.*, 2006), and they contain occasionally rutile and ilmenite which could further account for the strong Nb and Ta depletion in some samples (e.g., Ke 785*). The available compositional data from the websterites, however, do not indicate metasomatic modification of websteritic garnet (Olker, 2001; Kaeser, unpublished data).

Careful SEM scanning rules out the presence of exotic phases such as zircon or Ti-oxides, described from other xenolith suites (e.g., Rudnick *et al.*, 1999, Bodinier *et al.*, 1996). Nevertheless, it cannot be excluded that the metasomatising agent percolated through mantle domains containing these phases before infiltrating the studied rocks.

The preservation of pre-metasomatic compositional heterogeneities is another possibility which must be considered. That such 'rock signals' partly overlap with the 'metasomatic signal' is indicated by the HREE variation in Type III-a clinopyroxene (see above) and also by other compositional parameters. For example, both Mg-katophorite and phlogopite growing at the expense of spinel have very high Cr_2O_3 contents, whereas euhedral Mg-katophorite in the amphibole dunite (Ke 1965/25) or in phlogopite inclusions in opx_m are comparably Cr_2O_3-poor (Fig. 3.6b; Table 3.4 and 3.5). Pre-existing heterogeneities would essentially be preserved by elements that are relatively compatible in a given mineral, i.e. which are not mobilised during metasomatism. This would be in agreement with the preserved HREE variations in Type III-a clinopyroxene, high Cr_2O_3 in amphiboles and phlogopite and Ti spikes in amphibole from Ke 1965/15.

Further, very high Mg#s in replacive amphiboles support melt (fluid)-rock interaction at low melt (fluid)/rock ratios, where Mg and Fe contents are buffered by the ambient peridotite (Tiepolo *et al.*, 2001). The slightly lower Mg# of euhedral amphiboles in Ke 1965/25, combined with their lower Cr_2O_3 contents (Fig. 3.6b), suggest a stronger 'melt signal'. Higher melt/rock

ratio in Ke 1965/25 is further supported by considerably lower Mg# in associated ol-I (~Fo88; Table 3.3).

The limited number of investigated samples does not allow us to decide which of the processes described above acted to which extent. However, given the heterogeneity observed in the numerous non-metasomatised xenoliths from Marsabit (Kaeser *et al.*, 2006), pre-metasomatic features certainly affect the final product of the melt-rock reaction process to a considerable degree.

The nature of the metasomatising agent(s)

Graphite stability and oxygen fugacity considerations

The Marsabit xenoliths are unusual in that they occur in an off-cratonic setting yet bear macroscopic graphite. The latter usually occurs in kimberlite-hosted peridotites (on-craton) or in pyroxenites from alpine-type peridotite bodies (e.g., Pearson *et al.*, 1994). In the phlogopite peridotites from Finero, graphite has recently been reported as nanoscopic layers in phlogopite (Ferraris *et al.*, 2004). In xenoliths from Marsabit, graphite occurs in the same textural relationship as in kimberlite-hosted peridotite xenoliths (i.e. mm-sized flakes, typically associated with orthopyroxene; see Fig. 3.2c-e and Pearson *et al.*, 1994). Graphite inclusions in phlogopite and Opx_m could indicate crystallisation during metasomatism by a 'reduced' C-bearing fluid or melt. However, precipitation of graphite more likely reflects relatively reducing conditions of the uppermost mantle prior to metasomatism. We used the oxygen barometer of Ballhaus *et al.* (1991) to constrain oxygen fugacity (fO_2) conditions prior to metasomatism in the Marsabit xenoliths (Fig. 3.14). The results show that non-metasomatised Group I and IV samples reflect similarly reducing conditions as the cryptically metasomatised Type III-a samples. Spinels from the heated Group II lherzolites, on the other hand, have considerably higher Fe^{3+} contents, in line with metasomatism through mafic alkaline melts (Dick & Bullen, 1984), and in line with the fact that mantle metasomatism, in almost all described cases, is an oxidising process (e.g., Ballhaus, 1993; Parkinson & Arculus, 1999; Woodland & Koch, 2003).

Although assessing Fe^{3+}/Fe^{2+} ratios in spinel based on microprobe analyses can be problematic (Wood & Virgo, 1989; Ballhaus *et al.*, 1991), all microprobe analyses were obtained by the same operational settings and, therefore, give at least the relative fO_2 variation between different samples. The relatively reducing conditions in the pre-metasomatic, cold and highly deformed mantle, well below carbon-carbonate-silicate equilibria ($Mg_2Si_2O_6 + 0.5\ CaMg(CO_3)_2 = Mg_2SiO_4 + 0.5\ CaMgSi_2O_6 + C + O_2$; see Fig. 3.14; Eggler & Baker, 1982) and close to the CCO oxygen buffer are in agreement with the presence of graphite in the Group III harzburgites. Moreover, the low *P-T* conditions at which the Group III xenoliths partially re-equilibrated are close to the subsolidus decarbonation reaction of model carbonated lherzolite (Fig 1; see Lee & Wyllie, 2000 and references therein), in agreement with the observed phase assemblage including orthopyroxene, olivine, clinopyroxene and graphite.

Evidence for low-temperature SiO_2-Na_2O-CO_2-H_2O-rich melts/fluids

Potential metasomatic agents, inferred from the presence of graphite, are C-O-H-rich fluids, carbonated melts or CO_2-rich silicate melts. The resulting phase assemblages and geochemical signatures, however, are the result of infiltration of fluid or melt in a cold (~750-850°C), shallow (<1.5 GPa; Fig. 3.1) and locally reduced lithospheric mantle. Compositional modifications under such disequilibrium conditions in an open system result in a complex interplay between pre-existing compositional heterogeneities and various metasomatic signatures evolving upon melt/rock reaction (see above). This makes it particularly difficult to constrain the exact nature of the 'original' metasomatic agent.

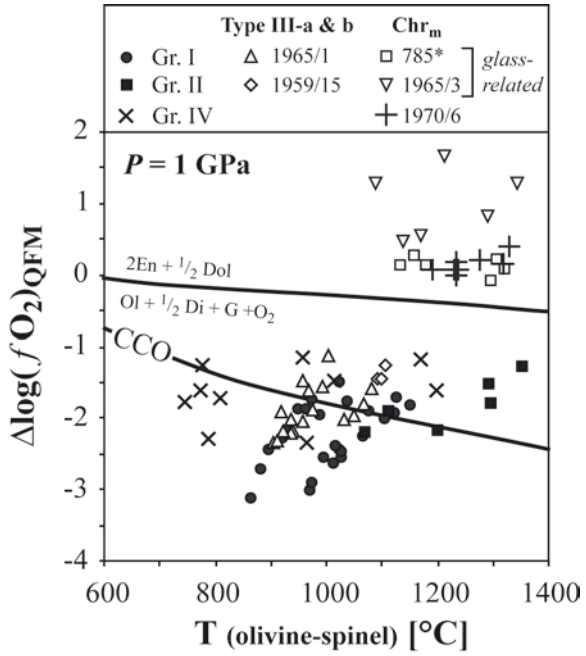


Fig. 3.14. *Oxygen fugacities relative to the quartz-fayalite-magnetite buffer (QFM; equation of O'Neill, 1987) as a function of temperature at assumed pressure of 1 GPa calculated using the composition of co-existing spinel and olivine (ol-I – spl-I pairs and Chr_m – Ol_m pairs, respectively) based on the oxygen-barometer of Ballhaus et al. (1991). The graphite-CO_2 equilibrium was calculated after Frost & Wood (1998), and the graphite-carbonate-silicate equilibrium was calculated with the equation proposed by Eggler & Baker (1982). See text for further explanations.*

Type III-c xenolith Ke 1965/25 contains the highest fraction of metasomatic phases and the least fractionated amphibole trace element patterns; 'magmatic' textures of the Mg-katophorites in this sample indicate crystallisation from a melt or a fluid (in contrast to replacement of a pre-existing phase). Therefore, hypothetical melts in equilibrium with the amphiboles in this xenolith could yield the composition of the initial metasomatic agents. Fig. 3.15 presents the trace element patterns of such melts and fluids, calculated using sets of experimentally or empirically determined mineral/melt (fluid) partition coefficients, including carbonated melt, silicate melt and hydrous fluid (for references see Fig. 3.15).

Common features for all calculated agents are negative Zr-Hf-Ti anomalies and LREE-enrichment (Fig. 3.15). However, previous studies have shown that these signatures may be indicative for almost all types of metasomatism, including interaction of peridotite with carbonated melts (Green and Wallace, 1988; Dautria *et al.*, 1992; Hauri *et al.*, 1993; Rudnick *et al.*, 1993; Ionov *et al.*, 1996; Yaxley *et al.*, 1998; Coltorti *et al.*, 2000), with hydrous fluids and/or melts originating from dehydration of altered subducting lithosphere (Maury *et al.*, 1992; Zanetti *et al.*, 1999; Laurora *et al.*, 2001; Grégoire *et al.*, 2001; Parkinson *et al.*, 2003), and interaction of peridotite with volatile- and Si-rich melts evolved through reactive porous flow (Bedini *et al.*, 1997; Ionov *et al.*, 2002; Bodinier *et al.*, 2004; Rivalenti *et al.*, 2004).

In our case, integration of the trace element characteristics, thermobarometric inferences and mineralogical constraints, favours a Na_2O-SiO_2-CO_2-H_2O-rich fluid or silicate melt. Carbonated melts can most likely be ruled out due to major element and mineralogical considerations. First, amphiboles are Ca-poor, in conflict with carbonate melt metasomatism which is generally characterised by Ca-enrichment (Rudnick *et al.*, 1993; Neumann *et al.*, 2002). Further, orthopyroxene is a stable phase and probably even crystallises during metasomatism in some samples (e.g., Ke 785*). At near-solidus conditions coexistence of orthopyroxene and carbonate melt is only possible at pressures ≥ 2.0 GPa (see Fig. 3.1; e.g., Lee and Wyllie, 2000 and references therein), which is considerably higher than the maximum pressures indicated by spinel (< 1.5 GPa). At such low pressures, carbonated melts turn lherzolite and harzburgite immediately into wehrlite, which is the major peridotite type in all xenolith suites where carbonate melt metasomatism is well constrained (Rudnick *et al.*, 1993; Yaxley *et al.*, 1998; Neumann *et al.*, 2002). In Marsabit wehrlites are absent, however.

Na_2O-SiO_2-CO_2-H_2O-rich melt or fluid, on the other hand, would explain the Na-rich nature of amphibole and phlogopite, as well as the pres-

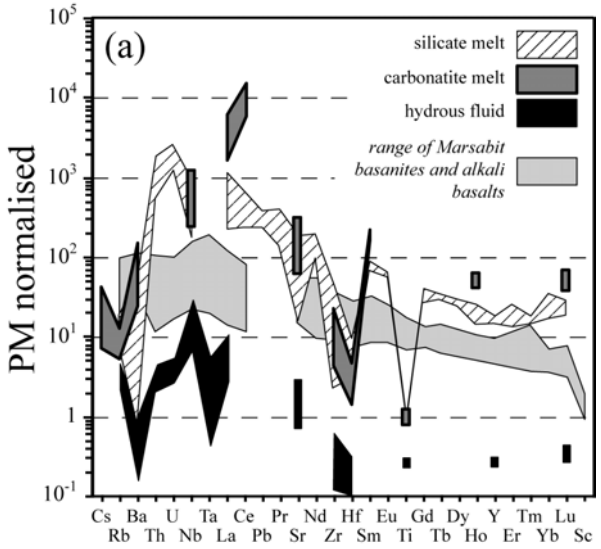


Fig. 3.15. *Calculated metasomatic agents in equilibrium with the euhedral Mg-katophorites from the Type III-c amphibole dunite Ke 1965/2. Amphibole/hydrous fluid and amphibole/carbonatite melt partition coefficients are from Adam et al. (1997) and Adam & Green (2001), respectively. Silicate melts have been calculated using amphibole/Si-rich melt partition coefficients from Chazot et al. (1996b) and amphibole/basanite partition coefficients from La Tourrette et al. (1995). The compositional range of the Marsabit basanites and alkali basalts (Volker, 1990) is shown for comparison.*

ence of orthopyroxene. Growth of metasomatic (and Al-poor) orthopyroxene has been described from several places where peridotites were infiltrated either by hydrous fluids or Si-rich melts (Smith *et al.*, 1999; McInnes *et al.*, 2001; Morishita *et al.*, 2003). At these sites metasomatised peridotite is occasionally accompanied by phlogopite-rich orthopyroxenites (e.g., Franz *et al.*, 2002). Na-rich phlogopite is commonly found as a reaction product between anhydrous mafic to ultramafic rocks and H_2O-rich evolved liquids (Costa *et al.*, 2001 and references therein) or H_2O-bearing fluids (e.g., Odling, 1994). The latter study was an experiment at 2.0 GPa simulating the effects of decreasing temperatures on the phase assemblages and their composition during metasomatism using a model peridotite + C-O-H fluid. The coolest part of Odling's (1994) experiment (<1075°C) contained a strikingly similar phase assemblage (katophorite, phlogopite with ~2 wt% Na_2O, and Al-poor orthopyroxene) compared to our samples, interpreted to have formed during sub-solidus fluid-solid interaction.

The observed trace element signatures of Group III-c Mg-katophorite and the patterns of the calculated metasomatic agents, however, suggest that the metasomatising agent in our case was a melt rather than a fluid. Hypothetical fluids in equilibrium with euhedral Mg-katophorite from sample Ke 1965/25 have high Nb/LILE (e.g., Rb, Ba) and low LILE/REE ratios (Fig. 3.15). Since experimental data predict the opposite for fluids (LILE enriched over HFSE and REE; e.g., Manning, 2004, and references therein), a fluid with a signature such as that indicated in Fig. 3.15 is unrealistic. Owing to the low maximum pressures (<1.5 GPa), a supercritical liquid is not expected either (Manning, 2004; Kessel *et al.*, 2005). In conclusion, the metasomatising agent was most likely a Na_2O-SiO_2-CO_2-H_2O-rich melt.

Comparisons with experimental studies further constrain the low temperature regime in which metasomatism occurred. In ultramafic (e.g., Niida & Green, 1999), basaltic (e.g., Rapp, 1995) and Si-enriched systems (e.g., trachybasaltic; Barclay & Carmichael, 2004), occurrence of amphibole (in the latter study together with phlogopite) is confined to temperatures lower than 1000-1050°C at pressures around 1.5 GPa (Fig. 3.1). This would be in agreement with a cooling Si-rich melt crystallising the euhedral Mg-katophorites and phlogopite during infiltration of the cold ambient peridotite (700-800°C; Fig. 3.1), similar to the findings of Odling (1994; see above) but at lower pressure. Relatively cold conditions would also explain the very high compositional gradients developed on small scales (Fig. 3.13). Replacement of clinopyroxene by amphibole, besides indicating hydration, possibly reflects the low temperatures as well. Clinopyroxene-replacement by amphibole in strongly Si-enriched (dacitic) systems, for example, occurs around 850-950°C (at 0.96 GPa) depending on H_2O contents in the melt (Fig. 3.1; Prouteau & Scaillet, 2003).

The low-pressure (0.92 GPa) peridotite-melt reaction experiments of Prouteau & Scaillet (2003) showed the formation of high amounts of orthopyroxene, Si-rich amphibole (hornblende), as well as Na-rich phlogopite. Moreover, in these experiments there is evidence for Si-enrichment and Ca-depletion in amphibole at decreasing temperatures. Consequently, low temperatures during the formation of the early metasomatic assemblages can further account for the anomalous Si-rich and Ca-poor Mg-katophorites in the xenoliths investigated here (Fig. 3.6a; Table 3.4). The more sodic composition (e.g., katophorite instead of hornblende) reflects the more alkaline characteristics of the melt compared to the experiments of Prouteau & Scaillet (2003).

The presence of apatite, often taken as evidence for carbonatite-type metasomatism (e.g., Yaxley *et al.*, 1998), is not in conflict with such a scenario. Apatite has also been shown to crystallise from volatile and alkali-rich melts formed during reactive porous flow of originally mafic silicate melts (Bedini *et al.*, 1997; Bodinier *et al.*, 2004).

Timing constraints

The age of formation of the early metasomatic assemblages is difficult to assess. Relative age information can be obtained from textural relationships. Metasomatism partly overprints the strongly deformed fabric of the pre-metasomatic Group III rocks. Since pervasive deformation occurred most likely during the development of the Mesozoic Anza Graben (Kaeser *et al.*, 2006), metasomatism should be younger. In the geodynamic context of Marsabit, this would then most likely be in relation with the young (Tertiary-Quaternary) magmatic activity connected to the development of the Kenya Rift (EARS).

The origin of the metasomatising agents

The occurrence of an orthopyroxene-saturated Na_2O-SiO_2-H_2O-CO_2-rich melts in a region characterised by voluminous alkaline magmatism is enigmatic. If we consider the geodynamic setting – a continental rift environment – it seems most plausible that the Si-rich melts evolved from alkaline mafic melts through complex melt-rock reaction during reactive porous flow, as in models of Bedini *et al.* (1997) or Bodinier *et al.* (2004). In their study, Bedini *et al.* (1997) explained metasomatism in the enriched and deformed harzburgite xenoliths from southern Ethiopia (~200 km north of Marsabit) by complex reactive porous flow processes, starting with an 'ordinary' OIB-type mafic silicate melt. Their hypothetical melts in equilibrium with the metasomatised xenoliths include compositions strikingly similar to the calculated silicate melts in equilibrium with euhedral Mg-katophorite (Fig. 3.15). In Marsabit, the heated (1000-1200°C) and recrystallised Group II lherzolites provide evidence for recent, EARS-related metasomatism through alkaline mafic melts, possibly parental to the basanites extruded at the surface (Kaeser *et al.*, 2006). Similar to the process invoked for the Ethiopian xenoliths, continuous melt-rock reaction and fractionation could have led to the formation of highly evolved SiO_2-Na_2O-H_2O-CO_2-rich melts infiltrating and metasomatising the cold and deformed Group III harzburgites. A relation between metasomatism in Group II and III peridotites is supported by one Group II (grt)-spl lherzolite (sample Ke 1958/13), characterised by Mg-calcite-bearing melt patches and transitional (Group II – Group III) trace element signatures (i.e., strong U-Th-LREE enrichment in clinopyroxene; Kaeser *et al.*, 2006).

In other xenolith studies from intra-plate settings, highly silicic melts have been described to evolve from basaltic veins (e.g., Wulff-Pedersen *et al.*, 1999), while crystallisation of ilmenite or rutile in such veins could explain the negative HFSE anomalies in the Group III samples (Moine *et al.*, 2001). This remains, however, speculative as such phase assemblages have not been observed in the investigated xenoliths.

Finally, we emphasise that in terms of composition and phase assemblages, the early meta-

somatic assemblages bear striking similarities to phlogopite and amphibole-bearing peridotites commonly interpreted to result from interaction with subduction-related melts or fluids (e.g., Finero: Zanetti *et al.*, 1999, or Lihir, Papua New Guinea: McInnes *et al.*, 2001; Grégoire *et al.*, 2001; Fig. 3.6 and 3.8). Despite textures indicating a young EARS-related age of formation, involvement of older, possibly subduction-related components cannot be ruled out entirely. The initial metasomatic agent(s) may have tapped reservoirs containing older components, e.g. lithosphere modified or metasomatised during Pan-African subduction and accretion.

Late assemblages – metasomatic mechanisms

Formation of the glass-bearing melt pockets

Textures strongly suggest that (1) the glass-bearing assemblages formed after the early metasomatic phase assemblages and (2) they form to a certain extent at the expense of the early metasomatic assemblages (i.e. incongruent amphibole melting; Fig. 3.3d). Moreover, clinopyroxene, a phase replaced by the early metasomatic assemblage, appears again (Na-rich Cr diopside microlites). BSE imaging reveals that the phases becoming unstable are mainly amphibole and orthopyroxene, as well as spl-I, phlogopite, cpx-I and apatite. Compositional (inter- and intra-xenolith) differences between silicate glass are texture-controlled and vary as a function of the associated precursor phases (Fig. 3.10a-f). TiO_2, for example, shows higher concentrations in glass from Group I xenoliths containing Ti-pargasite (Fig. 3.10c). High-alkali glass occurs in Mg-katophorite-bearing samples (Fig. 3.10a), while K_2O contents are highest in phlogopite-rich samples (e.g., Ke 785*; Fig. 3.10d). The virtually anhydrous Group II (grt)-spl lherzolite (Ke 1959/25), on the other hand, contains glass with very low K_2O (Fig. 3.10d) and Cl contents (Table 3.6), in agreement with the lack of evidence for any former K- and volatile-bearing phases. Interestingly, this glass composition is quite similar to melt compositions obtained from peridotite melting experiments (e.g., Mysen & Boettcher 1975; Robinson *et al.*, 1998), supporting the hypothesis that it is the peridotitic assemblage (cpx-I + spl-I) that melts (see also Ionov *et al.*, 1994). Elevated P_2O_5 contents are found in glass adjacent to apatite (Fig. 3.10e), which mirrors at the same time the high Th and LREE contents of apatite (fig. 3.10f). Significant Si-enrichment is found in glass lining orthopyroxene (Fig. 3.10d), supporting incongruent orthopyroxene melting (see details below). Even though melt pockets are connected along grain boundaries, the strong compositional variation (on inter- and intra-xenolith scale) suggests that the mobility of the melt was limited, or that the melting event was very short (for timing constraints see below).

The co-variation plots in Fig. 3.10 further reveal considerable compositional differences between all types of xenolith glass and the host basanite. This indicates that glass cannot be derived from xenolith-host lava interaction during ascent to the surface. Also, back-mixing of microlites into melt fails to derive glass from host-related melt (Fig. 3.10b). Glass from xenolith margins, however, is compositionally closer to the bulk basanite (e.g., Fig. 3.10b), in line with a direct derivation from xenolith-host lava interaction. Its more evolved major element composition (e.g., higher SiO_2, lower Mg numbers; Fig. 3.10b) is most likely the result of fractionation of basanite phenocrysts (e.g., olivine, augite and titanomagnetite; Volker, 1990). Host lava-xenolith interaction is further supported by the trace element signature of glass at the margin, which is closely similar to Marsabit basanites (Fig. 3.11b; Volker, 1990). The same is observed for intra-xenolith glass in the unusual kaersutite-bearing sample (Ke 1959/27). The significance of this xenolith will be further outlined below.

Xenolith glass unrelated to host lavas, with microlites of similar compositions as those reported here, in association with residual amphibole, has now been reported from many xenolith localities (e.g., Ionov *et al.*, 1994; Chazot *et al.*,

1996a,b; Ionov *et al.*, 1996; Yaxley *et al.*, 1997; Laurora *et al.*, 2001; Bali *et al.*, 2002). Recently, very detailed studies on glass-bearing xenoliths from the West Eifel (Shaw & Klügel, 2002; Ban *et al.*, 2005) have shown that in-situ incongruent amphibole melting is a suitable process to produce such typical glass-microlite pockets in peridotite xenoliths. Ban *et al.* (2005) demonstrated that the weight proportions of glass and the associated microlites match the composition of the parent amphibole. We used the same approach and performed simple mass-balance calculations (least-square fitting), in order to constrain the conclusions drawn from petrography, and to test which phase contributed to which extent to the formation of the melt pockets. The results, reported in Table 3.8, show that in most case amphibole-melting can account successfully for the melt pocket composition only when a certain amount of other phases (orthopyroxene and/or phlogopite) is added to the reactant. Such a contribution of other phases agrees with textural observation (e.g. Fig. 3.3a showing Aug_m growing on resorbed opx-I), as well as with the conclusions of Ban *et al.* (2005), who state that more Si-rich glass (i.e. > 54 wt%) necessitates orthopyroxene contributing to the the melt.

Trace element patterns of the bulk glass + microlites pockets, calculated using the measured trace element abundances of glass and microlites and the respective mass balance parameters (Table 3.8), are broadly identical to the measured amphibole composition (Fig. 3.16a-b). Higher LILE (Cs, Rb, Ba) concentrations in the calculated bulk patches of sample Ke 785* can be balanced by adding ~7 wt% of phlogopite (Fig. 3.16b), which is in line with mass balance (Table 3.8). This demonstrates that no extraneous melt acting as a metasomatising agent is required, and apparently no trace elements were added during the formation of the late glass-bearing assemblages.

Further, the obtained phase proportions for the melt patches are in good agreement with the results from image analysis (Table 3.1). Besides, they are similar to glass-cpx-ol proportions measured in recent experiments on the melting behaviour of amphibole in wehrlites at temperatures between 1175-1250°C and pressures of 0.5-1.0 GPa (Médard *et al.*, 2006). These temperatures are in good agreement with the estimates for the formation of olivine and chromite microlites in the melt patches (Fig. 3.14). The heat supply required for amphibole melting in the formerly low-T metasomatised Group III xenoliths (ΔT ~200-300°C) may be explained by local heating shortly before or during xenolith entrainment in the host lava.

Finally, formation of the most Si-enriched melt (adjacent to Opx_m in Group III-c samples) can be modelled assuming progressing interaction between melt and orthopyroxene where the latter melts incongruently:

(1) opx + melt1 $\Rightarrow$ ol + melt2 $\pm$ cpx (Table 3.8)

To calculate reaction (1) we chose the least evolved glass found in melt patches of sample Ke 1965/3 (SiO_2 = 59.21 wt%; Mg# = 64.65) to represent the initial melt1, whereas melt2, adjacent to opx, is SiO_2-rich (65.89 wt%). Trace element abundances in glass next to orthopyroxene are shifted to lower concentrations (Table 3.6), which is in agreement with dilution due to adding of a trace element-poor orthopyroxene component. The obtained phase proportions are similar to those observed at orthopyroxene-melt interfaces (i.e. high olivine/low cpx abundances), and are in agreement with experimental studies (Shaw *et al.*, 1998).

An alternative way to account for the Si-rich nature of glass is to infer that amphibole melting was triggered by infiltration of the mantle by already Si-enriched melts. Such melts can be in equilibrium with a harzburgitic mineral assemblage as shown on the basis of both experimental investigation (Draper and Green 1997) and natural samples (e.g., Schiano and Clocchiatti 1994; Zinngrebe and Foley 1995; Wulff-Pedersen *et al.*, 1999). In this case, amphibole melting would represent an open-system process. If this was the case for our samples, these melts did not obviously modify the trace element budget of the system (Fig. 3.16).

Table 3.8: Results of mass balance calculations to test melt pocket formation by incongruent melting of the early metasomatic assemblages

Sample*	**1960/2**		**1959/15**	**785***		**1965/25**		**1965/3**
Reactant:								
amph	*1.000*	*0.405*	*1.000*	*1.000*	*0.820*	*1.000*	*0.944*	-
opx	-	*0.411*	-	-	*0.078*	-	*0.056*	*0.406*
phl	-	-	-	-	*0.102*	-	-	-
glass	-	-	-	-	-	-	-	*0.594* [a]
SiO_2	43.86	48.97	44.84	49.89	49.64	51.29	51.67	58.98
TiO_2	3.04	1.82	0.14	0.39	0.36	0.25	0.24	0.18
Cr_2O_3	0.51	0.45	2.32	2.91	2.58	1.27	1.21	0.09
Al_2O_3	14.93	9.83	13.68	7.62	7.69	8.00	7.57	9.61
$FeO_{(tot)}$	3.66	4.74	3.36	3.14	3.33	3.43	3.57	3.94
MnO	0.07	0.10	0.06	0.08	0.08	0.12	0.12	0.10
NiO	0.13	0.11	0.09	0.13	0.14	0.11	0.11	0.04
MgO	17.55	24.27	18.44	20.29	21.97	20.40	21.22	16.25
CaO	11.98	7.17	8.54	7.83	6.44	9.66	9.13	0.78
Na_2O	3.51	2.10	4.60	5.00	4.36	5.04	4.76	8.43
K_2O	0.75	0.45	0.49	0.32	0.96	0.42	0.40	0.60
Product:								
glass	*0.281*	*0.419*	*0.389*	*0.322*	*0.335*	*0.292*	*0.284*	*0.703* [b]
ol	*0.143*	*0.394*	*0.243*	*0.259*	*0.315*	*0.266*	*0.286*	*0.273*
cpx	*0.477*	*0.186*	*0.288*	*0.373*	*0.308*	*0.442*	*0.431*	*0.024*
spl	*0.100*	-	*0.052*	*0.032*	*0.028*	-	-	-
carb	-	-	*0.028*	*0.014*	*0.014*	-	-	-
SiO_2	44.90	49.18	44.77	50.27	49.86	52.07	51.81	59.03
TiO_2	1.69	1.36	0.13	0.41	0.39	0.15	0.14	0.17
Cr_2O_3	1.29	0.30	2.13	3.14	2.72	1.09	1.06	0.15
Al_2O_3	15.77	10.14	13.64	7.64	7.70	7.98	7.76	9.57
$FeO_{(tot)}$	3.91	4.34	3.74	3.31	3.51	3.22	3.32	3.50
MnO	0.06	0.05	0.07	0.07	0.07	0.09	0.09	0.06
NiO	0.09	0.09	0.11	0.13	0.15	0.11	0.12	0.07
MgO	18.03	24.54	18.34	20.24	21.96	20.63	21.41	16.35
CaO	12.32	7.42	8.54	7.59	6.32	9.52	9.29	0.80
Na_2O	1.77	2.31	4.49	3.85	3.88	4.99	4.85	8.60
K_2O	0.18	0.26	0.60	0.96	1.00	0.15	0.14	0.91
Σr^2	**8.03**	**0.75**	**0.23**	**2.00**	**0.35**	**0.84**	**0.28**	**0.33**

*: prefix Ke omitted; [a]: low-Si glass; [b]: high-Si glass (see text for explanations)

Formation of carbonates

Another point which needs further explanation is the amount of carbonate found in the late metasomatic assemblage. High Ca/(Ca+Mg) values (Table 3.7), oscillatory zoning (Fig. 3.4a-b), and low REE concentrations (Fig. 3.12) suggest that the carbonates are cumulate crystals, precipitated from a CO_2-rich melt or fluid, and not quenched carbonated-melts (Lee *et al.*, 2000;

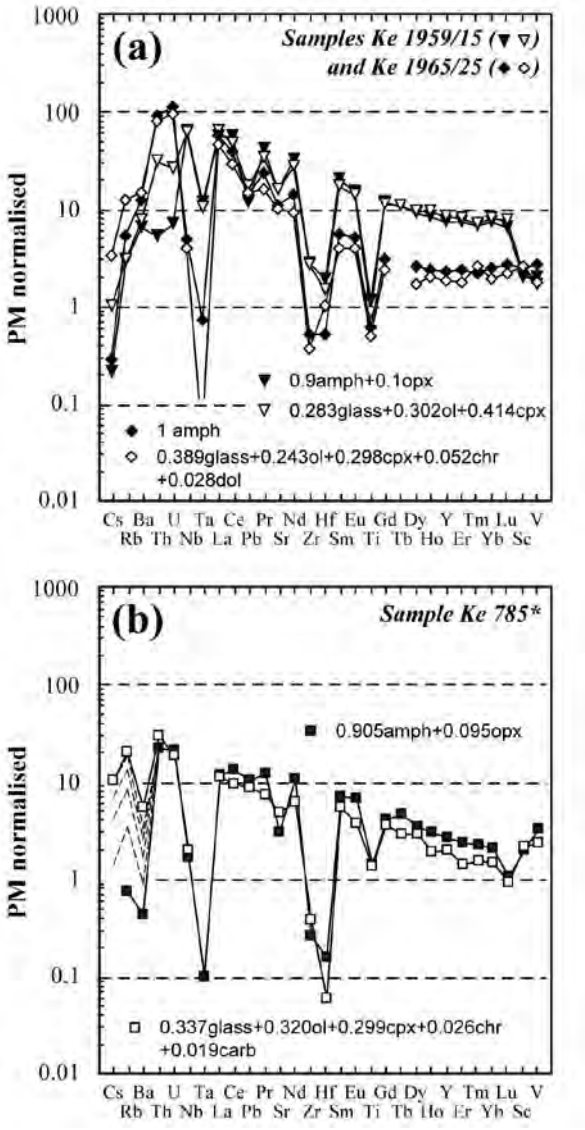


Fig. 3.16. *Calculated trace element characteristics of reactants (in most cases amphibole + orthopyroxene; filled symbols) and products (melt pockets; empty symbols) of the 'amphibole melting' model (see equation 1 in text). The relative phase proportions were obtained by mass balance calculations and are given in Table 3.8. The dashed lines in* ***(b)*** *show that the high LILE concentrations obtained for the product (bulk melt pocket) can be explained by adding about 7 wt% of phlogopite to the reactant (amphibole + orthopyroxene; Table 3.8). Further explanations are given in the text.*

Ionov & Harmer, 2002). The rounded contacts toward glass (globules) are in line with this interpretation. Similar forms were reported from experimental studies (e.g., Lee & Wyllie, 1996), and do not *a priori* imply the presence of immiscible carbonate and silicate melts. However, the amphibole breakdown reaction (1) does not account for the CO_2 required for carbonate precipitation during amphibole melting. Therefore, amphibole breakdown either occurred in an open system with addition of at least CO_2 (e.g., Ban *et al.*, 2005), or another pre-existing phase acted as a source of carbon. Simple mass balance calculations suggest that graphite, texturally identified as a part of the early assemblage (e.g., Fig. 3.2d), could deliver the CO_2 necessary for carbonate formation. The most graphite-rich sample of our collection, for example, contains maximum 0.25 Vol% graphite (Table 3.1), corresponding to approximately 1600 μg/g C in a dunitic bulk rock (d = 3.32 g/cm^3). Oxidising the elemental carbon to CO_2 would allow the formation of ~0.6 wt% $CaCO_3$. This corresponds well with the amount of carbonate found in Ke 1965/3 (~1 Vol% from image analysis corresponding to ~0.8 wt% $CaCO_3$ taking $d_{calcite}$ = 2.71 g/cm^3). Thus, the transition from a graphite-bearing Group III-c sample, devoid of carbonate (Ke 1965/25), to a sample which lacks graphite, but is relatively carbonate-rich (Ke 1965/3), can be entirely explained by increasing fO_2 conditions during partial melting of the early metasomatic assemblage.

Higher oxygen fugacities are indeed obtained when the composition of glass-related spinel (Chr_m) is used for calculations (well on the oxidised side of C-carbonate-silicate buffer plotted in Fig. 3.14). Thus, in the case of Marsabit, no 'exotic' CO_2 bearing fluids or melts are required to account for the formation of mantle carbonates.

To conclude, the major and trace element composition of glass and associated microlites, as well as the presence of carbonates can be fully explained by the breakdown of the early metasomatic assemblages, mainly dominated by am-

phibole and orthopyroxene, including variable but minor contribution of graphite, phlogopite, apatite, and clinopyroxene. The dominant control of amphibole to account for the trace element budget of melt pockets is similar to results found in other suites of glass-bearing xenoliths (Chazot *et al.*, 1996a; Yaxley & Kamenetsky 1999; Laurora *et al.*, 2001).

Time constraints

Glass-bearing assemblages formed at the expense of the early metasomatic assemblages, and are therefore younger. Most Type III-b and c samples contain high amounts of interstitial glass and fine-grained microlites. The preservation of such features clearly indicates that the late assemblages are very young, possibly formed shortly before or even while the xenoliths were transported in the host magma. Evidence that late metasomatism started prior to the entrainment comes mainly from the textures and phase relationships in the particular Type III-d xenolith (Ke 1970/6), as well as from the kaersutite-bearing Type III-c sample (Ke 1959/27).

The Type III-d xenolith contains clinopyroxene that is almost identical to glass-related Na-rich Cr diopside microlites from Type III-c rocks (Table 3.2; Fig. 3.5b). Further, Opx_m in this sample contains abundant melt inclusions, concentrated along cleavage planes, which suggest a similar mode of formation as for melt films penetrating opx in glass-bearing A-III-c xenoliths. The completely statically recrystallised texture of the Type III-d xenolith, however, indicates that enough time elapsed to allow this rock to anneal completely after the late metasomatic assemblage had formed. This implies that the process of melt generation and formation of the late mineral assemblage already started at mantle depth.

A similar conclusion can be drawn for the clearly host-related glass found in xenolith Ke 1959/27 (e.g., Fig. 3.11b). This Type III-c sample is characterised by the presence of Na-rich Cr diopside microlites partly overgrown by mineral rims clearly related to basanite magmas (kaersutite, Ti-augite and olivine with ~Fo88.5; Table 3.3-3.4, and supplementary data in Appendix A3). Kaersutite has major and trace element characteristics similar to typical basanitic and alkali basaltic amphibole phenocrysts (Fig. 3.7d). The special phase assemblages in this xenolith indicates that host-related basanitic melts intruded some Type III-c xenoliths and partly overprinted the assemblage formed slightly earlier by *in-situ* derived alkali-rich peraluminous melts, fully preserved in other samples (e.g., Ke 1965/3 or Ke 785*).

SUMMARY & CONCLUSIONS

(1) Detailed textural and geochemical investigation of peridotite xenoliths reveals that the lithospheric mantle beneath Marsabit, after rifting-induced deformation, decompression and cooling during the formation of the Anza graben (Mesozoic-Paleogene), experienced various styles of metasomatism (a cartoon illustrating the relative timing and possible spatial relationship of the different styles of metasomatism is given in Fig. 3.17). The metasomatised Group III spl peridotite xenoliths provide evidence for a first event of melt-rock reaction resulting in the formation of an early, volatile-bearing metasomatic phase assemblage (Mg-katophorite, Na-rich phlogopite, apatite, graphite, orthopyroxene), followed by a later event that resulted in the formation of glass-bearing melt pockets.

(2) While a SiO_2-Na_2O-CO_2-H_2O-rich melt was most likely responsible for the early event, mass balance calculations showed that no further melts or fluids are required to account for the formation of the melt pockets. They can be fully explained by incongruent melting of the early metasomatic assemblage (namely amphibole) which took place possibly shortly before or during transport of the xenoliths to the surface (Fig. 3.17c).

(3) Most of the uncommon compositional characteristics of the early metasomatic assemblage (presence of Mg-katophorite, graphite, orthopyroxene, LREE-U-Th enrichment) can be explained by an infiltrating silicic melt

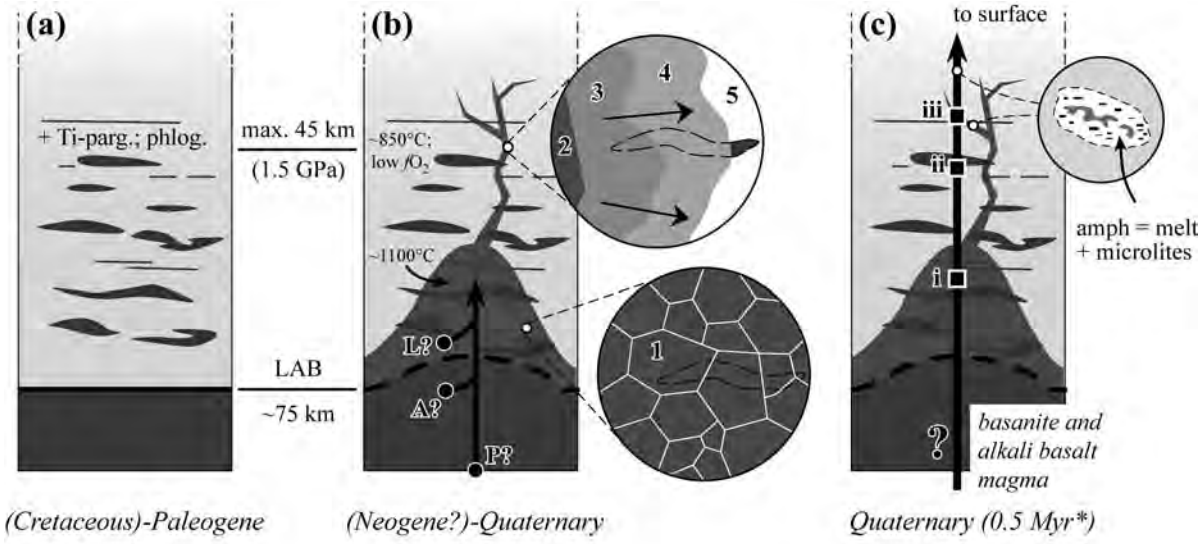


Fig. 3.17. *Cartoon showing the possible spatial and temporal relationships between the different metasomatic processes recorded by the investigated mantle xenoliths from Marsabit:* ***(a)*** *state of the lithosphere beneath Marsabit after Mesozoic rifting (decompression and cooling; Kaeser et al., 2006). LAB = Lithosphere-Asthenosphere boundary (Henjes-Kunst & Altherr, 1992). Penetrative deformation is indicated by thin horizontal lines. Dark grey boudins indicate compositional heterogeneities including deformed pyroxenite bands and cpx-rich lherzolite (Group I xenoliths), including associated Ti-pargasite and phlogopite.* ***(b)*** *Schematic representation of the EARS-related heating as a result of mafic silicate melt impregnation (Kaeser et al., 2006; bold arrow), and propagation (and associated melt-rock reaction) of residual melts in colder and relatively reduced lithospheric domains (this study). L?, A?, and P? represent possible, yet unconstrained components in the initial melt, either deriving from the lower lithosphere, the asthenosphere or a mantle plume, respectively. Close-ups: 1 = possible location of statically recrystallised silicate melt metasomatised Group II lherzolite; 2 = SiO_2-Na_2O-CO_2-H_2O-rich melt/fluid responsible for metasomatism in Group III peridotites; 3 = position of Type III-c amphibole-harzburgite and dunite (close to the metasomatising agent); 4 = position of Type III-b harzburgite; 5: position of Type III-a harzburgite (least metasomatised). Percolation through and/or reaction with pre-existing heterogeneities (dashed lines) may account for several trace element characteristics (see text). Small arrows indicate melt percolation away from the initial source (e.g., a vein).* ***(c)*** *sampling of the xenoliths by Quaternary basanites and alkali basalts (*: Brotzu et al., 1984); i: Group II (grt)-spl lherzolites; ii; non-metasomatised Group I (grt)-spl lherzolites; iii: strongly metasomatised Type III-a to -d harzburgites and dunites. Close up: melt pocket formation during this late-stage event. Note that the vertical differences are purely hypothetical owing to the lack of accurate constraints on the sampling depth. The relationship between Group II and III could also be lateral (e.g., away from a larger melt conduit).*

or fluid in a cold mantle (~750-850°C) at low pressures (<1.5 GPa; Fig. 3.17b), associated with melt-rock reaction processes and inherence of pre-existing heterogeneities. The occurrence of graphite most likely reflects locally reduced conditions prior to metasomatism, and not an exotic 'reduced' metasomatising agent. Preserved low oxygen fugacities in the mantle beneath Marsabit, possibly lower than beneath other off-craton localities, might be an explanation for the scarcity of graphite in off-cratonic mantle peridotite.

(4) The interpretation of the origin of the SiO_2-Na_2O-CO_2-H_2O-rich melt/fluid and some of the trace element features (e.g. strong Hf-Zr-Ti depletion) remains speculative. It is possible that such liquids derive from complex melt-rock reaction processes, starting with an ordinary alkaline mafic melt, but it may reflect also a component in the source of the metasomatising agent related to much older modification in the context of an ancient Pan-African subduction-zone. These issues necessitate further investigation.

ACKNOWLEDGMENTS

We would like to thank Edwin Gnos and Alfons Berger (Bern), and Hans-Peter Meyer (Heidelberg) for assistance with microprobe work, as well as André Villard who provided top-quality thin sections. Discussion with Othmar Müntener, Dmitri Ionov, Rainer Altherr, Alan Woodland helped to clarify many aspects of this work. This publication is part of a project financed by the Swiss National Science Foundation (grant Nr. 200021-100647/1 to AK).

Chapter 4: Li, Be and B Abundances in Minerals of Peridotite Xenoliths from Marsabit (Kenya): Disequilibrium Processes and Implications for Subduction Zone Signatures

Benjamin Kaeser[1], Angelika Kalt[1] & Thomas Ludwig[2]

[1] Institut de Géologie et d'Hydrogéologie, Université de Neuchâtel, Rue Emile-Argand 11, CH-2009 Neuchâtel, Switzerland
[2] Mineralogisches Institut, Universität Heidelberg, Im Neuenheimer Feld 236, D-69120 Heidelberg, Germany

Manuscript submitted to Geochemistry, Geophysics, Geosystems

ABSTRACT

The light elements Li, Be and B have been analysed *in-situ* in minerals from 3 groups of peridotite xenoliths hosted in Quaternary basanites from the Marsabit volcanic field (northern Kenya). Group I and II are relatively fertile lherzolites that experienced deformation, decompression and cooling in the context of Mesozoic rifting (Group I), followed by heating, static recrystallisation and associated cryptic metasomatism (Group II) as a result of Tertiary-Quaternary rifting and magmatism. Group III xenoliths are spl harzburgites and dunites which experienced strong cryptic and modal metasomatism. The Li-Be-B systematics in minerals of Group I and II deviate only slightly from estimates for un-metasomatized sub-continental lithospheric mantle. In contrast, Group III samples are characterized by significant enrichment in all light elements, with concentration levels similar to or higher than reported from mantle rocks metasomtized by melts and fluids released from subducting slabs. However, detailed investigation of textures and chemical zoning shows that the light element systematics were considerably modified during late-stage melting and/or melt percolation (formation of silicate glass, clinopyroxene, olivine and chromite melt pockets) in the course of Tertiary-Quaternary alkaline magmatism in Marsabit. These late modifications resulted in disequilibrium partitioning of light elements (Li in particular) between different minerals. Mass balance calculations show that the melt pockets formed at the expense of earlier metasomatic phases, namely amphibole. During this process, the bulk melt pockets mostly preserved the Be and B budget, whereas Li concentrations were modified.
Light element and REE signatures (i.e., Ce/B, Li/Yb and B/Be ratios) of metasomatic phases prior to late melting (preserved in mineral cores) may be explained to result from metasomatism by a melt/fluid carrying a signature from a subducting slab. Alternatively, residual melts deriving from basaltic (OIB-like) melt-peridotite interaction can lead to similar signatures. This implies that the inference of a 'slab signature' exclusively based on trace element data of metasomatized peridotite is ambiguous.

Keywords: light element geochemistry, Secondary ion mass spectrometry, mantle xenoliths, metasomatism,

INTRODUCTION

The geochemistry of the low atomic mass elements Li, Be and B (hereafter called 'light elements') is increasingly used to constrain metasomatic and magmatic processes in the Earth's mantle and in mantle-derived volcanic rocks. Li, Be and B systematics (including Li and B isotopes) are significantly modified in the oceanic lithosphere during interaction with seawater. This makes the light elements particularly useful to detect and track subducted components released from the subducting lithospheric slab, either in volcanic products or in mantle rocks situated above convergent plate boundaries [e.g., *Ryan and Langmuir,* 1987, 1988, 1993; *Ishikawa and Nakamura,* 1994; *Brenan et al.,* 1998a and b; *Chan & Kastner,* 2000; *Leeman & Sisson,* 2002; *Tomascak et al.,* 2002; *Elliott,* 2003; *Elliott et al.,* 2004; *Scambelluri et al.,* 2004; *Paquin et al.,* 2004].

Further, light element signatures similar to those inferred for peridotite metasomatized by slab fluids have now been reported from mantle-derived rocks from rift-related tectonic settings at places far away from any modern subduction zones [e.g., *Brooker et al.,* 2004; *Nishio et al.,* 2004]. This invokes the potential of Li, Be and B to detect old lithospheric mantle domains modified during earlier subduction-related processes.

However, up to now, there is only sparse information on Li-Be-B budgets in rift-related and/or intra-plate magmatic settings [*Dostal et al.,* 1996, *Ryan et al.,* 1996; *Ryan,* 2002; *Chan & Frey,* 2003; *Ryan and Kyle,* 2004; *Tanaka and Nakamura,* 2005; *Elliott et al.,* 2006]. Also, most studies of light elements in intra-continental mantle rocks mainly aimed at the characterisation of non-metasomatized sub-continental lithospheric mantle and contain only limited information on light element systematics related to intra-continental mantle metasomatism [*Chaussidon and Libourel,* 1993; *Seitz and Woodland,* 2000; *Woodland et al.,* 2002; *Seitz et al.,* 2004; *Woodland et al.,* 2004; *Ottolini et al.,* 2004]. Considering the highly mobile character of light elements (especially Li [e.g., *Lundström et al.,* 2005; *Coogan et al.,* 2005]), detailed *in-situ* investigation of metasomatized mantle rocks is clearly needed. This is especially the case for mantle xenoliths as they often record complex metasomatic processes. This includes very late-stage features such as interstitial silicate glass, often interpreted to reflect processes related to the xenolith transport in the host magma, which may significantly alter the older compositional evolution of the lithospheric mantle [e.g., *Shaw et al.,* 2006]. With respect to the light elements, *Jeffcoate et al.* [2006] showed recently that in the case of Li, such late-stage processes can produce strong heterogeneity on a mineral grain scale. Moreover, as a result of very late-stage diffusive isotope fractionation, Li isotope zoning in single mineral grains can approach the entire range of Li isotope variation in all terrestrial whole rock. Such results highlight the importance of *in-situ* trace element investigation in order to reasonably attribute trace element signatures in minerals to a particular geotectonic environment.

In this study we report Li, Be and B abundances in minerals from peridotite xenoliths (Marsabit, Kenya) showing various styles of metasomatic modification. These peridotite xenoliths are very well studied in terms of textures, *P-T* evolution, and metasomatism [*Henjes-Kunst and Altherr,* 1992; *Kaeser et al.,* 2006; *Kaeser et al.,* submitted (chapter 3 of this thesis)]. They are characterized by different early metasomatic assemblages that clearly formed within the mantle. These were partly replaced by late metasomatic assemblages, formed shortly before or during ascent to the surface. The effects of these late, glass-forming events on the Li-Be-B signature of the earlier mineral assemblages will be discussed. Then, we will further put forward constraints on the light element signature of the earlier metasomatic events, and their possible relation with subduction-related processes.

GEODYNAMIC CONTEXT

The xenoliths investigated in this study were collected from Quaternary basanitic and

Table 4.1: Details of the investigated peridotite xenoliths

Sample	Group	Lithology	*Pre-metasomatic and phases* former garnet[1]	ol-I	opx-I	cpx-I	spl-I	*modal metasomatism* early metasomatic phases[2]	melt pockets (m.p.)	*P-T estimates* final stage[3] *P [GPa]*	*T [°C]*	m.p.[4] *T [°C]*
1963/2	I	porphyroclastic (grt)-spl lherzolite	15.5	41.1	23.2	19.2	0.1	Ti-pargasite (0.8), phlogopite (0.1)	-	< 1.47	799 ± 25	-
1958/13	II	recrystallised (grt)-spl lherzolite	9.9	58.0	20.2	10.3	0.2	-	-	< 1.66	908 ± 40	-
1958/20	II	recrystallised (grt)-spl lherzolite	14.8	52.0	23.7	9.3	0.3	-	-	< 1.63	1068 ± 20	-
1965/1	III-a	porphyroclastic spl harzburgite	1.5	70.8	22.9	3.9	0.9	graphite (tr.)	-	< 1.62	834 ± 37	-
1965/15	III-b	porphyroclastic spl harzburgite	-	71.9	17.7	6.8	0.4	Mg-katophorite (0.15), phlogopite (0.1)[5], graphite (0.1), apatite (tr.)	3 Vol% (cpx_m, ol_m, chr_m, Mg-calcite, silicate glass)	-	837 ± 46	-
1965/3	III-c	porphyroclastic spl dunite	-	80.1	-	-	0.7[5]	low-Al opx_m (3.2); phlogopite (tr.; inclusions in opx_m)	16 Vol% (cpx_m, ol_m, chr_m, Mg-calcite, silicate glass)	-	719 ± 6	1246 ± 136
785*	III-c	porphyroclastic spl harzburgite	-	64.0	-	-	0.6[5]	low-Al opx_m (18.7), Mg-katophorite (1.1), phlogopite (0.6), graphite (tr.)	14.4 Vol% (cpx_m, ol_m, chr_m, Mg-calcite, silicate glass)	< 1.89	751 ± 10	1234 ± 85

ol-I, opx-I, cpx-I and opx-I: primary (i.e. not metasomatic) olivine, orthopyroxene, clinopyroxene and spinel, respectively (porphyroclasts and neoblasts undifferentiated); Di_m, Ol_m, Chr_m: Na-rich Cr-diopside, olivine, and chromite microlites, respectively; [1]: spl-opx-cpx symplectites; [2]: formed prior to glass-bearing melt pockets (see text for details); numbers in brackets are Vol%; tr. = traces); 3: after cooling and decompression (max. P obtained using the Cr content in spinel [*Carroll Webb and Wood,* 1986]; *T* based on the Ca-in-opx thermometer of Brey and Köhler [1990] and calculated for an assumed P of 1.2 GPa); [4]: *T* obtained from the Fe-Mg partitioning between ol_m and chr_m (thermometer of *Ballhaus et al.,* [1991]; calculated at assumed *P* of 1.2 GPa); [5]: no phlogopite was found in the thin section used for SIMS analysis; n.d.: not detected; -: not calculated

alkali-basaltic scoriae from the Marsabit shield volcano (northern Kenya). Quaternary volcanism in Marsabit is related to the development of the Tertiary-Quaternary Kenya Rift (the eastern branch of the East African Rift System; EARS). However, the volcano is located about 150 km eastward of the rift axis, within the Anza Graben (a Mesozoic rift perpendicular to the Kenya rift). Detailed studies of the xenoliths in terms of textures, *P-T* evolution and trace element geochemistry [*Henjes-Kunst and Altherr,* 1992; *Kaeser et al.,* 2006] provide evidence for a complex evolution of the uppermost mantle beneath the Marsabit complex.

The earliest events recognised include decompression and cooling from *P-T* conditions around 1000°C at 2.0-2.9 GPa to temperatures of 750-900°C at pressures < 1.5 GPa. The corresponding lithospheric thinning of about 30-40 km was accompanied by strong, penetrative deformation indicated by abundant porphyroclastic fabrics in peridotite and pyroxenite xenoliths. This process is most likely related to the formation of the Mesozoic Anza Graben [*Kaeser et al.*, 2006]. Some of the formerly porphyroclastic rocks show evidence for later static recrystallisation and heating (to about 1000-1200°C), accompanied by metasomatism through infiltrating mafic silicate melts. Heating and infiltration of melts is related to the formation of the EARS and the development of the Marsabit shield volcano.

MINERALOGICAL AND GEOCHEMICAL CHARACTERISTICS OF THE SAMPLES

Lithium, beryllium and boron concentrations in minerals and glass were analysed in seven xenoliths representative of the major peridotite types from Marsabit (see Table 4.1 for a summary, and *Kaeser et al.* [2006]). Each sample was previously analysed in terms of major and trace element composition of the constituent minerals, and the *P-T* evolution was quantified. Based on the classification of *Kaeser et al.* [2006], the peridotite xenoliths can be subdivided in the following rock types (note that in the following, primary olivine (ol), clinopyroxene (cpx) and orthopyroxene (opx), also when cryptically enriched, will be referred to as ol-I, cpx-I, and opx-I, whereas newly crystallised ol, cpx, chromite and opx will be named Ol_m, Cpx_m, Chr_m and Opx_m, respectively (where m stands for 'metasomatic'):

Group I: porphyroclastic formerly garnet-bearing spinel lherzolite [(grt)-spl lherzolite]

Xenoliths of this type are porphyroclastic, cpx-rich lherzolites (Fig. 4.1a). Symplectites of spinel, ortho- and clinopyroxene as well as increasing Heavy Rare Earth Elements (HREE) abundances from cores to rims in cpx-I indicate decompression from garnet to spinel stability. Thermobarometry and the evaluation of major element zoning patterns in pyroxenes revealed that decompression was accompanied by cooling. The rocks passed from an early high-pressure/high-temperature stage in the garnet stability-field (966-1075°C at pressures of 2.33-2.87 GPa) to a medium temperature stage (800-900°C at P ≤ 1.5 GPa). After the garnet-spinel transition, ongoing cooling resulted in partial equilibration at very low final temperatures (around 750°C). The ambient pressure at the time the xenoliths were sampled by the host lava was probably between 1.2 and 1.0 GPa (calculated from associated, still garnet-bearing websterites; [*Henjes-Kunst and Altherr,* 1992; *Olker,* 2001]). Incompatible trace element patterns of cpx-I (Fig. 4.2a), together with Mg# of ol-I (Table 4.2) are in line with relatively fertile, non-metasomatized lherzolite [e.g., *Eggins et al.,* 1998]. However, high modal clinopyroxene contents (Table 4.1) and textures indicate that Group I lherzolites were mechanically mingled with pyroxenite during pervasive deformation [*Kaeser et al.,* 2006]. The representative Group I xenolith included in this study (sample Ke 1963/2) contains small amounts of Ti-pargasite (0.8 vol%) and phlogopite (0.1 Vol%) that most likely derived from this pyroxenitic component.

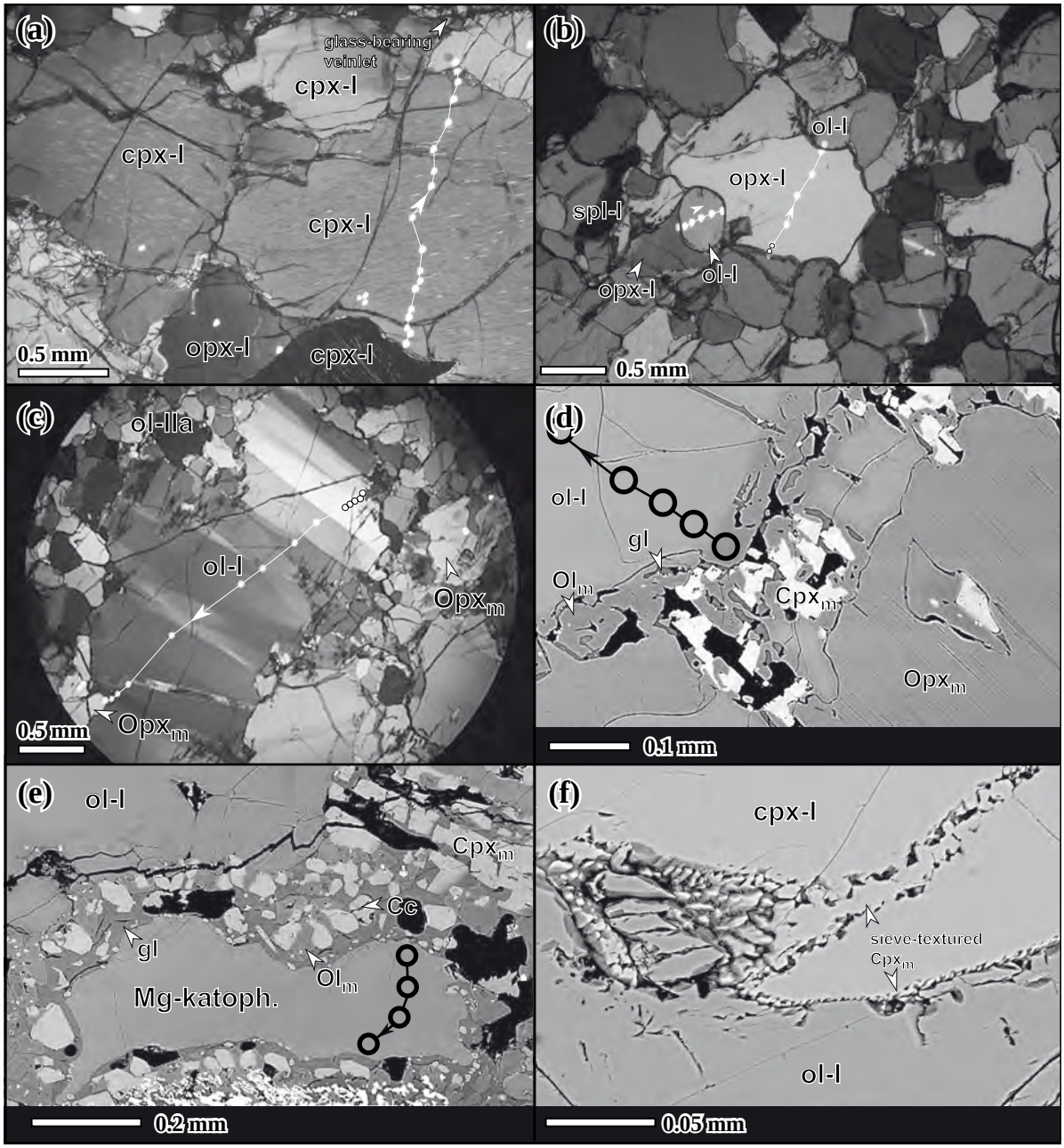


Fig. 4.1: *Photomicrographs (a-c; crossed polarizers) and back-scattered electron images (d-f) showing textural aspects of the investigated peridotite xenoliths from Marsabit. (a) Cpx-I (with opx exsolution lamellea) and opx-I in Group I, xenolith Ke 1963/2 [porphyroclastic (grt)-spl lherzolite]. White dots are SIMS spots of the profile depicted in Fig. 4.4a (arrow=from right to left); (b) strainfree, granular fabric in Group II, xenolith Ke 1958/20 (recrystallised (grt)-spl lherzolite). White dots are SIMS spots of profiles across opx-I (Fig. 4.4e) and ol-I (Fig. 4.4f); (c) fabric of Group III-c, xenolith Ke 1965/3 (porphyroclastic spl dunite). Note strongly kinked olivine porphyroclast (ol-I) and strainfree, polygonal neoblasts (ol-IIa). White dots are SIMS spots of the profile depicted in Fig. 4. 7a; (d) glass + microlites at contact between ol-I and Opx_m in Group III-c, xenolith Ke 785* (porphyroclastic spl harzburgite). Black circles indicate the SIMS profile depicted in Fig. 4. 7c; (e) residual Mg-katophorite in a melt pocket (glass + microlites) in Group III-c, xenolith Ke 785*. Black circles indicate SIMS profile depicted in Fig. 4.7f. (f) late-stage 'sieve-textured' Cpx_m developing at a glass-free contact between cpx-I and ol-I in Group II, xenolith Ke 1958/13 [recrystallised (grt)-spl lherzolite];*

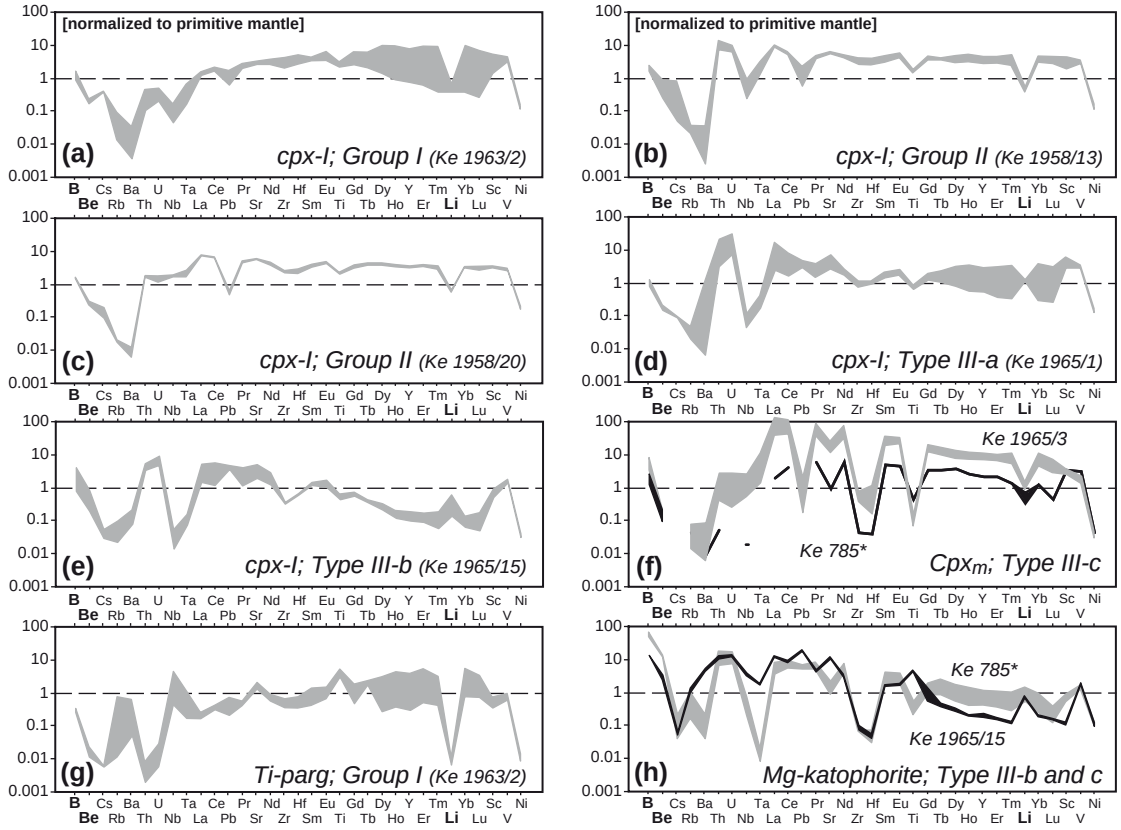


Fig. 4.2: *Li, Be and B signatures of clinopyroxene (a-e) and amphibole (f-h) in peridotite xenoliths from Marsabit compared to other trace elements (LA-ICPMS data from Kaeser et al. [2006] and Kaeser et al. [submitted; Chapter 3 of this thesis]; concentrations normalized to the primitive mantle estimate of McDonough and Sun [1995]).*

Group II: Recrystallised (grt)-spl lherzolites

In these samples, the early history was partly overprinted by static recrystallisation in the course of a thermal event (up to 1200°C; *Kaeser et al.* [2006]). The result is a fabric of equant, mostly strain-free and polygonal grains (Fig. 4.1b). Compositional features of some Group II samples [Fe-Ti enrichment, Light REE (LREE) enrichment but lack of High Field Strength Elements (HFSE) depletion; Fig. 4.2b and c] indicate metasomatism by a silicate melt. Calculated melts in equilibrium with the calculated bulk rocks provide evidence for this melt, yet modified during melt-peridotite interaction, to be parental to the Quaternary basanite and alkali basalt lavas erupted at the surface [*Kaeser et al.*, 2006].

Group III: porphyroclastic spl harzburgite and dunite

Porphyroclastic spl harzburgites and dunites (Fig. 4.1c) record a similar *P-T* evolution as the Group I lherzolites. Rare symplectites after garnet indicate earlier decompression. Thermometry reveals cooling from medium (~800-900°C) to low temperatures (~750°C). All Group III samples were modified by metasomatism (cryptic and modal). Texturally different types are characterized by an increasing degree of metasomatic overprint and obliteration of 'primary' textures (from Type III-a to -c; see Table 4.1). Type III-a consists of cpx-I -bearing harzburgite characterized by cryptically enriched cpx-I (LREE-U-Th enrichment; Fig. 4.2d) but devoid of volatile-bearing phases. In Type III-b, cpx-I is partially replaced by amphi-

bole (Mg-katophorite) and contains clusters and veinlets of Mg-katophorite, Na-rich phlogopite, graphite and apatite. Opx-I is replaced by metasomatic low-Al orthopyroxene (Opx_m). Type III-c is finally devoid of 'primary' clinopyroxene and ranges from harzburgite to dunite. Opx_m contains phlogopite inclusions. Mg-katophorite, phlogopite and occasionally graphite form clusters around partly resorbed spl-I.

The trace element signature of clinopyroxene and amphibole in all Group III samples is characterized by enrichment of LREEs, U, and Th, while HFSEs (Zr, Hf, Ti) and the HREEs are strongly depleted (Fig. 4.2e-h). Compositional similarities between Type III-a to -c, as well as implications derived from phase assemblages and thermobarometry indicate that Group III harzburgites were metasomatized by an evolved Si-rich melt and/or fluid. A more detailed discussion related to this topic is given in below, as well as in a separate paper [*Kaeser et al.*, submitted].

Late-stage textures (melt pockets)

All Type III-b and -c some Group I and II xenoliths contain a texturally secondary assemblage, so-called 'melt-pockets', consisting of broadly trachy-andesitic to phonolitic glass (Table 4.2) associated with microlites of Cpx_m (Na-rich Cr diopside; Table 4.2), Ol_m and chromite (Chr_m; see Fig. 4.1d and e). Melt pockets in Type III-b and -c samples further include globules of Mg-calcite. Generally, late-stage textures in Type III-b and -c xenoliths are by far more abundant and larger than in Group I and II xenoliths.

The major and trace element composition of these secondary phases, their relative modal abundances, and textural constraints, strongly suggest that melt pockets formed through incongruent melting of the earlier modal metasomatic phases, namely amphibole. In Group II samples cpx-I may further show minute (<10 μm) sieve textured rims (Fig. 4.1f) made of 'residual' Cpx_m (i.e. depleted in basaltic components such as Ti, Ca and Na). The implications of late metasomatic processes on the light element systematics will be discussed in detail in below.

Li, Be AND B ABUNDANCES IN MINERALS

Abundances of the light elements Li, Be and B were measured in all silicates and in melt pocket glass. We analysed mineral pairs (rim-rim contacts), as well as traverses across single grains to obtain information on zoning (for analytical methods see Chapter 8: Analytical Methods). Representative concentrations and relative analytical uncertainties (2σ), along with major element data, are given in Table 4.2. The complete dataset is presented in Appendix A5. The ranges and average abundances of Li, Be and B for each mineral are further illustrated in Fig. 4.3. Generally, the minerals in both, porphyroclastic and statically recrystallised formerly grt-bearing lherzolites (Group I and II) carry less light elements than the metasomatic spl harzburgites (Type III-a to -c). The latter are further characterized by a larger variation of light element abundances which is mainly due to significant zoning of minerals (Fig. 4.4-4.7). In the modally metasomatized harzburgites (Group III-b and -c) both, the primary anhydrous silicates and the newly formed volatile-bearing minerals (amphibole and phlogopite) are variably enriched in Li, Be, and B compared to Group I and II samples. Silicate glass turned out to be the phases with the highest light element concentrations, but shows strong variation from one sample to another (Table 4.2; Fig. 4.3).

Lithium

Among the primary anhydrous minerals (ol-I, opx-I, cpx-I) in the studied mantle xenoliths, olivine is the major carrier of Li. In the formerly grt-bearing rocks (Groups I and II), Li abundances decrease from olivine (1.27-1.86 μg/g) via clinopyroxene (0.59-1.10 μg/g) to orthopyroxene (0.56-1.02 μg/g). Group I Ti-pargasite and phlogopite have the lowest Li

Table 4.2: Representative major (wt%) and light element (µg/g) composition of minerals in the investigated peridotite xenoliths from Marsabit

Sample	Ke 1963/2: Group I (grt)-spl lherzolite								Ke 1958/13: Group II recrystallised (grt)-spl lherzolite				
Mineral	ol-I	ol-I	cpx-I	cpx-I	opx-I	opx-I	Ti-prg	Phl	ol-I	ol-I	cpx-I	cpx-I	opx-I
Location	core	core	rim (cpx-I)	core	rim (cpx-I)	core	core	core	rim (cpx-I)	core	rim (opx-I)	core	rim (ol-I)
SiO_2	41.11	40.30	53.13	53.05	56.60	56.38	43.24	38.97	40.75	40.69	53.00	52.33	55.81
TiO_2	n.d.	n.d.	0.66	0.71	0.05	0.18	2.96	4.62	0.00	0.01	0.33	0.43	0.06
Al_2O_3	0.03	0.01	5.34	5.30	2.19	2.48	14.68	15.00	0.01	0.03	5.69	6.47	3.45
Cr_2O_3	n.d.	0.01	0.84	0.78	0.19	0.31	0.37	0.84	0.04	0.03	0.69	0.99	0.24
FeO (tot)	10.25	10.53	2.54	2.74	6.79	6.64	3.73	3.96	9.82	9.34	2.51	2.44	6.14
MnO	0.15	0.21	0.07	0.09	0.18	0.15	0.06	0.03	0.19	0.14	0.08	0.10	0.19
NiO	0.37	0.34	0.08	0.00	0.08	0.02	0.11	0.21	0.36	0.40	0.00	0.00	0.00
MgO	48.95	48.61	14.95	15.15	34.48	34.02	17.50	21.74	49.26	49.10	15.81	14.61	33.64
CaO	0.02	0.02	20.98	20.04	0.31	0.42	11.54	0.09	0.05	0.06	20.19	20.38	0.65
Na_2O	n.d.	n.d.	1.91	2.20	0.04	0.04	3.67	0.81	0.01	0.02	1.79	2.08	0.11
K_2O	n.d.	n.d.	n.d.	n.d.	n.d.	n.d.	0.41	9.28	n.d.	n.d.	n.d.	n.d.	n.d.
Total	**100.88**	**100.01**	**100.50**	**100.06**	**100.91**	**100.64**	**98.27**	**95.55**	**100.49**	**99.81**	**100.10**	**99.84**	**100.28**
Mg-number	*89.49*	*89.17*	*91.30*	*90.80*	*90.05*	*90.13*	*89.33*	*90.73*	*89.94*	*90.36*	*91.82*	*91.45*	*90.72*
Li	1.337 (37)	1.270 (31)	0.675 (34)	0.804 (21)	0.617 (31)	0.635 (34)	0.695 (30)	0.857 (32)	1.441 (29)	1.536 (33)	0.779 (26)	0.905 (28)	0.684 (22)
Be	n.d.	n.d.	0.093 (6)	0.094 (7)	0.008 (3)	0.010 (2)	0.195 (14)	0.126 (6)	*0.002 (1)*	*0.001 (1)*	0.130 (9)	0.157 (15)	0.035 (3)
B	0.059 (15)	0.041 (9)	0.067 (19)	0.067 (9)	0.044 (13)	0.063 (7)	0.137 (28)	0.708 (31)	0.086 (21)	0.086 (11)	0.100 (16)	0.089 (16)	0.055 (8)

Sample	Ke 1958/13	Ke 1958/20: Group II recrystallised (grt)-spl lherzolite						Ke 1965/1: Type III-a spl harzburgite					
Mineral	opx-I	ol-I	ol-I	cpx-I	cpx-I	opx-I	opx-I	ol-I	ol-I	cpx-I	cpx-I	opx-I	opx-I
Location	core	rim (opx-I)	core	rim (opx-I)	core	rim (ol-I)	core	core	core	rim (ol-I)	core	rim	core
SiO_2	55.07	40.60	40.67	51.61	51.60	53.92	54.10	41.05	41.01	53.92	53.43	57.27	56.78
TiO_2	0.08	0.01	0.02	0.49	0.48	0.14	0.13	n.d.	0.01	0.15	0.14	0.03	0.01
Al_2O_3	3.78	0.04	0.03	7.21	6.93	5.43	5.16	0.01	0.03	3.31	3.84	1.86	2.53
Cr_2O_3	0.38	0.05	0.01	0.71	0.76	0.40	0.41	0.01	0.01	0.83	1.06	0.18	0.50
FeO (tot)	6.25	10.09	9.99	3.33	3.29	6.56	6.45	8.36	8.06	2.15	1.90	5.30	5.46
MnO	0.11	0.13	0.18	0.09	0.07	0.17	0.17	0.14	0.12	n.d.	n.d.	0.11	0.15
NiO	0.00	0.35	0.34	0.00	0.00	0.10	0.03	0.33	0.36	0.06	0.07	0.06	0.10
MgO	33.47	48.87	48.79	16.25	16.24	32.42	32.33	49.99	50.40	16.32	16.11	35.07	34.32
CaO	0.35	0.11	0.09	19.71	19.50	1.00	1.00	0.03	0.04	22.65	22.23	0.33	0.40
Na_2O	0.09	0.01	0.01	1.29	1.35	0.14	0.09	0.03	n.d.	1.18	1.31	0.05	0.04
K_2O	n.d.	0.01	n.d.	n.d.	n.d.	n.d.	n.d.	n.d.	n.d.	n.d.	0.00	n.d.	n.d.
Total	**99.59**	**100.27**	**100.14**	**100.69**	**100.23**	**100.29**	**99.88**	**99.95**	**100.02**	**100.57**	**100.10**	**100.26**	**100.28**
Mg-number	*90.51*	*89.62*	*89.70*	*89.69*	*89.79*	*89.80*	*89.93*	*91.42*	*91.77*	*93.11*	*93.79*	*92.19*	*91.80*
Li	0.757 (30)	1.828 (51)	1.811 (21)	1.078 (36)	1.049 (43)	0.976 (27)	0.940 (22)	2.465 (60)	3.363 (57)	1.237 (33)	1.979 (38)	0.891 (25)	1.100 (30)
Be	0.040 (4)	*0.002 (1)*	0.003 (1)	0.100 (6)	0.101 (8)	0.045 (2)	0.043 (5)	*0.001 (1)*	n.d.	0.056 (7)	0.062 (5)	0.026 (4)	0.018 (4)
B	0.065 (7)	0.071 (12)	0.078 (9)	0.092 (10)	0.079 (11)	0.063 (13)	0.061 (6)	0.058 (9)	0.051 (9)	0.045 (12)	0.050 (12)	0.050 (11)	0.046 (11)

Mg-numbers: atomic $Mg/(Mg+Fe_{tot})$ x 100; numbers in brackets are analytical uncertainties (expressed as 2σ); values in italic are below the minimal detectable value [*Currie*,1968]
n.d.: not detected; n.a.: not analysed

Table 4.2: (continued)

Sample	Ke 1965/15: Type III-b spl harzburgite											
Mineral	ol-I	ol-I	ol-I	ol_m	cpx-I	cpx-I	di_m	opx-I	opx-I	opx_m	katoph.	glass
Location	core	rim (opx-I)	rim (glass)	in melt pocket	core	rim (glass)	in melt pocket	core	rim	core	relic in melt pocket	
SiO_2	41.18	41.23	41.57	41.40	54.67	54.52	51.94	56.21	56.96	57.66	45.70	57.45
TiO_2	0.01	0.02	0.01	0.01	0.25	0.13	0.25	0.08	0.03	0.01	0.25	1.09
Al_2O_3	0.02	0.10	n.d.	0.03	3.05	2.46	4.61	2.32	1.87	0.60	12.59	20.41
Cr_2O_3	0.03	n.d.	0.04	0.82	1.15	1.67	4.06	0.39	0.42	0.18	2.51	0.00
FeO (tot)	8.41	8.49	7.41	5.84	1.81	1.84	1.74	5.77	5.56	5.45	2.96	1.91
MnO	0.12	0.14	0.11	0.10	0.06	0.04	0.05	0.16	0.13	0.15	0.05	0.02
NiO	0.40	0.35	0.37	0.43	0.00	0.00	0.08	0.09	0.07	0.12	0.14	1.64
MgO	50.41	50.08	50.68	51.85	16.47	17.23	16.84	34.62	35.02	35.43	19.08	1.52
CaO	0.01	0.03	0.07	0.18	21.08	21.14	19.52	0.30	0.27	0.30	9.38	2.91
Na_2O	n.d.	0.03	n.d.	0.03	1.85	1.53	1.44	0.07	0.07	0.07	4.49	9.36
K_2O	n.d.	n.d.	0.01	0.02	n.d.	n.d.	n.d.	n.d.	0.00	0.01	0.33	0.97
Total	**100.59**	**100.48**	**100.26**	**100.71**	**100.39**	**100.57**	**100.53**	**100.01**	**100.40**	**99.96**	**97.48**	**97.27**
Mg-number	*91.44*	*91.31*	*92.42*	*94.05*	*94.18*	*94.35*	*94.52*	*91.45*	*91.83*	*92.06*	*91.99*	*58.63*
Li	4.444 (76)	4.100 (97)	5.014 (85)	4.675 (67)	0.954 (51)	1.116 (63)	4.18 (11)	3.53 (11)	3.33 (11)	1.539 (30)	2.962 (79)	18.15 (66)
Be	*0.003 (2)*	*0.004 (2)*	*0.002 (2)*	0.007 (2)	0.146 (20)	0.477 (24)	0.809 (83)	0.016 (5)	0.137 (9)	0.050 (5)	1.293 (29)	3.752 (83)
B	0.119 (23)	0.098 (20)	0.354 (44)	0.095 (26)	0.522 (49)	0.320 (36)	0.649 (99)	0.060 (19)	0.275 (22)	0.374 (40)	1.88 (12)	4.57 (14)

Sample	Ke 1965/3: Type III-c spl dunite									
Mineral	ol-I	ol-I	ol_m	di_m	di_m	opx_m	opx_m	phl	glass	glass
Location	core	rim (glass)	core	in glass	in glass	core	rim (glass)	incl. in opx_m	next di_m	next opx_m
SiO_2	40.93	40.72	41.35	54.13	55.23	58.33	58.58	41.40	60.63	62.47
TiO_2	n.d.	n.d.	n.d.	0.11	0.04	0.01	0.01	0.22	0.24	0.23
Al_2O_3	0.01	0.03	n.d.	2.02	1.42	0.24	0.24	13.89	15.29	13.85
Cr_2O_3	0.02	0.15	0.22	5.35	3.46	0.13	0.15	1.48	n.d.	n.d.
FeO (tot)	8.12	6.86	5.52	1.76	2.07	5.09	5.44	2.70	2.64	3.01
MnO	0.16	0.13	0.14	0.05	0.03	0.23	0.21	0.01	0.03	0.12
NiO	0.50	0.32	0.34	0.01	0.05	0.02	0.14	0.15	n.d.	n.d.
MgO	50.61	51.66	52.22	15.88	16.93	35.93	35.87	25.58	3.42	3.25
CaO	0.01	0.11	0.09	18.11	19.65	0.19	0.19	0.04	1.26	0.83
Na_2O	n.d.	0.04	0.03	2.73	2.01	0.06	0.06	2.88	13.05	12.55
K_2O	n.d.	0.01	n.d.	0.01	n.d.	n.d.	n.d.	6.39	1.03	0.86
Total	**100.35**	**100.05**	**99.91**	**100.17**	**100.89**	**100.23**	**100.90**	**94.74**	**97.59**	**97.16**
Mg-number	*91.75*	*93.07*	*94.40*	*94.14*	*93.58*	*92.64*	*92.15*	*94.41*	*69.79*	*65.77*
Li	5.159 (69)	6.905 (84)	9.36 (10)	5.537 (97)	3.651 (58)	2.133 (47)	2.737 (49)	0.626 (11)	19.74 (23)	12.24 (40)
Be	0.007 (3)	0.016 (3)	0.013 (3)	0.822 (17)	0.464 (13)	0.295 (7)	0.301 (13)	3.798 (40)	32.98 (16)	32.55 (15)
B	0.237 (24)	0.662 (44)	0.153 (17)	0.126 (18)	0.128 (13)	0.550 (42)	0.597 (36)	0.884 (37)	10.66 (23)	10.36 (17)

ol_m and di_m are melt pocket olivine and diopside microlites, respectively; katoph. = Mg-katophorite

Table 4.2: (continued)

Sample	Ke 785*: Type III-c spl harzburgite												
Mineral	ol-I	ol-I	ol-I	ol-I	ol_m	di_m	di_m	opx_m	opx_m	katoph.	katoph.	phl	phl
Location	core	core	rim (glass)	rim (glass)				core	rim (ol-I)	core	rim glass	relic in melt pocket	incl. in opx_m
SiO_2	40.68	40.77	40.77	41.47	41.58	55.08	54.70	57.17	57.25	49.70	49.58	41.02	41.37
TiO_2	0.01	0.02	0.03	0.01	0.01	0.14	0.21	0.08	0.09	0.24	0.26	0.41	0.43
Al_2O_3	0.01	n.d.	0.04	0.01	0.03	1.33	2.06	1.01	1.19	7.72	7.71	13.85	13.74
Cr_2O_3	n.d.	n.d.	0.01	0.19	0.21	3.26	3.73	0.30	0.23	2.56	2.62	1.75	1.50
FeO (tot)	9.16	8.95	8.72	7.18	6.24	2.05	2.01	5.65	5.77	3.090	2.94	2.92	2.97
MnO	0.12	0.17	0.13	0.06	0.08	0.05	0.13	0.17	0.18	0.100	0.09	0.03	0.01
NiO	0.42	0.43	0.36	0.18	0.45	n.a.	n.a.	0.13	0.07	0.080	0.11	0.24	0.20
MgO	50.48	49.24	50.38	50.95	51.68	18.62	17.71	35.04	34.71	20.910	20.93	25.95	26.17
CaO	0.01	0.03	0.02	0.09	0.12	18.51	18.39	0.34	0.32	7.810	7.87	0.01	0.00
Na_2O	n.d.	0.03	0.01	0.05	0.06	1.57	1.93	0.12	0.06	5.230	5.25	2.48	2.51
K_2O	n.d.	n.d.	0.01	0.01	0.02	0.01	n.d.	n.d.	0.03	0.28	0.27	7.13	7.24
Total	**100.89**	**99.64**	**100.47**	**100.19**	**100.46**	**100.61**	**100.86**	**100.03**	**99.90**	**97.72**	**97.63**	**95.79**	**96.14**
Mg-number	*90.76*	*90.75*	*91.15*	*92.68*	*93.66*	*94.19*	*94.01*	*91.70*	*91.47*	*92.34*	*92.70*	*94.06*	*94.01*
Li	4.85 (11)	5.705 (116)	5.71 (11)	8.13 (20)	7.79 (11)	2.284 (55)	3.148 (60)	2.399 (80)	2.909 (94)	3.838 (65)	4.781 (99)	3.59 (11)	1.027 (33)
Be	*0.001 (1)*	0.005 (2)	*0.003 (2)*	0.005 (5)	0.072 (12)	0.214 (15)	0.314 (14)	0.204 (17)	0.149 (9)	4.163 (33)	4.199 (70)	1.402 (51)	1.279 (48)
B	0.065 (22)	0.626 (58)	0.109 (19)	0.098 (16)	0.322 (56)	0.176 (24)	0.218 (23)	0.532 (52)	0.354 (27)	5.96 (16)	5.999 (95)	1.44 (13)	1.166 (71)

Sample	Ke 785* (continued)		
Mineral	phl	glass	glass
Location	incl. in ol-I	in melt pocket	in melt pocket
SiO_2	41.02	61.85	62.61
TiO_2	0.43	0.57	0.71
Al_2O_3	13.59	19.28	17.328
Cr_2O_3	1.15	0.05	0.208
FeO (tot)	2.94	1.48	1.247
MnO	0.06	0.04	0.045
NiO	0.19	n.a.	n.a.
MgO	26.15	0.95	1.11
CaO	0.10	0.40	0.67
Na_2O	2.28	11.04	9.52
K_2O	7.15	3.06	3.38
Total	**95.06**	**98.72**	**96.83**
Mg-number	*94.07*	*53.33*	*61.32*
Li	0.639 (22)	13.05 (19)	16.78 (16)
Be	1.170 (30)	7.88 (10)	7.542 (79)
B	1.311 (92)	11.94 (19)	11.04 (23)

concentrations (0.48-0.69 and 0.73-0.86 μg/g, respectively).

Compared to Groups I and II, all minerals from the metasomatized spl harzburgites (Group III-a to -c) are enriched in Li and show considerable inter- and intra-grain variations (Fig. 4.3). Average abundances (Fig. 4.3) are in the order of 2.5-5.3 μg/g (ol-I), 1.6-2.0 μg/g (cpx-I), and 1.4-3.2 μg/g (opx-I and Opx_m). Mg-katophorite and Na-rich phlogopite contain 2.48-5.17 μg/g and 0.63-5.14 μg/g Li. High concentrations are found in Ol_m and Cpx_m microlites in melt pockets (up to 9.54 μg/g and 5.71 μg/g, respectively). The associated glass shows the highest Li abundances (9.72-22.0 μg/g; Fig. 4.3). These concentrations are higher than those reported from glass of mineralogically similar melt pockets found in xenoliths from Victoria, Australia [*Woodland et al.*, 2004].

Beryllium

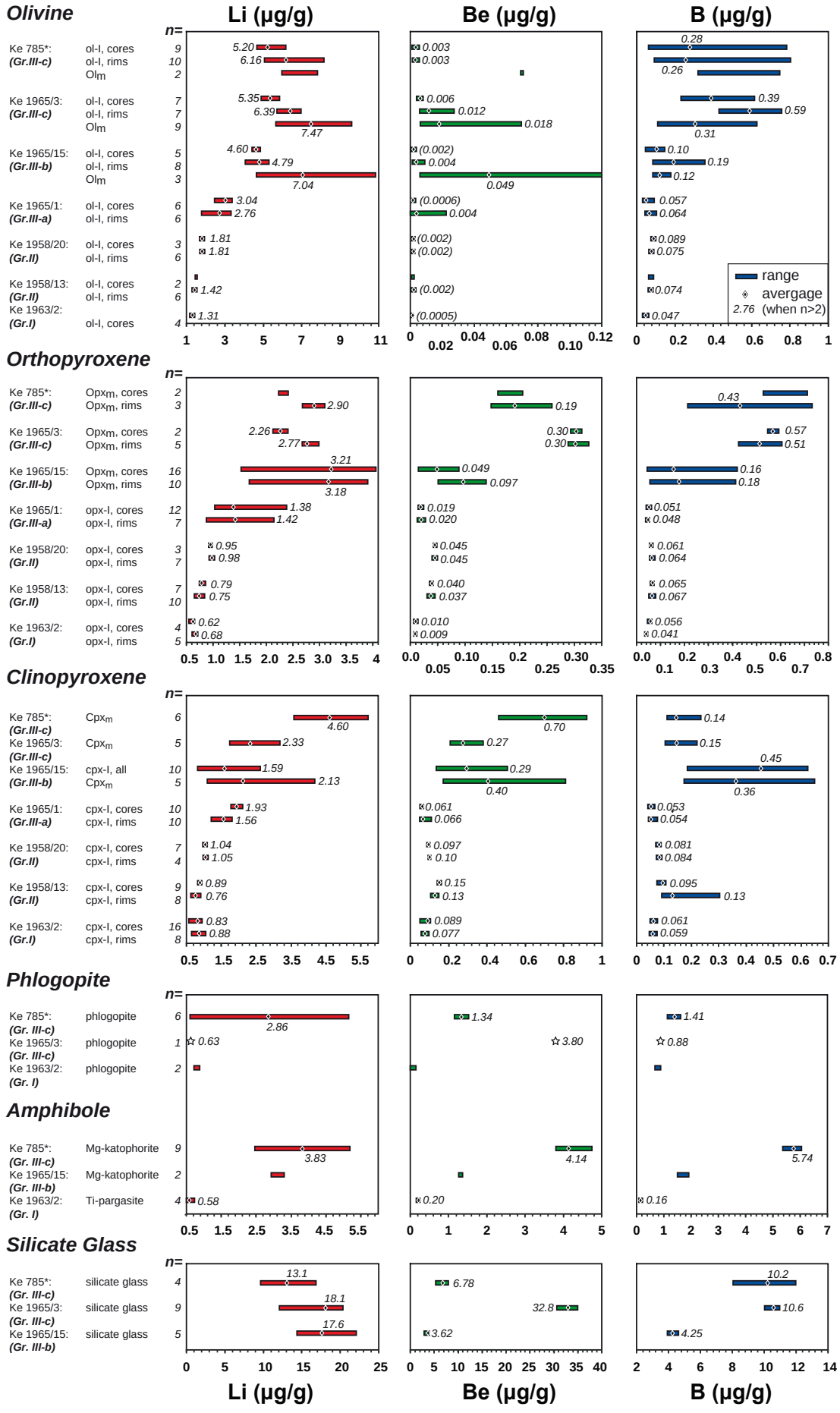
Besides glass, amphibole and phlogopite are the major hosts for Be (up to 4.72 μg/g in Type III-c Mg-katophorite, and 3.80 μg/g in Type III-c phlogopite). However, large variations were observed between different samples (e.g. very low Be abundances in Ti-pargasite and phlogopite from the Group I xenolith; Fig. 4.3). In anhydrous silicates of Groups I, II, and Type III-a, Be exhibits only limited variation (Fig. 4.3). Concentrations decrease from cpx-I (0.055-0.16 μg/g), via opx-I (0.007-0.049 μg/g), to olivine (at the ng/g level, mostly close or below the minimal detectable value). Clinopyroxene and orthopyroxene in the modally metasomatized spl harzburgites (Group III-b to -c), on the other hand, show considerable Be enrichment (0.14-0.50 μg/g in cpx-I, and 0.016-0.32 μg/g in opx-I and Opx_m; Fig. 4.3). Clinopyroxene in melt pockets shows the highest Be concentrations (0.17-0.91 μg/g), and even olivine microlites (Ol_m) contain detectable amounts of Be (up to 0.12 μg/g). By far the highest Be concentrations were measured in silicate glass (up to 34.9 μg/g; Table 4.2).

Boron

B in anhydrous silicates from Group I and II lherzolites shows only limited variation and is evenly distributed between ol-I (0.038-0.099 μg/g), cpx-I (0.049-0.092 μg/g; one analysis with 0.30 μg/g), and opx-I (0.039-0.074 μg/g). Minerals in the Group III-a spl harzburgite show the same range of B abundances. The modally metasomatized spl harzburgites (Group III-b and -c) show variable B enrichment in ol-I (0.050-0.80 μg/g) and orthopyroxene (up to 0.73 μg/g B in Opx_m). The high B contents in cpx-I from sample Ke 1965/15 result most likely from tiny amphibole lamellae, inevitably included in some analyses (Table 4.2). Ti-pargasite (0.13-0.20 μg/g) and phlogopite (0.71-0.87 μg/g) in sample Ke 1963/2 (Group I) show slightly elevated concentrations, but nonetheless, compared with Mg-katophorite and Na-rich phlogopite from Group III-b and -c xenoliths, they are rather B-depleted (Fig. 4.3). Mg-katophorite in sample Ke 785* contains up to 6.02 μg/g B. Within the melt pocket assemblage, silicate glass is the major host for B (4.01-11.9 μg/g), followed by Ol_m (0.088-0.75 μg/g), and Cpx_m (0.11-0.65).

Light element zoning

Mineral zoning profiles for light elements and major elements (where available) are illustrated in Figs. 4.3-4.6. Considering the relative analytical uncertainties (2σ), zoning is in most cases restricted to Li and is generally more developed in the cryptically and modally metasomatized spl harzburgites (Type III-a to -c). Further, core-rim zoning strongly depends on the phase adjacent to the analysed grain. All minerals in contact with silicate glass – irrespective of xenolith group – display Li enrichment on the outermost ~150 μm (e.g. Fig. 4.6c or 4.7). Further, Li enrichment of olivine adjacent to glass can be accompanied either by increasing (Fig. 4.6c and 4.6a, d) or decreasing B contents (Fig. 4.7c). The latter is confined to zones were olivine is in


Olivine
Orthopyroxene
Clinopyroxene
Phlogopite
Amphibole
Silicate Glass
Li (µg/g)
Be (µg/g)
B (µg/g)
n=
Ke 785*: (Gr.III-c)
Ke 1965/3: (Gr.III-c)
Ke 1965/15: (Gr.III-b)
Ke 1965/1: (Gr.III-a)
Ke 1958/20: (Gr.II)
Ke 1958/13: (Gr.II)
Ke 1963/2: (Gr.I)
ol-I, cores
ol-I, rims
Olm
Opxm, cores
Opxm, rims
opx-I, cores
opx-I, rims
Cpxm
cpx-I, all
cpx-I, cores
cpx-I, rims
phlogopite
Mg-katophorite
Ti-pargasite
silicate glass
range
avergage
2.76 (when n>2)

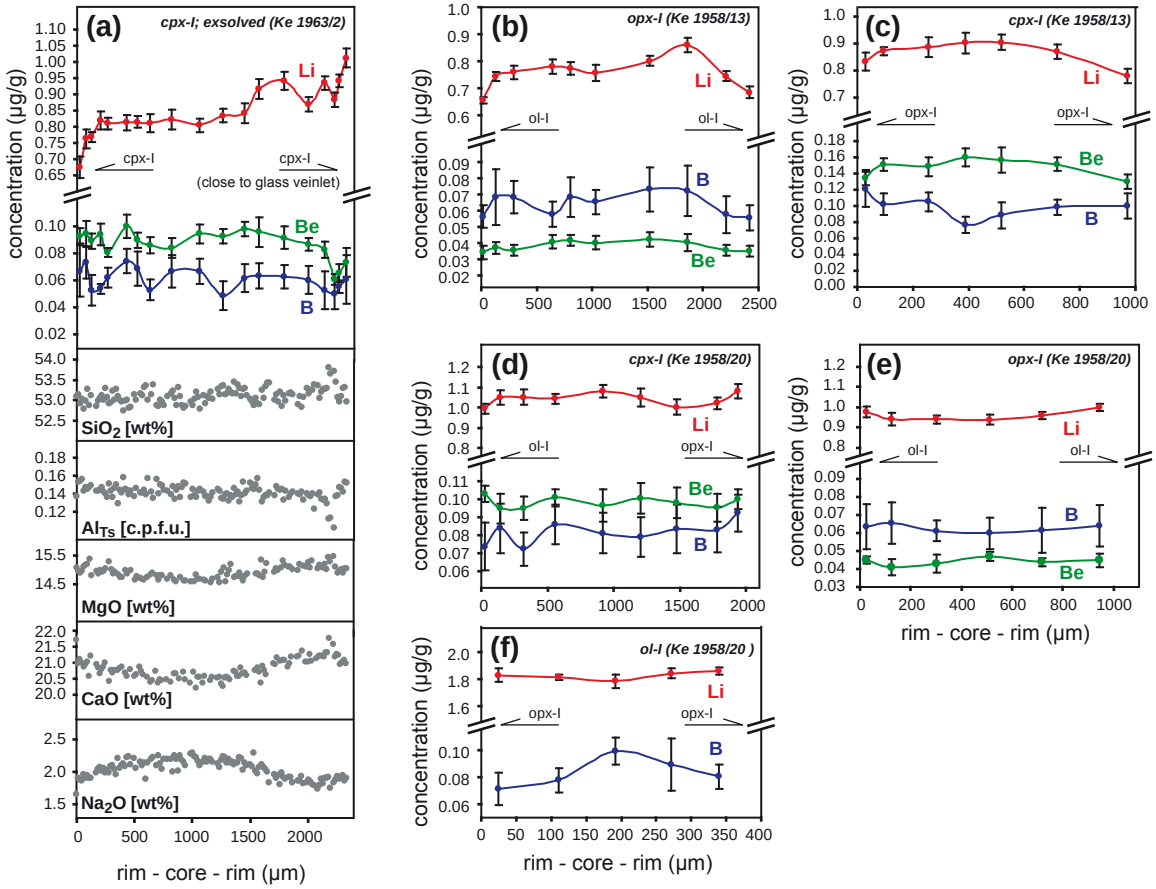


Fig. 4. 4: *Li, Be, and B (SIMS) and major element (electron microprobe) profiles across minerals from Group I and Group II peridotite xenoliths from Marsabit. (a): Li-Be-B and major element zoning in a clinopyroxene porphyroclast (cpx-I) from Group I sample Ke 1963/2; (b) and (c): Li-Be-B zoning in a opx-I and a cpx-I grain, respectively, from Group II, sample Ke 1958/13; (d)-(f): Li-Be-B zoning in a cpx-I, opx-I and ol-I grain, respectively, from Group II, sample Ke 1958/20. Arrows pointing to the left and to the right indicate the respective neighbouring phase. Error bars correspond to 2σ.*

contact with resorbed Opx_m or Cpx_m-poor melt pockets (such as displayed in Fig. 4.1d).

A second type of zoning pattern occurs in pyroxenes (but not in olivine) in sample zones devoid of glass. There – irrespective of the neighbouring phases – Li abundances decrease on the outermost 150-200 µm (Fig. 4.4a-c; 4.5a-d), whereas Be and B may increase (e.g. opx-I in Fig. 4.6a). It is important to note that the different behaviour of Li, depending on the presence of glass, can be observed on a very small scale. For example, the analysed cpx-I from the Group I xenolith (Ke 1963/2; Fig. 4.4a) shows decreasing Li abundances at the contact with another cpx-I grain, whereas the other side of the grain (at ~2.5 mm distance), in the vicinity of a tiny glass veinlet (Fig. 4.1a), is significantly enriched in Li.

Profiles where major element data is available show that that light element zoning is sometimes coupled with major element variation. Mg#s in olivine adjacent to glass, for example, always increase simultaneously with Li abundances (Fig. 4.7c). In pyroxenes from Group III harzburgites, decreasing Li abundances coincide with decreasing $^{[IV]}Al$, CaO and Na_2O,

Fig. 4.3: *Averages and ranges of Li, Be and B concentrations in minerals and silicate glass of peridotite xenoliths from Marsabit. Numbers in brackets (Be in olivine) are concentrations below the minimal detectable value [Currie, 1968]*

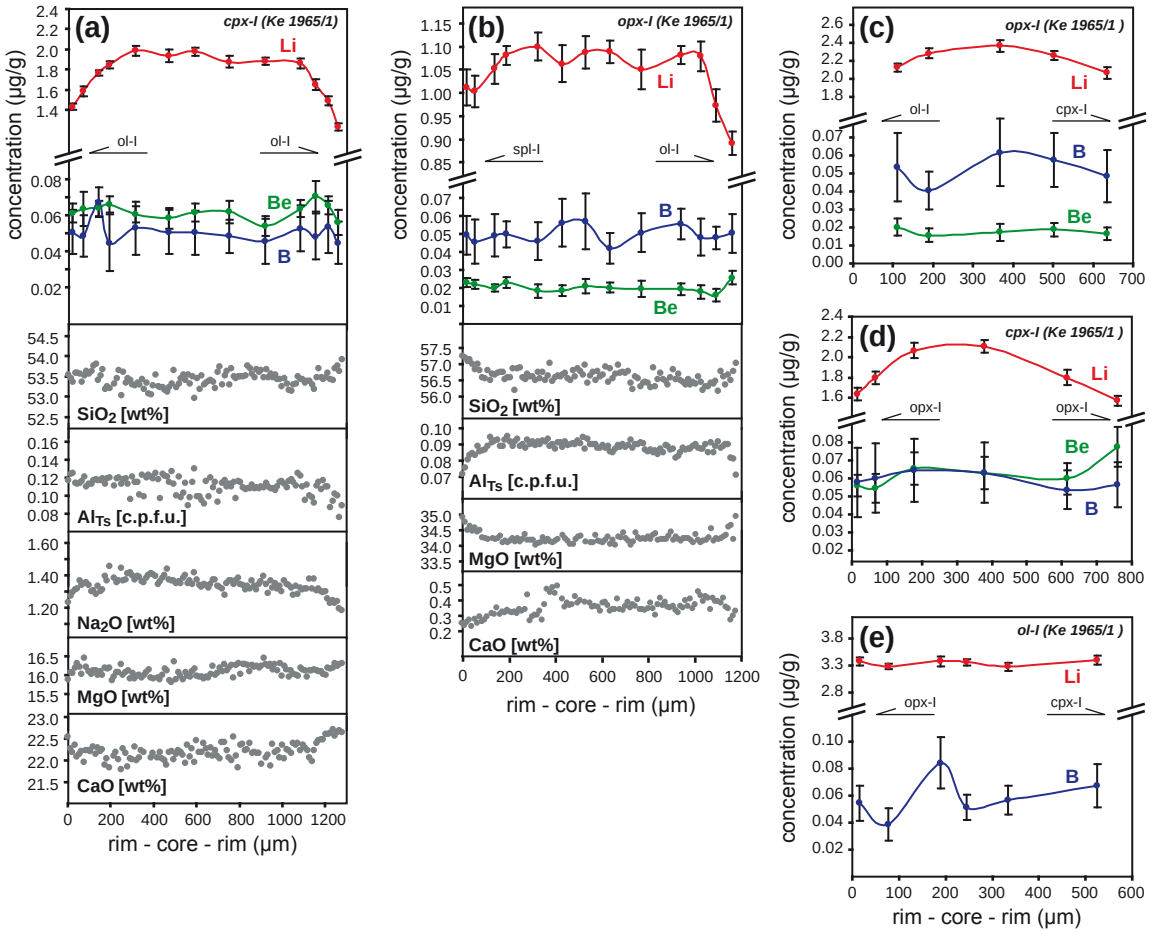


Fig. 4. 5: *Li, Be, and B (SIMS) and major element (electron microprobe) profiles across minerals from Type III-a spl harzburgite xenolith Ke 1965/1. (a) and (d): clinopyroxene porphyroclasts (cpx-I); (b) and (c): orthopyroxene porphyroclasts (opx-I); (d) olivine porphyroclast (ol-I). Error bars correspond to 2σ.*

while SiO_2 and MgO contents slightly increase. In a composite orthopyroxene grain (Fig. 4.6b; metasomatic low-Al Opx_m on the left-hand side and relic opx-I on the right-hand side) Li and Be patterns are parallel to the $^{[IV]}Al$ profile, whereas B mimics the SiO_2 and MgO patterns (Fig. 4.6a-b).

INTER-MINERAL AND MINERAL / MELT PARTITIONING OF Li, Be AND B: DEGREE OF (DIS)EQUILIBRIUM

As the xenoliths from Marsabit display complex metasomatic features, it is important to constrain to which extent chemical equilibrium was attained in the different phase assemblages during their evolution. In the following we will show that minerals from Group I and II xenoliths exhibit near-equilibrium partitioning of light elements. In the case of the Group III spl harzburgites and dunites minerals are mostly out of equilibrium with respect to the light element. Only direct mineral contacts and microlites in melt pockets may occasionally attain mutual light element equilibration.

Group I and II

Minerals from the investigated Group I and II lherzolites are all characterized by limited variations in light elements at concentration levels

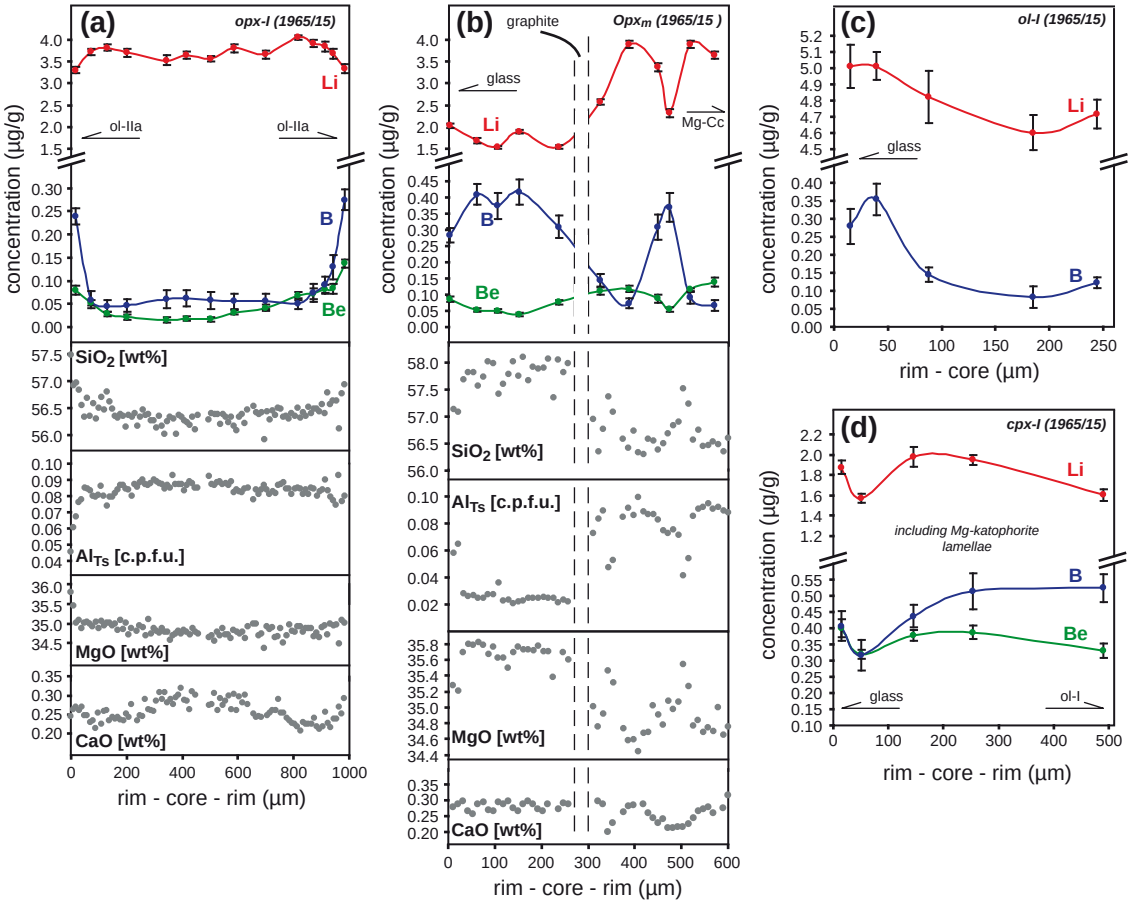


Fig. 4.6: *Li, Be, and B (SIMS) and major element (electron microprobe) profiles across minerals from Type III-b spl harzburgite xenolith Ke 1965/15. (a) and (b): orthopyroxene porphyroclast (opx-I) and composite opx-I – metasomatic low-Al Opx$_m$ grain, respectively; (c): olivine porphyroclast (ol-I); (d) clinopyroxene porphyroclast (cpx-I). Error bars correspond to 2σ.*

broadly corresponding to those defined for normal mantle peridotite [Fig. 4.3 et 4.8; *Seitz and Woodland*, 2000; *Ottolini et al.*, 2004]. Further, LA-ICPMS studies of minerals of the Group I lherzolite (Ke 1963/2) showed that this rock is well equilibrated with respect to the incompatible trace elements (i.e., LREEs, U, Th, LILE, HFSEs; see Fig. 4.2 and *Kaeser et al.* [2006]). Zoning with respect to major elements and some trace elements such as the HREEs and Sc (e.g., Fig. 4.2a), can be explained by partial subsolidus re-partitioning resulting from cooling, decompression and the associated garnet-spinel transition [*Kaeser et al.*, 2006]. Group II xenoliths re-equilibrated almost completely at higher temperatures (Table 4.1) during later EARS-related heating of parts of the lithosphere [*Kaeser et al.*, 2006]. Accordingly, Group II minerals, in terms of major and trace elements, are mostly homogeneous (e.g., Fig. 4.2b and c). Partial (low temperatures; Group I) and complete (high-temperature; Group II) re-equilibration of elements with intermediate or even slow diffusivities (Ca and REEs, or Al, respectively [e.g., *Sautter et al.*, 1988; *van Orman et al.*, 2001]) allows to assume equilibrium for the light elements as well, at least at contacts between different phases. This is especially the case for Li which is known for very high diffusivity [e.g., *Coogan et al.*, 2005]. We therefore used Li, Be and B contents at contacts between mineral pairs from Group I and II xenoliths (samples Ke 1963/2, 1958/13, and

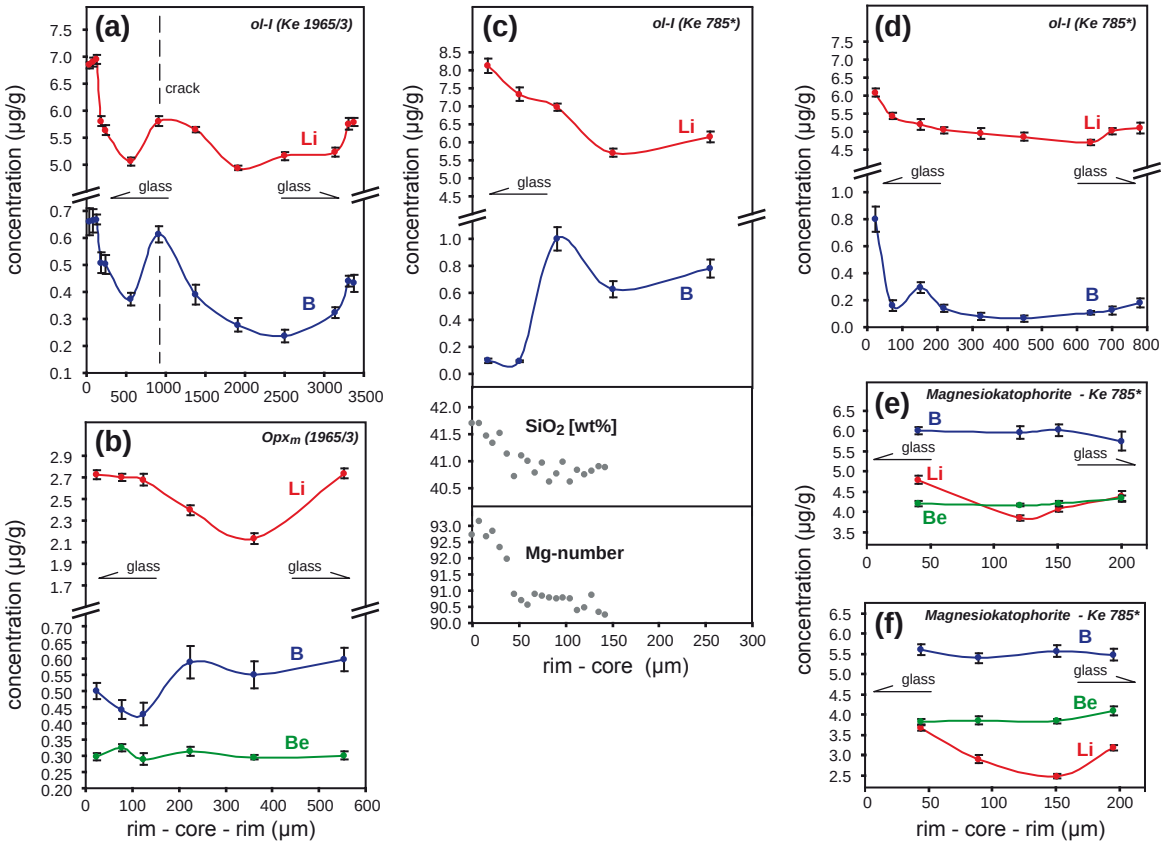


Fig. 4.7: *Li, Be, and B (SIMS) and major element (electron microprobe) profiles across minerals from Type III-c spl dunite Ke 1965/3 and spl harzburgite Ke 785*, respectively. (a) and (b) olivine porphyroclast (ol-I) and metasomatic low-Al orthopyroxene (Opx$_m$), respectively, in sample Ke 1965/3; (c) and (d): olivine porphyroclasts (o-I) in sample Ke 785*; (e) and (f): amphibole (Mg-katophorite) grains in sample Ke 785*. Error bars correspond to 2σ.*

1958/20) to calculate equilibrium mineral/mineral partition coefficients ($^{element}D_{min1/min2}$). Mean values for individual mineral pairs are given in Table 4.3. The values obtained for Li and B (Fig. 4.8) are, within the relative uncertainties, in good agreement with previously published equilibrium partition coefficients [*Seitz and Woodland*, 2000; *Kaliwoda*, 2004; *Ottolini et al.*, 2004]. Even though Group I and II lherzolites recorded a different thermal evolution, their constituent minerals exhibit a fairly similar light element signature. Based on this and the low number of investigated samples, our data does not allow to constrain a possible temperature-dependence of the light element partitioning.

Group III

In the case of phlogopite and Mg-katophorite in sample Ke 785* (Type III-c), equilibrium is indicated texturally by straight contacts and subhedral crystal forms. Calculated partition coefficients indicate Li distribution close to unity. Both Be and B are strongly partitioned into Mg-katophorite (Table 4.3). Preferential incorporation of Be in amphibole is well known [e.g. *Brenan et al.*, 1998a; *Adam and Green*, 2006]. However, in the case of Li and B, experiments in basanitic systems (1050°C at 2.0 GPa; *Adam and Green* [2006]) revealed amphibole/phlogopite partition coefficients well below 1 (0.51 for

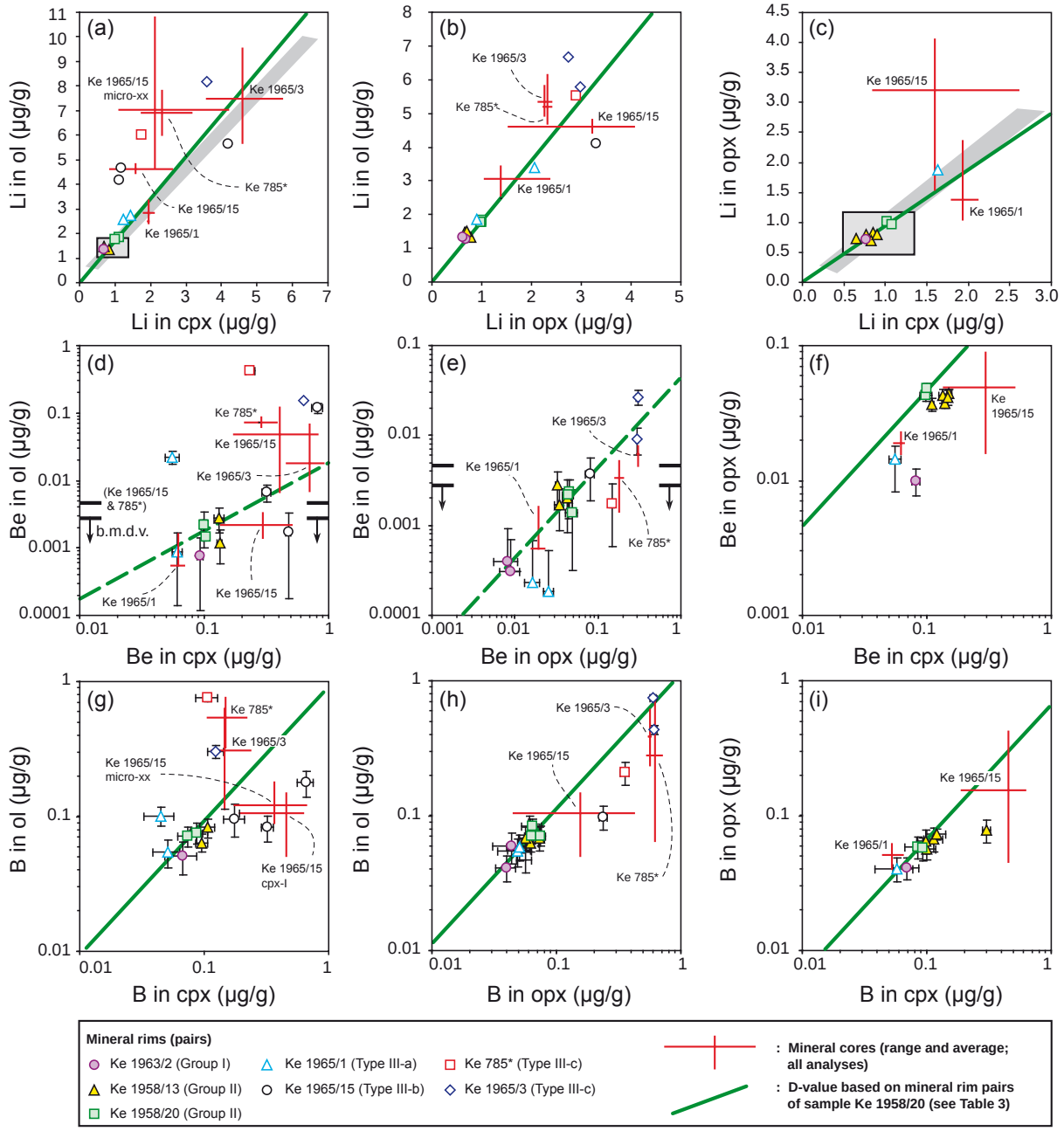


Fig. 4.8: *Partitioning of Li, Be and B between olivine and clinopyroxene (a, d, and g, respectively), olivine and orthopyroxene (b, e, and h, respectively) and orthopyrxoxene and clinopyroxene (c, f, and i, respectively). Symbols correspond to mineral pairs in direct contact with each other. The grey rectangle and field in (a) and (c) correspond to the 'normal mantle' values and equilbrium partitioning, respectively, of Seitz & Woodland [2000]. b.m.d.v.: below the minimal detectable value (after Curie [1968]; for Be in olivine; note higher value for samples Ke 1965/15 and 785* due to shorter analysis times; see Chapter 8).*

Table 4.3: Average apparent mineral/mineral and mineral/melt partition coefficients obtained from minerals and glass in peridotite xenoliths from Marsabit

Sample	ol / cpx			ol / opx			opx / cpx			phl / amph			cpx / glass			ol / glass		
	Li	Be	B	Li	Be	B	Li	Be	B	Li	Be	B	Li	Be	B	Li	Be	B
Ke 1963/2 (G. I)	2.01 (10)	*0.008 (7)*	0.75 (26)	2.03 (9)	*0.041 (55)*	1.19 (42)	1.04 (4)	0.19 (5)	0.59 (18)	1.23 (7)	0.64 (6)	5.18 (1.09)	-	-	-	-	-	-
Ke 1958/13 (G. II)	1.89 (9)	*0.015 (7)*	0.72 (14)	2.04 (8)	*0.062 (29)*	1.05 (24)	0.97 (5)	0.30 (3)	0.61 (15)	-	-	-	-	-	-	-	-	-
Ke 1958/20 (G. II)	1.71 (7)	*0.018 (11)*	0.91 (21)	1.80 (7)	*0.044 (22)*	1.13 (23)	0.94 (5)	0.46 (6)	0.66 (17)	-	-	-	-	-	-	-	-	-
Ke 1965/15 (G. III-b)	-	-	-	-	-	-	-	-	-	-	-	-	0.053 (3)	0.082 (7)	0.041 (8)	0.21 (1)	0.0017 (5)	0.022 (6)
Ke 785* (G. III-c)	-	-	-	-	-	-	-	-	-	1.00 (3)	0.34 (1)	0.26 (2)	0.28 (1)	0.048 (3)	0.024 (3)	-	-	-
Ke 1965/3 (G. III-c)	-	-	-	-	-	-	-	-	-	-	-	-	0.25 (1)	0.021 (1)	0.014 (1)	0.53 (1)	0.0007 (1)	0.011 (2)

only analyses of in direct contact with each other have been used (see text for explanations); numbers in brackets = fully propagated errors (last significant digits)
D-values in italic have to be treated with caution as Be concentrations in olivine are often close/below the minimal detectable value (see Table 4.2)

Li and 0.76 for B). The disagreement with our data either reflects disequilibrium between amphibole and phlogopite in sample Ke 785*, or varying partition coefficients depending on the strongly different amphibole composition (katophorite instead of Ti pargasite obtained by *Adam and Green* [2006]).

As for Mg-katophorite and phlogopite, textures indicate that silicate glass + microlite pockets in the Type III-b and -c xenoliths might represent small equilibrated 'sub-systems' (e.g. euhedral shapes of Ol_m and Cpx_m in contact with glass; see Fig. 4.1e). Therefore we used the melt pocket phases to calculate $D_{mineral/melt}$-values for Li, Be and B (Table 4.3 and Fig. 4.9). $D_{cpx/melt}$ obtained from the glass-rich xenolith Ke 1965/3 compare quite well with the experimental data set of *Brenan et al.* [1998a]. $^{Li}D_{cpx/melt}$ (Fig. 4.9a) fit particularly well with experimental values obtained at relatively low pressure (1 atm [*Brenan et al.,* 1998a], and 1.2 GPa [*Gaetani et al.,* 2003]; except values from sample 1965/15; Fig. 4.9b). This would be in line with melt pocket formation at shallow depths (<1.5 GPa) and/or during the transport of the xenoliths to the surface, but may also reflect the relatively high Na contents in cpx of our data (and resulting high $^{Na}D_{cpx/melt}$; *Brenan et al.* [1998a]). $^{Li}D_{ol/melt}$ (Fig. 4.9b) agree well with literature data [*Brenan et al.,* 1998a; *Taura et al.,* 1998; *Zanetti et al.*, 2004], whereas $^{B}D_{ol/melt}$ is slightly higher than most published values, resulting in Ol_m-Cpx_m pairs deviating from the equilibrium partitioning line (Fig. 4.8a; preferential enrichment in Ol_m). In the case of Li, comparison between Ol_m and Cpx_m reveals near equilibrium partitioning (in sample Ke 1965/3) to preferential Li incorporation in Ol_m. Chemical equilibrium for Li has also been observed in melt pockets from Australian xenoliths [*Woodland et al.,* 2004], whereas disequilibrium is often observed in xenoliths which experienced metasomatism by carbonated melts [Seitz and Woodland, 2000]. The melt pockets from this study are small carbonated systems (containing Mg-calcite), which may thus explain the relative Li enrichment in olivine in some of them (samples Ke 1965/15 and 785*; Fig. 4.8a).

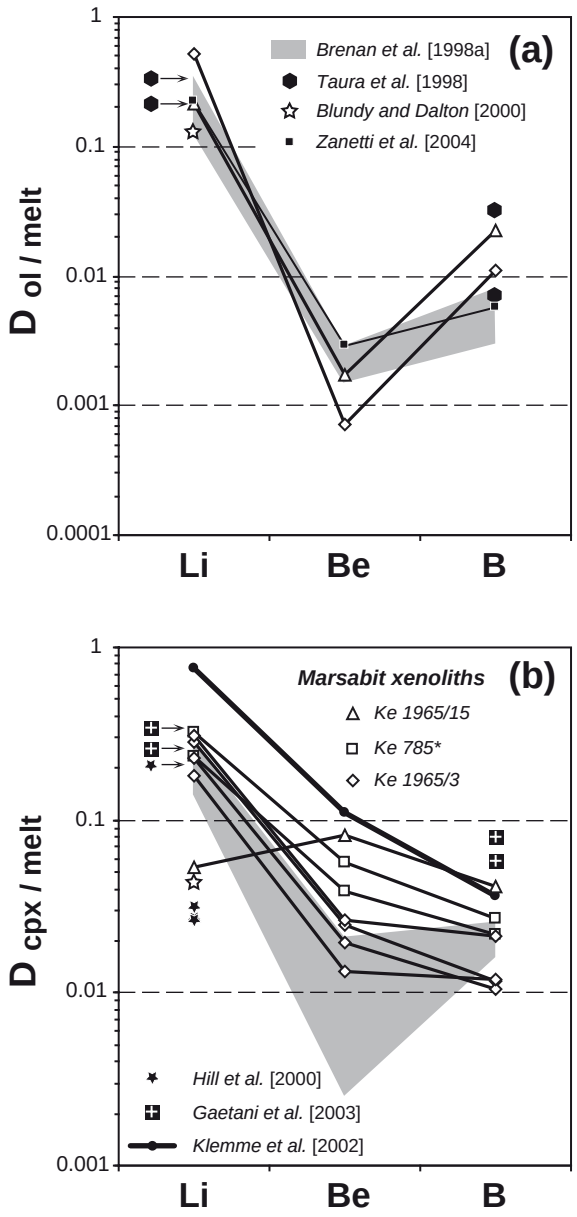


Fig. 4.9: *Olivine/melt (a) and clinopyroxene/melt (b) partition coefficients obtained from melt pockets (Ol_m and Cpx_m microlites and silicate glass) in peridotite xenoliths from Marsabit, in comparison with experimental results.*

In Group III harzburgites, 'primary', cryptically metasomatized silicates (ol-I, cpx-I, opx-I) are variably enriched in Li, Be and B compared to Group I and II. Further, apparent mineral/mineral partition coefficients commonly deviate from equilibrium values (i.e. higher $^{Li}D_{ol/cpx}$, and lower $^{B}D_{ol/cpx}$, $^{B}D_{opx/cpx}$ and $^{Be}D_{opx/cpx}$; Fig. 4.8). In the case of $^{Li}D_{ol/opx}$ and $^{Li}D_{opx/cpx}$, however, values close to equilibrium are often maintained (Fig. 4.8b and c). There seems to be a systematic enrichment of Be in opx relative to ol (Fig. 4.8a). However, $^{Be}D_{ol/cpx}$ and $^{Be}D_{ol/opx}$ have high uncertainties because Be concentrations in olivine are close to the limit of detection (Table 4.2). These ratios must therefore be treated with caution. Finally, Fig. 4.8 further illustrated that mineral cores are clearly out of equilibrium with respect to all light elements. In summary, together with features highlighted by the zoning patterns, light element systematics in primary minerals from the metasomatized spl harzburgite (Type IIIa to -c) point to important disequilibrium processes compared to normal mantle partitioning and exhibit heterogeneity on small scales.

CAUSES FOR DISEQUILIBRIUM: LATE-STAGE DIFFUSION AND REACTION

The late-stage melt formed mainly at the expense of the early metasomatic assemblage (namely amphibole) and obviously strongly modified the light element signature of the primary minerals. This modification of Li, Be and B contents in minerals needs to be understood and quantified before the light element systematics related to the earlier metasomatism can be discussed. In this respect, compositional modification of the pre-existing phases by melt may be achieved either by diffusional re-equilibration during melt percolation along grain-boundaries, and/or by overgrowth or replacement by secondary, melt-related phases of different major and trace element composition. In the following we present evidence for both (most likely interacting) processes.

Diffusion

The well expressed Li zoning profiles in all phases with contacts towards glass (Fig. 4.6 and 4.7) indicate diffusional re-equilibration with a melt. Similar Li concentration patterns were re-

ported from peridotite xenoliths from southern Siberia and San Carlos, USA [*Jeffcoate et al.*, 2006]. There, it was shown that rapid Li diffusion would result in quick re-equilibration and thus indicates a very young age of the melt-mineral interaction. Diffusion coefficients in diopside, for example, are several orders of magnitude higher than for other cations (e.g., Ca and Mg; see *Coogan et al.*, [2005]). The diffusion of B and Be has only been investigated in Si-rich melts indicating diffusion coefficients ~10 orders of magnitude lower than in the case of Li [*Jambon and Semet*, 1978; *Mungall et al.*, 1999]. Therefore, if diffusion is the only process acting, Li can be decoupled from Be and B during melt percolation processes [see also *Tomascak et al.*, 2000 and 2002]. This effect may explain why some zoning patterns show varying Li but constant Be and B concentrations. However, most profiles (except those across Mg-katophorite; Fig. 4.7e and f) show very low Be and B concentrations (and resulting higher relative uncertainties) compared to Li, and do not allow a precise estimation of the relative Be and B zoning.

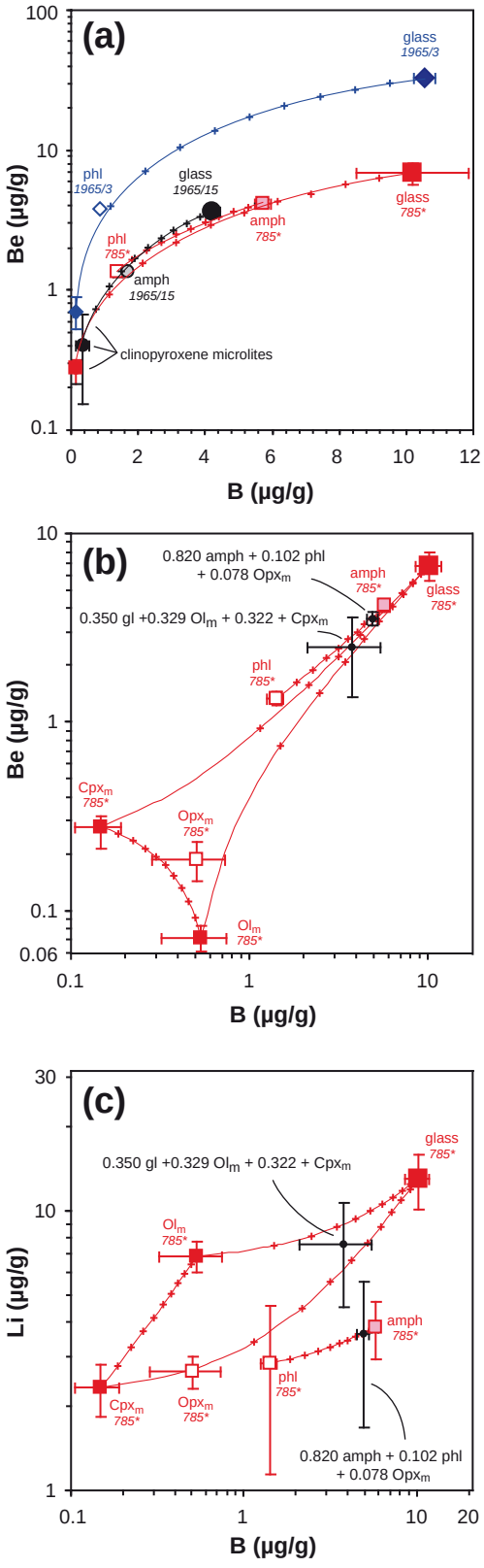
The preservation of glass in mantle xenoliths is another indication for a very young age of formation, as this implies that the melt was still present (or even formed) at the time when the xenoliths were transported to the surface. Quantitative constraints on the duration of the late metasomatic event can be obtained provided that zoning profiles are solely due to diffusional re-equilibration. As zoning is commonly restricted to a narrow zone at the grain's rims, major element profiles are better suited for diffusion modelling due to the better spatial resolution of the microprobe traverses compared to the relatively large SIMS spots (~25 μm). Mg-Fe interdiffusion in olivine is very well understood [e.g., *Chakraborty*, 1997] and gradients in ol-I adjacent to melt pockets (Fig. 4.7c) can be used to calculate the duration of olivine-melt reaction until the melt was quenched to glass [see also *Wulff-Pedersen et al.*, 1999; *Shaw and Klügel*, 2002; *Shaw et al.*, 2006 for similar modelling]. Time (t) may be estimated using the approximate relation $\chi = \sqrt{(Dt)}$ [*Crank*, 1975], where χ is the distance from the olivine-melt contact at which the concentration of the given element is the average of the (initial) core and the rim concentration. D is the diffusion coefficient for a given element. We calculated t for two olivine profiles (not shown) in the glass-rich xenolith Ke 1965/3 (Type III-c). During the diffusion event we assumed a constant temperature of 1246 ± 136 °C (average based on the olivine-spinel thermometer of *Ballhaus et al.* [1991], using the composition of Chr_m and Ol_m microlites; see Table 4.1). Owing to the temperature uncertainties of our temperature data we calculated time periods using Mg-Fe interdiffusion-coefficients of 5.5×10^{-18} m^2/s (for Fo_{92} at 1100°C) and 2×10^{-16} m^2/s (for Fo_{93} at 1300°C; *Chakraborty* [1997]). The resulting time spans calculated for two olivine profiles lie between 4 and 206 days, indicating that melt-olivine reaction occurred shortly before and/or during the transport of the xenolith in the host magma.

Reaction

In reality, diffusion was probably not the only process influencing light element partitioning. Textures indicate that the melt pockets (glass + microlites) are the result of incongruent melting of pre-existing phases (mainly amphibole) according to reactions such as:

$$\text{amph} (\pm \text{phl}, \pm \text{apatite}, \pm \text{graphite}) = Cpx_m + Ol_m\ Chr_m + \text{Mg-calcite} + \text{melt1} \quad (1)$$

More Si-rich glass associated with orthopyroxene (Table 4.2) most likely formed during reaction of orthopyroxene with melt produced during reaction (1) [see also *Shaw*, 1999, for example]. Mass balance calculations based on the major element composition of minerals indicate that even though a fluid phase probably triggered melting, the reaction products, to the greatest extent, inherited the compositional features of the precursor assemblage [*Kaeser et al.*, submitted]. According to this, the light element signature in the newly formed phases (microlites and reaction rims) will, on one hand, reflect



the light element composition of the precursor phase(s). On the other hand, the Li-Be-B systematics will vary depending on the mechanism upon which the new phases form; (a) crystallisation from the melt (e.g. microlite), (b) resorption and/or overgrowth of the pre-cursor primary phase (e.g. Ol_m at the expense of ol-I), and (c) chemical 'overprint' of the primary phase (e.g. cryptic enrichment of ol-I). Mechanism (a) would mainly depend on mineral/melt partition coefficients, whereas (b) and (c) would be in addition strongly influenced by the initial light element composition of the primary phase, as well as by the different diffusion coefficients of the light elements. Interfering effects of these processes are possibly the main reason for the variable B zoning in Ol_m and ol-I adjacent to glass (Figs. 4.6c, 4.7a, c and d). Olivine associated with melt pockets containing abundant Cpx_m and/or relic amphibole has commonly higher B contents than olivine associated with cpx-poor melt pockets. The latter are commonly related to the incongruent melting of orthopyroxene (Fig. 4.1d). Replacement of B-poor Opx_m, relative to B-rich amphibole, can thus explain the large compositional variation of olivine on a rather small scale.

In the case of cpx-rich melt pockets, the major element-based relative phase proportions

Fig. 4.10: *Melt pocket formation by amphibole (± phlogopite, ± orthopyroxene) melting with respect to the Li-Be-B budget. (a): B vs. Be concentrations and binary mixing lines (10% increments) between silicate glass and clinopyroxene microlites (Cpx_m) compared to amphibole and phlogopite in samples Ke 1965/15 (black); 1965/3 (blue) and 785* (red). (b) Mutual mixing lines between microlites (Ol_m and Cpx_m) and glass, and phlogopite and amphibole from sample Ke 785* with respect to B and Be concentrations. Black symbols: bulk composition of melt pockets (glass+Ol_m+Cpx_m) and reactants (amph+phl+Opx_m) using the phase proportions obtained from major element mass balance [Kaeser et al., submitted]. (c): Mutual mixing lines between microlites (Ol_m and Cpx_m) and glass, and phlogopite and amphibole from sample Ke 785* with respect to B and Be concentrations [black symbols as in (b)]. For explanations see text.*

(annotated in Fig. 4.10) can be used to calculate the bulk melt pocket trace element signature. With respect to the 'classical' trace elements, this shows that the melt pockets fully inherit the trace element budget of the reactant, i.e. amphibole and minor amounts of phlogopite (*Kaeser et al.* [submitted]). Here, we used the same mass balance parameters to test whether the light element signature can be explained by the same process. This is illustrated in Fig. 4.10. With respect to B and Be, amphibole and/or phlogopite from all samples plot close to a binary mixing line between the respective composition of silicate glass and the related Cpx_m (Fig. 4.10a). The position of amphibole close to 1:1 mixing between glass and Cpx_m is in agreement with the relative phase proportions in the melt pockets obtained from major element mass balance (e.g. glass/Cpx_m ratio of 1.087 in melt pockets of sample Ke 785*). The influence of the olivine microlites (Ol_m) on the mixing curves and the resulting bulk melt pocket composition can be depicted from Fig. 4.10b. The B-Be signature of the reactant (amph+phl+opx), plots close to the bulk melt pocket (cpx+ol+glass) composition (Fig. 4.10b). This illustrates that the B-Be signature of silicate glass and microlites inherit the signature of the previous metasomatic assemblage (mainly amphibole), and that the melt (i.e. the glass) does not represent a metasomatizing agent that greatly modified the B-Be budget of the whole rock. In contrast, Li abundances are less well reproduced (Fig. 4.10c), mainly due to slightly higher concentrations in the bulk melt pockets (Fig. 4.10c). Since Li is extremely mobile, diffusional modification, either of the relict reactant phases or of the products may explain this mismatch.

Li zoning at glass-free mineral contacts

Pyroxenes that are not in contact with glass are commonly characterized by decreasing Li concentrations towards the rim (Figs. 4.4a-c, 4.5a-c, 4.6a). This may reflect a relatively Li-poor signature of the melt responsible for the early metasomatic events (mafic silicate melt in Group II and evolved Si-rich melt in Group III, prior to melt pocket formation; see below for more details). Alternatively, it could be also related to late modification, similar to the formation of the melt pockets. Given the fast diffusion rates of Li in diopside, a late event seems more plausible. Applying the Li diffusion coefficient determined by *Coogan et al.* [2005] to the profile in Fig. 4.5a shows that even at the low temperatures at which this xenolith partly re-equilibrated (834±37°C; Table 4.1), the observed gradient, and the decoupling from Be and B, could be attained in only 1-23 days. Moreover, the trace element patterns obtained by LA-ICPMS from the pyroxene's cores show already the enriched signature characteristic for the early metasomatic events (e.g. high LREE-U-Th in clinopyroxene; Fig. 4.2d). This signature corresponds to the high-Li plateaus (Fig. 4.5a). The extreme differences in diffusivities, e.g. between Li [*Coogan et al.*, 2005] and REEs [*van Orman et al.*, 2001] are in favour of the hypothesis that Li depletion of the rims occurred significantly later than LREE-U-Th enrichment. Likewise, Li depletion has been observed in magmatic augite and pigeonite from Martian meteorites [e.g. *McSween et al.*, 2001; *Lentz et al.*, 2001], interpreted to reflect late-stage loss of a water-rich fluid (related to the ascent of the lava to the Martian surface). Extraction of such a fluid (resulting in texturally 'dry' grain boundaries), may explain the Li depletion in pyroxenes from this study. Its origin could be related to partial melting of clinopyroxene during heating and decompression of the xenolith in the host magma. Clinopyroxene melting has been invoked to explain sieve-textured clinopyroxene rims from lavas [*Hibbard and Sjöberg*, 1994] and xenoliths [e.g. *Carpenter et al.*, 2002; *Shaw et al.*, 2006,], and would be in line with the occurrence of similar textures observed in this study (Fig. 4.1f). The high diffusivity of Li explains why other trace elements are not affected by this process.

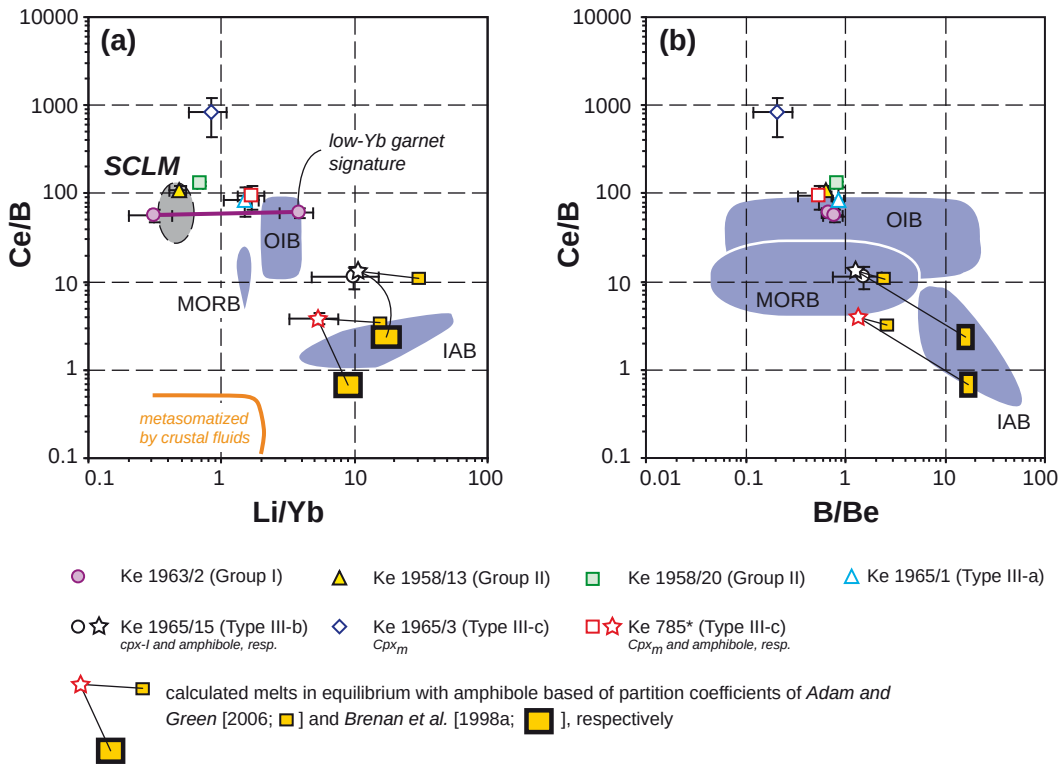


Fig. 4.11: *Li/Yb vs. Ce/B (a) and B/Be vs. Ce/B ratios in clinopyroxene, Mg-katophorite and melts in equilibrium with Mg-katophorite from Marsabit peridotite xenoliths: Li/Yb and Ce/B ratios for fluid metasomatized peridotite, MORB and OIB as in Ottolini et al. [2004]. B/Be ratios for MORB and OIB based on data from Ryan and Langmuir [1988], Dostal et al. [1996] and Bach et al. [2001] for Be, and on Ryan & Langmuir [1993], Chaussidon and Marty [1995] and Dostal et al. [1996] for B (considering only analyses from MORB with > 7 wt% MgO). Field for IAB (for all ratios) based data from the Panama [Defant et al., 1991; Tomascak et al., 2000] and Vanuatu arc [Peate et al., 1997].*

THE NATURE OF EARLY METASOMATISM BENEATH MARSABIT AS DEDUCED FROM CLASSICAL TRACE AND LIGHT ELEMENT DATA

The preservation of glass and the light element zoning patterns indicate that late metasomatism (melt pocket formation) occurred shortly before eruption of the xenoliths and modified only the rims of the primary minerals. Hence, the cores of the primary minerals, even in the glass-bearing xenoliths, still record an earlier compositional stage of the mantle beneath Marsabit, including early metasomatic event(s). These are cryptic metasomatism in Group II (grt)-spl lherzolites and the formation of the volatile-bearing phase assemblages in Group III spl harzburgites. In Fig. 4.11, Li and B abundances in clinopyroxene and amphiboles are compared to REEs of similar compatibility (LA-ICPMS data; *Kaeser et al.* [2006; and submitted]). The Li/Yb *vs.* Ce/B plot was used by *Ottolini et al.* [2004] to identify different types of metasomatized peridotite and to define the Li-B systematics of the (hypothetical) 'non-metasomatized sub-continental lithospheric mantle' (SCLM; Fig. 4.11a). Amphibole and clinopyroxene from the different xenolith types of Marsabit cover a large spectrum of Li/Yb, Ce/B, as well as B/Be ratios. These features and their implications for the nature of variable metasomatism in the lithosphere beneath Marsabit will be discussed in the following.

Group I

Although the Group I lherzolites contain small amounts of Ti-pargasite and phlogopite, their constituent cpx-I are LREE-depleted and compare well with the signature found in typical non-metasomatized peridotite [*Eggins et al.*, 1998; *Kaeser et al.*, 2006]. In line with this, light element concentrations in cpx-I (as well as in ol-I and opx-I) fall within the range of the 'normal mantle' values (Fig. 4.8; *Seitz and Woodland* [2000]). Consequently, as expected, their incompatible element ratio (i.e. Ce/B) is in good agreement with the SCLM estimate of *Ottolini et al.* [2004]. On the other hand, the low HREE contents in the cores of cpx-I from Group I lherzolites drives Li/Yb ratios to much higher values than those of the SCLM. This is obviously due to the preservation of a garnet-facies signature preserved in the Group I clinopyroxenes [*Kaeser et al.*, 2006], and does not imply metasomatism. This highlights that Li/Yb ratios of clinopyroxene can only be applied to discriminate melt signatures from different tectonic settings when other processes such as sub-solidus decoupling of Li from Yb can be clearly excluded. Given the strongly different diffusion rates of Li compared to HREEs (see above), it might be argued that melt percolation processes can have a similar effect.

Group II

Clinopyroxenes from the two heated Group II lherzolites (Ke 1958/13 and 1958/20) are LREE-enriched. The light element abundances are only slightly higher than in LREE-depleted Group I lherzolites, resulting only in small deviations from the SCLM (Fig. 4.11a) or 'normal mantle' fields (Fig. 4.8). Due to the cryptic enrichment (LREE-U-Th) we cannot distinguish to which extent the slightly different light element contents in Group I and II clinopyroxenes reflect metasomatism or an eventual influence of the higher temperature. In our earlier study, we proposed that Group II lherzolites interacted with a mafic silicate melt of an already evolved composition, resulting from chromatographic trace element fractionation [*Kaeser et al.*, 2006]. Considering the relatively high bulk Li partition coefficient in a peridotitic matrix (resulting from high $^{Li}D_{ol/melt}$ values; e.g. *Brenan et al.* [1998a]), Li would be effectively absorbed by olivine close to the metasomatizing agent's source. Such a scenario would explain the lack of strong Li enrichment in Group II clinopyroxene (as well as in olivine; Fig. 4.8a). Similarly, Yb would be quickly absorbed by clinopyroxene. Consequently, the fractionated melts at the top of the metasomatic front would enrich clinopyroxene in incompatible elements (e.g. LREEs, B, Be), but leave Yb and Li concentrations broadly unchanged (Fig. 4.11a). The slightly elevated Ce/B ratios of the Group II clinopyroxene (compared to the SCLM; Fig. 4.11a) are in line with this interpretation and coincide with other samples interpreted in the context of chromatographic fractionation processes [*Ottolini et al.*, 2004]. Group II minerals exhibit only minor Be and B enrichment relative to Group I minerals (only opx-I shows slightly higher Be abundances; Fig. 4.8e and f). This indicates most likely that the metasomatising agent did not carry significant amounts of these elements. At the same time, cpx-I shows no fractionation of B from Be (Fig. 4.11b). Given the similar $^{B}D_{cpx/melt}$ and $^{Be}D_{cpx/melt}$ [*Brenan et al.*, 1998a], this is what can be expected as long as no agent with strongly differing B and Be solubilities (e.g. hydrous fluids), and no minerals able to fractionate B from Be (e.g. amphibole; *Brenan et al.*, [1998a]) are present.

Group III

Minerals from Group III harzburgites are characterized by the strongest light element enrichment (Fig. 4.3 and 4.8) and cpx-I (where present) and amphibole show fractionated Li/Yb and Ce/B and B/Be ratios (Fig. 4.11a and b). Many textural and compositional features common to Type III-a to -c (see section 'Mineralogical and

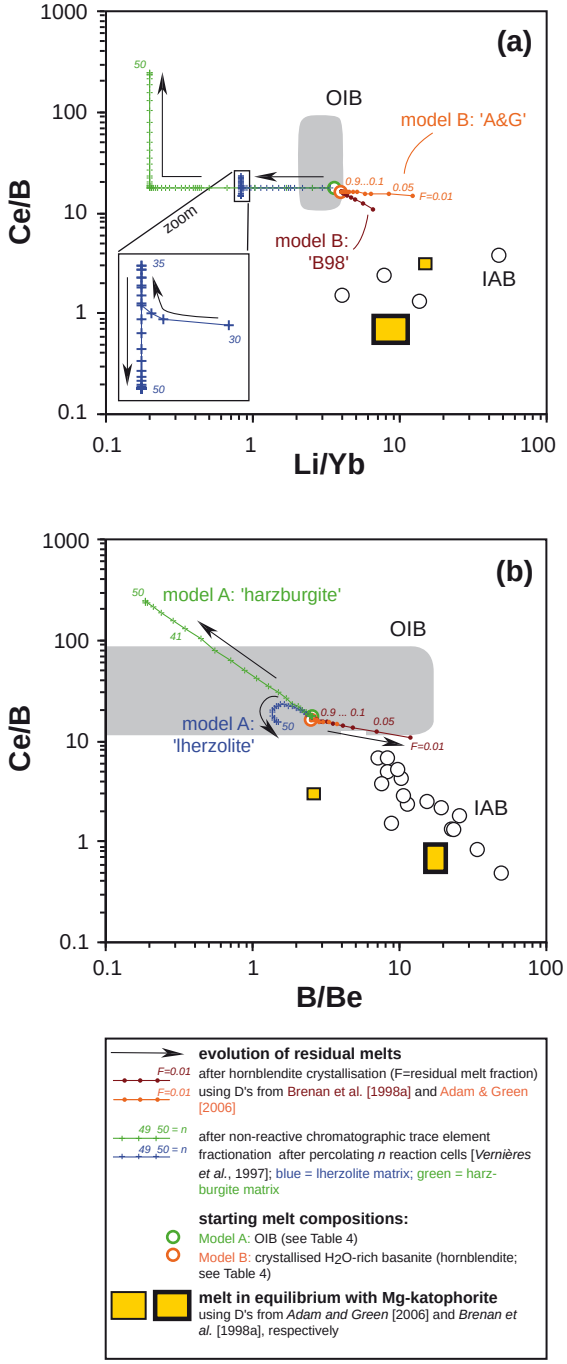
Geochemical characteristics of the samples') indicate that one single metasomatizing event formed different products depending on the position of the peridotite rock relative to the source of the metasomatizing agent. In this context, the different Group III samples describe a sequence of harzburgite modified by melt-rock reaction, whereby the degree of modification increases from Type III-a to -c. Type III-c xenoliths thus represent fragments of the wall rock closest to the metasomatizing source. This is in line with high amounts of volatile-bearing phases present in these rocks (e.g., sample Ke 785*). Even though trace element patterns of cpx-I and amphibole exhibit typical 'carbonatitic' signatures (LREE-enrichment and very low HFSE/REE ratios [e.g., *Green and Wallace,* 1988]), co-existence of Na-rich volatile-bearing phases, graphite and low-Al orthopyroxene (Opx_m) at pressures <1.5 GPa implies that the metasomatising agent was a SiO_2-Na_2O-H_2O-CO_2-rich melt or fluid, and precludes carbonated melts [e.g., *Lee and Wyllie,* 2000 and references therein]. The Be concentration in minerals would be in line with a silicate melt as metasomatising agent. Be in pyroxenes (especially Opx_m; Fig. 4.3) is considerably enriched relative to Group I xenoliths (Fig. 4.8), and B/Be ratios in both Mg-katophorite and cpx-I are only slightly above 1, well within the range of mantle-derived melts (e.g., MORB and OIB; see Fig. 4.11b). The lack of Be and B enrichment in minerals of the studied Type III-a sample (Ke 1965/1; Fig. 4.3) may reflect depletion of the residual metasomatizing agent in these elements due to previous crystallization of high amounts of B- and Be-rich Mg-katophorite and phlogopite (Fig. 4.3) in peridotite closer the initial agent's source (i.e. Type III-b and -c samples).

Is there a subduction-related component in the Group III harzburgites?

Metasomatism by fluids or melts released from subducting lithosphere is expected to produce similar trace element signatures in peridotite like carbonated melts. There, fractionation of REEs from HFSEs may reflect both low HFSE solubilities in hydrous fluids and minerals (e.g., rutile) in the residual subducting slab retaining HFSEs [e.g., *Brenan et al.*, 1995; *Keppler,* 1996; *Stalder et al.*, 1998; *Klemme et al.*, 2005; *Kessel et al.,* 2005]. Accordingly, such metasomatic signatures in mantle samples from tectonic settings above or close to subduction zones are commonly interpreted to result from the percolation of slab-derived melts or fluids [e.g., *Maury et al.,* 1992; *Kepezhinskas et al.,* 1996; *Grégoire et al.,* 2001; *Laurora et al., 2001*; *Parkinson et al.,* 2003]. Metasomatised peridotite xenoliths from subduction zone settings further contain several other characteristics strikingly similar to the Group III peridotites from Marsabit, such as the presence of metasomatic orthopyroxene or particularly Na-rich phase assemblages [*McInnes and Cameron,* 1994; *Kepezhinskas et al.,* 1995; *Smith et al.*, 1999; *McInnes et al.*, 2001; *Franz et al.,* 2002; *Arai et al.*, 2004].

Given the enrichment of light elements (at least Li and B) in subducting slabs compared to the depleted upper mantle [*Ryan and Langmuir,* 1987; *Leeman & Sisson,* 1996; *Ryan,* 2002], slab-released fluids could explain the light element signature in the Group III peridotites from Marsabit, such as invoked for other cases [e.g., *Paquin et al.,* 2004; *Scambelluri et al.,* 2006; *Raffone et al.,* 2006]. Moreover, hypothetical melts in equilibrium with Type III-b and -c amphibole show Li/Yb, Ce/B and B/Be similar to those of Island Arc Basalts carrying a typical slab signature [e.g., *Peate et al.,* 1997; *Tomascak et al.,* 2000; see Fig. 4.12].

The last tectonic event that potentially led to subduction-related metasomatism in the lithospheric mantle beneath Marsabit was the formation of the East African Orogen in Pan-African times (720-550 Myr; e.g., *Meert* [2003]). However, early metasomatism in the Group III samples is texturally young, and clearly overprints the penetratively deformed fabric of the pre-metasomatic 'protolith' [*Kaeser et al.,*



2006]. Deformation and associated decompression and cooling was attributed to Mesozoic rifting (formation of the Anza Graben; *Kaeser et al.* [2006]). Metasomatism must thus be related to the Tertiary-Quaternary magmatic activity at Marsabit. Consequently, if the early metasomatic assemblage in Group III xenoliths contains a subduction-related component, it must be an old mantle domain modified by ancient slab fluids that re-melted in the Tertiary-Quaternary. Preliminary Pb and Sr isotope data on minerals from sample Ke 785*, however, do not point to any 'slab-related' component (E. Bourdon, personal communication).

Whatever the origin of the light element enrichment in Marsabit is, we would like to emphasize that it is in any case not straightforward to postulate 'subduction signatures' based only on trace element patterns from single minerals, especially in cases where ample evidence for extensive melt-rock reaction and disequilibrium processes exists (such as the Group III xenoliths; see above). There are several recent studies which highlight the potential of melt-rock reaction, reactive porous flow, and chromatographic trace element fractionation to produce residual volatile-enriched melt fractions and various trace element signatures starting from relatively 'ordinary' mantle melts such as alkali basalts or basanites [e.g. *Bedini et al.*, 1997; *Xu et al.*, 1998; *Ionov et al.*, 2002; *Bodinier et al.*, 2004; *Rivalenti et al.*, 2004]. Similarly, the propagation and crystallisation of alkaline melts in cracks and veins may produce highly evolved residual melts which ultimately metasomatize the adjacent peridotite wall-rock creating trace element signatures similar to those observed in

Fig. 4.12: *Evolution of Li/Yb vs. Ce/B (a) and B/Be vs. Ce/B (b) ratios in residual melts deriving from two 'end-member' metasomatic fractionation processes. Model A: Evolution of a residual melt modified by non-reactive chromatographic trace element fractionation during porous melt flow through lherzolite and harzburgite, respectively. Model B: Residual melt after fractional crystallisation of hornblendite from a basanite melt in a hypothetical vein [using partition coefficients of Brenan et al. [1998a] (B'98) and Adam and Green [2006] (A&G), respectively] . See Table 4.4 for model parameters and text for further explanations. Lava fields and composition of calculated melts in equilibrium with Mg-katophorite as in Fig. 4.11. (c) Trace element pattern of Model B residual melts (F = residual melt fraction) in comparison with melts calculated to be in equilibrium with Type III-c Mg-katohorite (grey field; Kaeser et al.[submitted]). For further explanations see text.*

Table 4.4: Parameters for models illustrated in Fig. 4.12

Model A: non-reactive chromatographic trace element fractionation simulated during porous flow						
Partition coefficients		Li	Be	B	Ce	Yb
ol/melt		0.35[a]	0.0015[a]	0.008[a]	0.0008[c]	0.036[c]
cpx/melt		0.20[a]	0.016[a]	0.018[a]	0.0016[b]	0.0787[b]
opx/melt		0.27[a]	0.021[a]	0.025[a]	0.094[b]	0.399[b]
initial melt composition (µg/g)						
OIB[d]		7.58	1.11	2.67	103	41.6
		[46.01 wt% SiO_2; 6.73 wt% MgO; Mg/(Mg+Fe) = 0.51]				
matrix composition (µg/g)						
lherzolite[e]	(0.09cpx, 0.21opx, 0.70ol)	1.20	0.011	0.034	0.39	0.252
harzburgite[f]	(0.04cpx, 0.24opx, 0.72ol)	0.28	0.009	0.0039	0.021	0.17
percolated macro-volumes (reaction cells)		50				
Model B: formation of residual liquids by fractional crystallisation of amphibole-rich veins						
bulk partition coefficient [i]						
i: amph/melt for Li, Be, B: Brenan et al. [1998]		0.183	0.248	0.022	0.086	0.259
ii: amph/melt for Li, Be, B: Adam and Green [2006]		0.095	0.134	0.071	0.086	0.259
initial melt composition (µg/g)						
hornblendite from Kerguelen[g]	(0.95amph, 0.04ilm, 0.01phl)	7.58[h]	1.11[h]	2.67[h]	95	1.9
		[40.89 wt% SiO_2; 15.82 wt% MgO; Mg/(Mg+Fe) = 0.80]				

[a]: *Brenan et al.* [1998a]; [b]: as in *Vernières et al.* [1997]; [c]: *Zanetti et al.* [2004]; [d]: MUR of *Dostal et al.*, [1996]; [e]: sample D58 from Eifel [*Ottolini et al.*, 2004; *Stosch*, 1982; *McDonough et al.* 1992]
[f]: Type III-a sample Ke 1965/1 from Marsabit with bulk-rock B, Be and Ce concentrations arbitrarily set to 0.13 x primitive mantle [*McDonough and Sun*, 1995]; [g]: *Moine et al.* [2001]; [h]: from *Dostal et al.* [1996]; [i]: mineral-melt partition coefficients for phlogopite and ilmenite from *Adam and Green* [2006] and *Moine et al.* [2001], respectively.

the Group III peridotites [e.g., *Woodland et al.*, 1996; *Moine et al.*, 2001; Bodinier et al., 2004]. The complexity of such processes demonstrated by the latter studies, combined with the complexities of light element distribution during metasomatism demonstrated by the present study, makes realistic modelling of Li/Yb and B/Be ratios, for example, more than challenging. Even more problems arise when taking into account that partitioning between light elements and melts/fluids in compositionally different systems shows considerable variation (i.e., systems relevant for alkaline settings as considered by *Adam and Green* [2006] and more Si-rich compositions relevant for Island Arc settings studied by *Brenan et al.*, [1998a,b]). And finally, the light element budgets in OIBs and alkaline magmas from continental rifts are still very poorly known, which hampers realistic assumptions on the light element concentrations in metasomatic agents without slab components.

Keeping the above mentioned limitations in mind we performed some modelling of well known simple metasomatic mechanisms that can drive an initially 'normal' OIB melt towards an evolved residual liquid (see above cited studies): chromatographic trace element fractionation (or non-reactive porous melt flow; Model

A; see Table 4.4; Fig. 4.12), and crystallisation of hornblendite veins (Model B). Both mechanisms produce residual liquids which can serve as potential metasomatizing agents able to precipitate volatile- and incompatible element-enriched phase assemblages during interaction with peridotite, such as those observed in the Group III peridotites from Marsabit. Although very simplified, these 'end-member' models can still serve to test what type of metasomatic mechanism could drive an OIB melt to a residual melt with 'slab-fluid'-like light element/REE ratios.

Comparing the OIB and IAB fields in Fig. 4.12, a mechanism is needed that is able to increase Li/Yb and B/Be and to decrease Ce/B ratios in the residual melt. Olivine, the dominant mineral in peridotite, preferentially incorporates Li and B relative to REEs [*Zanetti et al.*, 2004], as well as B relative to Be [*Brenan et al.*, 1998a]. Thus, the case of pervasive melt percolation through peridotite predicts that chromatographic trace element fractionation will decrease B/Be and Li/Yb and increase Ce/B in the residual melts. This effect is demonstrated in Fig. 4.12 (Model A) which simulates percolation of an alkaline melt [REE and light element composition of OIB from French Polynesia; *Dostal et al.*, 1996] that evolves by non-reactive chromatographic trace element fractionation (using the plate-model of *Vernières et al.* [1997], simulating propagation of fluid/melt batches through macro-volumes of mantle peridotite, i.e., the 'reaction cells'). We calculated percolation through two different matrix compositions (depleted harzburgite and fertile lherzolite; Table 4.4). The variation of the matrix composition has a great influence on the path of the melt evolution. However, in both cases the residual melt moves away from the IAB field. These results imply that simple non-reactive porous melt flow through peridotite is unlikely to produce apparent 'slab-fluid' signatures unless important amounts of another mineral with different light element/REE and B/Be partitioning is present in high modal abundances. Thus, more complex processes, such as reactive melt percolation [e.g., *Vernières et al.*, 1997] or the presence/formation of other rock types during metasomatism must be taken into account.

During metasomatism at mantle conditions beyond the stability of plagioclase (as inferred for the Group III xenoliths; *Kaeser et al.* [2006]), amphibole crystallisation is the most plausible mechanism able to fractionate Be from B and to produce residual melts with higher B/Be ratios. Amphibole-rich veins, for example, are widespread metasomatic features in mantle rocks [e.g., *Wilshire et al.*, 1980; *Kempton*, 1987; *Witt and Seck*, 1989] and their crystallisation potentially releases evolved liquids which subsequently metasomatize the adjacent peridotite wall-rock [e.g., *Kempton*, 1987; *Bodinier et al.*, 1990; *Moine et al.*, 2001; *Woodland et al.*, 1996; *Witt-Eickschen et al.*, 1998; *Bodinier et al.*, 2004].

Such residual liquids should have higher B/Be ratios than the parental melts (most likely alkaline basalt or basanite). This hypothesis is tested with Model B (Fig. 4.12; Table 4.4) simulating the crystallisation of a hornblendite vein in mantle peridotite. As model parameters we used the composition and phase assemblage of a typical hornblendite vein representing crystallised H_2O-rich basanite melt [*Moine et al.*, 2001]. Assuming a simplified (i.e., closed) system, the trace element composition of residual melts after the injection and crystallisation the melt can be calculated using the Rayleigh law $C_m/C_p = F^{(D-1)}$ (C_p and C_m: concentration of an element in the parental and residual melt, respectively; F: residual melt fraction; D: mineral/melt partition coefficient). Such a melt would be Si-rich, with strongly fractionated REE patterns, similar to those inferred to be in equilibrium with Mg-katophorite [*Kaeser et al.*, submitted]. Such residual melts could represent potential agents responsible for metasomatism in the Group III peridotites. Moreover, Fig. 4.12a and b exhibit that Li/Yb, Ce/B and B/Be ratios will be driven towards more IAB-like compositions (i.e., creating 'slab fluid signature'), in the direction of calculated melts in equilibrium with Mg-katophorite from Type III-b and -c peridotite. It must be empha-

sised, however, that none of the studied xenolith from Marsabit contains hornblendite veins, and, in addition, the modelled residual melts do not reproduce the calculated melts perfectly. On the other hand, the model shows that during metasomatism simple reaction processes can lead to strong modifications of trace element signatures in an initial OIB-like melt. Extreme caution must therefore be taken when trace element signatures in metasomatic minerals are used to distinguish between metasomatic agents specific to different tectonic settings. This is especially the case for mantle rock suites were ample evidence for peridotite-melt/fluid interaction is given – such as for the Group III peridotites from Marsabit. Further, the mismatch between modelled melts and melts in equilibrium with Mg-katophorite is – as aforementioned – certainly to a part due to the poor knowledge of light element concentrations in alkaline intra-plate melts (i.e., defining the starting point in Fig. 4.12) and to mineral/melt partitioning data. This highlights the clear need for further investigation in this field.

SUMMARY AND CONCLUSIONS

(1) The Li-Be-B systematics in minerals from the deformed, decompressed and cooled Group I lherzolite and subsequently re-heated and modally metasomatized Group II lherzolite are similar. This indicates that only little light element modification occurred during Anza Graben-related rifting (deformation, decompression, cooling), and during EARS-related high temperature metasomatism.

(2) In contrast, modal metasomatism in Group III harzburgite and dunite shows evidence for metasomatic addition of Li, Be and B during low-temperature, EARS-related metasomatism in the shallow lithospheric mantle, comparable to peridotite possibly metasomatized by fluids/melts containing a slab-derived component.

(3) The light element systematics, along with other trace element data, however, do not allow to conclude whether the metasomatic agent carried a 'subducted slab-derived' signature. However, simple modelling illustrates that metasomatic processes in the mantle can alter light element/REE ratios towards values which are typically used as constraints to invoke the presence of slab-derived components in lavas and mantle rocks.

(4) Late melting/crystallisation events (i.e. the formation of typical melt pockets) can strongly modify the light element systematics in mantle xenoliths. This is especially the case for the very mobile element Li. Interpreting Li systematics (including Li isotopes; see *Jeffcoate et al.*, 2006) thus necessitates careful knowledge of late-stage features, especially in the case of mantle xenolith as they often react with their host magma [e.g. *Shaw et al.*, 2006]. If late metasomatic events last longer than several days or occur at higher temperatures, Li may be quickly obliterate older signatures and becomes decoupled from other trace elements. Interpretation of trace element ratios, such as the widely used Li/Yb values, are therefore prone for erroneous interpretation.

ACKNOWLEDGMENTS

This work was financially supported by the Swiss National Science Foundation (grant Nr. 200021-100647/1 to AK). Field work in Kenya was financially supported by the Deutsche Forschungsgemeinschaft within the frame of the Collaborative Research Centre 108 (RFB 108) at the University of Karlsruhe. Fruitful discussions with Erwan Bourdon, Rainer Altherr, Dmitri Ionov, Alan Woodland and Othmar Müntener helped to improve an earlier version of this paper. Ilona Fin and Oliver Wienand (Heidelberg) are thanked for the preparation of top-quality thin sections for SIMS analysis.

Chapter 5: Mafic Xenoliths from Marsabit (Northern Kenya): Evidence for Multiple Magmatic Events in the Lithospheric Mantle and Interaction between Peridotite and Pyroxenite

Benjamin Kaeser[1], Bettina Olker[2], Angelika Kalt[1] & Rainer Altherr[2,*]

[1] Institut de Géologie et d'Hydrogéologie, Université de Neuchâtel, Rue Emile-Argand 11, CH-2009 Neuchâtel, Switzerland
[2] Mineralogisches Institut, Universität Heidelberg, Im Neuenheimer Feld 236, D-69120 Heidelberg, Germany

1st version manuscript; to be prepared for publication

ABSTRACT

Mantle xenoliths from Marsabit include, besides peridotite, two groups of mafic lithologies: garnet websterite and garnet-free (spinel-olivine) websterite and clinopyroxenite. Mineralogical, major and trace element, as well as textural features indicate that the two groups are the product of temporally different magmatic episodes that modified the lithospheric mantle beneath Marsabit.

Garnet websterites experienced a similar *P-T* evolution as formerly garnet-bearing lherzolites from Marsabit (decompression and cooling from ~970-1100 °C at ~2.3-2.6 GPa, and ~700-800°C at ~0.5-1.0 GPa), accompanied by garnet-spinel transition (garnet-olivine reaction to form spinel-pyroxene symplectite). This *P-T* evolution is best explained by lithospheric stretching during Mesozoic-Paleogene rifting (formation of the Anza Graben). During this process, both websterites and peridotites underwent penetrative deformation, accompanied by partial sub-solidus chemical re-equilibration and possibly disruption and dispersion of thinner pyroxenite layers into peridotite (i.e., 'mechanical mingling'). Textures indicate that the availability of olivine (i.e., to drive garnet breakdown) was a function of the degree of deformation (i.e. olivine addition to pyroxenite during stretching of pyroxenite layers). This would explain complete garnet preservation in the least deformed websterites.

The major and trace element composition of clinopyroxene, garnet and calculated bulk rocks, along with relic magmatic minerals (included in garnet from an almost undeformed xenolith) suggest that garnet websterite formed as crystal segregates during high-pressure fractionation of opx-saturated (tholeiitic or calc-alkaline) melts. Such melts could have intruded the sub-continental lithosphere during multiple accretion events in Pan-African times, prior to the onset of continental rifting during the Mesozoic.

Garnet-free pyroxenites, on the other hand, are compositionally very similar to cumulates from alkaline basaltic melts. The presence of undeformed, cumulate-like textures indicates a young age, related to the Mesozoic-Quaternary alkaline magmatic activity in the Marsabit area. The lack of feldspar and garnet indicate crystallisation in the shallow mantle (i.e., at ~25-50 km depths).

PREFACE

The Marsabit xenolith suite contains a considerable portion of mafic lithologies (47 xenoliths out of ~300) including garnet-bearing websterite, garnet-free websterite and clinopyroxenite, as well as one gabbro xenolith. Among these, the garnet websterites have already been the subject of the Heidelberg working group (Altherr and co-workers) prior to this thesis. Some compositional data as well as thermobarometric data has been published in an earlier reconnaissance study by Henjes-Kunst & Altherr (1992). Further, the garnet websterites were the subject of the PhD thesis of Bettina Olker at the University of Heidelberg (Olker, 2001). Most of the major element geochemistry as well as the thermobarometric data presented in this chapter (indicated in the respective figures and tables) are compiled from Olker (2001). The present study further contributes some major element compositional data for four additional garnet websterites (samples Ke 784/1, 1959/18, 1960/8, 1964) not analysed by Olker (2001), as well as data for the garnet-free pyroxenites. In addition trace elements have been analysed in-situ (LA-ICPMS) in three garnet websterites and in one spinel-olivine clinopyroxenite.

INTRODUCTION

The presence of pyroxenite in the mantle beneath Marsabit testifies to magmatic and/or metasomatic processes that significantly modified the peridotitic lithospheric mantle beneath this region. The study of these rocks, besides contributing to our understanding of the formation of mafic rocks within the mantle, puts further constraints on the development of the lithosphere beneath Marsabit.

Worldwide, occurrences of mantle rock almost always include minor amounts of pyroxenite, indicating that mafic lithologies form important heterogeneities in the otherwise peridotitic mantle (for recent reviews see Pearson *et al.*, 2003 and Bodinier & Godard, 2003, for example). Most tectonically exhumed ultramafic massifs and ophiolite complexes, which allow large-scale structural studies, exhibit mm-dm scaled websterite and/or clinopyroxenite bands or layers, typically aligned parallel to the main foliation of the tectonised peridotite (Bodinier & Godard, 2003). Among these, most are spinel-bearing while garnet-bearing pyroxenite is rarer but occurs in several localities. Very similar to the Marsabit garnet websterites are occurrences from the Pyrenees (the so-called 'arièges': Kornprobst & Conquéré. 1972; Conquéré, 1977; Bodinier *et al.*, 1987 and 1988; Fabriès *et al.*, 1998 and 2001), from Zabargad (Piccardo *et al.*, 1988; Kurat *et al.*, 1993), from the Liguride ophiolites (Montanini *et al.*, 2006), and from Malenco (Müntener & Hermann, 1996).

In the case of xenolith localities, almost all suites include different varieties of spinel-facies pyroxenite. Kimberlite-hosted (on-craton) mantle rocks occasionally include eclogite (garnet+omphacite) which is rare in basalt-hosted (off-craton) xenolith suites (Jacob, 2004). Off-craton xenoliths, on the other hand, almost always include spinel (± olivine) pyroxenite typically belonging to the Al-augite or Cr-diopside series (Wilshire & Shervais, 1975; Downes, 2001; Pearson *et al.*, 2003). Garnet-bearing pyroxenite is widespread but not abundant (Pearson *et al.*, 2003). Orthopyroxene- and amphibole-bearing varieties similar to ariègite (such as grt websterite from Marsabit) were reported from off-craton settings such as the Baikal rift (Ionov *et al.*, 1998; Litasov et al., 2000), the Taiwan Strait (Ho *et al.*, 2000), Western Victoria, Australia (Griffin *et al.*, 1984), Spitsbergen (Amundsen *et al.*, 1987), or Nushan, SE China (Xu *et al.*, 1998b).

With respect to their petrogenesis, there is general consensus that mantle pyroxenites crystallised from mantle-derived melts (or fluids). However, different processes have been proposed to explain their mode of occurrence and

relation with the peridotitic host. On the one hand, several authors propose that pyroxenites (in general, and garnet-bearing varieties in particular) may represent remnants of subducted mafic oceanic crust, streaked out during recycling through the convecting asthenosphere, until they become re-incorporated into the lithosphere (e.g., Allègre & Turcotte, 1986; Hamelin & Allègre, 1988; Kornprobst *et al.*, 1990; Kerr *et al.*, 1995; Morishita *et al.*, 2004). On the other hand, the characteristics of many pyroxenite occurrences are well explained as mantle melts propagating along and crystallising in hydraulically opened cracks, which may evolve later into parallel layers by plastic (sub-solidus) deformation (Nicolas, 1986; Nicolas & Jackson, 1982). However, irrespective of which final emplacement process is preferred, the composition of most pyroxenites implies that they cannot represent crystallised melt batches, but formed as crystal segregates or cumulates with residual melts that must have escaped the system (e.g., Wilshire & Shervais, 1975; Irving, 1975a and b; Irving, 1980; Loubet & Allègre, 1982; Suen & Frey, 1986; Bodinier *et al.*, 1987; Pearson *et al.*, 1993; Wilkinson & Stolz, 1997, Kopylova *et al.*, 1999; Ho *et al.*, 2000; Fabriès *et al.*, 2001 and many others).

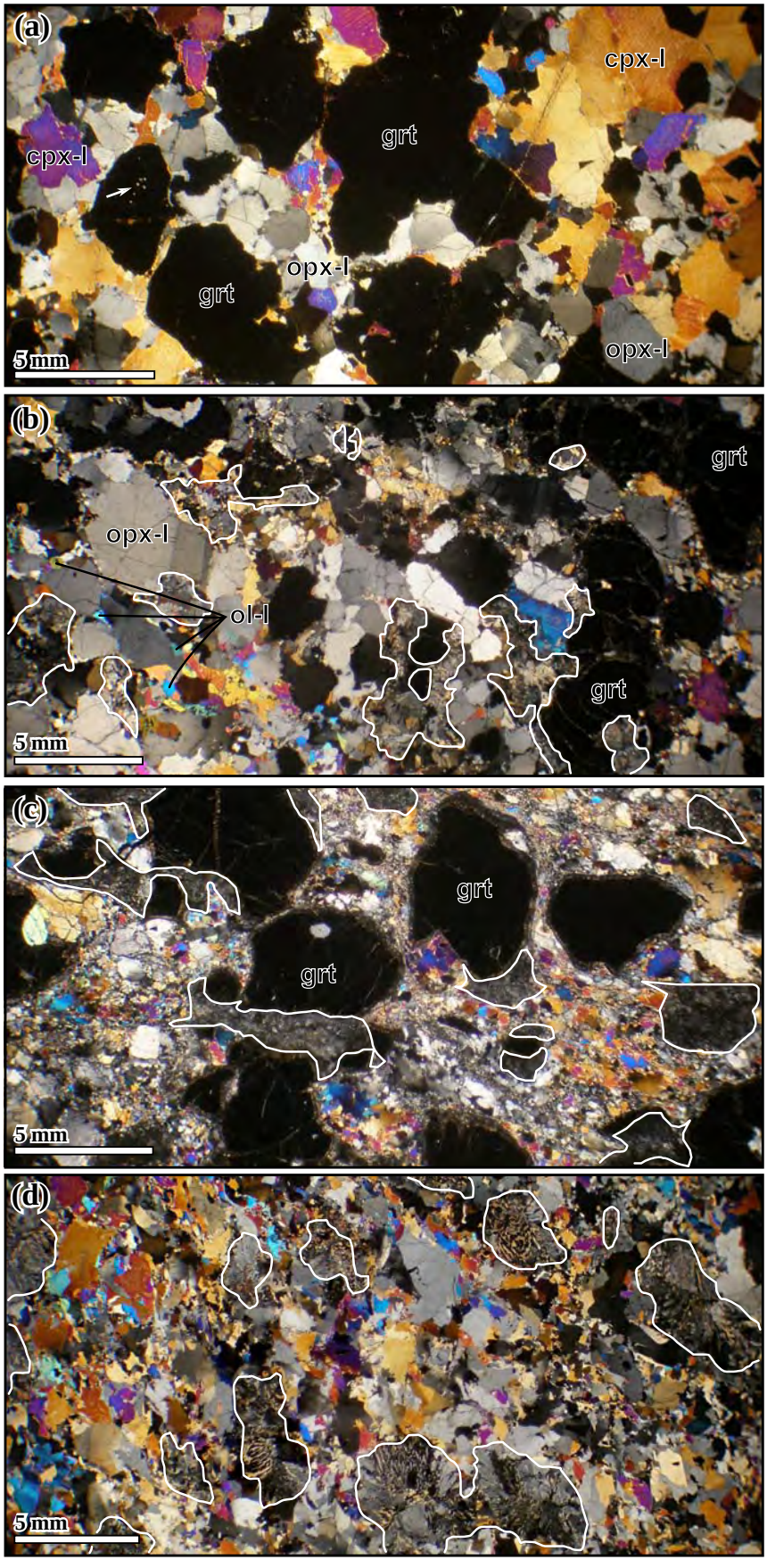
In addition to magmatic fractionation such as the flow crystallisation mechanism proposed by Irving (1980), the formation of mantle pyroxenites is complicated by interaction between the parental melts and surrounding wall rock on one hand, and by later partial re-equilibration and recrystallisation at sub-solidus conditions on the other hand. This often obliterates the 'primary' composition of pyroxenite (Bodinier *et al.*, 1987; Rivalenti *et al.*, 1995; Garrido & Bodinier, 1999; Zanetti *et al.*, 1999; Litasov et al., 2000; Liu *et al.*, 2005).

In the following we will present a detailed petrographic and geochemical investigation of the mafic xenoliths from Marsabit. The results will demonstrate that, based on different textures and composition, garnet-bearing and garnet-free pyroxenites are most likely genetically not linked. The garnet pyroxenites most likely represent crystal segregates from relatively Si-rich tholeiitic or calcalkaline basaltic melts introduced to the Marsabit lithosphere prior to the onset of continental rifting in East Africa (i.e. the formation of the Mesozoic Anza Graben). Throughout Mesozoic and Tertiary-Quaternary rifting, they were metamorphosed and experienced the same evolution as their host peridotites. During this process, the attained mineralogical, compositional and textural features remarkably similar to several garnet pyroxenite occurrences from mantle rocks sections finally exhumed during rifting processes.

The garnet-free pyroxenites, on the other hand, show indications to be much younger and to have crystallised from alkaline basaltic melts, probably in the context of the development of the Kenya Rift.

PETROGRAPHY

Following the classification of the Marsabit peridotites of Kaeser *et al.* (2006; Group I to IV), the mafic xenoliths will be subdivided in Group V (garnet websterite) and Group VI (garnet-free pyroxenite). The following mineral abbreviations will be used (see also Kaeser *et al.*, 2006): grt for garnet; opx-I, cpx-I, ol-I, and spl-I for first generation (i.e. porphyroclasts or texturally equilibrated grains) orthopyroxene, clinopyroxene, olivine and spinel, respectively; neoblasts are indicated by the suffix 'IIa', whereas 'IIb' indicates minerals occurring in symplectites resulting from garnet-breakdown. Ti-pargasite is subdivided in amph-i (large, subhedral grains in textural equilibrium with the surrounding grains), and amph-ii (Ti-pargasite associated with the breakdown products of garnet). Minerals associated with late stage metasomatic modification (e.g. sieve textured clinopyroxene rims, glass and/or plagioclase bearing reaction zones associated with breakdown products of garnet) are identified with a subscript 'm' for 'metasomatic': cpx_m, spl_m, pl_m, $amph_m$.


(a)
cpx-I
grt
cpx-I
opx-I
grt
opx-I
5 mm
(b)
grt
opx-I
ol-I
grt
5 mm
(c)
grt
grt
5 mm
(d)
5 mm

Group V – Garnet websterites

Texturally, the most noticeable feature of the garnet websterites (Fig. 1a-c) is their textural similarity to Group I (grt)-spl lherzolite xenoliths (Kaeser *et al.*, 2006; Fig. 5.1d). The difference compared to Group I is the absence (or very rarely occurring) ol-I, and the preservation of large garnet crystals (Fig. 5.1a-c). Garnet (cm-sized) and clinopyroxene (~5 mm) are the most abundant minerals (Fig. 5.1), with grt/cpx ratios often exceeding 1. Orthopyroxene contents are generally >5 vol%, while abundances of up to more than 20 Vol% were observed in sample Ke 1958/18 (hereafter referred to 'opx-rich grt websterite'). The latter sample comprises a zone of grt-cpx-rich and opx-poor websterite grading into a zone of cpx- and ol-bearing orthopyroxenite (Fig. 5.1b). All grt websterites show indications for more or less strong deformation (Fig. 5.1a-c) and are texturally very similar to pyroxenite layers described from exhumed peridotite massifs (e.g., Lherz: Conquéré, 1977; the Ligurides; Montanini *et al.*, 2006; Zabargad: Piccardo *et al.*, 1988; Kurat *et al.*, 1993; Malenco: Müntener & Hermann, 1996; Müntener, 1997). The degree of deformation ranges from undulous extinction, grain-boundary migration and subgrain formation in pyroxenes from the least deformed samples (Fig. 5.1a and 5.2a), via samples with porphyroclastic textures (pyroxene porphyroclasts surrounded by smaller neoblasts; Fig. 1b and 2b), to mylonitic textures (domains consisting exclusively of neoblasts with grain sizes down to <50 µm; e.g., sample Ke 1964; see Fig. 5.1c). The grain fabric in the least deformed sample (xenolith Ke 784/1) is similar to ad-cumulates (Fig. 5.1a and 5.2a). The pyroxene microtextures are strikingly similar to those observed in Group I lherzolites (Kaeser *et al.*, 2006; Fig. 5.1d). Clinopyroxene porphyroclasts (cpx-I) always contain orthopyroxene exsolution lamellae (Fig. 5.1a and 5.2a). This type of exsolution occurred before the main deformation event, as the lamellae are often bent. Clinopyroxene lamellae in opx-I less abundant and obviously result from the deformation event as they always occur normal to kinkbands. One of the studied samples (Ke 1958/2) contain almost strain- and exsolution-free pyroxenes exhibiting polygonal shapes (120° triple-junctions), somewhat similar to the Group II recrystallised (grt)-spl lherzolites (Kaeser *et al.*, 2006).

Garnet crystals are in most cases round to ovoid, and responded to deformation by the formation of abundant cracks (Fig. 5.2b-d). The cores of garnet grains contain several types of mineral inclusions. The largest (up to ~0.5 mm) are subhedral clinopyroxene crystals containing opx exsolution lamellae (Fig. 5.1c and 5.2c). They are texturally similar to cpx-I outside garnet but lack deformation-related features. Of much smaller size (several µm) are very abundant oriented rutile needles (Fig. 5.2e). Similar, though less abundant, are euhedral clinopyroxene, kaersutite or orthopyroxene (sometimes polyphase) inclusions (Fig. 5.2e).

Ti-pargasite occurs further outside garnet, either as texturally equilibrated large crystals (up to 1 mm; amph-i; Fig. 5.2a) or growing at the expense of pyroxenes (amph-ii; Fig. 5.2b). Further, amphibole was observed occasionally in reaction zones associated with the breakdown products of garnet ($amph_m$). Various amounts of Fe-Ni sulphides are present either as inclusions (secondary trails) in, or interstitial between py-

Fig. 5.1: *Textural features of Group V grt websterites compared to Group I (grt)-spl lherzolites.* ***(a)*** *sample Ke 784/1 characterised by very little deformation and ad-cumulate-like textures (note clinopyroxene and amphibole inclusions in grt indicated by the white arrow);* ***(b)****: porphyroclastic, opx-rich grt websterite (sample Ke 1959/18). Note that no garnet is preserved in the orthopyroxene-rich and olivine-bearing zone to the left;* ***(c)*** *mylonitic grt websterite (sample Ke 1964). Note the euhedral clinopyroxene inclusion in garnet;* ***(d)*** *porphyroclastic Group I (grt)-spl lherzolite (sample Ke 1963/2) shown for comparison. Note that no garnet is preserved. White lines outline spinel-orthopyroxene-clinopyroxene symplectites representing the breakdown-product of former garnet. All photomicrographs taken with crossed polarisers.*

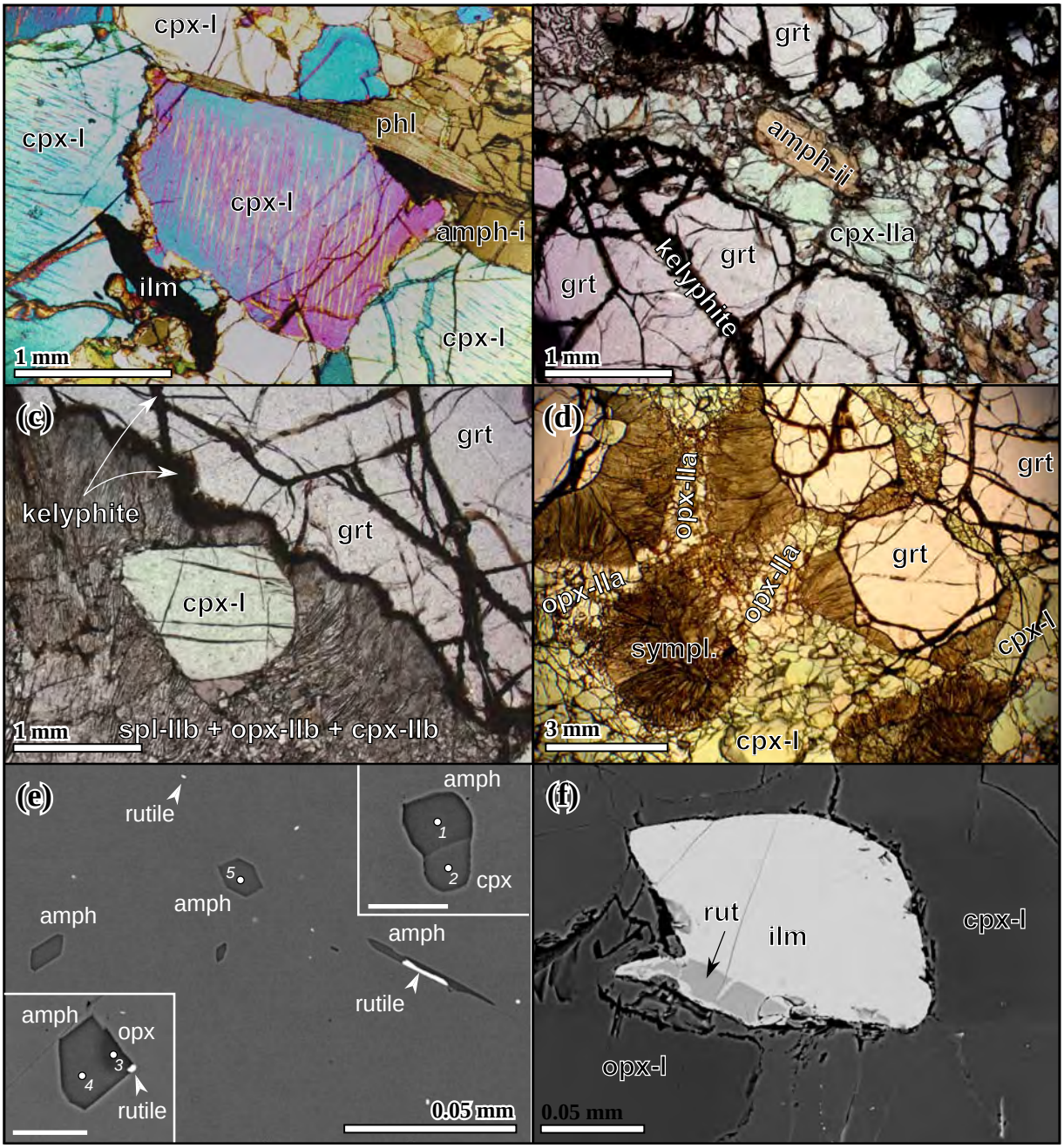


Fig. 5.2: *Textural details of Group V grt websterites.* ***(a)*** *phlogopite (phl), amphibole (amph-i), and ilmenite (ilm) in textural equilibrium with primary clinopyroxene (cpx-I) in least deformed grt websterite (sample Ke 784/1; crossed polarisers);* ***(b)*** *amphibole neoblasts in textural equilibrium with clinopyroxene neoblasts (cpx-IIa). Note that kelyphites developing along cracks within garnet (porphyroclastic grt websterite; sample Ke 1960/9; uncrossed polarisers);* ***(c)*** *former primary clinopyroxene inclusion in garnet, now preserved within symplectite (porphyroclastic grt websterite; sample Ke 1960/9; uncrossed polarisers);* ***(d)*** *primary kaersutite (amph), clinopyroxene, orthopyroxene and rutile inclusions in garnet (least deformed grt websterite Ke 784/1; BSE images). Scale bars in inlets correspond to 20 µm. Small white dots correspond to electron microprobe analyses listed in Table 5.3.* ***(e)*** *interstitial ilmenite mantling relic rutile (least deformed grt websterite Ke 784/1; BSE image).*

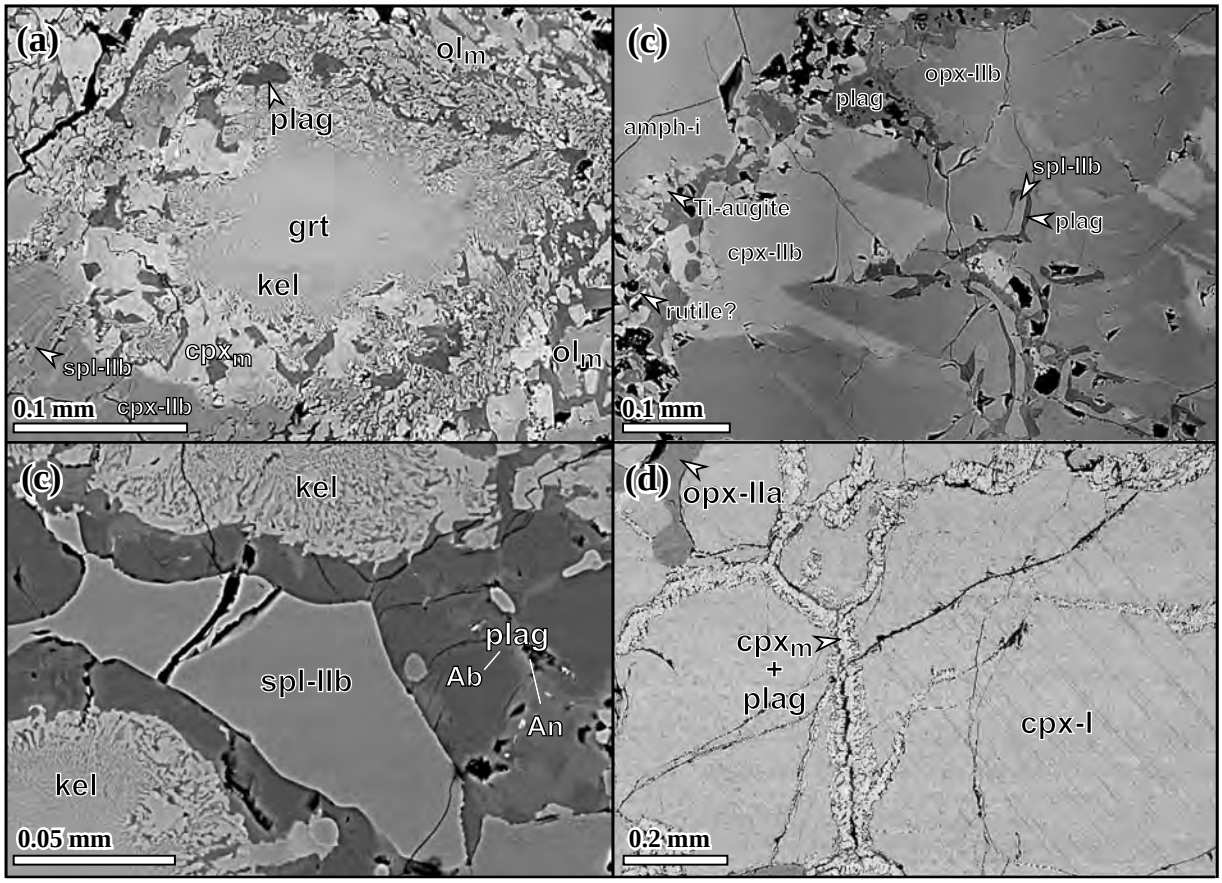


Fig. 5.3: *Late-stage reaction zones (RZ) in Group V grt websterite (all BSE images from sample Ke 1959/18).* ***(a)*** *RZ between relic garnet and symplectite (spl-IIb + cpx-IIb) composed of ultrafine-grained kelyphite with straight contacts towards garnet and coarser grained reaction zone (RZ1) made of secondary clinopyroxene (cpx_m), olivine (ol_m), and plagioclase (plag);* ***(b)*** *RZ1 in between Ti-pargasite (amph-i) and symplectite (spl-IIb, opx-IIb, cpx-IIb). Clinopyroxene developing at the expense of Ti-pargasite corresponds to Ti-augite. Note plagioclase coronas developing around spl-IIb rods;* ***(c)*** *plagioclase corona around spl-IIb. Note the patchy aspect of plagioclase corresponding to albite- (Ab) and anorthite-rich (An) domains;* ***(d)*** *Sieve-textured cpx_m and plagioclase (RZ2) developing around and within primary clinopyroxene (cpx-I with orthopyroxene exsolution lamellae).*

roxenes. In addition, one sample (Ke 784/1) contains ilmenite and phlogopite as interstitial, texturally equilibrated grains between pyroxenes. Ilmenite encloses occasionally rutile (Fig. 5.2f).

The reaction products associated with the breakdown of garnet consist of fine-grained symplectitic intergrowths of greenish to slightly reddish spinel (spl-IIb), opx-IIb and cpx-IIb (± amph-ii). They are identical to symplectites described for the Group I lherzolites (Kaeser *et al.,* 2006). Finally, two types of late-stage reaction zones can be distinguished: reaction zones 1 (RZ1; Fig. 5.3a-c) developed at the expense of the spl-IIb-opx-IIb-cpx-IIb symplectites. They include clinopyroxene (cpx_m), spinel (spl_m), plagioclase, olivine (ol_m). Kaersutitic amphibole ($amph_m$) and Ti oxides (rutile?) may occur as well (Fig. 5.3c). RZ2 consist of cpx_m and plagioclase forming sieve-textured rims on, or domains in cpx-I, cpx-IIa and/or cpx-IIb (Fig. 5.3d; similar to those reported from Chyulu Hills pyroxenites, see Ulianov & Kalt, 2006).

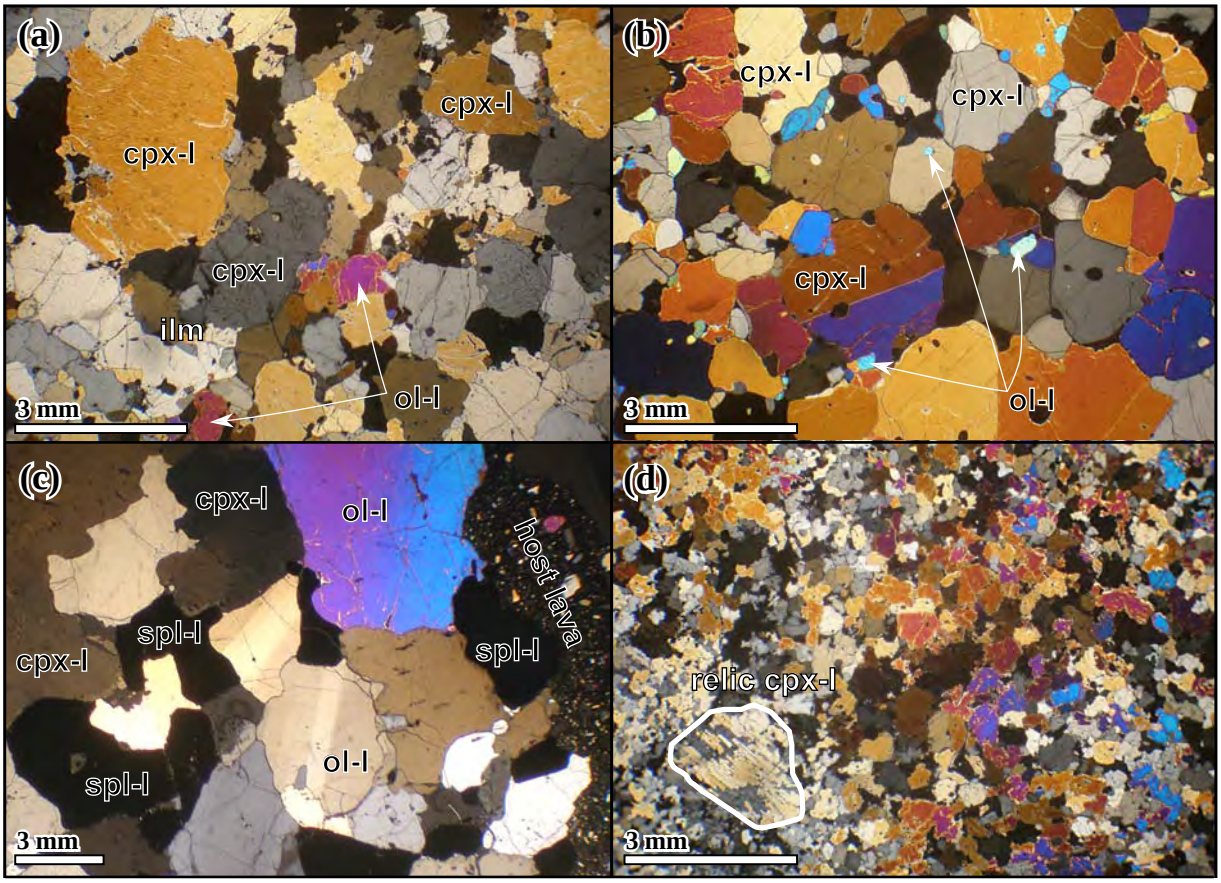


Fig. 5.4: *Textural aspect of Group VI garnet-free pyroxenites from Marsabit.* ***(a)*** *slightly deformed spl-ol websterite (sample Ke 782/2). Note lamellae and bleb-like micro-inclusions in cpx-I (orthopyroxene and spinel; white arrows) and the ragged grainboundaries indicating sub-solidus exsolution and grainboundary migration;* ***(b)*** *undeformed spl clinopyroxenite (sample Ke 1973/2). Note magmatic twin (orange-blue) in the labelled cpx-I grain;* ***(c)*** *coarse-grained spl-ol clinopyroxenite. Note kinkbands in olivine indicating deformation;* ***(d)*** *granular recrystallised ol websterite (sample Ke 782/1). Note lamellar intergrown ortho- and clinopyroxene (white outlined) most likely representing a former exsolved clinopyroxene porphyroclast. All photomicrographs taken with crossed polarisers.*

Group VI – grt-free pyroxenites

The four investigated garnet-free pyroxenite xenoliths are all texturally distinct. Sample Ke 782/2 (Fig. 5.4a) is a spl-ol websterite characterised by a granuloblastic fabric, composed mainly of cpx-I (up to 4 mm) and subordinate interstitial ol-I (polygonal; ~0.5 mm), small opx-I and dark-green spl-I (both interstitial; ~0.2 mm). Grain boundaries between cpx-I are typically ragged and tightly lobe-shaped (Fig. 5.4a). Cpx-I hosts orthopyroxene and spinel lamellae, as well as abundant sulphide and rare carbonate inclusions.

Sample Ke 1973/2 (Fig. 5.4b) is a typical composite xenolith, similar to those reported by Irving (1980). It consists of undeformed spl-ol clinopyroxenite enclosing a lherzolite 'xenolith' texturally similar to the recrystallised Group II (grt)-spl lherzolites. The pyroxenitic part has a granular texture, composed mainly of equant (2.5-3.0 mm) polygonal cpx-I grains (Fig. 5.4b). They are devoid of lamellae but developed (magmatic?) twins (Fig. 5.4b). Ol-I occurs as bleb-like inclusions in cpx-I, or as interstitial grains. Spl-I grains exhibit rounded shapes and are of dark-green colour. No orthopyroxene was observed. The contact between pyroxenite and

peridotite is marked by a spl-rich layer. The lack of deformation in the pyroxenitic part, as well as the presence of a Group II lherzolite enclave indicates that the clinopyroxenitic part may be cognate to the host lava that transported this sample to the surface.

Sample Ke 726 (Fig. 5.4c) contains more or less equal amounts of cpx-I, ol-I and somewhat less abundant spl-I. Grain sizes range from 0.5 to 1.5 cm. The rock fabric resembles that of an ad-cumulate, however, ol-I shows quite abundant kinkbands (Fig. 5.4c), indicating that this xenolith type is probably not cognate to the host basanite. Cpx-I contains very abundant primary Ni-Fe-Cu sulphide inclusions.

Sample Ke 782/1 (Fig. 5.4d), in turn, is a spl-free websterite exhibiting a metamorphic fabric. It is characterised by large (up to cm-sized) lamellar aggregates of clino- and orthopyroxene (probably representing former exsolved cpx-I porphyroclast; see Fig. 5.4d), surrounded by a matrix of equant (~0.3 mm) polygonal cpx-IIa and opx-IIa grains. Cpx-opx aggregates contain carbonate inclusions. In addition, the sample is cross-cut by a layer including small, slightly altered olivine of greenish colour.

COMPOSITION OF MINERALS

The major element composition of minerals is mostly compiled from Olker (2001; see annotations in Table 5.1 and 5.2). The compositions of reaction zone minerals and garnet inclusions are given in Table 5.2 and 5.3. The trace element data set is given in Appendix A4 of this thesis. For the analytical techniques, the reader is referred to Chapter 8.

Garnet

Group V – grt websterites

Garnets are pyrope-rich (Prp_{57-70}) and grossular-poor (Grs_{9-13}), with strongly variable Cr_2O_3 contents (0.04-1.66 wt%; Table 5.1). There is a considerable variation between texturally different samples. The lowest Prp contents, Mg-numbers [atomic $Mg/(Mg+Fe_{tot})$] and Cr_2O_3 contents are found in the least deformed samples. Garnet from the more strongly deformed xenoliths has the highest Prp and Cr_2O_3 contents, and is more calcic as well.

Besides inter-xenolith heterogeneity, significant compositional zoning within single grains can be observed (Fig. 5.5). Zoning patterns (from cores to rims) are generally characterised by decreasing Mg-numbers, TiO_2 contents and sometimes Cr-numbers [atomic $Cr/(Cr+Al)$]. MnO contents, on the other hand, increase.

Bulk analyses of garnet-rimming kelyphites (obtained with a defocused electron beam) are show considerable Na_2O enrichment compared to the garnet composition (analyses are listed in Appendix A4). This indicates Na-addition during kelyphite formation, probably in accordance with the appearance of plagioclase in RZ1 and RZ2.

The trace element composition of garnet has been measured in samples Ke 784/1, 1959/18 and 1960/4 (Fig. 5.6). Garnet is the major host for the HREEs (with almost flat patterns from Dy to Lu), whereas LREEs and Sr are strongly depleted (Fig. 5.6b). Some analyses exhibit a slight positive La inflection, possibly pointing to metasomatic modification.

Clinopyroxene

Group V – grt websterites

Clinopyroxene compositions range from Cr diopside to Al-rich augite (Table 5.1). They are similar to clinopyroxene from other grt pyroxenites, especially to the so-called 'ariègite'-facies from Lherz (cpx + opx + spl + amphibole ± grt; e.g., Conquéré, 1977; Bodinier *et al.*, 1987; Fabriès *et al.*, 2001), but clearly distinct compared to alkali basalt-hosted clinopyroxene megacrysts (Fig. 5.7).

Further, there is a clear relationship between the degree of deformation and the composition of clinopyroxene. This is displayed in Fig. 5.7a

Table 5.1: Major element composition (ranges) of minerals in mafic xenoliths from Marsabit (concentrations in wt%)

Sample	Min.	SiO_2	TiO_2	Al_2O_3	Cr_2O_3	FeO*	MnO	NiO	MgO	CaO	Na_2O	K_2O	Mg#	Cr#
*** Ke 771/1**	Grt	40.61-41.65	0.00-0.22	22.33-23.37	0.04-0.20	13.68-15.28	0.22-0.49	n.a.	15.99-17.65	3.59-4.29	0.00-0.09	n.d.	65.7-72.0	-
(grt web)	Cpx	51.15-54.09	0.39-0.69	6.52-9.44	0.03-0.22	3.10-4.415	0.00-0.13	n.a.	11.77-14.01	17.72-18.49	3.13-3.91	n.d.	83.2-86.1	-
little def.	Opx	53.32-55.05	0.00-0.11	2.11-4.52	0.00-0.11	10.96-12.86	0.05-0.20	n.a.	28.81-30.06	0.21-0.36	0.02-0.10	n.d.	80.1-82.9	-
	Amph	42.05-42.72	2.25-3.05	14.98-16.18	0.10-0.34	4.07-4.53	0.00-0.08	n.a.	14.69-15.63	10.07-10.78	3.94-4.51	0.05-0.15	80.4-82.3	-
*** Ke 771/2**	Grt	41.30-42.43	0.01-0.19	22.58-23.69	0.19-0.67	9.83-12.12	0.31-0.93	n.a.	17.65-19.76	3.65-4.14	0.00-0.06	n.d.	72.3-78.7	-
(grt web)	Cpx	51.57-53.31	0.52-0.89	6.51-7.48	0.48-0.65	2.34-2.84	0.00-0.16	n.a.	13.02-14.20	18.73-20.99	2.06-3.26	n.d.	89.6-91.1	-
p.clastic	Opx	54.83-56.57	0.02-0.18	1.50-3.27	0.06-0.23	6.85-7.83	0.07-0.23	n.a.	32.61-33.86	0.23-0.39	0.01-0.07	n.d.	87.8-89.6	-
	Amph	41.69-43.40	2.62-3.50	14.72-16.34	0.29-0.36	2.63-2.94	0.02-0.09	n.a.	15.89-16.77	10.82-11.31	3.88-4.31	0.02-0.05	87.1-88.9	-
Ke 784/1	Grt	40.92-42.33	0.02-0.22	22.07-23.23	0.17-0.44	12.28-13.87	0.22-0.57	0.00-0.01	17.08-18.56	4.19-4.91	0.00-0.07	n.d.	70.4-74.4	-
(grt web)	Cpx	52.19-53.11	0.52-0.83	4.98-5.83	0.11-0.27	3.31-3.76	0.00-0.13	0.00-0.11	14.31-14.74	20.86-21.23	1.89-2.26	n.d.	87.3-88.5	-
little def.	Opx	53.69-54.82	0.12-0.23	3.82-5.12	0.00-0.11	8.26-9.13	0.03-0.21	0.01-0.23	31.10-31.94	0.27-0.40	0.02-0.08	n.d.	85.9-87.0	-
	Amph	42.38-43.14	3.88-5.21	13.87-14.80	0.08-0.30	3.33-3.73	0.00-0.11	0.05-0.19	15.49-16.39	10.48-11.10	3.83-4.18	0.00-0.05	84.5-85.9	-
	Phl	37.61-37.90	6.80-7.04	14.08-14.99	0.29-0.37	7.82-8.05	0.00-0.04	0.22-0.26	17.53-17.89	0.01-0.03	1.01-1.10	8.74-8.81	79.7-80.3	-
	Ilm	0.01-0.03	57.44-58.96	0.25-0.44	0.12-0.33	27.63-31.76	0.26-0.41	0.03-0.20	10.00-12.43	0.04-0.23	n.d.	n.d.	36.0-44.5	-
	Rut*	0.01-0.03	98.59-99.47	0.11-0.17	0.16-0.21	0.38-0.45	0.00-0.02	0.01-0.02	0.00-0.01	0.06-0.08	n.d.	n.d.	-	-
*** Ke 1958/2**	Grt	41.93-42.61	0.03-0.18	22.90-23.65	0.16-0.34	8.49-9.37	0.40-0.67	n.a.	19.83-20.85	4.45-4.85	0.00-0.05	n.d.	79.6-80.8	
(grt web)	Cpx	51.01-53.00	0.40-0.59	6.68-9.34	0.14-0.42	2.60-3.19	0.02-0.18	n.a.	14.42-15.37	19.22-21.05	1.57-2.07	n.d.	89.5-91.0	-
granular	Opx	54.46-54.83	0.07-0.12	4.76-5.98	0.06-0.19	6.55-7.45	0.11-0.17	n.a.	32.33-33.16	0.41-0.78	0.07-0.12	n.d.	89.2-89.9	
	Amph	42.03-42.54	2.03-2.65	15.50-16.80	0.25-0.54	2.82-3.35	0.04-0.18	n.a.	16.29-17.03	10.28-10.63	3.10-3.55	0.79-1.37	85.9-88.2	-
Ke 1959/18	Grt	42.23-42.93	0.00-0.18	22.66-23.14	0.14-0.46	9.10-12.51	0.28-0.64	n.d.	18.61-20.93	3.76-4.14	0.00-0.07	n.d.	74.6-81.7	-
(grt web)	Cpx	53.00-54.14	0.61-0.80	6.61-8.89	0.25-0.44	2.23-2.95	0.00-0.13	0.00-0.09	12.74-14.19	18.06-19.43	2.80-3.69	n.d.	89.0-91.3	-
p.clastic	Opx	54.03-56.43	0.04-0.18	2.28-5.01	0.06-0.23	7.32-8.57	0.07-0.22	0.04-0.20	32.10-33.33	0.26-0.48	0.02-0.10	n.d.	87.1-88.9	-
	Amph	42.87-43.49	3.26-3.73	14.81-15.50	0.34-0.45	3.15-3.40	0.03-0.11	n.a.	15.78-16.29	10.07-10.45	4.09-4.16	0.17-0.26	85.4-86.5	-
	Ol	40.54-41.15	n.d.	n.d.	n.d.	12.84-13.28	0.10-0.21	0.47-0.64	47.22-47.60	0.01-0.04	-	n.d.	86.5-86.7	-
*** Ke 1960/3**	Grt	41.55-42.57	0.10-0.25	22.79-23.58	0.27-0.38	8.13-9.11	0.29-0.38	n.a.	19.76-20.84	4.35-4.96	0.01-0.08	n.d.	81.2-85.0	-
(grt web)	Cpx	52.33-53.64	0.50-0.92	5.34-8.48	0.25-0.55	1.80-2.56	0.00-0.13	n.a.	13.02-15.50	20.21-21.21	2.02-3.12	n.d.	91.0-93.0	-
p.clastic	Opx	55.42-56.63	0.10-0.17	2.14-2.82	0.06-0.11	7.25-7.73	0.10-0.15	n.a.	32.50-33.33	0.26-0.40	0.01-0.08	n.d.	88.4-89.2	-
	Amph	43.11	3.61	15.53	0.35	2.98	0.05	n.a.	15.67	10.752	3.69	0.09	86.8	-

*: analyses compiled from Olker (2001); little def. = low degree of deformation; p.clastic = porphyroclastic fabric; [1]: rutile in Ke 784/1 includes 0.03-0.04 wt% Nb_2O_5 and 0.04-0.05 wt% Zr_2O; Mg# = 100*Mg/(Mg+Fe^{tot}); Cr# = 100*Cr/(Cr+Al)

Table 5.1: (continued)

Sample	Min.	SiO_2	TiO_2	Al_2O_3	Cr_2O_3	FeO*	MnO	NiO	MgO	CaO	Na_2O	K_2O	Mg#	Cr#
*** Ke 1960/4**	Grt	41.14-42.50	0.04-0.20	22.28-23.34	0.66-0.89	8.48-11.07	0.31-0.63	n.a.	18.35-20.38	4.41-5.25	0.00-0.07	n.d.	76.4-82.7	-
(grt web)	Cpx	51.74-53.95	0.42-0.74	4.33-7.70	0.49-0.79	1.48-2.43	0.02-0.12	n.a.	13.62-15.49	20.63-22.51	1.19-2.82	n.d.	91.5-94.5	-
p.clastic	Opx	54.58-56.93	0.02-0.19	1.78-4.54	0.13-0.30	6.52-7.95	0.05-0.20	n.a.	32.26-34.34	0.17-0.40	0.00-0.07	n.d.	88.0-90.3	-
	Amph	41.35-42.47	3.07-4.39	15.22-15.96	0.45-0.67	2.30-2.77	0.01-0.10	n.a.	15.54-16.83	11.52-11.86	3.25-3.61	0.15-0.35	87.5-90.0	-
*** Ke 1960/5**	Grt	41.71-42.71	0.04-0.26	22.83-23.83	0.13-0.53	8.55-10.44	0.25-0.51	n.a.	19.14-20.61	4.21-4.79	0.00-0.07	n.d.	76.9-82.3	-
(grt web)	Cpx	52.84-54.34	0.55-0.89	5.38-6.40	0.21-0.39	2.12-2.69	0.00-0.12	n.a.	13.80-14.67	20.34-21.05	2.06-2.45	n.d.	90.2-92.4	-
p.clastic	Opx	55.08-57.10	0.03-0.22	1.748-4.95	0.04-0.21	6.58-7.60	0.04-0.23	n.a.	31.84-33.75	0.19-0.47	0.01-0.08	n.d.	88.3-90.0	-
	Amph	42.26-42.97	2.88-4.15	15.49-16.22	0.32-0.49	2.26-2.66	0.01-0.08	n.a.	15.60-16.51	10.68-11.14	3.52-4.18	0.13-0.27	88.0-90.0	-
*** Ke 1960/6**	Grt	41.41-42.59	0.03-0.24	22.72-23.62	0.34-0.59	8.11-9.86	0.25-0.55	n.a.	19.04-20.66	4.33-4.80	0.00-0.07	n.d.	78.4-84.2	-
(grt web)	Cpx	52.03-52.92	0.69-1.10	6.04-7.21	0.44-0.58	1.97-2.32	0.03-0.09	n.a.	14.04-14.82	20.09-20.79	2.00-2.47	n.d.	91.8-92.7	-
p.clastic	Opx	54.66-56.70	0.07-0.24	25.12-5.43	0.08-0.27	6.12-6.86	0.06-0.23	n.a.	32.82-34.43	0.24-0.46	0.03-0.10	n.d.	89.6-90.8	-
	Amph	41.67-42.64	3.39-3.87	15.37-16.49	0.45-0.59	2.87-3.24	0.04-0.07	n.a.	15.59-15.88	10.53-11.18	3.32-3.58	0.00-0.79	85.9-87.1	-
*** Ke 1960/8**	Grt	41.81-42.41	0.05-0.12	23.05-23.70	1.32-1.66	8.22-10.15	0.29-0.61	0.00-0.01	18.37-20.12	4.99-5.21	0.01-0.06	n.d.	76.3-81.3	-
(grt web)	Cpx	52.63-53.40	0.24-0.33	5.73-7.59	0.45-1.48	2.14-2.47	0.05-0.10	0.01-0.06	13.59-14.57	21.03-22.08	2.17-2.49	n.d.	91.0-91.9	-
p.clastic	Opx	54.74-56.42	0.01-0.05	3.13-4.86	0.18-0.48	6.67-7.09	0.11-0.18	0.05-0.10	31.98-33.17	0.20-0.38	0.02-0.09	n.d.	89.1-89.7	-
	Amph	n.a.	n.a.	n.a.	n.a.	n.a.	n.a.		n.a.	n.a.	n.a.	n.a.	n.a.	-
Ke 1964	Grt	42.14-43.01	0.03-0.10	23.75-24.26	0.78-1.14	6.92-8.67	0.26-0.42	0.00-0.04	18.82-21.23	4.49-5.38	0.00-0.08	n.d.	78.2-85.6	-
(grt web)	Cpx	53.72-54.59	0.21-0.29	4.16-4.92	0.6-0.93	1.39-1.62	0.02-0.08	0.02-0.10	15.05-15.71	22.11-23.17	1.37-1.95	n.d.	94.3-95.1	-
mylonitic	Opx	55.09-57.35	0.01-0.07	2.12-5.10	0.09-0.42	5.39-6.57	0.08-0.16	0.07-0.14	32.43-34.46	0.19-0.33	0.01-0.08	n.d.	89.8-91.6	-
	Amph	n.a.	n.a.	n.a.	n.a.	n.a.	n.a.	n.a.	n.a.	n.a.	n.a.	n.a.	n.a.	-
Ke 726	Cpx	48.21-48.65	1.13-1.49	8.48-8.94	0.00-0.08	5.72-6.37	0.08-0.18	0.00-0.08	12.93-14.17	19.91-20.46	1.03-1.24	n.d.	78.9-81.0	-
(spl-ol	Ol	38.78-39.50	0.00-0.06	0.04-0.07	0.00-0.03	16.09-18.62	0.19-0.31	0.07-0.19	42.06-44.16	0.17-0.33	0.01-0.04	n.d.	80.1-83.0	-
cpx-ite)	Spl	0.06-0.17	0.42-0.67	58.75-61.41	0.55-0.81	18.11-22.23	0.07-0.20	0.12-0.20	17.69-19.48	0.00-0.04	n.a.	n.a.	58.9-65.7	0.62-0.89
Ke 782/1	Cpx	50.20-51.55	0.45-0.6	5.89-6.77	0.18-0.43	4.91-5.99	0.09-0.17	0.00-0.08	14.29-15.95	19.21-21.79	0.89-0.78	n.d.	82.5-84.1	-
(web)	Opx	52.80-53.59	0.12-0.22	5.01-5.38	0.13-0.35	10.44-11.72	0.17-0.25	0.04-0.10	27.86-28.89	0.68-1.33	0.04-0.12	n.d.	81.0-83.0	-
	Ol	39.78-40.86	0.00-0.02	0.01-0.06	0.00-0.11	15.35-16.05	0.20-0.25	0.19-0.27	41.57-43.33	0.18-0.23	0.00-0.03	n.d.	82.2-83.3	-

Table 5.1: (continued)

Sample	Min.	SiO_2	TiO_2	Al_2O_3	Cr_2O_3	FeO*	MnO	NiO	MgO	CaO	Na_2O	K_2O	Mg#	Cr#
Ke 782/2	Cpx	48.19-50.85	0.72-1.45	5.87-8.49	0.12-0.67	4.70-5.85	0.04-0.17	0.01-0.06	13.60-15.14	19.67-21.29	0.81-1.22	n.d.	81.2-84.7	-
(ol-spl web)	Opx	52.78-53.85	0.18-0.28	4.26-4.80	0.22-0.32	10.19-12.03	0.09-0.27	0.02-0.09	29.04-29.84	0.7-0.93	0.03-0.10	n.d.	81.4-83.8	-
	Ol	38.90-39.49	0.00-0.04	0.01-0.06	0.00-0.05	15.84-18.03	0.14-0.30	0.15-0.25	42.33-43.32	0.08-0.25	0.00-0.04	n.d.	80.9-83.0	-
	Spl	0.05-0.15	0.40-0.68	52.02-55.45	6.20-9.41	18.77-20.99	0.00-0.17	0.16-0.28	16.44-17.83	0.00-0.25	n.a.	n.d.	58.5-62.9	6.98-10.75
	Calcite	0.05-0.06	0.00-0.03	0.00-0.01	0.00-0.01	0.08-0.09	0.00-0.02	0.00-0.05	0.50-0.63	56.49-57.15	n.d.	n.d.	92.1-92.9	-
Ke 1973/2	Cpx	48.36-48.95	1.02-1..30	8.75-9.21	0.03-0.15	5.41-5.84	0.09-0.14	0.00-0.06	13.35-13.79	20.51-21.44	0.88-1.16	n.d.	80.8-82.8	-
(spl-ol	Ol (1)	39.43-39.76	0.00-0.03	0.05-0.10	0.00-0.06	15.91-16.19	0.19-0.24	0.09-0.15	42.78-43.96	0.23-0.35	0.01-0.05	n.d.	82.6-83.1	-
cpx-ite)	Ol (2)	40.67-41.05	0.00-0.02	0.04-0.09	0.00-0.03	12.53-12.60	0.17-0.20	0.28-0.33	46.08-46.40	0.20-0.23	0.01-0.03	n.d.	86.7-86.8	-
	Spl (1)	0.11-0.13	0.35-0.44	61.42-63.15	0.67-1.02	12.82-15.70	0.10-0.13	0.25-0.36	19.77-20.62	0.00-0.03	n.a.	n.a.	67.3-72.1	0.71-1.10
	Spl (2)	0.14-0.15	0.38-0.39	56.85-58.94	5.02-6.72	13.95-14.16	0.15-0.19	0.33-0.37	19.55-20.16	0.00-0.01	n.a.	n.d.	69.5-69.8	5.40-7.35

(1) ol and spl in clinopyroxenite; (2) ol in peridotite enclave, spl at peridotite-clinopyroxenite contact

and b, showing that cpx from highly deformed samples approach the composition of clinopyroxene in Group I (grt)-spl lherzolite (i.e., Cr diopside with high Mg-numbers). The highest Mg-numbers (>95; Table 5.1, Fig. 5.7) are observed in the mylonitic sample, at the same time characterised by low TiO_2 contents (Fig. 5.7a). The less deformed samples (e.g., Ke 784/1) contain less magnesian Al-rich augite. Na_2O contents are not in systematic relation with the rock texture and display a relatively broad range between different samples (1.2-3.7 wt% Na_2O).

On the tectonic discrimination diagram of Koloskov & Zharinov (1993; based on the major element composition of cpx from mantle rocks) clinopyroxene from grt websterites of Marsabit plot in the fields of spl peridotite, while the least deformed samples (Ke 784/1 and 771/1) show a clear affinity with clinopyroxene from kimberlite-hosted eclogite and pyrope-bearing pyroxenite xenoliths (Fig. 5.8).

Secondary, sieve-textured clinopyroxenes (cpx_m) growing at the expense of cpx-I, -IIa or -IIb are depleted in TiO_2, Al_2O_3 and Na_2O (Table 5.2). Cpx_m adjacent to Ti-pargasite in symplectites (amph-ii; sample Ke 1959/18) has a Ti-enriched augitic composition.

Compositional zoning in cpx-I is mainly restricted to Al, Ca and Na (zoning patterns for cpx-I are displayed in Fig. 5.9). The cpx-I cores are characterised by an Al and $Al^{(IV)}$ plateau followed by either slightly decreasing (Fig. 5.8a) or increasing concentrations toward rims (Fig. 5.9b and c). Ca patterns always mirror the Na zoning pattern. The resulting Ca* value [the temperature sensitive term Ca/(1-Na); see Brey *et al.,* 1990] is therefore broadly constant (Fig. 5.9).

The trace element composition of clinopyroxene has been analysed in one little deformed (Ke 784/1), one porphyroclastic (Ke 1960/4) and in the opx-rich grt websterite (Ke 1958/18). The results are illustrated in Fig. 5.10 and 5.11. The trace element patterns of clinopyroxene from samples Ke 784/1 and 1960/4 are strikingly similar to those of Group I (grt)-spl lherzolites (Fig. 5.10a-b, 5.10e-f). Further, sample

Table 5.2: Major element composition of minerals in reaction zones

mineral	**spl-IIb (in symplectite)**								
	*	*		*	*	*	*		
sample	771/2	1958/2	1958/18	1960/3	1960/4	1960/5	1960/6	1960/8	1964
texture	p.clast.	gran.	p.clast.	p.clast.	p.clast.	p.clast.	p.clast	p.clast	p.clast
RZ									
SiO_2	0.44	0.03	0.03	0.12	0.08	0.03	0.19	0.12	0.01
TiO_2	0.02	0.07	0.05	0.22	3.12	0.06	0.44	n.d.	0.01
Al_2O_3	64.70	66.54	65.45	65.76	65.02	63.09	64.06	62.33	63.79
Cr_2O_3	1.66	0.71	1.64	0.60	0.09	4.75	1.50	5.95	5.79
Fe_2O_3	0.83	1.43	1.08	1.24	0.00	0.55	1.77	0.33	0.32
FeO	9.84	9.27	10.66	8.83	9.07	10.23	10.51	9.65	7.26
MnO	0.10	0.11	0.09	0.18	0.03	0.12	0.21	0.14	0.18
NiO	n.a.	n.a.	0.68	n.a.	n.a.	n.a.	n.a.	0.30	0.26
MgO	21.21	21.66	20.22	21.71	22.14	20.52	20.70	20.72	22.46
CaO	n.d.	0.01	0.07	0.05	n.d.	0.08	0.16	0.02	0.06
Na_2O	0.01	n.d.	n.a.	n.d.	0.01	0.01	0.01	n.d.	n.d.
K_2O	0.01	0.02	n.a.	0.02	n.d.	0.01	n.d.	n.d.	n.d.
Total	**98.82**	**99.85**	**99.96**	**98.73**	**99.56**	**99.45**	**99.55**	**99.55**	**100.13**
Mg#	79.3	80.6	77.2	81.4	81.3	78.1	77.8	79.3	84.6
Cr#	1.69	0.71	1.65	0.61	0.09	4.81	1.55	6.02	5.74
An	-	-	-	-	-	-	-	-	-
Ab	-	-	-	-	-	-	-	-	-
Or	-	-	-	-	-	-	-	-	-

mineral	**cpx_m (in RZ1 and RZ2)**						
	*			*	*	*	*
sample	771/1	1959/18	1959/18	1960/3	1960/4	1960/4	1960/6
texture	undef.	p.clastic	p.clastic	p.clastic	p.clastic	p.clastic	p.clastic
RZ	RZ2	RZ1[1]	RZ2	RZ2	RZ1	RZ2	RZ2
SiO_2	51.08	48.99	52.12	52.19	52.64	52.78	51.89
TiO_2	0.26	2.32	0.57	0.49	0.89	0.53	0.47
Al_2O_3	6.12	7.00	4.55	4.10	5.74	5.99	6.23
Cr_2O_3	0.19	0.56	0.40	0.37	0.25	0.15	0.45
Fe_2O_3	-	-	-	-	-	-	-
FeO	3.89	4.38	2.85	2.44	1.98	2.21	1.99
MnO	0.05	0.25	0.12	0.06	0.08	0.08	0.04
NiO	n.a.	n.a.	n.a.	n.a.	n.a.	n.a.	n.a.
MgO	14.62	15.09	16.06	16.61	14.93	15.01	15.08
CaO	21.74	20.09	21.74	22.16	22.64	21.88	22.03
Na_2O	1.30	0.96	1.00	0.76	1.13	1.45	1.42
K_2O	n.d.	n.d.	n.d.	n.d.	0.01	0.01	n.d.
Total	**99.25**	**99.63**	**99.43**	**99.18**	**100.29**	**100.09**	**99.60**
Mg#	87.0	86.0	90.9	92.4	93.1	92.4	93.1
Cr#							
An	-	-	-	-	-	-	-
Ab	-	-	-	-	-	-	-
Or	-	-	-	-	-	-	-

Sample numbers annotated with a * are analyses compiled from Olker (2001); undef.: little deformation; p.clast.: porphyroclastic; gran.: granularrecrystallised; mylo: mylonitic; RZ = recation zone; [1]: sieve-textured Ti augite around Ti-pargasite; the composition of opx-IIb and cpx-IIb are identical to the rims of porphyroclasts and neoblasts and are not reported here; n.a.: not analysed; n.d.: not detected; -: not calculated

Table 5.2: continued

mineral	plagioclase (RZ1 and RZ2)							
	*	*	*				*	*
sample	771/1	771/1	1958/2	1959/18	1959/18	1959/18	1960/3	1960/5
texture	undef.	undef.	p.clastic	p.clastic	p.clastic	p.clastic	p.clastic	p.clastic
RZ	RZ1	RZ2	RZ1	RZ1	RZ1	RZ2	RZ2	RZ1
SiO_2	61.87	58.46	57.74	62.14	54.33	55.71	58.06	51.76
TiO_2	n.d.	0.12	n.d.	n.a.	n.a.	n.a.	0.06	0.09
Al_2O_3	23.95	25.73	26.69	24.21	28.65	28.19	26.27	28.54
Cr_2O_3	0.00	0.03	n.d.	n.a.	n.a.	n.a.	n.d.	0.06
Fe_2O_3	0.18	0.36	0.16	0.23	0.48	0.28	0.17	1.49
FeO	-	-	-	-	-	-	-	-
MnO	n.d.	0.01	n.a.	n.a.	n.a.	n.a.	0.03	n.d.
NiO	n.d.	n.d.	n.d.	n.a.	n.a.	n.a.	n.a.	n.a.
MgO	n.d.	0.16	n.d.	n.a.	n.a.	n.a.	0.11	0.84
CaO	4.79	8.39	7.91	5.00	10.44	9.64	8.99	11.92
Na_2O	8.88	6.96	6.72	9.04	5.89	6.28	6.47	3.81
K_2O	0.02	0.01	0.39	0.06	0.05	0.04	0.01	0.43
Total	**99.70**	**100.23**	**99.61**	**100.68**	**99.84**	**100.14**	**100.17**	**98.94**
Mg#	-		-	-	-	-	-	-
Cr#	-		-	-	-	-	-	-
An	0.23	0.40	0.39	0.23	0.49	0.46	0.43	0.62
Ab	0.77	0.60	0.59	0.76	0.50	0.54	0.57	0.36
Or	0.00	0.00	0.02	0.00	0.00	0.00	0.00	0.03

mineral	ol_m (in RZ1 and RZ2)					$amph_m$ (RZ1)		
			*	*		*		*
sample	1959/18	1959/18	1960/3	1960/6		771/1	1959/18	1960/5
texture	p.calstic	p.calstic	p.calstic	p.calstic		undef.	p.calstic	p.clastic
RZ	RZ1	RZ1	RZ1	RZ1		RZ1	RZ1	RZ1
SiO_2	40.52	40.64	40.64	39.58		42.19	40.01	41.67
TiO_2	0.03	0.07	n.d.	0.03		2.73	7.47	3.48
Al_2O_3	0.06	0.06	0.05	0.04		14.98	14.09	16.39
Cr_2O_3	0.03	0.05	0.07	0.05		0.30	0.78	0.53
Fe_2O_3	-	-	-	-		-	-	-
FeO	10.39	12.53	10.17	12.99		6.17	4.75	4.11
MnO	0.14	0.42	0.27	0.39		0.04	0.15	0.04
NiO	0.22	0.22	n.a.	n.a.		n.a.	n.a.	n.a.
MgO	48.60	46.34	48.29	46.35		15.63	15.66	15.83
CaO	0.22	0.26	0.20	0.29		10.69	12.40	10.54
Na_2O	0.01	0.02	0.01	0.01		3.94	2.83	3.44
K_2O	n.d.	n.d.	n.d.	n.d.		0.05	0.15	0.79
Total	**100.22**	**100.61**	**99.70**	**99.73**		**96.72**	**98.29**	**96.82**
Mg#	89.3	86.8	89.4	86.4		81.9	85.5	87.3
Cr#	-	-	-	-		-	-	-
An	-	-	-	-		-	-	-
Ab	-	-	-	-		-	-	-
Or	-	-	-	-		-	-	-

Table 5.3: Major element composition of primary inclusions in garnet of Group V grt websterite Ke 784/1 from Marsabit

Mineral	kaers.	kaers.	kaers.	cpx	opx
Nr. [1]	*1*	*4*	*6*	*2*	*3*
SiO_2	43.05	42.36	42.38	51.22	54.64
TiO_2	4.01	4.32	3.81	1.60	0.16
Al_2O_3	14.09	14.75	14.64	7.98	3.71
Cr_2O_3	0.43	0.47	0.43	0.34	0.13
$FeO_{(tot)}$	5.53	5.66	5.62	3.14	9.55
MnO	0.03	0.01	0.04	0.04	0.07
NiO	0.11	0.09	0.06	0.05	0.04
MgO	15.88	15.49	15.61	13.05	30.89
CaO	10.22	10.22	10.15	19.71	0.40
Na_2O	3.92	4.03	4.09	2.60	0.07
K_2O	0.02	n.d.	0.01	n.d.	0.01
H_2O [2]	2.10	2.09	2.08	-	-
Total	**99.40**	**99.49**	**98.91**	**99.70**	**99.66**
Stoich.	**23O**	**23O**	**23O**	**6O**	**6O**
Si	6.160	6.067	6.101	1.861	1.919
Ti	0.432	0.465	0.412	0.044	0.004
Al	2.377	2.489	2.484	0.342	0.153
Cr	0.049	0.053	0.049	0.010	0.004
Fe^{2+}	0.662	0.678	0.676	0.095	0.280
Mn	0.003	0.001	0.004	0.001	0.002
Ni	0.013	0.011	0.006	0.001	0.001
Mg	3.387	3.306	3.349	0.707	1.617
Ca	1.567	1.568	1.565	0.767	0.015
Na	1.087	1.117	1.143	0.183	0.005
K	0.004	0.000	0.002	-	0.001
H	2.000	2.000	2.000	-	-
Total [3]	**15.741**	**15.756**	**15.792**	**4.011**	**4.001**
Mg#	***83.7***	***83.0***	***83.2***	***88.1***	***85.2***

kaers. = kaersutite; [1]: see Fig. 5.2e for point localisation;
[2]: calculated on the basis of 2 OH per formula unit;
[3]: without H

Ke 1960/4 shows a similar HREE variation as observed in Group I samples, i.e., higher HREE-concentrations towards cpx-I rims and in cpx-IIa cores (Fig. 5.11). This is in good agreement with re-partitioning HREEs during the breakdown of garnet as indicated by the presence of symplectites, and is consistent with the results of Kaeser *et al.*, (2006). The more incompatible REEs are progressively depleted (from Eu to La). Extended trace element plots show negative inflections for Nb, Ta, and Pb, and very weak negative anomalies for Zr, Hf, and Ti. Sample Ke 784/1 is characterised by a weak positive Sr anomaly (Fig. 5.10b). Cpx-I from the opx-rich sample has slightly higher incompatible element abundances (i.e. MREE, LREE, U and Th).

Secondary cpx_m was analysed only in sample Ke 1959/18 (Fig. 5.10c-d). Sieve-textured cpx_m obviously inherited the trace element budget of the associated cpx-I (i.e. convex upward REE pattern; Fig. 5.10d). Ti-augite in reaction zones within symplectites is enriched in HREEs (Fig. 5.10d). Negative Sr spikes (Fig. 5.10c) of both cpx_m are in line with the presence of plagioclase.

Group VI – grt-free pyroxenites

The grt-free pyroxenites typically contain Al-rich augite with variable TiO_2, Cr_2O_3 and Na_2O contents (Table 5.1; Fig. 5.7), similar to the Al-augite series defined by Wilshire & Shervais (1975). Mg-numbers range from 78.9-84.7 (Table 5.1). They are negatively correlated with TiO_2, and positively correlated with Cr_2O_3 (Fig. 5.7a and b). Generally, the most primitive rocks (i.e. clinopyroxene with highest Mg-number and Cr_2O_3, and lowest Na_2O and TiO_2 contents) have at the same time lowest modal olivine. In contrast to Group V, clinopyroxenes overlap with compositions characteristic for clinopyroxene megacrysts hosted by alkaline melts. Zoning profiles (not shown) are either flat or exhibit slightly decreasing Al and increasing Ca contents towards rims.

Trace elements were analysed in the slightly deformed spl-ol websterite Ke 782/2. Compared to clinopyroxene from Group V grt websterites, trace element patterns show variable enrichment in LREEs and LILEs (Fig. 5.10g and h). The HFSEs are slightly depleted relative to the neighbouring REEs (Fig. 5.10g). The REE patterns (Fig. 5.10h) are convex upward with some analyses showing a positive deflection for La and Ce.

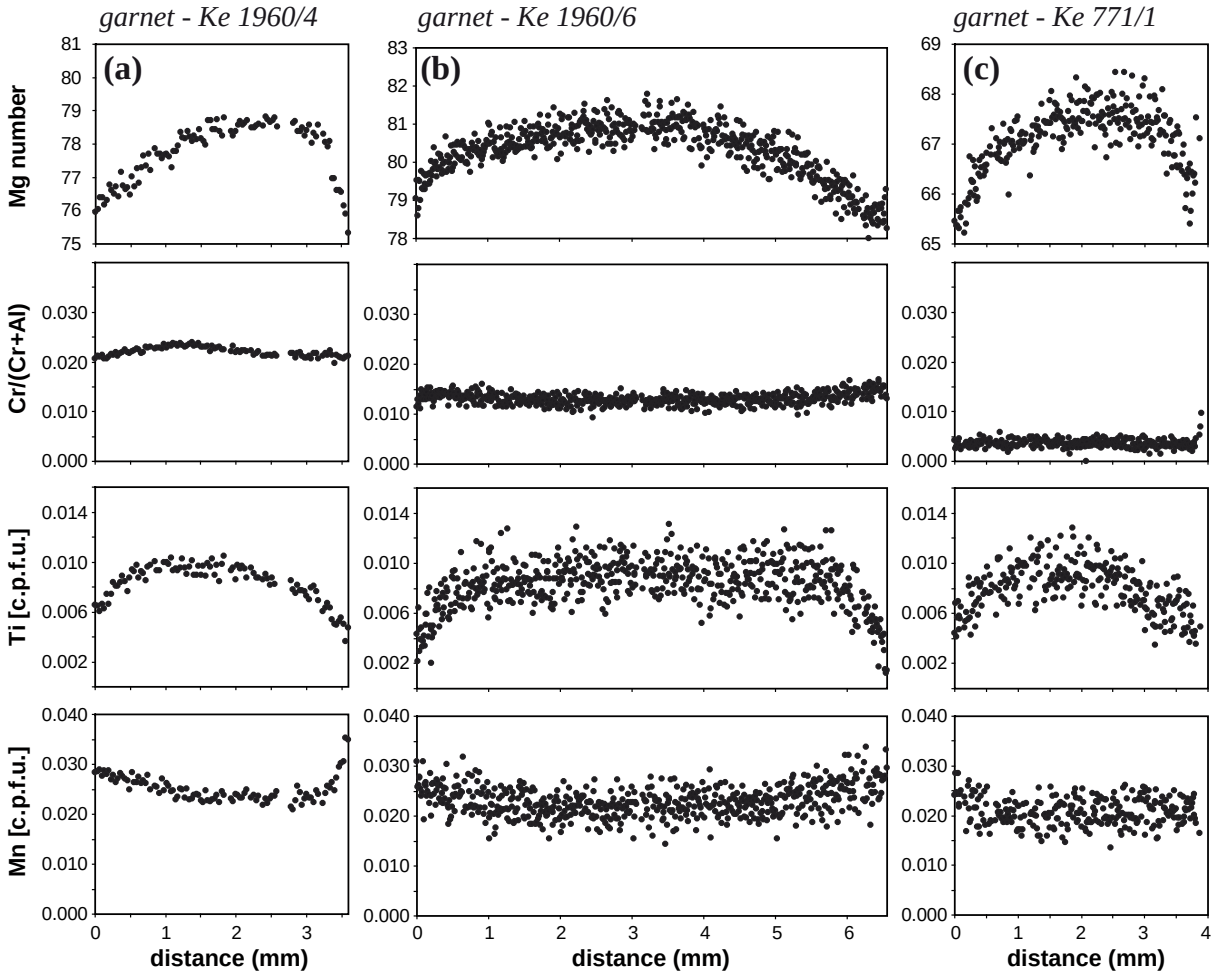


Fig. 5.5: *Electron microprobe traverses (rim-core-rim) across three garnet grains in different Group V grt websterites from Marsabit (Ke 1960/4 and 1960/6: porphyroclastic grt websterites; Ke 771/1: slightly deformed grt websterite; c.p.f.u. = cations per formula unit). Electron microprobe analyses from Olker (2001).*

Orthopyroxene

Group V – grt websterites

Orthopyroxenes in all grt websterites are Al-rich enstatites (Table 5.1). As clinopyroxene, the composition of orthopyroxene can be related to the rock texture, being more 'primitive' (i.e. higher Mg-numbers and Cr_2O_3 contents) in the strongly deformed samples compared to the less deformed ones. Orthopyroxene from the deformed grt websterites again approaches the composition of orthopyroxene from the Group I lherzolites. Compositional zoning is broadly limited to Al and Ca (Fig. 5.12). The shape of the patterns depends on the textural context of the individual grains (e.g., adjacent phase; Fig. 5.12) , as well as on deformation and the presence of exsolution lamellae (e.g., 5.12c). Grains isolated from garnet or symplectites show only limited zoning (e.g. Fig. 5.12a, c and d), typically characterised by increasing Al concentrations from cores to rims, sometimes followed by again decreasing contents towards the outermost rims. These patterns are very similar to those observed in opx-I from Group I xenoliths (Kaeser *et al.*, 2006). Decreasing Al contents are also observed towards clinopyroxene exsolution lamel-

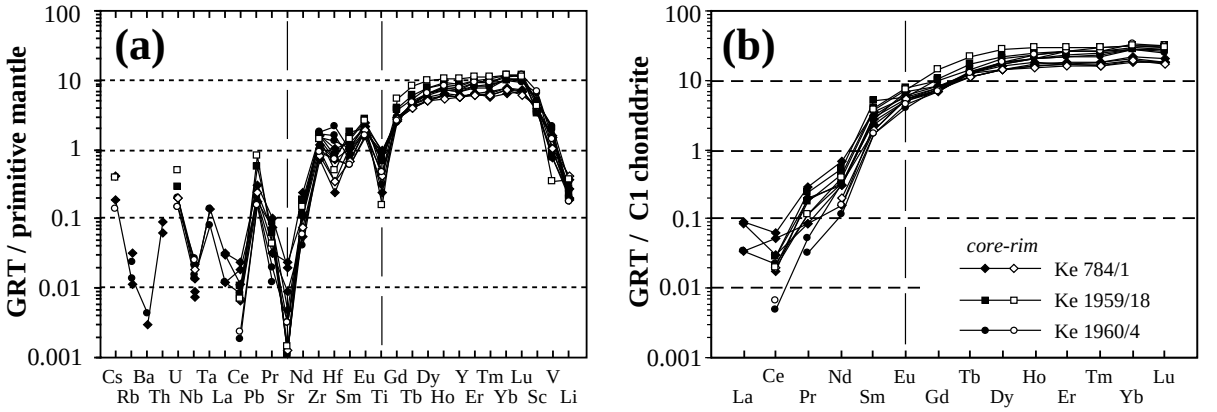


Fig. 5.6: *Trace element composition of garnet from Group V grt websterites. Extended trace element patterns* ***(a)*** *are normalised to the primitive mantle and REE patterns* ***(b)*** *are normalised to C1 chondrite (normalising values from McDonough & Sun, 1995).*

lae (Fig. 5.12c). Towards contacts with garnet or kelyphites, Al concentrations strongly increase (Fig. 5.12b). Ca profiles are relatively flat, with very weak decreases in concentrations towards the outermost rims (Fig. 5.12b). In some samples, however a plateau of higher Ca contents, similar to Group I opx-I (Kaeser *et al.*, 2006) is preserved (Fig. 5.12d).

The trace element compositions of orthopyroxene is almost identical to those in Group I lherzolite, i.e., patterns (not shown) are characterised by low REE concentrations and positive excursions for Pb, Zr, Hf, and Ti.

Group VI – grt-free pyroxenites

Orthopyroxenes, restricted to the more magnesian grt-free pyroxenites, are Al-rich enstatites and bronzites (En79.7-82.2; Table 5.1). Zoning profiles reveal decreasing Al_2O_3 and increasing CaO contents towards rims (not shown). Compared to Group V grt websterites, orthopyroxene is enriched in TiO_2 and shows elevated CaO concentrations (Table 5.2).

Trace elements were only measured in the slightly deformed spl-ol clinopyroxenite Ke 782/2, which display LREE-depleted patterns characterised by positive inflections for Zr, Hf and Ti (not shown).

Olivine, spinel, plagioclase

Group V – grt websterites

Ol-I (only observed in the opx-rich grt websterite Ke 1959/18) has Mg-numbers of ~86.6 and is characterised by NiO contents slightly higher than those in Group I xenoliths (0.47-0.61 wt% instead of 0.27-0.40 in Group I; see Table 5.1). Ol_m in reaction zones have Mg-numbers increasing from undeformed to porphyroclastic samples (from 86.9 to 89.1; Table 5.2).

Spinel in symplectites is an Mg-rich and Cr-poor pleonast (Table 5.2). Slightly higher Cr_2O_3 contents and Cr-numbers occur in stronger deformed samples. Trace elements in olivine and spinel from grt websterites were not analysed.

Plagioclase in the grt websterites (in RZ1 and RZ2) shows a broad compositional diversity, ranging from oligoclase to labradorite (Ab32.4-77.6 and An22.2-67.4). Only two samples (Ke 1958/2 and 1960/6) contain plagioclase with significant orthoclase components (up to Or0.3). Considerable compositional variation occurs within single plagioclase aggregates (e.g. Ab42.2-76.4 in sample Ke 1959/18), optically recognisable by their patchy aspect on BSE-images (Fig. 5.3c).

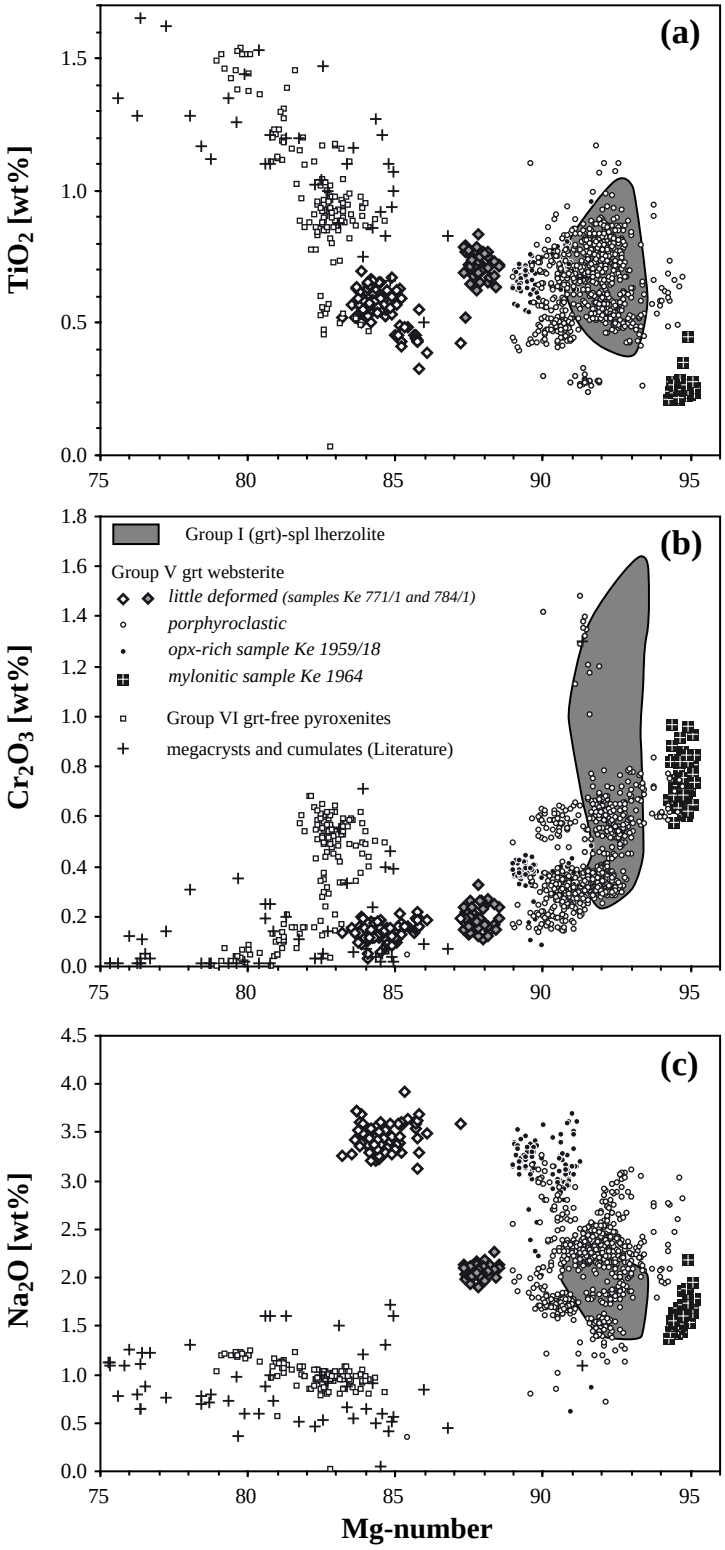
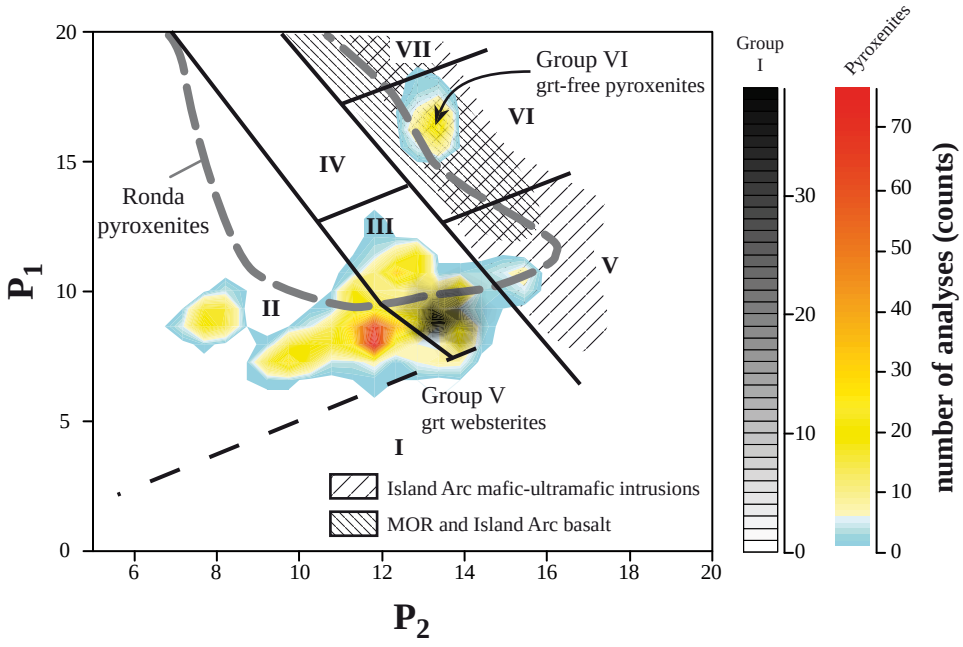


Fig. 5.7: *Compositional variation of clinopyroxene in Group V and Group VI pyroxenite xenoliths from Marsabit. The grey field outlines the compositional range of clinopyroxene from Group I (grt)-spl lherzolites (Kaeser et al., 2006). Data for augite megacrysts and cumulates (spl-ol clinopyroxenite) from Irving (1974a), Righter & Carmichael (1993), Shaw & Eyzaguirre (2000) and Downes et al. (2004).*



P_1: $-0.02SiO_2 + 0.09TiO_2 + 0.64Al_2O_3 + 0.59Cr_2O_3 + 1.35FeO + 9.65MnO - 0.50MgO + 0.29CaO - 2.26Na_2O + 8.0$
P_1: $0.93TiO_2 + 0.07Al_2O_3 + 1.23Cr_2O_3 - 0.46FeO + 1.74MnO - 0.36MgO + 0.10CaO - 1.66Na_2O + 8.0$

Cpx in equil. with:	Field:	
grt	**I:**	peridotite xenoliths from kimberlites
grt	**II:**	eclogites and pyrope-bearing pyroxenites in kimberlites
spl	**III:**	spl peridotites
spl	**IV:**	spl pyroxenites
plag	**V:**	Island Arc peridotites
plag	**VI:**	Island Arc pyroxenites
plag	**VII:**	plagioclase-bearing xenoliths in Island Arc volcanics

[see Koloskov & Zharinov (1993) and Santos *et al.* (2002) for further details]

Fig. 5.8: *Tectonic discrimination diagram for clinopyroxenes from mafic and ultramafic rocks (Koloskov & Zharinov, 1993). Group V and Group I clinopyroxenes both plot within the spl peridotite field, while Group V clinopyroxenes (from the least deformed samples) extend into the eclogite xenolith field, in line with preservation of compositions in equilibrium with garnet. Group VI clinopyroxenes fall within the range of plagioclase-facies peridotite, MORB, and Island Arc mafic and ultramafic intrusions from Kohistan, Aleutians-Tonsina, Kamchatka (data sources: Koloskov & Zharinov, 1993 and Santos et al., 2002, and references therein).*

Group VI – grt-free pyroxenites

Mg-numbers in olivine from the grt-free pyroxenites ranges from 80.1-83.3 (Table 5.1). CaO contents are elevated (0.08-0.3 wt%), whereas NiO contents are lower than in peridotitic olivine (0.05-0.27 wt%; Table 5.1).

Spl-I in Group VI xenoliths are pleonasts with hercynite contents between 0.20-0.35 Mol%. Cr contents are low (Cr-numbers < 10; Table 5.1) and Mg-numbers range from 65.4-79.2. Spinel close to the peridotite-clinopyroxenite contact in the composite xenolith Ke 1973/2 is enriched in Cr_2O_3 compared to spinel away from the contact (Table 5.1).

Amphibole and phlogopite

Group V – grt websterites

Amphibole compositions range from Cr_2O_3-poor Ti-pargasite to kaersutite (Table 5.1). They

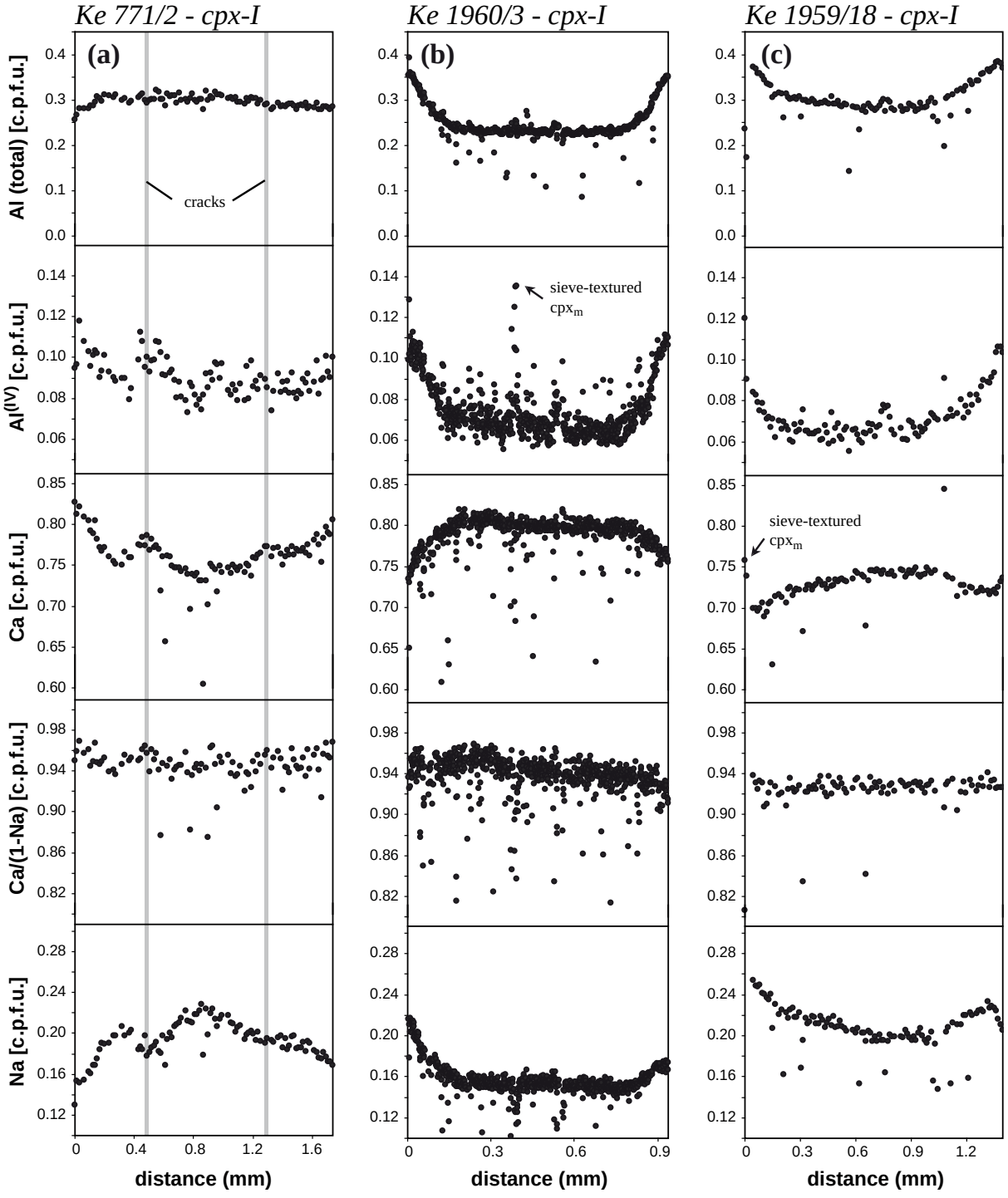


Fig. 5.9: *Major element zoning (in c.p.f.u. = cations per formula unit) of primary clinopyroxene grains (cpx-I) from three different Group V grt websterite samples. Profile* ***(a)*** *exhibits different Al and Ca patterns than profiles* ***(b)*** *and* ***(c)****. Nevertheless, its* $Al^{(IV)}$ *and Ca/(1-Na) patterns are similar to those in* ***(b)*** *and* ***(c)****. This indicates that the P-T evolution of all three samples was similar (since Al[IV] and Ca/(1-Na) are the pressure and temperature dependent terms; e.g., Brey et al., 1990). Note that profiles of type* ***(a)*** *were only observed in this sample (Ke 771/2). All other samples show cpx-I patterns similar to* ***(b)*** *and* ***(c)****. Outliers in* ***(b)*** *and* ***(c)*** *(e.g., deviating from the low-Al core plateau) are hybrid analyses between orthopyroxene lamellae and their clinopyroxene host.*

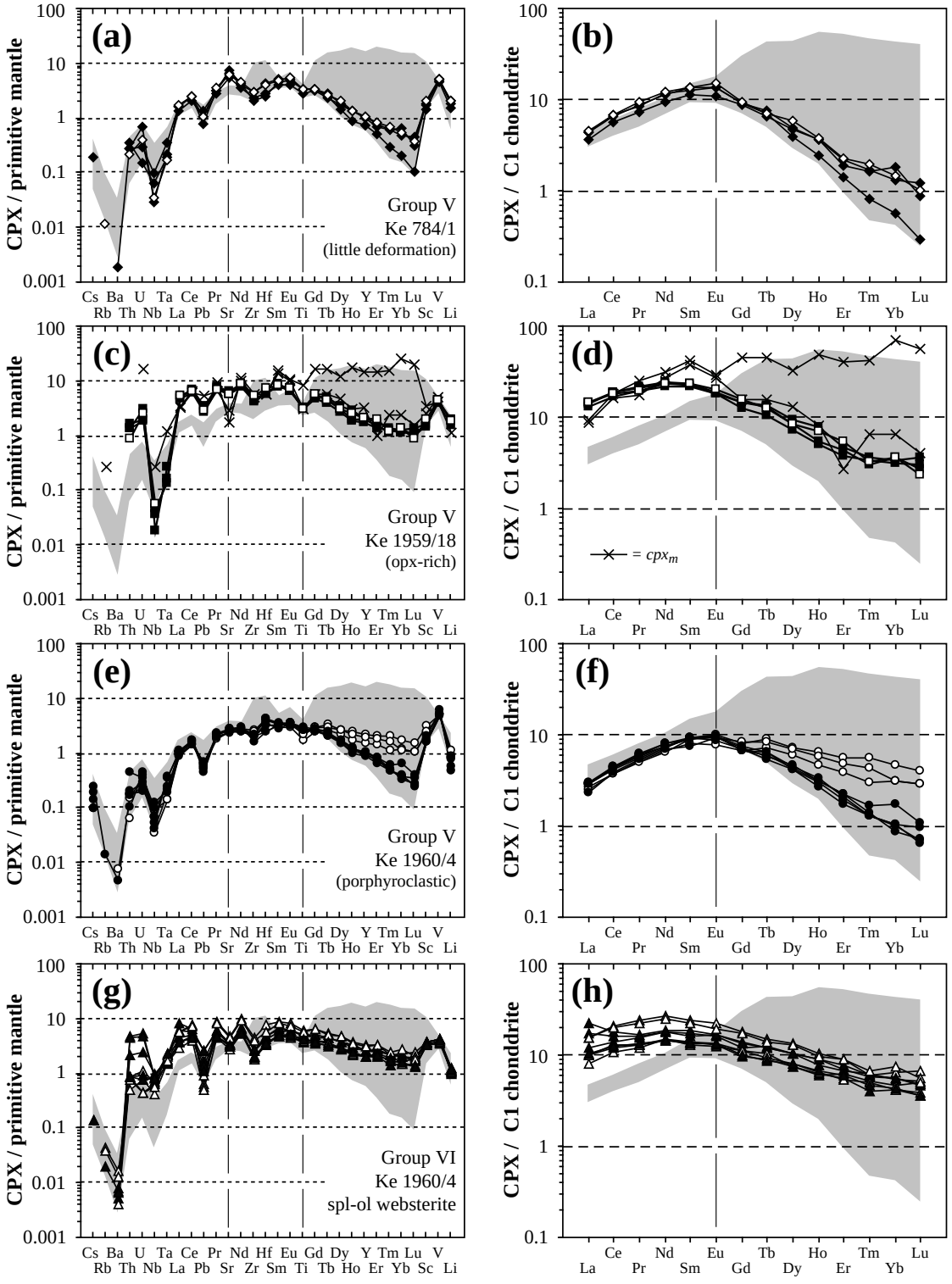


Fig. 5.10: *Trace element composition of clinopyroxene in Marsabit pyroxenite xenoliths:* ***(a)*** *and* ***(b)****, least deformed grt websterite Ke 784/1;* ***(c)*** *and* ***(d)*** *orthopyroxene-rich grt websterite Ke 1959/18 (cpx$_m$ = secondary clinopyroxene in late-stage reaction zones);* ***(e)*** *and* ***(f)****, porphyroclastic grt websterite Ke 1960/4;* ***(g)*** *and* ***(h)*** *Group VI spl-ol websterite Ke 782/2. Extended trace element patterns are normalised to the primitive mantle and REE patterns to C1 chondrite (normalising values from McDonough & Sun, 1995). They grey-shaded field illustrates the clinopyroxene composition of Group I (grt)-spl lherzolite xenoliths.*

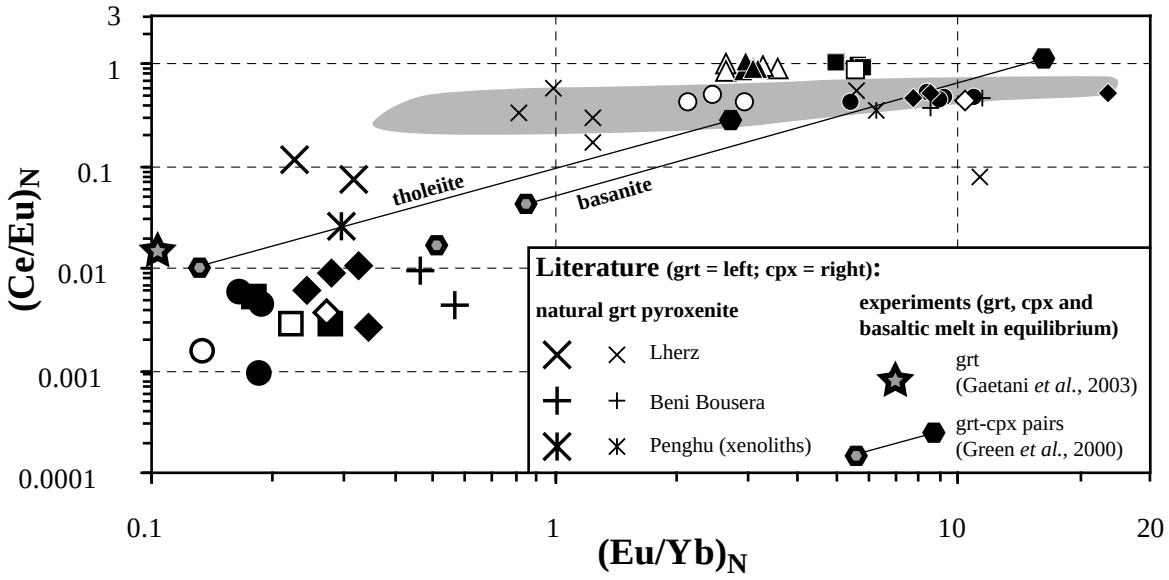


Fig. 5.11: *REE systematics in clinopyroxene and garnet in Group V grt websterite xenoliths from Marsabit (same symbols as in Fig. 5.10), compared to literature data [analyses of natural samples from Bodinier et al., (1987; Lherz), Kumar et al., (1996; Beni Bousera) and Ho et al., (2000; Penghu, Taiwan Strait)]. The grey-shaded field outlines the range shown by the Group I clinopyroxenes indicating the sub-solidus garnet-spinel transition (HREE-redistribution). Note that the tie-lines of co-existing clinopyroxene and garnet (and melt) in both experiments of Green et al., (2000; tholeiite and basanite at 3GPa and 1230 and 1200°C, respectively) exhibit the same length and slope. This line can thus be used as a proxy for garnet and clinopyroxene crystallising in mutual equilibrium from a basaltic melt. The fact that most garnets and clinopyroxenes from the natural samples (including those from Marsabit) cannot be related by a similar tie-line indicates re-equilibration and redistribution of REEs at sub-solidus conditions.*

overlap with the compositional range of Ti-pargasites from the Group I (grt)-spl lherzolites (Kaeser *et al.*, 2006). Amphibole inclusions in garnet (in sample Ke 784/1) are compositionally distinct, being Si-enriched and Al-depleted (Table 5.3). Trace element patterns for amph-i are given in Fig. 5.13a. The REE patterns mimic those of associated clinopyroxene. Amphibole from the porphyroclastic sample shows incompatible trace element patterns identical to those in Group I lherzolites. Kaersutite from the undeformed Ke 784/1 is depleted in LILEs, in agreement with low K_2O contents (Table 5.1). Amphibole from the opx-rich sample (Ke 1959/18) is slightly enriched in LREEs, U and Th (Fig. 5.13a).

Phlogopite – only observed in the non-deformed sample Ke 784/1 – is very TiO_2-rich (6.18-7.04 wt%), Cr_2O_3-poor and has Mg-numbers between 79.7 and 82.2 (Table 5.1). Trace element patterns are typical for mantle phlogopites and are comparable to phlogopite found in the Group I xenoliths (Fig. 5.13b; Kaeser *et al.*, 2006).

Fe-Ti oxides

Group V – grt websterites

Group V xenoliths contain both ilmenite and rutile (Fig. 5.2a and f) . Ilmenite is MgO-rich and contains small amounts of Al_2O_3 and Cr_2O_3 (Table 5.1). This composition is typical for mantle ilmenite (e.g., Kalfoun *et al.*, 2002). Rutile contains small amounts of Cr_2O_3, Al_2O_3 and Fe_2O_3, as well as detectable amounts of Nb_2O_5 and ZrO_2 (Table 5.1; analysed with the electron microprobe). Ilmenite and rutile were not analysed by LA-ICPMS.

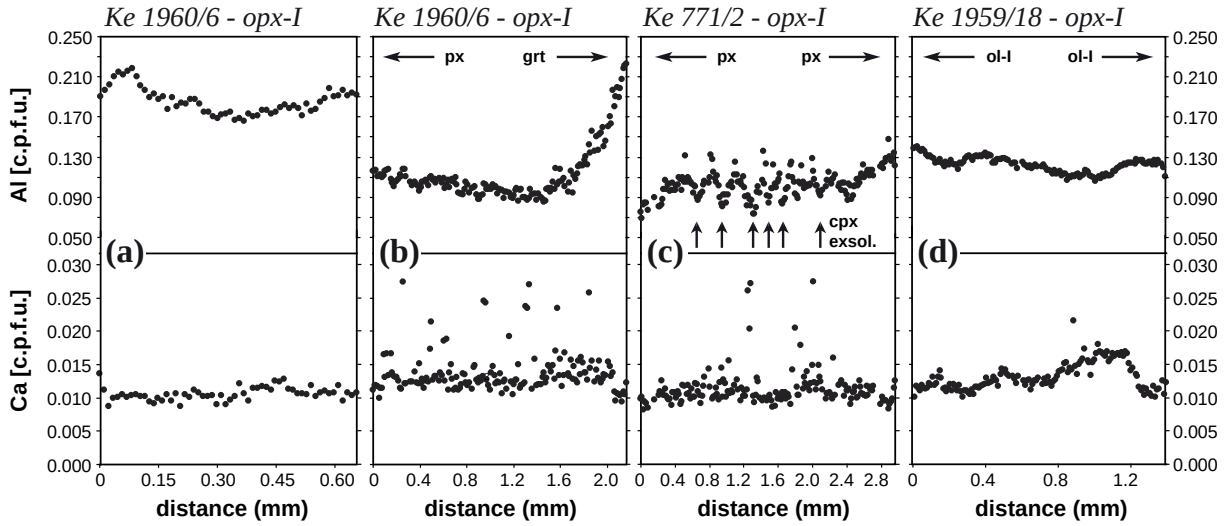


Fig. 5.12: *Major element zoning (in c.p.f.u. = cations per formula unit) of primary orthopyroxene grains (opx-I) from three different Group V grt websterite samples. Note that zoning patterns can be very heterogeneous (e.g., b and c), but are generally characterised by increasing Al contents (core to rim). The high-Ca plateau in cores* ***(d)*** *is only rarely preserved. Note further that Al[IV] and Ca/(1-Na) patterns (not shown) mimic those of Al and Ca.*

CALCULATED BULK ROCK COMPOSITIONS

Due to the small size we did not analyse the whole rock samples. We calculated bulk rock compositions using the average mineral compositions and the modal phase proportions obtained by different image analysis approaches (for details see the Analytical Methods section in Kaeser *et al.*, 2006). We performed these calculations for the four samples where major and trace element data is available, i.e., for three Group V (Ke 784/1; Ke 1960/4; Ke 1959/18) and one Group VI spl-ol websterite (Ke 782/2). Two Group I (grt)-spl lherzolites are included for comparison (Kaeser *et al.*, 2006). The results are given in Table 5.4 and 5.5. The major and trace element results are illustrated in Fig. 5.14 and 5.15, respectively (along with literature data).

The aim was to estimate the bulk rock composition prior to late stage modifications, i.e., the formation of plagioclase-bearing reaction zones. Phases included in the calculations were garnet, clinopyroxene, orthopyroxene, primary olivine (ol-I), Ti pargasite, phlogopite, ilmenite and rutile. The relatively large uncertainties on calculated Al_2O_3 contents (Fig. 5.14a) result from compositional zoning in pyroxenes (see Fig. 5.9 and 5.12). Rutile was included in the calculations (for sample Ke 784/1; see Table 5.4) to obtain realistic HFSE bulk concentrations. Nb and Zr contents were taken from microprobe analysis (see Appendix A4), while Ta and Hf concentrations were calculated using the Nb/Ta and Zr/Hf ratios for mantle rutile as reported by Kalfoun *et al.* (2002).

The compositional range of the three main constituent phases garnet, clinopyroxene and orthopyroxene is shown in Fig. 5.14 as well, in order to account for the broad range of modal compositions exhibited by the Marsabit grt pyroxenites. This illustrates that any calculated bulk rock composition will fall within the range of known mantle pyroxenite compositions. They are further similar to other similar 'ariègite-facies' grt clinopyroxenite and websterite (data shown for Pyrenean and Malenco pyroxenites; Bodinier et al., 1987; Müntener, 1997; see Fig. 5.14). Moreover, the grt websterites show high Al_2O_3 contents, distinguishing them from lower

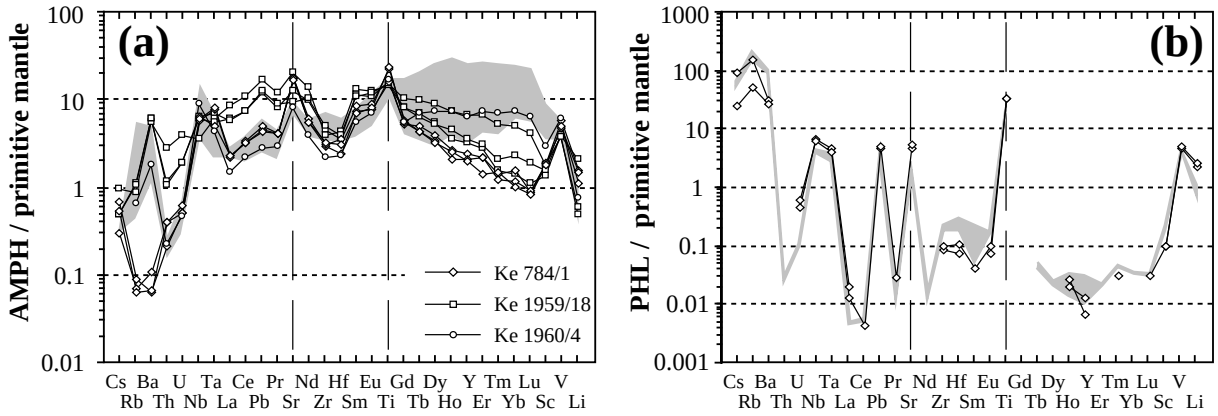


Fig. 5.13: *Trace element patterns of amphibole* ***(a)*** *and phlogopite* ***(b)*** *in Group V grt websterite xenoliths. The grey-shaded fields correspond to amphiboles and phlogopites in Group I (grt)-spl lherzolites (Kaeser et al., 2006). Normalising values (primitive mantle) from McDonough & Sun (1995).*

crustal - upper mantle Island Arc cumulate pyroxenite (IAC pyroxenites; Fig. 5.14a). This is in line with the clinopyroxene classification illustrated in Fig. 5.8.

The composition of the Group I (grt)-spl lherzolite, shown for comparison, plots close to the most 'fertile' end of non-cratonic mantle peridotite from world-wide locations (e.g., Griffin *et al.*, 1999; Pearson *et al.*, 2003). The two investigated Group I samples are in fact more fertile than primitive mantle estimates (McDonough & Sun, 1995) and tend to be more fertile than other grt- and cpx-rich lherzolites from off-craton settings (e.g. Stern *et al.*, 1999; Xu *et al.*, 2000; Ionov *et al.*, 2005). This fact is best explained by a model invoking mechanical (sub-solidus) mingling of peridotite and grt websterite during rifting-induced deformation (see below and Kaeser *et al.*, 2006).

DISCUSSION I: ORIGIN AND EVOLUTION OF THE GRT WEBSTERITES

The Group V grt websterites show a strongly metamorphic fabric with textural characteristics pointing to low-temperature deformation (e.g., mylonites; Fig. 5.2c) most likely at shallow lithospheric conditions (e.g. garnet-spinel transition and the formation of plagioclase). As we will show in the following, metamorphism is due to the relatively late, rift-related evolution of the mantle beneath Marsabit. Deformation and metamorphism strongly obliterates earlier signatures (i.e., related to the magmatic pyroxenite emplacement) and need therefore to be discussed first. In a second part, the question on the pyroxenite emplacement and on their parental melts will be addressed.

Metamorphic evolution of the grt websterites and their relation with peridotite xenoliths

From our earlier study (Kaeser *et al.*, 2006) we concluded that the porphyroclastic peridotite xenoliths – mainly the formerly garnet-bearing Group I – essentially reflect the result of pervasive deformation associated with decompression and cooling in the context of multiple rifting episodes to which the lithospheric mantle in this region was subjected (Anza Graben and Kenya Rift; e.g., Winn *et al.*, 1993; Morley, 1999; Morley, 2006a & b).

A close relation between the grt websterites (Group V) and the formerly garnet-bearing lherzolites (Group I) was already suggested, mainly based on the anomalous modal composition of

Table 5.4: Calculated bulk rock major element compositions (modal contents in vol%; major elements in wt%)

Group	**V**		**V**		**V**		**VI**		**I**		**I**	
Sample	**784/1**		**1959/18**		**1960/4**		**782/2**		**1963/2**		**1965/4**	
Grt[1]	39.3		27.4		36.5		-		15.5		19.4	
Spl[2]	-		-		-		0.7		0.05		0.05	
Cpx[2]	51.7		48.9		52.2		91.0		19.2		15.7	
Opx[2]	6.4		21.0		9.6		0.5		23.2		23.9	
Ol[2]	-		1.2		-		7.8		41.1		41.0	
Amph	2.3		1.5		0.7		-		0.8		tr.	
Phl	0.1		-		-		-		0.1		-	
Rutile	0.05		-		-		-		-		-	
Ilmenite	0.01		-		-		-		-		-	
		1 σ		*1 σ*		*1 σ*		*1 σ*		*1 σ*		*1 σ*
SiO_2	47.70	*0.19*	50.80	*0.03*	49.36	*0.48*	48.85	*0.45*	46.86	*0.39*	46.32	*0.56*
TiO_2	0.58	*0.07*	0.44	*0.01*	0.37	*0.07*	0.87	*0.11*	0.21	*0.03*	0.19	*0.08*
Al_2O_3	12.27	*0.30*	10.38	*0.18*	11.53	*0.66*	6.34	*0.51*	4.77	*0.50*	5.13	*0.57*
Cr_2O_3	0.25	*0.05*	0.51	*0.01*	0.73	*0.06*	0.51	*0.13*	0.37	*0.09*	0.49	*0.18*
FeO(tot)	7.15	*0.23*	5.94	*0.28*	5.12	*0.38*	6.43	*0.26*	7.17	*0.25*	7.22	*0.26*
MnO	0.19	*0.05*	0.20	*0.02*	0.20	*0.04*	0.13	*0.04*	0.14	*0.03*	0.14	*0.05*
NiO	0.02	*0.01*	0.03	*0.01*	0.01	*0.00*	0.02	*0.00*	0.17	*0.01*	0.16	*0.02*
MgO	17.00	*0.18*	19.83	*0.06*	18.61	*0.55*	16.78	*0.35*	34.91	*0.38*	35.97	*0.73*
CaO	12.97	*0.19*	10.48	*0.15*	13.01	*0.43*	18.89	*0.41*	5.07	*0.26*	4.16	*0.37*
Na_2O	1.17	*0.04*	1.61	*0.19*	0.98	*0.20*	0.89	*0.05*	0.49	*0.08*	0.35	*0.12*
K_2O	0.01	*0.00*	0.00	*0.00*	0.00	*0.00*	n.c.		0.01	*0.00*	n.c.	
Total	**100.17**		**100.12**		**99.93**				**100.17**		**100.12**	
Mg#	80.9	*0.3*	85.6	*0.6*	86.7	*0.5*	82.3	*0.3*	89.7	*0.2*	89.9	*0.1*

[1]: garnet contents in Group I samples correspond to symplectite and thus represent maximum values (as sympl = grt + ol); [2]: only primary minerals (spl-I, cpx-I and opx-I, respectively); 1σ: propagated errors from the mean values of each mineral analyses; n.c.: not calculated; modes of Group I (grt)-spl lherzolites are from Kaeser *et al.* (2006);

the Group I lherzolites (i.e., showing extremely high clinopyroxene and former garnet contents), as well as on the preservation of layered structures reflecting cpx- and grt-rich domains in the peridotitic host rock (e.g. Fig. 2a of Kaeser *et al.*, 2006). The close spatial relationship was explained to result from sub-solidus mingling of peridotite and pyroxenite during pervasive deformation.

In the following we use textural observations and *P-T* data (qualitative from mineral zoning and phase assemblages and quantitative from thermobarometry) in order to (1) decipher the metamorphic (*P-T*) history experienced by the Group V grt websterites and (2) to further constrain the role of deformation and metamorphism during peridotite-pyroxenite mingling.

The P-T evolution

An assessment of qualitative indications reflecting changing pressures and temperatures shows that the Group V grt websterites record a *P-T* evolution almost identical to the Group I

Table 5.5: Calculated bulk rock trace element compositions (concentrations in μg/g)

Group	V	V	V	VI	I	I
Sample	784/1	1959/18	1960/4	782/2	1963/2	1965/4
Li	1.96	1.78	0.90	1.92	1.68	1.64
P	105	100	40.7	37.1	39.3	34.2
K	92.3	29.9	18.1	6.46	137	1.54
Sc	40.0	30.9	51.6	52.9	19.7	15.6
Ti	3193	2318	2046	5177	1174	1015
V	264	207	283	306	104	101
Ni	229	308	226	315	1558	1593
Zn	26.4	11.3	8.19	28.6	57.4	73.3
Ga	11.9	8.34	8.16	9.54	5.76	6.61
Rb	0.069	0.009	0.011	0.019	0.13	0.004
Sr	73.3	61.1	27.4	63.8	14.7	12.8
Y	12.0	15.2	14.4	9.63	6.35	4.22
Zr	19.2	28.4	17.0	25.9	10.8	8.32
Nb	0.37	0.066	0.070	0.43	0.082	0.034
Cs	0.006	0.002	0.003	0.003	0.004	0.001
Ba	0.21	0.58	0.11	0.051	0.79	0.020
La	0.56	1.68	0.35	2.90	0.22	0.17
Ce	2.16	5.61	1.36	8.48	0.81	0.60
Pr	0.43	0.96	0.28	1.38	0.15	0.11
Nd	2.82	5.41	1.80	7.62	0.94	0.74
Sm	1.20	1.88	0.81	2.29	0.42	0.33
Eu	0.54	0.65	0.37	0.82	0.18	0.14
Gd	1.60	2.09	1.31	2.35	0.71	0.53
Tb	0.31	0.40	0.30	0.38	0.14	0.11
Dy	2.07	2.64	2.30	2.19	1.07	0.70
Ho	0.45	0.57	0.54	0.39	0.26	0.17
Er	1.26	1.60	1.65	1.01	0.73	0.48
Tm	0.19	0.24	0.25	0.12	0.10	0.068
Yb	1.37	1.63	1.92	0.78	0.69	0.49
Lu	0.19	0.25	0.28	0.11	0.099	0.071
Hf	0.79	0.92	0.63	1.17	0.35	0.29
Ta	0.033	0.007	0.007	0.066	0.006	0.004
Pb	0.11	0.28	0.061	0.18	0.072	0.052
Th	0.014	0.052	0.008	0.13	0.006	0.003
U	0.006	0.027	0.005	0.035	0.002	0.002

for modal composition of each sample see Table 5.4

(grt)-spl lherzolite xenoliths, which are characterised by decompression and cooling (Kaeser *et al.*, 2006). The formation of spl-opx-cpx symplectites reflects the garnet-spinel transition certainly associated to decompression [Ca zoning patterns in pyroxenes and Mg-number patterns in garnet (see below) exclude a heating-induced garnet-spinel transition]. Increasing Al concentrations (from cores to rims) in opx-I and cpx-I (Fig. 5.9 and 5.12) are in line with decompression. This also holds true for increasing HREE abundances in cpx-I rims and cpx-IIa neoblasts in some samples (Fig. 5.10 and 5.11). Further, decreasing Ti concentrations towards garnet rims (Fig. 5.5) may also indicate decompression (Brey *et al.*, 1990; O'Reilly & Griffin, 1995), as do rutile relics preserved in ilmenite. Continuous cooling is indicated by the presence of exsolution lamellae in cpx-I and core-rim zoning patterns such as decreasing Al in opx and cpx in some samples (Fig. 5.9a, 5.12a), decreasing Ca contents in opx (e.g. Fig. 5.12d) and decreasing Mg-numbers in garnet (Fig. 5.5). Slightly increasing (opx) and decreasing (cpx) Ca concentrations towards rims of the polygonal exsolution-free pyroxenes of sample Ke 1958/2 (not shown) point to later heating. This latter relation between texture (static recrystallisation) and temperature (heating) suggests that some pyroxenites were subjected to the EARS-related heating event similar to the recrystallised (and metasomatised) Group II (grt)-spl lherzolites (Kaeser *et al.*, 2006).

In order to quantitatively constrain the *P-T* evolution, pressures and temperatures were calculated based on the Ca distribution between opx and cpx (the two-pyroxene thermometer $T_{2Px\text{-}BK90}$ and the Ca-in-opx thermometer $T_{Ca\text{-}opx\text{-}BK90}$ of Brey & Köhler, 1990) and thermometers calibrations based on the Mg/Fe partitioning between cpx and grt ($T_{grt\text{-}cpx\text{-}K88}$: Krogh, 1988), as well as opx and grt ($T_{grt\text{-}opx\text{-}H84}$: Harley, 1984 and $T_{grt\text{-}opx\text{-}BK90}$: Brey & Köhler 1990). Pressures were calculated based on the Al partitioning between opx and grt ($P_{Al\text{-}opx\text{-}BK90}$; Brey & Köhler, 1990).

Results from thermobarometry are given in Table 5.6. The largest part of these data are compiled from Olker (2001; see annotation in Table 5.6). Generally, the obtained results are in agreement with the qualitative interpretations (see above), i.e., the higher temperatures based on the core compositions of cpx-I, opx-I and grt-I compared to temperatures based on por-

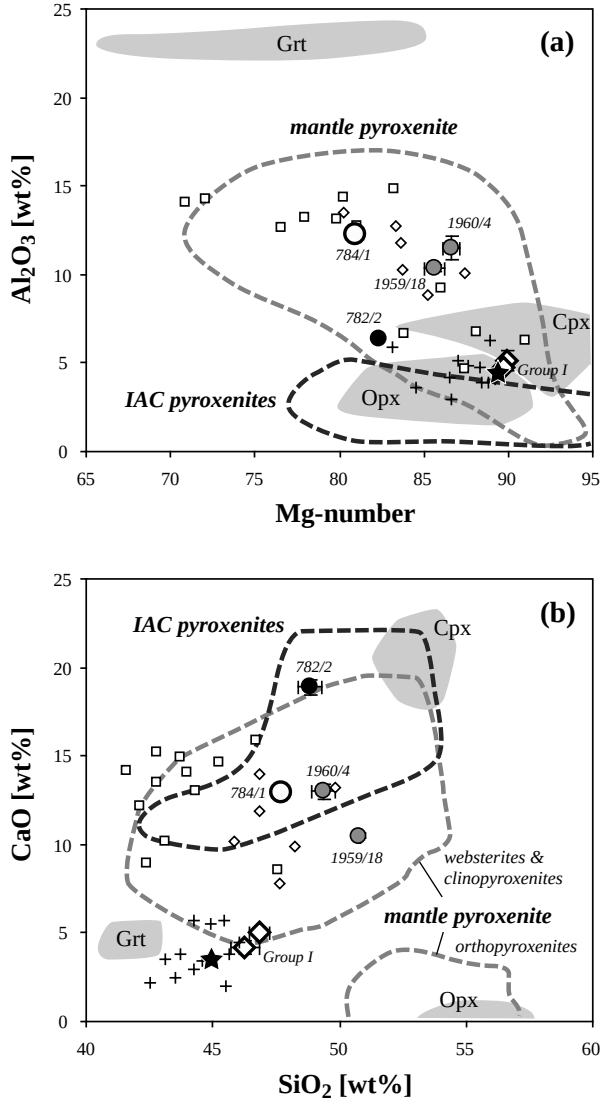


Fig. 5.14: *Mg-number [100*Mg/(Mg+Fe^{tot})] vs. Al_2O_3 and SiO_2 vs. CaO contents for calculated bulk Group V and VI pyroxenites (sample numbers in italic) and Group I lherzolites, compared to the compositional ranges of mantle-derived pyroxenite and Island Arc crustal (IAC) pyroxenites (data sources: Hirschmann & Stolper, 1996 and Berly et al., 2006 and references therein). Data further discussed in the text are plotted individually: crosses = Pyrenean 'arièGite' (cpx+opx+spl+amph±grt; Bodinier et al., 1987); diamonds = Pyrenean cpx-rich lherzolite (at peridotite-pyroxenite contacts; Bodinier et al., 1988); squares = Malenco grt clinopyroxenites (Müntener, 1997). The star corresponds to the primitive mantle estimate of McDonough & Sun (1995). Light grey fields: composition of grt, cpx-I and opx-I of all Group V grt websterites from Marsabit. This indicates that calculated bulk rock using any realistic modal compositions will fall broadly within the field for mantle-derived pyroxenite. See text for further discussion.*

phyroclast rims and/or neoblast cores are in line with cooling, while pressure calculations yield higher values for grt and opx cores than for rims, reflecting the decompression event (Table 5.6; Fig. 5.16).

However, Olker (2001) found that the use of different thermometers results in significant temperature variations, in some cases reaching up to 200°C (Table 5.6). This is especially the case when looking at values based on the mineral cores, whereas temperatures for the mineral rims show less variation [Table 5.6; the different assumed pressures for cores and rims (2.0 and 1.0 GPa,) were chosen to account for the effect of decompression which accompanied cooling (see below)]. Independent tests of the here applied thermobarometers have shown that they yield reliable results in the range of 800-1000°C (e.g., Brey *et al.*, 1990; Smith, 1999). Thus, the discrepancy obtained by different thermometers is most likely due to disequilibrium with respect to some compositional parameters between cpx, opx and grt and not to the thermometer calibration. Generally, temperatures based on the Fe-Mg distribution between opx and grt ($T_{grt\text{-}opx\text{-}BK90}$ and $T_{grt\text{-}opx\text{-}H86}$) yield the highest temperatures while the diopside-enstatite solvus based $T_{2Px\text{-}BK90}$ and $T_{Ca\text{-}in\text{-}opx\text{-}BK90}$ give the lowest estimates. This implies that Ca in pyroxenes already re-equilibrated to the lower temperature stage, whereas the Fe/Mg ratios in garnet and opx still preserve higher temperatures. This is, however, not in accordance with diffusion coefficients which are known to be much higher in the case of Mg and Fe (in both garnet and opx; Chakraborty & Ganguly, 1992; Ganguly & Tazzoli, 1994; Ganguly *et al.*, 1998) compared to Ca in pyroxenes (Sautter *et al.*, 1988; Dimanov & Jaoul, 1998). This apparent contradiction may be explained by taking the high degree of pyroxene deformation into account. Textural features such as abundant undulous extinction and subgrain formation indicate a high dislocation density in the pyroxene grains which will significantly shorten diffusion ways and fasten chemical re-equilibration. In contrast, garnet crystals absorb strain by the for-

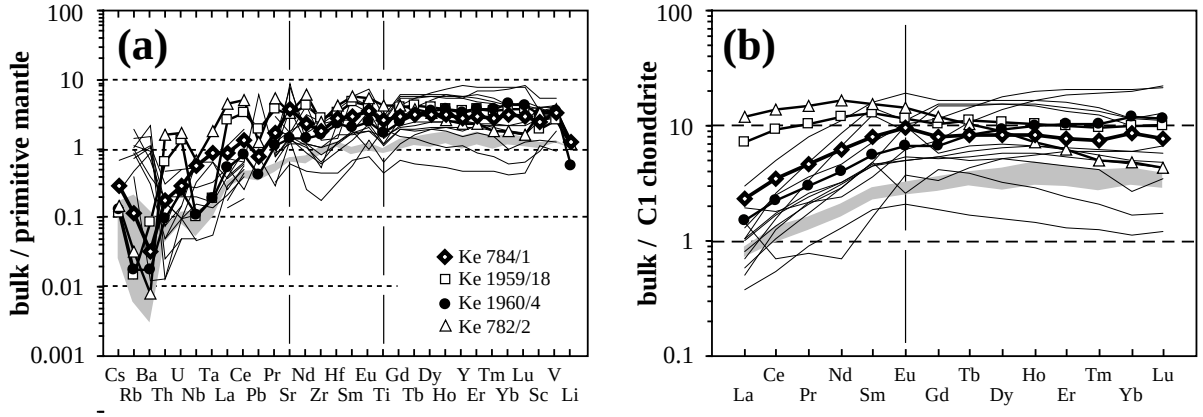


Fig. 5.15: *Calculated bulk trace element patterns of Group V (Ke 784/1, 1959/18 and 1960/4) and Group VI (Ke 782/2) pyroxenites from Marsabit. Thin lines are grt clinopyroxenites from Malenco (Müntener, 1997; for discussion see text). They grey-shaded field illustrates the calculated bulk trace element composition of Group I (grt)-spl lherzolite xenoliths. Extended trace element patterns are normalised to the primitive mantle and REE patterns to C1 chondrite (normalising values from McDonough & Sun, 1995).*

mation of relatively widely spaced cracks (Fig. 5.2b). In the intact zones between cracks elements are impeded to use 'fast diffusion ways'. This explanation would, on the other hand, imply disequilibrium between Fe-Mg contents in the cores of opx-I and grt-I. However, it can be shown that the Fe/Mg ratios in opx suffer only little change during cooling and that the temperatures calculated with $T_{\text{grt-opx-BK90}}$ and $T_{\text{grt-opx-H86}}$ mainly depend on the Fe/Mg ratio in garnet (Olker, 2001). This can be depicted from Fig. 5.17a (redrawn from Olker, 2001) illustrating the change in Fe/Mg ratios in grt and opx as a function of decreasing temperature in a model bulk rock (Fe/Mg = 0.2) of 35vol% grt, 25vol% opx, and 40vol% cpx (for the calculation method see caption of Fig. 5.17). Consequently, $T_{\text{opx-grt-BK90}}$ only slightly underestimate the temperature prior to cooling. Conversely, equal changes of Fe/Mg ratios are obtained in the case of cpx and grt (Fig. 5.17b). Thus, since deformation facilitated Fe/Mg re-equilibration in cpx-I cores but not in garnet, temperatures obtained by $T_{\text{cpx-grt-K88}}$ do no longer represent former equilibrium conditions. Similarly, $T_{\text{2px-BK90}}$ and $T_{\text{Ca-in-opx}}$ represent temperatures along the cooling path rather than former equilibrium, depending to which degree Ca contents in opx-I and cpx-I already re-equilibrated.

In contrast to Ca and Mg-numbers, both opx-I and cpx-I exhibit well-preserved low-Al cores (Fig. 5.9 and 5.12), pointing to former equilibrium with garnet. Preservation of Al zoning is in line with much slower Al diffusion coefficients compared to Ca (e.g. Sautter *et al.*, 1988; Smith & Barron, 1991). Consequently, using the increasing Al contents in opx-I with $P_{\text{Al-in-opx-BK90}}$ most likely reflect well the decompression path (Fig. 5.16).

Following the above argumentations the combination of $T_{\text{grt-opx-BK90}}$ with $P_{\text{Al-opx-BK90}}$ probably yields the most appropriate estimates for the *P-T* stages before and after cooling and decompression (Table 5.6). *P-T* data based on mineral cores and rims of the more or less deformed grt websterites cover a field with maximum and minimum conditions of about ~970-1100 °C at ~2.3-2.6 GPa, and ~700-800°C at ~0.5-1.0 GPa, respectively (Fig. 5.16). These conditions overlap broadly with the *P-T* stages defined on the basis of the peridotite xenoliths from Marsabit, and thus constrain the transition from the HP/HT versus an MT to a LT stage (Kaeser *et al.*, 2006). This is in line with textural features indi-

Table 5.6: Results of *P-T* calculations for Group V garnet websterite xenoliths from Marsabit (*P* in GPa, *T* in °C)

Sample	*P* assumed	$T_{2Px\text{-}BK90}$	$T_{Ca\text{-}opx\text{-}BK90}$	$T_{grt\text{-}opx\text{-}BK90}$	$T_{grt\text{-}opx\text{-}H84}$	$T_{cpx\text{-}grt\text{-}K88}$	$T_{grt\text{-}opx\text{-}BK'90}$ / $P_{Al\text{-}opx\text{-}BK'90}$	P_{max} RZ[2]
* Ke 771/1 - cores[1]	2.0	833 ± 46	838 ± 29	966 ± 50	960 ± 50	887 ± 35	**926 ± 50** / **1.46 ± 0.09**	
* Ke 771/1 - rims[1]	1.0	768 ± 33	788 ± 12	812 ± 57	837 ± 43	746 ± 22	**805 ± 57** / **0.90 ± 0.14**	0.75 ± 0.08 / 0.83 ± 0.12
* Ke 771/2 - cores	2.0	823 ± 44	820 ± 21	914 ± 42	918 ± 32	812 ± 42	**926 ± 42** / **2.17 ± 0.03**	
* Ke 771/2 - rims	1.0	747 ± 51	770 ± 13	775 ± 17	807 ± 13	-	**748 ± 17** / **0.87 ± 0.16**	-
* Ke 1958/2 - cores	2.0	975 ± 33	919 ± 45	1015 ± 36	1002 ± 27	956 ± 45	**970 ± 36** / **1.41 ± 0.05**	
* Ke 1958/2 - rims	1.0	1019 ± 16	968 ± 16	1042 ± 46	1011 ± 42	1055 ± 32	**1066 ± 46** / **1.29 ± 0.04**	-
Ke 1959/18 - cores	2.0	965 ± 71	832 ± 34	1022 ± 80	1001 ± 60	867 ± 38	**1044 ± 81** / **2.31 ± 0.40**	
Ke 1959/18 - rims	1.0	818 ± 16	767 ± 17	777 ± 35	804 ± 28	-	**757 ± 35** / **0.78 ± 0.11**	-
* Ke 1960/3 - cores	2.0	781 ± 36	826 ± 38	1000 ± 46	991 ± 34	929 ± 37	**1034 ± 46** / **2.45 ± 0.20**	
* Ke 1960/3 - rims	1.0	726 ± 66	771 ± 22	743 ± 48	782 ± 39	776 ± 51	**712 ± 48** / **0.52 ± 0.10**	0.31 ± 0.07 / 0.22 ± 0.10
* Ke 1960/4 - cores	2.0	755 ± 36	802 ± 32	944 ± 55	988 ± 41	847 ± 32	**1030 ± 55** / **2.48 ± 0.57**	
* Ke 1960/4 - rims	1.0	731 ± 54	791 ± 48	770 ± 49	809 ± 40	746 ± 38	**716 ± 49** / **0.18 ± 0.12**	-
* Ke 1960/5 - cores	2.0	770 ± 24	810 ± 22	1026 ± 46	1009 ± 34	865 ± 22	**1066 ± 46** / **2.51 ± 0.19**	
* Ke 1960/5 - rims	1.0	860± 137	769 ± 23	781 ± 17	810 ± 13	-	**753 ± 17** / **0.58 ± 0.22**	0.92 ± 0.03 / 1.06 ± 0.04
* Ke 1960/6 - cores	2.0	825 ± 26	850 ± 29	997 ± 41	989 ± 30	871 ± 21	**1031 ± 41** / **2.45 ± 0.07**	
* Ke 1960/6 - rims	1.0	888 ± 41	859 ± 24	864 ± 20	880 ± 16	850 ± 54	**859 ± 20** / **0.93 ± 0.09**	-
Ke 1964 - cores	2.0	851 ± 23	812 ± 48	975 ± 11	979 ± 7	844 ± 52	**996 ± 11** / **2.31 ± 0.12**	
Ke 1964 - rims	1.0	-	767 ± 30	784 ± 93	822 ± 73	-	**752 ± 91** / **0.55 ± 0.15**	-

*: thermobarometric data compiled from Olker (2001); [1]: cores and rims indicate whether P and T are calculated based on porphyroclast cores (grt, opx-I, cpx-I), or rims (including neoblasts cores/rims), respectively. [2]: maximum pressures for the formation of the plagioclase-bearing reaction zones based on the jadeite-albite-quartz barometer from Holland (1980) at assumed T=700°C, and T=1100°C, respectively.

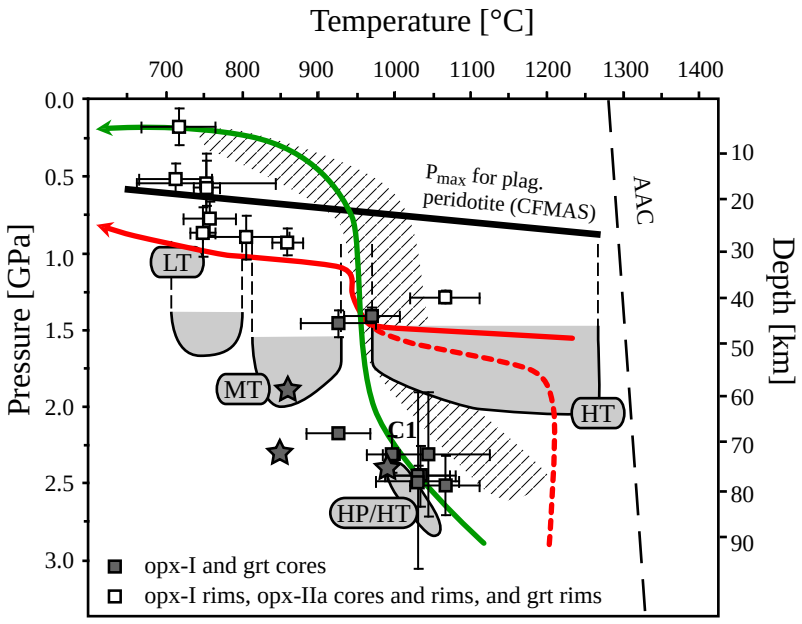


Fig. 5.16: *Pressure-temperature stages preserved by Group V grt websterites (based on orthopyroxene-garnet thermobarometry: $T_{opx\text{-}grt\text{-}BK90}$ and $P_{opx\text{-}grt\text{-}BK90}$; Brey & Köhler, 1990). The results are in good agreement with the temperature estimates for the HP/HT, MT and LT stages based on Marsabit peridotite xenoliths (Kaeser et al., 2006) and further constrain their depth range. Also indicated for comparison are P-T evolution paths for three mantle rock massifs which have been exhumed during continental rifting: Malenco [red; Müntener (1997); dashed line = peridotite; continuous line = grt clinopyroxenite intrusion]; Ligurian grt clinopyroxenites and peridotites [green; Montanini et al. (2006)]; Zabargad, former garnet-bearing websterites and spl peridotites [hachured field; Piccardo et al. (1988)].*

cating a close spatial relationship and a similar metamorphic evolution of Group V grt websterites and porphyroclastic peridotite types. The HP/HT stage can be explained to reflect the *P-T* conditions of a former re-equilibrated pyroxenite-bearing subcontinental mantle, similar to present-day thermal conditions observed in southern parts of Kenya (e.g., Chyulu), where rifting-induced lithospheric thinning is much less advanced than beneath the Anza Graben (Henjes-Kunst & Altherr, 1992; Kaeser *et al.*, 2006; Altherr *et al.*, submitted).

Mesozoic to Paleogene rifting-related deformation was accompanied by further cooling and decompression (to ~900-750°C at 0.5-1.3 GPa; Table 5.6), in agreement with thermobarometric studies of the associated peridotites (Fig. 5.16: the MT and LT stages; Kaeser *et al.*, 2006). The low temperatures and pressure estimates using the rim compositions minerals (both neoblasts and porphyroclasts) from porphyroclastic and mylonitic Group V grt websterites (mostly <800°C at pressures < 1.0 GPa; Table 5.6) further constrain the shallow (i.e., ≤ 30 km) position of deformed grt websterites and porphyroclastic peridotites prior to their entrainment in the Marsabit basanites. The pressure estimates based on garnet and opx rims (mostly <1.0 GPa; Table 5.6; Fig. 5.16) are in good agreement with the observed mineral assemblages. The garnet-spinel transition in pyroxenitic assemblages was determined experimentally to occur at 1.3-1.7 GPa (Irving, 1974b; Hirschmann & Stolper, 1996). In these systems, plagioclase appears at 0.9 GPa (Irving, 1974b), in line with the development of plagioclase reaction zones in the here investigated xenoliths.

The *P-T* conditions obtained for the MT and LT stage are similar to the metamorphic high-stress deformation stage reported for exhumed

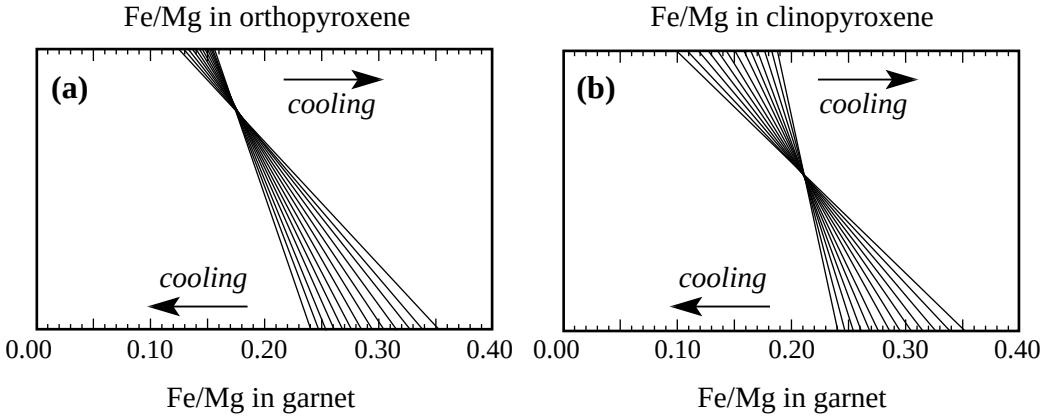


Fig. 5.17: *Changing Fe/Mg ratio in orthopyroxene and garnet as a function of temperature calculated for a garnet websterite bulk-rock (Fe/Mg = 0.2; grt = 35 Vol%, opx = 25 Vol%, cpx = 40 Vol%; ρ_{grt} = 3.582 g/cm^3; ρ_{opx} = 3.21 g/cm^3; ρ_{cpx} = 3.22 g/cm^3).* ***(a)*** *Fe/Mg calculated in opx and grt based on the $T_{grt\text{-}opx\text{-}BK90}$, $T_{grt\text{-}cpx\text{-}K88}$ and $T_{2Px\text{-}BK90}$ thermometers.* ***(b)*** *Fe/Mg calculated in cpx and grt based on the $T_{grt\text{-}opx\text{-}BK90}$, $T_{grt\text{-}cpx\text{-}K88}$ and $T_{2Px\text{-}BK90}$ thermometers. Each line corresponds to a 50°C temperature decrement (arrow; from 1300-700°C). For discussion see text.*

peridotite massifs, such as Lherz (early recrystallisation at ~950°C/1.2-1.5 GPa and formation of porphyroclastic fabrics and foliation at 0.8-1.3 GPa; see Vétil *et al.*, 1988; Fabriès *et al.*, 2001). Mylonites, both in pyroxenite (e.g. sample Ke 1964) and peridotite (Group IV; see Kaeser *et al.*, 2006) are in accordance with similar observations from Pyrenean massifs as well (Fabriès *et al.*, 1998 and 2001). In fact, the deciphered *P-T* path, as well as textures and compositional features of the Marsabit pyroxenites are strikingly similar to pyroxenites from ultramafic massifs exhumed during continental rifting processes, namely from Malenco (Müntener & Hermann, 1996), the Ligurides (Montanini *et al.*, 2006), and from Zabargad (Piccardo et al., 1988; Kurat *et al.*, 1993; Vannucci *et al.*, 1993; see Fig. 5.16). This highlights that similar uplift and deformation processes take and/or took place beneath Marsabit.

Finally, the mineral rims of the granular recrystallised sample Ke 1958/2 partly re-equilibrated at higher temperatures (Table 5.6), within the range of the HT stage defined by the Group II lherzolite xenoliths (Fig. 5.16 and Kaeser *et al.*, 2006). This result is in agreement with the fabric of this sample indicating static recrystallisation, most likely in response to the young, EARS-related, thermal modification of the Marsabit lithosphere.

Formation of kelyphites and plagioclase-bearing reaction zones

Some pressures estimates based on mineral rims yield very low values, implying depths which are too shallow for a mantle origin (e.g. sample Ke 1960/4; see Table 5.6). These values most likely reflect partial re-equilibration of opx and grt during the formation of kelyphites. Pressures estimates for the formation of the plagioclase-bearing parageneses were obtained (Olker, 2001) using a barometer based on co-existing jadeite, albite and quartz (Holland, 1980). As quartz is missing in the studied samples the results represent maximum values. The pressure range (0.24-1.10 GPa; Table 5.6) broadly overlaps with values based on the grt-opx barometry. The sometimes very low pressures, together with the fine-grained aspect of the reaction zones growing at the expense of all mineral generations (porphyroclasts, neoblasts and symplectite assemblages) indicate a very late-stage formation. The presence of plagioclase in the

kelyphite but not in the spl-opx-cpx symplectites led Henjes-Kunst & Altherr (1992) to the conclusion that the latter still formed within the mantle, whereas the kelyphite formed presumably during the ascent of the xenoliths to the surface. A likewise formation can be suggested for the sieve-textured clinopyroxene rims which are texturally and compositionally very similar to 'late-stage' textures formed upon decompression during the ascent and/or heating of the xenolith in the host magma (e.g., Shaw & Edgar, 1997; Carpenter *et al.*, 2002; Ulianov & Kalt, 2006). High Na contents in bulk kelyphites and abundant Na-rich plagioclase indicate that reaction zone formation was not a completely isochemical process, i.e., occurring in the presence of intergranular fluid or melt.

Peridotite-pyroxenite mingling: the result from pyroxenite emplacement and/or sub-solidus reactions?

Thermobarometry (see above) gave evidence that porphyroclastic peridotites and grt websterites experienced a very similar *P-T*-deformation history. In addition, the compositional data clearly revealed that increasingly deformed pyroxenite xenoliths show increasing compositional overlaps with the Group I (grt)-spl lherzolites (e.g., Fig. 5.7, 5.8, 5.13 and 5.15), implying an interaction between peridotite and pyroxenite, e.g., through sub-solidus deformation-induced mingling (Kaeser *et al.*, 2006). However, as we will show in the following, the well-preserved microtextures in the Marsabit grt websterites and compositional features indicate that peridotite-pyroxenite interaction most likely occurred during two stages: first during melt-rock reaction in the context of pyroxenite intrusion, and second, during later sub-solidus deformation and re-equilibration in the context of continental rifting. Sub-solidus modification is more evident in the present case and will be thus discussed first.

A close relation between deformation and metamorphism (i.e., the garnet-spinel transition) is indicated texturally: strongly deformed grt websterites contain much more symplectite, while in the undeformed samples, symplectites are virtually missing (Fig. 5.1a). The above features would be in line with a close link between the strain rate and the metamorphic reaction rates (e.g., Brodie & Rutter, 1985; Baxter & DePaolo, 2004; Terry & Heidelbach, 2006; and references therein), in this case enhancing the garnet-spinel transition. However, the garnet-breakdown further depends on the textural context of the garnet crystal, indicating a further mineralogical control of the phase transition. This is highlighted by the fact that symplectites are restricted to opx-rich zones, while no reaction is visible at grt – cpx interfaces (Fig. 5.2c and d). The reason for this may be the association of orthopyroxene with olivine, and the availability of olivine to drive the sub-solidus reaction grt + ol = opx + cpx + spl. Restriction of ol-I to opx-rich zones is texturally indicated in the opx-rich zone of sample Ke 1959/18 (Fig. 5.1c). In this part of the sample garnet was completely transformed to symplectite (Fig. 5.1c). The same was systematically observed in the Group I lherzolites, where no garnet was preserved (see Fig. 5.1d and Kaeser *et al.*, 2006). If we assume that less opx-rich pyroxenites also contained less olivine, then the latter will be exhausted before all garnet reacted to form symplectite. This would explain the textural control of symplectite formation and the absence of olivine in all pyroxenites except the opx-rich sample Ke 1959/18.

Besides the availability of olivine, garnet break-down depends also on the *P-T* conditions, as well as on the composition of the 'bulk system'. *P-T* estimates (Fig. 5.16) are in the range of the generally assumed position of the garnet-spinel transition in pyroxenitic rocks (1.3-1.7 GPa). With respect to the bulk composition, adding peridotite to pyroxenite would enhance the grt-spl transition in the sense that it will be shifted to higher pressures, given the Cr-rich nature of peridotite compared to pyroxenite (e.g., Klemme & O'Neill, 2000).

All the above observations are principally in agreement with deformation-induced sub-solidus mingling and chemical re-equilibration

between pyroxenite and peridotite. In addition, field observations made in mantle rock bodies where the peridotite-pyroxenite relationship is better visible than in xenoliths support such a model (e.g., Kornprobst, 1966; Bodinier *et al.*, 1987; Tabit *et al.*, 1997; Van der Wal & Vissers, 1996). The over-fertile bulk-rock compositions of Group I lherzolites (depicted in Fig. 5.14; see also Kaeser *et al.*, 2006) compositionally overlap (Fig. 5.14) with cpx-rich lherzolites found at the contact between peridotite and pyroxenite veins in Lherz, which are explained by a similar deformation-related model (Bodinier *et al.*, 1988).

The deformation behaviour of pyroxene and olivine aggregates (Chopra & Paterson, 1981; Bystricky & Mackwell, 2001) indicates that pyroxenite dykes, at *P-T* conditions relevant to the MT and LT stage (750-850°C at ~1.0-2.0 GPa; Fig. 5.16), will be stretched and probably disaggregated into a more plastically deforming olivine matrix. This process would provide olivine to drive to completion the garnet breakdown reaction in thin pyroxenitic layers (such as those preserved in Group I lherzolites; see Fig. 2a of Kaeser *et al.*, 2006) or at the rims of larger pyroxenite bands.

The low *P-T* conditions, however, also imply that chemical re-equilibration of peridotite and pyroxenite depends strongly on the diffusivities of a given element. Fast diffusing elements such as Mg and Fe will potentially re-equilibrate (on both intra- and inter-grain scale), even at relatively low temperatures (see discussion of the pyroxene and garnet zoning patterns). In contrast slowly diffusing elements, such as trivalent ions like Al and Cr (e.g., Freer, 1981), will preserve earlier, i.e., magmatic signatures. In this respect, higher Cr contents in more strongly deformed websterites (e.g., Fig. 5.7a) more likely reflect melt-peridotite interaction (e.g., at the margin of pyroxenite layers) during pyroxenite emplacement rather than diffusional Cr addition at low temperatures. High Cr contents coinciding with strong deformation could then simply reflect that deformation was more intense at the margins of pyroxenite dykes, where also previous melt-peridotite interaction occurred. Melts crystallised in the centre of pyroxenite bodies, in turn, interacted less with peridotite and were shielded against later deformation (e.g., during boudinage). Similar models of interfering 'magmatic' and sub-solidus signatures were reported from peridotite massifs such as Lherz (Bodinier *et al.*, 1987); Balmuccia (Rivalenti *et al*., 1995), Ronda (Garrido & Bodinier, 1999) and Beni Bousera (Tabit *et al.*, 1997; Kumar *et al.*, 1996), as well as from xenolith studies (Litasov *et al.*, 2000; Liu *et al.*, 2005).

Finally, earlier melt-peridotite reaction could also explain the presence of opx-rich pyroxenite (see sample Ke 1959/18), presumably localised at pyroxenite dyke margins (e.g., Fabriès *et al.*, 2001). Replacement of olivine by orthopyroxenite typically occurs during interaction of peridotite and opx-saturated (e.g., tholeiitic) basaltic melt (Kelemen, 1990; Sen & Dunn, 1995). In line with this, opx-rich zones are commonly observed at peridotite-pyroxenite interfaces in orogenic peridotite bodies (e.g., Fabriès *et al.*, 2001). The very Ni-rich composition of ol-I in sample Ke 1959/18 (Table 5.1) would be in agreement with such an origin, i.e. reflecting Ni re-partitioning from an originally olivine-rich into an olivine-poor orthopyroxenitic rock [note that the inverse is observed where harzburgite is transformed into dunite during melt-rock reaction processes (Suhr, 1999)].

Summarised, grt websterites from Marsabit most likely reflect the result of variable degrees of melt-rock reaction during emplacement and subsequent sub-solidus mingling with peridotite during decompression and deformation. The least deformed samples were shown to contain less peridotitic components. Together with the preservation of primary textures (i.e., ad-cumulate-like), they can therefore be used to constrain their 'pre-metamorphic' origin.

The origin of the grt websterites

Pyroxenite xenoliths found with continental intraplate volcanism can, on the one hand, represent crystal segregates (i.e., cumulates) of

alkaline melts, either cognate to their host lava or related to earlier magmatic activity, but in the same tectonic setting. Alternatively, they may be the result of earlier magmatism in other geodynamic settings. Among these, there are several mantle-rock suites (both exhumed massifs and xenolith occurrences) containing mafic rocks with clear affinities to calc-alkaline magmas formed in supra-subduction zone settings. These are, on the one hand, massif, medium- to high-pressure pyroxenitic cumulates formed in magma chambers within the lower crust and/or at the crust-mantle boundary (e.g., DeBari & Coleman, 1989, Pearson *et al.*, 1993; Santos *et al.*, 2002; Ulianov *et al.*, 2006). On the other hand, there are also several studies reporting mantle-derived pyroxenite testifying to melt-rock reaction and veining of the mantle in convergent tectonic settings, e.g., in a supra-subduction zone mantle wedge (e.g., McInnes *et al.*, 2001; Zanetti *et al.*, 1999; Brooker *et al.*, 2004; Berly *et al.*, 2006). In the context of the Tertiary-Quaternary Afro-Arabian rift system, evidence for ancient (Pan-African) mantle magmatism/metasomatism in a convergent tectonic regime comes from mafic xenoliths (granulites and pyroxenites) from the Chyulu Hills (Ulianov & Kalt, 2005; Ulianov *et al.*, 2006), as well as from mantle websterites exhumed at Zabargad (Brooker *et al.*, 2002). Both cases represent old features not directly related to the Tertiary-Quaternary continental rifting and intraplate magmatism.

Group V grt websterites are all, even the least deformed samples, characterised by high Mg-numbers (>80 in calculated bulk rocks; see Table 5.4) and show depleted REE patterns (Fig. 5.15). These features, along with ad-cumulate-like textures in the least deformed samples (Fig. 5.1a), are entirely in line with crystal segregates or cumulates. With respect to the geodynamic evolution of east Africa, Group V grt websterites thus most likely represent 'meta-cumulate' rocks either crystallised from melts either formed in a convergent setting during t Pan-African times, or from mantle melts formed in the context of the 'continental' evolution of the lithosphere, including multiple rifting events from Mesozoic times until present days.

Information on the compositional nature of the melt(s) parental to the Group V grt websterites would allow to constrain the tectonic setting in which the pyroxenites crystallised. However, the composition of the liquidus phase(s), required to calculate precisely the parental melts, was modified and partly obliterated during recrystallisation and partial re-equilibration at lower pressure and temperature (see Figs. 5.11). On the other hand, the least deformed sample Ke 784/1 preserves compositional and textural features pointing to the nature of the initial melt. In the following, we show that sample Ke 784/1 provides evidence to have crystallised not from an alkaline but from an opx-saturated, relatively H_2O-rich melt. Such cumulates are not typical for a continental rift environment. This, together with their metamorphic evolution suggesting that they formed prior to rifting, leads to the hypothesis that the Marsabit grt websterites could have formed as veins in the lithospheric mantle during accretion events in Pan-African times.

The primary crystallisation sequence of sample Ke 784/1 – constraints on the parental melt

Cpx-I, opx-I and partly grt in sample Ke 784/1 preserve crystal shapes similar to ad-cumulates. Among these minerals, clinopyroxene is a liquidus phase in all basaltic liquids crystallising at high pressures [e.g., Green & Ringwood, 1967; Yoder & Tilley, 1968; Kushiro et al., 1972; Mysen & Boettcher, 1975, and many others (e.g., Ulmer, 2001 or Kogiso *et al.*, 2004 for more complete reference lists)]. Olivine would appear even earlier, however, judging from the lack of any spl-opx-cpx symplectite (Fig. 5.1a) it can be supposed that sample Ke 784/1 contained no magmatic olivine.

Garnet can either be a cumulus phase or may form at sub-solidus conditions (exsolving from clinopyroxene, for example; see Fabriès *et al.*, 2001 or Ulianov & Kalt, 2005, for example).

Although garnet compositions indicate mutual sub-solidus re-equilibration with cpx-I (see Fig. 5.11), its high HREE concentrations (Fig. 5.6) and its high modal abundance (Table 5.4), as well as partly preserved subhedral crystal shapes (Fig. 5.1a) suggest formation as a cumulus phase. Crystallisation of garnet from basaltic liquids is restricted to high pressure (>1.0-3.0 GPa depending on the bulk composition; see Kogiso *et al.*, 2004 and references therein). Such conditions would be in line with crystallisation at conditions corresponding to the HP/HT stage (Fig. 5.16).

The cores of garnet contain variable amounts of primary cpx-I, kaersutite, rutile and rare orthopyroxene inclusions which are critical for constraining the primary liquid. It should be emphasised that almost all of them (except rutile) are unlikely or even impossible to explain by sub-solidus exsolution processes. Orthopyroxene exsolution, for example, would imply an earlier ultrahigh-pressure stage (majoritic garnet), for which we do not have any indication. Moreover, amphibole exsolution is probably impossible, given the low Na_2O in mantle-derived garnet.

The nature of the parental melt (i.e., SiO_2 and H_2O contents), in fact, strongly depends on how the appearance of orthopyroxene and kaersutite are interpreted. Both minerals also occur texturally similar to cpx-I (i.e., porphyroclasts in more deformed samples), outside of garnet. There, however, it is difficult to conclude whether they are former cumulus phases or whether they grew in the sub-solidus regime, i.e. from late-stage magmatic fluids in the case of amphibole (e.g., Fabriès *et al.,* 2001), or exsolved from initially Ca-poor clinopyroxene in the case of orthopyroxene. The fact that both, amphibole and orthopyroxene occur as inclusions in garnet clearly indicate that both minerals crystallised earlier or contemporaneously with garnet from the parental melt. Consequently the melt – at the time of garnet crystallisation – was Si-rich (opx-saturated) and contained about 4 wt% H_2O (to stabilise amphibole). Based on the garnet inclusions, we prefer to interpret texturally equilibrated kaersutite (amph-i) and opx-I outside of garnet to represent magmatic phases as well. The same probably holds true for texturally equilibrated phlogopite (Fig. 5.2a). Neither replacement textures nor geochemical arguments (e.g., incompatible element enrichment in other minerals) indicate a later metasomatic origin.

Finally, the occurrence of Ti oxides has to be considered as well. Rutile mantled by ilmenite (Fig. 5.2f) is a clear indication for decreasing pressures. This suggests that rutile already existed at the HP/HT stage (prior to decompression), and possibly crystallised as magmatic phase. The co-existence of rutile and Ti-rich phlogopite points to Ti saturation in the initial melt.

Rutile needles in garnet are often explained as exsolution products, mainly based on their appearance oriented along the isometric garnet crystal lattice (e.g., Roden *et al.*, 2006). Notwithstanding, they could be co-magmatic with garnet as well, simply coating the isomorphic faces of a growing garnet crystal. Support for this hypothesis comes from the fact that rutile forms also composite inclusions with kaersutite (Fig. 5.2e). The latter cannot exsolve from garnet (see above).

Concluding from the above descriptions, the crystallisation sequence of xenolith Ke 784/1 is either cpx → (opx, amph, phl, rutile) → garnet or cpx → (grt, opx, amph, phl, rutile). It might be argued that the grt websterites crystallised from more residual melts, e.g., evolved from Si-undersaturated liquids that fractionated olivine as an early crystallising phase. This is however unlikely, as in such a case stronger incompatible trace element enrichment and higher alkali contents, even in cumulates, would be expected (i.e. trends towards alkali pyroxenites or ijolite series rocks). The solidus temperature of basaltic melts with some H_2O (i.e., H_2O undersaturated conditions), required to account for kaersutite to crystallise earlier than or contemporaneously with garnet, is at about 1000-1100°C (at ~2.0 GPa; e.g., Niida & Green, 1999; Ulmer, 2001, and references therein). The presence of garnet and co-existence of amphibole and phlogopite

are 'high-pressure indicators', in line with crystallising depths ≥ 60 km (i.e., 2.0 GPa) in agreement with emplacement conditions in the range of the high-pressure / high-temperature stage (~970-1100 °C at ~2.3-2.6 GPa; Fig. 5.16).

The opx/cpx ratio during high-pressure fractionation of opx-saturated liquids (websterite crystallisation) decreases with decreasing temperature and/or increasing H_2O content in the melt (Müntener *et al.*, 2001). In their experiments, Müntener *et al.* (2001) found grt pyroxenite (with 4.9 wt% opx) to crystallise at 1110°C and amph-bearing grt pyroxenite (8.8 wt% opx; 8.9 wt% amph) at 1070°C (in both cases at 1.2 GPa with ~5 wt% H_2O in the melt). Similar phase proportions and thermal conditions (but higher pressures; see Fig. 5.16) are obtained for the Marsabit grt websterites and define the HP/HT stage preserved in the Marsabit lithosphere. This stage corresponds probably well to the *P-T* conditions to which the melts cooled during intrusion and crystallised the Marsabit grt websterites.

Mantle pyroxenite formation in an ancient (Pan-African) supra-subduction zone setting?

The opx-saturated nature of melts parental to the Marsabit grt websterites (tholeiitic or calc-alkaline) is in good agreement with their metamorphic history that indicates emplacement prior to continental rifting and intraplate alkaline magmatism. In this context, a relation to ancient, Pan-African, convergent tectonic events are at least plausible. The crustal basement of the Marsabit volcanic field consists mostly of Precambrian rocks (the Mozambique mobile belt) recording polymetamorphic events resulting from multiple Pan-African accretion events (e.g., Key *et al.*, 1989; Nyamai *et al.*, 2003). The preservation of rocks in the lithospheric mantle recording the same events would be the logical consequence.

In (sub)-recent examples of such convergent tectonic settings, pyroxenite is typically observed in subduction-zone related magmatic rock suites, e.g., forming massif bodies representing mafic cumulates in lower crustal to uppermost mantle levels beneath island arcs (e.g., DeBari & Coleman, 1989; Spandler *et al.*, 2003; Berly *et al.*, 2006). Alternatively, pyroxenites may occur as dykes in the supra-subduction zone mantle (McInnes *et al.*, 2001; Zanetti *et al.*, 1999; Brooker *et al.*, 2004; Berly *et al.*, 2006).

In the present case, calculated bulk rock major and trace element compositions, as well as the clinopyroxene classification are fairly distinct to typical island arc cumulates (Fig. 5.14a), thus arguing more in favour of an ancient Pan-African veined lithospheric mantle. On the basis of only one sample studied in detail, and keeping the complex modifying processes in mind (i.e., melt-rock reaction and later metamorphism), we have no conclusive evidence clearly favouring whether the parental melts were related to a subduction-zone (e.g., island arc) or to another setting in a convergent regime (e.g., back-arc spreading).

DISCUSSION II: ORIGIN AND EVOLUTION OF THE GRT-FREE PYROXENITES

Grt-free pyroxenites: cumulates from alkaline melts

The mineralogy and textures of the Group VI pyroxenites, dominated by olivine and clinopyroxene, are very similar to mafic xenoliths described from numerous xenoliths occurrences in intraplate alkaline magmatic settings (Wilshire & Shervais, 1975; Frey, 1980; Irving, 1974a and b, 1980; Griffin *et al.*, 1988; Wilkinson & Stolz, 1997). These rocks are typically interpreted in terms of cumulates or crystal segregates precipitated from alkaline melts at depths and may be cognate to their host lava (Irving & Frey, 1984). A similar origin is indicated for Group VI pyroxenites by the trace element signature of cpx-I from xenolith Ke 782/2 exhibiting a convex-upward REE pattern. This signature is typical for

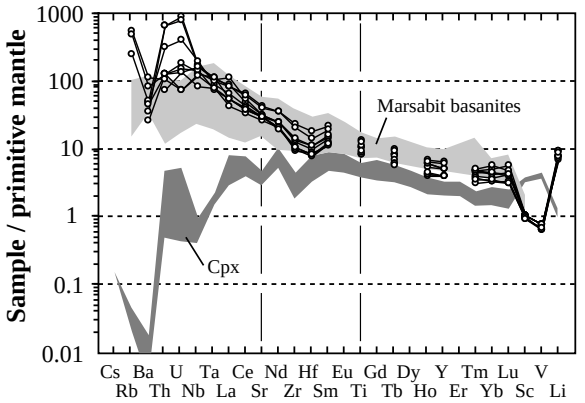


Fig. 5.18: *Calculated melts in equilibrium with clinopyroxene (cpx) from the Group VI spl-ol websterite xenoliths compared to the trace element composition of Quaternary basanites from Marsabit (Volker, 1990). Cpx/basanite melt partition coefficients from Adam & Green (2006): run R79 (1075°C at 1.0 GPa). Normalising values (primitive mantle) from McDonough & Sun (1995).*

intraplate alkaline magmas and their clinopyroxene and amphibole megacrysts (Irving & Frey, 1984, Shaw & Eyzaguirre, 2000; Downes *et al.*, 2004). Trace element patterns of calculated melts in equilibrium with cpx-I of sample Ke 782/2 are closely similar to the Quaternary Marsabit basanites (Fig. 5.18), suggesting that this sample formed at least during the same magmatic episode. The lack of any volatile-bearing phases in all Group VI pyroxenites compared to the generally volatile-rich character of alkaline melts strongly argues in favour of cumulates and against a completely crystallised melt.

The occurrence of orthopyroxene is restricted to the two samples (Ke 782/1 and 782/2) characterised by sub-solidus and deformation-related textures (i.e. exsolution lamellae in cpx-I of Ke 782/2 and porphyroclastic fabric of Ke 782/1). Further, opx-I in sample Ke 782/2 occurs exclusively as small irregular grains in interstices between large cpx-I grains. These textural features point to a sub-solidus origin of orthopyroxene in the grt-free pyroxenites, e.g., exsolved from clinopyroxene during cooling. This is in agreement with an alkaline parental melts undersaturated in orthopyroxene and/or with relatively low pressure (i.e., <2.5 GPa) where olivine replaces orthopyroxene as a liquidus phase (e.g., Adam, 1990; Adam & Green, 2006). Spinel developed similar grain shapes as orthopyroxene in similar textural positions and was also observed as exsolution lamellae in sample Ke 782/2. This type of spinel is thus possibly of sub-solidus origin as well. In contrast, spinel in sample Ke 726 forms large, subhedral grains, pointing towards a magmatic origin. This is in agreement with megacryst studies which indicate that spinel is a typical cumulus phase from alkaline melts (O'Reilly & Griffin, 1987; Wilkinson & Stolz, 1997).

The lack of feldspar and garnet allows confining the pressure to be in between ~0.9 GPa (no plagioclase) and 1.3-1.7 GPa (no garnet; Irving, 1974b; Hirschmann & Stolper, 1996). These estimates are in the range of maximum pressure calculations (1.4-1.7 GPa; based on the Cr contents in spinels of sample Ke 726, 782/1 and 782/2 using the calibration of Carroll Webb & Wood, 1987). Temperature estimates were only obtained for the sub-solidus stage using $T_{2Px\text{-}BK90}$ based orthopyroxene and clinopyroxene pairs. The results indicate partial re-equilibration and opx exsolution at about 1015 ± 70 °C and 1022 ± 68 °C (at 1.2 GPa for samples Ke 782/2 and 782/1, respectively). The presence of orthopyroxene and spinel exsolution lamellae in cpx-I from sample Ke 782/2 indicates somewhat higher earlier temperatures (i.e., corresponding to the magmatic crystallisation). This *P-T* evolution – cooling from crystallisation temperatures to ~950-1100°C at pressures between 0.9-1.7 GPa – is similar to other pyroxenite xenoliths entrained by intraplate alkaline magma (Wilkinson & Stolz, 1997).

Out of the four studied Group VI xenoliths, three show sub-solidus features (orthopyroxene and spinel exsolution, recrystallisation and kink-bands in olivine; Fig. 5.4a, c and d) indicating that they are not cognate to their host lava. The occurrence of deformed cumulates from alkaline melts can be explained by the long-time mag-

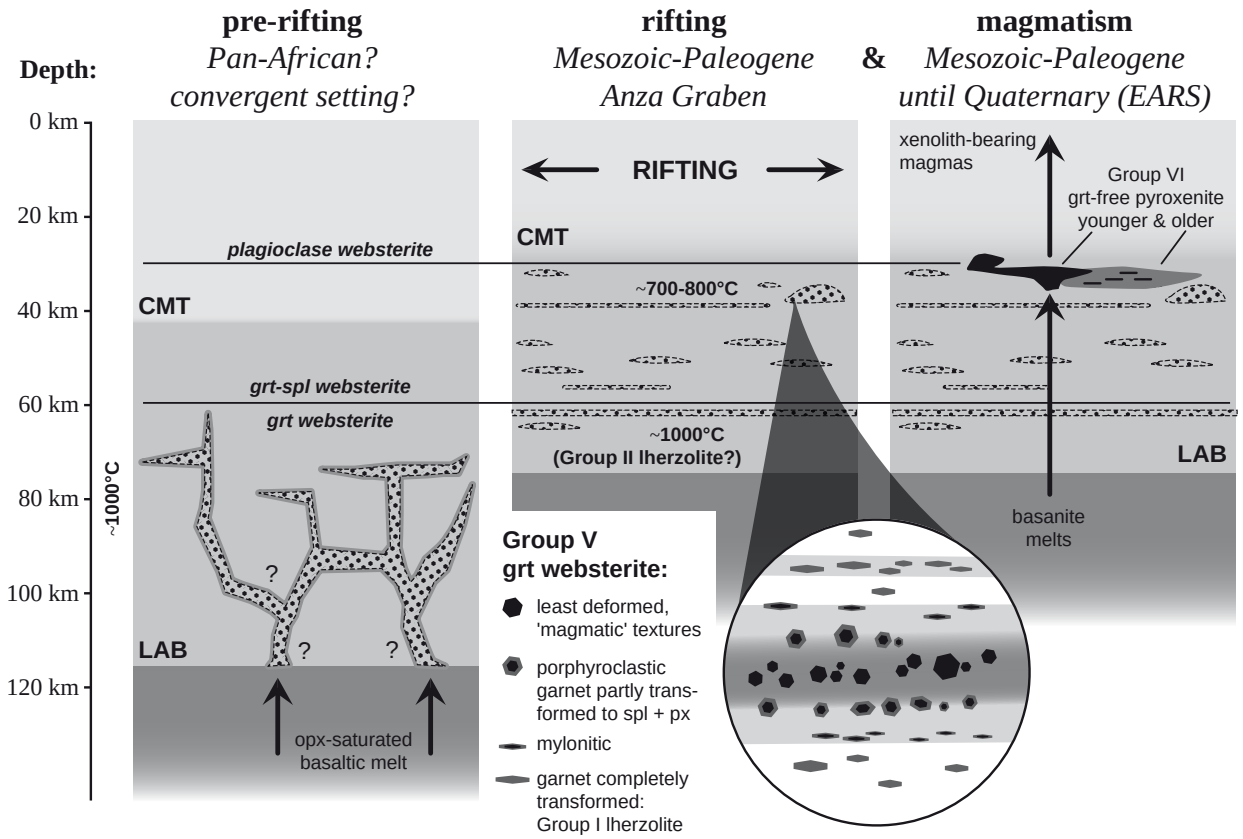


Fig. 5.19: *Cartoon illustrating the two magmatic events resulting in the formation of Group V and VI pyroxenites. LAB = lithosphere-asthenosphere; CMT = crust-mantle transition (depths from Henjes-Kunst & Altherr, 1992). The pre-rift stage* ***(a)*** *corresponds to the present-day thermal stage beneath the Chyulu Hills (southern Kenya; Henjes-Kunst & Altherr, 1992); Temperature estimates as in Fig. 5.16. Phase transitions in websterite after Hirschmann & Stolper (1996; grt-spl) and Irving (1974b; spl-plagioclase). For further explanations see text.*

matic activity in the region of Marsabit, starting in Mesozoic-Paleogene times (i.e., diabase intrusion associated with the development of the Anza Graben; Winn *et al.*, 1993; Morley *et al.*, 2006c), until the development of the Marsabit shield volcano. The xenolith-bearing basanites and alkali basalts represent the youngest volcanic products (1.8-0.5 Myr; Brotzu *et al.*, 1984; Key *et al.*, 1987) and thus potentially sampled mafic lithologies accumulated earlier. This explanation is supported by seismic evidence which confirms the presence of mafic material at the lowermost crust beneath the rift flanks of the Kenya Rift (Mechie *et al.*, 1997).

SUMMARY

Textures and compositional features of pyroxenite xenoliths suggest two magmatic events adding mafic material to the lithospheric mantle beneath Marsabit. Pyroxenite emplacement and later modification could be summarised by four evolutionary stages (see Fig. 5.19):

1) Basaltic melts intrude the thick sub-continental lithospheric mantle (at depths > 60 km) prior to the onset of Mesozoic-Paleogene continental rifting. High-pressure fractional crystallisation and melt-peridotite interaction during cooling from magmatic to the ambient mantle

temperatures (the HP/HT stage) presumably resulted in a veined mantle made of peridotite and grt websterite.

The melts were opx-saturated and most likely tholeiitic or calc-alkaline in composition. They possibly formed in a convergent tectonic setting, i.e., during the East African orogenesis in Pan-African times.

2) Onset of continental rifting leads to the formation of the Anza Graben and to thinning (uplift) of the lithospheric mantle. Rifting was accompanied by cooling and pervasive deformation affecting both peridotite and grt websterite. Given the rheological contrast between peridotite and pyroxenite, the latter may have undergone boudinage. Disruption of grt websterite and chemical re-equilibration led to mechanical, sub-solidus mingling between peridotite and pyroxenite.

3) Multiple continental rifting events were accompanied by magmatic activity (Mesozoic? until present days). Throughout this period, presumably multiple episodes of alkaline magma intrusion added mafic material to the lithosphere. Earlier intruded material underwent sub-solidus modification by ongoing rifting (related to the Anza Graben and onset of EARS-related rifting), whereas young material prevented modification. Tertiary-Quaternary magmas finally sampled xenoliths of all types of mafic rocks and transported them to the surface.

Chapter 6: An Analcime-bearing Olivine Gabbro Xenolith from Marsabit (northern Kenya): Evidence for Alkalic Crustal Intrusions?

Benjamin Kaeser[1]

[1] Institut de Géologie et d'Hydrogéologie, Université de Neuchâtel, Rue Emile-Argand 11, CH-2009 Neuchâtel, Switzerland

ABSTRACT

The xenolith collection from the Marsabit volcanic field includes a single olivine gabbro xenolith. The sample is characterised by an igneous ophitic-intersertal fabric. Major minerals are (with decreasing abundance): euhedral plagioclase (An52.4-40.4 with anorthoclase-orthoclase rich rims), intergrown with subhedral-skeletal clinopyroxene (diopside-hedenbergite), euhedral (partially altered) olivine (~Fo50), and interstitial anhedral ilmenite (Ti-poor ilmenite exsolved into Ti-rich ilmenite and Ti-rich hematite). Interstices between all minerals are filled by (partly altered) analcime associated with euhedral apatite.

Compositional zoning of minerals is in line with differentiation of a magma during *in-situ* crystallisation. Textures indicate a crystallisation sequence typical for basaltic liquids with olivine and plagioclase representing the earliest crystallising phases, followed by (or contemporaneously with) clinopyroxene crystallisation. Ilmenite and apatite are late crystallising phases. Analcime most likely crystallised as a late stage mineral, or formed at the expense of nepheline (which is not preserved, however). The presence of analcime indicates that the parental melts were probably alkalic. The occurrence of gabbro xenoliths could indicate the presence of alkalic plutonic bodies in the crust beneath Marsabit.

INTRODUCTION

This is a short complementary chapter on the mineralogy and composition of a single olivine gabbro xenolith (sample Ke 772/2) from Marsabit (Group VII xenoliths according to the classification in the previous chapters). The xenolith is characterised by remarkably fresh igneous textures. The phase assemblage and composition of minerals are similar to gabbro xenoliths from Hawaii, interpreted to represent plutonic crustal intrusions of alkalic to transitional basaltic magma. A similar origin is proposed for the Marsabit gabbro.

TEXTURES

The main minerals in the unique gabbro xenolith are olivine (eu- to subhedral; partly iddingsitised), euhedral, elongated feldspar crystals, surrounded by irregular, optically zoned, brownish clinopyroxene (cpx-I) and interstitial ilmenite (Fig. 6.1a-d). Tiny spinel crystals are rarely observed in association with olivine. The texture of the rock is subophitic to intersertal (Vernon, 2004), devoid of deformation- and recrystallisation-related features. Plagioclase crystals are further surrounded by irregular selvages of analcime containing abundant euhedral inclusions of apatite and a rare REE-Ti-rich silicate (titanite?). Larger analcime crystals (containing apatite needles; Fig. 6.1b) occur interstitial between plagioclase laths. Analcime is commonly partially replaced by zeolites (chabacite) and spherulitic alteration products (nanoscopic mixtures of carbonate and silicates); however, fresh domains occur (Fig. 6.1b).

BSE-imaging reveals that ilmenite grains consist of tight lamellar aggregates of more Fe-rich and Fe-poor compositions (Fig. 6.1b). At analcime-ilmenite interfaces, symplectitic intergrowths between these two minerals are observed. Similar intergrowths occur between ilmenite and apatite, especially at contacts with clinopyroxene.

MINERAL COMPOSITION

Representative analyses of the minerals are given in the Appendices volume of this thesis (Appendix A3). Zoning profiles across clinopyroxene, olivine and plagioclase are illustrated in Figs. 6.2, 6.3 and 6.4, respectively.

Clinopyroxene

The gabbro xenolith contains clinopyroxene showing either symmetric (Fig. 6.2a) or sector zoning (Fig. 6.2b). Mineral cores are of augitic composition (Morimoto, 1988) grading into more Ti-augite-rich rims. The cores are relatively primitive, i.e., characterised by high Mg-numbers and elevated Cr_2O_3 contents. Rims show more evolved compositions (enriched in FeO, MnO, and Na_2O, with variable TiO_2 and Al_2O_3 contents). The rims of some grains grade into Ti- and Al-depleted and Na- and Mn-enriched ferroaugite (e.g., right side of the profile depicted in Fig. 6.2b).

Olivine and spinel

Ol-I in the gabbro xenolith is Fe-rich (Mg-numbers = 49.8-47.9) and contains elevated CaO (0.31-0.35 wt%) and MnO contents (0.66-0.77 wt%). NiO contents are low (0.01-0.08 wt%). Mg-numbers decrease towards rims, whereas Mn contents increase (Fig. 6.3), which is consistent with magmatic differentiation.

Accessory spinel corresponds to a titanian chromite with low MgO and Al_2O_3 contents. It contains considerable magnetite (0.19 Mol%) and ulvöspinel components (0.20 Mol%).

Feldspar, analcime and zeolite

Feldspar crystals in the gabbro xenolith show strong compositional zoning (Fig. 6.4). Mineral cores consist of andesine (An52.4-40.4), grading into oligoclase- and anorthoclase-rich rims (Fig. 6.4). The outermost rims occasionally con-

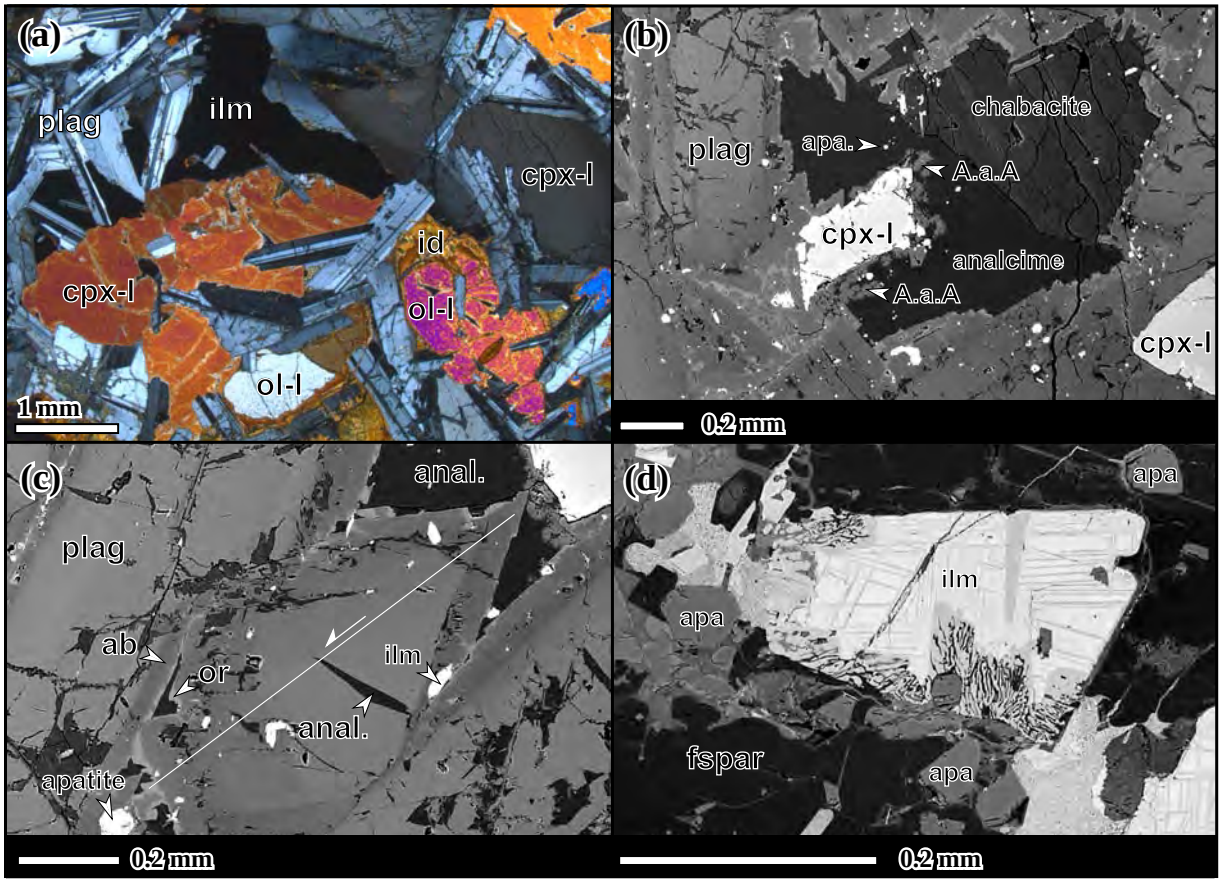


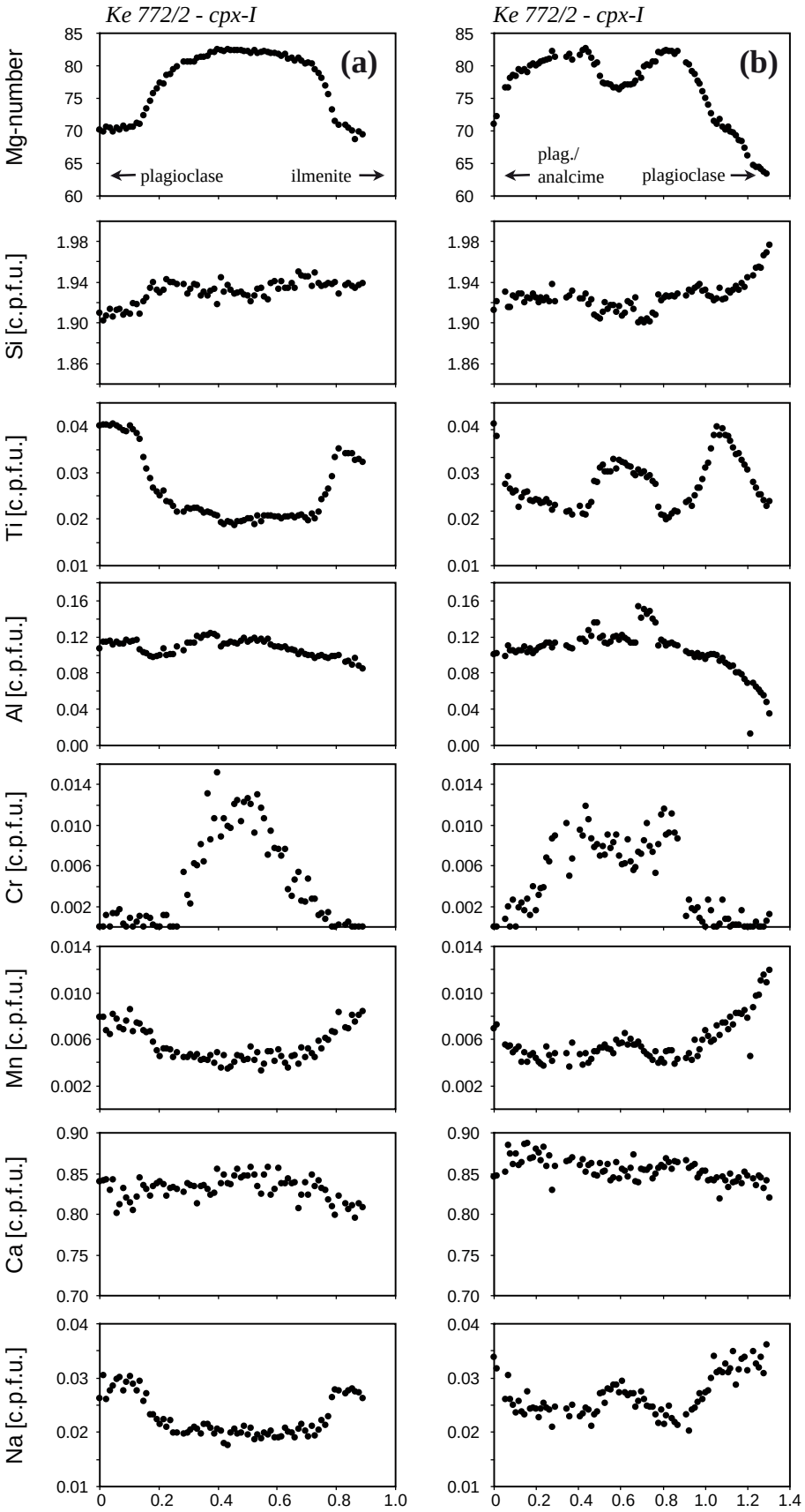
Fig. 6.1: *Photomicrographs (a; crossed polarisers) and BSE images showing textural aspects of the unique ol gabbro xenolith (sample Ke 772/2).* ***(a)*** *Ophitic to intersertal fabric made of plagioclase (plag), olivine (ol-I), clinopyroxene (cpx-I) and ilmenite (ilm). Note optically zoned cpx-I and red-brown iddingsite (id) replacing olivine (photomicrograph; crossed polarisers);* ***(b)*** *analcime and chabacite interstitial between plagioclase and clinopyroxene. A.a.A. = 'alteration after analcime' (microcrystalline carbonates and silicates). Note primary inclusions in analcime (white dots) representing sections of apatite needles;* ***(c)*** *euhedral, compositionally zone feldspar (plag: plagioclase; ab: albite-rich; or; almost pure orthoclase). The white line corresponds to the microprobe profile depicted in Fig. 6.4;* ***(d)*** *primary ilmenite (ilm) exsolved in ilmenite (white) + Ti-rich hematite (light grey). Note symplectitic intergrowth between hematite and analcime or apatite. The fine-grained bright material are alteration products after analcime and ilmenite, composed of carbonates, Fe-(hydr)oxides and (phyllo?)silicates.*

sist of almost pure orthoclase. Ti, $Fe_{(tot)}$ and Mg contents decrease significantly from cores to rims (Fig. 6.4).

Analcime shows a homogeneous composition characterised by very low CaO and K_2O contents. Si/Al ratios range from 1.99-2.09 indicating compositions close to 'ideal' analcime ($NaAlSi_2O_6 \cdot H_2O$) and only limited NaAl ↔ Si substitution. The composition of zeolite occasionally occurring together with analcime corresponds broadly to a chabacite ($Ca_2Al_4Si_8O_{24} \cdot 12H_2O$) with small amounts of Na and K substituting for Ca and Al for Si.

Fe-Ti oxides

The gabbro xenolith contains exsolved Fe-Ti oxide grains composed of ilmenite and ilmenite-rich hematite lamellae. Re-integration of the respective lamellae proportions yields an original ilmenite composition with approximately ~40 wt% TiO_2. MgO contents are low (~1.2 wt%).


Ke 772/2 - cpx-I
(a)
plagioclase
ilmenite
Ke 772/2 - cpx-I
(b)
plag./
analcime
plagioclase
Mg-number
Si [c.p.f.u.]
Ti [c.p.f.u.]
Al [c.p.f.u.]
Cr [c.p.f.u.]
Mn [c.p.f.u.]
Ca [c.p.f.u.]
Na [c.p.f.u.]

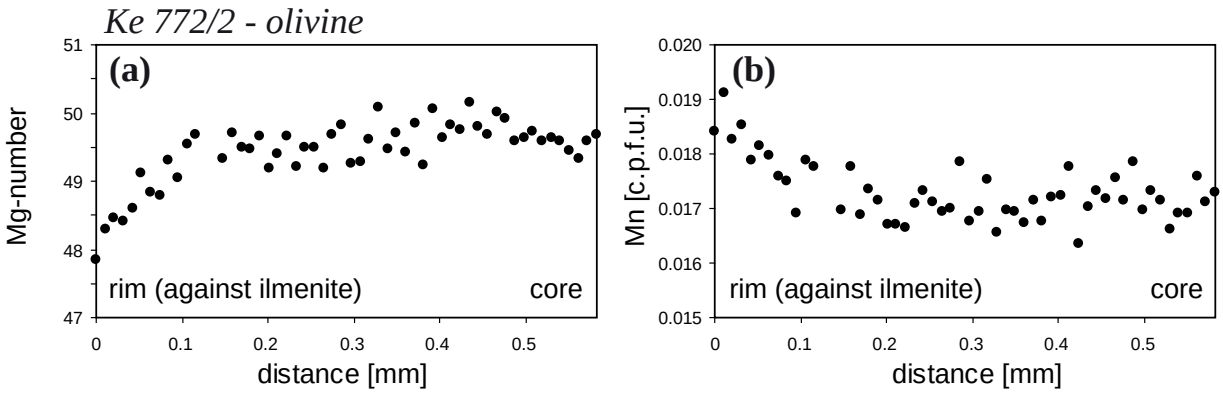
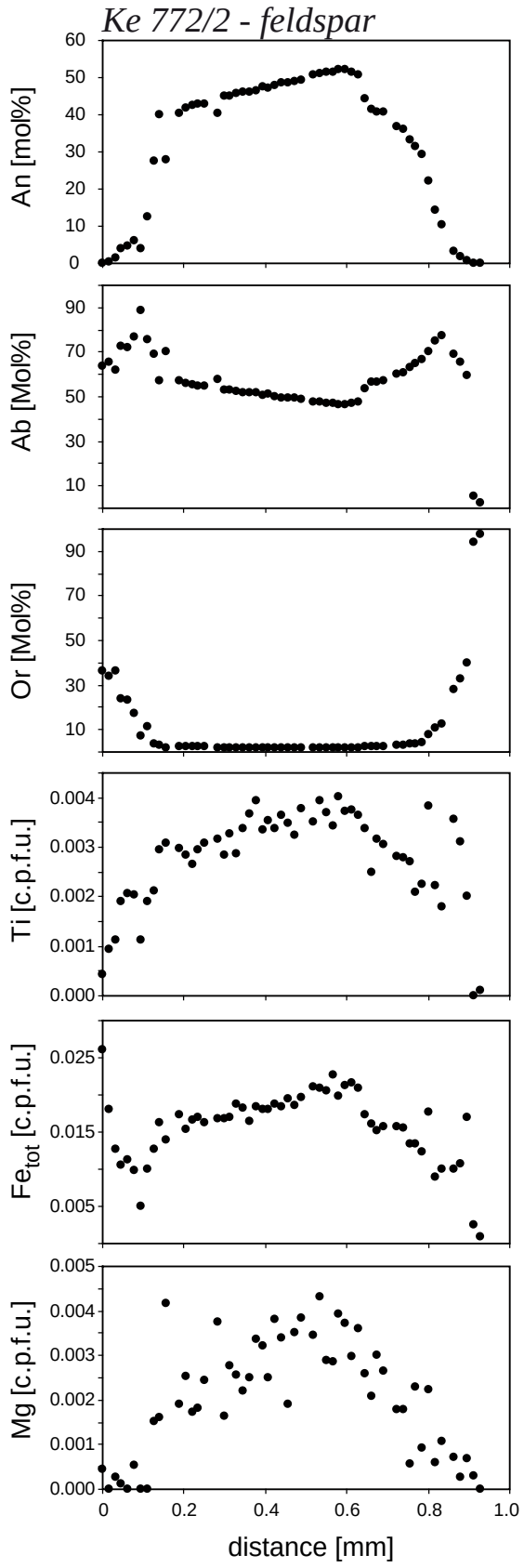


Fig. 6.3: *Mg-number [Mg/(Mg+Fe^{tot})] and Mn zoning pattern in olivine from ol gabbro Ke 772/2.*

Group VII gabbro – crystallised, slightly evolved alkali basaltic melt

The perfect subophitic-intersertal microtexture, together with the lack of deformation-related features, suggests a plutonic origin, most likely related to the Tertiary-Quaternary magmatic activity in Marsabit. Subophitic fabrics and the presence of interstitial minerals such as ilmenite and apatite can be explained by *in-situ* crystallisation of a cooling melt. Idiomorphic olivine and plagioclase, surrounded by clinopyroxene and interstitial ilmenite suggest a crystallisation sequence such as (ol+plag) → cpx → ilm, which is the typical sequence observed in basalt crystallisation experiments, with ilmenite appearing as the latest crystallising phase at about 1105 ± 5 °C (Thy & Lofgren, 1994). Alternatively, ophitic textures between plagioclase and clinopyroxene have been demonstrated experimentally to develop by simultaneous crystallisation with higher nucleation rates for plagioclase than for clinopyroxene (Lofgren, 1983). *In-situ* crystallisation and differentiation is in line with the compositional zoning of olivine, plagioclase and clinopyroxene, which are all characterised by relatively 'primitive' core compositions and more evolved mineral rims (i.e., Mg-numbers and MnO in olivine, Mg-numbers, Cr_2O_3, and Na_2O in clinopyroxene, and anorthite or orthoclase components in feldspars). Strongly decreasing TiO_2 and increasing SiO_2 towards rims of some clinopyroxene crystals could be explained by the appearance of ilmenite as late crystallising phase, which would lead to strong Si-enrichment and Ti-depletion in the residual melt (Thy & Lofgren, 1994). Such residual liquids would also become enriched in phosphorous and volatiles, allowing to crystallise apatite, and even analcime. The latter can coexist with Si-undersaturated melts at temperatures between 600 and 640 °C (P = 0.5-1.3 GPa; Wilkinson & Hensel, 1994 and references therein). Further cooling from magmatic temperatures is indicated by exsolution of primary ilmenite into Ti-enriched ilmenite and hematite (Fig. 6.1d). Euhedral apatite needles included in analcime further support a magmatic origin of analcime. Alternatively, analcime may form as devitrification product of glass or derive form former nepheline by low-temperature sub-solidus reaction involving hydrothermal fluids (Wilkinson & Hensel, 1994). The structure-less and 'pure'

Fig. 6.2: *Electron microprobe traverses across two clinopyroxene grains in the ol gabbro (Ke 772/2) showing almost symmetrical zoning* ***(a)*** *and sector zoning* ***(b)****; Mg-numbers = 100*Mg/(Mg+Fe^{tot}); c.p.f.u. = cations per formula unit. Arrows indicate adjacent phases.*



aspect of analcime argues against a devitrification product. An argument for former nepheline could be the relatively high SiO_2 contents in analcime (54.18-56.13 wt%; compared to ~51 wt% of high-temperature analcime; Wilkinson & Hensel, 1994).

Due to strong compositional zoning of minerals, the bulk rock composition cannot be estimated accurately. However, considering the composition of plagioclase and olivine cores indicates a relatively evolved nature of the parental melt (i.e. Mg/Fe of about 0.30-0.36 using a $K_D^{ol/melt}$ of 0.30-0.35; Roeder & Emslie, 1970). The mineral assemblage and compositions are similar to leucocratic slightly alkalic to tholeiitic gabbro xenoliths from Hawaii (Shamberger & Hammer, 2006, and references therein). These xenoliths, however, commonly contain orthopyroxene. The lack of this phase in the Marsabit ol gabbro, as well as magmatic analcime (or the former presence of nepheline), supports rather an alkaline parental melt.

The presence of plagioclase suggests crystallisation pressures of less than ~0.9 GPa (Irving, 1974b), which favours a crustal origin. It can be speculated that evolved alkaline melts crystallised small plutonic bodies within the crust beneath the Marsabit shield volcano, similar to models invoked for the Hawaiian gabbros (Shamberger & Hammer, 2006).

Fig. 6.4: *Electron microprobe traverse across a euhedral feldspar grain in ol gabbro Ke 772/2 (see textural context in Fig. 6.1c). An = anorthite, Ab = albite, Or = orthoclase.*

Chapter 7:

Summary, Conclusions

and

Outlook

SUMMARY AND CONCLUSIONS

The results of the previous 5 chapters led to the recognition of different evolutionary stages recorded in mantle xenoliths from Marsabit. A summary of the different events and the relationship between the different xenolith types is given in Fig. 7.1.

Four major objectives were defined in the introduction to this work: (1) to characterise the nature and compositional heterogeneity of the lithosphere underlying Marsabit with respect to major and trace elements; (2) to constrain the evolution of the lithospheric mantle beneath Marsabit in the *P-T-X* space; (3) to characterise metasomatic events which modified this lithosphere; and (4) to get temporal information of the different events, wherever possible. The major conclusions on these topics are as follows:

Mineralogical composition of the lithospheric mantle beneath Marsabit - The nature of the lithospheric mantle beneath the Marsabit volcanic field was constrained by detailed petrographic and geochemical investigation of mantle xenoliths. The results show that the mantle is strongly heterogeneous. It comprises the entire spectrum of peridotite ranging from clinopyroxene-rich lherzolite to dunite, associated with considerable amounts of mafic rocks. Structurally, two domains were identified:

a) strongly deformed (tectonised) lherzolite to dunite ranging from fertile to depleted (with respect to major elements), associated with metamorphosed garnet websterite and igneous garnet-free pyroxenite and gabbro. The deformed mantle domain represents (at present-day) the uppermost lithosphere (depths less than 30 km) that recorded partial re-equilibration at low temperatures (~750-850°C).
b) relatively fertile granular recrystallised lherzolite associated with minor granular garnet websterite and with peridotite specimens showing textural features transitional between domain a) and b). The strongly recrystallised lherzolites are partly to completely equilibrated at high temperatures (950-1100°C) and interacted to variable degrees with mafic silicate melt (cryptic metasomatism characterised by Fe-Ti enrichment and/or U-Th-LREE enrichment).

Textures and compositions of the deformed xenoliths (domain a) seem to be very similar to xenoliths from the Merille volcanics [only data from Suwa *et al.* (1975) available yet] which also sampled the mantle beneath the Anza graben (see Fig. 1.2). The recrystallised and heated xenoliths (domain b), on the other hand are comparable to xenoliths erupted within the Sidamo region (South Ethiopia), which were metasomatised by percolating basaltic melts in the context of EARS-related magmatism. Further, the deformed Marsabit mantle xenoliths are very similar to ultramafic massifs which were up-lifted during rifting in the context of continent-ocean transitions, suggesting a similar tectonic evolution of the lithosphere beneath Marsabit. These processes may still be going on in the context of the N-S propagating EARS, or, much more likely (see below), they occurred during the development of the Anza Graben in Mesozoic times.

Evolution of the lithospheric mantle in the* P-T-X-t *space - Detailed investigation of textures and mineral grains was used to constrain the *P-T-X-t* evolution of the lithospheric mantle beneath Marsabit. Thermobarometric results indicate that the deformed shallow-seated xenoliths were once equilibrated at greater depths and higher temperatures. This former high pressure / high-temperature stage corresponded broadly to the present-day thermal state of the lithospheric mantle beneath the eastern flank of the EARS in southern Kenya (as deduced from xenoliths from the Chyulu Hills), which is more or less characteristic for off-craton, non-rifted

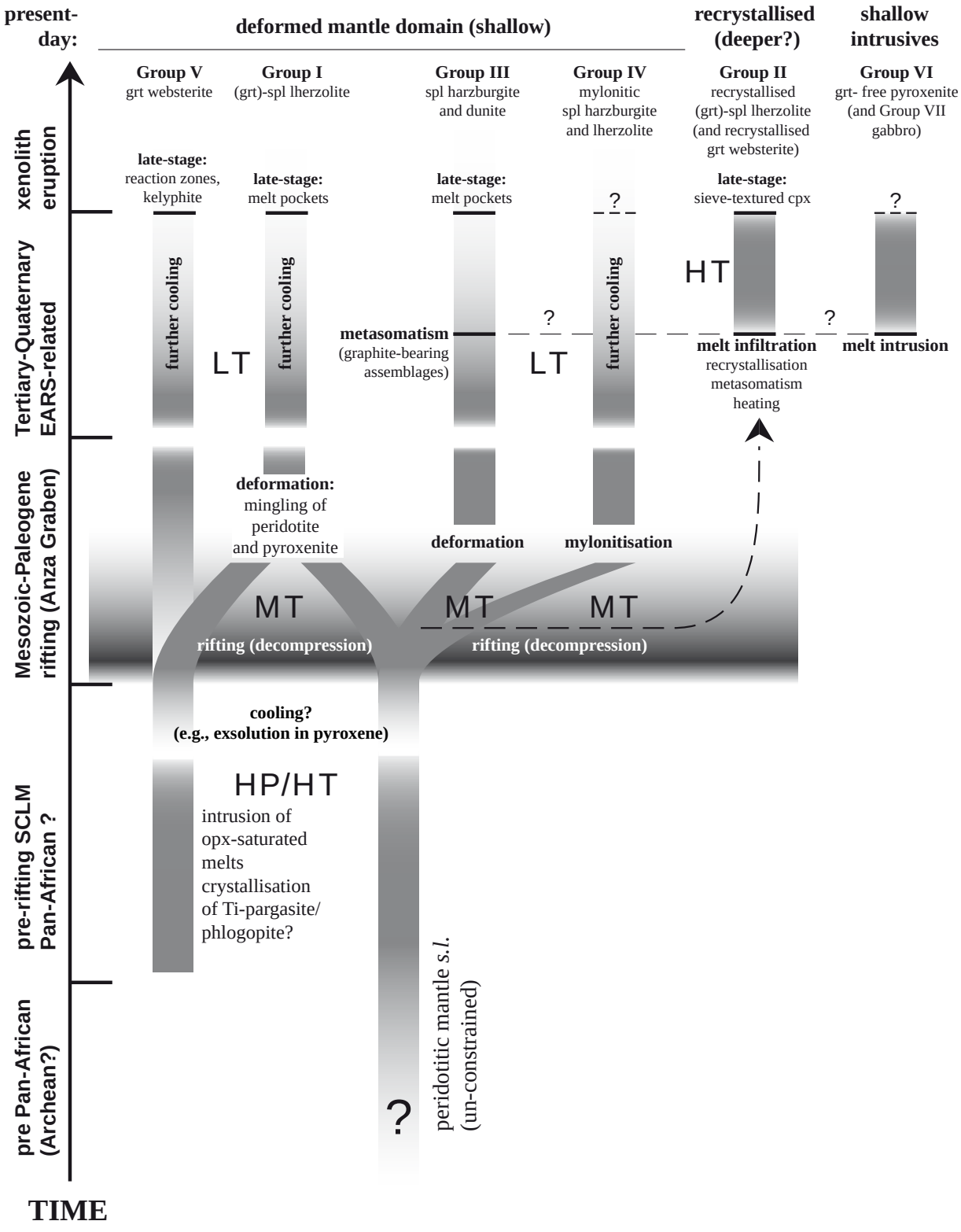


Fig. 7.1. Schematic summary of the results of this thesis: relative chronology of events recorded by the Marsabit xenoliths and relationship between the xenolith types and their record with respect to changing pressure, temperature and composition. HP/HT, MT and LT stages correspond to the high-pressure / high-temperature, medium-temperature and low-temperature stage as defined in Chapter 2. SCLM = Subcontinental Lithospheric Mantle

continental lithosphere. These results confirm in fact the major findings of earlier studies made in the course of this KRISP-related petrological xenolith project (Henjes-Kunst & Altherr, 1992; Olker, 2001; see Chapter 1).

After the high-pressure / high-temperature stage, the Marsabit lithosphere underwent cooling and decompression in the course of lithospheric thinning, accompanied by pervasive deformation. These events led to the formation of the strongly deformed rock fabrics, exsolution features in pyroxenes, and to the complete (lherzolites) and partial (pyroxenites) transformation of garnet into spinel-pyroxene symplectites. At the same time, formerly igneous (cumulate-like) garnet pyroxenite was mechanically mingled with the peridotitic mantle, while both, peridotite and pyroxenite, experienced different degrees of chemical re-equilibration.

An important implication arising from this pyroxenite-peridotite relationship is that probably most of the cpx-rich lherzolites do not represent fertile peridotitic mantle (i.e., that avoided earlier melt extraction), but rather reflects the result of deformation-induced sub-solidus mingling with pyroxenite, ultimately leading to variable degrees of 're-fertilisation'. High initial garnet contents of the lherzolites ('over-fertility') can thus be explained to result from the incorporation of websteritic garnet (i.e., mechanical out-streaking and disruption of websterite layers). Consequently, it cannot be concluded with certainty whether the peridotitic mantle represented by these xenoliths resided in the garnet peridotite stability field or whether all garnet was added by incorporation of websterite.

The deformation-decompression-cooling history of the porphyroclastic xenoliths can be easily explained as the result of continental rifting, thus confining it to either Mesozoic (Anza Graben) or Tertiary-Quaternary (EARS) times. Conclusions derived from the investigation of the second, recrystallised group of mantle samples clearly favour Mesozoic rifting. Many features in this rock type indicate a similar earlier *P-T* evolution including deformation (e.g., preservation of porphyroclasts in transitional samples), decompression (e.g., preservation of garnet breakdown products) and cooling (e.g., mineral zoning patterns of slowly diffusing elements). These early events were followed by later heating, static recrystallisation and melt impregnation (variable degrees of metasomatism; see below). The latter features are similar to the characteristics of mantle xenoliths from farther north that sampled the mantle beneath the Afar plateau (the Sidamo or Mega xenoliths; see Fig. 1.2). Concluding from this, the recrystallised peridotites and websterites provide evidence that the formerly rifted and cooled lithospheric mantle (Mesozoic-Paleogene) subsequently experienced re-heating (Tertiary-Quaternary), most likely in the context of hot upwelling asthenosphere or a mantle plume, similar to the late evolution of the mantle north of the Anza Graben. However, it must be emphasised that the spatial relation between the recrystallised mantle domain(s) and the deformed mantle (i.e. vertical or lateral) remains unconstrained (due to the lack of precise pressure constraints). However, an origin at slightly greater depth compared to the deformed xenoliths would be realistic when hot upwelling mantle material (asthenospheric or plume-related) indeed impinges the base of the lithosphere beneath Marsabit.

The nature and age of metasomatism - Based on textures and compositions, two 'early' and one 'late' metasomatic events within the Marsabit lithospheric mantle can be distinguished. Here, 'early' means that metasomatic (or metasomatised) phases formed prior to the entrainment of the xenoliths and, at least partially, re-equilibrated with the host peridotite. In contrast, 'late' indicates onset of metasomatism in the mantle, but only shortly (i.e., days to hours) before and/or during the transport of the xenolith to the surface:

- A first 'eraly' assemblage (Ti-pargasite and rare phlogopite) shows evidence to have formed during the magmatic garnet websterite intrusion (high-pressure crystallisation of basaltic melts prior to continental rifting; see below). Ti-pargasite and phlogopite

in the formerly garnet-bearing lherzolites most likely derived/recrystallised from former garnet websterite that was streaked out in the peridotitic matrix during pervasive Mesozoic deformation (see above). The formation of this metasomatic assemblage is thus most likely related to pre-rift events (see below).

- A second 'early' metasomatic assemblage clearly developed after the main deformation (i.e., is itself strain-free and overgrows the deformed fabric) and consists of rather unusual minerals, including low-Ti Mg-katophorite (amphibole), Na-rich phlogopite, low-Al orthopyroxene, apatite and graphite. Although the trace element signature of the metasomatic minerals is similar to products of carbonatite melt metasomatism, the major element compositions, as well as considerations of phase assemblages and *P-T* constraints argue in favour of an evolved Si-rich melt interacting with peridotite. Detailed major and trace element analysis indicates that the final compositional nature comprises signatures added by the metasomatic agent (mainly incompatible elements) and signatures inherited from the pre-existing heterogeneous mantle (mainly more compatible elements). Metasomatism occurred most likely at low pressures (<1.5 GPa) and in a relatively reduced protolith allowing for the precipitation of graphite.
  According to xenolith studies from other localities such volatile-enriched melts or fluids can form as derivates of extensive melt-rock reaction and fractionation processes (i.e., reactive porous flow and chromatographic trace element fractionation). In this respect it is likely that cryptic metasomatism (porous flow of basaltic melt in the high-temperature recrystallised mantle domain; see above) and modal metasomatism in the shallow deformed mantle (reaction of evolved volatile-rich melts with cold peridotite allowing crystallisation of volatile-bearing minerals) are genetically related.
  Replacement of deformed minerals by undeformed metasomatic phases suggests that this metasomatic event occurred in the context of EARS-related magmatism. It is thus plausible that the Si-rich liquids formed by melt-peridotite reaction of primary alkaline basaltic melts in the course of EARS-related Tertiary-Quaternary magmatism at Marsabit. It is further plausible that such melt-rock reaction occurred slightly prior to the main magmatic event that ultimately disrupted and entrained fragments of this metasomatised mantle.
- Finally, a 'late' metasomatic assemblage consisting of silicate glass and associated silicate, oxide and carbonate microlites ('melt pockets') was shown to partly replace all types of early assemblages, as well as primary (non-metasomatic) minerals. Relative abundances, compositional features and mass balance calculations indicate that the formation of the glass-bearing assemblages is dominated by the incongruent breakdown of pre-existing amphibole (with minor contribution of all other phases, especially orthopyroxene). High amounts of Mg-calcite and now empty bubbles (vugs) indicate presence of a CO_2-rich fluid during melt pocket formation. This fluid most likely triggered amphibole breakdown and the *in-situ* formation of silicate melt. The silicate melt itself does not represent a metasomatic agent (in the sense of deriving from an external source and adding components to the system).
  The preservation of silicate glass and implications from Mg-Fe diffusion modelling in olivine (and Li in clinopyroxene; see below) show that the melt pockets formed during days or hours, shortly before incorporation of the xenoliths in their host magma. The absence of plagioclase, however, indicate that initial melting started at mantle depths.

The detailed study of metasomatism in the Marsabit mantle suggests at least two events

(graphite-bearing 'early' assemblages and melt pockets) to have formed in the context of recent EARS-related melt infiltration and heat input. These findings are in line with the results of numerous petrological and geochemical studies on the volcanic rocks extruded in the context of EARS magmatism (including those from the Marsabit volcanic field; Volker, 1990), indicating that most lavas are the products of sub-lithospheric melts that interacted with the lithospheric mantle. The results from this study, however, allow not to conclude whether the melt contained components of a deep-seated mantle plume.

Pyroxenites: evidence for pre-rift (Pan-African?) and EARS-related mafic cumulates **–** Both garnet websterite and garnet free pyroxenites indicate crystallisation from basaltic melt at relatively high pressure. However garnet-bearing and garnet-free rocks show textural and compositional differences indicating two different events of melt intrusion within the mantle:

- Garnet websterite shows a transition from cumulate-like via porphyroclastic to mylonitic textures, accompanied by an increasing degree of re-equilibration with peridotite. Together with thermobarometric results, these features indicate that garnet websterite underwent the same rifting history (deformation-decompression-cooling) as the shallow peridotitic mantle. Preservation of 'magmatic' (cumulate-like) relics could be explained by the presence of thicker websterite layers or boudins whose central parts escaped shearing. While their metamorphic evolution indicates that garnet websterites were emplaced prior to Mesozoic rifting, the preservation of magmatic features allows putting constraints on the nature of their parental melts. Primary orthopyroxene and kaersutite inclusions in igneous garnet strongly suggest that the parental melts were not alkaline in character, but rather tholeiitic or calc-alkaline. The latter possibility, together with the pre-rift origin of garnet websterite, could be an argument in favour of formation during Pan-African times (or earlier).

- Garnet-free clinopyroxenite and websterite exhibit mineralogical and compositional features (major and trace element data) typical for cumulates crystallised from alkali basaltic or basanitic melt at elevated pressure (0.9-1.7 GPa, indicated by the absence of plagioclase and garnet). Sub-solidus modifications, such as exsolution of orthopyroxene and spinel from clinopyroxene and kink-bands in olivine suggest that most xenoliths are not cognate to the host lava, but crystallised earlier. This may be in the context of Mesozoic magmatism relate to the Anza Graben or in the course of EARS-related magmatism.
  The single olivine gabbro xenolith shows perfect igneous textures. In analogy to similar slightly alkaline gabbro xenolith suites (e.g., Hawaii), it testifies most likely to the presence of plutonic gabbroic bodies in the Marsabit crust, formed during EARS-related magmatism.

Li, Be and B in minerals: evidence for slab-derived fluids? - The *in-situ* investigation of Li, Be and B in minerals from the deformed and the recrystallised (heated) formerly garnet-bearing lherzolites show light element systematics similar to those inferred to represent non-metasomatised fertile sub-continental lithopsheric mantle. On the other hand, the modally metasomatised (graphite-bearing) harzburgite and dunite xenoliths show much higher light element concentrations. Their light element signature together with other trace element patterns (e.g., U-Th-LREE enrichment) is similar to what would be expected in the case of peridotite metasomatised by fluids released from a subducting slab. Moreover, melts from which metasomatic phases such as Mg-katophorite crystallised (calculated compositions) show key trace element ratios (e.g., B/Be, Li/Yb) very similar to Island

Arc Basalts. These features thus raise the question whether the metasomatic agent(s) carried a slab-derived component. Since metasomatism itself has been shown to be young (EARS-related; see above), such a component would necessarily originate from an old mantle domain (e.g., in the source of, or tapped by the metasomatic agent). Considering the geodynamic evolution of the Marsabit lithosphere (subjected to multiple accretion events during Pan-African orogenesis), as well as the nature of the pre-rift garnet websterites (see above), preservation of 'subduction-modified' mantle domains is absolutely plausible. However, detailed SIMS investigation of Li, Be and B in single mineral grains also indicate that these elements may be strongly modified by late-stage processes such as the formation of melt pockets (see above). This creates ubiquitous concentration gradients, disequilibrium between minerals, and possibly de-coupling of light elements from other trace elements (e.g., REEs). Moreover, metasomatic processes such as the crystallisation of amphibole may produce residual melts/fluids with light element signatures mimicking those of slab-derived fluids. These results illustrate that, although Li, Be and B are succesfully used to trace slab-components in modern subduction zone rocks, caution must be paid when inferring ancient subduction processes. This applies in particular to intraplate mantle xenoliths. For this geodynamic context eventual late stage melting and metasomatic events that may strongly alter initial light element signatures must be well constrained and quantified in terms of geochemistry.

OUTLOOK

This xenolith study provides a fairly detailed picture of mineralogical and geochemical features as well as of mantle processes in a small portion of the lithospheric mantle related to the EARS. The study, however, also leaves some questions poorly or un-resolved, and also raises new ones. Whilst some deal with particular issues related to the regional geodynamic setting, others apply to mantle petrology and geochemistry in general. Three points may be mentioned in particular and are an outlook for further research:

1) Regional geology I: constraining the age of the lithosphere domains: There is ample (especially textural) evidence which allows to place relative age constraints on the different structural, metasomatic and magmatic events recorded in the lithosphere. Other methods are, however, needed to date mantle processes beneath Marsabit more precisely. Isotope geochemistry has undoubtedly the potential to resolve some of these issues. K-Ar and Ar-Ar dating, for example, may give indications on the age of the metasomatising events that led to the formation of the phlogopite-bearing assemblages in the low-*T* spl harzburgites and dunites. Further topics to be addressed (e.g., by Os and/or Nd isotope studies) are the age of pre-rift lithosphere stabilisation (also in the light of the possible presence of pre-Pan-African cratonic material, as suggested for the mantle beneath southern Ethiopia; Reisberg *et al.*, 2004). Further, isotope studies will shed additional light on the nature and age of garnet pyroxenites (i.e., their possible relation to Pan-African subduction processes). In fact, O, Nd, Sr and Pb, as well as Os isotope (including PGE systematics) investigation were already initiated and will follow up this study (E. Bourdon, A. Kalt *et al.*, in preparation).

2) Regional geology II: the mantle plume issue: As stated in the introduction, magmas from the EARS – including those from Marsabit and adjoining Huri Hills – are often interpreted to reflect asthenosphere- or plume-derived melts that interacted with the lithosphere. There, most lavas carry components typically attributed to hypothetical mantle reservoirs indicating the compositional contribution of a deep-seated mantle plume (e.g., the so-called HIMU component – high $^{238}U/^{204}Pb$ ratios – interpreted to indicate old deeply subducted mafic crust, sampled and recycled to the surface by a plume).
In this context, the above mentioned isotope

studies will allow to better characterise the 'lithospheric component' with which lavas at the surface potentially interacted, and its influence on the enigmatic and still lively debated 'plume signature' in the erupted lavas.

3) Li, Be and B and their capabilities as tracers in intraplate settings: The light element studies of the Marsabit peridotites highlighted that their use as tracers for recycled components (i.e., mantle metasomatised by slab fluids) in intraplate settings is not unproblematic. This is also due to the fact that their behaviour in intraplate magmas (e.g., carbonatite or basanite melts) is yet only poorly constrained (with respect to natural lavas, as well as in terms of sparse experimental constraints). There, more work is clearly needed.

Chapter 8:

Analytical Methods

Petrography (Optical Microscopy and Secondary Electron Microscopy, SEM)

Prior to compositional analysis each sample was investigated in detail by optical and secondary electron microscopy. SEM was conducted using the Phillips XL 30 environmental secondary electron microscope (ESEM) at the Institute of Microtechniques (University of Neuchâtel) and a FEI XL30 Sirion electron microscope at the department of geosciences (University of Fribourg, Switzerland). Back-Scattered Electron (BSE) imaging was used to illustrate textural features and to determine the mineralogical compositions of the samples.

Electron Microprobe

The major element composition of minerals has been determined using electron microprobe facilities at the Universities of Bern (Switzerland) and Heidelberg (Germany). The largest part of the analytical work was done on a CAMECA SX50 microprobe (Bern) equipped with 4 wavelength-dispersive spectrometers. Additionally, a CAMECA SX 51 (Heidelberg) and a new JEOL JXA 8200 (Bern), both equipped with five wavelength-dispersive spectrometers were used for completation. Pyroxenes, olivine and spinel were analysed using routine operating conditions (focused beam with a diameter of ~1-2 μm, accelerating voltage of 15 kV, beam current of 20 nA). Peak counting times were between 20 and 30 s for most elements, and the backgrounds were measured for the half of the peak counting times on each side of the peak position. Amphiboles and phlogopites were analysed with a slightly defocused beam (~5 μm), preventing alkali diffusion. For the same reason, as well as to avoid destruction, silicate glass was analysed with a larger beam size (~10-15 μm) and a lower beam current (15 nA). Natural and synthetic silicates and oxides were used as standards. Carbonates were analysed with a beam current of 10 nA and a beam size of 10 μm, while natural carbonates and sulfates were used as standards. The concentrations of H_2O (in amphibole and phlogopite), CO_2 (in carbonates) and Fe^{3+} (in spinel) were calculated based on stoichiometry. The raw data of all microprobe analyses were corrected with a routine PAP program (CAMECA SX 50 and 51) and a Phi-Rho-Z correction algorithm (JEOL JXA 8200).

Laser Ablation – Inductively Coupled Mass Spectrometry (LA-ICPMS)

LA-ICPMS was used to analyse trace elements in all phases of the investigated xenoliths. Forty isotopes (^{7}Li, ^{11}B, ^{23}Na, ^{25}Mg, ^{27}Al, ^{31}P, ^{39}K, ^{42}Ca, ^{45}Sc, ^{49}Ti, ^{51}V, ^{62}Ni, ^{66}Zn, ^{71}Ga, ^{85}Rb, ^{88}Sr, ^{89}Y, ^{90}Zr, ^{93}Nb, ^{133}Cs, ^{137}Ba, ^{139}La, ^{140}Ce, ^{141}Pr, ^{146}Nd, ^{147}Sm, ^{151}Eu, ^{157}Gd, ^{159}Tb, ^{163}Dy, ^{165}Ho, ^{167}Er, ^{169}Tm, ^{173}Yb, ^{175}Lu, ^{178}Hf, ^{181}Ta, ^{208}Pb, ^{232}Th, ^{238}U) where measured *in-situ* on polished thin sections using the facility at the Institut für Isotopengeologie und Mineralische Rohstoffe, ETH Zürich. This consists of a pulsed 193 nm ArF Excimer laser (Lambda Physik, Germany) with an energy-homogenised (Günther *et al.*, 1997) beam profile, coupled with an ELAN6100 ICP quadrupole mass spectrometer (Perkin Elmer, Canada). The following descriptions of working conditions and instrumental capabilities are compiled from Günther *et al.* (1997), Heinrich *et al.* (2003), and Pettke *et al.* (2004).

The instrumental design is illustrated in Fig. 8.1. An output energy of 60-80 mJ was used, translating into an energy density of ca. 10-15 J/cm^2 on the sample surface. The optical setup is described in detail by Günther *et al.*, (1997). It allows laterally homogeneous UV ablation (depth-controlled, at a rate of 0.1-0.2 μm/shot depending on the matrix, resulting in flat-bottomed craters), combined with simultaneous TV-observation of the ablation process (through a modified petrographic microscope; Fig. 8.1). This allows having control on the textural context of the analysed material (e.g., avoiding im-

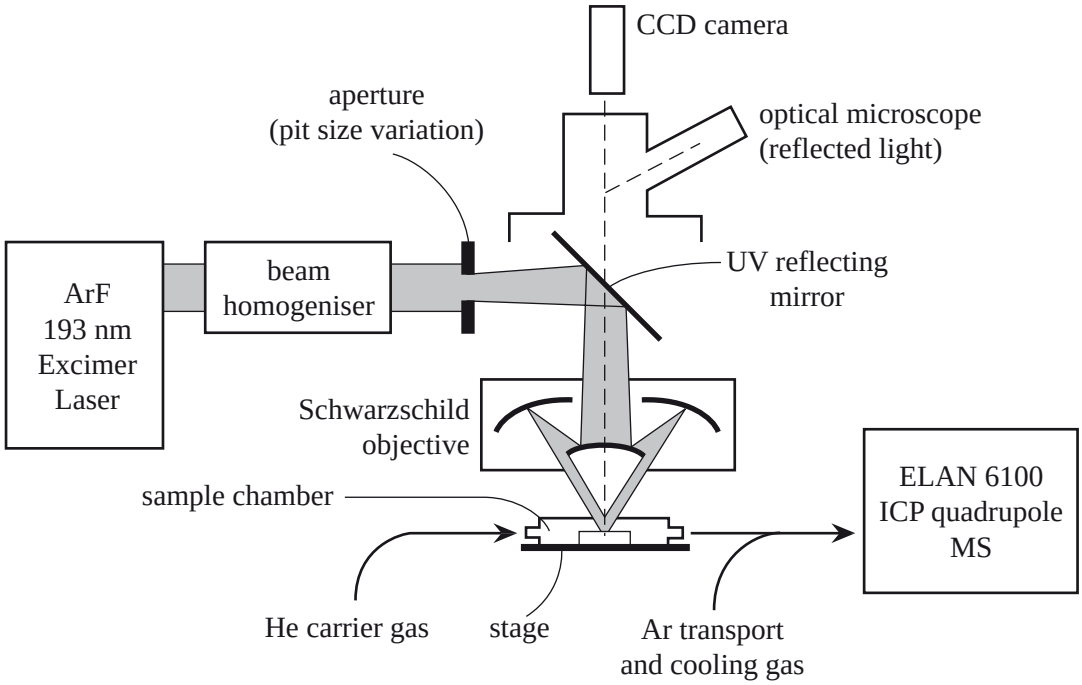


Fig. 8.1: Setup of the LA-ICPMS installation at the Institute for Isotope Geochemistry and Mineral Resources, ETH Zürich (modified after Günther *et al.*, 1997).

purities or fluid/solid inclusions). An aperture in the beam path allows the use of different pit sizes (8-100 µm), which were chosen depending on grain size and the absence / presence of mineral, fluid or melt inclusions and of exsolution lamellae.

The thin sections were placed along with the NIST SRM 610 glass standard in a 5 or 10 cm^3 ablation chamber and placed on the stage of the modified microscope (Fig. 8.1). The ablation chamber was flushed with He, and the aerosol was transported to the ICPMS by a mixed Ar-He carrier gas. The mass spectrometer records elements sequentially and each ablation was stored individually as time-resolved (transient) signal acquired in peak-hopping mode. The ELAN6100 ICP quadrupole MS has 3 ms quadrupole settling times and, together whith dwell times of 10ms, allows recording of statistically relevant data for up to 40 elements from an ablation time as short as 10s (Heinrich *et al.*, 2003). Ions were counted in a dual detector mode (cross-calibrated pulse counting and analog detection) allowing measurement of major (<100 wt%) and trace elements (≥ a few tens of ng/g) during a single shot.

One series of measurements always comprises up to 16 analyses of unknowns bracketed by 2 analyses of a known standard (SRM 610). These are required as an external standard to calibrate analyte sensitivities. Bracketing standardisation further provides a linear drift correction. Raw data were reduced using the LAMTRACE program (modified version from Simon E. Jackson). This allows quantification using an internal standard (known element concentration in the analysed material in wt% oxides), and calculation of detection limits. Preceding calculations the transient signal of each element, the background and ablation signal intervals were filtered for eventual spikes (manual substitution by a value corresponding to the mean count rates of neighbouring sweep recordings). Detection limits for each element are calculated

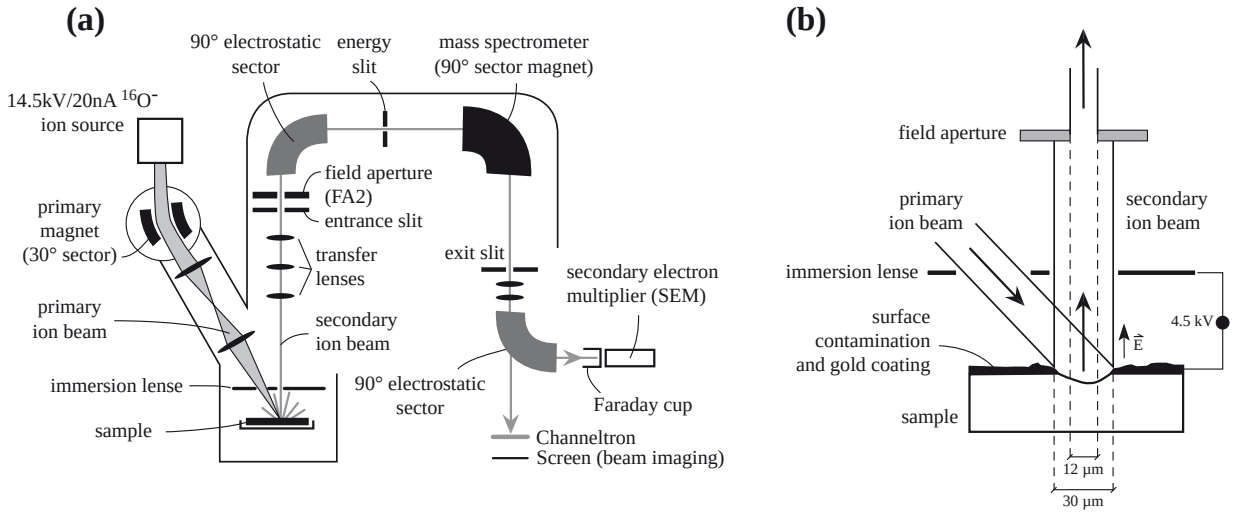


Fig. 8.2: (a) Setup of the SIMS installation at the Mineralogical Institute, Universität Heidelberg. (b) Schematic illustration of the sputtering process during SIMS analysis (modified after Marschall & Ludwig, 2004).

from the minimum detectable signal intensity, defined by 3 times the standard deviation of the background signal divided by element sensitivity (Longerich *et al.*, 1996). Compositional data previously obtained by electron microprobe analysis were used as the internal standard (CaO for clinopyroxene, amphibole, apatite, carbonate, and glass; MgO for olivine, orthopyroxene, and phlogopite; Al_2O_3 for Ca-poor glass).

Secondary Ion Mass Spectrometry (SIMS)

The concentrations of the low atomic mass elements Li, Be and B (hereafter called 'light elements') in silicates (olivine, orthopyroxene, clinopyroxene, amphibole, phlogopite) and silicate glass have been measured *in-situ*, on polished thin sections by Secondary Ion Mass Spectrometry (SIMS) using a modified CAMECA IMS 3f ion microprobe (Mineralogisches Institut, Universität Heidelberg, Germany), equipped with a primary beam mass filter (Fig. 8.2). A 14.5kV/20nA $^{16}O^-$ primary ion beam was used. The surface imaged by the secondary ions was reduced from ~30 µm to ~12 µm by applying a field apperture (FA2; 750 µm). Positive secondary ions were accelerated to a nominal energy of 4.5 keV and the mass spectrometer's energy window was set to 40 eV. Secondary ^{7}Li, ^{9}Be, and ^{11}B ions were collected applying the energy filtering method (Ottolini *et al.*, 1993) using an offset of 75 eV at a mass resolution (m/Δm) of 1030. The latter allows differentiation between ^{7}Li ions and ^{6}LiH molecules. The intensities were normalised to the count rates of ^{30}Si and calibrated against the NIST SRM 610 glass standard (concentrations from Pearce *et al.*, 1997). SiO_2 (wt%) concentrations in the respective phase were obtained by electron microprobe analysis. One analysis comprises 10 cycles for each element with an integartion time of 8 s/cycle for Li, 16 s/cycle for Be and B, and 2 s/cycle for Si. The total analysis time was ~12 min (including ~400 s pre-sputtering). The minimal detectable values (Currie, 1968) are 4.7 ng/g Li, 2.9 ng/g Be, and 7.5 ng/g B (two samples, Ke 1965/15 and Ke 785*, have been analysed with 4 s/cylce for Li and 8 s/cycle for Be and B, which increases the minimal detectable values to 7.7 ng/g Li, 4.7 ng/g Be, and 12.1 ng/g B).

As SIMS is a method were material is removed from a polished surface, contamination, especially in the case of boron (Shaw *et al.*,

1988), is always present. Owing to this and to the generally low concentrations of Li, Be and B in mantle rocks, careful sample preparation is essential. Thin sections for this study have been prepared at the Institute of Mineralogy (University of Heidelberg, Germany) following a standard protocol to minimise surface contamination (Marschall & Ludwig, 2004). Pure glycol was used as lubricant and cooling liquid for sawing and polishing and all products containing boric acid were avoided. Samples were then coated with carbon for BSE investigation (textures) and electron microprobe analyses (major element composition of minerals; see above). After this, the carbon was removed using γ-alumina powder and distilled water. Subsequently, the samples were cleaned in an ultrasonic bath using ultra-pure water from a Milli-Q water purification system (Millipore). Ultrasonic cleaning was repeated three times for about 10 min. Thin sections were then coated with gold. During SIMS analysis, pre-sputtering further removes possible surface contamination. Applying the field aperture that limits the imaged field's diameter to less than the diameter of the primary beam avoids that surface contamination at the sputtering crater's edge is reaches the mass spectrometer (Fig. 8.2b). Following this procedure described by Marschall & Ludwig (2004), the boron contamination level is < 2 ng/g. Lithium contamination is typically ~50 times lower than for boron, and beryllium does not show any sign of contamination.

Cited References

CITED REFERENCES

Achauer, U. & KRISP Teleseismic Working Group (1994). New ideas on the Kenya rift based on the inversion of the combined dataset of the 1985 and 1989/90 seismic tomography experiments. *Tectonophysics* **236**, 305-329.

Adam, J. (1990). The geochemistry and experimental petrology of sodic alkaline basalts from Oatlands, Tasmania. *Journal of Petrology* **31**, 1201-1223.

Adam, J. & Green, T. (2001). Experimentally determined partition coefficients for minor and trace elements in peridotite minerals and carbonatitic melt, and their relevance to natural carbonatites. *European Journal of Mineralogy.* **13**, 815-827.

Adam, J. & Green, T. (2006). Trace element partitioning between mica- and amphibole-bearing garnet lherzolite and hydrous basanitic melt: 1. Experimental results and the investigation of controls on partitioning behaviour. *Contributions to Mineralogy and Petrology* **152**, 1-17.

Adam, J., Green, T. H., Sie, S. H. & Ryan, C. G. (1997). Trace element partitioning between aqueous fluids, silicate melts and minerals. *European Journal of Mineralogy* **9**, 569-584.

Allègre, C. J. & Turcotte, D. L. (1986). Implications of a 2-component marble-cake mantle. *Nature* **323**, 123-127.

Altherr, R., Garasic, V., Ulianov, A. & Kalt, A. Composition and thermal evolution of the lithospheric mantle beneath the Chyulu Hills (Southern Kenya, East African Rift) as deduced from xenoliths. *submitted to Journal of Petrology*.

Amundsen, H. E. F., Griffin, W. L. & O'Reilly, S. Y. (1987). The lower crust and upper mantle beneath northwestern Spitsbergen: evidence from xenoliths and geophysics. *Tectonophysics* **139**, 169-185.

Anderson, D. L. (2005). Scoring hotspots: the plume and plate paradigms. In: Foulger, G. R., Natland, J. H., Presnall, D. C. & Anderson, D. L. (eds.) *Plates, plumes, and paradigms*. Boulder, Colorado: Geological Society of America Special Paper, 31-54.

Anderson, D. L. & Schramm, K. A. (2005). Global hotspot maps. In: Foulger, G. R., Natland, J. H., Presnall, D. C. & Anderson, D. L. (eds.) *Plates, plumes, and paradigms*. Boulder, Colorado: Geological Society of America Special Paper, 19-29.

Appel, P., Möller, A. & Schenk, V. (1998). High-pressure granulite facies metamorphism in the Pan-African belt of eastern Tanzania: P-T-t evidence against granulite formation by continent collision. *Journal of Metamorphic Geology* **16**, 491-509.

Arai, S., Takada, S., Michibayashi, K. & Kida, M. (2004). Petrology of peridotite xenoliths from Iraya volcano, Philippines, and its implication for dynamic mantle-wedge processes. *Journal of Petrology* **45**, 369-389.

Bach, W., Alt, J. C., Niu, Y. L., Humphris, S. E., Erzinger, J. & Dick, H. J. B. (2001). The geochemical consequences of late-stage low-grade alteration of lower ocean crust at the SW Indian Ridge: Results from ODP Hole 735B (Leg 176). *Geochimica et Cosmochimica Acta* **65**, 3267-3287.

Baker, B. H. (1987). Outline of the petrology of the Kenya rift alkaline province. In: Fitton, J. G. & Upton, B. G. J. (eds.) *Alkaline Igneous Rocks*. London: Geological Society, Special Publications, 293-311.

Baker, B. H. & Wohlenberg, J. (1971). Structure and evolution of Kenya Rift Valley. *Nature* **229**, 538-542.

Baker, B. H., Williams, L. A. J., Miller, J. A. & Fitch, F. J. (1971). Sequence and geochronology of the Kenya rift volcanics. *Tectonophysics* **11**, 191-215.

Bali, E., Szabó, C., Vaselli, O. & Török, K. (2002). Significance of silicate melt pockets in upper mantle xenoliths from the Bakony-Balaton highland volcanic field, Western Hungary. *Lithos* **61**, 79-102.

Ballhaus, C. (1993). Redox states of lithospheric and asthenospheric upper-mantle. *Contributions to Mineralogy and Petrology* **114**, 331-348.

Ballhaus, C., Berry, R. F. & Green, D. H. (1991). High pressure experimental calibration of the olivine-orthopyroxene-spinel oxygen geobarometer: implications for the oxidation state of the upper mantle. *Contributions to Mineralogy and Petrology* **107**, 27-40.

Ban, M., Witt-Eickschen, G., Klein, M. & Seck, H. A. (2005). The origin of glasses in hydrous mantle xenoliths from the West Eifel, Germany: incongruent break down of amphibole. *Contributions to Mineralogy and Petrology* **148**, 511-523.

Barclay, J. & Carmichael, I. S. E. (2004). A hornblende basalt from western Mexico: water-saturated phase relations constrain a pressure-temperature window of eruptibility. *Journal of Petrology* **45**, 485-506.

Baxter, E. F. & DePaolo, D. J. (2004). Can metamorphic reactions proceed faster than bulk strain? *Contributions to Mineralogy and Petrology* **146**, 657-670.

Bedini, R. M. (1994). Studio geochemico-petrologico degli xenoliti ultrafemici di Mega (Sidamo, Ethiopia -Rift Africano Orientale-): implicazioni sui processi di interazione magma-roccia nel mantello litosferico subcontinentale. *unpublished PhD thesis, University of Bologna, 278 pp.*

Bedini, R. M. & Bodinier, J.-L. (1999). Distribution of incompatible trace elements between the constituents of spinel peridotite xenoliths: ICP-MS data from the East African Rift. *Geochimica et Cosmochimica Acta* **63**, 3883-3900.

Bedini, R. M., Bodinier, J.-L., Dautria, J.-M. & Morten, L. (1997). Evolution of LILE-enriched small melt fractions in the lithospheric mantle: a case study from the East African Rift. *Earth and Planetary Science Letters* **153**, 67-83.

Bell, K. & Dodson, M. H. (1981). The geochronology of the Tanzanian shield. *Journal of Geology* **89**, 109-128.

Benoit, M. H., Nyblade, A. A. & VanDecar, J. C. (2006). Upper mantle P-wave speed variations beneath Ethiopia and the origin of the Afar hotspot. *Geology* **34**, 329-332.

Berly, T. J., Hermann, J., Arculus, R. J. & Lapierre, H. (2006). Supra-subduction zone pyroxenites from San Jorge and Santa Isabel (Solomon Islands). *Journal of Petrology* **47**, 1531-1555.

Betton, P. J. & Civetta, L. (1984). Strontium and neodymium isotopic evidence for the heterogeneous nature and development of the mantle beneath Afar (Ethiopia). *Earth and Planetary Science Letters* **71**, 59-70.

Binks, R. M. & Fairhead, J. D. (1992). A Plate Tectonic Setting for Mesozoic Rifts of West and Central Africa. *Tectonophysics* **213**, 141-151.

Blundy, J. & Dalton, J. (2000). Experimental comparison of trace element partitioning between clinopyroxene and melt in carbonate and silicate systems, and implications for mantle metasomatism. *Contributions to Mineralogy and Petrology* **139**, 356-371.

Bodinier, J. L. & Godard, M. (2003). Orogenic, ophiolitic, and abyssal peridotites. In: Holland, H. D. & Turrekian, K. K. (eds.) *Treatise on Geochemistry*. Amsterdam: Elsevier, 103-170.

Bodinier, J. L., Guiraud, M., Fabriès, J., Dostal, J. & Dupuy, C. (1987). Petrogenesis of layered pyroxenites from the Lherz, Freychinede and Prades ultramafic bodies (Ariège, French Pyrenees). *Geochimica et Cosmochimica Acta* **51**, 279-290.

Bodinier, J. L., Dupuy, C. & Dostal, J. (1988). Geochemistry and petrogenesis of eastern Pyrenean peridotites. *Geochimica et Cosmochimica Acta* **52**, 2893-2907.

Bodinier, J. L., Vasseur, G., Vernieres, J., Dupuy, C. & Fabriès, J. (1990). Mechanisms of mantle metasomatism - geochemical evidence from the Lherz orogenic peridotite. *Journal of Petrology* **31**, 597-628.

Bodinier, J. L., Merlet, C., Bedini, R. M., Simien, F., Remaidi, M. & Garrido, C. J. (1996). Distribution of niobium, tantalum, and other highly incompatible trace elements in the lithospheric mantle: the spinel paradox. *Geochimica et Cosmochimica Acta* **60**, 545-550.

Bodinier, J.-L., Menzies, M. A., Shimizu, N., Frey, F. A. & McPherson, E. (2004). Silicate, hydrous and carbonate metasomatism at Lherz, France: Contemporaneous derivates of silicate melt-harzburgite reaction. *Journal of Petrology* **45**, 299-320.

Borg, G. & Krogh, T. (1999). Isotopic age data of single zircons from the Archean Sukumaland Greenstone Belt, Tanzania. *Journal of African Earth Sciences* **29**, 301-312.

Bosworth, W. (1992). Mesozoic and early Tertiary rift tectonics in East-Africa. *Tectonophysics* **209**, 115-137.

Bosworth, W. & Morley, C. K. (1994). Structural and stratigraphic evolution of the Anza rift, Kenya. *Tectonophysics* **236**, 93-115.

Brenan, J. M., Shaw, H. F., Ryerson, F. J. & Phinney, D. L. (1995). Mineral-aqueous fluid partitioning of trace elements at 900°C and 2.0 GPa: constraints on the trace element chemistry of mantle and deep crustal fluids. *Geochimica et Cosmochimica Acta* **59**, 3331-3350.

Brenan, J. M., Neroda, E., Lundström, C. C., Shaw, H. F., Ryerson, F. J. & Phinney, D. L. (1998a). Behaviour of boron, beryllium, and lithium during melting and crystallization: constraints from mineral-melt partitioning experiments. *Geochimica et Cosmochimica Acta* **62**, 2129-2141.

Brenan, J. M., Ryerson, F. J. & Shaw, H. F. (1998b). The role of aqueous fluids in the slab-to-mantle transfer of boron, beryllium, and lithium during subduction: Experiments and models. *Geochimica et Cosmochimica Acta* **62**, 3337-3347.

Brey, G. P. & Köhler, T. (1990). Geothermobarometry in four-phase lherzolites II. New thermobarometers, and practical assessment of existing thermobarometers. *Journal of Petrology* **31**, 1353-1378.

Brey, G. P., Köhler, T. & Nickel, K. G. (1990). Geothermobarometry in four-phase lherzolites I. Experimental results from 10 to 60 kb. *Journal of Petrology* **31**, 1313-1352.

Brodie, K. H. & Rutter, E. H. (1985). On the relationship between deformation and metamorphism, with special reference to the behaviour of basic rocks. In: Thompson, A. B. & Rubie, D. C. (eds.) *Metamorphic reactions: kinetics, textures, and deformation*. Berlin: Springer, 138-179.

Brooker, R. A., James, R. H. & Blundy, J. D. (2004). Trace element and Li isotope systematics in Zabargad peridotites: evidence of ancient subduction processes in the Red Sea mantel. *Chemical Geology* **212**, 179-204.

Brotzu, P., Morbideli, L., Nicoletti, M., Piccirillo, E. M. & Traversa, G. (1984). Miocene to quaternary volcanism in eastern Africa: sequence and chronology. *Tectonophysics* **101**, 75-86.

Burke, K. (1996). The African plate. *South African Journal of Geology* **99**, 341-409.

Burton, K. W., Schiano, P., Birck, J.-L., Allègre, C. J., Rehkämper, M., Halliday, A. N. & Dawson, J. B. (2000). The distribution and behaviour of rhenium and osmium amongst mantle minerals and the age of the lithospheric mantle beneath Tanzania. *Earth and Planetary Science Letters* **183**, 93-106.

Bystricky, M. & Mackwell, S. (2001). Creep of dry clinopyroxene aggregates. *Journal of Geophysical Research* **106**, 13443-13454.

Carpenter, R. L., Edgar, A. D. & Thibault, Y. (2002). Origin of spongy textures in clinopyroxene and spinel from mantle xenoliths, Hessian Depression, Germany. *Mineralogy and Petrology* **74**, 149-162.

Carroll Webb, S. A. & Wood, B. J. (1986). Spinel-pyroxene-garnet relationship and their dependence on Cr/Al ratio. *Contributions to Mineralogy and Petrology* **92**, 471-480.

Chakraborty, S. (1997). Rates and mechanisms of Fe-Mg interdiffusion in olivine at 980°-1300°C. *Journal of Geophysical Research* **102**, 12317-12331.

Chakraborty, S. & Ganguly, J. (1992). Cation diffusion in aluminosilicate garnets - experimental-determination in spessartine-almandine diffusion couples, evaluation of effective binary diffusion-coefficients, and applications. *Contributions to Mineralogy and Petrology* **111**, 74-86.

Chakraborty, S., Farver, J. R., Yund, R. A. & Rubie, D. C. (1994). Mg tracer diffusion in synthetic forsterite and San Carlos olivine as a function of P, T and fO_2. *Physics and Chemistry of Minerals* **21**, 489-500.

Chan, L. H. & Kastner, M. (2000). Lithium isotopic compositions of pore fluids and sediments in the Costa Rica subduction zone: Implications for fluid processes and sediment contribution to the arc volcanoes. *Earth and Planetary Science Letters* **183**, 275-290.

Chan, L. H. & Frey, F. A. (2003). Lithium isotope geochemistry of the Hawaiian plume: Results from the Hawaii Scientific Drilling Project and Koolau volcano. *Geochemistry Geophysics Geosystems* **4**. doi: 10.1029/2002GC000365.

Chaussidon, M. & Libourel, G. (1993). Boron partitioning in the upper mantle: an experimental and ion microprobe study. *Geochimica et Cosmochimica Acta* **57**, 5053-5062.

Chaussidon, M. & Marty, B. (1995). Primitive boron isotope composition of the mantle. *Science* **269**, 383-386.

Chazot, G., Menzies, M. A. & Harte, B. (1996a). Determination of partition coefficients between apatite, clinopyroxene, amphibole, and melt in natural spinel lherzolites from Yemen: implications for wet melting of the lithospheric mantle. *Geochimica et Cosmochimica Acta* **60**, 423-437.

Chazot, G., Menzies, M. A. & Harte, B. (1996b). Silicate glasses in spinel lherzolites from Yemen: origin and chemical composition. *Chemical Geology* **134**, 159-179.

Chesley, J. T., Rudnick, R. L. & Lee, C. T. (1999). Re-Os systematics of mantle xenoliths from the East African Rift: age, structure, and history of the Tanzanian craton. *Geochimica et Cosmochimica Acta* **63**, 1203-1217.

Chopra, P. N. & Paterson, M. S. (1981). The experimental deformation of dunite. *Tectonophysics* **78**, 453-473.

Class, C., Altherr, R., Volker, F., Eberz, G. & McCulloch, M. T. (1994). Geochemistry of pliocene to quaternary alkali basalts from the Hurri Hills, northern Kenya. *Chemical Geology* **113**, 1-22.

Cohen, R. S., O'Nions, R. K. & Dawson, J. B. (1984). Isotope geochemistry of xenoliths from East-Africa - implications for development of mantle reservoirs and their interaction. *Earth and Planetary Science Letters* **68**, 209-220.

Coltorti, M., Beccaluva, L., Bonadiman, C., Salvini, L. & Siena, F. (2000). Glasses in mantle xenoliths as geochemical indicators of metasomatic agents. *Earth and Planetary Science Letters* **183**, 303-320.

Coltorti, M., Bonadiman, C., Hinton, R. W., Siena, F. & Upton, B. G. J. (1999). Carbonatite metasomatism of the oceanic upper mantle: evidence from clinopyroxenes and glasses in ultramafic xenoliths of Grande Comore, Indian Ocean. *Journal of Petrology* **40**, 133-165.

Conquéré, F. (1977). Pétrologie des pyroxènites litées dans les complexes ultramafiques de l'Ariège (France) et autres gisements de lherzolite à spinelle. Compositions minéralogiques et chimiques, évolution des conditions d'équilibre des pyroxénites. *Bulletin de la Société Française de Minéralogie et de Cristallographie* **100**, 42-80.

Conticelli, S., Sintoni, M. F., Abebe, T., Mazzarini, F. & Manetti, P. (1999). Petrology and geochemistry of ultramafic xenoliths and host lavas from the Ethiopian volcanic province: an insight into the upper mantle under eastern Africa. *Acta Vulcanologica* **11**, 143-159.

Coogan, L. A., Kasemann, S. A. & Chakraborty, S. (2005). Rates of hydrothermal cooling of new oceanic upper crust derived from lithium-geospeedometry. *Earth and Planetary Science Letters* **240**, 415-424.

Costa, F., Dungan, M. A. & Singer, B. S. (2001). Magmatic Na-rich phlogopite in a suite of gabbroic crustal xenoliths from Volcán San Pedro, Chilean Andes: evidence for a solvus relation between phlogopite and aspidolite. *American Mineralogist* **86**, 29-35.

Courtillot, V., Davaille, A., Besse, J. & Stock, J. (2003). Three distinct types of hotspots in the Earth's mantle. *Earth and Planetary Science Letters* **205**, 295-308.

Cox, K. G. (1970). Tectonics and vulcanism of the Karroo period and their bearing on the postulated fragmentation of Gondwanaland. In: Clifford, T. N. & Gass, I. G. (eds.) *African Magmatism and Tectonics*. Edinburgh: Longman Group, 211-235.

Crank, J. (1975) *The mathematics of diffusion, 2nd edition*. Oxford: Clarendon Press.

Currie, L. A. (1968). Limits for qualitative detection and quantitative determination. *Analytical Chemistry* **40**, 586-593.

Dautria, J. M. & Girod, M. (1987). Cenozoic volcanism associated with swells and rifts. In: Nixon, P. H. (ed.) *Mantle Xenoliths*. Chichester: John Wiley & Sons, 195-214.

Dautria, J.-M., Dupuy, C., Takherist, D. & Dostal, J. (1992). Carbonate metasomatism in the lithospheric mantle: peridotitic xenoliths from a melilitic district of the Sahara basin. *Contributions to Mineralogy and Petrology* **111**, 37-52.

Dawson, J. B. (1964). Carbonate tuff cones in northern Tanganyika. *Geological Magazine* **101**, 129-137.

Dawson, J. B. (1987). Metasomatised harzburgites in kimberlite and alkaline magmas; enriched restites and flushed lherzolites. In: Menzies, M. & Hawkesworth, C. J. (eds.) *Mantle Metasomatism*. London: Academic Press, 125-144.

Dawson, J. B. (1992). Neogene tectonics and volcanicity in the north Tanzania sector of the Gregory rift-valley - contrasts with the Kenya sector. *Tectonophysics* **204**, 81-92.

Dawson, J. B. (2002). Metasomatism and partial melting in upper-mantle peridotite xenoliths from the Lashaine volcano, Northern Tanzania. *Journal of Petrology* **43**, 1749-1777.

Dawson, J. B. & Powell, D. G. (1969). Mica in the upper mantle. *Contributions to Mineralogy and Petrology* **22**, 233-237.

Dawson, J. B. & Smith, J. V. (1973). Alkalic Pyroxenite xenoliths from the Lashaine volcano, northern Tanzania. *Journal of Petrology* **14**, 113-131.

Dawson, J. B. & Smith, J. V. (1992). Olivine-mica pyroxenite xenoliths from northern Tanzania: metasomatic products of upper mantle peridotite. *Journal of Volcanology and Geothermal Research* **50**, 131-142.

Dawson, J. B. & Smith, J. V. (1988). Metasomatized and veined upper mantle xenoliths from Pello Hill, Tanzania: evidence for anomalously light mantle beneath the Tanzanian sector of the East-African Rift Valley. *Contributions to Mineralogy and Petrology* **100**, 510-527.

Dawson, J. B., Powell, D. G. & Reid, A. M. (1970). Ultrabasic xenoliths and lava from the Lashaine Volcano, northern Tanzania. *Journal of Petrology* **11**, 519-548.

Dawson, J. B., Paslick, J. D. & Halliday, A. N. (1997). Ultrabasic potassic low-volume magmatism and continental rifting in north-central Tanzania: association with enhanced heat flow. Proceedings of the Sixth International Kimberlite Conference. *Russian Geology and Geophysics* **38**, 69-81.

DeBari, S. M. & Coleman, R. G. (1989). Examination of the deep levels of an island arc: evidence from the Tonsina ultramafic-mafic assemblage, Tonsina, Alaska. *Journal of Geophysical Research* **94**, 4373-4391.

Debayle, E., Leveque, J. J. & Cara, M. (2001). Seismic evidence for a deeply rooted low-velocity anomaly in the upper mantle beneath the northeastern Afro/Arabian continent. *Earth and Planetary Science Letters* **193**, 423-436.

Defant, M. J., Richerson, P. M., Deboer, J. Z., Stewart, R. H., Maury, R. C., Bellon, H., Drummond, M. S., Feigenson, M. D. & Jackson, T. E. (1991). Dacite genesis via both slab melting and differentiation - petrogenesis of La Yeguada colcanic complex, Panama. *Journal of Petrology* **32**, 1101-1142.

Delaney, J. S., Smith, J. V., Carswell, D. A. & Dawson, J. B. (1980). Chemistry of micas from kimberlites and xenoliths - II. Primary- and secondary-textured micas from peridotite xenoliths. *Geochimica et Cosmochimica Acta* **44**, 857-872.

Demény, A., Vennemann, T. W., Hegner, E., Nagy, G., Milton, J. A., Embey-Isztin, A., Homonnay, Z. & Dobosi, G. (2004). Trace element and C-O-Sr-Nd isotope evidence for subduction related carbonate-silicate melts in mantle xenoliths (Pannonian Basin, Hungary). *Lithos* **75**, 89-113.

Dick, H. J. B. & Bullen, T. (1984). Chromian spinel as a petrogenetic indicator in abyssal and alpine-type peridotites and spatially associated lavas. *Contributions to Mineralogy and Petrology* **86**, 54-76.

Dimanov, A. & Jaoul, O. (1998). Calcium self-diffusion in diopside at high temperature: Implications for transport properties. *Physics and Chemistry of Minerals* **26**, 116-127.

Dindi, E. W. (1994). Crustal structure of the Anza graben from gravity and magnetic investigations. *Tectonophysics* **236**, 359-371.

Dostal, J., Dupuy, C. & Dudoignon, P. (1996). Distribution of boron, lithium and beryllium in ocean island basalts from French Polynesia: Implications for the B/Be and Li/Be ratios as tracers of subducted components. *Mineralogical Magazine* **60**, 563-580.

Downes, H. (2001). Formation and modification of the shallow sub-continental lithospheric mantle: a review of geochemical evidence from ultramafic xenolith suites and tectonically emplaced ultramafic massifs of western and central Europe. *Journal of Petrology* **42**, 233-250.

Downes, H., Beard, A. & Hinton, R. (2004). Natural experimental charges: an ion-microprobe study of trace element distribution coefficients in glass-rich hornblendite and clinopyroxenite xenoliths. *Lithos* **75**, 1-17.

Draper, D. S. & Green, T. H. (1997). P-T phase relations of silicic, alkaline, aluminous mantle-xenolith glasses under anhydrous and C-O-H fluid-saturated conditions. *Journal of Petrology* **38**, 1187-1224.

Ebinger, C. J. (1989). Tectonic development of the western branch of the East African rift system. *Geological Society of America Bulletin* **101**, 885-903.

Ebinger, C. J. & Ibrahim, A. (1994). Multiple episodes of rifting in Central and East-Africa: a re-evaluation of gravity data. *Geologische Rundschau* **83**, 689-702.

Ebinger, C. J. & Sleep, N. H. (1998). Cenozoic magmatism throughout east Africa resulting from impact of a single plume. *Nature* **395**, 788-791.

Ebinger, C. J., Yemane, T., Woldegabriel, G., Aronson, J. L. & Walter, R. C. (1993). Late Eocene - recent volcanism and faulting in the southern main Ethiopian rift. *Journal of the Geological Society* **150**, 99-108.

Eggins, S. M., Rudnick, R. L. & McDonough, W. F. (1998). The composition of peridotites and their minerals: a laser-ablation ICP-MS study. *Earth and Planetary Science Letters* **154**, 53-71.

Eggler, D. H. & Baker, D. R. (1982). Reduced volatiles in the system C-O-H: implications to mantle melting, fluid formation and diamond genesis. In: Akimoto, S. & Manghnani, M. H. (eds.) *High Pressure Research in Geophysics*. Tokyo: Center for Academic Publications Japan.

Elliott, T. (2003). Tracers of the slab. In: Eiler, J. (ed.) *Inside the subduction factory*. Washington: American Geophysical Union.

Elliott, T., Jeffcoate, A. & Bouman, C. (2004). The terrestrial Li isotope cycle: light-weight constraints on mantle convection. *Earth and Planetary Science Letters* **220**, 231-245.

Elliott, T., Thomas, A., Jeffcoate, A. & Niu, Y. L. (2006). Lithium isotope evidence for subduction-enriched mantle in the source of mid-ocean-ridge basalts. *Nature* **443**, 565-568.

Ernst, R. E. & Buchan, K. L. (2001) *Mantle plumes: their identification through tims*. Boulder, Colorado: Geological society of America Special Paper.

Fabriès, J., Lorand, J. P. & Bodinier, J. L. (1998). Petrogenetic evolution of orogenic lherzolite massifs in the central and western Pyrenees. *Tectonophysics* **292**, 145-167.

Fabriès, J., Lorand, J. P. & Guiraud, M. (2001). Petrogenesis of the amphibole-rich veins from the Lherz orogenic Iherzolite massif (Eastern Pyrenees, France): a case study for the origin of orthopyroxene-bearing amphibole pyroxenites in the lithospheric mantle. *Contributions to Mineralogy and Petrology* **140**, 383-403.

Fairhead, J. D. (1988). Mesozoic plate tectonic reconstructions of the central south-Atlantic ocean - the role of the west and central African rift system. *Tectonophysics* **155**, 181-191.

Ferraris, C., Grobéty, B., Früh-Green, G. L. & Wessicken, R. (2004). Intergrowth of graphite within phlogopite from Finero ultramafic complex (Italian Western Alps): implications for mantle crystallization of primary-texture mica. *European Journal of Mineralogy* **16**, 899-908.

Foster, A., Ebinger, C. J., Mbede, E. & Rex, D. (1997). Tectonic development of the northern Tanzanian sector of the East African Rift System. *Journal of the Geological Society of London* **154**, 689-700.

Foulger, G. R., Natland, J. H., Presnall, D. C. & Anderson, D. L. (2005) *Plates, plumes, and paradigms*. Boulder, Colorado: Geological Scociety of America Special Paper.

Franz, L., Becker, K.-P., Kramer, W. & Herzig, P. M. (2002). Metasomatic mantle xenoliths from the Bismarck microplate (Papua New Guinea) - thermal evolution, geochemistry and extent of slab-induced metasomatism. *Journal of Petrology* **43**, 315-343.

Freer, R. (1981). Diffusion in silicate minerals and glasses - a data digest and guide to the literature. *Contributions to Mineralogy and Petrology* **76**, 440-454.

Frey, F. A. (1980). The origin of pyroxenites and garnet pyroxenites from Salt-Lake Crater, Oahu, Hawaii - trace-element evidence. *American Journal of Science* **280**, 427-449.

Frey, F. A. & Green, D. H. (1974). Mineralogy, geochemistry and origin of Ilherzolite inclusions in Victorian basanites. *Geochimica et Cosmochimica Acta* **38**, 1023-1059.

Fritz, H., Tenczer, V., Hauzenberger, C. A., Wallbrecher, E., Hoinkes, G., Muhongo, S. & Mogessie, A. (2005). Central Tanzanian tectonic map: a step forward to decipher Proterozoic structural events in the East African Orogen. *Tectonics* **24**, TC6013.

Frost, D. J. & Wood, B. J. (1998). The fugacity of carbon dioxide and the graphite/diamond CO equilibrium between 35 and 77 kbar at 925 to 1650 degrees C. (vol 61, pg 1565, 1997). *Geochimica et Cosmochimica Acta* **62**, 725-725.

Fuchs, K., Altherr, R., Müller, B. & Prodehl, C. (1997). Structure and dynamic processes in the lithosphere of the Afro-Arabian rift system. *Tectonophysics (special issue)* **278**, 352 pp.

Furman, T. & Graham, D. (1999). Erosion of lithospheric mantle beneath the East African Rift system: geochemical evidence from the Kivu volcanic province. *Lithos* **48**, 237-262.

Furman, T., Bryce, J. G., Karson, J. & Iotti, A. (2004). East African rift system (EARS) plume structure: insights from quaternary mafic lavas of Turkana, Kenya. *Journal of Petrology* **45**, 1069-1088.

Furman, T., Kaleta, K. M., Bryce, J. G. & Hanan, B. B. (2006). Tertiary mafic lavas of Turkana, Kenya: Constraints on East African plume structure and the occurrence of high-mu volcanism in Africa. *Journal of Petrology* **47**, 1221-1244.

Gaetani, G. A., Kent, A. J. R., Grove, T. L., Hutcheon, I. D. & Stolper, E. M. (2003). Mineral/melt partitioning of trace elements during hydrous peridotite partial melting. *Contributions to Mineralogy and Petrology* **145**, 391-405.

Ganguly, J. & Tazzoli, V. (1994). Fe2+-Mg interdiffusion in ortho-pyroxene - retrieval from the data on intracrystalline exchange-reaction. *American Mineralogist* **79**, 930-937.

Ganguly, J., Cheng, W. J. & Chakraborty, S. (1998). Cation diffusion in aluminosilicate garnets: experimental determination in pyrope-almandine diffusion couples. *Contributions to Mineralogy and Petrology* **131**, 171-180.

Garasic, V. (1997). Mantelxenolithe als Dokumente der thermischen Entwicklung des Erdmantels unter den Chyulu Hills, Kenia. *PhD thesis, University of Heidelberg, Germany*.

Garrido, C. J. & Bodinier, J. L. (1999). Diversity of mafic rocks in the Ronda peridotite: evidence for pervasive melt-rock reaction during heating of subcontinental lithosphere by upwelling asthenosphere. *Journal of Petrology* **40**, 729-754.

Gasparik, T. (1987). Orthopyroxene thermobarometry in simple and complex systems. *Contributions to Mineralogy and Petrology* **96**, 357-370.

George, R. M. & Rogers, N. W. (2002). Plume dynamics beneath the African plate inferred from the geochemistry of the Tertiary basalts of southern Ethiopia. *Contributions to Mineralogy and Petrology* **144**, 286-304.

George, R., Rogers, N. & Kelley, S. (1998). Earliest magmatism in Ethiopia: evidence for two mantle plumes in one flood basalt province. *Geology* **26**, 923-926.

Glaser, S. M., Foley, S. F. & Günther, D. (1999). Trace element compositions of minerals in garnet and spinel peridotite xenoliths from the Vitim volcanic field, Transbaikalia, eastern Siberia. *Lithos* **48**, 263-285.

Godard, M., Bodinier, J.-L. & Vasseur, G. (1995). Effects of mineralogical reactions on trace element redistributions in mantle rocks during percolation processes: a chromatographic approach. *Earth and Planetary Science Letters* **133**, 449-461.

Green, D. H. & Ringwood, A. E. (1967). The genesis of basaltic magmas. *Contributions to Mineralogy and Petrology* **15**, 103-190.

Green, D. H. & Wallace, M. E. (1988). Mantle metasomatism by ephemeral carbonatite melts. *Nature* **336**, 459-462.

Green, T. H., Blundy, J. D., Adam, J. & Yaxley, G. M. (2000). SIMS determination of trace element partition coefficients between garnet, clinopyroxene and hydrous basaltic liquids at 2-7.5 GPa and 1080-1200° C. *Lithos* **53**, 165-187.

Green, W. V., Achauer, U. & Meyer, R. P. (1991). A 3-dimensional seismic image of the crust and upper mantle beneath the Kenya rift. *Nature* **354**, 199-203.

Greene, L. C., Richards, D. R. & Johnson, R. A. (1991). Crustal structure and tectonic evolution of the Anza rift, northern Kenya. *Tectonophysics* **197**, 203-211.

Grégoire, M., McInnes, B. I. A. & O'Reilly, S. Y. (2001). Hydrous metasomatism of oceanic sub-arc mantle, Lihir, Papua New Guinea, Part 2. Trace element characteristics of slab-derived fluids. *Lithos* **59**, 91-108.

Grégoire, M., Bell, D. R. & Le Roex, A. P. (2002). Trace element geochemistry of phlogopite-rich mafic mantle xenoliths: their classification and their relationship to phlogopite-bearing peridotites and kimberlites. *Contributions to Mineralogy and Petrology* **142**, 603-625.

Gregory, J. W. (1896) *The Great Rift Valley*. London: John Murray.

Gregory, J. W. (1921) *Rift Valleys and the Geology of East African*. London: Seeley Service.

Griffin, W. L., Wass, S. Y. & Hollis, J. D. (1984). Ultramafic xenoliths from Bullenmerri and Gnotuk maars, Victoria, Australia: petrology of a sub-continental crust-mantle transition. *Journal of Petrology* **25**, 53-87.

Griffin, W. L., O'Reilly, S. Y. & Stabel, A. (1988). Mantle metasomatism beneath western Victoria, Australia. 2. Isotopic geochemistry of Cr-diopside Iherzolites and Al-augite pyroxenites. *Geochimica et Cosmochimica Acta* **52**, 449-459.

Griffin, W. L., O'Reilly, S. Y. & Ryan, C. G. (1999). The composition and origin of sub-continental lithospheric mantle. In: Fei, Y., Bertka, C. M. & Mysen, B. O. (eds.) *Mantle Petrology: Field Observation and High-Pressure Experimentation. A Tribute to Francis R. (Joe) Boyd*: Geochem. Soc. Spec. Pub., 13-45.

Guiraud, R. & Bellion, Y. (1995). Late Carboniferous to recent, geodynamic evolution of the west Gondwanian, cratonic, Tethyan margins. In: Nairn, A. E. M. (ed.) *The Ocean Basins and Margins*. New York: Plenum Press, 101-124.

Günther, D., Frischknecht, R., Heinrich, C. A. & Kahlert, H. J. (1997). Capabilities of an Argon Fluoride 193 nm excimer laser for laser ablation inductively coupled plasma mass spectrometry microanalysis of geological materials. *Journal of Analytical Atomic Spectrometry* **12**, 939-944.

Hamelin, B. & Allègre, C. J. (1988). Evidence for the 'marble-cake' structure of the mantle: a lead isotope study of orogenic lherzolite massifs. *Earth and Planetary Science Letters* **91**, 117-131.

Harley, S. L. (1984). An experimental study of the partitioning of Fe and Mg between garnet and orthopyroxene. *Contributions to Mineralogy and Petrology* **86**, 359-373.

Hauri, E. H., Shimizu, N., Dieu, J. J. & Hart, S. R. (1993). Evidence for hotspot-related carbonatite metasomatism in the oceanic upper mantle. *Nature* **365**, 221-227.

Heinrich, C. A., Pettke, T., Halter, W. E., Aigner-Torres, M., Audetat, A., Günther, D., Hattendorf, B., Bleiner, D., Guillong, M. & Horn, I. (2003). Quantitative multi-element analysis of minerals, fluid and melt inclusions by laser-ablation inductively-coupled-plasma mass-spectrometry. *Geochimica et Cosmochimica Acta* **67**, 3473-3497.

Hendrie, D. B., Kusznir, N. J., Morley, C. K. & Ebinger, C. J. (1994). Cenozoic extension in northern Kenya: a quantitative model of rift basin development in the Turkana region. *Tectonophysics* **236**, 409-438.

Henjes-Kunst, F. & Altherr, R. (1992). Metamorphic petrology of xenoliths from Kenya and northern Tanzania and implications for geotherms and lithospheric structures. *Journal of Petrology* **33**, 1125-1156.

Hibbard, M. J. & Sjöberg, J. J. (1994). Signs of incongruent melting of clinopyroxene in limburgite, Thetford Hill, Vermont. *Can. Mineral.* **32**, 307-317.

Hill, E., Wood, B. J. & Blundy, J. D. (2000). The effect of Ca-Tschermaks component on trace element partitioning between clinopyroxene and silicate melt. *Lithos* **53**, 203-215.

Hirschmann, M. M. & Stolper, E. M. (1996). A possible role for garnet pyroxenite in the origin of the ''garnet signature'' in MORB. *Contributions to Mineralogy and Petrology* **124**, 185-208.

Ho, K. S., Chen, J. C., Smith, A. D. & Juang, W. S. (2000). Petrogenesis of two groups of pyroxenite from Tungchihsu, Penghu Islands, Taiwan Strait: implications for mantle metasomatism beneath SE China. *Chemical Geology* **167**, 355-372.

Hofmann, A. W. (1997). Mantle geochemistry: the message from oceanic volcanism. *Nature* **385**, 219-229.

Holland, T. J. B. (1980). The reaction albite = jadeite + quartz determined experimentally in the range 600-1200°C. *American Mineralogist* **65**, 129-134.

Holmes, A. (1951). The sequence of Precambrian orogenic belts in south and central Africa. In: *Proceedings of the 18th International Geological Congress, Vol.14*. London: Assoc. Seros. Geol. Afr., 254-269.

Ionov, D. A. (1998). Trace element composition of mantle-derived carbonates and coexisting phases in peridotite xenoliths from alkali basalts. *Journal of Petrology* **39**, 1931-1941.

Ionov, D. A. (2004). Chemical variations in peridotite xenoliths from Vitim, Siberia: inferences for REE and Hf behaviour in the garnet-facies upper mantle. *Journal of Petrology* **45**, 343-367.

Ionov, D. A. & Hofmann, A. W. (1995). Nb-Ta-rich mantle amphiboles and micas - implications for subduction-related metasomatic trace-element fractionations. *Earth and Planetary Science Letters* **131**, 341-356.

Ionov, D. A. & Harmer, R. E. (2002). Trace element distribution in calcite-dolomite carbonatites from Spitskop: inferences for differentiation of carbonatite magmas and the origin of carbonates in mantle xenoliths. *Earth and Planetary Science Letters* **198**, 495-510.

Ionov, D. A., Dupuy, C., O'Reilly, S. Y., Kopylova, M. G. & Genshaft, Y. S. (1993). Carbonated peridotite xenoliths from Spitsbergen: implications for trace element signature of mantle carbonate metasomatism. *Earth and Planetary Science Letters* **119**, 283-297.

Ionov, D. A., Hofmann, A. W. & Shimizu, N. (1994). Metasomatism-induced melting in mantle xenoliths from Mongolia. Journal of Petrology 35, 753-785.

Ionov, D. A., Griffin, W. L. & O'Reilly, S. Y. (1997). Volatile-bearing minerals and lithophile trace elements in the upper mantle. *Chemical Geology* **141**, 153-184.

Ionov, D. A., O'Reilly, S. Y., Genshaft, Y. S. & Kopylova, M. G. (1996). Carbonate-bearing mantle peridotite xenoliths from Spitsbergen: phase relationship, mineral compositions and trace-element residence. *Contributions to Mineralogy and Petrology* **125**, 375-392.

Ionov, D. A., O'Reilly, S. Y. & Griffin, W. L. (1998). A geotherm and lithosphere section for central Mongolia (Tariat region). In: Flower, M., Chung, S. L., Lo, C. H. & Lee, T. Y. (eds.) *Mantle dynamics and plate interactions in East Asia*. Washington, D.C.: American Geophysical Union Geodynamics, 127-154.

Ionov, D. A., Bodinier, J.-L., Mukasa, S. B. & Zanetti, A. (2002). Mechanisms and sources of mantle metasomatism: major and trace element compositions of peridotite xenoliths from Spitsbergen in the context of numerical modelling. *Journal of Petrology* **43**, 2219-2259.

Ionov, D. A., Ashchepkov, I. & Jagoutz, E. (2005). The provenance of fertile off-craton lithospheric mantle: Sr-Nd isotope and chemical composition of garnet and spinel peridotite xenoliths from Vitim, Siberia. *Chemical Geology* **217**, 41-75.

Ionov, D. A., Chazot, G., Chauvel, C., Merlet, C. & Bodinier, J. L. (2006). Trace element distribution in peridotite xenoliths from Tok, SE Siberian craton: a record of pervasive, multi-stage metasomatism in shallow refractory mantle. *Geochimica et Cosmochimica Acta* **70**, 1231-1260.

Irving, A. J. (1974a). Pyroxene-rich ultramafic xenoliths in the Newer Basalts of Victoria, Australia. *Neues Jahrbuch für Mineralogie Abhandlungen* **120**, 147-167.

Irving, A. J. (1974b). Geochemical and high-pressure experimental studies of garnet pyroxenite and pyroxene granulite xenoliths from the Delegate basaltic pipes, Australia. *Journal of Petrology* **15**, 1-40.

Irving, A. J. (1980). Petrology and geochemistry of composite ultramafic xenoliths in alkalic basalts and implications for magmatic processes within the mantle. *American Journal of Science* **280**, 389-426.

Irving, A. J. & Frey, F. A. (1984). Trace element abundances in megacrysts and their host basalts - constraints on partition-coefficients and megacryst genesis. *Geochimica et Cosmochimica Acta* **48**, 1201-1221.

Ishikawa, T. & Nakamura, E. (1994). Origin of the slab component in arc lavas from across-arc variation of B and Pb isotopes. *Nature* **370**, 205-208.

Ito, M. (1986). Kimberlites and their ultramafic xenoliths from Western Kenya. *Tschermaks Mineralogische und Petrographische Mitteilungen* **35**, 193-216.

Jacob, D. E. (2004). Nature and origin of eclogite xenoliths from kimberlites. *Lithos* **77**, 295-316.

Jambon, A. & Semet, M. P. (1978). Lithium diffusion in silicate-glasses of albite, orthoclase, and obsidian composition - ion-microprobe determination. *Earth and Planetary Science Letters* **37**, 445-450.

Jeffcoate, A. B., Elliott, T., Kasemann, S. A., Ionov, D., Cooper, K. & Brooker, R. (2006). Li isotope fractionation in peridotites and mafic melts. *Geochimica et Cosmochimica Acta*, doi: 10.1016/j.gca.2006.06.1611.

Johnson, L. H., Jones, A. P., Church, A. A. & Taylor, W. R. (1997). Ultramafic xenoliths and megacrysts from a melilitite tuff cone, Deeti, northern Tanzania. *Journal of African Earth Sciences* **25**, 29-42.

Johnson, M. C. & Plank, T. (1999). Dehydration and melting experiments constrain the fate of subducted sediments. *Geochemistry Geophysics Geosystems* **1**, doi:1999GC000014.

Johnson, S. P., Cutten, H. N. C., Muhongo, S. & De Waele, B. (2003). Neoarchaean magmatism and metamorphism of the western granulites in the central domain of the Mozambique belt, Tanzania: U-Pb shrimp geochronology and PT estimates. *Tectonophysics* **375**, 125-145.

Jones, A. P. (1983). Metamorphism, partial melting, and K-metasomatism of garnet-scapolite-kyanite granulite xenoliths from Lashaine, Tanzania. *Journal of Geology.* **91**, 143-165.

Jones, A. P., Smith, J. V. & Dawson, J. B. (1983). Glasses in mantle xenoliths from Olmani, Tanzania. *Journal of Geology.* **91**, 167-178.

Kabeto, K., Sawada, Y., Iizumi, S. & Wakatsuki, T. (2001). Mantle sources and magma-crust interactions in volcanic rocks from the northern Kenya rift: geochemical evidence. *Lithos* **56**, 111-139.

Kaeser, B., Kalt, A. & Pettke, T. (2006). Evolution of the lithopsheric mantle beneath the Marsabit volcanic field (northern Kenya): constraints from textural, P-T and geochemical studies on xenoliths. *Journal of Petrology* **47**, 2149-2184.

Kalfoun, F., Ionov, D. & Merlet, C. (2002). HFSE residence and Nb/Ta ratios in metasomatised, rutile-bearing mantle peridotites. *Earth and Planetary Science Letters* **199**, 49-65.

Kaliwoda, M. (2004). Mantel-Xenolithe des Harrat Uwayrid (Saudi-Arabien): Archive des stofflichen und thermischen Entwicklung des lithopshärischen Erdmantels im Bereich eines passiven Kontinentalrandes. *PhD thesis, University of Heidelberg, Germany*, pp. 365.

Kalt, A., Hegner, E. & Satir, M. (1997). Nd, Sr, and Pb isotopic evidence for diverse lithospheric mantle sources of East African Rift carbonatites. *Tectonophysics* **278**, 31-45.

Kampunzu, A. B. & Mohr, P. (1991). Magmatic evolution and petrogenesis in the East African Rift System. In: Kampunzu, A. B. & Lubala, R. T. (eds.) *Magmatism in extensional structural settings; the phanerozoic African plate*. Berlin: Springer.

Kampunzu, A. B., Bonhomme, M. G. & Kanika, M. (1998). Geochronology of volcanic rocks and evolution of the Cenozoic Western Branch of the East African Rift System. *Journal of African Earth Sciences* **26**, 441-461.

Kempton, P. D. (1987). Metasomatism and enrichment in lithospheric peridotites. In: Menzies, M. A. & Hawkesworth, C. J. (eds.) *Mantle Metasomatism.* London: Academic Press, 45-89.

Kepezhinskas, P. K., Defant, M. J. & Drummond, M. S. (1995). Na metasomatism in the island-arc mantle by slab melt-peridotite interaction: evidence from mantle xenoliths in the north Kamchatka arc. *Journal of Petrology* **36**, 1505-1527.

Kepezhinskas, P., Defant, M. J. & Drummond, M. S. (1996). Progressive enrichment of island arc mantle by melt-peridotite interaction inferred from Kamchatka xenoliths. *Geochimica et Cosmochimica Acta* **60**, 1217-1229.

Keppler, H. (1996). Constraints from partitioning experiments on the composition of subduction-zone fluids. *Nature* **380**, 237-240.

Kerr, A. C., Saunders, A. D., Tarney, J., Berry, N. H. & Hards, V. L. (1995). Depleted mantle-plume geochemical signatures: no paradox for plume theories. *Geology* **23**, 843-846.

Kessel, R., Schmidt, M. W., Ulmer, P. & Pettke, T. (2005). Trace element signature of subduction-zone fluids, melts and supercritical liquids at 120-180 km depth. *Nature* **437**, 724-727.

Key, R. M., Rop, B. P. & Rundle, C. C. (1987). The development of the late Cenozoic alkali basaltic Marsabit shield volcano, northern Kenya. *Journal of African Earth Sciences* **6**, 475-491.

Key, R. M., Charsley, T. J., Hackman, B. D., Wilkinson, A. F. & Rundle, C. C. (1989). Superimposed upper Proterozoic collision-controlled orogenies in the Mozambique orogenic belt of Kenya. *Precambrian Research* **44**, 197-225.

King, B. C. (1970). Vulcanicity and rift tectonics in east Africa. In: Clifford, T. N. & Gass, I. G. (eds.) *African Magmatism and Tectonics*. Edinburgh: Longman Group, 263-285.

King, S. D. & Ritsema, J. (2000). African hot spot volcanism: small-scale convection in the upper mantle beneath cratons. *Science* **290**, 1137-1140.

Klemme, S. & O'Neill, H. S. (2000). The near-solidus transition from garnet lherzolite to spinel lherzolite. *Contributions to Mineralogy and Petrology* **138**, 237-248.

Klemme, S., Blundy, J. D. & Wood, B. J. (2002). Experimental constraints on major and trace element partitioning during partial melting of eclogite. *Geochimica et Cosmochimica Acta* **66**, 3109-3123.

Klemme, S., Prowatke, S., Hametner, K. & Günther, D. (2005). Partitioning of trace elements between rutile and silicate melts: implications for subduction zones. *Geochimica et Cosmochimica Acta* **69**, 2361-2371.

Kogiso, T., Hirschmann, M. M. & Pertermann, M. (2004). High-pressure partial melting of mafic lithologies in the mantle. *Journal of Petrology* **45**, 2407-2422.

Koloskov, A. V. & Zharinov, S. E. (1993). Multivariate statistical analysis of clinopyroxene compositions from mafic and ultramafic xenoliths in volcanic rocks. *Journal of Petrology* **34**, 173-185.

Kopylova, M. G., Russell, J. K. & Cookenboo, H. (1999). Petrology of peridotite and pyroxenite xenoliths from Jericho kimberlite: implications for the thermal state of the mantle beneath the Slave craton, northern Canada. *Journal of Petrology* **40**, 79-104.

Kornprobst, J. (1966). A propos des peridotites du massif des Beni-Bouchera (Rif septentrional Maroc). *Bulletin de la Société Française de Minéralogie et de Cristallographie* **89**, 399-404.

Kornprobst, J. & Conquéré, F. (1972). Les pyroxenolites à grenat du massif de lhérzolite de Moncaup (Haute Garonne - France); caractères communs avec certaines enclaves des basaltes alcalins. *Earth and Planetary Science Letters* **16**, 1-14.

Kornprobst, J., Piboule, M., Roden, M. & Tabit, A. (1990). Corundum-bearing garnet clinopyroxenites at Beni Bousera (Morocco): original plagioclase-rich gabbros recrystallized at depth within the mantle. *Journal of Petrology* **31**, 717-745.

Krogh, E. J. (1988). The garnet-clinopyroxene Fe-Mg geothermometer - a reinterpretation of existing experimental data. *Contributions to Mineralogy and Petrology* **99**, 44-48.

Kumar, N., Reisberg, L. & Zindler, A. (1996). A major and trace element and strontium, neodymium, and osmium isotopic study of a thick pyroxenite layer from the Beni Bousera ultramafic complex of northern Morocco. *Geochimica et Cosmochimica Acta* **60**, 1429-1444.

Kurat, G., Palme, H., Embeyisztin, A., Touret, J., Ntaflos, T., Spettel, B., Brandstatter, F., Palme, C., Dreibus, G. & Prinz, M. (1993). Petrology and geochemistry of peridotites and associated vein rocks of Zabargad-Island, Red-Sea, Egypt. *Mineralogy and Petrology* **48**, 309-341.

Kushiro, I., Nakamura, Y., Akimoto, S. & Shimizu, N. (1972). Compositions of coexisting liquid and solid phases formed upon melting of natural garnet and spinel lherzolites at high pressures. A preliminary report. *Earth and Planetary Science Letters* **14**, 19-&.

Lambiase, J. J. (1989). The framework of African rifting during the Phanerozoic. *Journal of African Earth Sciences* **8**, 183-190.

Latin, D., Norry, M. J. & Tarzey, R. J. E. (1993). Magmatism in the Gregory rift, east-Africa - evidence for melt generation by a plume. *Journal of Petrology* **34**, 1007-1027.

LaTourrette, T., Hervig, R. L. & Holloway, J. R. (1995). Trace-element partitioning between amphibole, phlogopite, and basanite melt. *Earth and Planetary Science Letters* **135**, 13-30.

Laurora, A., Mazzucchelli, M., Rivalenti, G., Vannucci, R., Zanetti, A., Barbieri, M. A. & Cingolani, C. A. (2001). Metasomatism and melting in carbonated peridotite xenoliths from the mantle wedge: the Gobernador Gregores case (southern Patagonia). *Journal of Petrology* **42**, 69-87.

Le Bas, M. J. (1987). Nephelinites and carbonatites. In: Fitton, J. G. & Upton, B. G. J. (eds.) *Alkaline Igneous Rocks*. London: Geological Society, Special Publication, 53-83.

Leake, B. E., Woolley, A. R., Arps, C.E.S., Birch, W.D., Gilbert, M.C., Grice, J.D., Hawthorne, F.C., Kato, A., Kisch, H.J., Krivovichev, V.G., Linthout, K., Laird, J., Mandarino, J.A., Maresch, W.V., Nickel, E.H., Rock, N.M.S., Schumacher,

J.C., Smith, D.C., Stephenson, N.C.N., Ungaretti, L., Whittaker, E.J.W. & Guo, Y.Z. (1997). Nomenclature of amphiboles: report of the subcommittee on amphiboles of the International Mineralogical Association, commission on new minerals and mineral names. *American Mineralogist* **82**, 1019-1037.

Lee, C.-T. & Rudnick, R. (1999). Compositionally stratified cratonic lithosphere; petrology and geochemistry of peridotite xenoliths from the Labait Volcano, Tanzanie. In: Gurney, J., Gurney, J. L., Pascoe, M. D. & Richardson, S. H. (eds.) *Proceedings of the 7th international Kimberlite Conference*. Cape Town: Red Roof Design, 503-521.

Lee, C.-T., Rudnick, R. L., McDonough, W. F. & Horn, I. (2000). Petrologic and geochemical investigation of carbonates in peridotite xenoliths from northeastern Tanzania. *Contributions to Mineralogy and Petrology* **139**, 470-484.

Lee, W. J. & Wyllie, P. J. (1996). Liquid immiscibility in the join $NaAlSi_3O_8$-$CaCO_3$ to 2.5 GPa and the origin of calciocarbonatite magmas. *Journal of Petrology* **37**, 1125-1152.

Lee, W. J. & Wyllie, P. J. (2000). The system CaO-MgO-SiO_2-CO_2 at 1 Gpa, metasomatic wehrlites, and primary carbonatite magmas. *Contributions to Mineralogy and Petrology* **138**, 214-228.

Leeman, W. P. & Sisson, V. B. (1996). Geochemistry of boron and its implications for crustal and mantle processes. In: Grew, E. S. & Anovitz, L. M. (eds.) *Boron: mineralogy, petrology and geochemistry, Reviews in Mineralogy*: Mineralogical Society of America, 645-708.

Lentz, R. C. F., McSween, H. Y., Ryan, J. & Riciputi, L. R. (2001). Water in martian magmas: Clues from light lithophile elements in shergottite and nakhlite pyroxenes. *Geochimica et Cosmochimica Acta* **65**, 4551-4565.

Lin, S. C., Kuo, B. Y., Chiao, L. Y. & van Keken, P. E. (2005). Thermal plume models and melt generation in East Africa: A dynamic modeling approach. *Earth and Planetary Science Letters* **237**, 175-192.

Lippard, S. J. (1973). The petrology of phonolites from the Kenya rift. *Lithos* **6**, 217-234.

Litasov, K. D., Foley, S. F. & Litasov, Y. D. (2000). Magmatic modification and metasomatism of the subcontinental mantle beneath Vitim volcanic field (East Siberia): evidence from trace element data on pyroxenite and peridotite xenoliths from miocene picrobasalt. *Lithos* **54**, 83-114.

Lithgow-Bertelloni, C. & Silver, P. G. (1998). Dynamic topography, plate driving forces and the African superswell. *Nature* **395**, 269-272.

Liu, Y. S., Gao, S., Lee, C. T. A., Hu, S. H., Liu, X. M. & Yuan, H. L. (2005). Melt-peridotite interactions: links between garnet pyroxenite and high-Mg# signature of continental crust. *Earth and Planetary Science Letters* **234**, 39-57.

Lloyd, F. E. & Bailey, D. K. (1975). Light element metasomatism of the continental mantle: the evidences and the consequences. *Physics and Chemistry of the Earth* **9**, 389-416.

Lloyd, F. E., Nixon, P. H., Hornung, G. & Condliffe, E. (1987). Regional K-metasomatism in the mantle beneath the west branch of the East African Rift: alkali clinopyroxenite xenoliths in highly potassic magmas. In: Nixon, P. H. (ed.) *Mantle Xenoliths*. Chichester: John Wiley & Sons, 641-659.

Lofgren, G. E. (1983). Effect of heterogeneous nucleation on basaltic textures - a dynamic crystallization study. *Journal of Petrology* **24**, 229-255.

Longerich, H. P., Jackson, S. E. & Günther, D. (1996). Laser ablation inductively coupled plasma mass spectrometric transient signal data acquisition and analyte concentration calculation. *Journal of Analytical Atomic Spectrometry* **11**, 899-904.

Lorand, J. P., Reisberg, L. & Bedini, R. M. (2003). Platinum-group elements and melt percolation processes in Sidamo spinel peridotite xenoliths, Ethiopia, East African Rift. *Chemical Geology* **196**, 57-75.

Loubet, M. & Allègre, C. J. (1982). Trace-elements in orogenic Iherzolites reveal the complex history of the upper mantle. *Nature* **298**, 809-814.

Lundström, C. C., Chaussidon, M., Hsui, A. T., Kelemen, P. & Zimmerman, M. (2005). Observations of Li isotopic variations in the Trinity Ophiolite: Evidence for isotopic fractionation by diffusion during mantle melting. *Geochimica et Cosmochimica Acta* **69**, 735-751.

Maboko, M. A. H. (2000). Nd and Sr isotopic investigation of the Archean-Proterozoic boundary in north eastern Tanzania: constraints on the nature of Neoproterozoic tectonism in the Mozambique Belt. *Precambrian Research* **102**, 87-98.

Macdonald, R. (1994). Petrological evidence regarding the evolution of the Kenya rift-valley. *Tectonophysics* **236**, 373-390.

Macdonald, R., Williams, L. A. J. & Gass, I. G. (1994). Tectonomagmatic evolution of the Kenya Rift valley: some geological perspectives. *Journal of the Geological Society of London* **151**, 879-888.

Macdonald, R., Rogers, N. W., Fitton, J. G., Black, S. & Smith, M. (2001). Plume-litosphere interactions in the generation of the basalts of the Kenya Rift, East Africa. *Journal of Petrology* **42**, 877-900.

Manning, C. E. (2004). The chemistry of subduction-zone fluids. *Earth and Planetary Science Letters* **223**, 1-16.

Manya, S. & Maboko, M. A. H. (2003). Dating basaltic volcanism in the Neoarchaean Sukumaland Greenstone Belt of the Tanzania Craton using the Sm-Nd method: implications for the geological evolution of the Tanzania Craton. *Precambrian Research* **121**, 35-45.

Marschall, H. R. & Ludwig, T. (2004). The low-boron contest: minimising surface contamination and analysing boron concentrations at the ng/g-level by secondary ion mass spectrometry. *Mineralogy and Petrology* **81**, 265-278.

Maury, R. C., Defant, M. J. & Joron, J. L. (1992). Metasomatism of the sub-arc mantle inferred from trace-elements in Philippine xenoliths. *Nature* **360**, 661-663.

McCall, G. J. H. (1958). Geology of the Gwasi area. *Geological Survey of Kenya* **Report No. 45**, 68 pps.

McCall, G. J. H. (1970). Gabbroic and ultramafic nodules: high level intracrustal nudular occurrences in alkalic basalts and associated volcanics from Kenya, described and compared to with those of Hawaii. *Physics of the Earth and Planetary Interiors* **3**, 255-272.

McDonough, W. F., Stosch, H. G. & Ware, N. G. (1992). Distribution of titanium and the rare earth elements between peridotitic minerals. *Contributions to Mineralogy and Petrology* **110**, 321-328.

McDonough, W. F. & Sun, S. S. (1995). The composition of the Earth. *Chemical Geology* **120**, 223-253.

McDougall, I. & Watkins, R. T. (2006). Geochronology of the Nabwal Hills: a record of earliest magmatism in the northern Kenyan Rift Valley. *Geological Magazine* **143**, 25-39.

McInnes, B. I. A. & Cameron, E. M. (1994). Carbonated, alkaline hybridizing melts from a sub-arc environment - mantle wedge samples from the Tabar-Lihir Tanga-Feni arc, Papua-New-Guinea. *Earth and Planetary Science Letters* **122**, 125-141.

McInnes, B. I. A., Grégoire, M., Binns, R. A., Herzig, P. M. & Hannington, M. D. (2001). Hydrous metasomatism of oceanic sub-arc mantle, Lihir, Papua New Guinea: petrology and geochemistry of fluid-metasomatised mantle wedge xenoliths. *Earth and Planetary Science Letters* **188**, 169-183.

McKenzie, D. & Bickle, M. J. (1988). The volume and composition of melt generated by extension of the lithosphere. *Journal of Petrology* **29**, 625-679.

McSween, H. Y., Grove, T. L., Lentz, R. C. F., Dann, J. C., Holzheid, A. H., Riciputi, L. R. & Ryan, J. G. (2001). Geochemical evidence for magmatic water within Mars from pyroxenes in the Shergotty meteorite. *Nature* **409**, 487-490.

Mechie, J., Keller, G. R., Prodehl, C., Khan, M. A. & Gaciri, S. J. (1997). A model for the structure, composition and evolution of the Kenya rift. *Tectonophysics* **278**, 95-119.

Médard, E., Schmidt, M. W., Schiano, P. & Ottolini, L. (2006). Melting of amphibole-bearing wehrlites: an experimental study on the origin of ultra-calcic nepheline-normative melts. *Journal of Petrology* **47**, 481-504.

Meert, J. G. (2003). A synopsis of events related to the assembly of eastern Gondwana. *Tectonophysics* **362**, 1-40.

Meert, J. G., Vandervoo, R. & Patel, J. (1994). Paleomagnetism of the late Archean Nyanzian system, western Kenya. *Precambrian Research* **69**, 113-131.

Menzies, M. A. & Hawkesworth, C. J. (1987) *Mantle Metsomatism*. London: Academic Press.

Menzies, M., Kempton, P. & Dungan, M. (1985). Interaction of continental lithosphere and asthenospheric melts below the Geronimo volcanic field, Arizona, USA. *Journal of Petrology* **26**, 663-693.

Moine, B. N., Grégoire, M., O'Reilly, S. Y., Sheppard, S. M. F. & Cottin, J. Y. (2001). High field strength element fractionation in the upper mantle: Evidence from amphibole-rich composite mantle xenoliths from the Kerguelen Islands (Indian Ocean). *Journal of Petrology* **42**, 2145-2167.

Moine, B. N., Grégoire, M., O'Reilly, S. Y., Delpech, G., Sheppard, S. M. F., Lorand, J. P., Renac, C., Giret, A. & Cottin, J. Y. (2004). Carbonatite melt in the upper mantle beneath the Kerguelen Archipelago. *Lithos* **75**, 239-252.

Möller, A., Mezger, K. & Schenk, V. (1998). Crustal age domains and the evolution of the continental crust in the Mozambique Belt of Tanzania: Combined Sm-Nd, Rb-Sr, and Pb-Pb isotopic evidence. *Journal of Petrology* **39**, 749-783.

Montanini, A., Tribuzio, R. & Anczkiewicz, R. (2006). Exhumation history of a garnet pyroxenite-bearing mantle section from a continent-ocean transition (northern Apennine ophiolites, Italy). *Journal of Petrology* **47**, 1943-1971.

Montelli, R., Nolet, G., Dahlen, F. A., Masters, G., Engdahl, E. R. & Hung, S. H. (2004). Finite-frequency tomography reveals a variety of plumes in the mantle. *Science* **303**, 338-343.

Morishita, T. & Arai, S. (2003). Evolution of spinel-pyroxene symplectite in spinel-lherzolites from the Horoman Complex, Japan. *Contributions to Mineralogy and Petrology* **144**, 509-522.

Morishita, T., Arai, S. & Green, D. H. (2003). Evolution of low-Al orthopyroxene in the Horoman peridotite, Japan: An unusual indicator of metasomatizing fluids. *Journal of Petrology* **44**, 1237-1246.

Morishita, T., Arai, S. & Green, D. H. (2004). Possible non-melted remnants of subducted lithosphere: Experimental and geochemical evidence from corundum-bearing mafic rocks in the Horoman peridotite complex, Japan. *Journal of Petrology* **45**, 235-252.

Morley, C. K., Wescott, W. A., Stone, D. M., Harper, R. M., Wigger, S. T. & Karanja, F. M. (1992). Tectonic evolution of the northern Kenya Rift. *Journal of the Geological Society of London* **149**, 333-348.

Morley, C. K. (1999). Tectonic evolution of the East African Rift System and the modifying influence of magmatism: a review. *Acta Vulcanologica* **11**, 1-19.

Morley, C. K., Ngenoh, D. K. & Ego, J. K. (2006a). Introduction to the East African Rift System. In: Morley, C. K. (ed.) *Geoscience of Rift Systems - Evolution of East Africa.* Tulsa, Oklahoma: AAPG Studies in Geology **44**, 1-18.

Morley, C. K., Wescott, W. A., Stone, D. M., Harper, R. M., Wigger, S. T., Day, R. A. & Karanja, F. M. (2006b). Geology and geophysics of the western Turkana basin, Kenya. In: Morley, C. K. (ed.) *Geoscience of Rift Systems - Evolution of East Africa.* Tulsa, Oklahoma: AAPG Studies in Geology **44**, 19-54.

Morley, C. K., Day, R. A., Lauck, R., Bosher, R., Stone, D. M., Wigger, S. T., Wescott, W. A., Haun, D., Bassett, N. & Bosworth, W. (2006b). Geology and geophysics of the Anza Graben. In: Morley, C. K. (ed.) *Geoscience of Rift Systems - Evolution of East Africa*. Tulsa, Oklahoma: AAPG Studies in Geology **44**, 67-90.

Morten, L., Defrancesco, A. M., Bonavia, F. F., Haileselassie, G., Bargossi, G. M. & Bondi, M. (1992). A new mantle xenolith locality from southern Ethiopia. *Mineralogical Magazine* **56**, 422-425.

Mungall, J. E., Dingwell, D. B. & Chaussidon, M. (1999). Chemical diffusivities of 18 trace elements in granitoid melts. *Geochimica et Cosmochimica Acta* **63**, 2599-2610.

Müntener, O. (1997). The Malenco peridotites (Alps): petrology and geochemistry of subcontinental mantle and Jurassic exhumation during rifting. *PhD thesis, ETH Zürich, Switzerland*.

Müntener, O. & Hermann, J. (1996). The Val Malenco lower crust - upper mantle complex and its field relations (Italian Alps). *Schweizerische Mineralogische und Petrographische Mitteilungen* **76**, 475-500.

Müntener, O., Kelemen, P. B. & Grove, T. L. (2001). The role of H_2O during crystallization of primitive arc magmas under uppermost mantle conditions and genesis of igneous pyroxenites: an experimental study. *Contributions to Mineralogy and Petrology* **141**, 643-658.

Mysen, B. O. & Boettcher, A. L. (1975). Melting of a hydrous mantle: 2. Geochemistry of crystals and liquids formed by anatexis of mantle peridotite at high-pressures and high-temperatures as a function of controlled activities of water, hydrogen, and carbon-Dioxide. *Journal of Petrology* **16**, 549-593.

Navon, O. & Stolper, E. (1987). Geochemical consequences of melt percolation: the upper mantle as a chromatographic column. *Journal of Geology.* **95**, 285-307.

Neumann, E.-R. & Wulff-Pedersen, E. (1997). The origin of highly silicic glass in mantle xenoliths from the Canary Islands. *Journal of Petrology* **38**, 1513-1539.

Neumann, E.-R., Wulff-Pedersen, E., Pearson, N. J. & Spencer, E. A. (2002). Mantle xenoliths from Tenerife (Canary Islands): evidence for reactions between mantle peridotites and silicic carbonatite melts inducing Ca metasomatism. *Journal of Petrology* **43**, 825-857.

Ni, S. D. & Helmberger, D. V. (2003). Seismological constraints on the South African superplume; could be the oldest distinct structure on Earth. *Earth and Planetary Science Letters* **206**, 119-131.

Nicolas, A. (1986). A melt extraction model based on structural studies in mantle peridotites. *Journal of Petrology* **27**, 999-1022.

Nicolas, A. & Jackson, M. (1982). High temperature dikes in peridotites: origin by hydraulic fracturing. *Journal of Petrology* **23**, 568-582.

Nielson, J. E. (1989). Nature and sequence of mantle magmatic events indicated by compositional variations in a composite xenolith from Lashaine volcano, Tanzania. In: Ross, J. (ed.) *Kimberlite and Related Rocks*: Geological Society of Australia, Special Volume, 700-708.

Niida, K. & Green, D. H. (1999). Stability and chemical composition of pargasitic amphibole in MORB pyrolite under upper mantle conditions. *Contributions to Mineralogy and Petrology* **135**, 18-40.

Nishio, Y., Nakai, S., Yamamoto, J., Sumino, H., Matsumoto, T., Prikhod'ko, V. S. & Arai, S. (2004). Lithium isotopic systematics of the mantle-derived ultramafic xenoliths: implications for EM1 origin. *Earth and Planetary Science Letters* **217**, 245-261.

Nixon, P. H. (1987). Kimberlitic xenoliths and their cratonic setting. In: Nixon, P. H. (ed.) *Mantle Xenoliths*. Chichester: John Wiley & Sons, 215-239.

Nyamai, C. M., Mathu, E. M., Opiyo-Akech, N. & Wallbrecher, E. (2003). A reappraisal of the geology, geochemistry, structures and tectonics of the Mozambique belt in Kenya, east of the rift system. *African Journal of Science and Technology* **4**, 51-71.

Nyblade, A. A. (2002). Crust and upper mantle structure in East Africa: implications for the origin of Cenozoic rifting and volcanism and the formation of magmatic rifted margins. In: Menzies, M. A., Klemperer, S. L., Ebinger, C. J. & Baker, J. (eds.) *Volcanic Rifted Margins*. Boulder, Colorado: Geological Society of America Special Paper, 15-26.

Nyblade, A. A. & Brazier, R. A. (2002). Precambrian lithospheric controls on the development of the East African rift system. *Geology* **30**, 755-758.

Nyblade, A. A., Pollack, H. N., Jones, D. L., Podmore, F. & Mushayandebvu, M. (1990). Terrestrial heat flow in east and southern Africa. *Journal of Geophysical Research* **95**, 17371-17384.

Nyblade, A. A., Owens, T. J., Gurrola, H., Ritsema, J. & Langston, C. A. (2000). Seismic evidence for a deep upper mantle thermal anomaly beneath east Africa. *Geology* **28**, 599-602.

O'Neill, H. S. (1987). Quartz-fayalite-iron and quartz-fayalite-magnetite equilibria and the free-energy of formation of fayalite (Fe_2SiO_4) and magnetite (Fe_3O_4). *American Mineralogist* **72**, 67-75.

O'Reilly, S. Y. & Griffin, W. L. (1987). Eastern Australia - 4000 kilometers of mantle samples. In: Nixon, P. H. (ed.) *Mantle Xenoliths*. Chichester: John Wiley & Sons, 267-280.

O'Reilly, S. Y. & Griffin, W. L. (1995). Trace-element partitioning between garnet and clinopyroxene in mantle-derived pyroxenites and eclogites: P-T-X controls. *Chemical Geology* **121**, 105-130.

O'Reilly, S. Y. & Griffin, W. L. (2000). Apatite in the mantle: implications for metasomatic processes and high heat production in Phanerozoic mantle. *Lithos* **53**, 217-232.

Odling, N. W. A. (1994). An experimental simulation of upper-mantle metasomatism. *American Mineralogist* **79**, 148-153.

Olker, B. (2001). Entwicklung und Anwendung eines Computerprogrammes zur numerischen Modellierung von Diffusionsprofilen in Mineralkörnern. *unpublished PhD thesis, University of Heidelberg, 269 pp.*

Ottolini, L., Bottazzi, P. & Vannucci, R. (1993). Quantification of Lithium, Beryllium, and Boron in silicates by secondary ion mass spectrometry using conventional energy filtering. *Anal. Chem.* **65**, 1960-1968.

Ottolini, L., Le Fèvre, B. & Vannucci, R. (2004). Direct assessement of mantle boron and lithium contents and distribution by SIMS analyses of peridotite minerals. *Earth and Planetary Science Letters* **228**, 19-36.

Ottonello, G. (1980). Rare earth abundances and distribution in some spinel peridotite xenoliths from Assab (Ethiopia). *Geochimica et Cosmochimica Acta* **44**, 1885-1901.

Ottonello, G., Piccardo, G. B., Joron, J. L. & Treuil, M. (1978a). Evolution of the upper mantle beneath the Assab region (Ethiopia): suggestions from petrology and geochemistry of tectonic ultramafic xenoliths and host basaltic lavas. *Geologische Rundschau* **67**, 547-576.

Ottonello, G., Piccardo, G. B., Mazzucotelli, A. & Cimmino, F. (1978b). clinopyroxene-orthopyroxene major and rare-earth elements partitioning in spinel peridotite xenoliths from Assab (Ethiopia). *Geochimica et Cosmochimica Acta* **42**, 1817-1828.

Pallister, T. C. (1971). Tectonics of East Africa. In: *Tectonics of Africa*. Geneva: UNESCO.

Paquin, J., Altherr, R. & Ludwig, T. (2004). Li-Be-B systematics in the ultrahigh-pressure garnet peridotite from Alpe Arami (central Swiss Alps): Implications for slab-to-mantle wedge transfer. *Earth and Planetary Science Letters* **218**, 507-519.

Park, Y. & Nyblade, A. A. (2006). P-wave tomography reveals a westward dipping low velocity zone beneath the Kenya Rift. *Geophysical Research Letters* **33**.

Parkinson, I. J. & Arculus, R. J. (1999). The redox state of subduction zones: insights from arc-peridotites. *Chemical Geology* **160**, 409-423.

Parkinson, I. J., Arculus, R. J. & Eggins, S. M. (2003). Peridotite xenoliths from Grenada, Lesser Antilles island arc. *Contributions to Mineralogy and Petrology* **146**, 241-262.

Pasteels, P., Villeneuve, M., Depaepe, P. & Klerkx, J. (1989). Timing of the volcanism of the southern Kivu province: implications for the evolution of the western branch of the East-African Rift System. *Earth and Planetary Science Letters* **94**, 353-363.

Pearce, N. J. G., Perkins, W. T., Westgate, J. A., Gorton, M. P., Jackson, S. E., Neal, C. R. & Chenery, S. P. (1997). A compilation of new and published major and trace element data for NIST SRM 610 and NIST SRM 612 glass reference materials. *Geostandard Newslett.* **21**, 115-144.

Pearson, D. G., Davies, G. R. & Nixon, P. H. (1993). Geochemical constraints on the petrogenesis of diamond facies pyroxenites from the Beni Bousera peridotite massif, North Morocco. *Journal of Petrology* **34**, 125-172.

Pearson, D. G., Boyd, F. R., Haggerty, S. E., Pasteris, J. D., Field, S. W., Nixon, P. H. & Pokhilenko, N. P. (1994). The characterization and origin of graphite in cratonic lithospheric mantle: a petrological carbon-isotope and Raman-spectroscopic study. *Contributions to Mineralogy and Petrology* **115**, 449-466.

Pearson, D. G., Canil, D. & Shirey, S. B. (2003). Mantle samples included in volcanic rocks: xenoliths and diamonds. In: Holland, H. D. & Turrekian, K. K. (eds.) *Treatise on Geochemistry*. Amsterdam: Elsevier, 171-275.

Peate, D. W., Pearce, J. A., Hawkesworth, C. J., Colley, H., Edwards, C. M. H. & Hirose, K. (1997). Geochemical variations in Vanuatu arc lavas: the role of subducted material and a variable mantle wedge composition. *Journal of Petrology* **38**, 1331-1358.

Pettke, T., Halter, W. E., Webster, J. D., Aigner-Torres, M. & Heinrich, C. A. (2004). Accurate quantification of melt inclusion chemistry by LA-ICPMS: a comparison with EMP and SIMS and advantages and possible limitations of these methods. *Lithos* **78**, 333-361.

Piccardo, G. B., Messiga, B. & Vannucci, R. (1988). The Zabargad peridotite-pyroxenite association: petrological constraints on its evolution. *Tectonophysics* **150**, 135-162.

Pik, R., Marty, B. & Hilton, D. R. (2006). How many mantle plumes in Africa? The geochemical point of view. *Chemical Geology* **226**, 100-114.

Pike, J. E. N., Meyer, C. E. & Wilshire, H. G. (1980). Petrography and chemical composition of a suite of ultramafic xenoliths from Lashaine, Tanzania. *Journal of Geology.* **88**, 343-352.

Pinna, P., Jourde, G., Calvez, J. Y., Mroz, J. P. & Marques, J. M. (1993). The Mozambique belt in northern Mozambique: Neoproterozoic (1100-850 Ma) crustal growth and tectogenesis, and superimposed Pan-African (800-550 Ma) tectonism. *Precambrian Research* **62**, 1-59.

Pollack, H. N. & Chapman, D. S. (1977). Regional variation of heat-flow, geotherms, and lithospheric thickness. *Tectonophysics* **38**, 279-296.

Powell, W., Zhang, M., O'Reilly, S. Y. & Tiepolo, M. (2004). Mantle amphibole trace-element and isotope signatures trace multiple metasomatic episodes in lithospheric mantle, western Victoria, Australia. *Lithos* **75**, 141-171.

Prodehl, C., Keller, G. R., Khan, M. A. & (eds.) (1994). Crustal and upper mantle structure of the Kenya rift. *Tectonophysics* **236**, 483 pp.

Prouteau, G. & Scaillet, B. (2003). Experimental constraints on the origin of the 1991 Pinatubo dacite. *Journal of Petrology* **44**, 2203-2241.

Rabinowitz, P. D., Coffin, M. F. & Falvey, D. (1983). The separation of Madagascar and Africa. *Science* **220**, 67-69.

Raffone, N., Le Fèvre, B., Ottolini, L., Vannucci, R. & Zanetti, A. (2006). Light-lithophile element metasomatism of Finero peridotite (W Alps): a secondary-ion mass spectrometry study. *Microchimica Acta* **155**, 251-255.

Rampone, E., Bottazzi, P. & Ottolini, L. (1991). Complementary Ti and Zr anomalies in orthopyroxene and clinopyroxene from mantle peridotites. *Nature* **354**, 518-520.

Rapp, R. P. (1995). Amphibole-out phase-boundary in partially melted metabasalt, its control over liquid fraction and Composition, and source permeability. *Journal of Geophysical Research* **100**, 15601-15610.

Reeves, C. V., Karanja, F. M. & MacLeod, I. N. (1987). Geophysical evidence for a failed Jurassic rift and triple junction in Kenya. *Earth and Planetary Science Letters* **81**, 299-311.

Rehkämper, M., Halliday, A. N., Barfod, D., Fitton, J. G. & Dawson, J. B. (1997). Platinum group element abundance patterns in different mantle environments. *Science* **278**, 1595-1598.

Reid, A. M. & Dawson, J. B. (1972). Olivine- garnet reaction in peridotites from Tanzania. *Lithos* **5**, 115-124.

Reid, A. M., Donaldson, C. H., Brown, R. W., Ridley, W. I. & Dawson, J. B. (1975). Mineral chemistry of peridotite xenoliths from the Lashaine volcano, Tanzania. *Physics and Chemistry of the Earth* **9**.

Reisberg, L., Lorand, J. P. & Bedini, R. M. (2004). Reliability of Os model ages in pervasively metasomatized continental mantle lithosphere: a case study of Sidamo spinel peridotite xenoliths (East African Rift, Ethiopia). *Chemical Geology* **208**, 119-140.

Rhodes, J. M. & Dawson, J. B. (1975). Major and trace element chemistry of peridotite inclusions from the Lashaine volcano, Tanzanie. *Physics and Chemistry of the Earth* **9**, 545-557.

Ridley, W. I. & Dawson, J. B. (1975). Lithophile trace element data bearing on the origin of peridtite xenoliths, ankaramite and carbonatite from the Lashaine volcano, northern Tanzania. *Physics and Chemistry of the Earth* **9**, 559-569.

Righter, K. & Carmichael, I. S. E. (1993). Mega-xenocrysts in alkali olivine basalts: fragments of disrupted mantle assemblages. *American Mineralogist* **78**, 1230-1245.

Ritsema, J. & van Heijst, H. (2000). New seismic model of the upper mantle beneath Africa. *Geology* **28**, 63-66.

Ritsema, J. & Allen, R. M. (2003). The elusive mantle plume. *Earth and Planetary Science Letters* **207**, 1-12.

Rivalenti, G., Mazzucchelli, M., Vannucci, R., Hofmann, A. W., Ottolini, L., Bottazzi, P. & Obermiller, W. (1995). The relationship between websterite and peridotite in the Balmuccia peridotite massif (NW Italy) as revealed by trace-element variations in clinopyroxene. *Contributions to Mineralogy and Petrology* **121**, 275-288.

Rivalenti, G., Zanetti, A., Mazzucchelli, M., Vannucci, R. & Cingolani, C. A. (2004). Equivocal carbonatite markers in the mantle xenoliths of the Patagonia backarc: the Gobernador Gregores case (Santa Cruz Province, Argentina). *Contributions to Mineralogy and Petrology* **147**, 647-670.

Robinson, J. A. C., Wood, B. J. & Blundy, J. D. (1998). The beginning of melting of fertile and depleted peridotite at 1.5 GPa. *Earth and Planetary Science Letters* **155**, 97-111.

Roden, M. F., Patino-Douce, A. E., Jagoutz, E. & Laz'ko, E. E. (2006). High pressure petrogenesis of Mg-rich garnet pyroxenites from Mir kimberlite, Russia. *Lithos* **90**, 77-91.

Roeder, P. L. & Emslie, R. F. (1970). Olivine liquid equilibrium. *Contributions to Mineralogy and Petrology* **29**, 275-&.

Roger, S., Dautria, J. M., Coulon, C., Pik, R., Yirgu, G., Michard, A., Legros, P. & Ayalew, D. (1999). An insight on the nature, composition and evolution of the lithospheric mantle beneath the north-western Ethiopian plateau: the ultrabasic xenoliths from the Tana Lake province. *Acta Vulcanologica* **11**, 161-168.

Rogers, N., MacDonald, R., Fitton, J. G., George, R., Smith, M. & Barreiro, B. (2000). Two mantle plumes beneath the East African rift system: Sr, Nd and Pb isotope evidence from Kenya rift basalts. *Earth and Planetary Science Letters* **176**, 387-400.

Rooney, T. O., Furman, T., Yirgu, G. & Ayalew, D. (2005). Structure of the Ethiopian lithosphere: xenolith evidence in the Main Ethiopian Rift. *Geochimica et Cosmochimica Acta* **69**, 3889-3910.

Rudnick, R. L., McDonough, W. F. & Chappell, B. W. (1993). Carbonatite metasomatism in the northern Tanzanian mantle: petrographic and geochemical characteristics. *Earth and Planetary Science Letters* **114**, 463-475.

Rudnick, R. L., McDonough, W. F. & Orpin, A. (1994). Northern Tanzania peridotite xenoliths: a comparison with Kapvaal xenoliths and inferences of metasomatic reactions. In: Meyer, H. O. A. & Leonardos, O. H. (eds.) *Kimberlites, Realted Rocks, and Mantle Xenoliths. Proceeding Volumes, 5th International Kimberlite Conference, Araxa, Barzil 1*. Brasilia: Companhia de Pesquisa de Recursos Minerais, 336-353.

Rudnick, R. L., Ireland, T. R., Gehrels, G., Irving, A. J., Chesley, J. T. & Hanchar, J. M. (1999). Dating mantle metasomatism: U-Pb geochronology of zircons in cratonic mantle xenoliths from Montana and Tanzania. In: Gurney, J., Gurney, J. L., Pascoe, M. D. & Richardson, S. H. (eds.) *Proceedings of the 7th international Kimberlite Conference*. Cape Town: Red Roof Design, 728-735.

Ryan, J. G. (2002). Trace-element systematics of beryllium in terrestrial materials. In: Grew, E. S. (ed.) *Beryllium: mineralogy, petrology and geochemistry*, Reviews in Mineralogy: Mineralogical Society of America, 121-145.

Ryan, J. G. & Langmuir, C. H. (1987). The systematics of Lithium abundances in young volcanic rocks. *Geochimica et Cosmochimica Acta* **51**, 1727-1741.

Ryan, J. G. & Langmuir, C. H. (1988). Beryllium systematics in young volcanic rocks: implications for ^{10}Be. *Geochimica et Cosmochimica Acta* **52**, 237-244.

Ryan, J. G. & Langmuir, C. H. (1993). The systematics of boron abundances in young volcanic rocks. *Geochimica et Cosmochimica Acta* **57**, 1489-1498.

Ryan, J. G. & Kyle, P. R. (2004). Lithium abundance and lithium isotope variations in mantle sources: insights from intraplate volcanic rocks from Ross Island and Marie Byrd Land (Antarctica) and other oceanic islands. *Chemical Geology* **212**, 125-142.

Ryan, J. G., Leeman, W. P., Morris, J. D. & Langmuir, C. H. (1996). The boron systematics of intraplate lavas: Implications for crust and mantle evolution. *Geochimica et Cosmochimica Acta* **60**, 415-422.

Sachtleben, T. & Seck, H. A. (1981). Chemical control of Al-solubility in orthopyroxene and its implications on pyroxene geothermometry. *Contributions to Mineralogy and Petrology* **78**, 157-165.

Santos, J. F., Scharer, U., Ibarguchi, J. I. G. & Girardeau, J. (2002). Genesis of pyroxenite-rich peridotite at Cabo Ortegal (NW Spain): Geochemical and Pb-Sr-Nd isotope data. *Journal of Petrology* **43**, 17-43.

Sautter, V., Jaoul, O. & Abel, F. (1988). Aluminum diffusion in diopside using the ^{27}Al(p,γ)^{28}Si nuclear reaction: preliminary results. *Earth and Planetary Science Letters* **23**, 109-114.

Scambelluri, M., Hermann, J., Morten, L. & Rampone, E. (2006). Melt-versus fluid-induced metasomatism in spinel to garnet wedge peridotites (Ulten Zone, Eastern Italian Alps): clues from trace element and Li abundances. *Contributions to Mineralogy and Petrology* **151**, 372-394.

Scambelluri, M., Müntener, O., Ottolini, L., Pettke, T. & Vannucci, R. (2004). The fate of B, Cl and Li in the subducted oceanic mantle and in the antigorite breakdown fluids. *Earth and Planetary Science Letters* **222**, 217-234.

Schiano, P. & Clocchiatti, R. (1994). Worldwide occurence of silica-rich melts in sub-continental and sub-oceanic mantle minerals. *Nature* **368**, 621-624.

Schiano, P., Clocchiatti, R., Bourdon, B., Burton, K. W. & Thellier, B. (2000). The composition of melt inclusions in minerals at the garnet-spinel transition zone. *Earth and Planetary Science Letters* **174**, 375-383.

Schubert, W. (1977). Reactions in Alpine Type Peridotite of Ronda (Spain) and in Its Partial Fusion Products. *Contributions to Mineralogy and Petrology* **62**, 205-220.

Schull, T. J. (1988). Rift basins of interior Sudan - petroleum-exploration and discovery. *AAPG Bulletin* **72**, 1128-1142.

Seitz, H.-M. & Woodland, A. B. (2000). The distribution of lithium in peridotitic and pyroxenitic mantle lithologies - an indicator of magmatic and metasomatic processes. *Chemical Geology* **166**, 47-64.

Seitz, H.-M., Altherr, R. & Ludwig, T. (1999). Partitioning of transition elements between orthopyroxene and clinopyroxene in peridotitic and websteritic xenoliths: new empirical geothermometers. *Geochimica et Cosmochimica Acta* **63**, 3967-3982.

Seitz, H.-M., Brey, G. P., Lahaye, Y., Durali, S. & Weyer, S. (2004). Lithium isotopic signatures of peridotite xenoliths and isotopic fractionation at high temperature between olivine and pyroxenes. *Chemical Geology* **212**, 163-177.

Sen, C. & Dunn, T. (1995). Experimental modal metasomatism of a spinel Iherzolite and the production of amphibole-bearing peridotite. *Contributions to Mineralogy and Petrology* **119**, 422-432.

Shackleton, R. M. (1973). Correlation of structures across Precambrian orogenic belts in Africa. In: Tarling, D. H. & Runcorn, S. K. (eds.) *Implications of Continental Drift to the Earth Sciences*. London: Academic Press, 1091-1095.

Shackleton, R. M. (1993). Tectonics of the Mozambique Belt in East Africa. In: Prichard, H. M., Alabaster, T., Harris, N. B. & Neary, C. R. (eds.) *Magmatic Processes and Plate Tectonics, Geological Society of London Special Publiactions*, 345-362.

Shamberger, P. J. & Hammer, J. E. (2006). Leucocratic and gabbroic xenoliths from Hualalai volcano, Hawai'i. *Journal of Petrology* **47**, 1785-1808.

Shaw, C. S. & Edgar, A. D. (1997). Post-entrainment mineral-melt reactions in spinel peridotite xenoliths from Inver, Donegal, Ireland. *Geological Magazine* **134**, 771-779.

Shaw, C. S. & Klügel, A. (2002). The pressure and temperature conditions and timing of glass formation in mantle-derived xenoliths from Baarley, West Eifel, Germany: the case for amphibole breakdown, lava infiltration and mineral - melt reaction. *Mineralogy and Petrology* **74**, 163-187.

Shaw, C. S. J. & Eyzaguirre, J. (2000). Origin of megacrysts in the mafic alkaline lavas of the West Eifel volcanic field, Germany. *Lithos* **50**, 75-95.

Shaw, C. S., Thibault, Y., Edgar, A. D. & Lloyd, F. E. (1998). Mechanism of orthopyroxene dissolution in silica-undersaturated melts at 1 atmosphere and implications for the origin of silica-rich glass in mantle xenoliths. *Contributions to Mineralogy and Petrology* **132**, 354-370.

Shaw, S. J., Heidelbach, F. & Dingwell, D. B. (2006). The origin of reaction textures in mantle peridotite xenoliths from Sal Island, Cape Verde: the case for „metasomatism" by the host lava. *Contributions to Mineralogy and Petrology* **151**, 681-697.

Shaw, D. M., Higgins, M. D., Truscott, M. G. & Middleton, T. A. (1988). Boron contamination in polished thin-sections of meteorites - implications for other trace-element studies by alpha-track image or ion microprobe. *American Mineralogist* **73**, 894-900.

Simiyu, S. M. & Keller, G. R. (1997). An integrated analysis of lithospheric structure across the East African plateau based on gravity anomalies and recent seismic studies. *Tectonophysics* **278**, 291-313.

Skulski, T., Minarik, W. & Watson, E. B. (1994). High-pressure experimental trace-element partitioning between clinopyroxene and melt. *Chemical Geology* **117**, 127-147.

Slack, P. D., Davis, P. M., Dahlheim, H. A., Glahn, A., Ritter, J. R. R., Green, W. V., Maguire, P. K. H. & Meyer, R. P. (1994). Attenuation and velocity of P-waves in the mantle beneath the East-African rift, Kenya. *Tectonophysics* **236**, 331-358.

Sleep, N. H. (1990). Hotspots and mantle plumes - some phenomenology. *Journal of Geophysical Research* **95**, 6715-6736.

Sleep, N. H. (2006). Mantle plumes from top to bottom. *Earth-Science Reviews* **77**, 231-271.

Smith, D. (1999). Temperatures and pressures of mineral equilibration in peridotite xenoliths: review, discussion, and implications. In: Fei, Y., Bertka, C. M. & Mysen, B. O. (eds.) *Mantle Petrology: Field Observation and High-Pressure Experimentation. A Tribute to Francis R. (Joe) Boyd*: Geochem. Soc. Spec. Pub., 171-188.

Smith, D. & Barron, B. R. (1991). Pyroxene-garnet equilibration during cooling in the mantle. *American Mineralogist* **76**, 1950-1963.

Smith, D., Riter, J. C. A. & Mertzman, S. A. (1999). Water-rock interactions, orthopyroxene growth, and Si-enrichment in the mantle: evidence in xenoliths from the Colorado Plateau, southwestern United States (vol 165, pg 45, 1999). *Earth and Planetary Science Letters* **167**, 347-356.

Smith, M. (1994). Stratigraphic and structural constraints on mechanisms of active rifting in the Gregory Rift, Kenya. *Tectonophysics* **236**, 3-22.

Smith, M. & Mosley, P. (1993). Crustal heterogeneity and basement influence on the development of the Kenya Rift, East Africa. *Tectonics* **12**, 501-606.

Sommer, H., Kröner, A., Hauzenberger, C., Muhongo, S. & Wingate, M. T. D. (2003). Metamorphic petrology and zircon geochronology of high-grade rocks from the central Mozambique Belt of Tanzania: crustal recycling of Archean and Palaeoproterozoic material during the Pan-African orogeny. *Journal of Metamorphic Geology* **21**, 915-934.

Spandler, C. J., Arculus, R. J., Eggins, S. M., Mavrogenes, J. A., Price, R. C. & Reay, A. J. (2003). Petrogenesis of the Greenhills Complex, Southland, New Zealand: magmatic differentiation and cumulate formation at the roots of a Permian island-arc volcano. *Contributions to Mineralogy and Petrology* **144**, 703-721.

Späth, A., le Roex, A. P. & Opiyo-Akech, N. (2001). Plume-lithosphere interaction and the origin of continental rift-related alkaline volcanism - the Chyulu Hills volcanic province, southern Kenya. *Journal of Petrology* **42**, 765-787.

Stalder, R., Foley, S. F., Brey, G. P. & Horn, I. (1998). Mineral aqueous fluid partitioning of trace elements at 900-1200 °C and 3.0-5.7 GPa: new experimental data for garnet, clinopyroxene, and rutile, and implications for mantle metasomatism. *Geochimica et Cosmochimica Acta* **62**, 1781-1801.

Stern, C. R., Kilian, R., Olker, B., Hauri, E. H. & Kyser, T. K. (1999). Evidence from mantle xenoliths for relatively thin (< 100 km) continental lithosphere below the Phanerozoic crust of southernmost South America. *Lithos* **48**, 217-235.

Stern, R. J. (1994). Arc assembly and continental collision in the Neoproterozoic East-African Orogen - implications for the consolidation of Gondwanaland. *Annual Review of Earth and Planetary Sciences* **22**, 319-351.

Stern, R. J. & Dawoud, A. S. (1991). Late Precambrian (740 Ma) charnockite, enderbite, and granite from Jebel Moya, Sudan - a link between the Mozambique belt and the Arabian-Nubian shield. *Journal of Geology* **99**, 649-659.

Stewart, K. & Rogers, N. (1996). Mantle plume and lithosphere contributions to basalts from southern Ethiopia. *Earth and Planetary Science Letters* **139**, 195-211.

Stosch, H. G. (1982). Rare earth element partitioning between minerals from anhydrous spinel peridotite xenoliths. *Geochimica Et Cosmochimica Acta* **46**, 793-811.

Suen, C. J. & Frey, F. A. (1987). Origins of the mafic and ultramafic rocks in the Ronda peridotite. *Earth and Planetary Science Letters* **85**, 183-202.

Suhr, G. (1999). Melt migration under oceanic ridges: Inferences from reactive transport modelling of upper mantle hosted dunites. *Journal of Petrology* **40**, 575-599.

Suwa, K., Yusa, Y. & Kishida, N. (1975). Petrology of peridotite nodules from Ndonyuo Olnchoro, Samburu district central Kenya. *Physics and Chemistry of the Earth* **9**, 273-286.

Tabit, A., Kornprobst, J. & Woodland, A. B. (1997). The garnet peridotites of the Beni Bousera massif (Morocco): tectonic mixing and iron-magnesium interdiffusion. *Comptes Rendus De L Academie Des Sciences Serie Ii Fascicule a-Sciences De La Terre Et Des Planetes* **325**, 665-670.

Takazawa, E., Frey, F., Shimizu, N. & Obata, M. (1996). Evolution of the Horoman peridotite (Hokkaido, Japan): implications from pyroxene compositions. *Chemical Geology* **134**, 3-26.

Tanaka, R. & Nakamura, E. (2005). Boron isotopic constraints on the source of Hawaiian shield lavas. *Geochimica et Cosmochimica Acta* **69**, 3385-3399.

Taura, H., Yurimoto, H., Kurita, K. & Sueno, S. (1998). Pressure dependence on partition coefficients for trace elements between olivine and the coexisting melts. *Physics and Chemistry of Minerals* **25**, 469-484.

Taylor, W. R. (1998). An experimental test of some geothermometer and geobarometer formulations for upper mantle peridotites with applications to the thermobarometry of fertile lherzolites and garnet websterites. *Neues Jahrbuch für Mineralogie Abhandlungen* **172**, 381-408.

Terry, M. P. & Heidelbach, F. (2006). Deformation-enhanced metamorphic reactions and the rheology of high-pressure shear zones, Western Gneiss Region, Norway. *Journal of Metamorphic Geology* **24**, 3-18.

Thy, P. & Lofgren, G. E. (1994). Experimental constraints on the low-pressure evolution of transitional and mildly alkalic basalts - the effect of Fe-Ti oxide minerals and the origin of basaltic andesites. *Contributions to Mineralogy and Petrology* **116**, 340-351.

Tiepolo, M., Bottazzi, P., Foley, S. F., Oberti, R., Vannucci, R. & Zanetti, A. (2001). Fractionation of Nb and Ta from Zr and Hf at mantle depths: The role of titanian pargasite and kaersutite. *Journal of Petrology* **42**, 221-232.

Tomascak, P. B., Ryan, J. G. & Defant, M. J. (2000). Lithium isotope evidence for light element decoupling in the Panama subarc mantle. *Geology* **28**, 507-510.

Tomascak, P. B., Widom, E., Benton, L. D., Goldstein, S. L. & Ryan, J. G. (2002). The control of lithium budgets in island arcs. *Earth and Planetary Science Letters* **196**, 227-238.

Ulianov, A. (2005). Formation and metamorphism of aluminous upper mantle and lower crustal rocks: a case study on websterite and granulite xenoliths from basanites of the Chyulu Hills volcanic field, Kenya. *PhD thesis, University of Neuchâtel, Switzerland*, pp. 181.

Ulianov, A. & Kalt, A. (2006). Mg-Al sapphirine- and Ca-Al hibonite-bearing granulite xenoliths from the Chyulu Hills Volcanic Field, Kenya. *Journal of Petrology* **47**, 901-927.

Ulianov, A., Kalt, A. & Pettke, T. (2005). Hibonite, Ca(Al,CrTi,Si,Mg,Fe2+)(12)O19, in granulite xenoliths from the Chyulu Hills volcanic field, Kenya. *European Journal of Mineralogy* **17**, 357-366.

Ulianov, A., Kalt, A. & Pettke, T. (2006). Aluminous websterite and granulite xenoliths from the Chyulu Hills volcanic field, Kenya: gabbro-troctolitic cumulates subjected to lithospheric foundering. *Contributions to Mineralogy and Petrology* **152**, 459-483.

Ulmer, P. (2001). Partial melting in the mantle wedge - the role of H_2O in the genesis of mantle-derived 'arc-related' magmas. *Physics of the Earth and Planetary Interiors* **127**, 215-232.

Vail, J. R. (1985). Pan-African (Late Precambrian) Tectonic Terrains and the Reconstruction of the Arabian-Nubian Shield. *Geology* **13**, 839-842.

van der Wal, D. & Vissers, R. L. M. (1996). Structural petrology of the Ronda peridotite, SW Spain: deformation history. *Journal of Petrology* **37**, 23-43.

van der Wal, D. & Bodinier, J. L. (1996). Origin of the recrystallisation front in the Ronda peridotite by km-scale pervasive porous melt flow. *Contributions to Mineralogy and Petrology* **122**, 387-405.

van Orman, J. A., Grove, T. L. & Shimizu, N. (2001). Rare earth element diffusion in diopside: influence of temperature, pressure, and ionic radius, and an elastic model for diffusion in silicates. *Contributions to Mineralogy and Petrology* **141**, 687-703.

Vannucci, R., Piccardo, G. B., Rivalenti, G., Zanetti, A., Rampone, E., Ottolini, L., Oberti, R., Mazzucchelli, M. & Bottazzi, P. (1995). Origin of LREE-depleted amphiboles in the subcontinental mantle. *Geochimica et Cosmochimica Acta* **59**, 1763-1771.

Vannucci, R., Shimizu, N., Piccardo, G. B., Ottolini, L. & Bottazzi, P. (1993). Distribution of trace elements during breakdown of mantle garnet: an example from Zabargad. *Contributions to Mineralogy and Petrology* **113**, 437-449.

Vasseur, G., Vernières, J. & Bodinier, J. L. (1991). Modelling of trace element transfer between mantle melt and hetero-granular peridotite matrix. *Journal of Petrology, Special Lherzolite Issue*, 41-54.

Vauchez, A., Dineur, F. & Rudnick, R. (2005). Microstructure, texture and seismic anisotropy of the lithospheric mantle above a mantle plume: Insights from the Labait volcano xenoliths (Tanzania). *Earth and Planetary Science Letters* **232**, 295-314.

Vernières, J., Godard, M. & Bodinier, J. L. (1997). A plate model for the simulation of trace element fractionation during partial melting and magma transport in the Earth's upper mantle. *Journal of Geophysical Research* **102**, 24771-24784.

Vernon, R. H. (2004) *A practical guide to rock microstructures*. Cambridge: University Press.

Vétil, J. Y., Lorand, J. P. & Fabriès, J. (1988). Conditions de mise en place des filons de pyroxénites à amphibole du massif ultramafique de Lherz (Ariège, France). *Comptes Rendus de l'Académie des Sciences Série II* **307**, 587-593.

Volker, F. (1990). Geochemie der quartären Vulkanite auf der Ostschulter des Kenia-Rifts. *PhD thesis, University of Karlsruhe, Germany*.

Wallace, R. C. (1975). Mineralogy and petrology of xenoliths in a diatreme from South Westland, New Zealand. *Contributions to Mineralogy and Petrology* **49**, 191-199.

Weeraratne, D. S., Forsyth, D. W., Fischer, K. M. & Nyblade, A. A. (2003). Evidence for an upper mantle plume beneath the Tanzanian craton from Rayleigh wave tomography. *Journal of Geophysical Research* **108**, 2427, doi: 10.1029/2002JB002273.

Werling, F. & Altherr, R. (1997). Thermal evolution of the lithosphere beneath the French Massif Central as deduced from geothermobarometry on mantle xenoliths. *Tectonophysics* **275**, 119-141.

Wescott, W. A., Wigger, S. T., Stone, D. M. & Morley, C. K. (2006). Geology and geophysics of the Lotikipi plain. In: Morley, C. K. (ed.) *Geoscience of Rift Systems: Evolution of East Africa*. Tulsa: AAPG Studies in Geology, 55-65.

Wilkinson, J. F. G. & Hensel, H. D. (1994). Nephelines and analcimes in some alkaline igneous rocks. *Contributions to Mineralogy and Petrology* **118**, 79-91.

Wilkinson, J. F. G. & Stolz, A. J. (1997). Subcalcic clinopyroxenites and associated ultramafic xenoliths in alkali basalt near Glen Innes, northeastern New South Wales, Australia. *Contributions to Mineralogy and Petrology* **127**, 272-290.

Williams, L. A. J. (1978). Character of quaternary volcanism in the Gregory rift valley. In: Bishop, W. W. (ed.) *Geological Background to Fossil Man*. Edinburgh: Scottish Academic Press, 55-69.

Wilshire, H. G. & Shervais, J. W. (1975). Al-augite and Cr-diopside ultramafic xenoliths in in basaltic rocks from the Western United States. *Physics and Chemistry of Minerals* **9**, 257-272.

Wilshire, H. G., Pike, J. E. N., Meyer, C. E. & Schwarzman, E. C. (1980). Amphibole-rich veins in lherzolite xenoliths, Dish Hill and Deadman Lake, California. *American Journal of Science* **280**, 576-593.

Winn, R. D., Steinmetz, J. C. & Kerekgyarto, W. L. (1993). Stratigraphy and rifting history of the mesozoic-cenozoic Anza rift, Kenya. *AAPG Bulletin* **77**, 1989-2005.

Witt, G. & Seck, H. A. (1989). Origin of amphibole in recrystallized and porphyroclastic mantle xenoliths from the Rhenish Massif: implications for the nature of mantle metasomatism. *Earth and Planetary Science Letters* **91**, 327-340.

Witt-Eickschen, G. & Seck, H. A. (1991). Solubility of Ca and Al in orthopyroxene from spinel peridotite: an improved version of an empirical geothermometer. *Contributions to Mineralogy and Petrology* **106**, 431-439.

Witt-Eickschen, G. & O'Neill, H. S. (2005). The effect of temperature on the equilibrium distribution of trace elements between clinopyroxene, orthopyroxene, olivine and spinel in upper mantle peridotite. *Chemical Geology* **221**, 65-101.

Witt-Eickschen, G., Kaminsky, W., Kramm, U. & Harte, B. (1998). The nature of young vein metasomatism in the lithosphere of the West Eifel (Germany): Geochemical and isotopic constraints from composite mantle xenoliths from the Meerfelder Maar. *Journal of Petrology* **39**, 155-185.

Witt-Eickschen, G., Seck, H. A., Mezger, K., Eggins, S. M. & Altherr, R. (2003). Lithospheric mantle evolution beneath the Eifel (Germany): constraints from Sr-Nd-Pb isotopes and trace element abundances in spinel peridotite and pyroxenite xenoliths. *Journal of Petrology* **44**, 1077-1095.

Woermann, E. & Rosenhauer, M. (1985). Fluid phases and the redox state of the Earth's mantle - extrapolations based on experimental, phase-theoretical and petrological data. *Fortschritte der Mineralogie* **63**, 263-349.

Wood, B. J. & Virgo, D. (1989). Upper mantle oxidation-state: ferric iron contents of lherzolite spinels by Fe^{57} Mössbauer-spectroscopy and resultant oxygen fugacities. *Geochimica et Cosmochimica Acta* **53**, 1277-1291.

Wood, B. J., Blundy, J. D. & Robinson, J. A. C. (1999). The role of clinopyroxene in generating U-series disequilibrium during mantle melting. *Geochimica et Cosmochimica Acta* **63**, 1613-1620.

Woodland, A. B., Kornprobst, J., McPherson, E., Bodinier, J. L. & Menzies, A. (1996). Metasomatic interactions in the lithospheric mantle: petrologic evidence from the Lherz massif, French Pyrenees. *Chemical Geology* **134**, 83-112.

Woodland, A. B., Seitz, H. M., Altherr, R., Marschall, H., Olker, B. & Ludwig, T. (2002). Li abundances in eclogite minerals: a clue to a crustal or mantle origin? *Contributions to Mineralogy and Petrology* **143**, 587-601.

Woodland, A. B. & Koch, M. (2003). Variation in oxygen fugacity with depth in the upper mantle beneath the Kaapvaal craton, Southern Africa. *Earth and Planetary Science Letters* **214**, 295-310.

Woodland, A. B., Seitz, H.-M. & Yaxley, G. M. (2004). Varying behaviour of Li in metasomatised spinel peridotite xenoliths from western Victoria, Australia. *Lithos* **75**, 55-66.

Wulff-Pedersen, E., Neumann, E.-R., Vannucci, R., Bottazzi, P. & Ottolini, L. (1999). Silicic melts produced by reaction between peridotite and infiltrating basaltic melts: ion probe data on glasses and minerals in veined xenoliths from La Plama, Canary Islands. *Contributions to Mineralogy and Petrology* **137**, 59-82.

Xu, Y., Menzies, M. A., Vroon, P., Mercier, J.-C. & Lin, C. (1998a). Texture-temperatures-geochemistry relationships in the upper mantle as revealed from spinel peridotite xenoliths from Wangqing, NE China. Journal of Petrology 39, 469-493.

Xu, X., O'Reilly, S. Y., Griffin, W. L., Zhou, X. & Huang, X. (1998b). The nature of Cenozoic lithosphere at Nushan, eastern China. In: Flower, M., Chung, S. L., Lo, C. H. & Lee, T. Y. (eds.) *Mantle dynamics and plate interactions in East Asia*. Washington, D.C.: American Geophysical Union Geodynamics, 127-154.

Xu, X., O'Reilly, S. Y., Griffin, W. L. & Zhou, X. (2000). Genesis of young lithospheric mantle in southeastern China: an LAM-ICPMS trace element study. *Journal of Petrology* **41**, 111-148.

Xu, Y. & Bodinier, J.-L. (2004). Contrasting enrichments in high- and low-temperature mantle xenoliths from Nushan, eastern China: results of a single metasomatic event during lithospheric accretion? *Journal of Petrology* **45**, 321-341.

Xu, Y. G., Menzies, M. A., Bodinier, J. L., Bedini, R. M., Vroon, P. & Mercier, J. C. C. (1998b). Melt percolation and reaction atop a plume: evidence from the poikiloblastic peridotite xenoliths from Boree (Massif Central, France). *Contributions to Mineralogy and Petrology* **132**, 65-84.

Yaxley, G. M., Green, D. H. & Kamenetsky, V. (1998). Carbonatite metasomatism in the southeastern Australian lithosphere. *Journal of Petrology* **39**, 1917-1930.

Yaxley, G. M., Kamenetsky, V., Green, D. H. & Falloon, T. J. (1997). Glasses in mantle xenoliths from western Victoria, Australia, and their relevance to mantle processes. *Earth and Planetary Science Letters* **148**, 433-446.

Yaxley, G. M. & Kemenetsky, V. (1999). In situ origin for glass in mantle xenoliths from southeastern Australia: insights from trace element compositions of glasses and metasomatic phases. *Earth and Planetary Science Letters* **172**, 97-109.

Yu, J. H., O'Reilly, S. Y., Zhang, M., Griffin, W. L. & Xu, X. S. (2006). Roles of melting and metasomatism in the formation of the lithospheric mantle beneath the Leizhou Peninsula, South China. *Journal of Petrology* **47**, 355-383.

Zanetti, Z., Vannucci, R., Bottazzi, P., Oberti, R. & Ottolini, L. (1996). Infiltration metasomatism at Lherz as monitored by systematic ion-microprobe investigations close to a hornblendite vein. *Chemical Geology* **134**, 113-133.

Zanetti, A., Mazzucchelli, M., Rivalenti, G. & Vannucci, R. (1999). The Finero phlogopite-peridotite massif: an example of subduction-related metasomatism. *Contributions to Mineralogy and Petrology* **134**, 107-122.

Zanetti, A., Tiepolo, M., Oberti, R. & Vannucci, R. (2004). Trace-element partitioning in olivine: modelling of a complete data set from a synthetic hydrous basanite melt. *Lithos* **75**, 39-54.

Zeyen, H., Volker, F., Wehrle, V., Fuchs, K., Sobolev, S. V. & Altherr, R. (1997). Styles of continental rifting: crust-mantle detachment and mantle plumes. *Tectonophysics* **278**, 329-352.

Zindler, A. & Hart, S. (1986). Chemical geodynamics. *Annual Review of Earth and Planetary Sciences* **14**, 493-571.

Zinngrebe, E. & Foley, S. F. (1995). Metasomatism in mantle xenoliths from Gees, West Eifel, Germany: evidence for the genesis of calc-alkaline glasses and metasomatic Ca-enrichment. *Contributions to Mineralogy and Petrology* **122**, 79-96.

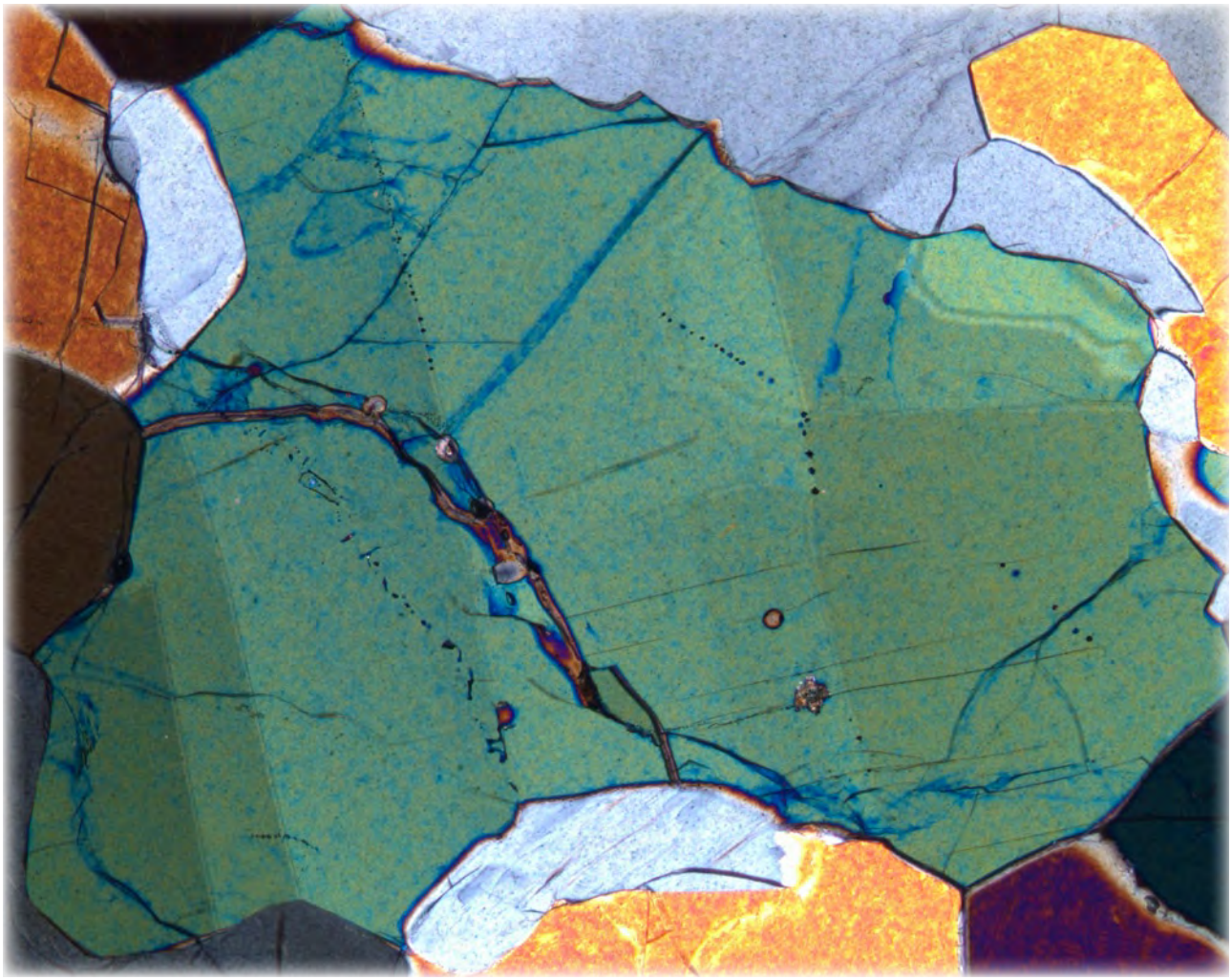
Mantle Xenoliths from the Marsabit Volcanic Field:

A Case Study on the Evolution

of the Lithopsheric Mantle in a Continental Rift Environment

Benjamin Kaeser

Appendices



November 2006

Université de Neuchâtel

Content:

Page

5 ***Appendix A1:****Petrographic descriptions of individual mantle xenoliths from Marsabit 5*

15 ***Appendix A2:*** *Electron Microprobe (EMP) data - microprobe transects 15*

93 ***Appendix A3:*** *Electron Microprobe (EMP) data - Representative Analyses 93*

151 ***Appendix A4:*** *LA-ICPMS data 151*

175 ***Appendix A5:*** *SIMS (Li, Be, and B) data 175*

Appendix A1

Petrographic descriptions of

individual mantle xenoliths

from Marsabit

Sample Nr. / Lithology	Textures	'early' metasomatism	'late' metas. glass+microlites	Particularities
604/11 Group I – III-a (grt)-spl lherzolite	ol-rich; coarse-grained (2.5-3 mm) ol-I; strongly deformed (kinked ol-I); slightly foliated no exsolution in px; important amounts of (holly-leaf) spl-I; some sympl.	few Ti-pargasite, associated with sympl.	no	sharp xenolith-lava contact; no signs for interaction, resorption
725/5 Group I - II (grt)-spl lherzolite	transitional p.clastic-recrystallised; curvilinear gr.bdr.; ol-I with kinkbands; no exsolution in px; slightly recrystallised sympl.	not	Ol_m, Chr_m, glass; associated with sympl; glass films along gr.bdr.	sharp xenolith-lava contact; no signs for interaction, resorption
726 Group VI spl-ol clinopyroxenite	very coarse-grained (cm's); cpx with irregular gr.bdr.; spl-I eu- to subhedral; ol-I with kinkbands	no	glass + microlites at the xenolith's edge	abundant primary sulphide inclusions in cpx-I, ol, spl-I
772/2 Group VII ol gabbro	euhedral plagioclase partly enclosed by cpx-I (ophitic-intersertal texture); magmatic fabric; strainfree; cpx-I optically zoned; abundant apatite needles in interstices	no	no	unique xenolith
780/5 Group V grt websterite	granular recrystallised; no porphyroclasts preserved; no exsolution in px; grt almost completely transformed to sympl; interstitial ol-I (altered)	no	glass (devitrified) along gr.bdr.	-
781/5 Group III-a spl harzburgite	transitional p.clastic to recrystallised fabric; ol-I with kinkbands; straight to curvilinear gr.bdr. neoblasts rel. large, polygonal; no exsolution in px; no sympl.	no	no	ol-I slightly iddingsitised
781/6 Group III-a spl harzburgite	similar to 781/5	no	few; brown glass, Chr_m; Cpx_m; carbonate	-
781/7 Group III-a spl harzburgite	equigranular; straight-curvilinear gr.bdr.; ol-I slightly kinked; no sympl.; no exsolution in px	no	no	cpx-I often enclosed by tiny opx rims
782/1 Group VI spl-free websterite	polygonal equigranular except some relic p.clasts (lamellar intergrowth of opx and cpx; assoc. with carbonate); ol-I (altered) in layer-like bands; no spl, no garnet	no	no	-
782/2 Group VI spl-ol websterite	add-cumulate-like texture; cpx-I with spl and opx exsolution; spl-I and opx-I (both small) only in interstices; rare carbonate inclusions in cpx-I; ol-I kinked	no	no	fluid inclusions (vibrating bubble + fluid)
784/1 Group V grt websterite	add-cumulate-like texture; deformation limited to subgrain formation and gr.bdr. migration; amph, phl and ilm in textural equilibrium; garnet with euhedral amph, opx and cpx incl.; no sympl	Kaersutite (both in garnet and interstitial), phl, ilmenite (with rutile cores); altered interst. Fe-Ni-Cu sulfides	no	-

Sample Nr. / Lithology	Textures	'early' metasomatism	'late' metas. glass+microlites	Particularities
785* Group III-c spl harzburgite	strongly porphyroclastic; ol-I strongly kinked; ol-IIa polygonal and strainfree; spl-I strongly resorbed (replaced by katophorite and phl)	abundant Mg-katophorite, phl and Opx_m (including graphite); phl around resorbed spl-I or as incl in Opx_m	abundant glass + microlites (incl. carbonate); replacing amph + phl	few sulphide globules in glass; vugs (in glass) sometimes coated with carbonate rhombs; melt inclusions in ol-I
785/1 Group III-c spl harzburgite	see 785* (most likely part of the same initial xenolith)			
787/1 Group III-b spl harzburgite	foliated; strongly strained p.clasts; almost strainfree neoblasts; strongly resorbed cpx-I relics; spl-I strongly resorbed	Opx_m; no amphibole (preserved)	very abundant melt pockets	strongly altered (iddingsite; oxides)
1921/2 Group IV spl harzburgite	mylonitic; equigranular polygonal neoblasts (<0.25 mm); p.clasts relatively rare and small; very fine-grained spl-rich layers	no	no	-
1958/1 Group II (grt)-spl lherzolite	polygonal grains; equigranular; px strainfree, no exsolution; ol-I with kinks; sympl. recrystallised to spl-px clusters strongly aligned (defining foliation)	no	no	some interstitial sulfides
1958/2 composite Group V, I (to II) grt websterite – (grt)-spl lherzolite	recrystallised grt websterite; garnet partly replaced by sympl.; (grt)-spl lherzolite: p.clastic – recrystallised; px still with exsolution lamellae; all garnet transformed to sympl.; contact between peridotite and websterite strongly metasomatised	at the contact peri-webs.: abundant (residual) amphibole + rare phl	m.p. at contact peri-webs.: replacing all sympl minerals, amph, phl	-
1958/5 Group II (grt)-spl lherzolite	transitional p.clastic-recrystallised; curvilinear gr.bdr.; round sympl., slightly recrystallised; opx-I often as selvages, interst. between ol-I and cpx-I	no	devitr. glass; sieve-textured cpx	considerably altered (iddingsite)
1958/6 Group II (grt)-spl lherzolite	polygonal equigranular fabric; all minerals strainfree; slightly poikilitic; sympl- recrystallised to spl-px clusters (elongated, defining foliation)	no	sieve-textured spl and cpx	-
1958/8 Group II (grt)-spl lherzolite	transitional p.clastic-recrystallised; some cpx with exsol. lamellae; opx-I resorbing cpx-I?; sympl. slightly recrystallised	no	Ol_m, Chr_m, devitr. glass; sieve-text. cpx	-
1958/13 Group II (grt)-spl lherzolite	tabular polygonal fabric; sympl. slightly recrystallised; rare exsol. lamellae in large opx-I and cpx-I	no	abundant; within sympl; incl. carbonate	sulfides in interstices; abundant fluid inclusion trails
1958/14 Group II (grt)-spl lherzolite	transitional p.clastic-recrystallised; lobed gr.bdr.; few kinks in ol-I; poor foliation; slightly recryst. sympl.; opx often vermiform/irregular in interstices along ol-I and cpx-I gr.bdr.	no	within/around sympl.	-

Sample Nr. / Lithology	Textures	'early' metasomatism	'late' metas. glass+microlites	Particularities
1958/15 Group III-b spl harzburgite	strongly p.clastic; ol-I with convex, px with concave gr.bdr.; opx-I as stringers interstitial between ol-I; ol-IIa strainfree; cpx-I extremely resorbed (sieve-textured); spl-I resorbed	no	intensive; sieve textured cpx; melt pockets around spl-I	abundant fluid/ melt incl. in cpx-I
1958/16 Group III-a spl harzburgite	p.clastic; lobed gr.bdr.; ol-I strongly kinked; neoblasts with 120° triple junctions; cpx-I small with concave gr.bdr.; spl-I resorbed	no	sieve-textured cpx and spl	fluid inclusion trails in cpx-I
1958/20 Group II (grt)-spl lherzolite	equigranular polygonal fabric; strainfree; some large cpx-I grains contain elongated opx blebs (former exsol. lamellae); sympl. partly recrystallised to px-spl clusters (elongated, defining foliation)	no	no	contains a macroscopically visible cpx (sympl) rich layer (~2 cm), interpreted to represent former grt websterite
1959/1 Group III-b spl harzburgite	strongly p.clastic; very large and strongly kinked ol-I (up to 5 mm); lobed gr.bdr; cpx-I very turbid, irregular grains, associated with spl	no	abundant; glass and sieve-textured cpx and spl; glass along gr.bdr. of ol-I	abundant melt inclusions in cpx
1959/15 Group III-b spl harzburgite	highly p.clastic; large, strongly kinked ol-I (up to 5 mm); opx-I and cpx-I irregular (concave gr.bdr.) between ol-l; rare exsolution in cpx-I; sympl. completely replaced by melt pockets; spl-I strongly resorbed	edenite-katoph. (residual in melt pockets)	very abundant; compl. replacing sympl; around spl; with dolomite and apatite globules	melt inclusions in resorbed (metas.) cpx-I and cpx-IIa
1959/16 Group I – IIIa (grt)-spl lherzolite	p.clastic (kinked ol-I); lobed gr.bdr.; low amount of sympl (fine-grained); some spl-I; no exsolution in cpx-I	no	within sympl.	opx growing at the expense of ol? (resorption textures, ol inclusions in opx); lots of Fe-Ni sulphide inclusion trails
1959/18 Group V grt websterite	p.clastic fabric; cpx-I exsolved; opx-I with lamellae normal to kink bands; contains a more opx-rich zone (ol-I bearing), where all garnet transformed to sympl; sympl. subsequently transformed to plag-bearing assemblages (RZ1)	abundant Ti pargasite; primary Fe-Ni sulphide inclusions	sieve textures on cpx and Ti pargasite	RZ1 and kelyphite contain Ti-oxide (rutile?)
1959/19 Group I to II (grt)-spl lherzolite	p.clastic with strained p.clasts and large polygonal strainfree neoblasts; opx-I often strainfree; sympl recrystallised to spl-px clusters	no	associated with spl-px clusters	ol-I replaced by opx (strainfree opx 'penetrates' kinked ol-I along kinkbands) conspicuous exsolutions in cluster pyroxenes (?)
1959/23 Group I (grt)-spl lherzolite	p.clastic; irregular-ragged gr.bdr.; cpx-I exsolved; fine-grained sympl.	no	few; within sympl.	altered (iddingsite)

Sample Nr. / Lithology	Textures	'early' metasomatism	'late' metas. glass+microlites	Particularities
1959/24 Group II (grt)-spl lherzolite	equigranular polygonal fabric; strainfree; no exsolution in px; sympl. recrystallised to px-spl clusters (elongated defining foliation)	no	no	xenolith-host lava interaction (up to 2 mm from contact)
1959/25 Group II (grt)-spl lherzolite	transitional p.clastic – recrystallised; ol-I with kinkbands; lobed gr.bdr; no exsolution in px; sympl. recrystallised to spl-px clusters	no	glass, sieve-textured cpx-IIb and spl-IIb	abundant melt(?) inclusions concentrated on kinks in ol-I
1959/26 Group I to II (grt)-spl lherzolite	transitional p.clastic – recrystallised; ol-I with kinkbands; lobed gr.bdr.; no exsolution in px; fine-grained round sympl.	no	abundant; within sympl.	-
1959/27 Group III-c dunite	strongly p.clastic; no spl, no Opx_m preserved; all gr.bdr. coated with glass	no	very abundant; Di_m rimmed by Aug_m; abundant kaersutite in m.p.	unique xenoliths; glass chemically similar to host basanite
1959/29 Group II (grt)-spl lherzolite	equigranular strainfree; sympl. recrystallised to elongated spl-px clusters defining weak foliation; kinkbands only in (rare) large ol-I	no	sieve-textured spl-IIb and cpx-IIb assoc. with brown glass	-
1959/35 Group I to II (grt)-spl lherzolite	transitional p.clastic – recrystallised; sympl. slightly recrystallised; ol-I are kinked; no exsolution in px		within sympl; with devitrified glass	abundant sulphide (?) trails; rel. abundant interstitial sulphides
1960/1 Group I (grt)-spl lherzolite	strongly p.clastic; very fine-grained sympl. (round, sectored); cpx-I with exsol. lamellae	Ti-pargasite (amph-ii and iii)	few; within sympl. (along recrystallised zones)	considerably altered (iddingsite)
1960/2 Group I (grt)-spl lherzolite	p.clastic but abundant non-strained cpx-I grains (exsolved); curvilinear gr.bdr.; very fine grained sympl. (round); very and sympl. px-rich	few Ti-pargasite (amph-i and ii)	few; rimming Ti-pargasite	slightly altered (iddingsite)
1960/3 Group V grt websterite (analysed by Olker, 2001)	p.clastic along shear zones between large fractured grt crystals; irregular px neoblasts; px in 'pressure shadows' less deformed; no ol-I; fine-grained sympl. replacing grt; grt cores full of inclusions	few Ti pargasite	RZ1; ol_m and plagioclase RZ2: sieve-textured cpx-I and cpx-IIa	abundant fluid/ melt inclusion trails in cpx-I
1960/4 Group V grt websterite (analysed by Olker, 2001)	strongly p.clastic; fractured grt; kinked px p.clasts with bent exsolution lamellae; grt cores full of inclusions (rutile, Ti pargasite, ilm?)	Ti pargasite (amph-ii and iii)	RZ1; with plagioclase	lots of fluid inclusion trails (within both neoblasts and p.clasts)
1960/8 Group V grt websterite	p.clastic; irregular p.clasts; strainfree neoblasts; cpx-I with exsol. lamellae; grt breakdown (abundant sympl) restricted to opx-rich zones; no sympl at cpx-grt interfaces	rare Ti-pargasite (amph-ii)	no	-

Sample Nr. / Lithology	Textures	'early' metasomatism	'late' metas. glass+microlites	Particularities
1961/1 Group IV spl harzburgite	ultramylonite; extremely deformed ol-I (kinkbands, undulous extinction; 'Böhm'sch lines'); extremely deformed opx-I (undulous extinct.; extremely stretched; bent cpx and spl lamellae); cpx-I with opx and spl lamellae; spl-I cracked; neoblasts from 0.2-0.01 mm; completely strainfree and polygonal	no	no	abundant sulphides along spl-I gr.bdr and along cpx-I gr.bdr.
1963/1 Group I (grt)-spl lherzolite	p.clastic; dynamic recryst; ragged gr.bdr.; fine-grained sympl.; ol-I with kinkbands	no	abundant; within sympl, also outside; with Aug_m; Chr_m; Ol_m; sulphides; glass	abundant sulphide trails in cpx-I; xenolith-host interaction (melt infiltration) on about 1 mm from the contact
1963/2 Group I (grt)-spl lherzolite	p.clastic; ragged gr.bdr.; dynamic recryst.; very abundant cpx-I (exsolved) and sympl.; fine-grained sympl., slightly elongated; opx-I kinked with cpx lamellae normal to kinks; macroscopically layered (ol-rich alternating with cpx-rich bands)	abundant Ti-pargasite (amph-i, ii, iii), rare phlogopite	rare; within sympl; along a crack	sulphide trails in amph-i and cpx-I
1963/3 Group I (grt)-spl lherzolite	p.clastic; lobed to curvilinear gr.bdr.; slightly foliated; elongated, very fine-grained sympl	no	abundant; within sympl.	slightly altered (iddingsite; oxides)
1963/4 Group I (grt)-spl lherzolite	p.clastic; lobed gr.bdr; cpx-I exsolved; opx-I kinked; fine-grained sympl.; some holly-leaf textured spl-I	no	abundant; within sympl.	-
1963/6 Group I (grt)-spl lherzolite	p.clastic; ragged gr.bdr.; dynamic recryst; strongly kinked ol-I; cpx-I rarely exsolved	no	few, in sympl.	altered
1963/17 Group I (grt)spl lherzolite	p.clastic; intermediate strain; irregular-lobed gr.bdr; px rarely exsolved; fine-grained sympl.	very abundant Ti-pargasite (amph-i, ii, iii) Ti-poor pargasite repl. cpx; graphite-bearing veinlet	very few; at lava-xenoliths contact	-
1964 Group V grt websterite	mylonitic (p.clastic zones grading into very fine-grained mylonitic shear-zones; grt with cracks and kelyph rims; ultra-fine-grained sympl.; cpx-I exsolved and strongly strained	no	RZ1 (plagioclase + spl)	contains opaques in sympl. and RZ1
1965/1 Group III-a spl harzburgite	p.clastic; lobed-irregular gr.bdr.; large cpx-I p.clasts sometimes exsolved; large holly-leaf spl-I; macroscopically zoned: grading from Type III-a (with rare sympl.) into Type III-b (amph lamellae in cpx-I; rare graphite)	rare katophorite lamellae in cpx-I some graphite	devitrified glass + microlites in zone of Type III-b	spl-I contains sulphide and (rare) carbonate inclusions
1965/2 Group III-c spl harzburgite	p.clastic; coarse p.clasts; polygonal neoblasts; no cpx-I; strongly kinked ol-I; exclusively 120° triple junctions	some relic amphibole in melt pockets	very abundant; glass along gr.bdr.; with apatite globules	some inclusion trails in p.clasts

Sample Nr. / Lithology	Textures	'early' metasomatism	'late' metas. glass+microlites	Particularities
1965/3 Group III-c spl dunite	see 1965/2	no preserved amph; abundant Opx_m with rarely preserved phlogopite; interstitial apatite (full of fluid inclusions)	very abundant; rel. coarse grained microlites; abundant carbonates	-
1965/4 Group I (grt)-spl lherzolite	strongly p.clastic; ragged-lobed gr.bdr.; px exsolved; very fine grained sympl.; some holly-leaf spl-I	rare Ti-pargasite (amph-ii, iii)	associated with sympl.	fluid incl. trails in cpx-I; also Fe-Ni sulphides
1965/12 Group III-b spl harzburgite	strongly p.clastic; kinked ol-I; polygonal strainfree neoblasts; holly-leaf spl-I; px not exsolved; foliated;	thin amphibole coronas around spl-I	no	-
1965/14 Group III-a spl harzburgite	p.clastic; irregular-ragged gr.bdr.; strongly kinked ol-I; px not exsolved; holly-leaf spl-I	rare amphibole	no	-
1965/15 Group III-b spl harzburgite	strongly p.clastic; irregular-ragged gr.bdr.; contacts between ol-I and opx-I lobed (replacement textures?); foliated; cpx-I with amph lamellae	Mg-katophorite, phlogopite and graphite in veinlets; Mg-katoph. residual in m.p. katoph. lamellae & blebs in cpx-I	abundant; around spl-I, cpx-I and katophorite; contain carbonate and microlites, and apatite globules	host-xenoliths reaction on 1 mm from contact
1965/17 Group III-a spl harzburgite	strongly p.clastic; undeformed opx-I often interstitial between kinked ol-I (replacement?); no exsolution in px; foliated	rare amphibole interst. and assoc. with spl-I and cpx-I	no	strong alteration (iddingsite)
1965/25 Group III-c amph dunite	p.clastic; primary minerals = exclusively ol-I (kinked) and ol-IIa (strainfree);	clusters of euhedral (twinned) Mg-katophorite with phl inclusions; Mg-katoph. sometimes relic in m.p.; very abundant graphite	very abundant; glass + Di_m + Ol_m + sulphide globules; no carbonate, no Chr_m	altered ol-I (iddingsite)
1965/26 Group I to III-a (grt)-spl lherzolite - harzburgite	strongly p.clastic; ragged-irregular gr.bdr.; neoblasts often polygonal; no exsolution in px; fine-grained sympl.; no foliation	Ti-pargasite (amph-i) assoc. with sympl.	no	strongly altered (iddingsite, oxides)
1965/29 Group I to III-a (grt)-spl lherzolite	strongly p.clastic; lobed-ragged gr.bdr.; ol-rich; large kinked ol-I clasts; cpx-I (exsolved) only in the vicinity of sympl; very fine-grained sympl.;	abundant Ti-pargasite (amph-i and ii)	rare; around Ti-pargasite and within sympl.	considerably altered (iddingsite)
1965/35 Group III-a spl harzburgite	contained grt (fine-grained sympl.); abundant spl-I; intermediate p.clastic; curvilinear-irregular gr.bdr.; opx-I often as stringers or irregular grains between ol-I; no exsolution in px	rare Ti-pargasite within sympl. (amp-ii)	no	altered (iddingsite); sharp lava-xenolith contact
1968/1 Group IV spl lherzolite	mylontic; cpx-I sometimes with opx exsolution; cross-cutting neoblast 'shear-zones'	no	some glass along gr.bdr.?	some fluid inclusion trails in cpx-I

Sample Nr. / Lithology	Textures	'early' metasomatism	'late' metas. glass+microlites	Particularities
1968/3 Group IV spl harzburgite	mylonitic; very fine-grained neoblast 'shear zones'; opx-I sometimes contain bent lamellae;	rare ilmenite -plagioclase (?) clusters	no	black (Fe-Ni sulphide) inclusion trails; also interst. sulphide
1968/7 Group III-a spl harzburgite	strongly p.clastic; ragged gr.bdr.; ol-I highly kinked; neoblasts often polygonal and strainfree; spl-I aligned defining foliation	no	no	lots of fluid inclusion trails; considerably altered (iddingsite)
1968/8 Group I (grt)-spl lherzolite	p.clastic; lobed gr.bdr.; weakly foliated; large (up to 5 mm) kinked ol-I; cpx-I only rarely exsolved; very fine-grained round sympl.	rare interst. phlogopite	devitrified glass?	altered (iddingsite; serpentine along cracks)
1968/15 Group III-b spl harzburgite	strongly p.clastic; lobed gr.bdr.; px generally not (or less) deformed than ol; sometimes poikilitic opx-I; no exsolution in cpx-I; opx-I sometimes with cpx exsolution	no	devitrified glass, Di_m, Ol_m, Chr_m and sulphide globules along gr.bdr. and cracks	considerably altered (iddingsite)
1968/16 Group III-a spl harzburgite	slightly p.clastic (kinked ol-I); mostly polygonal grains; lobed-curvilinear gr.bdr.; opx-I often irregular un-strained with concave gr.bdr. against (replacing?) ol-I; rounded spl-I	no	slightly sieve-textured cpx-I	rare fluid incl. trails in cpx-I
1970/1 Group II (grt)-spl lherzolite	equigranular recrystallised fabric; curvilinear gr.bdr.; almost strainfree (some kinkbands in ol-I; no deformation of px); no exsolution in px; sympl. slightly recrystallised to px-spl clusters; very opx-rich sample	no	dark-brown glass + Ol_m + Aug_m; associated with sympl. and in cracks; sieve-textured spl-I and cpx-I	interstitial sulphides
1970/2 Group II (grt)-spl lherzolite	transitional p.clastic-recrystallised; irregular to curvilinear gr.bdr.; ol-I mostly kinked; opx sometimes with undulous extinct.; sympl. partly recrystallised to px-spl clusters	no	dark-brown glass + Ol_m + Aug_m; associated with sympl.; sieve-textured rims on cpx-I and spl	interstitial sulphides
1970/6 Group III-d spl harzburgite	slightly p.clastic (ol-I kinked); all grains polygonal; slightly poikilitic (opx inclusions in ol-I); opx (=Opx_m) typically with melt inclusions along cleavage planes; spl (=Chr_m) mantled by polygonal cpx (=Di_m) clusters	no	glass inclusions in Di_m and Opx_m	unique xenolith
1970/15 Group II (grt)-spl lherzolite	equigranular recrystallised; strainfree; curvilinear gr.bdr.; sympl. recrystallised to px-spl clusters (elongated, define foliation); no exsolution in px	no	brown glass + Ol_m in clusters; px and spl in clusters strongly resorbed (sieve-textured)	-
1970/17 Group III-b spl harzburgite	p.clastic (strongly kinked ol-I); lobed gr.bdr.; abundant 120° triple junctions; opx-I kinked; spl-I only rarely preserved (in m.p.); clearly foliated; cpx-I strongly resorbed by m.p.	no	m.p. (with Dim, Olm, Chrm and apatite globules) interconnected along gr.bdr. melt films; cpx-I strongly resorbed (contained amph lamellae?)	

Sample Nr. / Lithology	Textures	'early' metasomatism	'late' metas. glass+microlites	Particularities
1970/21 Group I to II (grt)-spl lherzolite	almost strainfree; irregular to curvilinear gr.bdr.; cpx-I with opx exsolution lamellae preserved; opx-I kinked with lamellae normal to kinks; medium-grained sympl.	no	abundant; within sympl.	-
1970/22 Group II (grt)-spl lherzolite	transitional p.clastic to recrystallised; lobed gr.bdr.; ol-I strongly kinked; px commonly strainfree; opx-I typically with concave gr.bdr. against ol-I (penetrating ol-I along kink bands); sympl. completely recrystallised to px-spl clusters	no	abundant brown glass + Olm in spl-px clusters; cpx-IIb and spl-IIb strongly resorbed (with sieve textured rims)	-
1970/23 Group II to III-b (grt)-spl lherzolite-harzburgite	transitional p.clastic to recrystallised; kinked ol-I and opx-I; cpx not strained; neoblasts often polygonal and strainfree; sympl. recrystallised to px-spl clusters; no exsolution in px	no	abundant; brown glass and Olm in spl-cpx clusters; spl-IIb and cpx-I and cpx-IIb strongly resorbed (sieve-textured)	-
1971/2 Group V grt websterite	p.clastic; lobed straight to curvilinear gr.bdr. (p.clasts); neoblasts commonly polygonal; cpx-I exsolved; grt strongly cracked and kelyphitised; sympl. completely replaced by plag-bearing RZ	Ti-pargasite (amph-i); interstitial neoblasts	RZ1 (plagioclase bearing)	-
1973/2 Group VI spl-ol clinopyroxenite	ad-cumulate-like texture; poikilitic (cpx-I with ol-I inclusions); spl-I at cpx-I triple points; cpx-I without exsolutions but sometimes twinned; xenolith encloses a Group II (grt)-spl lherzolite 'xenolith'; margin of the latter coated by a spl-I-rich layer	no	no	abundant fluid inclusion trails in the clinopyroxenite cpx-I
1978/5 Clinopyroxene (augite) megacryst	contains abundant sulphide and melt inclusions			

Appendix A2

Electron Microprobe (EMP) data

microprobe transects

used abbreviations:

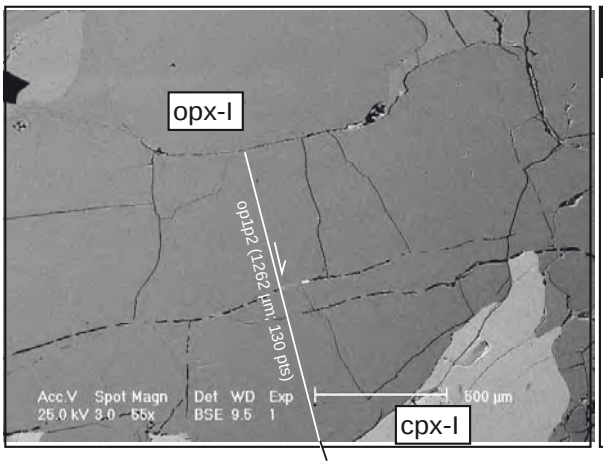
op, cp, sp, ol, gt:	otho-, clinopyroxene, spinel, olivine and garnet, respectively
am, amph:	amphibole
ph, phl, bt:	phlogopite
cc, carb:	carbonates
gl:	glass
mp, m.p.:	melt pockets (silicate glass + ol + cpx ± spl ± carbonate)
ilm:	ilmenite
rut, rt:	rutile
exso., exs.:	exsolution lamellae

Labels:

op1p2, for example, denotes '***profile Nr. 2 orthopyroxene Nr. 1*** (note: successive numbering without reference to mineral generations)

Remarks:

for Group V (grt websterite) only data obtained during this study are reported. Additional data (also discussed in Chapter 5) can be found in Olker (2001).

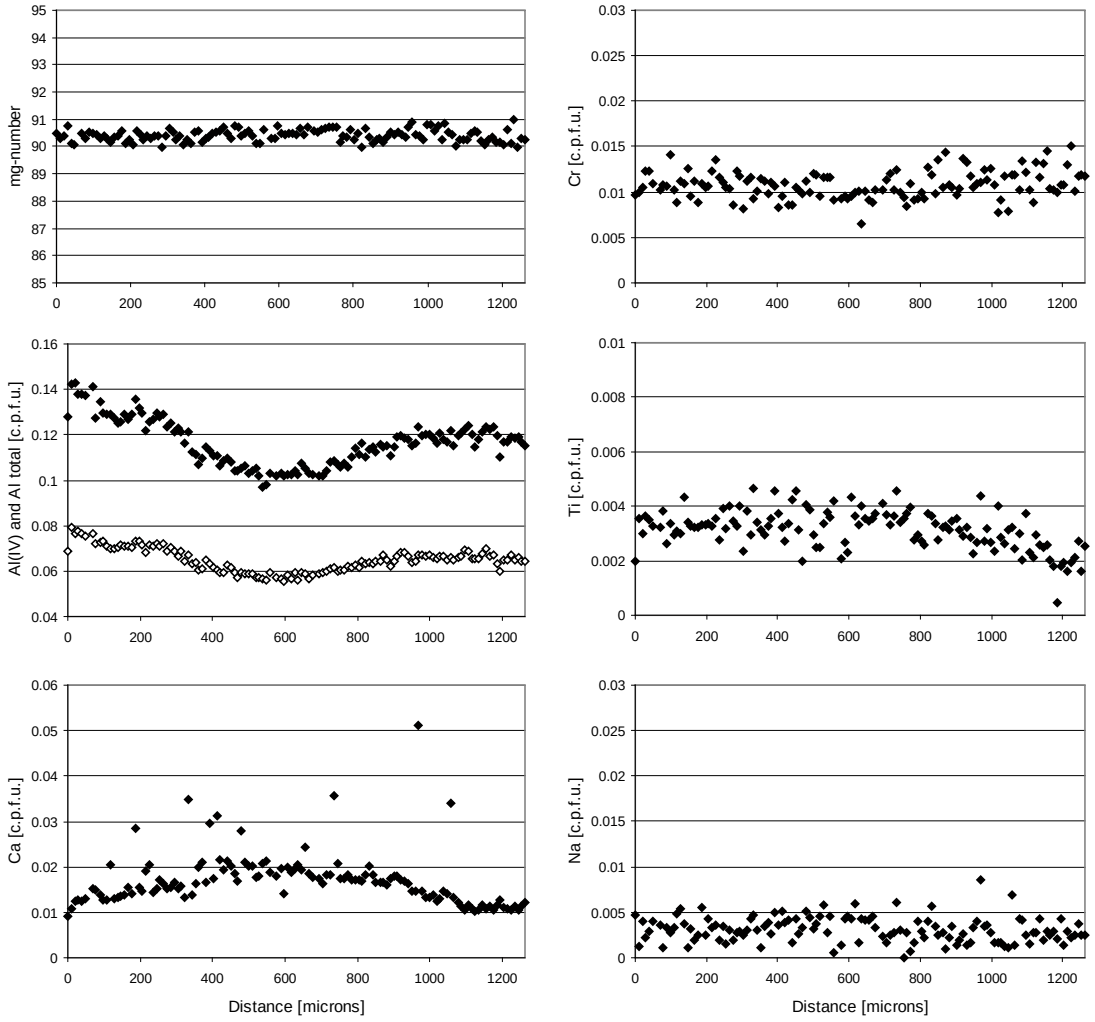


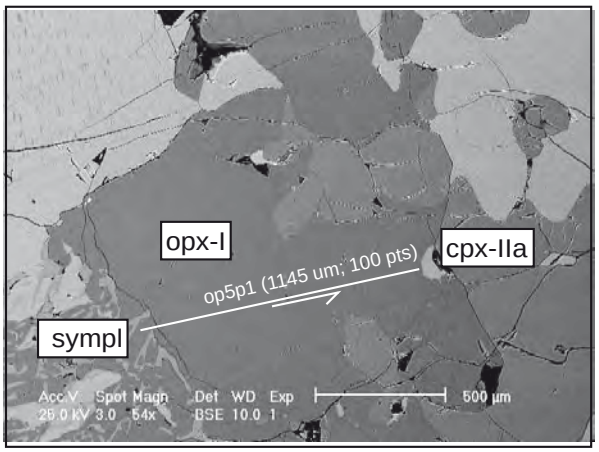
Group II: Orthopyroxene

Sample: 1960/2 - Group I (grt)-spl lherzolite

opx-I: large porphyroclast (with minute cpx exsolution lamellae; see spikes in Ca pattern)

EMP-analysis: Session17 / op1p2



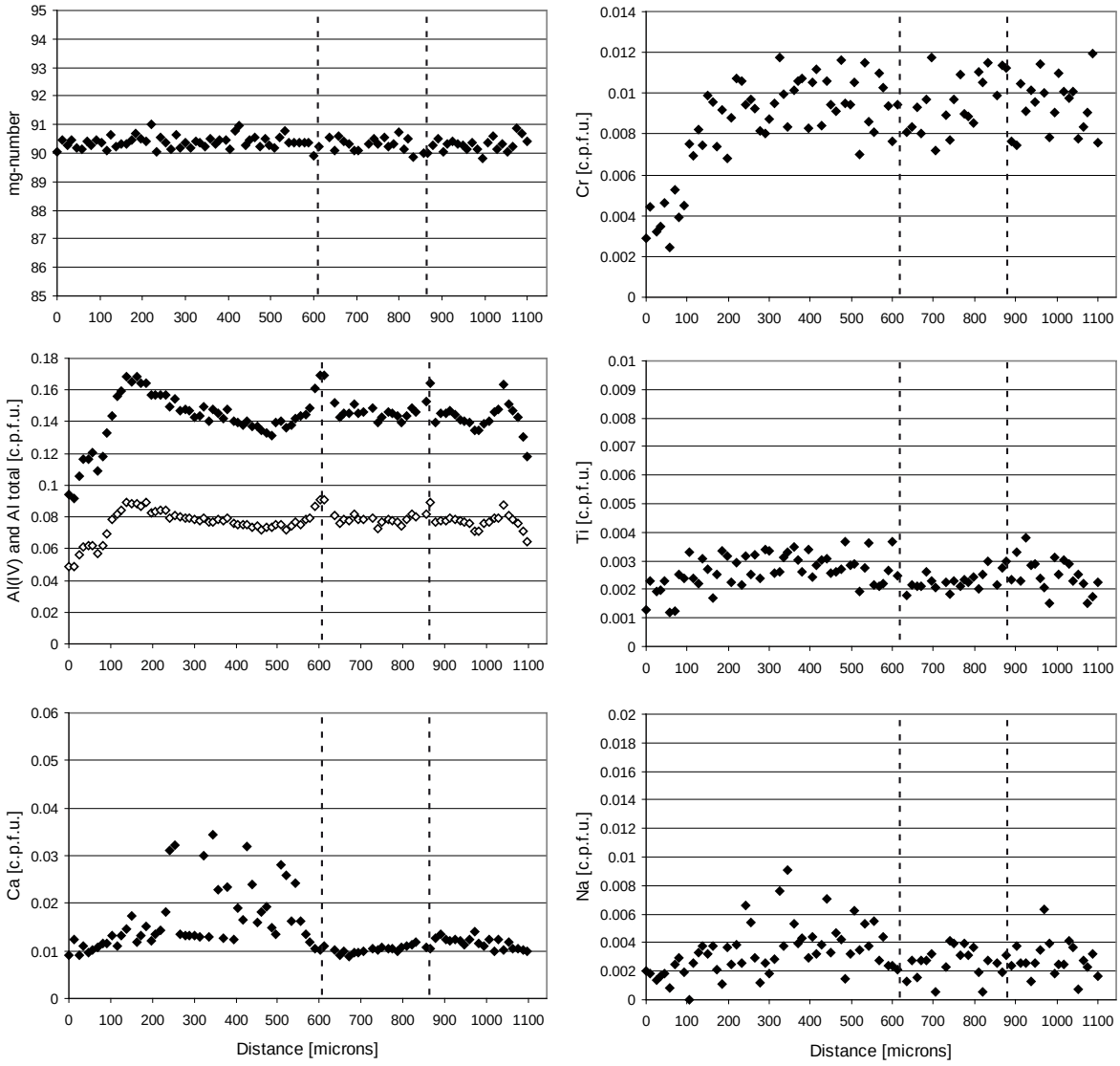


Group I: Orthopyroxene

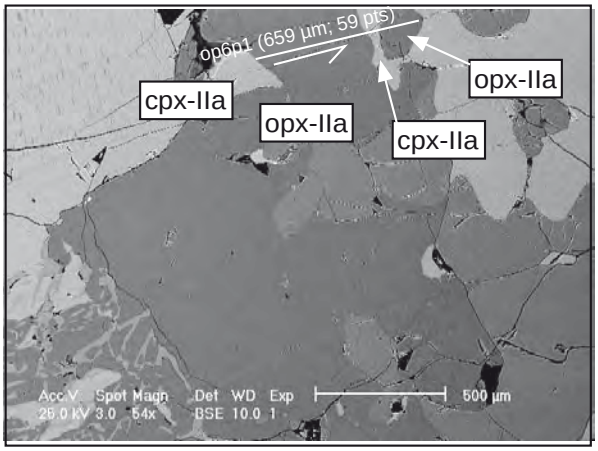
Sample: 1960/2 - Group I (grt)-spl lherzolite

opx-I: strongly deformed porphyroclast

EMP-analysis: Session17 / op5p1



kinkbands - - - - - - -

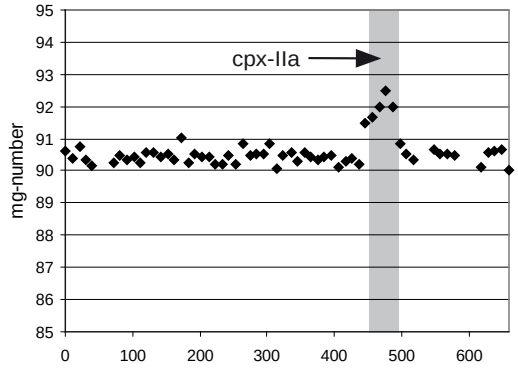


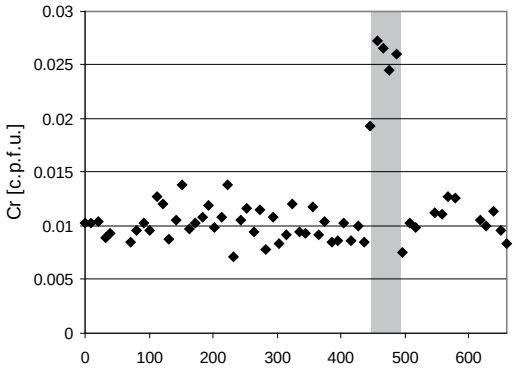
Group I: Orthopyroxene

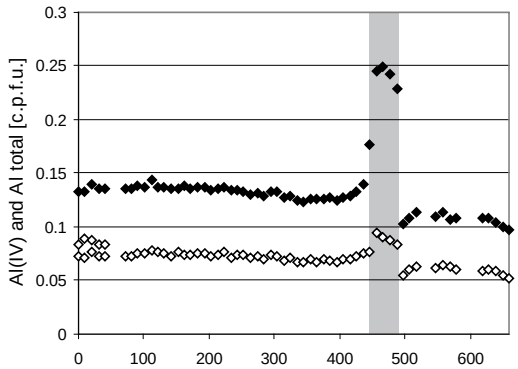
Sample: 1960/2 - Group I (grt)-spl lherzolite

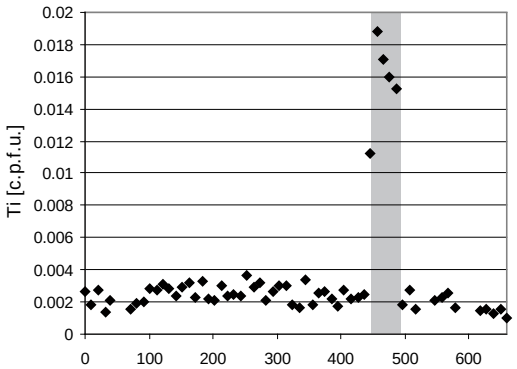
transect through neoblasts:
opx-IIa (large) - cpx-IIa - opx-IIa (small)

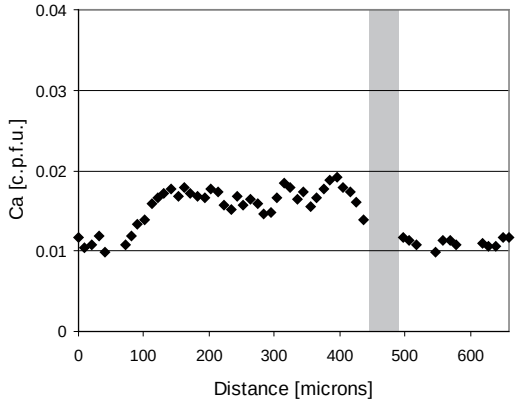
EMP-analysis: Session17 / op6p1

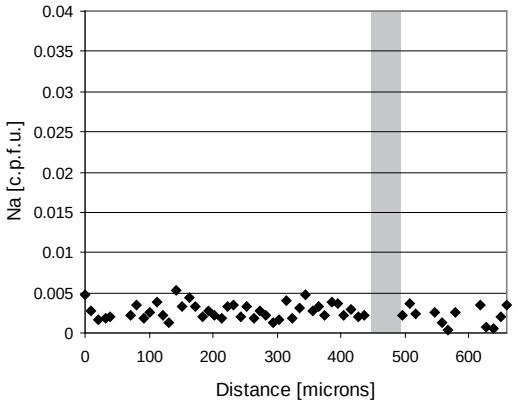


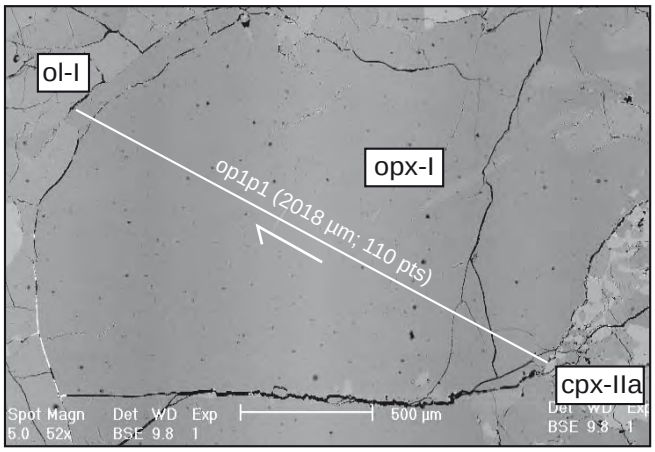












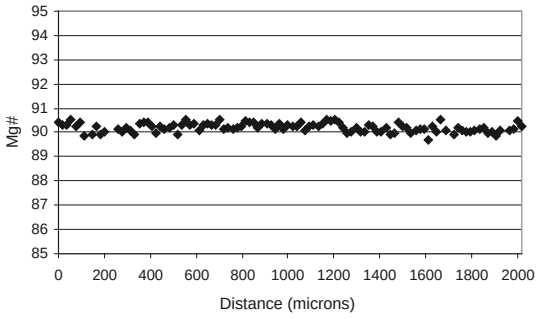
Group I: Orthopyroxene

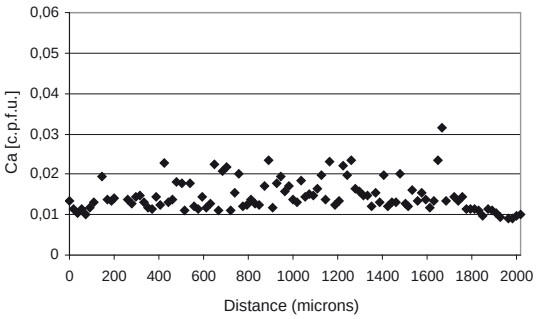
Sample: 1963/02 - Group I (grt)-spl lherzolite

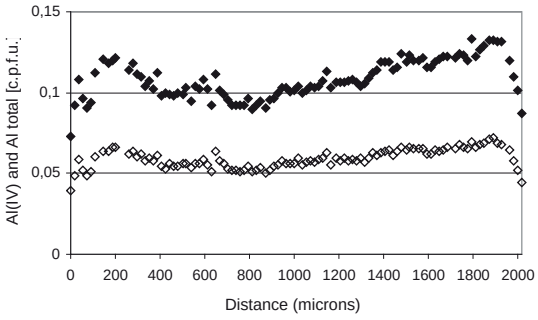
opx-I porphyroclast (with rare cpx exsolution lamellae normal to kinks)

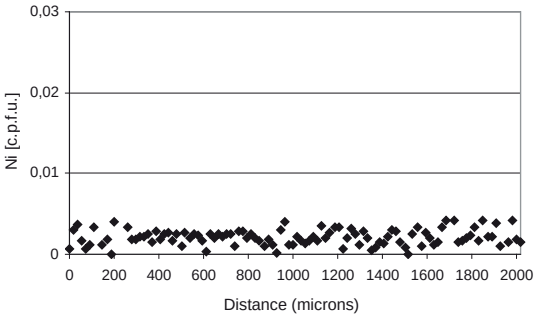
EMP-analysis: Session9 / op1p1

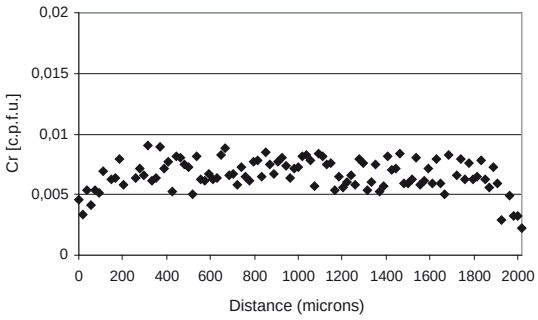
Files: 6302o11.tif; 6302o12.tif; opx(session9).xls; 6302op1p1.ai

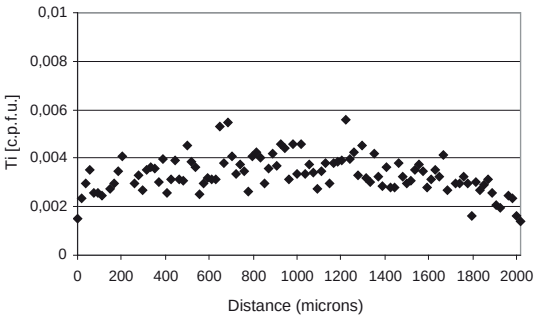


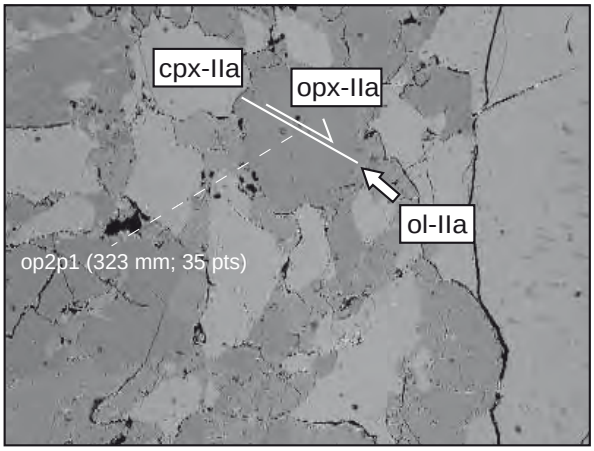










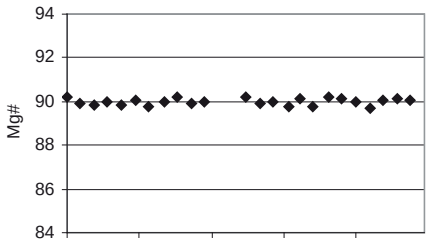


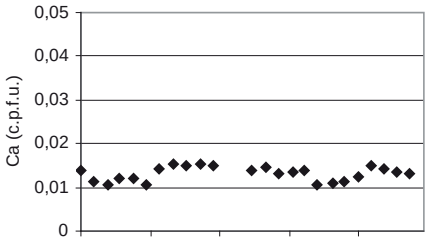
Group I: Orthopyroxene

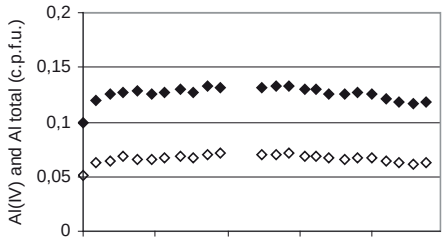
Sample: 1963/2 - Group I (grt)-spl lherzolite

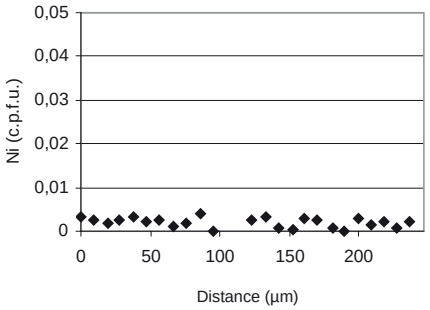
opx-IIa: strainfree neoblast

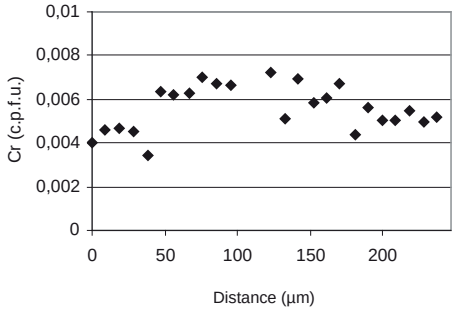
EMP-analysis: Session5 / op2p1

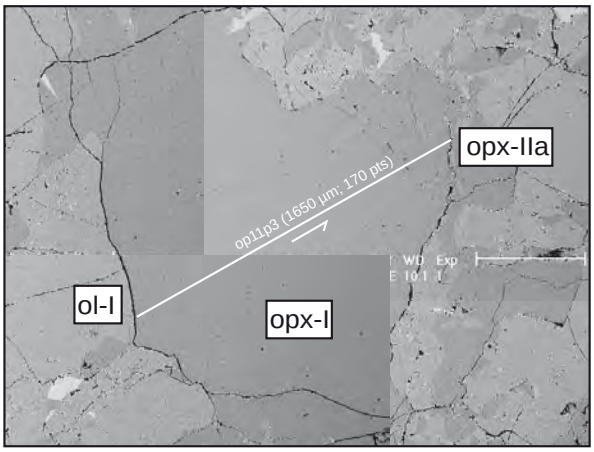










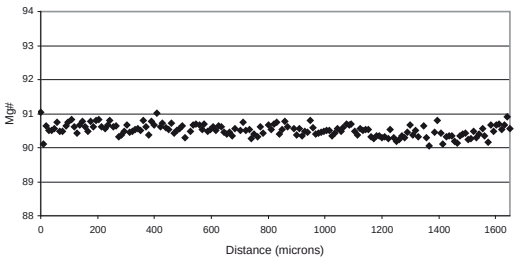


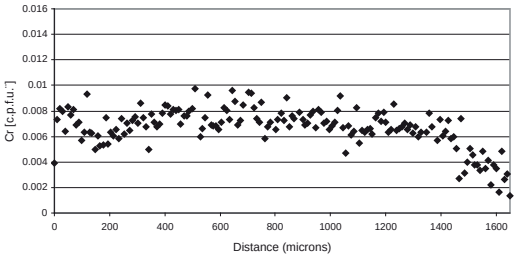
Group I: Orthopyroxene

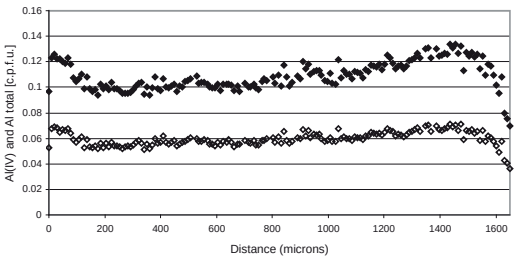
Sample: 1963/2 - Group I (grt)-spl lherzolite

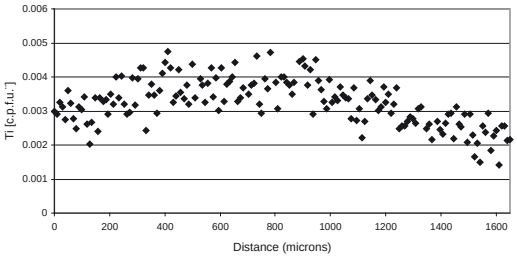
opx-I porphyroclast

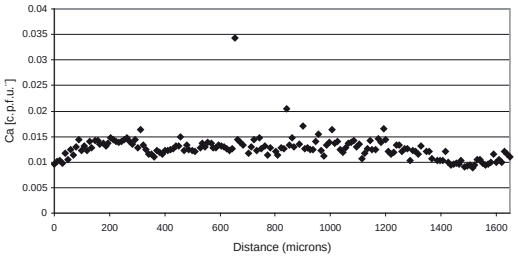
EMP-analysis: Session11 / op11p3

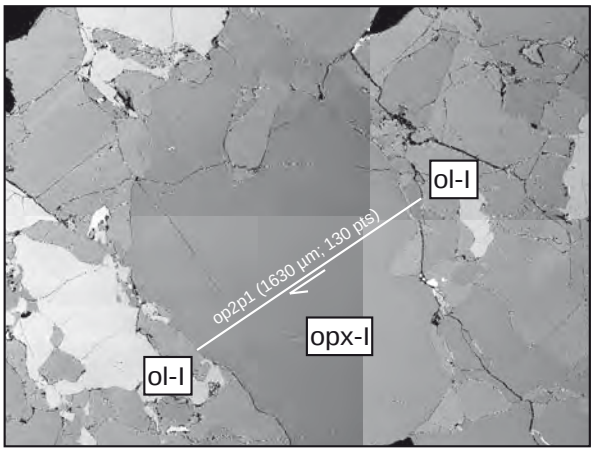










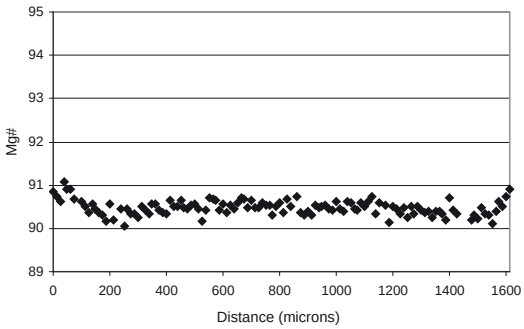


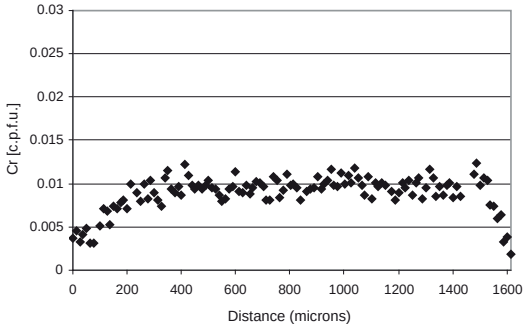
Group I: Orthopyroxene

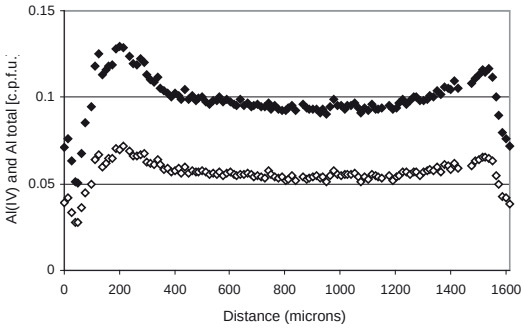
Sample: 1965/4 - Group I (grt)-spl lherzolite

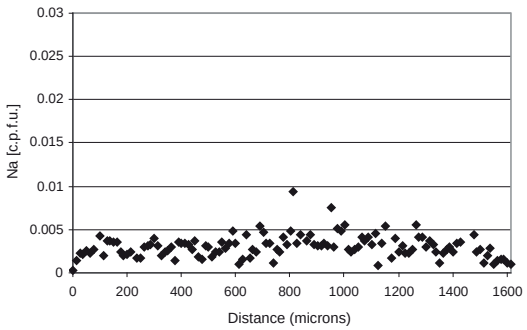
opx-I porphyroclast with rare cpx exsolution lamellae

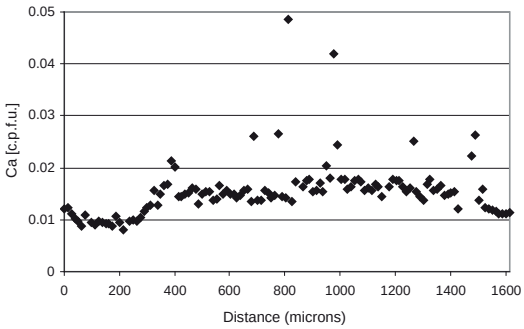
EMP-analysis: Session10 / op2p1

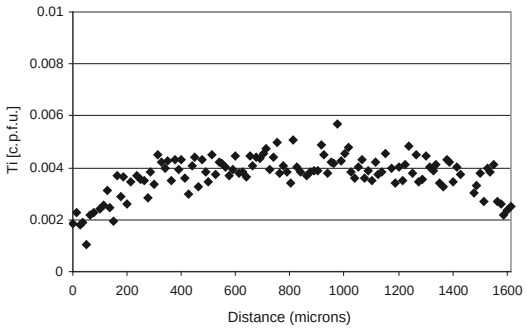


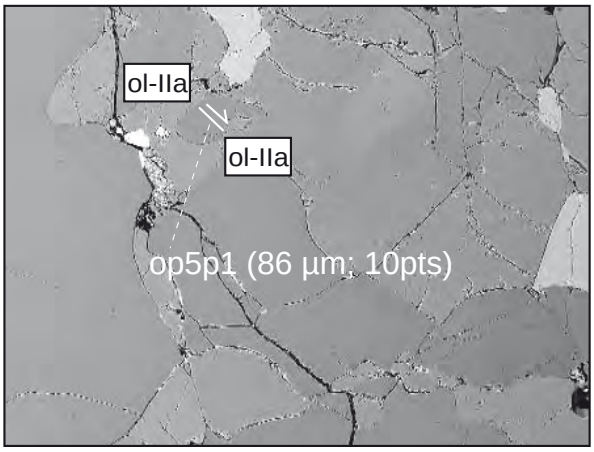










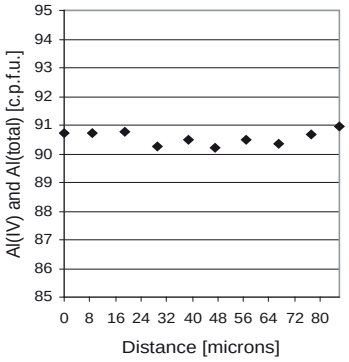


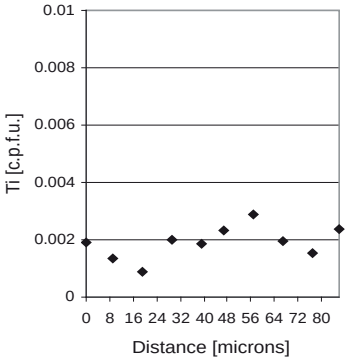
Group I: Orthopyroxene

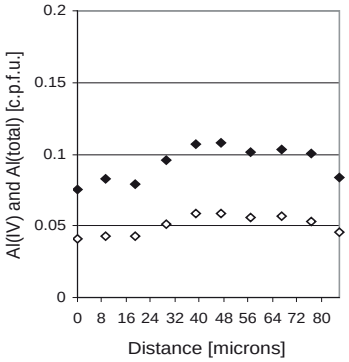
Sample: 1965/4 - Group (grt)-spl lherzolite

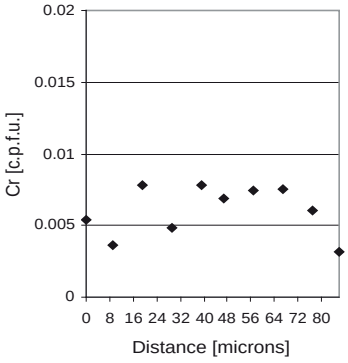
strainfree opx-IIa neoblast

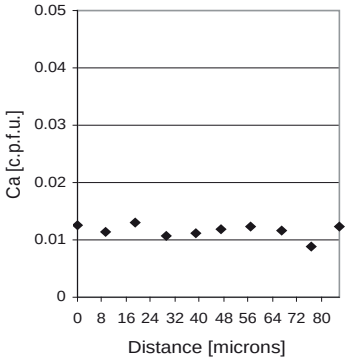
EMP-analysis: Session15 / op5p1

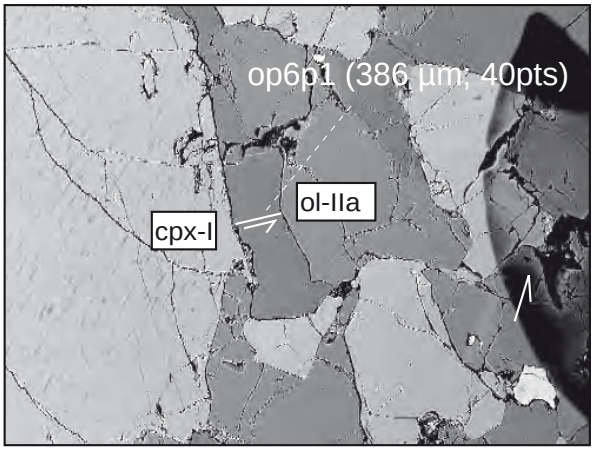










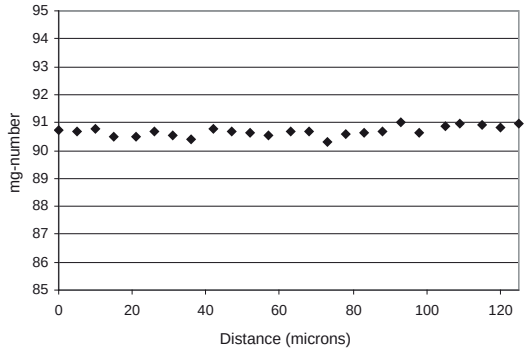


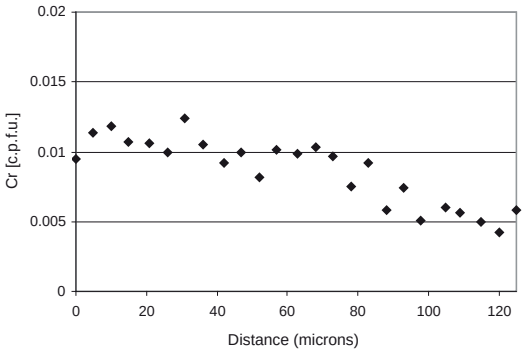
Group I: Orthopyroxene

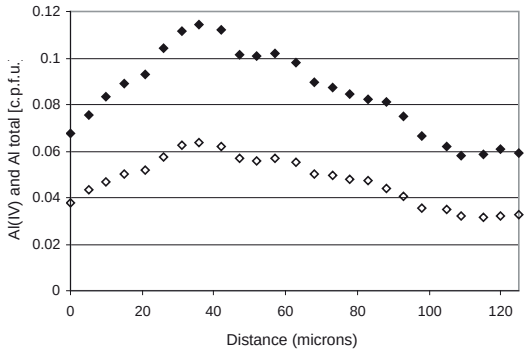
Sample: 1965/4 - Group I (grt)-spl lherzolite

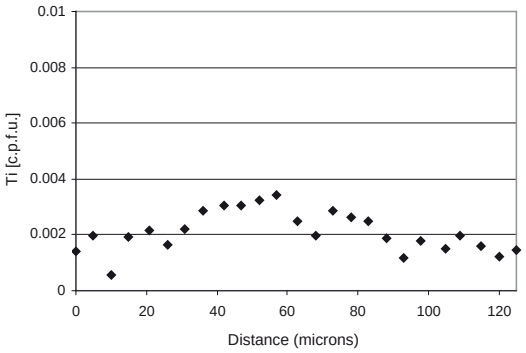
strainfree opx-IIa neoblast

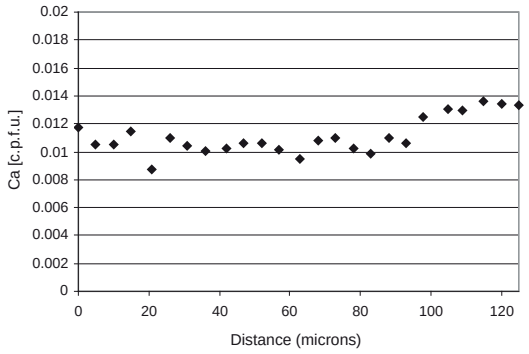
EMP-analysis: Session13 / op2p1 (2)

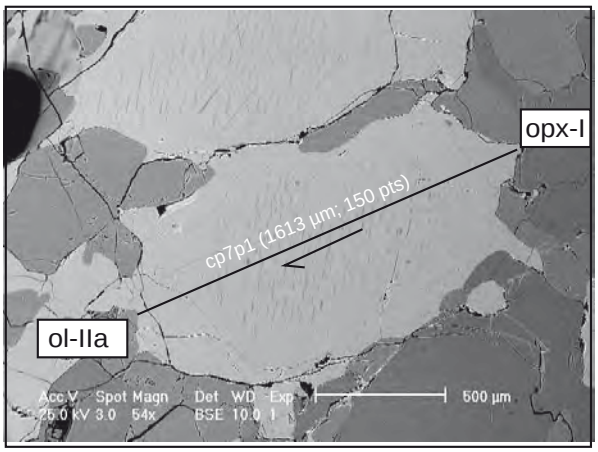










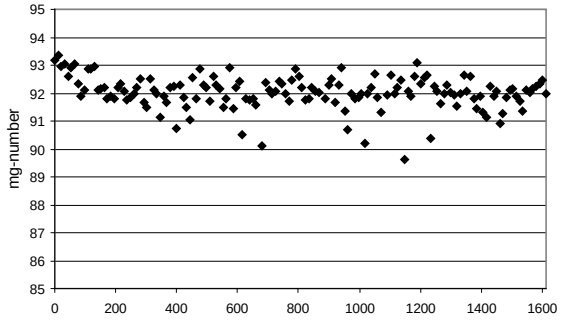


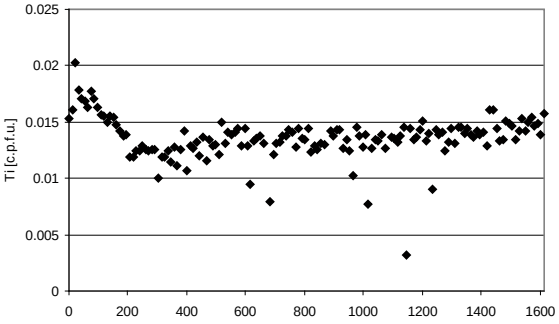
Group I: Clinopyroxene

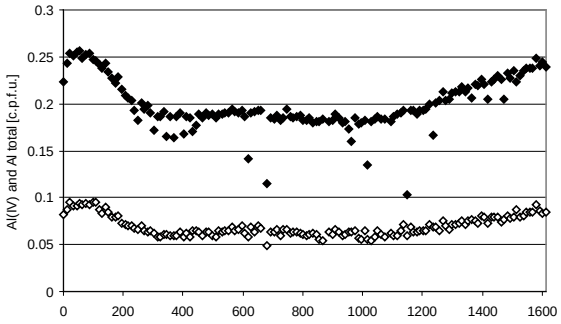
Sample: 1960/2 - Group I (grt)-spl lherzolite

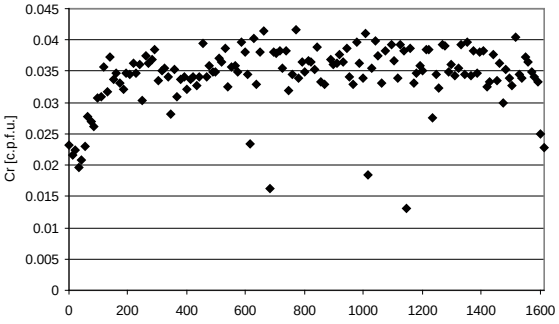
cpx-I: exsolved clinopyroxene porphyroclast

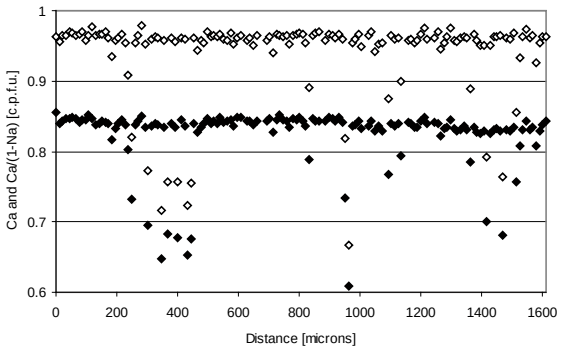
EMP-analysis: Session17 / cp7p1

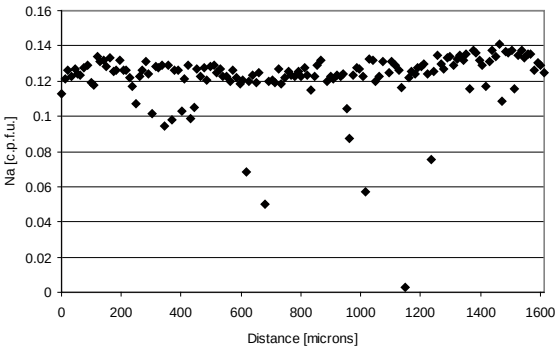


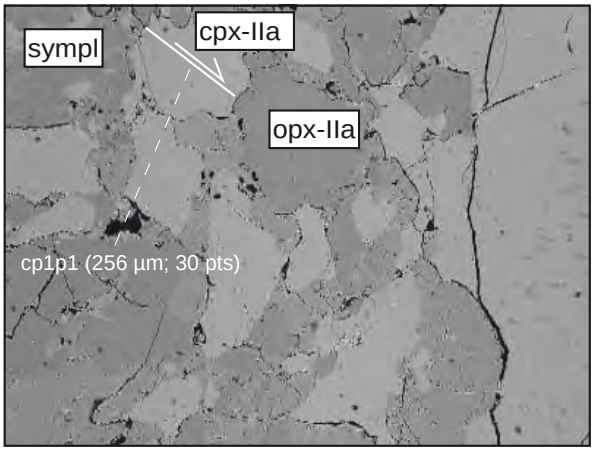










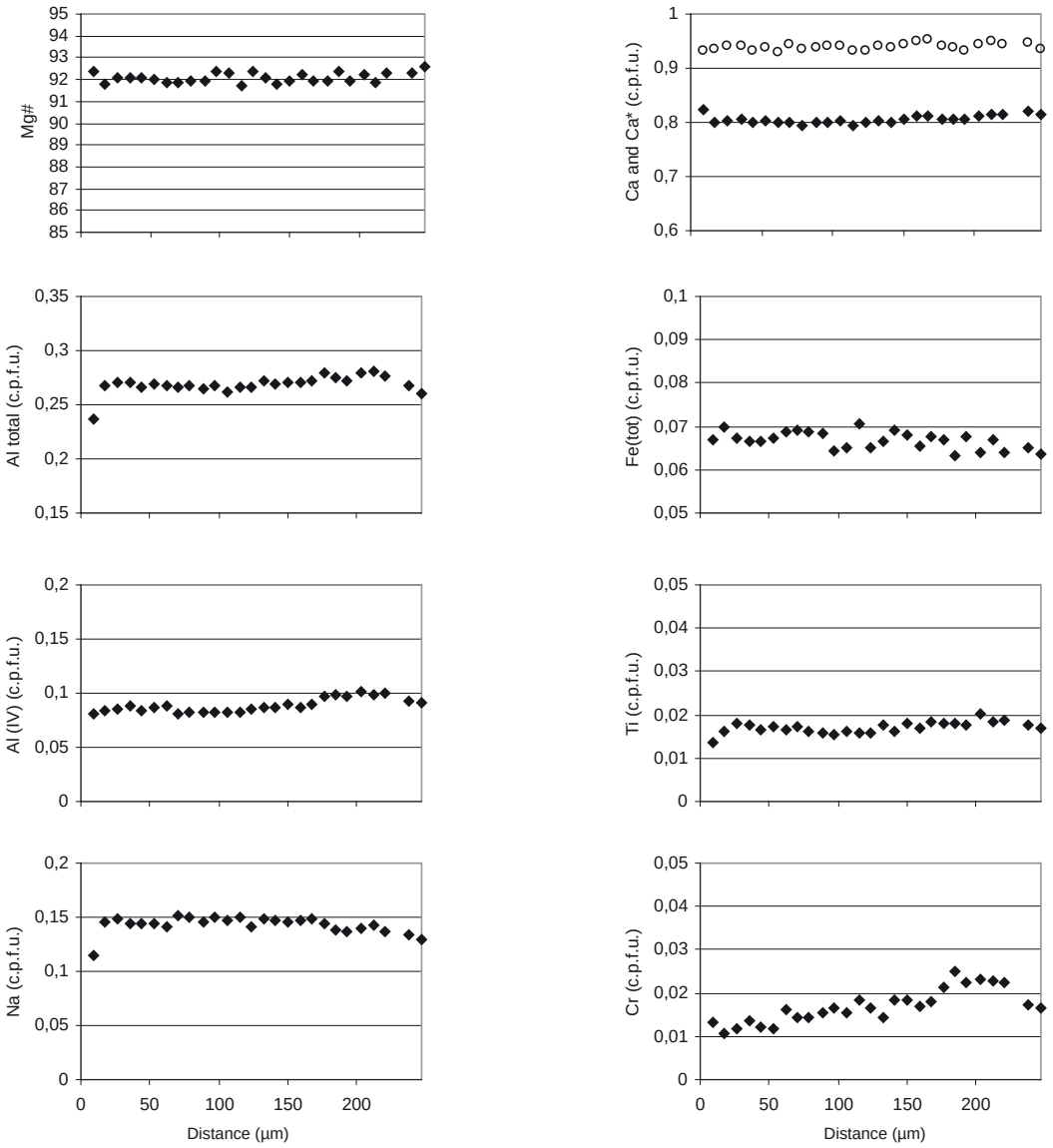


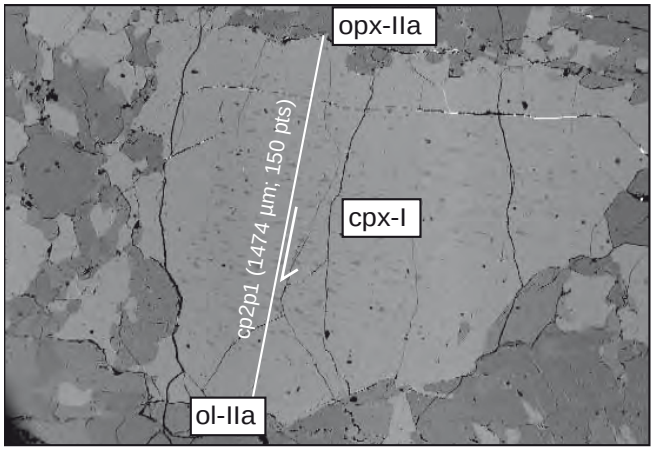
Group I: Clinopyroxene

Sample: 1963/2 - Group I (grt)-spl lherzolite

cpx-IIa neoblast adjacent to spl-IIb - opx-IIb - cpx-IIb symplectite

EMP-analysis: Session5 / cp1p1



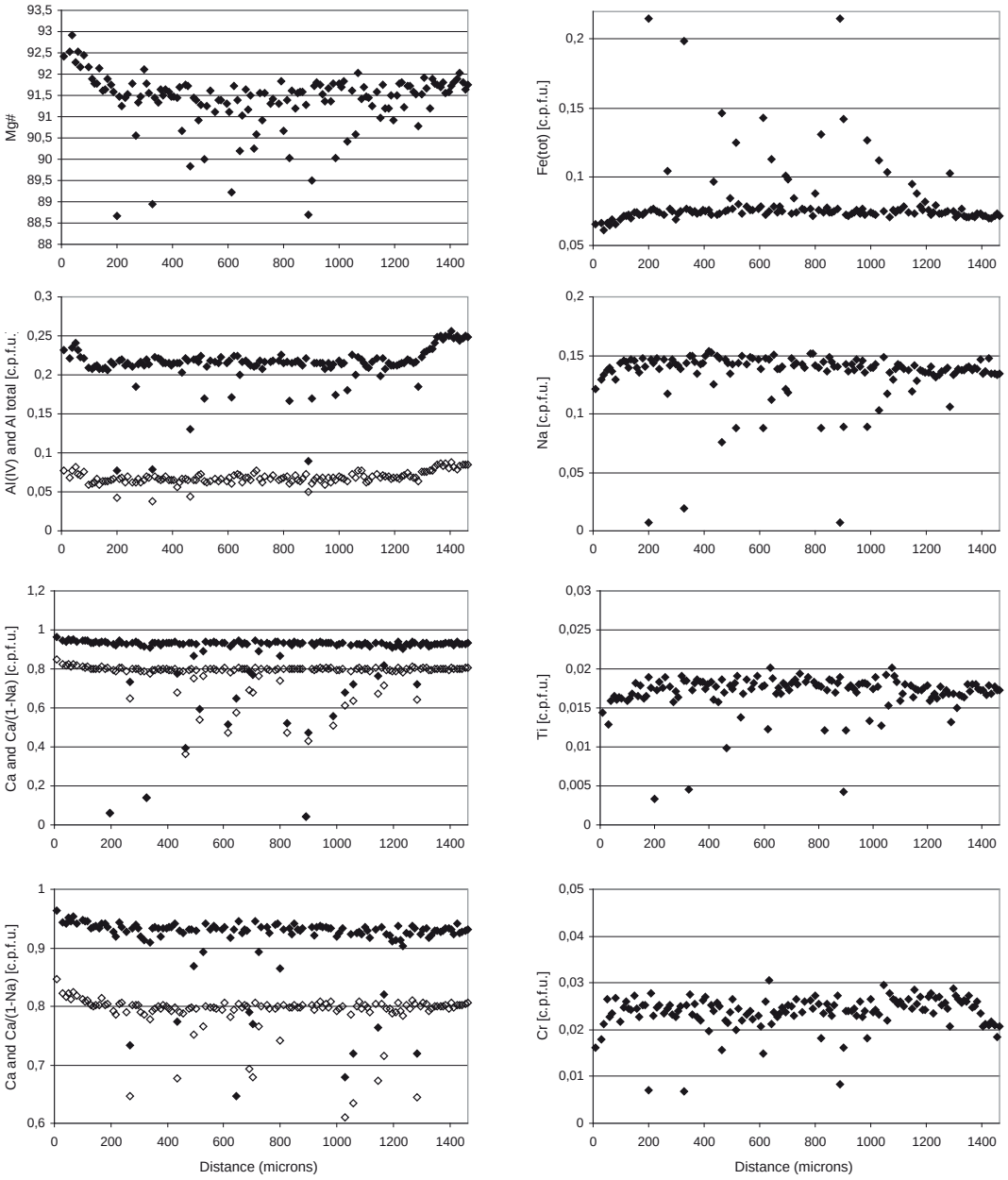


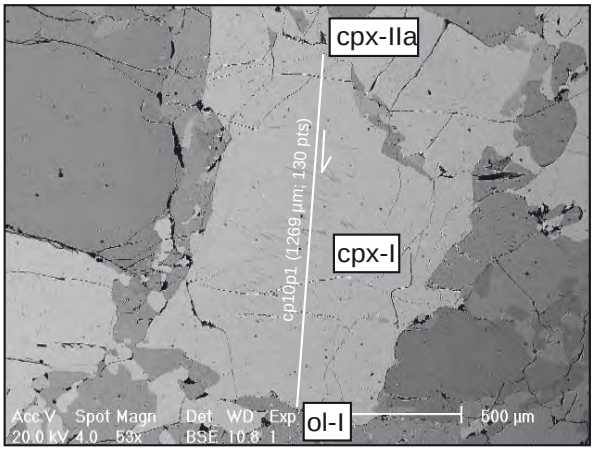
Group I: Clinopyroxene

Sample: 1963/02 - Group I (grt)-spl lherzolite

cpx-I porphyroclast (with opx exsolution lamellae; see spikes in patterns below)

EMP-analysis: Session9 / cp2p1



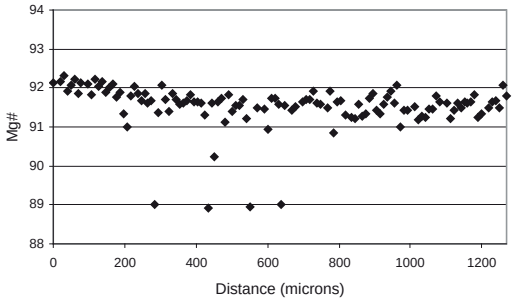


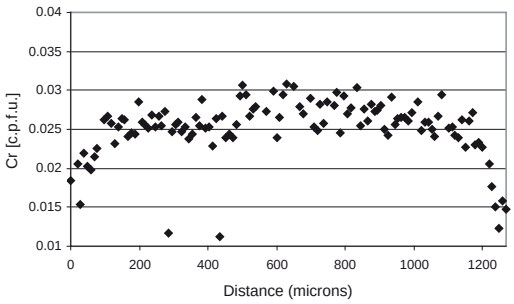
Group I: Clinopyroxene

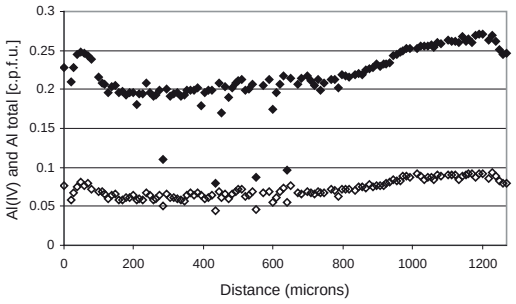
Sample: 1963/2 - Group I (grt)-spl lherzolite

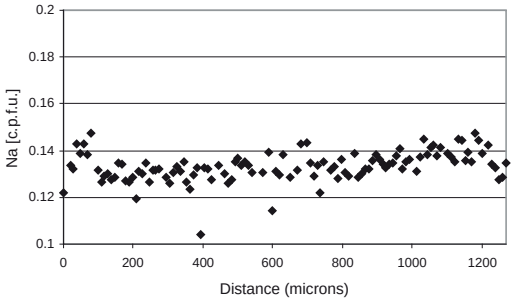
cpx-I porphyroclast (with opx exsolution lamellae)

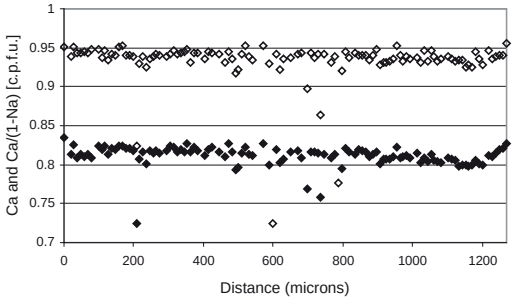
EMP-analysis: Session11 / cp10p1

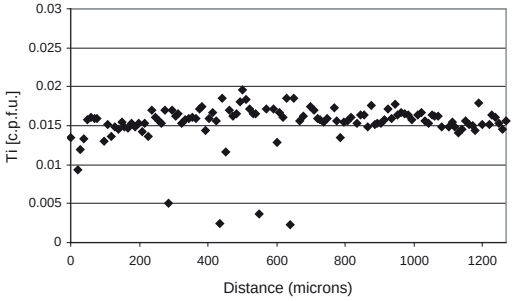


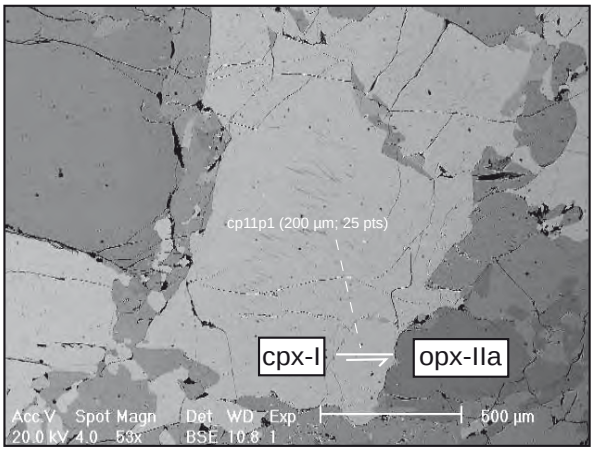










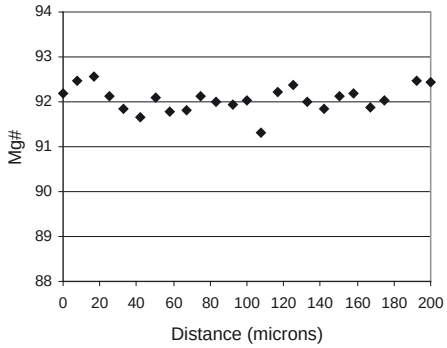


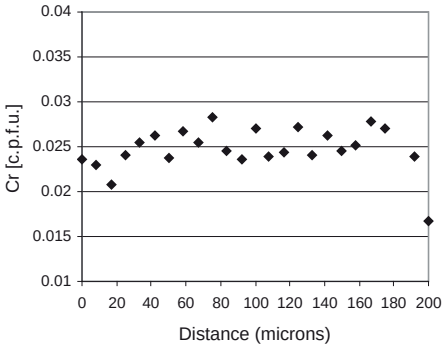
Group I: Clinopyroxene

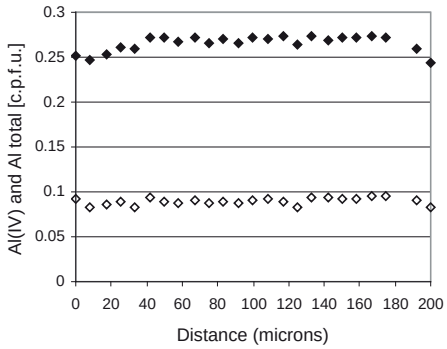
Sample: 1963/2 - Group I (grt)-spl lherzolite

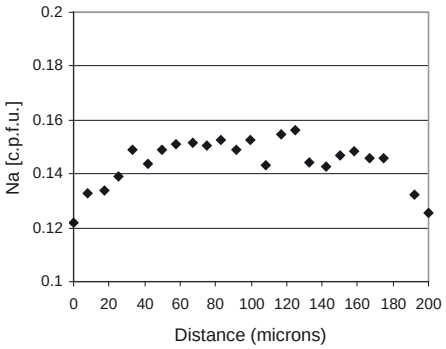
cpx-IIa neoblast

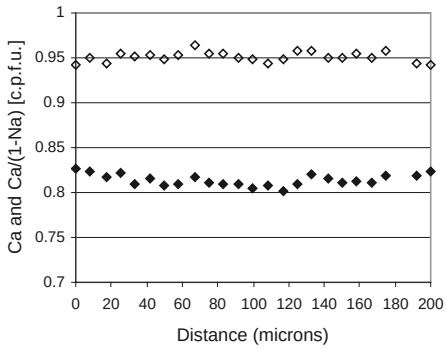
EMP-analysis: Session11 / cp11p1

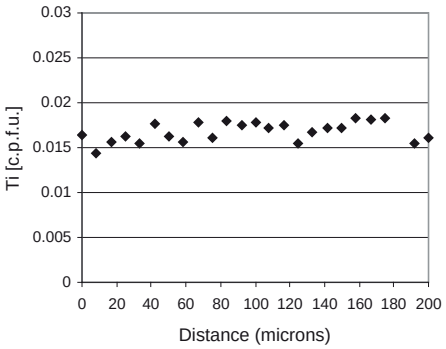


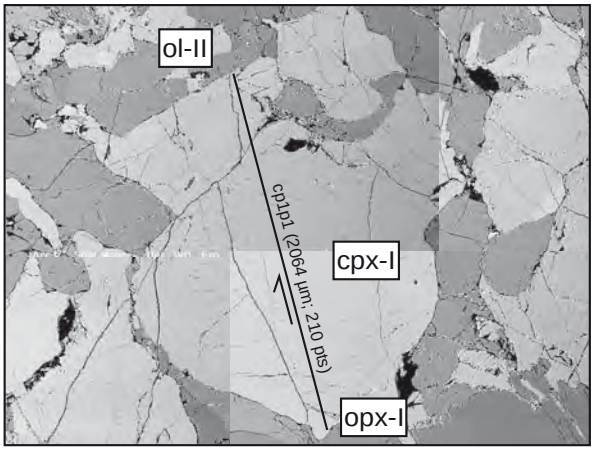










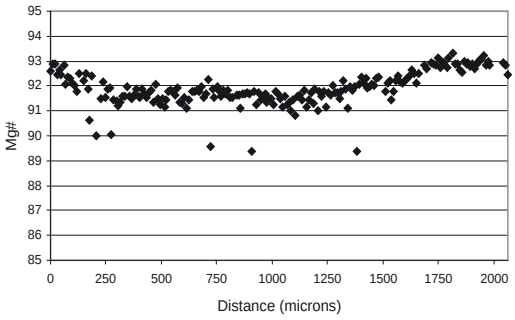


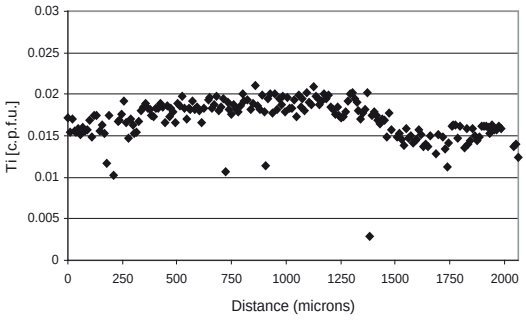
Group I: Clinopyroxene

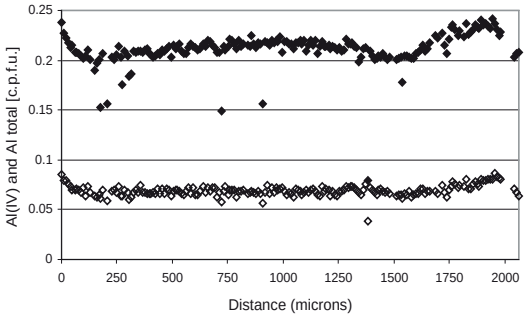
Sample: 1965/4 - Group I (grt)-spl lherzolite

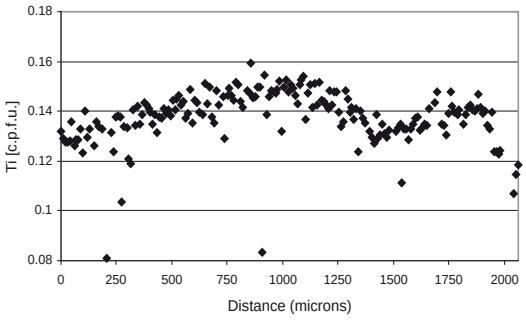
cpx-I porphyroclast (with opx exsolution lamellae)

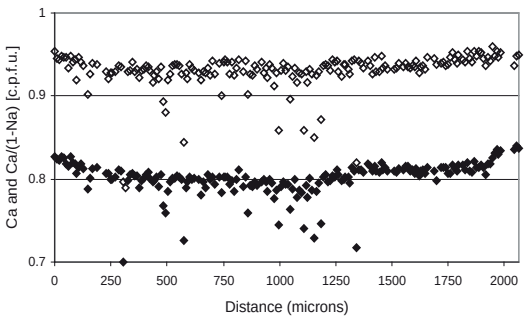
EMP-analysis: Session11 / cp1p1

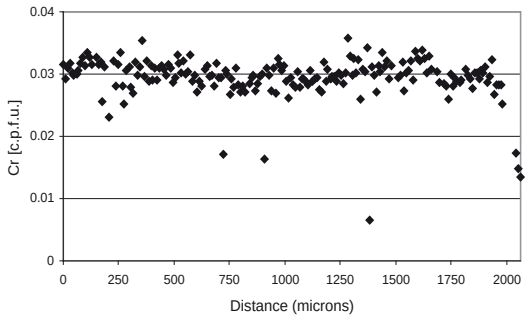


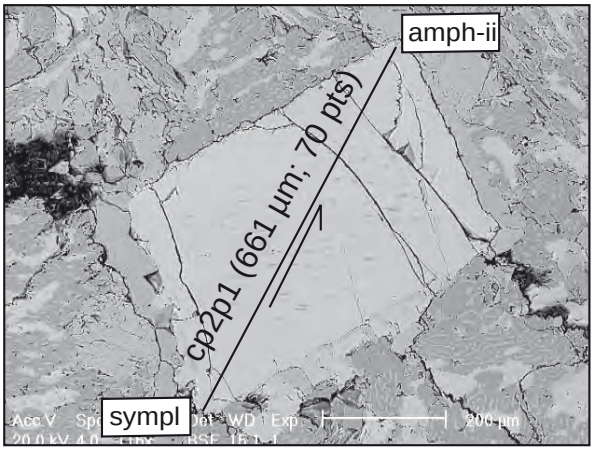












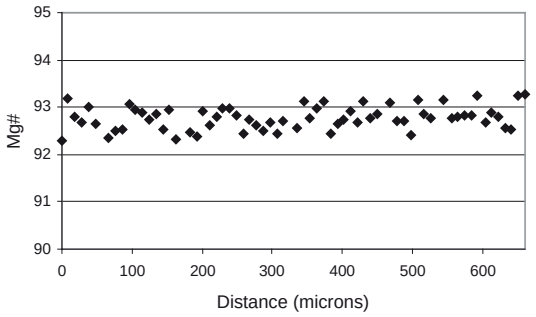
Group I: Clinopyroxene

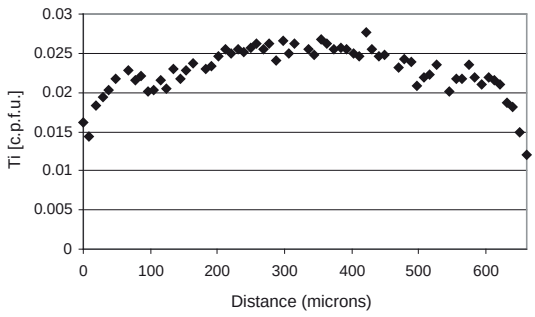
Sample: 1965/4 - Group I (grt)-spl lherzolite

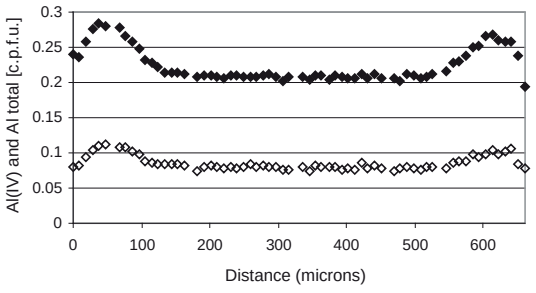
relich euhedral cpx-I inclusion in former garnet (now spl-IIb - opx-IIb - cpx-IIb symplectite)

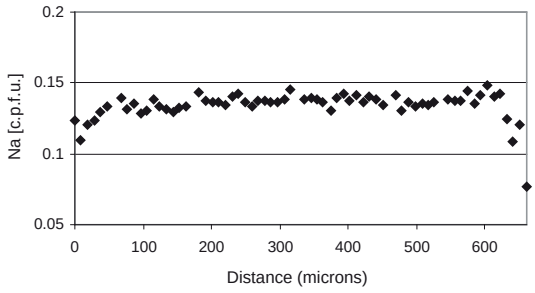
cpx-I is partly rimmed by Ti-pargasite (amph-ii)

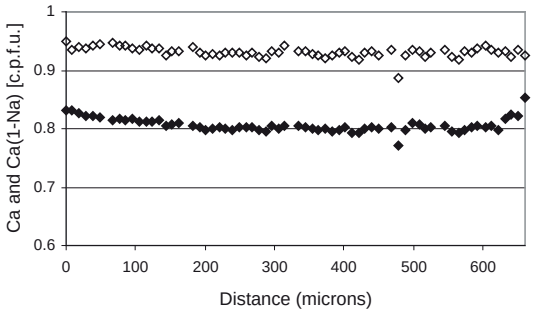
EMP-analysis: Session13 / cp2p1

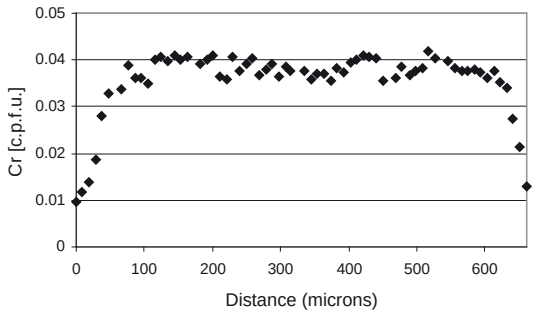


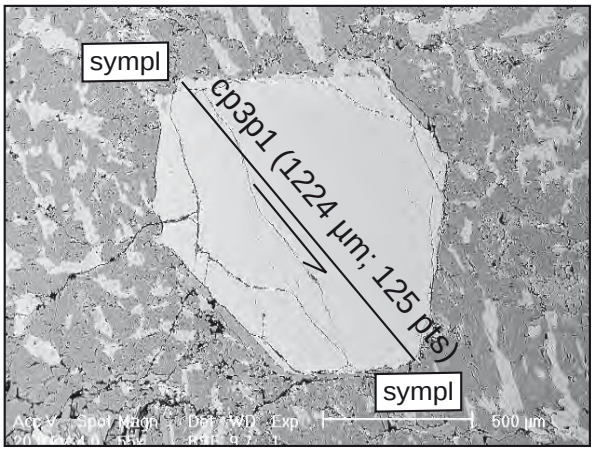












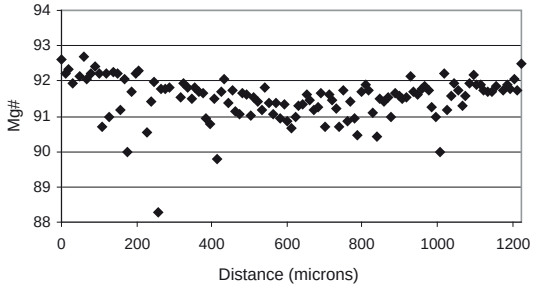
Group I: Clinopyroxene

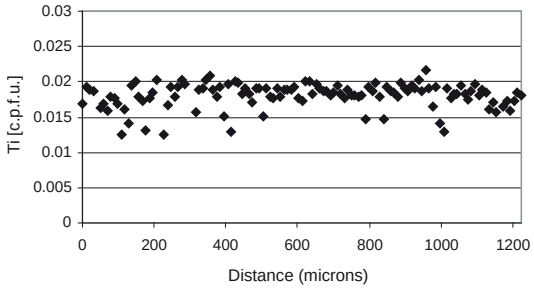
Sample: 1965/4 - Group I (grt)-spl lherzolite

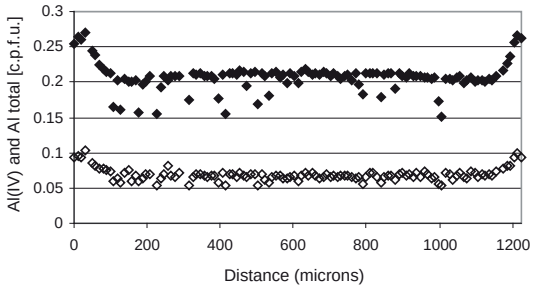
cpx-I: relic euhedral inclusion in former garnet (now spl-IIb - opx-IIb - cpx-IIb symplectite)

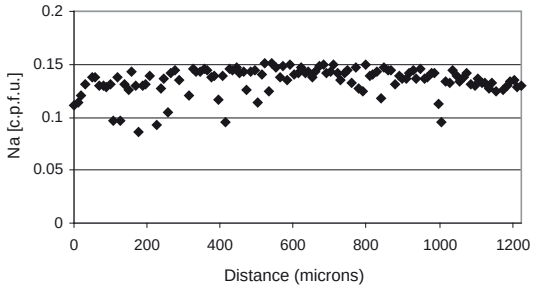
(with cpx exsolution lamellae responsible for spiky patterns)

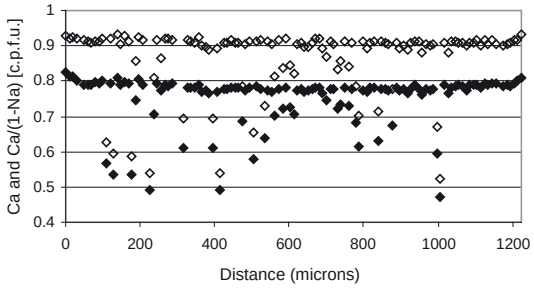
EMP-analysis: Session13 / cp3p1

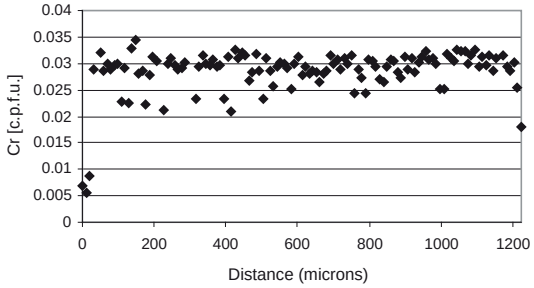


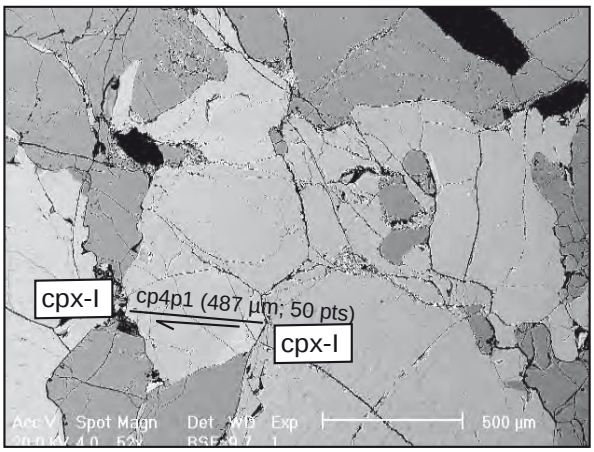










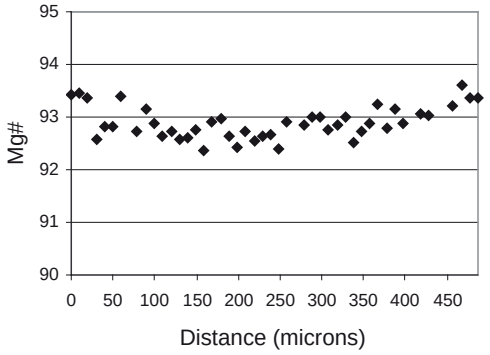


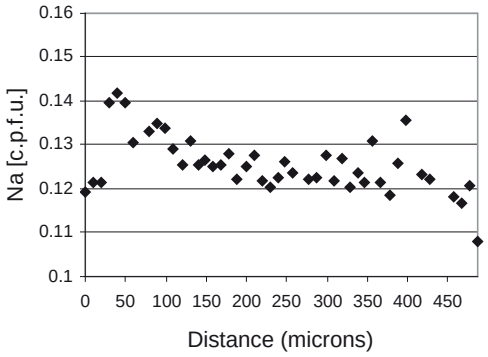
Group I: Clinopyroxene

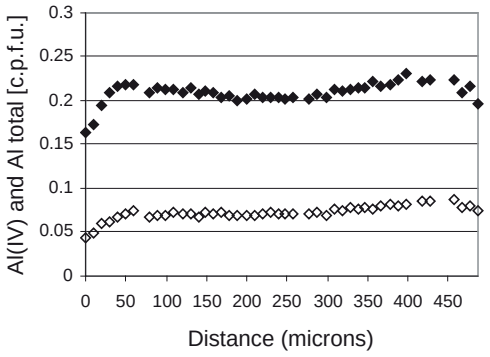
Sample: 1965/4 - Group I (grt)-spl lherzolite

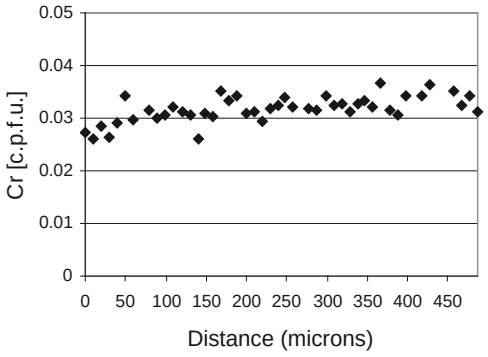
Large slightly strained but un-exsolved cpx-IIa neoblast

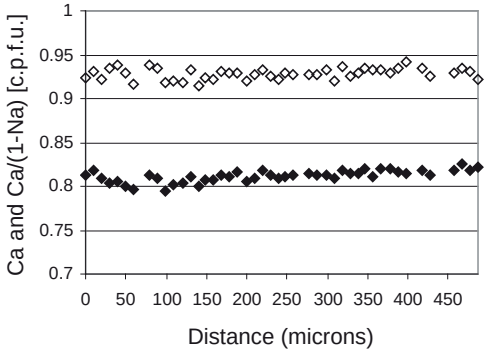
EMP-analysis: Session13 / cp4p1

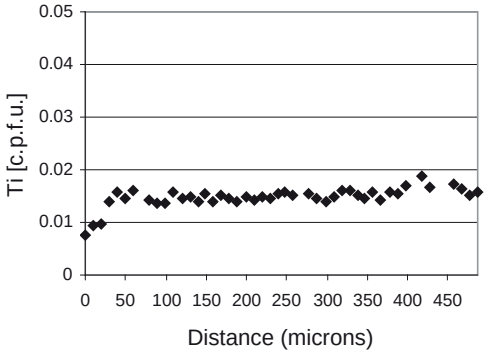


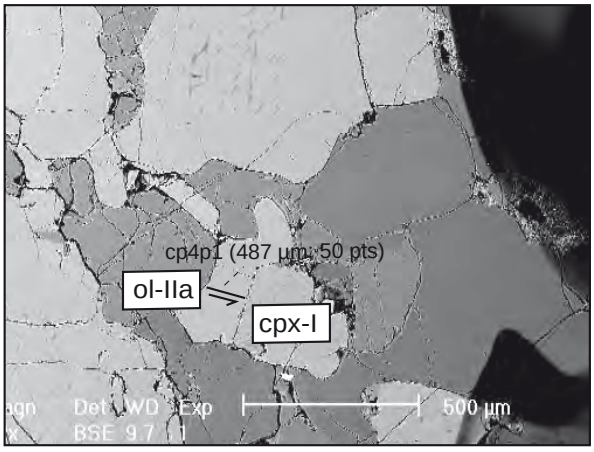










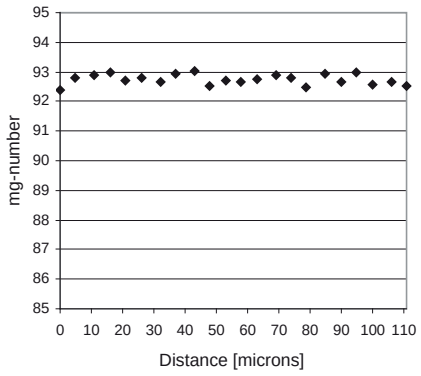


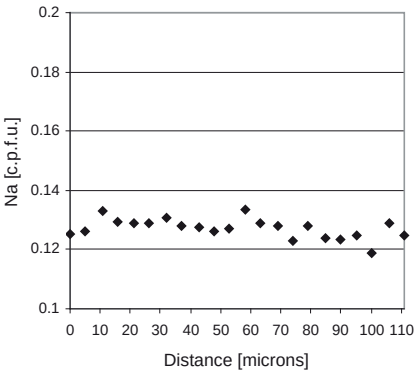
Group I: Clinopyroxene

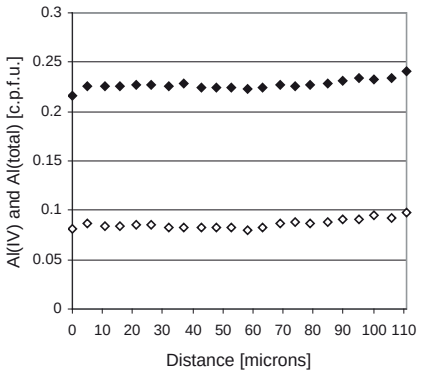
Sample: 1965/4 - Group I (grt)-spl lherzolite

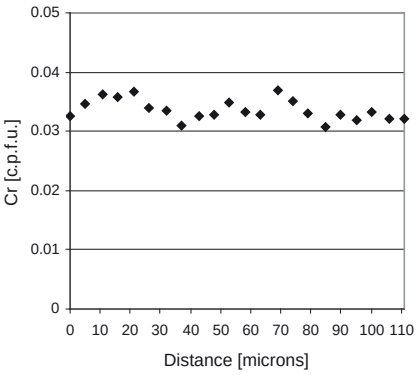
strainfree cpx-IIa neoblast adjacent to small exsolved cpx-I porphyroclast

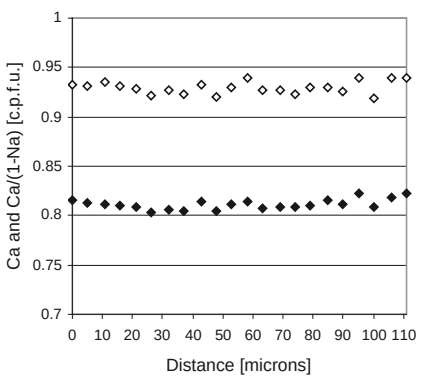
EMP-analysis: Session13 / cp5p1

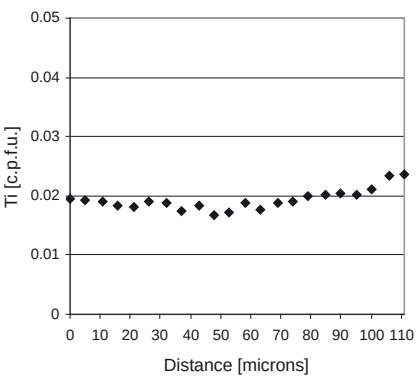


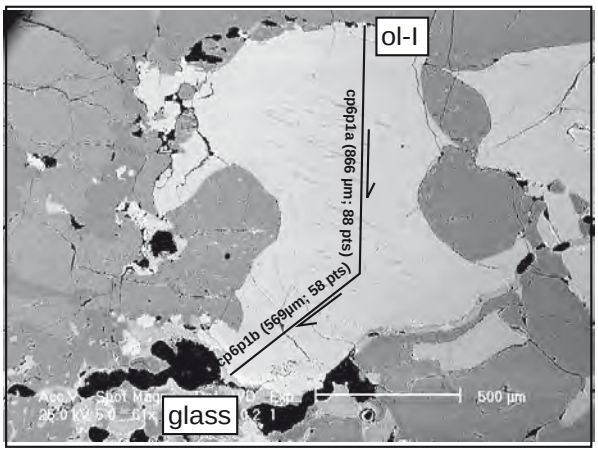










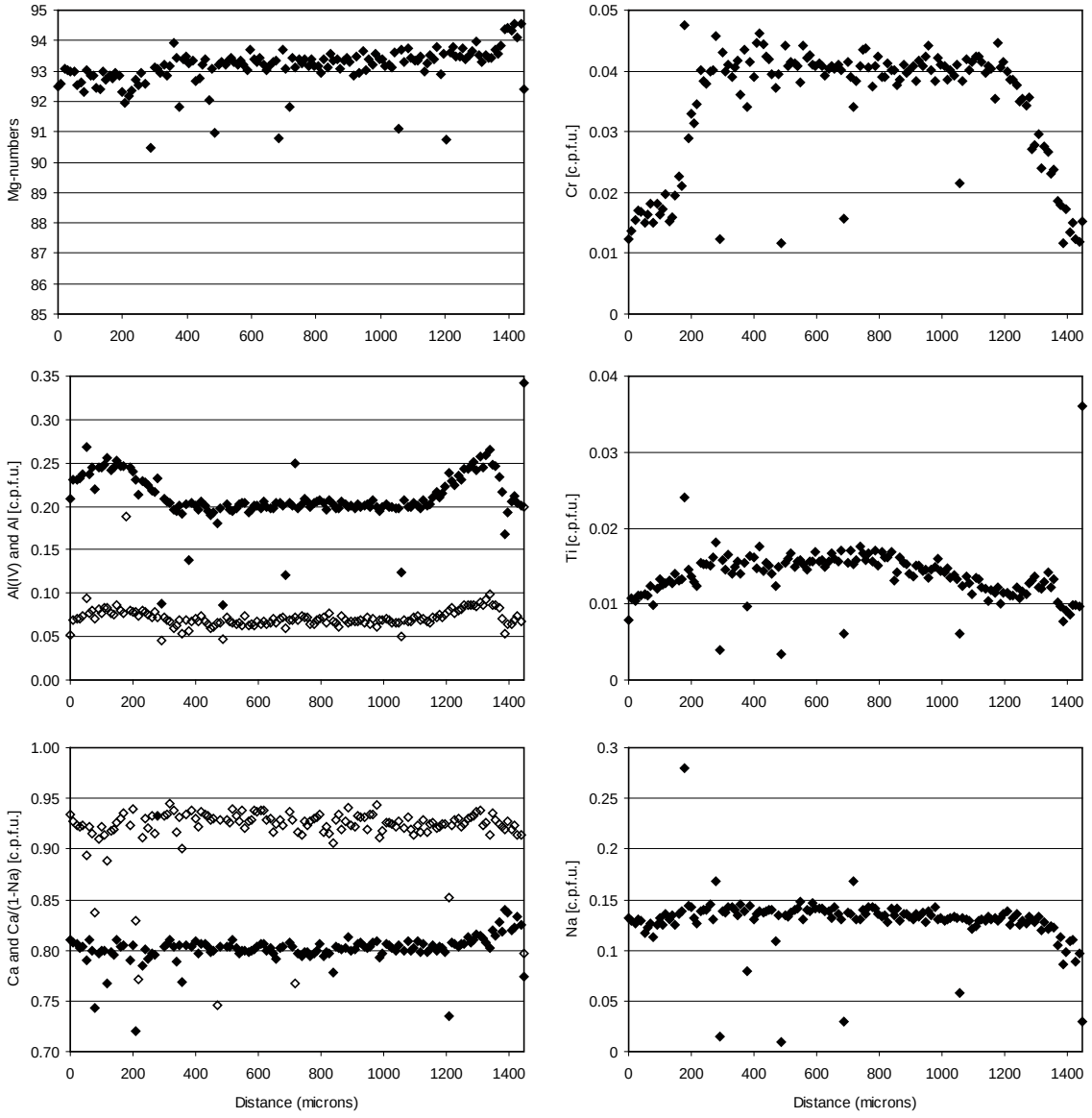


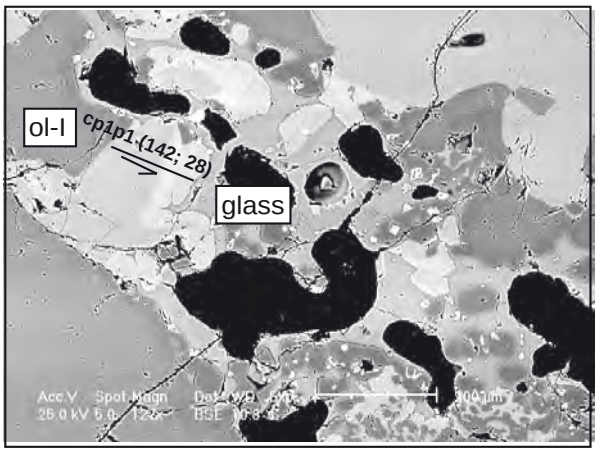
Group I: Clinopyroxene

Sample: 1963/1 - Group I (grt)-spl lherzolite (with abundant melt pockets)

cpx-I: clinopyroxene porphyroclast (with opx exsolution lamellae) lined by glass

EMP-analysis: Session14 / cp6p1 (a & b)



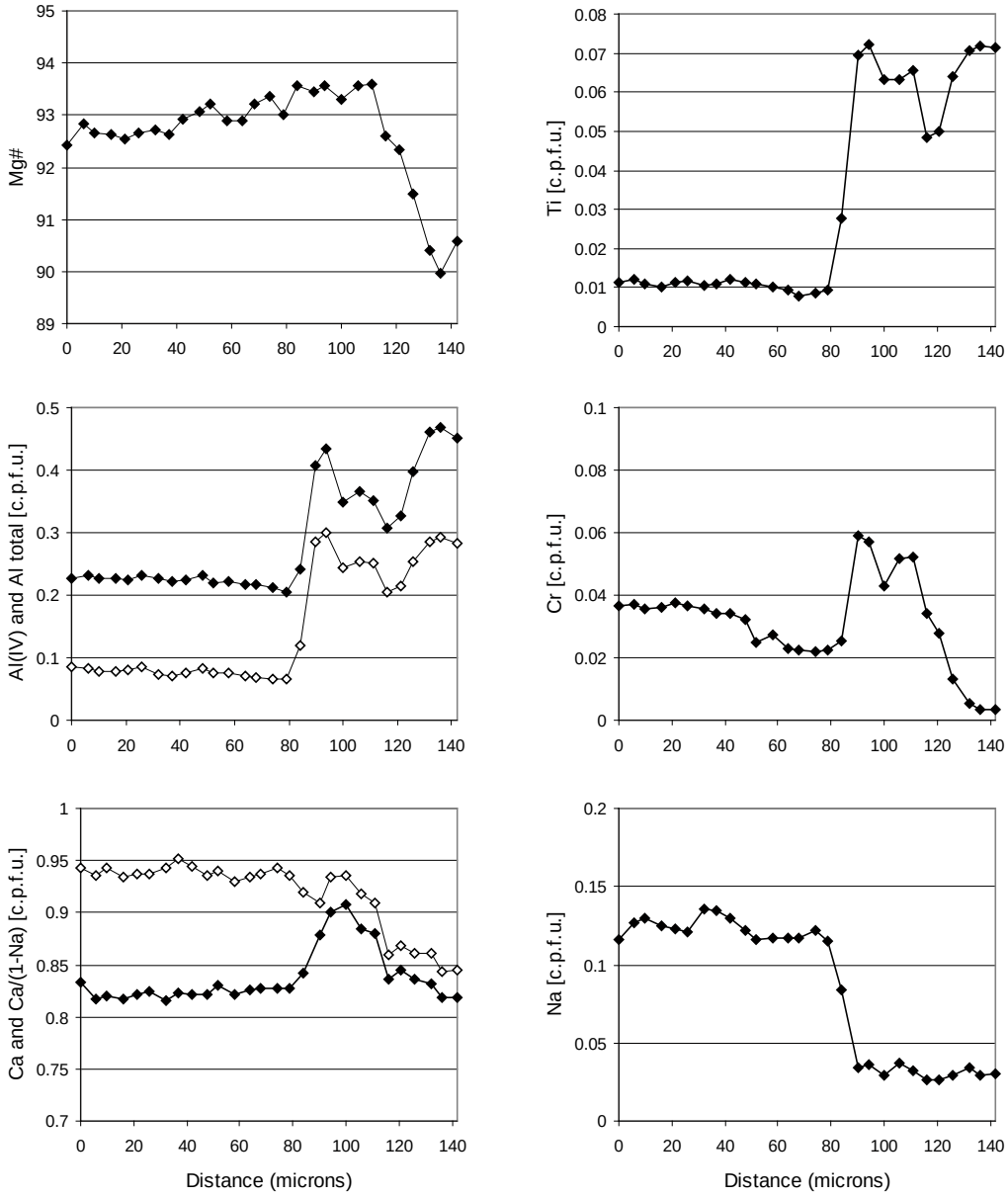


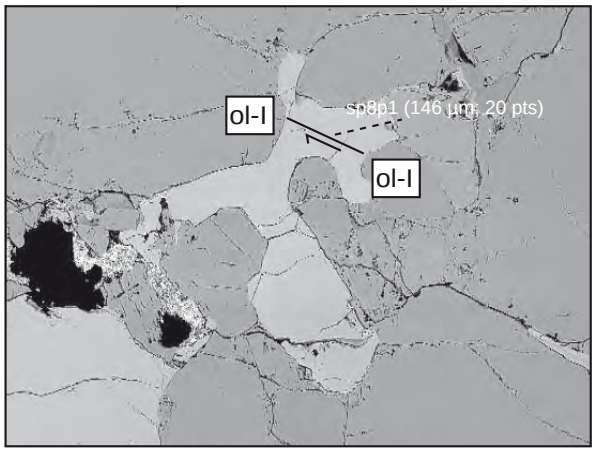
Group I: Clinopyroxene

Sample: 1960/2 - Group I (grt)-spl lherzolite (with abundant melt pockets)

cpx-IIa grading into Aug_m: recation rim on clinopyroxene adjacent to a melt pocket

EMP-analysis: Session14 / cp1p1



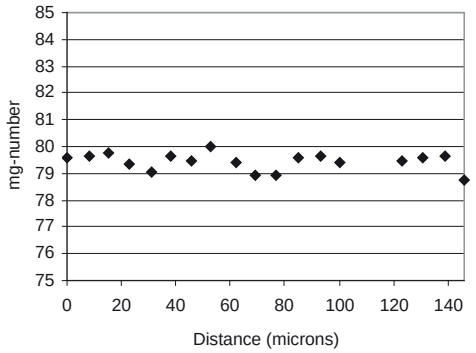


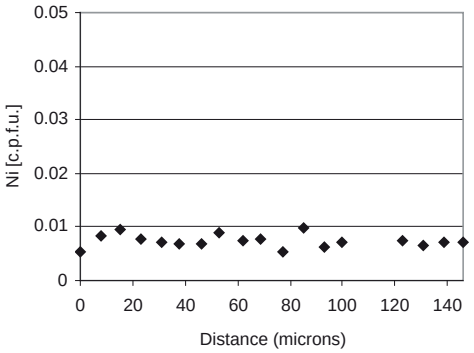
Group I: Spinel

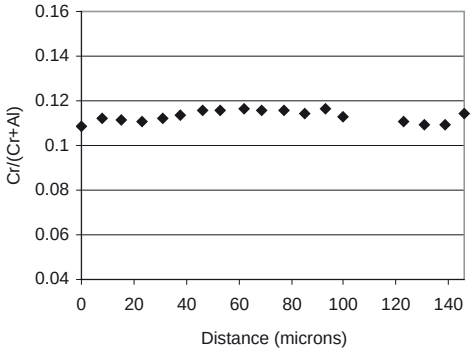
Sample: 1965/4 - Group I (grt)-spl lherzolite

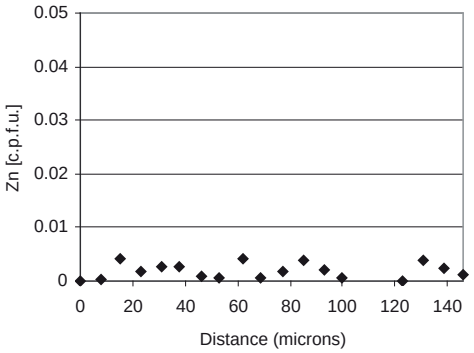
spl-II: spinel outside of symplectites, interstitial between pyroxene and olivine

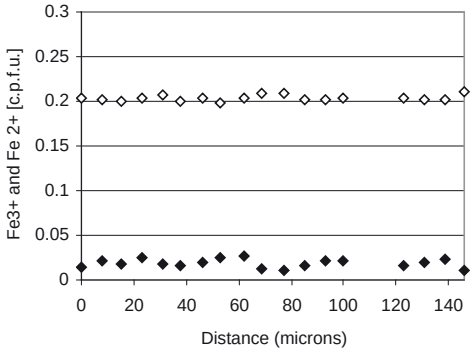
EMP-analysis: Session15 / sp8p1

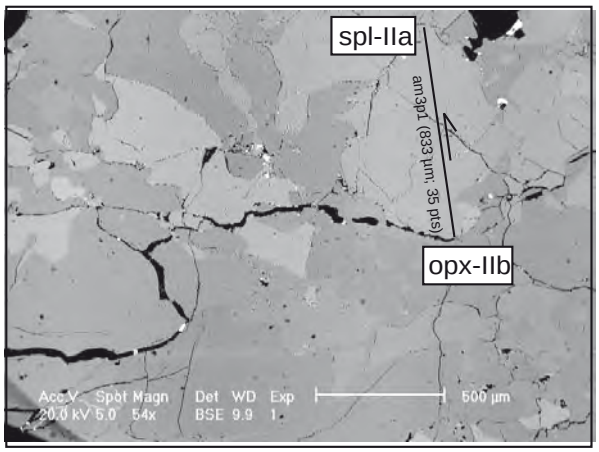










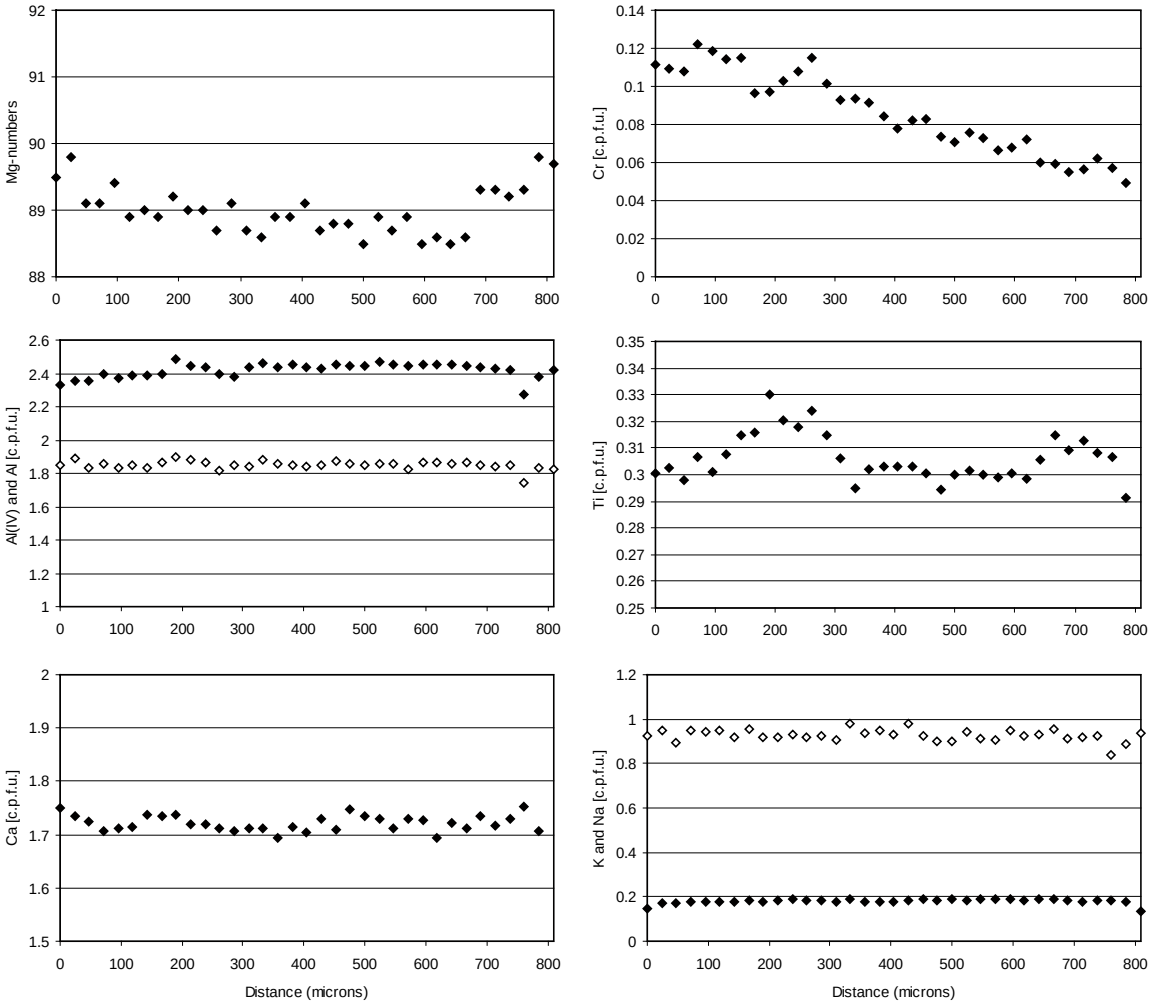


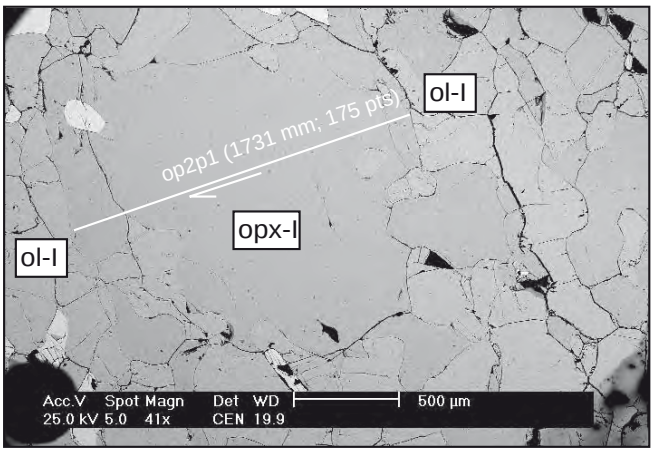
Group I: Ti-Pargasite

Sample: 1963/2 - Group I (grt)-spl lherzolite

amph-i: large, texturally equilibarted Ti-pargasite adjacent to a former garnet

EMP-analysis: Session14 / cp1p1



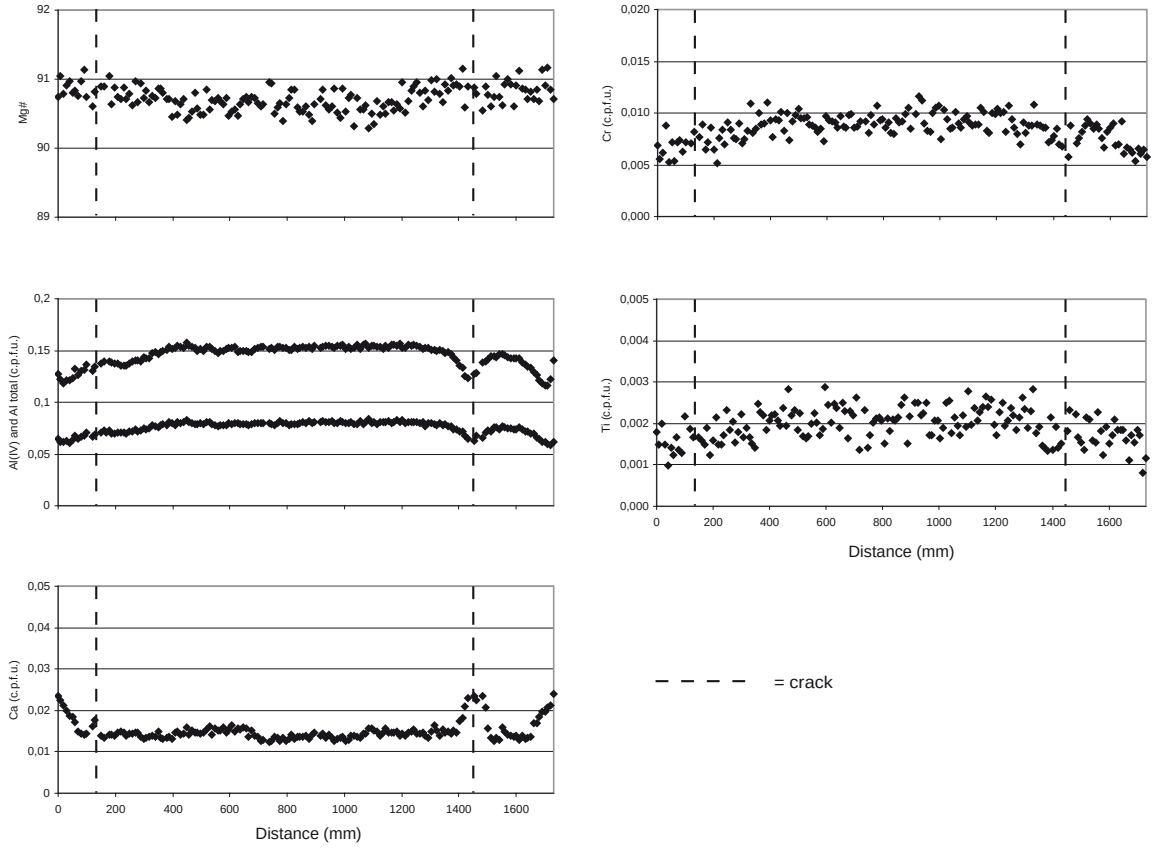


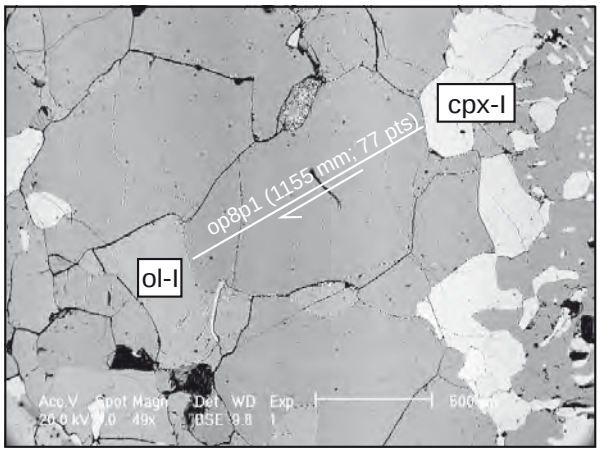
Group II: Orthopyroxene

Sample: 1958/13 - Group II
(grt)-spl lherzolite (tabular fabric)

opx-I (relic porphyroclast)

EMP-analysis: Session3 / op2p1



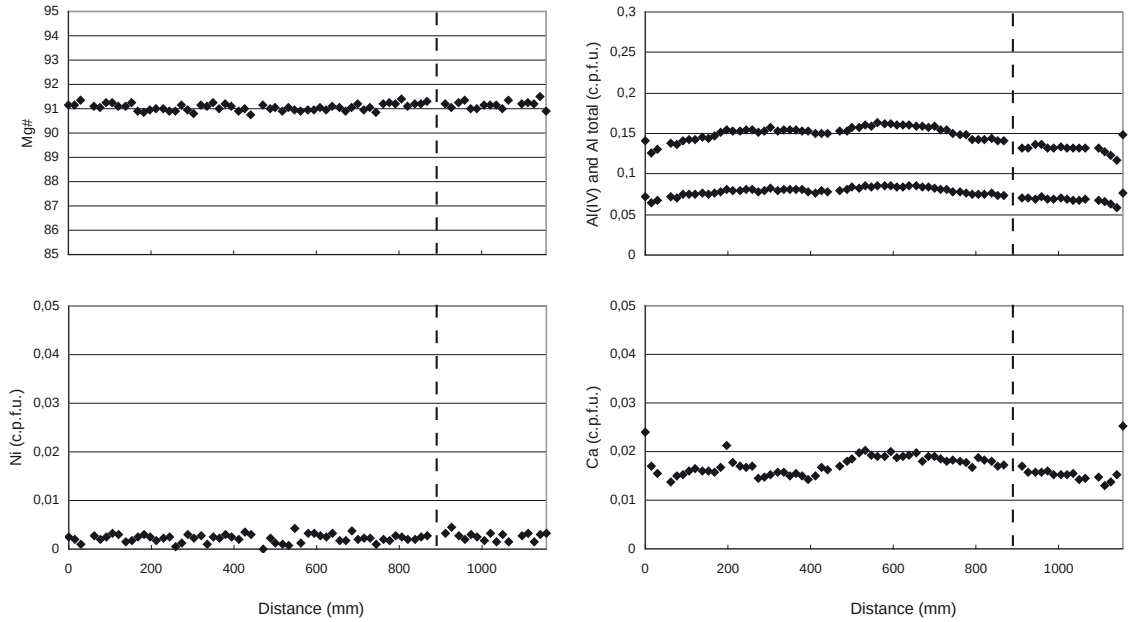


Group II: Orthopyroxene

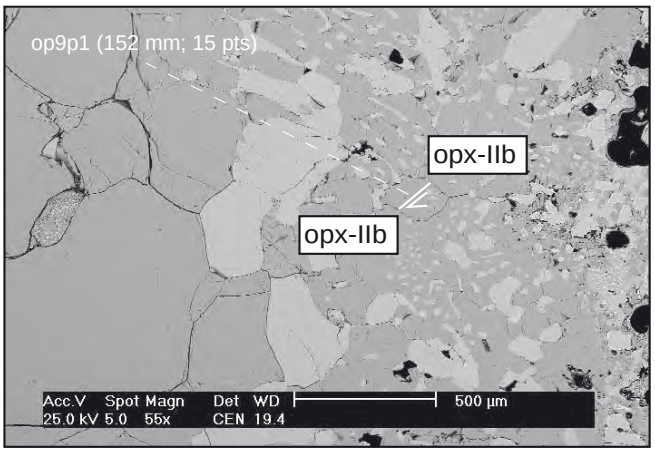
Sample: 1958/13 - Group II
(grt)-spl lherzolite (tabular fabric)

strainfree opx-I

EMP-analysis: Session5 / op8p1



– – – = crack

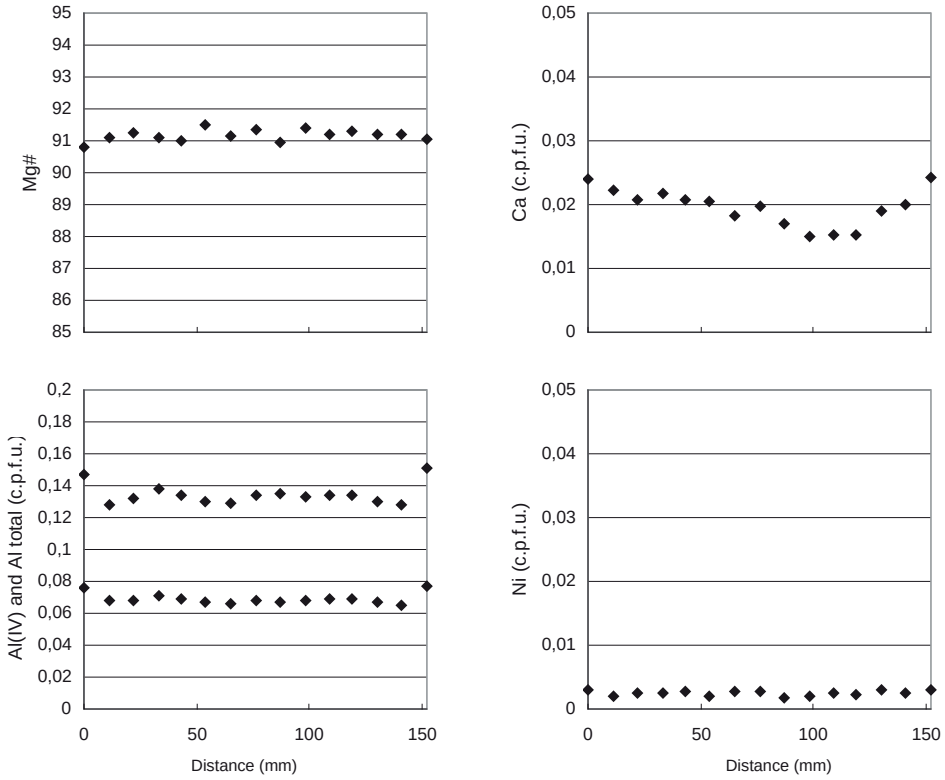


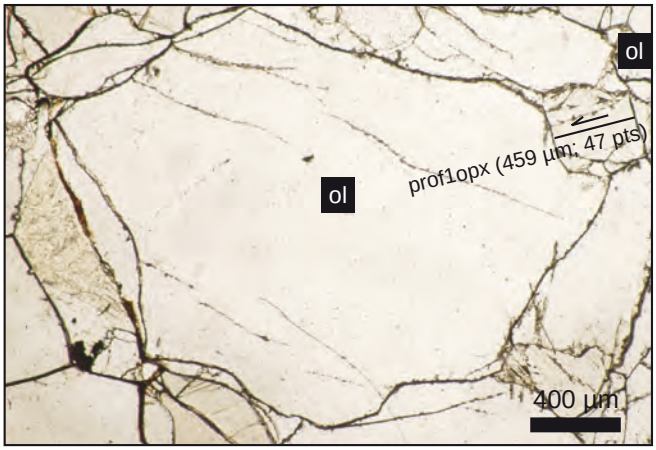
Group II: Orthopyroxene

Sample: 1958/13 - Group II
(grt)-spl lherzolite

opx-IIb within a partly recrystallised spl-IIb - opx-IIb - cpx-IIb symplectite

EMS-analysis: Session5 / op9p1



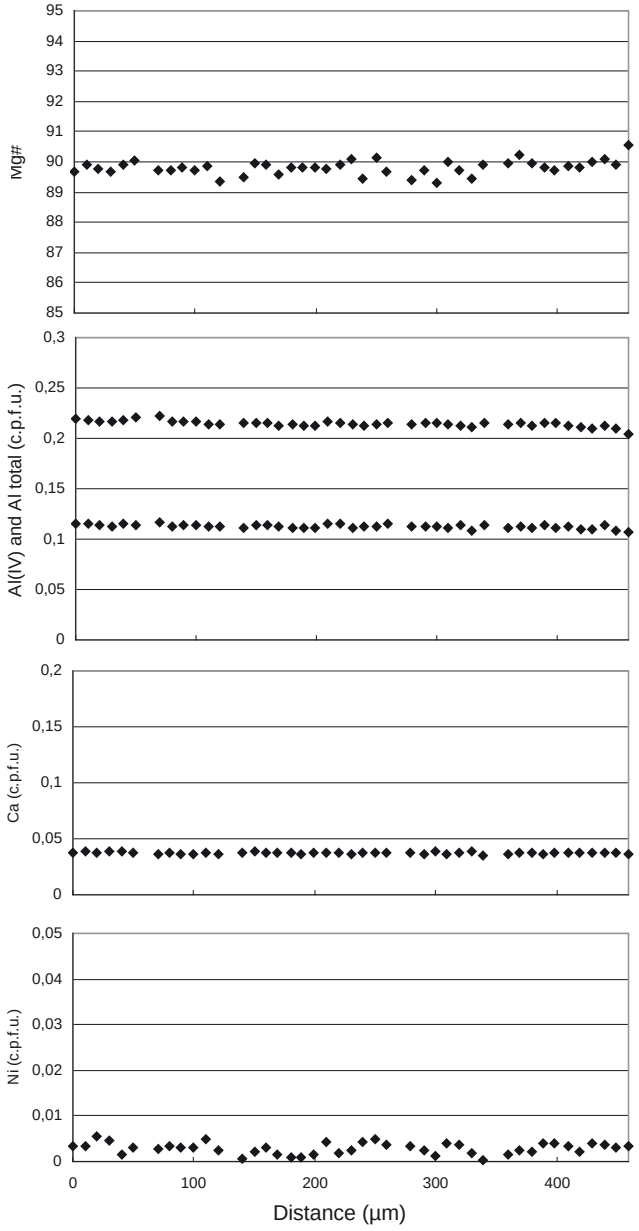


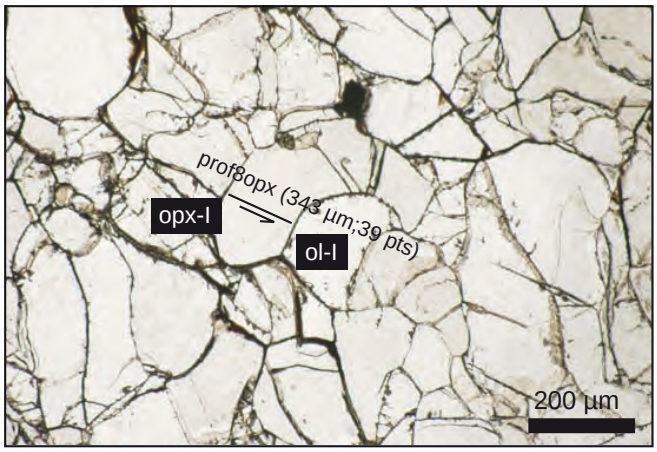
Group II: Orthopyroxene

Sample: 1958/20 - Group II
(grt)-spl lherzolite

opx-I; small strainfree grain

EMP-analysis: Session1 / prof1opx



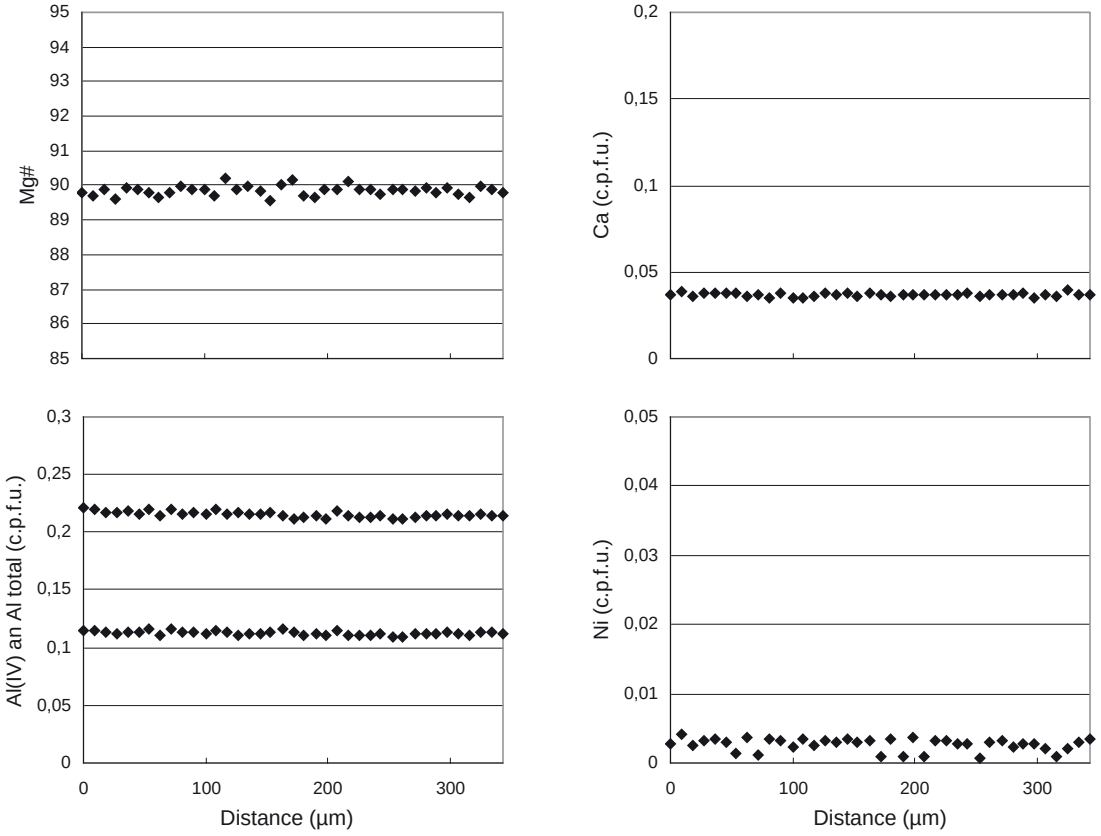


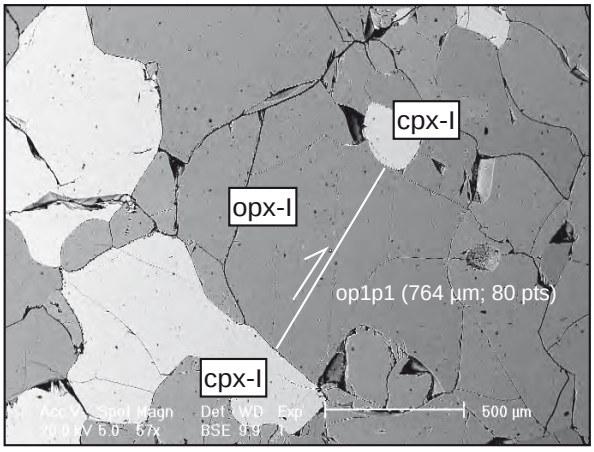
Group II: Orthopyroxene

Sample: 1958/20 - Group II
(grt)-spl lherzolite

opx-I; strainfree, statically recrystallised small grain

EMP-analysis: Session1 / prof8opx



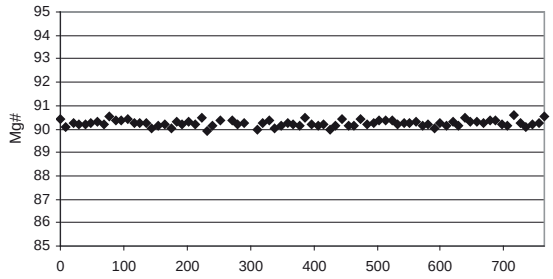


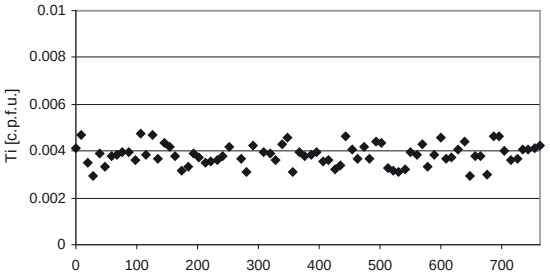
Group II: Orthopyroxene

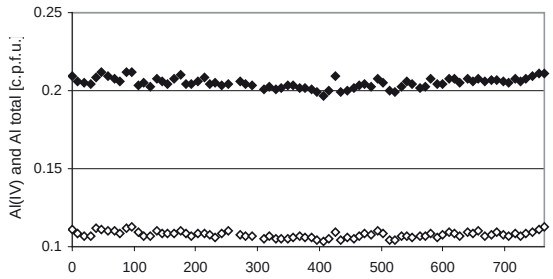
Sample: 1959/24 - Group II
(grt)-spl lherzolite

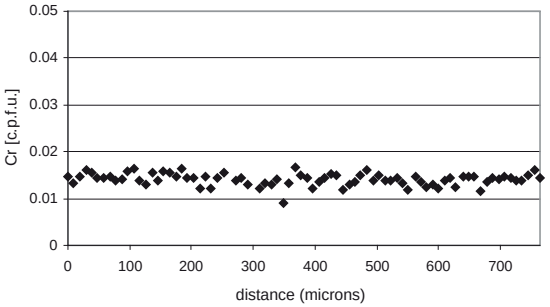
opx-I; large, strainfree grain

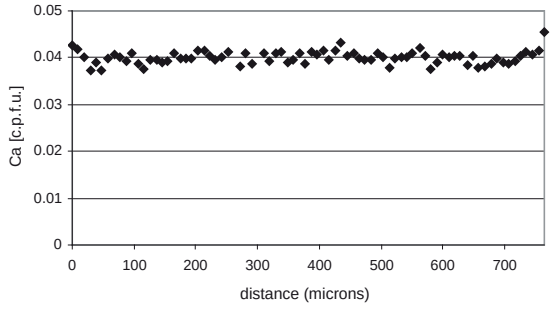
EMP-analysis: Session10 / op1p1

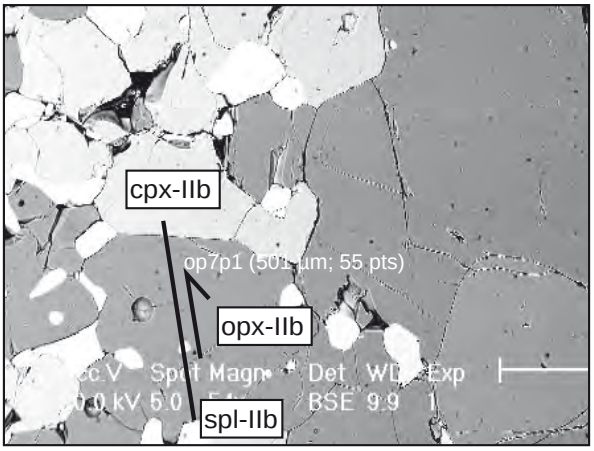










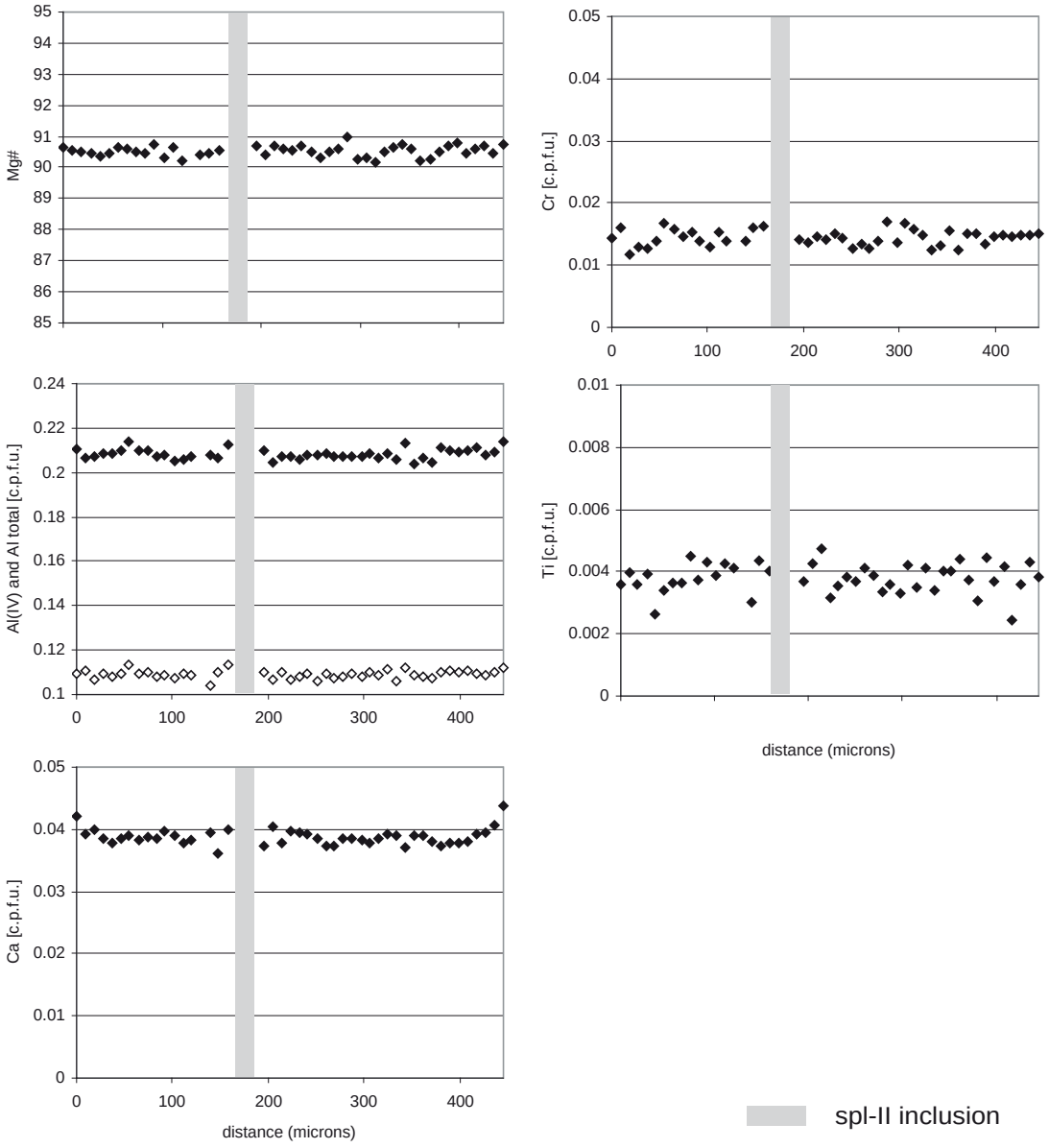


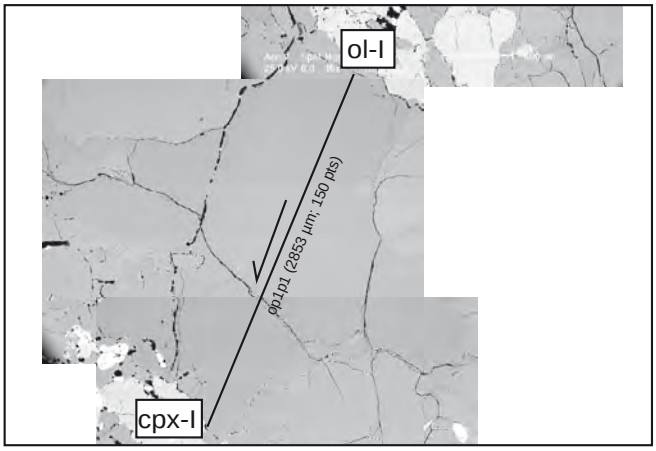
Group II: Orthopyroxene

Sample: 1959/24 - Group II (grt)-spl lherzolite

opx-II: within a recrystallised spl-IIb - opx-IIb - cpx-IIb cluster; strainfree

EMP-analysis: Session10 / op7p1



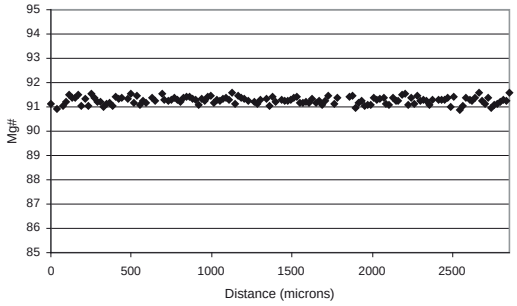


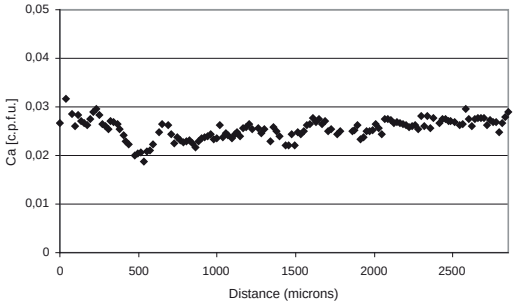
Group II: Orthopyroxene

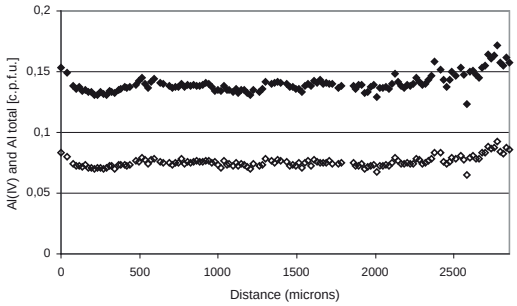
Sample: 1959/25 - Group II (grt)-spl lherzolite (less recrystallised)

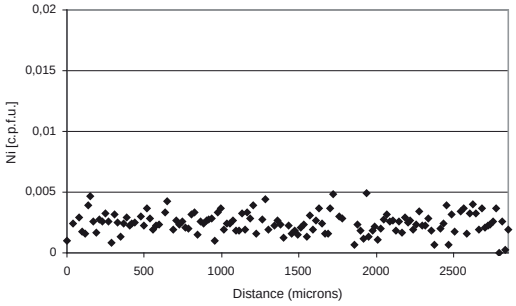
opx-I: relic porphyroclast

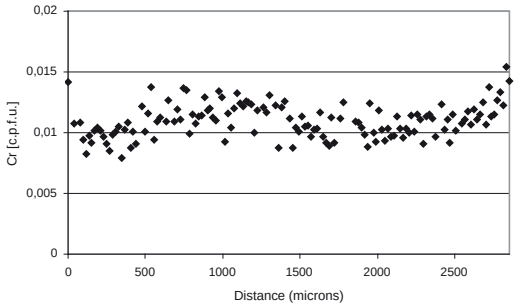
EMP-analysis: Session7 / op1p1

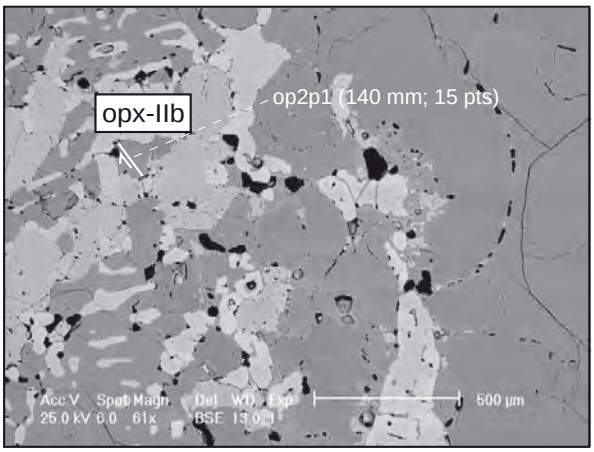










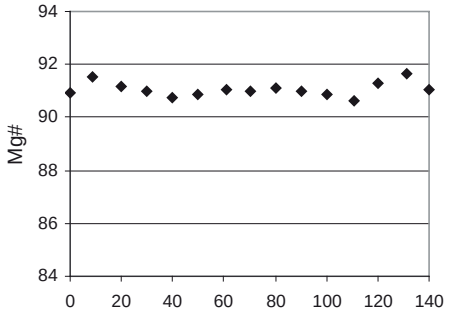


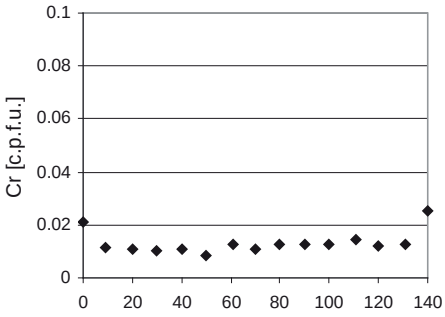
Group II: Orthopyroxene

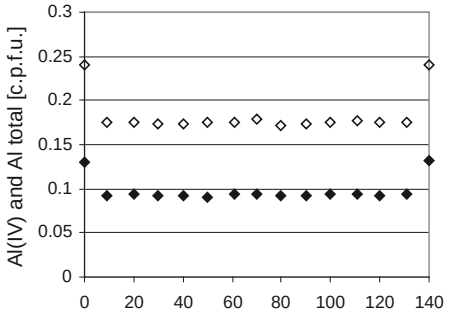
Sample: 1959/25 - Group II (grt)-spl lherzolite

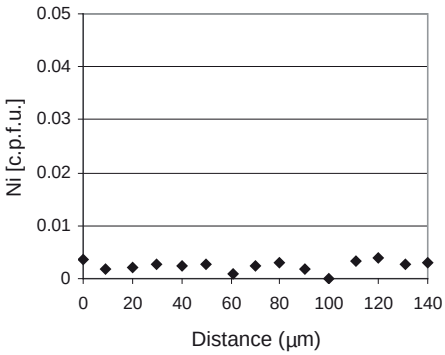
opx-IIb in contact with silicate glass, within a partly recrystallised spl-IIb - opx-IIb - cpx-IIb cluster

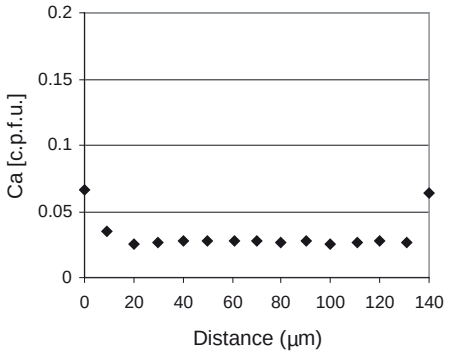
EMP-analysis: Session8 / op2p1

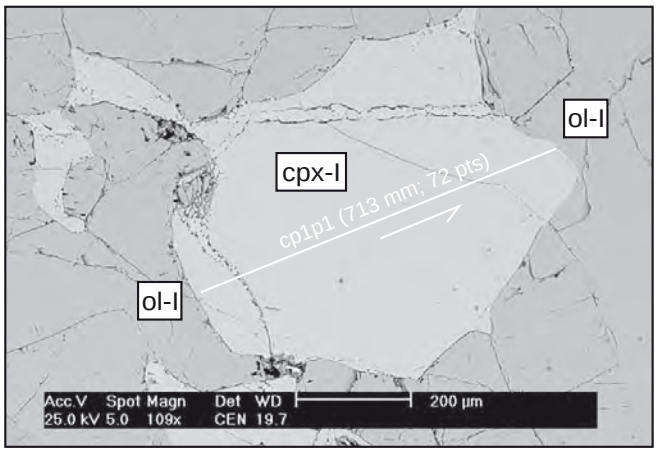










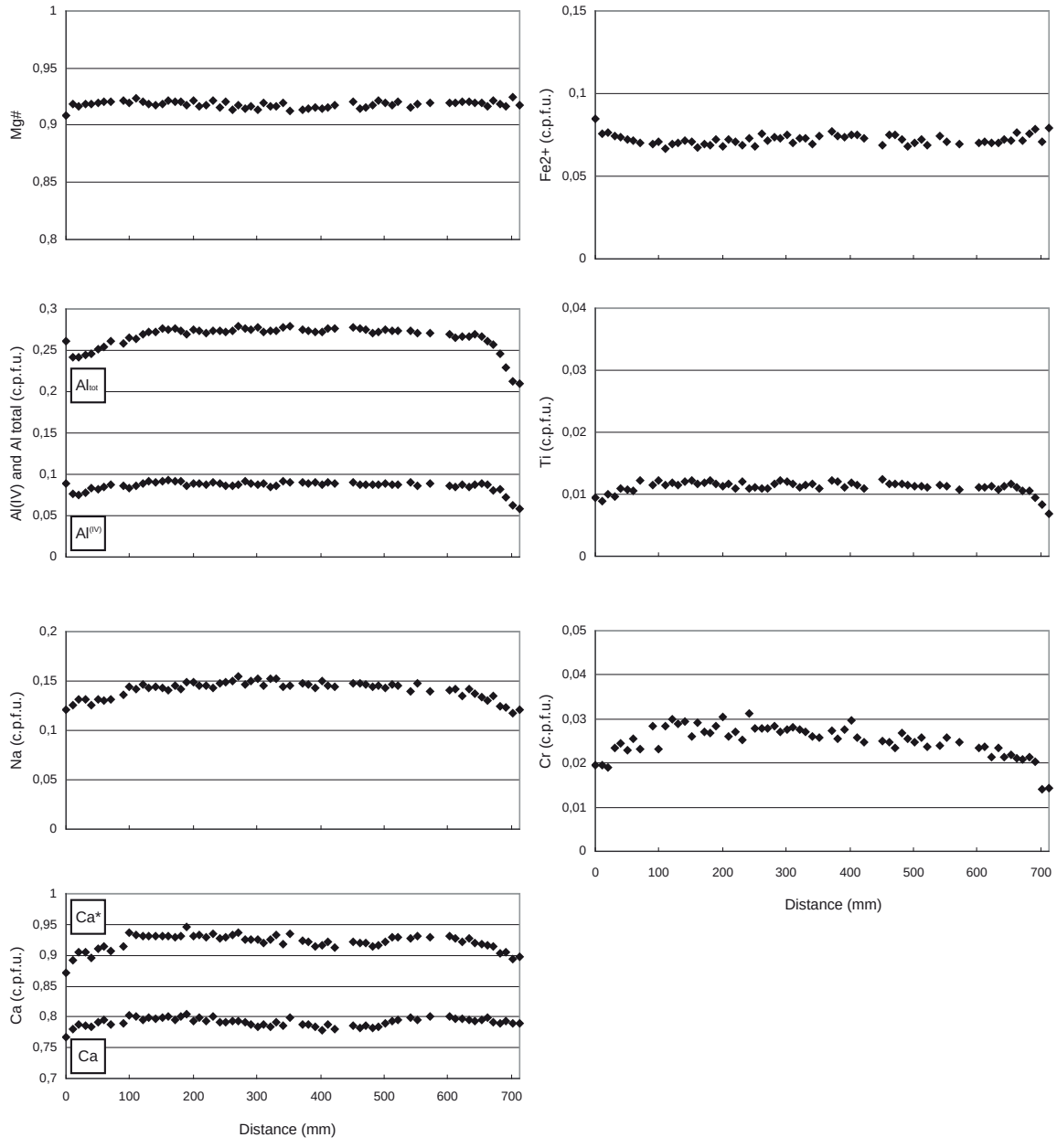


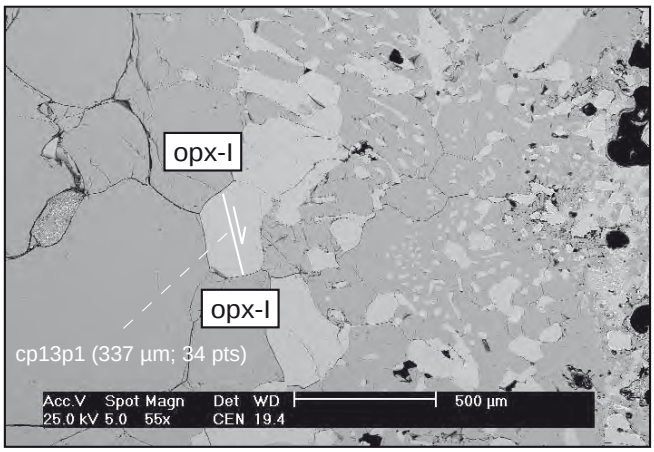
Group II: Clinopyroxene

Sample: 1958/13 - Group II
(grt)-spl lherzolite (tabular farbric)

relic cpx-I porphyroclast
(including stringers of secondary 'sieve-textured' Cpx_m)

EMP-analysis: Session3 / cp1p1



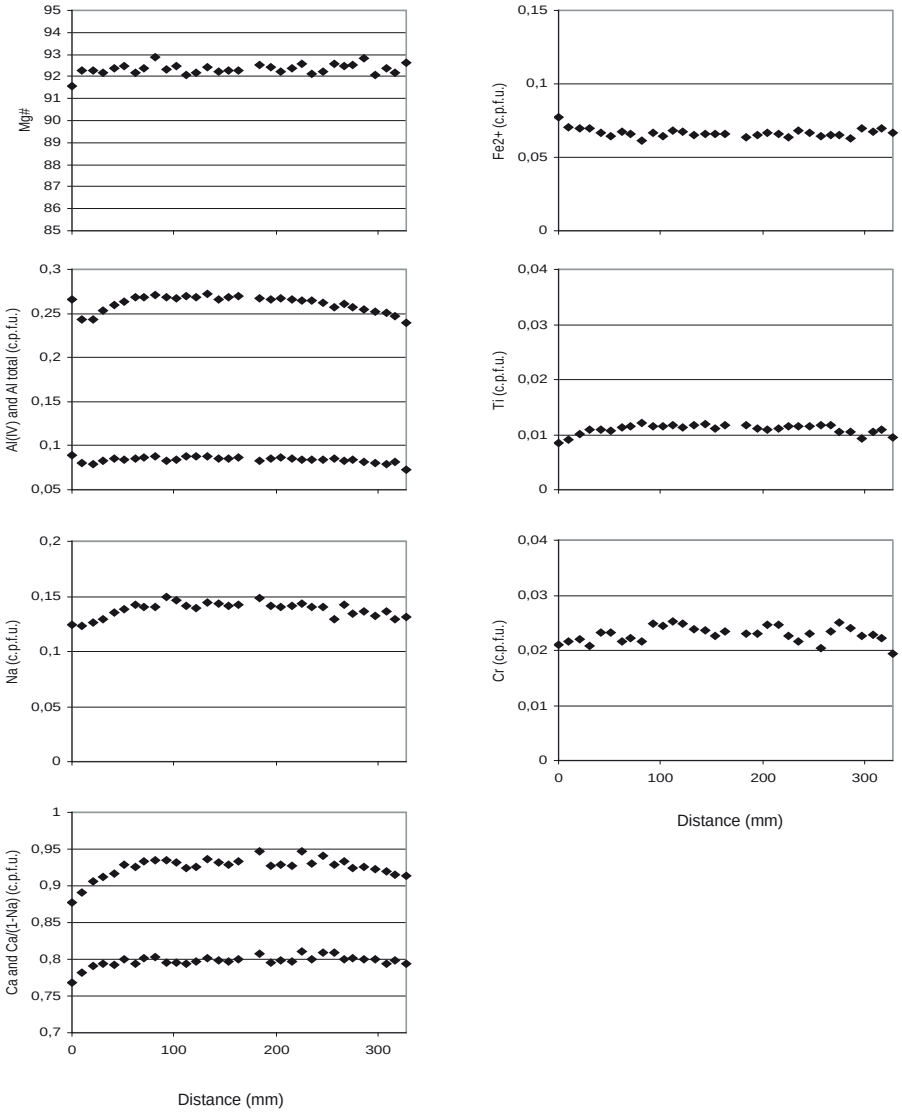


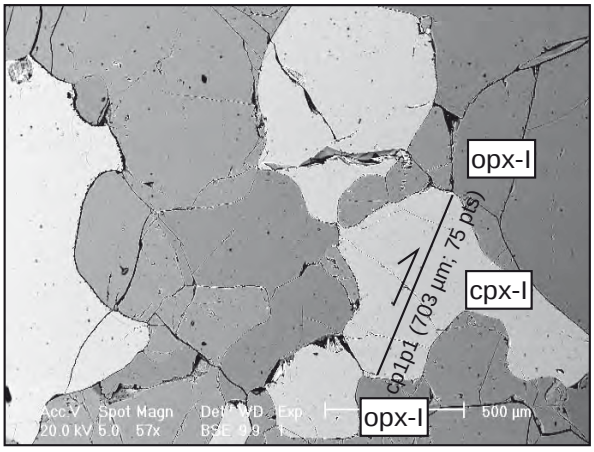
Group II: Clinopyroxene

Sample: 1958/13 - Group II
(grt)-spl lherzolite (tabular fabric)

cpx-IIa (neoblast) at the edge of a partly recrystallised spl-IIb - opx-IIb - cpx-IIb symplectite

EMP-analysis: Session5 / cp13p1



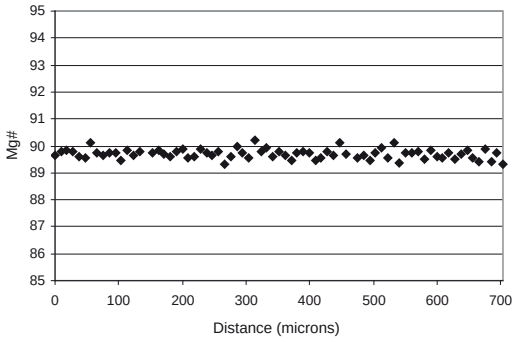


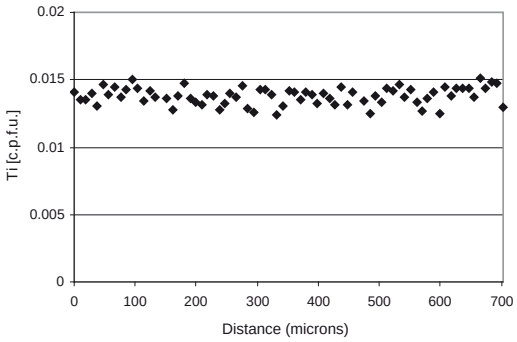
Group II: Clinopyroxene

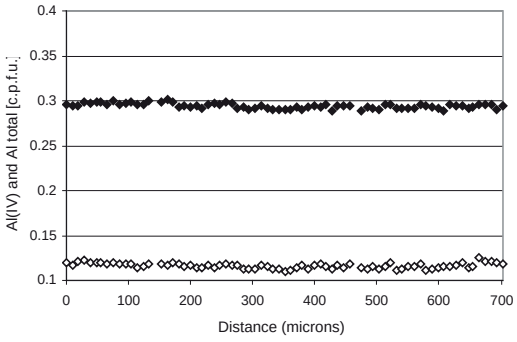
Sample: 1959/24 - Group II (grt)-spl lherzolite

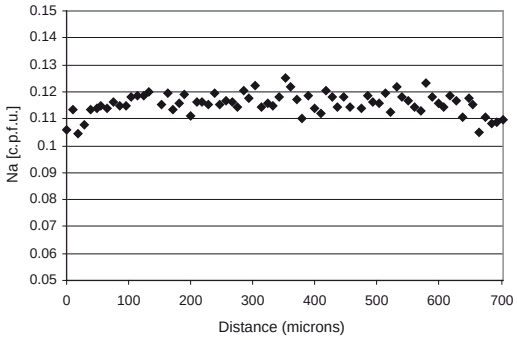
cpx-I: strainfree, no exsolution

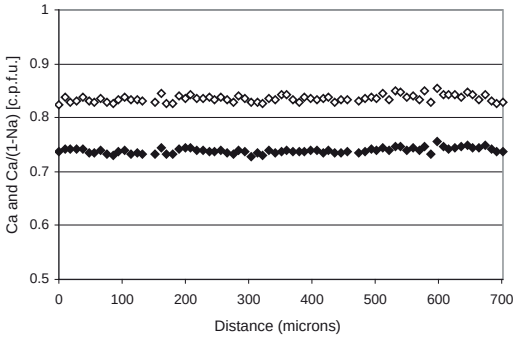
EMP-analysis: Session10 / cp1p1

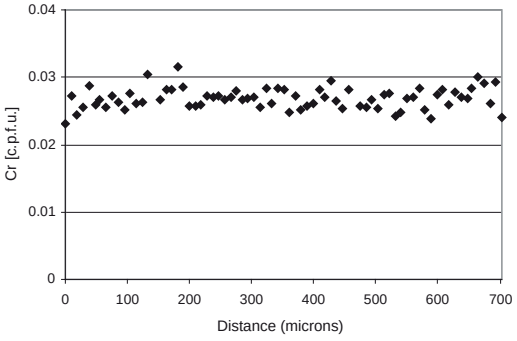


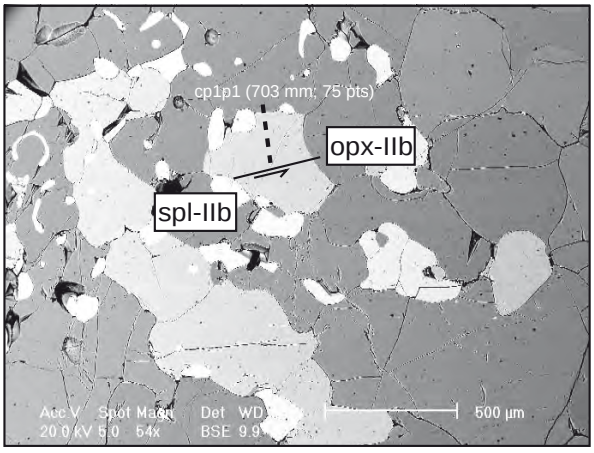










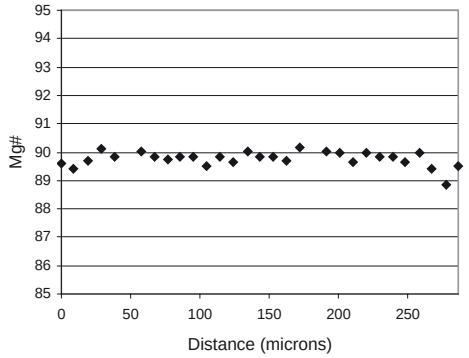


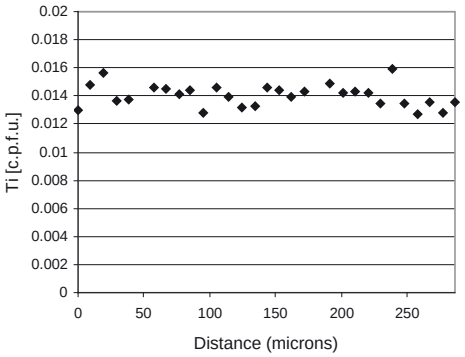
Group II: Clinopyroxene

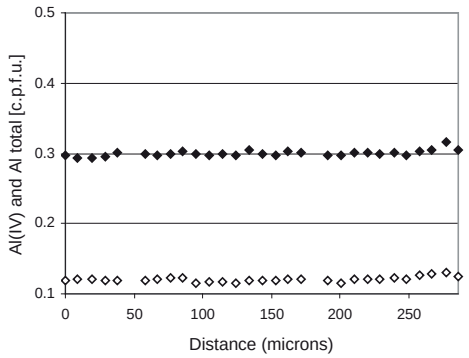
Sample: 1959/24 - Group II
(grt)-spl lherzolite

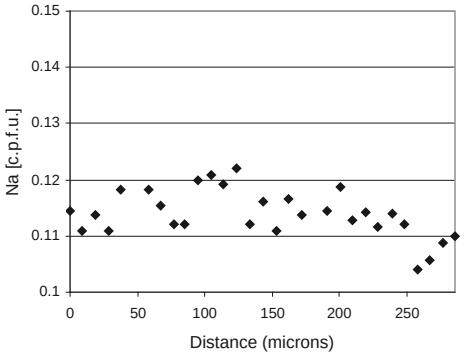
cpx-IIb: within a recrystallised spl-IIb - cpx-IIb - opx-IIb cluster, not strained, no exsolution

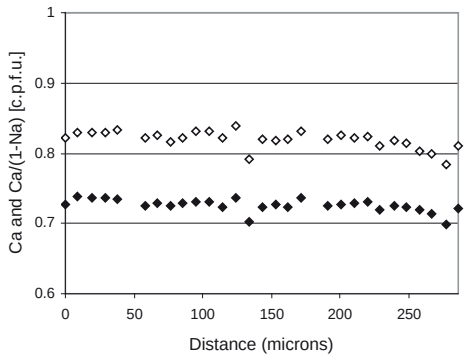
EMP-analysis: Session10 / cp10p1

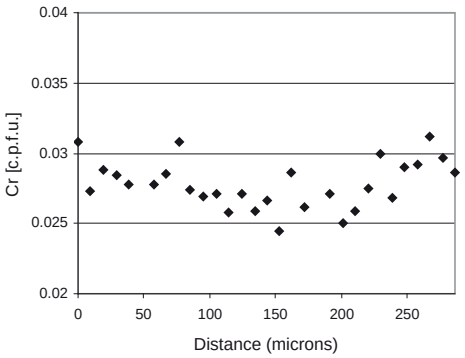


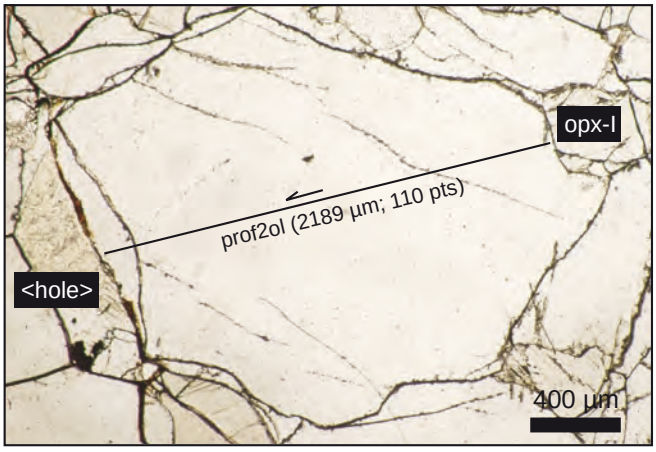










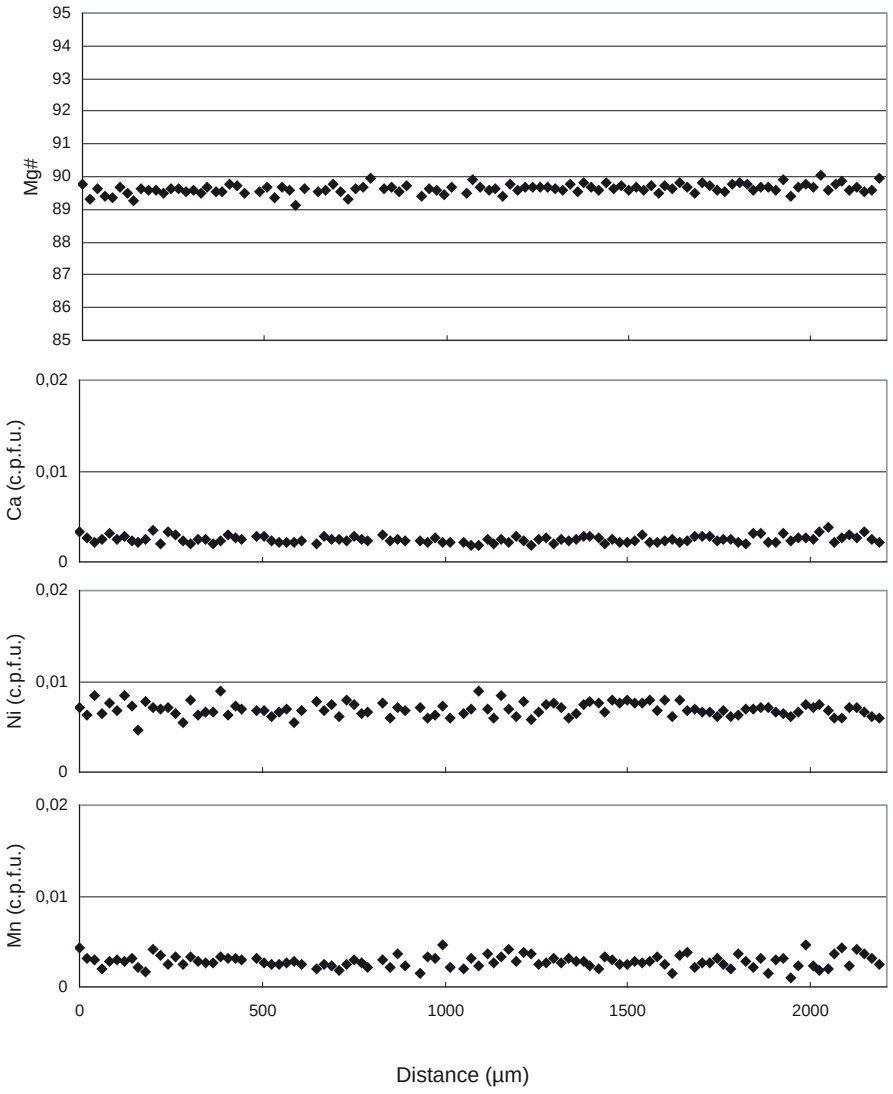


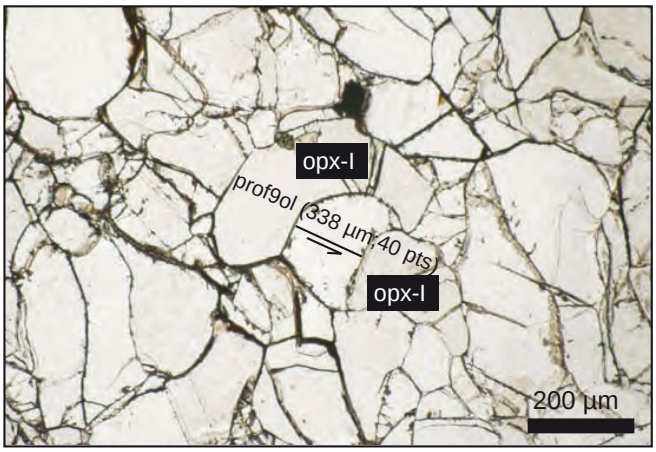
Group II: Olivine

Sample: 1958/20 - Group II
(grt)-spl lherzolite

ol-I; large, strainfree grain

EMP-analysis: Session1 / prof2ol



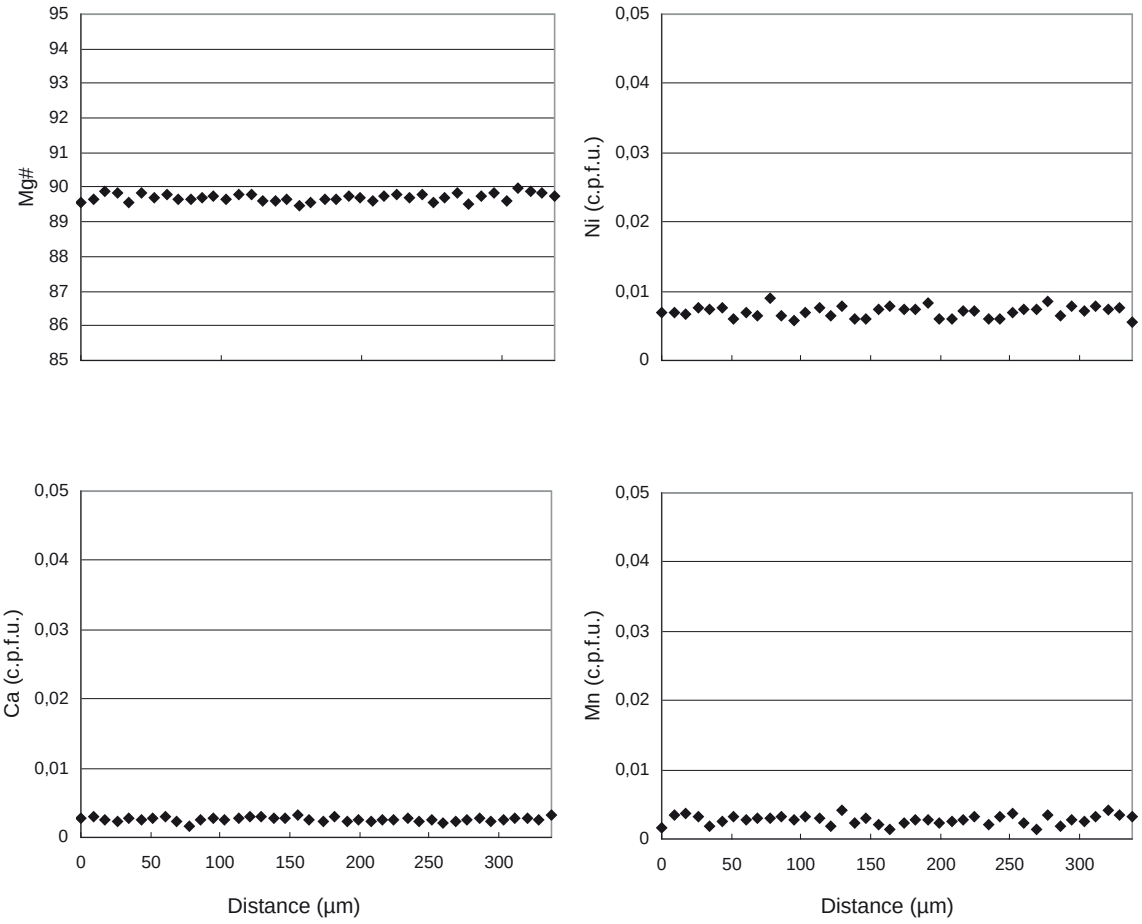


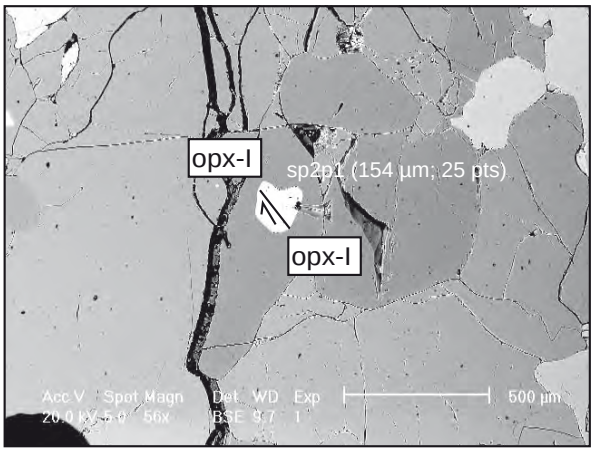
Group II: Olivine

Sample: 1958/20 - Group II
(grt)-spl lherzolite

ol-I; strainfree, statically recrystallised small grain

EMP-analysis: Session1 / prof8opx



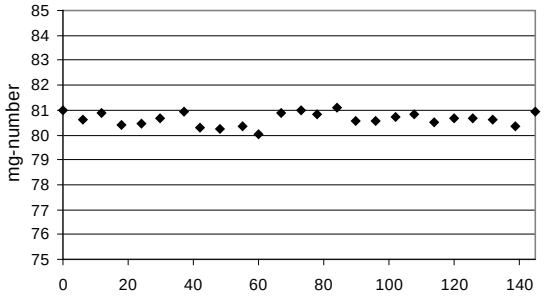


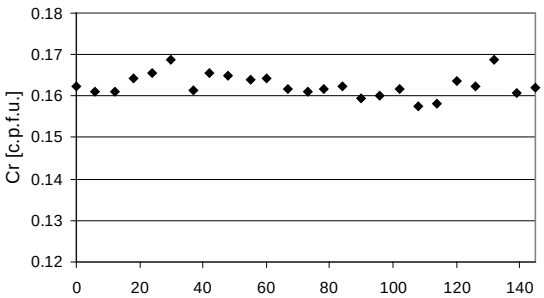
Group II: Spinel

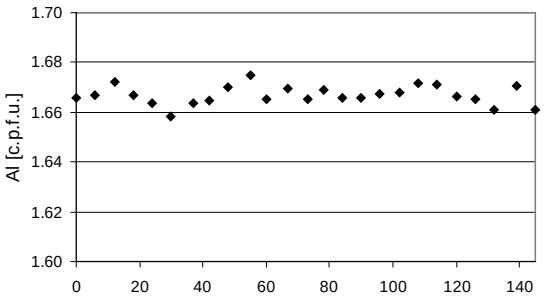
Sample: 1959/24 - Group II (grt)-spl lherzolite

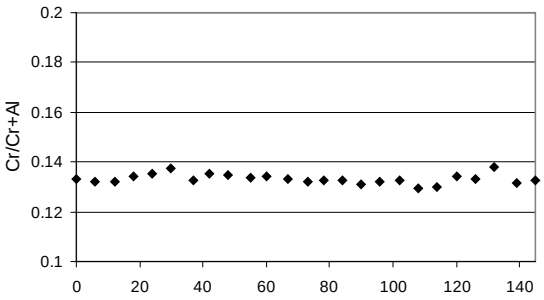
spl-I (inclusion in opx-I)

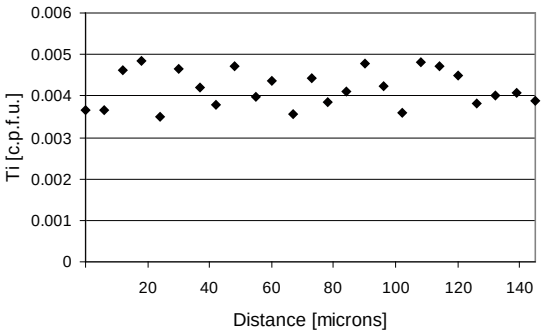
EMP-analysis: Session17 / sp2p1

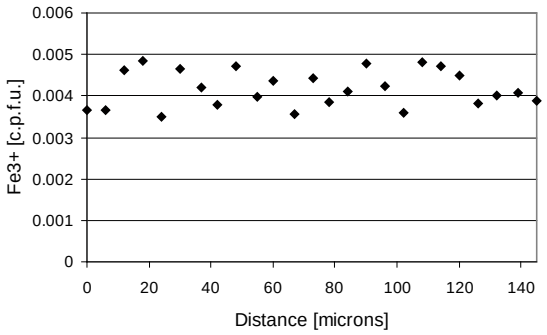


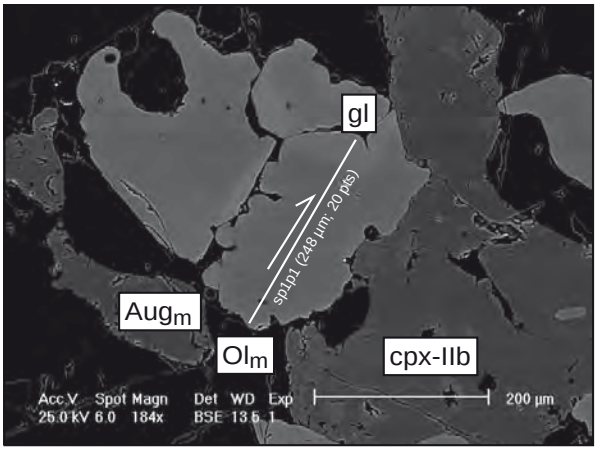










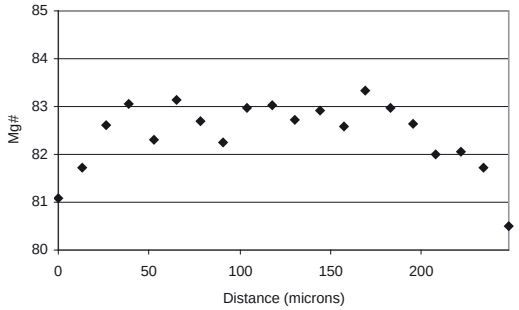


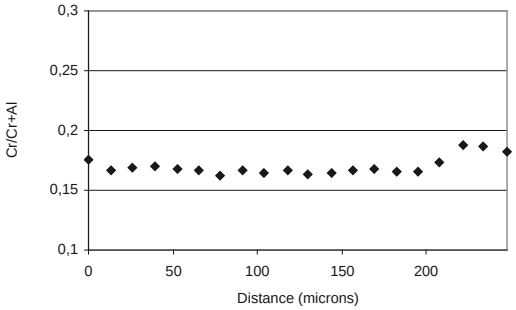
Group II: Spinel

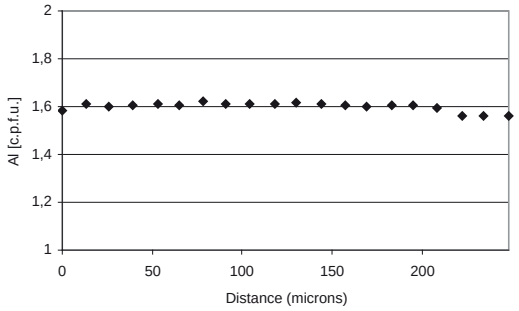
Sample: 1959/25 - Group II (grt)-spl lherzolite (less recrystallised)

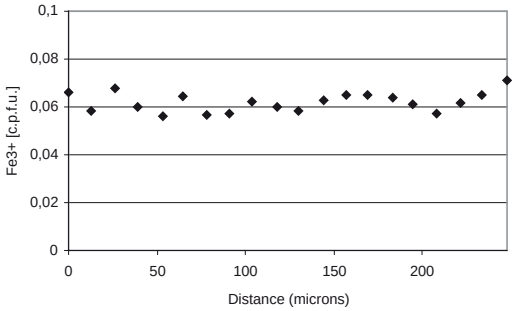
spl-IIb: residual (with sieve-textured rims) in a partially molten (glass-bearing) spl-IIb - opx-IIb - cpx-IIb cluster

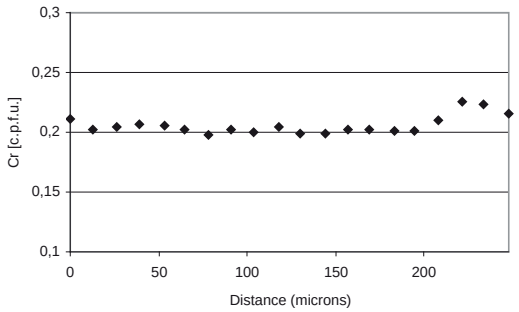
EMP-analysis: Session7 / sp1p1

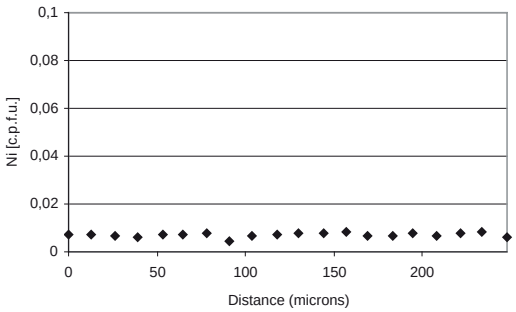


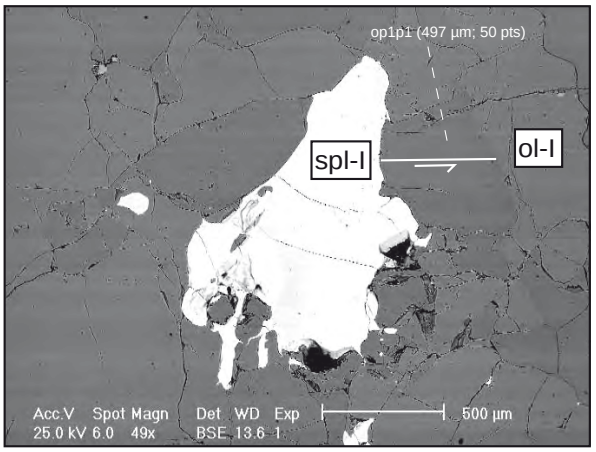










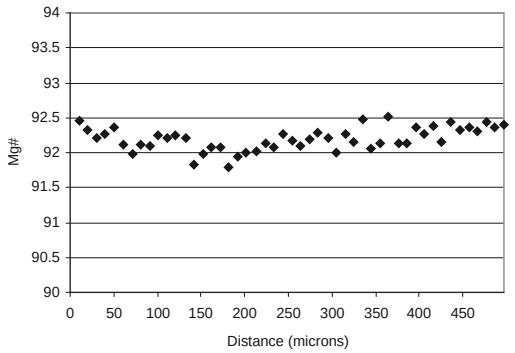


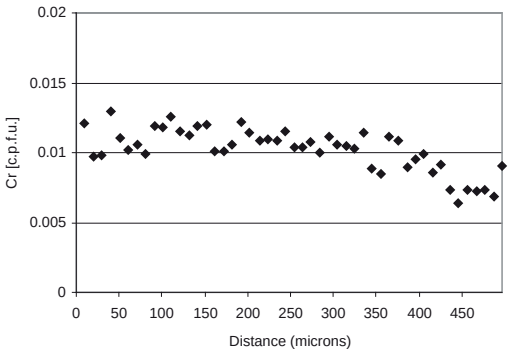
Group III-a: Orthopyroxene

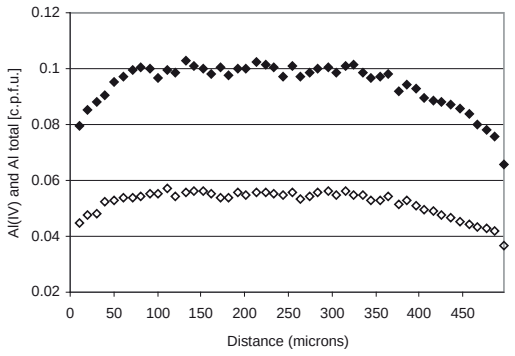
Sample: 1965/1 - Group III-a spl harzburgite

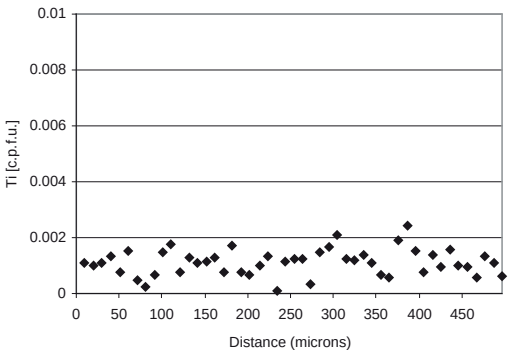
opx-I porphyroclast adjacent to spl-I

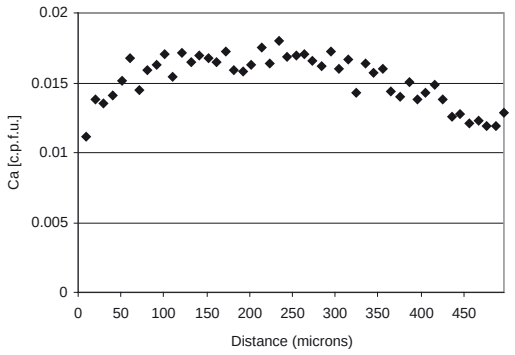
EMP-analysis: Session10 / op1p1

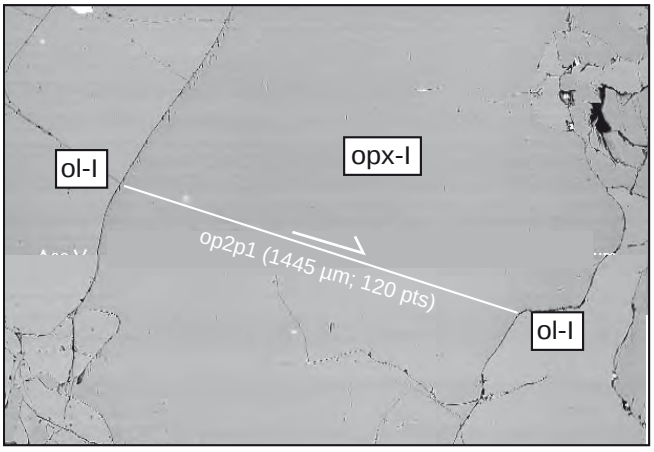










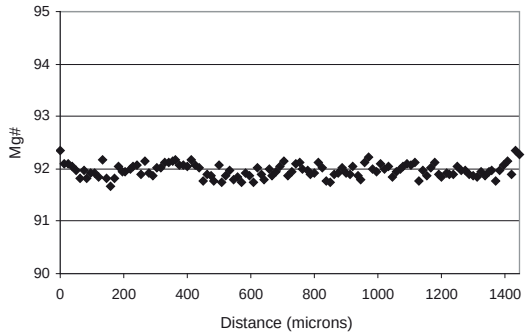


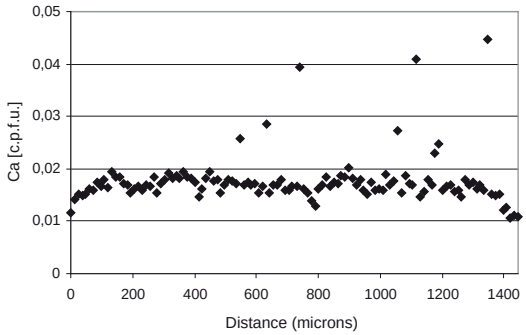
Group III-a: Orthopyroxene

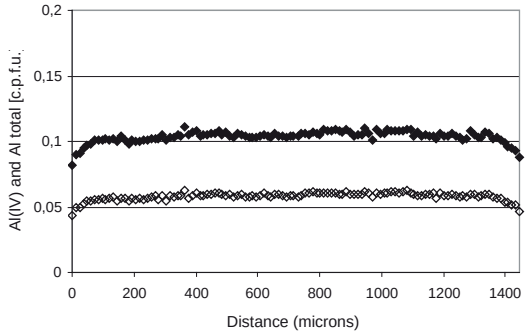
Sample: 1965/1 - Group III-a spl harzburgite

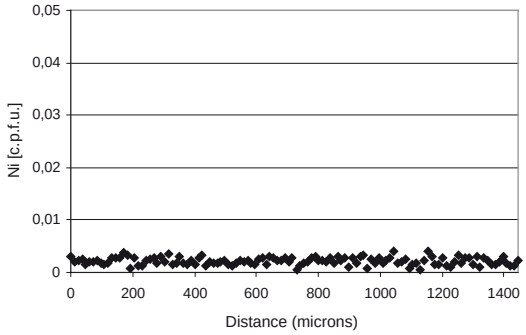
opx-I: large porphyroclast

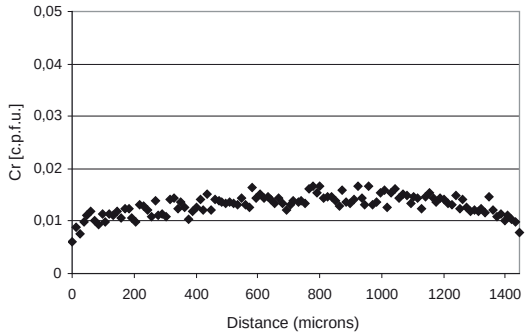
EMP-analysis: Session9 / op2p1

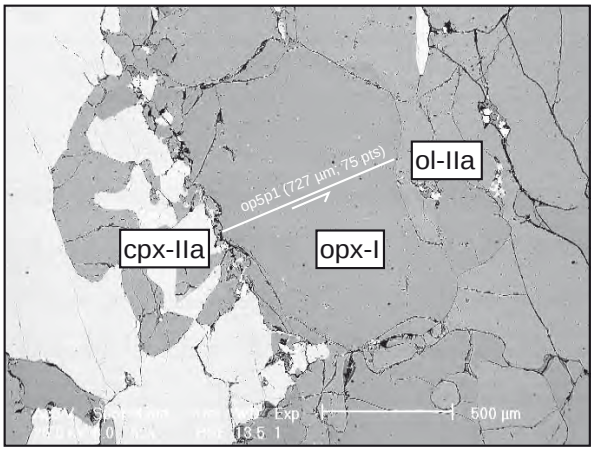










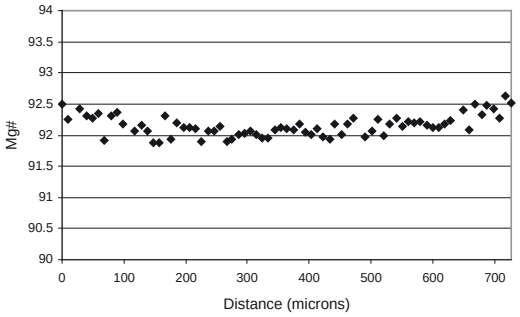


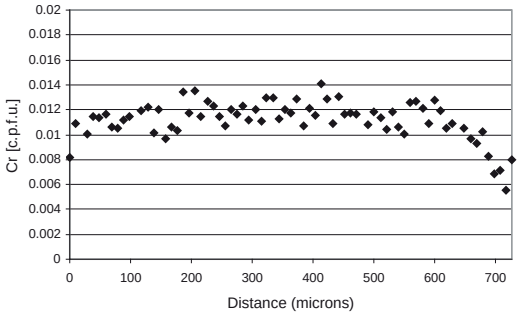
Group III-a: Orthopyroxene

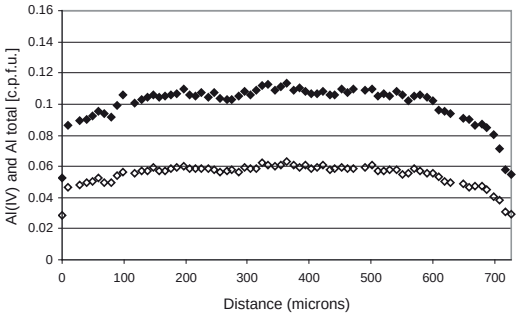
Sample: 1965/1 - Group III-a spl harzburgite

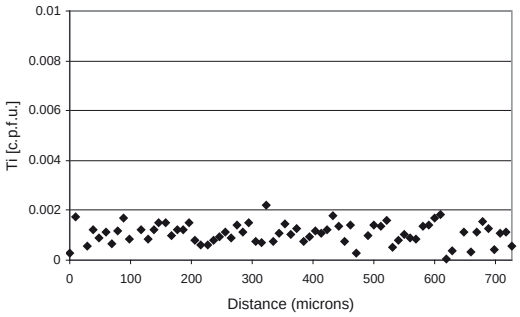
large opx-I porphyroclast

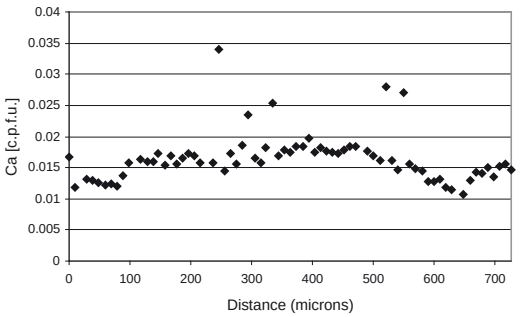
EMP-analysis: Session10 / op5p1

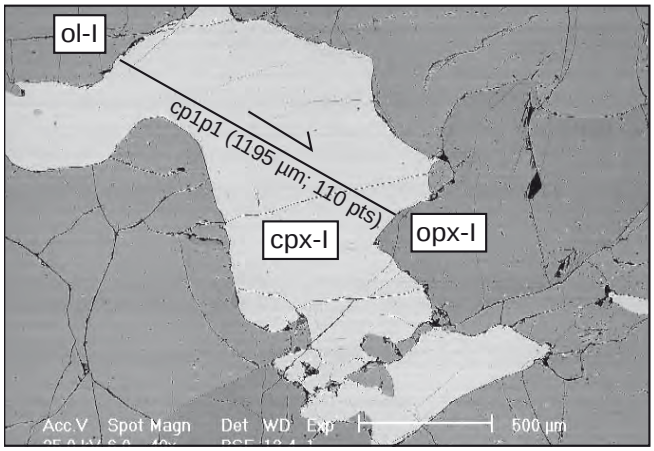










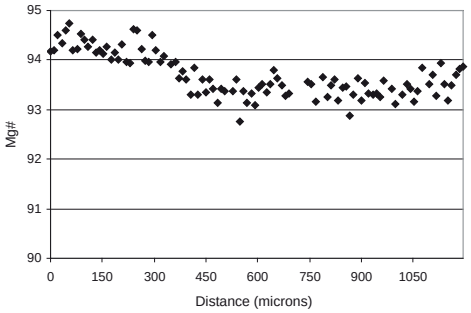


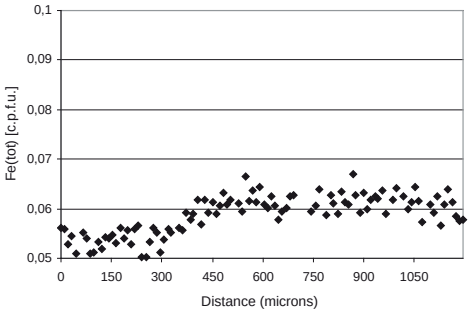
Group III-a: Clinopyroxene

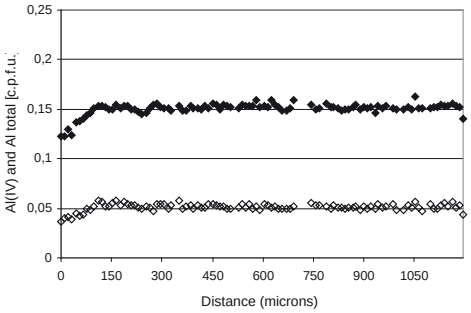
Sample: 1965/01 - Group III-a spl harzburgite

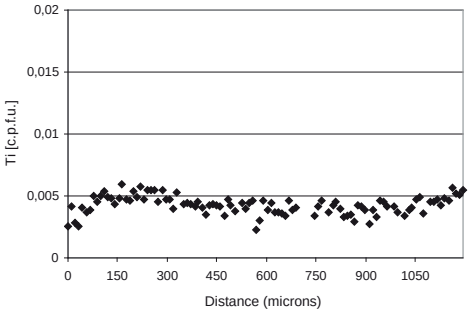
cpx-I porphyroclast (exsolution-free)

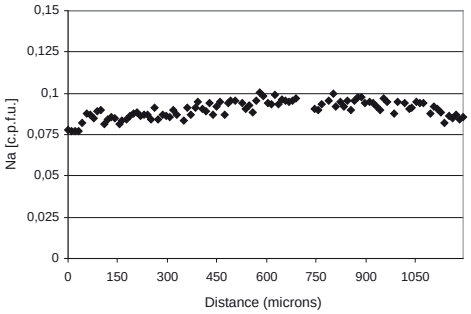
EMP-analysis: Session9 / cp1p1

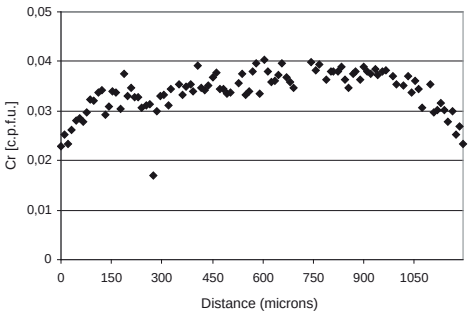


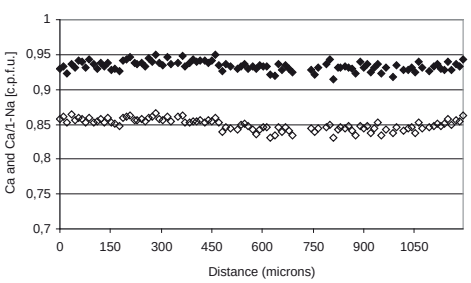


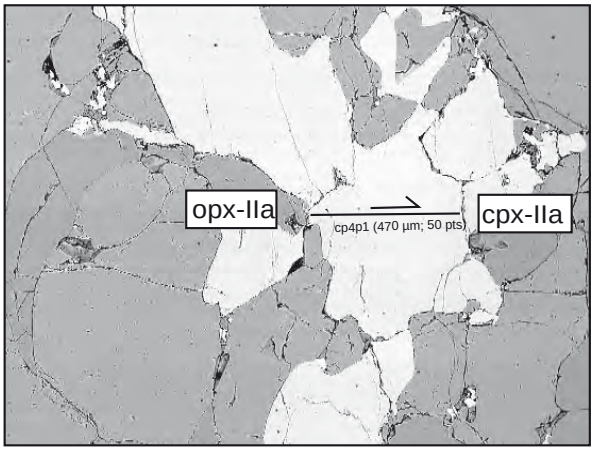










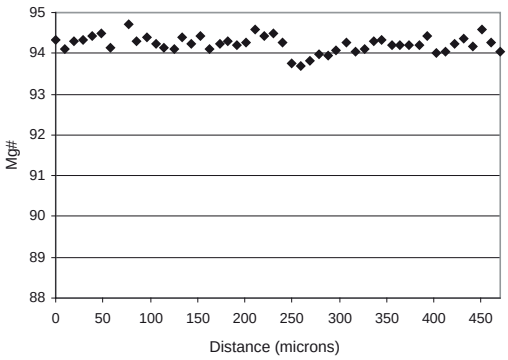


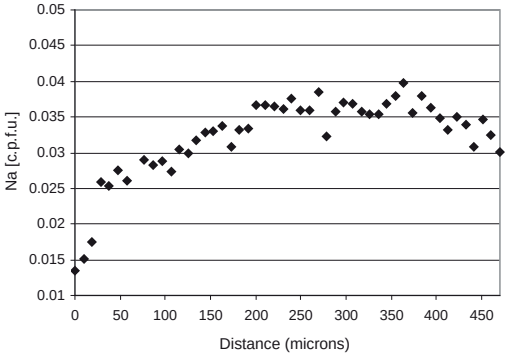
Group III-a: Clinopyroxene

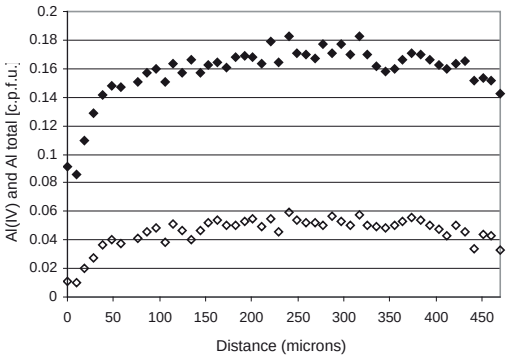
Sample: 1965/1 - Group III-a spl harzburgite

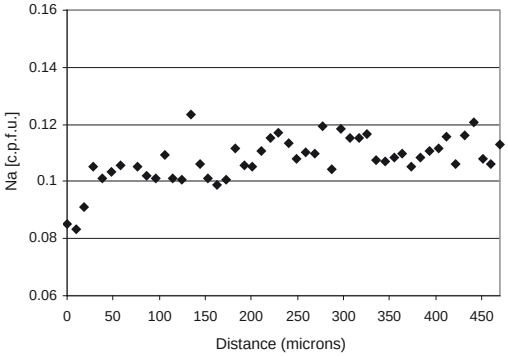
cpx-I porphyroclast

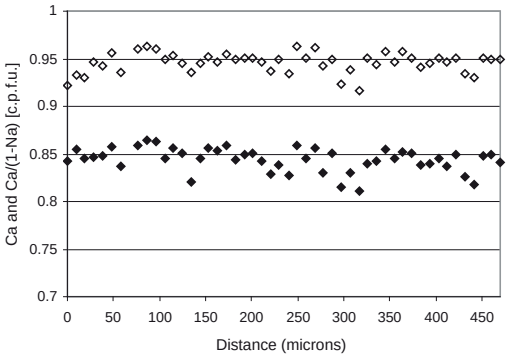
EMP-analysis: Session10 / cp4p1

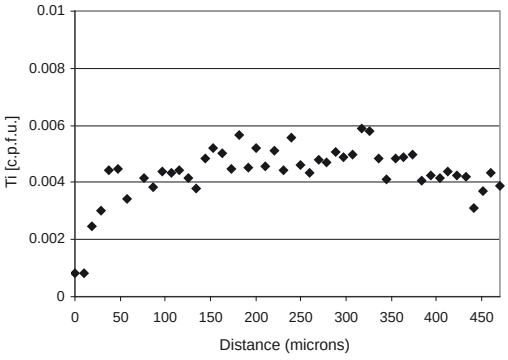


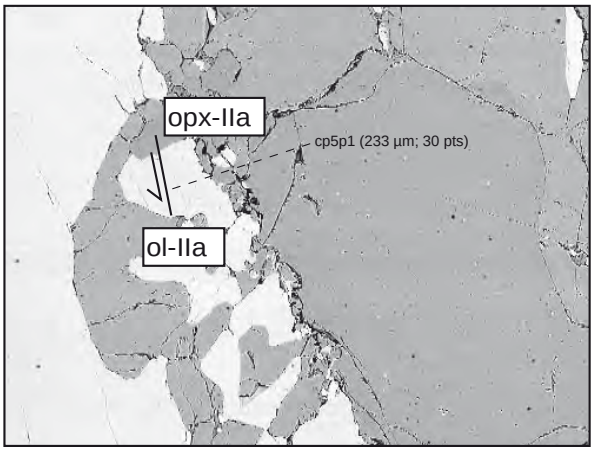










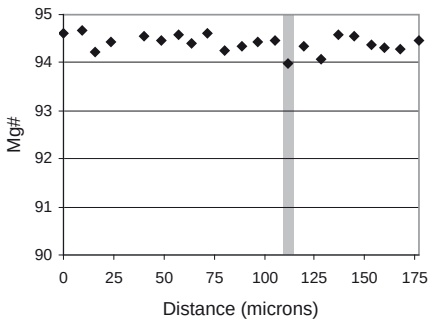


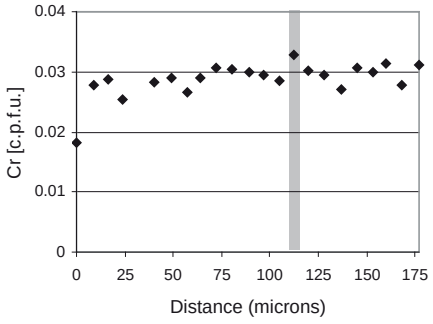
Group III-a: Clinopyroxene

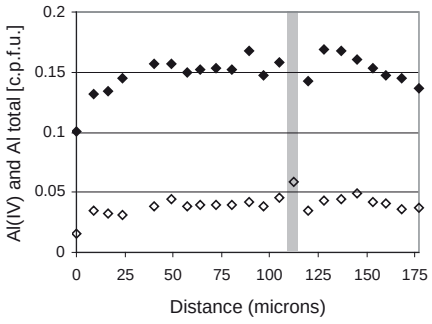
Sample: 1965/1 - Group III-a spl harzburgite

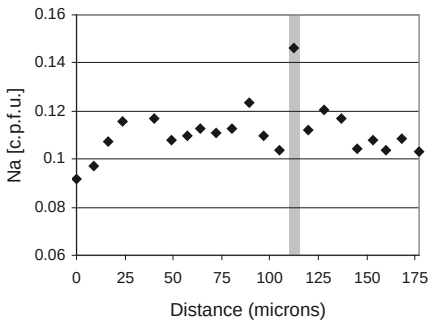
cpx-IIa neoblast with katophorite lamellae

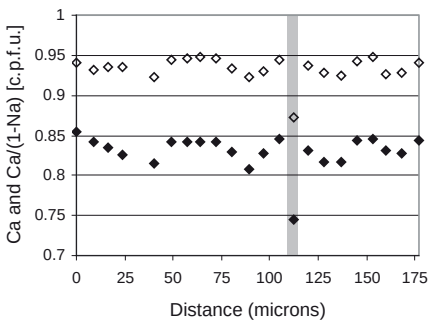
EMP-analysis: Session10 / cp5p1

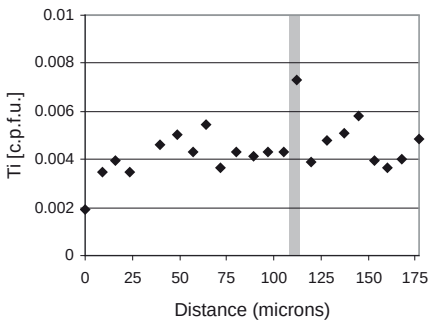




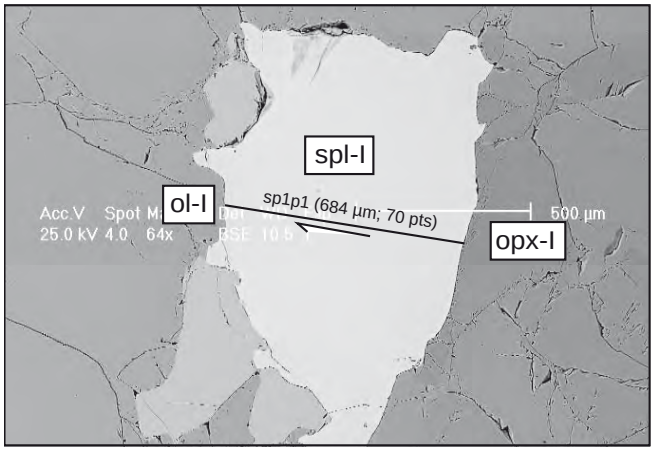








amphibole lamellae

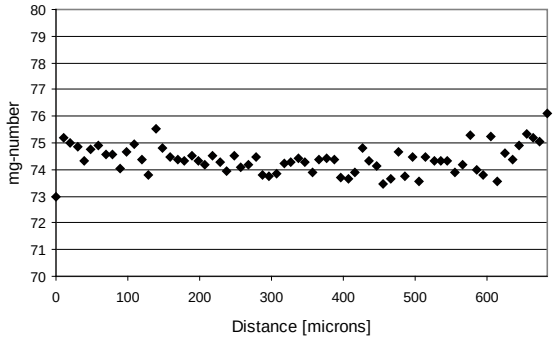


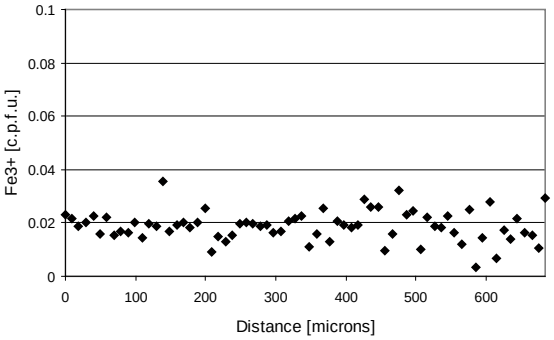
Group III-a: Spinel

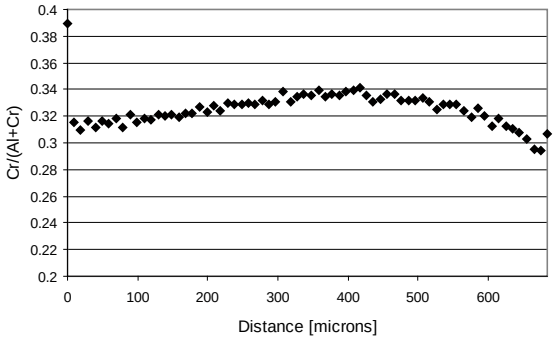
Sample: 1965/01 - Group III-a spl harzburgite

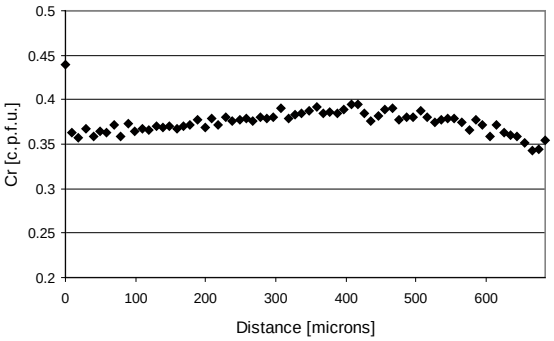
spl-I porphyroclast

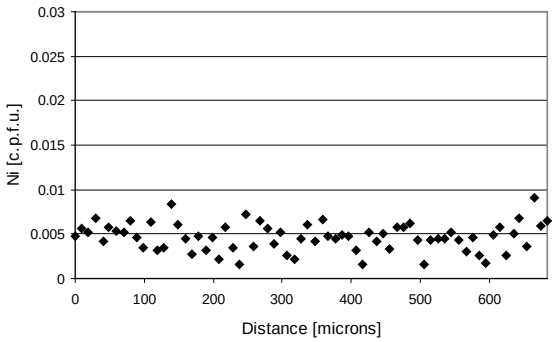
EMP-analysis: Session18 / sp1p1

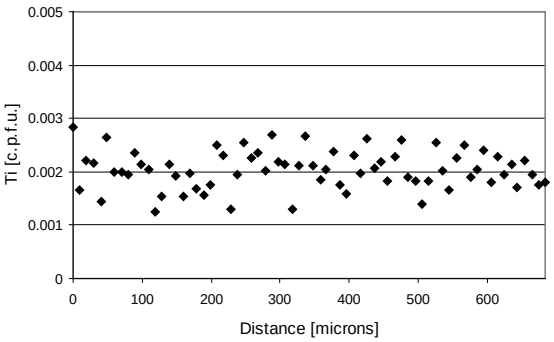


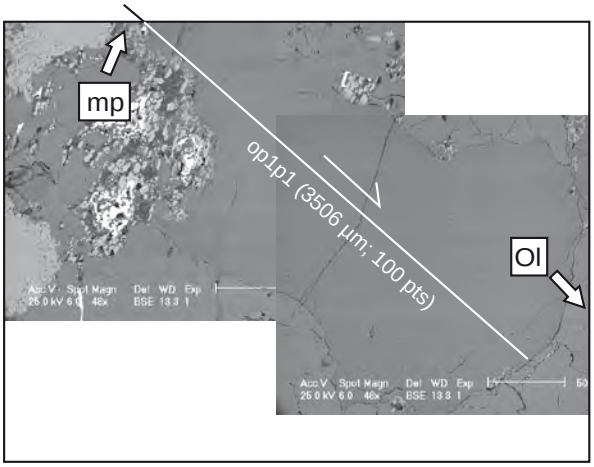










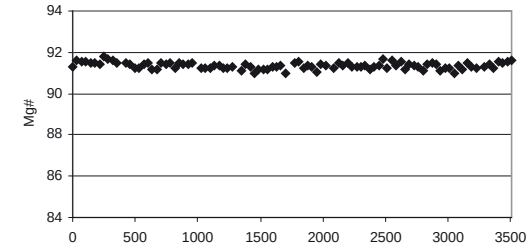


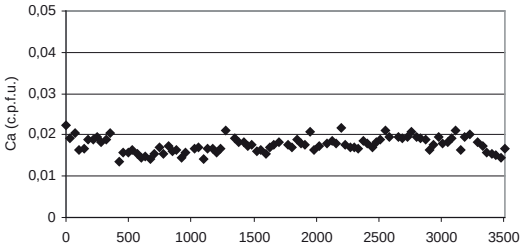
Group III-b: Orthopyroxene

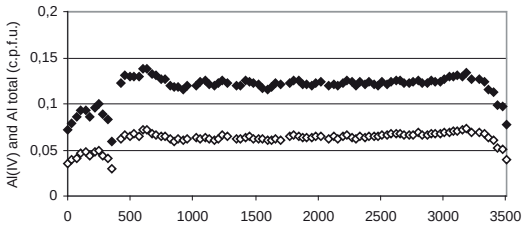
Sample: 1959/15: - Group III-b spl harzburgite (formerly garnet-bearing)

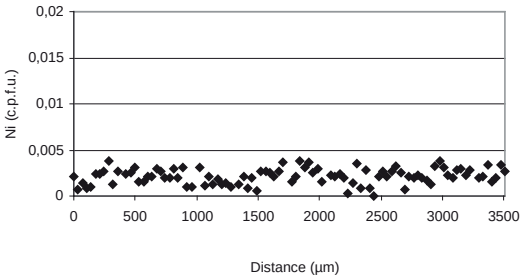
large, strongly deformed opx-I porphyroclast

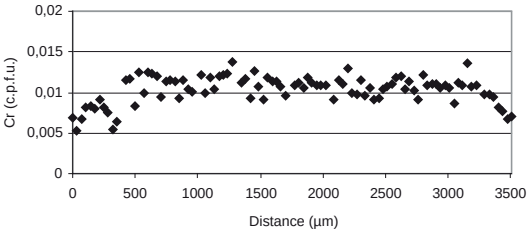
EMP-analysis: Session7 / op1p1

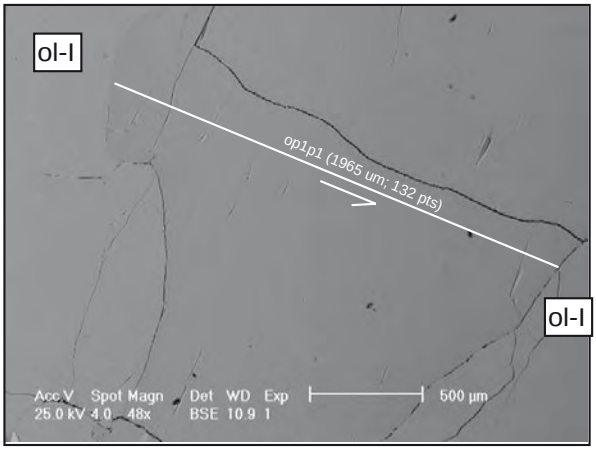










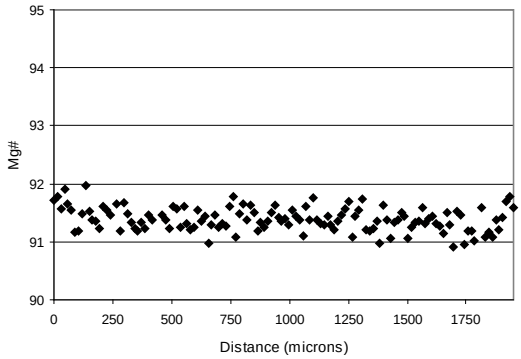


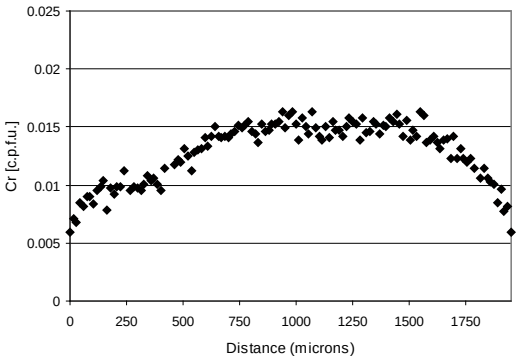
Group III-b: Orthopyroxene

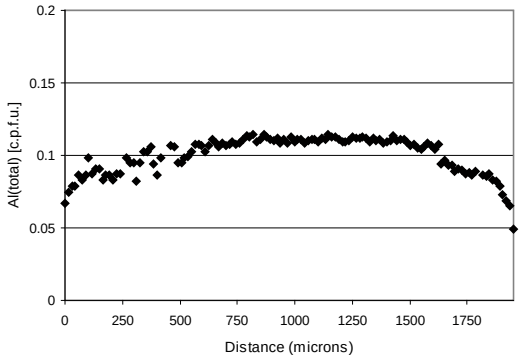
Sample: 1965/15 - Group III-b spl harzburgite

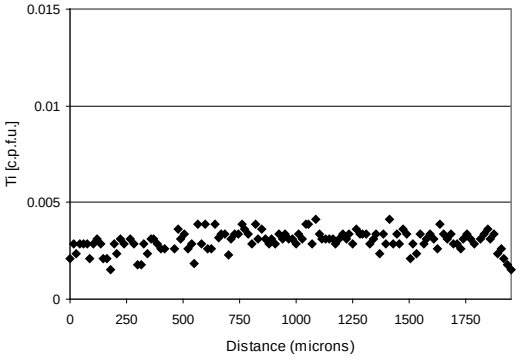
opx-I porphyroclast

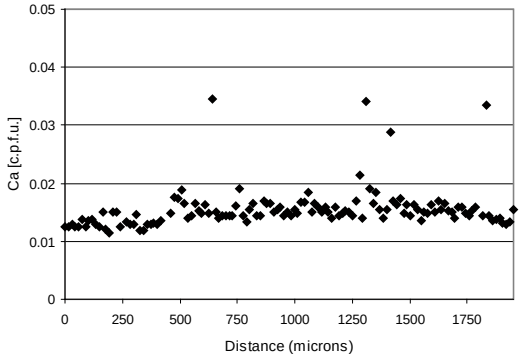
EMP-analysis: SessionHe1 / op1p1

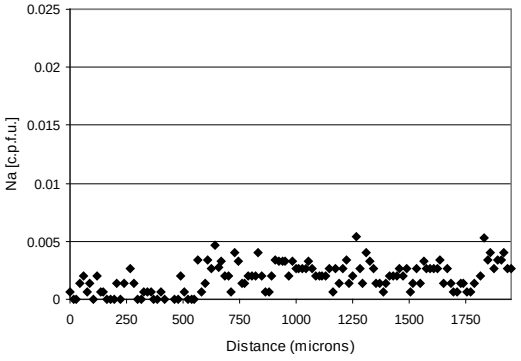


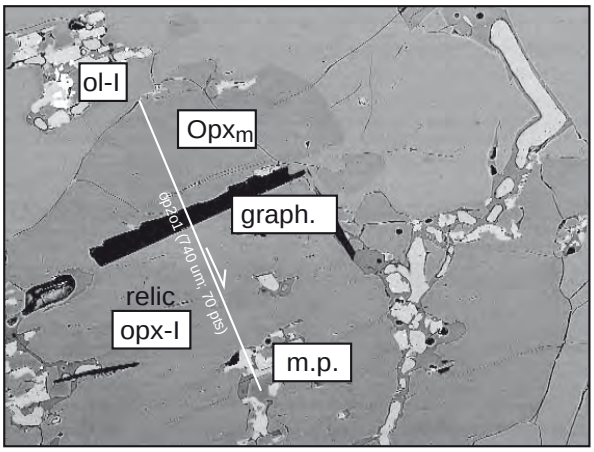










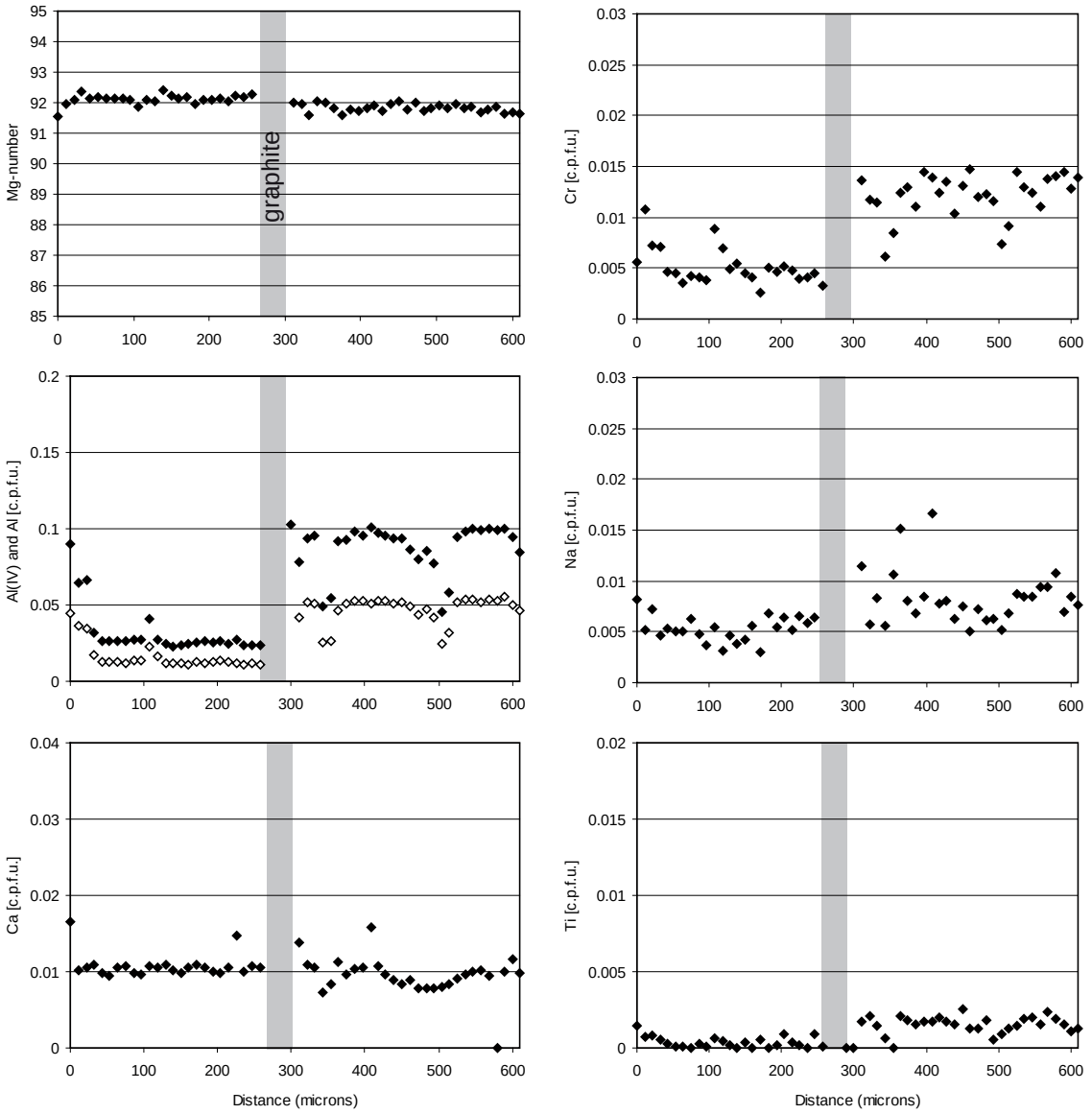


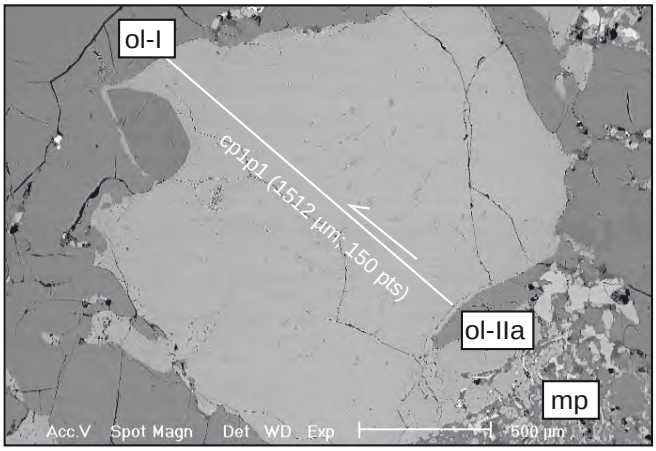
Group III-b: Orthopyroxene

Sample: 1965/15 - Group III-b spl harzburgite

relic opx-I overgrown by low-Al Opx$_m$ and enclosing graphite

EMP-analysis: Session16 / op2p1



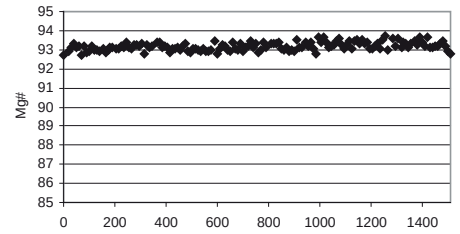


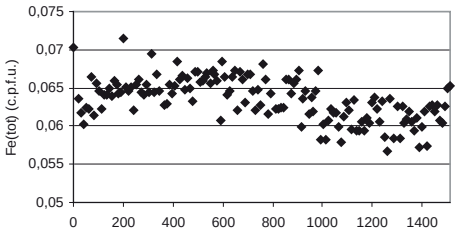
Group III-b: Clinopyroxene

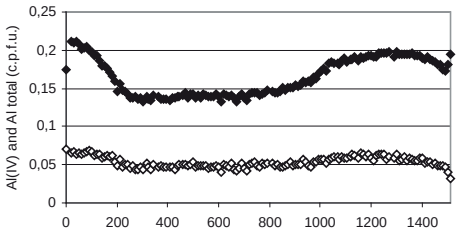
Sample: 1959/15 - Group III-b
spl harzburgite (formerly garnet-bearing)

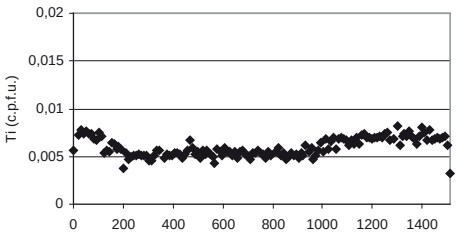
large cpx-I porphyroclast (with opx exsolution lamellae)

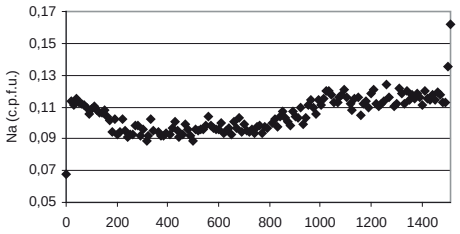
EMS-analysis: Session7 / cp1p1

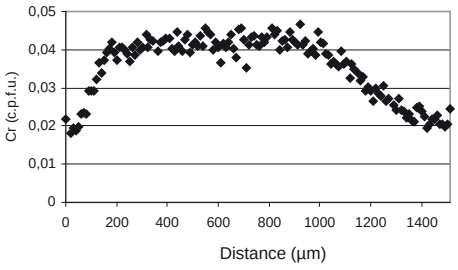


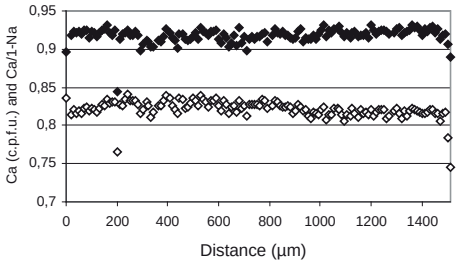


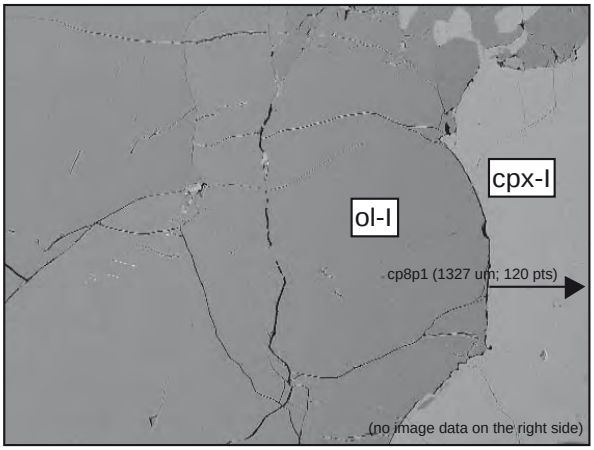












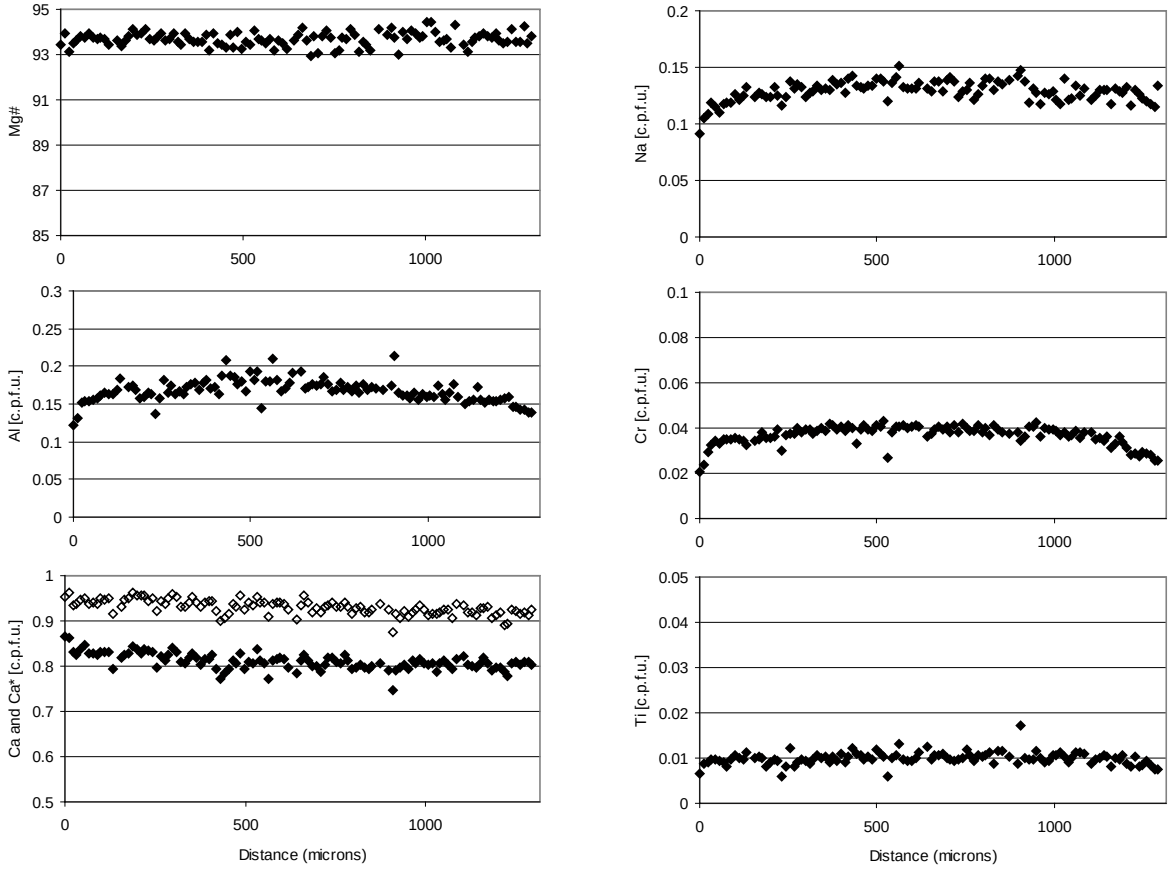
Group III-b: Clinopyroxene

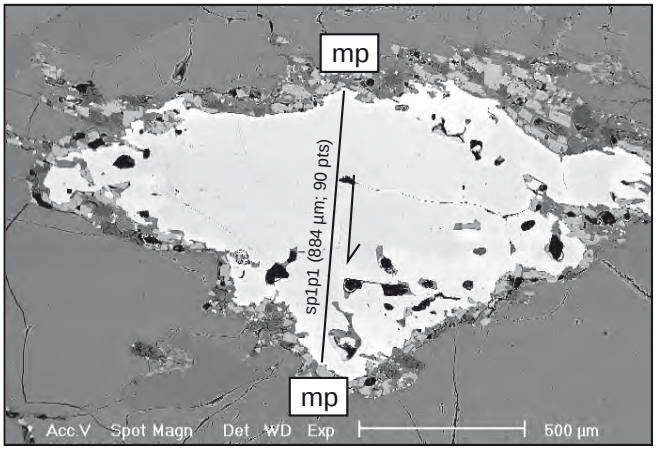
Sample: 1965/15 - Group III-b spl harzburgite

cpx-I porphyroclast (devoid of amphibole lamellae in this case*)

(*many other cpx-I in this sample are replaced by Mg-katophorite (lamellar or blebs)

EMP-analysis: SessionHe1 / cp8p1



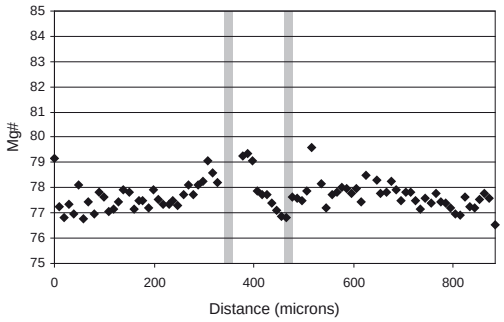


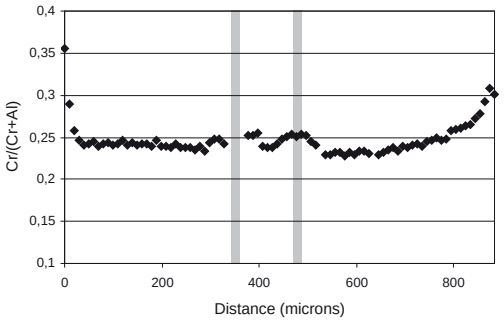
Group III-b: Spinel

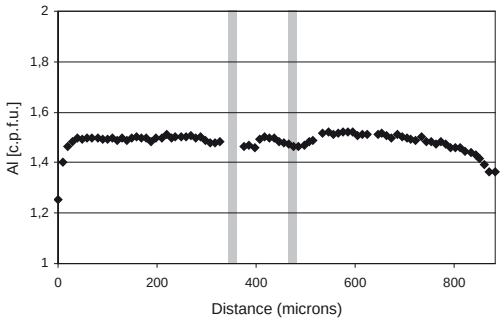
Sample: 1959/15 - Group III-b
spl harzburgite

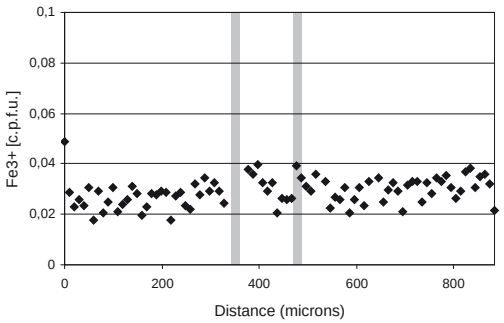
relic spl-I, partly resorbed and lined by melt pockets (mp)

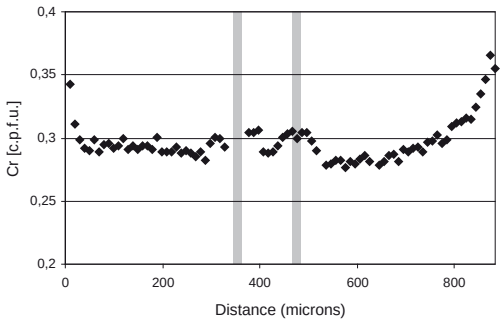
EMP-analysis: Session7 / sp1p1

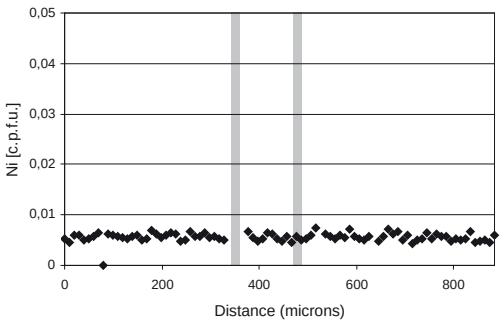




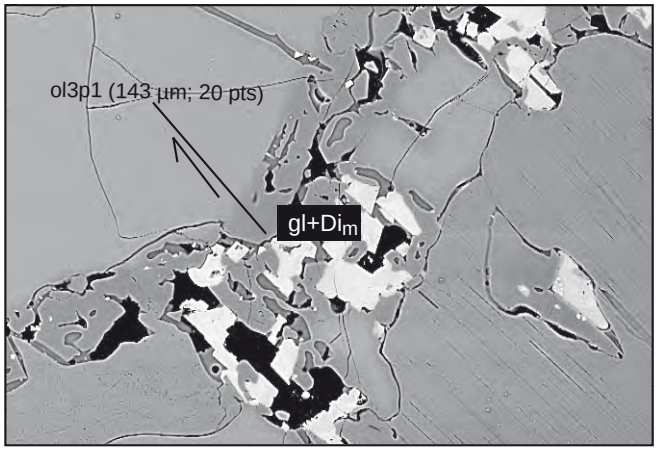








= melt chanel

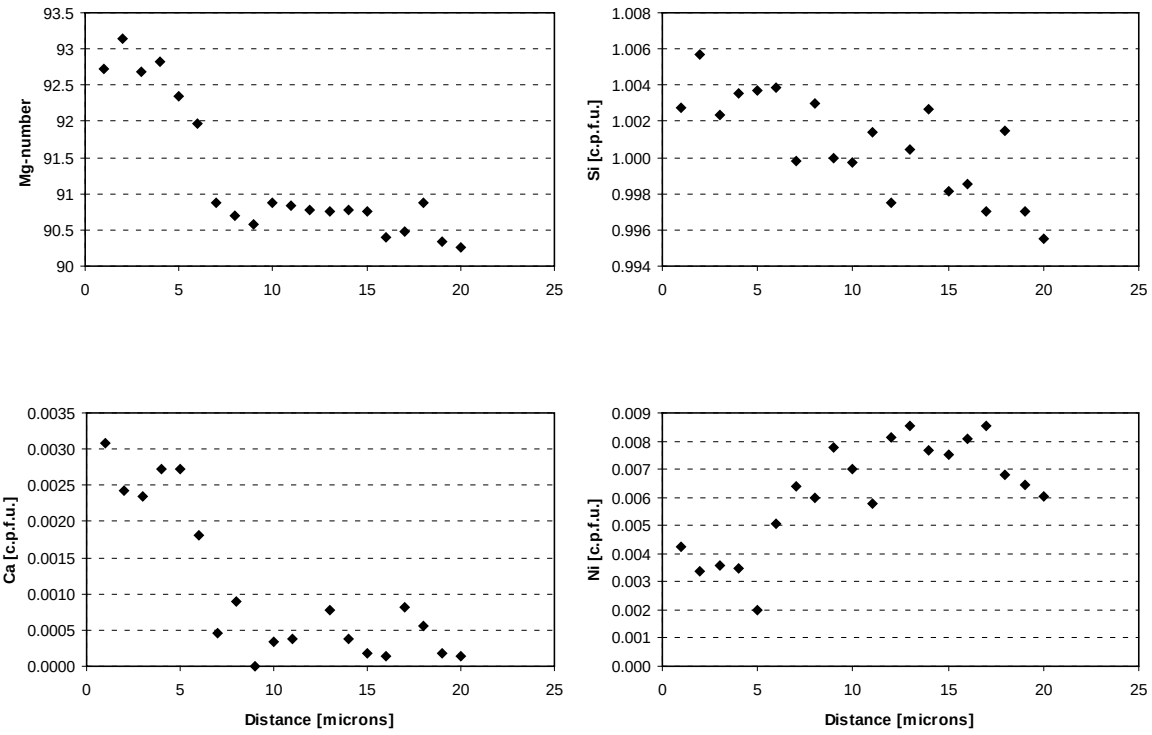


Group III-c: Olivine

Sample: 785* - Group III-c
spl harzburgite

olivine porphyroclast in contact with melt pocket

EMP-analysis: Session15 / ol3p1

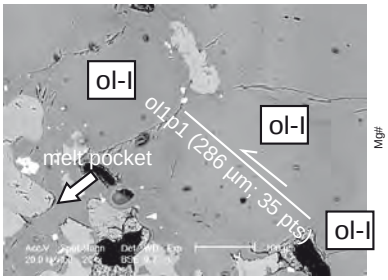


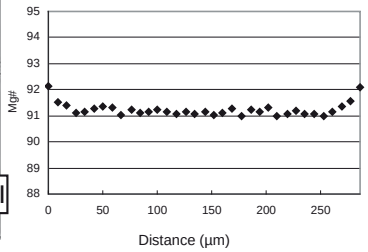
Group III-c: Olivine

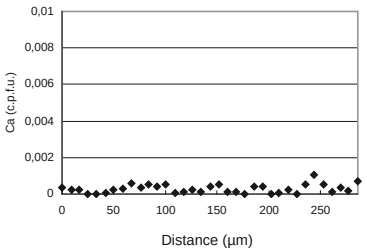
Sample: 1965/3 - Group III-c spl dunite

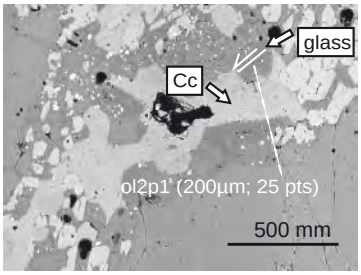
a) ol-I porphyroclast lined by glass films
b) and c) Ol_m microlites within melt pockets

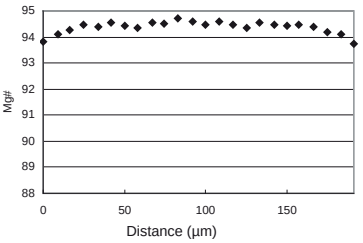
EMP-analysis: Session4 / ol1p1 [(a)], ol2p1 [(b)], ol4p1[(c)]

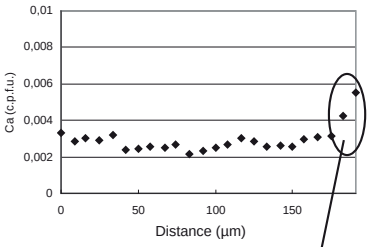


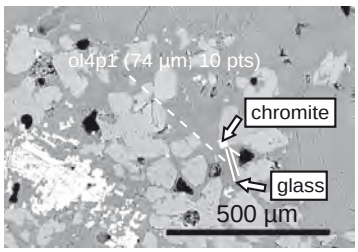


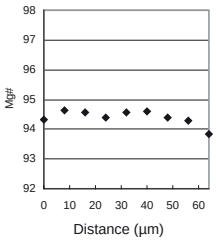


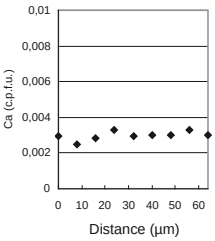




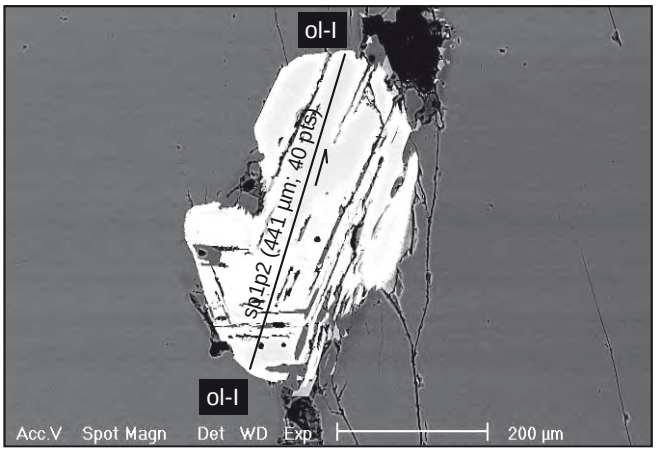








probably secondary fluorescence
(Ca from calcite)

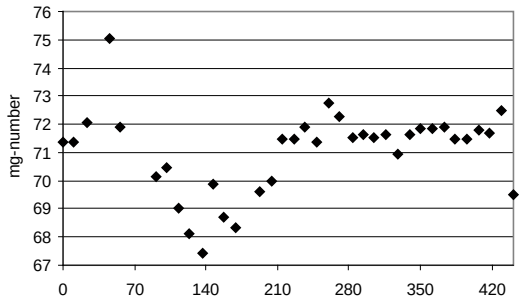


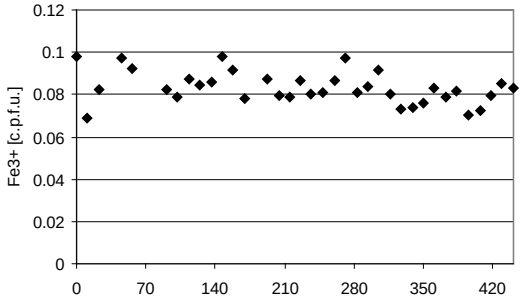
Group III-c: spinel

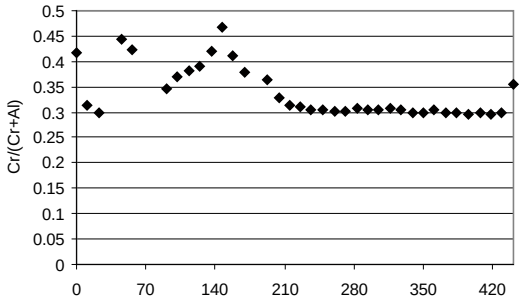
Sample: 785* - Group III-c
spl harzburgite

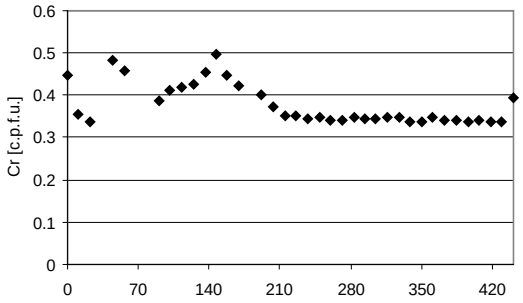
relic (partly resorbed) spl-I (inclusion in ol-I)

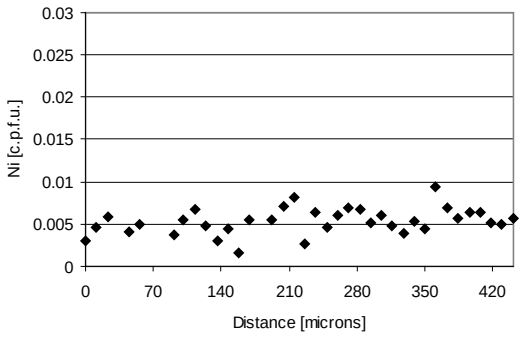
EMP-analysis: Session18 / sp1p2

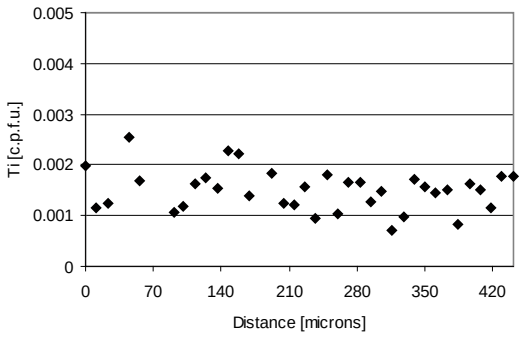


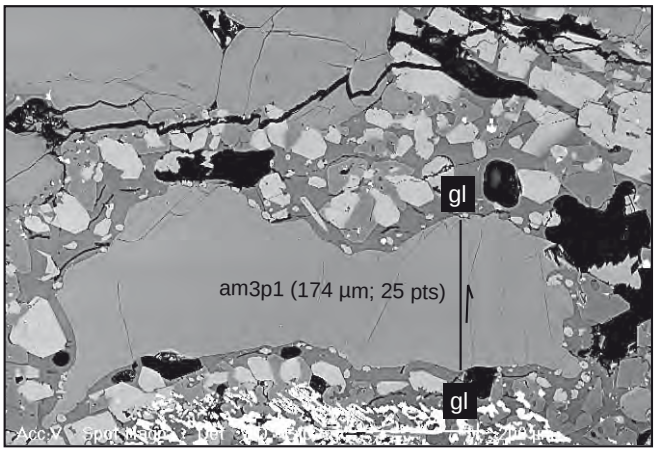










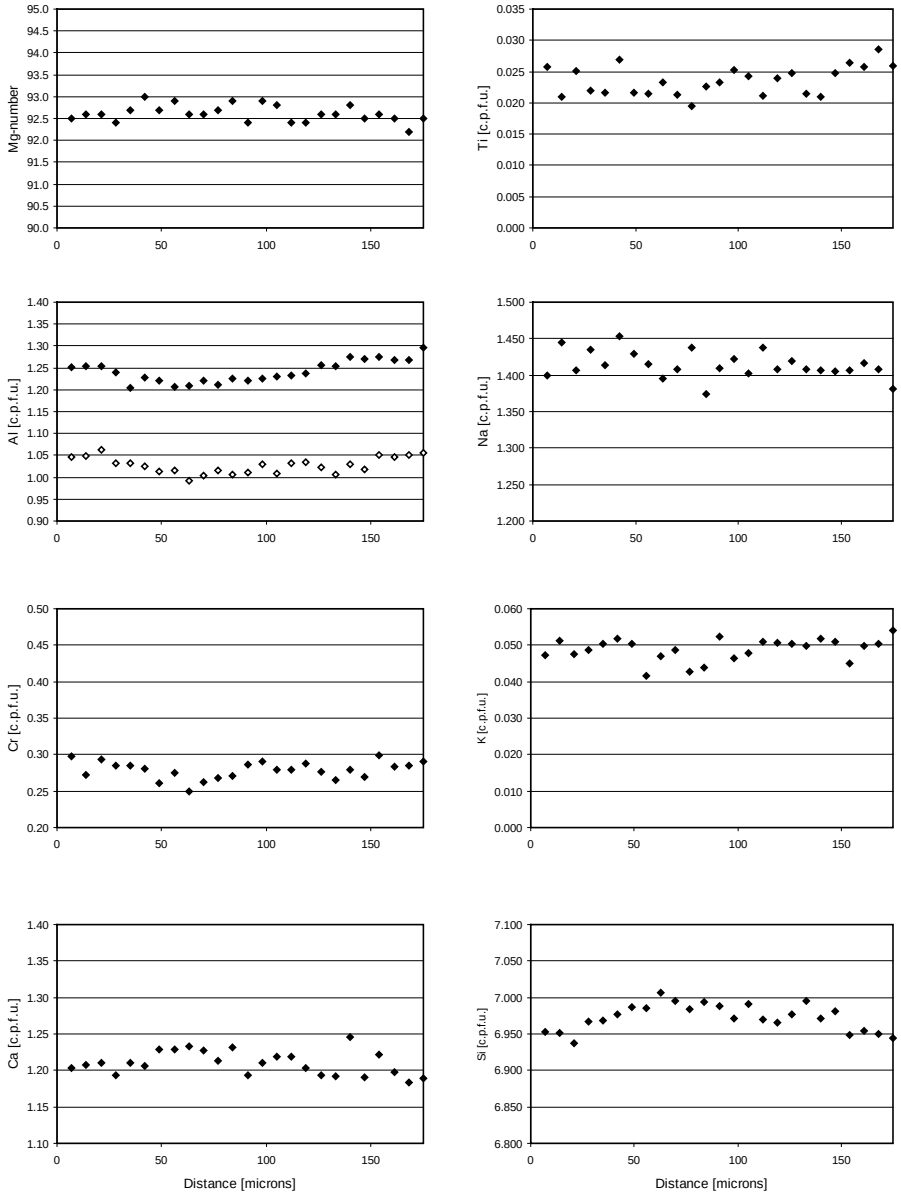


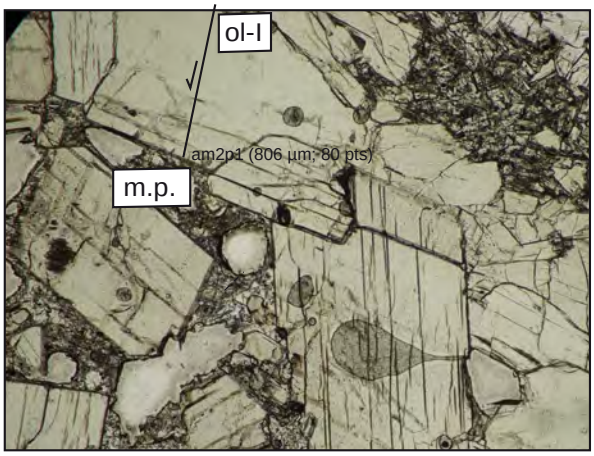
Group III-c: Katophorite

Sample: 785* - Group III-c
spl harzburgite

residual Mg-katophorite in melt pocket

EMP-analysis: Session1 / prof1opx



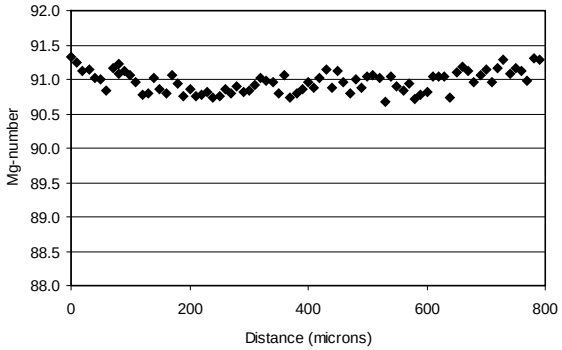


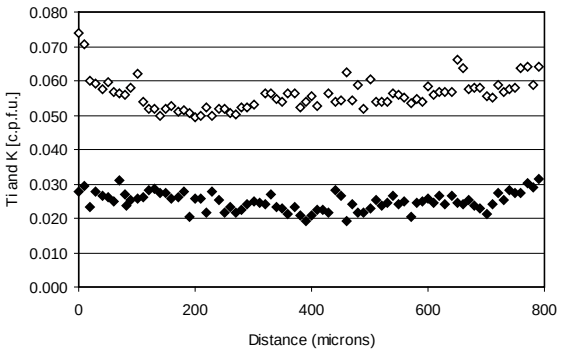
Group III-c: Mg-katophorite

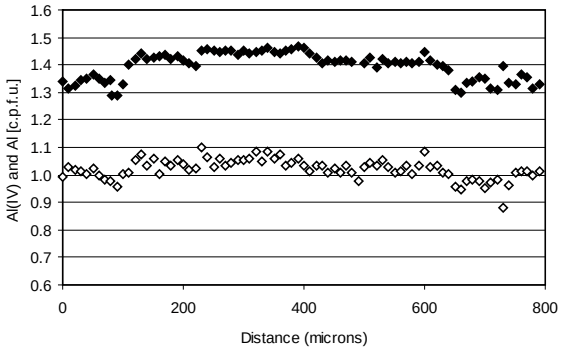
Sample: 1965/25 - Group III-c amph dunite

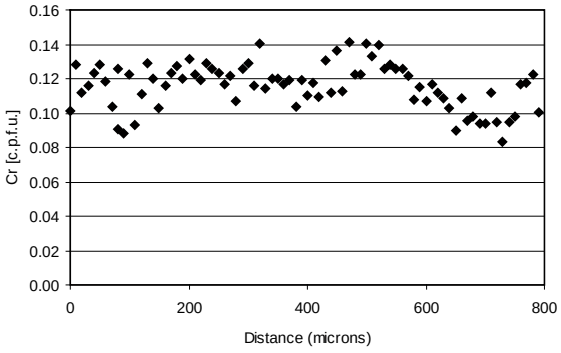
euhedral Mg-katophorite

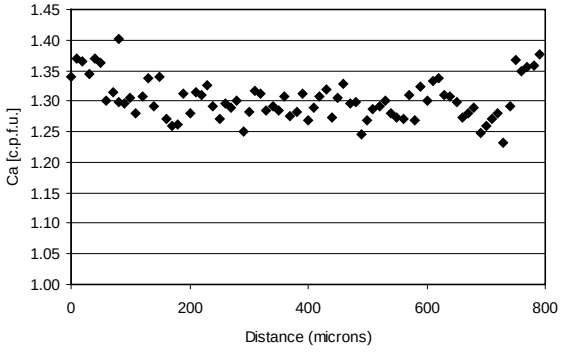
EMP-analysis: SessionJEOL2 / am2p1

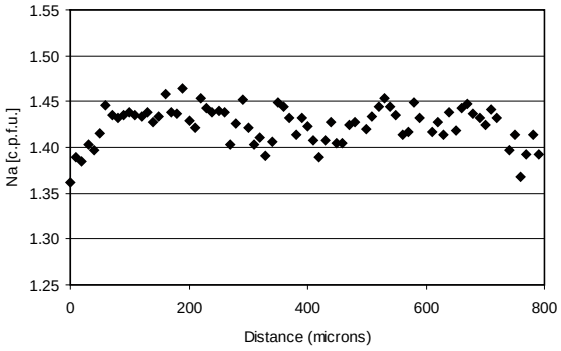


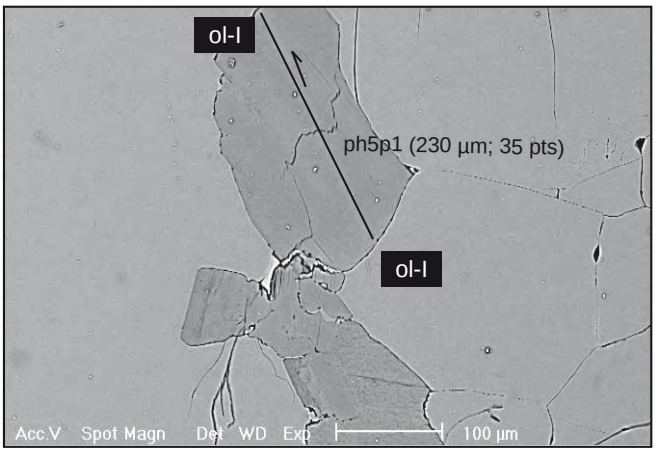










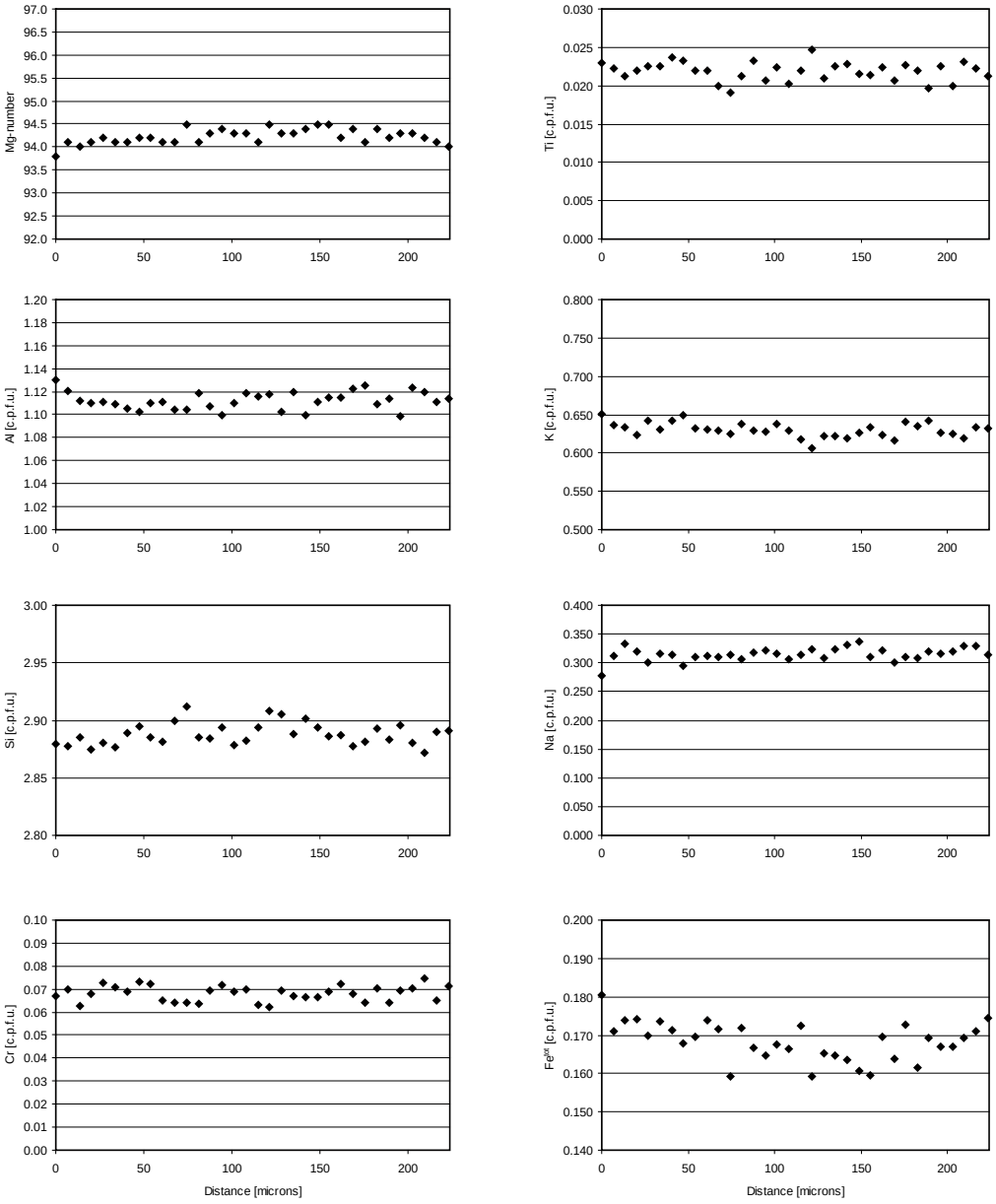


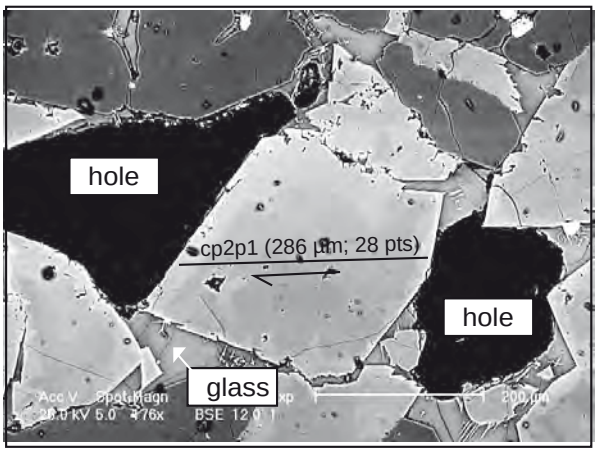
Group III-c: Phlogopite

Sample: 785* - Group III-c
spl harzburgite

Na-rich phlogopite interstitial between olivine porphyroclasts

EMP-analysis: Session12 / ph5p1



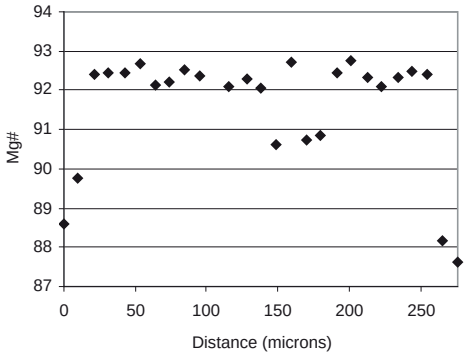


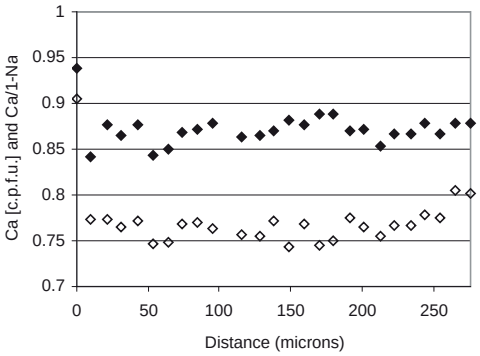
Group III-c: Clinopyroxene

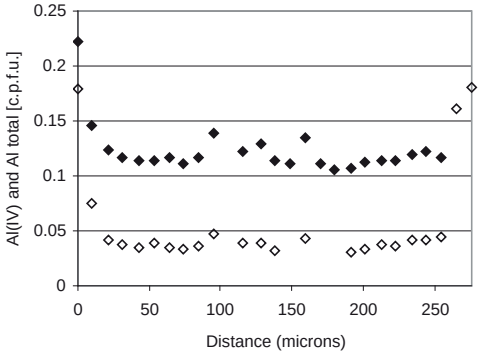
Sample: 1959/27 - kaersutite-bearing dunite

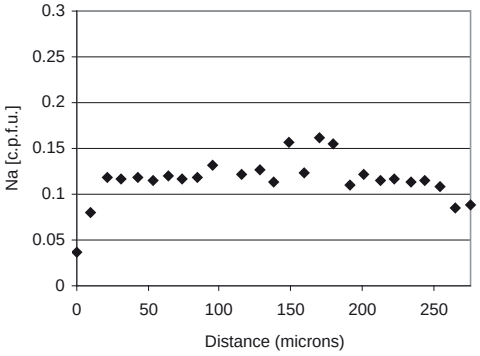
Di_m with Aug_m rims in a melt pocket (glass composition with affinity to host basanite)

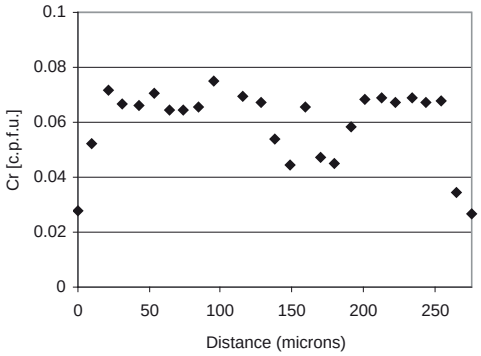
EMP-analysis: Session8 / cp2p1

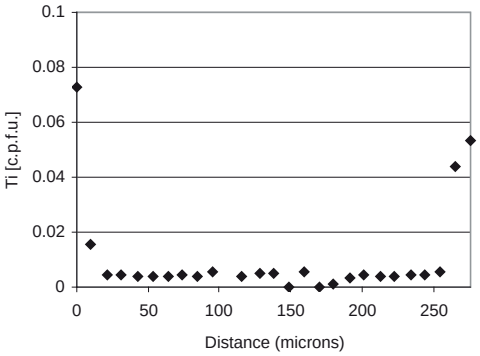


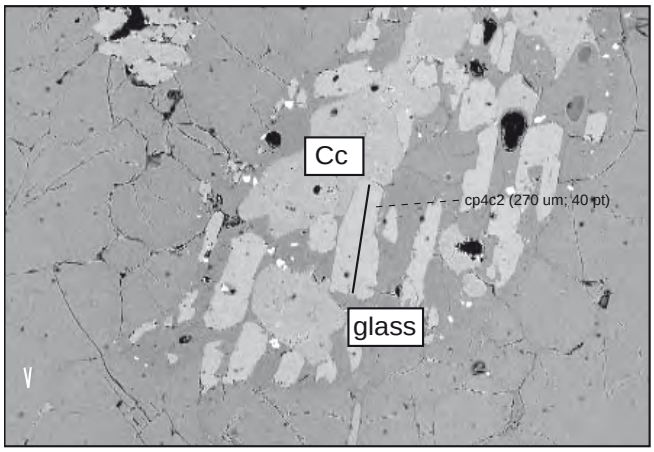










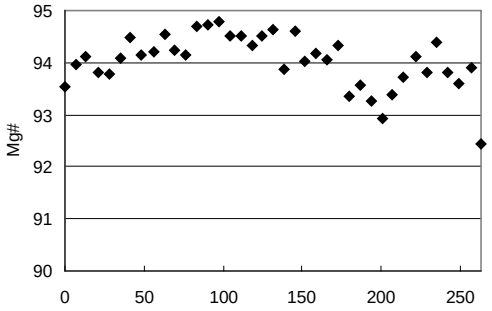


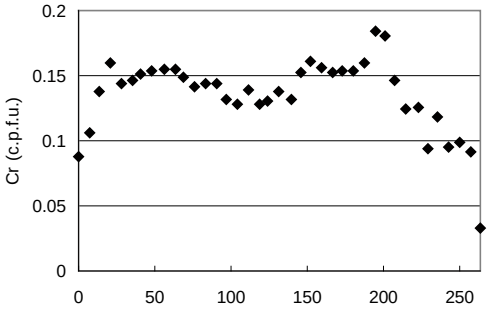
Group III-c: Clinopyroxene

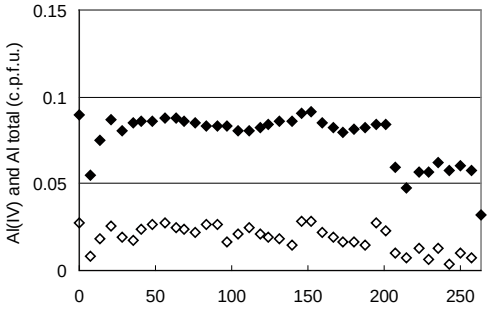
Sample: 1965/3 - Group III-a spl dunite

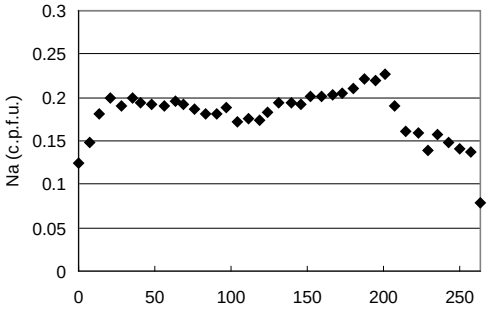
Na-rich Cr diopside (Di_m) microlite in melt pocket showing sector zoning

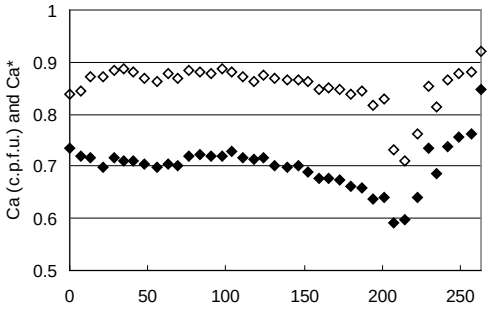
EMP-analysis: Session5 / cp4p2

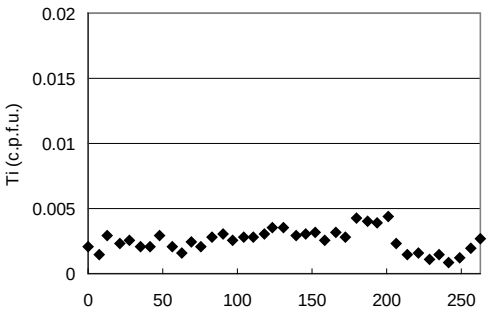


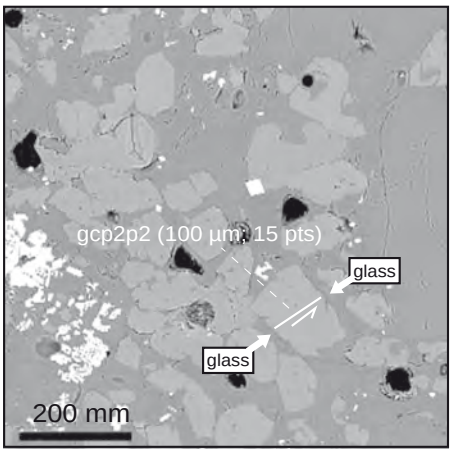










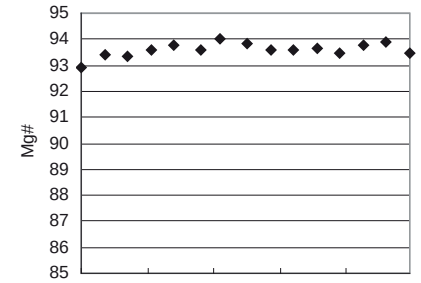


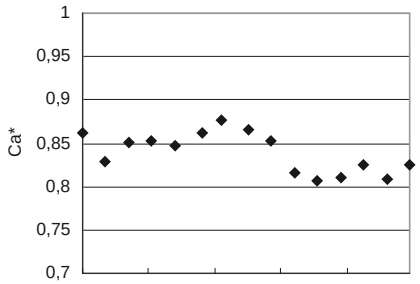
Group III-c: Clinopyroxene

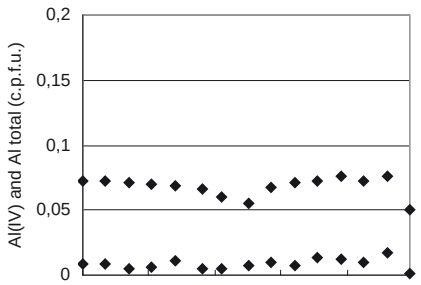
Sample: 1965/3 - Group III-c spl dunite

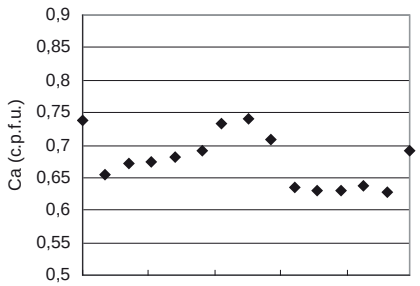
Euhedral Na-rich Cr diopside microlite (Di_m) in melt pocket

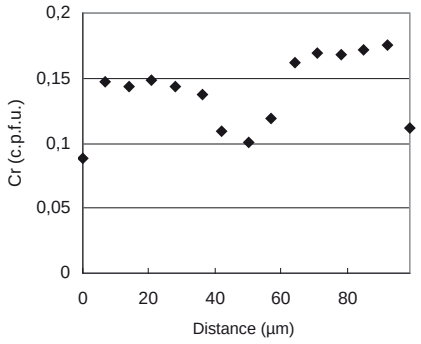
EMP-analysis: Session4 / gcp2p2 (green micropheno-xx)

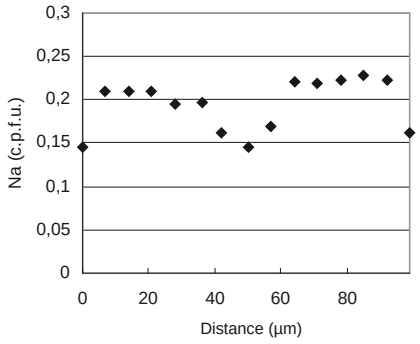


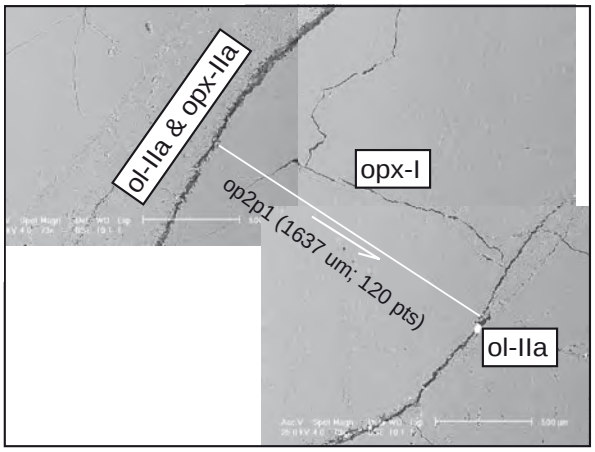










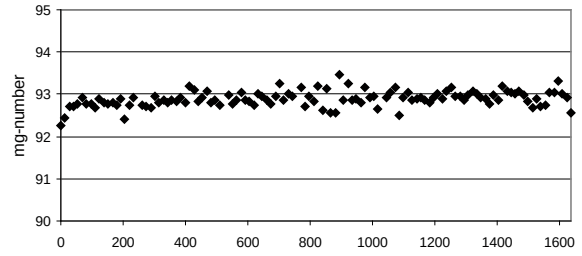


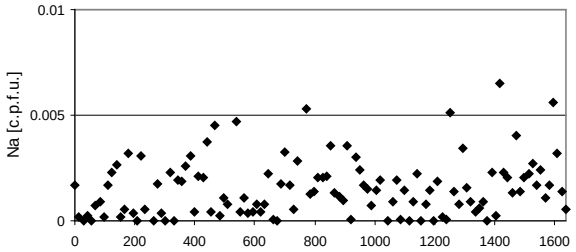
Group IV: Orthopyroxene

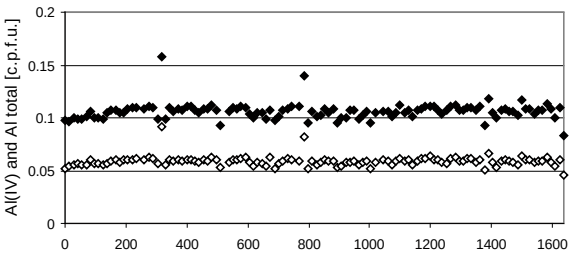
Sample: 1961/1 - Group IV spl harzburgite (ultramylonitic)

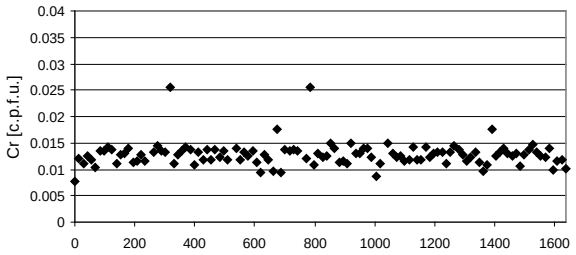
opx-I: large opx porphyroclast (stringer, with abundant bent cpx and spl exsolution lamellae)

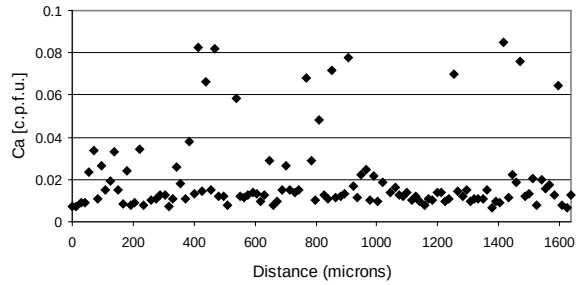
EMP-analysis: Session17 / op1p2

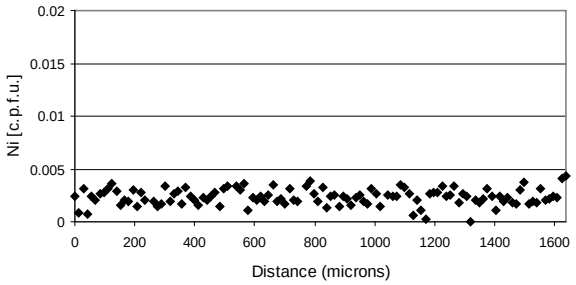


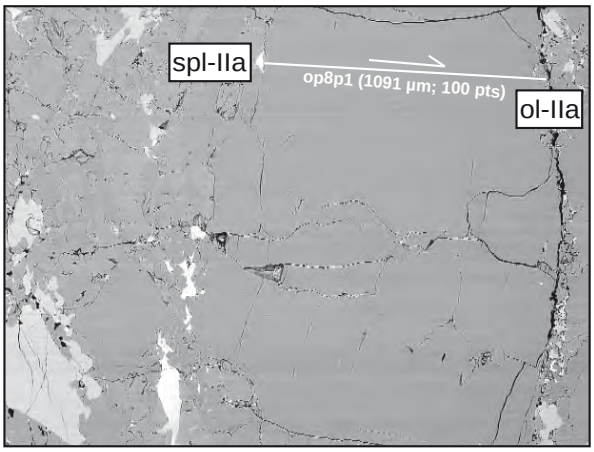










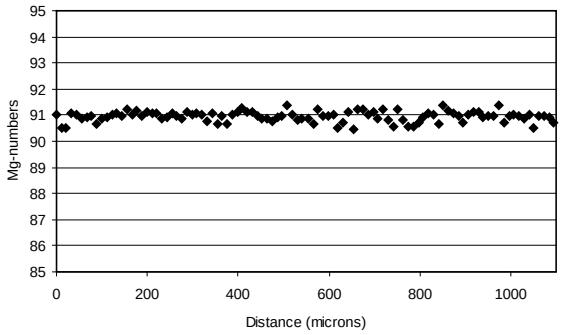


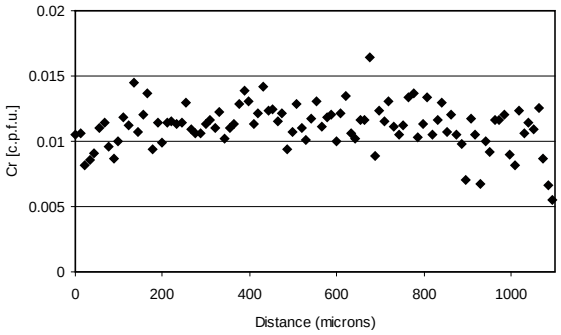
Group IV: Orthopyroxene

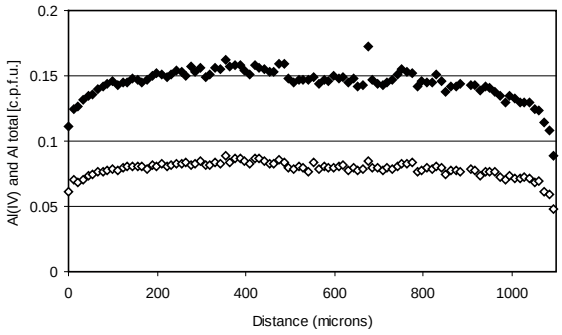
Sample: 1968/1 - Group IV spl lherzolite (mylonitic)

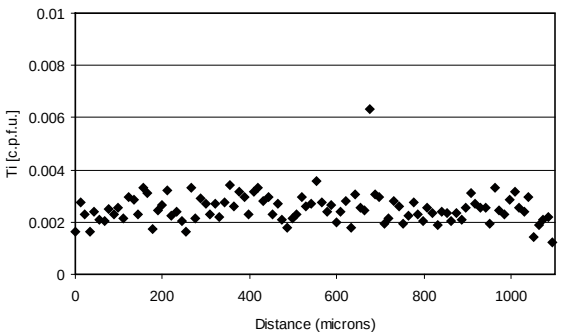
opx-I porphyroclast (stringer)

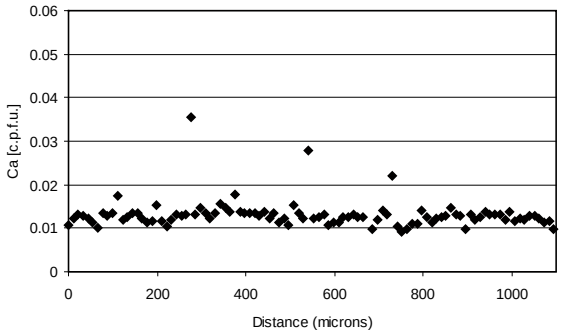
EMP-analysis: Session18 / op8p1

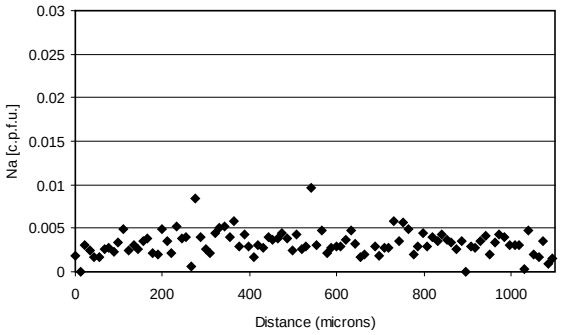


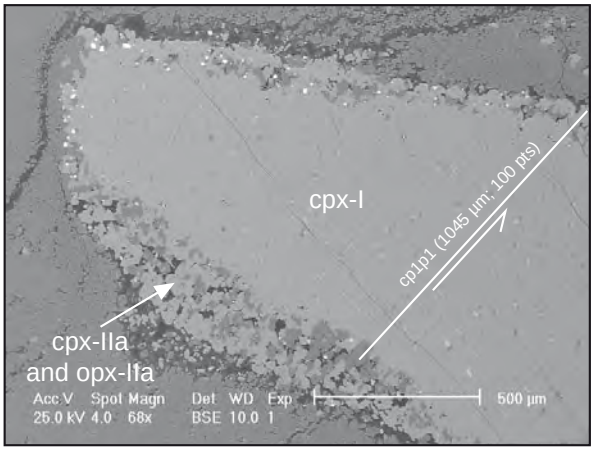










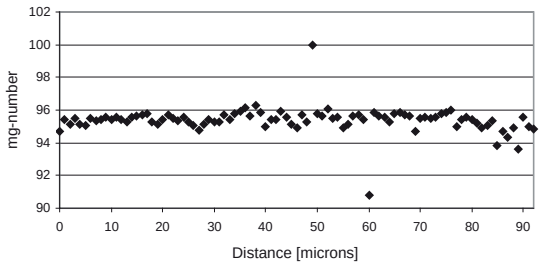


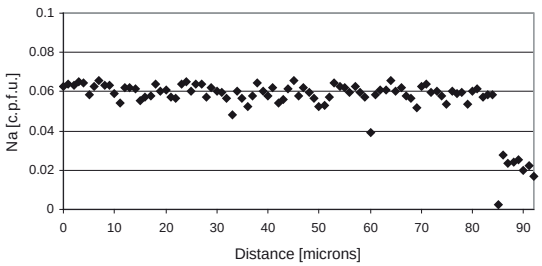
Group IV: Clinopyroxene

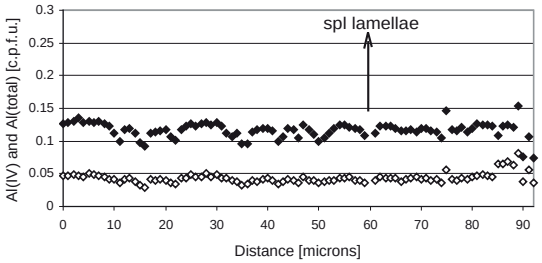
Sample: 1961/1 - Group IV spl harzburgite (ultramylonitic)

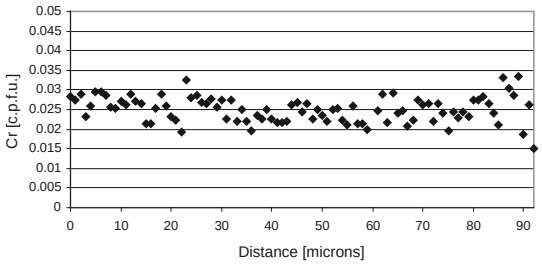
cpx-I: porphyroclast with spl and opx exsolution lamellae

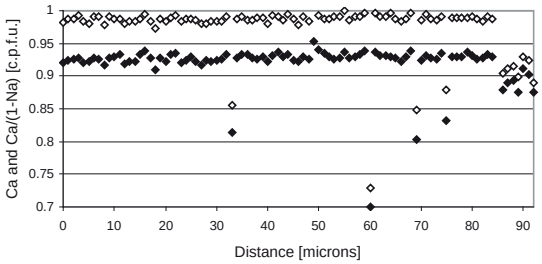
EPS-analysis: Session15 / cp1p1

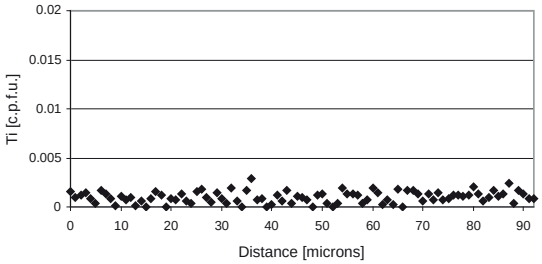


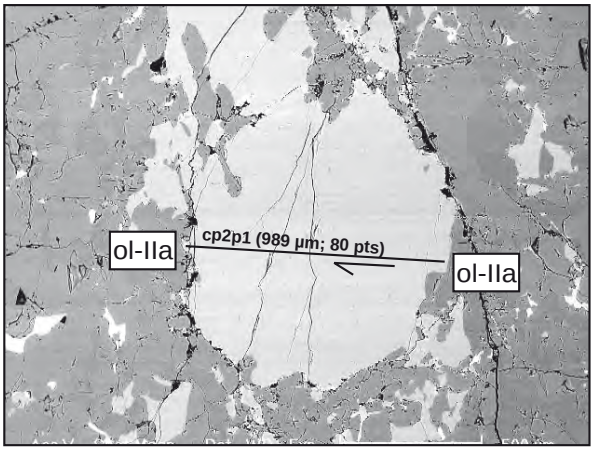










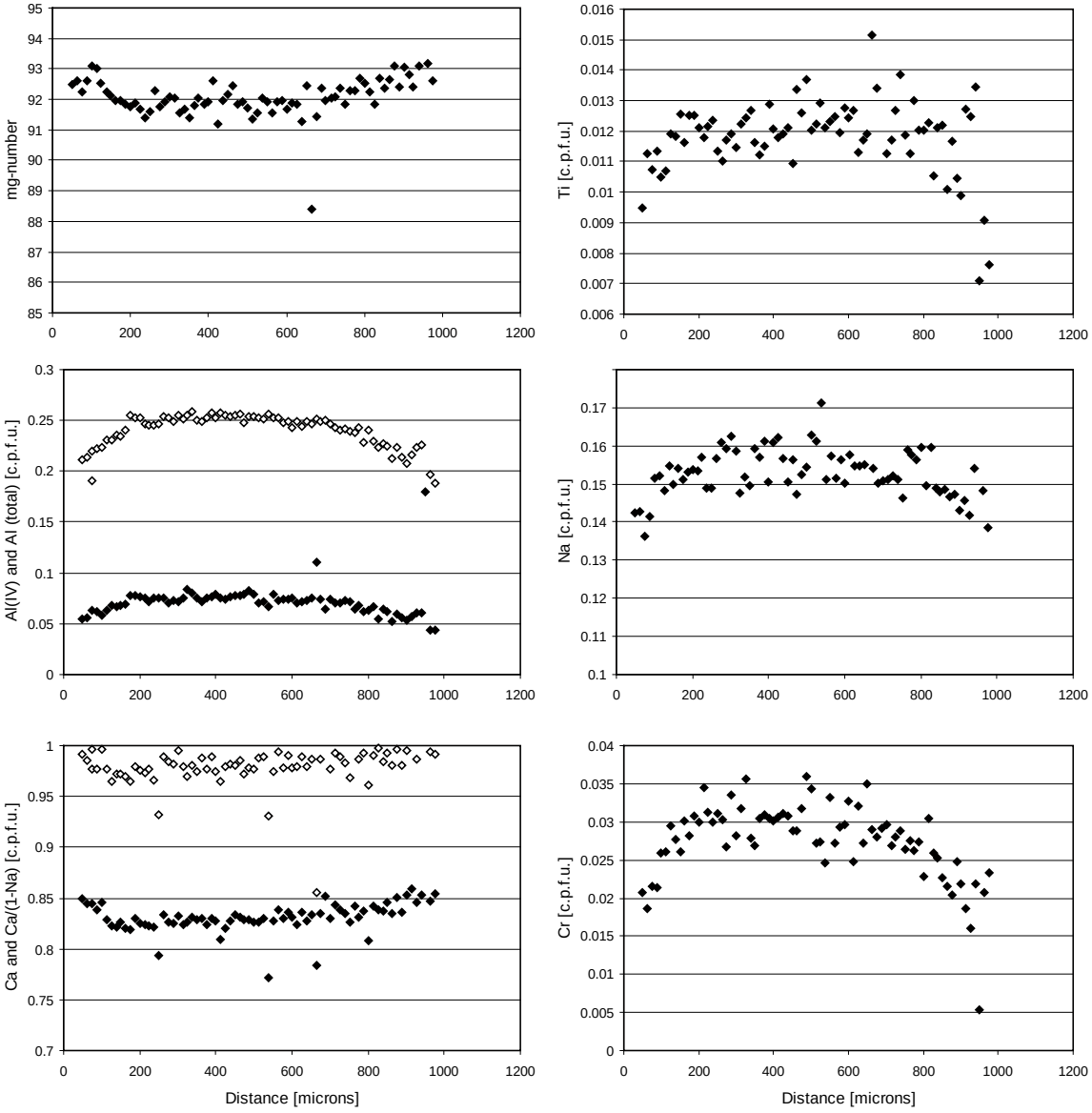


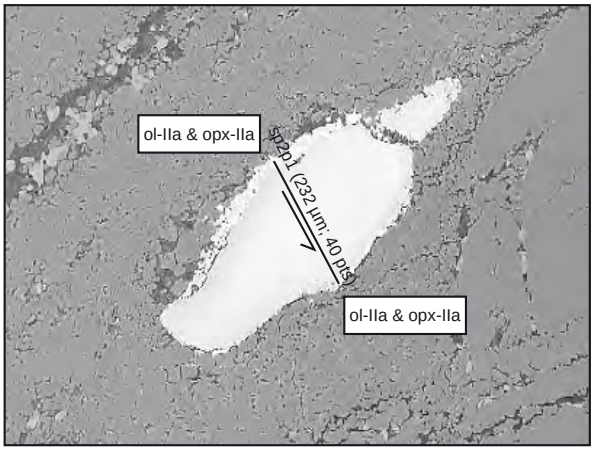
Group IV: Clinopyroxene

Sample: 1968/1 - Group IV spl lherzolite (mylonitic)

strongly deformed cpx-I porphyroclast

EMP-analysis: Session18 / cp2p1



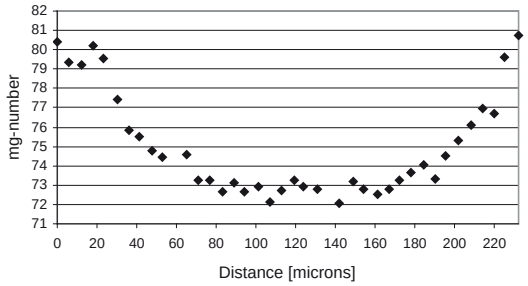


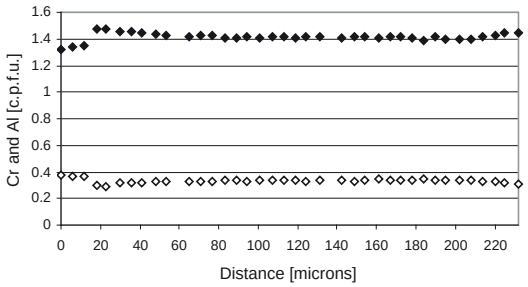
Group IV: Spinel

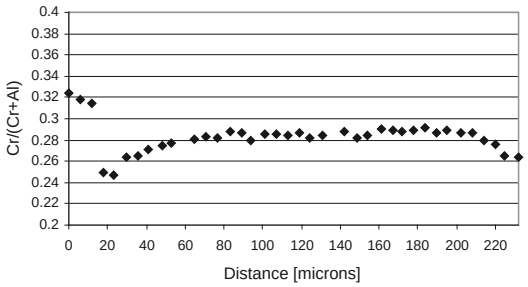
Sample: 1961/1 - Group IV spl harzburgite (ultramylonitic)

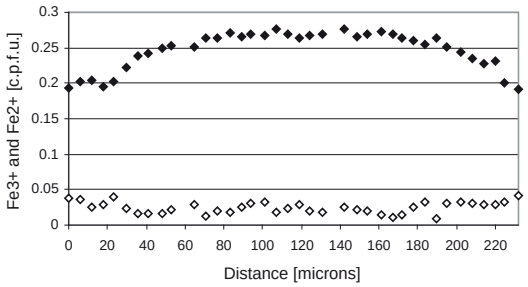
spl-I porphyroclast embedded in ol and opx neoblasts

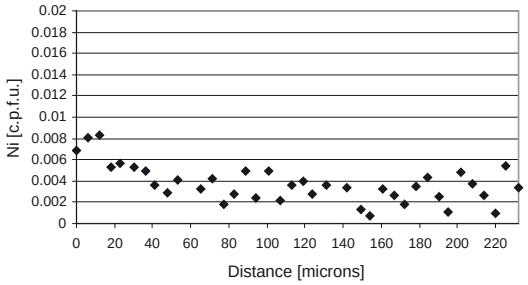
EMP-analysis: Session15 / sp2p1

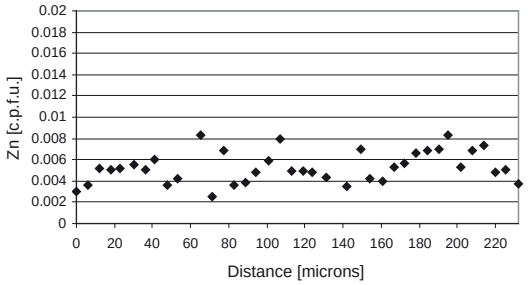


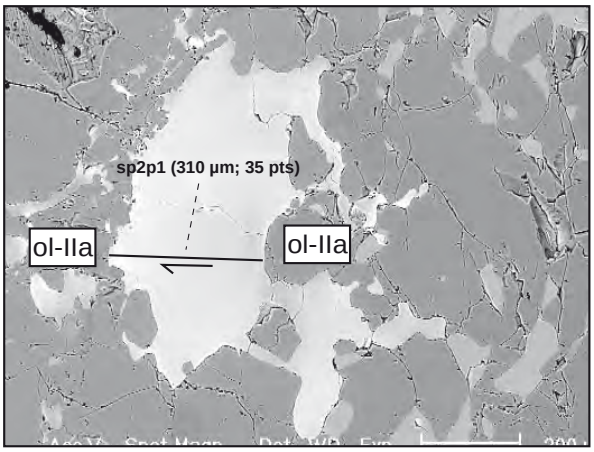










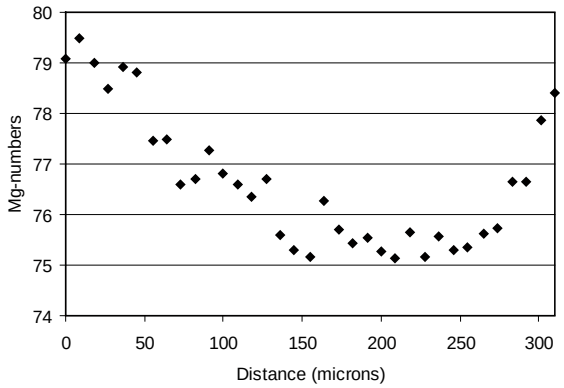


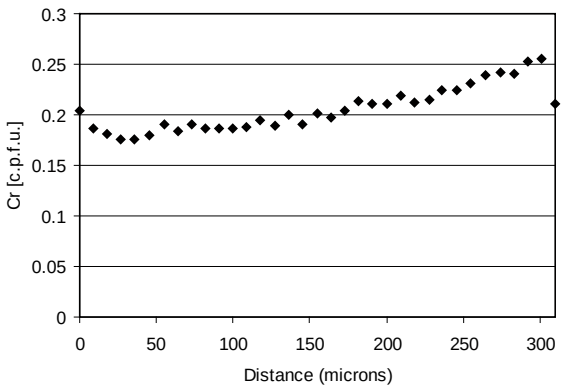
Group IV: Spinel

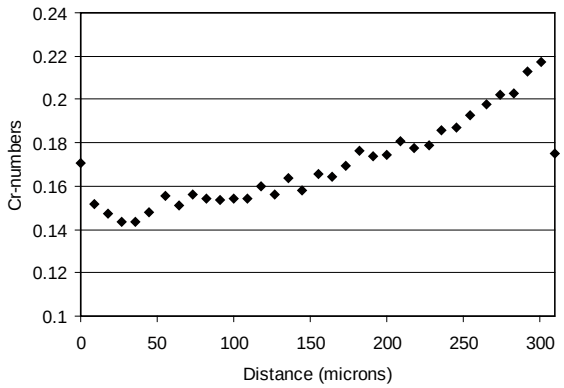
Sample: 1968/1 - Group IV spl lherzolite (mylonitic)

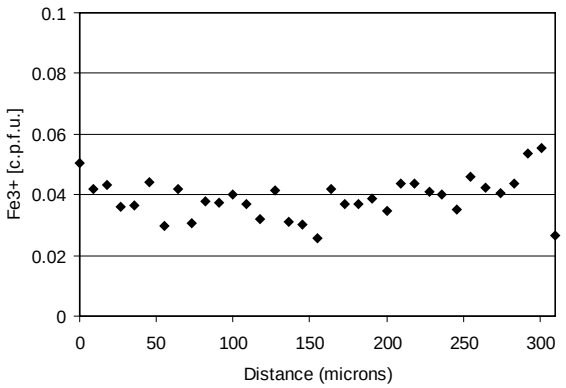
spl-I porphyroclast

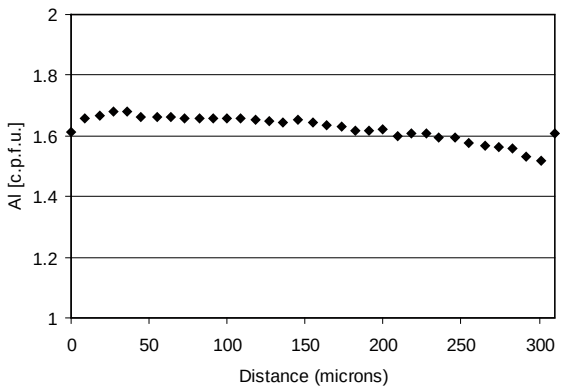
EMP-analysis: Session18 / sp2p1

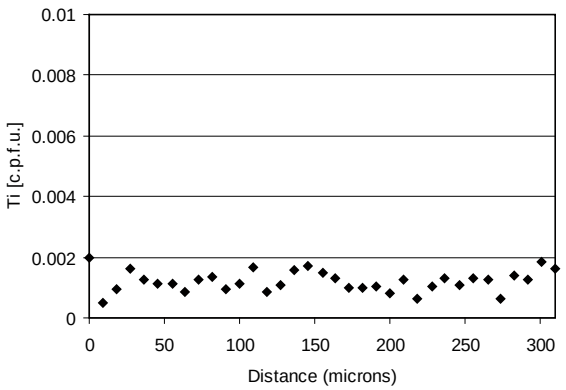


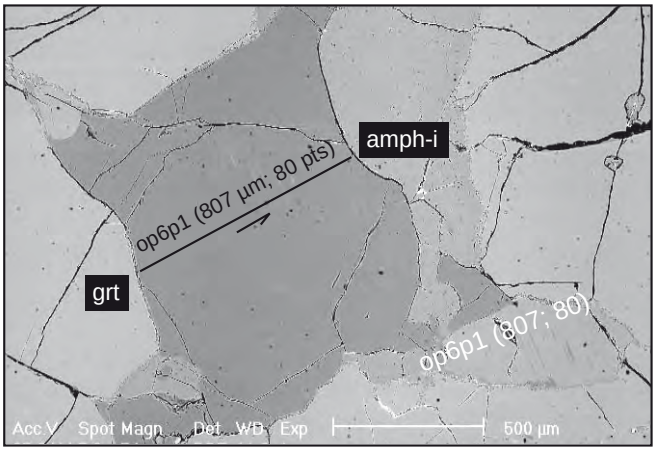










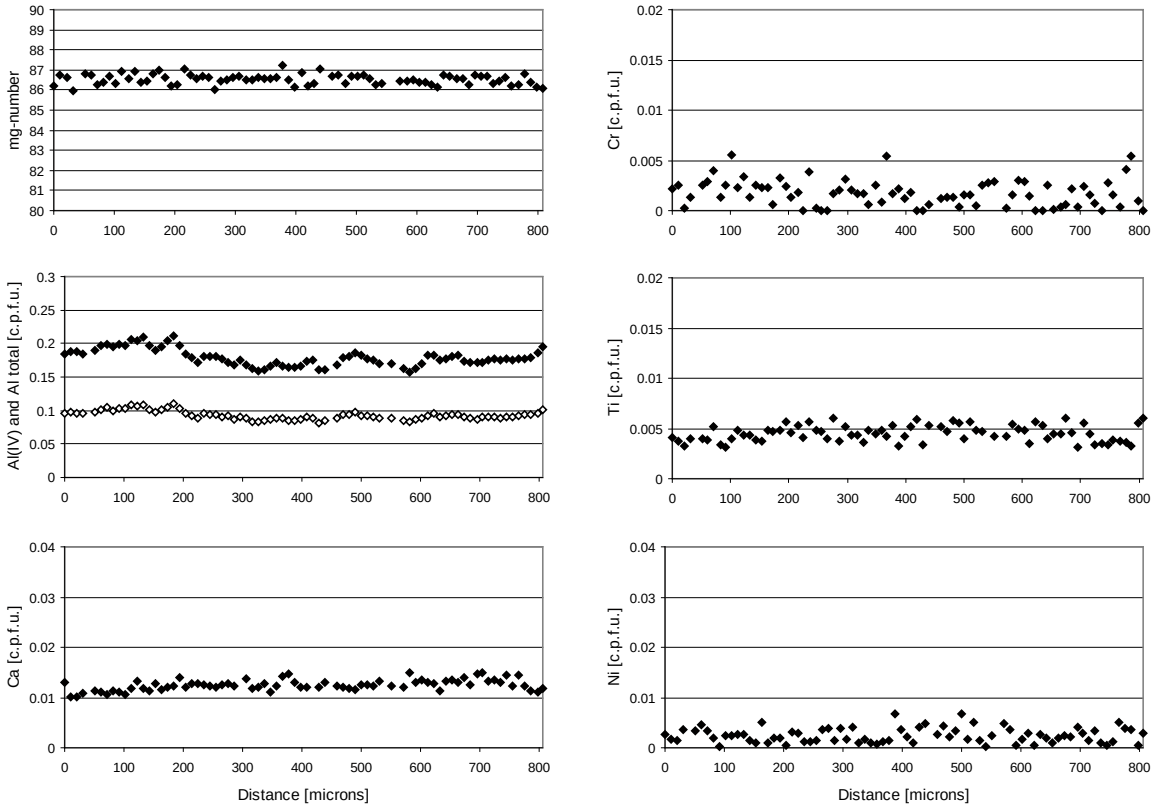


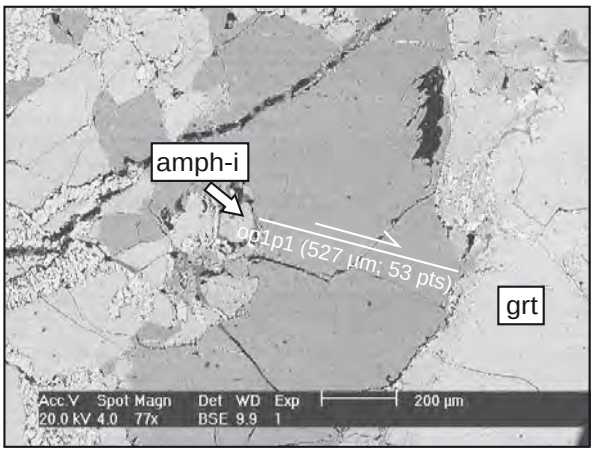
Group V: Orthopyroxene

Sample: 784/1 - Group V
grt websterite (cumulate-like textures)

primary, exsolved orthopyroxene (opx-I)

EMP-analysis: Session15 / op6p1



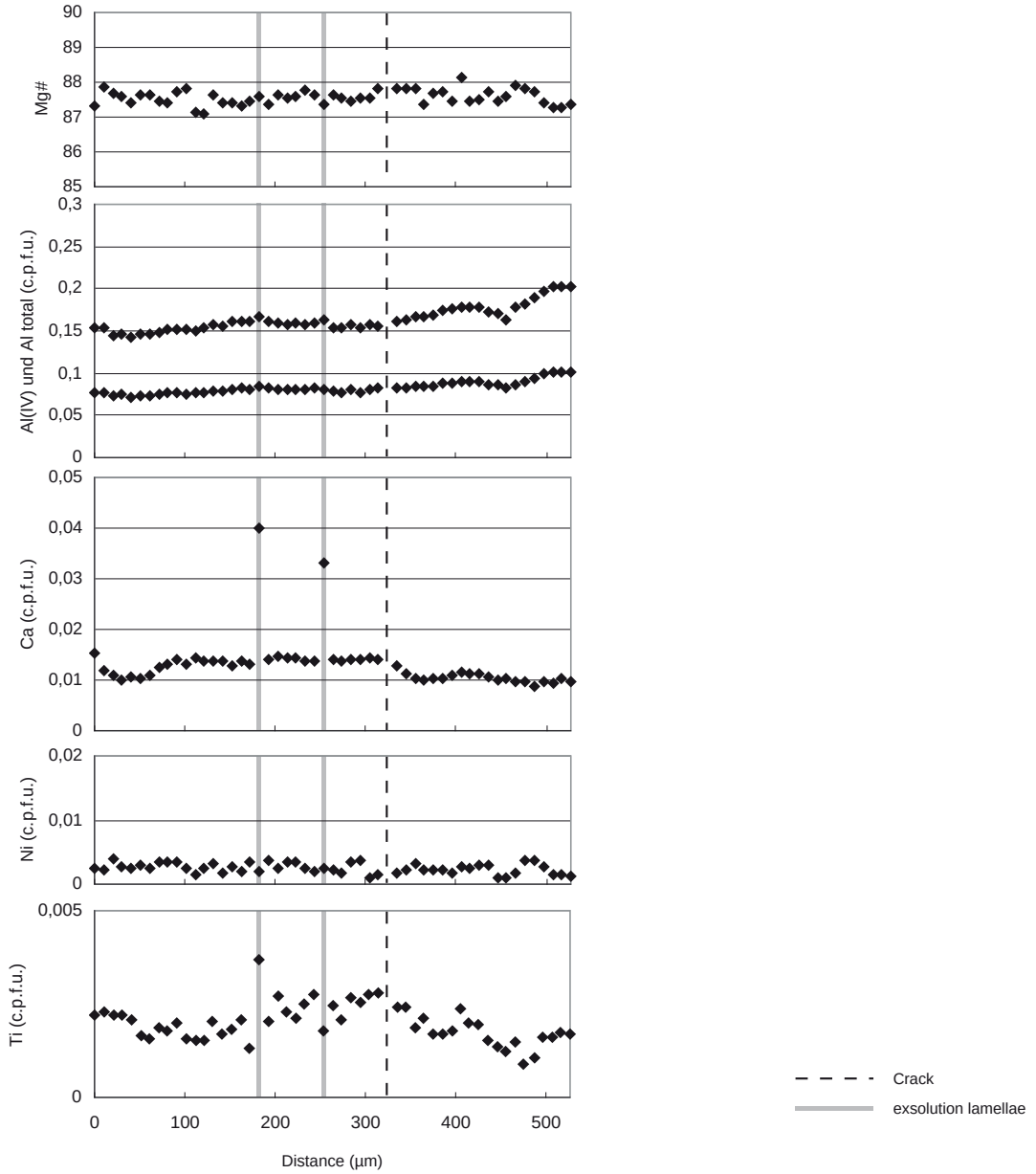


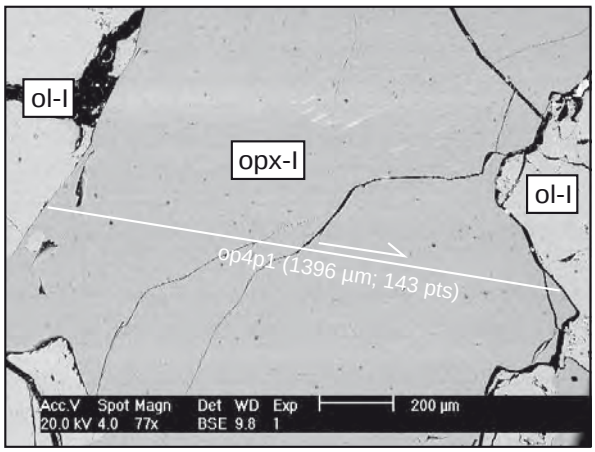
Group V: Orthopyroxene

Sample: 1959/18 - Group V grt websterite (opx-rich variety)

large opx-I porphyroclast

EMP-analysis: Session2 / op1p1



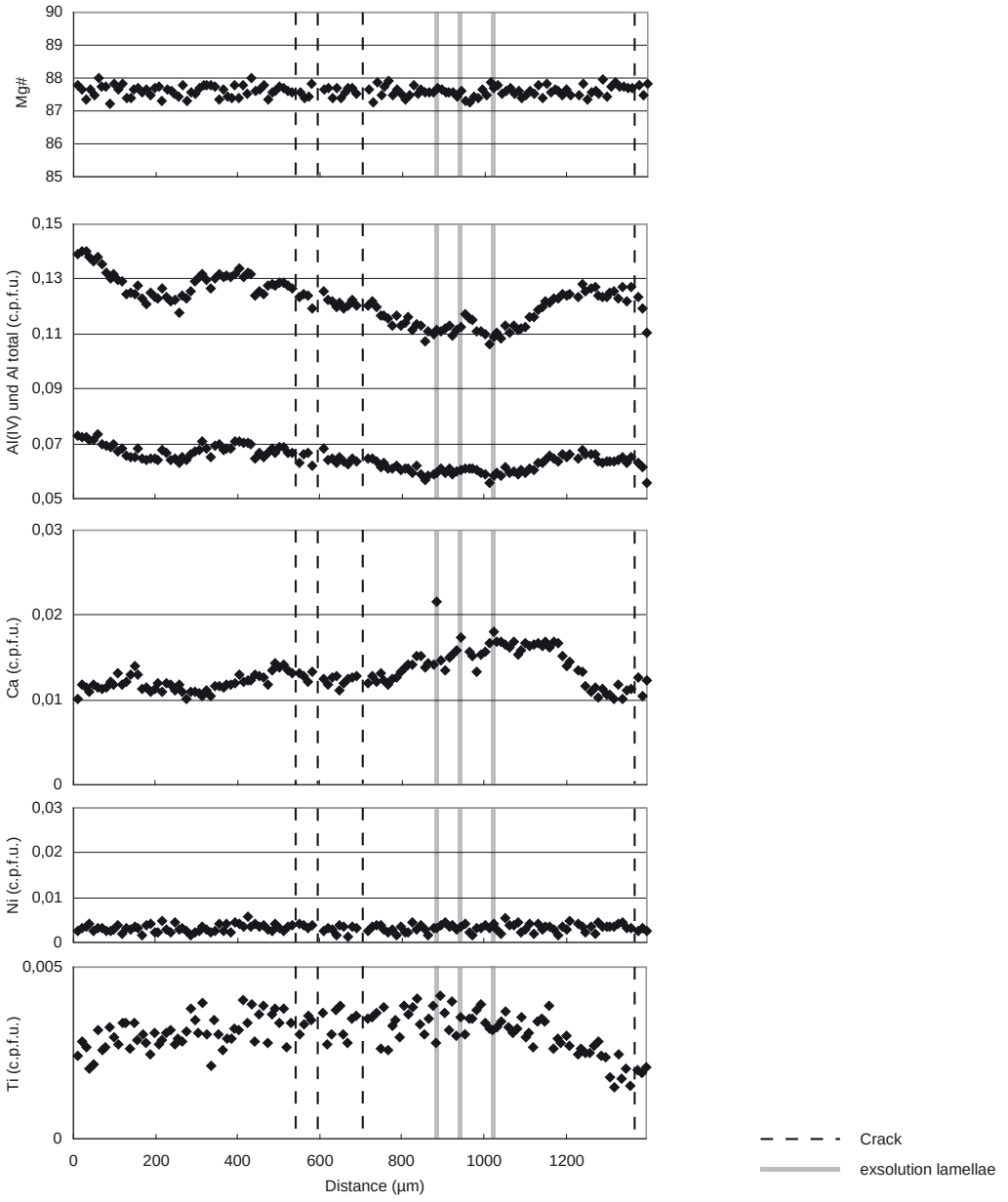


Zonation Profiles:

Sample: 1959/18 - Group V grt websterite (opx-rich variety)

opx-I porphyroclast with adjacent ol-I

EMP-analysis: Session2 / op4p1



NO IMAGE AVAILABLE

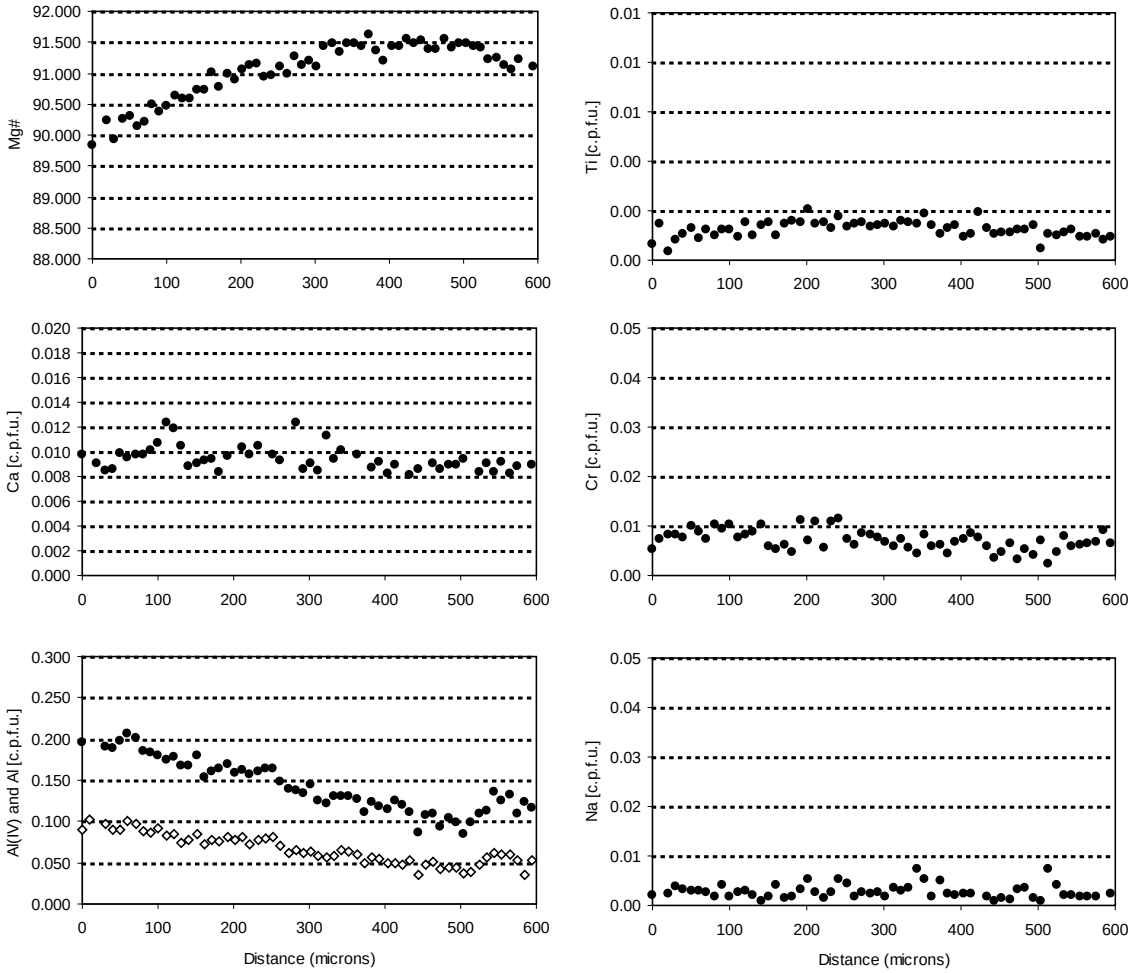
from cpx-IIa to cpx-IIa
(595 µm; 60 pts)

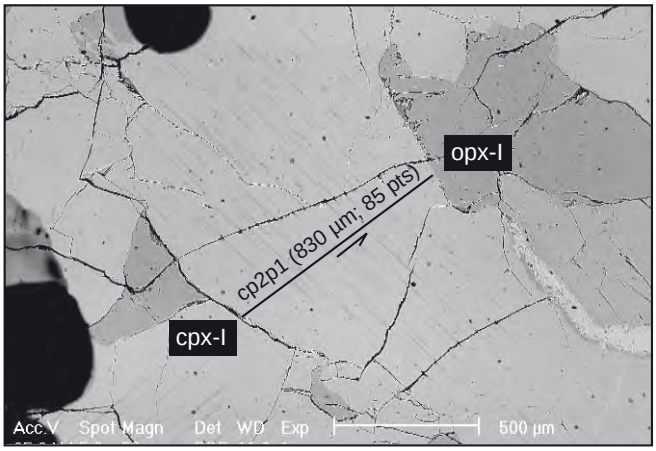
Group V: Orthopyroxene

Sample: 1964 - Group V grt websterite (mylonitic)

large strained opx-I porphyroclast embedded in very small-grained opx-IIa and cpx-IIa neoblasts

EMP-analysis: SessionJEOL3 / op1p1



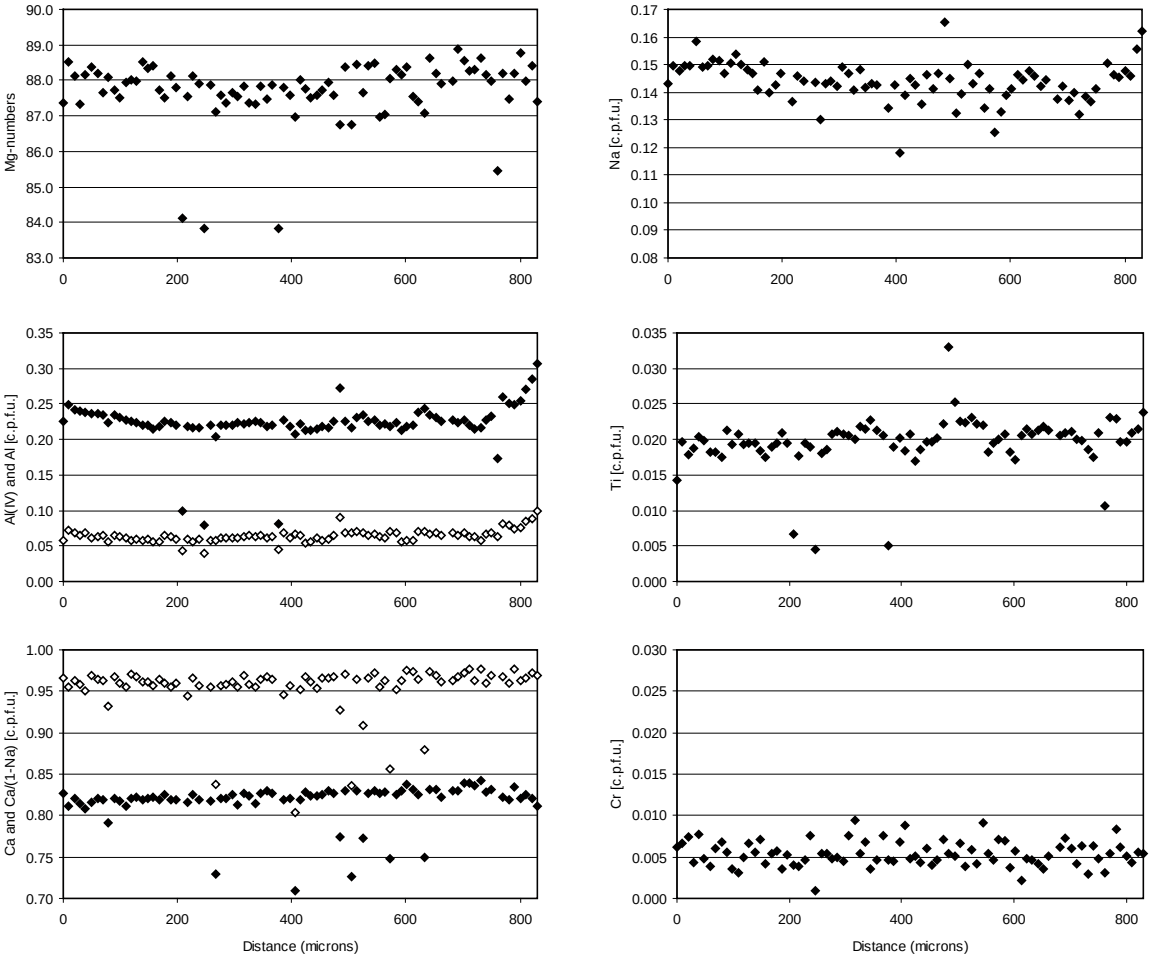


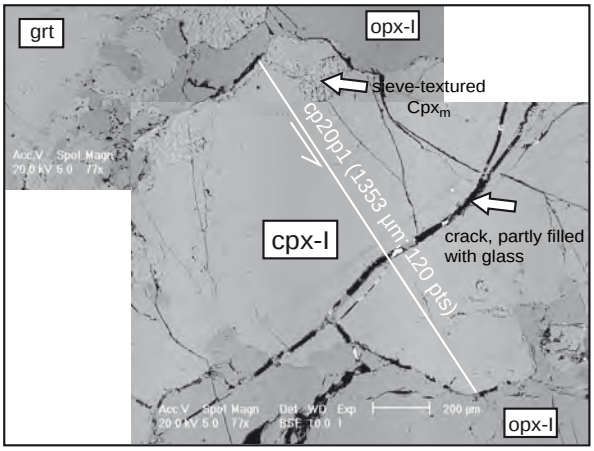
Group V: Clinopyroxene

Sample: 784/1 - Group V
grt websterite (cumulate-like textures)

primary, exsolved clinopyroxene (cpx-I)

EMP-analysis: Session15 / cp2p1



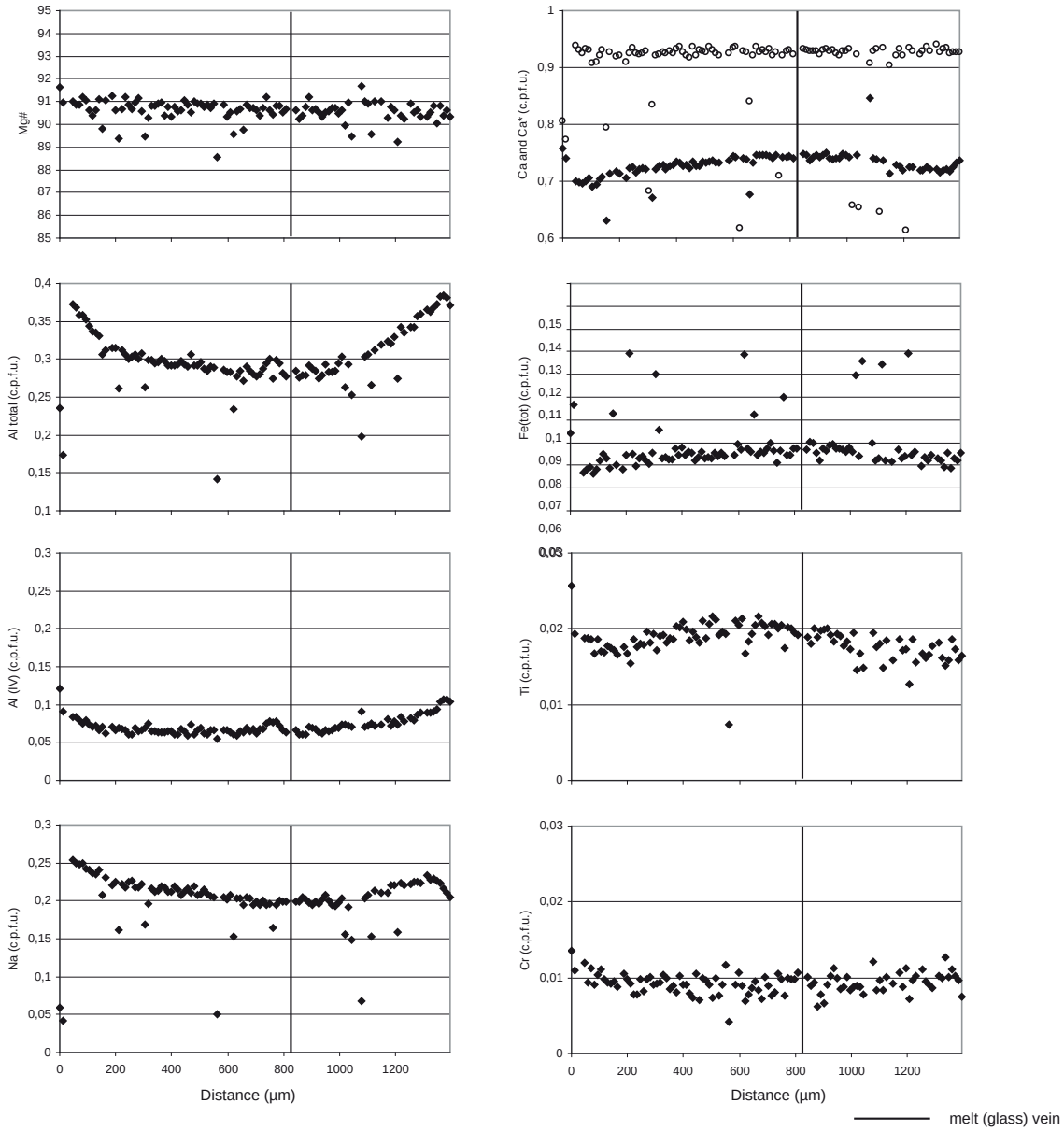


Group V: Clinopyroxene

Sample: 1959/18 - Group V grt websterite (opx-rich variety)

large deformed and exsolved cpx-I

EMP-analysis: Session5 / cp20p1



NO IMAGE AVAILABLE

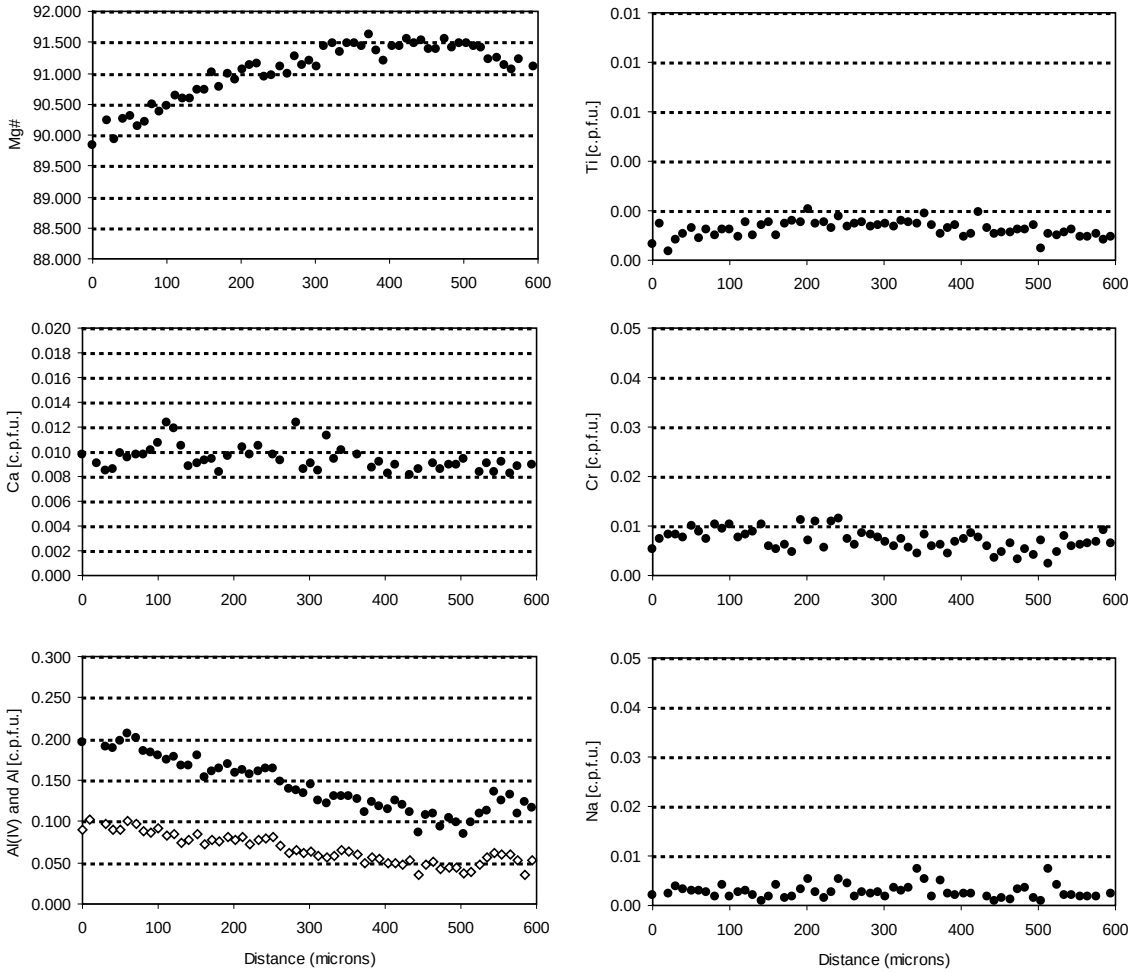
from cpx-IIa to cpx-IIa
(595 µm; 60 pts)

Group V: Orthopyroxene

Sample: 1964 - Group V grt websterite (mylonitic)

large strained opx-I porphyroclast embedded in very small-grained opx-IIa and cpx-IIa neoblasts

EMP-analysis: SessionJEOL3 / op1p1



Appendix A3

Electron Microprobe (EMP) data

Representative Analyses

Table A3-1: Representative major element composition and stoichiometry of ***olivine*** in peridotite xenoliths from Marsabit

Group	**I**	**I**	**I**	**I**	**I**	**I**	**I**	**I**	**I**	**I**	**I**	**I**	**I**	**I**	**I**	**II**	**II**
sample	1960/2	1960/2	1960/2	1960/2	1960/2	1963/1	1963/1	1963/1	1963/1	1963/2	1963/2	1963/2	1965/4	1965/4	1965/4	1958/6	1958/6
mineral	**ol-I**	**ol-I**	**ol-IIa**	**ol-IIa**	**Ol_m**	**ol-I**	**ol-I**	**Ol_m**	**Ol_m**	**ol-I**	**ol-I**	**ol-IIa**	**ol-I**	**ol-I**	**ol-IIa**	**ol-I**	**ol-I**
loaction	core	core	rim (opx)	rim (spl)	core	core	core	core	core	core	core	core	core	rim (opx)	rim (spl)	rim (ol)	core
SiO_2	40.69	40.93	40.84	40.96	41.31	40.88	40.75	41.30	40.86	40.68	41.11	40.56	40.74	40.80	40.76	40.24	40.71
TiO_2	0.01	0.01	n.d.	0.01	0.03	n.d.	n.d.	0.03	0.03	0.02	n.d.	n.d.	0.02	0.01	0.01	0.03	0.02
Al_2O_3	0.02	0.01	0.01	0.01	0.06	n.d.	0.01	0.05	0.04	n.d.	0.03	n.d.	0.01	0.02	0.03	0.08	0.06
Cr_2O_3	0.02	n.d.	0.06	n.d.	0.01	0.04	0.04	0.10	0.16	0.01	n.d.	0.02	n.d.	0.02	0.10	0.04	0.02
FeO	9.88	9.54	9.82	10.06	6.98	9.47	9.42	7.03	7.85	10.21	10.25	10.45	9.78	9.86	10.28	12.32	11.65
MnO	0.18	0.15	0.24	0.21	0.04	0.11	0.16	0.01	0.11	0.14	0.15	0.19	0.13	0.15	0.21	0.18	0.22
NiO	0.25	0.39	0.36	0.43	0.13	0.41	0.32	0.25	0.26	0.40	0.37	0.37	0.35	0.37	0.25	0.31	0.34
MgO	48.96	49.28	49.30	49.26	51.45	48.93	48.87	50.75	50.03	48.60	48.95	48.54	48.86	49.18	48.72	46.91	47.71
CaO	0.02	0.03	0.04	0.03	0.21	0.04	0.03	0.16	0.17	0.01	0.02	0.01	0.03	0.04	0.04	0.21	0.22
Na_2O	n.d.	0.02	0.01	n.d.	n.d.	0.02	n.d.	0.02	n.d.	n.d.	n.d.	0.01	n.d.	n.d.	0.03	0.01	0.04
K_2O	0.01	0.01	0.02	0.01	0.01	n.d.	0.01	0.01	n.d.	0.01	n.d.	n.d.	0.00	0.02	n.d.	n.d.	n.d.
Total	***100.02***	***100.36***	***100.67***	***100.97***	***100.23***	***99.91***	***99.60***	***99.72***	***99.52***	***100.08***	***100.88***	***100.14***	***99.93***	***100.47***	***100.44***	***100.34***	***100.99***
Stoich.	**4O**	**4O**	**4O**	**4O**	**4O**	**4O**	**4O**	**4O**	**4O**	**4O**	**4O**	**4O**	**4O**	**4O**	**4O**	**4O**	**4O**
Si	0.998	0.999	0.996	0.997	0.997	1.002	1.002	1.002	0.999	0.999	1.001	0.997	1.000	0.997	0.998	0.996	0.998
Ti	0.000	0.000	-	0.000	0.001	-	-	0.001	0.001	0.000	-	-	0.000	0.000	0.000	0.001	0.000
Al	0.000	0.000	0.000	0.000	0.002	-	0.000	0.002	0.001	-	0.001	-	0.000	0.001	0.001	0.002	0.002
Cr	0.000	-	0.001	-	0.000	0.001	0.001	0.002	0.003	0.000	-	0.000	-	0.000	0.002	0.001	0.000
Fe	0.203	0.195	0.200	0.205	0.141	0.194	0.194	0.143	0.160	0.210	0.209	0.215	0.201	0.202	0.210	0.255	0.239
Mn	0.004	0.003	0.005	0.004	0.001	0.002	0.003	0.000	0.002	0.003	0.003	0.004	0.003	0.003	0.004	0.004	0.005
Ni	0.005	0.008	0.007	0.008	0.003	0.008	0.006	0.005	0.005	0.008	0.007	0.007	0.007	0.007	0.005	0.006	0.007
Mg	1.791	1.794	1.792	1.787	1.852	1.788	1.791	1.836	1.823	1.780	1.777	1.779	1.788	1.791	1.778	1.731	1.743
Ca	0.001	0.001	0.001	0.001	0.005	0.001	0.001	0.004	0.005	0.000	0.001	0.000	0.001	0.001	0.001	0.006	0.006
Na	-	0.001	0.000	-	-	0.001	-	0.001	-	-	-	0.000	-	-	0.001	0.000	0.002
K	0.000	0.000	0.001	0.000	0.000	-	0.000	0.000	-	0.000	-	-	0.000	0.001	-	-	-
Total	***3.002***	***3.001***	***3.004***	***3.003***	***3.001***	***2.998***	***2.998***	***2.996***	***2.999***	***3.001***	***2.999***	***3.003***	***3.000***	***3.003***	***3.001***	***3.002***	***3.002***
Mg#	***89.84***	***90.21***	***89.95***	***89.72***	***92.93***	***90.20***	***90.24***	***92.79***	***91.91***	***89.46***	***89.49***	***89.23***	***89.90***	***89.89***	***89.41***	***87.16***	***87.95***

the abbreviation in brackets under location indicates the adjacent mineral phase of the respective rim analysis; n.a.: not analysed; n.d.: not detected;

Stoich.: cations calculated on the basis of 4 oxygens

Table A3-1: Representative major element composition and stoichiometry of ***olivine*** in peridotite xenoliths from Marsabit (continued)

Group	**II**	**II**	**II**	**II**	**II**	**II**	**II**	**II**	**II**	**II**	**II**	**II**	**II**	**III-a**	**III-a**	**III-a**
sample	1958/6	1958/13	1958/13	1958/13	1958/13	1958/20	1958/20	1958/20	1959/24	1959/24	1959/25	1959/25	1959/25	781/6	781/6	1965/1
mineral	**ol-I**	**ol-I**	**ol-I**	**ol-I**	**Ol_m**	**ol-I**	**ol-I**	**ol-I**	**ol-I**	**ol-I**	**ol-I**	**ol-I**	**Ol_m**	**ol-I**	**ol-I**	**ol-I**
loaction	core	core	core	rim (cpx)	core	core	core	rim (spl)	core	rim (spl)	core	rim (ol)	core	core	rim (spl)	core
SiO_2	40.05	41.15	41.48	41.46	41.81	40.51	40.84	40.75	40.97	40.97	41.03	41.26	40.64	40.29	40.30	41.17
TiO_2	n.d.	0.02	n.d.	0.01	0.03	0.02	n.d.	0.01	n.d.	0.02	0.01	0.01	0.01	n.d.	0.03	0.02
Al_2O_3	0.08	0.02	0.03	0.02	0.03	0.03	0.05	0.07	0.06	0.03	0.04	0.04	0.01	0.05	0.04	n.d.
Cr_2O_3	0.04	0.02	0.03	0.01	0.10	0.05	0.02	0.10	0.03	0.14	0.03	0.04	0.18	n.d.	0.19	n.d.
FeO	12.48	9.28	9.87	9.37	6.06	9.51	9.92	9.57	9.28	9.80	9.10	9.23	9.02	8.35	8.75	8.04
MnO	0.13	0.15	0.15	0.10	0.15	0.11	0.18	0.14	0.18	0.13	0.16	0.09	0.10	0.17	0.18	0.12
NiO	0.28	0.34	0.38	0.38	0.28	0.35	0.32	0.50	0.36	0.39	0.36	0.37	0.38	0.38	0.32	0.37
MgO	47.01	49.80	49.97	49.90	52.17	48.68	49.01	49.19	49.32	48.93	49.59	49.97	50.00	49.02	48.70	50.35
CaO	0.23	0.05	0.04	0.09	0.29	0.11	0.08	0.13	0.12	0.13	0.18	0.15	0.15	0.04	0.13	0.04
Na_2O	0.04	0.02	0.01	0.04	0.01	n.d.	n.d.	0.01	n.d.	0.04	n.d.	0.01	n.d.	n.d.	n.d.	0.03
K_2O	0.01	n.d.	n.d.	n.d.	n.d.	0.02	n.d.	n.d.	n.d.	n.d.	n.d.	0.01	n.d.	0.01	n.d.	n.d.
Total	***100.34***	***100.85***	***101.95***	***101.40***	***100.93***	***99.40***	***100.42***	***100.47***	***100.32***	***100.59***	***100.49***	***101.18***	***100.49***	***98.30***	***98.63***	***100.15***
Stoich.	**4O**	**4O**	**4O**	**4O**	**4O**	**4O**	**4O**	**4O**	**4O**	**4O**	**4O**	**4O**	**4O**	**4O**	**4O**	**4O**
Si	0.992	0.998	0.998	1.000	0.999	0.999	0.998	0.995	1.000	1.000	0.999	0.998	0.990	1.000	0.999	1.000
Ti	-	0.000	-	0.000	0.001	0.000	-	0.000	-	0.000	0.000	0.000	0.000	-	0.001	0.000
Al	0.002	0.001	0.001	0.001	0.001	0.001	0.001	0.002	0.002	0.001	0.001	0.001	0.000	0.001	0.001	-
Cr	0.001	0.000	0.001	0.000	0.002	0.001	0.000	0.002	0.001	0.003	0.001	0.001	0.003	-	0.004	-
Fe	0.259	0.188	0.199	0.189	0.121	0.196	0.203	0.195	0.189	0.200	0.185	0.187	0.184	0.173	0.181	0.163
Mn	0.003	0.003	0.003	0.002	0.003	0.002	0.004	0.003	0.004	0.003	0.003	0.002	0.002	0.003	0.004	0.002
Ni	0.006	0.007	0.007	0.007	0.005	0.007	0.006	0.010	0.007	0.008	0.007	0.007	0.007	0.008	0.006	0.007
Mg	1.736	1.801	1.792	1.795	1.859	1.790	1.786	1.791	1.794	1.780	1.800	1.801	1.816	1.813	1.799	1.824
Ca	0.006	0.001	0.001	0.002	0.008	0.003	0.002	0.003	0.003	0.003	0.005	0.004	0.004	0.001	0.003	0.001
Na	0.002	0.001	0.000	0.002	0.000	-	-	0.001	-	0.002	-	0.000	-	-	-	0.001
K	0.000	-	-	-	-	0.001	-	-	-	-	-	0.000	-	0.000	-	-
Total	***3.007***	***3.001***	***3.002***	***3.000***	***2.999***	***3.000***	***3.001***	***3.003***	***2.999***	***2.999***	***3.000***	***3.002***	***3.008***	***3.000***	***2.998***	***3.000***
Mg#	***87.03***	***90.54***	***90.03***	***90.47***	***93.89***	***90.13***	***89.80***	***90.16***	***90.45***	***89.90***	***90.67***	***90.61***	***90.81***	***91.28***	***90.85***	***91.78***

Table A3-1: Representative major element composition and stoichiometry of ***olivine*** in peridotite xenoliths from Marsabit (continued)

Group	**III-a**	**III-a**	**III-a**	**III-b**	**III-b**	**III-b**	**III-b**	**III-b**	**III-b**	**III-b**	**III-b**	**III-b**	**III-b**	**III-b**	**III-c**	**III-c**
sample	1965/1	1965/1	1965/1	1959/15	1959/15	1959/15	1959/15	1959/15	1959/15	1965/15	1965/15	1965/15	1965/15	1965/15	785*	785*
mineral	**ol-IIa**	**ol-I**	**ol-I**	**ol-I**	**ol-I**	**Ol_m**	**Ol_m**	**Ol_m**	**Ol_m**	**ol-I**	**ol-I**	**ol-IIa**	**Ol_m**	**Ol_m**	**ol-I**	**ol-I**
loaction	core	rim (opx)	rim (spl)	core	core	core (glass)	rim (glass)	rim (Chrm)	rim (glass)	core	rim (opx)	core	core	core	core	core
SiO_2	41.25	41.13	40.61	41.09	41.48	41.51	41.52	40.84	41.40	41.25	41.23	41.40	41.27	41.40	40.76	40.95
TiO_2	n.d.	n.d.	n.d.	n.d.	n.d.	n.d.	n.d.	n.d.	n.d.	0.03	0.02	n.d.	0.02	0.01	0.03	0.01
Al_2O_3	0.02	0.01	0.01	0.00	0.02	0.04	0.02	0.01	0.05	0.01	0.10	n.d.	0.03	0.03	0.02	0.01
Cr_2O_3	0.02	0.01	0.26	0.04	0.02	0.08	0.12	0.22	0.11	0.05	n.d.	0.05	0.14	0.82	0.01	n.d.
FeO	8.08	8.38	8.64	8.77	8.87	5.52	5.35	9.34	6.20	8.58	8.49	8.51	5.91	5.84	9.51	9.63
MnO	0.12	0.14	0.16	0.14	0.17	0.09	0.13	0.12	0.11	0.09	0.14	0.16	0.12	0.10	0.09	0.17
NiO	0.36	0.33	0.39	0.34	0.34	0.32	0.38	0.43	0.33	0.38	0.35	0.40	0.37	0.43	0.42	0.43
MgO	50.59	50.08	49.29	49.80	50.20	52.75	52.74	49.28	51.48	50.25	50.08	50.27	51.48	51.85	49.00	49.06
CaO	0.03	0.03	0.01	0.03	0.04	0.26	0.28	0.00	0.32	0.01	0.03	0.04	0.15	0.18	0.01	0.02
Na_2O	0.01	0.03	0.01	n.d.	0.02	n.d.	0.03	0.00	0.01	0.03	0.03	0.01	0.04	0.03	0.01	0.01
K_2O	n.d.	n.d.	n.d.	0.01	n.d.	n.d.	0.00	0.01	n.d.	n.d.	n.d.	n.d.	0.01	0.02	n.d.	n.d.
Total	***100.49***	***100.14***	***99.39***	***100.23***	***101.17***	***100.57***	***100.56***	***100.25***	***100.02***	***100.69***	***100.48***	***100.86***	***99.52***	***100.71***	***99.85***	***100.30***
Stoich.	**4O**	**4O**	**4O**	**4O**	**4O**	**4O**	**4O**	**4O**	**4O**	**4O**	**4O**	**4O**	**4O**	**4O**	**4O**	**4O**
Si	0.999	1.001	0.998	1.001	1.001	0.994	0.994	0.998	1.000	0.999	1.000	1.001	1.000	0.993	1.000	1.001
Ti	-	-	-	-	-	-	-	-	-	0.001	0.000	-	0.000	0.000	0.000	0.000
Al	0.001	0.000	0.000	0.000	0.000	0.001	0.000	0.000	0.001	0.000	0.003	-	0.001	0.001	0.001	0.000
Cr	0.000	0.000	0.005	0.001	0.000	0.002	0.002	0.004	0.002	0.001	-	0.001	0.003	0.016	0.000	-
Fe	0.164	0.170	0.178	0.179	0.179	0.111	0.107	0.191	0.125	0.174	0.172	0.172	0.120	0.117	0.195	0.197
Mn	0.002	0.003	0.003	0.003	0.003	0.002	0.003	0.002	0.002	0.002	0.003	0.003	0.002	0.002	0.002	0.004
Ni	0.007	0.006	0.008	0.007	0.007	0.006	0.007	0.008	0.006	0.007	0.007	0.008	0.007	0.008	0.008	0.009
Mg	1.826	1.817	1.806	1.808	1.806	1.883	1.883	1.795	1.853	1.814	1.811	1.812	1.860	1.855	1.792	1.788
Ca	0.001	0.001	0.000	0.001	0.001	0.007	0.007	0.000	0.008	0.000	0.001	0.001	0.004	0.005	0.000	0.001
Na	0.000	0.001	0.001	-	0.001	-	0.001	0.000	0.001	0.001	0.002	0.001	0.002	0.001	0.000	0.000
K	-	-	-	0.000	-	-	0.000	0.000	-	-	-	-	0.000	0.000	-	-
Total	***3.001***	***3.000***	***2.999***	***2.999***	***2.999***	***3.005***	***3.005***	***3.000***	***2.999***	***3.000***	***2.999***	***2.999***	***2.999***	***2.999***	***2.999***	***2.999***
Mg#	***91.77***	***91.42***	***91.05***	***91.01***	***90.98***	***94.45***	***94.62***	***90.40***	***93.67***	***91.26***	***91.31***	***91.33***	***93.95***	***94.05***	***90.18***	***90.08***

Table A3-1: Representative major element composition and stoichiometry of ***olivine*** in peridotite xenoliths from Marsabit (continued)

Group	**III-c**	**III-c**	**III-c**	**III-c**	**III-c**	**III-c**	**III-c**	**III-c**	**III-c**	**III-c**	**III-c**	**III-c**	**III-c**	**III-c**	**III-c**	**III-c**
sample	785*	785*	785*	1959/27	1959/27	1959/27	1959/27	1959/27	1965/3	1965/3	1965/3	1965/3	1965/3	1965/3	1965/3	1965/25
mineral	**ol-I**	**Ol_m**	**Ol_m**	**ol-I**	**ol-I**	**ol-I**	**Ol_m**	**Ol_m**	**ol-I**	**ol-I**	**ol-I**	**ol-I**	**ol-I**	**Ol_m**	**Ol_m**	**ol-I**
loaction	rim (glass)	core	rim (Opxm)	core	core	rim (glass)	core	rim (glass)	core	core	rim (Opxm)	rim (glass)	rim (glass)	core	core	core
SiO_2	41.51	41.58	41.45	40.63	41.22	40.78	40.72	40.59	41.32	41.15	40.72	41.38	41.17	41.37	41.35	40.78
TiO_2	0.01	0.01	0.01	0.03	n.d.	0.03	0.01	0.02	n.d.	0.02	0.01	0.01	0.02	n.d.	0.01	0.01
Al_2O_3	0.04	0.03	0.02	0.02	0.01	0.02	0.01	0.02	n.d.	n.d.	n.d.	0.01	n.d.	n.d.	0.01	n.d.
Cr_2O_3	0.07	0.21	0.10	0.02	0.01	n.d.	0.05	0.02	n.d.	n.d.	0.02	0.01	0.20	0.12	0.29	0.01
FeO	6.27	6.24	7.18	10.07	10.79	11.19	11.03	11.05	8.15	8.22	8.45	6.60	6.04	6.63	5.83	11.33
MnO	0.09	0.08	0.10	0.19	0.27	0.29	0.29	0.31	0.16	0.20	0.24	0.13	0.03	0.18	0.13	0.27
NiO	0.44	0.45	0.19	0.38	0.27	0.32	0.28	0.33	0.46	0.37	0.40	0.31	0.31	0.34	0.24	0.37
MgO	51.66	51.68	51.04	48.54	49.03	48.02	47.94	48.27	50.41	50.71	50.34	52.36	52.26	51.83	51.82	47.39
CaO	0.11	0.12	0.08	0.07	0.10	0.17	0.16	0.17	0.02	0.01	0.01	0.12	0.10	0.12	0.08	0.02
Na_2O	0.02	0.06	0.01	0.02	0.04	0.00	0.01	0.02	0.02	n.d.	0.01	0.02	0.03	0.03	0.04	n.d.
K_2O	n.d.	0.02	n.d.	n.d.	n.d.	0.02	n.d.	0.01	n.d.	n.d.	0.01	0.01	n.d.	n.d.	n.d.	n.d.
Total	***100.21***	***100.46***	***100.18***	***99.99***	***101.74***	***100.85***	***100.51***	***100.79***	***100.53***	***100.69***	***100.21***	***100.94***	***100.16***	***100.62***	***99.80***	***100.18***
Stoich.	**4O**	**4O**	**4O**	**4O**	**4O**	**4O**	**4O**	**4O**	**4O**	**4O**	**4O**	**4O**	**4O**	**4O**	**4O**	**4O**
Si	1.000	1.000	1.002	0.999	0.998	0.999	1.000	0.995	1.001	0.996	0.992	0.992	0.992	0.995	0.999	1.005
Ti	0.000	0.000	0.000	0.001	-	0.001	0.000	0.000	-	0.000	0.000	0.000	0.000	-	0.000	0.000
Al	0.001	0.001	0.001	0.001	0.000	0.001	0.000	0.000	-	-	-	0.000	-	-	0.000	-
Cr	0.001	0.004	0.002	0.000	0.000	-	0.001	0.000	-	-	0.000	0.000	0.004	0.002	0.006	0.000
Fe	0.126	0.125	0.145	0.207	0.218	0.229	0.226	0.226	0.165	0.166	0.172	0.132	0.122	0.133	0.118	0.234
Mn	0.002	0.002	0.002	0.004	0.005	0.006	0.006	0.006	0.003	0.004	0.005	0.003	0.001	0.004	0.003	0.006
Ni	0.008	0.009	0.004	0.008	0.005	0.006	0.006	0.006	0.009	0.007	0.008	0.006	0.006	0.007	0.005	0.007
Mg	1.856	1.853	1.839	1.779	1.770	1.754	1.755	1.764	1.820	1.829	1.828	1.871	1.877	1.859	1.865	1.741
Ca	0.003	0.003	0.002	0.002	0.003	0.004	0.004	0.004	0.001	0.000	0.000	0.003	0.002	0.003	0.002	0.000
Na	0.001	0.003	0.000	0.001	0.002	-	0.001	0.001	0.001	-	0.001	0.001	0.001	0.001	0.002	-
K	-	0.001	-	-	-	0.001	-	0.000	-	-	0.000	0.000	-	-	-	-
Total	***2.999***	***2.999***	***2.997***	***3.001***	***3.002***	***3.000***	***2.999***	***3.005***	***3.000***	***3.004***	***3.008***	***3.008***	***3.006***	***3.004***	***2.999***	***2.994***
Mg#	***93.63***	***93.66***	***92.69***	***89.57***	***89.01***	***88.44***	***88.57***	***88.62***	***91.69***	***91.66***	***91.39***	***93.40***	***93.91***	***93.30***	***94.06***	***88.17***

Table A3-1: Representative major element composition and stoichiometry of ***olivine*** in peridotite xenoliths from Marsabit (continued)

Group	**III-c**	**III-c**	**III-d**	**III-d**	**III-d**	**IV**	**IV**	**IV**	**IV**	**IV**	**IV**	**IV**	**IV**	**IV**
sample	1965/25	1965/25	1970/6	1970/6	1970/6	1961/1	1961/1	1961/1	1961/1	1961/1	1961/1	1968/1	1968/1	1968/1
mineral	**ol-I**	**ol-I**	**ol-I**	**ol-I**	**ol-I**	**ol-I**	**ol-I**	**ol-I**	**ol-I**	**ol-IIa**	**ol-IIa**	**ol-I**	**ol-IIa**	**ol-IIa**
loaction	core	core	core	core	core	core	core	rim (opx)	rim (spl)	core (next opx)	core (next spl)	core	core	rim (spl)
SiO_2	40.91	40.90	41.07	41.05	41.26	41.48	41.04	41.32	40.63	41.46	40.95	41.20	41.19	40.67
TiO_2	n.d.	0.01	0.04	n.d.	n.d.	n.d.	0.02	n.d.	0.01	0.01	n.d.	0.03	0.03	n.d.
Al_2O_3	n.d.	0.02	0.03	0.02	0.03	n.d.	0.01	n.d.	0.02	0.02	0.01	0.02	n.d.	0.04
Cr_2O_3	0.08	0.03	0.08	0.07	n.d.	0.01	0.05	n.d.	0.22	0.05	0.32	n.d.	0.02	0.10
FeO	11.36	11.48	8.05	7.74	7.69	7.48	7.25	7.36	8.53	7.40	8.24	9.21	9.37	10.26
MnO	0.27	0.28	0.12	0.11	0.14	0.14	0.09	0.13	0.12	0.10	0.14	0.07	0.09	0.14
NiO	0.34	0.37	0.33	0.33	0.44	0.43	0.50	0.42	0.35	0.35	0.31	0.35	0.35	0.34
MgO	48.03	47.65	50.81	50.91	50.97	51.12	50.53	51.02	49.92	51.00	50.06	49.71	49.62	48.51
CaO	0.03	0.03	0.08	0.06	0.07	0.01	0.04	0.07	0.07	0.11	0.10	0.01	0.01	0.05
Na_2O	0.01	n.d.	n.d.	0.01	0.01	0.03	0.02	0.01	n.d.	0.01	n.d.	n.d.	0.02	0.02
K_2O	n.d.	n.d.	n.d.	n.d.	0.02	0.01	0.01	n.d.	n.d.	n.d.	n.d.	n.d.	n.d.	0.02
Total	***101.04***	***100.77***	***100.62***	***100.31***	***100.64***	***100.70***	***99.55***	***100.33***	***99.87***	***100.52***	***100.12***	***100.61***	***100.71***	***100.15***
Stoich.	**4O**	**4O**	**4O**	**4O**	**4O**	**4O**	**4O**	**4O**	**4O**	**4O**	**4O**	**4O**	**4O**	**4O**
Si	1.001	1.003	0.994	0.995	0.997	1.000	1.000	0.999	0.994	1.001	0.997	1.001	1.001	0.999
Ti	-	0.000	0.001	-	-	0.000	0.000	-	0.000	0.000	-	0.001	0.001	-
Al	-	0.001	0.001	0.000	0.001	-	0.000	-	0.001	0.001	0.000	0.001	-	0.001
Cr	0.002	0.001	0.002	0.001	-	0.000	0.001	-	0.004	0.001	0.006	-	0.000	0.002
Fe	0.232	0.235	0.163	0.157	0.155	0.151	0.148	0.149	0.174	0.149	0.168	0.187	0.190	0.211
Mn	0.006	0.006	0.003	0.002	0.003	0.003	0.002	0.003	0.002	0.002	0.003	0.001	0.002	0.003
Ni	0.007	0.007	0.007	0.007	0.009	0.008	0.010	0.008	0.007	0.007	0.006	0.007	0.007	0.007
Mg	1.751	1.742	1.833	1.840	1.836	1.837	1.836	1.840	1.820	1.835	1.817	1.800	1.797	1.776
Ca	0.001	0.001	0.002	0.002	0.002	0.000	0.001	0.002	0.002	0.003	0.002	0.000	0.000	0.001
Na	0.001	-	-	0.001	0.001	0.001	0.001	0.000	-	0.001	-	-	0.001	0.001
K	-	-	-	-	0.001	0.000	0.000	-	-	-	-	-	-	0.001
Total	***2.999***	***2.996***	***3.004***	***3.004***	***3.003***	***3.001***	***2.999***	***3.001***	***3.004***	***2.999***	***3.000***	***2.998***	***2.999***	***3.000***
Mg#	***88.29***	***88.09***	***91.84***	***92.14***	***92.20***	***92.42***	***92.55***	***92.51***	***91.26***	***92.47***	***91.55***	***90.59***	***90.42***	***89.40***

Table A3-2: Representative major element composition and stoichiometry of ***spinel*** in peridotite xenoliths from Marsabit

Group	**I**	**I**	**I**	**I**	**I**	**I**	**I**	**I**	**I**	**I**	**I**	**I**	**I**	**I**	**I**	**I**	**I**
sample	1960/2	1960/2	1960/2	1960/2	1960/2	1960/2	1960/2	1963/2	1963/2	1963/2	1963/2	1963/2	1963/2	1965/4	1965/4	1965/4	1965/4
mineral	**spl-IIa**	**spl-IIa**	**spl-IIa**	**spl-IIa**	**spl-IIb**	**spl-IIb**	**spl-IIb**	**spl-IIa**	**spl-IIa**	**spl-IIa**	**spl-IIb**	**spl-IIb**	**spl-IIb**	**spl-IIa**	**spl-IIa**	**spl-IIa**	**spl-IIa**
loaction	core	core	rim (cpx)	rim (ol)	sympl.	sympl.	sympl.	core	core	core	sympl.	sympl.	sympl.	core	core	rim (ol)	rim (ol)
SiO_2	n.d.	0.00	0.06	0.03	0.04	0.02	n.d.	0.05	0.03	0.01	0.02	n.d.	0.07	n.d.	n.d.	0.01	n.d.
TiO_2	0.06	0.04	0.07	0.00	0.01	0.03	0.03	0.06	0.02	0.09	0.01	0.02	0.03	0.07	0.04	0.06	0.04
Al_2O_3	51.51	53.58	52.74	53.56	63.70	62.34	63.01	57.24	57.76	54.86	63.80	64.09	63.41	57.16	53.63	57.92	53.07
Cr_2O_3	17.62	15.08	15.36	15.12	4.32	4.59	4.74	10.44	10.55	13.01	3.82	3.47	4.01	11.17	14.92	11.14	15.96
Fe_2O_3	0.72	0.61	1.04	0.81	0.94	1.48	1.21	0.91	0.70	1.50	0.71	0.83	0.77	1.05	1.14	0.56	1.22
FeO	10.72	10.80	10.52	10.69	8.91	8.57	9.03	9.83	9.89	10.25	8.82	8.69	9.01	9.39	10.01	9.77	9.88
MnO	0.18	0.06	0.09	0.06	0.12	0.11	0.08	0.14	0.14	0.14	0.10	0.09	0.12	0.10	0.18	0.06	0.17
NiO	0.33	0.29	0.28	0.27	0.41	0.45	0.44	0.40	0.36	0.34	0.41	0.46	0.46	0.33	0.35	0.35	0.24
MgO	18.89	19.13	19.21	19.24	21.31	21.06	21.11	19.92	20.02	19.52	21.17	21.26	20.98	20.37	19.57	20.32	19.76
CaO	0.01	0.00	0.03	0.00	0.03	0.10	0.07	n.d.	n.d.	0.02	n.d.	n.d.	0.02	n.d.	0.01	0.02	n.d.
ZnO	0.18	0.00	0.00	0.00	n.a.	0.08	n.a.	0.06	0.03	0.16	0.11	0.10	0.16	0.05	0.00	0.06	0.06
Total	***100.21***	***99.60***	***99.40***	***99.79***	***99.78***	***98.83***	***99.74***	***99.06***	***99.51***	***99.90***	***98.98***	***99.01***	***99.04***	***99.69***	***99.87***	***100.27***	***100.39***
Stoich.	**4O**	**4O**	**4O**	**4O**	**4O**	**4O**	**4O**	**4O**	**4O**	**4O**	**4O**	**4O**	**4O**	**4O**	**4O**	**4O**	**4O**
Si	-	0.000	0.002	0.001	0.001	0.000	-	0.001	0.001	0.000	0.001	-	0.002	-	-	0.000	-
Ti	0.001	0.001	0.001	0.000	0.000	0.001	0.001	0.001	0.000	0.002	0.000	0.000	0.001	0.001	0.001	0.001	0.001
Al	1.613	1.671	1.651	1.667	1.894	1.877	1.881	1.761	1.767	1.696	1.908	1.914	1.900	1.748	1.665	1.759	1.643
Cr	0.370	0.315	0.322	0.316	0.086	0.093	0.095	0.216	0.217	0.270	0.077	0.070	0.081	0.229	0.311	0.227	0.331
Fe^{3+}	0.014	0.012	0.021	0.016	0.018	0.029	0.023	0.018	0.014	0.030	0.014	0.016	0.015	0.020	0.023	0.011	0.024
Fe^{2+}	0.238	0.239	0.234	0.236	0.188	0.183	0.191	0.215	0.215	0.225	0.187	0.184	0.192	0.204	0.221	0.211	0.217
Mn	0.004	0.001	0.002	0.001	0.003	0.002	0.002	0.003	0.003	0.003	0.002	0.002	0.003	0.002	0.004	0.001	0.004
Ni	0.007	0.006	0.006	0.006	0.008	0.009	0.009	0.008	0.008	0.007	0.008	0.009	0.009	0.007	0.007	0.007	0.005
Mg	0.748	0.754	0.760	0.757	0.802	0.802	0.797	0.775	0.775	0.763	0.801	0.803	0.795	0.788	0.769	0.781	0.774
Ca	0.000	0.000	0.001	0.000	0.001	0.003	0.002	-	-	0.000	-	-	0.000	-	0.000	0.001	-
Zn	0.003	0.000	0.000	0.000	-	0.002	-	0.001	0.001	0.003	0.002	0.002	0.003	0.001	0.000	0.001	0.001
Total	***3.000***	***3.000***	***3.000***	***3.000***	***3.000***	***3.000***	***3.000***	***3.000***	***3.000***	***3.000***	***3.000***	***3.000***	***3.000***	***3.000***	***3.000***	***3.000***	***3.000***
Mg#	***75.86***	***75.94***	***76.50***	***76.24***	***81.00***	***81.41***	***80.64***	***78.32***	***78.29***	***77.24***	***81.05***	***81.35***	***80.59***	***79.46***	***77.70***	***78.75***	***78.08***
Cr#	***18.53***	***15.78***	***16.17***	***15.79***	***4.31***	***4.64***	***4.75***	***10.80***	***10.85***	***13.52***	***3.83***	***3.48***	***4.04***	***11.47***	***15.55***	***11.37***	***16.59***

the abbreviation in brackets under location indicates the adjacent mineral phase of the respective rim analysis; n.a.: not analysed; n.d.: not detected; Stoich.: cations calculated on the basis of 4 oxygens; Mg# = 100*Mg/(Mg+Fe^{2+}); Cr# = 100*Cr/(Cr+Al+Fe^{3+}); Fe_2O_3 calculated assuming perfect stoichiometry

Table A3-2: Representative major element composition and stoichiometry of ***spinel*** in peridotite xenoliths from Marsabit (continued)

Group	**I**	**I**	**I**	**II**	**II**	**II**	**II**	**II**	**II**	**II**	**II**	**II**	**II**	**II**	**II**	**II**
sample	1965/4	1965/4	1965/4	1958/13	1958/13	1958/13	1958/13	1958/13	1958/13	1958/13	1958/20	1958/20	1958/20	1958/20	1958/20	1958/20
mineral	**spl-IIb**	**spl-IIb**	**spl-IIb**	**spl-IIb**	**spl-IIb**	**spl-IIb**	**spl-IIb**	**spl-IIb**	**spl-IIb**	**Chr_m**	**spl-I**	**spl-I**	**spl-I**	**spl-I**	**spl-IIb**	**spl-IIb**
loaction	sympl.	sympl.	sympl.	core	core	rim (ol)	rim (opx)	sympl.	sympl.	core	core	core	rim (ol)	rim (opx)	sympl.	sympl.
SiO_2	0.09	0.06	0.05	0.04	0.04	0.07	0.05	0.06	0.04	0.08	0.06	0.05	0.08	0.03	0.05	0.08
TiO_2	0.02	0.04	0.07	0.06	0.06	0.08	0.05	0.06	0.08	0.74	0.19	0.19	0.19	0.20	0.17	0.17
Al_2O_3	60.95	62.54	63.66	58.90	56.56	58.80	56.77	57.39	56.75	46.60	56.97	57.49	57.98	56.76	56.87	57.52
Cr_2O_3	7.03	5.76	4.32	9.48	11.47	9.90	11.07	10.72	10.76	20.87	8.99	8.40	8.58	9.14	9.11	8.88
Fe_2O_3	1.02	1.03	0.78	1.03	1.53	0.85	1.32	1.43	1.67	3.52	3.36	3.23	2.60	3.18	3.39	3.24
FeO	9.01	8.45	8.76	8.50	8.46	8.56	8.44	8.20	8.38	5.87	7.69	7.83	8.05	8.10	7.98	8.21
MnO	0.10	0.07	0.10	0.08	0.09	0.05	0.17	0.11	0.13	0.11	0.16	0.14	0.08	0.13	0.11	0.03
NiO	0.30	0.36	0.45	0.34	0.36	0.32	0.29	0.30	0.28	0.30	0.41	0.43	0.43	0.38	0.37	0.29
MgO	20.94	21.54	21.34	21.11	20.88	21.20	20.77	21.18	20.85	22.10	21.37	21.29	21.29	21.05	21.15	21.35
CaO	0.04	0.03	0.03	0.01	n.d.	0.01	0.04	0.01	0.01	0.08	0.02	n.d.	n.d.	0.01	0.02	n.d.
ZnO	0.22	0.21	0.13	0.12	0.07	0.10	0.07	0.07	0.13	0.04	0.03	0.08	0.12	0.07	0.16	0.12
Total	***99.71***	***100.08***	***99.70***	***99.66***	***99.52***	***99.94***	***99.06***	***99.51***	***99.08***	***100.32***	***99.26***	***99.12***	***99.40***	***99.06***	***99.39***	***99.88***
Stoich.	**4O**	**4O**	**4O**	**4O**	**4O**	**4O**	**4O**	**4O**	**4O**	**4O**	**4O**	**4O**	**4O**	**4O**	**4O**	**4O**
Si	0.002	0.002	0.001	0.001	0.001	0.002	0.001	0.002	0.001	0.002	0.002	0.001	0.002	0.001	0.001	0.002
Ti	0.000	0.001	0.001	0.001	0.001	0.002	0.001	0.001	0.002	0.015	0.004	0.004	0.004	0.004	0.003	0.003
Al	1.833	1.861	1.894	1.783	1.730	1.776	1.742	1.748	1.741	1.458	1.740	1.755	1.763	1.740	1.738	1.746
Cr	0.142	0.115	0.086	0.193	0.235	0.201	0.228	0.219	0.221	0.438	0.184	0.172	0.175	0.188	0.187	0.181
Fe^{3+}	0.020	0.020	0.015	0.020	0.030	0.016	0.026	0.028	0.033	0.070	0.065	0.063	0.050	0.062	0.066	0.063
Fe^{2+}	0.192	0.178	0.185	0.183	0.184	0.183	0.184	0.177	0.182	0.130	0.167	0.170	0.174	0.176	0.173	0.177
Mn	0.002	0.001	0.002	0.002	0.002	0.001	0.004	0.002	0.003	0.002	0.003	0.003	0.002	0.003	0.002	0.001
Ni	0.006	0.007	0.009	0.007	0.007	0.007	0.006	0.006	0.006	0.006	0.009	0.009	0.009	0.008	0.008	0.006
Mg	0.797	0.811	0.803	0.808	0.808	0.810	0.806	0.816	0.809	0.875	0.825	0.822	0.819	0.816	0.818	0.820
Ca	0.001	0.001	0.001	0.000	-	0.000	0.001	0.000	0.000	0.002	0.001	-	-	0.000	0.001	-
Zn	0.004	0.004	0.002	0.002	0.001	0.002	0.001	0.001	0.003	0.001	0.001	0.001	0.002	0.001	0.003	0.002
Total	***3.000***	***3.000***	***3.000***	***3.000***	***3.000***	***3.000***	***3.000***	***3.000***	***3.000***	***3.000***	***3.000***	***3.000***	***3.000***	***3.000***	***3.000***	***3.000***
Mg#	***80.56***	***81.97***	***81.28***	***81.58***	***81.48***	***81.53***	***81.44***	***82.16***	***81.61***	***87.03***	***83.21***	***82.89***	***82.50***	***82.25***	***82.54***	***82.26***
Cr#	***7.11***	***5.76***	***4.32***	***9.65***	***11.80***	***10.06***	***11.42***	***10.98***	***11.10***	***22.28***	***9.25***	***8.64***	***8.80***	***9.44***	***9.38***	***9.09***

Table A3-2: Representative major element composition and stoichiometry of ***spinel*** in peridotite xenoliths from Marsabit (continued)

Group	**II**	**II**	**II**	**II**	**II**	**II**	**II**	**II**	**II**	**II**	**III-a**	**III-a**	**III-a**	**III-a**	**III-a**	**III-a**
sample	1959/24	1959/24	1959/24	1959/24	1959/24	1959/24	1959/25	1959/25	1959/25	1959/25	781/1	781/1	781/1	781/1	1965/1	1965/1
mineral	**spl-I**	**spl-I**	**spl-I**	**spl-I**	**spl-IIb**	**spl-IIb**	**spl-IIb**	**spl-IIb**	**spl-IIb**	**Chr_m**	**spl-I**	**spl-I**	**spl-I**	**spl-I**	**spl-I**	**spl-I**
loaction	core	core	rim (opx)	rim (ol)	sympl.	sympl.	sympl. core	sympl. core	sympl. rim (ol)	core	core	core	rim (ol)	rim (cpx)	core	core
SiO_2	0.04	0.10	0.07	0.08	0.04	0.05	0.03	0.05	0.12	0.15	n.d.	n.d.	n.d.	n.d.	n.d.	n.d.
TiO_2	0.18	0.23	0.20	0.25	0.18	0.21	0.16	0.19	0.23	0.26	0.09	0.06	0.09	0.09	0.10	0.10
Al_2O_3	53.75	53.77	53.82	53.93	53.62	53.92	52.06	51.70	50.51	49.69	52.37	51.95	52.47	52.47	40.06	40.28
Cr_2O_3	12.29	12.45	12.20	12.57	12.93	12.48	15.50	15.54	16.05	17.00	15.87	16.08	15.34	15.34	29.47	30.14
Fe_2O_3	3.30	3.15	3.42	3.58	3.08	2.84	3.03	3.28	3.32	3.26	2.45	2.08	2.39	2.39	0.77	1.23
FeO	8.62	8.57	8.64	8.64	8.26	8.59	7.66	7.53	8.49	8.19	8.82	8.78	8.39	8.39	11.08	11.07
MnO	0.06	0.10	0.12	0.13	0.13	0.12	0.10	0.13	0.09	0.10	0.14	0.16	0.11	0.11	0.20	0.10
NiO	0.40	0.43	0.30	0.35	0.45	0.33	0.36	0.32	0.35	0.38	0.37	0.33	0.30	0.30	0.23	0.20
MgO	20.47	20.53	20.54	20.77	20.65	20.53	21.05	21.11	20.43	20.52	20.32	20.12	20.50	20.50	17.45	17.87
CaO	n.d.	0.04	n.d.	n.d.	0.03	n.d.	n.d.	0.01	0.02	0.01	0.01	n.d.	0.01	0.01	n.d.	0.01
ZnO	0.02	0.12	0.11	0.07	0.04	0.06	0.12	0.10	0.02	0.10	0.12	0.15	0.14	0.14	0.11	0.16
Total	***99.12***	***99.48***	***99.42***	***100.39***	***99.42***	***99.13***	***100.06***	***99.97***	***99.63***	***99.66***	***100.55***	***99.71***	***99.73***	***99.73***	***99.46***	***101.15***
Stoich.	**4O**	**4O**	**4O**	**4O**	**4O**	**4O**	**4O**	**4O**	**4O**	**4O**	**4O**	**4O**	**4O**	**4O**	**4O**	**4O**
Si	0.001	0.003	0.002	0.002	0.001	0.001	0.001	0.001	0.003	0.004	-	-	-	-	-	-
Ti	0.004	0.004	0.004	0.005	0.004	0.004	0.003	0.004	0.005	0.005	0.002	0.001	0.002	0.002	0.002	0.002
Al	1.669	1.665	1.667	1.657	1.661	1.673	1.611	1.602	1.581	1.559	1.619	1.620	1.630	1.630	1.325	1.312
Cr	0.256	0.259	0.254	0.259	0.269	0.260	0.322	0.323	0.337	0.358	0.329	0.336	0.320	0.320	0.654	0.658
Fe^{3+}	0.065	0.062	0.068	0.070	0.061	0.056	0.060	0.065	0.066	0.065	0.048	0.041	0.047	0.047	0.016	0.026
Fe^{2+}	0.190	0.188	0.190	0.188	0.182	0.189	0.168	0.166	0.189	0.182	0.193	0.194	0.185	0.185	0.260	0.256
Mn	0.001	0.002	0.003	0.003	0.003	0.003	0.002	0.003	0.002	0.002	0.003	0.004	0.002	0.002	0.005	0.002
Ni	0.008	0.009	0.006	0.007	0.010	0.007	0.007	0.007	0.007	0.008	0.008	0.007	0.006	0.006	0.005	0.004
Mg	0.804	0.804	0.805	0.807	0.809	0.806	0.824	0.827	0.809	0.814	0.795	0.793	0.805	0.805	0.730	0.736
Ca	-	0.001	-	-	0.001	-	-	0.000	0.001	0.000	0.000	-	0.000	0.000	-	0.000
Zn	0.000	0.002	0.002	0.001	0.001	0.001	0.002	0.002	0.000	0.002	0.002	0.003	0.003	0.003	0.002	0.003
Total	***3.000***	***3.000***	***3.000***	***3.000***	***3.000***	***3.000***	***3.000***	***3.000***	***3.000***	***3.000***	***3.000***	***3.000***	***3.000***	***3.000***	***3.000***	***3.000***
Mg#	***80.89***	***81.02***	***80.91***	***81.08***	***81.67***	***80.98***	***83.04***	***83.33***	***81.09***	***81.72***	***80.42***	***80.33***	***81.34***	***81.34***	***73.74***	***74.22***
Cr#	***12.86***	***13.02***	***12.75***	***13.05***	***13.50***	***13.06***	***16.15***	***16.24***	***16.99***	***18.05***	***16.48***	***16.84***	***16.01***	***16.01***	***32.77***	***32.99***

Table A3-2: Representative major element composition and stoichiometry of ***spinel*** in peridotite xenoliths from Marsabit (continued)

Group	**III-a**	**III-a**	**III-a**	**III-a**	**III-b**	**III-b**	**III-b**	**III-b**	**III-b**	**III-c**	**III-c**	**III-c**	**III-c**	**III-c**	**III-c**	**III-c**
sample	1965/1	1965/1	1965/1	1965/1	1959/15	1959/15	1959/15	1959/15	1959/15	758*	758*	1965/3	1965/3	1965/3	1959/27	1959/27
mineral	**spl-I**	**spl-I**	**spl-IIb**	**spl-IIb**	**spl-I**	**spl-I**	**spl-I**	**spl-I**	**Chr_m**	**spl-I**	**Chr_m**	**Chr_m**	**Chr_m**	**Chr_m**	**Chr_m**	**Chr_m**
loaction	rim (ol)	rim (ol)	sympl.	sympl.	core	core	rim (glass)	rim (glass)	core	core	core	residual	core	core	core	rim (glass)
SiO_2	n.d.	n.d.	0.01	0.03	0.03	0.01	0.05	0.02	0.08	n.d.	n.d.	0.09	0.12	0.10	0.05	0.21
TiO_2	0.09	0.13	0.02	0.05	0.01	0.02	0.01	0.02	0.04	0.07	0.91	0.06	0.44	0.04	0.94	1.57
Al_2O_3	42.71	36.90	59.75	59.20	47.58	47.04	46.87	41.92	35.96	40.54	16.77	5.48	12.23	6.19	14.49	29.50
Cr_2O_3	26.62	31.98	8.82	9.27	21.44	22.08	22.21	27.75	33.55	25.93	52.01	66.38	54.54	65.07	50.99	33.48
Fe_2O_3	0.73	1.36	0.84	0.49	1.33	1.40	1.14	1.55	1.82	3.74	3.26	2.37	5.54	3.29	4.07	5.09
FeO	10.54	10.98	8.10	8.64	9.79	9.82	10.09	9.62	9.04	11.78	9.94	13.10	11.14	12.07	15.97	14.39
MnO	0.08	0.16	0.05	0.04	0.13	0.15	0.03	0.13	0.19	0.20	0.16	0.25	n.a.	n.a.	0.31	0.22
NiO	0.41	0.14	0.37	0.29	0.25	0.32	0.23	0.20	0.20	0.30	0.31	0.09	0.15	0.08	0.13	0.21
MgO	17.94	17.10	21.36	20.97	19.17	18.98	18.92	18.66	18.30	16.91	16.24	12.95	14.80	13.80	11.99	15.26
CaO	0.02	n.d.	0.01	n.d.	n.d.	n.d.	n.d.	0.10	0.04	n.d.	0.02	0.03	0.03	0.03	0.05	0.07
ZnO	0.19	0.23	0.12	0.16	0.05	0.19	0.14	0.11	0.20	0.25	0.15	0.07	0.12	0.06	0.11	0.16
Total	***99.33***	***98.99***	***99.46***	***99.15***	***99.78***	***100.01***	***99.69***	***100.09***	***99.42***	***99.71***	***99.78***	***100.86***	***99.10***	***100.74***	***99.10***	***100.15***
Stoich.	**4O**	**4O**	**4O**	**4O**	**4O**	**4O**	**4O**	**4O**	**4O**	**4O**	**4O**	**4O**	**4O**	**4O**	**4O**	**4O**
Si	-	-	0.000	0.001	0.001	0.000	0.001	0.001	0.002	-	-	0.003	0.004	0.003	0.002	0.006
Ti	0.002	0.003	0.000	0.001	0.000	0.000	0.000	0.000	0.001	0.002	0.021	0.001	0.011	0.001	0.023	0.035
Al	1.397	1.243	1.804	1.798	1.513	1.498	1.497	1.361	1.203	1.342	0.611	0.212	0.461	0.238	0.551	1.025
Cr	0.584	0.722	0.179	0.189	0.457	0.472	0.476	0.605	0.753	0.576	1.271	1.721	1.380	1.675	1.301	0.780
Fe^{3+}	0.015	0.029	0.016	0.009	0.027	0.028	0.023	0.032	0.039	0.079	0.076	0.059	0.133	0.081	0.099	0.113
Fe^{2+}	0.245	0.262	0.174	0.186	0.221	0.222	0.229	0.222	0.215	0.277	0.257	0.359	0.298	0.329	0.431	0.355
Mn	0.002	0.004	0.001	0.001	0.003	0.003	0.001	0.003	0.004	0.005	0.004	0.007	0.000	0.000	0.009	0.005
Ni	0.009	0.003	0.008	0.006	0.005	0.007	0.005	0.004	0.005	0.007	0.008	0.002	0.004	0.002	0.004	0.005
Mg	0.742	0.729	0.816	0.806	0.771	0.765	0.764	0.767	0.774	0.708	0.748	0.633	0.706	0.670	0.577	0.671
Ca	0.001	-	0.000	-	-	-	-	0.003	0.001	-	0.001	0.001	0.001	0.001	0.002	0.002
Zn	0.004	0.005	0.002	0.003	0.001	0.004	0.003	0.002	0.004	0.005	0.003	0.002	0.003	0.001	0.003	0.003
Total	***3.000***	***3.000***	***3.000***	***3.000***	***3.000***	***3.000***	***3.000***	***3.000***	***3.000***	***3.000***	***3.000***	***3.000***	***3.000***	***3.000***	***3.000***	***3.000***
Mg#	***75.20***	***73.52***	***82.45***	***81.22***	***77.73***	***77.51***	***76.98***	***77.57***	***78.30***	***71.90***	***74.45***	***63.78***	***70.32***	***67.09***	***57.23***	***65.41***
Cr#	***29.25***	***36.23***	***8.94***	***9.46***	***22.90***	***23.61***	***23.84***	***30.26***	***37.74***	***28.84***	***64.92***	***86.42***	***69.88***	***84.04***	***66.69***	***40.69***

Table A3-2: Representative major element composition and stoichiometry of ***spinel*** in peridotite xenoliths from Marsabit (continued)

Group	**III-d**	**IV**	**IV**	**IV**	**IV**	**IV**	**IV**	**IV**	**IV**	**IV**	**IV**	**IV**	**IV**	**IV**	**IV**
sample	1970/6	1961/1	1961/1	1961/1	1961/1	1961/1	1961/1	1968/1	1968/1	1968/1	1968/1	1968/1	1968/1	1968/1
mineral	**Chr_m**	**spl-I**	**spl-I**	**spl-I**	**spl-I**	**spl-IIa**	**spl-L**	**spl-I**	**spl-I**	**spl-I**	**spl-I**	**spl-I**	**spl-IIb**	**spl-IIb**
loaction	core	core	core	rim (ol)	rim (ol)	core	lamellae in cpx-I	core	core	rim (ol)	rim (ol)	rim (opx)	core	core
SiO_2	0.04	n.d.	n.d.	n.d.	n.d.	0.01	0.01	n.d.	n.d.	n.d.	n.d.	n.d.	n.d.	n.d.
TiO_2	0.21	n.d.	0.04	0.01	0.03	0.02	0.02	0.07	0.05	0.03	0.09	0.16	0.06	0.02
Al_2O_3	18.70	43.24	43.98	54.70	46.22	46.51	46.68	50.08	50.96	53.48	47.57	55.87	58.20	58.63
Cr_2O_3	49.82	25.66	25.08	13.54	22.93	23.50	22.21	17.03	16.25	14.27	19.65	11.39	9.46	8.69
Fe_2O_3	3.61	1.09	0.75	1.44	1.40	1.13	0.88	1.97	1.83	2.12	2.72	1.88	2.04	1.95
FeO	11.72	11.62	11.14	8.06	8.62	9.16	10.17	10.68	10.79	9.16	9.66	8.33	7.93	7.73
MnO	0.04	0.11	0.16	0.15	0.14	0.00	0.10	0.18	0.12	0.15	0.13	0.09	0.05	0.13
NiO	0.14	0.16	0.16	0.26	0.24	0.23	0.37	0.32	0.24	0.37	0.29	0.34	0.39	0.51
MgO	15.07	17.37	17.75	20.68	19.56	19.68	18.56	18.51	18.58	19.93	19.05	20.72	21.34	21.21
CaO	0.01	0.02	n.d.	0.01	n.d.	n.d.	n.a.	n.d.	0.01	n.d.	n.d.	n.d.	n.d.	0.01
ZnO	0.05	0.24	0.17	0.29	0.25	n.a.	0.15	0.20	0.25	0.26	0.20	0.21	0.13	0.17
Total	***99.41***	***99.52***	***99.23***	***99.15***	***99.40***	***100.25***	***99.16***	***99.04***	***99.07***	***99.77***	***99.36***	***99.01***	***99.60***	***99.05***
Stoich.	**4O**	**4O**	**4O**	**4O**	**4O**	**4O**	**4O**	**4O**	**4O**	**4O**	**4O**	**4O**	**4O**	**4O**
Si	0.001	-	-	-	-	0.000	0.000	-	-	-	-	-	-	-
Ti	0.005	-	0.001	0.000	0.001	0.000	0.000	0.001	0.001	0.001	0.002	0.003	0.001	0.000
Al	0.683	1.414	1.434	1.691	1.478	1.475	1.501	1.594	1.615	1.660	1.520	1.721	1.766	1.784
Cr	1.221	0.563	0.549	0.281	0.492	0.500	0.479	0.364	0.346	0.297	0.421	0.235	0.192	0.177
Fe^{3+}	0.084	0.023	0.016	0.028	0.029	0.023	0.018	0.040	0.037	0.042	0.055	0.037	0.040	0.038
Fe	0.304	0.270	0.258	0.177	0.196	0.206	0.232	0.241	0.243	0.202	0.219	0.182	0.171	0.167
Mn	0.001	0.003	0.004	0.003	0.003	0.000	0.002	0.004	0.003	0.003	0.003	0.002	0.001	0.003
Ni	0.003	0.004	0.004	0.006	0.005	0.005	0.008	0.007	0.005	0.008	0.006	0.007	0.008	0.011
Mg	0.696	0.719	0.732	0.809	0.791	0.790	0.755	0.745	0.745	0.782	0.770	0.808	0.819	0.816
Ca	0.000	0.001	-	0.000	-	-	-	-	0.000	-	-	-	-	0.000
Zn	0.001	0.005	0.004	0.006	0.005	-	0.003	0.004	0.005	0.005	0.004	0.004	0.003	0.003
Total	***3.000***	***3.000***	***3.000***	***3.000***	***3.000***	***3.000***	***3.000***	***3.000***	***3.000***	***3.000***	***3.000***	***3.000***	***3.000***	***3.000***
Mg#	***69.62***	***72.71***	***73.97***	***82.06***	***80.18***	***79.30***	***76.49***	***75.56***	***75.44***	***79.49***	***77.86***	***81.60***	***82.74***	***83.02***
Cr#	***61.41***	***28.15***	***27.46***	***14.03***	***24.61***	***25.02***	***23.98***	***18.20***	***17.29***	***14.86***	***21.10***	***11.81***	***9.63***	***8.87***

Table A3-3: Representative major element composition and stoichiometry of ***orthopyroxene*** in peridotite xenoliths from Marsabit

Group	**I**	**I**	**I**	**I**	**I**	**I**	**I**	**I**	**I**	**I**	**I**	**I**	**I**	**I**	**I**	**I**	**I**
sample	1960/2	1960/2	1960/2	1960/2	1960/2	1960/2	1960/2	1960/2	1960/2	1960/2	1963/1	1963/1	1963/1	1963/2	1963/2	1963/2	1963/2
mineral	**opx-I**	**opx-I**	**opx-I**	**opx-I**	**opx-I**	**opx-IIa**	**opx-IIa**	**opx-IIb**	**opx-L**	**opx-L**	**opx-I**	**opx-I**	**opx-IIb**	**opx-I**	**opx-I**	**opx-I**	**opx-I**
loaction	Al trough	Al trough	Al bulge	Al bulge	rim (cpx)	core	rim (spl)	sympl	lamellae in cpx	lamellae in cpx	core	rim (ol)	sympl	Al trough	Al trough	Al bulge	Al bulge
SiO_2	56.03	56.18	56.10	55.35	56.47	55.29	56.94	56.26	56.03	55.94	56.59	57.70	56.22	56.89	56.24	55.57	56.20
TiO_2	0.12	0.17	0.07	0.12	0.09	0.13	0.07	0.04	0.09	0.05	0.07	0.04	0.05	0.16	0.13	0.10	0.10
Al_2O_3	2.58	2.51	3.03	4.16	2.25	3.33	2.32	2.97	2.31	2.33	2.12	1.70	2.17	2.38	2.26	3.23	3.48
Cr_2O_3	0.40	0.35	0.38	0.27	0.16	0.40	0.26	0.19	0.39	0.46	0.18	0.10	0.14	0.27	0.24	0.26	0.19
FeO	6.55	6.31	6.40	6.43	6.42	6.38	6.43	6.32	7.03	7.25	5.59	5.50	6.11	6.55	6.58	6.57	6.42
MnO	0.21	0.17	0.19	0.16	0.18	0.18	0.13	0.18	0.13	0.17	0.20	0.09	0.21	0.16	0.18	0.19	0.19
NiO	n.a.	n.a.	0.08	0.09	0.07	0.06	0.09	0.06	n.a.	n.a.	0.03	0.14	0.11	n.d.	0.10	0.08	0.11
MgO	33.57	33.63	33.60	33.31	34.07	33.17	34.53	33.82	33.49	33.51	34.30	35.04	33.92	34.51	33.76	33.36	34.15
CaO	0.55	0.54	0.29	0.40	0.34	0.45	0.25	0.25	0.44	0.38	0.36	0.26	0.35	0.37	0.54	0.30	0.24
Na_2O	0.06	0.06	0.04	0.06	0.03	0.03	0.05	0.04	0.05	0.04	0.05	0.03	0.04	0.03	0.05	0.01	0.03
K_2O	0.01	n.d.	n.d.	0.01	0.02	0.01	0.01	0.01	n.d.	n.d.	0.01	n.d.	0.01	0.01	n.d.	n.d.	0.01
Total	***100.08***	***99.92***	***100.18***	***100.36***	***100.10***	***99.41***	***101.07***	***100.13***	***99.96***	***100.13***	***99.50***	***100.59***	***99.32***	***101.32***	***100.08***	***99.67***	***101.12***
Stoich.	**6O**	**6O**	**6O**	**6O**	**6O**	**6O**	**6O**	**6O**	**6O**	**6O**	**6O**	**6O**	**6O**	**6O**	**6O**	**6O**	**6O**
Si	1.936	1.941	1.933	1.906	1.947	1.922	1.944	1.937	1.941	1.938	1.955	1.968	1.951	1.939	1.943	1.926	1.919
Ti	0.003	0.004	0.002	0.003	0.002	0.003	0.002	0.001	0.002	0.001	0.002	0.001	0.001	0.004	0.003	0.003	0.003
Al	0.105	0.102	0.123	0.169	0.091	0.136	0.094	0.120	0.094	0.095	0.086	0.068	0.089	0.095	0.092	0.132	0.140
Cr	0.011	0.010	0.010	0.007	0.004	0.011	0.007	0.005	0.011	0.013	0.005	0.003	0.004	0.007	0.007	0.007	0.005
Fe	0.189	0.182	0.185	0.185	0.185	0.185	0.183	0.182	0.204	0.210	0.161	0.157	0.177	0.187	0.190	0.191	0.183
Mn	0.006	0.005	0.006	0.005	0.005	0.005	0.004	0.005	0.004	0.005	0.006	0.003	0.006	0.005	0.005	0.005	0.005
Ni	-	-	0.002	0.003	0.002	0.002	0.002	0.002	-	-	0.001	0.004	0.003	-	0.003	0.002	0.003
Mg	1.729	1.732	1.726	1.709	1.752	1.719	1.757	1.736	1.730	1.730	1.766	1.782	1.755	1.754	1.739	1.724	1.738
Ca	0.020	0.020	0.011	0.015	0.012	0.017	0.009	0.009	0.016	0.014	0.013	0.009	0.013	0.013	0.020	0.011	0.009
Na	0.004	0.004	0.003	0.004	0.002	0.002	0.003	0.002	0.003	0.003	0.003	0.002	0.003	0.002	0.004	0.000	0.002
K	0.000	-	-	0.000	0.001	0.000	0.000	0.000	-	-	0.001	-	0.000	0.000	-	-	0.000
Total	***4.005***	***4.001***	***4.000***	***4.005***	***4.004***	***4.002***	***4.006***	***4.001***	***4.006***	***4.009***	***4.000***	***3.997***	***4.003***	***4.007***	***4.006***	***4.002***	***4.007***
Mg#	***90.13***	***90.48***	***90.34***	***90.23***	***90.44***	***90.26***	***90.55***	***90.51***	***89.47***	***89.18***	***91.63***	***91.91***	***90.82***	***90.37***	***90.14***	***90.05***	***90.47***

the abbreviation in brackets under location indicates the adjacent mineral phase of the respective rim analysis; n.a.: not analysed; n.d.: not detected; Stoich.: cations calculated on the basis of 6 oxygens; Mg# = $100*Mg/(Mg+Fe^{tot})$;

Table A3-3: Representative major element composition and stoichiometry of ***orthopyroxene*** in peridotite xenoliths from Marsabit (continued)

Group	**I**	**I**	**I**	**I**	**I**	**I**	**I**	**I**	**I**	**I**	**I**	**I**	**I**	**I**	**I**	**I**
sample	1963/2	1963/2	1963/2	1963/2	1963/2	1963/2	1963/2	1963/2	1963/2	1963/2	1965/4	1965/4	1965/4	1965/4	1965/4	1965/4
mineral	**opx-I**	**opx-I**	**opx-IIa**	**opx-IIa**	**opx-IIa**	**opx-IIa**	**opx-IIb**	**opx-IIb**	**opx-L**	**opx-L**	**opx-I**	**opx-I**	**opx-I**	**opx-I**	**opx-I**	**opx-I**
loaction	rim (ol)	rim (ol)	core	core	rim (cpx)	rim (cpx)	sympl	sympl	lamellae in cpx	lamellae in cpx	Al trough	Al trough	Al bulge	Al bulge	rim	rim
SiO_2	56.93	56.29	55.70	56.15	56.39	57.08	55.72	55.70	56.24	57.15	56.22	55.86	55.43	55.32	56.36	57.11
TiO_2	0.06	0.05	0.10	0.07	0.07	0.10	0.08	0.05	0.15	0.11	0.17	0.17	0.13	0.12	0.10	0.07
Al_2O_3	1.86	2.14	3.46	3.29	2.44	1.82	3.11	2.76	2.50	1.72	2.24	2.28	3.16	3.32	1.76	1.27
Cr_2O_3	0.09	0.08	0.28	0.19	0.15	0.13	0.08	0.05	0.38	0.17	0.36	0.39	0.36	0.25	0.07	0.15
FeO	6.26	6.56	6.88	6.65	6.55	6.44	6.66	6.69	7.27	7.85	6.36	6.36	6.53	6.64	6.16	6.06
MnO	0.18	0.17	0.18	0.18	0.12	0.17	0.17	0.14	0.24	0.22	0.16	0.17	0.16	0.14	0.14	0.18
NiO	0.10	0.05	n.a.	0.11	0.12	0.10	0.10	0.04	n.a.	n.a.	n.a.	0.04	n.a.	0.07	n.a.	n.a.
MgO	34.50	34.08	33.61	33.37	33.70	34.29	33.41	33.53	33.56	33.57	34.08	33.91	33.68	33.22	34.47	34.70
CaO	0.28	0.28	0.42	0.40	0.37	0.29	0.26	0.30	0.50	0.45	0.46	0.46	0.22	0.36	0.31	0.28
Na_2O	0.04	0.04	0.03	0.05	0.04	0.05	0.02	0.02	0.04	0.06	0.05	0.05	0.04	0.04	0.01	0.03
K_2O	n.d.	0.01	n.d.	n.d.	0.02	n.d.	0.01	n.d.	n.d.	n.d.	0.01	n.d.	0.01	0.01	0.01	0.03
Total	***100.28***	***99.76***	***100.65***	***100.46***	***99.97***	***100.49***	***99.61***	***99.28***	***100.88***	***101.30***	***100.12***	***99.71***	***99.72***	***99.47***	***99.38***	***99.89***
Stoich.	**6O**	**6O**	**6O**	**6O**	**6O**	**6O**	**6O**	**6O**	**6O**	**6O**	**6O**	**6O**	**6O**	**6O**	**6O**	**6O**
Si	1.957	1.948	1.915	1.931	1.947	1.959	1.932	1.938	1.934	1.959	1.940	1.937	1.921	1.923	1.954	1.969
Ti	0.001	0.001	0.003	0.002	0.002	0.003	0.002	0.001	0.004	0.003	0.004	0.004	0.003	0.003	0.003	0.002
Al	0.075	0.087	0.140	0.133	0.099	0.074	0.127	0.113	0.101	0.069	0.091	0.093	0.129	0.136	0.072	0.052
Cr	0.002	0.002	0.008	0.005	0.004	0.004	0.002	0.001	0.010	0.005	0.010	0.011	0.010	0.007	0.002	0.004
Fe	0.180	0.190	0.198	0.191	0.189	0.185	0.193	0.195	0.209	0.225	0.183	0.184	0.189	0.193	0.178	0.175
Mn	0.005	0.005	0.005	0.005	0.004	0.005	0.005	0.004	0.007	0.006	0.005	0.005	0.005	0.004	0.004	0.005
Ni	0.003	0.001	-	0.003	0.003	0.003	0.003	0.001	-	-	-	0.001	-	0.002	-	-
Mg	1.768	1.758	1.723	1.711	1.735	1.755	1.727	1.739	1.721	1.715	1.753	1.752	1.740	1.721	1.782	1.783
Ca	0.010	0.010	0.015	0.015	0.014	0.011	0.009	0.011	0.019	0.017	0.017	0.017	0.008	0.013	0.011	0.010
Na	0.003	0.003	0.002	0.003	0.003	0.003	0.001	0.002	0.003	0.004	0.003	0.003	0.002	0.002	0.001	0.002
K	-	0.000	-	-	0.001	-	0.000	-	-	-	0.000	-	0.000	0.000	0.001	0.001
Total	***4.004***	***4.007***	***4.009***	***4.000***	***4.001***	***4.001***	***4.002***	***4.005***	***4.008***	***4.003***	***4.007***	***4.009***	***4.008***	***4.004***	***4.007***	***4.003***
Mg#	***90.76***	***90.25***	***89.70***	***89.94***	***90.17***	***90.47***	***89.94***	***89.94***	***89.17***	***88.40***	***90.53***	***90.48***	***90.18***	***89.92***	***90.89***	***91.08***

Table A3-3: Representative major element composition and stoichiometry of ***orthopyroxene*** in peridotite xenoliths from Marsabit (continued)

Group	**I**	**I**	**I**	**I**	**I**	**I**	**I**	**I**	**II**	**II**	**II**	**II**	**II**	**II**	**II**	**II**
sample	1965/4	1965/4	1965/4	1965/4	1965/4	1965/4	1965/4	1965/4	1958/6	1958/6	1958/6	1958/6	1958/13	1958/13	1958/13	1958/13
mineral	**opx-IIa**	**opx-IIa**	**opx-IIa**	**opx-IIa**	**opx-IIb**	**opx-IIb**	**opx-L**	**opx-L**	**opx-I**	**opx-I**	**opx-IIb**	**opx-IIb**	**opx-I**	**opx-I**	**opx-IIb**	**opx-IIb**
loaction	core	core	rim (opx)	rim (cpx)	sympl	sympl	lamellae in cpx	lamellae in cpx	core	rim (cpx)	sympl/ core	sympl/rim (spl)	core	rim	sympl/ core	sympl/ rim
SiO_2	55.18	55.77	56.60	56.28	56.21	56.23	55.90	55.98	54.24	54.10	54.12	53.54	55.68	56.53	56.17	56.17
TiO_2	0.11	0.15	0.09	0.14	0.04	0.09	0.08	0.16	0.18	0.19	0.23	0.22	0.06	0.06	0.05	0.02
Al_2O_3	3.20	2.98	1.48	2.01	2.61	2.90	2.39	2.44	5.06	5.46	5.31	5.74	3.72	3.04	3.31	3.17
Cr_2O_3	0.30	0.48	0.15	0.28	0.14	0.16	0.39	0.31	0.49	0.49	0.55	0.61	0.32	0.20	0.26	0.27
FeO	6.44	6.47	6.32	6.56	6.59	6.45	7.16	7.20	7.22	7.64	8.07	8.08	6.17	6.00	5.82	5.84
MnO	0.24	0.17	0.22	0.10	0.18	0.12	0.20	0.19	0.17	0.18	0.21	0.19	0.13	0.10	0.10	0.13
NiO	0.08	0.03	n.a.	0.01	0.00	0.14	n.a.	n.a.	n.a.	n.a.	n.a.	n.a.	n.a.	n.a.	0.09	0.09
MgO	33.38	33.70	34.57	34.22	34.12	33.76	32.85	32.98	31.44	30.96	30.83	30.14	33.86	34.20	33.89	33.93
CaO	0.29	0.33	0.28	0.40	0.41	0.35	0.55	0.48	1.30	1.58	1.25	1.59	0.36	0.61	0.41	0.54
Na_2O	0.02	0.03	0.03	0.05	0.03	0.01	0.07	0.07	0.14	0.18	0.17	0.19	0.10	0.11	0.10	0.10
K_2O	n.d.	n.d.	0.02	n.d.	n.d.	n.d.	0.02	n.d.	0.02	0.03	0.01	0.01	n.d.	n.d.	n.d.	0.02
Total	***99.24***	***100.11***	***99.76***	***100.04***	***100.32***	***100.20***	***99.61***	***99.81***	***100.26***	***100.81***	***100.73***	***100.31***	***100.38***	***100.86***	***100.20***	***100.28***
Stoich.	**6O**	**6O**	**6O**	**6O**	**6O**	**6O**	**6O**	**6O**	**6O**	**6O**	**6O**	**6O**	**6O**	**6O**	**6O**	**6O**
Si	1.922	1.925	1.958	1.944	1.936	1.936	1.945	1.944	1.883	1.873	1.877	1.867	1.913	1.931	1.930	1.930
Ti	0.003	0.004	0.002	0.004	0.001	0.002	0.002	0.004	0.005	0.005	0.006	0.006	0.002	0.001	0.001	0.001
Al	0.131	0.121	0.060	0.082	0.106	0.118	0.098	0.100	0.207	0.223	0.217	0.236	0.151	0.123	0.134	0.128
Cr	0.008	0.013	0.004	0.008	0.004	0.004	0.011	0.009	0.013	0.013	0.015	0.017	0.009	0.006	0.007	0.007
Fe	0.188	0.187	0.183	0.190	0.190	0.186	0.208	0.209	0.210	0.221	0.234	0.236	0.177	0.171	0.167	0.168
Mn	0.007	0.005	0.006	0.003	0.005	0.003	0.006	0.006	0.005	0.005	0.006	0.006	0.004	0.003	0.003	0.004
Ni	0.002	0.001	-	0.000	0.000	0.004	-	-	-	-	-	-	-	-	0.003	0.003
Mg	1.733	1.734	1.782	1.762	1.751	1.733	1.704	1.707	1.627	1.598	1.594	1.567	1.734	1.742	1.735	1.738
Ca	0.011	0.012	0.011	0.015	0.015	0.013	0.021	0.018	0.048	0.058	0.046	0.060	0.013	0.022	0.015	0.020
Na	0.001	0.002	0.002	0.004	0.002	0.000	0.004	0.005	0.009	0.012	0.011	0.013	0.006	0.008	0.007	0.006
K	-	-	0.001	-	-	-	0.001	-	0.001	0.001	0.001	0.000	-	-	-	0.001
Total	***4.006***	***4.005***	***4.009***	***4.010***	***4.009***	***4.000***	***4.001***	***4.000***	***4.007***	***4.010***	***4.007***	***4.007***	***4.009***	***4.007***	***4.002***	***4.005***
Mg#	***90.23***	***90.28***	***90.70***	***90.28***	***90.23***	***90.31***	***89.11***	***89.09***	***88.59***	***87.85***	***87.20***	***86.93***	***90.73***	***91.04***	***91.21***	***91.20***

Table A3-3: Representative major element composition and stoichiometry of ***orthopyroxene*** in peridotite xenoliths from Marsabit (continued)

Group	**II**	**II**	**II**	**II**	**II**	**II**	**II**	**II**	**II**	**II**	**II**	**II**	**III-a**	**III-a**	**III-a**	**III-a**
sample	1958/20	1958/20	1958/20	1958/20	1959/24	1959/24	1959/24	1959/24	1959/25	1959/25	1959/25	1959/25	781/6	781/6	781/6	781/6
mineral	**opx-I**	**opx-I**	**opx-IIb**	**opx-IIb**	**opx-I**	**opx-I**	**opx-IIb**	**opx-IIb**	**opx-I**	**opx-I**	**opx-IIb**	**opx-IIb**	**opx-I**	**opx-I**	**opx-I**	**opx-I**
loaction	core	rim (ol)	core	rim (cpx)	core	rim (cpx)	core	rim (cpx)	core	rim (cpx)	core	sympl	core	rim (cpx)	core	rim (spl)
SiO_2	53.73	53.71	54.19	53.96	54.92	54.30	54.55	54.74	55.83	55.79	55.12	55.37	55.49	55.80	55.45	55.46
TiO_2	0.15	0.13	0.14	0.15	0.12	0.16	0.15	0.15	0.12	0.13	0.11	0.06	0.07	0.08	0.08	0.05
Al_2O_3	5.24	5.30	5.30	5.42	5.04	5.16	5.05	5.29	3.52	3.74	4.39	4.39	3.42	3.33	3.56	3.25
Cr_2O_3	0.44	0.42	0.44	0.50	0.50	0.54	0.47	0.56	0.37	0.40	0.40	0.44	0.44	0.33	0.44	0.55
FeO	6.41	6.38	6.24	6.44	6.33	6.17	6.21	5.95	5.88	5.75	5.85	5.82	5.19	5.39	5.55	5.43
MnO	0.17	0.11	0.17	0.11	0.12	0.15	0.14	0.14	0.09	0.09	0.10	0.15	0.20	0.20	0.16	0.18
NiO	0.11	0.12	0.10	0.11	n.a.	n.a.	n.a.	n.a.	0.12	0.08	0.09	0.11	0.17	0.16	0.20	0.11
MgO	32.05	31.96	32.06	32.23	32.87	32.61	32.45	32.69	33.86	33.51	33.14	33.17	34.04	33.90	33.80	33.63
CaO	1.02	1.02	1.08	1.04	1.08	1.15	1.05	1.19	0.75	0.98	0.75	0.75	0.44	0.60	0.44	0.56
Na_2O	0.09	0.09	0.15	0.14	0.16	0.17	0.16	0.18	0.07	0.15	0.09	0.10	0.05	0.03	0.04	0.06
K_2O	n.d.	n.d.	0.01	0.02	0.01	n.d.	0.02	0.01	n.d.	0.01	0.01	n.d.	0.01	0.01	n.d.	n.d.
Total	***99.40***	***99.25***	***99.88***	***100.12***	***101.15***	***100.40***	***100.25***	***100.91***	***100.61***	***100.63***	***100.05***	***100.35***	***99.53***	***99.84***	***99.73***	***99.29***
Stoich.	**6O**	**6O**	**6O**	**6O**	**6O**	**6O**	**6O**	**6O**	**6O**	**6O**	**6O**	**6O**	**6O**	**6O**	**6O**	**6O**
Si	1.874	1.875	1.879	1.869	1.880	1.874	1.883	1.877	1.915	1.913	1.901	1.903	1.918	1.924	1.916	1.924
Ti	0.004	0.003	0.004	0.004	0.003	0.004	0.004	0.004	0.003	0.003	0.003	0.001	0.002	0.002	0.002	0.001
Al	0.215	0.218	0.217	0.221	0.203	0.210	0.205	0.214	0.142	0.151	0.178	0.178	0.139	0.135	0.145	0.133
Cr	0.012	0.012	0.012	0.014	0.013	0.015	0.013	0.015	0.010	0.011	0.011	0.012	0.012	0.009	0.012	0.015
Fe	0.187	0.186	0.181	0.187	0.181	0.178	0.179	0.171	0.169	0.165	0.169	0.167	0.150	0.155	0.160	0.158
Mn	0.005	0.003	0.005	0.003	0.004	0.004	0.004	0.004	0.003	0.003	0.003	0.004	0.006	0.006	0.005	0.005
Ni	0.003	0.003	0.003	0.003	-	-	-	-	0.003	0.002	0.003	0.003	0.005	0.005	0.005	0.003
Mg	1.666	1.664	1.657	1.665	1.678	1.677	1.670	1.671	1.731	1.713	1.704	1.700	1.754	1.742	1.741	1.739
Ca	0.038	0.038	0.040	0.038	0.040	0.043	0.039	0.044	0.028	0.036	0.028	0.028	0.016	0.022	0.016	0.021
Na	0.006	0.006	0.010	0.009	0.010	0.012	0.011	0.012	0.005	0.010	0.006	0.007	0.003	0.002	0.003	0.004
K	-	-	0.000	0.001	0.000	-	0.001	0.001	-	0.000	0.000	-	0.000	0.000	-	-
Total	***4.011***	***4.010***	***4.008***	***4.014***	***4.013***	***4.016***	***4.009***	***4.012***	***4.008***	***4.008***	***4.005***	***4.004***	***4.006***	***4.003***	***4.005***	***4.003***
Mg#	***89.91***	***89.93***	***90.15***	***89.92***	***90.25***	***90.41***	***90.31***	***90.74***	***91.12***	***91.23***	***90.98***	***91.04***	***92.11***	***91.81***	***91.56***	***91.69***

Table A3-3: Representative major element composition and stoichiometry of ***orthopyroxene*** in peridotite xenoliths from Marsabit (continued)

Group	**III-a**	**III-a**	**III-a**	**III-a**	**III-a**	**III-a**	**III-b**	**III-b**	**III-b**	**III-b**	**III-b**	**III**	**III**	**III**	**III**	**III**
sample	1965/1	1965/1	1965/1	1965/1	1965/1	1965/1	1959/15	1959/15	1959/15	1959/15	1959/15	1965/15	1965/15	1965/15	1965/15	1965/15
mineral	**opx-I**	**opx-I**	**opx-I**	**opx-I**	**opx-IIa**	**opx-IIa**	**opx-I**	**opx-I**	**opx-I**	**opx-IIa**	**opx-IIa**	**opx-I**	**opx-I**	**opx-I**	**opx-I**	**opx-IIa**
loaction	core	core	rim (ol)	rim (spl)	core	rim (cpx)	core	core	rim (ol)	core	rim (opx)	core	core	rim (ol)	rim (ol)	core
SiO_2	56.54	56.70	57.22	57.10	57.28	57.80	56.56	56.31	56.93	56.75	57.49	56.31	56.41	57.42	56.94	57.04
TiO_2	0.05	0.03	0.04	0.04	0.00	0.06	0.04	0.04	0.04	0.07	0.03	0.15	0.10	0.08	0.03	0.11
Al_2O_3	2.51	2.65	1.89	1.97	1.92	1.28	3.02	3.43	1.90	2.29	2.07	2.68	2.70	1.83	2.07	1.84
Cr_2O_3	0.40	0.59	0.25	0.45	0.27	0.23	0.40	0.45	0.26	0.31	0.20	0.57	0.54	0.25	0.38	0.26
FeO	5.29	5.42	5.22	5.10	5.23	4.94	5.74	5.82	5.63	5.74	5.68	5.68	5.51	5.63	5.62	5.33
MnO	0.16	0.11	0.17	0.15	0.13	0.10	0.14	0.18	0.09	0.14	0.10	0.15	0.14	0.21	0.12	0.15
NiO	n.a.	0.08	n.a.	n.a.	n.a.	n.a.	0.10	0.08	0.09	0.03	0.04	0.10	0.07	0.10	0.07	0.07
MgO	34.81	34.66	35.38	35.08	35.26	35.62	34.06	33.78	34.60	34.51	34.74	34.11	34.22	35.10	35.02	34.93
CaO	0.45	0.51	0.33	0.30	0.39	0.57	0.48	0.40	0.45	0.46	0.52	0.56	0.45	0.33	0.29	0.32
Na_2O	0.04	0.07	0.02	0.06	0.07	0.04	0.15	0.15	0.12	0.15	0.14	0.10	0.06	0.07	0.13	0.09
K_2O	0.01	0.01	n.d.	n.d.	n.d.	n.d.	n.d.	n.d.	n.d.	n.d.	n.d.	n.d.	n.d.	n.d.	n.d.	n.d.
Total	***100.28***	***100.84***	***100.53***	***100.26***	***100.55***	***100.63***	***100.69***	***100.64***	***100.13***	***100.44***	***101.01***	***100.40***	***100.18***	***101.02***	***100.68***	***100.14***
Stoich.	**6O**	**6O**	**6O**	**6O**	**6O**	**6O**	**6O**	**6O**	**6O**	**6O**	**6O**	**6O**	**6O**	**6O**	**6O**	**6O**
Si	1.938	1.935	1.953	1.954	1.955	1.969	1.934	1.927	1.956	1.945	1.957	1.933	1.937	1.955	1.946	1.956
Ti	0.001	0.001	0.001	0.001	0.000	0.001	0.001	0.001	0.001	0.002	0.001	0.004	0.002	0.002	0.001	0.003
Al	0.101	0.107	0.076	0.080	0.077	0.051	0.122	0.139	0.077	0.093	0.083	0.108	0.109	0.073	0.083	0.074
Cr	0.011	0.016	0.007	0.012	0.007	0.006	0.011	0.012	0.007	0.008	0.005	0.015	0.015	0.007	0.010	0.007
Fe	0.152	0.155	0.149	0.146	0.149	0.141	0.164	0.167	0.162	0.164	0.162	0.163	0.158	0.160	0.161	0.153
Mn	0.005	0.003	0.005	0.004	0.004	0.003	0.004	0.005	0.003	0.004	0.003	0.004	0.004	0.006	0.004	0.004
Ni	-	0.002	-	-	-	-	0.003	0.002	0.003	0.001	0.001	0.003	0.002	0.003	0.002	0.002
Mg	1.779	1.763	1.800	1.789	1.794	1.808	1.737	1.723	1.772	1.764	1.763	1.746	1.752	1.782	1.784	1.786
Ca	0.016	0.019	0.012	0.011	0.014	0.021	0.018	0.015	0.017	0.017	0.019	0.021	0.016	0.012	0.011	0.012
Na	0.003	0.005	0.002	0.004	0.005	0.002	0.010	0.010	0.008	0.010	0.009	0.007	0.004	0.004	0.009	0.006
K	0.000	0.001	-	-	-	-	-	-	-	-	-	-	-	-	-	-
Total	***4.006***	***4.006***	***4.005***	***4.002***	***4.005***	***4.002***	***4.003***	***4.001***	***4.005***	***4.007***	***4.003***	***4.004***	***4.000***	***4.005***	***4.011***	***4.003***
Mg#	***92.14***	***91.93***	***92.35***	***92.46***	***92.32***	***92.78***	***91.36***	***91.19***	***91.64***	***91.47***	***91.60***	***91.46***	***91.72***	***91.75***	***91.74***	***92.12***

Table A3-3: Representative major element composition and stoichiometry of ***orthopyroxene*** in peridotite xenoliths from Marsabit (continued)

Group	**III**	**III-b**	**III-b**	**III-b**	**III-b**	**III-c**	**III-c**	**III-c**	**III-c**	**III-c**	**III-c**	**III-c**	**III-c**	**III-c**	**III-c**	**III-c**
sample	1965/15	1965/15	1965/15	1965/15	1965/15	785*	785*	785*	785*	785*	785*	1959/27	1959/27	1959/27	1959/27	1965/3
mineral	**opx-IIa**	**Opx_m**	**Opx_m**	**Opx_m**	**Opx_m**	**Opx_m**	**Opx_m**	**Opx_m**	**Opx_m**	**Opx_m**	**Opx_m**	**Opx_m**	**Opx_m**	**Opx_m**	**Opx_m**	**Opx_m**
loaction	rim (cpx)	core	core	rim (graph)	rim (glass)	core	core	core	rim (phl)	rim (glass)	rim (glass)	core	core	rim (Di_m)	rim (Di_m)	core
SiO_2	57.80	57.60	57.75	57.98	57.14	57.88	58.28	56.84	57.71	58.20	58.05	57.96	58.16	57.83	57.82	58.07
TiO_2	0.03	0.02	0.01	0.00	0.03	0.03	0.04	0.08	0.02	0.01	0.00	0.02	0.01	0.02	0.00	0.01
Al_2O_3	0.87	0.68	0.57	0.58	1.61	0.36	0.33	1.00	0.55	0.24	0.29	0.60	0.62	0.61	0.61	0.46
Cr_2O_3	0.16	0.26	0.17	0.12	0.40	0.24	0.22	0.30	0.19	0.12	0.20	0.26	0.14	0.19	0.17	0.32
FeO	5.55	5.46	5.37	5.32	5.50	6.06	5.89	5.62	5.65	5.99	5.85	6.32	6.10	6.10	6.09	5.38
MnO	0.05	0.15	0.12	0.14	0.14	0.14	0.19	0.17	0.19	0.10	0.14	0.24	0.26	0.30	0.27	0.12
NiO	0.13	0.12	0.09	0.05	0.12	0.10	0.12	0.13	0.05	0.11	0.12	0.07	0.04	0.13	0.07	0.07
MgO	35.31	35.62	35.76	35.60	35.27	34.94	35.39	34.83	34.92	35.22	35.12	34.28	34.34	34.39	34.34	35.61
CaO	0.53	0.29	0.27	0.29	0.28	0.25	0.23	0.34	0.23	0.23	0.26	0.80	0.77	0.99	0.82	0.20
Na_2O	0.07	0.05	0.06	0.07	0.08	0.10	0.07	0.12	0.07	0.05	0.07	0.15	0.16	0.11	0.09	0.09
K_2O	0.02	n.d.	n.d.	n.d.	n.d.	0.01	n.d.	n.d.	0.10	0.02	0.01	n.d.	n.d.	0.01	n.d.	n.d.
Total	***100.51***	***100.23***	***100.18***	***100.16***	***100.56***	***100.11***	***100.75***	***99.44***	***99.65***	***100.29***	***100.12***	***100.71***	***100.62***	***100.68***	***100.29***	***100.34***
Stoich.	**6O**	**6O**	**6O**	**6O**	**6O**	**6O**	**6O**	**6O**	**6O**	**6O**	**6O**	**6O**	**6O**	**6O**	**6O**	**6O**
Si	1.977	1.975	1.979	1.986	1.955	1.991	1.990	1.968	1.990	1.996	1.994	1.987	1.992	1.984	1.989	1.986
Ti	0.001	0.000	0.000	0.000	0.001	0.001	0.001	0.002	0.000	0.000	0.000	0.001	0.000	0.001	0.000	0.000
Al	0.035	0.027	0.023	0.023	0.065	0.015	0.013	0.041	0.022	0.010	0.012	0.024	0.025	0.025	0.025	0.019
Cr	0.004	0.007	0.005	0.003	0.011	0.007	0.006	0.008	0.005	0.003	0.005	0.007	0.004	0.005	0.005	0.009
Fe	0.159	0.157	0.154	0.152	0.157	0.174	0.168	0.163	0.163	0.172	0.168	0.181	0.175	0.175	0.175	0.154
Mn	0.002	0.004	0.003	0.004	0.004	0.004	0.005	0.005	0.005	0.003	0.004	0.007	0.007	0.009	0.008	0.004
Ni	0.004	0.003	0.002	0.001	0.003	0.003	0.003	0.004	0.001	0.003	0.003	0.002	0.001	0.004	0.002	0.002
Mg	1.800	1.821	1.827	1.817	1.799	1.791	1.802	1.798	1.795	1.801	1.798	1.752	1.754	1.759	1.760	1.816
Ca	0.019	0.011	0.010	0.011	0.010	0.009	0.008	0.013	0.008	0.008	0.010	0.029	0.028	0.036	0.030	0.007
Na	0.005	0.003	0.004	0.005	0.005	0.007	0.004	0.008	0.005	0.003	0.005	0.010	0.011	0.007	0.006	0.006
K	0.001	-	-	-	-	0.000	-	-	0.004	0.001	0.000	-	-	0.001	-	-
Total	***4.005***	***4.009***	***4.009***	***4.003***	***4.010***	***4.002***	***4.001***	***4.010***	***4.000***	***4.000***	***4.000***	***4.001***	***3.998***	***4.005***	***4.000***	***4.003***
Mg#	***91.90***	***92.08***	***92.23***	***92.26***	***91.96***	***91.13***	***91.46***	***91.70***	***91.68***	***91.29***	***91.45***	***90.62***	***90.93***	***90.95***	***90.95***	***92.18***

Table A3-3: Representative major element composition and stoichiometry of ***orthopyroxene*** in peridotite xenoliths from Marsabit (continued)

Group	**III-c**	**III-c**	**III-c**	**III-c**	**III-c**	**III-d**	**III-d**	**III-d**	**III-d**	**III-d**	**III-d**	**IV**	**IV**	**IV**	**IV**	**IV**
sample	1965/3	1965/3	1965/3	1965/3	1965/3	1970/6	1970/6	1970/6	1970/6	1970/6	1970/6	1961/1	1961/1	1961/1	1961/1	1961/1
mineral	**Opx_m**	**Opx_m**	**Opx_m**	**Opx_m**	**Opx_m**	**Opx_m**	**Opx_m**	**Opx_m**	**Opx_m**	**Opx_m**	**Opx_m**	**opx-I**	**opx-I**	**opx-I**	**opx-I**	**opx-IIa**
loaction	core	core	rim (glass)	rim (glass)	rim (phl)	core	core	core	rim (Ol_m)	rim (Ol_m)	rim (Ol_m)	core (reint.)	core (reint)	rim (ol)	rim (ol)	core
SiO_2	58.31	58.37	58.24	58.21	58.29	57.29	57.36	57.03	57.67	57.31	57.66	56.48	56.31	56.97	57.71	57.41
TiO_2	0.04	0.02	n.d.	0.01	n.d.	0.03	0.03	0.04	0.05	0.03	0.03	0.02	0.01	0.02	0.01	0.01
Al_2O_3	0.27	0.32	0.17	0.23	0.26	1.96	1.79	1.91	1.46	1.56	1.35	2.75	2.79	2.40	1.65	0.69
Cr_2O_3	0.16	0.17	0.14	0.16	0.13	0.52	0.44	0.52	0.51	0.60	0.34	0.45	0.55	0.45	0.31	0.09
FeO	5.29	5.16	5.33	5.33	5.23	5.04	4.91	5.06	4.93	4.99	4.88	4.94	4.87	5.18	5.03	5.33
MnO	0.14	0.06	0.14	0.13	0.13	0.20	0.14	0.10	0.14	0.06	0.13	0.10	0.13	0.16	0.11	0.14
NiO	0.13	0.06	0.09	0.05	0.08	0.11	0.13	0.10	0.07	0.11	0.10	0.08	0.10	0.03	0.09	0.05
MgO	36.01	35.84	35.91	35.72	35.73	34.77	34.92	34.63	34.72	34.34	34.88	34.63	34.61	35.59	35.73	35.41
CaO	0.20	0.19	0.19	0.18	0.19	0.54	0.51	0.53	0.90	0.95	0.86	0.58	0.67	0.20	0.18	0.22
Na_2O	0.06	0.08	0.06	0.06	0.06	0.14	0.15	0.14	0.17	0.17	0.18	0.02	0.03	0.00	0.03	0.01
K_2O	n.d.	0.02	n.d.	n.d.	0.01	n.d.	n.d.	0.01	n.d.	0.01	n.d.	0.01	0.01	n.d.	0.01	0.01
Total	***100.62***	***100.30***	***100.29***	***100.08***	***100.11***	***100.60***	***100.38***	***100.04***	***100.62***	***100.11***	***100.40***	***100.05***	***100.08***	***101.01***	***100.85***	***99.38***
Stoich.	**6O**	**6O**	**6O**	**6O**	**6O**	**6O**	**6O**	**6O**	**6O**	**6O**	**6O**	**6O**	**6O**	**6O**	**6O**	**6O**
Si	1.988	1.994	1.992	1.994	1.995	1.956	1.961	1.957	1.969	1.967	1.971	1.937	1.932	1.936	1.961	1.982
Ti	0.001	0.001	-	0.000	-	0.001	0.001	0.001	0.001	0.001	0.001	0.000	0.000	0.001	0.000	0.000
Al	0.011	0.013	0.007	0.009	0.010	0.079	0.072	0.077	0.059	0.063	0.054	0.111	0.113	0.096	0.066	0.028
Cr	0.004	0.005	0.004	0.004	0.004	0.014	0.012	0.014	0.014	0.016	0.009	0.012	0.015	0.012	0.008	0.002
Fe	0.151	0.147	0.153	0.153	0.150	0.144	0.140	0.145	0.141	0.143	0.139	0.142	0.140	0.147	0.143	0.154
Mn	0.004	0.002	0.004	0.004	0.004	0.006	0.004	0.003	0.004	0.002	0.004	0.003	0.004	0.005	0.003	0.004
Ni	0.004	0.002	0.002	0.001	0.002	0.003	0.004	0.003	0.002	0.003	0.003	0.002	0.003	0.001	0.003	0.001
Mg	1.830	1.825	1.831	1.824	1.823	1.770	1.779	1.772	1.767	1.757	1.778	1.771	1.771	1.803	1.810	1.822
Ca	0.007	0.007	0.007	0.007	0.007	0.020	0.019	0.019	0.033	0.035	0.031	0.021	0.025	0.007	0.007	0.008
Na	0.004	0.005	0.004	0.004	0.004	0.009	0.010	0.009	0.011	0.011	0.012	0.001	0.002	0.000	0.002	0.001
K	-	0.001	-	-	0.001	-	-	0.000	-	0.000	-	0.000	0.000	-	0.000	0.001
Total	***4.005***	***4.000***	***4.004***	***4.001***	***4.000***	***4.001***	***4.002***	***4.001***	***4.000***	***3.999***	***4.002***	***4.001***	***4.004***	***4.009***	***4.003***	***4.003***
Mg#	***92.38***	***92.52***	***92.31***	***92.27***	***92.41***	***99.51***	***99.54***	***99.52***	***99.18***	***99.13***	***99.22***	***92.59***	***92.68***	***92.45***	***92.69***	***92.22***

Table A3-3: Representative major element composition and stoichiometry of ***orthopyroxene*** in peridotite xenoliths from Marsabit (continued)

Group	**IV**	**IV**	**IV**	**IV**	**IV**	**IV**	**IV**	**IV**	**IV**	**IV**	**IV**
sample	1961/1	1961/1	1961/1	1968/1	1968/1	1968/1	1968/1	1968/1	1968/1	1968/1	1968/1
mineral	**opx-IIa**	**opx-L**	**opx-L**	**opx-I**	**opx-I**	**opx-I**	**opx-I**	**opx-IIa**	**opx-IIa**	**opx-IIa**	**spl-IIb**
loaction	core	lamellae in cpx	lamellae in cpx	core	core	rim (ol)	rim (cpx)	core	rim (spl)	rim (cpx)	core
SiO_2	57.45	56.82	56.93	55.02	55.06	55.76	57.05	56.78	56.80	57.63	n.d.
TiO_2	0.05	n.d.	n.d.	0.11	0.09	0.05	0.02	0.04	0.05	0.05	0.02
Al_2O_3	1.09	2.00	2.09	3.80	3.61	2.17	1.61	2.38	1.70	1.11	58.63
Cr_2O_3	0.13	0.31	0.22	0.37	0.44	0.20	0.15	0.27	0.55	0.10	8.69
FeO	4.92	4.95	5.20	5.86	5.89	6.23	6.28	6.18	6.14	5.84	7.73
MnO	0.08	0.14	0.12	0.22	0.13	0.25	0.23	0.16	0.14	0.20	0.13
NiO	0.05	0.12	0.01	0.12	n.a.	0.02	0.01	n.a.	0.16	0.05	0.51
MgO	35.97	35.17	34.97	33.55	33.49	34.05	34.66	34.35	34.56	34.99	21.21
CaO	0.19	0.36	0.39	0.42	0.31	0.26	0.29	0.23	0.21	0.23	0.01
Na_2O	0.02	0.00	0.01	0.08	0.04	0.02	0.04	0.04	0.05	0.05	
K_2O	0.02	n.d.	0.01	n.d.	0.01	n.d.	n.d.	0.02	0.02	0.01	0.17
Total	***99.98***	***99.88***	***99.94***	***99.53***	***99.08***	***99.03***	***100.34***	***100.46***	***100.37***	***100.27***	***99.05***
Stoich.	**6O**	**6O**	**6O**	**6O**	**6O**	**6O**	**6O**	**6O**	**6O**	**6O**	**4O**
Si	1.968	1.951	1.954	1.908	1.915	1.943	1.960	1.947	1.953	1.976	-
Ti	0.001	-	-	0.003	0.002	0.001	0.000	0.001	0.001	0.001	0.000
Al	0.044	0.081	0.085	0.155	0.148	0.089	0.065	0.096	0.069	0.045	1.784
Cr	0.004	0.009	0.006	0.010	0.012	0.006	0.004	0.007	0.015	0.003	0.177
Fe	0.141	0.142	0.149	0.170	0.171	0.181	0.181	0.177	0.177	0.168	0.167
Mn	0.002	0.004	0.003	0.006	0.004	0.008	0.007	0.005	0.004	0.006	0.003
Ni	0.002	0.003	0.000	0.003	-	0.001	0.000	-	0.004	0.001	0.011
Mg	1.837	1.801	1.789	1.734	1.737	1.769	1.775	1.756	1.771	1.789	0.816
Ca	0.007	0.013	0.014	0.016	0.011	0.010	0.011	0.009	0.008	0.008	0.000
Na	0.001	0.000	0.001	0.005	0.003	0.002	0.003	0.003	0.003	0.003	0.003
K	0.001	-	0.001	-	0.001	-	-	0.001	0.001	0.000	0.003
Total	***4.008***	***4.004***	***4.002***	***4.010***	***4.004***	***4.009***	***4.006***	***4.002***	***4.006***	***4.001***	***3.000***
Mg#	***92.87***	***92.68***	***92.30***	***91.07***	***91.03***	***90.70***	***90.77***	***90.83***	***90.93***	***91.44***	***8.87***

Table A3-4: Representative major element composition and stoichiometry of ***clinopyroxene*** in peridotite xenoliths from Marsabit

Group	**I**	**I**	**I**	**I**	**I**	**I**	**I**	**I**	**I**	**I**	**I**	**I**	**I**	**I**	**I**	**I**	**I**
sample	1960/2	1960/2	1960/2	1960/2	1960/2	1960/2	1960/2	1960/2	1960/2	1960/2	1960/2	1960/2	1960/2	1960/2	1963/1	1963/1	1963/1
mineral	**cpx-I**	**cpx-I**	**cpx-I**	**cpx-I**	**cpx-I**	**cpx-I**	**cpx-IIa**	**cpx-IIa**	**cpx-IIa**	**cpx-IIa**	**cpx-IIb**	**cpx-IIb**	**Aug$_m$**	**Aug$_m$**	**cpx-I**	**cpx-I**	**cpx-I**
loaction	Al trough	Al trough	Al bulge	Al bulge	rim (ol)	rim (opx)	core	core	rim (opx)	rim (opx)	sympl	sympl	in glass	in glass	Al trough	Al trough	Al bulge
SiO_2	52.78	52.61	52.17	51.87	52.94	52.27	52.52	52.71	52.72	52.55	53.08	52.69	46.12	48.94	53.70	53.53	53.21
TiO_2	0.52	0.46	0.61	0.62	0.53	0.56	0.51	0.57	0.46	0.72	0.64	0.62	2.95	1.96	0.58	0.56	0.47
Al_2O_3	4.44	4.20	5.74	5.89	4.60	5.20	5.24	5.79	4.88	5.57	5.63	5.85	9.89	7.00	4.72	4.78	5.76
Cr_2O_3	1.44	1.34	0.99	0.91	0.68	0.80	1.33	1.23	0.83	1.02	0.40	0.35	1.62	1.25	1.44	1.35	0.56
FeO	2.47	2.26	2.14	2.26	2.15	1.96	2.40	2.27	2.14	2.03	2.07	2.07	2.40	2.73	1.98	2.08	2.07
MnO	0.13	0.05	0.07	0.09	0.11	0.10	0.05	0.09	0.06	0.06	0.09	0.10	0.05	0.08	0.07	0.05	0.09
NiO	0.02	n.d.	0.02	0.05	0.13	0.03	0.02	0.05	n.a.	0.03	0.02	0.03	0.03	n.d.	0.04	n.d.	0.08
MgO	14.80	15.01	14.66	14.32	15.31	15.00	14.67	14.51	15.04	14.85	15.06	14.88	14.83	16.64	14.86	15.22	15.38
CaO	21.43	21.62	21.72	21.60	21.82	21.90	21.53	21.17	21.79	21.93	22.10	22.05	21.48	20.52	20.74	20.91	20.63
Na_2O	1.77	1.73	1.82	1.83	1.56	1.60	1.86	1.96	1.62	1.77	1.49	1.66	0.71	0.57	2.10	1.94	1.94
K_2O	0.03	n.d.	0.01	n.d.	0.02	n.d.	0.02	n.d.	0.01	n.d.	0.02	0.03	0.02	0.02	n.d.	0.02	n.d.
Total	***99.83***	***99.29***	***99.95***	***99.43***	***99.84***	***99.43***	***100.15***	***100.34***	***99.56***	***100.53***	***100.59***	***100.33***	***100.09***	***99.72***	***100.24***	***100.43***	***100.18***
Stoich.	**6O**	**6O**	**6O**	**6O**	**6O**	**6O**	**6O**	**6O**	**6O**	**6O**	**6O**	**6O**	**6O**	**6O**	**6O**	**6O**	**6O**
Si	1.921	1.924	1.893	1.893	1.921	1.905	1.904	1.903	1.918	1.895	1.908	1.901	1.688	1.786	1.935	1.927	1.915
Ti	0.014	0.013	0.017	0.017	0.014	0.015	0.014	0.015	0.013	0.019	0.017	0.017	0.081	0.054	0.016	0.015	0.013
Al	0.190	0.181	0.246	0.253	0.197	0.223	0.224	0.246	0.209	0.237	0.238	0.249	0.426	0.301	0.201	0.203	0.244
Cr	0.041	0.039	0.029	0.026	0.020	0.023	0.038	0.035	0.024	0.029	0.011	0.010	0.047	0.036	0.041	0.038	0.016
Fe	0.075	0.069	0.065	0.069	0.065	0.060	0.073	0.069	0.065	0.061	0.062	0.063	0.073	0.083	0.060	0.063	0.062
Mn	0.004	0.002	0.002	0.003	0.003	0.003	0.002	0.003	0.002	0.002	0.003	0.003	0.001	0.002	0.002	0.002	0.003
Ni	0.001	-	0.000	0.002	0.004	0.001	0.000	0.001	-	0.001	0.001	0.001	0.001	-	0.001	-	0.002
Mg	0.803	0.818	0.793	0.779	0.828	0.815	0.793	0.781	0.816	0.799	0.807	0.800	0.809	0.906	0.799	0.817	0.825
Ca	0.836	0.847	0.844	0.844	0.848	0.855	0.836	0.819	0.849	0.847	0.851	0.852	0.842	0.803	0.801	0.806	0.795
Na	0.125	0.123	0.128	0.129	0.110	0.113	0.131	0.137	0.114	0.124	0.104	0.116	0.050	0.041	0.147	0.135	0.135
K	0.001	-	0.001	-	0.001	-	0.001	-	0.001	-	0.001	0.001	0.001	0.001	-	0.001	-
Total	***4.012***	***4.015***	***4.018***	***4.015***	***4.012***	***4.013***	***4.016***	***4.009***	***4.010***	***4.015***	***4.003***	***4.012***	***4.020***	***4.012***	***4.002***	***4.006***	***4.010***
Mg#	***91.44***	***92.21***	***92.43***	***91.87***	***92.71***	***93.19***	***91.60***	***91.93***	***92.59***	***92.89***	***92.83***	***92.75***	***91.69***	***91.57***	***93.04***	***92.86***	***92.98***

the abbreviation in brackets under location indicates the adjacent mineral phase of the respective rim analysis; n.a.: not analysed; n.d.: not detected; Stoich.: cations calculated on the basis of 6 oxygens; Mg# = 100*Mg/(Mg+Fe^{tot});

Table A3-4: Representative major element composition and stoichiometry of ***clinopyroxene*** in peridotite xenoliths from Marsabit (continued)

Group	**I**	**I**	**I**	**I**	**I**	**I**	**I**	**I**	**I**	**I**	**I**	**I**	**I**	**I**	**I**	**I**
sample	1963/1	1963/1	1963/1	1963/1	1963/1	1963/1	1963/1	1963/1	1963/1	1963/1	1963/1	1963/2	1963/2	1963/2	1963/2	1963/2
mineral	**cpx-I**	**cpx-I**	**cpx-IIa**	**cpx-IIa**	**cpx-IIb**	**cpx-IIb**	**Aug$_m$**	**Aug$_m$**	**Aug$_m$**	**Aug$_m$**	**Aug$_m$**	**cpx-I**	**cpx-I**	**cpx-I**	**cpx-I**	**cpx-I**
loaction	Al bulge	rim (ol)	core	rim (ol)	sympl	sympl	core	core	rim (gl)	rim (gl)	rim (gl)	Al trough	Al trough	Al bulge	Al bulge	rim (cpx)
SiO_2	50.67	53.86	52.54	52.63	52.82	52.63	45.53	48.90	45.76	47.57	46.47	53.18	53.14	53.10	52.81	53.09
TiO_2	0.43	0.29	0.42	0.42	0.39	0.41	2.60	1.76	3.10	2.34	2.60	0.70	0.59	0.65	0.56	0.50
Al_2O_3	5.82	4.92	5.38	5.28	5.34	5.61	9.95	7.13	12.17	9.79	10.84	5.23	4.90	5.92	6.40	5.38
Cr_2O_3	1.00	0.43	1.28	1.28	0.67	0.61	1.95	1.17	0.43	0.04	0.12	0.78	1.00	0.92	0.80	0.65
FeO	1.76	2.23	2.09	2.16	2.09	2.20	1.73	2.32	3.15	2.92	2.96	2.50	2.49	2.43	2.49	2.29
MnO	0.12	0.07	0.03	0.08	0.07	0.05	0.07	0.07	0.09	0.12	0.15	0.07	0.10	0.10	0.07	0.04
NiO	0.04	0.01	n.d.	n.d.	0.06	0.07	0.10	0.06	n.d.	0.03	0.02	0.03	n.a.	0.04	n.a.	n.a.
MgO	14.25	15.39	14.84	14.83	15.37	15.06	14.15	16.30	14.44	15.36	14.89	14.88	15.20	14.77	14.76	15.05
CaO	20.22	21.01	21.15	21.44	21.47	21.17	22.76	21.35	21.22	20.81	20.85	20.53	21.05	20.89	20.78	21.62
Na_2O	1.82	1.89	1.71	1.65	1.48	1.75	0.50	0.37	0.45	0.39	0.42	2.11	1.93	1.99	2.00	1.74
K_2O	n.d.	0.01	0.03	n.d.	n.d.	n.d.	0.02	n.d.	0.03	n.d.	n.d.	0.01	n.d.	0.02	0.01	n.d.
Total	***96.14***	***100.11***	***99.49***	***99.77***	***99.74***	***99.56***	***99.36***	***99.45***	***100.83***	***99.38***	***99.31***	***100.02***	***100.40***	***100.83***	***100.69***	***100.36***
Stoich.	**6O**	**6O**	**6O**	**6O**	**6O**	**6O**	**6O**	**6O**	**6O**	**6O**	**6O**	**6O**	**6O**	**6O**	**6O**	**6O**
Si	1.903	1.940	1.910	1.910	1.913	1.911	1.682	1.789	1.658	1.739	1.703	1.922	1.918	1.905	1.896	1.914
Ti	0.012	0.008	0.012	0.011	0.011	0.011	0.072	0.048	0.084	0.064	0.072	0.019	0.016	0.017	0.015	0.013
Al	0.257	0.209	0.231	0.226	0.228	0.240	0.433	0.307	0.519	0.422	0.468	0.223	0.209	0.251	0.271	0.228
Cr	0.030	0.012	0.037	0.037	0.019	0.017	0.057	0.034	0.012	0.001	0.003	0.022	0.028	0.026	0.023	0.018
Fe	0.055	0.067	0.064	0.066	0.063	0.067	0.053	0.071	0.096	0.089	0.091	0.076	0.075	0.073	0.075	0.069
Mn	0.004	0.002	0.001	0.002	0.002	0.001	0.002	0.002	0.003	0.004	0.005	0.002	0.003	0.003	0.002	0.001
Ni	0.001	0.000	-	-	0.002	0.002	0.003	0.002	-	0.001	0.001	0.001	-	0.001	-	-
Mg	0.798	0.826	0.805	0.802	0.830	0.815	0.779	0.889	0.780	0.837	0.814	0.802	0.818	0.790	0.790	0.809
Ca	0.814	0.811	0.824	0.834	0.833	0.823	0.901	0.837	0.824	0.815	0.819	0.795	0.814	0.803	0.799	0.835
Na	0.133	0.132	0.121	0.116	0.104	0.123	0.036	0.026	0.032	0.028	0.030	0.148	0.135	0.139	0.139	0.122
K	-	0.001	0.002	-	-	-	0.001	-	0.001	-	-	0.001	0.000	0.001	0.000	-
Total	***4.008***	***4.008***	***4.005***	***4.005***	***4.005***	***4.011***	***4.019***	***4.005***	***4.009***	***4.000***	***4.004***	***4.010***	***4.016***	***4.009***	***4.011***	***4.010***
Mg#	***93.53***	***92.49***	***92.67***	***92.44***	***92.93***	***92.42***	***93.58***	***92.60***	***89.09***	***90.35***	***89.97***	***91.39***	***91.59***	***91.56***	***91.35***	***92.15***

Table A3-4: Representative major element composition and stoichiometry of ***clinopyroxene*** in peridotite xenoliths from Marsabit (continued)

Group	**I**	**I**	**I**	**I**	**I**	**I**	**I**	**I**	**I**	**I**	**I**	**I**	**I**	**I**	**I**	**I**
sample	1963/2	1963/2	1963/2	1963/2	1963/2	1963/2	1963/2	1963/2	1965/4	1965/4	1965/4	1965/4	1965/4	1965/4	1965/4	1965/4
mineral	**cpx-I**	**cpx-IIa**	**cpx-IIa**	**cpx-IIa**	**cpx-IIa**	**cpx-IIb**	**cpx-IIb**	**Aug$_m$**	**cpx-I**	**cpx-I**	**cpx-I**	**cpx-I**	**cpx-I**	**cpx-I**	**cpx-IIa**	**cpx-IIa**
loaction	rim (opx)	core	core	rim (opx)	rim (opx)	sympl	sympl	in glass	Al trough	Al trough	Al bulge	Al bulge	rim (opx)	rim (ol)	core	core
SiO_2	53.77	52.75	53.06	53.20	53.18	52.89	52.83	48.36	53.05	52.85	52.24	53.33	53.23	53.27	53.68	51.99
TiO_2	0.48	0.66	0.67	0.60	0.63	0.62	0.53	2.51	0.69	0.98	0.81	0.60	0.53	0.46	0.57	0.78
Al_2O_3	5.26	6.44	6.40	5.75	6.16	6.01	5.48	9.09	5.03	4.90	6.65	5.69	5.57	4.90	4.81	5.72
Cr_2O_3	0.64	0.90	0.65	0.59	0.58	0.25	0.30	0.23	1.03	1.28	1.15	1.07	0.41	0.47	1.13	1.23
FeO	2.21	2.28	2.27	2.20	2.12	2.38	2.21	2.85	2.44	2.17	2.08	2.08	2.04	2.26	2.12	2.10
MnO	0.08	0.09	0.11	0.06	0.07	0.05	0.08	0.07	0.05	0.10	0.06	0.05	0.10	0.10	0.09	0.02
NiO	0.03	n.a.	0.04	n.a.	n.a.	n.a.	n.a.	n.a.	n.a.	n.a.	n.a.	n.a.	n.a.	n.a.	n.a.	n.a.
MgO	15.31	14.39	14.44	15.08	14.85	15.15	15.40	15.58	15.06	15.34	14.75	14.96	15.65	15.49	15.61	14.74
CaO	21.45	21.29	20.98	21.42	21.19	21.65	21.66	21.34	20.75	20.83	21.30	21.33	21.68	21.67	21.20	21.50
Na_2O	1.87	2.18	2.09	1.81	1.86	1.82	1.62	0.60	2.10	1.95	1.92	2.04	1.58	1.69	1.78	1.87
K_2O	n.d.	n.d.	n.d.	0.01	0.01	0.01	0.01	n.d.	n.d.	n.d.	n.d.	n.d.	0.02	n.d.	n.d.	n.d.
Total	***101.09***	***100.99***	***100.69***	***100.71***	***100.65***	***100.83***	***100.11***	***100.63***	***100.21***	***100.40***	***100.97***	***101.15***	***100.80***	***100.30***	***100.99***	***99.95***
Stoich.	**6O**	**6O**	**6O**	**6O**	**6O**	**6O**	**6O**	**6O**	**6O**	**6O**	**6O**	**6O**	**6O**	**6O**	**6O**	**6O**
Si	1.922	1.892	1.903	1.909	1.907	1.898	1.908	1.748	1.917	1.906	1.874	1.907	1.907	1.921	1.921	1.887
Ti	0.013	0.018	0.018	0.016	0.017	0.017	0.014	0.068	0.019	0.027	0.022	0.016	0.014	0.012	0.015	0.021
Al	0.221	0.272	0.271	0.243	0.260	0.254	0.233	0.388	0.214	0.208	0.281	0.240	0.235	0.208	0.203	0.244
Cr	0.018	0.025	0.018	0.017	0.017	0.007	0.009	0.007	0.029	0.036	0.033	0.030	0.012	0.013	0.032	0.035
Fe	0.066	0.069	0.068	0.066	0.064	0.071	0.067	0.086	0.074	0.065	0.062	0.062	0.061	0.068	0.064	0.064
Mn	0.002	0.003	0.003	0.002	0.002	0.002	0.002	0.002	0.001	0.003	0.002	0.002	0.003	0.003	0.003	0.001
Ni	0.001	-	0.001	-	-	-	-	-	-	-	-	-	-	-	-	-
Mg	0.816	0.769	0.772	0.807	0.794	0.810	0.829	0.840	0.811	0.825	0.789	0.797	0.836	0.833	0.833	0.798
Ca	0.821	0.818	0.806	0.823	0.814	0.832	0.838	0.827	0.803	0.805	0.818	0.817	0.832	0.837	0.813	0.836
Na	0.129	0.152	0.145	0.126	0.129	0.127	0.114	0.042	0.147	0.137	0.134	0.142	0.109	0.118	0.124	0.131
K	-	-	-	0.000	0.000	0.000	0.000	-	-	-	-	-	0.001	-	-	-
Total	***4.010***	***4.017***	***4.007***	***4.008***	***4.003***	***4.018***	***4.014***	***4.008***	***4.016***	***4.013***	***4.015***	***4.013***	***4.010***	***4.015***	***4.008***	***4.018***
Mg#	***92.51***	***91.82***	***91.90***	***92.44***	***92.59***	***91.91***	***92.56***	***90.70***	***91.66***	***92.66***	***92.66***	***92.77***	***93.18***	***92.45***	***92.91***	***92.60***

Table A3-4: Representative major element composition and stoichiometry of ***clinopyroxene*** in peridotite xenoliths from Marsabit (continued)

Group	**I**	**I**	**I**	**I**	**II**	**II**	**II**	**II**	**II**	**II**	**II**	**II**	**II**	**II**	**II**	**II**
sample	1965/4	1965/4	1965/4	1965/4	1958/6	1958/6	1958/6	1958/6	1958/6	1958/13	1958/13	1958/13	1958/13	1958/13	1958/13	1958/13
mineral	**cpx-IIa**	**cpx-IIa**	**cpx-IIb**	**cpx-IIb**	**cpx-I**	**cpx-I**	**cpx-I**	**cpx-I**	**cpx-I**	**cpx-I**	**cpx-I**	**cpx-I**	**cpx-I**	**cpx-IIb**	**cpx-IIb**	**Aug$_m$**
loaction	rim (ol)	rim (cpx)	sympl.	sympl.	core	core	rim (ol)	rim (opx)	rim (opx)	core	core	rim (ol)	rim (ol)	sympl/c	sympl/r (opx)	rim (gl)
SiO_2	52.16	54.19	53.41	52.69	50.76	51.27	51.32	51.22	51.15	52.44	52.28	53.27	53.00	52.96	53.09	44.17
TiO_2	0.67	0.35	0.72	0.62	0.73	0.76	0.69	0.56	0.63	0.41	0.44	0.31	0.33	0.42	0.34	3.12
Al_2O_3	4.97	4.12	5.86	5.65	7.02	7.11	7.01	6.61	6.96	6.40	6.49	5.01	5.69	6.23	5.76	11.04
Cr_2O_3	0.67	0.92	0.52	0.25	0.81	0.92	0.78	0.75	0.80	0.96	0.95	0.49	0.69	0.85	0.70	2.33
FeO	2.20	2.01	2.27	2.16	4.09	4.31	4.39	4.65	4.51	2.44	2.30	2.36	2.51	2.27	2.32	2.10
MnO	0.07	0.09	0.09	0.11	0.12	0.12	0.10	0.08	0.10	0.08	0.10	0.07	0.08	0.09	0.10	0.04
NiO	0.03	n.a.	n.a.	0.05	n.a.	n.a.	n.a.	n.a.	n.a.	n.a.	n.a.	n.a.	n.a.	n.a.	n.a.	n.a.
MgO	15.00	16.13	15.70	15.36	15.93	15.92	16.66	17.63	16.81	14.89	14.83	16.27	15.81	15.15	15.51	13.57
CaO	21.60	21.33	21.43	22.03	18.73	18.72	18.16	17.26	18.05	20.25	20.51	20.39	20.19	20.48	20.08	22.25
Na_2O	1.74	1.75	1.71	1.54	1.40	1.45	1.15	1.02	1.13	2.04	2.08	1.68	1.79	1.99	1.93	0.51
K_2O	0.01	n.d.	n.d.	n.d.	n.d.	0.01	n.d.	0.02	0.01	0.01	n.d.	n.d.	n.d.	n.d.	0.02	0.02
Total	***99.12***	***100.88***	***101.70***	***100.45***	***99.58***	***100.59***	***100.25***	***99.80***	***100.16***	***99.92***	***99.97***	***99.85***	***100.10***	***100.44***	***99.85***	***99.15***
Stoich.	**6O**	**6O**	**6O**	**6O**	**6O**	**6O**	**6O**	**6O**	**6O**	**6O**	**6O**	**6O**	**6O**	**6O**	**6O**	**6O**
Si	1.908	1.940	1.898	1.898	1.850	1.850	1.853	1.856	1.850	1.896	1.891	1.923	1.910	1.903	1.916	1.639
Ti	0.018	0.009	0.019	0.017	0.020	0.021	0.019	0.015	0.017	0.011	0.012	0.008	0.009	0.011	0.009	0.087
Al	0.214	0.174	0.245	0.240	0.301	0.303	0.298	0.282	0.297	0.273	0.277	0.213	0.242	0.264	0.245	0.483
Cr	0.019	0.026	0.015	0.007	0.023	0.026	0.022	0.021	0.023	0.028	0.027	0.014	0.020	0.024	0.020	0.068
Fe	0.067	0.060	0.068	0.065	0.125	0.130	0.133	0.141	0.137	0.074	0.069	0.071	0.076	0.068	0.070	0.065
Mn	0.002	0.003	0.003	0.003	0.004	0.004	0.003	0.002	0.003	0.002	0.003	0.002	0.002	0.003	0.003	0.001
Ni	0.001	-	-	0.002	-	-	-	-	-	-	-	-	-	-	-	-
Mg	0.818	0.861	0.832	0.825	0.865	0.857	0.897	0.953	0.907	0.803	0.799	0.876	0.849	0.811	0.835	0.751
Ca	0.847	0.818	0.816	0.850	0.731	0.724	0.703	0.670	0.699	0.784	0.795	0.789	0.780	0.788	0.776	0.885
Na	0.124	0.122	0.118	0.108	0.099	0.101	0.080	0.072	0.079	0.143	0.146	0.118	0.125	0.139	0.135	0.037
K	0.000	-	-	-	-	0.000	-	0.001	0.000	0.000	-	-	-	-	0.001	0.001
Total	***4.019***	***4.012***	***4.012***	***4.015***	***4.018***	***4.016***	***4.008***	***4.013***	***4.012***	***4.014***	***4.018***	***4.014***	***4.013***	***4.011***	***4.010***	***4.017***
Mg#	***92.39***	***93.46***	***92.49***	***92.70***	***87.41***	***86.82***	***87.12***	***87.12***	***86.91***	***91.59***	***92.01***	***92.49***	***91.82***	***92.24***	***92.26***	***92.03***

Table A3-4: Representative major element composition and stoichiometry of ***clinopyroxene*** in peridotite xenoliths from Marsabit (continued)

Group	**II**	**II**	**II**	**II**	**II**	**II**	**II**	**II**	**II**	**II**	**II**	**II**	**II**	**II**	**II**	**II**
sample	1958/13	1958/13	1958/13	1958/20	1958/20	1958/20	1958/20	1959/24	1959/24	1959/24	1959/24	1959/24	1959/24	1959/24	1959/25	1959/25
mineral	**Aug_m**	**Aug_m**	**Aug_m**	**cpx-I**	**cpx-I**	**cpx-I**	**cpx-I**	**cpx-I**	**cpx-I**	**cpx-I**	**cpx-I**	**cpx-I**	**cpx-IIb**	**cpx-IIb**	**cpx-I**	**cpx-I**
loaction	rim (gl)	spongy in cpx-I	spongy in cpx-I	core	core	rim (ol)	rim (ol)	core	core	rim (opx)	rim (spl)	rim (opx)	sympl/c	sympl/r (opx)	core	core
SiO_2	45.83	52.10	52.32	51.35	51.40	51.89	51.71	51.59	51.40	51.83	51.54	51.12	51.81	51.82	51.89	52.35
TiO_2	2.53	0.45	0.40	0.40	0.53	0.48	0.49	0.50	0.51	0.52	0.55	0.60	0.52	0.53	0.52	0.46
Al_2O_3	9.35	4.28	4.22	7.08	6.98	6.98	7.32	6.97	6.95	6.93	7.00	7.06	7.14	6.99	5.59	5.53
Cr_2O_3	2.62	1.06	1.16	1.17	0.98	0.65	0.69	0.95	1.19	0.97	1.07	0.91	1.01	0.93	1.36	1.56
FeO	1.95	2.63	2.20	3.42	3.26	3.35	3.31	3.37	3.23	3.40	3.46	3.27	3.31	3.28	2.72	2.68
MnO	0.04	0.05	0.12	0.12	0.09	0.17	0.08	0.12	0.11	0.09	0.08	0.11	0.10	0.12	0.05	0.14
NiO	n.a.	n.a.	n.a.	n.a.	n.a.	n.a.	n.a.	n.a.	n.a.	0.09	0.07	0.06	n.a.	n.a.	0.03	n.a.
MgO	14.66	17.10	16.80	16.25	16.35	16.56	16.46	16.20	15.89	16.47	16.38	16.35	16.17	16.23	15.80	15.88
CaO	21.86	21.96	22.52	18.97	19.33	19.43	19.51	19.05	19.06	19.01	18.74	18.67	18.80	19.30	20.17	20.69
Na_2O	0.47	0.47	0.39	1.33	1.28	1.28	1.34	1.72	1.69	1.53	1.53	1.56	1.67	1.51	1.55	1.53
K_2O	n.d	n.d	n.d	n.d.	0.02	n.d.	n.d.	n.d.	n.d.	0.03	n.d.	n.d.	0.01	0.01	0.02	n.d.
Total	***99.33***	***100.10***	***100.12***	***100.08***	***100.22***	***100.78***	***100.92***	***100.49***	***100.04***	***100.88***	***100.43***	***99.70***	***100.54***	***100.72***	***99.70***	***100.82***
Stoich.	**6O**	**6O**	**6O**	**6O**	**6O**	**6O**	**6O**	**6O**	**6O**	**6O**	**6O**	**6O**	**6O**	**6O**	**6O**	**6O**
Si	1.692	1.890	1.896	1.856	1.855	1.861	1.852	1.859	1.860	1.859	1.857	1.854	1.862	1.861	1.886	1.884
Ti	0.070	0.012	0.011	0.011	0.014	0.013	0.013	0.014	0.014	0.014	0.015	0.016	0.014	0.014	0.014	0.013
Al	0.407	0.183	0.180	0.302	0.297	0.295	0.309	0.296	0.296	0.293	0.297	0.302	0.302	0.296	0.239	0.234
Cr	0.077	0.030	0.033	0.033	0.028	0.018	0.020	0.027	0.034	0.028	0.030	0.026	0.029	0.026	0.039	0.044
Fe	0.060	0.080	0.067	0.103	0.098	0.101	0.099	0.102	0.098	0.102	0.104	0.099	0.099	0.099	0.083	0.081
Mn	0.001	0.002	0.004	0.004	0.003	0.005	0.003	0.004	0.004	0.003	0.003	0.003	0.003	0.004	0.002	0.004
Ni	-	-	-	-	-	-	-	-	-	0.002	0.002	0.002	-	-	0.001	-
Mg	0.807	0.925	0.907	0.876	0.880	0.885	0.879	0.870	0.857	0.881	0.880	0.884	0.866	0.869	0.856	0.852
Ca	0.864	0.853	0.874	0.735	0.747	0.747	0.749	0.735	0.739	0.730	0.723	0.725	0.724	0.742	0.786	0.798
Na	0.034	0.033	0.028	0.093	0.090	0.089	0.093	0.120	0.119	0.107	0.107	0.109	0.116	0.105	0.109	0.107
K	-	-	-	-	0.001	-	-	-	-	0.001	-	-	0.000	0.000	0.001	-
Total	***4.013***	***4.008***	***4.000***	***4.012***	***4.013***	***4.014***	***4.016***	***4.026***	***4.021***	***4.020***	***4.018***	***4.021***	***4.017***	***4.016***	***4.016***	***4.017***
Mg#	***93.04***	***92.05***	***93.15***	***89.45***	***89.95***	***89.80***	***89.86***	***89.54***	***89.76***	***89.62***	***89.40***	***89.92***	***89.70***	***89.81***	***91.20***	***91.35***

Table A3-4: Representative major element composition and stoichiometry of ***clinopyroxene*** in peridotite xenoliths from Marsabit (continued)

Group	**II**	**II**	**II**	**II**	**II**	**II**	**II**	**III-a**	**III-a**	**III-a**	**III-a**	**III-a**	**III-a**	**III-a**	**III-a**	**III-a**
sample	1959/25	1959/25	1959/25	1959/25	1959/25	1959/25	1959/25	781/6	781/6	781/6	781/6	1965/1	1965/1	1965/1	1965/1	1965/1
mineral	**cpx-I**	**cpx-I**	**cpx-I**	**cpx-IIb**	**Aug$_m$**	**Aug$_m$**	**Aug$_m$**	**cpx-I**	**cpx-I**	**cpx-I**	**cpx-I**	**cpx-I**	**cpx-I**	**cpx-I**	**cpx-I**	**cpx-I**
loaction	rim (ol)	rim (ol)	rim (opx)	sympl.	spongy (cpx-IIb)	spongy (cpx-IIb)	spongy (cpx-IIb)	core	core	rim (opx)	rim (spl)	core	core	core	rim (ol)	rim (ol)
SiO_2	52.27	53.08	52.70	52.62	50.77	51.12	50.59	52.06	52.14	52.85	52.47	53.07	53.57	53.40	53.92	54.03
TiO_2	0.41	0.43	0.38	0.35	0.89	0.72	0.93	0.27	0.33	0.25	0.24	0.16	0.12	0.21	0.15	0.10
Al_2O_3	5.33	5.61	5.22	5.99	6.89	6.46	6.95	5.38	5.24	4.57	4.58	4.12	3.47	3.97	3.31	2.89
Cr_2O_3	1.00	0.89	0.84	0.75	0.82	0.89	0.75	1.01	0.94	0.74	0.88	1.29	1.36	1.23	0.83	0.80
FeO	2.61	2.77	3.12	2.75	3.47	3.37	3.51	2.20	2.32	2.48	2.28	1.99	2.10	1.78	2.15	1.85
MnO	0.10	0.12	0.11	0.09	0.13	0.11	0.05	0.08	0.07	0.07	0.08	n.a.	0.08	0.05	0.00	0.08
NiO	0.11	n.a.	n.a.	0.03	n.a.	n.a.	n.a.	0.05	0.02	n.d.	0.12	0.06	0.01	n.a.	0.06	0.05
MgO	16.16	16.14	17.77	15.99	17.09	17.16	16.67	15.22	15.50	16.02	15.91	16.13	16.08	15.87	16.32	16.82
CaO	20.25	20.56	19.25	20.69	20.30	19.90	20.05	21.77	21.58	21.76	21.69	21.71	21.78	21.64	22.65	22.11
Na_2O	1.49	1.45	1.09	1.42	0.70	0.68	0.72	1.47	1.45	1.24	1.25	1.40	1.31	1.66	1.18	1.11
K_2O	0.01	0.01	0.01	0.01	n.d.	0.01	0.01	0.03	0.01	n.d.	n.d.	n.d.	n.d.	n.d.	n.d.	n.d.
Total	***99.74***	***101.07***	***100.48***	***100.68***	***101.06***	***100.42***	***100.22***	***99.56***	***99.59***	***99.98***	***99.50***	***99.95***	***99.88***	***99.80***	***100.57***	***99.84***
Stoich.	**6O**	**6O**	**6O**	**6O**	**6O**	**6O**	**6O**	**6O**	**6O**	**6O**	**6O**		**6O**	**6O**		**6O**
Si	1.897	1.899	1.893	1.890	1.825	1.845	1.831	1.897	1.898	1.915	1.912	1.923	1.942	1.935	1.943	1.956
Ti	0.011	0.012	0.010	0.009	0.024	0.020	0.025	0.008	0.009	0.007	0.007	0.004	0.003	0.006	0.004	0.003
Al	0.228	0.237	0.221	0.254	0.292	0.275	0.297	0.231	0.225	0.195	0.197	0.176	0.148	0.169	0.140	0.123
Cr	0.029	0.025	0.024	0.021	0.023	0.025	0.021	0.029	0.027	0.021	0.025	0.037	0.039	0.035	0.024	0.023
Fe	0.079	0.083	0.094	0.082	0.104	0.102	0.106	0.067	0.071	0.075	0.069	0.060	0.064	0.054	0.065	0.056
Mn	0.003	0.004	0.003	0.003	0.004	0.003	0.002	0.002	0.002	0.002	0.003	-	0.002	0.001	-	0.003
Ni	0.003	-	-	0.001	-	-	-	0.002	0.000	-	0.004	0.002	0.000	-	0.002	0.001
Mg	0.874	0.861	0.952	0.856	0.915	0.923	0.899	0.827	0.841	0.865	0.864	0.871	0.869	0.857	0.877	0.908
Ca	0.787	0.788	0.741	0.796	0.782	0.769	0.777	0.850	0.842	0.845	0.847	0.843	0.846	0.840	0.875	0.858
Na	0.105	0.100	0.076	0.099	0.049	0.048	0.051	0.104	0.102	0.087	0.088	0.098	0.092	0.116	0.083	0.078
K	0.000	0.000	0.000	0.000	-	0.001	0.000	0.001	0.001	-	-	-	-	-	0.000	0.000
Total	***4.017***	***4.009***	***4.013***	***4.012***	***4.018***	***4.010***	***4.010***	***4.018***	***4.018***	***4.013***	***4.015***	***4.015***	***4.007***	***4.015***	***4.012***	***4.008***
Mg#	***91.70***	***91.22***	***91.05***	***91.21***	***89.77***	***90.09***	***89.44***	***92.49***	***92.26***	***92.00***	***92.56***	***93.52***	***93.19***	***94.10***	***93.10***	***94.18***

Table A3-4: Representative major element composition and stoichiometry of ***clinopyroxene*** in peridotite xenoliths from Marsabit (continued)

Group	**III-a**	**III-a**	**III-a**	**III-b**	**III-b**	**III-b**	**III-b**	**III-b**	**III-b**	**III-b**	**III-b**	**III-b**	**III-b**	**III-b**	**III-b**	**III-b**
sample	1965/1	1965/1	1965/1	1959/15	1959/15	1959/15	1959/15	1959/15	1959/15	1959/15	1959/15	1959/15	1959/15	1965/15	1965/15	1965/15
mineral	**cpx-IIa**	**cpx-IIa**	**cpx-IIb**	**cpx-I**	**cpx-I**	**cpx-I**	**cpx-I**	**Di_m**	**Di_m**	**Di_m**	**Di_m**	**Di_m**	**Di_m**	**cpx-I**	**cpx-I**	**cpx-I**
loaction	core	rim (opx)	sympl.	core	core	rim (ol)	rim (ol)	core	core	core	core	rim (gl)	rim (gl)	core	core	rim (ol)
SiO_2	53.22	53.81	52.70	54.08	53.97	54.04	54.54	53.97	54.29	50.84	48.15	51.43	50.18	52.83	53.06	54.35
TiO_2	0.16	0.14	0.19	0.21	0.20	0.27	0.27	0.24	0.18	0.17	0.22	0.17	0.32	0.36	0.40	0.24
Al_2O_3	3.56	2.99	4.23	3.31	3.44	5.02	4.09	4.37	4.26	4.56	7.76	3.96	5.97	4.25	4.30	2.87
Cr_2O_3	1.21	0.91	0.50	1.44	1.40	0.64	0.70	1.29	1.44	2.56	3.89	1.90	2.70	1.42	1.38	0.73
FeO	1.79	1.73	2.03	2.19	2.07	2.13	2.09	2.07	2.19	1.99	2.11	1.90	2.17	1.87	1.98	2.04
MnO	0.06	0.02	0.08	0.05	0.13	0.07	0.06	0.08	0.03	0.06	0.06	0.07	0.02	0.08	0.07	0.04
NiO	n.a.	n.a.	n.d.	0.09	0.03	0.01	0.01	0.05	0.05	0.02	0.04	0.01	0.05	0.05	0.06	0.01
MgO	16.32	16.86	16.31	16.42	16.36	15.73	16.07	15.49	15.73	16.00	13.99	16.42	15.30	15.56	16.09	16.21
CaO	22.22	22.21	22.62	21.43	21.38	21.24	21.32	19.87	19.62	22.89	22.52	23.38	22.60	20.78	20.34	22.41
Na_2O	1.34	1.11	0.77	1.37	1.48	1.64	1.62	2.43	2.44	0.59	0.74	0.42	0.74	1.87	1.90	1.31
K_2O	n.d.	0.01	0.03	0.01	n.d.	0.00	0.00	n.d.	0.01	n.d.	n.d.	0.01	0.01	0.02	0.04	n.d.
Total	***99.89***	***99.78***	***99.47***	***100.59***	***100.47***	***100.79***	***100.79***	***99.84***	***100.23***	***99.67***	***99.49***	***99.66***	***100.05***	***99.09***	***99.60***	***100.22***
Stoich.	**6O**	**6O**	**6O**	**6O**	**6O**	**6O**	**6O**	**6O**	**6O**	**6O**	**6O**	**6O**	**6O**	**6O**	**6O**	**6O**
Si	1.931	1.949	1.918	1.946	1.944	1.933	1.951	1.949	1.953	1.864	1.778	1.882	1.834	1.929	1.925	1.962
Ti	0.004	0.004	0.005	0.006	0.005	0.007	0.007	0.006	0.005	0.005	0.006	0.005	0.009	0.010	0.011	0.007
Al	0.152	0.128	0.181	0.140	0.146	0.212	0.173	0.186	0.180	0.197	0.338	0.171	0.257	0.183	0.184	0.122
Cr	0.035	0.026	0.014	0.041	0.040	0.018	0.020	0.037	0.041	0.074	0.114	0.055	0.078	0.041	0.039	0.021
Fe	0.054	0.052	0.062	0.066	0.062	0.064	0.063	0.062	0.066	0.061	0.065	0.058	0.066	0.057	0.060	0.062
Mn	0.002	0.001	0.002	0.002	0.004	0.002	0.002	0.002	0.001	0.002	0.002	0.002	0.001	0.002	0.002	0.001
Ni	-	-	-	0.003	0.001	0.000	0.000	0.001	0.001	0.001	0.001	0.000	0.002	0.001	0.002	0.000
Mg	0.883	0.911	0.885	0.881	0.878	0.839	0.857	0.834	0.843	0.874	0.770	0.896	0.834	0.847	0.870	0.872
Ca	0.864	0.862	0.882	0.826	0.825	0.814	0.817	0.769	0.756	0.899	0.891	0.917	0.885	0.813	0.791	0.867
Na	0.095	0.078	0.055	0.095	0.104	0.114	0.112	0.170	0.170	0.042	0.053	0.029	0.052	0.132	0.133	0.092
K	-	0.001	0.001	0.000	-	0.000	0.000	-	0.000	-	-	0.001	0.000	0.001	0.002	-
Total	***4.019***	***4.010***	***4.007***	***4.006***	***4.010***	***4.002***	***4.002***	***4.018***	***4.017***	***4.017***	***4.017***	***4.015***	***4.016***	***4.016***	***4.020***	***4.006***
Mg#	***94.19***	***94.57***	***93.46***	***93.03***	***93.36***	***92.95***	***93.20***	***93.03***	***92.76***	***93.49***	***92.22***	***93.91***	***92.64***	***93.69***	***93.55***	***93.41***

Table A3-4: Representative major element composition and stoichiometry of ***clinopyroxene*** in peridotite xenoliths from Marsabit (continued)

Group	**III-b**	**III-b**	**III-b**	**III-b**	**III-b**	**III-b**	**III-b**	**III-c**	**III-c**	**III-c**	**III-c**	**III-c**	**III-c**	**III-c**	**III-c**	**III-c**
sample	1965/15	1965/15	1965/15	1965/15	1965/15	1965/15	1965/15	785*	785*	785*	785*	785*	785*	1959/27	1959/27	1959/27
mineral	**cpx-I**	**Di_m**	**Di_m**	**Di_m**	**Di_m**	**Di_m**	**Di_m**	**Di_m**	**Di_m**	**Di_m**	**Di_m**	**Di_m**	**Di_m**	**Di_m**	**Di_m**	**Di_m**
loaction	rim (opx)	core	core	core	rim (cpx-I)	rim (gl)	rim (gl)	core	core	core	rim (Ol_m)	rim (Opx_m)	rim (glass)	core	core	core
SiO_2	55.22	51.01	52.72	51.96	52.35	50.55	54.16	53.98	55.08	54.60	52.76	54.08	53.87	54.06	53.27	53.61
TiO_2	0.09	0.33	0.52	0.31	0.44	0.40	0.19	0.19	0.14	0.30	0.22	0.46	0.16	0.26	0.19	0.19
Al_2O_3	2.22	5.71	3.78	4.85	4.45	5.37	2.40	1.78	1.33	2.08	2.52	1.73	1.61	2.36	3.35	3.40
Cr_2O_3	0.57	2.56	2.63	2.79	2.45	5.42	2.17	3.64	3.26	4.12	4.81	3.92	2.84	2.17	2.96	2.70
FeO	2.00	1.54	1.57	1.73	1.84	1.64	1.86	2.02	2.05	1.99	1.88	2.45	1.87	2.76	2.32	2.35
MnO	0.07	0.06	0.03	0.07	0.04	0.02	0.09	0.05	0.05	0.11	0.07	0.11	0.12	0.13	0.12	0.07
NiO	0.05	0.00	0.00	0.10	0.00	0.08	0.06	0.07	0.00	0.00	0.07	0.06	0.04	0.03	0.00	0.07
MgO	17.04	16.01	17.09	16.59	16.22	15.93	19.27	16.80	18.62	17.37	15.21	16.22	17.29	17.68	16.07	16.41
CaO	22.04	21.49	20.98	20.63	20.07	19.34	19.51	19.08	18.51	18.32	19.46	18.07	20.76	19.48	19.77	19.15
Na_2O	1.31	1.00	1.33	1.31	1.39	1.60	1.03	1.83	1.57	2.01	2.19	2.37	1.27	1.41	1.81	2.08
K_2O	0.01	n.d.	0.01	0.02	0.01	n.d.	0.01	n.d.	0.01	n.d.	n.d.	n.d.	n.d.	n.d.	n.d.	n.d.
Total	***100.61***	***99.71***	***100.67***	***100.36***	***99.27***	***100.35***	***100.76***	***99.44***	***100.61***	***100.90***	***99.18***	***99.47***	***99.82***	***100.35***	***99.85***	***100.04***
Stoich.	**6O**	**6O**	**6O**	**6O**	**6O**	**6O**	**6O**	**6O**	**6O**	**6O**	**6O**	**6O**	**6O**	**6O**	**6O**	**6O**
Si	1.981	1.857	1.899	1.878	1.907	1.837	1.937	1.966	1.974	1.957	1.938	1.971	1.957	1.950	1.935	1.940
Ti	0.002	0.009	0.014	0.008	0.012	0.011	0.005	0.005	0.004	0.008	0.006	0.013	0.004	0.007	0.005	0.005
Al	0.094	0.245	0.161	0.207	0.191	0.230	0.101	0.076	0.056	0.088	0.109	0.074	0.069	0.100	0.143	0.145
Cr	0.016	0.074	0.075	0.080	0.071	0.156	0.061	0.105	0.092	0.117	0.140	0.113	0.082	0.062	0.085	0.077
Fe	0.060	0.047	0.047	0.052	0.056	0.050	0.056	0.062	0.061	0.060	0.058	0.075	0.057	0.083	0.070	0.071
Mn	0.002	0.002	0.001	0.002	0.001	0.001	0.003	0.002	0.002	0.003	0.002	0.003	0.004	0.004	0.004	0.002
Ni	0.002	0.000	0.000	0.003	0.000	0.002	0.002	0.002	0.000	0.000	0.002	0.002	0.001	0.001	0.000	0.002
Mg	0.911	0.869	0.917	0.894	0.881	0.863	1.027	0.912	0.995	0.928	0.833	0.882	0.936	0.951	0.870	0.885
Ca	0.847	0.838	0.809	0.799	0.783	0.753	0.748	0.744	0.711	0.703	0.766	0.706	0.808	0.753	0.769	0.742
Na	0.091	0.071	0.093	0.092	0.098	0.113	0.071	0.129	0.109	0.140	0.156	0.168	0.089	0.099	0.127	0.146
K	0.001	-	0.000	0.001	0.000	-	0.001	-	0.000	-	-	-	-	-	-	-
Total	***4.007***	***4.010***	***4.016***	***4.016***	***4.000***	***4.016***	***4.012***	***4.003***	***4.003***	***4.003***	***4.009***	***4.006***	***4.008***	***4.011***	***4.009***	***4.016***
Mg#	***93.82***	***94.88***	***95.08***	***94.47***	***94.01***	***94.54***	***94.85***	***93.68***	***94.19***	***93.97***	***93.53***	***92.20***	***94.28***	***91.94***	***92.51***	***92.57***

Table A3-4: Representative major element composition and stoichiometry of ***clinopyroxene*** in peridotite xenoliths from Marsabit (continued)

Group	**III-c**	**III-c**	**III-c**	**III-c**	**III-c**	**III-c**	**III-c**	**III-c**	**III-c**	**III-c**	**III-c**	**III-c**	**III-c**	**III-c**	**III-c**	**III-d**
sample	1959/27	1959/27	1959/27	1965/3	1965/3	1965/3	1965/3	1965/3	1965/3	1965/25	1965/25	1965/25	1965/25	1965/25	1965/25	1970/6
mineral	**Aug_m**	**Aug_m**	**Aug_m**	**Di_m**	**Di_m**	**Di_m**	**Di_m**	**Di_m**	**Di_m**	**Di_m**	**Di_m**	**Di_m**	**Di_m**	**Di_m**	**Di_m**	**Di_m**
loaction	rim (gl)	rim (gl)	rim (gl)	core	core	core	rim (glass)	rim (Opx_m)	rim (cc)	core	core	core	core	core	core	core
SiO_2	49.03	48.81	46.56	54.54	55.09	54.10	55.27	55.03	54.07	55.66	53.63	53.97	55.08	53.48	55.18	53.70
TiO_2	1.94	2.38	3.25	0.15	0.04	0.10	0.07	0.09	0.08	0.07	0.22	0.26	0.16	0.33	0.08	0.12
Al_2O_3	7.26	6.57	7.08	1.93	1.33	1.76	1.35	1.45	2.08	1.33	2.83	2.82	1.61	2.90	2.07	3.90
Cr_2O_3	0.92	1.11	1.27	5.58	3.32	5.85	3.20	4.62	3.07	0.89	3.84	3.05	2.14	3.01	1.47	2.82
FeO	3.77	3.73	3.67	1.95	2.06	2.04	1.95	2.25	2.11	2.21	1.86	2.07	2.05	1.97	2.37	2.63
MnO	0.16	0.12	0.10	0.08	0.13	0.09	0.07	0.12	0.12	0.12	0.04	0.07	0.08	0.07	0.10	0.04
NiO	0.10	0.07	0.03	0.01	0.05		0.03	0.06	0.01	0.08	0.04	0.07	0.03	0.05	0.09	0.13
MgO	14.96	14.82	14.16	15.86	17.53	16.36	16.84	16.89	17.11	17.30	14.69	15.33	16.41	15.09	17.18	16.17
CaO	20.39	21.05	22.25	16.97	19.08	16.15	19.74	17.21	18.86	20.83	20.41	21.29	21.43	20.68	20.04	18.75
Na_2O	1.23	0.92	0.70	3.14	2.00	3.17	1.96	2.71	1.76	0.95	1.97	1.72	1.23	1.71	1.39	2.39
K_2O	n.d.	0.04	0.02	0.01	n.d.	0.00	n.d.	0.00	0.04	n.d.	n.d.	n.d.	n.d.	n.d.	n.d.	0.01
Total	***99.77***	***99.63***	***99.09***	***100.21***	***100.62***	***99.63***	***100.49***	***100.44***	***99.30***	***99.43***	***99.53***	***100.64***	***100.21***	***99.29***	***99.97***	***100.66***
Stoich.	**6O**	**6O**	**6O**	**6O**	**6O**	**6O**	**6O**	**6O**	**6O**	**6O**	**6O**	**6O**	**6O**	**6O**	**6O**	**6O**
Si	1.798	1.797	1.737	1.973	1.980	1.968	1.989	1.983	1.968	2.014	1.957	1.950	1.988	1.954	1.989	1.933
Ti	0.054	0.066	0.091	0.004	0.001	0.003	0.002	0.002	0.002	0.002	0.006	0.007	0.004	0.009	0.002	0.003
Al	0.314	0.285	0.311	0.082	0.056	0.075	0.057	0.061	0.089	0.057	0.122	0.120	0.069	0.125	0.088	0.165
Cr	0.027	0.032	0.037	0.159	0.094	0.168	0.091	0.132	0.088	0.026	0.111	0.087	0.061	0.087	0.042	0.080
Fe	0.116	0.115	0.114	0.059	0.062	0.062	0.059	0.068	0.064	0.067	0.057	0.062	0.062	0.060	0.071	0.079
Mn	0.005	0.004	0.003	0.003	0.004	0.003	0.002	0.004	0.004	0.004	0.001	0.002	0.002	0.002	0.003	0.001
Ni	0.003	0.002	0.001	0.000	0.001		0.001	0.002	0.000	0.002	0.001	0.002	0.001	0.001	0.003	0.004
Mg	0.818	0.814	0.788	0.855	0.939	0.887	0.903	0.907	0.928	0.933	0.799	0.825	0.883	0.822	0.923	0.868
Ca	0.801	0.830	0.889	0.657	0.735	0.630	0.761	0.665	0.735	0.807	0.798	0.824	0.829	0.809	0.774	0.723
Na	0.088	0.066	0.050	0.221	0.139	0.224	0.137	0.189	0.124	0.066	0.139	0.121	0.086	0.121	0.097	0.167
K	-	0.002	0.001	0.000	-	0.000	-	0.000	0.002	-	-	-	-	-	-	0.000
Total	***4.022***	***4.012***	***4.023***	***4.013***	***4.013***	***4.019***	***4.003***	***4.013***	***4.005***	***3.976***	***3.991***	***4.000***	***3.985***	***3.991***	***3.992***	***4.024***
Mg#	***87.61***	***87.64***	***87.32***	***93.55***	***93.82***	***93.46***	***93.89***	***93.03***	***93.53***	***93.33***	***93.36***	***92.96***	***93.45***	***93.18***	***92.81***	***91.63***

Table A3-4: Representative major element composition and stoichiometry of ***clinopyroxene*** in peridotite xenoliths from Marsabit (continued)

Group	**III-d**	**III-d**	**III-d**	**III-d**	**III-d**
sample	1970/6	1970/6	1970/6	1970/6	1970/6
mineral	**Di_m**	**Di_m**	**Di_m**	**Di_m**	**Di_m**
loaction	core	core	rim (Ol_m)	rim (Ol_m)	rim (Chr_m)
SiO_2	53.49	53.90	53.63	54.02	53.61
TiO_2	0.07	0.07	0.08	0.05	0.09
Al_2O_3	3.77	3.89	3.65	3.58	3.62
Cr_2O_3	2.84	2.84	2.79	2.59	3.06
FeO	2.48	2.53	2.51	2.71	2.56
MnO	0.03	0.04	0.08	0.11	0.12
NiO	0.03	0.00	0.01	0.08	0.03
MgO	16.02	16.04	15.93	16.23	16.03
CaO	18.53	18.41	18.52	18.58	18.56
Na_2O	2.37	2.32	2.23	2.16	2.24
K_2O	n.d.	n.d.	0.01	0.03	n.d.
Total	***99.63***	***100.03***	***99.45***	***100.14***	***99.91***
Stoich.	**6O**	**6O**	**6O**	**6O**	**6O**
Si	1.942	1.946	1.949	1.951	1.942
Ti	0.002	0.002	0.002	0.001	0.002
Al	0.161	0.165	0.156	0.153	0.155
Cr	0.082	0.081	0.080	0.074	0.088
Fe	0.075	0.076	0.076	0.082	0.078
Mn	0.001	0.001	0.002	0.003	0.004
Ni	0.001	0.000	0.000	0.002	0.001
Mg	0.867	0.864	0.863	0.874	0.866
Ca	0.721	0.712	0.721	0.719	0.720
Na	0.167	0.162	0.157	0.151	0.157
K	-	-	0.000	0.001	-
Total	***4.018***	***4.010***	***4.009***	***4.011***	***4.013***
Mg#	***92.00***	***91.89***	***91.87***	***91.43***	***91.77***

Table A3-5: Representative major element composition and stoichiometry of ***amphibole*** in peridotite xenoliths from Marsabit

Group	**I**	**I**	**I**	**I**	**I**	**I**	**I**	**I**	**I**	**I**	**I**	**I**	**I**	**I**	**I**	**I**	**I**
sample	1960/2	1960/2	1960/2	1960/2	1963/2	1963/2	1963/2	1963/2	1963/2	1963/2	1963/2	1963/2	1965/4	1965/4	1965/4	1965/4	1965/4
mineral	**Ti parg**	**Ti parg**	**Ti parg**	**Ti parg**	**Ti parg**	**Ti parg**	**Ti parg**	**Ti parg**	**Ti parg**	**Ti parg**	**Ti parg**	**Ti parg**	**Ti parg**	**Ti parg**	**Ti parg**	**Ti parg**	**Ti parg**
loaction	amph-i core	amph-i core	amph-i rim (gl)	amph-i rim (gl)	amph-i core	amph-i core	amph-i rim (ol)	amph-i rim (spl)	amph-ii sympl.	amph-ii sympl.	amph-iii next cpx	amph-iii next cpx	amph-i core	amph-i core	amph-i rim (opx)	amph-i rim (spl)	amph-ii sympl.
SiO_2	42.56	42.86	42.66	42.65	43.15	43.42	43.21	43.82	43.94	43.72	43.81	43.55	43.72	43.74	43.87	44.02	44.13
TiO_2	3.01	2.89	3.00	2.94	2.85	2.84	2.84	2.75	3.40	2.78	2.96	2.78	3.35	3.56	2.92	2.66	2.12
Al_2O_3	14.40	14.45	14.65	14.61	13.84	14.58	13.91	14.58	13.96	14.27	13.31	13.61	13.81	13.69	13.78	14.35	14.72
Cr_2O_3	0.49	0.51	0.50	0.50	1.01	0.75	0.87	0.44	0.38	0.33	1.00	1.03	0.58	0.71	0.64	0.68	0.55
FeO	3.55	3.64	3.65	3.40	3.63	3.70	3.67	3.58	3.58	3.77	3.63	3.42	3.51	3.57	3.59	3.60	3.60
MnO	0.11	0.09	0.03	0.04	0.03	0.05	0.07	0.06	0.07	0.11	0.08	0.06	0.04	0.03	0.08	0.05	0.06
NiO	0.05	0.22	0.14	0.11	0.13	0.09	0.11	0.10	0.09	0.12	0.08	0.07	0.13	0.10	0.12	0.11	0.05
MgO	16.96	17.23	17.03	17.08	17.00	16.92	17.53	17.53	17.57	17.81	17.99	17.75	17.94	17.86	18.17	18.23	18.26
CaO	11.62	11.61	11.59	11.83	11.46	11.28	11.38	11.31	11.64	11.58	11.62	11.55	11.33	11.37	11.33	11.40	11.37
Na_2O	3.34	3.34	3.53	3.48	3.15	3.39	3.34	3.43	3.72	3.69	3.66	3.65	3.61	3.49	3.47	3.48	3.52
Na_2O	0.72	0.74	0.72	0.72	1.32	0.99	0.81	0.74	0.13	0.10	0.36	0.35	0.21	0.21	0.12	0.14	0.07
F	n.a.	n.a.	n.a.	n.a.	n.a.	0.09	0.09	n.d.	0.03	0.06	n.a.	n.a.	0.12	0.05	0.08	0.24	0.02
Cl	n.a.	n.a.	n.a.	n.a.	n.a.	n.a.	n.a.	n.a.	n.a.	n.a.	n.a.	n.a.	0.01	0.02	0.02	0.02	n.d.
H_2O*	2.09	2.10	2.10	2.10	2.10	2.07	2.06	2.13	2.12	2.10	2.12	2.11	2.06	2.10	2.08	2.02	2.13
Total***	***98.88***	***99.67***	***99.59***	***99.46***	***99.68***	***100.13***	***99.86***	***100.48***	***100.61***	***100.42***	***100.61***	***99.94***	***100.36***	***100.48***	***100.21***	***100.89***	***100.59***
Stoech.	**23O**	**23O**	**23O**	**23O**	**23O**	**23O**	**23O**	**23O**	**23O**	**23O**	**23O**	**23O**	**23O**	**23O**	**23O**	**23O**	**23O**
Si	6.110	6.110	6.087	6.100	6.170	6.156	6.150	6.173	6.177	6.162	6.183	6.178	6.163	6.161	6.188	6.166	6.186
Ti	0.325	0.310	0.322	0.316	0.306	0.303	0.304	0.291	0.359	0.294	0.314	0.297	0.355	0.378	0.309	0.280	0.224
Al	2.436	2.427	2.464	2.462	2.333	2.437	2.333	2.421	2.314	2.371	2.213	2.276	2.294	2.272	2.291	2.368	2.432
Cr	0.055	0.057	0.056	0.057	0.115	0.084	0.098	0.049	0.042	0.037	0.111	0.115	0.064	0.079	0.072	0.075	0.061
Fe	0.426	0.434	0.435	0.407	0.434	0.438	0.437	0.422	0.421	0.444	0.429	0.406	0.414	0.421	0.424	0.421	0.422
Mn	0.013	0.011	0.004	0.005	0.004	0.006	0.009	0.008	0.008	0.014	0.009	0.007	0.005	0.004	0.010	0.006	0.007
Ni	0.005	0.026	0.016	0.013	0.015	0.010	0.012	0.012	0.010	0.013	0.009	0.008	0.015	0.011	0.014	0.012	0.006
Mg	3.630	3.661	3.622	3.640	3.623	3.577	3.718	3.682	3.683	3.743	3.784	3.754	3.770	3.749	3.820	3.806	3.815
Ca	1.787	1.773	1.772	1.813	1.756	1.714	1.735	1.707	1.754	1.749	1.757	1.756	1.711	1.716	1.711	1.711	1.708
Na	0.930	0.923	0.976	0.966	0.872	0.933	0.923	0.938	1.015	1.009	1.002	1.004	0.986	0.952	0.947	0.945	0.958
K	0.132	0.134	0.131	0.131	0.240	0.178	0.148	0.133	0.023	0.019	0.065	0.064	0.037	0.038	0.021	0.026	0.012
F	-	-	-	-	-	0.042	0.041	-	0.011	0.029	-	-	0.056	0.022	0.035	0.107	0.010
Cl	-	-	-	-	-	-	-	-	-	-	-	-	0.003	0.005	0.004	0.004	-
H	2.000	2.000	2.000	2.000	2.000	1.958	1.960	2.000	1.989	1.971	2.000	2.000	1.941	1.973	1.961	1.889	1.990
Total****	***15.850***	***15.867***	***15.885***	***15.910***	***15.869***	***15.836***	***15.866***	***15.837***	***15.805***	***15.854***	***15.875***	***15.864***	***15.814***	***15.781***	***15.806***	***15.817***	***15.829***
Mg#	***89.50***	***89.41***	***89.27***	***89.95***	***89.30***	***89.08***	***89.48***	***89.72***	***89.74***	***89.40***	***89.82***	***90.24***	***90.11***	***89.91***	***90.01***	***90.03***	***90.05***
Cr#	***2.21***	***2.29***	***2.23***	***2.26***	***4.69***	***3.34***	***4.02***	***2.00***	***1.77***	***1.54***	***4.78***	***4.83***	***2.73***	***3.36***	***3.04***	***3.07***	***2.45***

Amphibole nomenclature according to Leake et al. (1997) - Ti parg = Ti pargasite; taram. = taramite; katoph. = katophorite; kaers. = kaersutite; n.a.: not analysed; n.d.: not detected;
Stoech.: cations calculated on the basis of *n* oxygens; *: calculated from 2 H per formula unit; **: corrected for F and Cl; ***: excluding F, Cl, and H;

Table A3-5: Representative major element composition and stoichiometry of ***amphibole*** in peridotite xenoliths from Marsabit (continued)

Group	**I**	**III-b**	**III-b**	**III-b**	**III-b**	**III-b**	**III-b**	**III-b**	**III-b**	**III-b**	**III-b**	**III-b**	**III-b**	**III-c**	**III-c**	**III-c**
sample	1965/4	1959/15	1959/15	1959/15	1959/15	1965/15	1965/15	1965/15	1965/15	1965/15	1965/15	1965/15	1965/15	785*	785*	785*
mineral	**Ti parg**	**katoph.**	**katoph.**	**katoph.**	**katoph.**	**katoph.**	**katoph.**	**katoph.**	**katoph.**	**katoph.**	**katoph.**	**kaers.**	**kaers.**	**katoph.**	**katoph.**	**katoph.**
loaction	amph-ii sympl.	residual core	residual core	residual rim	residual rim	veinlet core	veinlet core	residual core	residual core	lam. in cpx	lam. in cpx	rims adj.glass	rims adj.glass	residual core	residual core	residual core
SiO_2	43.71	45.24	45.26	44.92	45.77	46.03	46.57	46.41	45.70	49.12	49.01	42.59	41.64	49.59	49.32	49.76
TiO_2	2.73	0.15	0.15	0.16	0.13	1.90	2.29	0.24	0.25	0.99	1.12	4.64	4.88	0.29	0.27	0.22
Al_2O_3	14.51	13.66	13.84	13.90	13.61	11.45	10.01	12.26	12.59	8.89	8.93	12.97	13.34	8.07	8.18	7.28
Cr_2O_3	0.69	2.38	2.34	2.17	2.14	1.23	1.25	1.92	2.51	1.24	1.39	1.36	2.81	2.63	2.61	2.24
FeO	3.58	3.52	3.38	3.46	3.57	2.93	2.90	3.06	2.96	2.84	2.82	2.73	1.67	2.94	2.99	2.99
MnO	0.03	0.06	0.06	0.06	0.07	0.03	0.02	0.02	0.05	0.09	0.02	0.00	0.02	0.02	0.04	0.07
NiO	0.06	0.09	0.09	0.09	0.13	0.14	0.11	0.12	0.14	0.13	0.15	0.13	0.12	0.06	0.11	0.05
MgO	18.03	18.62	18.54	18.47	18.86	18.86	19.09	19.63	19.08	20.15	19.50	17.64	16.96	20.62	20.37	21.12
CaO	11.53	8.43	8.55	8.65	8.61	9.74	9.69	9.10	9.38	9.87	10.59	11.41	11.76	7.93	8.00	8.17
Na_2O	3.61	4.67	4.58	4.56	4.61	4.27	4.33	4.45	4.49	4.29	4.31	3.15	2.65	5.55	5.32	5.11
Na_2O	0.09	0.50	0.51	0.48	0.49	0.38	0.46	0.33	0.33	0.33	0.29	0.69	1.48	0.29	0.34	0.26
F	n.d.	0.08	0.16	n.d.	0.18	n.a.	n.a.	n.a.	n.a.	n.a.	n.a.	n.a.	n.a.	n.a.	0.07	n.a.
Cl	0.01	0.14	0.13	0.14	0.12	n.a.	n.a.	n.a.	n.a.	n.a.	n.a.	n.a.	n.a.	0.06	0.04	n.a.
H_2O*	2.13	2.04	2.01	2.07	2.02	2.11	2.11	2.13	2.12	2.14	2.14	2.10	2.09	2.13	2.09	2.13
Total**	***100.71***	***99.51***	***99.50***	***99.11***	***100.21***	***99.06***	***98.83***	***99.67***	***99.60***	***100.08***	***100.27***	***99.41***	***99.42***	***100.16***	***99.70***	***99.41***
Stoech.	**23O**	**23O**	**23O**	**23O**	**23O**	**23O**	**23O**	**23O**	**23O**	**23O**	**23O**	**23O**	**23O**	**23O**	**23O**	**23O**
Si	6.137	6.408	6.407	6.387	6.434	6.529	6.627	6.535	6.461	6.870	6.856	6.080	5.969	6.941	6.937	7.007
Ti	0.288	0.016	0.016	0.017	0.014	0.202	0.245	0.025	0.027	0.104	0.117	0.498	0.526	0.030	0.028	0.023
Al	2.401	2.281	2.309	2.329	2.256	1.915	1.679	2.035	2.098	1.465	1.473	2.183	2.254	1.332	1.356	1.209
Cr	0.077	0.267	0.261	0.244	0.238	0.138	0.141	0.214	0.281	0.137	0.154	0.154	0.318	0.291	0.290	0.250
Fe	0.420	0.417	0.400	0.412	0.419	0.347	0.345	0.360	0.350	0.332	0.329	0.326	0.200	0.344	0.352	0.352
Mn	0.004	0.007	0.007	0.007	0.008	0.004	0.002	0.002	0.006	0.011	0.003	0.000	0.002	0.003	0.005	0.008
Ni	0.007	0.010	0.010	0.010	0.015	0.016	0.013	0.014	0.016	0.015	0.017	0.015	0.014	0.007	0.012	0.006
Mg	3.772	3.931	3.911	3.913	3.951	3.988	4.049	4.120	4.020	4.202	4.065	3.754	3.624	4.301	4.270	4.432
Ca	1.733	1.279	1.296	1.317	1.296	1.480	1.477	1.373	1.421	1.479	1.587	1.745	1.806	1.189	1.206	1.233
Na	0.982	1.284	1.257	1.257	1.257	1.174	1.195	1.215	1.231	1.164	1.169	0.872	0.736	1.506	1.451	1.395
K	0.017	0.090	0.093	0.087	0.088	0.068	0.084	0.059	0.060	0.059	0.052	0.126	0.271	0.051	0.060	0.047
F	-	0.036	0.072	-	0.081	-	-	-	-	-	-	-	-	-	0.009	-
Cl	0.001	0.035	0.031	0.034	0.029	-	-	-	-	-	-	-	-	0.014	0.030	-
H	1.999	1.930	1.897	1.966	1.891	2.000	2.000	2.000	2.000	2.000	2.000	2.000	2.000	1.986	1.961	2.000
Total**	***15.836***	***15.989***	***15.967***	***15.981***	***15.977***	***15.863***	***15.857***	***15.952***	***15.969***	***15.836***	***15.824***	***15.753***	***15.722***	***15.996***	***15.967***	***15.961***
Mg#	***89.97***	***90.40***	***90.72***	***90.48***	***90.41***	***91.99***	***92.15***	***91.96***	***91.99***	***92.69***	***92.51***	***92.02***	***94.76***	***92.59***	***92.39***	***92.64***
Cr#	***3.10***	***10.47***	***10.17***	***9.50***	***9.56***	***6.73***	***7.73***	***9.51***	***11.79***	***8.53***	***9.45***	***6.57***	***12.38***	***17.94***	***17.61***	***17.13***

Amphibole nomenclature according to Leake et al. (1997) - Ti parg = Ti pargasite; taram. = taramite; katoph. = katophorite; kaers. = kaersutite; n.a.: not analysed; n.d.: not detected;
Stoech.: cations calculated on the basis of n oxygens; *: calculated from 2 H per formula unit; **: corrected for F and Cl; ***: excluding F, Cl, and H;

Table A3-5: Representative major element composition and stoichiometry of ***amphibole*** in peridotite xenoliths from Marsabit (continued)

Group	**III-c**	**III-c**	**III-c**	**III-c**	**III-c**	**III-c**	**III-c**	**III-c**	**III-c**	**III-c**	**III-c**	**III-c**	**III-c**	**III-c**	**III-c**	**III-c**
sample	785*	785*	785*	785*	785*	1965/25	1965/25	1965/25	1965/25	1965/25	1965/25	1965/25	1965/25	1965/25	1959/27	1959/27
mineral	**katoph.**	**katoph.**	**katoph.**	**katoph.**	**katoph.**	**katoph.**	**katoph.**	**katoph.**	**katoph.**	**katoph.**	**katoph.**	**katoph.**	**katoph.**	**katoph.**	**kaers.**	**kaers.**
loaction	residual rim	residual rim	residual rim	rims adj.glass	rims adj.glass	euhedr. core	euhedr. core	euhedr. core	euhedr. core	euhedr. rim	euhedr. rim	euhedr. rim	residual core	residual rim	in m.p. core	in m.p. core
SiO_2	49.58	49.70	49.29	46.44	44.67	49.91	49.77	49.61	50.70	49.71	49.56	50.97	50.87	50.90	41.29	40.71
TiO_2	0.27	0.27	0.33	0.91	1.22	0.26	0.20	0.18	0.26	0.26	0.29	0.27	0.23	0.27	5.80	6.13
Al_2O_3	7.94	7.69	7.44	9.16	10.38	7.83	8.81	8.54	8.73	8.08	8.00	7.93	7.85	7.94	14.03	14.07
Cr_2O_3	2.62	2.58	2.92	3.27	4.89	1.04	1.10	1.01	1.17	0.91	0.90	1.00	1.15	1.21	0.08	0.31
FeO	3.04	3.18	3.19	2.14	2.23	3.50	3.58	3.49	3.57	3.40	3.42	3.47	3.40	3.43	6.18	5.89
MnO	0.04	0.06	0.08	n.d.	n.d.	0.10	0.08	0.10	0.11	0.11	0.11	0.10	0.08	0.08	0.10	0.16
NiO	0.00	0.04	0.09	0.18	0.14	0.10	0.09	0.08	0.09	0.10	0.08	0.12	0.08	0.09	0.10	0.10
MgO	20.99	21.19	20.10	20.56	18.65	20.28	19.84	19.66	19.74	20.11	20.12	20.15	19.81	20.11	15.54	15.79
CaO	7.88	7.90	7.86	10.35	10.91	9.06	8.60	8.80	8.77	8.88	9.12	9.00	9.42	9.04	10.81	10.88
Na_2O	4.96	5.19	5.25	3.63	3.60	5.04	5.17	5.14	5.23	4.98	5.10	4.92	4.96	5.09	2.96	2.84
Na_2O	0.29	0.28	0.36	0.92	0.89	0.29	0.28	0.35	0.29	0.41	0.36	0.45	0.42	0.33	1.39	1.39
F	n.a.	n.a.	0.09	n.a.	0.01	0.02	0.04	n.d.	0.02	0.01	0.03	0.02	0.02	0.05	0.18	0.06
Cl	n.a.	n.a.	0.04	n.a.	0.01	0.03	0.03	0.05	0.04	0.04	0.03	0.04	0.05	0.04	0.02	0.00
H_2O*	2.14	2.14	2.06	2.11	2.09	2.11	2.11	2.11	2.14	2.11	2.10	2.14	2.13	2.13	2.00	2.06
Total***	***99.73***	***100.24***	***99.05***	***99.67***	***99.68***	***99.56***	***99.67***	***99.11***	***100.84***	***99.08***	***99.21***	***100.55***	***100.44***	***100.68***	***100.39***	***100.37***
Stoech.	**23O**	**23O**	**23O**	**23O**	**23O**	**23O**	**23O**	**23O**	**23O**	**23O**	**23O**	**23O**	**23O**	**23O**	**23O**	**23O**
Si	6.954	6.950	6.989	6.590	6.387	7.026	6.987	7.009	7.032	7.025	7.005	7.089	7.092	7.074	5.934	5.857
Ti	0.028	0.029	0.035	0.097	0.131	0.027	0.022	0.019	0.027	0.028	0.031	0.028	0.024	0.028	0.627	0.663
Al	1.312	1.268	1.244	1.532	1.750	1.299	1.458	1.422	1.427	1.345	1.333	1.300	1.290	1.301	2.377	2.387
Cr	0.290	0.286	0.327	0.367	0.553	0.116	0.122	0.113	0.128	0.102	0.101	0.110	0.126	0.133	0.009	0.035
Fe	0.357	0.371	0.378	0.254	0.267	0.412	0.420	0.412	0.415	0.402	0.405	0.404	0.396	0.399	0.743	0.709
Mn	0.005	0.008	0.010	-	-	0.012	0.009	0.011	0.013	0.013	0.013	0.012	0.010	0.009	0.012	0.020
Ni	0.000	0.005	0.011	0.021	0.016	0.012	0.010	0.009	0.010	0.011	0.010	0.013	0.009	0.010	0.012	0.012
Mg	4.387	4.416	4.247	4.348	3.975	4.255	4.151	4.139	4.081	4.235	4.239	4.178	4.115	4.166	3.328	3.385
Ca	1.184	1.184	1.195	1.573	1.671	1.366	1.293	1.332	1.303	1.344	1.381	1.341	1.406	1.345	1.664	1.677
Na	1.349	1.407	1.443	0.999	0.999	1.374	1.407	1.409	1.405	1.365	1.396	1.325	1.339	1.371	0.824	0.793
K	0.052	0.050	0.065	0.167	0.162	0.052	0.050	0.063	0.052	0.074	0.064	0.079	0.075	0.059	0.254	0.256
F	-	-	0.041	-	0.005	0.009	0.018	0.011	0.010	0.003	0.012	0.008	0.009	0.021	0.082	0.027
Cl	-	-	0.010	-	0.001	0.008	0.007	-	0.009	0.009	0.008	0.009	0.012	0.009	0.005	0.000
H	2.000	2.000	1.949	2.000	1.994	1.983	1.975	1.989	1.982	1.988	1.980	1.983	1.979	1.970	1.913	1.973
Total***	***15.917***	***15.973***	***15.944***	***15.946***	***15.911***	***15.952***	***15.930***	***15.940***	***15.893***	***15.943***	***15.978***	***15.880***	***15.883***	***15.895***	***15.785***	***15.793***
Mg#	***92.48***	***92.24***	***91.82***	***94.48***	***93.70***	***91.16***	***90.80***	***90.95***	***90.78***	***91.33***	***91.29***	***91.18***	***91.21***	***91.26***	***81.74***	***82.69***
Cr#	***18.11***	***18.38***	***20.83***	***19.32***	***24.01***	***8.20***	***7.71***	***7.37***	***8.22***	***7.02***	***7.03***	***7.78***	***8.92***	***9.27***	***0.38***	***1.46***

Amphibole nomenclature according to Leake et al. (1997) - Ti parg = Ti pargasite; taram. = taramite; katoph. = katophorite; kaers. = kaersutite; n.a.: not analysed; n.d.: not detected;
Stoech.: cations calculated on the basis of n oxygens; *: calculated from 2 H per formula unit; **: corrected for F and Cl; ***: excluding F, Cl, and H;

Table A3-5: Representative major element composition and stoichiometry of ***amphibole*** in peridotite xenoliths from Marsabit (continued)

Group	**III-c**	**III-c**	**III-c**
sample	1959/27	1959/27	1959/27
mineral	**kaers.**	**kaers.**	**kaers.**
loaction	in m.p. rim	in m.p. rim	in m.p. rim
SiO_2	40.96	41.42	41.55
TiO_2	6.00	5.52	5.18
Al_2O_3	14.19	13.73	13.10
Cr_2O_3	0.56	0.06	0.30
FeO	5.95	6.26	6.18
MnO	0.07	0.12	0.13
NiO	0.04	n.d.	0.04
MgO	15.87	15.82	15.81
CaO	10.96	10.63	10.88
Na_2O	2.88	2.91	2.94
Na_2O	1.35	1.34	1.40
F	0.28	0.08	0.14
Cl	0.02	0.03	0.03
H_2O*	1.96	2.03	1.99
Total*	***100.98***	***99.91***	***99.61***
Stoech.	**23O**	**23O**	**23O**
Si	5.858	5.975	6.022
Ti	0.645	0.598	0.565
Al	2.392	2.334	2.238
Cr	0.064	0.007	0.035
Fe	0.711	0.755	0.749
Mn	0.009	0.015	0.016
Ni	0.005	-	0.005
Mg	3.383	3.402	3.416
Ca	1.679	1.642	1.689
Na	0.800	0.813	0.827
K	0.247	0.247	0.258
F	0.128	0.037	0.064
Cl	0.005	0.007	0.007
H	1.867	1.956	1.928
Total**	***15.792***	***15.787***	***15.819***
Mg#	***82.62***	***81.84***	***82.02***
Cr#	***2.60***	***0.29***	***1.52***

Amphibole nomenclature according to Leake et al. (1997) - Ti parg = Ti pargasite; taram. = taramite; katoph. = katophorite; kaers. = kaersutite; n.a.: not analysed; n.d.: not detected; Stoech.: cations calculated on the basis of n oxygens; *: calculated from 2 H per formula unit; **: corrected for F and Cl; ***: excluding F, Cl, and H;

Table A3-6: Representative major element composition and stoichiometry of ***phlogopite*** in peridotite xenoliths from Marsabit

Group	**I**	**I**	**I**	**I**	**I**	**I**	**I**	**I**	**I**	**III-b**	**III-b**	**III-b**	**III-b**	**III-c**	**III-c**	**III-c**	**III-c**
sample	**1963/2**	**1963/2**	**1963/2**	**1963/2**	**1963/2**	**1963/2**	**1963/2**	**1963/2**	**1963/2**	**1965/15**	**1965/15**	**1965/15**	**1965/15**	**785***	**785***	**785***	**785***
mineral	phl	phl	phl	phl	phl	phl	phl	phl	phl	phl	phl	phl	phl	phl	phl	phl	phl
loaction	core	core	core	core	core	rim (cpx)	rim (ol)	rim (amph)	rim (phl)	veinlet core	veinlet core	veinlet rim	veinlet rim	cluster core	cluster core	cluster rim	cluster rim
SiO_2	38.94	38.59	38.40	38.46	38.97	38.50	38.95	38.57	38.74	39.64	40.07	40.07	39.53	41.08	41.54	41.27	40.79
TiO_2	4.66	4.71	4.81	4.70	4.62	4.62	4.73	4.60	4.76	3.16	2.95	3.12	3.10	0.36	0.36	0.37	0.40
Al_2O_3	15.32	15.52	15.52	15.16	15.00	15.38	15.35	15.21	15.24	15.59	15.49	15.70	15.99	13.40	13.84	14.06	13.73
Cr_2O_3	0.91	0.89	0.88	0.99	0.84	0.78	0.99	0.94	0.88	1.13	1.04	0.97	1.06	2.05	1.98	2.11	1.88
FeO	3.76	3.90	3.80	3.86	3.96	3.77	3.84	3.90	3.92	3.18	2.87	3.08	3.15	2.97	2.79	2.83	3.20
MnO	n.d.	0.01	0.01	n.d.	0.03	n.d.	0.06	0.04	0.01	n.d.	0.02	0.01	0.02	n.d.	0.02	0.04	n.d.
NiO	0.22	0.26	0.20	0.22	0.21	0.21	0.21	0.20	0.24	0.23	0.18	0.25	0.27	0.23	0.29	0.20	0.22
MgO	21.77	21.58	21.63	21.71	21.74	21.60	21.79	21.67	21.90	23.10	23.16	23.16	23.03	25.46	25.41	25.47	25.29
CaO	0.03	0.04	0.02	0.03	0.09	0.09	0.15	0.04	0.04	n.d.	0.01	0.01	0.02	n.d.	0.01	n.d.	0.03
BaO	n.a.	n.a.	n.a.	n.a.	n.a.	n.a.	n.a.	n.a.	n.a.	n.a.	n.a.	n.a.	n.a.	n.a.	n.a.	n.a.	n.a.
Na_2O	0.89	0.94	0.95	0.93	0.81	0.95	0.86	0.90	0.92	2.17	2.20	2.09	2.21	2.63	2.63	2.60	2.61
Na_2O	9.38	9.43	9.37	9.27	9.28	9.19	9.13	9.28	9.15	7.26	7.22	7.38	7.14	7.09	6.87	6.98	6.66
F	n.a.	n.a.	n.a.	n.a.	n.a.	n.a.	n.a.	n.a.	n.a.	n.a.	n.a.	n.a.	n.a.	0.07	0.03	0.05	0.07
Cl	n.a.	n.a.	n.a.	n.a.	n.a.	n.a.	n.a.	n.a.	n.a.	n.a.	n.a.	n.a.	n.a.	0.06	0.05	0.06	0.06
H_2O*	4.24	4.23	4.23	4.21	4.23	4.21	4.25	4.22	4.24	4.28	4.28	4.30	4.28	4.22	4.28	4.27	4.21
Total*	***100.11***	***100.09***	***99.82***	***99.52***	***99.78***	***99.28***	***100.30***	***99.57***	***100.03***	***99.76***	***99.51***	***100.14***	***99.81***	***99.57***	***100.08***	***100.27***	***99.10***
Stoech.	**22O**	**22O**	**22O**	**22O**	**22O**	**22O**	**22O**	**22O**	**22O**	**22O**	**22O**	**22O**	**22O**	**22O**	**22O**	**22O**	**22O**
Si	5.502	5.464	5.449	5.474	5.527	5.484	5.492	5.487	5.481	5.556	5.613	5.586	5.533	5.774	5.790	5.748	5.751
Ti	0.495	0.502	0.513	0.503	0.493	0.494	0.501	0.492	0.506	0.334	0.311	0.327	0.327	0.038	0.038	0.038	0.042
Al	2.551	2.590	2.596	2.543	2.508	2.582	2.551	2.551	2.541	2.576	2.558	2.579	2.638	2.221	2.274	2.309	2.282
Cr	0.102	0.100	0.099	0.112	0.094	0.088	0.110	0.105	0.099	0.125	0.115	0.107	0.118	0.227	0.218	0.232	0.210
Fe	0.445	0.462	0.451	0.460	0.470	0.449	0.453	0.464	0.464	0.373	0.336	0.360	0.369	0.349	0.325	0.329	0.377
Mn	-	0.001	0.001	-	0.003	-	0.007	0.005	0.001	-	0.002	0.001	0.003	-	0.003	0.005	-
Ni	0.025	0.029	0.023	0.025	0.024	0.024	0.024	0.023	0.027	0.026	0.021	0.028	0.030	0.026	0.032	0.022	0.025
Mg	4.585	4.555	4.575	4.606	4.595	4.586	4.578	4.594	4.618	4.826	4.835	4.813	4.804	5.335	5.278	5.288	5.315
Ca	0.004	0.006	0.003	0.004	0.014	0.014	0.022	0.007	0.006	-	0.001	0.002	0.003	-	0.002	-	0.004
Ba	-	-	-	-	-	-	-	-	-	-	-	-	-	-	-	-	-
Na	0.244	0.257	0.261	0.256	0.222	0.261	0.234	0.248	0.253	0.590	0.598	0.566	0.601	0.717	0.711	0.703	0.714
K	1.691	1.703	1.697	1.683	1.680	1.670	1.642	1.683	1.651	1.298	1.291	1.314	1.275	1.272	1.222	1.240	1.197
F	-	-	-	-	-	-	-	-	-	-	-	-	-	0.029	0.012	0.020	0.031
Cl	-	-	-	-	-	-	-	-	-	-	-	-	-	0.013	0.013	0.014	0.014
H	4.000	4.000	4.000	4.000	4.000	4.000	4.000	4.000	4.000	***4.000***	***4.000***	***4.000***	***4.000***	3.957	3.975	3.966	3.955
Total**	***15.644***	***15.669***	***15.669***	***15.665***	***15.630***	***15.652***	***15.614***	***15.659***	***15.646***	15.7038	15.6832	15.6832	15.7006	***15.958***	***15.893***	***15.915***	***15.917***
Mg#	***91.16***	***90.79***	***91.03***	***90.92***	***90.72***	***91.09***	***91.00***	***90.82***	***90.87***	***92.82***	***93.50***	***93.05***	***92.87***	***93.86***	***94.20***	***94.14***	***93.37***
Cr#	***3.83***	***3.72***	***3.66***	***4.20***	***3.62***	***3.30***	***4.14***	***3.97***	***3.74***	***4.62***	***4.32***	***4.00***	***4.27***	***9.28***	***8.75***	***9.13***	***8.43***

n.a.: not analysed; n.d.: not detected; Stoech.: cations calculated on the basis of 22 oxygens; *: calculated from 2 H per formula unit; **: corrected for F and Cl;
***: excluding F, Cl, and H;

Table A3-6: Representative major element composition and stoichiometry of ***phlogopite*** in peridotite xenoliths from Marsabit

Group	**III-c**	**III-c**	**III-c**	**III-c**	**III-c**	**III-c**	**III-c**	**III-c**	**III-c**	**III-c**
mineral	**785***	**785***	**785***	**785***	**785***	**1965/3**	**1965/3**	**1965/3**	**1965/3**	**1965/25**
sample	phl	phl	phl	phl	phl	phl	phl	phl	phl	phl
loaction	residual core	residual adj.glass	in opx core	in opx core	in opx core	in opx core	in opx core	in opx core	in opx core	in amph.
SiO_2	41.05	41.55	41.50	41.67	41.20	41.40	41.61	40.74	41.71	42.30
TiO_2	0.40	0.42	0.52	0.53	0.44	0.22	0.22	0.17	0.09	0.27
Al_2O_3	13.94	14.00	13.47	13.74	13.58	13.89	13.47	13.73	13.60	14.77
Cr_2O_3	1.88	1.77	1.46	1.38	1.44	1.48	1.55	1.57	1.32	0.63
FeO	2.91	2.68	3.02	3.17	3.02	2.70	2.88	2.77	2.71	3.40
MnO	0.03	0.05	n.d.	0.04	0.02	0.01	0.01	0.04	0.08	0.05
NiO	0.23	0.26	0.23	0.22	0.22	0.15	0.21	0.24	0.19	0.23
MgO	25.62	25.45	25.66	25.69	26.18	25.58	25.86	25.93	25.77	25.25
CaO	0.02	0.02	n.d.	0.01	n.d.	0.04	0.02	n.d.	0.01	0.02
BaO	n.a.	n.a.	n.a.	n.a.	n.a.	0.15	0.24	0.28	0.13	n.a.
Na_2O	2.54	2.54	2.56	2.50	2.47	2.88	2.58	2.65	2.82	2.08
Na_2O	6.83	6.85	6.99	6.95	7.12	6.39	6.84	7.18	7.04	6.83
F	0.08	0.09	0.02	0.07	n.a.	0.20	n.d.	0.22	0.12	0.04
Cl	0.04	0.08	0.06	0.06	n.a.	0.10	0.07	0.14	0.22	0.04
H_2O*	4.24	4.24	4.26	4.26	4.29	4.15	4.27	4.12	4.18	4.30
Total*	***99.78***	***99.95***	***99.71***	***100.26***	***99.97***	***99.24***	***99.81***	***99.64***	***99.89***	***100.20***
Stoech.	**22O**	**22O**	**22O**	**22O**	**22O**	**22O**	**22O**	**22O**	**22O**	**22O**
Si	5.743	5.790	5.807	5.799	5.757	5.804	5.819	5.734	5.832	5.854
Ti	0.042	0.044	0.054	0.056	0.046	0.023	0.023	0.018	0.009	0.028
Al	2.299	2.300	2.221	2.254	2.237	2.296	2.221	2.277	2.242	2.409
Cr	0.208	0.195	0.161	0.152	0.159	0.164	0.171	0.175	0.146	0.069
Fe	0.340	0.312	0.354	0.369	0.353	0.316	0.337	0.326	0.316	0.393
Mn	0.003	0.006	-	0.005	0.002	0.001	0.001	0.004	0.010	0.006
Ni	0.026	0.029	0.026	0.024	0.025	0.017	0.024	0.027	0.021	0.025
Mg	5.343	5.286	5.353	5.328	5.452	5.345	5.390	5.439	5.369	5.208
Ca	0.003	0.002	-	0.002	-	0.006	0.002	-	0.002	0.004
Ba	-	-	-	-	-	0.008	0.013	0.016	0.007	-
Na	0.690	0.686	0.693	0.674	0.670	0.782	0.699	0.722	0.765	0.558
K	1.219	1.218	1.247	1.233	1.269	1.143	1.221	1.289	1.256	1.206
F	0.037	0.041	0.011	0.032	-	0.091	0.000	0.096	0.051	0.018
Cl	0.010	0.018	0.014	0.015	-	0.024	0.018	0.032	0.051	0.011
H	3.953	3.940	3.975	3.953	4.000	***3.886***	***3.982***	***3.872***	***3.898***	***3.964***
Total**	***15.916***	***15.870***	***15.917***	***15.896***	***15.969***	15.9056	15.922	16.0272	15.9756	15.7607367
Mg#	***94.01***	***94.42***	***93.80***	***93.53***	***93.92***	***94.41***	***94.12***	***94.35***	***94.44***	***92.98***
Cr#	***8.29***	***7.81***	***6.78***	***6.31***	***6.64***	***6.65***	***7.17***	***7.12***	***6.11***	***2.78***

n.a.: not analysed; n.d.: not detected; Stoech.: cations calculated on the basis of 22 oxygens; *: calculated from 2 H per formula unit; **: corrected for F and Cl; ***: excluding F, Cl, and H;

Table A3-7: Representative analyses and stoichiometry of ***carbonates*** in peridotite xenoliths from Marsabit

Group	**II**	**II**	**II**	**II**	**III-b**	**III-b**	**III-b**	**III-b**	**III-b**	**III-b**	**III-b**	**III-b**	**III-c**	**III-c**	**III-c**	**III-c**
sample	**1958/13**	**1958/13**	**1958/13**	**1958/13**	**1959/15**	**1959/15**	**1959/15**	**1959/15**	**1965/15**	**1965/15**	**1965/15**	**1965/15**	**785***	**785***	**785***	**785***
mineral	Mg calc.	Mg calc.	Mg calc.	Mg calc.	Mg calc.	Mg calc.	Cal-Dol	Cal-Dol	Mg calc.	Mg calc.	Mg calc.	Mg calc.	Mg calc.	Mg calc.	Mg calc.	Mg calc.
loaction	in glass	in glass	in glass	in glass	in glass	in glass	in glass	in glass	in glass	in glass	in glass	xenolith edge	in glass	in glass	in glass	in glass
SiO_2	n.a.	n.a.	n.a.	n.a.	n.a.	n.a.	n.a.	n.a.	0.10	0.06	0.03	0.06	n.a.	n.a.	n.a.	n.a.
Al_2O_3	n.a.	n.a.	n.a.	n.a.	n.a.	n.a.	n.a.	n.a.	0.03	0.02	0.01	0.01	n.d.	n.d.	n.d.	n.d.
Fe_2O_3*	0.06	-	-	-	-	0.15	0.08	0.12	-	-	-	-	0.10	0.03	-	-
FeO	0.02	0.02	0.02	0.02	0.11	0.01	0.09	-	0.15	0.18	0.11	0.16	0.01	0.12	0.19	0.11
MnO	n.d.	0.04	0.02	n.d.	n.d.	n.d.	0.01	n.d.	0.04	n.d.	n.d.	0.09	n.d.	n.d.	n.d.	n.d.
NiO	n.a.	n.a.	n.a.	n.a.	n.a.	n.a.	n.a.	n.a.	0.07	0.12	0.02	n.d.	n.a.	n.a.	n.a.	n.a.
MgO	0.92	0.83	1.46	2.58	3.58	3.99	19.22	18.58	1.94	2.01	2.36	0.76	1.90	1.02	1.06	1.91
CaO	54.88	54.90	53.52	52.89	51.58	50.14	31.89	32.67	53.83	53.03	53.13	54.39	53.77	54.51	54.60	53.50
Na_2O	0.02	n.d.	n.d.	n.d.	n.d.	0.06	0.03	0.06	0.02	n.d.	n.d.	0.01	0.04	0.01	n.d.	n.d.
K_2O	n.a.	n.a.	n.a.	n.a.	n.a.	n.a.	n.a.	n.a.	n.d.	n.d.	0.02	0.01	n.a.	n.a.	n.a.	n.a.
SrO	0.07	n.d.	0.11	0.08	n.d.	0.06	0.03	0.06	n.d.	0.02	0.10	0.12	0.08	0.10	n.d.	0.20
BaO	0.03	0.02	n.d.	0.02	0.08	0.00	0.03	n.d.	0.01	0.04	n.d.	n.d.	n.d.	n.d.	n.d.	0.01
Cl	n.a.	n.a.	n.a.	n.a.	n.a.	n.a.	n.a.	n.a.	n.a.	n.a.	n.a.	n.a.	n.a.	n.a.	n.a.	n.a.
CO_2*	44.19	44.03	43.67	44.37	44.48	43.91	46.18	46.10	44.65	44.09	44.44	43.79	44.42	44.03	44.12	44.23
Total*	***100.19***	***99.84***	***98.80***	***99.95***	***99.83***	***98.32***	***97.56***	***97.59***	***100.85***	***99.58***	***100.21***	***99.39***	***100.32***	***99.82***	***99.97***	***99.96***
Stoech.	2O	2O	2O	2O	2O	2O	2O	2O	2O	2O	2O	2O	2O	2O	2O	2O
Si	-	-	-	-	-	-	-	-	0.001	0.000	0.000	0.000	-	-	-	-
Al	-	-	-	-	-	-	-	-	0.000	0.000	0.000	0.000	-	-	-	-
Fe3+	0.001	-	-	-	-	0.002	0.001	0.001	-	-	-	-	0.001	0.000	-	-
Fe2+	0.000	0.000	0.000	0.000	0.002	0.000	0.001	-	0.002	0.003	0.002	0.002	0.000	0.002	0.003	0.002
Mn	-	0.001	0.000	-	-	-	0.000	-	0.001	-	-	0.001	-	-	-	-
Ni	-	-	-	-	-	-	-	-	0.001	0.002	0.000	-	-	-	-	-
Mg	0.023	0.021	0.037	0.063	0.088	0.099	0.454	0.440	0.047	0.050	0.058	0.019	0.047	0.025	0.026	0.047
Ca	0.975	0.979	0.962	0.935	0.910	0.896	0.542	0.556	0.946	0.944	0.938	0.975	0.950	0.971	0.971	0.949
Na	0.001	-	-	-	-	0.002	0.001	0.002	0.001	-	-	0.000	0.001	0.000	-	-
K	-	-	-	-	-	-	-	-	-	-	0.001	0.000	-	-	-	-
Sr	0.001	0.000	0.001	0.001	-	0.001	0.000	0.001	-	0.000	0.001	0.001	0.001	0.001	-	0.002
Ba	0.000	0.000	-	0.000	0.001	0.000	0.000	-	0.000	0.000	-	-	-	-	-	0.000
Cl	-	-	-	-	-	-	-	-	-	-	-	-	-	-	-	-
C	1.000	1.000	1.000	1.000	1.000	1.000	1.000	1.000	1.000	1.000	1.000	1.000	1.000	1.000	1.000	1.000
Total	***2.000***	***2.000***	***2.000***	***2.000***	***2.000***	***2.000***	***2.000***	***2.000***	***2.000***	***2.000***	***2.000***	***2.000***	***2.000***	***2.000***	***2.000***	***2.000***
Mg#	***95.68***	***98.67***	***99.24***	***99.57***	***98.31***	***97.93***	***99.54***	***99.67***	***95.84***	***95.22***	***97.45***	***89.44***	***97.13***	***92.85***	***90.86***	***96.87***
Ca/(Ca+Mg)	***0.98***	***0.98***	***0.96***	***0.94***	***0.91***	***0.90***	***0.54***	***0.56***	***0.95***	***0.95***	***0.94***	***0.98***	***0.95***	***0.97***	***0.97***	***0.95***

Mg calc: Mg calcite; Cal-Dol: calcite-dolomite; *: calculated from stoichiometry; Mg# = 100*Mg/(Mg+Fetot); n.a.: not analysed; n.d.: not detected; -: not calculated

Table A3-7: Representative analyses and stoichiometry of ***carbonates*** in peridotite xenoliths from Marsabit (continued)

Group	**III-c**	**III-c**	**III-c**	**III-c**	**III-c**	**III-c**	**III-c**
sample	**1965/3**	**1965/3**	**1965/3**	**1965/3**	**1965/3**	**1965/3**	**1965/3**
mineral	Mg calc.	Mg calc.	Mg calc.	Mg calc.	Mg calc.	Mg calc.	Mg calc.
loaction	in glass core	in glass core	in glass core	in glass core	in glass rim	in glass rim	in glass rim
SiO_2	n.a.	n.d.	0.01	n.a.	0.04	0.03	n.a.
Al_2O_3	n.a.	n.d.	n.d.	n.a.	n.d.	n.d.	n.a.
Fe_2O_3*	0.01	0.02	0.06	0.04	0.06	-	0.03
FeO	0.07	0.09	-	-	-	0.06	-
MnO	n.d.	n.d.	0.01	n.d.	n.d.	n.d.	n.d.
NiO	n.a.	n.a.	n.a.	n.a.	n.a.	n.a.	n.a.
MgO	1.45	1.25	0.91	2.95	5.12	5.17	5.35
CaO	54.20	53.91	54.68	51.81	48.93	48.53	47.65
Na_2O	n.d.	n.d.	n.d.	0.03	0.05	0.03	0.12
K_2O	n.a.	0.01	0.01	n.d.	0.01	n.d.	n.a.
SrO	0.07	0.04	n.d.	0.30	0.19	0.21	0.79
BaO	n.d.	n.a.	n.a.	0.04	n.a.	n.a.	n.d.
Cl	n.a.	n.d.	0.02	n.a.	0.02	n.d.	n.a.
CO_2*	44.20	43.77	43.99	44.09	44.23	43.91	43.75
Total*	***99.99***	***99.09***	***99.71***	***99.27***	***98.64***	***97.94***	***97.68***
Stoech.	2O	2O	2O	2O	2O	2O	2O
Si	-	-	0.000	-	0.001	0.000	-
Al	-	-	-	-	-	-	-
Fe3+	0.000	0.000	0.001	0.001	0.001	-	0.000
Fe2+	0.001	0.001	-	-	-	0.001	-
Mn	-	-	0.000	-	-	-	-
Ni	-	-	-	-	-	-	-
Mg	0.036	0.031	0.022	0.073	0.126	0.129	0.133
Ca	0.962	0.967	0.975	0.922	0.868	0.867	0.855
Na	-	-	-	0.001	0.001	0.001	0.008
K	-	0.000	0.000	-	0.000	-	-
Sr	0.001	0.000	-	0.003	0.002	0.002	0.004
Ba	-	-	-	0.000	-	-	-
Cl	-	-	0.001	-	0.001	-	-
C	1.000	1.000	1.000	1.000	1.000	1.000	1.000
Total	***2.000***	***2.000***	***2.000***	***2.000***	***2.000***	***2.000***	***2.000***
Mg#	***97.03***	***95.54***	***96.80***	***99.32***	***99.44***	***99.31***	***99.72***
Ca/(Ca+Mg)	***0.96***	***0.97***	***0.98***	***0.93***	***0.87***	***0.87***	***0.87***

Mg calc: Mg calcite; Cal-Dol: calcite-dolomite; *: calculated from stoichiometry; Mg# = 100*Mg/(Mg+Fetot); n.a.: not analysed; n.d.: not detected; -: not calculated

Table A3-8: Major element composition of ***silicate glass*** from peridotite xenoliths from Marsabit

Group	**I**	**I**	**I**	**I**	**I**	**I**	**I**	**I**	**I**	**I**	**I**	**I**	**I**	**I**	**I**	**I**	**I**
sample	**1960/2**	**1960/2**	**1963/1**	**1963/1**	**1963/1**	**1963/1**	**1963/1**	**1963/1**	**1963/1**	**1963/1**	**1963/1**	**1963/1**	**1963/1**	**1963/1**	**1963/1**	**1963/1**	**1963/1**
loaction	next Ti-parg	next Ti-parg	m.p.	m.p.	m.p.	m.p.	m.p.	m.p.	m.p.	in sympl.	in sympl.	in sympl.	in sympl.	in sympl.	in sympl.	in sympl.	gr.bdr.
SiO_2	56.48	57.16	54.22	54.41	54.65	54.94	55.01	54.52	55.25	54.82	55.02	54.70	54.82	54.76	54.62	54.28	54.14
Al_2O_3	2.28	2.19	2.24	2.03	2.03	2.04	1.82	1.75	1.85	1.64	1.47	1.36	1.52	1.64	1.68	1.68	1.93
Fe_2O_3*	20.29	20.68	19.89	19.94	19.84	19.80	19.89	20.17	19.85	20.04	19.68	20.47	20.46	20.06	20.03	20.21	20.12
FeO	0.03	n.d.	0.02	0.02	0.04	0.08	0.00	0.03	0.00	n.d.	0.01	n.d.	0.05	0.08	0.02	n.d.	0.06
MnO	2.69	2.60	2.90	2.89	2.64	2.91	2.54	3.18	2.55	2.76	2.90	2.95	2.94	3.49	2.92	3.27	3.25
NiO	0.07	0.07	0.03	0.13	0.16	0.09	0.08	0.04	0.08	0.02	0.13	0.10	0.07	0.07	0.11	0.08	0.10
MgO	0.03	0.13	n.d.	n.d.	0.02	n.d.	0.03	0.04	0.01	n.d.	0.02	n.d.	0.04	0.04	0.11	n.d.	n.d.
CaO	3.20	3.00	3.69	3.40	3.57	3.54	3.56	3.85	3.25	3.49	3.71	3.12	3.18	3.85	3.53	3.72	3.72
Na_2O	8.55	7.73	8.26	8.34	8.02	8.12	8.06	8.07	7.56	8.51	8.48	8.75	9.12	9.37	9.38	9.95	8.81
K_2O	n.a.	n.a.	n.a.	n.a.	n.a.	n.a.	n.a.	n.a.	n.a.	n.a.	n.a.	n.a.	n.a.	n.a.	n.a.	n.a.	n.a.
SrO	5.04	5.36	3.87	3.72	4.03	3.72	3.85	3.79	4.08	3.90	3.72	4.14	4.17	3.66	3.98	3.92	4.23
BaO	0.57	0.64	2.13	2.30	2.08	2.26	2.00	1.77	2.20	1.48	1.56	0.97	0.49	0.43	0.43	0.42	0.43
F	n.a.	n.a.	n.d.	n.d.	0.23	0.11	0.02	0.13	0.10	0.06	0.20	0.19	0.05	0.05	0.07	0.10	0.24
Cl	n.a.	n.a.	n.d.	0.01	n.d.	0.03	n.d.	n.d.	n.d.	0.02	0.02	0.01	0.02	n.d.	0.01	0.01	0.03
P_2O_5	n.a.	n.a.	0.14	0.14	0.14	0.09	0.15	0.09	0.07	0.14	0.12	0.09	0.12	0.10	0.12	0.15	0.17
SO_2	n.a.	n.a.	n.a.	n.a.	n.a.	n.a.	n.a.	n.a.	n.a.	n.a.	n.a.	n.a.	n.a.	n.a.	n.a.	n.a.	n.a.
Total*	***99.23***	***99.57***	***97.38***	***97.35***	***97.45***	***97.74***	***97.00***	***97.41***	***96.84***	***96.87***	***97.03***	***96.85***	***97.04***	***97.59***	***97.00***	***97.78***	***97.24***
Mg#	***67.96***	***67.24***	***69.36***	***67.72***	***70.72***	***68.45***	***71.40***	***68.34***	***69.40***	***69.23***	***69.52***	***65.36***	***65.83***	***66.25***	***68.29***	***66.98***	***67.08***

Group	**I**	**II**	**II**	**II**	**II**	**II**	**II**	**II**	**II**	**II**	**II**	**II**	**II**	**II**	**II**	**III-b**	**III-b**
sample	**1963/1**	**1958/13**	**1958/13**	**1958/13**	**1958/13**	**1959/25**	**1959/25**	**1959/25**	**1959/25**	**1959/25**	**1959/25**	**1959/25**	**1959/25**	**1959/25**	**1959/25**	**1959/15**	**1959/15**
loaction	gr.bdr.	in sympl.	in sympl.	in sympl.	in sympl.	in sympl.	in sympl.	in sympl.	in sympl.	gr.bdr.	in sympl.	in sympl.	in sympl.	in sympl.	gr.bdr.	m.p.	next amph.
SiO_2	53.75	51.76	52.07	52.79	53.37	55.15	57.29	56.94	57.46	56.97	57.14	56.30	56.99	57.41	55.43	52.83	52.25
Al_2O_3	1.47	2.46	2.57	2.33	2.00	1.28	1.25	1.31	1.23	1.04	0.96	1.19	1.11	1.16	1.11	0.13	0.12
Fe_2O_3*	20.31	18.47	18.96	19.11	19.16	19.33	19.30	19.55	19.12	19.57	20.09	20.13	20.01	20.01	21.56	24.39	23.81
FeO	0.03	0.08	0.07	0.03	0.10	0.19	n.d.	0.07	0.11	0.03	0.13	n.d.	n.d.	n.d.	0.47	0.07	0.09
MnO	3.51	3.79	3.24	2.98	2.96	2.65	2.79	2.83	2.57	2.55	2.84	2.82	2.93	2.96	3.18	1.73	1.91
NiO	0.14	0.09	0.06	0.14	0.07	0.03	0.09	0.06	0.05	0.05	0.05	0.04	0.15	0.12	0.05	n.d.	n.d.
MgO	n.d.	n.a.	n.a.	n.a.	n.a.	n.d.	0.01	0.01	0.04	0.01	0.12	0.06	0.10	0.07	0.01	n.d.	0.01
CaO	3.99	4.70	3.79	3.01	3.26	3.04	2.69	3.19	3.14	2.58	2.85	2.95	3.27	2.68	3.57	1.67	1.69
Na_2O	8.94	11.71	11.87	11.19	10.72	6.44	6.69	6.67	6.67	6.50	6.16	7.51	7.36	7.26	7.01	4.47	4.45
K_2O	n.a.	0.06	0.06	0.08	0.14	n.a.	n.a.	n.a.	n.a.	n.a.	n.a.	n.a.	n.a.	n.a.	n.a.	n.a.	n.a.
SrO	4.13	3.43	3.25	3.53	3.80	6.22	6.23	6.36	6.13	6.58	6.40	5.88	6.02	5.99	5.67	10.80	8.67
BaO	0.43	0.84	0.75	0.94	0.92	0.01	0.05	0.04	0.04	0.01	0.01	0.03	0.05	0.07	0.03	1.60	1.53
F	0.20	n.a.	n.a.	n.a.	n.a.	n.a.	n.a.	n.a.	n.a.	n.a.	n.a.	n.a.	n.a.	n.a.	n.a.	n.a.	n.a.
Cl	0.02	0.17	0.22	0.18	0.18	n.d.	0.02	0.02	n.d.	0.02	0.01	n.d.	n.d.	0.02	n.d.	0.41	0.39
P_2O_5	0.12	0.11	0.15	0.21	0.15	0.08	0.07	0.15	0.10	0.08	0.09	0.09	0.09	0.13	0.04	0.35	0.34
SO_2	n.a.	0.02	n.d.	n.a.	n.a.	n.a.	n.a.	n.a.	n.a.	n.a.	n.a.	n.a.	n.a.	n.a.	n.a.	n.a.	n.a.
Total*	***97.05***	***97.70***	***97.04***	***96.51***	***96.83***	***94.42***	***96.48***	***97.20***	***96.65***	***95.99***	***96.85***	***97.01***	***98.07***	***97.88***	***98.12***	***98.43***	***95.25***
Mg#	***66.96***	***68.89***	***67.62***	***64.24***	***66.27***	***67.12***	***63.18***	***66.76***	***68.51***	***64.30***	***64.11***	***65.11***	***66.57***	***61.74***	***66.73***	***63.23***	***61.18***

Table A3-8: Major element composition of ***silicate glass*** from peridotite xenoliths from Marsabit (continued)

Group	III-b	III-b	III-b	III-b	III-b	III-b	III-b	III-b	III-b	III-b	III-b	III-b	III-b	III-b	III-b	III-b
sample	**1959/15**	**1959/15**	**1959/15**	**1959/15**	**1959/15**	**1959/15**	**1959/15**	**1959/15**	**1959/15**	**1959/15**	**1959/15**	**1959/15**	**1959/15**	**1959/15**	**1959/15**	**1965/15**
loaction	m.p.	m.p.	m.p.	m.p.	m.p.	next apatite	next apatite	m.p.	m.p.	m.p.	next apatite	next Opx_m	next Opx_m	next Opx_m	m.p.	next Opxm
SiO_2	52.76	52.92	52.78	53.04	53.06	59.02	57.64	55.82	55.98	56.27	61.77	58.51	58.47	58.71	56.51	59.10
Al_2O_3	0.15	0.08	0.12	0.20	0.17	0.45	0.47	0.28	0.24	0.29	0.41	0.43	0.45	0.42	0.31	1.62
Fe_2O_3*	24.34	25.07	24.50	24.22	24.12	19.32	19.70	22.69	22.75	22.98	18.10	20.27	20.70	19.44	20.97	19.64
FeO	0.04	0.12	0.01	0.04	0.05	0.05	0.08	0.08	0.08	0.07	0.03	0.01	n.d.	n.d.	0.24	0.04
MnO	1.83	2.19	1.87	1.56	1.88	1.97	1.95	1.88	1.95	1.77	1.21	1.67	1.82	1.68	1.68	1.76
NiO	0.10	0.03	0.06	0.06	0.07	n.d.	n.d.	0.06	0.05	0.02	0.01	0.07	0.03	0.01	0.07	0.03
MgO	n.d.	n.d.	0.08	0.02	n.d.	0.04	0.02	n.d.	0.10	n.d.	n.d.	n.d.	n.d.	0.06	0.01	n.a.
CaO	1.64	1.71	1.70	1.75	1.82	1.48	1.56	1.67	1.99	1.59	1.05	1.72	1.91	1.71	1.97	1.21
Na_2O	4.42	4.47	4.77	5.05	5.06	2.17	2.68	4.83	4.76	4.45	1.52	3.73	4.04	3.65	4.10	2.48
K_2O	n.a.	n.a.	n.a.	n.a.	n.a.	n.a.	n.a.	n.a.	n.a.	n.a.	n.a.	n.a.	n.a.	n.a.	n.a.	n.a.
SrO	10.80	10.84	10.49	11.01	11.07	8.88	9.47	9.82	9.57	10.15	9.56	8.82	8.97	8.66	9.85	9.65
BaO	1.56	1.49	1.48	1.57	1.54	1.67	1.61	0.87	0.86	0.88	1.88	0.91	0.95	0.83	1.05	1.94
F	n.a.	n.a.	n.a.	n.a.	n.a.	n.a.	n.a.	n.a.	n.a.	n.a.	n.a.	n.a.	n.a.	n.a.	n.a.	n.a.
Cl	0.29	0.37	0.34	0.35	0.31	0.33	0.33	0.41	0.40	0.40	0.21	0.28	0.31	0.33	0.36	0.87
P_2O_5	0.31	0.36	0.33	0.32	0.41	1.07	1.19	0.28	0.24	0.28	0.59	0.93	1.12	1.34	1.04	0.14
SO_2	n.a.	n.a.	n.a.	n.a.	n.a.	n.a.	n.a.	n.a.	n.a.	n.a.	n.a.	n.a.	n.a.	n.a.	n.a.	n.a.
Total*	***98.24***	***99.63***	***98.52***	***99.20***	***99.56***	***96.44***	***96.70***	***98.68***	***98.95***	***99.16***	***96.32***	***97.34***	***98.77***	***96.83***	***98.16***	***98.48***
Mg#	***61.49***	***58.24***	***61.87***	***66.70***	***63.29***	***57.21***	***58.72***	***61.34***	***64.59***	***61.66***	***60.86***	***64.67***	***65.11***	***64.50***	***67.61***	***55.06***

Group	III-b	III-b	III-b	III-b	III-b	III-b	III-b	III-b	III-b	III-b	III-b	III-b	III-b	III-b	III-c	III-c
sample	**1965/15**	**1965/15**	**1965/15**	**1965/15**	**1965/15**	**1965/15**	**1965/15**	**1965/15**	**1965/15**	**1965/15**	**1965/15**	**1965/15**	**1965/15**	**1965/15**	**785***	**785***
loaction	xenolith margin	m.p.	m.p.	m.p.	m.p.	m.p.	m.p.	m.p.	xenolith margin	xenolith margin	xenolith margin	xenolith margin	next Opx_m	next Opx_m	gr.bdr.	gr.bdr.
SiO_2	50.50	57.75	56.03	58.07	58.62	59.15	61.12	59.37	52.03	52.98	52.31	51.61	57.10	57.87	57.66	58.12
Al_2O_3	1.18	1.57	1.43	0.94	1.36	1.37	1.17	1.28	1.01	1.08	1.10	1.06	0.70	0.74	0.59	0.56
Fe_2O_3*	20.22	20.53	21.02	21.78	20.91	20.63	19.27	19.62	21.08	21.07	20.51	20.25	19.00	19.88	20.46	20.20
FeO	n.d.	0.01	0.06	0.02	n.d.	0.06	0.05	0.03	0.06	n.d.	n.d.	n.d.	0.02	n.d.	1.04	0.02
MnO	5.63	2.47	2.60	1.33	1.51	1.63	1.34	1.39	4.78	4.49	5.12	6.26	3.17	1.97	1.44	1.30
NiO	0.09	n.d.	0.12	0.03	0.03	n.d.	0.05	0.05	0.12	0.07	0.16	0.26	0.06	0.07	0.03	n.d.
MgO	n.a.	n.d.	0.05	0.02	0.05	n.d.	0.01	n.d.	0.04	n.d.	n.d.	n.d.	n.d.	n.d.	n.a.	n.a.
CaO	1.07	1.29	1.24	0.76	1.16	1.52	1.26	1.29	0.88	1.02	0.90	1.16	1.19	1.25	0.85	0.72
Na_2O	2.70	2.57	3.23	2.49	2.95	3.37	2.02	2.54	3.10	2.53	2.67	2.83	1.84	1.83	1.47	2.05
K_2O	n.a.	n.a.	n.a.	n.a.	n.a.	n.a.	n.a.	n.a.	n.a.	n.a.	n.a.	n.a.	n.a.	n.a.	n.a.	n.a.
SrO	9.44	9.66	9.74	8.63	8.98	8.99	8.57	8.92	10.13	10.34	9.56	9.69	9.29	10.10	10.37	10.29
BaO	4.52	1.97	1.78	2.65	1.46	1.44	1.52	1.51	4.69	3.83	4.71	4.65	3.85	3.44	3.72	3.21
F	n.a.	n.d.	0.29	n.d.	0.01	0.24	n.d.	0.07	0.27	n.d.	0.23	n.d.	n.d.	0.10	n.a.	n.a.
Cl	0.39	1.06	1.13	0.63	0.98	0.92	0.80	0.76	0.39	0.42	0.44	0.38	0.36	0.36	0.13	0.17
P_2O_5	0.49	0.08	0.15	0.22	0.35	0.34	0.32	0.49	0.63	0.56	0.56	0.44	0.50	0.48	0.06	0.08
SO_2	n.a.	n.a.	n.a.	n.a.	n.a.	n.a.	n.a.	n.a.	n.a.	n.a.	n.a.	n.a.	n.a.	n.a.	n.a.	n.a.
Total*	***96.23***	***98.96***	***98.89***	***97.56***	***98.35***	***99.65***	***97.47***	***97.33***	***99.22***	***98.39***	***98.26***	***98.60***	***97.09***	***98.07***	***97.81***	***96.70***
Mg#	***25.23***	***48.16***	***45.91***	***50.67***	***57.90***	***62.30***	***62.66***	***62.36***	***24.80***	***28.88***	***23.75***	***24.89***	***40.04***	***53.11***	***51.25***	***49.43***

gr.bdr. = grainboundary

Table A3-8: Major element composition of ***silicate glass*** from peridotite xenoliths from Marsabit (continued)

Group	**III-c**	**III-c**	**III-c**	**III-c**	**III-c**	**III-c**	**III-c**	**III-c**	**III-c**	**III-c**	**III-c**	**III-c**	**III-c**	**III-c**	**III-c**	**III-c**
sample	**785***	**785***	**785***	**785***	**785***	**785***	**785***	**785***	**785***	**785***	**785***	**785***	**785***	**785***	**785***	**785***
loaction	m.p.	m.p.	m.p.	m.p.	m.p.	next amph.	m.p.	m.p.	next amph.	m.p.	m.p.	next amph.	next Opxm	next Opxm	m.p.	next Opxm
SiO_2	60.96	60.09	60.96	60.09	60.27	57.80	60.33	62.09	60.80	62.76	63.56	61.84	65.30	64.02	59.29	65.38
Al_2O_3	0.62	0.59	0.62	0.59	0.58	0.50	0.51	0.57	0.63	0.67	0.60	0.53	0.49	0.57	0.51	0.67
Fe_2O_3*	17.79	18.95	17.79	18.95	19.27	19.64	18.27	17.09	18.54	16.83	17.05	18.10	15.33	18.46	19.69	16.36
FeO	0.01	n.d.	0.01	n.d.	0.04	n.d.	n.d.	0.07	0.10	0.04	0.08	0.15	n.d.	n.d.	0.37	0.01
MnO	1.26	1.33	1.26	1.33	1.27	0.97	1.23	1.31	1.25	1.29	1.33	1.39	1.31	1.01	1.29	1.39
NiO	0.01	n.d.	0.01	n.d.	0.02	n.d.	0.01	n.d.	0.02	0.00	0.02	0.05	0.02	0.06	n.d.	0.01
MgO	n.a.	n.a.	n.a.	n.a.	n.a.	n.a.	n.a.	n.a.	n.a.	n.a.	n.a.	n.a.	n.a.	n.a.	n.a.	n.a.
CaO	1.14	0.72	1.14	0.72	0.70	1.33	1.09	1.29	0.85	0.98	1.06	0.85	1.20	0.66	1.28	0.98
Na_2O	0.82	0.80	0.82	0.80	0.96	0.86	1.39	0.33	0.46	0.44	0.41	0.32	0.59	1.16	1.04	0.42
K_2O	n.a.	n.a.	n.a.	n.a.	n.a.	n.a.	n.a.	n.a.	n.a.	n.a.	n.a.	n.a.	n.a.	n.a.	n.a.	n.a.
SrO	9.71	9.95	9.71	9.95	9.90	8.47	10.13	9.50	9.53	9.74	10.22	10.33	8.95	9.69	10.98	9.56
BaO	3.57	3.85	3.57	3.85	3.71	4.87	3.41	2.94	3.20	2.78	2.92	2.99	3.33	3.45	3.19	2.02
F	n.a.	n.a.	n.a.	n.a.	n.a.	n.a.	n.a.	n.a.	n.a.	n.a.	n.a.	n.a.	n.a.	n.a.	n.a.	n.a.
Cl	0.12	0.12	0.12	0.12	0.15	0.15	0.11	0.15	0.11	0.08	0.15	0.13	0.09	0.06	0.14	0.12
P_2O_5	0.09	0.12	0.09	0.12	0.08	0.09	0.07	0.04	0.08	0.10	0.06	0.06	0.05	0.01	0.07	0.02
SO_2	n.a.	n.a.	n.a.	n.a.	n.a.	n.a.	n.a.	n.a.	n.a.	n.a.	n.a.	n.a.	n.a.	n.a.	n.a.	n.a.
Total*	***96.09***	***96.50***	***96.09***	***96.50***	***96.94***	***94.68***	***96.56***	***95.37***	***95.56***	***95.69***	***97.45***	***96.73***	***96.66***	***99.15***	***97.85***	***96.93***
Mg#	***61.75***	***49.08***	***61.75***	***49.08***	***49.77***	***70.97***	***61.26***	***63.65***	***54.86***	***57.57***	***58.66***	***52.26***	***61.98***	***53.82***	***63.81***	***55.60***

Group	**III-c**	**III-c**	**III-c**	**III-c**	**III-c**	**III-c**	**III-c**	**III-c**	**III-c**	**III-c**	**III-c**	**III-c**	**III-c**	**III-c**	**III-c**	**III-c**
sample	**785***	**785***	**785***	**785***	**785***	**785***	**785***	**785***	**785***	**785***	**785***	**1959/27**	**1959/27**	**1959/27**	**1959/27**	**1959/27**
loaction	gr.bdr.	next Opx_m	next Opx_m	gr.bdr.	m.p.	m.p.	m.p.	m.p.	m.p.	m.p.	m.p.	m.p.	m.p.	m.p.	m.p.	m.p.
SiO_2	65.80	65.43	66.37	65.98	60.53	60.36	64.18	62.61	62.84	61.85	61.63	48.54	48.80	48.66	48.39	49.36
Al_2O_3	0.57	0.48	0.54	0.57	0.76	0.70	0.68	0.71	0.63	0.57	0.65	3.74	3.84	3.74	3.69	3.46
Fe_2O_3*	15.81	16.21	16.21	16.09	19.61	19.63	17.35	17.33	16.94	19.28	18.72	18.52	19.13	18.97	18.65	19.46
FeO	0.02	n.d.	n.d.	0.04	0.06	0.10	0.02	0.21	n.d.	0.05	n.d.	0.06	0.00	0.02	0.06	n.d.
MnO	1.43	1.33	1.39	1.61	1.40	1.39	1.38	1.25	1.40	1.48	1.54	5.32	5.30	5.60	5.43	4.62
NiO	0.01	0.04	n.d.	0.05	0.03	0.05	0.06	0.05	0.02	0.04	n.d.	0.22	0.26	0.14	0.23	0.13
MgO	n.a.	n.a.	n.a.	n.a.	n.a.	n.a.	n.a.	n.a.	n.a.	n.a.	n.a.	0.04	0.02	n.d.	n.d.	n.d.
CaO	0.87	1.05	0.91	1.26	0.81	0.58	1.34	1.11	1.27	0.95	1.27	2.69	2.17	2.44	3.29	2.25
Na_2O	1.06	0.80	0.51	1.01	0.85	0.61	0.63	0.67	0.76	0.40	0.71	7.46	7.27	7.42	7.93	6.27
K_2O	n.a.	n.a.	n.a.	n.a.	n.a.	n.a.	n.a.	n.a.	n.a.	n.a.	n.a.	n.a.	n.a.	n.a.	n.a.	n.a.
SrO	8.68	9.00	9.40	9.50	10.16	9.89	10.26	9.52	9.41	11.04	10.38	6.61	7.10	7.03	6.65	7.31
BaO	2.07	2.40	2.16	2.00	2.89	3.00	3.12	3.38	3.19	3.06	3.15	3.03	2.90	3.06	2.82	3.50
F	n.a.	n.a.	n.a.	n.a.	n.a.	n.a.	n.a.	n.a.	n.a.	n.a.	n.a.	n.a.	n.a.	n.a.	n.a.	n.a.
Cl	0.10	0.09	0.09	0.11	0.11	0.13	n.a.	n.a.	n.a.	n.a.	n.a.	0.17	0.17	0.14	0.15	0.16
P_2O_5	0.03	0.06	0.04	0.06	0.08	0.13	n.a.	n.a.	n.a.	n.a.	n.a.	0.99	0.96	0.98	0.97	0.99
SO_2	n.a.	n.a.	n.a.	n.a.	n.a.	n.a.	n.a.	n.a.	n.a.	n.a.	n.a.	n.a.	n.a.	n.a.	n.a.	n.a.
Total*	***96.45***	***96.90***	***97.61***	***98.28***	***97.29***	***96.56***	***99.02***	***96.83***	***96.47***	***98.73***	***98.05***	***97.38***	***97.90***	***98.21***	***98.24***	***97.51***
Mg#	***51.96***	***58.53***	***53.90***	***58.21***	***50.77***	***42.60***	***63.52***	***61.32***	***61.79***	***53.33***	***59.52***	***47.42***	***42.26***	***43.68***	***51.90***	***46.43***

gr.bdr. = grainboundary

Table A3-8: Major element composition of ***silicate glass*** from peridotite xenoliths from Marsabit (continued)

Group	III-c	III-c	III-c	III-c	III-b	III-b	III-b	III-b	III-b	III-b	III-b	III-c	III-c	III-c	III-c	III-c
sample	**1959/27**	**1959/27**	**1959/27**	**1959/27**	**1965/3**	**1965/3**	**1965/3**	**1965/3**	**1965/3**	**1965/3**	**1965/3**	**1965/3**	**1965/3**	**1965/3**	**1965/3**	**1965/3**
loaction	gr.bdr.	gr.bdr.	m.p.	m.p.	m.p.	m.p.	m.p.	m.p.	m.p.	m.p.	gr.bdr.	m.p.	m.p.	gr.bdr.	next Opx_m	next Opx_m
SiO_2	49.10	48.88	48.64	49.02	60.44	60.51	59.61	59.38	60.70	59.81	61.61	59.21	59.41	61.03	66.04	65.30
Al_2O_3	3.92	4.05	3.95	3.66	0.29	0.27	0.27	0.24	0.24	0.26	0.22	0.30	0.27	0.24	0.21	0.23
Fe_2O_3*	19.35	19.11	18.40	18.53	15.92	15.54	15.40	15.75	15.24	15.67	14.89	15.99	15.78	14.96	13.68	13.55
FeO	n.d.	n.d.	0.03	n.d.	0.01	n.d.	n.d.	n.d.	0.01	0.66	0.02	0.04	0.01	0.03	0.01	n.d.
MnO	4.65	4.75	5.21	4.96	3.04	3.10	2.83	2.95	3.03	2.72	3.01	2.99	3.21	2.87	2.32	2.65
NiO	0.19	0.08	0.18	0.19	0.07	0.06	0.10	0.05	0.00	0.02	0.00	0.03	0.10	0.07	n.d.	0.07
MgO	n.d.	0.01	n.d.	n.d.	n.a.	n.a.	n.a.	n.a.	n.a.	n.a.	n.a.	n.a.	n.a.	n.a.	0.01	n.d.
CaO	1.66	1.74	2.59	3.09	3.10	3.11	3.09	3.04	2.97	2.66	2.62	3.06	2.76	2.77	2.85	2.52
Na_2O	8.93	9.69	9.52	8.38	1.01	0.98	1.59	1.24	1.81	1.55	0.58	1.13	0.56	1.79	0.36	0.39
K_2O	n.a.	n.a.	n.a.	n.a.	0.09	0.08	0.08	0.06	0.02	0.01	0.08	0.08	0.03	0.04	n.a.	n.a.
SrO	6.86	6.61	6.16	6.28	13.49	13.37	13.89	13.88	13.45	13.43	13.79	14.11	13.77	12.91	12.14	12.11
BaO	3.08	2.96	2.79	2.83	1.24	1.15	1.09	1.21	1.21	1.33	1.23	1.01	1.04	1.24	1.29	1.27
F	n.a.	n.a.	n.a.	n.a.	n.a.	n.a.	n.a.	n.a.	n.a.	n.a.	n.a.	n.a.	n.a.	n.a.	n.a.	n.a.
Cl	0.15	0.14	0.17	0.16	0.27	0.29	0.26	0.23	0.24	0.25	0.28	0.32	0.36	0.28	0.21	0.20
P_2O_5	1.08	0.94	1.02	1.04	0.53	0.54	0.48	0.49	0.46	0.41	0.55	0.86	0.83	0.50	0.19	0.18
SO_2	n.a.	n.a.	n.a.	n.a.	n.d.	0.06	0.05	n.d.	0.02	0.05	n.d.	0.03	0.02	0.01	n.a.	n.a.
Total*	***98.97***	***98.95***	***98.66***	***98.13***	***99.49***	***99.06***	***98.75***	***98.51***	***99.42***	***98.82***	***98.89***	***99.13***	***98.15***	***98.73***	***99.31***	***98.46***
Mg#	***38.94***	***39.49***	***46.94***	***52.65***	***64.53***	***64.08***	***66.07***	***64.74***	***63.61***	***63.53***	***60.79***	***64.65***	***60.50***	***63.22***	***68.63***	***62.89***

Group	III-c	III-c	III-c	III-c	III-c	III-c	III-c	III-c	III-c	III-c	III-c	III-c	III-c	III-c	III-c	III-c
sample	**1965/3**	**1965/3**	**1965/3**	**1965/3**	**1965/3**	**1965/3**	**1965/3**	**1965/3**	**1965/3**	**1965/3**	**1965/3**	**1965/3**	**1965/3**	**1965/3**	**1965/3**	**1965/3**
loaction	next Opx_m	next apatite	next apatite	next apatite	m.p.	m.p.	m.p.	m.p.	m.p.	m.p.	m.p.	m.p.	m.p.	m.p.	m.p.	m.p.
SiO_2	66.32	59.74	58.22	59.12	60.77	60.68	60.63	60.74	60.90	60.78	60.25	60.49	58.78	58.87	59.64	59.17
Al_2O_3	0.26	0.20	0.21	0.24	0.27	0.25	0.24	0.27	0.27	0.25	0.27	0.27	0.28	0.25	0.22	0.26
Fe_2O_3*	13.42	12.45	12.36	12.44	16.11	15.67	15.29	15.53	15.55	14.97	14.89	15.12	15.32	14.55	15.75	15.75
FeO	0.06	n.d.	0.05	n.d.	n.a.	n.a.	n.a.	n.a.	n.a.	n.a.	n.a.	n.a.	n.a.	n.a.	n.a.	n.a.
MnO	2.45	3.74	3.64	3.52	3.13	3.07	2.64	3.06	3.03	2.96	2.91	2.94	2.99	3.14	2.99	3.11
NiO	n.d.	0.08	0.01	0.15	0.09	0.03	0.03	0.01	0.05	0.17	0.03	0.07	0.02	0.09	0.03	n.d.
MgO	n.d.	0.06	n.d.	n.d.	n.a.	n.a.	n.a.	n.a.	n.a.	n.a.	n.a.	n.a.	n.a.	n.a.	n.a.	n.a.
CaO	2.52	3.82	4.52	4.21	3.45	3.23	3.42	3.29	3.05	3.64	3.57	3.53	3.75	4.17	3.07	3.52
Na_2O	0.78	1.01	1.36	1.41	1.32	1.19	1.26	1.09	0.87	1.85	1.89	1.84	1.39	1.59	1.38	1.32
K_2O	n.a.	n.a.	n.a.	n.a.	n.a.	n.a.	n.a.	n.a.	n.a.	n.a.	n.a.	n.a.	n.a.	n.a.	n.a.	n.a.
SrO	12.13	13.84	13.93	13.30	12.81	13.17	13.05	13.06	13.31	12.83	12.92	12.88	13.30	13.12	13.47	13.35
BaO	1.30	1.42	1.30	1.44	1.01	1.02	1.03	1.00	1.10	0.93	0.85	0.90	1.01	1.03	1.02	0.98
F	n.a.	n.a.	n.a.	n.a.	n.a.	n.a.	n.a.	n.a.	n.a.	n.a.	n.a.	n.a.	n.a.	n.a.	n.a.	n.a.
Cl	0.22	0.61	0.55	0.57	0.30	0.29	0.32	0.33	0.27	0.26	0.30	0.31	0.35	0.37	0.35	0.33
P_2O_5	0.25	2.33	2.72	2.44	n.a.	n.a.	n.a.	n.a.	n.a.	n.a.	n.a.	n.a.	n.a.	n.a.	n.a.	n.a.
SO_2	n.a.	n.a.	n.a.	n.a.	n.a.	n.a.	n.a.	n.a.	n.a.	n.a.	n.a.	n.a.	n.a.	n.a.	n.a.	n.a.
Total*	***99.69***	***99.29***	***98.87***	***98.85***	***99.20***	***98.53***	***97.84***	***98.28***	***98.34***	***98.58***	***97.82***	***98.27***	***97.11***	***97.10***	***97.83***	***97.71***
Mg#	***64.68***	***64.58***	***68.88***	***68.06***	***66.27***	***65.22***	***69.79***	***65.72***	***64.16***	***68.69***	***68.63***	***68.17***	***69.10***	***70.25***	***64.68***	***66.92***

gr.bdr.= grainboundarie

Table A3-8: Major element composition of ***silicate glass*** from peridotite xenoliths from Marsabit (continued)

Group	**III-c**	**III-c**	**III-c**	**III-c**	**III-c**	**III-c**	**III-c**	**III-c**	**III-c**	**III-c**
sample	**1965/3**	**1965/3**	**1965/3**	**1965/3**	**1965/25**	**1965/25**	**1965/25**	**1965/25**	**1965/25**	**1965/25**
loaction	m.p.	m.p.	next Opx_m	next Opx_m	m.p.	m.p.	m.p.	m.p.	m.p.	m.p.
SiO_2	59.63	60.82	61.26	62.47	56.61	57.27	56.95	56.79	56.57	56.75
Al_2O_3	0.24	0.27	0.26	0.23	0.26	0.41	0.38	0.37	0.30	0.32
Fe_2O_3*	15.63	15.64	15.33	13.85	24.05	23.09	22.46	21.99	23.13	21.53
FeO	n.a.	n.a.	n.a.	n.a.	0.05	0.06	0.01	n.d.	0.01	0.05
MnO	2.87	2.84	2.81	3.01	1.59	2.10	2.89	2.59	2.52	1.84
NiO	0.03	0.13	n.d.	0.12	0.04	0.05	0.06	0.04	0.04	0.01
MgO	n.a.	n.a.	n.a.	n.a.	n.d.	0.02	n.d.	n.d.	n.d.	0.03
CaO	3.15	3.18	3.23	3.25	0.66	0.65	2.85	1.60	1.22	1.61
Na_2O	1.00	1.25	1.22	0.83	1.05	0.75	1.03	0.89	0.44	1.56
K_2O	n.a.	n.a.	n.a.	n.a.	n.a.	n.a.	n.a.	n.a.	n.a.	n.a.
SrO	12.94	13.29	12.97	12.55	14.80	14.81	10.62	12.53	12.99	13.46
BaO	0.92	0.94	0.89	0.86	0.48	0.56	1.09	1.28	1.38	0.36
F	n.a.	n.a.	n.a.	n.a.	n.a.	n.a.	n.a.	n.a.	n.a.	n.a.
Cl	0.33	0.32	0.31	0.33	0.02	0.10	0.13	0.14	0.14	0.02
P_2O_5	n.a.	n.a.	n.a.	n.a.	0.14	0.11	0.17	0.15	0.12	0.14
SO_2	n.a.	n.a.	n.a.	n.a.	n.a.	n.a.	n.a.	n.a.	n.a.	n.a.
Total*	***96.67***	***98.61***	***98.22***	***97.41***	***99.76***	***99.96***	***98.62***	***98.38***	***98.88***	***97.67***
Mg#	***66.19***	***66.58***	***67.22***	***65.77***	***42.60***	***35.46***	***63.75***	***52.36***	***46.32***	***60.84***

Table A3-9: Representative major element composition (wt%) and stoichiometry of ***garnet*** in mafic xenoliths from Marsabit

	Grt websterites																	
Group	V	V	V	V	V	V	V	V	V	V	V	V	V	V	V	V	V	V
mineral	grt	grt	grt	grt	grt	grt	grt	grt	grt	grt	kelyph.*	kelyph.*	grt	grt	grt	cpx-I	cpx-I	cpx-I
sample	784/1	784/1	784/1	784/1	784/1	784/1	1959/18	1959/18	1959/18	1959/18	1959/18	1959/18	1960/8	1960/8	1960/8	1964	1964	1964
remark	core	core	core	rim (opx-I)	rim (cpx-I)	rim (cpx-I)	core	core	rim (opx-I)	rim (Ti-prg)	bulk	bulk	core	core	rim (cpx-I)	core	core	rim (cpx-IIb)
SiO_2	41.57	41.58	41.40	41.90	41.65	41.45	42.53	42.43	42.40	42.05	42.00	41.68	41.84	41.78	41.69	42.42	42.13	41.72
TiO_2	0.13	0.13	0.13	0.02	0.03	0.03	0.12	0.15	0.15	0.04	0.03	0.03	0.12	0.11	0.05	0.09	0.07	0.04
Al_2O_3	22.10	22.53	22.77	23.00	22.48	22.59	22.92	22.86	22.89	22.72	22.32	22.27	23.26	23.21	23.19	23.83	23.64	23.61
Cr_2O_3	0.29	0.37	0.39	0.24	0.27	0.17	0.23	0.19	0.23	0.42	0.31	0.32	1.31	1.47	1.64	1.00	1.03	0.98
FeO	12.48	12.77	12.82	12.96	13.40	13.14	9.41	9.43	10.18	11.92	11.45	11.58	8.16	8.56	8.85	7.49	7.58	9.55
MnO	0.35	0.39	0.41	0.37	0.31	0.57	0.35	0.32	0.44	0.43	0.58	0.54	0.31	0.35	0.35	0.29	0.29	0.63
NiO	n.d.	n.d.	0.01	0.03	0.01	0.01	n.a.	n.a.	n.a.	n.a.	0.01	0.00	n.d.	n.d.	0.01	n.d.	n.d.	0.01
MgO	17.97	17.96	17.89	18.13	17.08	17.37	20.74	20.68	19.93	18.81	18.39	18.28	19.91	19.78	19.22	20.40	20.33	18.63
CaO	4.66	4.43	4.54	4.25	4.79	4.96	3.87	3.95	3.98	3.83	3.99	4.45	5.14	5.16	5.13	5.35	5.14	5.19
Na_2O	0.03	0.03	0.00	0.00	0.03	0.04	0.06	0.06	0.04	0.04	0.68	0.23	0.01	0.05	0.01	0.04	0.03	0.03
K_2O	0.01	n.d.	0.01	0.01	0.01	n.d.	n.d.	n.d.	0.01	0.01	n.d.	n.d.	n.d.	0.01	n.d.	0.01	n.d.	0.01
Total	***99.59***	***100.18***	***100.37***	***100.91***	***100.05***	***100.32***	***100.23***	***100.08***	***100.26***	***100.27***	***99.75***	***99.38***	***100.04***	***100.48***	***100.14***	***100.93***	***100.26***	***100.40***
Stoech.	**12O**	**12O**	**12O**	**12O**	**12O**	**12O**	**12O**	**12O**	**12O**	**12O**	**12O**	**12O**	**12O**	**12O**	**12O**	**12O**	**12O**	**12O**
Si	3.018	3.003	2.987	3.001	3.020	3.000	3.014	3.013	3.016	3.015	3.031	3.022	2.974	2.966	2.973	2.977	2.977	2.975
Ti	0.007	0.007	0.007	0.001	0.002	0.002	0.006	0.008	0.008	0.002	0.001	0.002	0.006	0.006	0.003	0.005	0.004	0.002
Al	1.891	1.917	1.936	1.941	1.920	1.927	1.914	1.913	1.919	1.920	1.899	1.902	1.949	1.942	1.949	1.971	1.969	1.984
Cr	0.017	0.021	0.022	0.014	0.015	0.010	0.013	0.011	0.013	0.024	0.018	0.018	0.073	0.082	0.093	0.055	0.058	0.055
Fe^{2+}	0.757	0.771	0.774	0.776	0.812	0.795	0.557	0.560	0.606	0.715	0.691	0.702	0.485	0.508	0.528	0.440	0.448	0.570
Mn	0.021	0.024	0.025	0.022	0.019	0.035	0.021	0.019	0.027	0.026	0.035	0.033	0.018	0.021	0.021	0.017	0.018	0.038
Ni	-	-	0.000	0.002	0.001	0.000	-	-	-	-	0.001	0.000	-	-	0.001	n.d.	n.d.	0.001
Mg	1.945	1.933	1.924	1.936	1.846	1.874	2.191	2.188	2.114	2.011	1.978	1.976	2.110	2.093	2.043	2.134	2.142	1.980
Ca	0.363	0.343	0.351	0.326	0.372	0.384	0.294	0.301	0.304	0.294	0.309	0.346	0.391	0.392	0.392	0.402	0.389	0.396
Na	0.004	0.004	0.000	0.000	0.004	0.005	0.009	0.008	0.006	0.005	0.094	0.033	0.002	0.006	0.001	0.006	0.004	0.004
K	0.001	-	0.001	0.001	0.001	-	-	-	0.001	0.001	0.000	-	-	0.001	-	0.001	-	0.001
Total	8.024	8.023	8.027	8.021	8.013	8.033	8.020	8.021	8.013	8.013	8.057	8.033	8.009	8.019	8.004	8.008	8.008	8.006
Cr#	***0.87***	***1.08***	***1.14***	***0.70***	***0.80***	***0.50***	***0.67***	***0.56***	***0.66***	***1.22***	***0.93***	***0.96***	***3.63***	***4.06***	***4.54***	***2.73***	***2.85***	***2.71***
Mg#	***71.98***	***71.49***	***71.32***	***71.37***	***69.45***	***70.20***	***79.72***	***79.63***	***77.73***	***73.77***	***74.11***	***73.79***	***81.31***	***80.46***	***79.47***	***82.92***	***82.70***	***77.66***

Cr# = 100*Cr/(Cr+Al); *: kelyph. = kelyphite after garnet (bulk analyses obtained with defocused electron beam); the abbreviation in brackets under location indicates the adjacent mineral phase of the respective rim analysis; n.a.: not analysed; n.d.: not detected; Stoich.: cations calculated on the basis of 12 oxygens

Table A3-10: Representative major element composition (wt%) and stoichiometry of ***clinopyroxene*** in mafic xenoliths from Marsabit

	Grt websterites																	
Group	**V**	**V**	**V**	**V**	**V**	**V**	**V**	**V**	**V**	**V**	**V**	**V**	**V**	**V**	**V**	**V**	**V**	**V**
	cpx-I	**cpx-I**	**cpx-I**	**cpx-I**	**cpx-I**	**cpx-I**	**cpx-I**	**cpx-I**	**cpx-I**	**cpx-I**	**cpx-I**	**cpx-I**	**cpx-I**	**cpx-I**	**cpx-IIb**	**cpx-IIb**	**cpx$_S$**	**cpx$_S$**	**cpx$_S$**
sample	784/1	784/1	784/1	784/1	784/1	784/1	784/1	1959/18	1959/18	1959/18	1959/18	1959/18	1959/18	1959/18	1959/18	1959/18	1959/18	1959/18	1959/18
remark	core (cpx-I)	core (cpx-I)	core (cpx-I)	rim (cpx-I)	rim (opx-I)	rim (opx-I)	incl. in grt	core (exsol.)	core (exsol.)	core (exsol.)	rim (opx-I)	rim (opx-I)	rim (opx-I)	sympl./r (opx-IIb)	sympl. core	spongy (cpx-I)	spongy (cpx-I)	spongy (Ti-prg)	
SiO_2	52.30	52.34	52.16	52.24	51.55	50.78	51.22	53.87	53.62	53.62	53.14	52.76	53.63	52.75	52.16	52.12	52.26	48.99	
TiO_2	0.71	0.81	0.79	0.72	0.76	0.86	1.60	0.70	0.76	0.72	0.53	0.64	0.70	0.61	0.51	0.57	0.91	2.32	
Al_2O_3	4.97	5.26	5.19	5.81	6.28	7.06	7.98	6.60	6.71	6.85	8.60	9.12	8.89	7.43	9.92	4.55	4.02	7.00	
Cr_2O_3	0.21	0.25	0.19	0.23	0.15	0.19	0.34	0.22	0.38	0.41	0.50	0.36	0.43	0.19	0.16	0.40	0.36	0.56	
FeO	3.67	3.65	3.71	3.30	3.43	3.48	3.14	2.52	2.64	2.87	2.66	2.43	2.25	2.84	2.56	2.85	3.19	4.38	
MnO	0.10	0.03	0.04	0.11	0.01	0.09	0.04	0.07	0.09	0.09	0.08	0.09	0.08	0.04	0.06	0.12	0.11	0.25	
NiO	0.04	0.08	0.01	0.03	0.03	0.01	0.05	0.07	0.05	n.d.	n.d.	0.01	0.06	n.a.	n.d.	n.a.	n.d.	n.a.	
MgO	14.53	14.44	14.39	14.27	14.08	13.56	13.05	13.91	13.82	13.85	12.74	12.84	12.75	14.05	12.50	16.06	17.99	15.09	
CaO	21.00	21.19	21.00	20.79	21.05	20.58	19.71	19.29	19.37	18.69	17.97	18.92	18.38	19.91	18.70	21.74	19.81	20.09	
Na_2O	1.91	2.08	1.98	2.12	2.05	2.27	2.60	2.90	2.91	3.13	3.74	3.12	3.69	2.57	3.33	1.00	0.73	0.96	
K_2O	n.d.	0.02	0.01	0.02	n.d.	n.d.	n.d.	n.d.	0.02	0.01	n.d.	n.d.	n.d.	n.d.	n.d.	0.01	n.d.	0.01	n.d.
Total	***99.44***	***100.14***	***99.47***	***99.64***	***99.38***	***98.88***	***99.71***	***100.16***	***100.37***	***100.24***	***99.97***	***100.28***	***100.86***	***100.41***	***99.90***	***99.43***	***99.38***	***99.63***	
Stoich.	**6O**	**6O**	**6O**	**6O**	**6O**	**6O**	**6O**	**6O**	**6O**	**6O**	**6O**	**6O**	**6O**	**6O**	**6O**	**6O**	**6O**	**6O**	
Si	1.915	1.905	1.909	1.904	1.887	1.869	1.861	1.934	1.924	1.925	1.909	1.889	1.906	1.895	1.875	1.903	1.901	1.800	
Ti	0.020	0.022	0.022	0.020	0.021	0.024	0.044	0.019	0.020	0.019	0.014	0.017	0.019	0.017	0.014	0.016	0.025	0.064	
Al	0.214	0.226	0.224	0.250	0.271	0.306	0.342	0.279	0.284	0.290	0.364	0.385	0.373	0.315	0.420	0.196	0.172	0.303	
Cr	0.006	0.007	0.005	0.007	0.004	0.005	0.010	0.006	0.011	0.012	0.014	0.010	0.012	0.006	0.004	0.012	0.010	0.016	
Fe^{2+}	0.112	0.111	0.114	0.100	0.105	0.107	0.095	0.076	0.079	0.086	0.080	0.073	0.067	0.085	0.077	0.087	0.097	0.135	
Mn	0.003	0.001	0.001	0.003	0.000	0.003	0.001	0.002	0.003	0.003	0.002	0.003	0.002	0.001	0.002	0.004	0.003	0.008	
Ni	0.001	0.002	0.000	0.001	0.001	0.000	0.001	0.002	0.001	-	-	0.000	0.002	-	-	-	-	-	
Mg	0.793	0.783	0.785	0.775	0.768	0.744	0.707	0.745	0.739	0.741	0.682	0.685	0.675	0.753	0.670	0.874	0.975	0.826	
Ca	0.824	0.826	0.823	0.812	0.825	0.812	0.767	0.742	0.745	0.719	0.691	0.726	0.700	0.767	0.720	0.850	0.772	0.791	
Na	0.136	0.147	0.141	0.150	0.146	0.162	0.183	0.201	0.202	0.218	0.261	0.217	0.254	0.179	0.232	0.071	0.052	0.068	
K	-	0.001	0.001	0.001	-	-	-	n.d.	0.001	0.001	-	-	-	-	0.000	-	0.000	-	
Total	4.023	4.031	4.025	4.023	4.028	4.033	4.011	4.006	4.010	4.014	4.018	4.005	4.010	4.018	4.015	4.013	4.009	4.011	
Mg#	***87.60***	***87.58***	***87.36***	***88.53***	***87.99***	***87.42***	***88.11***	***90.78***	***90.33***	***89.59***	***89.51***	***90.39***	***91.00***	***89.81***	***89.70***	***90.93***	***90.96***	***85.99***	

the abbreviation in brackets under location indicates the adjacent mineral phase of the respective rim analysis; n.a.: not analysed; n.d.: not detected;
Stoich.: cations calculated on the basis of 6 oxygens

Table A3-10: Representative major element composition (wt%) and stoichiometry of ***clinopyroxene*** in mafic xenoliths from Marsabit (continued)

													Spl-ol websterite				
Group	**V**	**V**	**V**	**V**	**V**	**V**	**V**	**V**	**V**	**V**	**V**	**V**	**VI**	**VI**	**VI**	**VI**	**VI**
	cpx-I	**cpx-I**	**cpx-I**	**cpx-I**	**cpx-I**	**cpx-I**	**cpx-I**	**cpx-I**	**cpx-I**	**cpx-I**	**cpx-IIa**	**cpx-IIa**	**cpx-I**	**cpx-I**	**cpx-I**	**cpx-I**	**cpx-I**
sample	1960/8	1960/8	1960/8	1960/8	1960/8	1960/8	1964	1964	1964	1964	1964	1964	782/2	782/2	782/2	782/2	782/2
remark	core	core	rim (cpx-I)	rim (cpx-I)	sympl. core	sympl. core	core	core	rim (opx-I)	rim (grt)	core	rim (opx-IIa)	core	core	core	rim (cpx-I)	rim (opx-I)
SiO_2	53.21	52.87	52.31	52.52	52.80	52.95	54.21	53.58	52.89	53.08	52.06	52.05	50.27	50.15	50.11	49.77	50.70
TiO_2	0.29	0.26	0.27	0.27	0.28	0.28	0.24	0.24	0.35	0.45	0.30	0.38	0.92	0.91	1.00	0.87	0.72
Al_2O_3	5.90	5.99	7.07	5.99	7.34	7.29	4.33	4.52	6.17	6.60	8.25	6.99	6.58	6.56	6.70	7.08	5.79
Cr_2O_3	1.32	1.27	0.57	0.99	0.53	0.45	0.60	0.65	0.85	0.96	0.55	0.44	0.54	0.63	0.55	0.34	0.45
FeO	2.36	2.40	2.45	2.36	2.15	2.28	1.48	1.57	1.43	1.36	1.59	1.69	5.18	5.25	5.20	5.20	5.51
MnO	0.05	0.08	0.07	0.09	0.08	0.06	0.04	0.06	0.03	0.03	0.06	0.06	0.09	0.13	0.14	0.19	0.11
NiO	0.05	0.06	0.02	0.01	0.04	0.03	0.03	0.05	0.03	0.07	0.04	0.08	n.d.	n.a.	n.d.	0.04	n.a.
MgO	14.10	14.06	13.80	14.42	13.68	13.70	15.39	15.20	14.46	14.32	13.66	14.38	14.37	14.23	14.35	14.90	15.00
CaO	21.31	21.23	21.20	21.33	21.61	21.51	22.92	22.69	22.23	21.83	22.67	22.80	20.82	20.75	21.04	19.89	20.54
Na_2O	2.28	2.31	2.31	2.15	2.36	2.36	1.62	1.53	1.87	2.18	1.68	1.57	0.97	0.95	0.93	0.93	0.93
K_2O	0.01	n.d.	n.d.	0.01	0.01	n.d.	n.d.	n.d.	0.01	n.d.	0.01	n.d.	0.02	n.d.	n.d.	n.d.	n.d.
Total	***100.88***	***100.51***	***100.05***	***100.16***	***100.87***	***100.91***	***100.86***	***100.10***	***100.33***	***100.88***	***100.88***	***100.43***	***99.75***	***99.55***	***100.03***	***99.21***	***99.74***
Stoich.	**6O**	**6O**	**6O**	**6O**	**6O**	**6O**	**6O**	**6O**	**6O**	**6O**	**6O**	**6O**	**6O**	**6O**	**6O**	**6O**	**6O**
Si	1.912	1.908	1.893	1.901	1.893	1.897	1.942	1.935	1.904	1.899	1.865	1.876	1.847	1.848	1.839	1.835	1.864
Ti	0.008	0.007	0.007	0.007	0.008	0.008	0.006	0.007	0.009	0.012	0.008	0.010	0.025	0.025	0.028	0.024	0.020
Al	0.250	0.255	0.301	0.256	0.310	0.308	0.183	0.193	0.262	0.278	0.348	0.297	0.285	0.285	0.290	0.308	0.251
Cr	0.038	0.036	0.016	0.028	0.015	0.013	0.017	0.018	0.024	0.027	0.016	0.013	0.016	0.018	0.016	0.010	0.013
Fe^{2+}	0.071	0.072	0.074	0.071	0.064	0.068	0.044	0.048	0.043	0.041	0.048	0.051	0.159	0.162	0.160	0.160	0.169
Mn	0.001	0.002	0.002	0.003	0.002	0.002	0.001	0.002	0.001	0.001	0.002	0.002	0.003	0.004	0.004	0.006	0.003
Ni	0.002	0.002	0.001	0.000	0.001	0.001	0.001	0.001	0.001	0.002	0.001	0.002	-	-	-	0.001	-
Mg	0.755	0.756	0.744	0.778	0.731	0.732	0.822	0.818	0.776	0.764	0.729	0.773	0.787	0.781	0.785	0.819	0.822
Ca	0.820	0.821	0.822	0.828	0.830	0.826	0.880	0.878	0.857	0.837	0.870	0.880	0.820	0.819	0.827	0.786	0.809
Na	0.159	0.161	0.162	0.151	0.164	0.164	0.112	0.107	0.131	0.151	0.117	0.110	0.069	0.068	0.066	0.066	0.066
K	0.000	0.000	0.000	0.001	0.000	0.000	-	-	0.000	-	0.000	-	0.001	-	-	-	-
Total	4.016	4.020	4.022	4.025	4.019	4.017	4.008	4.007	4.009	4.012	4.004	4.014	4.012	4.010	4.014	4.015	4.017
Mg#	***91.42***	***91.27***	***90.96***	***91.60***	***91.90***	***91.46***	***94.88***	***94.51***	***94.74***	***94.94***	***93.87***	***93.81***	***83.19***	***82.86***	***83.10***	***83.62***	***82.93***

Table A3-10: Representative major element composition (wt%) and stoichiometry of ***clinopyroxene*** in mafic xenoliths from Marsabit (continued)

	Spl-ol web.		**Spl-ol clinopyroxenite**					**Spl-free websterite**						**Spl-Ol clinopyroxenite**			
Group	**VI cpx-I**	**VI cpx-I**	**VI cpx-I**	**VI cpx-I**	**VI cpx-I**	**VI cpx-I**	**VI cpx-I**	**VI cpx-I**	**VI cpx-I**	**VI cpx-I**	**VI cpx-I**	**VI cpx-I**	**VI cpx-I**	**VI cpx-I**	**VI cpx-I**	**VI cpx-I**	**VI cpx-I**
sample	782/2	782/2	726	726	726	726	726	782/1	782/1	782/1	782/1	782/1	782/1	1973/2	1973/2	1973/2	1973/2
remark	rim (spl-I)	rim (opx-I)	core	core	core	rim spongy	rim spongy	core	core	core	rim (opx-I)	rim (cpx-I)	rim (opx-I)	core	core	rim (cpx)	rim (cpx)
SiO_2	49.51	50.80	48.41	48.35	48.43	48.65	48.50	50.89	50.82	50.95	51.55	50.84	51.36	48.36	48.74	48.95	48.53
TiO_2	0.78	0.86	1.38	1.36	1.51	1.13	1.49	0.52	0.56	0.55	0.45	0.57	0.47	1.29	1.20	1.02	1.12
Al_2O_3	7.17	5.87	8.89	8.94	8.80	8.53	8.48	6.21	6.64	6.62	5.89	6.77	5.93	9.20	8.75	8.89	9.12
Cr_2O_3	0.68	0.43	0.04	0.05	0.06	0.05	0.00	0.34	0.28	0.31	0.35	0.29	0.29	0.10	0.10	0.07	0.05
FeO	5.85	4.98	6.12	5.79	6.04	5.93	6.37	5.01	5.78	5.81	5.90	5.80	5.99	5.58	5.54	5.52	5.68
MnO	0.18	0.09	0.13	0.15	0.12	0.17	0.10	0.17	0.14	0.15	0.16	0.15	0.12	0.14	0.12	0.11	0.12
NiO	n.a.	0.04	n.d.	0.01	0.01	0.02	n.d.	0.06	0.03	0.03	0.04	0.04	0.07	0.01	0.05	n.d.	0.04
MgO	15.14	14.79	13.43	13.33	13.42	14.17	13.39	14.44	15.33	15.58	15.69	15.62	15.95	13.45	13.48	13.79	13.60
CaO	19.47	21.03	20.33	20.33	20.31	20.41	20.46	21.47	19.95	19.83	19.41	19.63	19.21	20.88	20.90	21.36	20.67
Na_2O	0.85	0.94	1.17	1.12	1.21	0.57	1.03	0.81	0.89	0.80	0.87	0.80	0.86	1.12	1.11	0.88	0.97
K_2O	0.03	n.d.	0.02	n.d.	0.03	n.d.	n.d.	0.01	0.01	0.01	0.01	0.01	n.d.	0.01	0.01	n.d.	0.01
Total	***99.65***	***99.84***	***99.91***	***99.43***	***99.93***	***99.62***	***99.81***	***99.93***	***100.42***	***100.64***	***100.31***	***100.51***	***100.26***	***100.15***	***100.00***	***100.60***	***99.91***
Stoich.	**6O**	**6O**	**6O**	**6O**	**6O**	**6O**	**6O**	**6O**	**6O**	**6O**	**6O**	**6O**	**6O**	**6O**	**6O**	**6O**	**6O**
Si	1.823	1.864	1.784	1.787	1.784	1.793	1.791	1.866	1.852	1.852	1.878	1.849	1.872	1.776	1.792	1.788	1.784
Ti	0.022	0.024	0.038	0.038	0.042	0.031	0.041	0.014	0.015	0.015	0.012	0.015	0.013	0.036	0.033	0.028	0.031
Al	0.311	0.254	0.386	0.389	0.382	0.371	0.369	0.268	0.285	0.284	0.253	0.290	0.255	0.398	0.379	0.383	0.395
Cr	0.020	0.013	0.001	0.001	0.002	0.001	0.000	0.010	0.008	0.009	0.010	0.008	0.008	0.003	0.003	0.002	0.001
Fe^{2+}	0.180	0.153	0.188	0.179	0.186	0.183	0.197	0.154	0.176	0.177	0.180	0.176	0.183	0.171	0.170	0.169	0.175
Mn	0.006	0.003	0.004	0.005	0.004	0.005	0.003	0.005	0.004	0.005	0.005	0.005	0.004	0.004	0.004	0.003	0.004
Ni	-	0.001	-	0.000	0.000	0.000	-	0.002	0.001	0.001	0.001	0.001	0.002	0.000	0.001	-	0.001
Mg	0.831	0.809	0.738	0.734	0.737	0.779	0.737	0.789	0.833	0.844	0.852	0.847	0.866	0.736	0.739	0.751	0.745
Ca	0.768	0.827	0.803	0.805	0.802	0.806	0.809	0.843	0.779	0.772	0.757	0.765	0.750	0.822	0.823	0.836	0.814
Na	0.061	0.067	0.084	0.080	0.087	0.040	0.074	0.058	0.063	0.056	0.061	0.057	0.061	0.080	0.079	0.062	0.069
K	0.002	-	0.001	-	0.002	-	-	0.000	0.000	0.000	0.000	0.000	-	0.000	0.000	-	0.001
Total	4.022	4.013	4.027	4.020	4.026	4.010	4.021	4.010	4.018	4.015	4.010	4.014	4.014	4.028	4.024	4.023	4.021
Mg#	***82.18***	***84.10***	***79.66***	***80.42***	***79.85***	***81.00***	***78.94***	***83.71***	***82.54***	***82.70***	***82.58***	***82.76***	***82.60***	***81.12***	***81.26***	***81.66***	***81.02***

Table A3-10: Representative major element composition (wt%) and stoichiometry of ***clinopyroxene*** in mafic xenoliths from Marsabit (continued)

	Ol Gabbro							
Group	**VII**	**VII**	**VII**	**VII**	**VII**	**VII**	**VII**	**VII**
	cpx-I	**cpx-I**	**cpx-I**	**cpx-I**	**cpx-I**	**cpx-I**	**cpx-I**	**cpx-I**
sample	772/2	772/2	772/2	772/2	772/2	772/2	772/2	772/2
remark	core	core	core	core	rim (ilm)	rim (plag)	rim (plag)	rim (plag)
SiO_2	51.52	51.52	52.50	52.36	50.16	51.06	51.65	51.89
TiO_2	1.06	0.98	0.71	0.73	1.41	1.28	0.76	0.24
Al_2O_3	2.72	3.45	2.61	2.64	2.55	2.29	0.78	0.16
Cr_2O_3	0.28	0.29	0.38	0.44	0.00	0.00	0.04	0.00
FeO	7.88	6.77	6.07	6.08	10.26	10.00	14.91	22.98
MnO	0.15	0.16	0.16	0.14	0.25	0.22	0.37	0.75
NiO	0.01	0.02	0.03	0.05	n.d.	0.01	n.d.	0.02
MgO	14.53	15.04	15.79	15.81	13.35	13.75	10.85	6.62
CaO	21.19	21.61	21.75	21.49	20.69	21.07	19.99	17.31
Na_2O	0.40	0.36	0.32	0.27	0.41	0.47	0.55	0.91
K_2O	0.01	n.d.	n.d.	n.d.	n.d.	n.d.	0.03	n.d.
Total	***99.75***	***100.21***	***100.31***	***100.00***	***99.08***	***100.15***	***99.93***	***100.88***
Stoich.	**6O**	**6O**	**6O**	**6O**	**6O**	**6O**	**6O**	**6O**
Si	1.917	1.900	1.927	1.926	1.902	1.913	1.977	2.027
Ti	0.030	0.027	0.019	0.020	0.040	0.036	0.022	0.007
Al	0.119	0.150	0.113	0.114	0.114	0.101	0.035	0.007
Cr	0.008	0.009	0.011	0.013	0.000	0.000	0.001	0.000
Fe^{2+}	0.245	0.209	0.186	0.187	0.325	0.313	0.477	0.751
Mn	0.005	0.005	0.005	0.004	0.008	0.007	0.012	0.025
Ni	0.000	0.001	0.001	0.001	-	0.000	-	0.001
Mg	0.806	0.827	0.864	0.867	0.755	0.768	0.619	0.386
Ca	0.845	0.854	0.855	0.847	0.841	0.846	0.820	0.724
Na	0.029	0.026	0.023	0.020	0.030	0.034	0.041	0.069
K	0.000	n.d.	n.d.	n.d.	n.d.	n.d.	0.001	-
Total	4.004	4.007	4.003	4.000	4.016	4.018	4.004	3.997
Mg#	***76.67***	***79.84***	***82.26***	***82.25***	***69.87***	***71.02***	***56.47***	***33.94***

Table A3-11: Representative major element composition (wt%) and stoichiometry of ***orthopyroxene*** in mafic xenoliths from Marsabit

	Grt websterites																	
Group	**V**	**V**	**V**	**V**	**V**	**V**	**V**	**V**	**V**	**V**	**V**	**V**	**V**	**V**	**V**	**V**	**V**	**V**
mineral	**opx-I**	**opx-I**	**opx-I**	**opx-I**	**opx-I**	**opx-I**	**opx-I**	**opx-I**	**opx-I**	**opx-I**	**opx-I**	**opx-I**	**opx-I**	**opx-I**	**opx-IIb**	**opx-IIb**	**opx-I**	**opx-I**
sample	784/1	784/1	784/1	784/1	784/1	784/1	1959/18	1959/18	1959/18	1959/18	1959/18	1959/18	1959/18	1959/18	1959/18	1959/18	1960/8	1960/8
location	core	core	core	rim (Ti-prg)	rim (grt)	incl. in grt	Al-trough	Al-trough	Al-trough	Al-bulge	Al-bulge	Al-trough	rim (grt)	rim (ol-I)	sympl.	sympl.	core	core
SiO_2	54.82	54.32	54.23	53.96	54.48	54.64	55.76	56.00	56.33	55.05	54.91	55.36	54.91	56.28	55.70	55.99	55.82	55.97
TiO_2	0.20	0.18	0.06	0.23	0.14	0.16	0.14	0.07	0.13	0.09	0.10	0.07	0.42	0.08	0.06	0.05	0.03	0.04
Al_2O_3	3.98	4.36	4.83	4.71	4.57	3.71	2.76	3.74	2.37	4.37	3.91	4.85	5.93	2.72	3.45	3.14	3.38	3.50
Cr_2O_3	0.06	0.05	0.13	0.00	0.09	0.13	0.19	0.10	0.12	0.09	0.10	0.08	0.14	0.06	0.08	0.02	0.29	0.34
FeO	8.26	8.60	9.39	8.96	8.58	9.55	8.20	7.26	7.60	7.85	8.10	7.42	7.61	8.14	8.46	8.38	6.99	7.04
MnO	0.12	0.17	0.15	0.17	0.13	0.07	0.26	0.12	0.16	0.10	0.14	0.15	0.13	0.16	0.10	0.12	0.18	0.18
NiO	0.06	0.15	0.10	0.11	0.06	0.04	0.19	0.07	0.09	0.10	0.09	0.15	0.11	0.09	0.16	0.15	0.07	0.06
MgO	31.72	31.58	31.01	31.10	31.45	30.89	32.58	33.26	33.34	32.67	32.24	32.52	30.51	32.91	32.53	32.54	32.87	32.92
CaO	0.39	0.32	0.30	0.32	0.27	0.40	0.44	0.30	0.36	0.31	0.39	0.28	0.58	0.33	0.26	0.29	0.28	0.35
Na_2O	0.05	0.05	0.04	0.06	0.04	0.07	0.04	0.05	0.04	0.05	0.08	0.06	0.61	0.06	0.08	0.05	0.05	0.06
K_2O	0.02	0.02	n.d.	0.01	n.d.	0.01	n.d.	n.d.	0.01	n.d.	n.d.	n.d.	n.d.	0.01	n.d.	n.d.	n.d.	n.d.
Total	***99.68***	***99.79***	***100.23***	***99.63***	***99.81***	***99.66***	***100.58***	***100.97***	***100.55***	***100.68***	***100.07***	***100.94***	***100.94***	***100.85***	***100.87***	***100.74***	***99.95***	***100.46***
Stoich.	**6O**	**6O**	**6O**	**6O**	**6O**	**6O**	**6O**	**6O**	**6O**	**6O**	**6O**	**6O**	**6O**	**6O**	**6O**	**6O**	**6O**	**6O**
Si	1.914	1.899	1.893	1.893	1.901	1.919	1.932	1.920	1.944	1.899	1.910	1.900	1.890	1.940	1.923	1.933	1.932	1.928
Ti	0.005	0.005	0.002	0.006	0.004	0.004	0.004	0.002	0.003	0.002	0.003	0.002	0.011	0.002	0.002	0.001	0.001	0.001
Al	0.164	0.180	0.199	0.195	0.188	0.153	0.113	0.151	0.096	0.178	0.160	0.196	0.241	0.110	0.140	0.128	0.138	0.142
Cr	0.002	0.001	0.004	0.000	0.002	0.004	0.005	0.003	0.003	0.002	0.003	0.002	0.004	0.002	0.002	0.001	0.008	0.009
Fe^{2+}	0.241	0.251	0.274	0.263	0.250	0.280	0.238	0.208	0.219	0.227	0.236	0.213	0.219	0.235	0.244	0.242	0.202	0.203
Mn	0.003	0.005	0.004	0.005	0.004	0.002	0.008	0.003	0.005	0.003	0.004	0.004	0.004	0.005	0.003	0.004	0.005	0.005
Ni	0.002	0.004	0.003	0.003	0.002	0.001	0.005	0.002	0.002	0.003	0.003	0.004	0.003	0.002	0.004	0.004	0.002	0.002
Mg	1.651	1.646	1.613	1.626	1.637	1.617	1.683	1.700	1.715	1.681	1.671	1.664	1.565	1.691	1.674	1.675	1.695	1.690
Ca	0.015	0.012	0.011	0.012	0.010	0.015	0.016	0.011	0.013	0.012	0.015	0.010	0.021	0.012	0.010	0.011	0.011	0.013
Na	0.004	0.003	0.003	0.004	0.003	0.005	0.003	0.003	0.003	0.003	0.005	0.004	0.040	0.004	0.006	0.004	0.003	0.004
K	0.001	0.001	-	0.001	-	0.001	-	-	0.001	-	-	-	-	0.000	-	-	-	-
Total	4.000	4.008	4.006	4.007	4.001	4.001	4.007	4.003	4.005	4.010	4.009	4.001	3.998	4.004	4.007	4.003	3.997	3.997
Mg#	***87.26***	***86.75***	***85.48***	***86.09***	***86.73***	***85.22***	***87.62***	***89.09***	***88.67***	***88.12***	***87.65***	***88.66***	***87.72***	***87.81***	***87.27***	***87.38***	***89.34***	***89.29***

the abbreviation in brackets under location indicates the adjacent mineral phase of the respective rim analysis; n.a.: not analysed; n.d.: not detected;
Stoich.: cations calculated on the basis of 6 oxygens

Table A3-11: Representative major element composition (wt%) and stoichiometry of ***orthopyroxene*** in mafic xenoliths from Marsabit

	Grt websterites							Spl-ol websterite				Spl-free websterite				
Group	**V**	**V**	**V**	**V**	**V**	**V**	**V**	**VI**	**VI**	**VI**	**VI**	**VI**	**VI**	**VI**	**VI**	**VI**
mineral	**opx-I**	**opx-IIb**	**opx-I**	**opx-I**	**opx-I**	**opx-I**	**opx-IIb**	**opx-I**	**opx-I**	**opx-I**	**opx-I**	**opx-I**	**opx-I**	**opx-I**	**opx-I**	**opx-I**
sample	1960/8	1960/8	1964	1964	1964	1964	1964	782/2	782/2	782/2	782/2	782/1	782/1	782/1	782/1	782/1
location	rim (cpx-I)	sympl.	core	core	rim (cpx-IIb)	rim (cpx-IIb)	core	core	core	rim (cpx-I)	rim (cpx-I)	core	core	rim (cpx-I)	rim (cpx-I)	lam. in cpx-I
SiO_2	55.92	54.74	56.00	55.76	55.17	56.75	54.62	53.60	53.33	53.85	53.77	52.80	52.96	53.30	52.94	53.48
TiO_2	0.06	0.03	0.06	0.05	0.03	0.04	0.03	0.20	0.21	0.21	0.24	0.15	0.12	0.14	0.22	0.11
Al_2O_3	3.62	4.81	3.21	4.05	4.68	2.72	5.89	4.58	4.65	4.30	4.44	5.23	5.13	5.20	5.38	5.34
Cr_2O_3	0.32	0.18	0.16	0.28	0.30	0.25	0.17	0.28	0.23	0.23	0.29	0.21	0.23	0.13	0.22	0.28
FeO	6.99	6.82	5.62	5.82	6.55	5.85	5.91	11.11	11.70	10.36	10.64	11.64	11.09	10.57	10.67	11.15
MnO	0.17	0.16	0.11	0.12	0.16	0.11	0.14	0.16	0.21	0.22	0.21	0.24	0.18	0.19	0.17	0.22
NiO	0.10	0.07	0.10	0.13	0.11	0.11	0.09	0.08	n.a.	0.06	n.a.	0.09	0.10	0.06	0.09	0.10
MgO	33.11	31.98	33.87	33.41	32.80	34.13	32.12	29.20	29.20	29.60	29.70	27.86	28.85	28.78	28.15	28.85
CaO	0.33	0.27	0.27	0.26	0.23	0.24	0.29	0.75	0.73	0.83	0.79	1.17	0.68	1.03	1.33	0.72
Na_2O	0.03	0.07	0.11	0.07	0.06	0.03	0.20	0.05	0.05	0.07	0.08	0.07	0.04	0.09	0.12	0.07
K_2O	0.01	0.01	0.02	0.01	n.d.	n.d.	0.03	0.01	0.02	n.d.	0.01	0.01	0.01	0.01	n.d.	n.d.
Total	***100.65***	***99.14***	***99.54***	***99.96***	***100.10***	***100.23***	***99.49***	***100.02***	***100.33***	***99.71***	***100.17***	***99.47***	***99.39***	***99.50***	***99.29***	***100.31***
Stoich.	**6O**	**6O**	**6O**	**6O**	**6O**	**6O**	**6O**	**6O**	**6O**	**6O**	**6O**	**6O**	**6O**	**6O**	**6O**	**6O**
Si	1.923	1.908	1.934	1.919	1.903	1.947	1.890	1.894	1.884	1.902	1.894	1.884	1.883	1.889	1.884	1.884
Ti	0.001	0.001	0.001	0.001	0.001	0.001	0.001	0.005	0.006	0.006	0.006	0.004	0.003	0.004	0.006	0.003
Al	0.147	0.198	0.131	0.164	0.190	0.110	0.240	0.191	0.194	0.179	0.184	0.220	0.215	0.217	0.226	0.222
Cr	0.009	0.005	0.004	0.007	0.008	0.007	0.005	0.008	0.006	0.006	0.008	0.006	0.007	0.004	0.006	0.008
Fe^{2+}	0.201	0.199	0.162	0.168	0.189	0.168	0.171	0.328	0.346	0.306	0.313	0.347	0.330	0.313	0.317	0.328
Mn	0.005	0.005	0.003	0.004	0.005	0.003	0.004	0.005	0.006	0.007	0.006	0.007	0.006	0.006	0.005	0.007
Ni	0.003	0.002	0.003	0.003	0.003	0.003	0.003	0.002	-	0.002	-	0.003	0.003	0.002	0.002	0.003
Mg	1.697	1.661	1.744	1.714	1.687	1.745	1.656	1.538	1.538	1.559	1.559	1.481	1.529	1.520	1.493	1.515
Ca	0.012	0.010	0.010	0.010	0.009	0.009	0.011	0.028	0.028	0.031	0.030	0.045	0.026	0.039	0.051	0.027
Na	0.002	0.005	0.007	0.004	0.004	0.002	0.013	0.003	0.003	0.004	0.005	0.005	0.003	0.006	0.008	0.005
K	0.000	0.000	0.001	0.001	-	-	0.001	0.000	0.001	-	0.000	0.000	0.000	0.000	-	-
Total	3.999	3.993	4.001	3.996	3.999	3.995	3.994	4.003	4.012	4.002	4.007	4.002	4.004	4.000	3.999	4.001
Mg#	***89.41***	***89.31***	***91.48***	***91.10***	***89.93***	***91.23***	***90.64***	***82.41***	***81.65***	***83.59***	***83.27***	***81.01***	***82.26***	***82.92***	***82.46***	***82.18***

Table A3-12: Representative major element composition (wt%) and stoichiometry of ***olivine*** in mafic xenoliths from Marsabit

	Grt websterites					**Spl-ol websterite**				**Spl-Ol clinopyroxenite**				**Spl-free webst.**		**Spl-Ol cpx-ite**		**Ol Gabbro**				
Group	**V**	**V**	**V**	**V**	**V**	**VI**	**VI**	**VI**	**VI**	**VI**	**VI**	**VI**	**VI**	**VI**	**VI**	**VI**	**VI**	**VII**	**VII**	**VII**	**VII**	**VII**
mineral	**ol-I**	**ol-I**	**ol-I**	**ol-I**	**ol$_m$**	**ol-I**	**ol-I**	**ol-I**	**ol-I**	**ol-I**	**ol-I**	**ol-I**	**ol-I**	**ol-I**	**ol-I**	**ol-I**	**ol-I**	**ol-I**	**ol-I**	**ol-I**	**ol-I**	**ol-I**
sample	1959/18	1959/18	1959/18	1959/18	1959/18	782/2	782/2	782/2	782/2	726	726	726	726	782/1	782/1	1973/2	1973/2	772/2	772/2	772/2	772/2	772/2
location	core	core	rim (opx-I)	rim (opx-I)	react. around	core	core	rim (cpx-I)	rim (cpx-I)	core	core	rim (cpx-I)	rim (spl-I)	core	core	core	rim (cpx)	core	core	core	rim (ilm)	rim (ilm)
SiO_2	39.98	40.17	40.11	40.00	40.64	39.41	39.11	39.31	39.35	38.86	39.20	39.50	39.35	39.86	39.78	39.48	39.43	34.44	35.95	36.13	33.59	33.84
TiO_2	0.02	0.01	n.d.	0.01	0.07	0.02	0.02	n.d.	n.d.	n.d.	0.02	n.d.	0.03	0.01	0.01	n.d.	0.01	0.03	0.01	0.02	0.04	0.05
Al_2O_3	0.01	0.02	0.06	n.d.	0.06	0.02	0.03	0.04	0.02	0.06	0.04	0.07	0.07	0.01	0.02	0.05	0.05	0.00	0.02	0.02	0.02	0.02
Cr_2O_3	n.d.	0.03	0.01	0.01	0.05	n.d.	0.01	n.d.	0.02	n.d.	n.d.	0.01	0.02	0.04	0.00	0.06	0.06	0.02	n.d.	0.01	0.03	0.03
FeO	12.98	12.78	12.83	12.74	12.53	17.65	17.48	17.37	17.20	17.88	18.12	16.18	16.13	15.60	15.74	16.18	15.91	41.58	36.13	38.90	42.84	42.41
MnO	0.13	0.14	0.15	0.13	0.42	0.23	0.23	0.20	0.23	0.19	0.19	0.23	0.25	0.24	0.23	0.24	0.19	0.70	0.60	0.67	0.75	0.78
NiO	0.52	0.58	0.47	0.49	0.22	0.21	0.18	0.17	0.17	0.10	0.12	0.12	0.10	0.21	0.27	0.14	0.09	0.08	0.04	0.08	0.04	0.02
MgO	46.36	46.38	46.46	46.56	46.34	42.69	42.53	42.53	42.65	42.16	42.51	43.74	44.16	43.33	42.94	43.17	43.96	22.86	27.53	23.84	22.05	22.22
CaO	0.04	0.01	0.02	0.03	0.26	0.08	0.10	0.17	0.14	0.19	0.20	0.30	0.29	0.18	0.18	0.25	0.27	0.34	0.24	0.30	0.32	0.31
Na_2O	0.03	n.d.	0.03	0.03	0.02	0.01	n.d.	n.d.	0.03	0.02	0.01	0.02	0.02	n.d.	n.d.	0.01	0.02	0.01	n.d.	0.01	0.02	0.02
K_2O	n.d.	0.02	0.02	n.d.	n.d.	0.01	n.d.	n.d.	0.02	n.d.	n.d.	n.d.	0.01	n.d.	n.d.	n.d.	n.d.	n.d.	n.d.	n.d.	n.d.	0.01
Total	**100.06**	**100.14**	**100.18**	**99.99**	**100.61**	**100.33**	**99.69**	**99.80**	**99.84**	**99.46**	**100.41**	**100.18**	**100.41**	**99.49**	**99.17**	**99.60**	**100.00**	**100.06**	**100.52**	**99.99**	**99.70**	**99.70**
Stoich.	**4O**	**4O**	**4O**	**4O**	**4O**	**4O**	**4O**	**4O**	**4O**	**4O**	**4O**	**4O**	**4O**	**4O**	**4O**	**4O**	**4O**	**4O**	**4O**	**4O**	**4O**	**4O**
Si	0.996	0.999	0.997	0.996	1.004	0.999	0.998	1.001	1.001	0.996	0.995	0.997	0.991	1.009	1.011	1.002	0.996	0.992	0.999	1.022	0.980	0.985
Ti	0.000	0.000	-	0.000	0.001	0.000	0.000	-	-	-	0.000	-	0.001	0.000	0.000	-	0.000	0.001	0.000	0.000	0.001	0.001
Al	0.000	0.001	0.000	-	0.002	0.001	0.001	0.001	0.001	0.002	0.001	0.002	0.002	0.000	0.001	0.002	0.002	0.000	0.000	0.000	0.001	0.001
Cr	-	0.000	0.001	0.000	0.001	-	0.000	-	0.000	-	-	0.000	0.000	0.001	0.000	0.001	0.001	0.001	-	0.000	0.000	0.000
Fe^{2+}	0.270	0.266	0.267	0.265	0.259	0.374	0.373	0.370	0.366	0.383	0.385	0.341	0.340	0.330	0.335	0.343	0.336	1.002	0.839	0.920	1.046	1.032
Mn	0.003	0.003	0.003	0.003	0.009	0.005	0.005	0.004	0.005	0.004	0.004	0.005	0.005	0.005	0.005	0.005	0.004	0.017	0.014	0.016	0.018	0.019
Ni	0.010	0.012	0.009	0.010	0.004	0.004	0.004	0.003	0.004	0.002	0.002	0.002	0.002	0.004	0.006	0.003	0.002	0.002	0.001	0.002	0.001	0.001
Mg	1.722	1.719	1.722	1.728	1.707	1.614	1.618	1.614	1.617	1.611	1.609	1.646	1.658	1.635	1.627	1.633	1.654	0.981	1.140	1.006	0.959	0.964
Ca	0.001	0.000	0.001	0.001	0.007	0.002	0.003	0.005	0.004	0.005	0.006	0.008	0.008	0.005	0.005	0.007	0.007	0.010	0.007	0.009	0.010	0.010
Na	0.001	0.000	0.001	0.001	0.001	0.001	-	-	0.002	0.001	0.001	0.001	0.001	-	-	0.000	0.001	0.001	-	0.001	0.001	0.001
K	-	0.001	0.001	-	0.000	0.000	-	-	0.001	-	-	-	0.000	-	-	-	-	-	-	-	-	0.000
Total	*3.004*	*3.000*	*3.002*	*3.004*	*2.994*	*3.001*	*3.001*	*2.999*	*3.000*	*3.004*	*3.004*	*3.002*	*3.008*	*2.990*	*2.988*	*2.997*	*3.003*	*3.007*	*3.001*	*2.977*	*3.018*	*3.014*
Mg#	***86.43***	***86.61***	***86.59***	***86.69***	***86.83***	***81.18***	***81.26***	***81.36***	***81.55***	***80.78***	***80.71***	***82.82***	***83.00***	***83.20***	***82.94***	***82.63***	***83.12***	***49.49***	***57.59***	***52.21***	***47.85***	***48.29***

the abbreviation in brackets under location indicates the adjacent mineral phase of the respective rim analysis; n.a.: not analysed; n.d.: not detected; Stoich.: cations calculated on the basis of 4 oxygens

Table A3-13: Representative major element composition (wt%) and stoichiometry of ***oxydes*** (spinel, ilmenite, rutile) in mafic xenoliths from Marsabit

	Grt websterites																	
Group	V	V	V	V	V	V	V	V	V	V	V	V	V	V	V	V	V	V
Mineral	spl-IIb	spl-IIb	ilm	ilm	rut	rut	spl-IIb	spl-IIb	spl-IIb	spl-IIb	spl-IIb	spl-IIb	spl-IIb	spl-IIb	spl-IIb	spl-IIb	spl-IIb	spl-IIb
sample	784/1	784/1	784/1	784/1	784/1	784/1	1959/18	1959/18	1959/18	1959/18	1960/8	1960/8	1960/8	1960/8	1964	1964	1964	1964
location	sympl.	sympl.	inter-stitial	inter-stitial	incl. in ilm	incl. in ilm	sympl.	sympl.	sympl.	sympl.	sympl.	sympl.	sympl.	sympl.	sympl.	sympl.	sympl.	sympl.
SiO_2	0.01	0.01	0.03	0.03	0.03	0.01 #	0.02	0.04	0.03	0.03	0.05	0.12	0.01	0.01	n.d.	0.01	0.05	0.01
TiO_2	n.d.	0.06	56.85	58.96	98.59	99.47 #	n.d.	0.05	0.05	0.03	n.d.	n.d.	0.01	n.d.	0.01	0.01	0.02	0.01
Al_2O_3	66.05	65.34	0.44	0.25	0.11	0.17 #	66.27	64.56	65.45	65.75	62.11	62.33	65.86	63.58	63.89	64.57	64.19	63.79
Cr_2O_3	1.31	1.84	0.13	0.33	0.21	0.16 #	1.28	2.31	1.64	1.32	6.50	5.95	3.02	4.07	5.45	4.49	5.00	5.79
Fe_2O_3	0.37	0.14	-	-	0.50	0.42 #	0.76	1.77	1.08	0.96	0.27	0.33	0.44	0.07	0.54	0.46	0.54	0.32
FeO	13.24	13.22	31.35	27.63	-	-	10.44	10.04	10.66	10.30	9.90	9.65	9.51	10.57	8.94	7.95	8.33	7.26
MnO	0.04	0.01	0.26	0.41	0.02	0.00	0.10	0.09	0.09	0.07	0.18	0.14	0.13	0.13	0.24	0.16	0.15	0.18
NiO	n.a.	n.a.	0.20	0.03	0.01	0.02	0.44	0.75	0.68	0.42	0.29	0.30	0.28	0.33	0.31	0.36	0.34	0.26
MgO	18.90	18.80	9.89	12.43	0.01	n.d.	20.56	20.45	20.22	20.58	20.54	20.72	21.35	19.95	21.36	22.00	21.91	22.46
CaO	n.d.	0.01	0.23	0.14	0.08	0.06	0.01	0.12	0.07	n.d.	0.04	0.02	0.00	0.07	0.02	0.03	n.d.	0.06
ZnO	0.43	0.39	n.a.	n.a.	n.a.	n.a.	0.08	0.13	n.d.	0.07	0.02	0.07	0.05	0.06	0.13	0.08	0.07	0.04
Nb_2O_5	n.a.	n.a.	n.d.	n.d.	0.03	0.04 #	n.a.	n.a.	n.a.	n.a.	n.a.	n.a.	n.a.	n.a.	n.a.	n.a.	n.a.	n.a.
ZrO_2	n.a.	n.a.	n.d.	n.d.	0.05	0.04 #	n.a.	n.a.	n.a.	n.a.	n.a.	n.a.	n.a.	n.a.	n.a.	n.a.	n.a.	n.a.
Total	*100.35*	*99.81*	*99.39*	*100.20*	*99.64*	*100.40 #*	*99.95*	*100.33*	*99.96*	*99.53*	*99.90*	*99.62*	*100.67*	*98.84*	*100.89*	*100.12*	*100.60*	*100.17*
Stoich.	**4O**	**4O**	**3O**	**3O**	**2O**	**2O**	**4O**	**4O**	**4O**	**4O**	**4O**	**4O**	**4O**	**4O**	**4O**	**4O**	**4O**	**4O**
Si	0.000	0.000	0.001	0.001	0.000	0.000	0.000	0.001	0.001	0.001	0.001	0.003	0.000	0.000	-	0.000	0.001	0.000
Ti	-	0.001	1.006	1.018	0.989	0.990	-	0.001	0.001	0.001	-	-	0.000	-	0.000	0.000	0.000	0.000
Al	1.966	1.958	0.012	0.007	0.002	0.003	1.959	1.916	1.944	1.953	1.862	1.869	1.932	1.917	1.884	1.903	1.889	1.879
Cr	0.026	0.037	0.002	0.006	0.002	0.002	0.025	0.046	0.033	0.026	0.131	0.120	0.059	0.082	0.108	0.089	0.099	0.114
Fe^{3+}	0.007	0.003	-	-	0.005	0.004	0.014	0.034	0.021	0.018	0.005	0.006	0.008	0.001	0.010	0.009	0.010	0.006
Fe^{2+}	0.280	0.281	0.617	0.531	-	-	0.219	0.211	0.225	0.217	0.211	0.205	0.198	0.226	0.187	0.166	0.174	0.152
Mn	0.001	0.000	0.005	0.008	0.000	0.000	0.002	0.002	0.002	0.001	0.004	0.003	0.003	0.003	0.005	0.003	0.003	0.004
Ni	-	-	0.004	0.000	0.000	0.000	0.009	0.015	0.014	0.009	0.006	0.006	0.006	0.007	0.006	0.007	0.007	0.005
Mg	0.712	0.712	0.347	0.425	0.000	-	0.769	0.768	0.759	0.773	0.779	0.786	0.792	0.761	0.796	0.820	0.815	0.837
Ca	-	0.000	0.006	0.004	0.001	0.001	0.000	0.003	0.002	-	0.001	0.000	0.000	0.002	0.001	0.001	-	0.002
Zn	0.008	0.007	-	-	-	-	0.001	0.002	-	0.001	0.000	0.001	0.001	0.001	0.002	0.001	0.001	0.001
Nb	-	-	-	-	0.000	0.000	-	-	-	-	-	-	-	-	-	-	-	-
Zr	-	-	-	-	0.000	0.000	-	-	-	-	-	-	-	-	-	-	-	-
Total	*3.000*	*3.000*	*2.000*	*2.000*	*1.000*	*1.000*	*3.000*	*3.000*	*3.000*	*3.000*	*3.000*	*3.000*	*3.000*	*3.000*	*3.000*	*3.000*	*3.000*	*3.000*
Mg#	***71.79***	***71.71***	***36.00***	***44.50***	***-***	***-***	***77.83***	***78.41***	***77.17***	***78.08***	***78.71***	***79.29***	***80.00***	***77.08***	***80.99***	***83.15***	***82.43***	***84.65***
Cr# [1]	***1.30***	***1.85***	***16.84***	***46.52***	***55.18***	***37.73***	***1.27***	***2.30***	***1.63***	***1.32***	***6.54***	***6.00***	***2.97***	***4.11***	***5.38***	***4.44***	***4.94***	***5.72***

ilm: ilmenite; rut: rutile; hem: Ti-rich hematite; [1]: 100*Cr/(Cr+Al+Fe^{3+}); the abbreviation in brackets under location indicates the adjacent mineral phase of the respective rim analysis;
n.a.: not analysed; n.d.: not detected; Stoech.: cations calculated on the basis of n oxygens

Table A3-12: Representative major element composition (wt%) and stoichiometry of ***olivine*** in mafic xenoliths from Marsabit

	Grt websterites					Spl-ol websterite				Spl-Ol clinopyroxenite				Spl-free webst.		Spl-Ol cpx-ite		Ol Gabbro				
Group	**V**	**V**	**V**	**V**	**V**	**VI**	**VI**	**VI**	**VI**	**VI**	**VI**	**VI**	**VI**	**VI**	**VI**	**VI**	**VI**	**VII**	**VII**	**VII**	**VII**	**VII**
mineral	**ol-I**	**ol-I**	**ol-I**	**ol-I**	**ol_m**	**ol-I**	**ol-I**	**ol-I**	**ol-I**	**ol-I**	**ol-I**	**ol-I**	**ol-I**	**ol-I**	**ol-I**	**ol-I**	**ol-I**	**ol-I**	**ol-I**	**ol-I**	**ol-I**	**ol-I**
sample	1959/18	1959/18	1959/18	1959/18	1959/18	782/2	782/2	782/2	782/2	726	726	726	726	782/1	782/1	1973/2	1973/2	772/2	772/2	772/2	772/2	772/2
location	core	core	rim (opx-I)	rim (opx-I)	react. around	core	core	rim (cpx-I)	rim (cpx-I)	core	core	rim (cpx-I)	rim (spl-I)	core	core	core	rim (cpx)	core	core	core	rim (ilm)	rim (ilm)
SiO_2	39.98	40.17	40.11	40.00	40.64	39.41	39.11	39.31	39.35	38.86	39.20	39.50	39.35	39.86	39.78	39.48	39.43	34.44	35.95	36.13	33.59	33.84
TiO_2	0.02	0.01	n.d.	0.01	0.07	0.02	0.02	n.d.	n.d.	n.d.	0.02	n.d.	0.03	0.01	0.01	n.d.	0.01	0.03	0.01	0.02	0.04	0.05
Al_2O_3	0.01	0.02	0.06	n.d.	0.06	0.02	0.03	0.04	0.02	0.06	0.04	0.07	0.07	0.01	0.02	0.05	0.05	0.00	0.02	0.02	0.02	0.02
Cr_2O_3	n.d.	0.03	0.01	0.01	0.05	n.d.	0.01	n.d.	0.02	n.d.	n.d.	0.01	0.02	0.04	0.00	0.06	0.06	0.02	n.d.	0.01	0.03	0.03
FeO	12.98	12.78	12.83	12.74	12.53	17.65	17.48	17.37	17.20	17.88	18.12	16.18	16.13	15.60	15.74	16.18	15.91	41.58	36.13	38.90	42.84	42.41
MnO	0.13	0.14	0.15	0.13	0.42	0.23	0.23	0.20	0.23	0.19	0.19	0.23	0.25	0.24	0.23	0.24	0.19	0.70	0.60	0.67	0.75	0.78
NiO	0.52	0.58	0.47	0.49	0.22	0.21	0.18	0.17	0.17	0.10	0.12	0.12	0.10	0.21	0.27	0.14	0.09	0.08	0.04	0.08	0.04	0.02
MgO	46.36	46.38	46.46	46.56	46.34	42.69	42.53	42.53	42.65	42.16	42.51	43.74	44.16	43.33	42.94	43.17	43.96	22.86	27.53	23.84	22.05	22.22
CaO	0.04	0.01	0.02	0.03	0.26	0.08	0.10	0.17	0.14	0.19	0.20	0.30	0.29	0.18	0.18	0.25	0.27	0.34	0.24	0.30	0.32	0.31
Na_2O	0.03	n.d.	0.03	0.03	0.02	0.01	n.d.	n.d.	0.03	0.02	0.01	0.02	0.02	n.d.	n.d.	0.01	0.02	0.01	n.d.	0.01	0.02	0.02
K_2O	n.d.	0.02	0.02	n.d.	n.d.	0.01	n.d.	n.d.	0.02	n.d.	n.d.	n.d.	0.01	n.d.	n.d.	n.d.	n.d.	n.d.	n.d.	n.d.	n.d.	0.01
Total	**100.06**	**100.14**	**100.18**	**99.99**	**100.61**	**100.33**	**99.69**	**99.80**	**99.84**	**99.46**	**100.41**	**100.18**	**100.41**	**99.49**	**99.17**	**99.60**	**100.00**	**100.06**	**100.52**	**99.99**	**99.70**	**99.70**
Stoich.	**4O**	**4O**	**4O**	**4O**	**4O**	**4O**	**4O**	**4O**	**4O**	**4O**	**4O**	**4O**	**4O**	**4O**	**4O**	**4O**	**4O**	**4O**	**4O**	**4O**	**4O**	**4O**
Si	0.996	0.999	0.997	0.996	1.004	0.999	0.998	1.001	1.001	0.996	0.995	0.997	0.991	1.009	1.011	1.002	0.996	0.992	0.999	1.022	0.980	0.985
Ti	0.000	0.000	-	0.000	0.001	0.000	0.000	-	-	-	0.000	-	0.001	0.000	0.000	-	0.000	0.001	0.000	0.000	0.001	0.001
Al	0.000	0.001	0.000	-	0.002	0.001	0.001	0.001	0.001	0.002	0.001	0.002	0.002	0.000	0.001	0.002	0.002	0.000	0.000	0.000	0.001	0.001
Cr	-	0.000	0.001	0.000	0.001	-	0.000	-	0.000	-	-	0.000	0.000	0.001	0.000	0.001	0.001	0.001	-	0.000	0.000	0.000
Fe^{2+}	0.270	0.266	0.267	0.265	0.259	0.374	0.373	0.370	0.366	0.383	0.385	0.341	0.340	0.330	0.335	0.343	0.336	1.002	0.839	0.920	1.046	1.032
Mn	0.003	0.003	0.003	0.003	0.009	0.005	0.005	0.004	0.005	0.004	0.004	0.005	0.005	0.005	0.005	0.005	0.004	0.017	0.014	0.016	0.018	0.019
Ni	0.010	0.012	0.009	0.010	0.004	0.004	0.004	0.003	0.004	0.002	0.002	0.002	0.002	0.004	0.006	0.003	0.002	0.002	0.001	0.002	0.001	0.001
Mg	1.722	1.719	1.722	1.728	1.707	1.614	1.618	1.614	1.617	1.611	1.609	1.646	1.658	1.635	1.627	1.633	1.654	0.981	1.140	1.006	0.959	0.964
Ca	0.001	0.000	0.001	0.001	0.007	0.002	0.003	0.005	0.004	0.005	0.006	0.008	0.008	0.005	0.005	0.007	0.007	0.010	0.007	0.009	0.010	0.010
Na	0.001	0.000	0.001	0.001	0.001	0.001	-	-	0.002	0.001	0.001	0.001	0.001	-	-	0.000	0.001	0.001	-	0.001	0.001	0.001
K	-	0.001	0.001	-	0.000	0.000	-	-	0.001	-	-	-	0.000	-	-	-	-	-	-	-	-	0.000
Total	*3.004*	*3.000*	*3.002*	*3.004*	*2.994*	*3.001*	*3.001*	*2.999*	*3.000*	*3.004*	*3.004*	*3.002*	*3.008*	*2.990*	*2.988*	*2.997*	*3.003*	*3.007*	*3.001*	*2.977*	*3.018*	*3.014*
Mg#	***86.43***	***86.61***	***86.59***	***86.69***	***86.83***	***81.18***	***81.26***	***81.36***	***81.55***	***80.78***	***80.71***	***82.82***	***83.00***	***83.20***	***82.94***	***82.63***	***83.12***	***49.49***	***57.59***	***52.21***	***47.85***	***48.29***

the abbreviation in brackets under location indicates the adjacent mineral phase of the respective rim analysis; n.a.: not analysed; n.d.: not detected; Stoich.: cations calculated on the basis of 4 oxygens

Table A3-12: Representative major element composition (wt%) and stoichiometry of ***olivine*** in mafic xenoliths from Marsabit

	Grt websterites					Spl-ol websterite				Spl-Ol clinopyroxenite				Spl-free webst.		Spl-Ol cpx-ite		Ol Gabbro				
Group	V	V	V	V	V	VI	VI	VI	VI	VI	VI	VI	VI	VI	VI	VI	VI	VII	VII	VII	VII	VII
mineral	ol-I	ol-I	ol-I	ol-I	ol_m	ol-I	ol-I	ol-I	ol-I	ol-I	ol-I	ol-I	ol-I	ol-I	ol-I	ol-I	ol-I	ol-I	ol-I	ol-I	ol-I	ol-I
sample	1959/18	1959/18	1959/18	1959/18	1959/18	782/2	782/2	782/2	782/2	726	726	726	726	782/1	782/1	1973/2	1973/2	772/2	772/2	772/2	772/2	772/2
location	core	core	rim (opx-I)	rim (opx-I)	react. around	core	core	rim (cpx-I)	rim (cpx-I)	core	core	rim (cpx-I)	rim (spl-I)	core	core	core	rim (cpx)	core	core	core	rim (ilm)	rim (ilm)
SiO_2	39.98	40.17	40.11	40.00	40.64	39.41	39.11	39.31	39.35	38.86	39.20	39.50	39.35	39.86	39.78	39.48	39.43	34.44	35.95	36.13	33.59	33.84
TiO_2	0.02	0.01	n.d.	0.01	0.07	0.02	0.02	n.d.	n.d.	n.d.	0.02	n.d.	0.03	0.01	0.01	n.d.	0.01	0.03	0.01	0.02	0.04	0.05
Al_2O_3	0.01	0.02	0.06	n.d.	0.06	0.02	0.03	0.04	0.02	0.06	0.04	0.07	0.07	0.01	0.02	0.05	0.05	0.00	0.02	0.02	0.02	0.02
Cr_2O_3	n.d.	0.03	0.01	0.01	0.05	n.d.	0.01	n.d.	0.02	n.d.	n.d.	0.01	0.02	0.04	0.00	0.06	0.06	0.02	n.d.	0.01	0.03	0.03
FeO	12.98	12.78	12.83	12.74	12.53	17.65	17.48	17.37	17.20	17.88	18.12	16.18	16.13	15.60	15.74	16.18	15.91	41.58	36.13	38.90	42.84	42.41
MnO	0.13	0.14	0.15	0.13	0.42	0.23	0.23	0.20	0.23	0.19	0.19	0.23	0.25	0.24	0.23	0.24	0.19	0.70	0.60	0.67	0.75	0.78
NiO	0.52	0.58	0.47	0.49	0.22	0.21	0.18	0.17	0.17	0.10	0.12	0.12	0.10	0.21	0.27	0.14	0.09	0.08	0.04	0.08	0.04	0.02
MgO	46.36	46.38	46.46	46.56	46.34	42.69	42.53	42.53	42.65	42.16	42.51	43.74	44.16	43.33	42.94	43.17	43.96	22.86	27.53	23.84	22.05	22.22
CaO	0.04	0.01	0.02	0.03	0.26	0.08	0.10	0.17	0.14	0.19	0.20	0.30	0.29	0.18	0.18	0.25	0.27	0.34	0.24	0.30	0.32	0.31
Na_2O	0.03	n.d.	0.03	0.03	0.02	0.01	n.d.	n.d.	0.03	0.02	0.01	0.02	0.02	n.d.	n.d.	0.01	0.02	0.01	n.d.	0.01	0.02	0.02
K_2O	n.d.	0.02	0.02	n.d.	n.d.	0.01	n.d.	n.d.	0.02	n.d.	n.d.	n.d.	0.01	n.d.	n.d.	n.d.	n.d.	n.d.	n.d.	n.d.	n.d.	0.01
Total	**100.06**	**100.14**	**100.18**	**99.99**	**100.61**	**100.33**	**99.69**	**99.80**	**99.84**	**99.46**	**100.41**	**100.18**	**100.41**	**99.49**	**99.17**	**99.60**	**100.00**	**100.06**	**100.52**	**99.99**	**99.70**	**99.70**
Stoich.	4O	4O	4O	4O	4O	4O	4O	4O	4O	4O	4O	4O	4O	4O	4O	4O	4O	4O	4O	4O	4O	4O
Si	0.996	0.999	0.997	0.996	1.004	0.999	0.998	1.001	1.001	0.996	0.995	0.997	0.991	1.009	1.011	1.002	0.996	0.992	0.999	1.022	0.980	0.985
Ti	0.000	0.000	-	0.000	0.001	0.000	0.000	-	-	-	0.000	-	0.001	0.000	0.000	-	0.000	0.001	0.000	0.000	0.001	0.001
Al	0.000	0.001	0.000	-	0.002	0.001	0.001	0.001	0.001	0.002	0.001	0.002	0.002	0.000	0.001	0.002	0.002	0.000	0.000	0.000	0.001	0.001
Cr	-	0.000	0.001	0.000	0.001	-	0.000	-	0.000	-	-	0.000	0.000	0.001	0.000	0.001	0.001	0.001	-	0.000	0.000	0.000
Fe^{2+}	0.270	0.266	0.267	0.265	0.259	0.374	0.373	0.370	0.366	0.383	0.385	0.341	0.340	0.330	0.335	0.343	0.336	1.002	0.839	0.920	1.046	1.032
Mn	0.003	0.003	0.003	0.003	0.009	0.005	0.005	0.004	0.005	0.004	0.004	0.005	0.005	0.005	0.005	0.005	0.004	0.017	0.014	0.016	0.018	0.019
Ni	0.010	0.012	0.009	0.010	0.004	0.004	0.004	0.003	0.004	0.002	0.002	0.002	0.002	0.004	0.006	0.003	0.002	0.002	0.001	0.002	0.001	0.001
Mg	1.722	1.719	1.722	1.728	1.707	1.614	1.618	1.614	1.617	1.611	1.609	1.646	1.658	1.635	1.627	1.633	1.654	0.981	1.140	1.006	0.959	0.964
Ca	0.001	0.000	0.001	0.001	0.007	0.002	0.003	0.005	0.004	0.005	0.006	0.008	0.008	0.005	0.005	0.007	0.007	0.010	0.007	0.009	0.010	0.010
Na	0.001	0.000	0.001	0.001	0.001	0.001	-	-	0.002	0.001	0.001	0.001	0.001	-	-	0.000	0.001	0.001	-	0.001	0.001	0.001
K	-	0.001	0.001	-	0.000	0.000	-	-	0.001	-	-	-	0.000	-	-	-	-	-	-	-	-	0.000
Total	*3.004*	*3.000*	*3.002*	*3.004*	*2.994*	*3.001*	*3.001*	*2.999*	*3.000*	*3.004*	*3.004*	*3.002*	*3.008*	*2.990*	*2.988*	*2.997*	*3.003*	*3.007*	*3.001*	*2.977*	*3.018*	*3.014*
Mg#	***86.43***	***86.61***	***86.59***	***86.69***	***86.83***	***81.18***	***81.26***	***81.36***	***81.55***	***80.78***	***80.71***	***82.82***	***83.00***	***83.20***	***82.94***	***82.63***	***83.12***	***49.49***	***57.59***	***52.21***	***47.85***	***48.29***

the abbreviation in brackets under location indicates the adjacent mineral phase of the respective rim analysis; n.a.: not analysed; n.d.: not detected; Stoich.: cations calculated on the basis of 4 oxygens

Table A3-13: Representative major element composition (wt%) and stoichiometry of ***oxydes*** (spinel, ilmenite, rutile) in mafic xenoliths from Marsabit

	Grt websterites																	
Group	V	V	V	V	V	V	V	V	V	V	V	V	V	V	V	V	V	V
Mineral	**spl-IIb**	**spl-IIb**	**ilm**	**ilm**	**rut**	**rut**	**spl-IIb**	**spl-IIb**	**spl-IIb**	**spl-IIb**	**spl-IIb**	**spl-IIb**	**spl-IIb**	**spl-IIb**	**spl-IIb**	**spl-IIb**	**spl-IIb**	**spl-IIb**
sample	784/1	784/1	784/1	784/1	784/1	784/1	1959/18	1959/18	1959/18	1959/18	1960/8	1960/8	1960/8	1960/8	1964	1964	1964	1964
location	sympl.	sympl.	inter-stitial	inter-stitial	incl. in ilm	incl. in ilm	sympl.	sympl.	sympl.	sympl.	sympl.	sympl.	sympl.	sympl.	sympl.	sympl.	sympl.	sympl.
SiO_2	0.01	0.01	0.03	0.03	0.03	0.01 #	0.02	0.04	0.03	0.03	0.05	0.12	0.01	0.01	n.d.	0.01	0.05	0.01
TiO_2	n.d.	0.06	56.85	58.96	98.59	99.47 #	n.d.	0.05	0.05	0.03	n.d.	n.d.	0.01	n.d.	0.01	0.01	0.02	0.01
Al_2O_3	66.05	65.34	0.44	0.25	0.11	0.17 #	66.27	64.56	65.45	65.75	62.11	62.33	65.86	63.58	63.89	64.57	64.19	63.79
Cr_2O_3	1.31	1.84	0.13	0.33	0.21	0.16 #	1.28	2.31	1.64	1.32	6.50	5.95	3.02	4.07	5.45	4.49	5.00	5.79
Fe_2O_3	0.37	0.14	-	-	0.50	0.42 #	0.76	1.77	1.08	0.96	0.27	0.33	0.44	0.07	0.54	0.46	0.54	0.32
FeO	13.24	13.22	31.35	27.63	-	-	10.44	10.04	10.66	10.30	9.90	9.65	9.51	10.57	8.94	7.95	8.33	7.26
MnO	0.04	0.01	0.26	0.41	0.02	0.00	0.10	0.09	0.09	0.07	0.18	0.14	0.13	0.13	0.24	0.16	0.15	0.18
NiO	n.a.	n.a.	0.20	0.03	0.01	0.02	0.44	0.75	0.68	0.42	0.29	0.30	0.28	0.33	0.31	0.36	0.34	0.26
MgO	18.90	18.80	9.89	12.43	0.01	n.d.	20.56	20.45	20.22	20.58	20.54	20.72	21.35	19.95	21.36	22.00	21.91	22.46
CaO	n.d.	0.01	0.23	0.14	0.08	0.06	0.01	0.12	0.07	n.d.	0.04	0.02	0.00	0.07	0.02	0.03	n.d.	0.06
ZnO	0.43	0.39	n.a.	n.a.	n.a.	n.a.	0.08	0.13	n.d.	0.07	0.02	0.07	0.05	0.06	0.13	0.08	0.07	0.04
Nb_2O_5	n.a.	n.a.	n.d.	n.d.	0.03	0.04 #	n.a.	n.a.	n.a.	n.a.	n.a.	n.a.	n.a.	n.a.	n.a.	n.a.	n.a.	n.a.
ZrO_2	n.a.	n.a.	n.d.	n.d.	0.05	0.04 #	n.a.	n.a.	n.a.	n.a.	n.a.	n.a.	n.a.	n.a.	n.a.	n.a.	n.a.	n.a.
Total	*100.35*	*99.81*	*99.39*	*100.20*	*99.64*	*100.40 #*	*99.95*	*100.33*	*99.96*	*99.53*	*99.90*	*99.62*	*100.67*	*98.84*	*100.89*	*100.12*	*100.60*	*100.17*
Stoich.	**4O**	**4O**	**3O**	**3O**	**2O**	**2O**	**4O**	**4O**	**4O**	**4O**	**4O**	**4O**	**4O**	**4O**	**4O**	**4O**	**4O**	**4O**
Si	0.000	0.000	0.001	0.001	0.000	0.000	0.000	0.001	0.001	0.001	0.001	0.003	0.000	0.000	-	0.000	0.001	0.000
Ti	-	0.001	1.006	1.018	0.989	0.990	-	0.001	0.001	0.001	-	-	0.000	-	0.000	0.000	0.000	0.000
Al	1.966	1.958	0.012	0.007	0.002	0.003	1.959	1.916	1.944	1.953	1.862	1.869	1.932	1.917	1.884	1.903	1.889	1.879
Cr	0.026	0.037	0.002	0.006	0.002	0.002	0.025	0.046	0.033	0.026	0.131	0.120	0.059	0.082	0.108	0.089	0.099	0.114
Fe^{3+}	0.007	0.003	-	-	0.005	0.004	0.014	0.034	0.021	0.018	0.005	0.006	0.008	0.001	0.010	0.009	0.010	0.006
Fe^{2+}	0.280	0.281	0.617	0.531	-	-	0.219	0.211	0.225	0.217	0.211	0.205	0.198	0.226	0.187	0.166	0.174	0.152
Mn	0.001	0.000	0.005	0.008	0.000	0.000	0.002	0.002	0.002	0.001	0.004	0.003	0.003	0.003	0.005	0.003	0.003	0.004
Ni	-	-	0.004	0.000	0.000	0.000	0.009	0.015	0.014	0.009	0.006	0.006	0.006	0.007	0.006	0.007	0.007	0.005
Mg	0.712	0.712	0.347	0.425	0.000	-	0.769	0.768	0.759	0.773	0.779	0.786	0.792	0.761	0.796	0.820	0.815	0.837
Ca	-	0.000	0.006	0.004	0.001	0.001	0.000	0.003	0.002	-	0.001	0.000	0.000	0.002	0.001	0.001	-	0.002
Zn	0.008	0.007	-	-	-	-	0.001	0.002	-	0.001	0.000	0.001	0.001	0.001	0.002	0.001	0.001	0.001
Nb	-	-	-	-	0.000	0.000	-	-	-	-	-	-	-	-	-	-	-	-
Zr	-	-	-	-	0.000	0.000	-	-	-	-	-	-	-	-	-	-	-	-
Total	*3.000*	*3.000*	*2.000*	*2.000*	*1.000*	*1.000*	*3.000*	*3.000*	*3.000*	*3.000*	*3.000*	*3.000*	*3.000*	*3.000*	*3.000*	*3.000*	*3.000*	*3.000*
Mg#	***71.79***	***71.71***	***36.00***	***44.50***	***-***	***-***	***77.83***	***78.41***	***77.17***	***78.08***	***78.71***	***79.29***	***80.00***	***77.08***	***80.99***	***83.15***	***82.43***	***84.65***
Cr#[1]	***1.30***	***1.85***	***16.84***	***46.52***	***55.18***	***37.73***	***1.27***	***2.30***	***1.63***	***1.32***	***6.54***	***6.00***	***2.97***	***4.11***	***5.38***	***4.44***	***4.94***	***5.72***

ilm: ilmenite; rut: rutile; hem: Ti-rich hematite; [1]: 100*Cr/(Cr+Al+Fe^{3+}); the abbreviation in brackets under location indicates the adjacent mineral phase of the respective rim analysis;
n.a.: not analysed; n.d.: not detected; Stoech.: cations calculated on the basis of n oxygens

Table A3-13: Representative major element composition (wt%) and stoichiometry of ***oxydes*** (spinel, ilmenite, rutile) in mafic xenoliths from Marsabit (continued)

	Spl-ol websterite				Spl-ol clinopyroxenite				Spl-Ol clinopyroxenite			Ol Gabbro			
Group	**VI**	**VI**	**VI**	**VI**	**C**	**C**	**C**	**C**	**C**	**C**	**C**	**C**	**C**	**C**	**C**
Mineral	**spl-I**	**spl-I**	**spl-I**	**spl-I**	**spl-I**	**spl-I**	**spl-I**	**spl-I**	**spl-I**	**spl-I**	**spl-I**	**spl-I**	**ilm**	**hem**	**ilm**
sample	782/2	782/2	782/2	782/2	726	726	726	726	1973/2	1973/2	1973/2	772/2	772/2	772/2	772/2
location	core	core	rim (cpx)	rim (opx)	core	core	rim (cpx)	rim (spl)	contact w. perid.	bleb in cpx	core	core	lamellae	lamellae	re-integr.*
SiO_2	0.08	0.09	0.09	0.13	0.10	0.07	0.15	0.13	0.14	0.11	0.12	0.17	0.01	0.07	0.03
TiO_2	0.50	0.67	0.63	0.67	0.63	0.64	0.42	0.44	0.38	0.38	0.44	9.11	49.77	16.07	39.65
Al_2O_3	55.08	52.48	52.52	53.31	58.57	58.43	61.04	60.57	58.94	62.36	61.42	7.34	0.03	0.52	n.d.
Cr_2O_3	6.55	8.66	8.31	8.23	0.68	0.63	0.81	0.81	5.02	0.93	1.02	22.93	n.d.	n.d.	0.17
Fe_2O_3	5.22	6.35	6.41	5.83	7.66	8.09	6.40	6.66	4.35	5.15	4.91	17.68	5.69	69.88	24.96
FeO	15.08	15.09	14.59	13.52	14.23	14.29	12.35	12.42	10.25	10.70	11.28	38.20	41.22	13.10	32.78
MnO	0.13	0.10	0.09	0.08	0.09	0.20	0.10	0.10	0.15	0.10	0.13	0.77	0.69	0.48	0.63
NiO	0.19	0.22	0.23	0.17	0.19	0.15	0.17	0.14	0.33	0.27	0.25	0.04	0.03	0.03	0.03
MgO	16.80	16.79	16.93	17.83	17.89	17.83	19.48	19.36	20.16	20.39	19.77	3.00	1.54	0.31	1.17
CaO	0.00	0.02	0.07	0.04	0.01	0.01	0.03	0.00	0.01	0.02	n.d.	n.d.	0.02	0.03	0.02
ZnO	n.a.	n.a.	n.a.	n.a.	n.a.	n.a.	n.a.	n.a.	0.10	0.11	0.08	n.a.	0.02	0.19	0.07
Nb_2O_5	n.a.	n.a.	n.a.	n.a.	n.a.	n.a.	n.a.	n.a.	n.a.	n.a.	n.a.	n.a.	n.a.	n.a.	n.a.
ZrO_2	n.a.	n.a.	n.a.	n.a.	n.a.	n.a.	n.a.	n.a.	n.a.	n.a.	n.a.	n.a.	n.a.	n.a.	n.a.
Total	*99.64*	*100.47*	*99.85*	*99.81*	*100.04*	*100.35*	*100.94*	*100.62*	*99.82*	*100.51*	*99.42*	*99.24*	*99.03*	*100.66*	*99.52*
Stoich.	**4O**	**4O**	**4O**	**4O**	**4O**	**4O**	**4O**	**4O**	**4O**	**4O**	**4O**	**3O**	**2O**	**2O**	**2O**
Si	0.002	0.002	0.002	0.004	0.003	0.002	0.004	0.003	0.004	0.003	0.003	0.006	0.000	0.002	0.001
Ti	0.010	0.014	0.013	0.014	0.012	0.013	0.008	0.008	0.007	0.007	0.009	0.228	0.945	0.312	0.759
Al	1.733	1.657	1.664	1.675	1.805	1.799	1.837	1.832	1.793	1.865	1.862	0.193	0.001	0.016	0.000
Cr	0.138	0.183	0.177	0.173	0.014	0.013	0.016	0.016	0.102	0.019	0.021	0.898	-	-	0.003
Fe^{3+}	0.105	0.128	0.130	0.117	0.151	0.159	0.123	0.129	0.084	0.098	0.095	0.442	0.108	1.360	0.478
Fe^{2+}	0.337	0.338	0.328	0.302	0.311	0.312	0.264	0.266	0.221	0.227	0.243	1.062	0.871	0.283	0.698
Mn	0.003	0.002	0.002	0.002	0.002	0.004	0.002	0.002	0.003	0.002	0.003	0.022	0.015	0.010	0.014
Ni	0.004	0.005	0.005	0.004	0.004	0.003	0.003	0.003	0.007	0.006	0.005	0.001	0.001	0.001	0.001
Mg	0.669	0.670	0.678	0.709	0.698	0.694	0.741	0.740	0.776	0.771	0.758	0.149	0.058	0.012	0.044
Ca	0.000	0.000	0.002	0.001	0.000	0.000	0.001	0.000	0.000	0.001	-	-	0.000	0.001	0.001
Zn	-	-	-	-	-	-	-	-	0.002	0.002	0.002	-	0.000	0.004	0.001
Nb	-	-	-	-	-	-	-	-	-	-	-	-	-	-	-
Zr	-	-	-	-	-	-	-	-	-	-	-	-	-	-	-
Total	*3.000*	*3.000*	*3.000*	*3.000*	*3.000*	*3.000*	*3.000*	*3.000*	*3.000*	*3.000*	*3.000*	*3.000*	*2.000*	*2.000*	*2.000*
Mg#	***66.51***	***66.48***	***67.41***	***70.15***	***69.15***	***68.99***	***73.76***	***73.53***	***77.81***	***77.26***	***75.75***	***12.28***	***6.25***	***4.03***	***5.99***
Cr# [1]	***7.00***	***9.32***	***8.96***	***8.82***	***0.72***	***0.66***	***0.82***	***0.83***	***5.17***	***0.94***	***1.05***	***58.59***	-	-	-

ilm: ilmenite; rut: rutile; hem: Ti-rich hematite; [1]: 100*Cr/(Cr+Al+Fe^{3+}); the abbreviation in brackets under location indicates the adjacent mineral phase of the respective rim analysis;
n.a.: not analysed; n.d.: not detected; Stoech.: cations calculated on the basis of n oxygens; * re-integrated using the relative hematite and ilmenite proportions obtained by image analysis

Table A3-14: Representative major element composition (wt%) and stoichiometry of ***amphibole and phlogopite*** in mafic xenoliths from Marsabit

	Grt websterites															
Group	**V**	**V**	**V**	**V**	**V**	**V**	**V**	**V**	**V**	**V**	**V**	**V**	**V**	**V**	**V**	**V**
Mineral	**Ti-prg**	**Ti-prg**	**Ti-prg**	**Ti-prg**	**Ti-prg**	**Ti-prg**	**Ti-prg**	**Ti-prg**	**Ti-prg**	**phl**	**phl**	**Ti-prg**	**Ti-prg**	**Ti-prg**	**Ti-prg**	**Ti-prg**
sample	784/1	784/1	784/1	784/1	784/1	784/1	784/1	784/1	784/1	784/1	784/1	1959/18	1959/18	1959/18	1959/18	1959/18
remark	amph-i core	amph-i core	amph-i r/opx	amph-i r/grt	amph-ii core	amph-ii r/phl	amph-ii r/ilm	incl. in grt	incl. in grt	core	rim (cpx-I)	amph-i core	amph-i core	amph-i r/grt	amph-i r/grt	with plag
SiO_2	42.70	42.79	43.15	42.20	42.31	44.93	45.51	43.05	42.42	37.86	37.61	43.49	43.22	43.27	43.03	40.01
TiO_2	4.96	4.74	4.81	3.59	2.31	4.25	4.46	4.01	4.92	6.86	6.80	3.50	3.38	3.54	3.35	7.47
Al_2O_3	14.25	13.97	14.06	14.97	17.06	10.17	9.74	14.09	14.71	14.73	14.99	14.81	15.18	15.07	15.40	14.09
Cr_2O_3	0.21	0.22	0.20	0.21	0.26	0.33	0.40	0.43	0.49	0.35	0.37	0.25	0.28	0.34	0.36	0.78
FeO	5.03	4.97	4.97	5.86	5.31	7.17	7.18	5.54	6.01	8.05	7.93	4.89	4.84	4.72	4.69	4.75
MnO	0.04	0.07	n.d.	0.06	0.03	0.01	0.07	0.03	0.04	n.d.	0.01	0.10	0.03	0.09	0.06	0.15
NiO	0.11	0.11	0.08	0.12	0.12	0.08	0.18	0.11	0.05	0.26	0.22	n.a.	n.a.	n.a.	n.a.	n.a.
MgO	15.93	16.21	16.36	15.97	15.61	15.73	16.31	15.88	15.31	17.78	17.53	16.29	15.95	15.99	15.78	15.66
CaO	10.91	10.93	10.71	10.17	10.08	10.11	10.18	10.22	9.88	0.03	0.03	10.54	10.43	10.23	10.07	12.40
Na_2O	3.86	4.10	4.18	4.08	3.83	3.82	4.04	3.92	3.97	1.10	1.03	4.09	4.09	4.14	4.14	2.83
K_2O	0.02	0.02	0.02	n.d.	n.d.	0.95	0.22	0.02	n.d.	8.78	8.74	0.18	0.26	0.21	0.25	0.15
H_2O	2.11	2.11	2.12	2.09	1.98	2.20	2.03	1.98	1.99	4.16	4.14	2.12	2.11	2.11	2.10	2.09
Total	*100.130*	*100.230*	*100.660*	*99.330*	*99.630*	*99.620*	*100.510*	*99.680*	*100.240*	*99.970*	*99.390*	*100.256*	*99.773*	*99.713*	*99.237*	*100.375*
Stoech.	**23O**	**23O**	**23O**	**23O**	**23O**	**23O**	**23O**	**23O**	**23O**	**23O**	**23O**	**22O**	**22O**	**22O**	**22O**	**22O**
Si	6.069	6.083	6.097	6.058	6.048	6.488	6.505	6.160	6.053	5.456	5.446	6.154	6.142	6.148	6.139	5.728
Ti	0.531	0.507	0.511	0.388	0.248	0.461	0.479	0.431	0.528	0.744	0.740	0.372	0.361	0.378	0.359	0.804
Al	2.387	2.340	2.342	2.533	2.874	1.731	1.641	2.377	2.474	2.502	2.558	2.470	2.543	2.524	2.590	2.378
Cr	0.024	0.025	0.023	0.024	0.029	0.038	0.045	0.049	0.055	0.040	0.042	0.028	0.031	0.038	0.041	0.089
Fe^{2+}	0.598	0.590	0.588	0.703	0.635	0.866	0.858	0.662	0.718	0.970	0.960	0.578	0.575	0.561	0.560	0.569
Mn	0.005	0.008	-	0.007	0.004	0.001	0.008	0.004	0.005	-	0.001	0.012	0.004	0.011	0.007	0.018
Ni	0.013	0.012	0.010	0.014	0.014	0.009	0.021	0.013	0.006	0.030	0.026	-	-	-	-	-
Mg	3.374	3.435	3.445	3.418	3.326	3.385	3.475	3.387	3.256	3.821	3.784	3.435	3.378	3.386	3.356	3.342
Ca	1.661	1.665	1.621	1.564	1.544	1.564	1.559	1.567	1.510	0.004	0.005	1.598	1.588	1.557	1.539	1.902
Na	1.065	1.129	1.145	1.136	1.061	1.069	1.120	1.087	1.098	0.309	0.288	1.122	1.127	1.140	1.145	0.785
K	0.003	0.004	0.003	-	-	0.175	0.040	0.004	-	1.615	1.614	0.032	0.047	0.038	0.045	0.027
H	2.000	2.000	2.000	2.000	2.000	2.000	2.000	2.000	2.000	4.000	4.000	2.000	2.000	2.000	2.000	2.000
Total	***15.726***	***15.794***	***15.781***	***15.844***	***15.569***	***15.639***	***15.671***	***15.637***	***15.590***	***15.490***	***15.465***	***15.802***	***15.797***	***15.782***	***15.782***	***15.641***
Mg#	***84.95***	***85.33***	***85.42***	***82.93***	***83.96***	***79.64***	***80.20***	***83.64***	***81.94***	***79.75***	***79.76***	***85.59***	***85.44***	***85.78***	***85.70***	***85.46***
Cr# [1]	***0.01***	***0.01***	***0.01***	***0.01***	***0.01***	***0.02***	***0.03***	***0.02***	***0.02***	***0.02***	***0.02***	***0.01***	***0.01***	***0.01***	***0.02***	***0.04***

[1]: 100*Cr/(Cr+Al+Fe^{3+}); the abbreviation in brackets under location indicates the adjacent mineral phase of the respective rim analysis; n.a.: not analysed; n.d.: not detected;
Stoech.: cations calculated on the basis of n oxygens

Table A3-15: Representative major element composition and stoichiometry of ***feldspar, analcime, and zeolite*** in mafic xenoliths from Marsabit

	Grt websterites				Gabbro										
Group	**V**	**V**	**V**	**V**	**VII**	**VII**	**VII**	**VII**	**VII**	**VII**	**VII**	**VII**	**VII**	**VII**	**VII**
Mineral	**$plag_m$**	**$plag_m$**	**$plag_m$**	**$plag_m$**	**plag**	**plag**	**plag**	**plag**	**plag**	**plag**	**anal**	**anal**	**anal**	**zeol**	**zeol**
sample	1959/18	1959/18	1959/18	1959/18	772/2	772/2	772/2	772/2	772/2	772/2	772/2	772/2	772/2	772/2	772/2
remark	RZ1	RZ1	RZ1	RZ2	core	core	rim (Ab-rich)	rim (Ab-rich)	rim (Or-rich)	rim (Or-rich)	core	core	rim (plag)	core	core
SiO_2	62.14	61.58	54.33	55.71	54.49	55.26	63.70	65.77	66.71	64.37	54.66	54.50	54.85	50.77	50.99
TiO_2	n.a.	n.a.	n.a.	n.a.	0.10	0.10	0.05	0.06	0.01	n.d.	n.d.	0.01	0.01	0.02	n.d.
Al_2O_3	24.21	24.36	28.65	28.19	29.00	28.37	21.94	20.41	19.00	18.96	23.26	22.95	22.87	n.d.	n.d.
Cr_2O_3	n.a.	n.a.	n.a.	n.a.	n.a.	n.a.	n.a.	n.a.	n.a.	n.a.	n.d.	n.d.	n.d.	23.47	23.46
FeO	0.21	0.19	0.43	0.25	0.60	0.50	0.27	0.30	0.69	0.02	0.18	n.d.	n.d.	n.d.	n.d.
MnO	n.a.	n.a.	n.a.	n.a.	0.01	n.d.	n.d.	n.d.	0.02	0.01	0.02	n.d.	n.d.	0.02	n.d.
NiO	n.a.	n.a.	n.a.	n.a.	n.a.	n.a.	n.a.	n.a.	n.a.	n.a.	n.d.	n.d.	n.d.	n.d.	n.d.
MgO	n.a.	n.a.	n.a.	n.a.	0.04	0.06	0.02	n.d.	0.01	n.d.	n.d.	n.d.	n.d.	n.d.	0.01
CaO	5.00	4.89	10.44	9.64	10.85	10.07	2.22	0.95	0.03	n.d.	0.37	0.28	0.21	10.22	10.17
Na_2O	9.04	9.29	5.89	6.28	5.45	5.82	9.30	8.49	7.35	0.29	12.70	12.73	12.99	2.11	0.93
K_2O	0.06	0.06	0.05	0.04	0.27	0.30	2.28	4.18	6.38	16.50	0.03	0.04	0.03	0.33	0.39
Total	*100.66*	*100.37*	*99.79*	*100.11*	*100.81*	*100.49*	*99.79*	*100.16*	*100.20*	*100.17*	*91.21*	*90.51*	*90.97*	*86.94*	*85.95*
Stoich.	**8O**	**8O**	**8O**	**8O**	**8O**	**8O**	**8O**	**8O**	**8O**	**8O**	**6O**	**6O**	**6O**	**24O**	**24O**
Si	2.740	2.727	2.461	2.505	2.448	2.484	2.841	2.925	2.984	2.975	2.008	2.015	2.019	7.796	7.869
Ti	-	-	-	-	0.003	0.003	0.002	0.002	0.000	-	-	0.000	0.000	0.002	-
Al	1.258	1.271	1.530	1.494	1.536	1.503	1.153	1.070	1.002	1.033	1.007	1.000	0.992	-	-
Cr	-	-	-	-	-	-	-	-	-	-	-	-	-	4.248	4.268
Fe^{2+}	0.008	0.007	0.016	0.009	0.023	0.019	0.010	0.011	0.026	0.001	0.005	-	-	-	-
Mn	-	-	-	-	0.000	-	-	-	0.001	0.001	0.001	-	-	0.002	-
Ni	-	-	-	-	-	-	-	-	-	-	-	-	-	-	-
Mg	-	-	-	-	0.003	0.004	0.001	-	0.000	-	-	-	-	-	0.001
Ca	0.236	0.232	0.507	0.464	0.522	0.485	0.106	0.045	0.001	-	0.014	0.011	0.008	1.681	1.681
Na	0.773	0.797	0.517	0.547	0.474	0.508	0.804	0.732	0.638	0.026	0.904	0.913	0.927	0.628	0.278
K	0.003	0.003	0.003	0.002	0.016	0.017	0.130	0.237	0.364	0.973	0.001	0.002	0.001	0.064	0.076
Total	*5.019*	*5.038*	*5.034*	*5.023*	*5.026*	*5.023*	*5.048*	*5.022*	*5.016*	*5.008*	*3.941*	*3.941*	*3.949*	*14.423*	*14.174*
An	***0.23***	***0.22***	***0.49***	***0.46***	***0.52***	***0.48***	***0.10***	***0.04***	***0.00***	***0.00***	-	-	-	-	-
Ab	***0.76***	***0.77***	***0.50***	***0.54***	***0.47***	***0.50***	***0.77***	***0.72***	***0.64***	***0.03***	-	-	-	-	-
Or	***0.00***	***0.00***	***0.00***	***0.00***	***0.02***	***0.02***	***0.12***	***0.23***	***0.36***	***0.97***	-	-	-	-	-

plag: plagioclase; anal: analcite; zeol: zeolite; the abbreviation in brackets under location indicates the adjacent mineral phase of the respective rim analysis;
n.a.: not analysed; n.d.: not detected; Stoich.: cations calculated on the basis of n oxygens

Appendix A4

LA-ICPMS data

Table A4-1: Trace element composition of ***olivine*** (in µg/g) in peridotite and pyroxenite xenoliths from Marsabit

	Group I	**Group II**				**Group III-a**				**Group III-b**		**Group III-c**			
sample	**1963/1**	**1958/13**	**1958/20**	**1959/24**	**1959/25**	**1965/1**	**1965/1**	**1965/1**	**1965/1**	**1959/15**	**1959/15**	**785***	**1959/27**	**1965/3**	**1965/3**
location	ol-I	ol-I	ol-I	ol-I	ol-I	ol-I	ol-I	ol-I	ol-I	Ol_m	metas.	ol-I	ol-I	ol-I	ol-I
	core	core	core	core	core	core	core	core	core		ol-I	core	core	core	rim
anal. Nr.	ob28f07	ob29a12	ob29b04	ob28b04	dd09a07	mc22a04	mc22a08	mc22a11	mc22a15	dd09a07	ob29c13	ob28e08	dd08g03	dd08c18	dd08c17
Na	14.5	74.2	64.8	80.8	218	12.1	17.0	8.46	11.9	218	14.8	29.7	90.2	31.1	71.6
Al	21.2	122	190	213	360	27.1	29.3	30.5	25.2	360	15.9	8.93	83.2	11.2	20.5
P	45.0	40.2	67.5	57.2	39.3	21.8	26.0	18.4	26.2	39.3	17.1	42.1	109	43.6	201
K	<0.38	2.23	<0.36	0.33	2.01	0.46	0.60	<0.46	<0.41	2.01	<0.36	<0.3653	<0.27	0.49	<1.97
Ca	121	415	722	715	1279	218	185	200	221	1279	181	82.2	443	100	<114
Sc	0.72	1.57	2.91	2.62	4.53	3.27	2.47	5.19	4.05	4.53	0.93	0.61	2.40	0.97	1.37
Ti	9.23	7.73	24.0	36.6	38.6	4.21	3.25	2.18	2.28	38.6	6.25	1.56	5.29	0.85	<1.52
V	1.20	2.63	4.16	4.37	7.23	1.07	1.29	0.86	1.09	7.23	1.70	1.04	4.28	0.85	1.90
Ni	2768	2524	2462	2624	2864	2874	2895	2924	2863	2864	2870	2686	2306	2736	2871
Zn	18.7	47.0	57.2	66.5	75.8	45.3	37.9	49.9	39.5	75.8	50.6	63.0	120	75.4	93.0
Ga	0.014	0.028	0.063	0.11	n.a.	<0.010	0.036	<0.010	0.031	n.a.	0.018	0.015	n.a.	n.a.	n.a.
Rb	<0.004	0.008	<0.008	0.002	<0.033	0.006	0.008	<0.005	<0.006	<0.033	<0.008	<0.008	<0.006	<0.010	<0.046
Sr	<0.002	0.053	0.009	0.012	0.20	0.005	0.004	0.003	0.007	0.195	0.003	0.017	0.026	0.019	0.034
Y	0.004	0.015	0.071	0.061	0.063	0.032	0.018	0.047	0.033	0.063	0.006	0.015	0.11	0.064	0.087
Zr	0.006	0.023	0.034	0.062	0.060	0.025	0.024	0.028	0.012	0.060	<0.009	<0.005	0.034	<0.010	<0.066
Nb	<0.003	<0.003	0.009	0.008	<0.020	<0.003	<0.003	0.005	0.005	<0.020	<0.002	<0.003	0.003	0.021	<0.033
Cs	<0.001	<0.003	0.004	0.001	<0.014	0.003	0.007	0.006	0.002	<0.014	<0.001	<0.002	<0.004	0.004	<0.019
Ba	<0.014	0.03	0.009	0.003	<0.087	<0.009	<0.015	<0.019	<0.009	<0.087	0.010	<0.016	<0.020	<0.033	<0.13
La	<0.001	<0.004	0.008	0.001	<0.018	0.002	0.003	<0.001	0.002	<0.018	<0.001	0.021	<0.002	0.008	<0.035
Ce	0.001	0.008	0.006	0.001	0.026	<0.002	0.007	<0.002	0.003	0.026	<0.001	0.023	<0.003	0.022	<0.027
Pr	<0.001	<0.001	0.001	0.002	<0.009	<0.001	0.005	0.002	<0.002	<0.009	<0.001	<0.001	<0.002	0.004	0.024
Nd	0.004	0.025	<0.011	0.002	<0.058	<0.012	0.019	<0.009	0.008	<0.058	<0.005	<0.007	<0.007	<0.011	<0.099
Sm	<0.005	<0.011	<0.008	0.002	<0.087	0.007	<0.006	<0.006	<0.016	<0.087	<0.012	<0.006	0.009	<0.010	<0.14
Eu	<0.001	<0.003	<0.003	<0.001	<0.024	0.005	<0.003	<0.002	<0.002	<0.024	<0.002	<0.002	<0.004	<0.006	<0.043
Gd	<0.005	<0.009	0.006	0.005	<0.090	<0.010	<0.006	<0.008	<0.006	<0.090	<0.005	<0.006	<0.021	<0.019	<0.11
Tb	<0.001	<0.001	<0.001	<0.001	n.a.	<0.001	0.001	<0.001	0.003	n.a.	<0.001	<0.001	n.a.	n.a.	n.a.
Dy	<0.003	0.01	0.012	0.005	<0.053	<0.004	0.007	0.004	0.007	<0.053	<0.003	<0.003	<0.014	<0.030	<0.11
Ho	0.001	<0.001	0.003	0.001	<0.010	0.001	0.004	0.003	0.002	<0.010	<0.001	<0.001	<0.004	<0.004	<0.021
Er	<0.006	0.01	0.011	0.010	<0.041	0.009	<0.008	0.007	0.011	<0.041	<0.008	<0.006	0.012	0.019	<0.043
Tm	<0.001	0.004	0.003	0.004	<0.007	<0.001	0.002	0.004	0.001	<0.007	<0.001	<0.001	0.003	0.008	<0.014
Yb	0.007	0.009	0.022	0.021	<0.062	0.027	0.020	0.039	0.034	<0.062	<0.005	0.009	0.049	0.028	<0.094
Lu	0.001	0.004	0.010	0.007	<0.014	0.014	0.005	0.013	0.006	<0.014	<0.002	0.002	0.012	0.006	<0.021
Hf	<0.003	<0.004	<0.006	0.004	<0.056	<0.004	<0.006	0.006	0.010	<0.056	<0.004	<0.003	<0.011	<0.012	<0.084
Ta	0.002	0.003	<0.002	<0.001	<0.023	0.002	0.002	0.003	<0.001	<0.023	<0.001	0.001	<0.003	<0.005	<0.018
Pb	0.035	<0.024	0.026	0.019	<0.070	0.034	0.019	0.036	0.024	<0.070	<0.019	0.036	0.033	0.025	0.095
Th	<0.001	<0.002	<0.001	0.002	<0.013	0.002	0.004	0.002	<0.002	<0.013	0.002	0.050	<0.003	<0.004	0.022
U	<0.001	<0.001	<0.002	<0.002	<0.007	0.004	0.007	<0.002	<0.001	<0.007	<0.001	0.011	<0.003	0.005	0.026

n.a.: not analysed

Table A4-1: Trace element composition of ***olivine*** (in µg/g) in peridotite and pyroxenite xenoliths from Marsabit (continued)

	Group III-c			Group III-d	Group IV								Group VI	
sample	**1965/3**	**1965/25**	**1965/25**	**1970/6**	**1961/1**	**1961/1**	**1961/1**	**1961/1**	**1968/1**	**1968/1**	**1968/1**	**1968/1**	**782/2**	**782/2**
location	Ol_m	ol-I	ol-I	ol-I	ol-I	ol-I	ol-IIa	ol-IIa	ol-I	ol-I	ol-IIa	ol-IIa	ol-I	ol-I
	in glass	core	core	core	core	core	core	core	core	core	core	core	core	core
anal. Nr.	dd08d03	as12a16	as12a18	ob28g11	mc22c08	mc22c13	mc22c14	mc22c15	mc22b11	mc22b12	mc22b04	mc22b05	mc22f15	mc22f16
Na	262	37.4	64.7	230	16.2	0.93	8.36	8.29	5.47	6.22	6.36	6.68	80.9	74.2
Al	82.1	14.7	12.0	1201	19.1	5.34	39.1	88.4	8.35	8.39	38.0	38.4	150	141
P	292	44.2	105	244	13.8	15.8	20.1	15.5	22.8	25.8	26.3	30.7	51.4	48.2
K	<1.02	1.25	1.98	6.30	0.87	0.65	<1.17	<0.63	0.71	<0.44	<0.40	0.58	0.56	0.59
Ca	579	216	200	658	304	43.9	<42.9	50.5	58.2	56.3	35.4	33.8	707	603
Sc	4.32	0.86	0.94	2.86	1.63	1.70	1.09	0.84	0.70	0.66	0.66	0.70	2.76	2.65
Ti	8.71	3.51	1.70	20.4	1.33	1.08	5.10	1.29	5.07	3.00	2.26	3.26	45.6	47.4
V	3.77	1.01	0.96	28.3	0.56	0.38	<0.159	0.34	0.36	0.33	1.07	0.62	5.62	5.16
Ni	2875	2861	2920	2649	3011	3055	3193	3146	2935	2895	2851	2871	1543	1517
Zn	66.5	141	146	69.3	21.4	23.7	17.8	19.3	18.4	19.2	20.1	20.1	78.3	77.2
Ga	n.a.	0.031	0.035	0.77	0.047	0.033	0.034	0.048	0.013	<0.012	<0.012	0.041	0.104	0.084
Rb	<0.028	<0.011	<0.013	0.0	0.009	<0.005	<0.020	<0.010	<0.006	<0.004	0.007	0.010	0.006	<0.005
Sr	<0.013	0.034	0.045	0.52	0.056	0.009	<0.011	<0.007	0.013	0.006	0.009	0.006	0.013	0.008
Y	0.16	0.084	0.10	0.19	<0.003	0.008	<0.010	<0.003	0.005	0.003	<0.002	<0.002	0.042	0.028
Zr	<0.033	0.008	<0.006	0.15	0.028	0.032	<0.024	0.016	<0.006	0.010	<0.003	0.016	0.034	0.014
Nb	0.025	0.013	0.008	0.035	<0.002	<0.003	<0.015	0.003	<0.003	<0.004	<0.005	<0.002	0.010	0.007
Cs	<0.010	0.005	0.004	0.003	0.003	0.006	0.011	<0.003	0.006	<0.003	<0.002	0.003	<0.001	0.002
Ba	<0.071	0.018	0.17	0.13	<0.017	<0.014	<0.050	<0.019	<0.018	<0.009	0.017	<0.010	<0.014	<0.010
La	<0.004	<0.004	0.017	0.019	<0.002	<0.002	0.005	<0.002	<0.001	0.007	<0.001	<0.003	<0.003	<0.001
Ce	<0.012	0.010	0.027	0.15	<0.003	0.002	0.013	<0.003	<0.003	0.003	0.003	<0.003	<0.003	0.002
Pr	<0.011	<0.003	0.009	0.019	0.002	<0.001	<0.003	<0.002	0.002	0.002	<0.001	0.002	0.002	<0.001
Nd	<0.052	<0.016	0.018	0.11	0.007	<0.006	<0.018	<0.008	<0.006	0.009	<0.009	<0.006	<0.006	0.009
Sm	<0.051	<0.013	<0.009	0.032	0.006	<0.007	<0.029	<0.009	<0.007	<0.006	<0.011	<0.007	<0.007	0.008
Eu	<0.012	<0.006	<0.003	0.011	<0.002	<0.002	<0.006	<0.003	<0.002	<0.002	<0.003	0.003	<0.004	<0.003
Gd	<0.041	<0.009	<0.016	0.035	0.006	<0.007	<0.020	0.027	<0.009	<0.006	<0.006	<0.007	<0.007	<0.006
Tb	n.a.	0.004	<0.001	0.004	<0.001	<0.001	0.004	<0.002	<0.001	<0.001	<0.001	0.004	<0.001	0.002
Dy	<0.043	<0.013	<0.009	0.041	<0.003	<0.004	<0.012	0.006	<0.004	<0.004	<0.005	<0.004	<0.004	<0.004
Ho	<0.006	<0.001	0.004	0.010	0.001	<0.001	<0.003	<0.003	0.003	<0.001	<0.001	<0.001	<0.001	0.003
Er	0.058	0.028	0.018	0.027	<0.003	<0.004	<0.013	<0.006	<0.006	<0.007	<0.004	<0.005	0.010	0.007
Tm	0.010	0.002	0.003	0.004	0.001	<0.001	<0.004	<0.001	<0.001	0.002	<0.001	0.004	0.001	0.002
Yb	0.064	0.089	0.060	0.038	0.006	0.015	<0.028	0.010	<0.007	<0.009	0.009	<0.010	0.011	<0.009
Lu	0.040	0.018	0.018	0.008	0.001	0.002	<0.003	<0.001	<0.001	0.001	<0.001	<0.002	0.003	0.003
Hf	<0.017	<0.006	<0.009	<0.006	<0.006	<0.006	<0.012	0.006	0.005	<0.005	<0.006	<0.004	<0.004	<0.004
Ta	<0.018	<0.003	<0.001	<0.001	0.001	<0.001	<0.004	<0.002	<0.002	0.002	<0.001	0.006	<0.001	<0.002
Pb	0.075	0.039	0.042	0.046	0.025	0.031	0.050	0.048	0.044	0.029	0.012	0.018	0.018	0.023
Th	<0.006	<0.002	0.011	<0.001	0.002	<0.001	<0.010	<0.002	<0.001	<0.001	0.004	<0.001	0.002	<0.001
U	<0.006	<0.002	<0.001	<0.002	0.001	0.002	<0.004	<0.002	0.004	<0.002	0.002	0.002	<0.001	<0.001

n.a.: not analysed

Table A4-2: Trace element composition of ***spinel*** (in µg/g) in peridotite and pyroxenite xenoliths from Marsabit

	Group I	**Group II**				**Group III-a**			**Group III-d**	**Group IV**				**Group VI**	
sample	**1963/1**	**1958/13**	**1958/20**	**1959/24**	**1959/25**	**1965/1**	**1965/1**	**1965/1**	**1970/6**	**1961/1**	**1961/1**	**1968/1**	**1968/1**	**782/2**	**782/2**
location	spl-IIb	spl-IIb	spl-IIb	spl-IIb	spl-IIb	spl-I	spl-I	spl-I	Chr_m	spl-I	spl-I	spl-I	spl-I	spl-I	spl-I
	sympl.	sympl.	sympl.	sympl.	sympl.	core	core	core	core	core	core	core	core	core	core
anal. Nr.	ob29d11	ob29d11	ob29b10	ob28b11	dd09a08	mc22c16	mc22c17	ob28d03	ob28g07	mc22c16	mc22c17	mc22b17	mc22b18	mc22f17	mc22f18
Na	0.50	n.a.	95.3	3.55	331	1.52	1.91	1.19	4.38	1.52	1.91	0.92	1.22	1.48	2.72
P	20.7	20.6	19.9	19.6	39.3	21.8	18.1	24.2	19.8	21.8	18.1	13.2	13.1	15.8	20.6
Ca	<111	<165	729	12.4	<314.47	<92.9	<50.0	<81.9	n.a.	<92.9	<50.0	<42.9	<50.0	1.3	<1.49
K	<2.49	<3.27	2.79	0.32	17.0	<2.22	<1.68	<1.83	<0.86	<2.22	<1.68	2.32	<1.11	<50.0	<57.2
Sc	<0.093	0.47	0.70	0.58	1.52	0.35	0.38	0.61	2.80	0.35	0.38	0.11	0.093	0.97	1.00
Ti	162	319	892	1031	1816	54	75	560	956	54.0	75.1	164	247	2756	2472
V	242	321	363	417	661	678	663	832	925	678	663	424	439	660	653
Ni	4298	3271	3376	3092	3179	1089	1302	1510	1010	1089	1302	2402	2440	1626	1692
Zn	1166	1105	764	878	808	2478	1812	1577	732	2478	1812	1885	1823	925	937
Ga	93.7	84.1	76.4	90.5	n.a.	23.0	23.2	54.3	28.0	23.0	23.2	71.2	82.2	136	138
Rb	0.056	0.042	0.027	0.038	<0.161	0.061	0.029	0.061	0.028	0.061	0.029	0.042	0.023	0.021	0.069
Sr	0.059	0.035	0.52	0.04	0.57	0.078	0.10	0.062	0.089	0.078	0.10	0.054	0.049	0.058	0.076
Y	<0.008	<0.011	0.021	0.019	<0.077	0.027	0.039	0.023	0.025	0.027	0.039	0.024	0.012	0.018	<0.009
Zr	0.078	0.18	0.15	0.21	0.33	0.49	0.44	0.38	1.24	0.49	0.44	0.29	0.31	0.16	0.25
Nb	0.091	0.16	0.21	0.21	0.31	0.38	0.32	0.58	0.88	0.38	0.32	0.18	0.20	0.12	0.16
Cs	<0.013	0.032	0.013	0.051	<0.054	0.059	0.026	0.073	0.046	0.059	0.026	0.046	0.026	0.015	0.026
Ba	<0.045	0.10	<0.030	<0.030	0.61	<0.072	0.41	0.081	<0.028	<0.072	0.41	0.046	<0.044	<0.032	<0.070
La	0.010	0.022	0.026	0.029	<0.077	0.034	0.036	0.033	0.039	0.034	0.036	0.026	0.028	0.015	0.025
Ce	0.045	0.11	0.20	0.10	0.092	0.099	0.056	0.043	0.052	0.099	0.056	0.042	0.017	0.032	0.075
Pr	<0.011	0.060	0.019	0.016	<0.032	0.023	0.029	0.053	0.024	0.023	0.029	0.029	0.027	0.013	0.031
Nd	<0.076	0.091	0.060	0.022	<0.30	0.064	<0.023	<0.033	<0.029	0.064	<0.023	<0.038	0.036	<0.020	<0.037
Sm	<0.053	<0.060	<0.021	0.006	0.23	<0.036	0.031	0.077	0.022	<0.036	0.031	<0.045	0.042	<0.023	<0.050
Eu	0.015	0.035	0.009	0.031	<0.071	<0.011	<0.008	0.036	0.018	<0.011	<0.008	0.025	<0.006	<0.011	<0.007
Gd	<0.043	<0.073	<0.021	0.011	<0.31	<0.035	<0.043	<0.021	<0.026	<0.035	<0.043	0.074	<0.021	<0.022	<0.024
Tb	<0.008	<0.009	0.005	0.003	n.a.	0.013	0.010	0.014	<0.004	0.013	0.010	0.005	0.010	0.009	0.007
Dy	<0.026	<0.044	<0.013	<0.010	<0.23	0.036	0.028	0.036	0.010	0.036	0.028	<0.013	0.028	<0.019	<0.015
Ho	<0.005	<0.007	0.009	0.005	<0.057	<0.008	0.005	0.006	0.003	<0.008	0.005	0.012	<0.003	0.004	0.010
Er	<0.044	<0.038	<0.044	0.009	<0.17	<0.045	<0.016	<0.024	<0.015	<0.045	<0.016	<0.014	<0.024	0.020	<0.016
Tm	<0.004	<0.009	<0.005	0.014	0.056	0.028	0.006	<0.006	<0.003	0.028	0.006	0.009	0.005	0.004	0.019
Yb	<0.052	<0.042	<0.020	0.030	<0.36	0.036	<0.044	<0.030	<0.018	0.036	<0.044	<0.049	<0.022	0.030	<0.034
Lu	<0.005	<0.007	0.004	0.012	<0.041	0.040	0.012	<0.006	0.007	0.040	0.012	0.004	0.006	0.012	0.013
Hf	<0.018	<0.025	<0.017	0.020	0.18	0.037	0.053	<0.018	0.042	0.037	0.053	0.029	0.185	0.034	<0.015
Ta	<0.006	0.014	0.006	0.015	<0.078	0.056	0.011	0.031	0.015	0.056	0.011	0.020	0.025	0.011	0.005
Pb	<0.12	0.28	0.24	0.10	<0.28	0.19	0.10	0.38	0.146	0.19	0.10	0.11	0.10	0.075	0.11
Th	0.009	0.022	<0.008	0.023	<0.044	0.071	0.017	0.027	0.010	0.071	0.017	0.022	0.018	0.018	0.018
U	<0.007	<0.013	0.012	0.011	<0.062	0.043	0.058	0.052	0.017	0.043	0.058	0.043	0.043	0.013	0.022

Table A4-3: Trace element composition of ***orthopyroxene*** (in µg/g) in peridotite and pyroxenite xenoliths from Marsabit

	Group I												Group II				
sample	**1963/2**	**1963/2**	**1963/2**	**1963/2**	**1963/2**	**1963/2**	**1963/2**	**1963/2**	**1963/2**	**1965/4**	**1965/4**	**1965/4**	**1958/13**	**1958/13**	**1958/13**	**1958/20**	**1958/20**
location	opx-I	opx-I	opx-I	opx-I	opx-I	opx-I	opx-I	opx-IIa	opx-IIa	opx-I	opx-I	opx-I	opx-I	opx-I	opx-IIb	opx-I	opx-I
	Al trough	Al trough	Al trough	Al trough	Al bulge	Al bulge	rim	core	core	Al trough	Al bulge	rim	core	core	sympl.	core	core
anal. Nr.	ob28f04	ob28f06	ob29d16	ob29d17	dd08b09	ob28f03	ob28f05	ob29d06	ob29d07	ob28c10	ob28c09	ob28c08	ob29a04	ob29a11	dd08a14	ob29b09	ob29b12
P	20.7	22.3	20.1	17.2	26.2	25.1	27.9	21.1	21.2	13.7	14.9	23.7	20.4	16.0	39.3	24.5	19.8
K	<0.42	0.72	<0.76	<0.54	0.50	<0.67	<0.93	0.86	2.44	0.50	<0.61	<1.41	<0.61	2.33	4.94	<0.61	<0.46
Sc	4.48	5.17	8.76	7.37	9.10	5.36	3.55	6.47	8.88	9.29	9.96	7.01	10.9	11.5	12.6	19.1	18.9
Ti	857	863	780	766	804	654	343	366	520	879	716	404	443	471	308	730	763
V	70.7	72.8	66.1	64.5	64.2	87.2	54.2	56.1	72.8	69.4	75.5	46.5	74.3	84.6	61.4	101	105
Ni	624	622	600	608	647	574	623	618	547	562	534	582	594	602	614	743	773
Zn	16.1	16.0	18.7	19.7	15.1	13.8	14.4	14.6	13.1	19.0	16.3	19.6	22.8	32.5	33.3	40.2	44.0
Ga	4.15	4.19	2.49	2.46	N.A.	3.96	2.78	1.36	2.31	2.18	1.83	1.21	2.10	2.74	n.a.	4.26	4.65
Rb	<0.006	<0.008	<0.008	0.019	0.012	0.007	<0.018	<0.012	<0.012	<0.013	<0.009	<0.030	<0.011	<0.009	<0.030	0.011	<0.009
Sr	0.060	0.268	0.058	0.015	0.076	0.019	0.044	0.024	0.053	0.057	0.014	0.053	0.094	0.33	0.20	0.63	0.66
Y	0.22	0.38	0.53	0.34	0.55	0.19	0.14	0.32	0.58	0.58	0.45	0.30	0.54	0.54	0.94	1.17	1.25
Zr	0.43	0.68	0.57	0.39	0.50	0.35	0.17	0.33	0.76	0.44	0.49	0.21	0.90	1.32	1.00	2.31	2.41
Nb	0.004	0.005	0.010	0.007	<0.007	0.007	<0.007	<0.007	0.008	<0.004	0.007	0.008	0.021	0.011	<0.022	0.074	0.065
Cs	0.001	<0.002	<0.004	<0.002	<0.005	<0.004	<0.005	<0.002	0.002	<0.003	0.001	<0.007	<0.001	<0.003	<0.017	0.005	<0.002
Ba	<0.008	0.021	<0.024	0.012	<0.024	<0.019	<0.048	<0.018	<0.020	0.018	<0.023	<0.051	<0.012	0.044	<0.11	0.020	0.026
La	0.002	0.007	<0.003	<0.002	<0.002	<0.002	<0.005	<0.004	<0.002	<0.003	<0.002	<0.006	<0.003	0.013	<0.015	0.022	0.021
Ce	<0.002	0.022	<0.003	<0.002	<0.004	<0.004	<0.003	<0.006	<0.005	0.004	<0.003	<0.005	0.014	0.017	0.016	0.075	0.100
Pr	<0.002	0.002	0.002	<0.002	<0.003	<0.001	<0.003	0.001	<0.002	0.002	0.002	<0.004	0.002	0.006	<0.012	0.014	0.015
Nd	0.010	<0.010	<0.008	<0.006	<0.016	<0.008	<0.024	<0.011	<0.009	0.011	<0.009	<0.035	0.009	0.021	<0.043	0.064	0.048
Sm	0.008	<0.006	<0.013	<0.010	<0.010	<0.009	<0.019	<0.012	<0.010	<0.013	<0.010	<0.026	0.021	<0.015	<0.075	0.038	<0.014
Eu	0.002	0.005	0.006	<0.003	<0.006	<0.004	<0.004	<0.003	0.007	0.002	<0.003	<0.005	0.006	<0.003	<0.023	0.021	0.020
Gd	0.011	0.020	<0.013	<0.007	<0.014	<0.013	<0.019	0.020	0.030	0.037	0.008	<0.017	0.021	0.022	<0.030	0.068	0.038
Tb	0.004	0.007	0.004	0.002	n.a.	0.002	<0.002	<0.002	0.004	0.007	0.001	0.003	0.008	0.005	n.a.	0.018	0.010
Dy	0.036	0.048	0.11	0.037	0.058	<0.014	<0.012	0.058	0.050	0.052	0.035	<0.024	0.056	0.052	0.13	0.16	0.17
Ho	0.008	0.011	0.023	0.011	0.021	0.007	0.011	0.016	0.020	0.029	0.017	<0.004	0.025	0.014	0.017	0.045	0.047
Er	0.028	0.056	0.073	0.036	0.094	0.043	<0.031	0.035	0.089	0.057	0.092	0.027	0.088	0.077	0.156	0.19	0.15
Tm	0.008	0.008	0.014	0.012	0.020	0.007	0.006	0.013	0.018	0.019	0.014	0.007	0.018	0.017	0.014	0.031	0.036
Yb	0.064	0.090	0.11	0.12	0.17	0.073	0.054	0.11	0.17	0.23	0.21	0.16	0.15	0.22	0.32	0.26	0.29
Lu	0.008	0.014	0.033	0.023	0.034	0.015	0.012	0.032	0.050	0.037	0.031	0.024	0.035	0.031	0.032	0.049	0.044
Hf	0.017	0.015	<0.008	0.011	0.020	0.019	<0.012	0.019	0.030	0.011	0.019	<0.011	0.045	0.023	<0.043	0.073	0.089
Ta	<0.001	<0.002	<0.002	<0.002	<0.007	<0.002	<0.003	<0.003	<0.002	<0.001	<0.002	<0.003	<0.002	0.004	<0.019	0.005	0.004
Pb	0.039	0.043	0.053	0.038	0.043	0.052	<0.055	0.043	0.044	<0.036	<0.030	<0.080	0.041	0.067	<0.047	<0.027	0.033
Th	<0.001	<0.001	<0.003	<0.002	<0.004	<0.002	<0.003	0.002	<0.002	0.002	<0.001	<0.004	<0.003	<0.003	<0.012	<0.002	0.003
U	<0.001	0.001	<0.002	<0.002	<0.003	<0.002	<0.004	<0.002	<0.002	<0.002	<0.002	<0.006	0.007	0.003	<0.008	<0.002	<0.002

n.a.: mot analysed

Table A4-3: Trace element composition of ***orthopyroxene*** (in µg/g) in peridotite and pyroxenite xenoliths from Marsabit (continued)

	Group III-a												Group III-b			G. III-c
sample	**1959/24**	**1959/24**	**1959/24**	**1959/25**	**1959/25**	**1959/25**	**1965/1**	**1965/1**	**1965/1**	**1965/1**	**1965/1**	**1965/1**	**1959/15**	**1959/15**	**1965/15**	**1965/3**
location	opx-I	opx-I	opx-I	opx-I	opx-I	opx-IIb	opx-I	opx-I	opx-I	opx-IIa	metas.	metas.	metas.	metas.	metas.	Opx_m
	core	core	core	core	core	sympl.	core	core	core	core	opx-I/core	opx-I/rim	opx-I/core	opx-I/rim	opx-I/core	
anal. Nr.	ob28b03	ob28b07	ob28b12	dd09a13	ob28a05	dd09a12	mc22a09	mc22a10	mc22a12	mc22a03	ob28d09	ob28d08	dd09b11	dd09b10	ob29c12	dd08c03
P	26.7	24.5	24.9	21.8	16.6	34.9	11.1	10.8	16.7	12.0	15.6	23.2	17.5	21.8	14.5	17.5
K	0.23	0.56	1.77	<0.37	<0.58	<1.20	<0.48	<0.46	<0.46	<0.51	1.72	<1.36	<0.35	4.32	<0.44	98.1
Sc	16.1	15.4	15.5	16.9	14.3	17.0	23.9	21.4	50.9	29.0	8.05	6.19	17.3	13.1	5.46	2.44
Ti	796	796	812	532	555	489	263	267	177	227	239	175	366	140	619	44.9
V	96.4	97.7	100	91.2	87.4	95.3	70.2	69.3	48.8	54.3	76.8	60.3	77.2	54.7	90.6	14.9
Ni	754	760	804	710	723	736	592	647	600	600	568	646	585	640	646	588
Zn	47.2	46.5	45.6	35.4	37.6	33.2	25.2	29.2	30.0	28.6	25.6	30.9	24.5	55.9	30.1	60.6
Ga	4.77	4.36	4.42	n.a.	3.42	n.a.	1.45	1.53	0.71	0.91	1.81	1.38	n.a.	n.a.	3.50	n.a.
Rb	0.005	0.002	0.006	<0.013	0.024	<0.028	<0.006	<0.006	<0.007	<0.006	<0.009	<0.024	<0.011	0.010	<0.010	0.45
Sr	0.49	0.44	0.38	0.094	0.10	0.10	0.041	0.028	0.021	0.018	0.24	0.55	0.44	0.42	0.14	1.02
Y	1.32	1.22	1.26	1.07	0.89	1.03	0.84	0.96	1.64	0.98	0.081	0.069	0.49	0.32	0.073	0.69
Zr	2.35	2.24	2.28	1.18	1.04	1.27	0.42	0.45	0.96	0.48	0.23	0.059	0.51	0.15	0.28	0.038
Nb	0.045	0.044	0.038	<0.018	0.006	<0.015	0.012	0.014	0.010	0.007	<0.005	<0.015	<0.007	0.009	0.020	0.18
Cs	0.003	<0.002	0.002	<0.004	<0.004	<0.013	0.005	<0.002	<0.001	<0.002	<0.002	<0.005	<0.004	<0.003	<0.001	0.008
Ba	<0.023	<0.014	<0.011	<0.021	<0.011	<0.065	<0.017	<0.015	<0.016	<0.015	0.056	0.22	<0.021	0.023	<0.018	7.48
La	0.004	0.005	0.004	<0.003	0.004	<0.013	<0.002	<0.002	0.002	<0.002	0.019	0.028	0.055	0.025	<0.002	0.061
Ce	0.029	0.034	0.025	0.008	0.007	0.013	0.004	<0.003	0.008	0.010	0.020	0.075	0.046	0.066	0.005	0.11
Pr	0.009	0.011	0.006	<0.004	0.004	<0.009	0.002	<0.001	0.005	0.002	0.002	0.004	0.005	0.005	<0.001	0.007
Nd	0.047	0.030	0.045	<0.016	<0.014	<0.068	<0.006	0.013	0.008	<0.009	<0.008	0.038	0.043	0.033	0.010	0.039
Sm	0.067	0.054	0.008	0.044	0.021	<0.051	<0.007	<0.008	<0.011	<0.008	0.014	<0.018	0.016	<0.015	<0.009	<0.018
Eu	0.032	0.023	0.020	<0.008	0.004	<0.022	0.006	0.006	0.009	0.003	<0.003	<0.009	<0.005	<0.005	<0.002	0.012
Gd	0.093	0.11	0.040	0.042	0.031	0.061	0.009	0.030	0.023	0.018	<0.014	<0.042	0.028	<0.018	<0.006	0.021
Tb	0.020	0.015	0.017	n.a.	0.013	n.a.	0.008	0.006	0.009	0.006	0.002	<0.004	n.a.	n.a.	<0.001	n.a.
Dy	0.17	0.18	0.15	0.07	0.13	0.09	0.056	0.11	0.16	0.086	0.015	0.016	0.086	0.026	0.011	0.058
Ho	0.052	0.041	0.042	0.037	0.032	0.024	0.028	0.036	0.062	0.045	0.007	0.003	0.012	0.015	0.003	0.031
Er	0.20	0.16	0.17	0.16	0.11	0.11	0.14	0.14	0.30	0.19	<0.012	<0.011	0.043	0.052	0.008	0.094
Tm	0.035	0.026	0.027	0.024	0.019	0.019	0.035	0.031	0.066	0.040	0.002	<0.004	0.015	0.008	0.001	0.014
Yb	0.31	0.21	0.27	0.20	0.23	0.32	0.33	0.31	0.69	0.47	0.027	0.036	0.19	0.084	0.011	0.17
Lu	0.050	0.046	0.047	0.040	0.037	0.034	0.066	0.067	0.15	0.093	0.001	0.006	0.026	0.018	0.002	0.026
Hf	0.072	0.075	0.050	0.041	0.028	0.067	0.013	0.012	0.011	0.008	0.006	<0.018	0.014	<0.012	0.010	<0.009
Ta	0.004	0.003	0.001	<0.005	<0.002	<0.013	0.002	<0.001	<0.001	<0.001	<0.001	<0.003	<0.004	<0.004	<0.001	<0.005
Pb	0.081	0.035	0.059	0.047	0.048	<0.049	0.022	0.024	0.021	0.026	<0.028	<0.089	0.047	0.043	0.041	0.074
Th	<0.002	0.002	0.003	<0.003	<0.002	<0.005	<0.003	<0.002	0.002	0.002	0.009	0.072	0.069	0.092	<0.002	0.020
U	<0.002	0.004	0.003	<0.004	<0.001	0.008	<0.001	0.002	0.002	0.005	0.004	0.016	0.026	0.021	<0.001	0.017

Table A4-3: Trace element composition of ***orthopyroxene*** (in µg/g) in peridotite and pyroxenite xenoliths from Marsabit (continued)

	Group III-d		Group IV							Group V				Group VI		
sample	**1970/6**	**1970/6**	**1961/1**	**1961/1**	**1961/1**	**1961/1**	**1968/1**	**1968/1**	**1968/1**	**794/1**	**794/1**	**1960/4**	**1960/4**	**782/2**	**782/2**	**782/2**
location	Opx_m	Opx_m	opx-I	opx-I	opx-I	opx-I	opx-I	opx-I	opx-I	opx-I	opx-I	opx-II	opx-I	opx-I	opx-I	opx-I
	core	rim	core	core	core	core	core	core	core	rim	core	core	core	core	core	core
anal. Nr.	ob28g04	ob28g03	mc22c09	mc22c10	mc22c11	mc22c12	mc22b06	mc22b13	mc22b14	mc22d15	mc22d16	mc22e12	mc22e13	mc22f08	mc22f09	mc22f13
P	24.8	35.5	9.19	10.1	12.8	10.5	13.7	9.39	9.20	17.9	20.7	12.6	12.0	24.5	22.3	23.5
K	1.50	<1.10	<0.50	0.85	<0.50	<0.50	0.48	<0.48	<0.44	<0.54	<0.56	<1.19	<0.45	<1.38	<1.93	<0.82
Sc	12.4	11.2	17.9	17.9	18.5	18.2	9.70	7.08	7.46	7.02	6.54	6.30	5.60	20.1	19.6	20.1
Ti	227	110	58.1	56.0	56.4	55.1	522	352	354	817	1033	486	573	1284	1285	1308
V	63.4	51.2	75.4	79.4	75.5	74.9	81.2	68.5	67.5	150	125	82.9	103	145	143	153
Ni	748	743	657	638	591	637	663	566	569	689	666	628	691	466	444	423
Zn	37.3	36.9	23.9	25.6	23.7	22.1	29.8	21.1	20.9	112	108	23.4	30.8	61.8	67.5	50.9
Ga	1.33	1.09	0.87	1.05	0.96	0.85	3.01	1.96	2.10	14.7	12.4	4.525	5.981	7.28	6.69	7.08
Rb	<0.014	<0.013	<0.008	<0.008	<0.005	<0.005	0.004	<0.005	<0.006	<0.011	<0.007	<0.018	<0.006	<0.017	<0.030	<0.013
Sr	1.67	1.90	0.15	0.23	0.095	0.090	0.10	0.035	0.028	0.093	0.16	0.024	0.009	0.15	0.16	0.82
Y	2.02	2.44	0.18	0.19	0.18	0.18	0.18	0.12	0.11	0.13	0.14	0.18	0.19	0.69	0.70	0.67
Zr	0.88	1.33	1.08	1.14	1.15	1.24	0.50	0.17	0.13	1.35	1.08	0.15	0.47	1.68	1.72	1.77
Nb	0.051	0.040	0.017	0.018	0.009	0.006	0.007	0.007	0.010	<0.003	<0.003	0.012	0.009	0.022	<0.012	0.037
Cs	<0.004	<0.007	0.003	0.002	<0.003	<0.002	<0.002	<0.002	<0.002	<0.002	<0.002	<0.005	<0.002	<0.004	0.010	0.006
Ba	0.035	<0.022	<0.016	<0.012	0.039	<0.011	<0.011	<0.015	0.012	<0.014	<0.018	<0.029	<0.012	<0.035	<0.11	<0.035
La	0.045	0.042	0.003	0.003	<0.003	<0.003	<0.002	<0.002	0.005	<0.002	0.003	<0.006	0.002	0.009	0.008	0.028
Ce	0.27	0.25	0.005	0.013	0.005	0.017	0.004	0.002	0.004	0.006	0.015	<0.009	0.004	0.048	0.039	0.212
Pr	0.064	0.060	<0.002	0.003	0.003	<0.002	0.001	0.002	0.003	<0.001	0.003	<0.003	<0.002	0.010	0.021	0.024
Nd	0.42	0.59	0.051	<0.014	0.015	0.025	<0.007	<0.007	0.015	0.012	<0.011	<0.018	<0.010	0.037	0.032	0.088
Sm	0.19	0.23	0.023	0.011	<0.009	0.025	<0.012	<0.015	<0.007	<0.022	<0.015	<0.035	0.010	<0.035	<0.048	0.066
Eu	0.077	0.14	0.008	0.007	0.009	0.006	0.005	0.003	0.004	0.007	0.004	<0.006	<0.003	0.019	0.011	0.025
Gd	0.20	0.40	<0.008	0.018	0.022	<0.011	<0.008	0.015	<0.007	0.023	0.021	<0.020	<0.011	0.041	0.036	0.058
Tb	0.045	0.059	0.003	0.006	0.004	<0.002	0.007	0.003	0.002	0.004	0.008	<0.003	<0.002	<0.004	0.009	0.017
Dy	0.38	0.43	0.028	0.035	0.034	0.027	0.017	0.013	0.015	0.014	0.029	0.026	0.048	0.087	0.15	0.11
Ho	0.069	0.098	0.004	0.005	0.004	0.010	0.006	0.006	0.007	0.006	0.006	0.015	0.004	0.017	<0.009	0.024
Er	0.22	0.22	0.037	0.030	0.010	0.016	0.027	<0.005	<0.008	<0.012	0.016	0.016	0.018	0.100	0.057	0.10
Tm	0.031	0.032	0.005	0.008	0.009	0.006	0.005	0.003	0.002	0.003	0.003	0.010	0.006	0.019	0.011	0.017
Yb	0.28	0.33	0.049	0.082	0.064	0.080	0.038	0.025	0.026	0.028	0.048	0.10	0.035	0.12	0.16	0.13
Lu	0.033	0.025	0.021	0.014	0.013	0.012	0.007	0.009	0.007	0.007	0.003	0.013	0.007	0.024	0.022	0.022
Hf	0.013	0.016	0.024	0.021	0.022	0.027	0.010	0.007	<0.004	0.051	0.026	<0.017	<0.005	0.087	0.059	0.090
Ta	<0.002	0.008	<0.001	<0.002	<0.002	<0.001	<0.003	<0.001	<0.001	<0.002	<0.002	<0.004	<0.002	<0.007	<0.009	0.003
Pb	<0.041	<0.063	0.028	0.033	0.022	0.014	0.033	0.014	0.024	0.023	0.10	0.035	0.022	<0.034	<0.040	0.050
Th	<0.002	<0.003	<0.002	<0.002	<0.002	0.004	<0.002	0.003	<0.001	<0.002	<0.004	<0.009	<0.002	<0.005	0.011	0.003
U	0.004	<0.003	<0.002	<0.002	<0.002	<0.003	<0.002	<0.002	0.002	0.003	0.003	<0.004	0.005	0.006	0.037	0.003

n.a.: mot analysed

Table A4-4: Trace element composition of ***clinopyroxene*** (in µg/g) in peridotite and pyroxenite xenoliths from Marsabit

	Group I																			
sample	**1963/1**	**1963/1**	**1963/1**	**1963/1**	**1963/1**	**1963/1**	**1963/2**	**1963/2**	**1963/2**	**1963/2**	**1963/2**	**1963/2**	**1963/2**	**1963/2**	**1963/2**	**1963/2**	**1963/2**	**1965/4**	**1965/4**	**1965/4**
location	cpx-I	cpx-I	cpx-IIb	Aug_m	Aug_m	Aug_m	cpx-I	cpx-I	cpx-I	cpx-I	cpx-I	cpx-I	cpx-I	cpx-I	cpx-I	cpx-IIb	cpx-IIb	cpx-I	cpx-I	cpx-I
	low-Al	rim	core				low-Al	low-Al	low-Al	low-Al	Al bulge	rim	rim	rim	rim	core	core	low-Al	low-Al	low-Al
anal. Nr.	ob29e06	ob29e05	ob29e13	ob29e10	ob29e11	ob29e12	dd08b06	dd08b07	ob29d05	ob29d13	ob29d03	dd08b04	ob29d09	ob29d10	dd08b08	dd08b05	ob29d08	ob28c06	ob28c11	ob28c18
Li	n.a.	n.a.	n.a.	n.a.	n.a.	n.a.	n.a.	n.a.	n.a.	n.a.	n.a.	n.a.	n.a.	n.a.	n.a.	n.a.	n.a.	n.a.	n.a.	n.a.
P	28.5	41.4	34.4	37.1	39.1	28.9	30.5	30.5	31.2	29.0	54.6	65.5	71.0	46.7	43.6	56.7	35.3	29.7	33.3	29.4
K	1.74	1.72	9.72	28.9	18.0	<29.1	0.86	0.79	2.03	<0.60	<3.37	<2.02	18.61	3.20	<1.89	1.43	1.39	<0.63	1.99	1.41
Sc	27.4	88.6	70.5	158	169	161	26.4	25.6	27.7	23.9	70.8	81.8	81.8	50.9	73.5	84.7	40.1	30.4	27.5	26.1
Ti	3117	2480	2244	11497	11871	13196	3180	3383	3194	3424	2680	3388	3377	3372	2785	3312	3303	4844	3648	3674
V	385	282	311	809	784	804	326	310	357	335	280	264	286	314	308	230	326	392	330	330
Ni	276	213	245	470	380	426	270	268	285	276	233	273	298	231	246	220	228	236	276	281
Zn	5.72	4.36	4.88	9.37	6.68	5.19	3.86	3.89	4.44	4.87	3.50	2.95	3.03	3.05	2.45	2.47	2.72	4.21	6.66	4.67
Ga	9.26	2.62	3.48	3.72	3.55	3.11	n.a.	n.a.	8.53	8.93	3.54	n.a.	2.74	5.34	n.a.	n.a.	6.45	10.5	8.98	9.84
Rb	<0.007	0.01	<0.023	<0.13	<0.090	<0.23	0.008	0.009	<0.008	<0.009	0.058	<0.058	<0.092	<0.011	<0.043	<0.022	<0.008	<0.011	<0.010	<0.008
Sr	71.7	63.2	65.9	20.2	22.6	24.1	68.6	65.4	64.4	67.8	54.8	57.1	57.8	57.7	52.8	54.6	52.8	61.5	74.1	75.9
Y	4.27	20.9	13.7	23.4	23.7	27.2	3.12	3.74	4.15	3.93	19.6	33.5	25.4	18.8	26.7	35.2	15.2	8.03	3.37	2.38
Zr	20.6	43.1	29.2	16.2	16.6	20.6	25.4	26.1	24.1	21.9	38.2	45.7	46.3	36.1	36.3	41.1	29.2	41.5	23.2	23.0
Nb	0.064	0.062	0.021	<0.12	0.20	0.28	0.065	0.090	0.049	0.11	<0.017	0.029	0.11	0.066	<0.029	0.098	0.048	0.064	0.23	0.12
Cs	0.004	<0.003	<0.008	0.076	<0.035	<0.071	<0.004	<0.006	<0.002	<0.002	0.008	<0.018	<0.030	<0.003	<0.025	<0.007	<0.003	<0.002	<0.004	0.001
Ba	<0.014	<0.013	0.043	0.65	0.30	<0.59	<0.021	<0.025	<0.025	<0.011	0.071	<0.170	0.23	<0.015	<0.12	<0.053	0.024	<0.011	<0.021	<0.010
La	0.86	0.76	0.86	0.26	0.23	0.23	0.99	0.94	0.89	0.84	0.76	1.12	0.81	0.94	0.77	0.87	0.81	0.72	1.05	1.03
Ce	3.38	3.13	3.23	1.44	1.76	1.98	3.62	3.72	3.70	3.60	3.41	3.61	3.43	3.63	2.77	3.21	3.16	2.60	3.60	3.49
Pr	0.64	0.63	0.59	0.42	0.49	0.61	0.75	0.66	0.67	0.67	0.67	0.58	0.58	0.67	0.52	0.59	0.59	0.57	0.69	0.62
Nd	4.08	3.76	3.99	3.72	5.04	4.04	4.66	4.52	4.20	4.20	3.66	3.71	3.72	4.18	3.24	3.65	3.99	3.97	4.17	4.19
Sm	1.43	1.49	1.53	2.98	1.99	1.91	1.42	1.56	1.64	1.63	1.55	1.64	1.79	1.74	1.71	1.75	1.74	2.16	1.62	1.42
Eu	0.61	0.72	0.67	0.98	0.85	0.66	0.58	0.61	0.65	0.55	0.68	0.99	0.81	0.82	0.60	0.84	0.75	0.84	0.59	0.53
Gd	1.24	2.52	1.89	2.75	4.15	2.73	1.42	1.67	1.55	1.42	2.71	3.42	2.90	2.42	2.58	3.19	2.14	2.03	1.44	1.43
Tb	0.19	0.53	0.42	0.59	0.73	0.69	n.a.	n.a.	0.21	0.19	0.50	n.a.	0.63	0.48	n.a.	n.a.	0.40	0.28	0.21	0.18
Dy	0.95	3.73	2.57	3.85	3.81	5.61	0.93	1.10	0.96	1.04	3.08	5.61	4.34	3.20	4.86	6.49	2.57	1.63	0.98	0.71
Ho	0.18	0.87	0.50	0.93	1.09	0.70	0.13	0.15	0.16	0.14	0.76	1.42	1.01	0.74	1.12	1.45	0.58	0.30	0.15	0.11
Er	0.39	2.34	1.30	2.87	2.17	2.26	0.27	0.28	0.36	0.29	2.26	3.29	2.79	2.01	3.23	4.03	1.76	0.77	0.24	0.15
Tm	0.063	0.33	0.21	0.45	0.45	0.38	0.037	0.026	0.049	0.042	0.28	0.54	0.44	0.34	0.48	0.61	0.24	0.10	0.025	0.012
Yb	0.44	2.26	1.74	3.28	1.97	3.32	0.19	0.17	0.30	0.21	1.98	4.15	2.49	2.17	3.37	3.59	1.78	0.88	0.25	0.066
Lu	0.071	0.31	0.21	0.37	0.27	0.35	0.017	0.028	0.043	0.040	0.31	0.48	0.38	0.27	0.47	0.47	0.26	0.12	0.009	0.006
Hf	0.83	0.88	0.74	0.61	1.00	0.88	1.10	0.93	0.96	0.79	1.45	1.33	1.41	1.15	1.05	1.13	0.99	1.89	1.00	0.80
Ta	0.007	0.006	<0.006	<0.028	0.034	0.044	0.017	0.025	0.012	0.018	0.009	<0.022	<0.025	0.006	<0.016	<0.008	0.012	0.013	0.019	0.012
Pb	0.20	0.23	0.31	<0.57	<0.29	<0.57	0.18	0.20	0.16	0.16	0.25	0.23	<0.266	0.17	0.12	0.090	0.15	0.17	0.16	0.16
Th	0.011	0.002	0.013	<0.032	<0.026	<0.039	0.022	0.036	0.035	0.012	0.011	0.025	<0.029	0.009	<0.014	0.020	0.009	0.024	0.017	0.010
U	0.004	0.005	<0.012	<0.054	0.020	<0.039	0.004	0.009	0.005	0.009	<0.009	<0.016	<0.029	0.006	0.009	0.010	0.006	0.007	0.006	0.007

Table A4-4: Trace element composition of ***clinopyroxene*** (in µg/g) in peridotite and pyroxenite xenoliths from Marsabit (continued)

	Group I					Group II													
sample	**1965/4**	**1965/4**	**1965/4**	**1965/4**	**1965/4**	**1958/13**	**1958/13**	**1958/13**	**1958/13**	**1958/13**	**1958/13**	**1958/13**	**1958/13**	**1958/20**	**1958/20**	**1958/20**	**1958/20**	**1958/20**	**1959/24**	**1959/24**
location	cpx-I	cpx-I	cpx-I	cpx-IIb	cpx-IIb	cpx-I	cpx-I	cpx-I	cpx-I	cpx-I	cpx-I	cpx-IIa	cpx-IIa	cpx-I	cpx-I	cpx-I	cpx-I	cpx-I	cpx-I	cpx-I
	Al bulge	rim	rim	core	core	core	core	core	rim	rim	rim	sympl.	sympl.	core	core	core	rim	rim	core	core
anal. Nr.	ob28c17	ob28c16	ob28c07	ob28c04	ob28c15	ob29a05	ob29a06	ob29a10	dd08a04	dd08a03	ob29a03	dd08a05	ob29a09	ob29b03	ob29b06	ob29b07	ob29b05	ob29b08	ob28b05	ob28b06
Li	n.a.	n.a.	n.a.	n.a.	n.a.	n.a.	n.a.	n.a.	n.a.	n.a.	n.a.	n.a.	n.a.	n.a.	n.a.	n.a.	n.a.	n.a.	n.a.	n.a.
P	30.7	48.8	85.4	30.9	32.0	53.8	40.7	53.1	61.1	52.4	50.7	48.0	53.1	52.0	43.5	47.4	47.1	44.4	55.6	51.8
K	1.16	<1.65	<5.90	<0.72	0.91	3.51	3.44	4.77	5.00	3.89	4.49	6.77	15.3	20.8	20.5	21.7	21.6	21.4	18.9	21.7
Sc	28.5	60.7	173	29.7	49.4	69.4	33.4	66.9	70.4	74.7	72.5	67.8	67.9	51.1	56.4	55.3	55.5	54.4	46.8	46.4
Ti	3377	3098	4726	3275	3852	2230	1719	2277	2296	1964	1889	2201	2088	2492	2653	2617	2614	2575	2766	2807
V	367	309	297	350	358	269	301	259	251	263	257	252	260	222	235	228	225	229	226	224
Ni	277	227	277	249	241	312	258	298	232	303	287	294	313	349	363	348	382	356	370	391
Zn	4.25	3.39	3.78	3.82	3.55	8.86	5.09	6.18	4.75	7.78	7.99	4.24	7.18	12.1	11.8	12.1	12.8	12.6	14.2	14.2
Ga	8.73	2.80	3.14	7.18	4.31	2.77	4.15	3.16	n.a.	n.a.	2.92	n.a.	3.16	4.83	3.90	4.53	4.47	4.46	5.07	5.17
Rb	<0.009	<0.019	<0.080	<0.014	<0.011	<0.035	<0.006	<0.009	0.01	<0.039	<0.024	0.02	0.02	<0.017	<0.008	0.011	<0.011	<0.008	0.033	0.017
Sr	74.0	59.0	50.2	60.3	69.5	110	118	117	120	109	118	113	120	110	114	113	114	114	81.0	84.3
Y	4.45	16.4	69.6	14.7	10.3	15.9	12.5	16.0	19.4	17.4	16.0	18.8	15.4	13.4	14.4	14.8	15.0	14.9	15.3	15.5
Zr	22.3	29.4	102	22.7	25.9	39.8	28.1	40.1	45.9	45.3	42.1	44.5	38.0	23.2	26.0	27.4	26.9	27.1	29.1	28.7
Nb	0.092	0.060	0.047	0.083	0.12	0.16	0.33	0.33	0.53	0.18	0.17	0.66	0.49	1.09	1.10	1.20	1.07	1.13	0.72	0.55
Cs	<0.003	<0.003	<0.031	<0.003	<0.003	<0.006	0.001	<0.002	0.019	<0.010	<0.008	<0.007	<0.004	0.004	0.003	0.002	<0.003	<0.002	0.003	0.004
Ba	0.019	<0.028	<0.11	<0.027	<0.021	<0.050	0.026	0.017	0.052	0.13	<0.059	<0.040	0.25	0.055	0.049	0.083	<0.024	0.041	0.14	0.12
La	0.95	0.73	0.83	0.75	0.92	5.58	5.69	5.99	6.89	6.36	6.46	6.60	6.23	4.53	4.88	4.77	4.53	4.67	1.15	1.46
Ce	3.35	2.90	2.47	2.68	3.48	9.95	9.58	10.4	10.9	9.76	10.9	10.3	10.4	9.93	10.5	10.6	10.8	10.6	3.79	4.93
Pr	0.61	0.59	0.46	0.47	0.66	1.04	1.07	1.18	1.26	1.23	1.27	1.20	1.07	1.15	1.18	1.24	1.27	1.27	0.72	0.83
Nd	4.11	3.74	3.19	3.12	3.95	5.09	5.11	5.61	6.04	6.20	5.56	5.29	5.50	5.06	5.03	5.56	5.84	5.77	4.41	5.06
Sm	1.38	1.47	2.19	1.41	1.51	1.31	1.66	1.76	2.15	1.94	1.79	1.91	1.84	1.70	1.43	1.51	1.75	1.69	1.82	1.75
Eu	0.60	0.54	0.90	0.70	0.72	0.71	0.65	0.82	0.83	0.66	0.84	0.75	0.70	0.69	0.63	0.72	0.75	0.71	0.79	0.78
Gd	1.62	2.19	6.02	2.04	1.86	2.38	1.93	2.11	2.35	2.36	2.43	2.52	2.03	1.69	1.96	2.12	1.97	1.99	2.17	2.41
Tb	0.20	0.45	1.54	0.38	0.32	0.39	0.38	0.42	n.a.	n.a.	0.41	n.a.	0.41	0.37	0.39	0.38	0.41	0.40	0.42	0.44
Dy	1.01	2.69	10.8	2.49	1.96	2.46	2.27	2.92	3.42	3.38	2.84	3.37	2.79	2.55	2.78	2.80	2.68	2.65	2.87	2.76
Ho	0.14	0.61	2.89	0.50	0.36	0.61	0.48	0.67	0.71	0.65	0.64	0.80	0.65	0.51	0.59	0.58	0.57	0.57	0.61	0.61
Er	0.36	1.72	8.37	1.58	1.20	1.67	1.25	1.93	2.02	1.87	2.07	2.03	1.67	1.55	1.74	1.54	1.68	1.60	1.72	1.63
Tm	0.056	0.26	1.13	0.23	0.18	0.34	0.19	0.24	0.31	0.26	0.28	0.31	0.21	0.19	0.22	0.24	0.24	0.22	0.22	0.21
Yb	0.36	2.00	6.83	1.82	1.32	1.92	1.47	1.87	2.03	1.97	1.63	2.29	1.78	1.39	1.51	1.53	1.58	1.53	1.47	1.49
Lu	0.071	0.29	1.00	0.24	0.18	0.21	0.19	0.24	0.31	0.26	0.24	0.31	0.28	0.18	0.24	0.20	0.21	0.20	0.22	0.20
Hf	0.97	1.00	3.05	0.79	1.08	1.13	0.76	0.96	1.12	1.19	1.17	1.21	1.08	0.62	0.83	0.78	0.82	0.76	0.88	0.84
Ta	0.015	0.014	<0.033	0.009	0.014	0.045	0.047	0.064	0.12	0.068	0.045	0.077	0.081	0.063	0.075	0.10	0.085	0.10	0.057	0.055
Pb	0.21	0.23	<0.39	0.22	0.18	0.28	0.28	0.23	0.29	0.094	0.15	0.35	0.30	0.074	0.075	0.10	0.080	0.076	0.040	0.037
Th	0.010	0.005	<0.015	0.008	0.007	0.85	0.66	0.80	1.04	1.15	1.00	1.06	0.77	0.13	0.14	0.15	0.14	0.13	0.18	0.12
U	0.008	<0.004	0.016	0.006	0.003	0.16	0.17	0.19	0.21	0.14	0.19	0.20	0.19	0.036	0.023	0.037	0.032	0.034	0.047	0.021

Table A4-4: Trace element composition of ***clinopyroxene*** (in µg/g) in peridotite and pyroxenite xenoliths from Marsabit (continued)

	Group II												**Group III-a**							
sample	**1959/24**	**1959/24**	**1959/24**	**1959/24**	**1959/25**	**1959/25**	**1959/25**	**1959/25**	**1959/25**	**1959/25**	**1959/25**	**1959/25**	**1965/1**	**1965/1**	**1965/1**	**1965/1**	**1965/1**	**1965/1**	**1965/1**	**1965/1**
location	cpx-I	cpx-I	cpx-I	cpx-IIa	cpx-I	cpx-I	cpx-I	cpx-I	cpx-I	cpx-I	Aug_m	Aug_m	cpx-I	cpx-I	cpx-I	cpx-I	cpx-I	cpx-I	cpx-IIb	cpx-IIb
	core	core	core	sympl.	core	core	core	core	rim	rim	spongy	spongy	core/exsol.	core	core	core	rim	rim	core	core
anal. Nr.	ob28b08	ob28b09	ob28b10	ob28b13	dd09a09	ob28a03	ob28a04	ob28a08	dd09a10	ob28a09	dd09a11	ob28a07	mc22a16	mc22a17	ob28d13	mc22a13	mc22a14	ob28d12	ob28d14	mc22a05
Li	n.a.	n.a.	n.a.	n.a.	n.a.	n.a.	n.a.	n.a.	n.a.	n.a.	n.a.	n.a.	n.a.	n.a.	n.a.	n.a.	n.a.	n.a.	n.a.	n.a.
P	52.4	51.7	48.0	54.6	34.9	25.3	25.9	29.2	30.5	26.1	44	31	12.6	18.3	15.8	17.9	15.9	19.5	16.9	16.2
K	18.2	18.5	18.0	18.8	<0.33	<0.68	<0.64	<0.95	0.54	2.51	<2.80	<3.97	6.64	1.61	4.51	0.72	<0.48	<0.78	0.86	3.36
Sc	50.7	47.1	48.9	46.3	57.8	47.2	66.3	63.4	61.3	54.4	58.4	54.9	41.6	140	46.0	141	158	104	64.6	207
Ti	2795	2705	2747	2804	2659	2584	2881	2341	2468	2547	1885	2157	747	803	794	837	846	998	816	806
V	244	231	246	231	279	294	278	259	269	279	258	255	233	209	240	202	198	250	245	186
Ni	387	359	364	398	333	346	349	347	323	339	537	536	287	264	266	263	257	290	269	278
Zn	15.1	14.1	14.3	15.0	8.70	11.0	9.82	9.44	8.18	9.22	30.0	30.9	5.85	5.92	5.92	4.81	5.08	6.22	5.87	7.38
Ga	5.16	5.17	5.00	5.26	n.a.	4.10	4.27	3.73	n.a.	3.84	n.a.	5.92	2.32	1.12	1.95	1.34	1.21	1.54	1.68	1.06
Rb	0.001	0.015	0.012	0.011	<0.010	<0.010	0.014	<0.017	<0.006	0.015	<0.071	<0.055	0.015	0.026	0.015	0.010	0.016	<0.012	0.013	0.014
Sr	85.6	85.0	84.2	80.9	53.4	53.9	52.9	49.8	52.1	51.2	11.8	14.4	52.8	44.3	51.3	39.6	41.0	67.8	58.0	42.5
Y	15.1	14.8	14.6	14.7	15.8	13.8	15.2	15.4	15.1	14.8	11.2	13.1	3.62	42.1	8.27	41.2	39.1	13.1	10.6	38.8
Zr	28.0	26.8	27.1	27.4	23.2	19.9	23.8	23.6	22.4	21.6	4.81	5.98	8.35	22.9	9.26	22.3	22.8	12.5	10.0	21.5
Nb	0.70	0.71	0.71	0.68	0.052	0.053	0.059	0.041	0.036	0.047	<0.036	0.046	0.13	0.056	0.077	0.072	0.025	0.031	0.051	0.055
Cs	0.003	0.005	0.003	0.003	<0.004	<0.002	0.005	<0.005	<0.003	0.003	<0.020	<0.015	0.003	<0.002	<0.002	0.003	<0.001	<0.004	<0.002	0.005
Ba	0.025	0.037	0.057	0.035	<0.021	0.020	<0.011	<0.029	<0.025	<0.021	<0.20	<0.062	0.60	0.063	1.91	0.13	0.025	0.26	0.047	0.80
La	1.26	1.27	1.23	1.15	0.79	0.82	0.79	0.85	0.81	0.78	0.053	0.12	0.97	1.32	1.59	0.79	1.09	4.14	3.04	0.99
Ce	3.90	4.08	3.79	3.86	2.65	2.54	2.66	2.52	2.52	2.53	0.49	0.65	2.43	2.45	2.75	2.15	2.22	5.61	5.03	2.19
Pr	0.75	0.75	0.72	0.71	0.52	0.48	0.56	0.53	0.51	0.49	0.16	0.16	0.45	0.36	0.36	0.32	0.31	0.50	0.53	0.31
Nd	4.32	4.63	4.51	4.28	3.42	3.20	3.40	3.01	3.31	3.17	1.30	1.58	2.39	1.85	2.09	1.83	1.80	2.24	2.42	1.63
Sm	1.70	1.65	1.78	1.58	1.55	1.40	1.51	1.54	1.40	1.27	0.62	0.96	0.78	1.07	0.79	0.98	0.92	0.78	0.88	1.09
Eu	0.78	0.78	0.78	0.69	0.63	0.66	0.66	0.64	0.61	0.61	0.34	0.38	0.35	0.64	0.36	0.64	0.56	0.38	0.37	0.56
Gd	2.24	2.32	2.14	2.18	2.19	1.93	2.23	1.97	2.14	1.93	1.03	1.53	0.85	2.56	0.93	2.74	2.49	1.13	1.10	2.66
Tb	0.40	0.43	0.43	0.44	n.a.	0.40	0.45	0.40	n.a.	0.38	n.a.	0.32	0.13	0.76	0.19	0.74	0.68	0.25	0.24	0.69
Dy	2.87	2.81	2.70	2.65	2.84	2.35	2.79	2.72	2.78	2.75	2.36	2.05	0.72	6.49	1.42	6.50	5.95	2.09	1.72	5.87
Ho	0.57	0.60	0.57	0.54	0.61	0.53	0.64	0.61	0.58	0.58	0.45	0.43	0.13	1.60	0.31	1.61	1.54	0.51	0.38	1.48
Er	1.68	1.67	1.45	1.54	1.64	1.35	1.63	1.64	1.71	1.64	1.26	1.22	0.35	4.97	0.85	5.04	4.68	1.47	1.18	4.58
Tm	0.24	0.24	0.24	0.20	0.22	0.20	0.23	0.24	0.21	0.23	0.28	0.22	0.056	0.81	0.13	0.76	0.70	0.25	0.19	0.68
Yb	1.51	1.37	1.61	1.44	1.59	1.35	1.55	1.51	1.52	1.50	1.52	1.42	0.51	5.72	0.94	5.42	5.29	1.71	1.28	4.83
Lu	0.21	0.21	0.20	0.19	0.22	0.20	0.23	0.23	0.19	0.19	0.15	0.17	0.087	0.85	0.14	0.81	0.75	0.21	0.18	0.68
Hf	0.85	0.84	0.78	0.69	0.84	0.68	0.77	0.86	0.80	0.65	0.18	0.22	0.34	0.38	0.32	0.41	0.38	0.32	0.31	0.38
Ta	0.046	0.058	0.050	0.061	0.004	0.006	0.007	<0.004	0.005	0.008	<0.026	<0.019	0.011	0.010	0.009	0.015	0.006	0.009	0.007	0.006
Pb	0.039	0.060	0.073	0.055	0.12	0.11	0.10	0.089	0.092	0.076	<0.15	<0.23	0.37	0.40	0.47	0.38	0.32	0.72	0.50	0.32
Th	0.15	0.17	0.18	0.16	0.052	0.042	0.053	0.051	0.050	0.053	<0.017	<0.008	0.12	0.12	0.25	0.014	0.033	0.64	0.41	0.071
U	0.025	0.040	0.040	0.029	0.020	0.013	0.016	0.008	0.012	0.016	<0.021	<0.008	0.076	0.10	0.15	0.010	0.032	0.35	0.27	0.068

Table A4-4: Trace element composition of ***clinopyroxene*** (in µg/g) in peridotite and pyroxenite xenoliths from Marsabit (continued)

	Group III-a						Group III-b										Group III-c		
sample	**1965/1**	**1965/1**	**1965/1**	**1965/1**	**1965/1**	**1965/1**	**1959/15**	**1959/15**	**1959/15**	**1959/15**	**1959/15**	**1959/15**	**1959/15**	**1965/15**	**1965/15**	**1965/15**	**785***	**1959/27**	**1959/27**
location	cpx-IIb	cpx-IIb	metas.	metas.	metas.	metas.	metas.	metas.	Di_m	Di_m	Di_m	Di_m	Di_m	metas.	metas.	metas.	Di_m	Di_m	Di_m
	core	core	cpx-I	cpx-I	cpx-I	cpx-I	cpx-I	cpx-I	m.p.	m.p.	m.p.	m.p.	m.p.	c/cpx-I	cpx-I*	r/cpx-I	m.p.	m.p.	m.p.
anal. Nr.	mc22a06	mc22a07	ob28d06	ob28d07	ob28d10	ob28d11	dd09b07	dd09b08	dd09b17	dd09c07	dd09c08	dd09c09	dd09c10	ob29c15	ob29c05	ob29c14	ob28e04	dd08f06	dd08f11
Li	n.a.	n.a.	n.a.	n.a.	n.a.	n.a.	n.a.	n.a.	n.a.	n.a.	n.a.	n.a.	n.a.	n.a.	n.a.	n.a.	n.a.	n.a.	n.a.
P	12.8	12.8	19.6	17.7	16.8	18.5	56.7	65.5	61.1	<122	61.1	<61.1	109	21.6	53.6	23.9	47	48.0	48.0
K	3.59	7.24	19.0	10.9	9.85	14.9	38.4	18.6	<8.39	347	50.3	25.2	151	198	369	86	112	33.5	7.62
Sc	198	124	53.5	47.6	46.4	53.3	86.2	69.2	119	158	113	135	152	24.3	27.9	36.9	108.00	68.6	77.0
Ti	767	851	967	882	828	1060	1310	1053	875	1213	1297	1196	992	2027	1557	1896	1663	1218	1195
V	184	212	262	249	249	274	268	278	261	381	355	347	289	275	319	318	525	272	255
Ni	310	263	278	261	277	295	294	294	348	597	470	422	467	302	359	327	411	324	331
Zn	7.80	5.49	6.34	5.85	6.79	6.44	12.1	13.7	4.40	<11.8	<4.74	8.11	6.35	9.14	9.42	9.64	10.8	19.6	13.6
Ga	0.85	1.47	2.27	2.26	2.39	2.29	n.a.	n.a.	n.a.	n.a.	n.a.	n.a.	n.a.	4.73	4.73	3.81	4.4	n.a.	n.a.
Rb	0.018	0.013	0.029	0.015	0.016	0.015	<0.072	<0.076	<0.21	<1.17	<0.66	<0.53	<0.37	0.16	0.24	0.071	0.1	0.11	<0.031
Sr	51.7	56.9	145	84.1	118	138	97.7	106	47.4	53.8	46.5	46.5	52.4	98.6	174	81.3	47	191	186
Y	28.9	26.7	2.56	2.37	2.32	2.71	10.9	11.0	18.1	19.8	16.2	16.8	20.3	1.65	2.78	2.51	19.92	33.4	36.4
Zr	20.8	16.8	8.49	8.55	7.90	8.97	14.3	13.0	4.79	6.70	6.73	8.50	6.00	10.4	10.5	11.6	2.3	56.3	49.1
Nb	0.025	0.11	0.057	0.073	0.045	0.061	0.27	0.14	0.28	<0.59	<0.38	<0.38	<0.099	0.14	0.15	0.052	0.07	0.73	0.81
Cs	0.003	0.009	<0.003	<0.002	<0.002	0.002	<0.019	<0.032	<0.069	<0.52	<0.22	<0.24	<0.18	0.005	0.003	0.003	<0.020	<0.022	<0.018
Ba	0.079	2.29	7.39	3.98	4.23	7.19	0.85	0.28	<0.63	5.41	<1.54	<1.09	2.25	4.44	3.97	2.09	0.4	0.84	<0.083
La	3.06	4.05	11.6	3.98	6.81	9.58	12.9	13.9	12.2	16.9	15.1	16.0	12.8	2.59	6.15	2.16	2.8	7.65	7.76
Ce	4.56	7.45	13.4	4.67	7.05	10.2	20.7	21.6	37.7	47.1	45.5	42.0	36.0	5.48	16.5	4.84	13.7	32.0	32.1
Pr	0.40	0.72	0.94	0.50	0.56	0.71	1.72	1.66	4.78	5.13	5.68	5.03	4.05	0.73	1.87	0.68	2.64	5.77	6.07
Nd	1.68	2.90	3.27	2.28	2.38	2.63	5.30	5.38	19.6	17.9	21.4	20.3	17.7	3.57	7.24	3.49	13.28	30.3	35.8
Sm	0.76	1.02	0.65	0.73	0.71	0.63	0.91	1.10	2.41	3.20	3.52	5.08	3.63	1.17	1.38	1.14	3.85	10.1	10.8
Eu	0.42	0.54	0.29	0.28	0.28	0.27	0.35	0.37	1.22	1.94	1.56	1.17	0.99	0.43	0.57	0.41	1.36	3.27	3.51
Gd	1.88	1.96	0.69	0.69	0.79	0.82	1.54	1.10	3.11	4.84	3.44	1.93	2.60	0.87	1.06	0.84	3.87	9.18	10.3
Tb	0.51	0.53	0.10	0.12	0.11	0.11	n.a.	n.a.	n.a.	n.a.	n.a.	n.a.	n.a.	0.10	0.12	0.11	0.68	n.a.	n.a.
Dy	4.39	4.20	0.62	0.56	0.55	0.57	2.22	1.64	2.35	2.51	3.01	2.42	2.75	0.49	0.66	0.64	4.96	8.56	8.32
Ho	1.17	1.04	0.10	0.10	0.094	0.10	0.48	0.37	0.79	1.16	0.64	0.31	0.46	0.068	0.10	0.094	0.81	1.40	1.45
Er	3.72	3.11	0.23	0.19	0.17	0.23	1.30	1.17	1.24	3.28	1.69	1.62	1.20	0.15	0.25	0.19	2.09	3.42	3.77
Tm	0.54	0.46	0.029	0.023	0.027	0.025	0.19	0.16	0.24	0.67	<0.17	0.54	0.31	0.017	0.042	0.033	0.220	0.49	0.40
Yb	3.71	3.27	0.21	0.15	0.16	0.15	1.46	0.95	1.92	<2.170	2.29	1.24	1.65	0.12	0.23	0.20	1.37	2.34	2.60
Lu	0.54	0.44	0.021	0.018	0.022	0.026	0.18	0.22	0.28	<0.44	<0.16	0.17	0.30	0.015	0.040	0.022	0.089	0.35	0.32
Hf	0.33	0.31	0.29	0.29	0.28	0.27	0.37	0.25	0.40	<1.77	<0.74	0.91	<0.51	0.50	0.47	0.51	0.06	1.26	1.04
Ta	0.002	0.008	0.008	0.012	0.016	0.012	<0.029	<0.029	<0.080	<0.53	<0.16	<0.18	<0.17	0.021	0.011	0.012	<0.012	0.040	0.055
Pb	0.70	0.41	0.72	0.45	0.58	0.68	0.85	0.68	<0.35	<1.57	<0.82	<0.59	<0.49	1.15	1.30	1.02	<0.281	0.12	0.063
Th	0.32	0.16	1.74	0.80	1.31	1.81	5.67	4.94	0.38	0.31	0.48	0.71	0.49	0.73	0.56	0.59	0.02	0.028	0.062
U	0.21	0.071	0.54	0.33	0.47	0.61	1.39	1.29	<0.078	<0.29	0.15	<0.12	<0.10	0.28	0.18	0.25	<0.018	0.009	<0.018

Table A4-4: Trace element composition of ***clinopyroxene*** (in µg/g) in peridotite and pyroxenite xenoliths from Marsabit (continued)

	Group III-c															Group III-d			
sample	**1959/27**	**1959/27**	**1959/27**	**1959/27**	**1959/27**	**1959/27**	**1959/27**	**1959/27**	**1965/3**	**1965/3**	**1965/3**	**1965/3**	**1965/3**	**1965/3**	**1965/25**	**1965/25**	**1970/6**	**1970/6**	**1970/6**	**1970/6**
location	Di_m	Di_m	Di_m	Aug_m	Aug_m	Aug_m	Aug_m	Aug_m	Di_m	Di_m	Di_m	Di_m	Di_m	Di_m	Di_m	Di_m	Di_m	Di_m	Di_m	Di_m
	m.p.	m.p.	m.p.	m.p.	m.p.	m.p.	m.p.	m.p.	m.p.	m.p.	m.p.	m.p.	m.p.	m.p.	m.p.	m.p.	rim	core	rim	rim
anal. Nr.	dd08g10	dd08g12	dd08g14	dd08f03	dd08f05	dd08g09	dd08g13	dd08g15	dd08c09	dd08c10	dd08c14	dd08d05	dd08d15	dd08d16	as12a11	as12a14	ob28g05	ob28g06	ob28g09	ob28g10
Li	n.a.	n.a.	n.a.	n.a.	n.a.	n.a.	n.a.	n.a.	n.a.	n.a.	n.a.	n.a.	n.a.	n.a.	n.a.	n.a.	n.a.	n.a.	n.a.	n.a.
P	113	61.1	65.5	43.6	56.7	122	69.8	78.6	109	74.2	56.7	61.1	78.6	113	29.9	46.1	130	130	151	159
K	480	38.9	6.22	24.8	16.9	603	37.4	76.6	88.7	83.0	6.66	10.7	20.9	13.7	<5.79	17.2	14.3	11.8	72.8	64.1
Sc	70.8	76.2	62.8	56.3	58.8	56.1	60.5	60.4	97.7	102	87.9	96.4	108	97.0	85.1	79.6	75.5	84.6	80.6	81.9
Ti	2718	1068	449	4578	5165	6742	6166	9622	445	419	372	360	535	613	886	884	292	375	500	491
V	323	246	211	264	282	319	306	385	381	305	264	271	364	378	228	263	276	296	296	291
Ni	358	331	337	341	365	376	394	472	374	341	381	314	334	368	375	303	375	324	416	405
Zn	20.5	16.1	19.4	22.7	29.3	27.5	26.5	29.3	13.4	15.8	14.7	9.82	8.33	7.93	15.7	14.6	12.1	10.7	12.9	11.8
Ga	n.a.	n.a.	n.a.	n.a.	n.a.	n.a.	n.a.	n.a.	n.a.	n.a.	n.a.	n.a.	n.a.	n.a.	3.76	4.46	3.51	3.43	3.81	3.68
Rb	0.76	0.073	<0.036	<0.065	<0.056	1.26	<0.10	0.33	0.20	<0.22	<0.050	<0.068	<0.057	0.051	<0.068	<0.12	<0.032	<0.006	0.13	0.17
Sr	250	226	337	113	114	122	119	115	543	459	367	386	516	687	164	166	374	538	494	466
Y	41.6	43.1	54.0	20.7	21.0	18.6	22.1	22.9	72.4	55.3	71.5	71.0	58.6	73.9	62.3	57.2	45.6	49.2	47.6	50.2
Zr	85.2	63.6	61.0	43.1	44.5	46.0	45.8	53.6	19.7	12.2	13.2	19.1	15.7	22.6	20.5	13.1	42.4	13.4	62.6	61.1
Nb	2.35	0.96	0.53	0.47	0.49	2.21	0.56	0.72	3.46	2.35	0.99	2.15	1.54	3.58	0.63	0.64	1.26	1.14	1.41	1.27
Cs	<0.062	<0.019	<0.021	<0.020	<0.025	<0.065	<0.031	<0.079	<0.042	<0.067	<0.024	<0.028	<0.023	<0.019	<0.026	<0.073	<0.008	0.004	<0.016	<0.009
Ba	14.5	0.76	<0.15	<0.13	0.12	14.9	0.49	<0.79	2.29	1.16	<0.14	0.30	0.66	0.47	<0.22	0.46	<0.041	0.036	9.93	2.52
La	11.5	9.63	17.0	3.68	3.89	4.14	4.24	3.95	51.6	37.7	31.7	35.7	50.2	88.4	18.2	20.9	16.6	22.7	24.5	23.1
Ce	43.4	39.3	61.0	14.5	14.7	16.4	16.0	14.6	122	99.3	86.0	93.2	120	195	62.4	64.7	71.7	87.2	86.2	87.6
Pr	7.90	7.75	10.4	2.77	2.71	2.67	2.78	2.68	16.0	13.9	12.1	12.8	15.2	23.9	9.50	9.32	14.0	15.5	15.0	15.5
Nd	42.4	43.9	55.6	16.6	16.4	16.3	16.4	16.7	68.0	60.4	52.9	59.5	67.4	99.5	46.9	45.3	86.4	86.5	85.4	89.6
Sm	12.4	9.54	14.2	5.09	6.10	5.48	6.13	5.94	15.9	11.5	13.2	15.1	14.4	18.4	11.8	11.5	22.8	21.3	21.5	24.5
Eu	4.08	4.17	5.01	2.08	2.10	1.61	1.86	2.25	5.24	4.92	4.69	5.65	4.56	6.21	3.58	3.94	7.71	7.27	7.39	8.05
Gd	11.1	11.7	12.7	6.26	5.65	4.22	6.45	4.11	13.9	10.7	10.3	14.3	12.3	14.3	11.4	9.60	20.3	17.1	17.7	19.7
Tb	n.a.	n.a.	n.a.	n.a.	n.a.	n.a.	n.a.	n.a.	n.a.	n.a.	n.a.	n.a.	n.a.	n.a.	1.99	1.60	2.51	2.47	2.56	2.68
Dy	10.45	9.39	12.2	4.81	4.93	3.91	5.08	5.03	13.2	9.17	13.6	13.5	11.5	13.4	11.1	10.9	12.1	12.1	11.7	11.9
Ho	1.54	1.66	2.17	0.90	0.93	0.85	0.83	0.84	2.59	1.85	2.43	2.71	2.15	2.58	2.35	2.55	1.85	2.00	1.82	1.89
Er	3.35	3.65	5.19	2.47	2.06	1.34	2.30	1.86	6.87	6.76	6.49	6.46	5.23	7.07	6.76	5.25	3.65	4.08	4.07	4.35
Tm	0.57	0.51	0.67	0.23	0.25	0.18	0.25	0.24	0.92	1.11	1.01	0.86	0.70	0.95	0.88	0.69	0.38	0.47	0.42	0.47
Yb	3.83	3.44	4.59	2.04	1.70	1.92	1.56	2.80	7.42	3.68	6.31	5.23	4.81	5.67	5.90	5.23	1.91	2.35	2.20	2.56
Lu	0.45	0.44	0.64	0.24	0.28	0.31	0.20	0.15	0.77	0.40	0.83	0.72	0.55	0.70	0.81	0.88	0.24	0.25	0.25	0.27
Hf	2.29	1.14	1.30	1.72	1.96	2.07	1.19	2.42	0.61	0.17	0.23	0.52	0.69	0.81	0.55	0.31	0.53	0.20	1.10	0.78
Ta	0.073	0.082	<0.023	0.046	<0.045	<0.072	0.074	<0.19	0.22	0.13	0.12	0.35	0.22	0.66	<0.014	<0.035	0.061	0.045	0.093	0.11
Pb	<0.20	<0.093	0.19	<0.080	0.072	<0.22	0.26	<0.37	0.24	0.66	<0.12	0.10	0.11	0.23	0.17	<0.29	0.21	0.13	0.16	<0.17
Th	0.089	0.029	0.10	0.054	0.032	<0.050	0.11	<0.074	0.48	0.27	0.11	0.11	0.25	0.45	0.072	0.085	0.081	0.077	0.098	0.088
U	0.061	<0.014	<0.017	<0.015	<0.022	0.088	<0.028	<0.071	0.12	<0.10	<0.023	<0.016	0.018	0.049	0.017	<0.035	0.022	0.013	0.011	0.031

Table A4-4: Trace element composition of ***clinopyroxene*** (in µg/g) in peridotite and pyroxenite xenoliths from Marsabit (continued)

	G. III-d	Group IV												Group V					
sample	**1970/6**	**1961/1**	**1961/1**	**1961/1**	**1961/1**	**1961/1**	**1968/1**	**1968/1**	**1968/1**	**1968/1**	**1968/1**	**1968/1**	**1968/1**	**1959/18**	**1959/18**	**1959/18**	**1959/18**	**1959/18**	**1959/18**
location	Di_m	cpx-I	cpx-I	cpx-I	cpx-I	cpx-I	cpx-I	cpx-I	cpx-I	cpx-I	cpx-IIb	cpx-IIb	cpx-IIb	cpx-I	cpx-I	cpx-I	cpx-I	cpx-m	cpx-m
	core	core	core	core	rim	rim	core	core	core	rim	core	core	core	core	core	core	rim	r/cpx-I	r/cpx-I
anal. Nr.	ob28g12	mc22c03	mc22c05	mc22c07	mc22c04	mc22c06	mc22b10	mc22b15	mc22b16	mc22b09	mc22b03	mc22b07	mc22b08	ob29f06	ob29f07	ob29f16	ob29f05	ob29f08	ob29f10
Li	n.a.	n.a.	n.a.	n.a.	n.a.	n.a.	n.a.	n.a.	n.a.	n.a.	n.a.	n.a.	n.a.	2.98	2.46	3.11	2.94	<1.47	1.75
P	129	12.5	11.6	11.3	14.6	13.2	20.3	18.4	19.2	18.9	21.4	23.8	31.9	69.4	80.3	71.5	90.7	77.9	60.6
K	11.4	2.73	7.44	7.99	2.36	4.28	0.97	0.97	0.50	0.71	<1.00	<1.35	6.76	<1.06	0.95	<0.94	<2.51	24.7	52.4
Sc	78.6	63.3	66.2	68.5	71.5	69.0	53.4	51.9	57.8	63.2	65.4	65.7	66.8	24.9	25.3	22.9	31.4	39.9	56.8
Ti	439	164	156	158	170	161	2274	2234	2304	2108	2189	2127	2010	3887	3622	3591	3540	3733	9714
V	303	178	178	176	185	188	253	252	262	259	274	268	270	356	310	345	359	411	343
Ni	329	306	269	281	306	337	268	265	278	229	233	230	407	286	319	295	325	1306	318
Zn	10.9	3.53	22.1	3.37	3.53	24.6	5.42	5.00	5.40	3.17	5.23	5.10	5.32	5.49	8.04	4.16	6.20	6.30	4.29
Ga	3.58	0.91	0.88	0.69	0.87	1.15	3.13	3.36	3.19	3.41	2.95	2.61	3.20	11.6	11.9	11.4	11.9	9.31	10.8
Rb	<0.008	<0.007	0.043	0.024	0.013	<0.007	0.011	<0.007	<0.005	<0.007	<0.012	0.036	<0.028	<0.016	<0.007	<0.013	<0.026	<0.23	0.16
Sr	484	33.0	33.3	32.2	34.9	34.1	52.6	51.6	52.9	52.0	55.4	54.2	53.7	115	125	112	113	56.0	34.7
Y	43.6	3.38	3.52	3.69	4.05	3.55	5.97	5.86	5.83	5.91	6.00	6.36	6.40	8.17	8.99	7.33	9.06	13.5	62.9
Zr	17.4	20.4	21.5	21.9	23.5	21.3	16.9	15.9	16.8	17.0	17.9	17.9	17.5	46.7	45.2	44.3	54.9	50.8	60.7
Nb	1.16	0.10	0.084	0.083	0.097	0.087	0.038	0.047	0.036	0.031	0.040	0.026	0.091	0.012	0.029	0.023	0.037	<0.083	0.17
Cs	<0.002	<0.003	0.004	<0.003	<0.004	0.003	0.006	<0.002	<0.002	0.004	<0.002	<0.006	<0.014	<0.005	<0.002	<0.004	<0.010	<0.097	<0.041
Ba	0.085	0.033	0.16	0.13	0.028	0.047	<0.014	<0.009	<0.009	0.019	<0.021	<0.044	0.320	<0.020	<0.021	<0.022	<0.064	<0.427	<0.338
La	21.7	0.24	0.20	0.18	0.21	0.22	0.48	0.53	0.52	0.51	0.52	0.51	0.49	3.26	3.40	3.06	3.48	2.07	2.18
Ce	90.3	0.98	0.92	0.88	1.01	0.97	2.23	2.17	2.20	2.07	2.34	2.36	2.20	11.5	11.5	10.3	10.8	9.79	11.0
Pr	16.1	0.29	0.29	0.30	0.30	0.29	0.48	0.43	0.43	0.44	0.51	0.48	0.43	1.95	2.00	1.82	1.77	1.63	2.29
Nd	86.4	3.04	2.97	2.99	3.23	3.02	2.83	2.94	2.89	2.79	3.29	3.18	3.11	10.7	11.1	9.77	10.6	12.1	14.0
Sm	21.4	1.55	1.84	1.62	1.83	1.82	1.28	1.07	1.08	1.05	1.38	1.24	1.01	3.37	3.44	3.17	3.41	5.45	6.13
Eu	7.41	0.46	0.55	0.52	0.55	0.54	0.48	0.47	0.45	0.44	0.45	0.41	0.45	1.01	1.06	1.02	1.13	1.51	1.60
Gd	16.4	0.97	1.01	1.09	1.19	1.03	1.30	1.28	1.23	1.27	1.37	1.43	1.32	2.85	2.87	2.52	3.12	3.07	8.79
Tb	2.33	0.12	0.11	0.15	0.12	0.12	0.23	0.21	0.22	0.21	0.25	0.24	0.24	0.46	0.49	0.37	0.45	0.55	1.61
Dy	11.2	0.64	0.73	0.64	0.68	0.64	1.37	1.29	1.27	1.35	1.34	1.43	1.35	2.08	2.31	1.80	2.04	3.20	7.91
Ho	1.82	0.12	0.13	0.13	0.15	0.14	0.23	0.24	0.23	0.23	0.27	0.23	0.23	0.29	0.42	0.28	0.38	0.44	2.59
Er	3.79	0.38	0.41	0.42	0.45	0.36	0.55	0.55	0.56	0.61	0.61	0.68	0.70	0.68	0.75	0.590	0.85	0.44	6.45
Tm	0.39	0.056	0.059	0.056	0.073	0.065	0.084	0.076	0.071	0.069	0.086	0.076	0.063	0.07	0.09	0.08	0.08	0.16	1.03
Yb	2.11	0.49	0.52	0.53	0.50	0.43	0.52	0.48	0.51	0.46	0.44	0.44	0.47	0.57	0.54	0.50	0.58	1.05	11.2
Lu	0.24	0.079	0.075	0.087	0.086	0.092	0.061	0.058	0.055	0.070	0.058	0.069	0.050	0.07	0.09	0.07	0.06	0.10	1.37
Hf	0.23	0.37	0.34	0.41	0.44	0.36	0.58	0.46	0.63	0.59	0.60	0.70	0.70	1.70	1.59	1.67	1.99	1.57	1.55
Ta	0.056	0.023	0.021	0.018	0.019	0.016	0.006	0.004	0.001	0.003	0.006	<0.004	<0.008	0.010	0.005	0.006	<0.006	<0.056	0.043
Pb	0.11	0.55	0.52	0.49	0.52	0.55	0.085	0.090	0.092	0.11	0.091	0.089	0.12	0.45	0.51	0.40	0.42	0.78	<0.61
Th	0.062	0.016	0.003	0.010	0.010	0.015	0.005	0.006	0.006	0.004	0.006	<0.009	<0.009	0.11	0.13	0.10	0.067	<0.077	<0.036
U	0.017	0.003	0.007	0.015	0.010	0.013	0.004	0.005	0.006	0.003	0.006	<0.004	0.014	0.060	0.039	0.037	0.051	0.330	<0.036

Table A4-4: Trace element composition of clinopyroxene (in µg/g) in peridotite and pyroxenite xenoliths from Marsabit (continued)

													Group VI								
sample	**794/1**	**794/2**	**794/3**	**794/4**	**1960/4**	**1960/5**	**1960/6**	**1960/7**	**1960/8**	**1960/9**	**1960/10**	**1960/11**	**782/2**	**782/2**	**782/2**	**782/2**	**782/2**	**782/2**	**782/2**	**782/2**	**782/2**
location	cpx-I	cpx-I	cpx-I	cpx-I	cpx-II	cpx-II	cpx-I	cpx-I	cpx-I	cpx-I	cpx-I	cpx-I	cpx-I	cpx-I	cpx-I	cpx-I	c/cpx-I	cpx-I; core	cpx-I	cpx-I	cpx-I
	core	core	core	rim	core	core	core	core	core	core	in grt	rim	core	core	core	core	no exsol.	no exsol.	rim	rim	rim
anal. Nr.	mc22d03	mc22d06	mc22d13	mc22d14	mc22e03	mc22e05	mc22e08	mc22e15	mc22e16	mc22e17	mc22e18	mc22e07	mc22f04	mc22f05	mc22f11	mc22f14	mc22f06	mc22f12	mc22f03	mc22f07	mc22f10
Li	2.43	3.27	2.88	3.16	1.51	1.72	0.89	1.25	1.29	1.30	0.77	1.42	2.05	1.56	1.73	1.90	1.72	1.72	1.70	2.04	1.66
P	54.7	53.5	58.0	61.2	31.4	21.7	19.5	19.9	20.3	19.6	18.4	31.9	32.6	33.1	33.8	35.6	35.5	37.1	44.7	34.1	39.5
K	1.04	1.20	1.10	0.66	0.73	3.03	1.01	<0.46	0.60	<0.44	16.5	<0.81	2.49	3.83	3.37	3.67	3.50	3.07	18.3	8.27	16.9
Sc	22.2	27.9	29.3	32.2	49.1	37.5	29.8	26.1	26.2	26.7	31.9	38.7	59.1	60.5	53.2	54.7	59.6	55.5	61.0	55.7	60.9
Ti	4032	3281	3977	4095	2820	2022	3148	3058	3379	3401	3530	2537	5882	5912	4613	5138	6041	4832	7176	4556	6770
V	360	386	419	415	413	414	418	397	387	422	496	418	348	349	295	317	350	300	355	301	353
Ni	333	263	331	282	203	230	260	344	324	329	390	233	198	189	206	203	196	194	182	233	201
Zn	28.1	13.4	26.3	19.8	3.15	2.68	2.59	9.38	5.27	5.26	13.0	2.45	12.7	15.3	17.2	12.8	12.0	12.6	26.7	22.3	23.7
Ga	14.4	12.0	14.8	14.9	7.49	7.63	8.96	10.1	9.93	10.2	10.2	7.21	9.16	9.10	8.27	7.78	8.43	6.92	13.4	9.71	11.7
Rb	<0.008	<0.006	<0.005	0.007	<0.010	<0.005	<0.004	<0.006	<0.006	<0.006	0.008	<0.008	<0.008	0.012	<0.009	<0.007	<0.008	<0.007	0.0260	<0.023	0.023
Sr	144	107	128	124	45.6	48.2	47.7	54.8	53.7	52.5	52.7	47.1	68.5	65.4	63.8	63.6	69.8	63.6	92.1	55.8	88.9
Y	3.12	4.50	4.14	4.58	9.06	6.57	4.50	4.08	4.05	3.74	4.05	7.98	11.0	10.9	8.55	8.58	11.3	8.58	14.3	8.75	13.3
Zr	21.6	23.9	30.4	31.2	27.3	21.4	21.1	16.5	20.9	21.1	22.6	25.7	26.8	27.1	20.3	21.6	28.7	21.8	47.6	19.0	42.8
Nb	0.064	0.019	0.042	0.022	0.061	0.045	0.027	0.063	0.043	0.035	0.081	0.023	0.57	0.64	0.47	0.52	0.54	0.38	0.42	0.27	0.45
Cs	0.004	<0.002	<0.001	<0.003	<0.002	0.002	<0.002	0.004	0.002	0.003	0.005	<0.004	<0.003	<0.002	<0.001	0.003	0.003	<0.002	<0.007	<0.007	<0.004
Ba	<0.024	0.012	<0.013	<0.014	<0.019	0.049	<0.009	<0.011	<0.018	<0.018	0.031	<0.019	0.035	0.046	<0.017	0.043	0.051	0.026	0.11	<0.047	0.083
La	1.04	0.86	1.04	1.07	0.68	0.63	0.55	0.68	0.71	0.68	0.68	0.60	4.04	2.86	2.37	2.48	5.20	2.41	3.67	1.92	3.71
Ce	4.15	3.42	3.98	4.12	2.52	2.33	2.35	2.77	2.77	2.68	2.62	2.31	9.74	8.56	7.49	7.72	10.9	7.82	12.9	6.63	12.1
Pr	0.77	0.68	0.79	0.87	0.52	0.49	0.50	0.57	0.56	0.56	0.53	0.46	1.51	1.44	1.19	1.24	1.55	1.20	2.26	1.12	2.09
Nd	5.24	4.31	5.08	5.44	3.34	3.04	3.12	3.61	3.61	3.38	3.36	2.97	8.30	8.14	6.65	6.56	8.44	6.94	12.0	6.73	11.5
Sm	1.87	1.632	2.00	1.99	1.39	1.21	1.10	1.38	1.31	1.35	1.33	1.34	2.38	2.56	2.05	1.96	2.77	2.09	3.56	1.91	3.32
Eu	0.74	0.61	0.77	0.85	0.55	0.44	0.53	0.54	0.53	0.48	0.53	0.52	0.95	0.92	0.74	0.76	0.94	0.76	1.28	0.69	1.11
Gd	1.77	1.74	1.81	1.85	1.60	1.35	1.44	1.35	1.36	1.39	1.51	1.63	2.76	2.41	1.92	2.01	2.67	2.19	3.61	2.20	3.46
Tb	0.25	0.23	0.27	0.25	0.32	0.26	0.21	0.22	0.23	0.20	0.24	0.30	0.44	0.45	0.33	0.32	0.43	0.34	0.55	0.38	0.49
Dy	0.95	1.15	1.20	1.40	1.79	1.48	1.16	1.07	1.12	1.04	1.01	1.71	2.54	2.53	1.86	1.96	2.56	1.99	3.24	1.87	3.15
Ho	0.13	0.19	0.20	0.20	0.35	0.25	0.17	0.17	0.18	0.15	0.16	0.31	0.43	0.49	0.35	0.36	0.49	0.35	0.56	0.33	0.53
Er	0.22	0.34	0.30	0.36	0.88	0.63	0.36	0.36	0.34	0.27	0.31	0.78	1.06	1.13	0.90	0.97	1.22	0.87	1.44	0.98	1.42
Tm	0.02	0.04	0.04	0.05	0.14	0.08	0.04	0.03	0.03	0.03	0.03	0.11	0.15	0.15	0.10	0.12	0.15	0.12	0.15	0.13	0.17
Yb	0.091	0.21	0.29	0.24	0.74	0.51	0.28	0.14	0.17	0.16	0.17	0.50	0.88	0.89	0.67	0.71	0.91	0.66	1.03	0.74	1.20
Lu	0.01	0.03	0.021	0.03	0.10	0.07	0.03	0.02	0.02	0.02	0.02	0.07	0.13	0.12	0.090	0.09	0.12	0.09	0.16	0.12	0.14
Hf	0.71	0.78	1.22	1.13	1.17	0.92	0.97	0.67	0.70	0.87	1.19	1.11	1.18	1.33	0.92	0.98	1.31	0.97	2.15	1.04	1.65
Ta	0.013	0.008	0.007	0.006	0.005	<0.001	0.007	0.009	0.013	0.014	0.008	0.005	0.080	0.067	0.055	0.086	0.082	0.062	0.085	0.060	0.075
Pb	0.20	0.16	0.12	0.15	0.096	0.095	0.10	0.084	0.079	0.077	0.066	0.089	0.39	0.26	0.21	0.17	0.38	0.14	0.094	0.073	0.084
Th	0.021	0.021	0.027	0.017	0.014	0.012	0.008	0.036	0.016	0.013	0.014	0.005	0.37	0.18	0.069	0.069	0.355	0.069	0.060	0.040	0.069
U	0.006	0.014	0.003	0.008	0.004	0.008	0.009	0.007	0.006	0.005	0.004	<0.003	0.11	0.050	0.019	0.016	0.094	0.009	0.009	0.016	0.022

Table A4-5: Trace element composition of ***amphibole*** (in µg/g) in peridotite and pyroxenite xenoliths from Marsabit

	Group I - Ti-pargasite										**Group III-b - edenite-Mg-katophorite**						**Group III-c - Mg-katoph.**		
sample	**1963/2**	**1963/2**	**1963/2**	**1963/2**	**1963/2**	**1963/2**	**1963/2**	**1963/2**	**1965/4**	**1965/4**	**1959/15**	**1959/15**	**1959/15**	**1959/15**	**1965/15**	**1965/15**	**785***	**785***	**785***
location	amph-i	amph-i	amph-i	amph-i	amph-i	amph-i	amph-ii	amph-iii	amph-i	amph-ii	residual	residual	residual	residual	interst.	interst.	residual	residual	residual
	core	core	core	core	rim	rim	sympl.	next cpx	core	sympl.	in m.p.	in m.p.	in m.p.	in m.p.			in m.p.	in m.p.	in m.p.
anal. Nr.	dd08b11	dd08b13	ob29d14	ob29d15	dd08b10	dd08b12	dd08b03	ob29d04	ob28c03	ob28c05	dd09b18	dd09c06	dd09c16	dd09c17	ob29c07	ob29c08	ob28e10	ob28e12	ob28e14
P	100	118	109	124	131	109	257	137	86.1	257	454	467	463	445	222	235	130	184	179
K	9292	8614	2343	2157	9117	9173	1398	4109	1643	556	4703	4787	4749	4301	3916	3637	2203	2543	3171
Sc	55.1	61.3	64.3	63.2	57.5	63.3	86.0	55.9	65.1	139	40.4	39.7	40.8	40.2	7.04	6.63	28.4	24.7	24.9
Ti	14730	15013	19849	19641	15277	15323	18176	17163	17050	12194	716	709	754	720	9867	9917	863	1209	1266
V	384	396	433	421	387	410	421	475	401	270	213	226	219	216	317	332	246	270	258
Ni	784	745	829	861	763	713	922	884	830	915	765	777	788	726	842	828	739	783	791
Zn	3.06	4.36	6.02	7.86	4.49	4.18	9.14	6.77	10.3	13.1	29.4	32.2	31.9	29.8	16.3	15.9	18.9	21.8	20.2
Ga	n.a.	n.a.	4.33	3.74	n.a.	n.a.	n.a.	5.18	3.86	2.28	n.a.	n.a.	n.a.	n.a.	9.81	9.39	9.78	10.8	10.9
Rb	3.17	2.13	0.40	0.50	2.40	2.31	0.25	0.73	0.88	0.50	2.98	3.44	3.22	2.79	1.84	1.51	0.41	0.44	1.50
Sr	142	157	189	187	156	155	169	153	183	131	218	221	218	216	325	335	43.5	61.0	91.7
Y	13.1	27.0	43.8	45.3	30.9	23.7	59.7	39.1	43.9	112	9.48	9.11	10.5	10.1	2.69	3.15	5.45	10.1	10.9
Zr	35.0	36.9	43.9	43.9	35.2	37.8	52.8	41.6	44.7	71.5	5.25	5.63	5.23	5.39	3.70	3.31	3.23	3.03	3.04
Nb	8.63	7.70	9.90	10.0	7.82	8.25	3.56	2.44	8.52	6.44	3.05	2.87	3.47	3.39	4.13	4.47	0.47	1.07	1.03
Cs	<0.018	<0.008	<0.005	0.006	<0.017	<0.023	<0.067	<0.016	<0.009	<0.093	<0.011	<0.027	<0.014	0.006	<0.001	0.005	<0.002	0.004	0.015
Ba	31.7	24.2	7.03	9.11	27.1	22.1	7.38	12.8	12.4	7.45	79.4	83.0	77.9	78.1	61.4	54.0	1.26	3.13	5.00
La	1.50	1.65	1.44	1.48	1.81	1.51	1.40	1.70	1.37	1.38	36.4	35.7	36.4	35.7	11.6	11.0	4.88	6.75	8.80
Ce	5.49	5.51	5.16	5.27	5.57	5.52	6.02	6.19	4.64	3.25	65.1	65.5	66.7	62.7	22.5	23.1	16.8	22.9	24.1
Pr	0.93	1.11	0.96	0.98	1.03	1.02	1.13	1.09	0.77	0.52	5.67	5.68	6.01	5.74	2.08	2.24	2.31	3.17	3.31
Nd	6.57	6.66	5.52	5.38	6.12	6.04	5.92	7.43	5.22	4.51	17.5	15.5	17.8	17.7	7.20	7.79	9.35	13.5	13.6
Sm	1.50	2.62	2.24	2.41	2.63	2.03	2.50	3.20	2.54	3.08	2.30	2.03	2.59	2.08	1.43	1.43	1.72	2.96	3.03
Eu	0.75	1.15	1.29	1.29	1.05	1.10	1.07	1.29	1.21	1.75	0.76	0.69	0.83	0.80	0.58	0.60	0.63	1.03	1.17
Gd	2.19	3.44	3.98	4.27	3.72	3.57	4.85	4.91	4.31	9.24	1.42	1.43	1.90	1.82	0.85	0.88	1.26	2.19	2.25
Tb	n.a.	n.a.	0.90	1.02	n.a.	n.a.	n.a.	0.87	1.00	2.04	n.a.	n.a.	n.a.	n.a.	0.11	0.13	0.22	0.36	0.42
Dy	1.90	4.57	7.02	7.74	5.00	3.50	8.58	6.27	7.04	17.6	1.71	1.73	1.64	1.71	0.57	0.67	1.06	2.26	2.10
Ho	0.53	1.07	1.71	1.92	1.13	0.90	2.27	1.56	1.81	4.46	0.36	0.35	0.34	0.36	0.10	0.10	0.19	0.39	0.40
Er	1.80	2.81	5.27	5.63	3.56	2.64	7.46	4.29	5.03	11.8	1.03	0.81	1.24	1.06	0.24	0.27	0.50	0.85	0.98
Tm	0.26	0.40	0.73	0.73	0.51	0.44	0.81	0.61	0.65	1.66	0.11	0.16	0.15	0.16	0.030	0.033	0.063	0.11	0.13
Yb	2.59	2.46	5.23	5.31	3.40	3.66	7.23	4.16	4.69	10.8	1.12	0.75	1.30	1.20	0.28	0.30	0.35	0.75	0.68
Lu	0.36	0.36	0.66	0.74	0.52	0.46	0.87	0.52	0.69	1.56	0.18	0.18	0.19	0.19	0.036	0.038	0.033	0.067	0.073
Hf	1.04	1.10	1.08	1.01	1.04	0.94	1.61	1.41	1.14	1.65	0.13	0.17	0.14	0.15	0.067	0.054	0.070	0.044	0.088
Ta	0.23	0.15	0.24	0.24	0.25	0.15	<0.054	0.078	0.19	0.17	0.022	<0.040	0.024	0.033	0.14	0.14	<0.002	<0.002	<0.003
Pb	0.48	0.69	0.79	0.65	0.71	0.41	0.36	0.38	0.89	<0.93	1.93	2.14	2.17	2.01	3.60	3.74	1.72	1.64	1.42
Th	0.027	0.012	0.015	0.023	<0.017	<0.020	<0.050	<0.010	0.023	<0.037	7.45	7.05	7.14	6.82	1.50	1.34	0.92	1.70	2.09
U	<0.014	0.008	0.009	0.006	<0.015	<0.027	<0.041	0.015	0.014	<0.052	2.20	2.41	2.19	2.12	0.39	0.39	0.26	0.41	0.43

n.a.: not analysed

Table A4-5: Trace element composition of ***amphibole*** (in µg/g) in peridotite and pyroxenite xenoliths from Marsabit (continued)

	Group III-c - Mg-katophorite										Type III-c - kaersutite				Ti Pargasite / Kaersutite						
sample	**785***	**785***	**1965/25**	**1965/25**	**1965/25**	**1965/25**	**1965/25**	**1965/25**	**1965/25**	**1965/25**	**1959/27**	**1959/27**	**1959/27**	**1959/27**	**1959/18**	**1959/18**	**1959/18**	**794/1**	**794/1**	**794/1**	**1960/4**
location	residual	residual	euhedral	euhedral	euhedral	euhedral	euhedral	residual	residual	residual	glass-	glass-	glass-	glass-	Ti Parg	Ti Parg	Ti Parg	Kaers.	Kaers.	Kaers.	Ti Parg
	in m.p.	in m.p.	core	core	rim	rim	rim	in m.p.	in m.p.	in m.p.	related	related	related	related	core	core	core	core	rim	core	core
anal. Nr.	ob28e17	ob28e18	as12a07	as12a12	as12a04	as12a03	as12a08	as12a13	as12a15	as12a17	dd08f08	dd08f12	dd08g0404	dd08g05	ob29f09	ob29f13	ob29f14	mc22d07	mc22d17	mc22d18	mc22e04
P	196	175	171	206	147	156	120	182	154	113	266	301	231	214	273	285	322	280	205	181	105
K	2654	2393	2888	2955	3893	3122	3655	3432	3918	3274	12762	12597	14519	13289	1826	2185	1961	740	132	132	2246
Sc	34.5	35.8	31.5	31.1	35.0	32.5	35.2	34.4	34.0	32.9	27.0	31.6	31.4	37.5	21.0	24.4	28.4	29.1	30.4	27.9	45.2
Ti	1898	1732	1480	1421	1581	1542	1589	1564	1539	1517	32071	30443	30703	32154	17106	19349	18252	18939	26454	27703	19720
V	299	289	173	172	179	175	187	186	177	176	404	417	402	469	314	313	299	454	388	409	475
Ni	876	811	706	737	761	726	813	854	785	783	530	521	589	638	1182	735	716	644	811	829	567
Zn	21.4	18.8	44.1	45.1	44.1	42.0	45.7	42.0	39.2	41.0	54.8	53.8	52.2	46.3	20.2	6.54	7.09	37.9	46.7	43.2	2.52
Ga	11.4	10.3	8.64	8.67	9.02	8.18	8.72	9.18	9.08	8.26					15.2	4.39	4.17	12.9	19.6	17.7	4.00
Rb	0.50	0.35	0.96	0.96	2.14	1.21	1.50	1.10	1.96	1.09	7.13	6.67	8.37	7.44	0.52	0.64	0.62	0.040	0.052	0.036	0.37
Sr	66.7	70.8	127	95.5	338	154	117	123	348	107	668	683	622	618	408	244	185	347	343	335	157
Y	12.6	11.1	37.9	39.0	36.8	38.8	35.9	40.1	35.2	33.5	35.5	33.8	33.4	31.0	13.7	15.2	27.9	10.1	8.69	8.39	26.9
Zr	2.97	2.92	13.8	11.4	32.6	31.3	59.2	22.3	32.9	57.5	110	102	107	93.3	40.8	46.9	51.3	30.1	32.1	33.3	22.3
Nb	1.21	1.02	31.3	19.2	47.7	39.3	70.5	31.4	46.2	78.5	34.1	29.5	35.9	26.5	2.27	3.93	4.15	4.11	3.69	3.82	5.66
Cs	<0.009	0.006	0.003	0.008	0.004	0.014	0.018	<0.037	0.005	<0.005	<0.010	<0.020	<0.030	<0.019	0.020	0.010	0.010	0.006	0.014	0.011	<0.006
Ba	3.09	2.59	8.49	8.46	50.3	8.67	8.41	10.0	47.5	7.82	322	338	312	331	36.0	39.7	39.8	0.68	0.41	0.41	11.7
La	8.24	7.04	19.3	17.7	38.2	18.8	11.3	17.9	40.2	10.7	13.8	14.1	12.8	10.7	5.51	3.77	3.64	1.45	1.38	1.48	0.95
Ce	24.8	21.7	63.3	62.1	99.7	56.3	42.6	57.1	102.6	40.5	44.8	42.3	42.3	33.8	17.6	12.3	12.3	5.26	5.49	5.26	3.65
Pr	3.49	3.01	8.68	8.56	11.97	7.74	6.23	8.11	11.71	6.27	7.24	6.86	6.77	5.57	2.95	2.02	2.24	1.00	1.01	1.03	0.73
Nd	15.1	12.8	36.0	36.3	46.8	34.1	29.6	33.9	45.4	29.1	39.8	37.1	36.1	31.8	16.7	12.2	12.9	6.56	7.39	6.72	4.84
Sm	3.16	2.85	8.32	7.52	8.90	8.37	7.40	8.90	9.02	7.76	11.1	10.4	10.5	9.45	5.12	4.47	4.42	2.90	3.38	2.77	2.22
Eu	1.15	1.08	2.41	2.32	2.77	2.41	2.52	2.39	2.64	2.35	3.84	3.71	3.48	3.63	1.89	1.63	1.81	1.15	1.35	1.19	1.03
Gd	2.41	2.25	6.59	7.01	7.14	6.96	6.92	6.96	6.97	6.94	9.80	9.04	9.31	9.40	4.37	4.24	5.46	2.78	3.14	2.92	2.99
Tb	0.50	0.39	1.20	1.20	1.23	1.27	1.17	1.37	1.17	1.17	n.a.	n.a.	n.a.	n.a.	0.68	0.63	0.97	0.47	0.42	0.41	0.68
Dy	2.52	2.02	7.24	7.35	7.17	7.39	6.98	7.79	6.78	6.88	8.19	7.69	7.75	7.00	3.67	3.44	6.00	2.55	2.20	2.15	4.85
Ho	0.50	0.39	1.47	1.55	1.38	1.49	1.44	1.63	1.37	1.37	1.47	1.49	1.30	1.37	0.53	0.64	1.07	0.38	0.31	0.37	1.09
Er	1.14	0.97	3.97	4.05	3.66	4.00	3.82	3.91	3.59	3.36	3.36	3.30	2.98	2.96	1.18	1.29	2.80	0.92	0.95	0.61	3.08
Tm	0.17	0.12	0.61	0.60	0.49	0.59	0.58	0.62	0.51	0.52	0.39	0.41	0.35	0.27	0.10	0.14	0.34	0.092	0.081	0.10	0.47
Yb	0.99	0.77	4.01	4.00	3.72	3.99	3.86	3.79	3.66	3.37	2.72	2.49	2.19	2.43	0.60	0.98	2.18	0.65	0.50	0.44	3.18
Lu	0.077	0.079	0.52	0.58	0.51	0.54	0.44	0.67	0.48	0.46	0.31	0.30	0.32	0.33	0.07	0.12	0.28	0.056	0.061	0.053	0.42
Hf	0.048	0.065	0.30	0.28	0.49	0.43	0.78	0.30	0.60	0.91	3.76	3.70	3.55	3.31	1.20	0.97	1.06	0.66	1.00	0.84	0.64
Ta	0.004	0.002	0.15	0.10	0.47	0.48	1.07	0.15	0.49	1.34	1.98	1.71	2.15	1.67	0.21	0.20	0.26	0.18	0.29	0.30	0.15
Pb	1.73	1.42	1.90	1.95	2.02	1.88	2.22	1.40	1.92	1.94	0.39	0.33	0.33	0.22	2.48	1.77	1.88	0.65	0.73	0.62	0.41
Th	1.96	1.81	0.53	0.59	0.47	0.49	0.28	0.52	0.46	0.30	0.20	0.25	0.20	0.10	0.22	0.092	0.080	0.030	0.031	0.016	0.017
U	0.48	0.40	0.15	0.19	0.13	0.15	0.12	0.22	0.16	0.10	0.048	0.023	<0.036	0.018	0.079	0.037	0.037	0.012	0.010	0.010	0.009

n.a.: not analysed

Table A4-6: Trace element composition of ***phlogopite*** (in µg/g) in peridotite and pyroxenite xenoliths from Marsabit

	Group I			Group III-b			Group III-c								Group V	
sample	**1963/2**	**1963/2**	**1963/2**	**1965/15**	**1965/15**	**1965/15**	**785***	**785***	**785***	**785***	**785***	**1965/3**	**1965/3**	**1965/25**	**794/1**	**794/1**
location	interst.	interst.	interst.	interst.	interst.	interst.	incl.	cluster[1]	cluster[1]	cluster[1]	cluster[1]	incl.	incl.	incl.	interst.	interst.
	core	core	core				in Opx_m					in Opx_m	in Opx_m	in amph.	core	core
anal. Nr.	ob28f08	ob28f09	ob28f10	ob29c10	ob29c16	ob29c17	ob28e05	ob28e06	ob28e07	ob28e11	ob28e13	dd08c05	dd08c06	as12a05	mc22d04	mc22d05
P	26.7	21.5	19.8	18.7	36.9	15.6	33.9	24.2	18.8	19.2	20.6	48.0	<56.7	36.2	23.6	17.2
K	101263	82709	87391	72575	71711	71951	79052	74060	69992	70363	70997	60747	63845	70189	84838	86290
Sc	3.46	2.98	2.97	1.10	0.99	1.17	1.30	0.78	0.91	0.96	0.88	1.31	2.22	1.60	1.58	1.57
Ti	26930	23896	24541	16408	15500	16513	2839	2080	1807	2209	2096	890	1129	1736	38177	38106
V	378	330	354	284	255	288	142	111	130	113	108	89	103	78.8	389	398
Ni	1867	1773	1798	1727	1808	1755	2046	1957	1773	1797	1813	1744	1724	1905	2127	1953
Zn	8.72	8.98	9.00	22.1	23.4	22.0	38.2	34.5	32.1	30.8	31.7	35.8	33.0	69.5	76.8	74.3
Ga	9.98	6.64	6.95	9.84	11.1	9.90	21.0	18.7	18.8	17.8	19.0	n.a.	n.a.	23.5	23.6	23.4
Rb	118	106	89.8	147	185	114	183	155	133	161	133	289	167	342	89.9	31.2
Sr	38.1	33.5	35.6	116	102	122	32.5	33.3	35.0	40.4	36.3	77.5	80.9	101	94.0	104
Y	0.044	0.13	0.079	0.086	0.10	0.040	<0.054	<0.012	0.006	<0.007	0.021	<0.057	<0.19	0.052	0.055	0.029
Zr	1.93	2.04	2.21	0.19	0.19	0.20	<0.088	0.042	0.070	0.11	0.077	0.43	0.60	0.73	0.87	1.05
Nb	2.80	2.66	2.55	6.28	5.06	6.11	1.77	1.47	1.46	1.10	1.02	47.9	39.7	21.0	4.49	4.18
Cs	1.22	1.29	1.09	1.38	1.75	1.17	3.99	2.40	1.80	4.65	2.16	2.61	1.13	7.98	1.89	0.53
Ba	657	626	593	1096	1212	919	298	271	219	309	277	1343	1934	1124	205	177
La	<0.010	0.008	0.003	0.055	0.10	<0.006	<0.029	<0.011	<0.003	0.006	0.020	0.069	<0.12	<0.045	0.0130	0.0080
Ce	<0.005	0.007	0.008	0.011	0.027	<0.005	<0.019	<0.008	<0.003	0.021	0.14	<0.075	<0.14	0.078	<0.004	0.0070
Pr	0.007	<0.002	0.003	0.008	0.012	0.00	<0.024	<0.005	<0.003	0.003	0.012	<0.067	<0.14	<0.019	<0.002	0.0070
Nd	<0.020	0.015	<0.010	0.035	0.019	<0.011	<0.079	<0.031	<0.009	<0.016	0.065	<0.41	<0.78	<0.22	<0.015	<0.013
Sm	<0.040	<0.013	0.020	<0.011	0.015	0.02	<0.090	<0.055	<0.010	<0.013	0.016	<0.47	<0.65	<0.13	<0.012	0.0160
Eu	<0.013	0.014	0.025	0.017	0.022	0.01	<0.026	<0.017	0.010	<0.007	0.013	<0.10	<0.31	<0.095	0.0110	0.0150
Gd	<0.023	<0.015	<0.011	<0.011	<0.010	<0.012	<0.151	<0.025	0.012	<0.012	<0.011	<0.43	<0.68	0.17	<0.016	<0.010
Tb	<0.008	0.005	0.004	<0.002	<0.002	<0.002	<0.027	<0.004	<0.002	0.004	0.002	n.a.	n.a.	<0.028	<0.002	<0.002
Dy	<0.014	0.017	0.014	<0.017	<0.015	<0.007	<0.077	<0.015	<0.006	<0.008	<0.007	0.45	<1.28	<0.077	<0.012	<0.009
Ho	<0.004	0.005	0.002	<0.003	<0.002	<0.002	<0.020	<0.006	<0.002	<0.002	0.002	<0.043	<0.12	<0.028	0.0030	0.0040
Er	<0.021	0.009	<0.010	<0.013	<0.009	<0.011	<0.113	<0.028	<0.009	<0.014	<0.016	<0.25	<0.59	<0.11	<0.008	<0.007
Tm	<0.006	0.003	0.003	<0.002	<0.002	<0.004	<0.013	<0.007	0.003	<0.002	0.002	<0.088	<0.17	<0.018	0.0020	<0.002
Yb	<0.023	<0.015	0.014	<0.011	<0.014	<0.027	<0.150	<0.048	<0.019	<0.017	<0.011	<0.47	<0.90	<0.17	<0.017	<0.010
Lu	<0.006	0.002	<0.002	<0.002	0.002	<0.002	<0.014	<0.004	<0.002	<0.002	<0.002	<0.061	<0.20	<0.020	<0.002	0.0020
Hf	0.068	0.049	0.082	0.018	0.019	<0.007	<0.053	<0.026	<0.006	0.009	<0.012	<0.25	<0.58	<0.19	0.0200	0.0300
Ta	0.11	0.13	0.13	0.22	0.20	0.20	0.031	0.013	0.009	0.011	0.012	1.40	1.16	0.23	0.18	0.15
Pb	0.55	0.46	0.50	5.86	5.46	6.84	1.08	0.82	0.98	0.98	0.83	1.25	1.68	1.43	0.68	0.73
Th	<0.005	0.002	<0.002	<0.004	<0.004	<0.003	0.043	0.12	0.056	0.036	0.088	<0.080	<0.15	<0.021	<0.004	<0.003
U	<0.008	<0.002	0.002	0.011	0.012	0.01	<0.018	0.046	0.030	0.026	0.038	0.069	<0.25	0.031	0.009	0.012

[1]: clusters of euhedral phlogopite around resorbed chromite

Table A4-7: Trace element composition of ***garnet*** (in µg/g) in pyroxenite xenoliths from Marsabit

	Group V: grt websterite												
sample	**1959/18**	**1959/18**	**1959/18**	**794/1**	**794/1**	**794/1**	**794/1**	**794/1**	**1960/4**	**1960/4**	**1960/4**	**1960/4**	**1960/4**
location	core	core	rim	core	core	core	rim	rim	core	core	core	core	rim
anal. Nr.	ob29f03	ob29f04	ob29f12	mc22d09	mc22d11	mc22d12	mc22d08	mc22d10	mc22e06	mc22e10	mc22e11	mc22e14	mc22e09
Li	0.44	0.36	0.60	0.43	0.60	0.30	0.33	0.67	0.53	0.29	0.33	0.31	0.28
P	197	195	208	170	182	187	171	176	73.0	73.5	75.9	73.3	73.0
K	<1.35	<1.45	<1.26	<0.78	1.01	<0.83	1.05	<0.81	<0.86	<0.71	<0.62	<0.78	<0.76
Sc	54.5	57.3	68.4	57.0	58.9	62.5	65.2	68.0	77.6	82.0	82.2	102.5	113.7
Ti	809	572	188	869	1197	1092	296	498	1135	1054	945	365	571
V	75.2	60.9	28.7	123	122	129	60.9	83.5	177	169	160	82.7	113
Ni	36.2	28.3	11.1	20.5	29.8	29.1	16.5	14.1	25.0	26.4	31.5	14.8	8.62
Zn	10.4	11.8	4.95	16.3	21.6	23.2	12.6	13.4	7.95	9.86	9.57	7.72	1.99
Ga	6.89	6.07	2.44	9.26	9.92	9.76	5.43	8.35	8.86	9.40	9.37	5.84	6.91
Rb	<0.016	<0.029	<0.016	0.007	<0.009	<0.010	0.019	<0.011	0.008	0.014	<0.007	<0.010	<0.012
Sr	0.023	0.022	0.029	0.46	0.40	0.098	0.18	0.025	0.023	0.062	0.062	<0.010	0.063
Y	36.8	35.0	46.1	24.5	23.9	24.5	26.1	24.3	31.3	30.3	29.6	31.5	32.6
Zr	15.2	16.7	14.7	10.2	16.8	12.2	7.63	8.45	18.9	17.7	15.7	10.4	9.8
Nb	<0.014	<0.008	<0.007	0.005	0.015	0.006	0.009	0.012	0.018	0.010	0.014	0.009	0.017
Cs	<0.003	<0.008	0.008	0.004	<0.003	0.009	<0.005	<0.003	<0.003	<0.003	<0.004	<0.004	0.003
Ba	<0.026	<0.061	<0.026	<0.033	<0.018	0.020	<0.019	<0.027	0.029	<0.028	<0.027	<0.027	<0.018
La	<0.004	<0.006	<0.007	0.008	0.021	<0.003	0.020	<0.006	<0.003	0.008	<0.003	<0.003	<0.003
Ce	0.018	0.013	0.012	0.032	0.039	0.011	0.019	0.012	0.018	0.014	0.003	<0.004	0.004
Pr	0.023	0.016	0.011	0.008	0.026	0.019	0.008	<0.004	0.017	0.011	0.005	0.003	<0.004
Nd	0.24	0.20	0.18	0.14	0.31	0.14	0.070	0.094	0.15	0.15	0.15	0.052	0.072
Sm	0.73	0.60	0.56	0.45	0.52	0.41	0.34	0.27	0.39	0.29	0.43	0.25	0.25
Eu	0.32	0.43	0.40	0.33	0.33	0.38	0.29	0.30	0.28	0.30	0.30	0.23	0.25
Gd	2.10	1.97	2.87	1.63	1.54	1.64	1.40	1.46	1.47	1.35	1.53	1.55	1.39
Tb	0.61	0.52	0.81	0.41	0.40	0.45	0.45	0.40	0.45	0.49	0.48	0.44	0.46
Dy	5.26	5.12	6.74	3.51	3.48	3.52	3.89	3.46	4.46	4.42	4.12	4.30	4.41
Ho	1.38	1.30	1.59	0.91	0.90	0.89	0.97	0.82	1.15	1.09	1.11	1.14	1.24
Er	4.23	4.28	4.81	2.83	2.78	2.77	2.72	2.64	4.08	3.54	3.48	3.69	4.07
Tm	0.72	0.63	0.74	0.45	0.39	0.42	0.44	0.41	0.63	0.57	0.54	0.59	0.65
Yb	5.08	4.37	5.09	3.42	2.84	3.13	3.38	3.14	4.82	4.53	4.53	4.45	5.27
Lu	0.79	0.73	0.74	0.49	0.46	0.46	0.46	0.42	0.78	0.69	0.66	0.62	0.78
Hf	0.20	0.23	0.14	0.099	0.29	0.21	0.070	0.098	0.59	0.45	0.37	0.20	0.20
Ta	<0.003	<0.005	<0.003	<0.002	<0.002	<0.002	0.01	<0.003	<0.002	0.003	<0.003	0.01	<0.002
Pb	<0.075	0.084	0.125	0.027	0.045	0.027	<0.021	0.035	0.035	0.031	0.025	0.024	0.024
Th	<0.005	<0.004	<0.004	0.005	<0.003	0.007	<0.004	<0.003	<0.004	<0.002	<0.002	<0.003	<0.003
U	<0.005	0.006	0.010	<0.002	0.004	<0.005	<0.004	0.004	<0.004	0.004	<0.003	0.003	0.003

Table A4-8: Trace element composition of ***carbonates**** (in µg/g) in peridotite xenoliths from Marsabit

	Group II				Group III-b			Group III-c						
Sample	**1958/13**	**1958/13**	**1958/13**	**1958/13**	**1959/15**	**1965/15**	**1965/15**	**785***	**1965/3**	**1965/3**	**1965/3**	**1965/3**	**1965/3**	**1965/3**
Mineral	Mg-calcite	Mg-calcite	Mg-calcite	Mg-calcite	dolomite	Mg-calcite	Mg-calcite	Mg-calcite	Mg-calcite	Mg-calcite	Mg-calcite	Mg-calcite	Mg-calcite	Mg-calcite
anal. Nr.	dd08a07	dd08a09	dd08a10	dd08a11	dd09c12	ob29c03	ob29c06	ob28e15	dd08c11	dd08d06	dd08d07	dd08d09	dd08d10	dd08d1
P	196	170	161	253	220	499	334	137	655	528	415	236	580	589
K	8.7	6.2	10.3	10.9	9.70	<8.71	21.2	6.4	4.2	13.5	6.6	4.9	10.5	15.5
Sc	1.54	<0.39	<0.43	0.2	<0.65	<0.28	<0.15	0.27	<0.24	<0.078	<0.10	<0.28	<0.27	<0.076
Ti	111	29.1	36.0	19.2	9.75	11.5	18.9	24.2	17.3	2.75	4.27	2.00	5.28	1.96
V	0.96	<0.50	0.71	0.21	<0.85	<0.84	0.48	<0.42	0.66	0.23	0.14	<0.33	<0.37	0.21
Ni	11.6	11.6	17.8	34.1	9.00	18.0	6.73	5.17	1.83	4.37	1.66	<2.443	<2.936	5.93
Zn	1.72	3.05	2.85	1.24	4.59	2.08	<0.89	1.13	4.76	0.72	1.20	4.77	2.96	0.45
Ga	n.a.	n.a.	n.a.	n.a.	n.a.	0.74	<0.14	<0.13	n.a.	n.a.	n.a.	n.a.	n.a.	n.a.
Rb	<0.12	<0.073	<0.084	0.036	0.08	<0.14	<0.072	<0.074	<0.045	0.028	<0.018	<0.050	<0.060	0.046
Sr	55.8	58.1	99.4	47.3	593	812	860	371	674	3502	776	340	251	4274
Y	3.99	0.57	0.83	0.74	0.12	0.23	0.11	1.30	0.62	0.061	0.17	1.02	7.04	0.15
Zr	1.20	0.48	0.65	0.47	2.61	0.94	0.24	0.12	2.41	4.86	0.87	0.28	0.97	7.56
Nb	0.80	0.58	0.53	0.33	1.44	0.95	0.19	0.06	27.7	2.14	3.67	3.61	6.92	1.85
Cs	0.087	<0.030	<0.026	<0.018	<0.063	<0.037	<0.011	<0.018	<0.017	<0.005	0.014	<0.027	<0.039	<0.008
Ba	0.44	<0.092	0.35	0.27	1.26	6.54	2.30	<0.24	0.29	34.8	3.72	<0.19	0.29	27.13
La	0.88	0.19	0.56	0.17	0.34	0.38	0.57	0.84	2.41	0.13	0.55	1.85	13.6	0.25
Ce	1.70	0.089	0.25	0.12	0.32	0.22	0.13	1.34	1.76	0.16	0.58	1.18	10.0	0.23
Pr	0.17	<0.017	0.042	<0.012	0.06	0.041	0.062	0.18	0.12	0.008	0.048	0.12	0.95	0.026
Nd	0.89	<0.16	0.18	0.13	0.30	0.11	0.13	0.68	0.10	0.08	0.15	0.55	2.28	0.08
Sm	0.26	<0.19	<0.12	0.082	<0.44	<0.12	<0.091	0.074	0.16	<0.046	0.039	<0.14	0.48	<0.018
Eu	0.095	<0.058	<0.043	<0.019	<0.12	<0.050	<0.019	0.051	<0.018	<0.006	<0.012	0.036	0.20	<0.008
Gd	0.46	<0.15	0.22	0.12	<0.37	<0.12	<0.090	0.14	<0.13	0.10	<0.024	<0.11	0.51	0.026
Tb	n.a.	n.a.	n.a.	n.a.	n.a.	<0.019	<0.010	0.036	n.a.	n.a.	n.a.	n.a.	n.a.	n.a.
Dy	0.36	<0.13	<0.14	0.14	<0.19	<0.11	<0.039	0.089	0.12	<0.038	<0.060	<0.090	0.58	<0.038
Ho	0.097	0.020	0.037	<0.018	<0.029	<0.019	0.013	0.044	<0.010	<0.006	<0.007	0.031	0.11	<0.006
Er	0.38	<0.11	<0.13	0.04	<0.117	<0.11	<0.041	0.083	<0.094	<0.028	<0.036	0.26	0.33	<0.019
Tm	0.075	<0.045	<0.020	<0.008	<0.052	0.02	<0.013	0.016	0.01	<0.006	<0.005	<0.017	0.08	<0.006
Yb	0.24	<0.17	<0.24	<0.032	<0.43	<0.12	<0.063	0.14	<0.066	<0.038	<0.056	<0.12	0.27	<0.040
Lu	<0.023	<0.030	<0.029	0.010	<0.072	<0.019	<0.010	0.011	0.039	<0.006	<0.008	<0.021	0.066	<0.008
Hf	<0.065	<0.11	<0.13	0.037	<0.16	<0.074	<0.038	<0.036	<0.073	<0.028	<0.023	<0.075	<0.074	<0.013
Ta	<0.036	<0.026	<0.045	<0.016	0.048	<0.024	<0.012	<0.016	0.019	<0.007	<0.012	<0.033	<0.031	0.008
Pb	<0.15	0.13	0.17	0.21	<0.24	48.8	8.58	<0.21	1.54	0.10	0.20	0.44	0.74	0.18
Th	<0.039	<0.021	<0.032	<0.008	0.021	0.028	<0.020	<0.017	<0.011	<0.010	<0.006	<0.023	<0.028	<0.005
U	0.14	0.086	0.072	0.27	0.60	0.90	0.94	0.86	4.69	2.03	3.19	1.75	6.00	1.48

*: always rounded globules enclosed by silicate glass; n.a.: not analysed

Table A4-9: Trace element composition of ***apatite*** (in µg/g) in peridotite xenoliths from Marsabit

	Group II-b			Group II-c				
Sample	**1959/15**	**1959/15**	**1959/15**	**1965/3**	**1965/3**	**1965/3**	**1965/3**	**1965/3**
Texture	globules in glass	globules in glass	globules in glass	interstitial	interstitial	interstitial	interstitial	interstitial
anal. Nr.	dd09b14	dd09b15	dd09b16	dd08e03	dd08e04	dd08e06	dd08e07	dd08e09
P	129717	140632	141021	146367	153699	146537	139419	150168
K	109.7	42.6	41.5	85.6	60.9	90.0	89.7	64.4
Sc	2.42	2.11	1.87	<1.30	1.37	1.42	0.79	1.17
Ti	23.5	7.06	3.15	<7.19	<5.96	6.00	<2.94	<4.86
V	3.65	2.03	1.28	6.14	9.13	8.29	3.82	9.28
Ni	12.1	2.85	<5.57	<15.2	<13.46	<8.44	3.97	<9.72
Zn	1.19	2.93	0.84	<2.50	<1.55	<2.01	0.96	<2.11
Ga	n.a.	n.a.	n.a.	n.a.	n.a.	n.a.	n.a.	n.a.
Rb	0.15	0.082	0.11	<0.22	0.17	0.73	0.49	0.31
Sr	7138	7288	7792	28306	30727	40953	42233	32539
Y	98.8	104	103	1046	1143	1512	1454	1143
Zr	3.07	0.56	0.69	1.16	1.10	0.94	1.01	0.64
Nb	0.24	<0.046	0.036	0.17	0.27	0.20	0.20	0.25
Cs	<0.013	<0.022	<0.038	<0.14	<0.089	<0.090	<0.036	<0.080
Ba	139	117	139	93.9	69.4	103	126	81.7
La	7460	8053	8246	14841	17630	19588	19048	18376
Ce	6844	7230	7547	22143	26241	27034	25945	26781
Pr	380	396	394	1971	2251	2230	2212	2339
Nd	749	816	787	6317	7271	6609	6530	7378
Sm	51.5	55.3	50.8	692	805	766	747	791
Eu	14.7	14.9	15.2	181	202	194	189	198
Gd	31.4	34.1	33.2	457	467	468	451	474
Tb	n.a.	n.a.	n.a.	n.a.	n.a.	n.a.	n.a.	n.a.
Dy	19.8	18.3	19.7	231	231	287	281	238
Ho	3.59	3.81	3.97	38.6	39.3	51.7	51.1	42.4
Er	9.03	9.57	9.67	72.6	82.3	117.1	119.2	84.4
Tm	1.19	1.21	1.28	7.87	8.83	14.25	13.81	9.74
Yb	8.03	8.10	7.16	33.2	39.5	72.3	72.4	41.1
Lu	1.15	1.24	1.29	3.05	3.48	8.05	7.42	4.22
Hf	<0.023	<0.046	<0.088	<0.44	<0.22	<0.30	<0.12	<0.16
Ta	<0.015	<0.019	<0.051	<0.11	<0.078	<0.12	<0.075	<0.12
Pb	43.6	42.2	46.0	6.18	3.18	5.14	5.77	4.15
Th	2538	2659	2662	346	248	1278	1305	303
U	572	615	582	71.9	53.7	269	278	67.2

n.a.: not analysed

Table A4-10: Trace element composition of ***silicate glass*** (in µg/g) in peridotite xenoliths from Marsabit

	Group I							Group II							Group III-b				
Sample	**1963/1**	**1963/1**	**1963/1**	**1963/1**	**1963/1**	**1963/1**	**1963/1**	**1958/13**	**1958/13**	**1958/13**	**1958/13**	**1959/25**	**1959/25**	**1959/25**	**1959/15**	**1959/15**	**1959/15**	**1959/15**	**1959/15**
Texture	gr.bdr.	gr.bdr.	m.p.	m.p.	m.p.	within sympl.	within sympl.	within sympl.	within sympl.	within sympl.	within sympl.	within sympl.	within sympl.	within sympl.	m.p.	m.p.	m.p.	m.p.	m.p.
anal. Nr.	ob29e03	ob29e04	ob29e07	ob29e08	ob29e09	ob29e14	ob29e15	dd08a08	dd08a12	dd08a13	dd08a15	dd09a03	dd09a04	dd09a05	dd09c05	dd09c11	dd09c13	dd09c14	dd09c15
P	175	174	130	102	109	114	126	179	271	166	96.0	157	192	144	1061	1074	899	995	947
K	5085	4725	25085	23999	20232	15306	15555	8111	9424	9147	3553	254	283	419	12563	12628	13983	13562	13497
Sc	32.3	28.2	30.2	30.9	27.5	29.9	27.6	69.4	61.2	69.6	30.5	15.0	13.3	13.2	1.79	4.45	<1.87	1.57	1.65
Ti	11401	8807	12900	12442	10662	9008	9477	14226	14713	15877	6385	5925	6046	6346	665	732	591	626	718
V	69.7	50.5	95.6	87.3	74.3	67.3	65.9	390	415	447	167	118	121	119	107	144	108	112	120
Ni	55.8	30.9	27.6	77.1	72.9	18.7	21.6	49.1	<104	<40.4	38.0	23.0	<26.2	33.9	12.8	35.1	17.5	<12.9	<20.0
Zn	44.4	52.3	52.0	40.99	43.2	34.5	47.82	21.8	34.0	34.4	11.8	13.5	13.0	11.5	9.62	8.79	9.48	5.86	9.29
Ga	8.47	8.99	9.77	9.63	10.3	9.85	11.0	n.a.	n.a.	n.a.	n.a.	n.a.	n.a.	n.a.	n.a.	n.a.	n.a.	n.a.	n.a.
Rb	1.04	1.08	24.6	23.5	19.4	9.23	8.53	10.8	15.0	12.4	4.83	<0.32	<0.65	0.43	18.1	18.4	18.2	18.9	20.6
Sr	167	155	146	138	144	145	147	289	315	326	151	256	243	257	427	431	420	455	423
Y	29.2	29.8	16.3	17.2	17.1	18.3	19.3	33.9	26.1	34.7	15.6	13.3	13.2	13.9	5.43	6.41	5.45	6.86	7.39
Zr	54.3	57.6	36.1	34.1	38.7	45.4	43.1	59.8	59.5	71.5	26.0	70.9	66.8	74.3	4.66	5.28	4.25	4.95	5.83
Nb	5.66	3.94	4.94	5.38	4.83	3.82	4.57	63.8	68.4	65.1	27.0	2.55	1.93	2.88	4.16	4.54	6.18	6.56	10.2
Cs	<0.054	0.042	0.41	0.28	0.11	0.048	<0.12	0.078	<0.59	<0.39	<0.14	<0.13	<0.23	<0.085	0.14	0.19	<0.12	0.24	0.14
Ba	18.9	16.8	174	160	127	57.2	48.4	536	561	553	220	13.7	14.2	9.5	238	244	243	259	217
La	1.67	1.87	1.70	1.58	1.55	1.30	1.44	13.7	11.8	15.0	5.89	2.95	3.57	3.36	69.8	64.9	60.6	65.0	64.1
Ce	6.27	5.73	5.16	4.92	5.13	5.17	5.20	20.3	15.4	21.7	9.06	8.44	8.05	8.79	94.7	93.5	85.3	97.3	98.2
Pr	1.23	1.01	0.89	0.73	0.91	1.00	0.87	2.20	1.42	2.32	0.88	1.32	0.93	1.74	6.55	6.88	5.72	6.60	7.93
Nd	4.87	5.76	5.98	5.64	5.07	5.71	4.98	11.1	6.96	16.9	6.20	5.03	6.18	5.78	14.6	15.5	14.1	15.0	17.2
Sm	2.13	2.34	1.53	2.12	2.13	2.17	2.06	3.57	2.48	3.17	1.36	1.62	<1.27	1.81	1.42	1.54	1.41	1.43	1.55
Eu	1.52	1.07	0.73	0.93	0.75	0.90	0.71	1.18	<0.86	1.04	0.55	0.78	1.69	0.67	0.41	0.57	0.62	0.60	0.53
Gd	3.76	2.49	2.56	2.22	2.17	2.35	2.60	4.47	<3.29	4.65	2.34	2.57	1.31	2.00	0.62	<0.54	<0.55	0.90	1.43
Tb	0.62	0.76	0.44	0.36	0.37	0.45	0.50	n.a.	n.a.	n.a.	n.a.	n.a.	n.a.	n.a.	n.a.	n.a.	n.a.	n.a.	n.a.
Dy	5.19	4.41	2.83	2.82	2.88	3.35	2.87	5.72	7.27	4.61	2.03	1.88	2.32	2.68	0.90	1.22	<0.82	0.71	0.95
Ho	1.20	1.02	0.63	0.56	0.69	0.74	0.59	1.36	1.45	1.19	0.37	0.59	<0.20	0.76	0.23	0.22	0.16	0.29	0.35
Er	2.90	2.50	1.83	1.46	1.46	2.13	2.67	3.84	2.02	3.47	1.26	1.86	1.28	1.79	0.45	0.60	0.79	0.52	0.70
Tm	0.57	0.50	0.20	0.30	0.30	0.24	0.27	0.53	0.95	<0.44	0.29	0.15	0.34	0.15	0.09	<0.097	<0.11	<0.14	0.17
Yb	3.83	3.72	2.27	2.09	1.72	1.55	2.20	3.66	5.43	3.01	2.36	1.36	1.62	1.99	0.62	<0.66	<1.21	0.96	0.86
Lu	0.54	0.49	0.25	0.39	0.29	0.33	0.43	0.52	<0.59	0.49	0.45	0.22	0.17	0.25	0.14	<0.15	<0.11	0.20	<0.15
Hf	1.29	0.99	1.14	0.81	1.07	0.73	1.25	1.61	<4.20	2.98	0.77	1.54	<0.90	1.94	0.26	<0.21	<0.52	<0.23	<0.45
Ta	0.12	<0.12	0.18	0.068	0.065	0.12	0.17	2.05	2.88	1.99	0.77	<0.12	<0.33	0.15	<0.080	<0.11	<0.17	<0.098	<0.17
Pb	1.07	0.70	0.73	0.73	0.60	0.89	1.08	0.59	<3.41	<1.63	<0.40	0.64	<0.90	0.69	5.41	5.68	6.57	6.04	4.63
Th	<0.12	0.052	0.053	0.061	0.027	0.058	0.045	1.55	1.79	1.98	0.71	0.33	0.58	0.39	19.4	16.4	14.6	14.7	12.9
U	<0.11	<0.12	0.029	<0.035	<0.020	<0.025	<0.061	0.34	<0.72	0.35	0.15	<0.094	<0.15	0.055	5.45	5.13	4.61	4.67	4.11

gr.bdr.: glass lining olivine or pyroxenes along grain boundaries; m.p.: glass associated with microlites in melt pockets; n.a.: not analysed

Table A4-10: Trace element composition of ***silicate glass*** (in µg/g) in peridotite xenoliths from Marsabit (continued)

					Group III-c														
Sample	**1965/15**	**1965/15**	**1965/15**	**1965/15**	**785***	**785***	**785***	**1959/27**	**1959/27**	**1959/27**	**1959/27**	**1959/27**	**1959/27**	**1959/27**	**1965/3**	**1965/3**	**1965/3**	**1965/3**	**1965/3**
Texture	m.p.	m.p.	m.p.	xenolith edge	gr.bdr.	m.p.	m.p.	m.p.	m.p.	m.p.	m.p.	m.p.	m.p.	m.p.	next Opx_m	next Opx_m	m.p.	m.p.	m.p.
anal. Nr.	ob29c09	ob29c11	ob29c18	ob29c04	ob28e03	ob28e09	ob28e16	dd08f07	dd08f09	dd08f10	dd08f13	dd08g06	dd08g07	dd08g08	dd08c07	dd08c08	dd08c12	dd08c15	dd08c16
P	471	448	1177	1610	175	230	246	3596	3155	3435	3291	2763	2994	2837	755	676	2330	2178	1946
K	18786	16408	12789	39599	20093	32515	26196	29943	29622	27573	30114	25607	25900	23950	10377	10071	7991	8563	8506
Sc	2.34	1.84	4.90	1.26	7.35	4.06	6.21	13.7	15.6	11.5	9.46	6.92	6.91	8.54	7.78	8.48	9.02	9.82	9.76
Ti	7924	7329	7270	4974	3347	2953	3334	21334	21717	19200	21154	17158	18199	17677	1084	1055	1275	1208	1171
V	28.8	26.5	37.0	23.5	104	79.6	107	286	278	269	265	213	234	232	143	134	206	179	177
Ni	46.1	37.1	<16.2	9.21	198	<5.75	<40.8	29.8	35.9	29.6	40.7	32.3	19.9	20.1	<28.8	<29.8	8.20	7.58	9.04
Zn	9.02	10.3	7.59	109	15.6	11.0	12.4	94.4	85.0	76.5	94.2	84.4	81.9	87.7	24.9	30.9	41.0	36.5	35.4
Ga	15.3	17.3	19.4	27.3	18.5	19.4	20.6	n.a.	n.a.	n.a.	n.a.	n.a.	n.a.	n.a.					
Rb	38.2	26.3	14.8	124	23.4	54.6	36.4	67.3	63.4	61.9	64.7	56.1	57.7	52.0	35.9	36.9	8.62	15.4	14.9
Sr	440	488	583	1407	190	188	227	1142	1077	1007	1117	989	1062	963	1055	985	2349	1894	1816
Y	1.87	1.45	2.19	22.4	6.83	7.52	7.62	36.9	37.1	32.9	36.9	27.1	30.1	30.2	38.9	36.9	74.9	60.3	58.4
Zr	10.1	17.1	26.6	353	11.6	7.61	9.69	296	293	263	276	216	242	240	41.6	42.8	60.0	48.6	45.7
Nb	18.0	16.1	9.99	137	1.44	2.60	3.73	93.3	94.0	89.6	95.8	81.8	83.7	82.5	183	169	241	213	210
Cs	0.59	0.46	0.19	1.86	0.42	1.25	0.64	0.68	0.70	0.84	0.74	0.63	0.63	0.68	0.54	0.52	0.10	0.25	0.16
Ba	329	261	137	1064	48.2	129	107	689	654	609	687	597	625	562	660	641	316	371	365
La	16.8	18.3	28.4	84.8	15.2	14.4	19.5	67.2	64.5	59.5	63.7	52.3	53.7	55.4	116	106	385	323	303
Ce	24.7	25.6	37.4	131	29.5	30.8	35.7	128	126	114	125	100	104	103	187	164	559	453	433
Pr	2.01	1.94	2.94	12.0	3.26	3.30	3.30	15.4	14.9	13.0	14.5	11.3	12.0	12.2	15.9	16.0	47.0	39.8	38.2
Nd	5.58	6.03	9.62	40.8	10.86	10.13	11.59	60.7	59.7	54.0	58.1	42.2	46.3	51.2	52.8	56.4	143.7	127	117
Sm	1.15	0.48	0.85	5.70	1.11	1.79	3.19	13.0	14.5	11.6	11.5	8.07	10.5	9.15	7.70	6.79	20.1	16.9	14.8
Eu	0.58	0.35	0.34	2.28	0.72	0.82	0.48	4.80	4.92	3.54	3.61	3.28	3.45	3.47	2.65	2.41	5.75	6.03	4.63
Gd	0.69	0.51	0.57	4.15	1.12	1.58	2.27	9.39	10.82	8.58	8.92	6.35	6.77	8.89	2.58	5.66	13.3	12.0	10.8
Tb	<0.036	0.086	0.10	0.86	0.21	0.20	0.25	n.a.	n.a.	n.a.	n.a.	n.a.	n.a.	n.a.					
Dy	0.33	0.27	0.50	3.59	0.81	0.98	1.50	8.00	8.92	6.30	7.99	6.32	7.32	6.32	4.97	6.37	12.5	9.37	10.4
Ho	0.048	0.037	<0.044	1.05	0.18	0.25	0.13	1.41	1.61	1.53	1.40	1.27	1.17	1.06	1.79	1.04	2.13	1.95	2.00
Er	0.30	0.38	0.25	1.95	0.74	0.58	<0.55	3.09	4.12	3.16	3.31	2.53	3.05	3.09	1.82	2.64	6.85	5.31	5.38
Tm	<0.058	<0.039	0.032	0.33	0.043	0.081	0.12	0.36	0.48	0.53	0.54	0.28	0.36	0.34	0.52	<0.142	1.03	0.94	0.90
Yb	<0.23	0.23	<0.19	2.67	0.92	0.44	0.72	2.99	3.45	1.79	3.25	2.51	2.53	3.08	2.87	4.87	7.78	5.30	4.94
Lu	<0.051	0.050	<0.030	0.26	0.096	0.041	0.10	0.61	0.54	0.30	0.42	0.40	0.40	0.36	0.57	0.58	0.85	0.90	0.66
Hf	0.32	0.52	1.63	5.35	0.50	0.14	<0.33	7.22	5.91	6.86	6.75	3.96	5.68	4.30	1.38	1.24	0.54	0.94	0.65
Ta	0.44	0.33	0.16	6.38	<0.053	0.022	<0.073	4.73	5.05	4.21	5.29	4.28	3.94	3.96	7.33	8.01	9.83	9.16	8.61
Pb	46.9	44.8	34.3	28.0	3.44	2.55	3.86	5.20	4.80	4.68	5.57	4.57	4.93	4.51	5.50	7.49	10.5	7.66	7.57
Th	3.02	2.96	5.02	16.0	4.83	4.66	7.15	7.33	6.61	6.25	6.85	6.01	5.34	5.54	11.7	10.5	32.5	27.0	25.4
U	0.72	0.69	1.18	4.78	1.04	0.99	1.08	2.06	1.61	1.53	2.03	1.60	1.71	1.67	3.19	2.16	8.00	6.80	5.81

gr.bdr.: glass lining olivine or pyroxenes along grain boundaries; m.p.: glass associated with microlites in melt pockets; n.a.: not analysed

Table A4-10: Trace element composition of ***silicate glass*** (in µg/g) in peridotite xenoliths from Marsabit (continued)

Sample	**1965/3**	**1965/3**	**1965/3**	**1965/3**	**1965/3**	**1965/3**	**1965/3**	**1965/25**	**1965/25**	**1965/25**
Texture	m.p.	m.p.	m.p.	m.p.	m.p.	next apatite	next apatite	m.p.	m.p.	m.p.
anal. Nr.	dd08d04	dd08d08	dd08d12	dd08d13	dd08d14	dd08e05	dd08e08	as12a06	as12a09	as12a10
P	1440	1392	1466	1497	1519	6607	6738	413	326	372
K	9585	8790	9255	9111	9265	10340	11277	8175	10300	7919
Sc	12.3	9.75	10.3	10.0	9.70	15.7	13.6	3.61	0.98	7.17
Ti	1214	1172	1204	1219	1213	1091	1163	1463	1275	1900
V	195	191	202	200	210	146	151	75.3	59.7	128
Ni	11.1	10.1	12.0	17.4	17.0	<5.41	<19.9	7.19	6.38	45.6
Zn	33.9	39.4	39.5	36.1	44.0	55.2	50.8	38.8	29.8	36.1
Ga								15.2	14.3	16.2
Rb	18.5	17.9	18.8	18.4	17.6	39.3	39.8	4.50	4.06	4.08
Sr	1555	1501	1570	1548	1644	4564	4997	616	571	561
Y	56.0	56.8	60.5	57.5	61.9	165	158	27.1	17.0	33.4
Zr	56.9	54.2	58.9	57.2	57.8	39.2	36.5	51.9	42.8	51.9
Nb	232	222	235	233	234	161	164	95.6	88.2	98.7
Cs	0.32	0.30	0.33	0.33	0.22	0.78	1.02	<0.033	0.044	0.050
Ba	459	441	441	412	405	1048	1099	146	109	108
La	205	205	214	215	221	994	1008	89.3	57.7	83.5
Ce	316	306	323	323	333	1273	1265	138	89.3	152
Pr	30.4	28.5	29.8	28.1	30.4	94.3	97.5	10.7	7.53	14.2
Nd	94.4	91.1	102	95.3	99.3	260	256	35.5	21.4	46.8
Sm	14.3	13.4	14.5	16.0	14.1	32.8	37.9	4.86	2.72	7.75
Eu	4.11	4.49	4.17	3.81	4.38	9.67	10.3	1.42	0.73	2.29
Gd	8.35	9.80	10.4	9.82	10.6	22.4	24.5	4.22	2.61	6.00
Tb								0.77	0.46	0.99
Dy	8.67	9.34	10.0	10.0	10.4	23.9	17.1	4.40	2.81	5.73
Ho	2.20	1.93	2.05	2.11	2.06	4.49	4.46	0.93	0.62	1.21
Er	4.20	4.39	5.26	5.87	6.11	14.9	15.3	2.12	1.66	3.41
Tm	0.77	0.84	0.88	0.79	0.85	2.18	2.92	0.33	0.27	0.51
Yb	6.91	6.68	6.07	6.21	6.67	14.7	12.0	3.27	2.00	3.64
Lu	0.51	0.60	0.84	0.98	0.80	1.57	1.40	0.41	0.30	0.52
Hf	1.25	0.78	1.14	1.00	1.10	0.73	<0.87	0.67	0.49	0.57
Ta	9.55	9.22	10.1	9.62	10.1	6.31	7.84	0.93	0.80	0.99
Pb	7.61	6.98	8.05	8.14	7.97	22.9	26.0	6.69	5.45	5.51
Th	18.7	17.6	18.5	18.1	18.5	271	247	7.54	4.56	5.36
U	4.47	4.00	4.49	3.99	4.47	73.3	72.4	1.53	0.99	1.22

gr.bdr.: glass lining olivine or pyroxenes along grain boundaries; m.p.: glass associated with microlites in melt pockets; n.a.: not analysed

Appendix A5

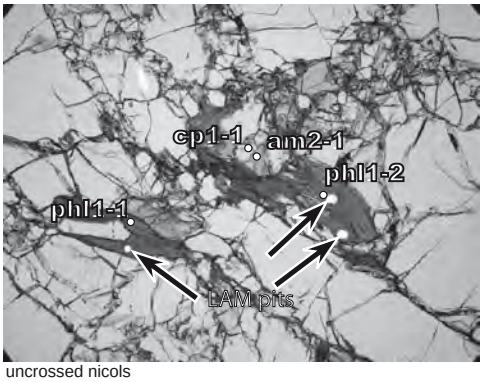
SIMS (Li, Be, and B) data

including
SIM spot localisation

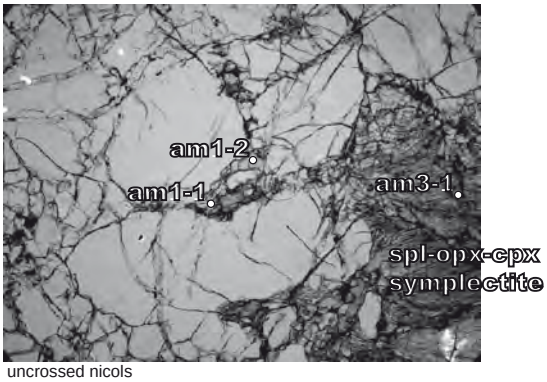
and

all analyses

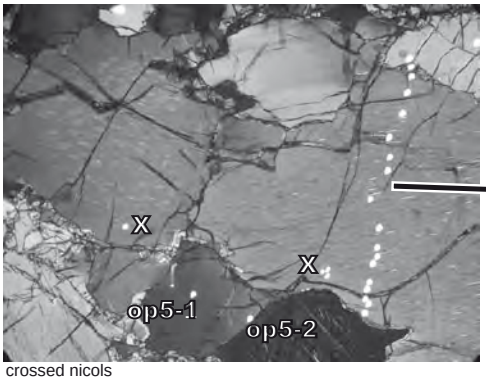
Ke 1963/2: Group I - porphyroclastic (grt)-spl lherzolite



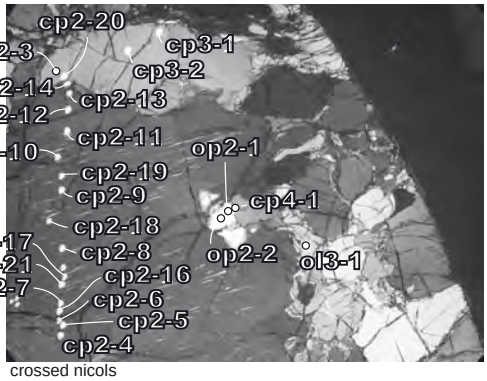
uncrossed nicols



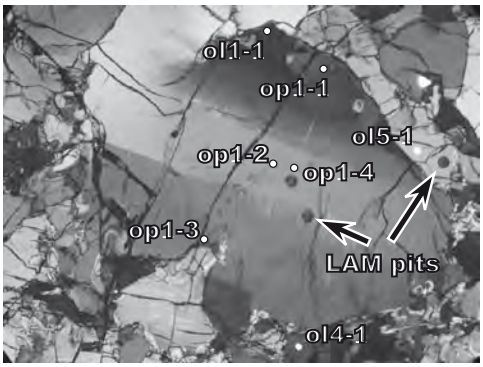
uncrossed nicols



crossed nicols



crossed nicols



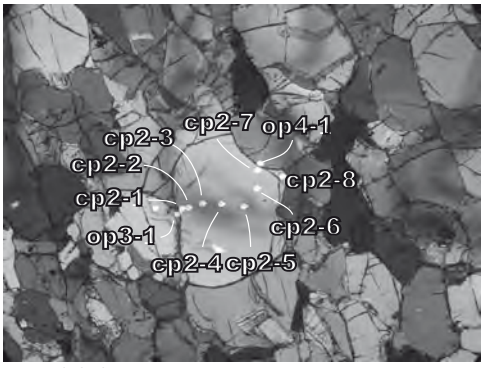
crossed nicols

op = orthopyroxene
cp = clinopyroxene
ol = olivine
am = amphibole
phl = phlogopite
gl = silicate glass
X = spots resulting from beam regulation

Ke 1958/13: Group II - tabular recrystallised (grt)-spl lherzolite



crossed nicols

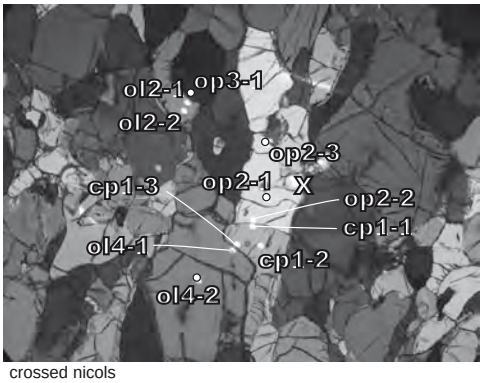


crossed nicols

Ke 1958/13: Group II -tabular recrystallised (grt)-spl lherzolite *(continued)*

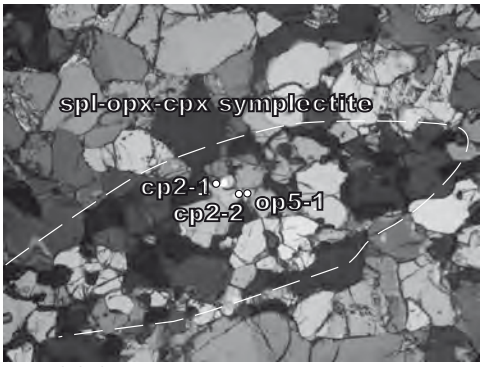


crossed nicols

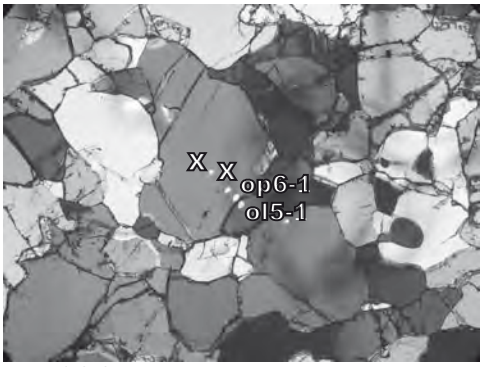


crossed nicols

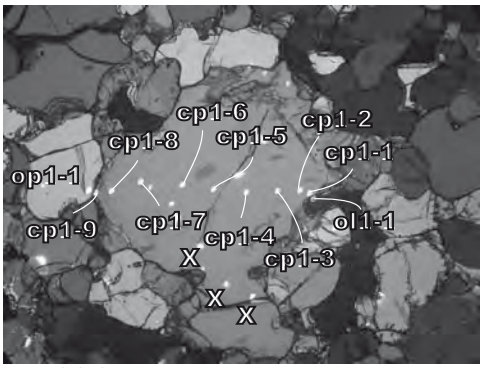
Ke 1958/20: Group II - granuloblastic recrystallised (grt)-spl lherzolite



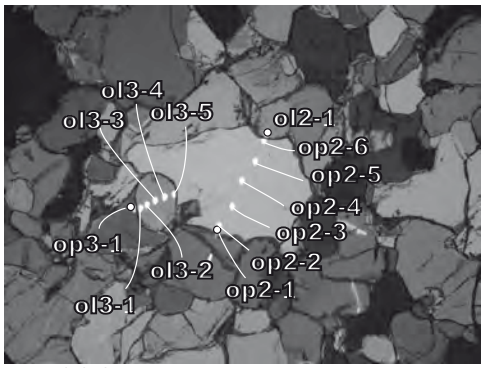
crossed nicols



crossed nicols

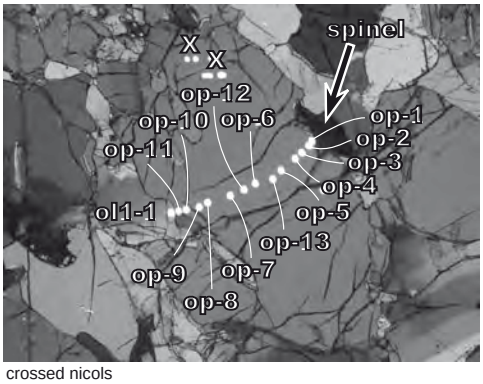


crossed nicols

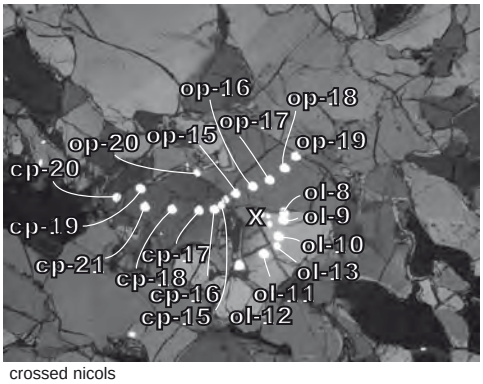


crossed nicols

Ke 1965/1: Group III-a - porphyroclastic spl harzburgite

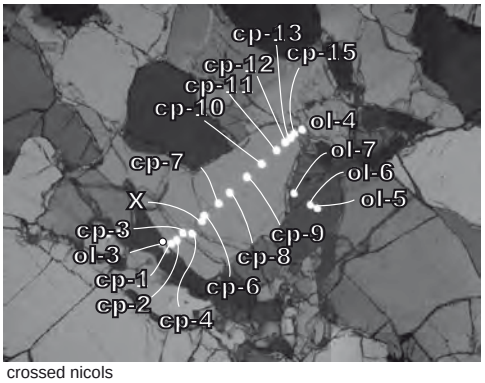


crossed nicols

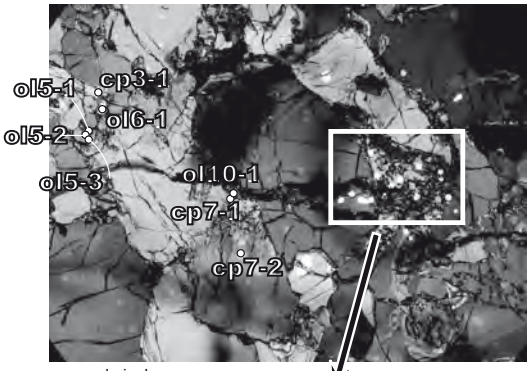


crossed nicols

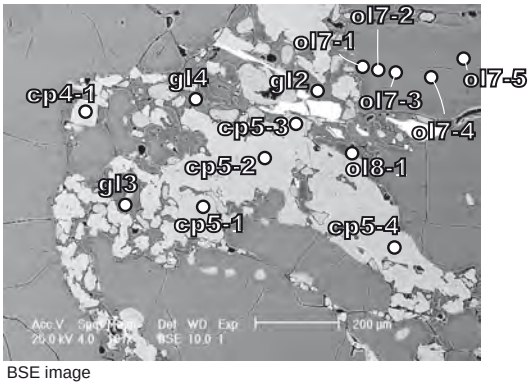
Ke 1965/1: Group III-a - porphyroclastic spl harzburgite *(continued)*



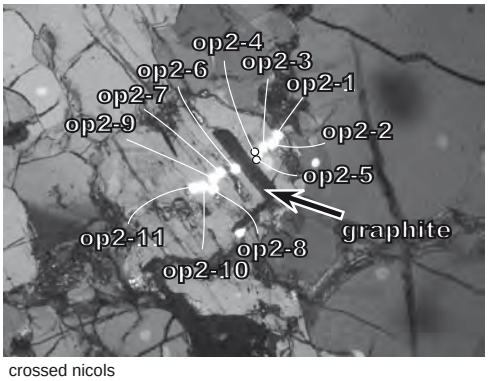
crossed nicols



crossed nicols

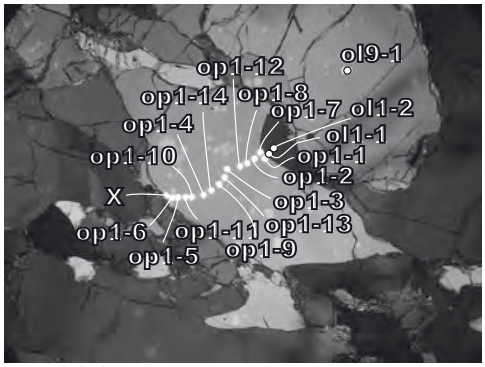


BSE image

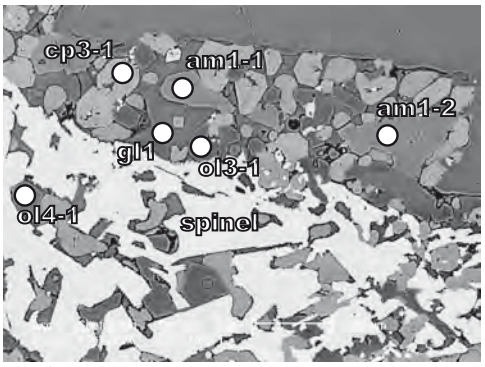


crossed nicols

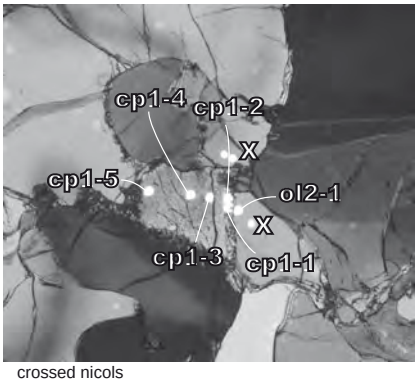
Ke 1965/15: Group III-b - porphyroclastic spl harzburgite



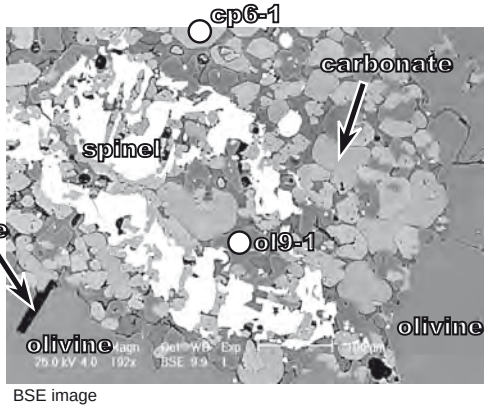
crossed nicols



BSE image

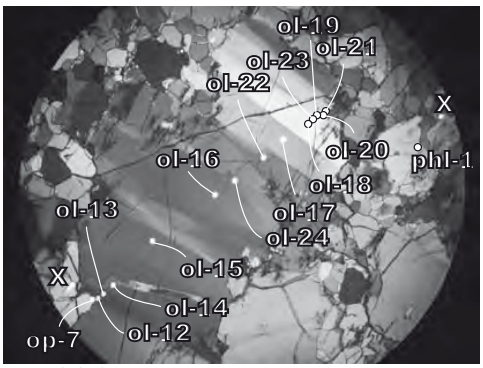


crossed nicols

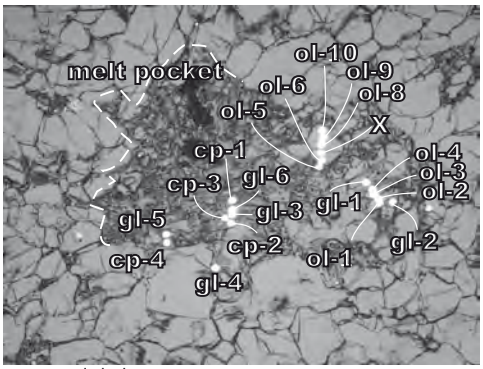


BSE image

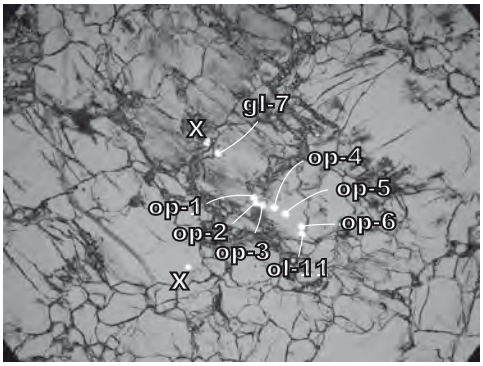
Ke 1965/3: Group III-c - porphyroclastic spl dunite *(continued)*



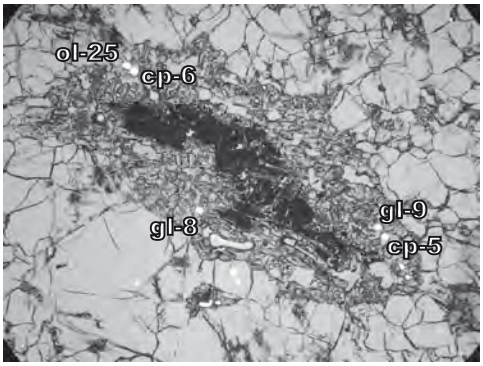
crossed nicols



uncrossed nicols

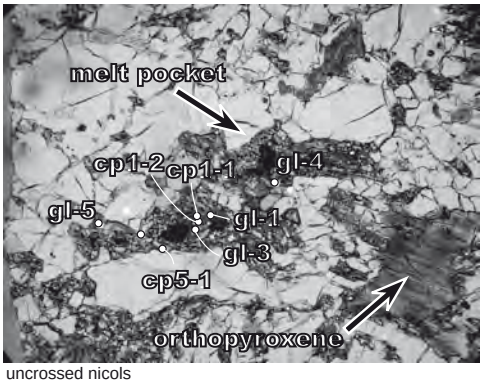


uncrossed nicols

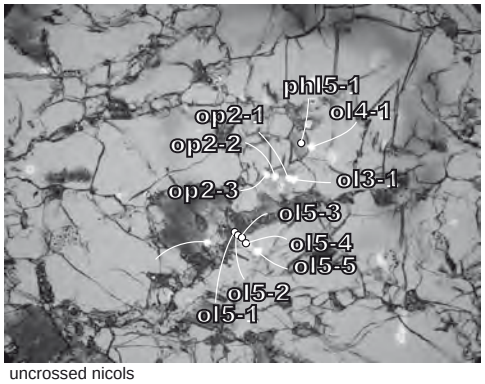


uncrossed nicols

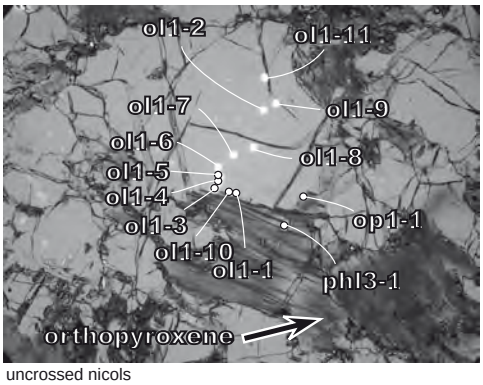
Ke 785*: Group III-c - porphyroclastic amph-phl-spl harzburgite



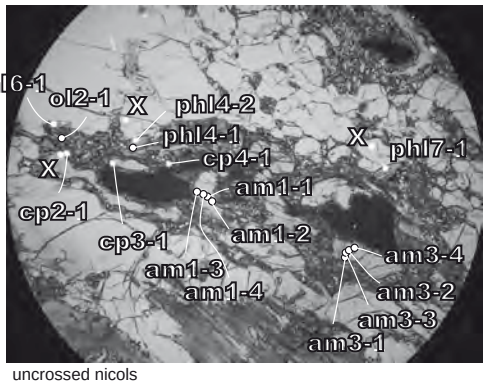
uncrossed nicols



uncrossed nicols



uncrossed nicols



uncrossed nicols

Table A5-1: Li, Be and B concentrations (µg/g) in minerals of xenolith Ke 1963/2 (Group I)

Nr.	Mineral	description	Distance [µm] (for profiles)	Li	2σ	Be	2σ	B	2σ
ol1-1	ol-I	rim; adjacent opx-I		1.337	0.037	0.0004	0.001	0.059	0.015
ol3-1	ol-IIa	core		1.357	0.026	0.001	0.001	0.050	0.014
ol4-1	ol-IIa	core		1.277	0.039	0.001	0.001	0.038	0.009
ol5-1	ol-IIa	rim; adjacent opx-I		1.270	0.031	0.0003	0.0004	0.041	0.009
op1-1	opx-I	rim; adjacent to cpx-I		0.672	0.016	0.009	0.002	0.040	0.007
op1-2	opx-I	core		0.645	0.023	0.012	0.002	0.059	0.009
op1-3	opx-I	rim; adjacent to cpx-Ia		0.617	0.031	0.008	0.003	0.044	0.013
op1-4	opx-I	core		0.635	0.034	0.010	0.002	0.063	0.008
op2-1	opx-IIa	rim; adjacent to cpx-IIa		0.710	0.019	0.010	0.002	0.041	0.008
op2-2	opx-IIa	core		0.704	0.020	0.010	0.002	0.039	0.008
op5-1	opx-I	core		0.558	0.016	0.007	0.002	0.048	0.007
op5-2	opx-I	rim; adjacent to cpx-I		0.642	0.025	0.013	0.004	0.054	0.012
cp2-4	cpx-I	rim; adjacent to cpx-I	21	0.675	0.034	0.093	0.006	0.067	0.019
cp2-5	cpx-I	rim; adjacent to cpx-I	82	0.763	0.029	0.094	0.009	0.073	0.012
cp2-15	cpx-I	core	122	0.768	0.015	0.089	0.006	0.053	0.011
cp2-6	cpx-I	core	204	0.820	0.028	0.094	0.008	0.054	0.004
cp2-16	cpx-I	core	265	0.810	0.019	0.081	0.003	0.062	0.007
cp2-7	cpx-I	core	429	0.813	0.024	0.100	0.009	0.074	0.009
cp2-21	cpx-I	core	520	0.815	0.019	0.090	0.006	0.069	0.012
cp2-17	cpx-I	core	632	0.811	0.028	0.086	0.006	0.053	0.008
cp2-8	cpx-I	core	816	0.823	0.030	0.084	0.007	0.067	0.012
cp2-18	cpx-I	core	1061	0.804	0.021	0.094	0.007	0.067	0.009
cp2-9	cpx-I	core	1265	0.835	0.020	0.093	0.005	0.049	0.011
cp2-19	cpx-I	core	1449	0.842	0.030	0.098	0.005	0.062	0.010
cp2-10	cpx-I	core	1571	0.916	0.031	0.096	0.011	0.064	0.009
cp2-11	cpx-I	core	1796	0.942	0.028	0.092	0.008	0.062	0.009
cp2-12	cpx-I	core	2000	0.870	0.022	0.087	0.005	0.060	0.010
cp2-13	cpx-I	core	2143	0.935	0.022	0.083	0.006	0.053	0.014
cp2-14	cpx-I	core	2225	0.883	0.022	0.061	0.004	0.050	0.012
cp2-20	cpx-I	rim; vicinity to glass	2265	0.941	0.019	0.065	0.007	0.056	0.005
cp2-3	cpx-I	rim; vicinity to glass	2326	1.012	0.029	0.073	0.011	0.061	0.018
cp1-1	cpx-IIa	neoblast; adjacent to pargasite		0.588	0.037	0.057	0.006	0.064	0.015
cp4-1	cpx-IIa	rim; adjacent to opx-IIa		0.771	0.017	0.081	0.006	0.070	0.017
cp3-1	cpx-I	rim; adjacent to phlogopite		0.921	0.025	0.066	0.006	0.052	0.009
cp3-2	cpx-I	core		1.053	0.025	0.076	0.005	0.061	0.011
am1-1	pargasite	amph-i; core		0.695	0.030	0.195	0.014	0.137	0.028
am1-2	pargasite	amph-i; core		0.643	0.024	0.205	0.009	0.196	0.019
am2-1	pargasite	amph-i; adjacent to phlogopite		0.488	0.025	0.198	0.019	0.129	0.026
am3-1	pargasite	amph-ii; within symplectite		0.480	0.016	0.216	0.018	0.168	0.011
phl1-1	phlogopite	core		0.858	0.032	0.126	0.006	0.708	0.031
phl1-2	phlogopite	core		0.732	0.030	0.040	0.005	0.867	0.064

Table A5-2: Li, Be and B concentrations (µg/g) in minerals of xenolith Ke 1958/13 (Group II)

Nr.	Mineral	decription	Distance [µm] (for profiles)	Li	2σ	Be	2σ	B	2σ
ol1_1	ol-I	rim; adjacent opx-I		1.481	0.033	0.002	0.001	0.068	0.014
ol2_1	ol-I	rim; adjacent opx-I		1.497	0.041	0.002	0.001	0.068	0.014
ol2_2	ol-I	core		1.421	0.033	0.003	0.001	0.076	0.011
ol3-1	ol-I	core		1.364	0.028	0.001	0.001	0.070	0.011
ol4_1	ol-I	rim; adjacent opx-I		1.465	0.044	0.001	0.001	0.082	0.012
ol4_2	ol-I	core		1.536	0.033	0.001	0.001	0.086	0.011
ol5_1	ol-I	rim; adjacent opx-I		1.441	0.029	0.002	0.001	0.086	0.021
ol6_1	ol-I	rim; adjacent cpx-I		1.331	0.043	0.003	0.001	0.063	0.010
op1_1	opx-I	rim; adjacent to ol-I	16	0.656	0.012	0.034	0.004	0.056	0.007
op1_2	opx-I	core	129	0.744	0.016	0.037	0.003	0.068	0.017
op1_3	opx-I	core	290	0.758	0.025	0.036	0.003	0.068	0.010
op1_4	opx-I	core	645	0.780	0.025	0.041	0.004	0.058	0.008
op1_11	opx-I	core	806	0.774	0.023	0.042	0.003	0.068	0.012
op1_5	opx-I	core	1032	0.757	0.030	0.040	0.004	0.065	0.007
op1_6	opx-I	core	1516	0.801	0.018	0.042	0.004	0.073	0.013
op1_7	opx-I	core	1855	0.861	0.026	0.040	0.005	0.072	0.016
op1_10	opx-I	core	2210	0.745	0.018	0.035	0.003	0.058	0.012
op1_9	opx-I	rim; adjacent to ol-I	2419	0.684	0.022	0.035	0.003	0.055	0.008
op2-1	opx-I	core		0.766	0.024	0.041	0.003	0.066	0.014
op2-2	opx-I	rim; adjacent to cpx-I		0.797	0.024	0.037	0.003	0.067	0.013
op3-1	opx-I	rim; adjacent to ol-I		0.701	0.012	0.042	0.005	0.073	0.007
op4-1	opx-I	rim; adjacent to cpx-I		0.827	0.023	0.044	0.003	0.065	0.013
op5-1	opx-IIb	rim; adjacent to cpx-IIb		0.799	0.033	0.041	0.005	0.078	0.015
op6-1	opx-IIb	rim; adjacent to cpx-IIb		0.730	0.021	0.037	0.004	0.057	0.010
op7-1	opx-I	rim; adjacent to ol-I		0.773	0.033	0.032	0.001	0.062	0.010
cp2_1	cpx-I	rim; adjacent to opx-I	28	0.834	0.034	0.135	0.009	0.121	0.022
cp2_2	cpx-I	core	94	0.872	0.015	0.151	0.008	0.102	0.013
cp2_3	cpx-I	core	255	0.886	0.038	0.149	0.012	0.105	0.012
cp2_4	cpx-I	core	387	0.902	0.038	0.160	0.011	0.077	0.010
cp2_5	cpx-I	core	519	0.905	0.028	0.157	0.015	0.089	0.016
cp2_6	cpx-I	core	717	0.871	0.027	0.152	0.008	0.099	0.009
cp2_8	cpx-I	rim; adjacent to opx-I	972	0.779	0.026	0.130	0.009	0.100	0.016
cp1_1	cpx-I	rim; adjacent to opx-I		0.772	0.021	0.138	0.006	0.114	0.019
cp1_2	cpx-I	core		0.890	0.026	0.146	0.009	0.083	0.010
cp1_3	cpx-I	rim; adjacent to ol-I		0.675	0.023	0.133	0.007	0.106	0.014
cp3_1	cpx-I	rim; adjacent to spl-IIb		0.627	0.025	0.126	0.007	0.103	0.013
cp3_2	cpx-I	core		0.919	0.034	0.151	0.016	0.101	0.022
cp3_3	cpx-I	core		0.897	0.022	0.143	0.006	0.103	0.016
cp3_4	cpx-I	rim; adjacent to ol-I		0.825	0.038	0.133	0.011	0.095	0.010
cp4_1	cpx-IIb	rim; adjacent to opx-IIb		0.901	0.026	0.147	0.008	0.301	0.022
cp5_1	cpx-IIb	rim; adjacent to opx-IIb		0.643	0.027	0.110	0.004	0.100	0.017

Table A5-3: Li, Be and B concentrations (µg/g) in minerals of xenolith Ke 1958/20 (Group II)

Nr.	Mineral	description	Distance [µm] (for profiles)	Li	2σ	Be	2σ	B	2σ
ol3-1	ol-I	rim; adjacent opx-I	25	1.828	0.051	0.002	0.001	0.071	0.012
ol3-2	ol-I	core	111	1.811	0.021	0.003	0.001	0.078	0.009
ol3-3	ol-I	core	191	1.783	0.047	0.002	0.001	0.099	0.010
ol3-4	ol-I	core	271	1.843	0.039	0.002	0.001	0.089	0.020
ol3-5	ol-I	rim; adjacent opx-I	340	1.861	0.026	0.002	0.001	0.080	0.009
ol1-1	ol-I	rim; adjacent cpx-I		1.762	0.047	0.001	0.001	0.070	0.012
ol2-1	ol-I	rim; adjacent opx-I		1.783	0.059	0.002	0.001	0.084	0.010
ol4-1	ol-I	rim; adjacent to sympl.		1.831	0.039	0.002	0.001	0.075	0.013
ol5-1	ol-I	rim; adjacent opx-I		1.777	0.037	0.001	0.001	0.071	0.009
op2-1	opx-I	rim; adjacent ol-I	25	0.976	0.027	0.045	0.002	0.063	0.013
op2-2	opx-I	core	123	0.941	0.030	0.041	0.005	0.066	0.012
op2-3	opx-I	core	302	0.940	0.022	0.043	0.005	0.061	0.006
op2-4	opx-I	core	512	0.940	0.023	0.047	0.002	0.060	0.009
op2-5	opx-I	core	716	0.960	0.018	0.044	0.002	0.061	0.013
op2-6	opx-I	rim; adjacent ol-I	944	1.002	0.018	0.045	0.004	0.064	0.011
op1-1	opx-I	rim; adjacent cpx-I		0.962	0.023	0.048	0.004	0.057	0.011
op3-1	opx-I	rim; adjacent ol-I		1.000	0.040	0.044	0.006	0.074	0.007
op5-1	opx-IIb	rim; adjacent cpx-IIb		1.018	0.032	0.043	0.004	0.059	0.011
op6-1	opx-I	rim; adjacent ol-I		0.987	0.027	0.049	0.008	0.064	0.008
cp1-1	cpx-I	rim; adjacent ol-I	26	0.994	0.024	0.103	0.005	0.074	0.013
cp1-2	cpx-I	rim	140	1.049	0.038	0.095	0.008	0.084	0.014
cp1-3	cpx-I	core	320	1.050	0.039	0.095	0.007	0.072	0.009
cp1-4	cpx-I	core	560	1.042	0.025	0.101	0.005	0.086	0.011
cp1-5	cpx-I	core	920	1.080	0.030	0.097	0.009	0.081	0.011
cp1-6	cpx-I	core	1200	1.049	0.043	0.101	0.008	0.079	0.011
cp1-7	cpx-I	core	1473	1.002	0.040	0.098	0.009	0.084	0.013
cp1-8	cpx-I	rim	1780	1.021	0.030	0.095	0.008	0.083	0.013
cp1-9	cpx-I	rim; adjacent opx-I	1940	1.078	0.036	0.100	0.006	0.092	0.010
cp2-1	cpx-IIb	rim; adjacent opx-I		1.107	0.048	1.107	0.048	0.086	0.010
cp2-2	cpx-IIb	rim; adjacent opx-I		1.023	0.046	1.023	0.046	0.085	0.017

Table A5-4: Li, Be and B concentrations (µg/g) in minerals of xenolith Ke 1965/1 (Group III-a)

Nr.	Mineral	description	Distance [µm] (for profiles)	Li	2σ	Be	2σ	B	2σ
ol-8	ol-I	rim; adjacent opx-I	15	3.381	0.075	0.000	0.000	0.055	0.013
ol-9	ol-I	core	78	3.282	0.051	0.001	0.001	0.039	0.012
ol-10	ol-I	core	190	3.383	0.092	0.001	0.001	0.084	0.019
ol-13	ol-I	core	245	3.363	0.057	0.000	0.000	0.051	0.009
ol-11	ol-I	core	334	3.280	0.076	0.000	0.000	0.057	0.011
ol-12	ol-I	rim; adjacent cpx-IIa	524	3.398	0.086	0.002	0.002	0.067	0.016
ol-1	ol-IIa	rim; adjacent opx-I		1.848	0.054	0.000	0.000	0.059	0.012
ol-3	ol-I	rim; adjacent cpx-I		2.719	0.066	0.001	0.001	0.053	0.012
ol-4	ol-IIa	rim; adjacent cpx-I		2.585	0.029	0.022	0.005	0.099	0.016
ol-5	ol-I	core		2.491	0.050	0.000	0.000	0.053	0.015
ol-6	ol-I	core		2.465	0.060	0.001	0.001	0.058	0.009
ol-7	ol-I	rim; adjacent cpx-I		2.600	0.037	0.000	0.000	0.049	0.013
op-1	opx-I	rim; adjacent spl-I	15	1.012	0.039	0.023	0.003	0.049	0.011
op-2	opx-I	rim	50	1.004	0.034	0.022	0.002	0.046	0.012
op-3	opx-I	core	136	1.052	0.032	0.020	0.002	0.049	0.012
op-4	opx-I	core	187	1.081	0.021	0.023	0.003	0.050	0.007
op-5	opx-I	core	323	1.100	0.030	0.018	0.004	0.046	0.011
op-13	opx-I	core	426	1.063	0.040	0.018	0.003	0.056	0.013
op-6	opx-I	core	528	1.088	0.035	0.021	0.004	0.057	0.016
op_12	opx-I	core	630	1.089	0.024	0.020	0.003	0.042	0.009
op-7	opx-I	core	767	1.051	0.044	0.019	0.004	0.051	0.011
op-8	opx-I	core	937	1.082	0.019	0.019	0.003	0.056	0.009
op-9	opx-I	core	1022	1.079	0.032	0.018	0.004	0.048	0.010
op-10	opx-I	rim	1090	0.973	0.035	0.016	0.003	0.048	0.006
op-11	opx-I	rim; adjacent ol-IIa	1159	0.891	0.025	0.026	0.004	0.050	0.011
op-20	opx-I	rim; adjacent cpx-I	15	1.878	0.050	0.014	0.004	0.041	0.008
op-15	opx-I	core	111	2.127	0.043	0.020	0.005	0.053	0.019
op-16	opx-I	core	190	2.284	0.058	0.016	0.004	0.041	0.010
op-17	opx-I	core	368	2.365	0.065	0.017	0.005	0.062	0.019
op-18	opx-I	core	502	2.262	0.050	0.019	0.004	0.058	0.015
op-19	opx-I	rim; adjacent ol-I	635	2.066	0.062	0.016	0.003	0.048	0.015
cp-1	cpx-I	rim; adjacent ol-I	15	1.435	0.031	0.061	0.005	0.051	0.012
cp-2	cpx-I	rim	67	1.587	0.045	0.064	0.009	0.048	0.012
cp-3	cpx-I	core	139	1.768	0.028	0.064	0.004	0.067	0.008
cp-4	cpx-I	core	191	1.845	0.035	0.066	0.005	0.045	0.016
cp-6	cpx-I	core	310	1.988	0.047	0.060	0.005	0.053	0.015
cp-7	cpx-I	core	465	1.942	0.062	0.058	0.006	0.051	0.012
cp-8	cpx-I	core	590	1.979	0.038	0.062	0.005	0.050	0.012
cp-9	cpx-I	core	750	1.877	0.057	0.062	0.006	0.048	0.009
cp-10	cpx-I	core	916	1.884	0.039	0.054	0.005	0.046	0.012
cp-11	cpx-I	core	1081	1.863	0.051	0.064	0.005	0.053	0.013
cp-12	cpx-I	core	1154	1.652	0.051	0.070	0.008	0.048	0.013
cp-13	cpx-I	rim	1211	1.489	0.044	0.065	0.005	0.053	0.015
cp-14	cpx-I	rim; adjacent ol-IIa	1257	1.237	0.033	0.056	0.007	0.045	0.012
cp-15	cpx-I	rim; adjacent opx-I	15	1.635	0.063	0.056	0.006	0.058	0.019
cp-16	cpx-I	core	66	1.793	0.060	0.055	0.008	0.060	0.019
cp-17	cpx-I	core	178	2.065	0.074	0.066	0.009	0.065	0.017
cp-18	cpx-I	core	379	2.106	0.059	0.063	0.009	0.063	0.017
cp-19	cpx-I	core	614	1.796	0.075	0.060	0.009	0.054	0.011
cp-21	cpx-I	rim; adjacent spl-I	759	1.571	0.049	0.078	0.011	0.057	0.013

Table A5-5: Li, Be and B concentrations (µg/g) in minerals of xenolith Ke 1965/15 (Group III-b)

Nr.	Mineral	description	Distance [µm] (for profiles)	Li	2σ	Be	2σ	B	2σ
ol5-1	ol-IIa	rim; adjacent to glass	15	4.784	0.092	0.004	0.001	0.087	0.021
ol5-2	ol-IIa	core	54	4.563	0.118	0.006	0.003	0.200	0.032
ol5-3	ol-IIa	rim; adjacent to apatite	108	4.823	0.098	0.002	0.002	0.211	0.036
ol7-1	ol-I	rim; adjacent to glass	15	5.010	0.133	0.002	0.001	0.279	0.049
ol7-2	ol-I	core	39	5.014	0.085	0.002	0.002	0.354	0.044
ol7-3	ol-I	core	88	4.823	0.161	0.001	0.002	0.146	0.020
ol7-4	ol-I	core	185	4.603	0.110	0.002	0.002	0.082	0.030
ol7-5	ol-I	core	244	4.716	0.088	0.002	0.002	0.123	0.015
ol1-1	ol-I	rim; adjacent to opx-I		4.100	0.097	0.004	0.002	0.098	0.020
ol1-2	ol-I	core		4.444	0.076	0.003	0.002	0.119	0.023
ol2-1	ol-I	rim; adjacent to cpx-I		4.751	0.131	0.002	0.002	0.090	0.019
ol4-1	Ol_m	microlite in melt pocket		4.675	0.067	0.007	0.002	0.095	0.026
ol6-1	ol-I	rim; adjacent to glass		5.254	0.086	0.009	0.003	0.220	0.043
ol8-1	Ol_m	microlite in melt pocket		10.802	0.104	0.021	0.005	0.088	0.022
ol8-1	Ol_m	microlite in melt pocket		5.653	0.120	0.120	0.020	0.176	0.038
ol9-1	ol-I	core		4.439	0.068	0.002	0.002	0.050	0.023
op1-7	opx-I	rim; adjacent to ol-IIa	15	3.298	0.073	0.080	0.010	0.239	0.018
op1-2	opx-I	rim	71	3.717	0.080	0.052	0.006	0.059	0.018
op1-8	opx-I	core	128	3.811	0.070	0.029	0.005	0.045	0.013
op1-12	opx-I	core	200	3.703	0.092	0.022	0.006	0.047	0.014
op1-3	opx-I	core	343	3.527	0.110	0.016	0.005	0.060	0.019
op1-13	opx-I	core	414	3.646	0.073	0.018	0.005	0.062	0.017
op1-9	opx-I	core	500	3.569	0.065	0.017	0.005	0.058	0.018
op1-14	opx-I	core	586	3.804	0.098	0.032	0.005	0.056	0.016
op1-4	opx-I	core	700	3.656	0.087	0.041	0.007	0.056	0.016
op1-15	opx-I	core	814	4.052	0.048	0.068	0.009	0.051	0.012
op1-10	opx-I	core	871	3.919	0.083	0.072	0.011	0.074	0.019
op1-11	opx-I	core	914	3.847	0.112	0.082	0.009	0.091	0.018
op1-5	opx-I	rim	943	3.680	0.109	0.083	0.010	0.129	0.026
op1-6	opx-I	rim; adjacent to ol-IIa	985	3.333	0.105	0.137	0.009	0.275	0.022
op2-1	Opx_m	rim; adjacent to glass	1	2.038	0.053	0.085	0.009	0.283	0.022
op2-2	Opx_m	core	60	1.697	0.056	0.053	0.005	0.409	0.032
op2-3	Opx_m	core	105	1.539	0.030	0.050	0.005	0.374	0.040
op2-4	Opx_m	core	150	1.898	0.036	0.039	0.005	0.417	0.039
op2-5	Opx_m	rim; adjacent to graphite	236	1.544	0.046	0.077	0.007	0.309	0.034
op2-6	opx-I	rim; adjacent to graphite	325	2.577	0.052	0.112	0.013	0.143	0.020
op2-7	opx-I	core	386	3.897	0.080	0.118	0.011	0.072	0.016
op2-9	opx-I	core	447	3.372	0.087	0.088	0.013	0.308	0.038
op2-8	opx-I	core	473	2.325	0.088	0.055	0.007	0.368	0.045
op2-10	opx-I	core	518	3.893	0.081	0.115	0.005	0.091	0.018
op2-11	opx-I	rim; adjacent to Mg-calcite	570	3.639	0.086	0.138	0.014	0.067	0.018

Table A5-5: continued

Nr.	Mineral	decription	Distance [µm] (for profiles)	Li	2σ	Be	2σ	B	2σ
cp1-1	cpx-I	rim; adjacent to glass	15	1.875	0.068	0.401	0.028	0.407	0.046
cp1-2	cpx-I	rim	50	1.568	0.045	0.320	0.014	0.317	0.047
cp1-3	cpx-I	core	145	1.975	0.096	0.378	0.017	0.437	0.036
cp1-4	cpx-I	core	254	1.948	0.048	0.387	0.021	0.514	0.055
cp1-5	cpx-I	rim; adjacent to ol-I	491	1.601	0.059	0.330	0.022	0.524	0.043
cp2-1	Cpx_m	microlite in melt pocket		2.614	0.080	0.243	0.019	0.219	0.024
cp3-1	Cpx_m	microlite in melt pocket		1.172	0.055	0.316	0.025	0.174	0.033
cp4-1	Cpx_m	microlite in melt pocket		1.552	0.053	0.174	0.011	0.448	0.058
cp5-1	cpx-I	relic; enclosed by melt pocket		0.961	0.053	0.207	0.018	0.473	0.051
cp5-2	cpx-I	relic; enclosed by melt pocket		0.954	0.051	0.146	0.020	0.522	0.049
cp5-3	cpx-I	relic; enclosed by melt pocket		1.587	0.052	0.139	0.016	0.189	0.055
cp5-4	cpx-I	relic; enclosed by melt pocket		0.850	0.037	0.138	0.012	0.531	0.054
cp6-1	Cpx_m	microlite in melt pocket		4.179	0.105	0.809	0.083	0.649	0.099
cp7-1	cpx-I	resorbed rim; adjacent to glass		1.116	0.063	0.477	0.024	0.320	0.036
cp7-2	cpx-I	core		2.599	0.063	0.504	0.021	0.622	0.069
am1-1	katoph.	relic in melt pocket		2.962	0.079	1.293	0.029	1.880	0.124
am1-2	katoph.	relic in melt pocket		3.296	0.122	1.361	0.045	1.527	0.107
gl-1	glass	in melt pocket around spl-I		22.024	0.182	3.852	0.052	4.244	0.205
gl-2	glass	in melt pocket around cpx-I		16.831	0.226	3.753	0.106	4.267	0.153
gl-3	glass	in melt pocket around cpx-I		18.148	0.658	3.752	0.083	4.572	0.136
gl-4	glass	in melt pocket around cpx-I		16.593	0.183	3.591	0.060	4.007	0.089
gl-5	glass	selvage rimming Opxm		14.474	0.166	3.101	0.044	4.134	0.112

Table A5-6: Li, Be and B concentrations (µg/g) in minerals of xenolith Ke 785* (Group III-c)

Nr.	Min.	description	Distance [µm] (for profiles)	Li	2σ	Be	2σ	B	2σ
ol1-3	ol-I	rim; adjacent to glass	24	6.077	0.114	0.004	0.003	0.798	0.094
ol1-4	ol-I	rim	71	5.433	0.092	0.003	0.002	0.160	0.038
ol1-5	ol-I	rim	152	5.201	0.145	0.003	0.002	0.293	0.039
ol1-6	ol-I	core	219	5.042	0.087	0.003	0.002	0.140	0.026
ol1-7	ol-I	core	324	4.942	0.154	0.004	0.003	0.078	0.026
ol1-8	ol-I	core	447	4.854	0.111	0.001	0.001	0.065	0.022
ol1-2	ol-I	core	638	4.700	0.078	0.004	0.001	0.109	0.013
ol1-9	ol-I	core	700	5.021	0.085	0.002	0.002	0.124	0.029
ol1-11	ol-I	rim; adjacent to glass	780	5.095	0.157	0.004	0.003	0.180	0.035
ol5-1	ol-I	rim; adjacent to glass next Opx_m	16	8.130	0.197	0.005	0.005	0.098	0.016
ol5-2	ol-I	rim	50	7.334	0.180	0.005	0.002	0.096	0.007
ol5-3	ol-I	core	91	6.970	0.107	0.002	0.002	1.001	0.088
ol5-4	ol-I	core	150	5.705	0.116	0.005	0.002	0.626	0.058
ol5-5	ol-I	core	255	6.145	0.155	0.005	0.005	0.780	0.066
ol1-1	ol-I	rim; adjacent to glass		5.441	0.075	0.002	0.002	0.281	0.048
ol2-1	Ol_m	microlite in melt pocket		5.998	0.121	0.428	0.024	0.746	0.045
ol3-1	ol-I	rim; adjacent to Opx_m		5.514	0.117	0.002	0.001	0.208	0.039
ol4-1	ol-I	rim; adjacent to phlogopite		5.916	0.131	0.003	0.002	0.385	0.037
op2-1	Opx_m	rim; adjacent to ol-I	27	2.909	0.094	0.149	0.009	0.354	0.027
op2-2	Opx_m	core	121	2.399	0.080	0.204	0.017	0.532	0.052
op2-3	Opx_m	rim; adjacent to ol-I	216	2.696	0.075	0.258	0.025	0.216	0.032
op1-1	Opx_m	rim; adjacent to glass		2.241	0.046	0.161	0.006	0.709	0.052
op3-1	Opx_m	rim; adjacent to glass		3.091	0.094	0.167	0.014	0.730	0.056
cp1-1	Cpx_m	microlite in melt pocket		2.284	0.055	0.214	0.015	0.176	0.024
cp1-2	Cpx_m	microlite in melt pocket		3.148	0.060	0.314	0.014	0.218	0.023
cp2-1	Cpx_m	microlite in melt pocket		1.761	0.078	0.235	0.020	0.106	0.021
cp3-1	Cpx_m	microlite in melt pocket		1.852	0.097	0.272	0.026	0.129	0.024
cp4-1	Cpx_m	microlite in melt pocket		2.531	0.071	0.381	0.022	0.117	0.019
cp5-1	Cpx_m	microlite in melt pocket		2.386	0.121	0.234	0.027	0.135	0.028
am3-1	katoph.	relic in melt pocket; rim	44	3.656	0.066	3.822	0.057	5.604	0.129
am3-3	katoph.	relic in melt pocket; core	89	2.897	0.094	3.854	0.097	5.390	0.118
am3-2	katoph.	relic in melt pocket; core	151	2.475	0.048	3.836	0.048	5.560	0.145
am3-4	katoph.	relic in melt pocket; rim	195	3.169	0.067	4.087	0.105	5.476	0.138
am1-2	katoph.	relic in melt pocket; rim	40	4.781	0.099	4.199	0.070	5.999	0.095
am1-1	katoph.	relic in melt pocket; core	120	3.838	0.065	4.163	0.033	5.963	0.157
am1-4	katoph.	relic in melt pocket; core	151	4.064	0.061	4.196	0.061	6.017	0.145
am1-3	katoph.	relic in melt pocket; rim	200	4.376	0.131	4.339	0.068	5.740	0.240
am4-1	katoph.	relic in melt pocket; rim		5.173	0.079	4.722	0.145	5.954	0.219
phl4-1	phl	relic in melt pocket; rim to glass		3.636	0.048	1.359	0.045	1.456	0.083
phl5-1	phl	incl. in ol-I; core		0.639	0.022	1.170	0.030	1.311	0.092
phl3-1	phl	incl. in Opx_m		1.027	0.033	1.279	0.048	1.166	0.071
ph4-2	phl	relic in melt pocket; rim to ol-I		3.590	0.114	1.402	0.051	1.444	0.133
ph6-1	phl	relic in melt pocket; core		5.136	0.072	1.510	0.036	1.592	0.066
ph7-1	phl	relic in melt pocket; core		3.126	0.044	1.305	0.044	1.474	0.081
gl-1	glass	in melt pocket		12.695	0.103	6.234	0.058	9.757	0.146
gl-5	glass	in melt pocket		16.777	0.158	7.542	0.079	11.041	0.228
gl-3	glass	in melt pocket		9.716	0.167	5.461	0.055	8.088	0.177
gl-4	glass	in melt pocket		13.050	0.193	7.875	0.104	11.937	0.187

Table A5-7: Li, Be and B concentrations (µg/g) in minerals of xenolith Ke 1965/3 (Group II-c)

Nr.	Mineral	description	Distance [µm] (for profiles)	Li	2σ	Be	2σ	B	2σ
ol-1	Ol_m	microlite in in melt pocket; rim	21	7.239	0.114	0.020	0.003	0.119	0.014
ol-2	Ol_m	microlite in in melt pocket; core	47	9.358	0.103	0.013	0.003	0.153	0.017
ol-3	Ol_m	microlite in in melt pocket; core	84	6.791	0.111	0.011	0.002	0.119	0.018
ol-4	Ol_m	microlite in in melt pocket; rim	136	9.546	0.126	0.022	0.004	0.112	0.017
ol-5	ol-I	rim; adjacent to glass	15	8.600	0.098	0.069	0.007	0.125	0.013
ol-6	ol-I	core	63	5.679	0.076	0.008	0.002	0.622	0.040
ol-8	ol-I	core	194	6.544	0.096	0.007	0.002	0.493	0.042
ol-9	ol-I	core	258	6.524	0.106	0.007	0.001	0.487	0.030
ol-10	ol-I	rim; adjacent to ol-I	316	6.952	0.068	0.007	0.002	0.531	0.043
ol-21	ol-I	rim; adjacent to melt pocket	30	6.846	0.062	0.008	0.002	0.660	0.049
ol-20	ol-I	rim	83	6.905	0.084	0.016	0.003	0.662	0.044
ol-19	ol-I	rim	129	6.945	0.082	0.007	0.002	0.668	0.019
ol-23	ol-I	core	185	5.805	0.094	0.008	0.002	0.508	0.039
ol-18	ol-I	core	242	5.639	0.087	0.008	0.002	0.502	0.035
ol-17	ol-I	core	557	5.060	0.070	0.005	0.002	0.374	0.025
ol-22	ol-I	core; close to crack	910	5.807	0.091	0.007	0.002	0.613	0.029
ol-24	ol-I	core	1373	5.651	0.052	0.007	0.002	0.388	0.037
ol-16	ol-I	core	1911	4.934	0.041	0.005	0.002	0.277	0.025
ol-15	ol-I	core	2504	5.159	0.069	0.007	0.003	0.237	0.024
ol-14	ol-I	core	3136	5.231	0.082	0.005	0.002	0.323	0.021
ol-13	ol-I	rim	3302	5.752	0.109	0.006	0.002	0.440	0.020
ol-12	ol-I	rim; adjacent to Opxm	3376	5.787	0.074	0.009	0.003	0.432	0.032
ol-11	ol-I	rim; adjacent to Opxm		6.684	0.083	0.027	0.005	0.753	0.028
ol-25	Ol_m	microlite in melt pocket		8.158	0.078	0.152	0.011	0.297	0.032
op-1	Opx_m	rim; adjacent to glass	23	2.724	0.041	0.298	0.011	0.501	0.026
op-2	Opx_m	core	77	2.703	0.034	0.326	0.012	0.442	0.029
op-3	Opx_m	core	123	2.679	0.055	0.290	0.018	0.429	0.034
op-4	Opx_m	core	223	2.396	0.043	0.313	0.014	0.589	0.051
op-5	Opx_m	core	361	2.133	0.047	0.295	0.007	0.550	0.042
op-6	Opx_m	rim; adjacent to ol-I	554	2.737	0.049	0.301	0.013	0.597	0.036
op-7	Opx_m	rim; adjacent to ol-I		2.982	0.066	0.293	0.008	0.604	0.042
cp-1	Cpx_m	microlite in melt pocket		5.712	0.086	0.917	0.026	0.231	0.019
cp-2	Cpx_m	microlite in melt pocket		5.537	0.097	0.822	0.017	0.126	0.018
cp-4	Cpx_m	microlite in melt pocket		4.536	0.054	0.659	0.014	0.114	0.013
cp-5	Cpx_m	microlite in melt pocket		3.651	0.058	0.464	0.013	0.128	0.013
cp-6	Cpx_m	microlite in melt pocket		3.581	0.054	0.636	0.010	0.123	0.018
ph-1	phl	inclusion in Opxm		0.626	0.011	3.798	0.040	0.884	0.037
gl-1	glass	in melt pocket		18.406	0.173	30.728	0.184	10.084	0.210
gl-2	glass	in melt pocket		19.010	0.175	31.682	0.241	10.238	0.197
gl-3	glass	in melt pocket		19.740	0.225	32.979	0.165	10.657	0.234
gl-4	glass	in melt pocket		16.249	0.182	32.626	0.150	10.748	0.153
gl-5	glass	in melt pocket		19.750	0.241	33.486	0.174	10.848	0.091
gl-6	glass	in melt pocket		18.479	0.776	34.457	0.358	10.961	0.136
gl-7	glass	lining Opxm		12.241	0.399	32.551	0.150	10.363	0.170
gl-8	glass	in melt pocket		18.777	0.184	32.030	0.211	10.344	0.176
gl-9	glass	in melt pocket		20.234	0.219	34.922	0.244	10.810	0.208